NASA Conference Publication 3214

Eighth International Workshop on Laser Ranging Instrumentation

8th International Workshop

Annapolis, Maryland
May 18-22,1992

Proceedings of a Workshop held
at Annapolis, Maryland
May 18-22, 1992

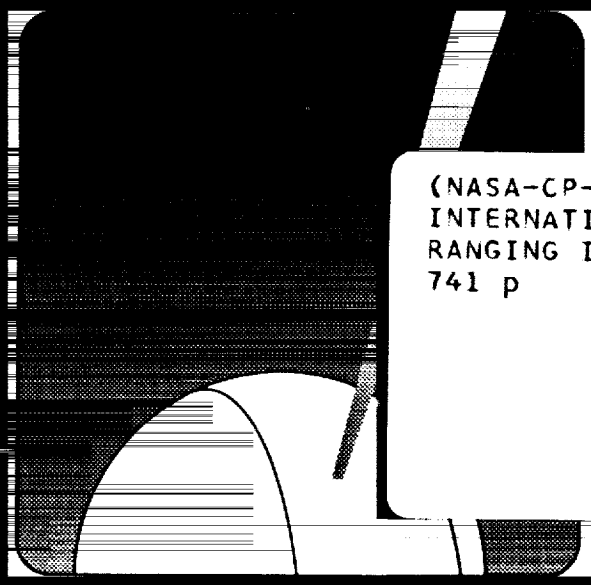

NASA Conference Publication 3214

Eighth International Workshop on Laser Ranging Instrumentation

Compiled and Edited by
John J. Degnan
Goddard Space Flight Center
Greenbelt, Maryland

National Aeronautics
and Space Administration

Goddard Space Flight Center
Greenbelt, Maryland 20771

1993

Proceedings of the Eighth International Workshop on Laser Ranging Instrumentation Annapolis, Maryland, USA May 18-22, 1992

TABLE OF CONTENTS

Page No.

Foreward vii

List of Participants viii

Workshop Agenda xv

Scientific Applications and Measurements Requirements

Laser Tracking for Vertical Control, P. Dunn et al., Hughes STX 1-1

Laser Ranging Network Performance and Routine Orbit Determination at D-PAF, F.-H. Massman et al., DGFI 1-19

Laser Ranging Application to Time Transfer Using Geodetic Satellite and to Other Japanese Space Programs, H. Kunimori et al., CRL 1-34

Applications of SLR, B. E. Schutz, Center for Space Research, University of Texas 1-43

Timely Issues

Satellite Signatures in SLR Observations, G.M. Appleby, Royal Greenwich Obs. 2-1

Work at Graz on Satellite Signatures, G. Kirchner, SLR Graz 2-15

The Precision of Today's Satellite Laser Ranging Systems, P.J. Dunn et al., Hughes STX 2-23

SLR Data Screening; Location of Peak of Data Distribution, A.T. Sinclair, Royal Greenwich Observatory 2-34

Adaptive Median Filtering for Preprocessing of Time Series Measurements, M. Paunonen, Finnish Geodetic Institute 2-44

SATCOP Mission Planning Software Package, S. Bucey, BFEC 2-51

Laser Technology

Nd:YLF Laser for Airborne/Spaceborne Laser Ranging, J.L. Dallas et al., NASA/GSFC 3-1

Alternative Wavelengths for Laser Ranging, K. Hamal, Czech Technical Univ. 3-7

New Methods of Generation of Ultrashort Laser Pulses for Ranging, H. Jelinkova et al., Czech Technical University 3-9

Simultaneously Compression of the Passively Mode-Locked Pulsewidth and Pulse Train, Yang Xiangchun et al., Shanghai Institute of Optics and Fine Mechanics . . 3-15

An Improved Light Source for Laser Ranging, K. Hamal et al, Czech Technical University 3-19

Epoch and Event Timing
Preliminary Results from the Portable Standard Satellite Laser Ranging Intercomparison with MOBLAS-7, M. Seldon et al., BFEC 4-1

Detector Technology
Performance Optimization of Detector Electronics for Millimeter Laser Ranging, S. Cova et al., Politecnico di Milano 5-1
Tracking Capabilities of SPADs for Laser Ranging, F. Zappa et al., Politecnico di Milano 5-19
How to Squeeze High Quantum Efficiency and High Time Resolution out of a SPAD, A. Lacaita et al., Politecnico di Milano 5-25
The Solid State Detector Technology for Picosecond Laser Ranging, I. Prochazka, Czech Technical University 5-31
Streak Camera Based SLR Receiver for Two Color Atmospheric Measurements, T. Varghese et al., BFEC 5-36
The First Satellite Laser Echoes Recorded on the Streak Camera, K. Hamal et al., Czech Technical University 5-47

Calibration Techniques/Targets
Experience and Results of the 1991 MTLRS#1 USSR Campaign, P. Sperber et al., IfAG 6-1
ETALON-1, -2 Center of Mass Correction and Array Reflectivity, N.T. Mironov et al., Main Astron. Obs. of the Academy of Sciences 6-9
Test Results from LAGEOS-2 Optical Characterization Using Pulsed Lasers, T. Varghese et al., BFEC 6-33
Analysis of TOPEX Laser Retroreflector Array Characteristics, T. Varghese, BFEC . 6-47
Historical MOBLAS System Characterization, V. Husson, BFEC 6-59

Multiwavelength Ranging/Streak Cameras
Optimum Wavelengths for Two Color Ranging, J. Degnan, NASA/GSFC 7-1
Two Color Satellite Laser Ranging Upgrades at Goddard's 1.2m Telescope Facility, T. Zagwodzki et al., NASA/GSFC 7-15
Measuring Atmospheric Dispersion with WLRS in Multiple Wavelength Mode, U. Schreiber et al., Fundamentalstation Wettzell 7-28
Millimeter Accuracy Satellites for Two Color Ranging, J. Degnan, NASA/GSFC . . . 7-36
Two Wavelength Satellite Laser Ranging Using SPAD, I. Prochazka et al., Czech Technical University 7-52
New Perspectives for High Accuracy SLR with Second Generation Geodesic Satellites, G. Lund, AEROSPATIALE 7-56

SLR Data Analysis/Model Errors
State-of-the-Art Satellite Laser Range Modeling for Geodetic and Oceanographic Applications, S.M. Klosko et al., Hughes STX 8-1
Geometric Analysis of Satellite Laser Ranging Data, B. Conklin et al., BFEC 8-15
Improvement of SLR Accuracy, A Possible New Step, M. Kasser, ESGT 8-23

Operational Software Developments
On the Accuracy of ERS-1 Orbit Predictions, R. Koenig et al., DGFI 9-1
Compensation for the Distortion in Satellite Laser Range Predictions Due to Varying Pulse Travel Times, M. Paunonen, Finnish Geodetic Institute 9-9
Timebias Corrections to Predictions, R. Wood et al., Satellite Laser Ranger Group, Herstmonceux Castle 9-13
Formation of On-Site Normal Points, G.M. Appleby et al., Royal Greenwich Obs. . . 9-19
Poisson Filtering of Laser Ranging Data, R.L. Ricklefs et al., McDonald Obs. 9-26
Computer Networking at SLR Stations, A. Novotny, Czech Technical Univ. 9-33
Upgrading NASA/*DOSE Laser Ranging System Control Computers*, R.L. Ricklefs et al., McDonald Observatory 9-43
HP Upgrade Operational Streamlining, D. Edge et al., BFEC 9-49
Application of the Robust Estimate in SLR Data Preprocessing, T. Detong et al., Shanghai Observatory 9-57

Lunar Laser Ranging
A Computer-Controlled x-y Offset Guiding Stage for the MLRS, P.J. Shelus et al., McDonald Observatory 10-1
Lunar Laser Ranging Data Processing in a Unix/X Windows Environment, R.L. Ricklefs et al., McDonald Observatory 10-6
LLR-Activities in Wettzell, U. Schreiber et al., Fundamentalstation Wettzell 10-14

Fixed Station Upgrades/Developments
Matera Laser Ranging Observatory (MLRO); An Overview, T. Varghese et al., BFEC 11-1
Performance of the Upgraded Orroral Laser Ranging System, J. Mck. Luck, Orroral Geodetic Observatory 11-6
SUB-CM Ranging and Other Improvements in Graz, G. Kirchner et al., SLR Graz . . 11-31
Upgrading of the Borowiec Laser Station, S. Schillak et al., Space Research Center of Polish Academy of Sciences 11-37
Development of Shanghai Satellite Laser Ranging Station, F.M. Yang et al., Shanghai Observatory 11-44
Status-Report on WLRS, R. Dassing et al., IfAG 11-51
Ground Based Laser Ranging for Satellite Location, G.C. Gilbreath et al., Naval Research Laboratory 11-54
New Progress of Ranging Technology at Wuhan Satellite Laser Ranging Station, Xia Zhizhong et al., Institute of Seismology 11-60

Mobile System Upgrades/Developments
TLRS-3 System Upgrades, R. Eichinger et al., BFEC 12-1
Results of the MTLRS-1 Upgrade, P. Sperber et al., IfAG 12-17
The new MTLRS#1 Receiving System, P. Sperber et al., IfAG 12-26
The new MTLRS Transmitting System, P. Sperber et al., IfAG 12-33
Transputer Based Control System for MTLRS, E. Vermaat et al., Kootwijk Observatory for Satellite Geodesy 12-40

Airborne and Spaceborne Systems

Airborne 2 Color Ranging Experiment, P.S. Millar et al., NASA/GSFC 13-1
GLRS 2-Colour Retroreflector Target Design and Predicted Performance, G. Lund, AEROSPATIALE 13-17
Effects of Turbulence on the Geodynamic Laser Ranging System, J.H. Churnside, NOAA Wave Propagation Laboratory 13-33
Development of the Mars Observer Laser Altimeter (MOLA), B.L. Johnson Jr. et al., NASA/GSFC 13-49
Bench Checkout Equipment for Spaceborne Laser Altimeter Systems, J.C. Smith et al., NASA/GSFC 13-52
Mars Laser Altimeter Based on a Single Photon Ranging Technique, I. Prochazka et al., Czech Technical University 13-74
Multi-Beam Laser Altimeter, J.L. Bufton, NASA/GSFC 13-78

Poster Presentations

Satellite Laser Station Helwan Status 1992, M. Cech et al., Czech Technical University 14-1
Optical Attenuation Mechanism Upgrades, MOBLAS and TLRS Systems, R. Eichinger et al., BFEC 14-2
The Third Generation SLR Station Potsdam No. 7836, H. Fischer et al., GeoForschungsZentrum Potsdam 14-14
Performance Comparison of High Speed Microchannel Plate Photomultiplier Tubes, T. Varghese et al., BFEC 14-20
Station Report on the Goddard Space Flight Center (GSFC) 1.2 Meter Telescope Facility, J.F. McGarry et al., NASA/GSFC 14-29

Session Summaries 15-1
Scientific Applications and Measurements Requirements 15-2
Timely Issues 15-5
Laser Technology 15-6
Epoch and Event Timing 15-7
Detector Technology 15-8
Calibration Techniques/Targets 15-9
Multiwavelength Ranging/Streak Cameras 15-10
SLR Data Analysis/Model Errors 15-11
Operational Software Developments 15-12
Lunar Laser Ranging 15-13
Fixed Station Upgrades/Developments 15-14
Mobile System Upgrades/Developments 15-15

Conference Summary/Resolutions 16-1

Business Meeting/Next Workshop 17-1

FOREWORD

At long last, the Proceedings of the Eighth International Workshop are "ready" for publication. As Chairman, I tried very hard to obtain 100 percent of the presentations in printed form so that they could be distributed in these proceedings. In spite of the fact that the original submission deadline of 1 August 1992 was extended twice into early 1993 and numerous personal contacts were made, there are still several fine papers missing. Nevertheless, this volume contains the vast majority of the presentations, and I felt I could not delay publication any longer. Besides, I desperately wanted to avoid the embarrassment of distributing these proceedings at the 1994 workshop in Australia. Thank you to all who contributed.

One does not take on the job of chairing a major international meeting without a lot of help, and I wish to take this opportunity to thank a number of people who made the Annapolis meeting a success.

A special thank you goes to Miriam Baltuck and Joe Engeln at NASA Headquarters who provided funding support for the meeting. Not only did this contribute substantially to the overall success of the workshop, but it permitted greater participation from many of our foreign colleagues.

I alsc wish to express my thanks to Karel Hamal of the Technical University of Prague, who kindly offered his laboratory as a meeting site for the Program Committee in January 1992, and to Ivan Prochazka for serving as unofficial recording secretary during our deliberations. Thanks also to Program Committee members Christian Veillet and Ben Greene for taking time from their busy schedules and coming to Prague to help plan the workshop.

I am grateful also for the support of the session chairmen who were responsible for soliciting papers and for organizing and summarizing the material presented in their sessions. These include Bob Schutz, Andrew Sinclair, Helena Jelinkova, Ben Greene, Tom Varghese, Jean Gaignebet, Karel Hamal, Ron Kolenkiewicz, Georg Kirchner, Christian Veillet, Erik Vermaat, Jim Abshire, Mike Pearlman, Carroll Alley, and Richard Eanes (for standing in on occasion).

Thanks also to Sarah Wager and Deborah Williams of Westover Consultants for their assistance in selecting the site for the meeting, helping with hotel and travel arrangements for the meeting, and general coordinating activities.

Last, but certainly not least, I want to thank my secretary, Mrs. Diana Elben, for her wonderful support during the entire effort - from mailing the initial circulars, through supporting the meeting itself (in countless ways), through the preparation of the proceedings for publication through their final distribution. I couldn't have done it without her.

John J. Degnan
Chairman
Eighth International Workshop on Laser Ranging Instrumentation

8TH INTERNATIONAL WORKSHOP ON LASER RANGING INSTRUMENTATION
MAY 18 - 22, 1992

LIST OF PARTICIPANTS

James Abshire
NASA/Goddard Space Flight Cntr.
Code 924
Greenbelt, MD 20771
USA
Phone: 301-286-2611

Robert Afzal
NASA/Goddard Space Flight Cntr.
Code 924
Greenbelt, MD 20771
USA

Fahad Al-Hussain
428-2 Ridge Road
Greenbelt, MD 20770
USA
Phone: 301-474-4787

Carroll Alley
Department of Physics
University of Maryland
College Park, MD 20742
USA
Phone: 301-405-6098
Fax: 301-699-9195

G.M. Appleby
Royal Greenwich Observatory
Madingley Road
Cambridge, CB30EZ
ENGLAND
Phone: 44-223-37437
Fax: 44-223-374700

Miriam Baltuck
NASA Headquarters
Code SEP-05
Washington, D.C. 20541

Aldo Banni
Via Ospedale 72
Cagliari, 09124
ITALY
Phone: 39-70-72-5246

Wiard Beek
Kootwijk Observatory
P.O. Box 581
Apeldoorn, 7300 AN
NETHERLANDS
Phone: 31-5769-8212
Fax: 31-5769-1344

Tammy Bertram
NASA/Goddard Space Flight Cntr.
Code 726.1
Greenbelt, MD 20771
USA
Phone: 301-286-8119
Fax: 301-286-2429

Giuseppe Bianco
Centro di Geodesia Spaziale
P.O. Box 11
Matera, 75100
ITALY
Phone: 39-835-377209
Fax: 39-835-339005

John Bosworth
NASA/Goddard Space Flight Cntr.
Code 901
Greenbelt, MD 20771
USA
Phone: 301-286-7052
Fax: 301-286-4943

Steven Bucey
BFEC
10210 Greenbelt Rd/Suite 700
Seabrook, MD 20706
USA
Phone: 301-794-3466
Fax: 301-794-3524

Jack L. Bufton
NASA/Goddard Space Flight Cntr.
Code 920
Greenbelt, MD 20771
USA
Phone: 301-286-8591
Fax: 301-286-9200

Alberto Cenci
via Tiburtina,
Rome, 965
ITALY
Phone: 39-640693861
Fax: 39-640693638

Jean Eugene Chabaudie
Ave. Copernic
Grasse, F06130
FRANCE
Phone: 33-93-365869
Fax: 33-93-368963

Jack Cheek
4400 Forbes Boulevard
Lanham, MD 20782
USA
Phone: 301-286-4076
Fax: 301-286-1620

Jim Churnside
NOAA - Wave Propagation
R/E/WP1, 325 Broadway
Boulder, CO 80303
USA
Phone: 303-497-6744
Fax: 303-497-6978

Brion Conklin
BFEC
10210 Greenbelt Rd/Suite 700
Seabrook, MD 20706
USA
Phone: 301-794-3510
Fax: 301-794-3524

Sergio Cova
p.z.a. Leonardo da Vinci 32
Politecnico di Milano
Milano, 20133
ITALY
Phone: 39-2-23996103
Fax: 39-2-2367604

William Crawford
BFEC
10210 Greenbelt Rd/Suite 700
Seabrook, MD 20706
USA
Phone: 301-794-3495
Fax: 301-794-3524

Don Cresswell
BFEC
10210 Greenbelt Rd/Suite 700
Seabrook, MD 20706
USA
Phone: 301-794-3493
Fax: 301-794-3524

Henry A. Crooks
BFEC
10210 Greenbelt Rd/Suite 700
Seabrook, MD 20706
USA
Phone: 301-794-3500
Fax: 301-794-3524

E. Cuot
Avenue Nicolas Copernic
Grasse 06130,
FRANCE
Phone: 33-93-126270
Fax: 33-93-092615

Joseph Dallas
NASA/Goddard Space Flight Cntr.
Code 726.1
Greenbelt, MD 20771
USA
Phone: 301-286-6041

Reiner Dassing
Fundamental Station Wettzell
Koetzting, 8493
GERMANY
Phone: 49-9941-603112
Fax: 49-9941-603222

Winfield M. Decker
BFEC
10210 Greenbelt Rd/Suite 700
Seabrook, MD 20706
USA
Phone: 301-794-3474
Fax: 301-794-3524

John J. Degnan
NASA/Goddard Space Flight Cntr.
Code 901
Greenbelt, MD 20771
USA
Phone: 301-286-8470
Fax: 301-286-4943

Domenico Del Rosso
Centro Spaziale Di Matera
ITALY
Phone: 39-835-334951
Fax: 39-835-3771

Howard Donovan
BFEC
10210 Greenbelt Rd/Suite 700
Seabrook, MD 20706
USA
Phone: 301-794-3491
Fax: 301-794-3524

Peter Dunn
Hughes STX
4400 Forbes Blvd.
Lanham, MD 20905
Phone: 301-796-5036
Fax: 301-306-1010

Richard Eanes
Cntr. for Space Research
University of Texas - Austin
Austin, TX 78712-1085
USA
Phone: 512-471-5573
Fax: 512-471-3570

David R. Edge
BFEC
10210 Greenbelt Rd/Suite 700
Seabrook, MD 20706
USA
Phone: 301-794-3474
Fax: 301-794-3524

Richard Eichinger
BFEC
10210 Greenbelt Rd/Suite 700
Seabrook, MD 20706
USA
Phone: 301-794-3508
Fax: 301-794-3524

Kenneth S. Emenheiser
BFEC
10210 Greenbelt Rd/Suite 700
Seabrook, MD 20706
USA
Phone: 301-794-3495
Fax: 301-794-3524

Joe Engeln
NASA Headquarters
Code SEP-05
Washington, D.C. 20541
Phone: 202-453-1725
Fax: 202-755-2552

Dominique Feraudy
CERGA
Ave. Copernic
Grasse, F06130
FRANCE
Phone: 33-93-365849
Fax: 33-93-092613

Thomas Fischetti
2609 Village Lane
Silver Spring, MD 20906
USA
Phone: 301-871-2425
Fax: 301-871-0269

J.C. Gaignebet
GRGS/CERGA/OCA
Av Copernic
Grasse, F06130
FRANCE
Phone: 33-93-365899
Fax: 33-93-368963

Virgil F. Gardner
NASA/Goddard Space Flight Cntr.
Code 901
Greenbelt, MD 20771
USA
Phone: 301-286-8437
Fax: 301-286-4943

Luciano Garramone
Centro Spaziale Di Matera
ITALY
Phone: 39-835-334951
Fax: 39-835-3771

G.C. Gilbreath
Code 8133
4555 Overlook Avenue, S.W.
Washington, DC 20375
USA
Phone: 202-767-2828
Fax: 202-767-1317

Carl Gliniak
EER Systems Corporation
10289 Aerospace Road
Seabrook, MD 20706
USA
Phone: 301-306-7840
Fax: 301-577-7493

Ben Greene
Electro Optic Systems Pty. Ltd.
55A Monaro Street
Queanbeyan, NSW 2820
AUSTRALIA
Phone: 61-6-2992470
Fax: 61-6-2992477

Ludwig Grunwaldt
Telegrafenberg A 17
Potsdam, 0-1561
GERMANY
Phone: 37-331-0325
Fax: 37-332-2824

Paci Guido
ESA/ESRIN
via G. Galilei
Frascati, 00044
ITALY
Phone: 49-6-94180386
Fax: 49-6-94180361

Karel Hamal
Technical University of Prague
Brehova 7
115 19 Prague 1
CZECHOSLOVAKIA
Phone: 42-2-84-8840
Fax: 42-2-84-8840

William Hanrahan III
BFEC
10210 Greenbelt Rd/Suite 700
Seabrook, MD 20706
USA
Phone: 301-794-3495

Jean Louis Hatat
GRGS/CERGA/OCA
Avenue Nicolas Copernic
Grasse 06130,
FRANCE
Phone: 33-93-126270
Fax: 33-93-092615

J. Michael Heinick
BFEC
10210 Greenbelt Rd/Suite 700
Seabrook, MD 20706
USA
Phone: 301-794-3469
Fax: 301-794-3524

Feng Hesheng
Chinese Academy of Sciences
P.O. Box 110, Kunming
Yunnan Province,
PEOPLE'S REP. OF CHINA
Phone: 86-0871-72946
Fax: 86-0871-71845

Van S. Husson
BFEC
10210 Greenbelt Rd/Suite 700
Seabrook, MD 20706
USA
Phone: 301-794-3470
Fax: 301-794-3524

Helena Jelinkova
Technical University of Prague
Brehova 7
115 19 Prague 1
CZECHOSLOVAKIA
Phone: 42-2-84-8840
Fax: 42-2-84-8840

Lawrence S. Jessie
NASA/Goddard Space Flight Cntr.
Code 901
Greenbelt, MD 20771
USA
Phone: 301-286-2052

Bert Johnson
NASA/Goddard Space Flight Cntr.
Code 924
Greenbelt, MD 20771
USA
Phone: 301-286-6179

Michel Kasser
18 Allee Jean Rostand
Evry Cedex, 91025
FRANCE
Phone: 33-160780042
Fax: 33-160779699

Waldemar Kielek
Warsaw University of Technology
Faculty of Electronics
Warsaw, 00667
POLAND
Fax: 48-22255248

Georg Kirchner
Lustbuhelstr 46
Graz, A-8042
AUSTRIA
Phone: 43-316-472231
Fax: 43-316-462678

Steve Klosko
Hughes STX
4400 Forbes Blvd.
Lanham, MD 20706
Phone: 301-794-5284
Fax: 301-306-1010

Rolf Koenig
DGFI
Marstallplatz 8
800 Munich 22
GERMANY
Phone: 49-8153-281353
Fax: 49-8153-281207

Yuri Kokurin
Lebedev Physical Institute
Russian Academy of Sciences
Leninski Prospect
Moscow, 53117924
RUSSIA
Phone: 7-95-132-7147

Ronald Kolenkiewicz
NASA/Goddard Space Flight Cntr.
Code 926
Greenbelt, MD 20771
USA
Phone: 301-286-5372
Fax: 301-286-9200

Danny Krebs
NASA/Goddard Space Flight Cntr.
Code 726.1
Greenbelt, MD 20771
USA
Phone: 301-286-7714

Hiroo Kunimori
4-2-1 Nukui-Kita-Machi Koganei
Tokyo, 184
JAPAN
Phone: 81-423-27-7560
Fax: 81-423-21-9899

Maurice Laplanche
CERGA/OCA
Ave. Copernic
Grasse, F06130
FRANCE
Phone: 33-93-426270
Fax: 33-93-092613

Dr. Kasimir Lapushka
Riga SLR Station
University of Riga
Riga
LATVIA

John Luck
AUSLIG, P.O. Box 2
Belconnen, ACT 2616
AUSTRALIA
Phone: 61-6-2357285
Fax: 61-6-2575883

Glenn Lund
Aerospatiale CA/TO/I
100 Blvd, du Midi
06322 Cannes La Bocca
FRANCE
Phone: 33-9292-7856
Fax: 33-9292-7190

Jan McGarry
NASA/Goddard Space Flight Cntr.
Code 901
Greenbelt, MD 20771
USA
Phone: 301-286-5020
Fax: 301-286-4943

Michael Maberry
Institute for Astronomy
P.O. Box 209
Kula, HI 96790
USA
Phone: 808-878-1215
Fax: 808-878-2862

Paul Malitson
BFEC
10210 Greenbelt Rd/Suite 700
Seabrook, MD 20706
USA
Phone: 301-794-3505
Fax: 301-794-3524

Jean Francois Mangin
CERGA/OCA
Ave. Copernic
Grasse, F06130
FRANCE
Phone: 33-93-365849
Fax: 33-93-092613

Franz-Heinrich Massmann
Pfarrangerweg 4
Petershalisen, D-8037
GERMANY
Phone: 49-8137-5965
Fax: 49-8153-28-1207

Timothy May
Electro Optic Systems Pty. Ltd.
55A Monaro Street
Queanbeyan, NSW 2820
AUSTRALIA
Phone: 61-6-2992470
Fax: 61-6-2992477

Pamela Millar
NASA/Goddard Space Flight Cntr.
Code 924
Greenbelt, MD 20771
USA
Phone: 301-286-3793
Fax: 301-286-2717

Joseph Miller
1130 Freeland Road
Freeland, MD 21053
Phone: 410-357-5818

Grant Moule
Electro Optic Systems Pty. Ltd.
55A Monaro Street
Queanbeyan, NSW
AUSTRALIA
Phone: 61-6-2992470
Fax: 61-6-2992477

Alan Murdoch
BFEC
10210 Greenbelt Rd/Suite 700
Seabrook, MD 20706
USA
Phone: 301-794-3497
Fax: 301-794-3524

Reinhart Neubert
Telegrafenberg A 17
Potsdam, 0-1561
GERMANY
Phone: 37-331-0325
Fax: 37-332-2824

Carey Noll
NASA/Goddard Space Flight Cntr.
Code 935
Greenbelt, MD 20771
USA
Phone: 301-286-9283
Fax: 301-286-4952

Antonin Novotny
Technical University of Prague
Brehova 7
115 19 Prague 1
CZECHOSLOVAKIA
Phone: 42-2-84-8840
Fax: 42-2-84-8840

Jacek Offierski
P.O. Box 581
7300 An Apeldoorn
NETHERLANDS
Phone: 31-5769-8211
Fax: 31-5769-1344

Thomas Oldham
BFEC
10210 Greenbelt Rd/Suite 700
Seabrook, MD 20706
USA
Phone: 301-794-3499
Fax: 301-794-3524

Klaus Otten
P.O. Box 581
7300 An Apeldoorn
NETHERLANDS
Phone: 31-5769-8211
Fax: 31-5769-1344

Linda Pacini
NASA/Goddard Space Flight Cntr.
Code 726
Greenbelt, MD 20771
USA
Phone: 301-286-4685

Jocelyn Paris
CERGA
Avenue Nicolas Copernic
Grasse, 06130
FRANCE
Phone: 33-93-126270
Fax: 33-93-092615

Kamoun Paul
Le Rocazur, Rue Cntr.so
Nice, 06100
FRANCE
Phone: 33-92-92-7517
Fax: 33-92-92-7620

Matti Paunonen
Ilmalankatu 1A
Helsinki, 00240
FINLAND
Phone: 353-0-264994
Fax: 353-0-264995

Michael R. Pearlman
SAO
60 Garden Street
Cambridge, MA 02138
USA
Phone: 617-495-7481
Fax: 617-495-7105

Peter Pendlebury
MOBLAS-5 Tracking Station
P.O. Box 137
Dongara, 6525
AUSTRALIA
Phone: 61-99-291011
Fax: 61-99-291060

Francis Pierron
OCA/CERGA
Ave N. Copernic
Grasse, F06130
FRANCE
Phone: 33-93-365849
Fax: 33-93-092613

James Pirozzoli
Naval Research Laboratory
4555 Overlook Ave.
Washington, D.C. 20375-5000
USA
Phone: 202-767-2828
Fax: 202-767-1317

E. Pop
Sidlerstr. 5
Bern, 3012
PEOPLE'S REP. OF CHINA
Phone: 4131658591
Fax: 4131653869

Ivan Prochazka
Technical University of Prague
Brehova 7
115 19 Prague 1
CZECHOSLOVAKIA
Phone: 42-2-84-8840
Fax: 42-2-84-8840

U.K. Rao
BFEC
10210 Greenbelt Rd/Suite 700
Seabrook, MD 20706
USA
Phone: 301-794-3478
Fax: 301-794-3524

Randall Ricklefs
McDonald Observatory
University of Texas
Austin, TX 78712-1083
USA
Phone: 512-471-1342
Fax: 512-471-6016

Giancarlo Ripamonti
p.z.a. Leonardo da Vinci 32
Politecnico di Milano
Milano, 20133
ITALY
Phone: 39-2-23996103

Gary D. Robinson
BFEC%CDSLR, Suite 750
10210 Greenbelt Road
Seabrook, MD 20706
USA
Phone: 301-794-3467
Fax: 301-794-3524

Norris J. Roessler
5844 Five Oaks Pkwy
St. Louis, MO 63128
Phone: 314-233-0421
Fax: 314-232-3393

Stanislaw Schillak
Astronomical Latitude Observ.
Borowiec 91
Kornik, 62-035
POLAND
Phone: 48-61-170187
Fax: 48-61-170219

Ulrich Schreiber
Fundamental Station Wettzell
Kotzting, Munich, 8493
GERMANY
Phone: 49-9941603113
Fax: 49-9941-60322

Bob E. Schutz
Cntr. for Space Research
University of Texas
Austin, TX 78712
USA
Phone: 512-471-4267
Fax: 512-471-3570

Bernard Seery
NASA/Goddard Space Flight Cntr.
Code 726
Greenbelt, MD 20771
USA
Phone: 301-286-8943

Paul J. Seery
BFEC
10210 Greenbelt Rd/Suite 700
Seabrook, MD 20706
USA
Phone: 301-794-3494
Fax: 301-794-3524

Michael Selden
BFEC
10210 Greenbelt Rd/Suite 700
Seabrook, MD 20706
USA
Phone: 301-794-3499
Fax: 301-794-3524

Mark Selker
NASA/Goddard Space Flight Cntr.
Code 726.1
Greenbelt, MD 20771
USA
Phone: 301-286-1013

Victor Shargorodsky
Science Research Institute for
Precision Device Engineering
53, Aviamotornaya Street
Moscow, 111024
RUSSIA
Phone: 7-95-273-47-19
Fax: 7-95-273-19-37

Peter Shelus
University of Texas at Austin
Austin, TX 78712
USA
Phone: 512-471-3339
Fax: 512-471-6016

Andrew T. Sinclair
Royal Greenwich Observatory
Madingley Road
Cambridge, CB30EZ
ENGLAND
Phone: 44-223-374741
Fax: 44-223-374700

David E. Smith
NASA/Goddard Space Flight Cntr.
Code 920
Greenbelt, MD 20771
USA
Phone: 301-286-8671
Fax: 301-286-9200

Jay Smith
NASA/Goddard Space Flight Cntr.
Code 924
Greenbelt, MD 20771
USA
Phone: 301-286-8525

Peter Sperber
Fundamental Station Wettzell
Koetzting, 8493
GERMANY
Phone: 49-9941-603205
Fax: 49-9961-603222

Charles A. Steggerda
BFEC
10210 Greenbelt Rd/Suite 700
Seabrook, MD 20706
USA
Phone: 301-794-3489
Fax: 301-794-3524

Mark Torrence
STX
4400 Forbes Boulevard
Lanham, MD 20706
USA
Phone: 301-794-5213
Fax: 301-794-1010

J. Utzinger
Sidlerstr. 5
Berm, 3012
PEOPLE'S REP. OF CHINA
Phone: 4131658591
Fax: 4131653869

M.R. van der Kraan
P.O. Box 155
2600 AD Delft,
NETHERLANDS
Phone: 31-15-692269
Fax: 31-15-692111

Carolus Vanes
P.O. Box 581
7300 An Apeldoorn
NETHERLANDS
Phone: 31-5769-8211
Fax: 31-5769-1344

Christian Veillet
CERGA
Ave. Copernic
Grasse, F06130
FRANCE
Phone: 33-93-365869
Fax: 33-93-368963

Erik Vermaat
Kootwijk Observatory
P.O. Box 581
7300 An Apeldoorn
NETHERLANDS
Phone: 31-5769-8211
Fax: 31-5769-1344

Huib Visser
P.O. Box 155
2600 AD Delft,
NETHERLANDS
Phone: 31-15-692160
Fax: 31-15-692111

Thomas Varghese
BFEC
10210 Greenbelt Rd/Suite 700
Seabrook, MD 20706
USA
Phone: 301-794-3498
Fax: 301-794-3524

Scott Wetzel
BFEC
10210 Greenbelt Rd/Suite 700
Seabrook, MD 20706
USA
Phone: 301-794-3492
Fax: 301-794-3524

Roger Wood
Satellite Laser Ranging Group
Herstmonceux Castle
Hailsham, East Sussex BN271RP
ENGLAND
Phone: 44-323-833888
Fax: 44-223-374700

Yao Xing-jia
Changchun,
PEOPLE'S REP. OF CHINA
Phone: 0431-42859

Fu-Min Yang
Shanghai Observatory
80 Nan Dan Road
Shanghai, 200030
PEOPLE'S REP. OF CHINA
Phone: 86-21-4386191
Fax: 86-21-4384618

Wenwei Ye
Wuhan SLR Station
Xiao Hongshan 430071
PEOPLE'S REP. OF CHINA

Lu Yu-Lin
Changchun,
PEOPLE'S REP. OF CHINA
Phone: 0431-42859

Xia Zhizhong
Wuhan SLR Station
Xiao Hongshan 430071
PEOPLE'S REP. OF CHINA
Phone: 86-027-81342
Fax: 86-027-712989

Thomas Zagwodzki
NASA/Goddard Space Flight Cntr.
Code 715
Greenbelt, MD 20771
USA
Phone: 301-286-5199

Ronald Zane
University of Hawaii
P.O. Box 209
Kula, HI 96790
USA
Phone: 808-878-1215
Fax: 808-878-2862

Barbara Zukowski
STX
4400 Forbes Boulevard
Lanham, MD 20706
USA
Phone: 301-286-2779
Fax: 301-286-2929

WORKSHOP AGENDA

EIGHTH INTERNATIONAL WORKSHOP ON LASER RANGING INSTRUMENTATION

Sunday Evening, May 17

6:00-10:00pm **Registration/Orientation (Governor Calvert Inn)**

8:00-10:00pm **Session Chairman Meeting (Calvert Chamber, Governor Calvert House)**

Monday Morning, May 18

8:30-10:00am **Registration (Joint Senate Hearing Room Lobby)**

10:00-11:30am **Welcome/Orientation - John Degnan**

Welcome/Introductions - J. Degnan, Program Chairman

Welcoming Address - M. Baltuck, Head, Geodynamics Branch, NASA Headquarters

Welcoming Address - J. Bosworth, Manager, NASA Crustal Dynamics Project

Orientation - John Degnan

Last Minute Agenda

Poster Papers

Submission Schedule for Proceedings - August 1, 1992

Conference Rooms/Splinter Meetings

Facilities (A-V equipment, xerox, etc.)

Local Phone Number for Workshop Participants

GGAO Tour/Cruise

Restaurants/Local Attractions

Monday Afternoon, May 18

1:00-3:30pm **Scientific Applications & Measurements Requirements - Bob Schutz**

Applications of SLR, B. E. Schutz, Center for Space Research, Univ. of Texas

SLR Tracking of Lageos and Etalon: Past Results and Future Trends, Richard J. Eanes, et al., Center for Space Research, Univ. of Texas

Applications of SLR to Gravity Field Modeling and Sea Surface Topography Determination, D. E. Smith et al., NASA/GSFC

Laser Tracking for Vertical Control, P. Dunn et al., Hughes STX

ESA's Intentions for Laser Tracking of Future European Earth Observation Satellites, Dr. Paci, ESA

ERS-1: Laser Ranging Network Performance and Routine Orbit Determination at the D-PAF, Ch. Reigber et al., DGFI

LASSO Experiments, Christian Veillet, OCA/CERGA

Laser Ranging Application to Time Transfer Using Geodetic Satellite and Other Japanese Space Programs, Hiroo Kunimori et al., CRL

Laser Ranging Support for TV Time Transfer, John McK. Luck, Orroral Geodetic Observatory

4:00-6:00pm **Timely Issues - Andrew Sinclair**

Satellite Signatures in SLR Data, G. M. Appleby et al., Royal Greenwich Observatory

Work at Graz on Satellite Signatures, G. Kirschner, Observatory Lustbuhel

SLR Data Quality Control, P. Dunn et al., Hughes STX

SLR Data Screening for Normal Points, A. T. Sinclair, Royal Greenwich Observatory

Adaptive Median Filtering for Preprocessing of Time Series Measurements, M. Paunonen, Finnish Geodetic Institute

SATCOP Mission Planning Software Package, S. Bucey, BFEC

Tuesday Morning, May 19

8:30-10:30am **Laser Technology - Helena Jelinkova**

Nd:YLF Laser for Airborne/Spaceborne Laser Ranging, J. L. Dallas et al., NASA/GSFC

Picosecond Laser Transmitter, J. Ferrario, QUANTA Systems

Alternative Wavelengths for Laser Ranging, K. Hamal, Faculty of Nuc. Sci. and Physical Engineering

Laser for Two Color Laser Ranging, J. Gaignebet, OCA/CERGA

New Methods of Generation of Ultrashort Laser Pulses for Ranging, H. Jelinkova, Faculty of Nuc. Sci. and Physical Engineering

Multi-Pulse Ranging to the Moon and Meteosat3 at OCA LLR Station, C. Veillet, OCA/CERGA

Recent Analyses and Laser Oscillator Breadboard Test Results for the Geoscience Laser Ranging System (GLRS), J. Gaignebet et al., OCA/CERGA

Simultaneous Compression of Passive Mode-locked Pulsewidth and Pulse Train, Yang Fu Min, Shanghai Observatory

11:00am-12:00pm **Epoch and Event Timing - Ben Greene**

Results of Accurate Timing Tests at Graz, G. Kirchner, Observatory Lustbuhel

Streak Camera Timing Resolution, J. Gaignebet, OCA/CERGA

Preliminary Results from the Portable Standard Satellite Laser Ranging Intercomparison with MOBLAS-7, M. Seldon et al., BFEC

Tuesday Afternoon, May 19

1:30-3:30pm **Detector Technology - Thomas Varghese**

Performance Optimization of Detector Electronics for Millimeter Ranging, S. Cova et al., Politecnico di Milano (Invited Talk)

Tracking Capabilities of SPADs for Laser Ranging, F. Zappa et al., Politecnico di Milano

How to Squeeze High Quantum Efficiency and High Temporal Resolution out of a SPAD, A. Lacaita et al., Politecnico di Milano

Solid State Detector Technology for Picosecond Laser Ranging, I. Prochazka, Faculty of Nuc. Sci. and Physical Engineering

Streak Camera Based SLR Receive System for High Accuracy Multiwavelength Atmospheric Differential Delay Measurements, T. K. Varghese et al., BFEC

Temporal Analysis of Picosecond Laser Pulses Reflected from Satellites, K. Hamal, Faculty of Nuc. Sci. and Physical Engineering

4:00-6:00pm **Calibration Techniques/Targets - Jean Gaignebet**

Experiences and Results of the MLTRS#1 USSR Collocation Campaign 1991, P. Sperber et al., IfAG

ETALON 1, 2 Center of Mass Correction and Array Reflectivity, Nikolai Mironov et al., Main Astron. Obs. of the Ukrainian Acad. of Science (presented by B. Schutz)

Test Results from LAGEOS-2 Optical Characterization Using Pulsed Lasers, T. Varghese et al., BFEC

Historical System Characterization of the NASA SLR Network of the NASA SLR Network Using Collocation and Special Analysis Techniques, V. Husson, BFEC

New Target Concept Based on Fizeau Effect, V. Shargorodsky

6:30pm **Buses leave for GGAO tour**

7:00-10:00pm **Barbecue/tour of the Goddard Geophysical and Astronomical Observatory (GGAO)**

10:30pm **Buses return to hotel**

Wednesday Morning, May 20

8:30-10:30am **Multiwavelength Ranging/Streak Cameras - Karel Hamal**

Two Color Laser Ranging: Potential and New Developments, J. Gaignebet, OCA/CERGA

Optimum Wavelengths for Two Color Ranging, J. Degnan, NASA/GSFC

Two Color Satellite Laser Ranging Upgrades at Goddard's 1.2m Telescope Facility, T. Zagwodzki et al., NASA/GSFC

Two Color Ranging at Wettzell, U. Schreiber, WLRS

Two Wavelengths Satellite Laser Ranging Using SPAD, I. Prochazka et al., Faculty of Nuc. Sci. and Physical Engineering

Millimeter Accuracy Satellites for Two Color Ranging, J. Degnan, NASA/GSFC

Low Pulse Spread Laser Retroreflector Array, I. Prochazka et al., Faculty of Nuc. Sci. and Physical Engineering

New Possibilities for High Precision 2 Color Ranging to Geodesic Satellites, G. Lund

11:00am-12:00pm **SLR Data Analysis/Model Errors - Ronald Kolenkiewicz**

State of the Art SLR Data Analysis at GSFC, S. Klosko, Hughes STX

SLR Modelling Errors, R. Eanes, Center for Space Research, Univ. of Texas

Geometric Analysis of Satellite Laser Ranging Data, J. Degnan et al., NASA/GSFC

Improvement of SLR Accuracy: A Possible New Step, M. Kasser, ESGT

Wednesday Afternoon, May 20

1:30-4:00pm **Operational Software Developments - Georg Kirchner**

On the Accuracy of ERS-1 Orbit Predictions, R. Koenig et al., DGFI

Compensation for the Distortion in Satellite Laser Range Predictions Due to Varying Pulse Travel Times, M. Paunonen, Finnish Geodetic Institute

Timebias Corrections to Predictions, Roger Wood, Satellite Laser Ranger, Herstmonceux

The Formation of On-Site Normal Points, G. Appleby, Royal Greenwich Obs.

Poisson Filtering of Laser Ranging Data, Randall L. Ricklefs et al., McDonald Obs., Univ. of Texas

Computer Networking at SLR Stations, Antonin Novotny, Czech Technical Univ.

Upgrading NASA/DOSE Laser Ranging System Control Computers, R.L. Ricklefs et al., McDonald Obs., University of Texas

HP Upgrade Operational Streamlining, D. Edge et al., BFEC

Application of the Robust Estimate in SLR Data Preprocessing, T. Detong, Shanghai Observatory

4:30-6:00pm **Lunar Laser Ranging - Christian Veillet**

A Computer-Controlled X-Y Offset Guiding Stage for the MLRS, P.J. Shelus et al., McDonald Obs., University of Texas

Lunar Laser Ranging Data Processing in a Unix/X Windows Environment, R.L. Ricklefs et al., McDonald Obs., University of Texas

LLR Activities in Wettzell, U. Schreiber et al., Wettzell Laser Ranging Station

Multi-Wavelength Ranging to the Moon and METEOSAT 3 at OCA LLR, J.F. Mangin, OCA/CERGA

Orroral LLR Activities, J. McK. Luck, Orroral Geodetic Obs.

Wednesday Evening, May 20

7:30-10:30pm **WEGENER/CSTG Splinter Meetings**

Thursday Morning, May 21

8:30-10:30am **Fixed Station Upgrades/Developments - John Degnan**

Design Principles of Fully Automated Ranging Systems, B. Greene et al., EOS Systems Inc.

Status of the Matera Laser Ranging Observatory, G. Bianco et al., ASI/CGS (presented by T. Varghese)

Performance of the Upgraded Orroral Laser Ranging System, J. McK. Luck, Orroral Geodetic Obs.

Sub-CM Ranging and Other Improvements in Graz, G. Kirchner et al., Laser Station Graz

Upgrading of the Borowiec Laser Station, S. Schillak et al., Space Research Center of Polish Academy of Sciences

New Progress in the Work of the Yunnan Laser Ranging Station, Feng Hesheng, Yunnan Observatory

Development of Shanghai SLR Station, Yang Fu Min, Shanghai Observatory

WLRS Status Report, R. Dassing and U. Schreiber, WLRS

NRL SLR Activities, C. Gilbreath, NRL

Status of Tokyo Station, Hiroo Kunimori, CRL

11:00am-12:00pm **Mobile System Upgrades/Developments - Erik Vermaat**

TLRS-3 System Upgrades, R. Eichinger, BFEC

Results of the MTLRS-1 Upgrade, P. Sperber et al., IfAG

A Transputer Based Control System for MTLRS, E. Vermaat et al., Delft Univ. of Technology

Presentation of the Highly Mobile French SLR Station, F. Pierron et al., ESGT

Thursday Afternoon, May 21

1:30-4:00pm **Airborne and Spaceborne Systems - James Abshire**

Airborne Laser/GPS Mapping of the Greenland Ice Sheet, W. B. Krabill et al., NASA/GSFC

Airborne 2 Color Ranging Experiment, P.S. Millar et al., NASA/GSFC

GLRS Phase B Extension Studies, K. Anderson, GE/ASD

GLRS-R 2 Color Retroreflector Target Design and Predicted Performance, G. Lund

Turbulence Effects on the Geodynamic Laser Ranging System, J.H. Churnside

Development of the Mars Observer Laser Altimeter, B.L. Johnson et al., NASA/GSFC

Bench Checkout Equipment for Spaceborne Laser Altimeter Systems, J. C. Smith

Single Photon Ranging Systems for Mars Altimetry and Atmospheric Studies, I. Prochazka et al., Faculty of Nuc. Sci. and Physical Engineering

Small Spacecraft Laser Altimeter Instrument Concepts for Topography Measurement from Low Earth Orbit, J.L. Bufton, NASA/GSFC

Satellite to Satellite Laser Ranging System for Lunar Gravity Measurements, J. Abshire et al., NASA/GSFC

4:00-6:00pm **Operational Software Splinter Meeting/Joint Hearing Room**
LASSO Splinter Meeting/Arundel Room/Maryland Inn
Poster Session/Governor Calvert Inn/Calvert Chamber

6:15pm **Boarding time for Conference Dinner Cruise (Annapolis Harbor)**

6:30-9:30pm **Conference Dinner Cruise**

9:30pm **Return to Annapolis Harbor**

Friday Morning, May 22

8:30-10:00am **Conference Summary/Resolutions - Michael Pearlman**

10:30am-12:00pm **Business Meeting/Next Workshop - Carroll Alley**

12:00pm **Adjourn**

POSTER PRESENTATIONS

Satellite Laser Station Helwan, NRIAG, Helwan, Egypt, and Czech Tech. Univ., Prague, Czechoslovakia

1.2 Meter Telescope Facility, Goddard Space Flight Center, Greenbelt, Md., T. W. Zagwodzki et al., NASA/GSFC

Ranging Data Quality Improvement from High Speed Detection Using 6m Core Microchannel Plate Photomultiplier Tube, T. Varghese et al., BFEC

The Optical Attenuation Mechanism, R. Eichinger, BFEC

Scientific Applications

and

Measurements Requirements

LASER TRACKING FOR VERTICAL CONTROL

Peter Dunn and Mark Torrence, Hughes STX Corp.,Lanham,MD
Erricos Pavlis, Univ. of Maryland,College Park,MD
Ron Kolenkiewicz and David Smith, GSFC LTP,Greenbelt,MD

ABSTRACT

The Global Laser Tracking Network has provided LAGEOS ranging data of high accuracy since the first MERIT campaign in late 1983 and we can now resolve centimeter-level three dimensional positions of participating observatories at monthly intervals. In this analysis, the station height estimates have been considered separately from the horizontal components, and can be determined by the strongest stations with a formal standard error of 2 mm. using eight years of continuous observations. The rate of change in the vertical can be resolved to a few mm./year, which is at the expected level of several geophysical effects. In comparing the behavior of the stations to that predicted by recent models of post-glacial rebound, we find no correlation in this very small effect. Particular attention must be applied to data and survey quality control when measuring the vertical component, and the survey observations are critical components of the geodynamic results. Seasonal patterns are observed in the heights of most stations, and the possibility of secular motion at the level of several millimeters per year cannot be excluded. Any such motion must be considered in the interpretation of horizontal inter-site measurements, and can help to identify mechanisms which can cause variations which occur linearly with time, seasonally or abruptly.

INTRODUCTION

LAGEOS laser ranging measurements have added significantly to our knowledge of horizontal motion at the observing stations and have helped to improve models of tectonic processes and regional deformation at plate boundaries (Frey and Bosworth,1988). The tectonic movements are as large as 17 cm/year between fast moving stations such as Huahine and Easter Island which lie astride the Pacific/Nacza plate boundary. The SLR data have demonstrated their ability to measure centimeter per year motions to a few mm/year, but geodesic lengths have usually been used in this work because they directly provide horizontal rates and are independent of vertical variations. The time grain of the horizontal measurements has progressed from annual values (Christodoulidis et al.,1985) to quarterly averages (Smith et al.,1990) as the network has grown and observation and force models have improved.

Accurate vertical control can assist the horizontal positioning in monitoring tectonic processes and the detection of pre- or post-seismic events. Accurate height determination also allows the measurement of post-glacial rebound and the investigation of atmospheric pressure loading at the stations. The scale of an Earth-centered reference system can be defined in a network of SLR stations to establish a global vertical datum. The systems can also be employed to calibrate altimeter instruments by determining the radial component of the orbit of the altimeter mission.

Degnan(1985) has described the various technical methods of accurate range measurement which include careful calibration for electronic path delays and atmospheric refraction, as well as accurate surveys of the distance between a system's electro-optical center and a ground bench-mark. Any systematic errors in the original observations will be preserved in the normal points which we employ in our analysis, and will affect the final position estimates for the stations. Characteristics of each instrument's laser transmitter and detection system must be monitored to ensure that the distribution of satellite returns is normally distributed. Any skewness in the range pattern would bias the normal points, and would usually be caused by errors which would delay the detection of the return, yielding normal points with a longer range value than that from a Gaussian distribution, although this system characteristic will vary with the detection scheme. The magnitude of the signature of the satellite retro-reflector array on the range measurement will also depend on the instrument. We have adopted a value of 251 mm. (Fitzmaurice et al.,1977) for the correction for the offset between the satellite's center-of-mass and its reflecting surface, which would be expected from the multiple photon, leading edge detection MOBLAS systems. Lower power transmitters with alternative detection methods may require corrections differing by a few millimeters.

Errors in station time-keeping can degrade the resolution of the horizontal component of station position, although modern systems using GPS time transfer for epoch time are synchronized to the microsecond, which is an insignificant error at the level of positioning accuracy currently dominated by errors in the satellite perturbation model. Systematic errors in the round-trip time measurement for range are more difficult to control. They will tend to cancel out in the horizontal position measurements of stations with adequate sky coverage, but will directly affect their height estimates. In this treatment we have restricted our analysis to the best calibrated observatories in the network, and have subjected their observations to particularly strict quality control standards. The locations of these stations are shown on the world map of Figure 1, and their positions listed in Table 1, with particular emphasis on the vertical component. The observations from these strong stations now allow us to reduce the interval for determination of 3-dimensional positions from a quarter of a year to a month, and thus provide improved resolution of the rate of any station movement.

DATA ANALYSIS METHOD

In our analysis, each SLR measurement constrains the solution of a numerically integrated satellite trajectory. A system of equations which satisfies all of the range information in a least squares sense is developed (Putney,1990) for orbits independently computed with an accurate perturbation model over time spans of approximately a month. The resulting linear system is subsequently solved to yield monthly three-dimensional coordinates of the tracking station positions, together with other geodetic parameters estimated at various time intervals. The motion of the satellite is computed in a reference frame which includes the effect of general relativity about the Earth with an adopted value of 398600.4415 km3/sec2 for GM, the product of mass and gravitational constant (Ries et al.,1992). The GEM-T3 geopotential model (Lerch et al.,1992) with expanded ocean tides to include significant LAGEOS perturbations was supplemented by third body perturbations from the sun and the moon, together with the planets Mercury through Neptune.

The effects of thermal drag on the satellite were represented by a model of the Earth Yarkovsky effect (Rubincam,1990) with an initial satellite spin axis orientation of 22 degrees,

decreasing by 50% every 6 years. To satisfy remaining unmodelled orbit effects, a secular along-track acceleration was adjusted every 15 days, as well as the phase and amplitude of an along-track component acting once per revolution of the orbit. This once per revolution adjustment parameter is related to the eccentricity excitation vector described by Yoder et al.(1983) and has been found to accommodate variations in the behavior of LAGEOS which have not yet been adequately described (cf. Eanes et al.,1991). The values of secular along-track acceleration determined by the full network over the experimental period is shown in Figure 2. This is a well-determined parameter with a formal uncertainty of about .1 picometer/sec2, and the regularly repeating patterns in the early part of the signature have been modelled by several workers (Anselmo et al.,1983; Afonso et al.,1989; Scharoo et al.,1991) using theories based on both Earth-reflected and direct solar heating. The unusual behavior of the along-track signature commencing in 1990 is not very well predicted by these models.

Figure 3 shows the orthogonal components of the once-per revolution acceleration estimates, which are more weakly determined than the direct effect, and have formal errors of about the same size as a typical value. The cosine function of orbital angle from equator crossing measures unmodelled perturbations in the equatorial plane, particularly those associated with solar position and radiation pressure. The unusual variation in it's amplitude indicates a change in the satellite's behavior in 1989 and again in 1991, and recent observations have shown that the irregular behavior continues in 1992. Bertotti and Iess (1991) have suggested that torques on the spacecraft due to eddy currents and gravity gradient would lead to chaotic spin dynamics in 1991 or 1992, and this could help explain these results. The once per revolution perturbations affect monthly orbital fits to the ranging observations by as much as ten centimeters, but when modelled according to the values of Figure 3, the root mean square fit of each month's data remains below five centimeters, and with this precision it is possible to resolve the vertical components of the selected stations at the centimeter level each month.

Ocean loading at appropriate locations was applied (IERS Standards: McCarthy, 1991), although this semi-diurnal effect would be very small when averaged over the monthly position estimates of stations with adequate sky coverage, but would have an effect on stations which track at favored times of the day (or night). Earth rotation and orientation parameters (EOP) were taken from a global solution in which they were adjusted daily in the J2000 reference system with the effects of dynamic polar motion included, and in which the UT1 time published by the International Earth Rotation Service was fixed for one day of each month to establish a longitude frame. In the global solution the station position for each site was estimated, but its motion was modelled according to Smith et al.(1990), resulting in a consistent reference frame throughout the eight year experimental period. In both the global solution for EOP and the monthly analysis which yielded the height values presented here, the stations' reference system was set by fixing the horizontal position components of Greenbelt (latitude and longitudes) and Maui (latitude). The results for monthly values of station height are reported only if coverage for both of the fiducial stations at Greenbelt and Maui reached a minimum of nine LAGEOS passes, and if there were adequate data from each individual station. A nutation series according to Wahr(1981) was adopted and the effect of solid Earth tides at the stations was also computed according to Wahr(1981)

LASER DATA QUALITY CONTROL

Each of the observatories whose vertical motion was monitored in this analysis contains a well calibrated system that has been in operation since late 1983. During the lifetime of each

station, continuous improvements are made to the system through up-grades in hardware and software. Any disturbance at an instrument is monitored with accurate resurveys of the system's eccentricity (optical center with respect to an associated ground marker) as well as of any change in the surveyed distance of the calibration tower used for system delay correction. The eccentricity offsets for the various MOBLAS instruments fielded by the Goddard Space Flight Center are listed in Table 2. They have been retrieved from the Crustal Dynamics Data Information System (CDDIS) in December 1991 and their correctness will directly affect the estimated heights given in Table 1, as well as any measure of vertical motion. The remaining observatories in the network were assumed stationary during the eight year period and their positions refer to the optical axis of each telescope, which is the estimated parameter in our data reduction. Any improved information on eccentricity surveys can be used to efficiently up-date the marker positions, and it is not necessary to repeat the full data reduction process. On the other hand, techniques for direct estimation of station velocity will require accurate eccentricity values at the outset of the analysis to connect the positions of each occupation at a site.

Information concerning calibration characteristics of each system is accessible through the CDDIS, although it is has already been used in the processing of the raw range measurements and is thus embedded in the normal points. As corrections to the calibration procedures are uncovered by subsequent analysis, it is necessary to compensate for any effects that retro-active improvements might exert on station position. Subtle engineering problems in the detection system must be remedied in a pre-processing stage using the original time-of-flight observations, but many of the data corrections can be represented by pass-by-pass or longer term range or timing bias parameters, and the design of our analysis facilitates the incorporation of historical updates using linear shifts based on the partial derivatives of range or clock bias computed in the initial time-consuming computation of normal equations. Several corrections to the released data were required. In particular, range corrections to Arequipa observations were applied: 4 cm to each measurement up to March 1986 to allow for the improved survey of the calibration tower noted in the CDDIS description of this station, as well as another 3 cm until July 1988 at which time improved system delay calibration procedures indicated this offset (Husson, 1988). Range errors of this magnitude would significantly affect any estimates of vertical motion occurring at the rate of a few mm/year, and the possibility of similar anomalies at other locations is closely monitored. The most compelling indication of engineering effects in station position is an abrupt change in station height to a subsequently maintained level: this was clearly seen when earlier, uncorrected Arequipa data was used in quarterly solutions shown in the lower frame of Figure 4. When the height of the station was held fixed at a value estimated over the 13 year data span, the monthly estimates of range bias shown in Figure 4 indicate error in the earlier observations of the correct magnitude.

ANALYSIS OF VERTICAL MEASUREMENTS

The independent monthly values of height at the three stations with the lowest month-to month variation seen in our analysis are given in Figures 5a,b and c. The least significant figures in millimeters of the distance from an average Earth semi-major axis of 6378136.3 m. appear on the vertical scale and the measurements are qualified by error estimates of twice their formal standard deviation based on the final fit of the range observations to each orbital arc. Although the ranges themselves are formally accurate to better than a centimeter, systematic residual signatures of several centimeters in amplitude are observed due to uncompensated errors in force, measurement and Earth orientation models. The effect of atmospheric refraction on the laser ranges is modelled according to Marini and Murray (1973) who assumed a spherically

stratified atmosphere based on surface pressure measurements. Herring (1988) has shown that range corrections due the refractivity formula, the zenith range correction and the elevation dependence of the range correction formula should only be a few millimeters at 20 degree elevation angle, which is the lower limit for most of the systems. However, any long term variations in station barometer accuracy or in the effects of lateral gradients in the atmosphere (see Abshire and Gardner,1985) will directly affect the vertical estimates. The SLR systems could thus be used to monitor aberrations in the dry component of atmospheric refraction which would not be separable from the wet component in nearby microwave instruments.

The possibility of errors in the adopted eccentricities must also be considered, particularly for stations which have undergone changes of system occupation, such as Greenbelt, Quincy and Huahine (see Table 2). The system changes at the North American sites coincided with collocation tests which cross-calibrated each instrument's ranging machine as well as its eccentricity. The transportable systems are periodically returned to Greenbelt for up-grades and collocation calibration against MOBLAS-7, but do not usually undergo a collocation test at their working location. The Huahine position shows more variation than the other sites but, because TLRS-2 eccentricity errors are minimized by employing a precise repositioning technique, this behavior is more likely to be due to the influence of the early, less accurate MOBLAS-1 measurements .

Considerable deviation from uniform motion can be noted in the height variation for some stations, and most of the estimated height rates shown in Table 3 are not significant compared to their quoted uncertainties, which are twice the formal standard error based on the fit of the individual values to a straight line. The measures of scatter of the height values about the mean listed in Table 1 are only reduced by a millimeter or two when a linear fit is substituted. The height statistic has been used as a quality control factor in earlier work measuring the horizontal component of motion (see, for example Table 3 of Smith et al.,1990). Considering the scatter of a station's height about a mean (or uniformly moving) value as a measure of the 'quality' of the station's performance, we see that it depends as much on system stability and careful calibration as upon the precision of the observations, and the lower values of height scatter at Greenbelt, Yarragadee and Arequipa testify to the reliability of these instruments.

Post-glacial rebound of the Earth from the melting of continental ice sheets starting roughly 18,000 years ago produces changes in the gravity field as it affects the long-term evolution of the LAGEOS orbit and have been reported by Yoder et al. (1983) and Rubincam (1984). Wagner and McAdoo (1986) present a simple uniform viscosity model for the rate of change of radial position due to post-glacial rebound based on the Ice-2 maps of Wu and Peltier(1983), and this model is complete enough to include all the SLR sites. The values of vertical uplift at each observatory predicted by the model have been taken from Figure 5 of Wagner and McAdoo(1986) and are compared in Table 3 with the height rates estimated from the laser data from the SLR stations, arranged for convenience by tectonic plate. Very little correlation can be seen between the modelled and observed values of up-lift, even in Europe, where the 4 mm/year rate expected from the model is within the detection capability of the SLR systems. On the other hand, neither the model nor the SLR observations taken at Greenbelt can confirm sinking of eastern North America as required by tide gauge data (see Trupin 1991) : the absence of higher degree terms due to the lack of a lithosphere in their treatment has been noted by Wagner and McAdoo and could explain the model results. James and Morgan (1990) have shown in more detail how modelling assumptions of the properties of the lithosphere can cause disagreement with sea level observations, and they have also indicated that horizontal motions due to post-glacial rebound in

North America and Fennoscandia can amount to 4 mm/year from plausible models. This movement is predicted in the Hudson Bay region where vertical movement can amount to over 10 mm/year, and both components are clearly within the resolution capability of a modern SLR system occupying this region in an extended campaign.

It is possible that further investigation of the SLR observations will uncover a source of instrument error which would alias into the vertical component of station position. However, the apparent rate of 4 mm/year observed at Arequipa is large enough that no SLR analysis should assume a stationary vertical component and expect accurate baseline measurements to distant stations. Only explicit separation from the vertical component by considering geodesic lengths will allow the definition of accurate horizontal motion.

CONCLUSIONS

The stability of the radial component of position at the strongest SLR observatories in an eight year time span suggests that vertical motion is bounded by 2 or 3 mm/year and this analysis does not confirm variations suggested by models of post-glacial rebound. Periodic signatures apparent in the height results may represent seasonal variations of a geophysical nature, but do not produce significant long term trends. These accurate estimates of station height can help in the calibration of satellite altimeters as well as to establish scale for positioning techniques which degrade as a function of distance on a global scale, such as GPS campaigns in close proximity to the SLR Observatories. The data quality control which must be exercised to retain the full scaling accuracy of the laser ranges is not so stringent in the analysis of GPS networks as they benefit from strong orbital geometry when multiple satellites are simultaneously tracked. On the other hand, accurate relative position measurements of each instrument's reception center from a ground marker is critical in both space techniques and must be carefully monitored. The capability with which the Global Laser Tracking Network can control vertical scale will grow with the increased number of retro-reflector-carrying satellites expected to be in high Earth orbit in the next few years. As observations from LAGEOS 2 are supplemented by concentrated tracking of the currently orbiting ETALON spacecraft, time resolution of any subtle vertical motion should also be improved.

REFERENCES

Abshire,J.B. and C.S.Gardner,"Atmospheric Refractivity Corrections in Satellite Laser Ranging", IEEE Trans. on Geosc. and Rem. Sense. GE-23, 1985

Afonso, G,F.Barlier,M.Carpino,P.Farinella,F.Mignard,M.Milani and A.M..Nobili," Orbital Effects of LAGEOS Seasons and Eclipses", Ann.Geophys.A 7(5),501-514,1989

Anselmo,L.,B.Bertotti,P.Farinella,A.Milani and A.M.Nobili,"Orbital Perturbations due to Radiation Pressure for a Spacecraft of Complex Shape", Celest. Mech. 29,27,1983

Bertotti,B.,and L.Iess,"The Rotation of LAGEOS", J.Geophys.Res., 96,2431-2440, 1991

Christodoulidis,D.C., D.E.Smith, R.Kolenkiewicz, S.M.Klosko, M.H.Torrence and P.J.Dunn,"Observing Tectonic Plate Motions and Deformations from Satellite Laser Ranging", J.Geophys.Res., 90(B11),9249-9263,1985

Degnan,J.J.,"Satellite Laser Ranging: Current Status and Future Prospects", IEEE Trans. on Geosc. and Rem. Sense. GE-23, 1985

Eanes,R.J. and M.M. Watkins,"Temporal Variability of Earth's Gravitational Field from Satellite Laser Ranging Observations", XX Gen. Ass. IUGG Symp. No.3,Vienna,1991

Fitzmaurice,M.W.,P.O.Minott,J.B.Abshire and H.E.Rowe,"Prelaunch Testing of the Laser Geodynamic Satellite (LAGEOS)", NASA Tech. Paper 1062,1977

Frey H.V. and J.M.Bosworth,"Measuring Contemporary Crustal Motions: NASA's Crustal Dynamics Project", Earthqu. and Volc. 20(3), 1988

Husson,V.S.,"First Six Month Data Processing Report",BFEC Report, October 1988

James,T.S.,and W.J.Morgan,"Horizontal Motions due to Post-Glacial Rebound", Geo. R.Lett. 17(7) 1990

Lerch,F.J," Geopotential Models of the Earth from Satellite Tracking, Altimeter and Surface Gravity Observations: GEM-T3 and GEM-T3S", NASA TM 104555, 1992

McCarthy D.D.(ed.), IERS Standards(1989), IERS Tech. Note 3, Central Bureau of IERS, Observatoire de Paris, 1989

Putney,B.,R.Kolenkiewicz,D.Smith,P.Dunn and M.H.Torrence,"Precision Orbit Determination at the NASA Goddard Space Flight Center", Adv. Space Res., 10(3),197-203, 1990

Ries,J.C.,R.J.Eanes,C.K.Shum and M.M.Watkins,"Progress in the Determination of the Gravitational Coefficient of the Earth", in press,1992

Rubincam,D.P.,"Postglacial Rebound Observed by LAGEOS and the Effective Viscosity of the Lower Mantle", J.Geophys.Res., 89(B2),1077-1087, 1984

Rubincam D.P.,"Drag on the LAGEOS Satellite",J. Geophys.Res., 95,4881-4886,1990

Scharoo,R.,K.F.Wakker,B.A.C.Ambrosius and R.Noomen,"On the Along-track Acceleration of the LAGEOS Satellite", J.Geophys.Res., 96,729-740, 1991

Smith,D.E.,R.Kolenkiewicz,P.J.Dunn,J.W.Robbins,M.H.Torrence,S.M.Klosko and R.G.Williamson,"Tectonic Motion and Deformation from Satellite Laser Ranging to LAGEOS", J.Geophys.Res., 95(B13),22013-22041, 1990

Trupin A.S.," The Effect of Global Change and Long Period Tides on the Earth's Rotation and Gravitational Potential", U. Col. Ph.D. Thesis, 1991

Wagner,C.A. and McAdoo,D.C.,"Time Variation in the Earth's Gravity Field Detectable With GRM Intersatellite Tracking",J.Geophys.Res. 91(B8), July,1986

Wahr,J.M.,"The Forced Nutations of an Ellipsoidal Rotating, Elastic and Oceanless Earth", Geophys.J.R.Astron.Soc.64, 1981

Wu, P.,and Peltier,W.P.," Glacial Isostatic Adjustment and the Free Air Gravity Anomaly as a Constraint on Deep Mantle Viscosity", Geophys. J. R. Astron. Soc.74, 1983

Yoder,C.F.,J.G.Williams,J.O.Dickey,B.E.Schutz,R.J.Eanes and B.D.Tapley,"Secular Variation of Earth's Gravitational J2 Coefficient from LAGEOS and Non-tidal Acceleration of Earth Rotation", Nature 303, 1983

TABLE 1 : STATION POSITIONS

		LATITUDE DEG MNSEC	LONGITUDE DEG MNSEC	HEIGHT METERS	ST.ERR. MILLIMETERS	ST.DEV	NO. MONTHS
GREENBELT	7105	39 1 14	283 10 20	19.931	2	16	69
QUINCY	7109	39 58 30	239 3 19	1107.119	2	18	67
MON.PEAK	7110	32 53 30	243 34 39	1839.746	2	20	73
YARAGADEE	7090	-29 2 47	115 20 48	242.080	2	16	69
HUAHINE	7123	-16 44 1	208 57 32	46.110	5	23	22
AREQUIPA	7907	-16 27 57	288 30 25	2492.945	2	17	52
MATERA	7939	40 38 56	16 42 17	536.551	2	19	60
WETZEL	7834	49 8 42	12 52 41	661.842	4	24	45
GRAZ	7839	47 4 2	15 29 36	540.125	3	20	55
RGO	7840	50 52 3	20 10	76.114	3	21	69
SIMOSATO	7838	33 34 40	135 56 13	100.175	4	25	51

TABLE 2 : ECCENTRICITY OFFSETS

			START	STOP	N(mm)	E(mm)	UP(mm)
GREENBELT	7105	MOBLAS-7	84 1 1	84 3 22	16	-26	3169
			84 3 22	85 7 29	17	-32	3169
			85 7 29	89 10 12	17	-31	3168
			89 10 12	90 7 25	35	-40	3162
			90 7 25	91 12 31	-14	-33	3153
	7918	TLRS-4	90 4 6	90 7 23	-7	-5	2613
QUINCY	7109	MOBLAS-8	84 1 1	86 9 18	-29	11	3124
			86 9 26	91 3 17	-27	12	3138
		TLRS-4	91 3 19	91 8 19	-5	0	2651
		MOBLAS-8	91 11 18	91 12 11	-19	5	3184
			91 12 12	91 12 31	-35	-3	3184
MON.PEAK	7110	MOBLAS-4	84 1 1	88 4 30	-33	-15	3210
			88 4 30	91 12 31	-33	-16	3213
YARAGADEE	7090	MOBLAS-5	84 1 1	87 8 13	3	11	3185
			87 8 13	91 12 31	3	10	3177
HUAHINE	7121	MOBLAS-1	84 1 1	86 3 13	8	1	3662
	7123	TLRS-2	87 7 14	87 10 8	0	0	1453
			88 3 16	88 9 1	0	0	1437
			89 4 24	89 9 3	0	0	1482
			90 3 15	90 8 20	-1	3	1459
			91 4 5	91 9 4	-2	4	1482

GROUND MARKER DISTANCES

	X(mm)	Y(mm)	Z(mm)
7105 TO 7918	-14419	5137	9457
7121 TO 7123	1458	807	501

TABLE 3 : COMPARISON WITH POST-GLACIAL REBOUND MODEL

TECTONIC PLATE	STATION	MODEL	OBSERVED	
N. AMERICAN	GREENBELT	3	1.7	+/-2 mm/year
	QUINCY	3	1.5	2
PACIFIC	MON.PEAK	1	2.6	2
	HUAHINE	1	3.2	4
AFRICAN	MATERA	1	2.3	2
EURASIAN	WETZEL	4	-1.5	3
	GRAZ	4	.9	2
	RGO	4	-.2	2
AUSTRO-INDIAN	YARAGADEE	1	1.4	2
S. AMERICAN	AREQUIPA	-2	4.1	2
UNKNOWN	SIMOSATO	-3	2.2	4

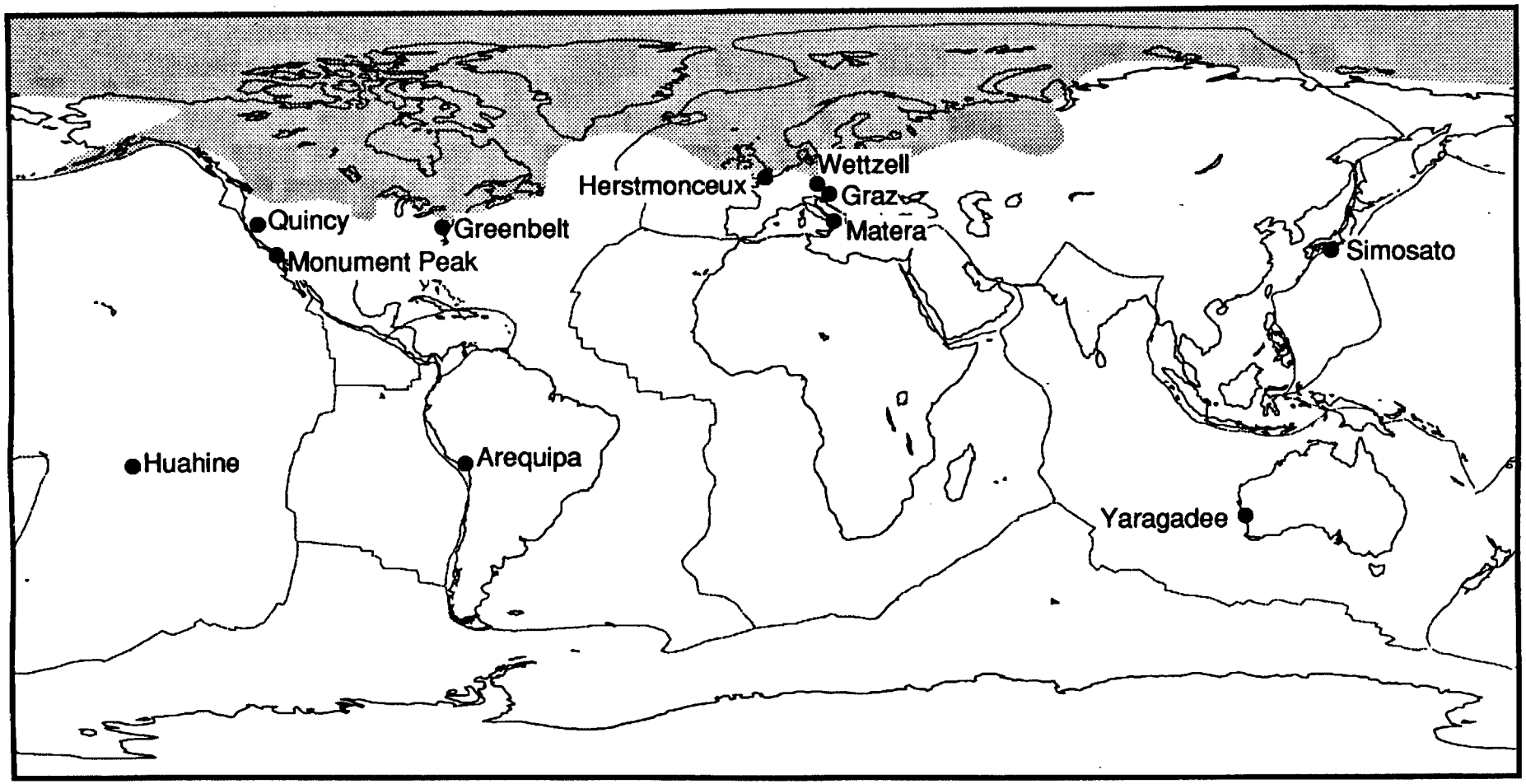

Figure 1 : A world map showing the selected stations and Tectonic and Ice Sheet Boundaries.

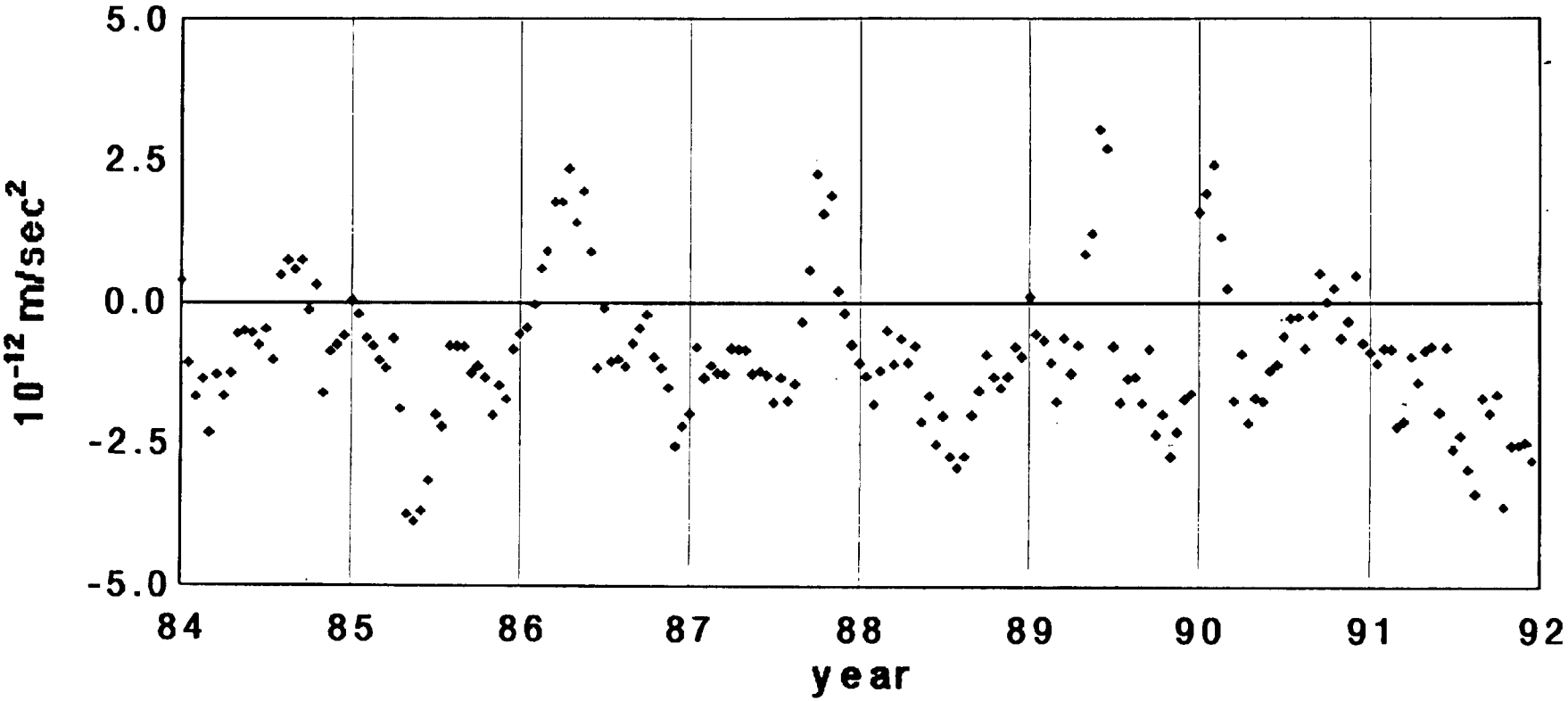

Figure 2 : Semi-monthly values of direct estimates of along-track accelerations.

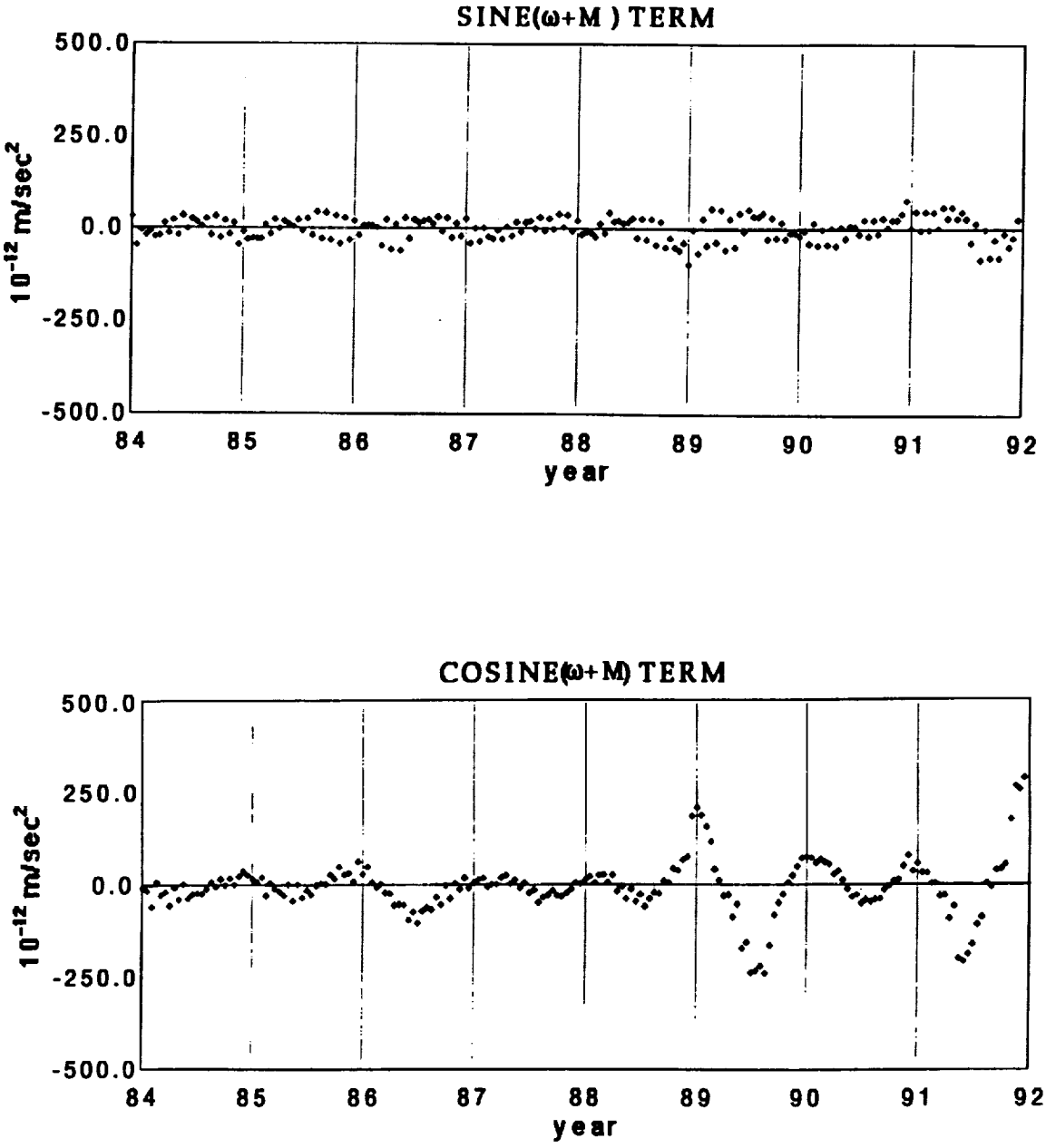

Figure 3 : Semi-monthly values of the once-per revolution acceleration

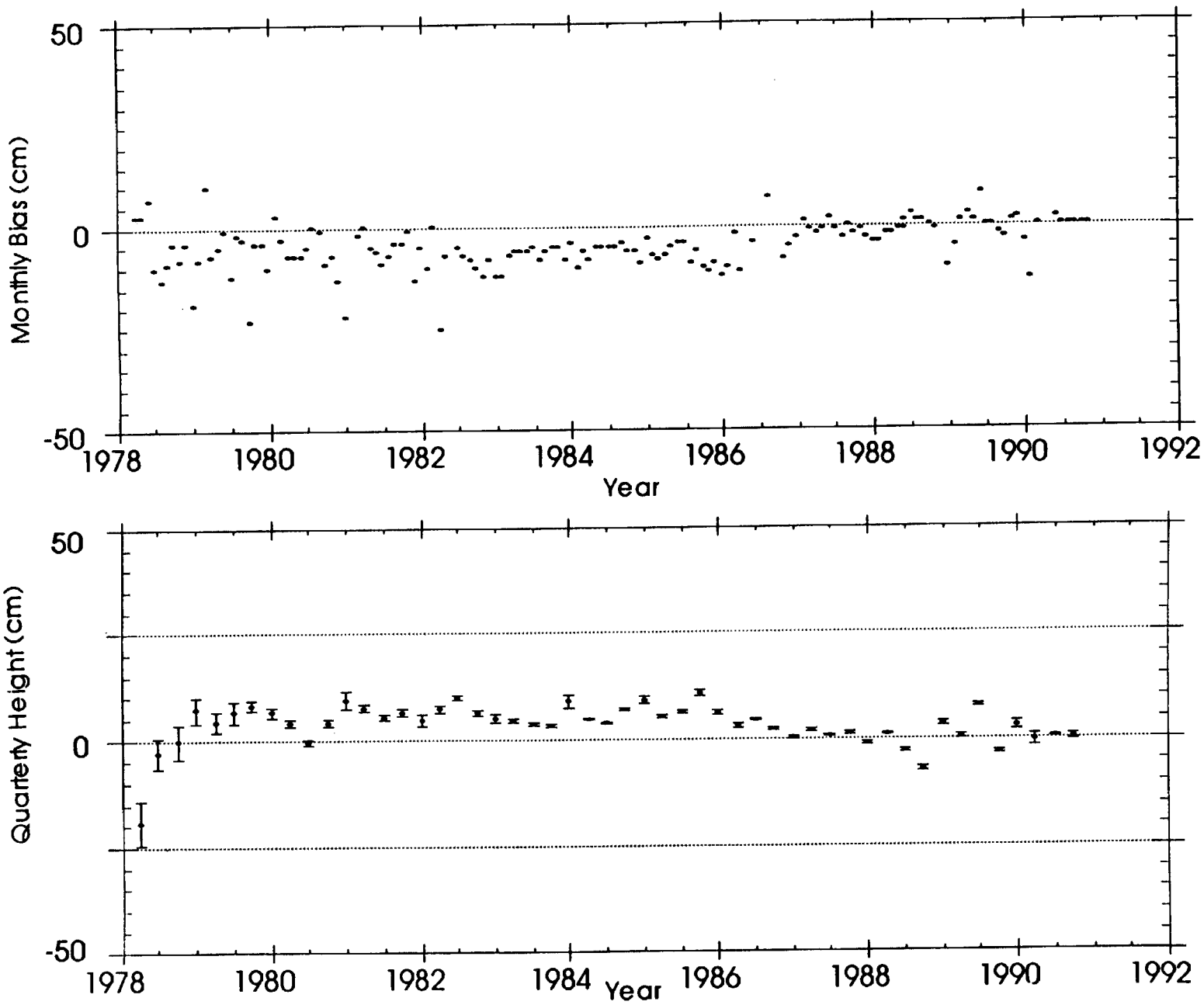

Figure 4 : Arequipa Range Bias Estimates and Equivalent Station Height Variations

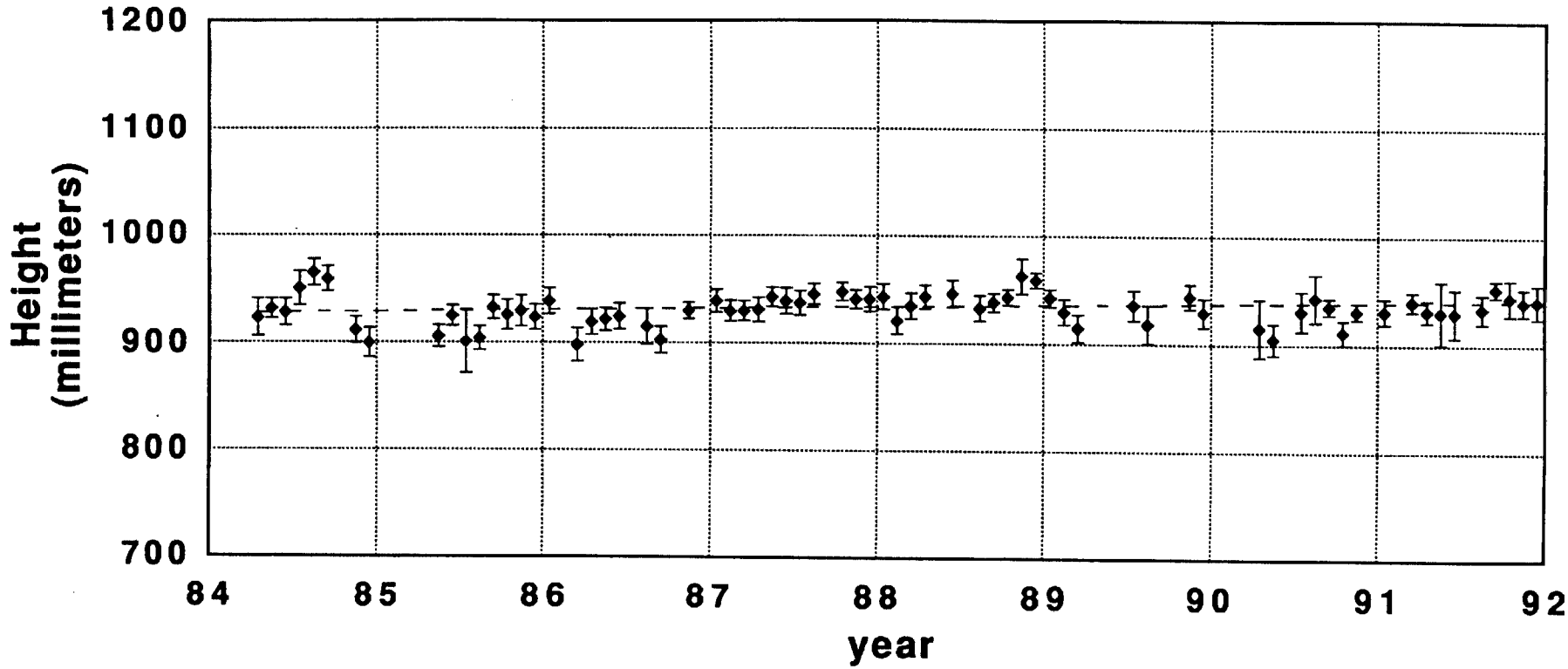

Figure 5a : Monthly estimates of the height of Greenbelt

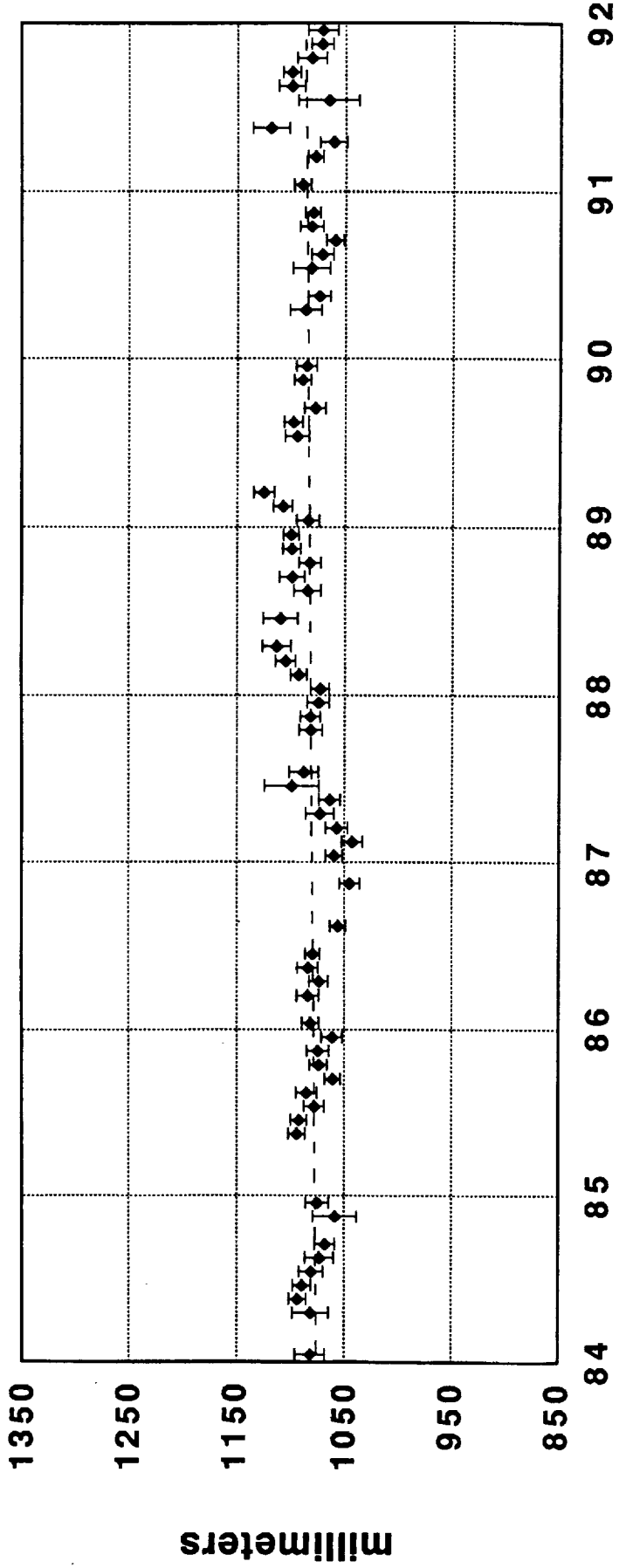

Figure 5b : Monthly estimates of the height of Yarragadee

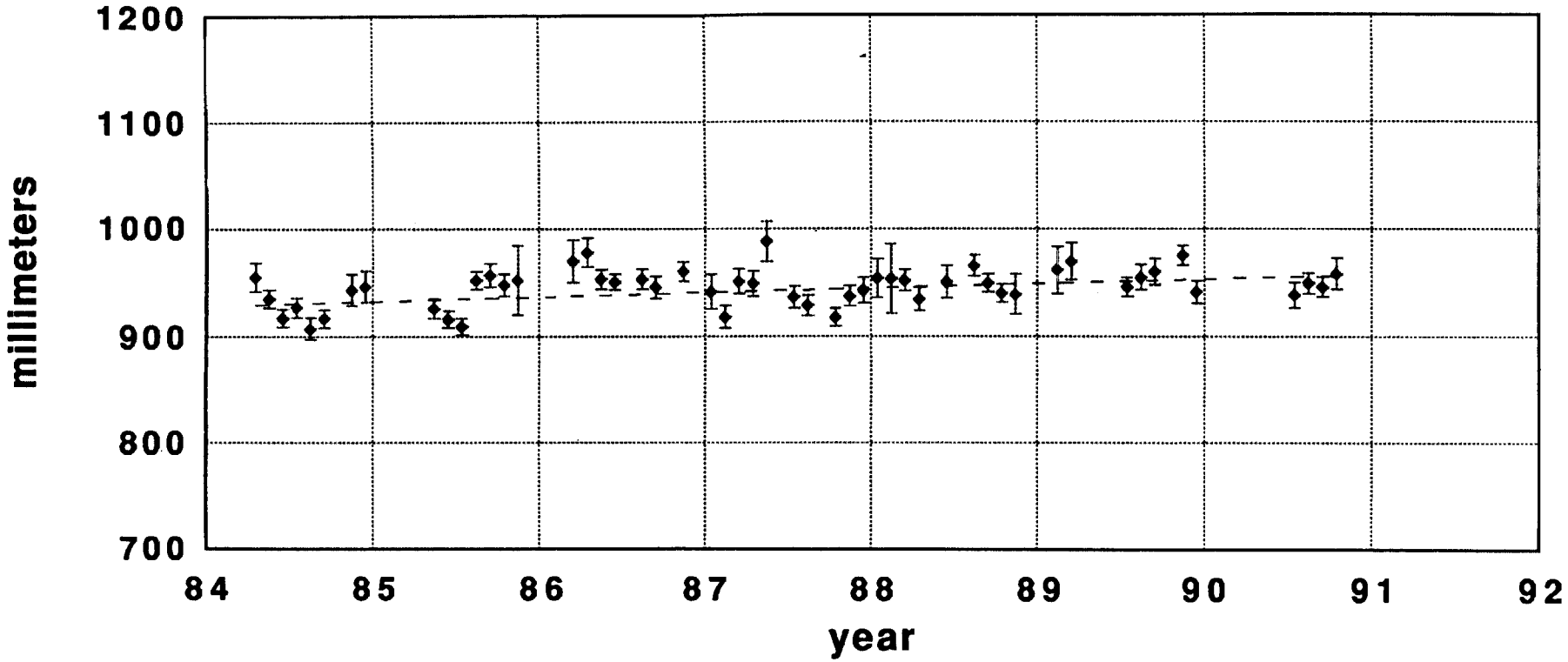

Figure 5c : Monthly Estimates of the height of Arequipa

Laser Ranging Network Performance and Routine Orbit Determination at D-PAF

F.-H. Massmann, Ch. Reigber, H. Li, R. König,
J.C. Raimondo, C. Rajasenan, M. Vei

Deutsches Geodätisches Forschungsinstitut (DGFI), Abt. I, and
German Processing and Archiving Facility (D-PAF)
Münchner Str. 20
D-8031 Oberpfaffenhofen
Germany

Summary

ERS-1 is now about 8 months in orbit and has been tracked by the global laser network from the very beginning of the mission. The German processing and archiving facility for ERS-1 (D-PAF) is coordinating and supporting the network and performing the different routine orbit determination tasks.

This paper presents details about the global network status, the communication to D-PAF and the tracking data and orbit processing system at D-PAF. The quality of the preliminary and precise orbits are shown and some problem areas are identified.

1. Background

On July 17, 1991, the first European (ESA) Remote Sensing Satellite (ERS-1) was successfully launched from Kourou, French Guayana. The satellite is equipped with a number of active microwave instruments for the monitoring of the Earth's environment (see figure 1). In order to make full use of the measurements the ERS-1 orbit has to be known very precisely. For this purpose ERS-1 is carrying a laser retro-reflector and, as an experiment, the Prare system (Precise Range and Range Rate Equipment). After the failure of the Prare system due to a radiation damage the satellite laser ranging (SLR) measurements are the basis for the precise orbit determination.

ERS-1 is flying in a sun-synchronous circular orbit (quasi-polar) at a mean altitude of 785 km and an inclination of 98.5 degrees with different ground repeat cycles (see table 1). The Kepler period is about 100.5 min.

To keep the satellite ground tracks within +-1 km deadband (first 6 months +- 2 km) so called maintenance manoeuvres have to be executed, which take place usually every two to four weeks depending mainly on the solar activity.

Figure 1: ERS-1 Satellite

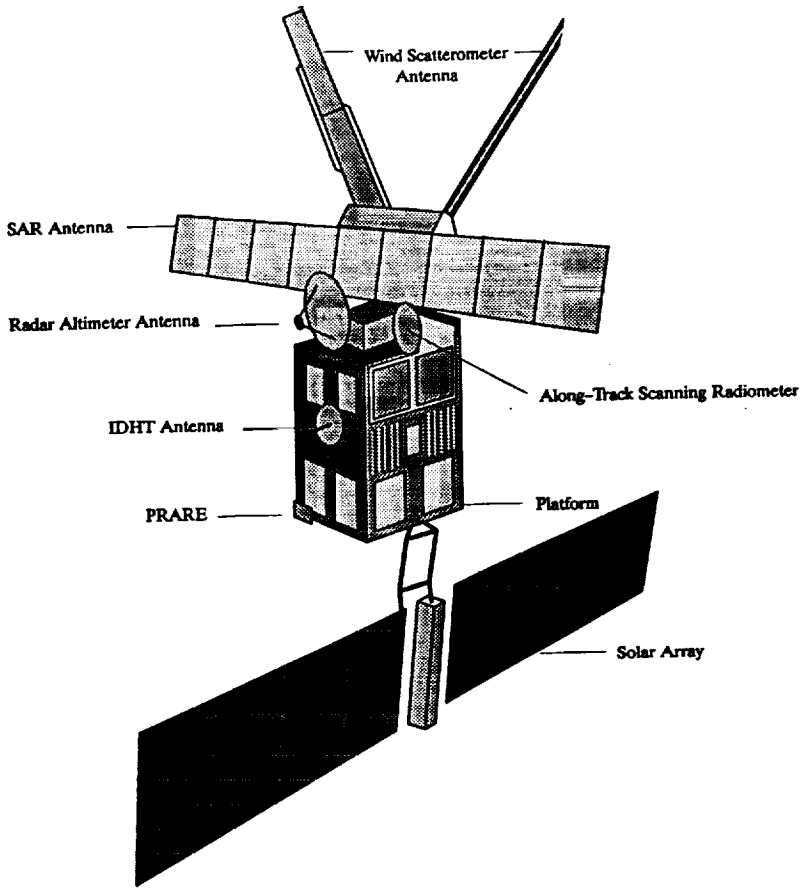

Table 1: ERS-1 Orbit Characteristics

	Repeat Cycle		
	3 days	**35 days**	**176 days**
Revolutions per cycle	43 revs	501 revs	2521 revs
Revs per day	14 + 1/3	14 + 11/35	14 + 57/176
Mean Semi-Major Axis [km]	7153.138	7159.4965	7156.30
Mean Inclination [Degrees]	98.516	98.5429	98.5114
Mean Eccentricity	1.165×10^{-3}	1.165×10^{-3}	1.165×10^{-3}
Mean Argument of Perigee	90.0 deg	90.0 deg	90.0 deg
Mean local solar time of descending node	10h 30min	10h 30min	10h 30min
Longitudinal phase (ascending node) [degrees]	24.36 East(1) 128.2 West(2)	20.9605 East	not decided
(1) Venice (2) ICE Orbit			
Duration	26/07/91-12/12/91 (1) 23/12/91-30/03/92 (2) 16/12/93-01/04/94 (2)	2/4/92-15/12/93	8/4/94-...

2. ERS-1 Laser Tracking Network

The ERS-1 satellite is tracked by a network of globally distributed stations which were funded by many different institutes. In table 2 the stations are listed along with their ERS-1 tracking periods.

In figures 2 to 4 the geographical distribution of the stations is plotted for the first three orbit phases (see table 1). As can be seen, most of the tracking stations are located in Europe and North America. The southern hemisphere is covered only by up to four SLR stations and none of them is located in the south African region. The plots show also the actual tracked ERS-1 orbital passes.

Figure 2: SLR Tracking Coverage within the Commissioning Phase (Venice Orbit)

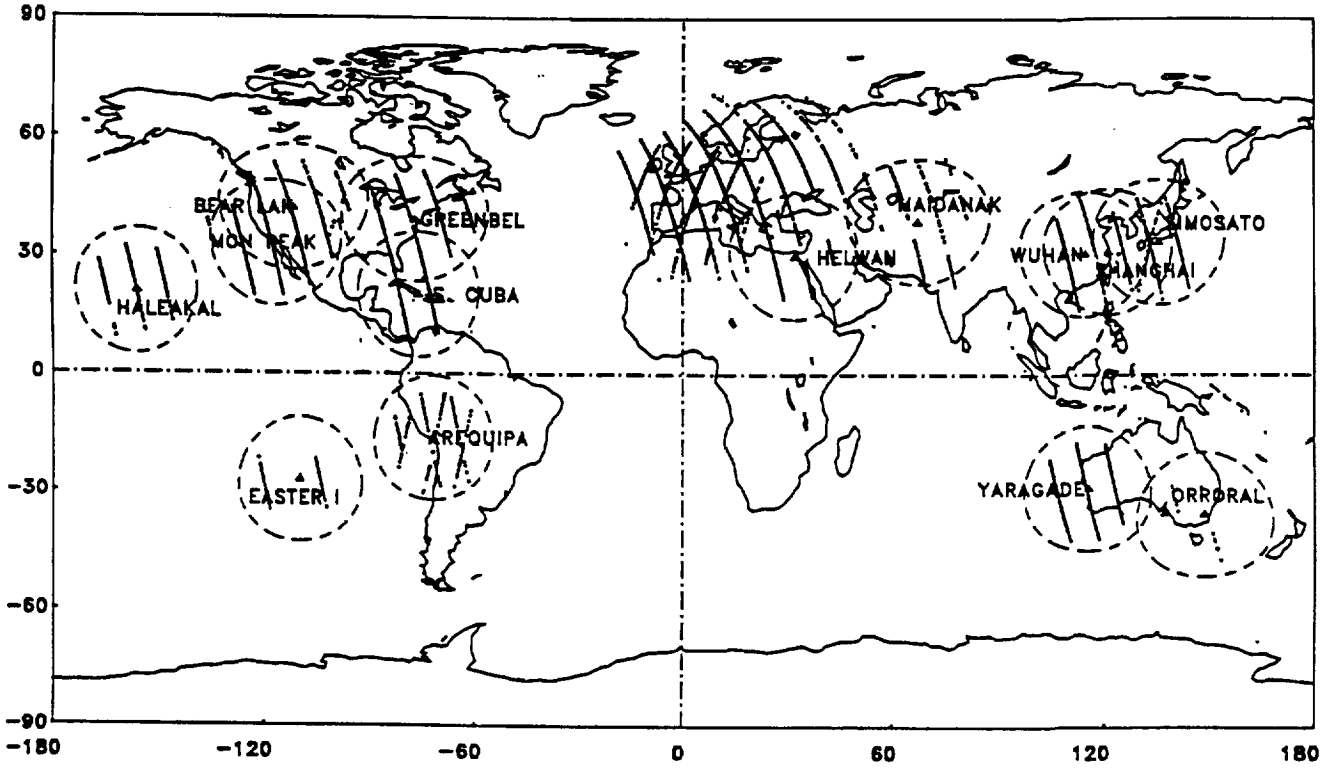

Table 2: ERS-1 Tracking Network Stations

ID	Name	Location	System	Tracking Periods
1181	Potsdam	Germany, Europe	fix	910720 ..
1863	Maidanak	Russia,	fix	910724 ..
1864	Maidanak	Russia,	fix	920421 ..
1873	Simeiz	Russia, Europe	fix	910723 .. 910829 920501 ..
1884	Riga	Latvia, Europe	fix	910731 .. 911028 920225 .. 920226 920401 ..
1893	Katzively	Russia, Europe	fix	920422 .. 920515
1953	Santiago de Cuba	Cuba, Carribean	fix	910808 .. 910922 911127 ..
7046	Bear Lake	USA, North America	TLRS-4	910906 .. 911015
7080	Fort Davis	USA, North America	fix	910822 .. 910822 911121 .. 920124 920318 ..
7090	Yarragadee	Australia	MOBLAS-5	910731 ..
7097	Easter Island	Chile, Pacific	TLRS-2	911018 .. 920311
7105	Greenbelt	USA, North America	MOBLAS-7	910802 ..
7109	Quincy	USA, North America	MOBLAS-8	911211 ..
7110	Monument Peak	USA, North America	MOBLAS-4	910725 .. 920306 920504 ..
7210	Haleakala	Hawaii, USA	fix	910731 ..
7236	Wuhan	China, Asia	fix	910929 .. 920222 920404 ..
7403	Arequipa	Chile, South America	TLRS-3	910731 .. 911010
7512	Kattavia	Greece, Europe	MTLRS-1	920328 .. 920426
7542	Monte Venda	Italy, Europe	MTLRS-2	910729 .. 910917
7810	Zimmerwald	Switzerland, Europe	fix	910719 ..
7811	Borowiec	Poland, Europe	fix	910807 .. 910818 911002 .. 911006 920107 .. 920121
7824	San Fernando	Spain, Europe	fix	911029 .. 920327 920505 ..
7831	Helwan	Egypt, North Africa	fix	910803 .. 911131 920226 ..
7835	Grasse	France, Europe	fix	910717 ..
7837	Shanghai	China, Asia	fix	910816 ..
7838	Simosato	Japan, Asia	fix	910720 ..
7839	Graz	Austria, Europe	fix	910722 ..
7840	Herstmonceux	Great Britain, Europe	fix	910719 ..
7843	Orroral	Australia	fix	910725 .. 910729 911117 .. 911117 920119 .. 920127 920414 ..
7882	Cabo San Lucas	Mexico	TLRS-4	920319 ..
7883	Ensenada	Mexico	TLRS-4	911113 .. 911126 920109 .. 920208
7907	Arequipa	Chile, South America	fix	911129 .. 911129
7918	Greenbelt	USA, North America	TLRS-3	920107 .. 920115 920404 ..
7939	Matera	Italy, Europe	fix	910724 ..
8834	Wettzell	Germany, Europe	fix	910918 .. 910918 920305 ..

MOBLAS	mobile laser system
MTLRS	modular transportable laser system
TLRS	transportable laser system

Figure 3: SLR Tracking Coverage within the First Ice Phase (Ice Orbit)

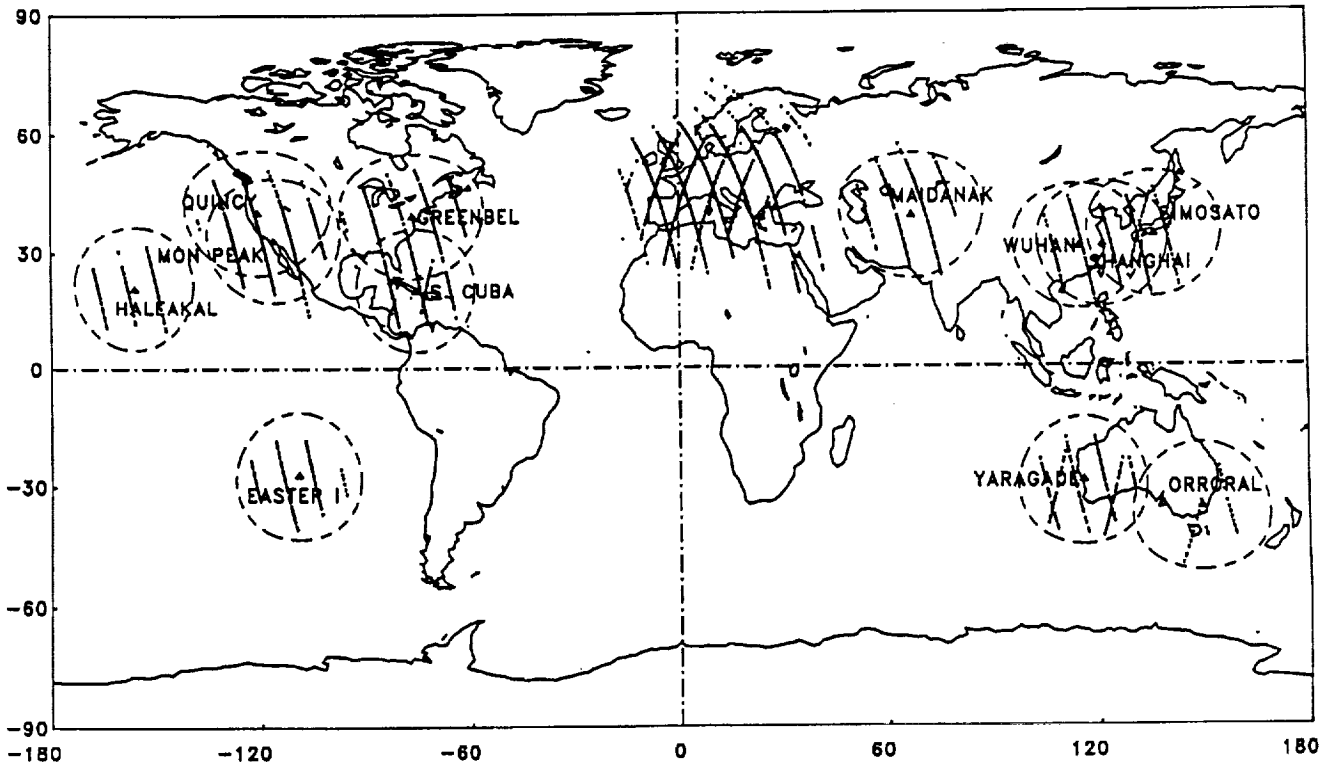

Figure 4: SLR Tracking Coverage within the first Month of the Multidisciplinary Phase

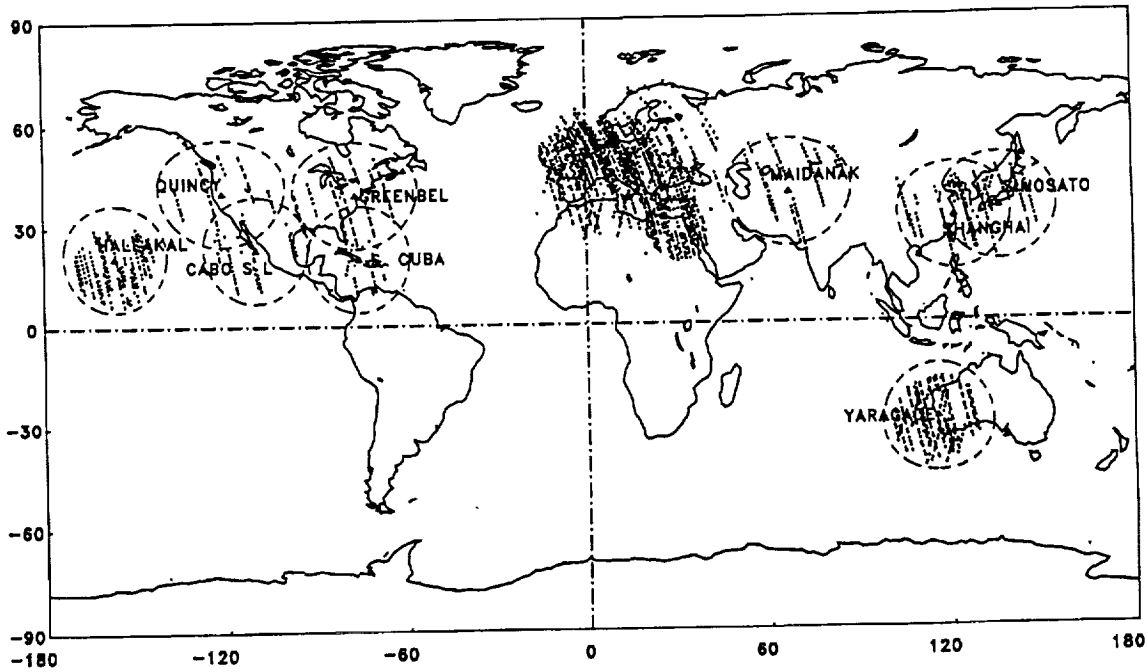

3. Data Flow to D-PAF Systems

Soon after the tracking of a satellite pass the SLR data is preprocessed at the station:

- a first data screening is performed by most of the stations;
- then from each pass about 50 data points were selected (quick-look (Q/L) data) or
- the measurements were compressed into onsite normal points (ONP).

This Q/L or ONP data is then transmitted to the Data Analysis Center at D-PAF. There are two centers collecting and forwarding the data: the data from the CDSLR stations is transmitted via existing internal links to the CDSLR headquarters and then forwarded to CDDIS; the second center is at the European Data Center (EDC) at DGFI. EDC is collecting all data from the European systems (EUROLAS) and also from stations in Russia, Cuba and China. From these two data centers D-PAF is retrieving the collected data files on a daily basis and merges them with data from those stations which have sent their data directly to D-PAF.

The data transmission is performed by using all currently available communication links: telex, Span, Bitnet, Internet, GE/MARK III and ftp.

After having applied all necessary corrections the full tracking data set (full-rate (FR)) is transmitted to the two centers, usually by CCT or Span. Again D-PAF retrieves the FR data sets from CDDIS and EDC and merges them with the directly received files.

It has to be noted, that all three parties exchange their data to have the full information available for all partners. In the beginning of the mission when EDC was not established D-PAF performed the EDC activities too.

According to the work distribution between the four European processing and archiving facilities (PAF) D-PAF is responsible for the generation of operational precision orbital products and for a processing of SAR data. In order to fulfill these tasks D-PAF has set up a number of processing systems. Used for the orbit generation are:

- the telecommunication system (TCS)
- the data management system (DMS)
- the **tracking and orbit determination system (TOS),** which consists of the following subsystems:

  preprocessing subsystem: preprocessing of incoming data, generation of normal points from laser and altimeter data

  orbit determination subsystem: differential orbit correction by numerical integration methods, quality control, generation of numerical and graphical products

  orbit prediction subsystem: orbit extrapolation, generation of orbit prediction sets in different formats, generation of time bias functions, quality control

  earth gravity modelling subsystem: processing of surface gravity data, reduction and solution of normal equation systems, quality control

4. Station Performance

At D-PAF all incoming data is checked for quality and statistics are generated. On a weekly basis Q/L reports are generated presenting incoming data statistics and data quality check information. This paragraphs will present some of the statistical information.

As already seen in figures 2 to 4 only a small part of the ERS-1 orbital path is observed by the ground stations and this is mainly located north of the equator. Especially over South America the situation became worse from the first to the second phase and in the first month of the multidisciplinary phase there is no tracking in that part of the world.

From the figures it is also visible that mainly the ascending arcs were observed by the stations, while only a few descending arcs were tracked. The reason probably is that the descending passes can be tracked only during daylight.

Figure 7 presents the variation in the number of stations observing ERS-1 per day. It ranges from 0 to 13 and shows clearly a decrease for the months October 91 to March 92, when ERS-1 was not in sunlight for many of the stations. A corresponding trend is visible in figure 9 which depicts the number of passes per week. For an arc of 7 days about 30 to 60 passes are available.

Figure 7: ERS-1 SLR Stations per Day

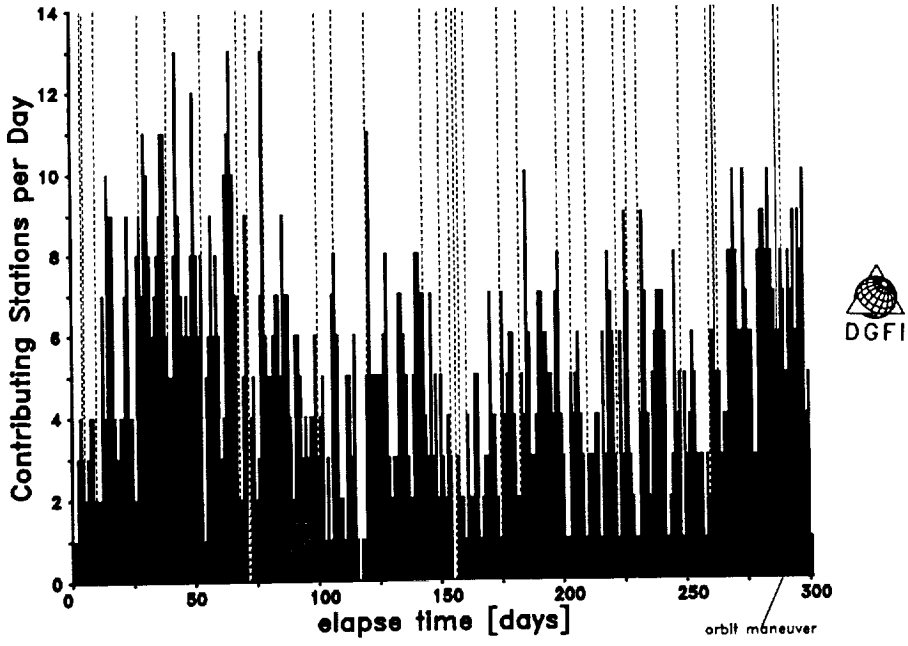

There is also a wide range in the number of passes being tracked by different stations. As can be seen from figure 8 this varies from 1 to 217. But one has to keep in mind that not all stations were continously tracking, some were occupied only for a short while (e.g. Monte Venda, see table 2). The tracking contribution of some stations to the total ERS-1 tracking ranges from a few percent to almost 15 percent (Grasse).

Figure 8: Acquired ERS-1 SLR Passes per Station

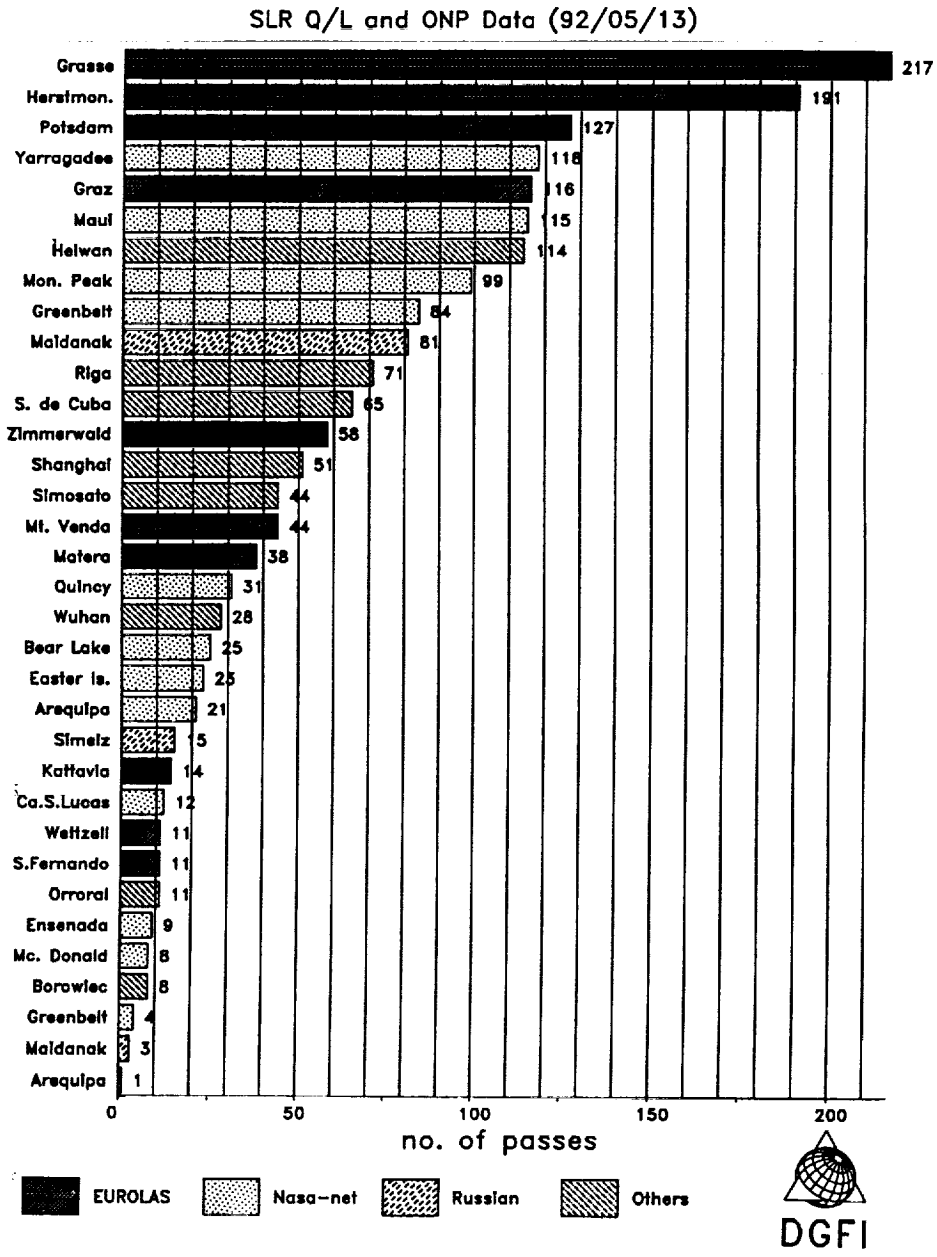

Not only the data quantity is varying from station to station, but also the data quality is different. There are some stations with single shot precision of about 20 cm and others with 1 cm and less. Figure 10 depicts the station performance in terms of single shot and 15 sec. normal point accuracy for some stations.

Figure 9: Acquired ERS-1 SLR Passes per Week

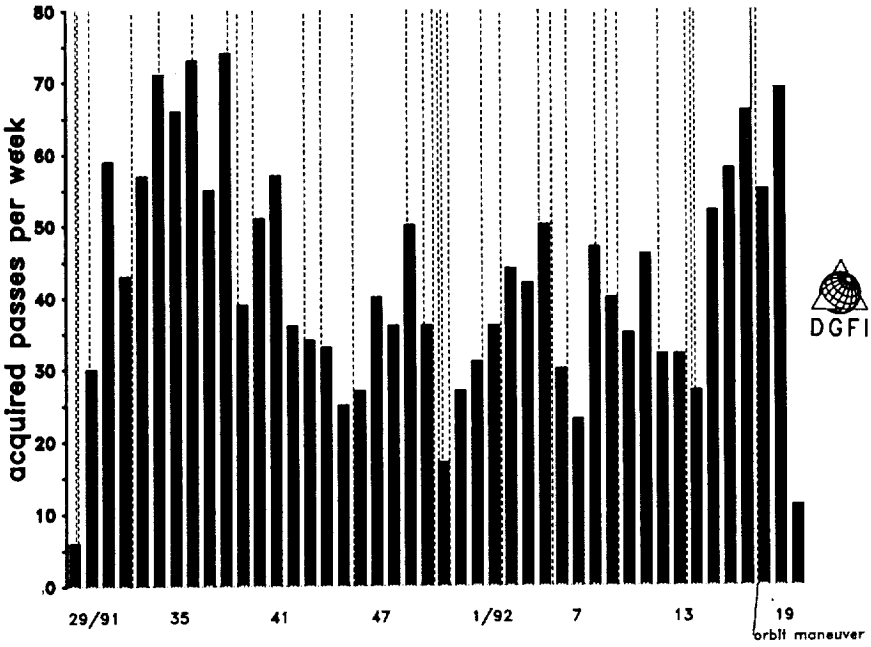

Figure 10: ERS-1 Tracking Precision per Station (cm)

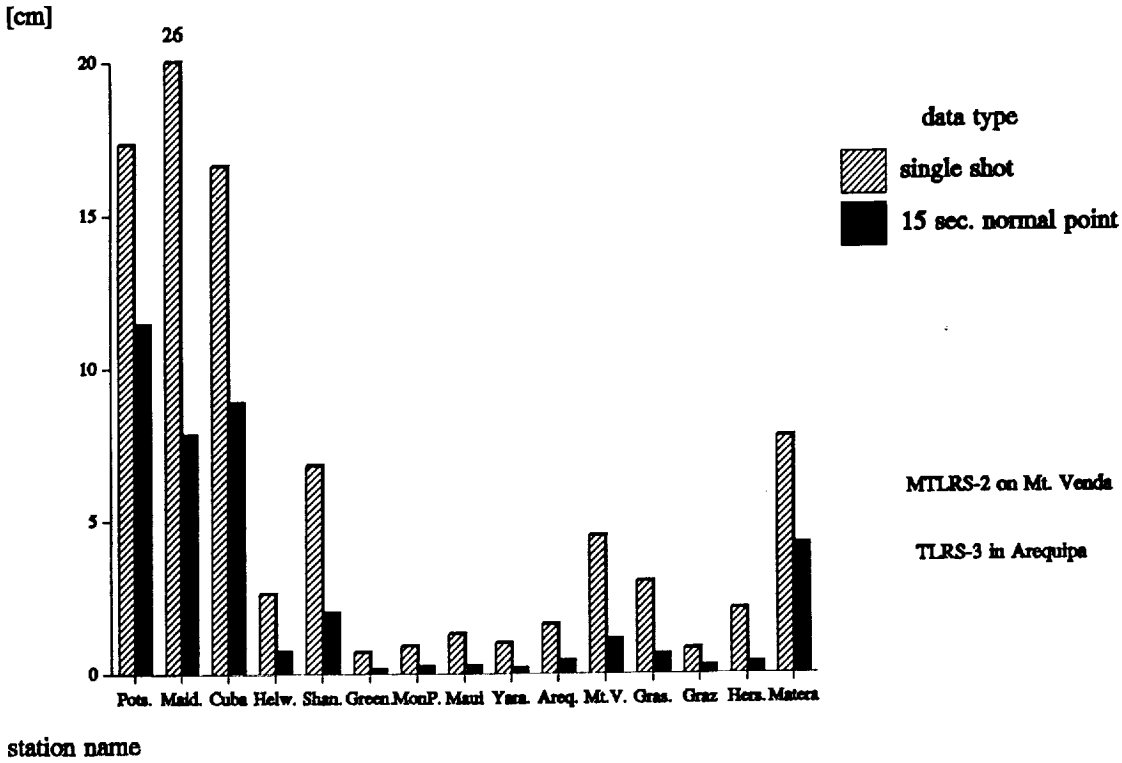

5. Orbit Determination at D-PAF

In order to provide ERS-1 precision orbits the following ERS-1 orbital products are routinely generated and distributed:

- orbit predictions and time bias functions
- preliminary orbits
- precise orbits

The latter two products are official ESA products, while the first one is an internal one. More details about the ERS-1 orbit predictions can be found in König et.al. (1992). A detailled description of all radar altimeter and tracking data products is presented in Bosch et.al. (1990).

The overall data flow for the orbit determination processes is explained in figure 11.

Figure 11: Orbit Determination Data Flow

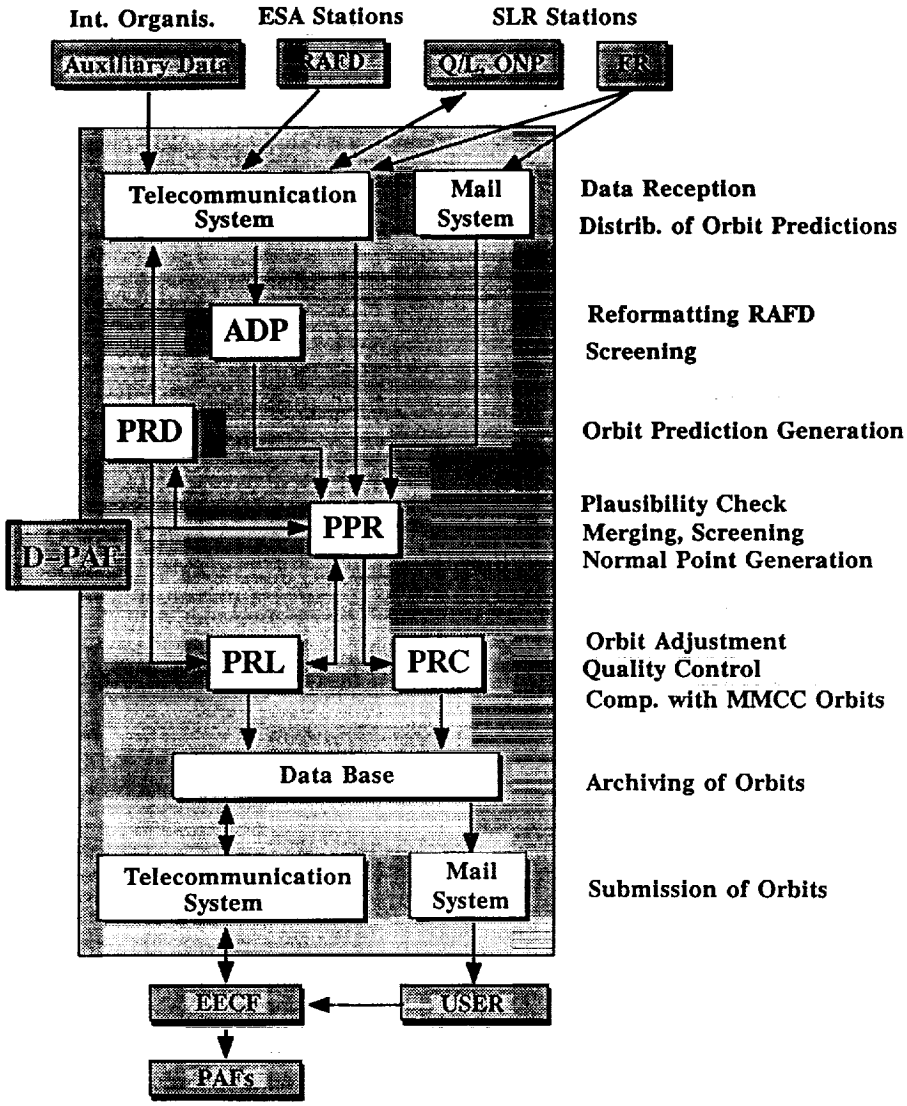

The processing schemes are outlined in figure 12 for manoeuvre free periods.

Figure 12: Processing Scheme

(for manoeuvre free periods)

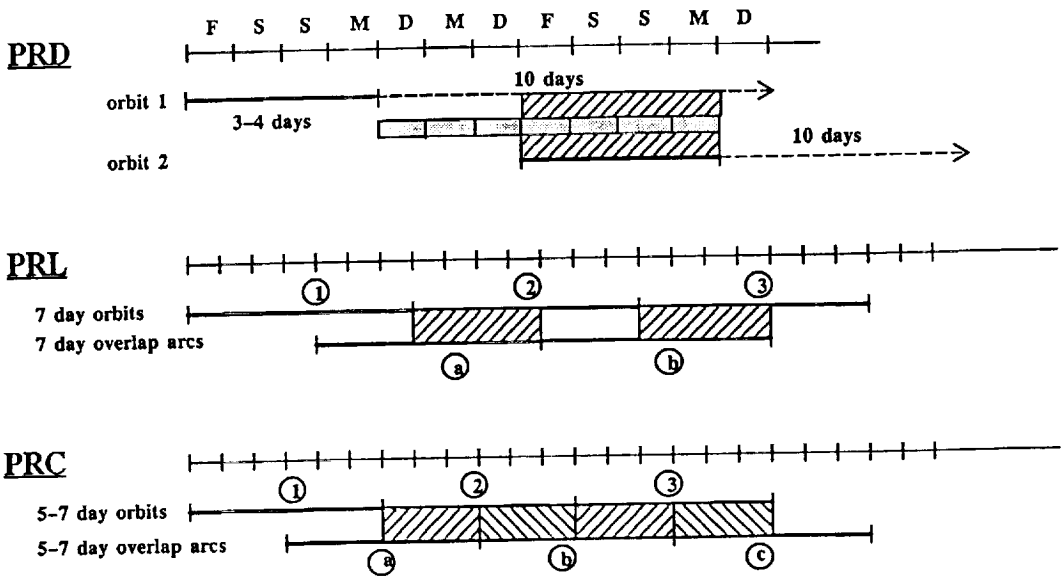

5.1 Preliminary Orbit Determination

Preliminary orbits are computed on a weekly basis by using Q/L laser and radar altimeter fast delivery (RA-FD) data and are usually available within two weeks. Both data sets are compressed into normal points (15 sec. bins for SLR, 10 sec. bins for RA-FD) after first quality checks. As can be seen from figure 14, the use of RA-FD data improves the global coverage especially for arc with only a few SLR passes.

In manoeuvre free periods weekly arcs are computed plus another 7-day arc which is overlapping by 3-4 days and is used for quality assessment (see figure 12). The models for the orbit determination are described in Zhu and Reigber (1991) and Massmann et.al. (1992). Solve-for parameters are the six orbital elements at epoch, one solar radiation coefficient, daily/half-daily drag coefficients, altimeter range bias (if RA-FD data is used) and station coordinates (for new stations only).

The resulting orbital fits are usually around 50-80 cm, in case of bad data coverage up to 130 cm. Figure 13 presents the quality control results from overlapping arcs for 1991 and 1992. The large values in November 91 are resulting from a period with no useful RA-FD data and only a very few laser passes. The same hold for the end of December 91.

Figure 13: PRL Precision Assessment by Overlapping Arc Comparison

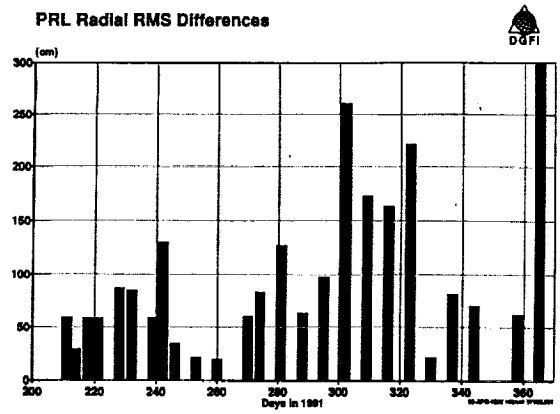

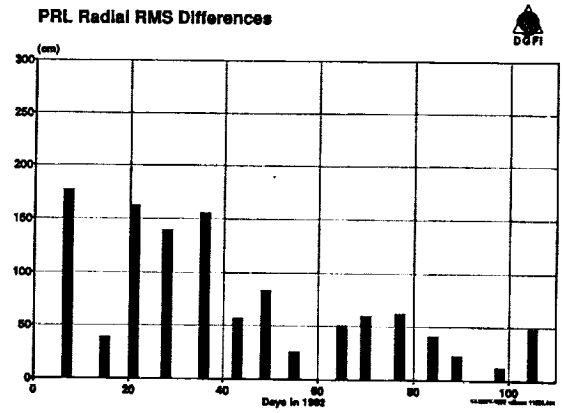

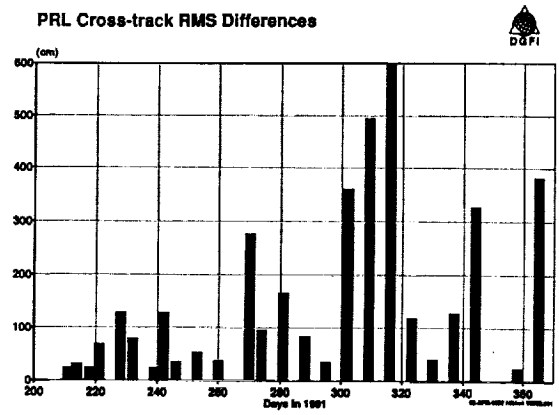

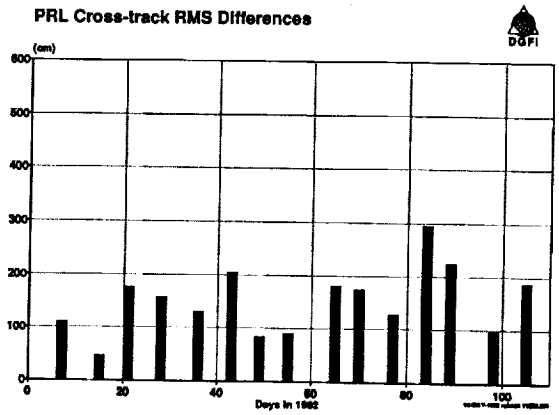

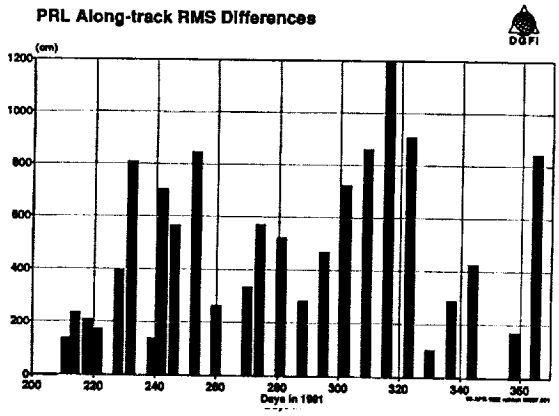

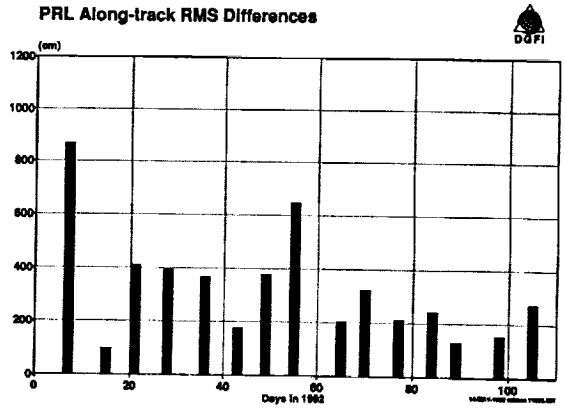

Figure 14: Input Example for the Preliminary Orbit Determination

(January 20-27, 1992)

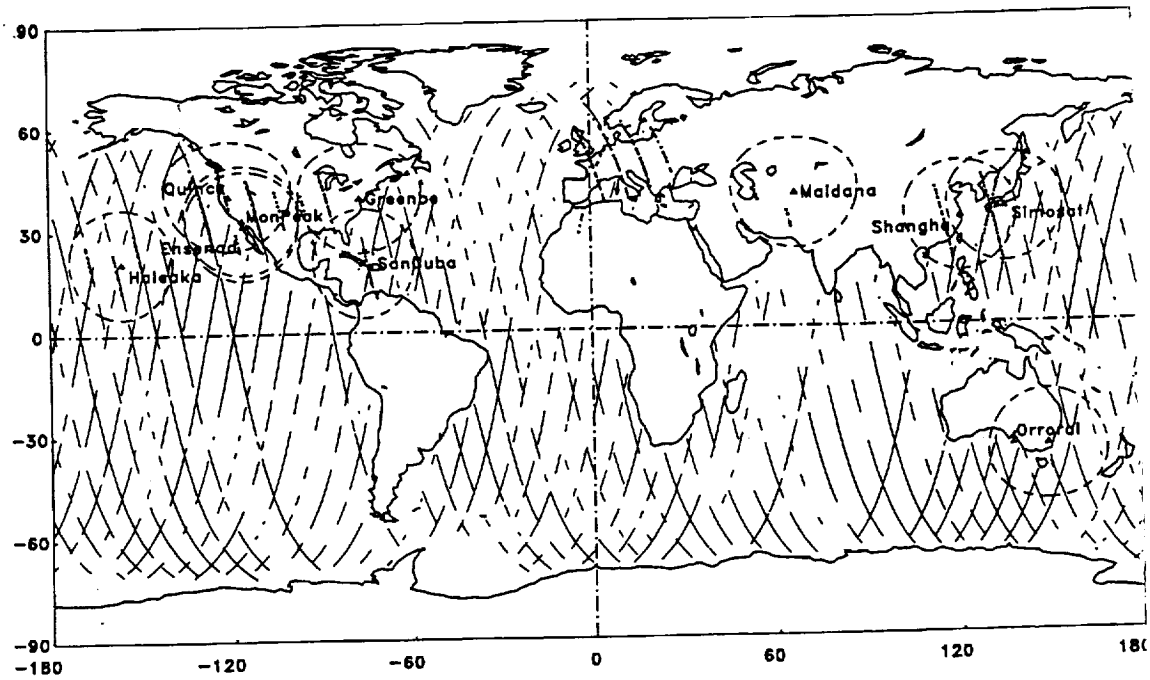

5.2 Precise Orbit Determination

The precise orbits are based up to now only on laser data which have been compressed into 15 sec. normal points. The orbits are computed with a delay of 3-6 months depending on the availability of all FR laser data at D-PAF. The arc length is choosen to fit as good as possible in between two manoeuvres and is usually in the range of 5-7 days. The quality control is also performed by overlapping arc comparison. Models and solve-for parameters are the same as for the preliminary orbits, except the earth rotation parameters, the geomagnetic indices and the solar flux data, which are now the official final values instead of predicted or preliminary ones.

Figure 15 presents the resulting rms orbital fit values for the precise orbit arcs generated up to now while figure 16 shows the quality estimates from the overlapping arc comparison. When comparing figure 13 and 16 one has to be careful, because the arcs are not the same. But generally one can say that the PRC results are more homogeneous and do not show large spikes due to better input data and a more intensive data handling. The most interesting radial component of the orbit seems to be accurate to 50 to 60 cm.

Figure 15: PRC Orbital Fits

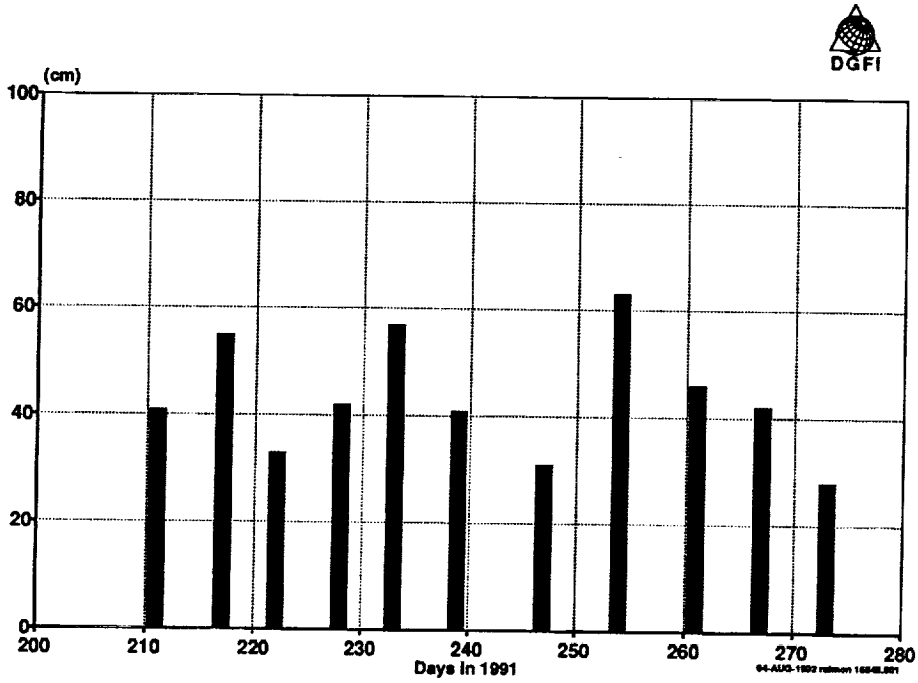

Figure 16: PRC Precision Assessment by Overlapping Arc Comparison

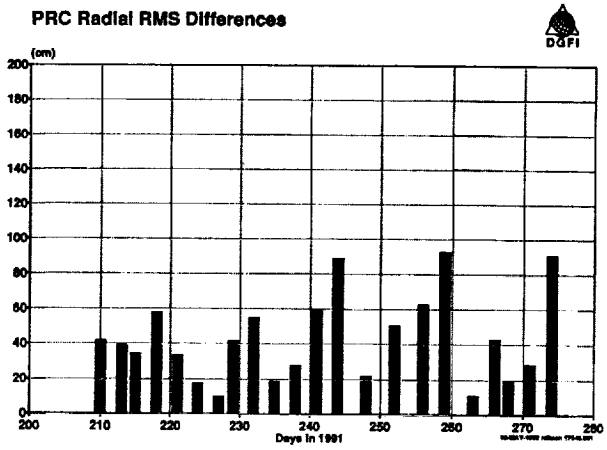

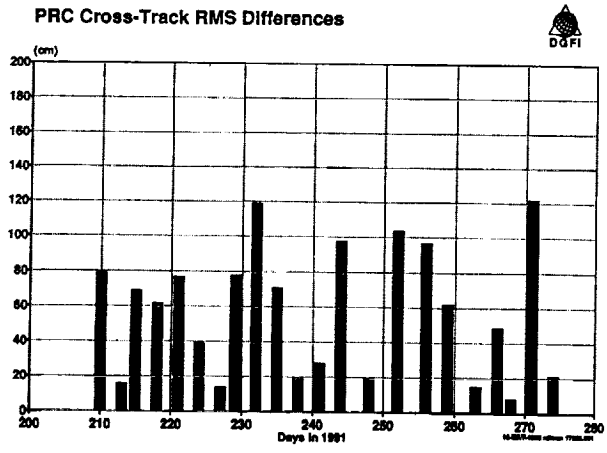

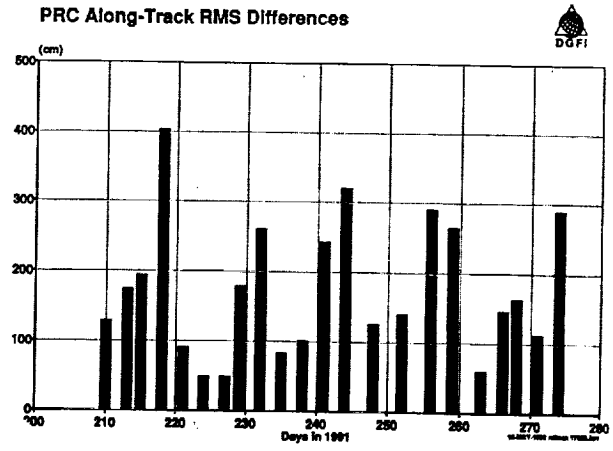

6. Conclusion

Soon after the ERS-1 launch DGFI/D-PAF has started the orbit computations and demonstrated its capability to generate good quality orbits on an operational basis. On the other hand the SLR stations have demonstrated their capability to track ERS-1 and provide high quality tracking data.

Nevertheless there are a few things that could be improved: The accuracy of the generated preliminary and precise orbits is very much limited by the spatial and temporal coverage of the SLR data.

Up to now there are only a few stations in the southern hemisphere of which only one has a good tracking record. On the African continent only one tracking station can be found and that is located in North Africa (Helwan). On the northern hemisphere some gaps can be identified over Russia.

The temporal coverage suffers from the fact that mostly the ascending ERS-1 arcs (night passes) were tracked by the stations. A reason for that is partly the missing daylight tracking capability of the station, partly tracking restrictions and partly man power problems.

Due to the data coverage it is difficult to model large ERS-1 drag perturbation, especially during periods with high solar activity. Tests are initiated to improve this by using either drag information derived from Spot2 Doris data or by using crossover altimeter data.

References

Bosch, W., Flechtner, F.,König, R., Massmann, F.-H., Reigber, Ch., Schwintzer, P. and Wilmes, H., 1990. **The German PAF for ERS-1: RAT Product Specification Document.** D-PAF/DGFI, Document ERS-D-PSD-30000, Issue 1.1, München.

König, R., Li, H., Massmann, F.-H., Raimondo, J.C. and Reigber, Ch., 1992. **On the Accuracy of ERS-1 Orbit Predictions,** this proceedings

Massmann, F.-H., Reigber, Ch., Raimondo, J.C. and Rajasenan, C., 1992. **Operational ERS-1 Orbit Determination at D-PAF,** Proceedings of the Sixth International Geodetic Symposium on Satellite Positioning, Columbus, Ohio

Zhu, S.Y. and Reigber, Ch., 1991. **The German PAF for ERS-1: ERS-1 Standards used at D-PAF.** D-PAF/DGFI, Document ERS-D-STD-31101, München.

Laser ranging application to time transfer using geodetic satellite and to other Japanese space programs

Hiroo KUNIMORI*, Fujinobu TAKAHASHI*, Toshikazu ITABE*
and Atsushi YAMAMOTO**

* Communications Research Laboratory, 4-2-1 Nukui-kita, Koganei-shi, Tokyo 184 Japan
** Maritime Safety Academy, Wakaba-Cho 5-1 Kure-shi, Hiroshima 737 Japan

ABSTRACT

Communications Research Laboratory (CRL) has been developing a laser time transfer system using a satellite laser ranging (SLR) system. We propose Japanese geodetic satellite 'AJISAI' , launched in 1986 as a target satellite. The surface is covered not only with corner cube reflectors but also with mirrors. The mirrors are originally designed for observation of flushing solar light reflected by the separate mirrors while the satellite is spinning. In the experiment, synchronized laser pulses are transferred via specified mirror from one station to another during the satellite is up on the horizon to both stations. The system is based on the epoch timing ranging system with 40 ps ranging precision, connected together with UTC(CRL). Simulation study indicates that two stations at thousands of km distance from each other can be linked with signal strength of more than 10 photons and the distributed images of laser beam from AJISAI mirrors give many chances to two stations to link each other during a single AJISAI pass.

In other topics on the application to Japanese space programs, Retro-reflector In Space for Advanced Earth Observation Satellite (ADEOS) and RendDezVous docking mission of Experimental Technology Satellite-VII (ETS-VII) are briefly presented.

1. Laser Time Transfer via Geodetic Satellite AJISAI

1.1 Introduction

Users of time and frequency standards have been able to take a variety of time comparison techniques even if they pursue the highest accuracy. The precision of GPS common view observation, for example, have got to several few nano seconds and 1 ns or higher precision have been attained by radio techniques such as two way time transfer via satellite (Ref.1). The requirement of such an extremely high precision may exist in deep space navigation, space geodesy, relativity physics and astronomy which always demand extreme precision and accuracy in their measurements. In addition to the radio techniques, time transfer using optical pulses has recently been suggested as one of potential for giving precision of sub-nano or picosecond time transfer to overcome the maximum bandwidth of radio waves (Ref.2).

Satellite laser ranging (SLR) have progressed as one of space geodetic techniques in the field of global geodesy and geophysics. Some SLR stations measure the range to as precise as 30 ps or higher (Refs. 3,4). Since the SLR system is essentially a highly precise epoch recorder transmitting and receiving of optical pulses, a combination of two or more SLR systems has potential as a highly precise time comparison and transfer system.

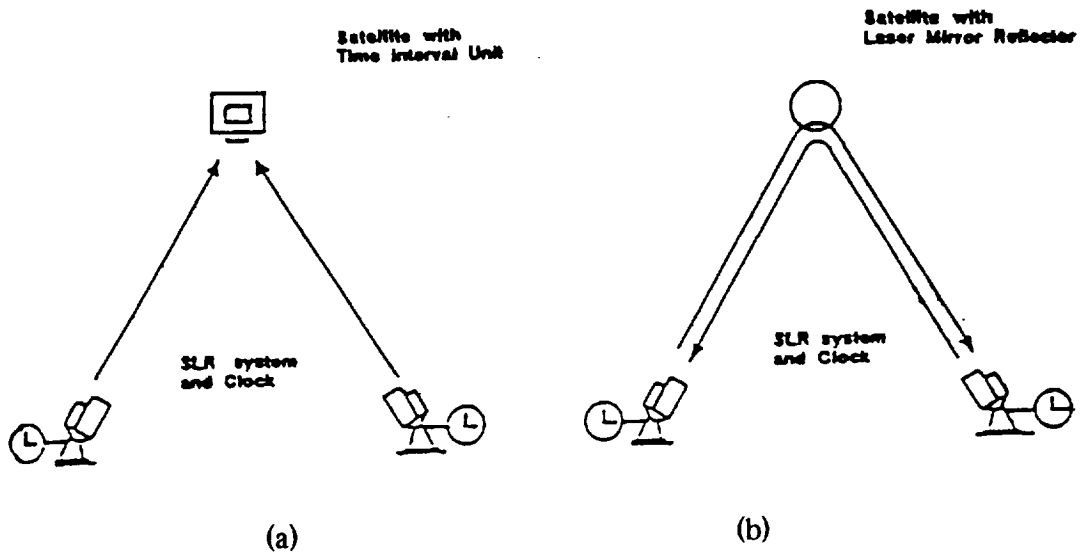

(a) (b)

Fig.1 Configuration of Laser time transfer
(a) One way uplink (LASSO) (b) Two way

There are two configurations considered for ground-based-laser time transfer system using a satellite (See Fig.1). The first is called the one-way up-link configuration. Both SLR stations transmit a laser pulse to the time interval unit (TIU) on the satellite and the TIU measures the interval between their arrival times. Such an optical time comparison has been performed in Europe in the LASSO experiment (Refs. 5,6). In the LASSO experiment of European phase, laser echoes were successfully received at Grasse, France and at other European laser ranging sites. The second is the two-way configuration. Each station transmits a laser pulse to the other station via a satellite with mirror reflectors. The satellite also has corner cube reflectors for conventional SLR, and they are used to determine the distance from each station to the satellite to give support to the time transfer solution. In this paper, we examines the two-way configuration using the Japanese SLR satellite AJISAI, including time transfer concept, calibration methods, signal strength and spatial distribution of the reflected beam. The system performance is based on the CRL SLR system (Refs. 7,8), including additions to be made for two-way time transfer.

1.2 Target satellite AJISAI

Table 1 : Major specifications of AJISAI

Launch Date:	August, 1986		
Configuration:	Polyhedron inscribed in sphere of diameter 2.15 m		
Weight:	685kg		
Corner cubes:	1436 pieces,	Effective area :91.2 cm^2	
Number of mirrors	:318 pieces,	Curvature of mirrors	:8.4-9 m
Reflective efficiency:	0.85,	Brightness :	1.5-3.5 star mag.
Duration of a flash :	. 5 msec,	Rate of flashing :	2 Hz
Spin rate:	40 rpm		
Launch orbit:	Altitude 1500 km,		
	Inclination 50 deg,	Eccentricity	0.001

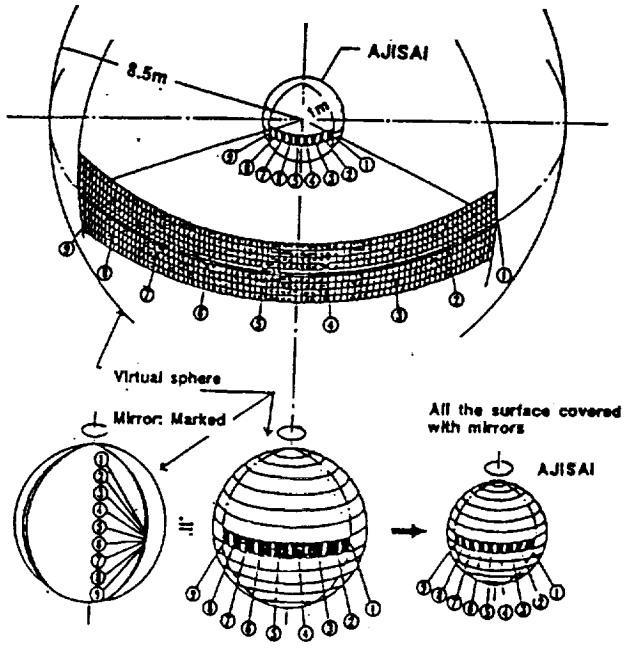

Fig.2 Arrangement of mirrors on AJISAI
Parts of an 8.5m radius virtual sphere (mirror) is placed on the surface of the 1-m radius AJISAI maintaining their latitude angles.

AJISAI is the Japanese geodetic satellite launched in 1986 by the National Space Development Agency (NASDA). The major specifications of AJISAI are listed in Table 1. The satellite is a hollow sphere 2.15 m in diameter and weighs 685 kg. The surface is covered with mirrors as well as corner cube reflectors. The orbit is a circular with an inclination of 50 degrees and an altitude of 1500 km (Ref.9). The mirrors were originally designed for observing flashing solar light reflected by separate mirrors while the satellite is spinning at about 40 rpm. Each mirror is a piece of a surface with a radius of curvature of 8.5 m. Three elements from the same latitude of the 8.5-m sphere at longitudes of 0, 120 and 240 degrees are put on the surface of a 1-m radius satellite retaining the phase angle of the original sphere (See Fig.2). The latitudes from which every set of three is taken are uniformly selected from the original surface so that a distant observer can observe the light reflected from the front surface flashing three times per rotation.

1.3 Two way time transfer

The equation for two-way time transfer via laser pulse is in principle the same as those being developed in radio frequency band (Ref. 1). The time difference d_{12} (: positive when clock 1 is ahead of clock 2) between the clocks of stations 1 and 2 is given by:

$$d_{12}= (t_{21}-t_{12}+t_1-t_2)/2 + (R_{12}-R_{21})/2c \quad (1),$$

where : $(i,j=1, 2)$,

t_i : Epoch of pulse departure at station i measured by station clock i ,

t_{ij} : $(i$ .NE.$j)$ Epoch of station i 's pulse reflected by a satellite mirror arriving at station j measured by station clock j,

R_{ij} : (i .NE.j) One-way distance of a laser pulse to travel from station i to station j via the satellite, and

c: speed of light.

The last term $(R_{12}-R_{21})/2c$ is expected to be nearly zero because of the good symmetry of travelling paths, but not negligible due to the effect on motions of both satellite and stations. It is related to the difference between the satellite position at the times the two laser pulses arrive. It approaches zero if the two pulses arrive at nearly the same time on the satellite. This is done by controlling the firing timing at both stations. Timing control within the precision of 1-ms is necessary to obtain a station to station link by a mirror of AJISAI with 20cm x 20cm size spinning at 40 rpm. If the laser fire timing is controllable to 1μs, $(R_{12}-R_{21})/2c$ is down to a few ps on the assumption that both the predicted position of the satellite and the clock synchronization are known with the accuracy of less than 1 μs (300 m in distance) before the experiment. The μs firing control can be performed by a fully active mode-locked laser operation. In this observation mode, we can apply the geometric method rather than dynamical one to the orbit solution using SLR range data (Ref.10).

1.4 Laser ranging system

We use an active-passive mode-locked Nd:YAG laser to generate 532 nm wavelength optical pulses 100 ps wide. The passive mode-locking is performed by saturable dye. The energy is 100 mJ per pulse and the nominal repetition rate is 10 pulses per second. The repetition rate can be controlled from 7 to 14 pps by real-time software. If the passive mode-locking by a saturable dye is replaced with an active component, the synchronization of firing timing can be controlled on nanosecond level (Ref.11) .

The receiving telescope aperture has diameter of 1.5 m. A micro-channel plate photo multiplier (MCP-PMT) is used for detector. It has a 300-ps rise time, 8% quantum efficiency and the transit time jitter of less than 30 ps with a constant fraction discriminator. The MCP detector can be also gated temporarily by the prediction of photons arrival in 20-ns time steps.

The timing system consists of a high performance disciplined quartz oscillator, a GPS receiver, and a time interval unit (TIU). Either a GPS timing receiver or cesium clock of UTC (CRL) can keep the reference to UTC. Timing epoch is measured for up to 4 stop events with a resolution of 40-ps.

1.5. Calibration system

In the actual experiment, we must consider that the reference signal of the atomic clock is transmitted to the SLR system via cables and electronics. Furthermore, the laser transmitting and receiving point is not at the telescope reference point.

The cables and electronics delay between the atomic clock and the TIU is monitored by an independent measurement system. Figure 3 is a block diagram of the monitoring system used in the experiment. The combined 5-MHz+1-pps signal from the cesium clock room is transmitted via a 500-m optical fiber. Output signal (50 MHz) of the quartz oscillator is phase-locked by the 5-MHz and used as the reference frequency in TIU. The 1 pps signal is used for the epoch reference of UTC. The 5-MHz and 1-pps signals are combined again at SLR site and are sent back to the clock room. Then delay and phase difference with respect to the original signals are continuously monitored at the clock room. It has been installed to get the characteristics of the long-term stability of the system.

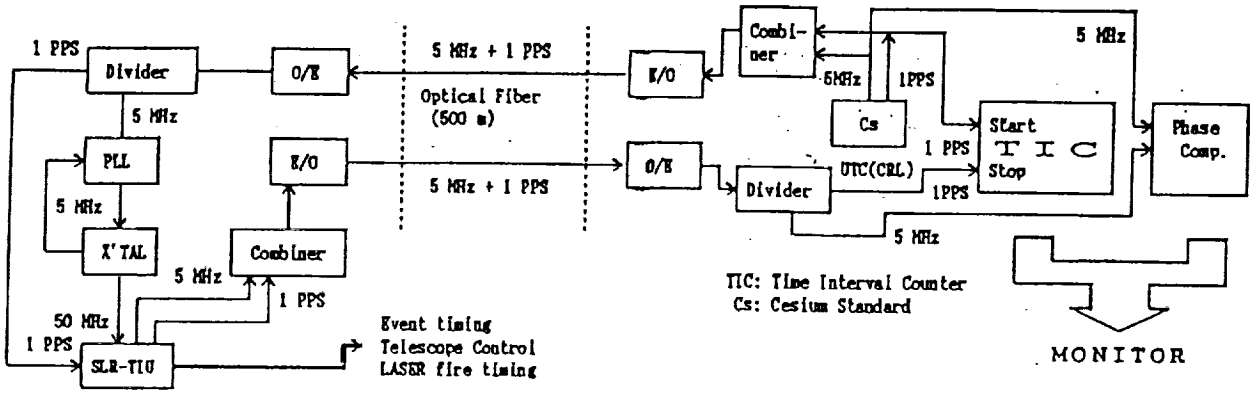

Fig.3 Reference signal monitoring system

The epoch latch point at each laser pulse start and stop must be treated as if these events occurred at the telescope reference point (intersection of two rotation axes). The calibration target is put on the telescope moving axis, as it takes partial reflection of transmitting beam and its physical distance from reference point must be measured precisely.

The time difference between clocks including calibration term (d'_{12}) is given by:

$$d'_{12} = (t_{21}-t_{12}+t_1-t_2)/2 + (R_{12}-R_{21})/2c + \{ (t_{1,a}-t_{1,b})-(t_{2,a}-t_{2,b})+(t_{2,x}+t_{2,y}) -(t_{1,x}+t_{1,y}) \}/2 \quad (2),$$

where : (i=1,2), in addition to the parameter defined in Eq.1,

$t_{i,a}$: Optical path delay from firing (laser input) point to telescope reference point at station i,

$t_{i,b}$: Optical path delay from telescope reference point to receiver point at station i,

$t_{i,x}$: Electronic delay from firing point to start-epoch latch gate at station i, and

$t_{i,y}$: Electronic delay from receiver point to stop-epoch latch gate at station i.

In order to calibrate the time difference between clock 1 and 2, each value of parameter in { } in the Eq.2 must be evaluated. The optical delay can be measured by a distance meter or by scales, and it will be stable in time unless optical design is changed. To cancel out the electronic delay, the common portable receiver can be collocated at two stations. This measurement would still have errors coming from the dependence on signal strength and temperature.

1.6 Link budget

In the laser time transfer experiment, the number of photons (N_p) detected at the remote ground station are calculated according to the following equation:

$$N_p=(E\lambda/hc)\cdot(r_1r_2r_3r_4^2)\cdot(16A_sA_r/\pi^2R_1^2R_2^2q_t^2q_s^2) \quad (3)$$

where E : Energy in a pulse, λ : Laser wavelength,

h : Planck's constant, c : Velocity of light,

r_1 : Transmission beam efficiency, r_2 : Receiving beam efficiency,

r_3 : Target reflector reflectivity,
r_4 : Atmospheric transmission efficiency (one-way),
A_s : Total reflector surface area, A_r : Received aperture surface area,
R_1 : Station 1 to satellite distance, R_2 : Station 2 to satellite distance,
q_t : Transmission beam divergence, and
q_s : Reflectors beam divergence for incident light return

Figure 4 shows the expected number of photons for AJISAI mirror reflection and the satellite elevation from stations, assuming the parameters have the values listed in Table 2. We also assume the position of AJISAI is roughly in the middle of the two station's common sky. From stations 2500 km apart, AJISAI is observed at above 40 degrees and more than 10 photons are expected.

Table 2 : Parameters for estimating the number of photons

Satellite Altitude	: 1500km (AJISAI)
Energy of pulse (E)	: 100 mJ
Wavelength (l)	: 532 nm
Transmission efficiency (r_1)	: 0.6 Receiving efficiency (r_2): 0.3
Target reflectivity (r_3)	: 0.9
Atmospheric transmission efficiency (r_4)	: 0.6
Reflector surface area (A_s)	: 0.04 m^2
Received surface area (A_r)	: 0.27 m^2 (60cm aperture)
Transmission beam divergence (q_t)	: 5 arcsec

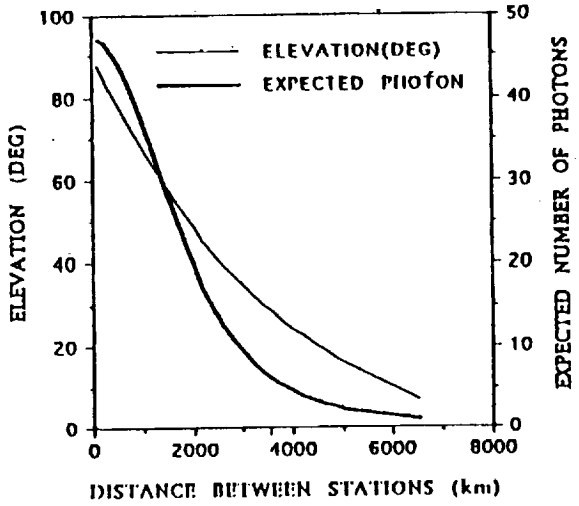

Fig.4 Elevation and Expected number of photon v.s. distance between stations in laser time transfer via AJISAI

1.7 Spatial distribution of laser reflection

We simulate the spatial distribution of laser reflection from AJISAI to study the possibility of an optical link for time synchronization between stations. We calculate first the rotation phase and the incident angle of AJISAI for a given transmitting station and epoch, then project the image onto the ground from all mirrors visible to both stations. The calculation continues according to the given time step.

In Fig.5, each rectangle is the image of the laser reflection on the ground for an instantaneous laser shot and the number by the rectangle shows the reflector number on AJISAI. In Fig.6, three steps of 50 msec (one AJISAI spin) are illustrated successively.

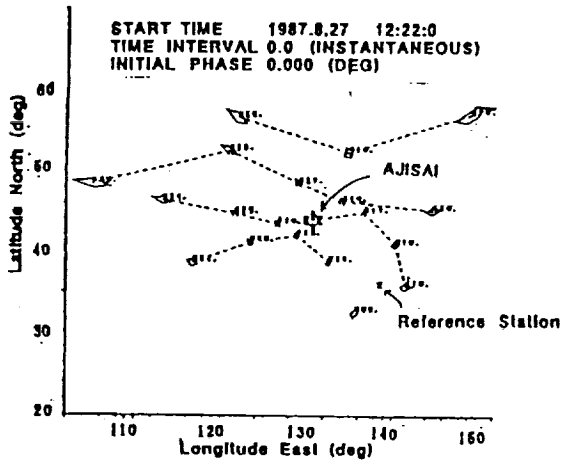

Fig.5 Instantaneous spatial distribution of reflected images on the ground via AJISAI mirror reflector. (The number next to each image indicates the mirror number on AJISAI)

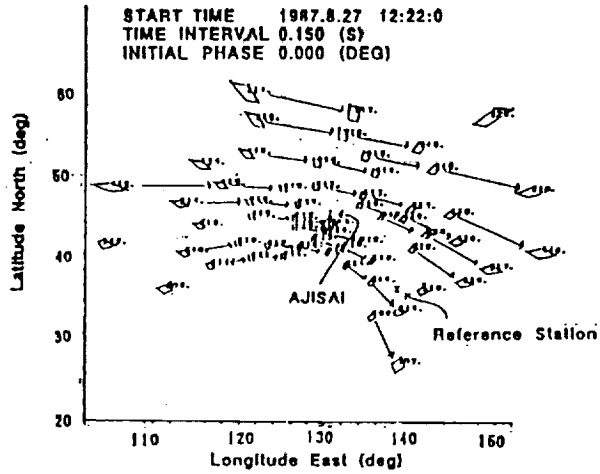

Fig.6 Spatial distribution of reflected images in three 50 msec steps. (The number next to each image indicates the mirror number on AJISAI)

A several percent of East Asia can locate an image, but there is a chance for many stations to get the link every AJISAI pass. If the timing of every shot is as accurate as the prediction, time comparison can be performed on average once every few seconds by simultaneously determining the rotation phase of AJISAI.

2. Application to Japanese Space Program

Table 3 lists the satellite name and its launching schedule in Japanese R&D space program. The schedule is released before the H-II rocket engine explosion which will cause at least one year delay shift from original schedule.

2.1 RIS

Retro-reflector In Space (RIS) is one of missions on ADEOS (Advanced Earth Observing Satellite) satellite which is scheduled for launch in 1996. The orbit is a sun synchronous sub-recurrent polar-orbit with an inclination of 98.6 deg. It has a period of 101 minutes and an altitude of approximately 800 km (Ref.12). RIS is a single element cube-corner

Table 3 R&D Satellite Launching Schedule (1992- 2001), released by NASDA in April 1992

Fiscal year/	Satellite name
1992	JERS-1,FMPT
1993	ETS-VI, SFU
1994	IML-2,SFU
1995	ADEOS
1996	COMETS
1997	TRMM, ETS-VII
1998	JEM-1,2, ADEOS-II
1999	JEM-n
2001	HOPE

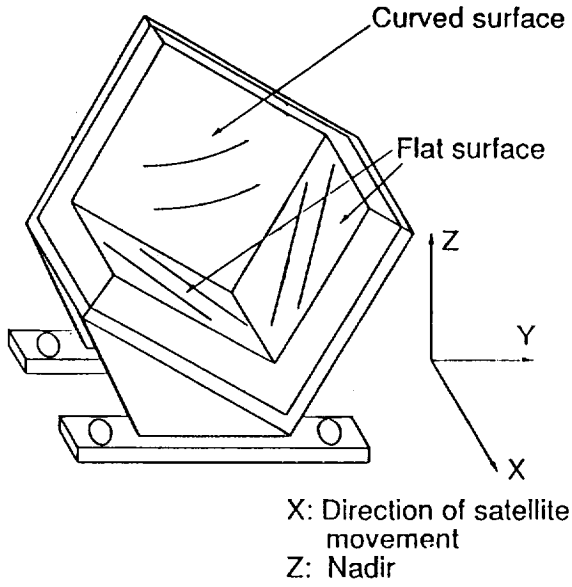

Fig.7 Structure of RIS
(Effective diameter : 50cm)

retro-reflector with a diameter of 0.5 m designed for earth-satellite-earth laser long-path absorption experiments. RIS is proposed by the National Institute for Environmental Studies collaborated with CRL.

In the experiment, laser beam transmitted from a ground station is reflected by RIS and received at the ground station. The absorption of the intervening atmosphere is measured in the round-trip optical path. Figure 7 shows the structure of RIS. We use a slightly curved mirror surface for one of three mirrors forming the retro-reflector, which diverges the reflected beam to overcome the velocity aberration caused by the satellite movement.

We have proposed a simple spectroscopic method which utilizes the Doppler shift of the reflected beam resulting from the satellite movement for measuring the high resolution transmission spectrum of the atmosphere. The wider laser beam is used for illuminating satellite and for autonomous tracking the satellite by guiding camera.

2.2 ETS-VII

NASDA will schedule to launch the Experimental Technology Satellite (ETS-VII) in 1998 whose objectives are development of space robotics and rendezvous control. It consists of two satellites, the chaser and the target, each has GPS receiver for orbit control of chaser. Tentative altitude is 550km and communication to the ground will utilize the data relay satellite.

We have proposed that each satellite should be loaded with corner cube reflector set, one of which is two-color sensitive and be monitored the rendezvous process from the ground. We will track the satellites with switching or simultaneously mode depending on two satellites being within one beam or not.

3. CONCLUSION

We have studied the feasibility of the sub-nanosecond precision laser time synchronization system with a target satellite of AJISAI based on CRL laser ranging system, whose timing system is connected with UTC(CRL).

Simulation study indicates that two stations at thousands of km distance from each other can be linked by laser beam with signal strength of more than 10 photons. The images of laser beam from AJISAI mirrors is uniformly distributed on the ground and two stations have many chances to link each other during a single AJISAI pass. It requires the μsec control of laser fire timing, however, it bring on the precise information of the orbit as well by using the self-returned satellite range data.

The system has been operating in geodetic mode since CRL started the SLR observations to the major geodetic satellites from 1990. While global position of the SLR station has been determined with the precision of several centimeters, we are re-designing our system so that current system has also for time synchronization mode operation as well as adapting for Japanese space program in future.

REFERENCES

1. Kirchner D.,1991, Two-way Time Transfer via communication satellites, Proc. IEEE, Vol.79, No.7, pp.983-990
2. Leschiutta S.,1991, Time synchronization using laser techniques, Proc. IEEE, Vol.79, No.7, pp.1001-1008.
3. Degnan J.J., 1985, Satellite Laser Ranging : Current Status and Future Prospects, IEEE Trans. Geosci. Remote Sensing, GE-23, 4, pp.398-4 13.
4. Pearlman M., & al. 1989 , Ground-based laser ranging measurement techniques and technology, Report of CDP-COOLFONT, section2.1, pp.1-26.
5. Serene B. and Albertinoli P. 1979, The LASSO Experiment, Proc.PTTI 11th conference, pp.145-167.
6. Veillet C. 1989, LASSO - the European Phase Aug.88-Sept.89, Proc.7th International Workshop on Laser Ranging Instrumentation, Matera 2-6 .
7. Kunimori H. & al. 1991, "Satellite Laser ranging system", Journal of CRL, Vol.38, No.2 ,pp.303-317 .
8. Greene B.A. 1984, Epoch timing for laser ranging, Proc. 5th International Workshop on Laser Ranging Instrumentation (Herstmoncex) , pp.247-250.
9. Sasaki M.and Hashimoto H. 1987, Launch and observation program of the experimental geodetic satellite of Japan, IEEE Trans.Geo.Rem., GE-25, 5, pp.526-533.
10. Yang F.M. 1986, The proposal of strictly simultaneous satellite laser ranging, The 6-th international workshop on laser ranging instrumentation, France, pp.549-557.
11. Electro Optic Systems 1991, EOS-V1 Active/Active Laser Characterization .
12. Sugimoto,A., Minato A. and Sasano Y.,1991, Retro-reflector in space for the ADEOS satellite, CREO'91 Baltimore.

APPLICATIONS OF SLR

B.E. Schutz
Center For Space Research
The University of Texas at Austin
Austin, TX 78712, USA

INTRODUCTION

Satellite Laser Ranging (SLR) has a rich history of development which began in the 1960s with 10 meter-level first generation systems. These systems evolved with order of magnitude improvements to the systems that now produce several millimeter single shot range precisions. What began, in part, as an interesting application of the new laser technology has become an essential component of modern, precision space geodesy, which in turn enables contributions to a variety of science areas.

Modern space geodesy is the beneficiary of technological developments which have enabled precision geodetic measurements. Aside fro SLR and its closely related technique, Lunar Laser Ranging (LLR), Very Long Baseline Interferometry (VLBI) has made prominent science contributions also. In recent years, the Global Positioning System (GPS) has demonstrated a rapidly growing popularity as the result of demonstrated low cost with high precision instrumentation. Other modern techniques such as DORIS have demonstrated the ability to make significant science contributions; furthermore, PRARE can be expected to contribute in its own right.

An appropriate question is "why should several techniques be financially supported"? While there are several answers, I offer the opinion that, in consideration of the broad science areas that are the benefactors of space geodesy, no single technique can meet all the requirements and/or expectations of the science areas in which space geodesy contributes or has the potential for contributing. The more well-known science areas include plate tectonics, earthquake processes, Earth rotation/orientation, gravity (static and temporal), ocean circulation, land and ice topography, to name a few applications.

It is unfortunate that the modern space geodesy techniques are often viewed as competitive, but this view is usually encouraged by funding competition, especially in an era of growing needs but diminishing budgets. The techniques are, for the most part, complementary and the ability to reduce the data to geodetic parameters from several techniques promotes confidence in the geophysical interpretations.

In the following sections, the current SLR applications are reviewed in the context of the other techniques. The strengths and limitations of SLR are reviewed and speculation about the future prospects are offered.

SLR Summary

Satellite Laser Ranging measures the round-trip time-of-flight for a laser pulse to travel from a transmitter to a target and back. Current and near-term satellite targets include Starlette (1000 km

altitude), Ajisai (1500 km), ERS-1 (800 km), Lageos (59000 km) and Etalon-1 and -2 (25000 km). Future satellites include TOPEX/POSEIDON (August 1992 launch) and Lageos-2 (October 1992 launch). The geodetic satellites (Starlette, Ajisai, Lageos and Etalon) have a long orbital lifetime measured in thousands of years to millions of years for the high altitude satellites, thereby offering a distinct advantage that the satellite will be available at no cost for a very long period of time. Only the ground segment requires operation and maintenance support. By contrast, all other satellite techniques (GPS, DORIS, PRARE) rely on an active space segment with a lifetime determined by the on-board power system, usually several years. VLBI, on the other hand, uses extragalactic radio sources which will, presumably, be available for a very long time.

Precision Orbit Determination/Gravity

The traditional strength of SLR has been in the ability to determine the orbits of target satellite with high accuracy. In the case of TOPEX/POSEIDON, SLR is the primary means of precisely determining the orbit to the required 13 cm in the radial component in support of radar altimeter analyses. SLR tracking of NASA altimeter satellites has been an important element in the accomplishment of the respective mission goals. SLR, however, has a distinct disadvantage created by dependency on atmospheric transparency. Radiometric systems, such as GPS and DORIS, are potentially able to provide essentially continuous tracking. Since TOPEX/POSEIDON includes SLR, GPS and DORIS, it will provide a unique opportunity to evaluate the performance of all systems. The focus of tracking systems on future satellites may be GPS with SLR as a backup. Nevertheless, it is important to note that the passive nature of SLR provides an extremely reliable space segment--it simply will not fail except under catastrophic circumstances. A cautionary note for the future is in order. The risk of regarding SLR as a backup system encourages the reduction in operating systems for budgetary reasons, but as systems close, it becomes more difficult to reactivate them in the event that the backup mode must be initiated.

Improvements in the gravity field, including the gravitational parameter GM, are other areas where SLR has made very significant contributions. The development of new models in preparation for TOPEX/POSEIDON have benefitted from the SLR data base that has been accumulated over the years, some of which has been used in previous fields and some has not. Gravity fields used for GPS applications, such as the Department of Defense WGS-84, have used SLR data from Lageos and Starlette which have particularly contributed to determination of low degree and order gravity coefficients. Current GPS applications use GEM-T3 or other, more recent fields, which have relied on SLR data. Furthermore, the Etalon satellites can be used to study gravitational effects that will be somewhat similar to those influencing the GPS satellites, except for the particular GPS effect of deep gravitational resonance.

SLR has made unique contributions to the study of temporal variations in the gravity field, both tidal and non-tidal variations. These studies have, in part, been made possible by the nature of low area-to-mass ratio satellites (Lageos and Starlette), which diminish the nongravitational forces. This diminishment enhances the opportunity to identify the spectral content of gravitational effects. Furthermore, the study of temporal changes in gravity has been enhanced by the ability to investigate the orbit evolution over long periods of time, spanning in some cases more than 15 years.

Earth Orientation/Reference Frame

All satellite techniques are, conceptually, able to define a reference frame coincident with the center of mass. VLBI, by using extragalactic radio sources, is insensitive to the center of mass; however, if VLBI is used to track artificial satellites, VLBI would have the sensitivity of the other satellite techniques. The SLR precision and long term continuity (Lageos was launched in 1976) has been a consideration in adopting the SLR origin to be the origin of the International Earth Rotation Service Terrestrial Reference Frame.

All space geodetic techniques have demonstrated sensitivity to polar motion. Current comparisons between polar motion series obtained from SLR and those obtained from VLBI show agreement at the 0.5 milliarcsecond level. GPS developments are underway, including the proof of concept International GPS Geodynamics Service (IGS) slated to begin in June 1992.

VLBI provides long term UT1 that cannot be matched by the satellite techniques at the present time. Lageos has been demonstrated to provide independent determinations of UT1 over a 50 day interval. The higher altitude of the Etalon satellites suggests that a much longer period of UT1 determination is possible, but the sparse SLR tracking of the Etalon satellites has allowed only limited demonstrations of the UT1 capability. It is worth emphasizing that the low area to mass ratio of Lageos and Etalon result in much smaller nongravitational forces than the GPS satellites. The nongravitational forces are a significant factor in the GPS satellites that limit the use of these satellites to very short term UT1 (sub-daily to a few days).

Comparisons have been made between SLR and VLBI reference frames using collocated instruments, either permanent or mobile. These comparisons have shown agreement at the 2 cm level.

FUTURE

With the launch of Lageos-2, there will be two Lageos and two Etalon satellites. Within a few years, a second Starlette satellite will be launched. Starlette and Lageos have provided much of our knowledge about variations in the gravity field as well as contributing to the development of gravity models for science applications and for precision orbit determination. Two Lageos satellites, for example, will enable improved Earth rotation determination and more rapid determination of site positions. New developments in on-site software have enhanced the ability of SLR to provide high precision quick-look data that can be used for science applications and to assure tracking of the diverse constellation of satellites now available for SLR tracking. Nevertheless, only one satellite can be ranged at a time and the involvement of the science community in the process of establishing priorities is essential.

No single space geodetic technique can meet all of the application requirements of the science community. Each technique provides some unique contribution, though most of the techniques overlap in some areas. In an era of diminishing budgets, the determination of the appropriate balance of techniques and the prospects of losing or eliminating some science applications must be considered as emphasis is redistributed.

The international collaboration in the SLR community has been outstanding. The promotion of further collaboration will enhance the prospects for long term availability of a global SLR network, thereby assuring the continued collection of data for the purpose of gaining better scientific understanding of our planet.

Timely Issues

Satellite Signatures in SLR Observations

G.M. Appleby
Royal Greenwich Observatory
Madingley Road
Cambridge CB3 0EZ, UK

Abstract.

We examine the evidence for the detection of satellite-dependent signatures in the laser range observations obtained by the UK single-photon SLR system. Models of the expected observation distributions from Ajisai and Lageos are developed from the published satellite spread functions and from the characteristics of the SLR system, and compared with the observations. The effects of varying return strengths are discused using the models and by experimental observations of Ajisai, during which a range of return levels from single to multiple-photons is achieved. The implications of these results for system-dependent centre of mass corrections are discussed.

1. Introduction.

The UK SLR system sited at Herstmonceux, and run by the Royal Greenwich Observatory, routinely observes the primary targets ERS-1, Lageos, Etalon-1 and -2, Starlette and Ajisai. The single-shot precision achieved by calibration ranging is close to 1 cm (1-sigma). The detection and timing hardware has recently been upgraded to include a Single Photon Avalanche Photodiode (SPAD, Prochazka et al, 1990), and an HP 5370 time interval counter. Epoch is derived at present from a Maryland 4-stop event timer, which is also used to make range measurements simultaneously and independently of the HP counter. Pass-averaged return rates are in general fairly low, varying from a few percent from the Etalon satellites, through about 20% from Lageos to up to 50% from Ajisai. Returns from the calibration targets are deliberately kept to similarly low levels (about 10-15%) using neutral density filters in the laser path. Under such conditions we can describe the system as a single photon return, single photon detection system. A detailed study of the system error budget was carried out following the upgrade of the detector from a PMT. During this investigation it became clear that the observational precision of in particular Lageos and Ajisai was consistently worse than that of the calibration targets. It was considered likely that the spacial distribution of the retroreflector arrays on the satellites would modify the distribution of the range residuals, when compared with those from the flat calibration targets. In this paper we examine the evidence for detection of satellite signatures in our range observations, compare the observations with models of the expected distributions from a selection of those satellites regularly observed, and discuss the implications in terms of the appropriate corrections required to reduce the observations to the centres of mass of the satellites

2. Observations.

This investigation is based upon the pass-by-pass range residuals that are formed during

the preprocessing stage to compute on-site normal points. All trends in the residuals due to errors in the predicted orbit of the satellite are removed during this process, which iteratively solves for corrections to a set of orbit-related parameters, rejecting at each stage residuals falling outside a 3-sigma band (Appleby and Sinclair, 1992, these proceedings). In a final stage of pre-processing, and as a useful check on system performance, the residuals are used to form a frequency distribution for each pass, by grouping the residuals in range bins. A normal distribution is fitted to the observed distribution by iterative least-squares, and the parameters of the fitted Gaussian are used to make a final selection of the original observations. Examples of the observed distributions and their fitted Gaussian distributions are shown in Figure 1. Also shown in the Figure is a typical distribution of ranges to a calibration target board, distant about 600 m from the SLR system. The observed range values are plotted relative to the mean of the fitted Gaussian distributions, which are also shown on each plot. The standard deviations of the fitted distributions are shown, along with higher moments of the data, expressed as skewness and kurtosis. For a perfect Gaussian distribution the values of skewness and kurtosis would be 0.0 and 3.0 respectively.

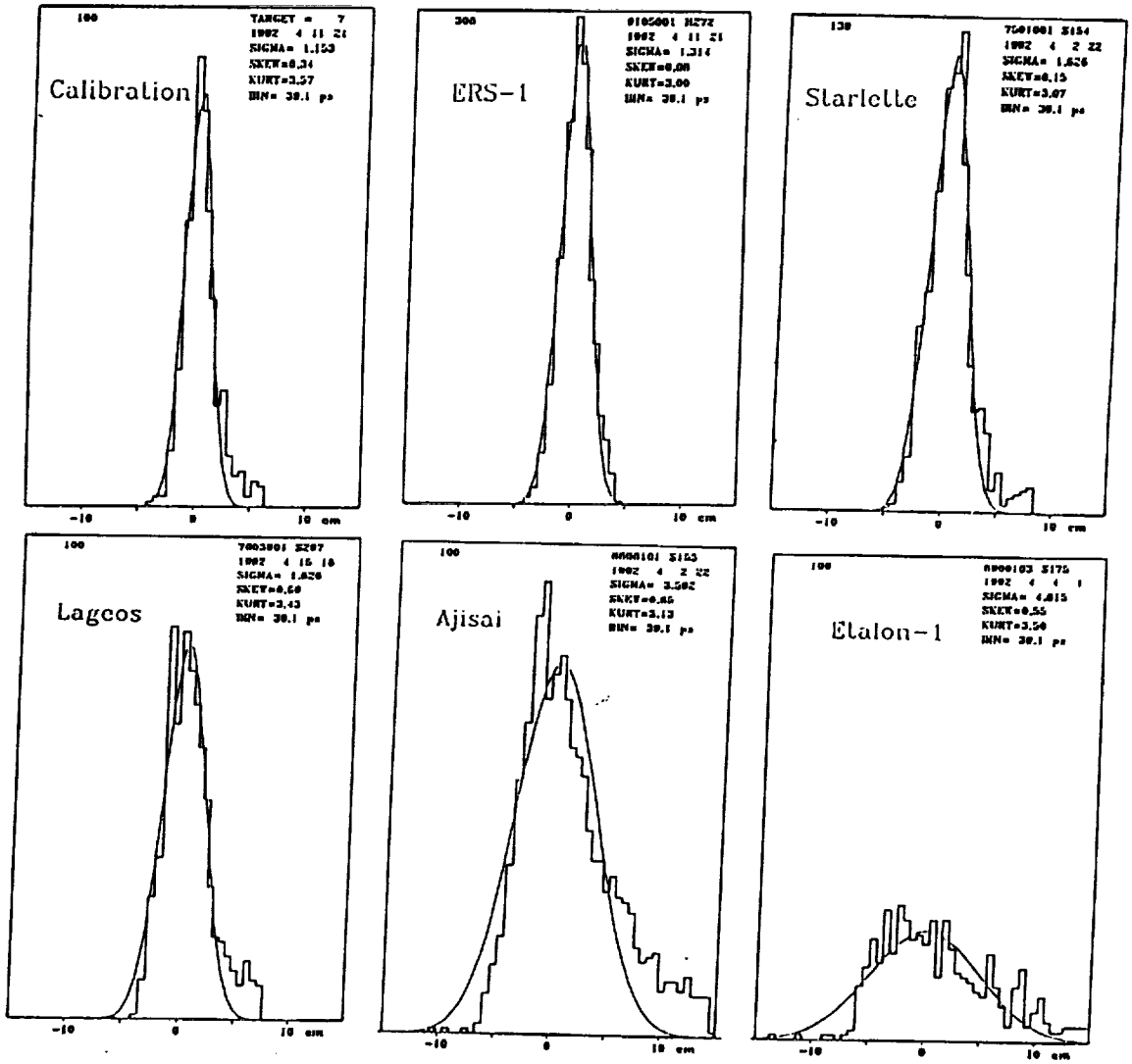

Figure 1. Observed distributions of range residuals from calibration and satellite targets.

2.1 Discussion.

From the distributions shown in Figure 1, we make the following observations. The distributions of the calibration ranges and those from Starlette and ERS-1 are clearly symmetric and well-fitted by the Gaussian distributions, but all have a significant 'tail' of observations outside the fitted curves. Skewness values for these 3 targets are between 0.05 and 0.1. The Lageos distribution is much less symmetric, and is less well fit by the Gaussian distribution. A chi-square goodness of fit test indicates significant departure, at a 5% level of significance, from the best-fit distribution shown in the plot. The results from Ajisai and Etalon 1 show large asymmetry, and are not at all well fit by the Gaussian distributions. Of particular significance to this investigation, are the 'widths' of the distributions, characterized by the standard deviations of the fitted distributions. Mean values of these standard deviations for a number of observations made during November and December 1991 are given in the Table below. These mean values of standard deviations confirm the impression given in Figure 1, that the calibration ranges have the smallest scatter, and those of Ajisai and Etalon-1 the largest, the range of standard deviations being from 1.1 cm to 4.8 cm.

Target	σ
	mm
Calib	11
ERS-1	12
Starlette	16
LAGEOS	18
Ajisai	32
Etalon	48

Before proceeding to investigate the hypothesis that satellite signatures are present in our observations, we first consider the possible causes of the 'tail' in the distributions, particularly evident in the calibration and Starlette data. We remark here that the existence of this tail does not constitute the thrust of our argument that we are detecting satellite signatures in our observations, since the tail is also present in the calibration ranges from a flat target board. We must therefore rule out such a target-induced effect and consider as probable cause the SPAD or the laser. In an experiment primarily designed to quantify the system time-walk under a large range of return signal strengths, calibration ranging was carried out using neutral density filters to vary the average number of photons reaching the detector. In this way the average number of photons was varied from about 0.5 to 50 photons per shot, as deduced from the observed return rates. A selection of the results is given in Figure 2, where the results are displayed in histogram form as before. The plots show, as expected, a reduction in the standard deviations of the distributions with increasing signal strength, since for a given laser pulse-width we would expect the contribution of the laser to the observational jitter to decrease with increasing number of photons in the return train, as the single-event detector increasingly receives photons originating nearer to the leading edge of the transmitted pulse. The plots also demonstrate that the extent of the tail in the distributions decreases with signal strength, suggesting an origin within the laser. However Prochazka (1992, private communication), points out that correct optical alignment

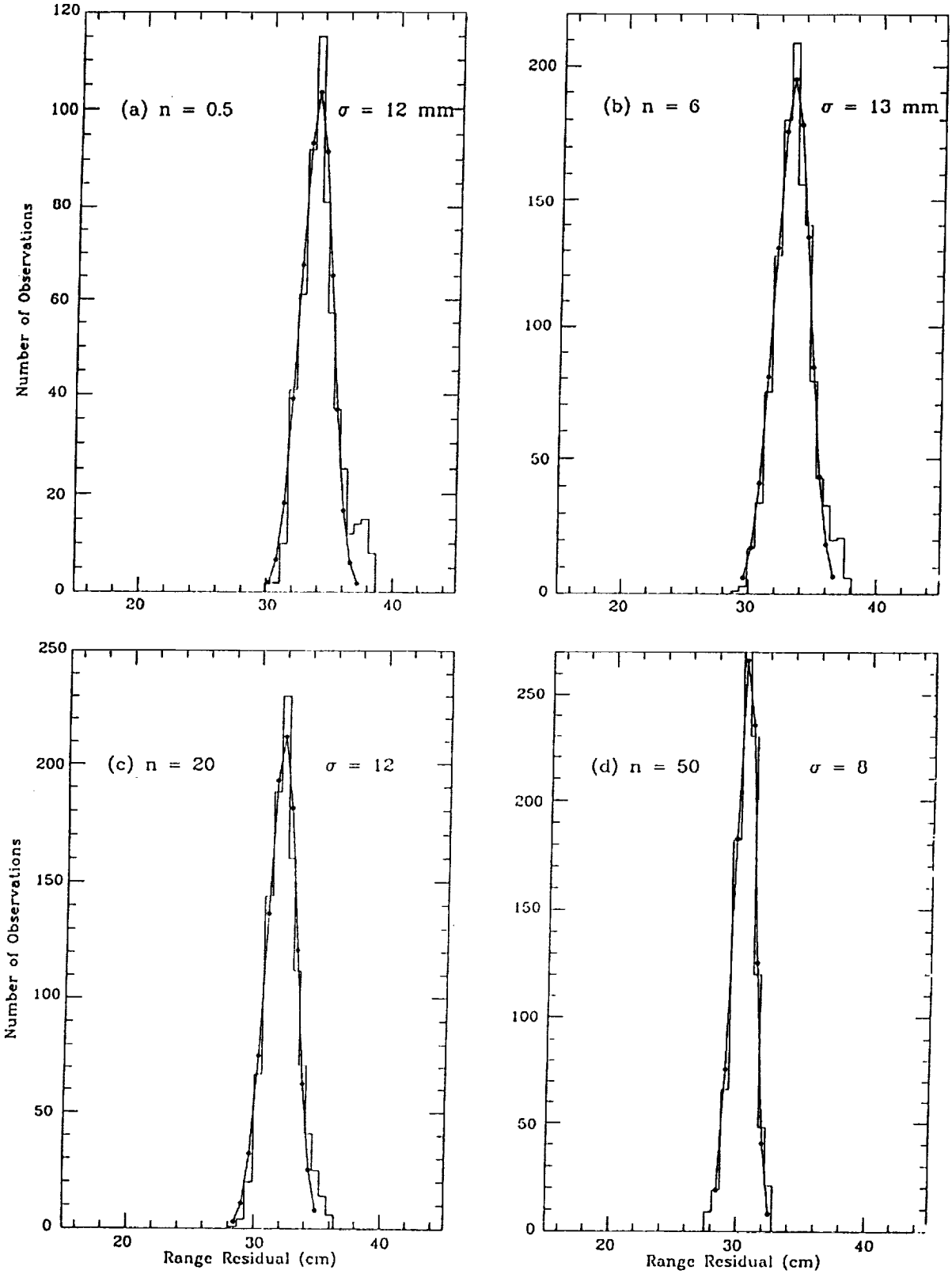

Figure 2. Calibration distributions as a function of average numbers n of returning photons.

of the SPAD detector is essential to avoid possible effects of non-uniformity within the chip. Resolution of this problem awaits further experimentation.

3. Satellite Signature Models.

We now take as our standard, single-photon system-signature the calibration distribution shown in Figure 1, and develop from it models of expected satellite return signatures, by convolution with the spread functions of Lageos and Ajisai. For Lageos, we take the model of cross-section parameters based upon row-by-row far-field diffraction pattern tests in polar orientation, presented in Fitzmaurice *et al* (1977). The parameters give, for the particular orientation, the lidar cross-section and number of corner cubes, in rows, contributing to the strength of returning signal. Also given is the optical distance of each row of reflectors from the spacecraft centre of gravity. We use the effective cross section of the cubes in their rings, of known distances from the centre of the satellite, to carry out a convolution of our system signature with that of Lageos. In this estimate of the shape of the returning pulse we ignore the effects of changing polarisation, which mainly affects the amplitude of the convolved pulse, and not its shape (Fitzmaurice *et al* 1977.) To model the return signatures from Ajisai we use the results of a computer simulation carried out by Sasaki and Hashimoto (1987). They find that the number of retroreflector sets contributing to the return signal from a given single laser pulse can only be 1, 2 or 3.5, and give the computed pulse shape in each of these 3 cases. The laser used in their simulation is gaussian in profile, of standard deviation 33 ps. From the published profiles, we can infer the spread distributions, consisting of lidar cross-sections and distances from spacecraft centre of gravity. We now have the information required to carry out a convolution with our system signature, in the same way as for Lageos. We assume that the rapid spin rate of Ajisai, of 40 rpm (Sasaki and Hashimoto, 1987) will ensure that for every pass all 3 possible orientations of the satellite will be sampled. We thus convolve our system signature with each of the spread distributions, and sum the resulting 3 distributions.

The results of the simulations for Lageos and Ajisai are shown in histogram form in Figures 3(a) and (b), where the quoted standard deviations are those of the fitted Gaussian distributions, also shown on the plots. For completeness we also present in Figure 3 the result of convolving our system separately with each of the 3 orientations of Ajisai.

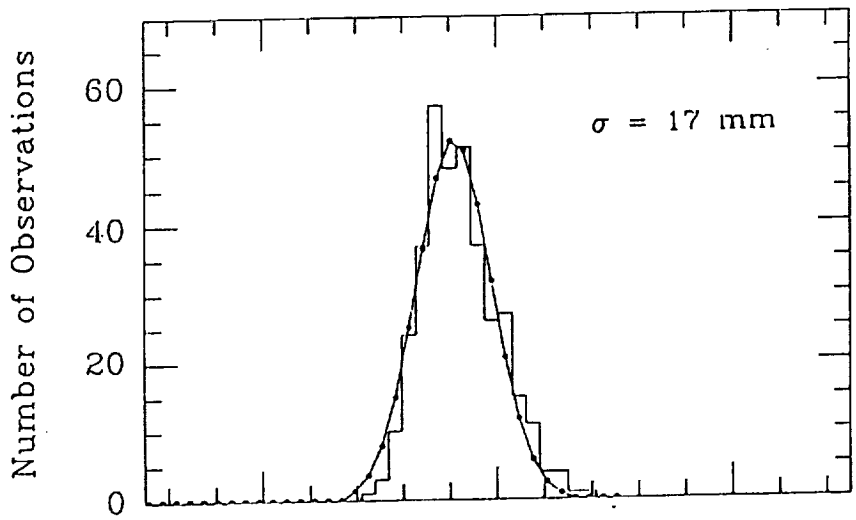

Figure 3. (a) Simulated Lageos range residual distributions.

of the SPAD detector is essential to avoid possible effects of non-uniformity within the chip. Resolution of this problem awaits further experimentation.

3. Satellite Signature Models.

We now take as our standard, single-photon system-signature the calibration distribution shown in Figure 1, and develop from it models of expected satellite return signatures, by convolution with the spread functions of Lageos and Ajisai. For Lageos, we take the model of cross-section parameters based upon row-by-row far-field diffraction pattern tests in polar orientation, presented in Fitzmaurice *et al* (1977). The parameters give, for the particular orientation, the lidar cross-section and number of corner cubes, in rows, contributing to the strength of returning signal. Also given is the optical distance of each row of reflectors from the spacecraft centre of gravity. We use the effective cross section of the cubes in their rings, of known distances from the centre of the satellite, to carry out a convolution of our system signature with that of Lageos. In this estimate of the shape of the returning pulse we ignore the effects of changing polarisation, which mainly affects the amplitude of the convolved pulse, and not its shape (Fitzmaurice *et al* 1977.) To model the return signatures from Ajisai we use the results of a computer simulation carried out by Sasaki and Hashimoto (1987). They find that the number of retroreflector sets contributing to the return signal from a given single laser pulse can only be 1, 2 or 3.5, and give the computed pulse shape in each of these 3 cases. The laser used in their simulation is gaussian in profile, of standard deviation 33 ps. From the published profiles, we can infer the spread distributions, consisting of lidar cross-sections and distances from spacecraft centre of gravity. We now have the information required to carry out a convolution with our system signature, in the same way as for Lageos. We assume that the rapid spin rate of Ajisai, of 40 rpm (Sasaki and Hashimoto, 1987) will ensure that for every pass all 3 possible orientations of the satellite will be sampled. We thus convolve our system signature with each of the spread distributions, and sum the resulting 3 distributions.

The results of the simulations for Lageos and Ajisai are shown in histogram form in Figures 3(a) and (b), where the quoted standard deviations are those of the fitted Gaussian distributions, also shown on the plots. For completeness we also present in Figure 3 the result of convolving our system separately with each of the 3 orientations of Ajisai.

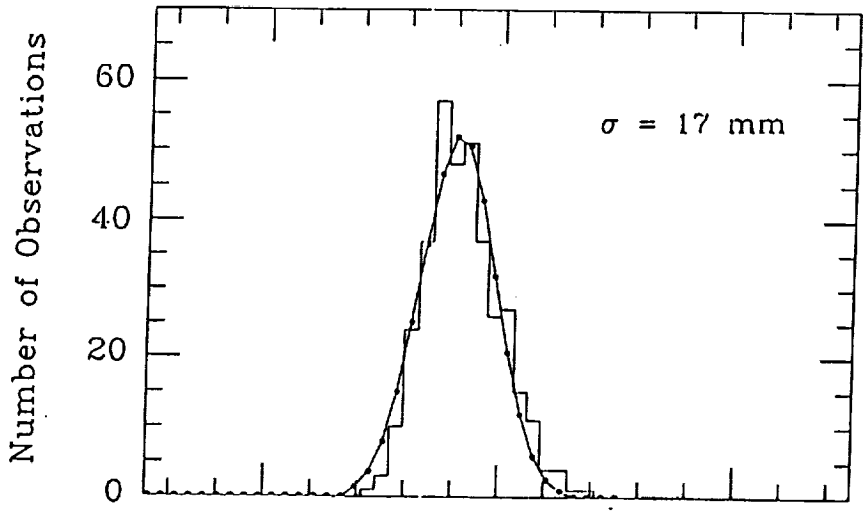

Figure 3. (a) Simulated Lageos range residual distribution

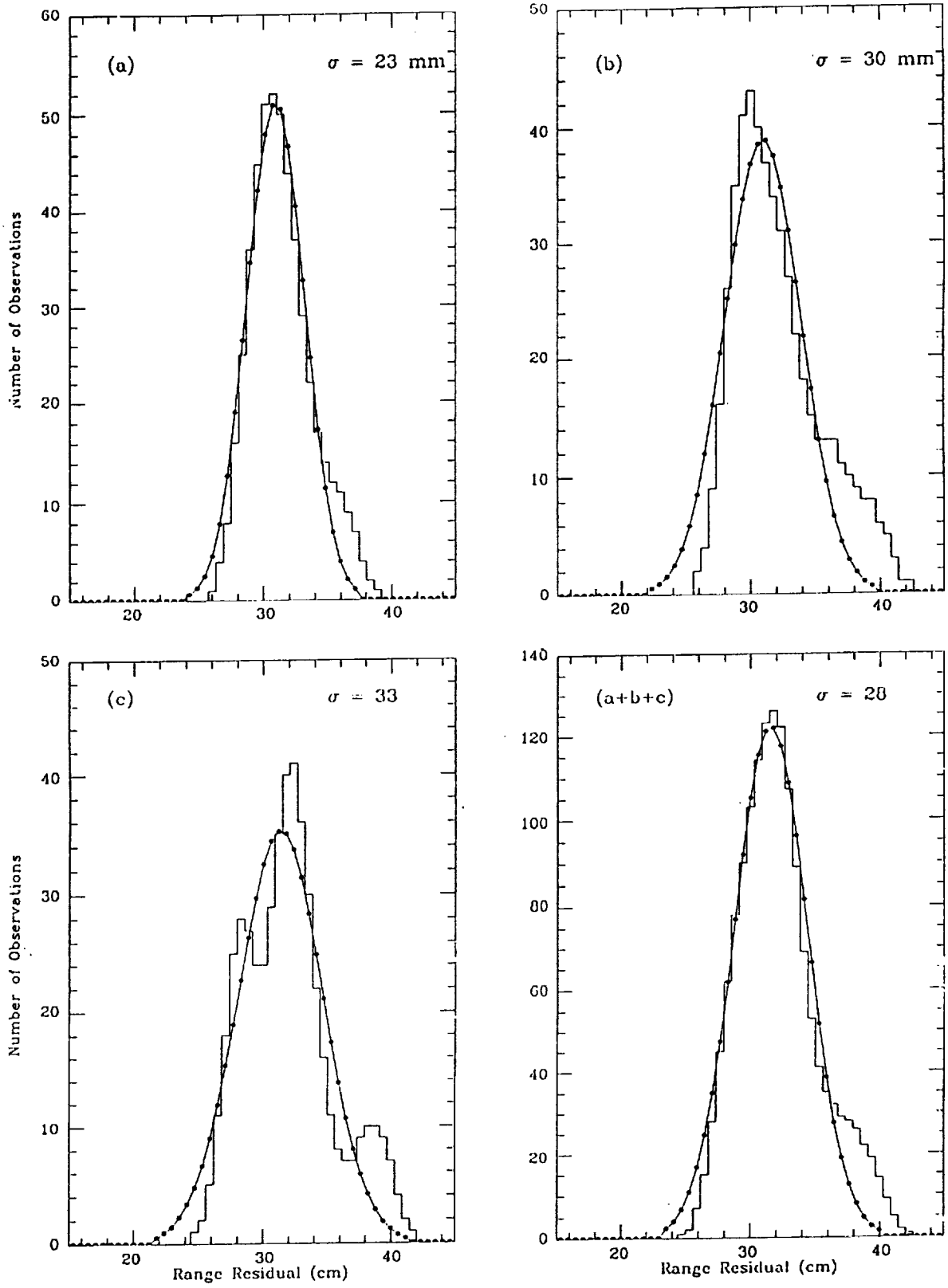

Figure 3. (b) Simulated Ajisai range residual distributions.

3.1 Discussion.

The standard deviation of the simulated Lageos data (1.7 cm) is close to our observational mean of 1.8 cm, and the appearance of the simulated and observed histograms is similar. The underestimate of the observed scatter by our model may be attributed to various causes; neglect of atmospheric turbulence (Gardner, 1976); neglect of coherency fading induced by the satellite, and the single satellite orientation chosen for the model. The models of the Ajisai return signatures give standard deviations of between 2.3 and 3.3 cm, which compare well with the observational results. There is some evidence in the Ajisai observations of variations of signature with pass circumstances, which may be due to the dominance of a particular satellite orientation or orientations for a given ground track.

4. Multi-photon Returns.

The foregoing discussion is based upon return energies at the single photon level; the detected photon is considered to be a random event taken from a population formed by the convolution of the laser pulse distribution with that of the satellite response. We now consider the effects of a larger number of photons reaching the single-photon detector, in order to quantify the subsequent systematic effects caused by a signal-strength-dependent variation of the mean reflection distance to the satellite.

4.1 Observations and reduction.

Experiments were carried out using Ajisai since it is relatively easy to obtain a large variation in received energy from the large target. The variation from single photon to multiple photon levels was achieved during the experimental passes by altering the divergence of the laser beam and hence the energy density at the satellite. The observations were filtered in the standard way, by using them to solve for corrections to the predicted orbit. However, it was found that this process did not remove all trends from the range residuals, indicating the presence of systematic range biases which varied during the passes. We found that it was necessary to divide each pass into a number (6) of segments, and use the processing software to filter the observations in each segment separately. The resulting scatter plot for one of the experimental passes is shown in Figure 4. The residuals from each of the six segments are shown in histogram form in Figure 5, along with the standard deviations of the fitted Gaussian distributions.

We calculate the average percentage return rates at intervals of 30 seconds throughout the passes by counting the numbers of satellite returns and the numbers of pre-return noise detections. Given that the laser fires 10 shots per second, the true percentage return rate in each 30-second interval is then

(number of true range measurements*100)/(30*10 - number of noise events)

On the assumption that the quantum efficiency of the SPAD is 20%, we calculate from these corrected return rates the average numbers of photons in each return. However we found that in several of the 30-second intervals the calculated return rate was nearly 100%. At such return levels we cannot reliably estimate the mean number of returning photons, which may be far in excess of the 16 estimated for a near 100% rate. Where possible, we have used these 30-second mean values to estimate the mean numbers of photons contributing to the observations in our 6 segments, and these averages are shown in Figure 5. For those 2

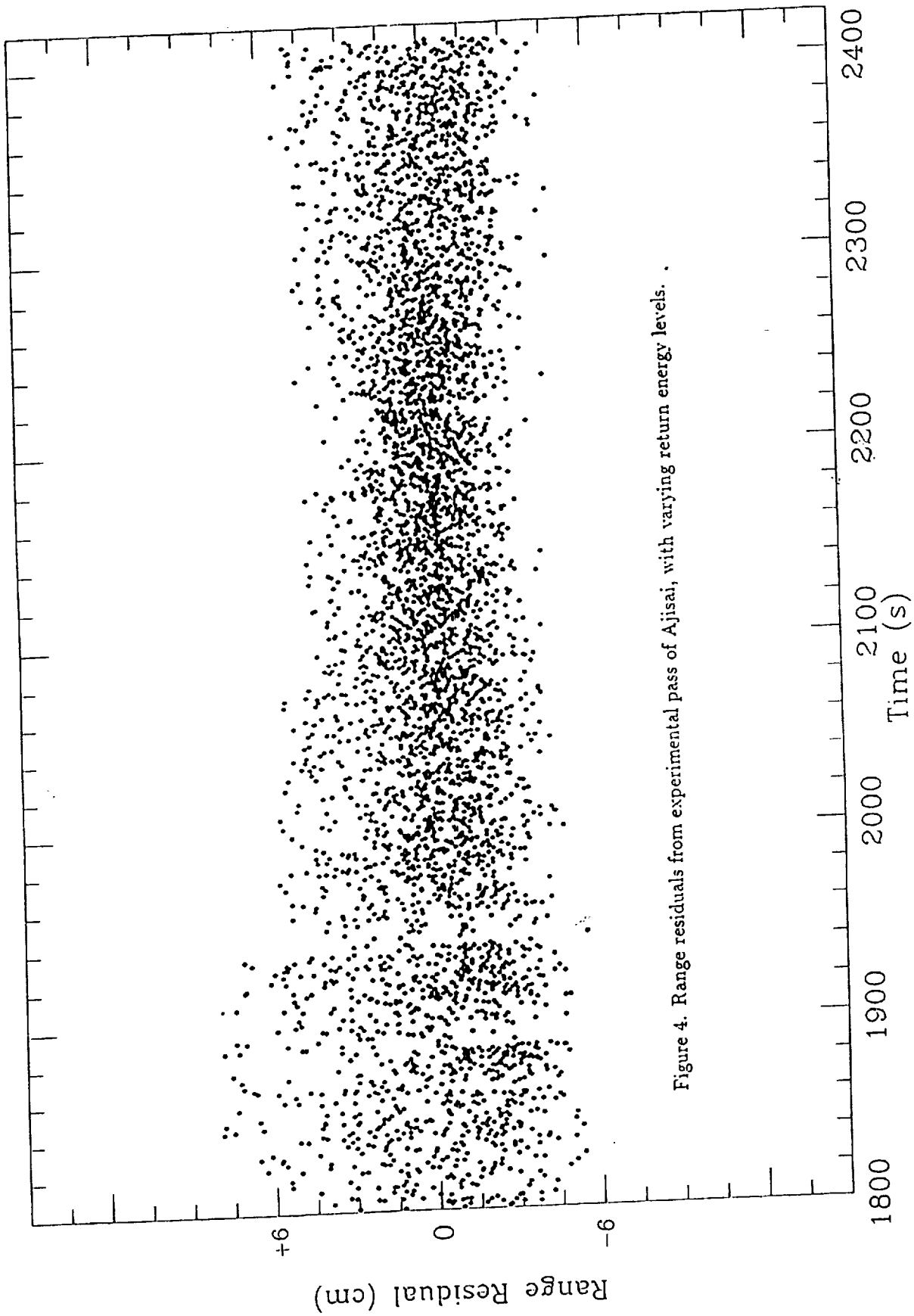

Figure 4. Range residuals from experimental pass of Ajisai, with varying return energy levels. .

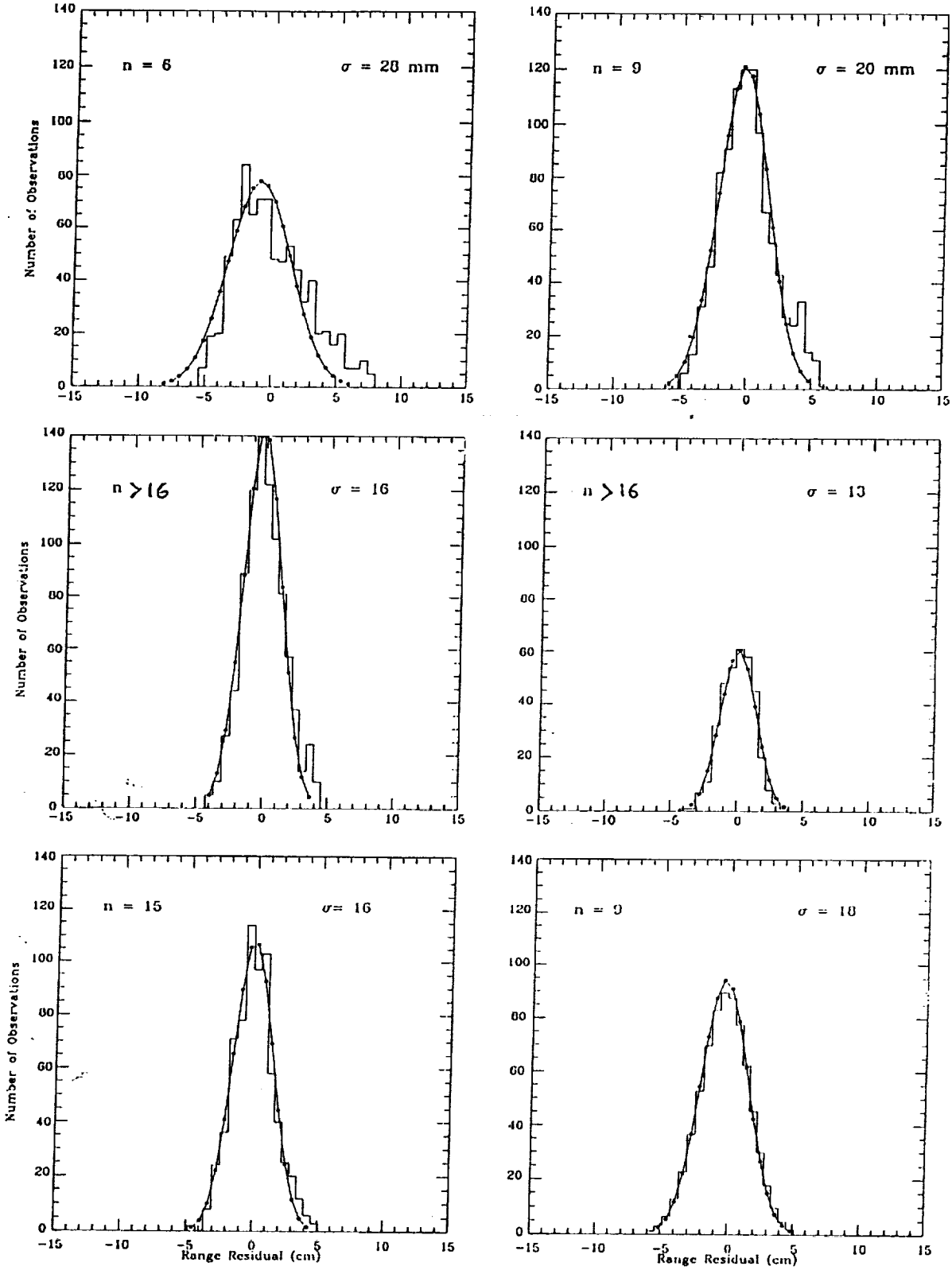

Figure 5. Distribution of range residuals from Ajisai pass as a function of average numbers n of returning photons.

segments where the average return rates were near 100%, we have asigned the numbers of photons as >16, but remark that the true numbers could be several times as large.

4.2 Model and Discussion.

There is a clear variation of histogram shape and single-shot precision with change of signal strength. At low return rates equivalent to single photon returns, the distribution of residuals is similar to the 'standard' Ajisai distribution (Figure 1). For the high return rates little of the satellite signature remains in the distributions, and the histograms qualitatively and quantitatively resemble those from Starlette or ERS-1 (Figure 1).

These results cannot be used to detect a systematic variation of satellite mean reflection distance during the passes, because the method of reducing the observations absorbs any such corrections. However we can use models to predict both the increase of precision and this change of mean reflection distance as a function of numbers of photons in each return. We model the time-distribution of the returning photons, from which we may sample a variable number, by convolution of the Ajisai spread distributions with a Gaussian distribution of FWHM 50 ps, to represent the laser. To model the effect of n photons reaching the detector, we use a random number generator to pick one 'photon' from our time-distribution of photons, then record its time-location within the distribution, and repeat the process n times. We then sort this sequence of n relative event times into chronological order of arrival at the detector. We model the 20% efficiency of the detector by stepping through the n events in time order, at each step generating an integer random number in the range 1-5. If the random number is 1, the event is accepted (detected). If the random number is not 1, the next event is 'tested'. In this way we generate a large number of event times each resulting from the selection of a single photon from a series of returns containing an average of n photons. The mean and standard deviation of these event times are computed and converted to range in cm. The standard deviation values are added quadratically to the estimated system jitter (0.8 cm) to fully model the observations. The results of simulations of range precision and biases from Ajisai for values of n between 1 and 50 are shown in Figures 6a and 6b, where the results have been joined by continuous lines. The 30-second average observed values of precision, where they can be reliably estimated (see section 4.1) from our experimental Ajisai passes, are shown as dots on the graph and agree well with those predicted. The predicted range bias curve in Figure 6b expresses the expected change of mean reflection distance from the satellite centre of mass as a result of increasing the number of photons reaching the detector in each laser return. Most of the bias, which contains a contribution from the finite pulse length of the laser (FWHM 50ps), is seen to take effect between signal strengths at the single photon level up to an average of about 40 photons per return. Little change is predicted with increasing numbers of photons beyond that point.

4.3 Lageos Centre-of-mass correction.

We can use the above techniques to estimate the magnitude of a systematic range-bias for Lageos, in the context of worldwide SLR systems working at different return-signal levels. Figure 6 shows the results of a computation of the range bias as a function of average number of photons reaching the detector, for 2 modelled laser pulse-lengths. The magnitude of the change of the effective reflection distance from the satellite centre of mass is about 1.3 cm for a variation of return level from single-photons to the 40 photon level. This result

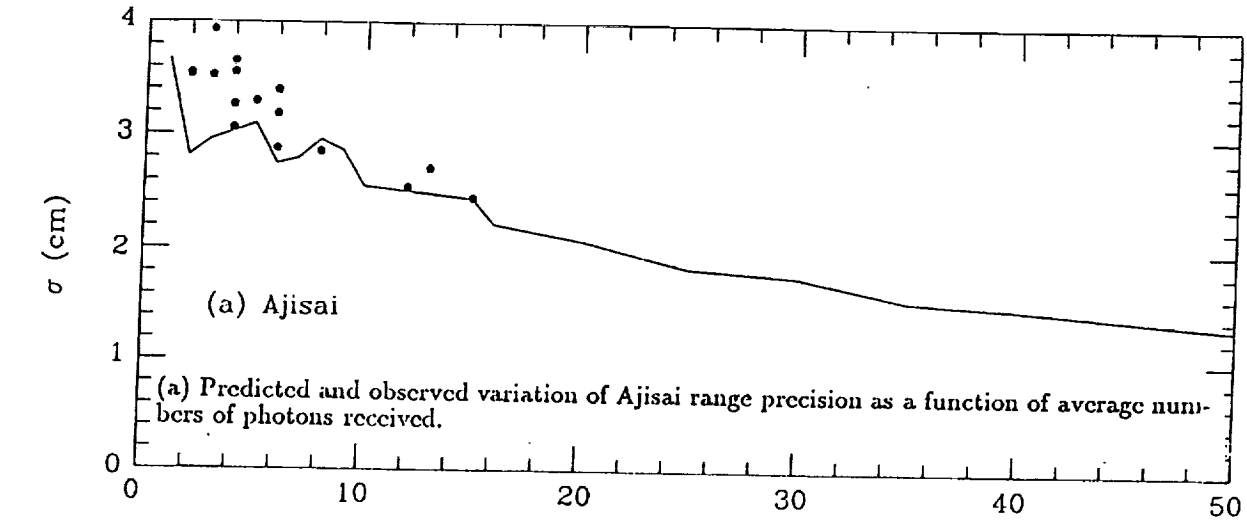

(a) Predicted and observed variation of Ajisai range precision as a function of average numbers of photons received.

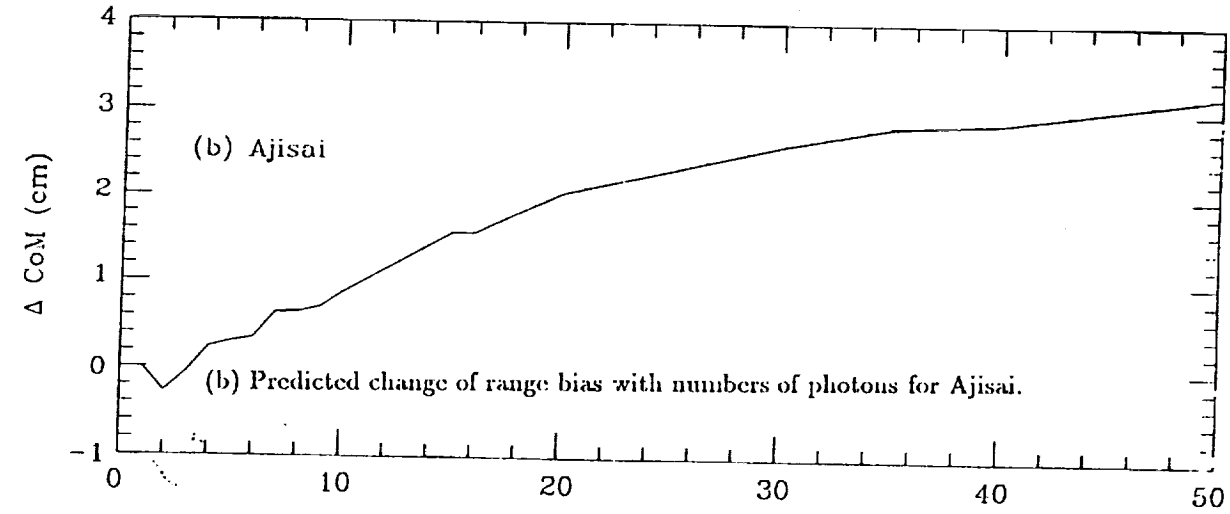

(b) Predicted change of range bias with numbers of photons for Ajisai.

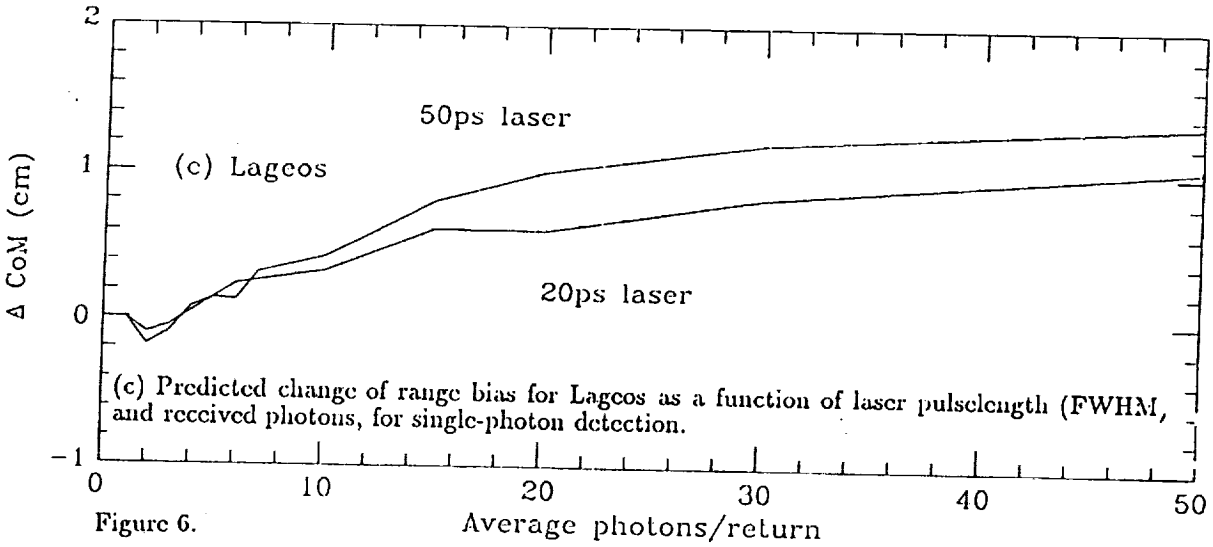

(c) Predicted change of range bias for Lageos as a function of laser pulselength (FWHM, and received photons, for single-photon detection.

Figure 6.

implies that an SLR system receiving and detecting single photons, and using a laser with a pulsewidth (FWHM) of 50 ps, is on average effectively observing a distance 1.3 cm closer to the satellite centre of mass than a single-photon detection system receiving more than about 40 photons per shot. Removing from this figure the effect of the length (FWHM) of the laser pulse, the satellite-induced range bias amounts to about 0.6 cm. The recommended centre-of-mass correction for Lageos is 25.1 cm for leading-edge, half-maximum detection of a large return pulse, and 24.9 for peak detection (Fitzmaurice *et al*, 1977). We assume that the electronic detection of the peak of a large return pulse is equivalent, in terms of distance from cenre of mass, to the formation of the mean of a set of range residuals arising from the detection of single photons. For the Herstmonceux system working at the level of single photon returns, the appropriate centre-of-mass correction should therefore be the same as for the large-pulse, peak-detection systems, *ie* 24.9 cm. However, for single-photon systems departing from the single photon regime, the implications of this investigation are that the centre of mass correction should be *increased* from the 24.9 cm by an amount as given in Figure 6, depending upon the laser pulse-length and the number of photons reaching the detector.

5. Conclusion

Using observations from the UK single-photon SLR system, we have demonstrated that the observational scatter contains a satellite-dependent signature, and that this signature varies as expected with the number of photons reaching the detector. The implications of this variation upon the corrections required to relate range observations to the centres-of-mass of the satellites is modelled and discussed. The magnitude of the effect is system-dependent since it depends both on the number of photons reaching the detector, and hence on laser energy level and local atmospheric conditions, and upon the laser pulse length. A graph is presented giving a calculated, energy and pulse-length dependent, center of mass correction for Lageos range data obtained using single-photon detection, which varies by 1.3 cm over the range of the parameters considered.

6. Acknowledgements

All of the observations reported here were carried out by the SLR team at Herstmonceux, East Sussex, UK, under the direction of the station manager Dr. Roger Wood. The team's interest in carrying out the non-standard observations is appreciated. I thank Dr. Andrew Sinclair, Head of the RGO Space Geodesy Group, for his comments throughout the work on this project.

7. References

Fitzmaurice, M.W., P.O. Minott, J.B. Abshire and H.E. Rowe. 1977. *Nasa Technical Paper 1062.*

Gardner, C.S. 1976. Effects of random path fluctuations on the accuracy of laser ranging systems. *App. Optics, Vol 15, No. 10.*

Prochazka, I., K. Hamal and B. Sopko, 1990. Photodiode Based Detector Package for Centimeter Satellite Ranging, *Proc. 7th Int. Workshop on Laser Ranging Instrumentation, Matera, Italy, 1989.*

Sasaki, M and H. Hashimoto. 1987. Launch and Observational Programme of the Experimental Geodetic Satellite of Japan. *IEEE Trans. on Geoscience and Remote Sensing, Vol GE-25, No. 5.*

N94-15558

Work at Graz on Satellite Signatures

Georg KIRCHNER, Franz KOIDL

SLR Graz / Institute for Space Research
Austrian Academy of Sciences
Observatory Lustbühel, Lustbühelstr. 46
A-8042 GRAZ, AUSTRIA

Tel.: +43-316-472231; Fax: +43-316-462678
E-Mail: kirchner@flubiw01.tu-graz.ac.at

Abstract

The size and shape of the satellites retroreflector arrays have a major impact on the distribution and scatter of the return signal; this can be seen clearly when reaching sub-cm ranging accuracies and when using Single-Photon Detectors with single- or multi-photon returns; for other receiver systems (using MCP's) it should be checked also. As a consequence, the necessary center-of-mass correction for some satellites will different, depending on the receiver systems.

While this effect is not yet visible on small satellites or small retro-reflector arrays (like STARLETTE, ERS1), it can be in the order of centimeters on AJISAI or ETALON.

1.0 Introduction

The SLR station Graz uses, since some years, Single Photon Avalanche Diodes (SPAD) to detect return signals from satellites; these diodes can detect single photons - which is used for ranging to ETALON, or, in worse atmospheric conditions, also for lower satellites -, but usually we use multiphoton returns to get maximum return rates; this results in better accuracies when using Normal-Point-Methods, and helps to avoid part of the

satellite signatures in the return signal distribution, as described later.

2.0 Ranging tests to the calibration target

Standard calibration to our target (distance about 400 m) gives an RMS of 6 to 7 mm for the routine SLR setup (with HP5370A counter, SPAD at 10 V above break, cooled to -27°C; 2.5σ limits); an example is shown in fig. 1, upper histogram; the distribution shows nice symmetry, with an RMS of 5.8 mm at 2.5σ ; there is no significant change of the mean value when using different sigma criteria, also indicating a proper distribution.

To check influences of the ranging system itself on the distribution of the return signals, different tests with various misadjustments of the involved devices were made; a worst-case example is shown in fig. 1, lower histogram: A similar calibration as before, but with misaligned SPAD, lower voltage above break, no cooling, and non-optimum start puls detection; this results in a non-symmetric distribution, higher RMS, and measurable shift of the mean value for varying sigma criteria.

After verifying the maximum contribution of the system itself, the distribution of returns from different satellites were analyzed.

3. ERS1 and STARLETTE

Due to their small size of the retroreflector arrays, there is no significant satellite signature visible in ERS1 and STARLETTE data; the average RMS is between 8 and 9 mm, close to the values obtained from the calibration target.

The distribution of the data (fig. 2, upper histogram) is more or less symmetric, with small irregularities due to lower number of returns; the 3 mm bin width for all these histograms was chosen in coincidence with the 20 ps resolution of the HP 5370A counter.

4.0 AJISAI

As a contrast to the previous satellites, AJISAI shows quite significant signatures; these are very dependant of the return signal strength (fig. 3).

With strong (multiphoton) return signals, AJISAI shows low RMS (11.8 mm, upper histogram), and only slightly non-symmetric distribution; when reducing the return signal level to mostly single photon-electrons (by switching off the last laser amplifier, and opening divergence; the return signal level is checked in real time by watching the return signal rate and/or the number of semi-train returns on a graphic screen), the RMS increases to 22 mm (lower histogram), while the distribution now follows the shape of the satellite.

Both histograms in fig. 3 are shown with editing criteria of 2.5 σ, which is used for our routine ranging procedures; using other σ values (4 σ, 3 σ, 2 σ), the mean value of the histogram will move - in the worst cases - between 1 and almost 2 cm.

5.0 LAGEOS

As expected from size and shape of LAGEOS, the satellite signature is much less visible than with AJISAI, but is still present (fig. 2); it is the main contribution to the increase of the RMS, from 6 to 7 mm from the target, to 11 to 14 mm from the satellite (again, this is valid for our single-photon detection system, using single photon and/or multi-photon return signals!!), with lower signal levels resulting in higher RMS.

When using different editing criteria again, the non-symmetric distribution causes a shift of the mean value of about 1 to 2 mm, only in extreme cases up to 4 mm.

6.0 ETALON

To complete the satellite's list, we show also the signature coming from ETALON ranging data, this time using a different way

of demonstrating the non-symmetric distribution. While fig. 4 shows the residuals of an ETALON-2 pass (demonstrating also the advantage of using the semitrain!), in fig. 5 the residuals are plotted after "folding", polynomial fitting and 2.5σ-editing. Due to the low return signal level from these satellites (most of the returns are single photons: We are ranging with 5 to 10 mJ Semitrain - this is about 2 or 3 mJ for the first pulse! - and 50 cm receiver to the ETALONS, still getting return rates of up to 1000 returns per hour), we see the full satellite's size and shape in the data, with an RMS of 3.5 to 4 cm

7.0 Conclusion

To keep systematic errors due to the influence of the satellite's shape as low as possible, we

- keep calibration and satellite return signals in the same level
- use the same editing criteria (2.5 σ) for calibration and for satellite data;
- try to minimize any contributions of the system itself to non-symmetric distributions.

As far as we know, in all analyzing calculations the satellites are treated as a "flat" reflecting surface, with a fixed center-of-mass correction, which was determined before launch using the detectors, techniques and accuracies available at that time. However, with the improvements in accuracy, we can see now the shape of the satellites in our data, which in turn can influence the values of the center-of-mass corrections; so it seems necessary to determine the center-of-mass correction with respect to different receiver systems, and using different values for the analysis.

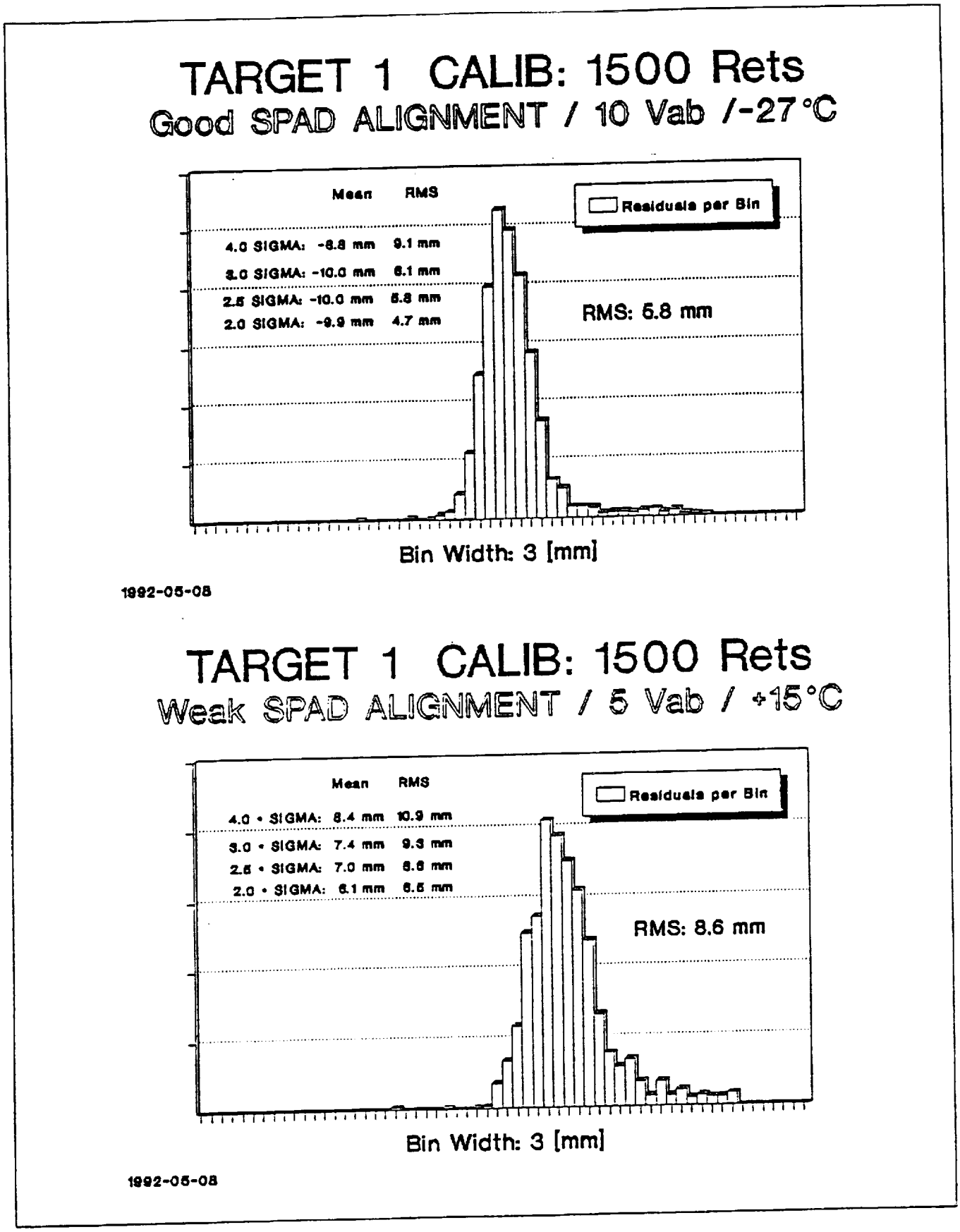

Figure 1: Histograms of calibration ranging to the target

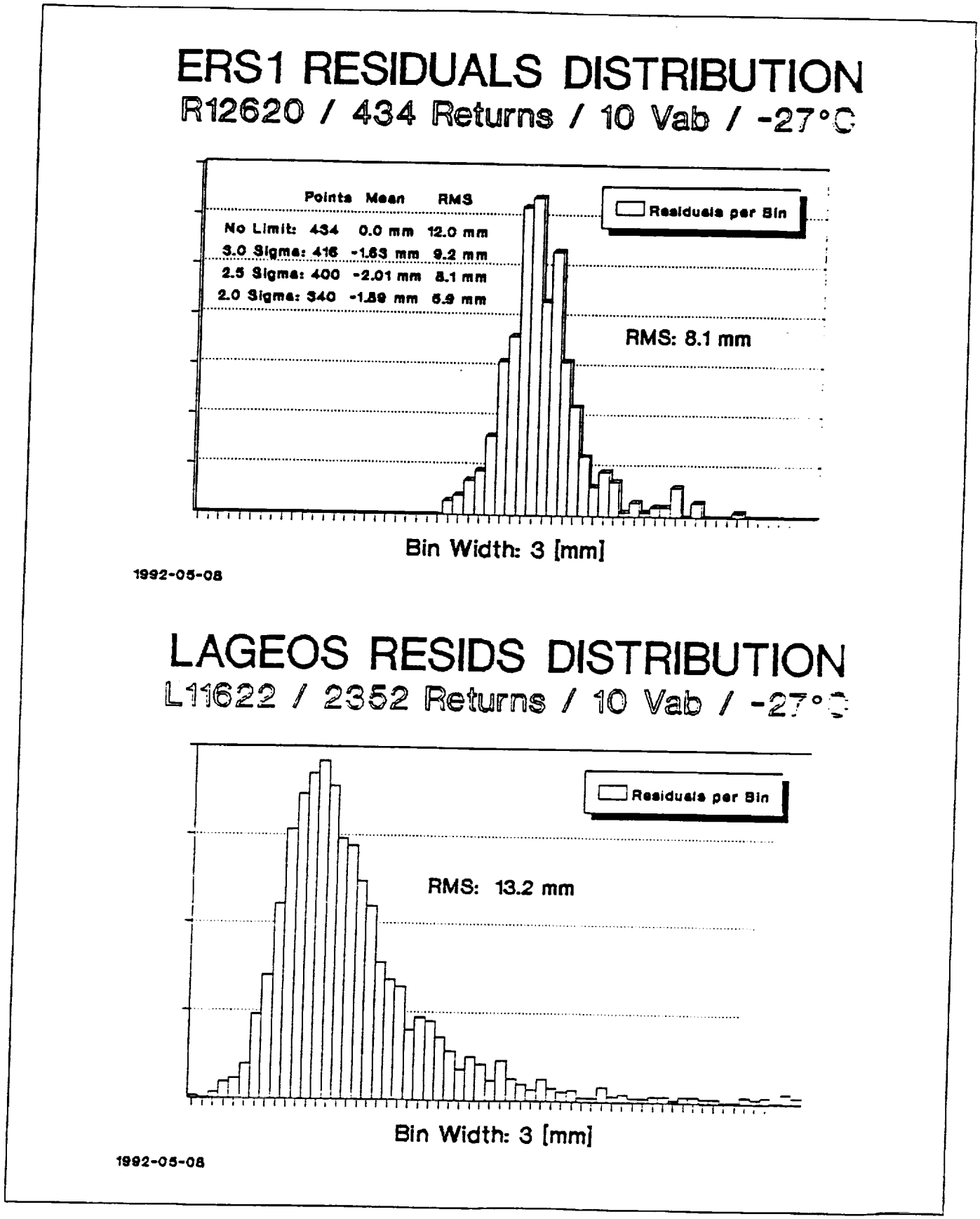

Figure 2: Histograms of ERS1 and LAGEOS returns

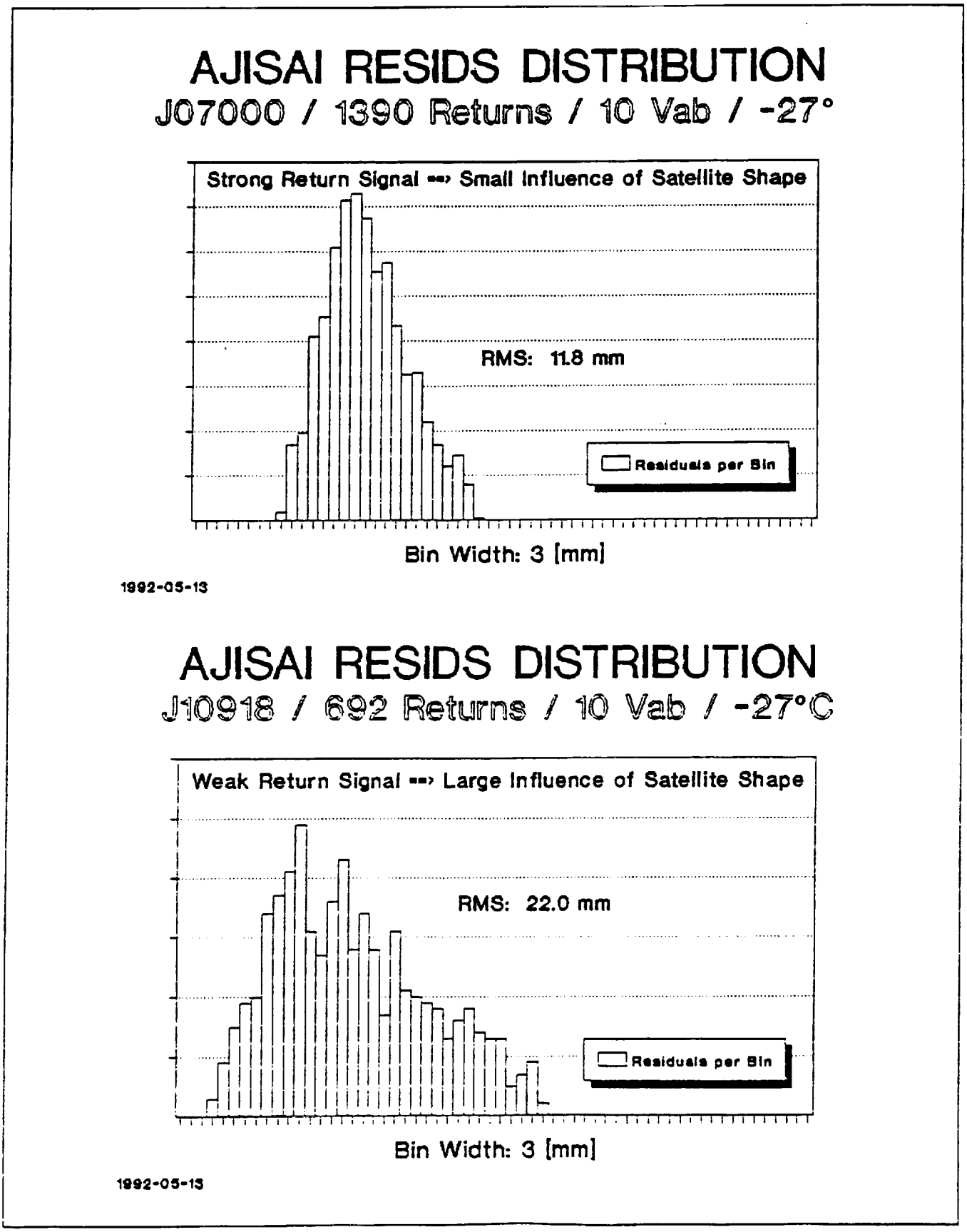

Figure 3: Histograms of AJISAI returns

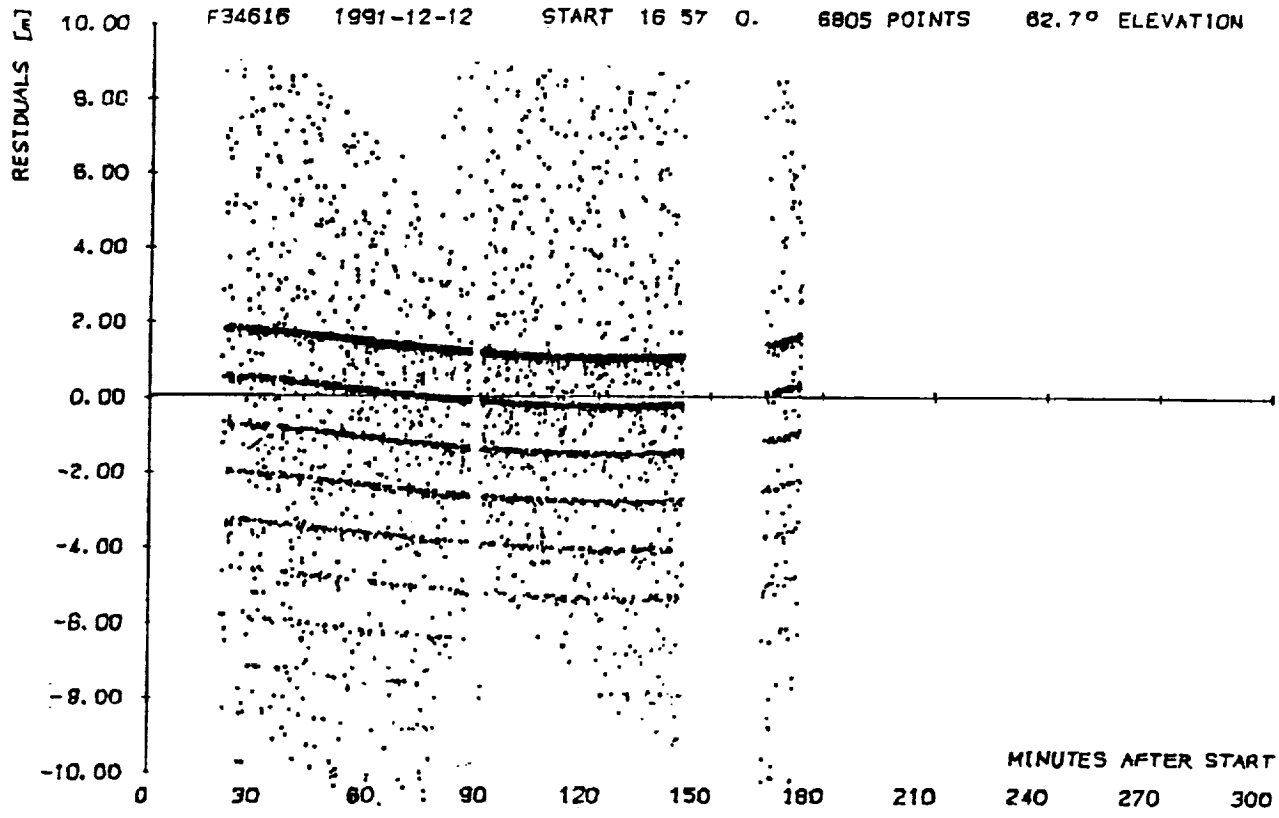

Figure 4: Residuals of ETALON-2, showing semitrain returns

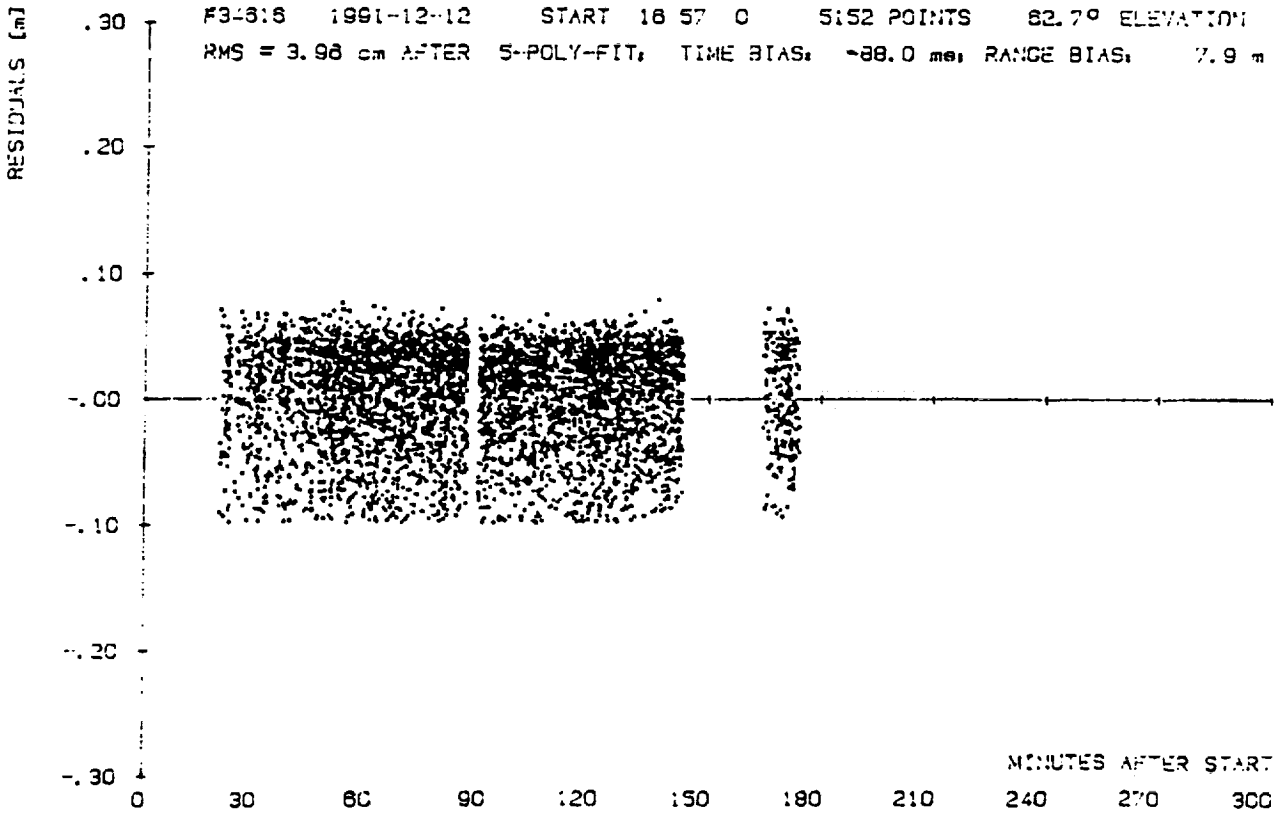

Figure 5: Same ETALON-2, with non-symmetric distribution

N94-15559

THE PRECISION OF TODAY'S SATELLITE LASER RANGING SYSTEMS

P.J.Dunn and M.H.Torrence, Hughes STX Corp., Lanham,MD
V.Hussen, Bendix Field Engineering Corporation, Greenbelt,MD
M.Pearlman, Smithsonian Astrophysical Observatory, Cambridge,Mass

Introduction

Recent improvements in the accuracy of modern SLR systems are strengthened by the new capability of many instruments to track an increasing number of geodetic satellite targets without significant scheduling conflict. This will allow the refinement of some geophysical parameters, such as solid Earth tidal effects and GM, and the improved temporal resolution of others, such as Earth orientation and station position. Better time resolution for the locations of fixed observatories will allow us to monitor more subtle motions at the stations, and transportable systems will be able to provide indicators of long term trends with shorter occupations. If we are to take advantage of these improvements, care must be taken to preserve the essential accuracy of an increasing volume of range observations at each stage of the data reduction process.

The Range Measurement

The SLR measurement is computed as one half of the product of an adopted value of the speed of light and the observed interval between the transmit time of the pulse and the time of a detected return. The essential simplicity of this process is tempered by the need for careful calibration for system delay and atmospheric refraction, as well as for an accurate survey of mount eccentricity and other important local coordinates to match the millimeter accuracy of the best current systems. The influence of satellite signature and detector time-walk must also be considered at this high accuracy level, and we consider here the particular need to preserve any details of these effects which may be lost in the current normal point compression process.

Normal Point Generation

The loss of detail at each stage of the process to reduce engineering data to normal points is illustrated in Table 1, which shows the information content of each of the parameters measured by most instruments for a typical satellite pass or pass sequence. Information on receive energy level is not necessary if all time-walk characteristics of the detector system have been eliminated or corrected before data compression. Neither will the absence of calibration details matter if the distribution of returns is identical to that from the satellite and the same algorithm is applied to reduce each observation. The accuracy of the satellite observations will be preserved as long as the return distribution is normal (or Gaussian) about the mean range.

Shape Factors

Two measures of the deviation of a distribution from normal are illustrated in Figure 1. Any skewness in the pattern of range residuals about the mean would bias normal points if we assume that the peak of the distribution is a better measure of the range. Skewness is computed from the third moment of the residual distribution, just as the standard deviation is based on the second moment: it is positive for a distribution with a tail towards long ranges, and negative (a rare

occurrence) when the noise is short. Another shape factor can be simply obtained as a combination of third and fourth moments: kurtosis gives an indication of flatness (low values) or peakiness (high values). A residual histogram with low kurtosis values can be produced by using a lower value of the sigma multiplier than three for data editing (clipping); high kurtosis values are obtained when a larger sigma multiplier than three is employed, and the return signal appears as a spike in the background noise.

Interpretative Aids

The utility of these shape factors can be demonstrated with examples from several different systems. To illustrate the mechanism used to build the basic contour picture which we have adopted for data quality assurance we refer to Figure 2, which is a three-dimensional accumulation of a number of pass histograms for LAGEOS ranges taken at the Grasse Observatory during a three month interval. The vertical scale shows the percentage of range measurements which lie within ten millimeter bins distributed about the mean value. An imaginative reader will observe a progression from a nearly symmetrical distribution in December 1990 to a significantly skewed pattern in February 1991: the front profile on 91-02-27 demonstrates the characteristic of long noise. The coarse grain caused by the centimeter bin width is softened in the contour of the same data which is shown in Figure 3. The grey band of the contour scale shows a shift in the distribution in early January 1991 and the lighter peaks also suggest a change in character at this time: the darker contour levels emphasize the asymmetrical tail towards long ranges in January and February 1991.

Quantifying the residual behavior

Numerical descriptors for the changing residual pattern are shown in the scatter plot to the left of the contour frame. The crosses depict a normalized skew factor which jumps from a low (moderately skewed) to a high value at the same time that a low (flat peak) kurtosis measure returns to a nominal level as shown by the open circles. The change in the pattern was caused by a relaxation of the tight data editing criterion applied to the earlier observations which clipped the distribution and muted the intrinsic asymmetry exposed with more liberal editing. The standard deviation of the full-rate data is recorded with the normal points in the currently adopted compression scheme, so this event would be flagged as an increase in noise level, but the skew and kurtosis shape factors provide improved diagnostics at a relatively low computational cost.

The cause of any data asymmetry can be isolated by inspecting the distribution of the calibration measurements: if the asymmetry is restricted to the satellite returns, the shift in the effective range measurement due to the editing change would amount to over a centimeter and would cause an even larger change in the apparent height of a station position determined from these observations. On the other hand, similar levels of asymmetry in the ground target returns would suggest a source in the detector rather than the satellite, and if the same editing scheme was used for each data type, there would be no bias in the satellite measurements.

Satellite and Calibration Target Data

We have considered the shape of distributions from calibration and satellite targets in an analysis of observations from six GSFC systems collected in early 1992. Figure 4 shows a collage of residual histogram contours from the systems tracking several different satellites: ERS-1(E), Starlette(S), LAGEOS(L), Ajisai(A), ETALON-1(E1), and ETALON-2(E2). This broad representation shows at a glance the higher noise level of the ETALON satellite returns, as well as the tight

precision of data from lower-orbiting satellites like ERS-1, which amounts to about 5 millimeters for MOBLAS-7. The same ten millimeter bin scale is used to describe the characteristics of these instruments as for the data from Grasse in the earlier example.

The patterns for the appropriate calibration passes are given in Figure 5: they show less variation than the satellite data, and allow us to discriminate satellite-dependent variations from detector characteristics. None of the systems depicted here shows a systematic bias of more than a millimeter, but subtle effects in the distribution for an individual system can be detected and quantified by the skew and kurtosis shape factors plotted in the Figures provided for a couple of the instruments. The satellite returns for Moblas-7 show no consistent kurtosis but a hint of the positive skew typical of all systems' observations of the ETALON satellites (at the bottom of the plot); the MOBLAS-7 calibration returns are slightly clipped (low kurtosis). On the other hand, TLRS-4's satellite returns show no significant skew, but indicate a hint of clipping; this instrument's calibration data possesses the rare property of slight negative skewness.

Summary

The effects of these idiosyncrasies in residual pattern for the GSFC systems is well below the accuracy threshold for any currently employed application of the data, but they could be used to characterize subtle changes in system characteristics. We have attempted to demonstrate in the above examples the enhanced ability to monitor data quality for any SLR system with some simple shape factors which can be computed economically in the normal point compression stage. Regular inspection of these parameters can flag changes in data characteristics which affect range accuracy, and also provide reassurance that our most advanced systems do indeed attain the millimeter accuracy of which they are capable.

LEVEL	DATA TYPE	GRANULARITY				
		ROUNDTRIP		RECEIVE ENERGY		MET.
		SAT.	CAL.	SAT.	CAL.	
0	RAW ENGINEERING	POINT	POINT	POINT	POINT	POINT
1a	PROCESSED FULL RATE	POINT	PASS	POINT		POINT
1b	NORMAL POINTS	BIN	PASS			BIN

TABLE 1: The information content of each data type is diluted in each step of the data compression process, although some statistical properties of the original distribution are recorded.

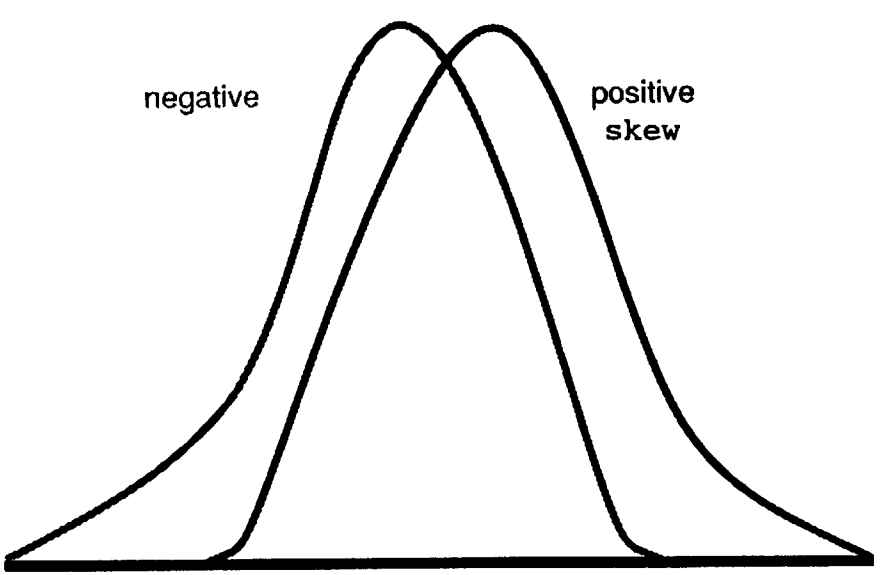

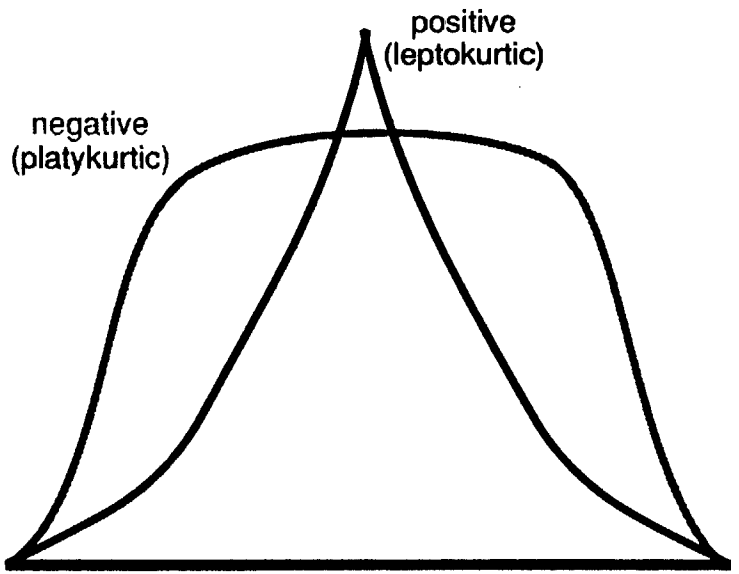

FIGURE 1: Shape factors which characterize the range deviation from normal can be used to supplement the root mean square value which is usually recorded. Slight positive skew is observed in almost all the systems; negative kurtosis(compared to a normal value of 3.0) is seen when a low editing multiplier (<3) "clips" the distribution and positive kurtosis is a symptom of loose editing (>3) which does not reject background noise.

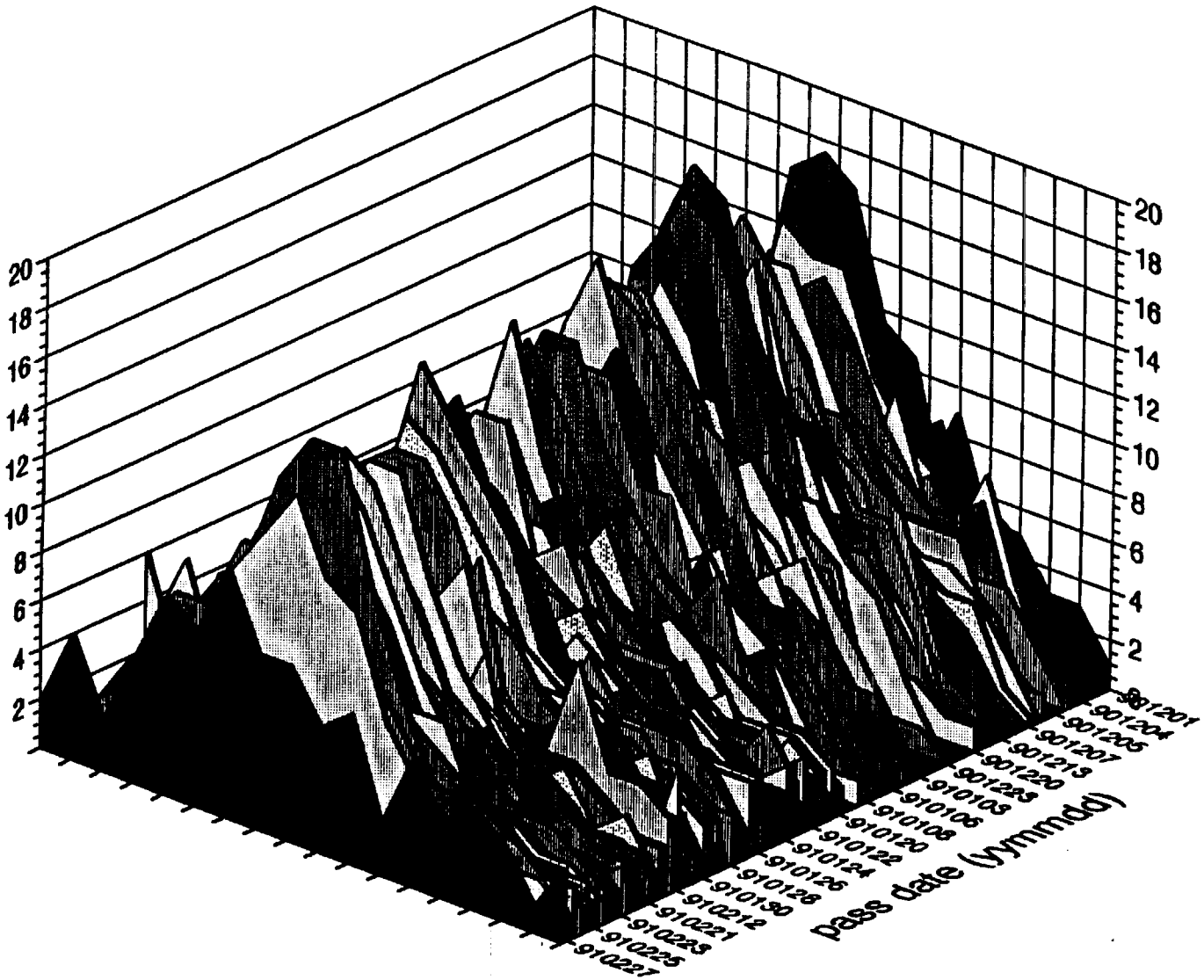

FIGURE 2: The build-up of pass histograms shows a progression towards a skewed distribution with time for LAGEOS data from the Grasse Observatory. The horizontal scale bin width is ten millimeters, and the ordinate gives the percentage of observations within each bin.

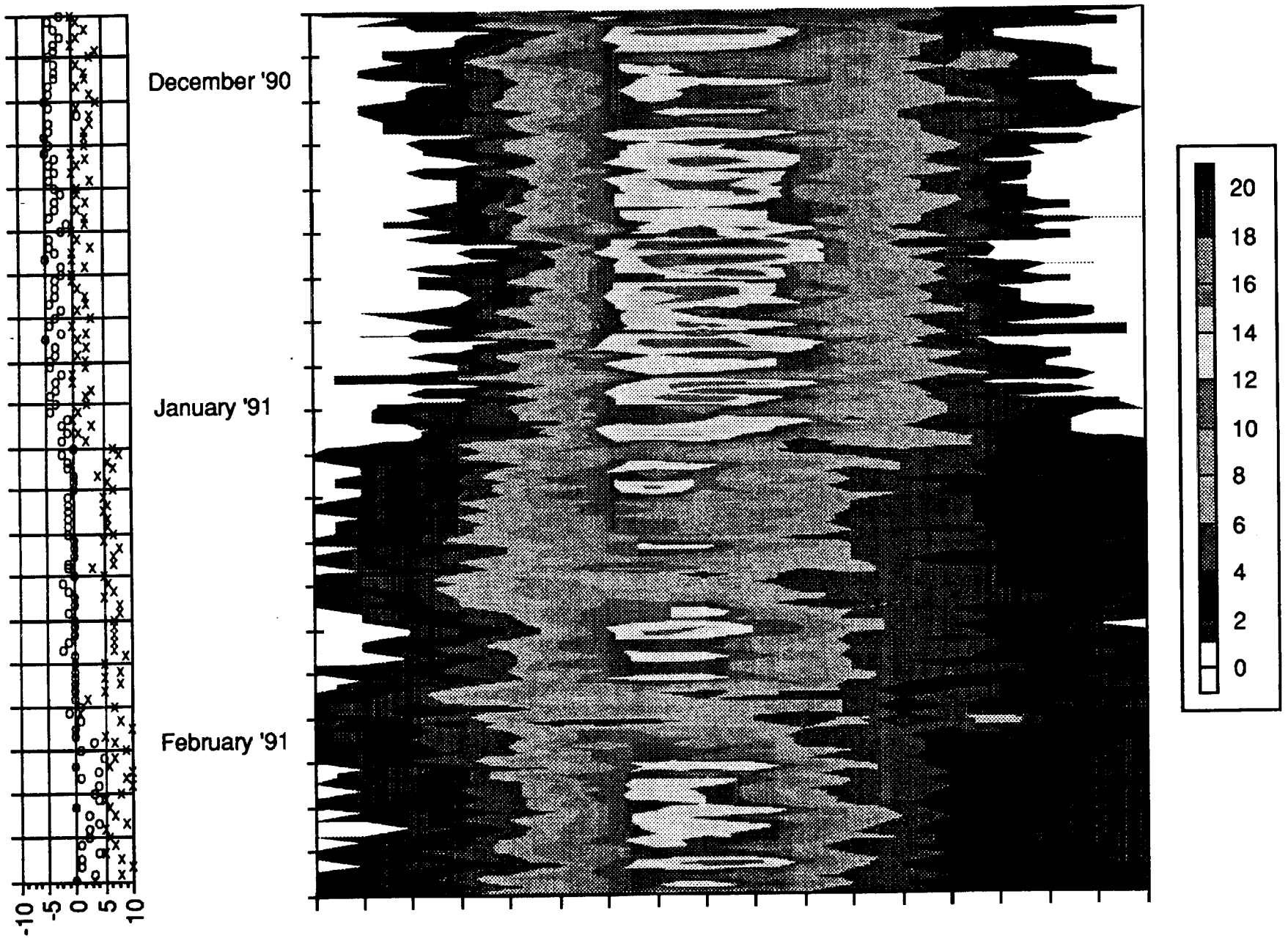

Figure 3. Pass-by-pass 10 mm binned LAGEOS residuals from Grasse.

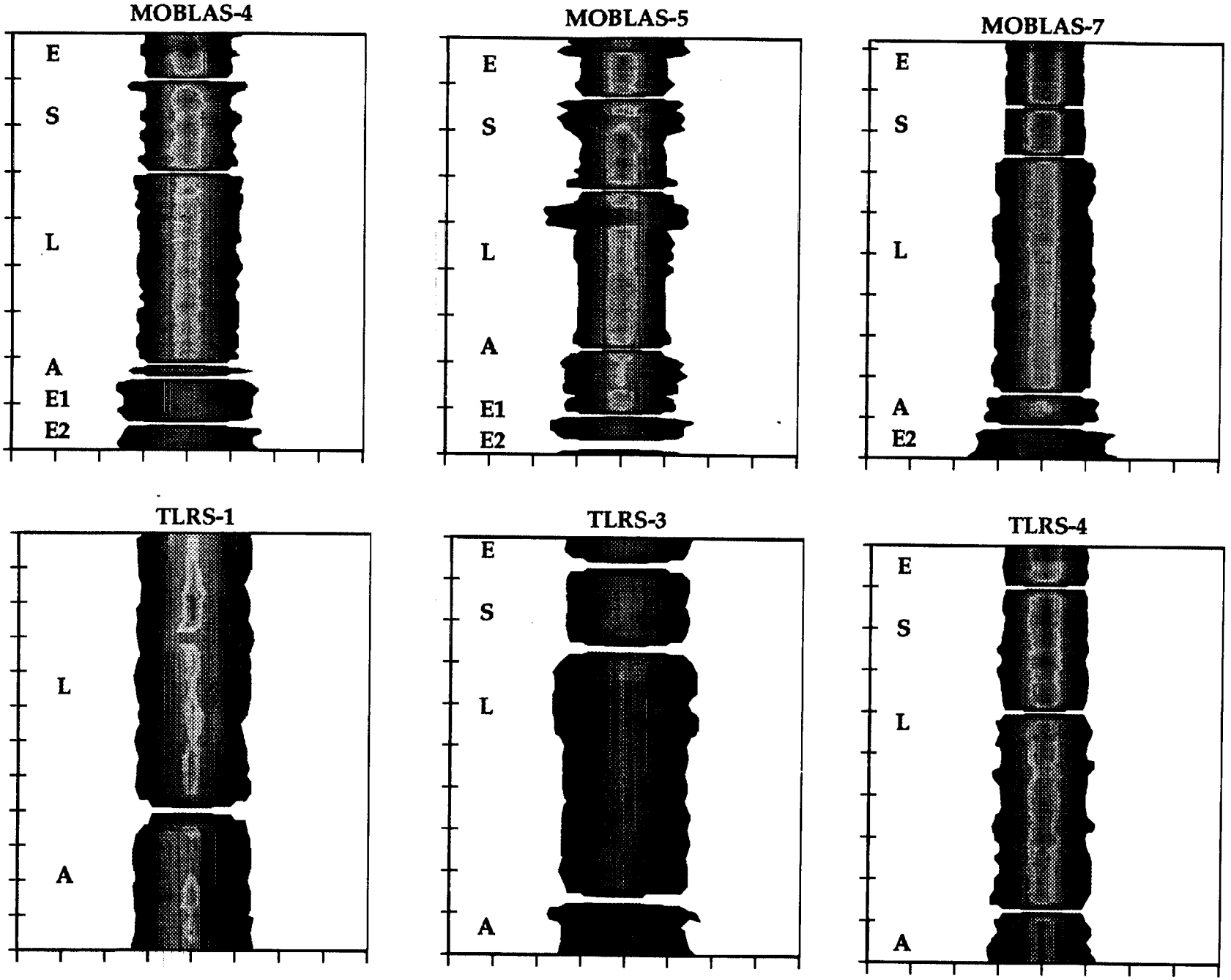

Figure 4. Satellite binned residuals.

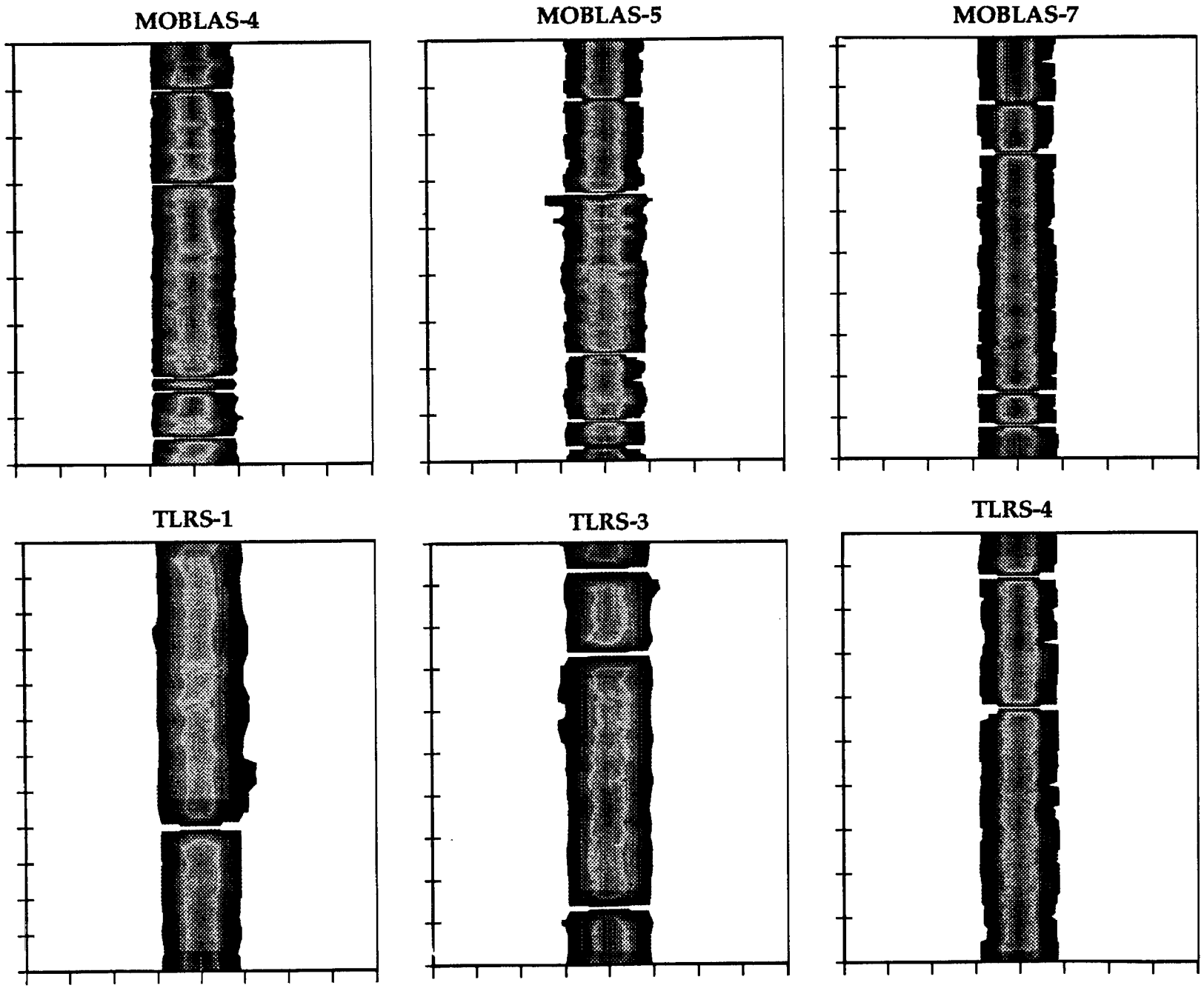

Figure 5. Calibration binned residuals

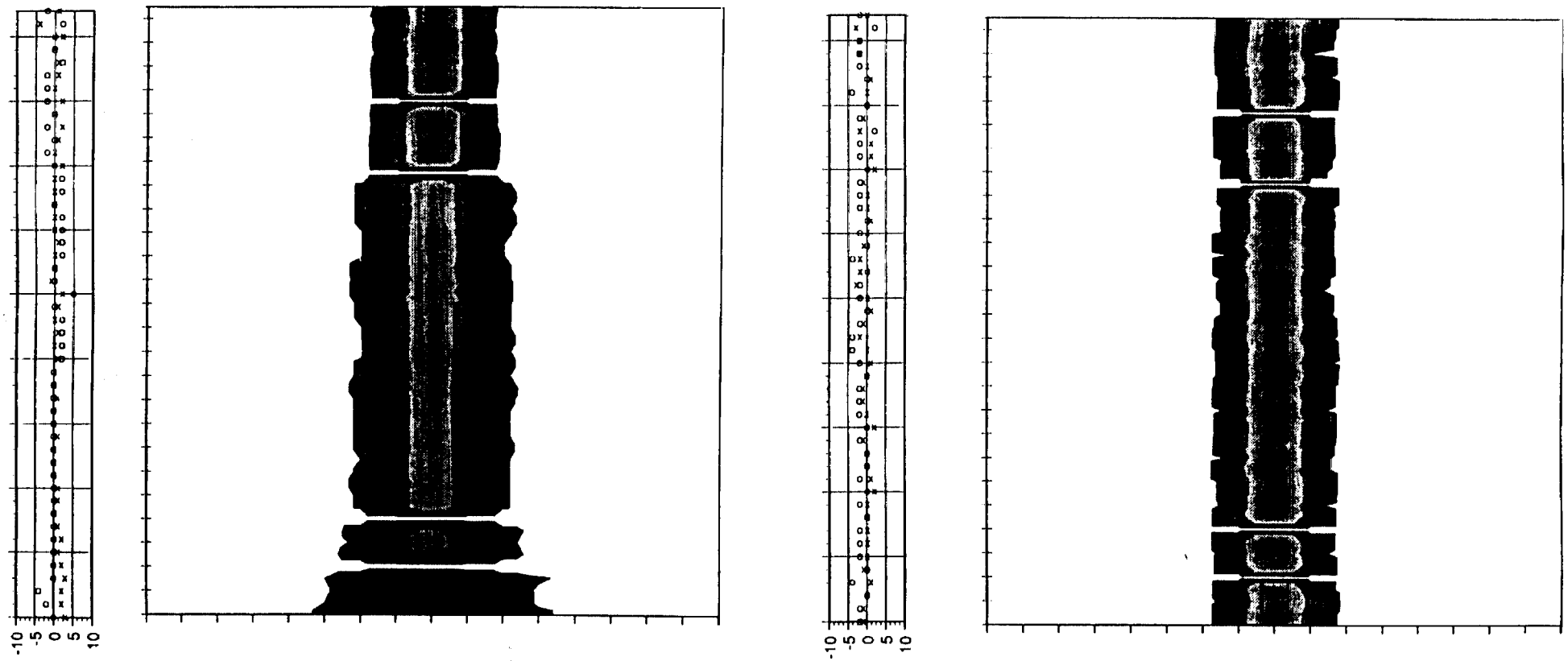

Figure 6a. Satellite and calibration binned residuals from MOBLAS-7

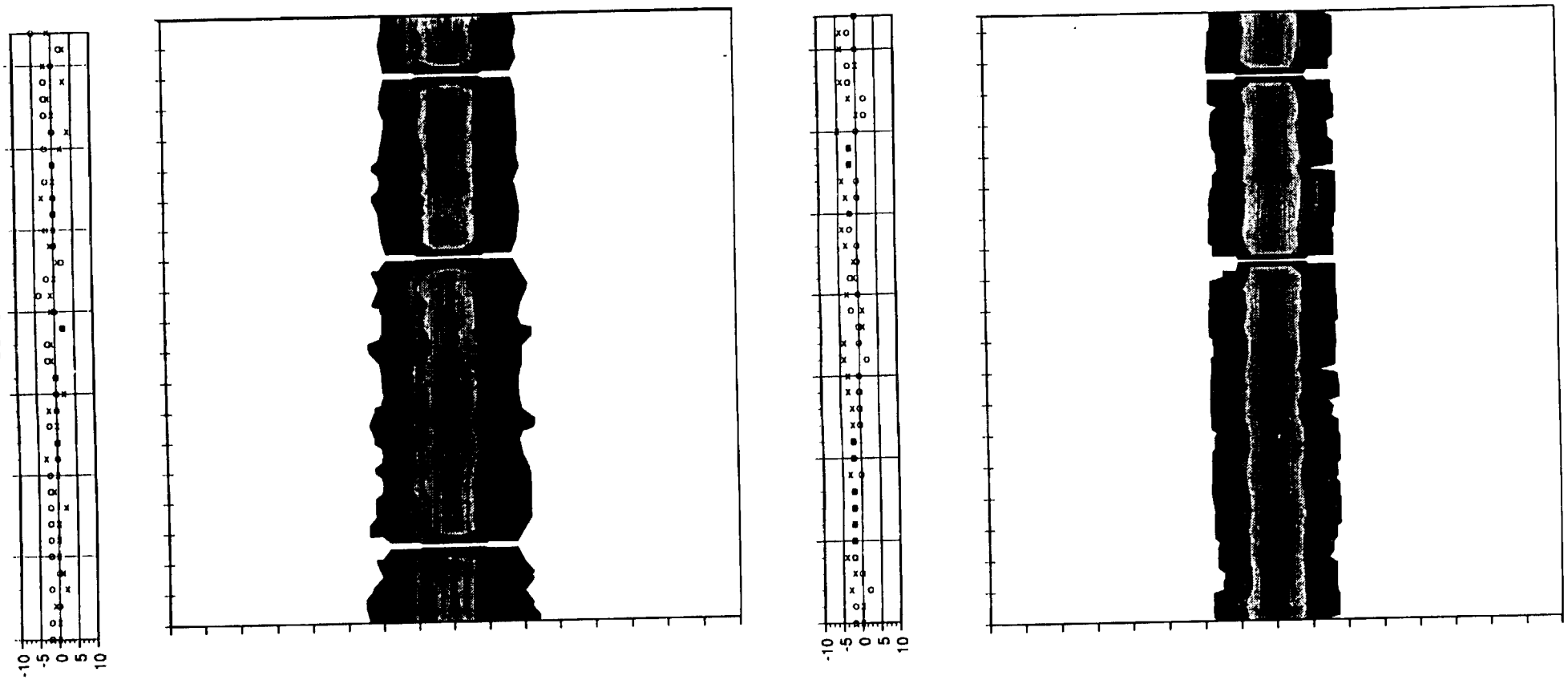

Figure 6b. Satellite and calibration binned residuals from TLRS-4.

N94-15560

SLR Data Screening; location of peak of data distribution

A.T. Sinclair

Royal Greenwich Observatory, Madingley Road, Cambridge CB3 0EZ, England

1. Introduction

At the 5th Laser Ranging Instrumentation Workshop held at Herstmonceux in 1984 consideration was given to the formation of on-site normal points by laser stations, and an algorithm was formulated. The algorithm included a recommendation that an iterated 3.0 × rms rejection criterion should be used to screen the data, and that arithmetic means should be formed within the normal point bins of the retained data. From 1990 September onwards this algoritm and screening criterion have been brought into effect by various laser stations for forming on-site normal points, and small variants of the algorithm are used by most analysis centres for forming normal points from full-rate data, although the data screening criterion they use ranges from about 2.5 to 3.0 × rms. At the CSTG SLR Subcommission a working group was set up in 1991 March to review the recommended screening procedure. The working group consists of A.T. Sinclair (chairman), G.M. Appleby, R.J. Eanes, P.J. Dunn and T.K. Varghese. This paper has been influenced by the discussions of this working group, although the views expressed are primarily those of this author.

The main thrust of this paper is that, particularly for single photon systems, a more important issue than data screening is the determination of the peak of a data distribution, and hence the determination of the bias of the peak from the mean. Several methods of determining the peak are discussed.

2. The effect of skew data

The first stage of forming normal points (described by Appleby in these proceedings) is to fit a trend-function to the raw ranges or to their residuals from a predicted orbit so that all signature from the orbit is removed, and then the distribution of the trend-removed data can be examined. Some level of screening is needed in the iterative process of fitting a trend-function, but this is not critical; 3.0 × rms or perhaps even tighter should be fine, and finally a wider band of trend-removed data, say 5.0 × rms, should be retained for examination of the distribution and then final screening. If these data have a symmetrical distribution about the peak then the criterion used for final screening is not critical, and a 3.0 × rms screening and use of the arithmetic mean should be fine. However if the data have a skew distribution then the arithmetic mean will be biased away from the peak, and the amount of bias will probably be dependent on the level of final screening used.

Analysis of the raw data from numerous stations shows that stations operating at a multi-photon return level per shot tend to have a fairly symmetrical distribution of data, whereas those operating at a single photon return level frequently show a significant skewness in the distribution of the data, usually skewed towards long ranges. As is described in papers by

Appleby and by Kirchner in these proceedings, some satellites (particulary Ajisai) impose their own signature on the laser data and can cause skewness as has been detected by some single-photon systems. However it is probable that some of the skewness is caused by the laser systems themselves, and it is certainly not the intention to explain away features of the system as being due the satellite. However if the skewness is due to the satellite then a means must be found in software of handling it. If it is due to the system then one view is that it is an engineering problem and that the hardware should be adjusted, but another view is that hardware will never be perfectly adjusted, and that one should accept some level of mal-adjustment and calibrate the effect out with software. Also it is possible that some detectors such as avalanche photo-diodes have an inherent skewness which would be very difficult to remove by adjustment of the hardware.

Systems which operate at a multi-photon return level and use pulse-level detection are in effect using hardware to form a mean of the individual photon returns obtained each shot, and so will see little effect from the distribution structure of the individual returns. Systems which operate at multi-photon level and detect the first photon received will primarily see the leading part of the distribution and will see little effect of any skew tail. Hence these system use a hardware method to eliminate any effects of satellite signature, and must ensure that the hardware is set up so as not to cause any biases. The objective of this paper is to devise an equivalent software scheme for systems operating at single photon return levels.

3. Choice of reference point of data distribution

The current recommendation is that the reference point of a data distribution should be the arithmetic mean of the data retained after a 3.0 × rms screening. This may not be ideal for a skew distribution of data.

If a skew data distribution is entirely caused by the laser ranging system, and if the ranges to the terrestrial calibration target have the same skew distribution as the satellite ranges, then it probably does not matter what screening criterion is used, provided the same is used for both calibration and satellite ranging, and it will probably be satisfactory to take the arithmetic mean of the data, even though this does not give the peak of a skew data distribution. However if the satellite is adding a significant contribution to the distribution, or if for some other reason the distributions of calibration and satellite data are different, then it is probably best that some means of processing the data should be devised such that the peak can be located. This is because, in the complicated convolution of the signatures of the system and the satellite, the range represented by the peak corresponds to the distance travelled by a photon from the peak of the laser pulse to the peak reflection point of the satellite (and so the centre of mass correction for the satellite should be that corresponding to peak reflection as determined in pre-launch testing).

Note that for a satellite pass it is not the peak of the trend-removed data for the whole pass that is required, but the peak of the distribution of the data within each normal point bin. This is a problem as there may not be sufficient points within a bin to give a reasonable indication of the distribution. The solution we recommend is that both the peak and arithmetic mean of the whole pass should be determined, and the difference, or bias, of the mean from the peak should thus be determined for the whole pass. Then within each normal point bin

just the arithmetic mean should be determined, but it should be corrected by applying to it the bias of the whole pass.

4. Methods of determining the peak of the data distribution

The usual method to determine the distribution of data is to plot a histogram, but this by itself does not give a good indication of the precise location of the peak. There is some arbitrariness introduced by the choice of bin width, and this is likely to be much coarser than the resolution required for the peak. An improvement can be made by fitting a curve such as a Gaussian profile to the histogram, but this total process is rather complicated, and as a Gaussian profile is symmetrical it will to some extent be influenced by a skew data set and be pulled away from the peak. In this paper we propose and examine three simpler techniques, and compare their performance on a variety of passes tracked by RGO Herstmonceux.

4.1 Data smoothing

After fitting and removing of a trend function, a plot of the data against time should be just a scatter plot about the mean, exhibiting no trend, but possibly not uniformly distributed about the mean. In order to examine this distribution we no longer consider the data as a time series, but just as points as lying along an x-axis, and our requirement is to plot in the y-direction some function describing the distribution of the points. The usual procedure is to plot a histogram, but we consider an alternative, in which each plotted residual is regarded as the most probable location of the measurement, and so we spread (or smooth) the effect of the residual each side of it using a Gaussian probability distribution. The result is that at any given location on the x-axis there will be contributions from all of the residuals, which can be summed and plotted on the y-axis. The peak of this plotted curve will give the most probable mean value of all of the residuals. The mathematical description of the method is very simple. Let $x_i, (i = 1, n)$ be the residuals of the range values from the trend function. Then for a range of values of x at, say, 10 ps intervals, evaluate and plot the quantity y, given by:

$$y = k \sum_{i=1}^{n} \exp[-\frac{1}{2}(x - x_i)^2/\sigma^2]$$

where σ is the somewhat arbitrary standard deviation of the smoothing function, although it would be reasonable to choose a value close to the single shot precision of the system. We regard the scale of y as arbitrary, and k is an arbitrary factor chosen to give some convenient maximum value of y.

Figure 1 shows a series of plots of this distribution function for a pass of Ajisai for a range of values of σ, with the conventional histogram plotted also. Apart from very small values of σ the peak is well-defined, and can be determined precisely. These plots are centred on the arithmetic mean of the distribution, so it is seen that the peak differs from the mean by about 2 cm, showing the large effect of the skewness (which is primarily caused by Ajisai - see paper by Appleby in this proceedings). A problem with the method is that the location of the peak depends on σ. As σ is increased the skewness has an increasing effect on the location of the peak, and in the plots the peak moves to the right by 2.3 mm as σ varies from 40 to 80 ps. A further problem is that for very sparse passes, possibly affected by a

significant amount of noise, the method fails to give a single main peak, or requires a large value of σ in order to do so.

4.2 Tight rejection criterion

The arithmetic mean of a set of data will be biased away from the peak due to any skewness of the data, but the amount of bias will be reduced if a tighter rejection level is used in forming the mean. We look at the effect of using various rejection levels, expressed as multiples of the root mean square difference from the mean (rms). However the rms of the retained data varies and usually gets smaller as the rejection limit is reduced, so for clarity we first determine the mean and rms using a 3.0 × rms iterated rejection level. Then subsequent rejection levels are expressed as multiples of this fixed rms. It also aids convergence with a tight rejection level if the rejection level itself does not vary as the iterations proceed. The table below gives the results of using various rejection levels on the Ajisai pass shown in Figure 1, with the various determinations of the mean given relative to the mean obtained using 3.0 × rms rejection.

Rej.	Mean(cm)	No.Pts.
3.0 × rms	0.00	1104
2.5 × rms	0.19	1081
2.0 × rms	0.58	1030
1.5 × rms	1.18	936
1.0 × rms	1.72	799
0.5 × rms	2.13	501

The peak of the distribution, as given by the smoothing method, is about 2 cm from the initial mean, and it is seen that the successive estimates of the mean move closer to the peak as the rejection level is reduced. For the rejection level of 0.5 × rms a large number of points have been rejected, and also in tests on various passes some difficulty was experienced in obtaining convergence. So for subsequent tests we have adopted a level of 1.0 × rms.

Objections that are frequently raised to using a tight rejection level are that too much data is being discarded, and that the data are being made to look better than they really are. However what we are proposing is that this tight rejection level is used only for the purpose of obtaining an estimate of the peak of the pass distribution, so that the bias of the peak from the 3.0 × rms mean can be determined. The means in the normal point bins and the value of the rms of the whole pass will be calculated from the data that remain after making a 3.0 × rms rejection.

4.3 Pearson curves

A distribution of n points x_i with mean $\bar{x}$ is characterised to a large extent by its moments μ_2, μ_3, μ_4 where

$$\mu_j = \frac{1}{n} \sum_{i=1}^{n} (x_i - \bar{x})^j$$

The second moment is the square of the standard deviation. The following quantities are also defined:

Skewness $= \mu_3^2/\mu_2^3$ indicates deviation from symmetry, $= 0$ for symmetry about $\bar{x}$

Kurtosis $= \mu_4/\mu_2^2$ indicates degree of peakiness, $= 3$ for Gaussian distribution.

These quantities are dimensionless and of restrained magnitude, and so are in some applications more convenient than the 3rd and 4th moments. This conventional definition of skewness has the disadvantage that the sign of the 3rd moment is lost, and it is this which describes the direction of the skewness. (It may be better to define skewness as $\mu_3/\mu_2^{3/2}$.) In the plots in this paper we attach the sign of the 3rd moment to the skewness.

There is a method in statistics of deriving a distribution function from values of these three moments obtained from a set of data. These are the Pearson distributions (see description by M.G. Kendall, The Advanced Theory of Statistics, Vol 1, 1947). The distribution function f of the quantity x is defined by a differential equation

$$\frac{df}{dx} = \frac{(x-a)f}{b_0 + b_1 x + b_2 x^2}$$

where

$$a = -\mu_3(\mu_4 + 3\mu_2^2)/A$$

$$b_0 = -\mu_2(4\mu_2\mu_4 - 3\mu_3^2)/A$$

$$b_1 = -\mu_3(\mu_4 + 3\mu_2^2)/A$$

$$b_2 = -(2\mu_2\mu_4 - 3\mu_3^2 - 6\mu_2^3)/A$$

$$A = 10\mu_4\mu_2 - 18\mu_2^3 - 12\mu_3^2$$

and where the origin of x is now at its mean value. The peak of the distribution curve is at $x = a$.

This differential equation has several forms of analytical solution depending on the values of the moments. For values likely to be met in practice its solution is of the form

$$f = k(1 + \frac{x}{a_1})^{m_1}(1 - \frac{x}{a_2})^{m_2}$$

but for the precise values of the moments corresponding to a Gaussian distribution this solution becomes singular, and it has an alternative solution which is in fact the Gaussian distribution. So unfortunately the analytical solution is close to a singularity in the region likely to be met in practice, and so is not a very useful way of deriving the shape of the curve. However it is easy to solve the differential equation by numerical integration starting from the peak, although there can be problems as the singularity on the x axis is approached

which require a little fudging. Some solution curves are shown in Figure 2 for a range of values of skewness and kurtosis. No attempt has been made to normalise the area under the curves; they are all plotted with the same height at the peak. It is seen that the shapes of the curves are close to a Gaussian curve until fairly extreme values of the parameters are reached, eg., skewness of 0.6 or kurtosis of 2.2, and then the shapes are not particulary typical of what is seen in some SLR data, and so it can be expected that this method will give a good estimate of the peak for distributions close to Gaussian, but not be so useful in more extreme cases.

This discussion of how to plot the Pearson curves is given here for completeness, but it is not proposed that this should be a normal procedure for SLR data handling. However the method provides a simple estimator of the location of the peak of a distribution of data. Expressed in terms of the standard deviation σ, the skewness s, and the kurtosis k, with consideration given to the sign of the 3rd moment, the displacement of the peak from the mean is

$$a = \frac{-s^{1/2}\sigma(k+3) \times \mathrm{sign}(\mu_3)}{10k - 18 - 12s}$$

5. Comparison of methods of peak determination

Figure 3 shows the results of applying these various methods of peak determination to a number of passes tracked by RGO Herstmonceux. The passes were selected to provide a good test of the methods, and are not necessary typical passes from the station. The figures give the following information:

- the conventional histogram, using a bin of 40 ps (= 6 mm)
- the smoothing-method distribution function plotted as a solid curve
- the Pearson distribution function plotted as a dashed curve
- the 3 × rms-rejection mean shown as a solid vertical line from the top
- the 1 × rms-rejection mean shown as a dashed vertical line from the top.

The two distribution curves are plotted with slightly different peak heights for clarity, and the peak height of the histogram is limited if necesssary to be slightly below these two curves.

The information given in the captions includes:

- Smoothing parameter σ in ps (multiply by 0.15 to get mm)
- Bias(1): difference of smoothing-method peak from 3 × rms mean
- Bias(2): difference of 1 × rms mean from 3 × rms mean
- Bias(3): difference of Pearson peak from 3 × rms mean.

Figures 3(a) and 3(b) show passes with insignificant skewness, in which all methods of determining the peak and mean agree well.

Figures 3(c), 3(d) and 3(e) show passes with significant skewness, in which smoothing, Pearson and 1 × rms agree well, but are significantly different from the 3 × rms mean.

Figures 3(f) and 3(g) show passes in which smoothing and 1 × rms agree well, but the Pearson peak stands off, and all differ from the 3 × rms mean.

Figures 3(h) and 3(i) show passes in which the Pearson peak and 1 × rms agree fairly well, but the smoothing peak stands off.

From these and tests on numerous other passes we conclude that:

- for a single-photon station there is often a significant difference of the peak from the 3 × rms-rejection mean
- the 1 × rms-rejection mean usually agrees with one or other of the smoothing peak and Pearson peak, and often with both.

6. Recommendations

In conclusion we recommend the following:

a) the ranges to a calibration target or the trend-removed data from a whole satellite pass should be screened at an iterated 3 × rms level, and in the process determine *rms* and *mean* of the retained data

b) the skewness and kurtosis of the retained data should be determined

c) using this fixed value of *rms* a second determination of the mean should be made using an iterated 1 × *rms* rejection. This provides an estimate of *peak*. Then the bias of the calibration or pass is $bias = peak - mean$

d) for a calibration run, use the value of *peak* as the calibration value

e) for a satellite pass, form normal points from the screened data within each bin in the usual way, but add the correction *bias* to the normal point.

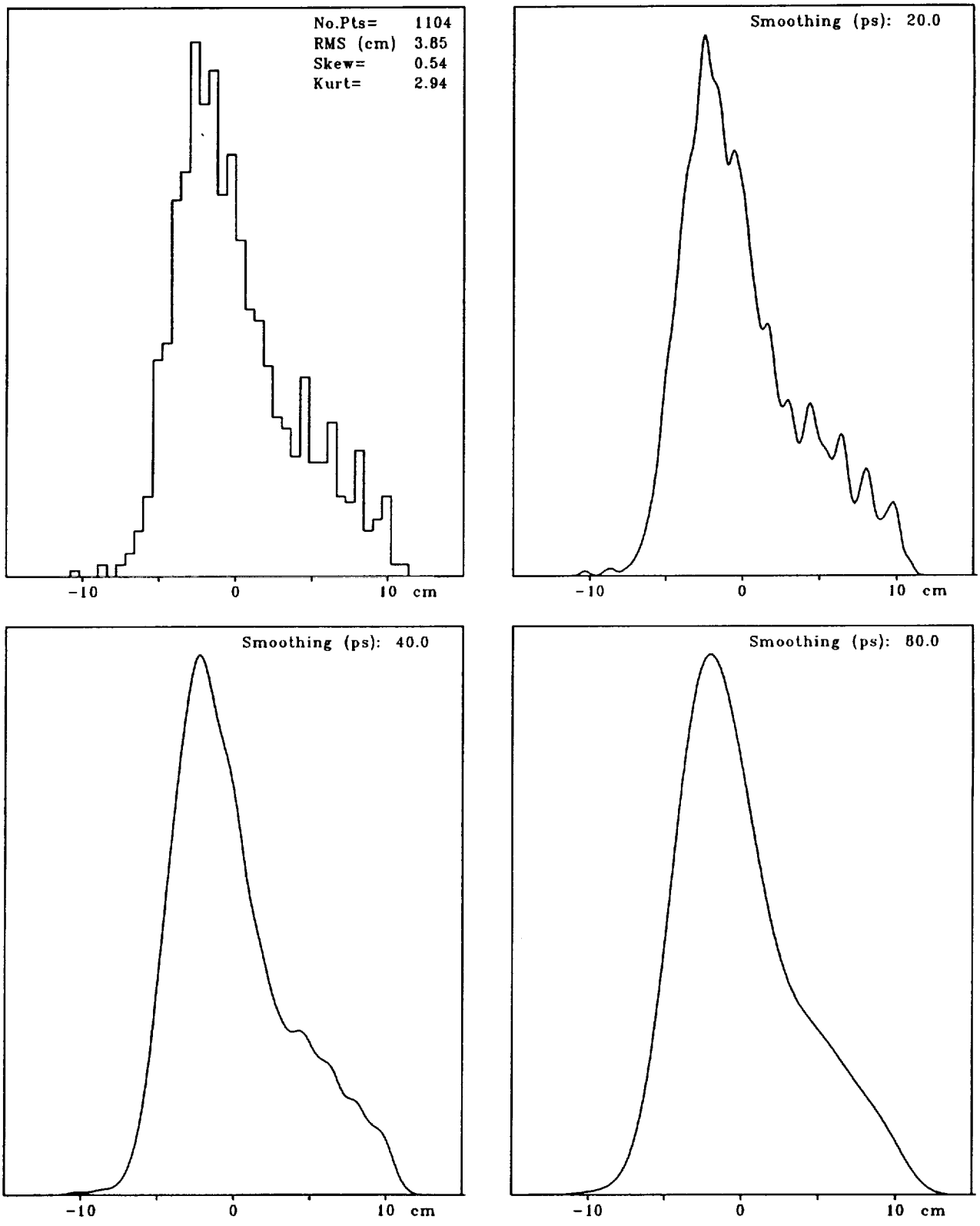

Figure 1. Use of the smoothing method to determine the distribution of an Ajisai pass.

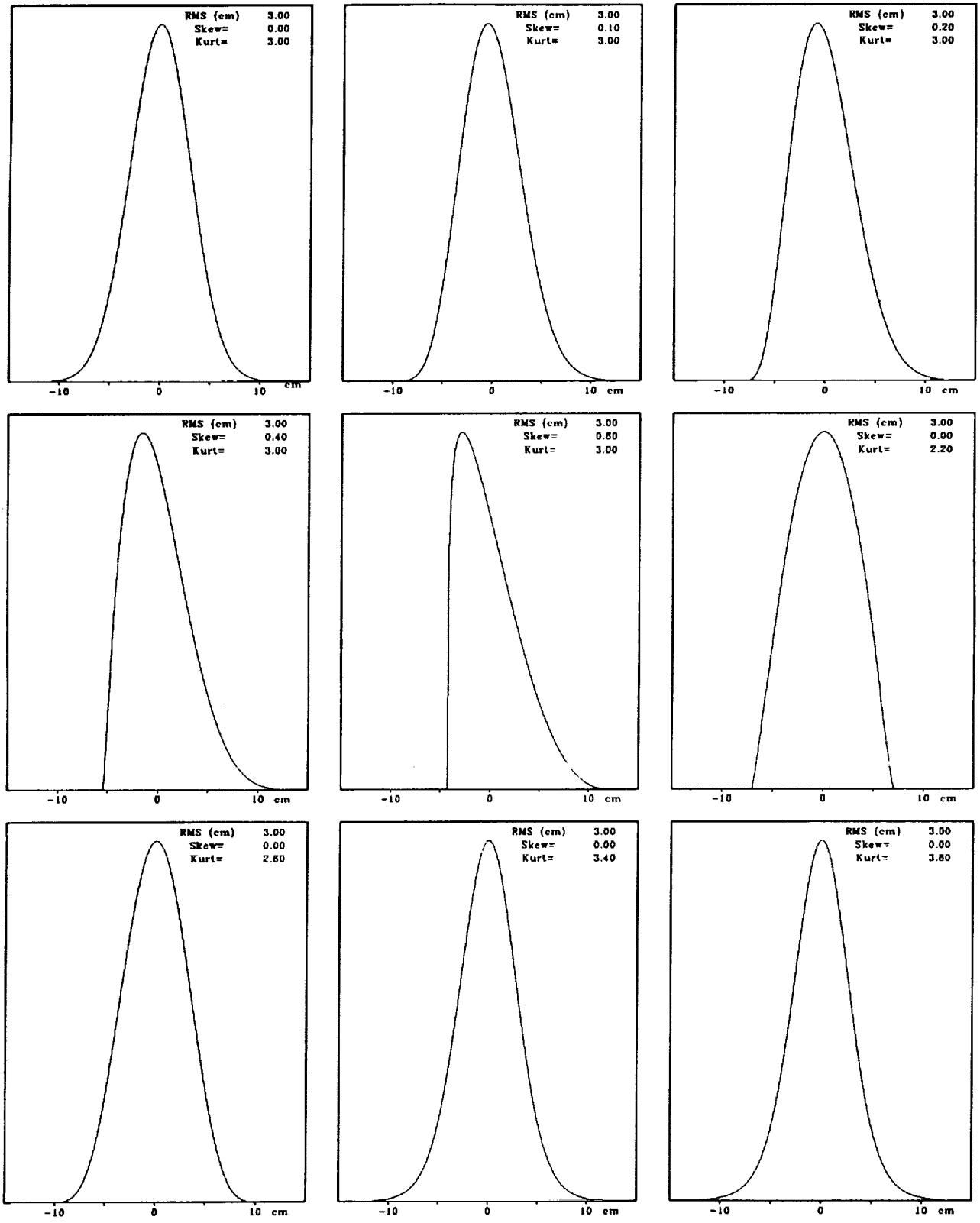

Figure 2. A range of Pearson distribution curves.

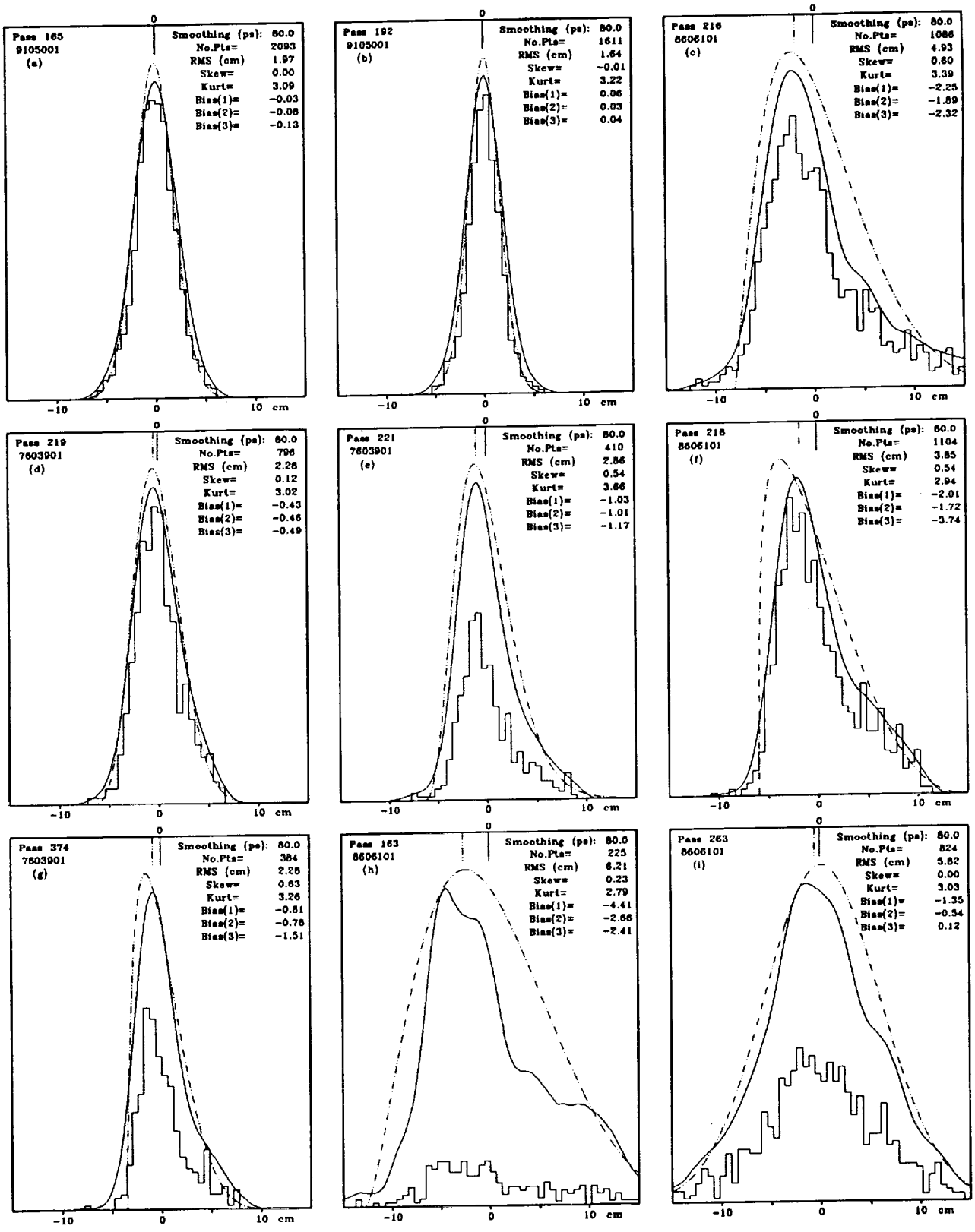

Figure 3. Comparison of methods of peak determination.

ADAPTIVE MEDIAN FILTERING FOR PREPROCESSING OF TIME SERIES MEASUREMENTS

Matti Paunonen

Finnish Geodetic Institute
Ilmalankatu 1A
SF-00240 Helsinki, Finland
Telefax:358-0-264995

ABSTRACT.

A median (L1-norm) filtering program using polynomials was developed. This program was used in automatic recycling data screening. Additionally a special adaptive program to work with asymmetric distributions was developed. Examples of adaptive median filtering of satellite laser range observations and TV satellite time measurements are given. The program proved out versatile and time saving in data screening of time series measurements.

1. INTRODUCTION

The advantages of data screening of satellite laser range measurements using median (or L1-norm) instead of least squares were shown earlier (Paunonen 1989). The median is known to be insensitive to outlying observations, which is a useful property in preliminary data screening of any time series measurements. Asymmetric distributions often arise for various reasons; saturation of the laser detector and the receiver electronics, laser prepulses etc. This cannot be easily treated with least squares methods.
In response to multiple needs, a median program permitting use of a higher order polynomial of up to ten was developed. A second version used automatic recycling of the fitting loop until a specified fit was obtained and a special program to work with unsymmetric distributions was devised. Examples of screening satellite laser range observations and TV satellite time measurements are given.

2.1 MEDIAN PROGRAM

The median program was constructed with the Fortran-procedure published by Barrodale and Roberts (1974), modified for polynomial use. The function to be minimized in the overdetermined case is

$$\sum_{1}^{M} \left| y_i - a_0 - a_1 x_i - a_2 x_i^2 - \ldots - a_N x_i^N \right| \quad , \tag{1}$$

where y_i are the observations, x_i the observing times (here), M the number of observations and N the degree of the polynomial to be fitted to the observations, and a_j (j=0...N) the coefficients of the polynomial.

2.2 AUTOMATIC MEDIAN FILTER PROGRAM

A versatile data screening program should be able to run automatically, without any manual interface. The median is good basis for a filtering program, because it selects reliably the densest part of the measurements as a reference. This means that any erratic points, that is outliers, are of true size, and not evened out as in the least squares method. Operation of the sequential median filtering program is started by forming the residuals of all the observations and calculating their average. Observations below a certain rejection limit are selected for the next cycle only. The problem is to find a suitable limit which is neither too inclusive nor too exclusive. Good operation was obtained by using the rejection level, R,

$$R = 3.5 * AVR \quad , \tag{2}$$

where AVR is the average of the residuals in the earlier round. For a Gaussian-shaped distribution the width between the zero and the point corresponding to one standard deviation is 1.46 times the width corresponding to the average. Thus the limit used is roughly equivalent to 2.4 times the standard deviation used in the least squares method. The repeated rounds are limited to four, but the final selection is generally ready after three rounds.

2.3 ADAPTIVE AUTOMATIC MEDIAN FILTER PROGRAM

In practice, the distribution of the data may be asymmetric and may include separated peaks. In satellite laser ranging, a distribution as shown in Fig.1 can easily arise with mode-locked lasers. The transmitted pulse may contain a small prepulse if selection of a single laser pulse from a train of mode-locked laser pulses is incomplete. Even if the parasitic pulse is small, it causes stops in the photon counting mode. This poses difficulties for normal screening methods using least squares. Use of only

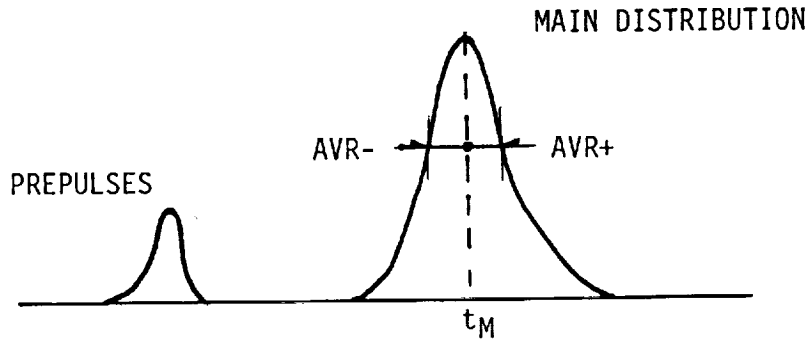

Fig. 1. An asymmetric distribution of possible range residuals in satellite laser ranging.

a two sigma-limit (Appleby and Sinclair 1991) is possible, but it may also fail if the contamination is severe. The median is expected to perform better because it finds the location of the main pulse more easily. The main part may also show unbalanced distribution (skewness) due, for instance, to saturation effects in the receiving electronics.

A modified method for asymmetric distributions is proposed as a refinement of the median filter described. Because the median produces separate average values for positive and negative residuals, AVR+ and AVR-, respectively, the program is allowed to select a minimum of the absolute values, and use it as the basis for the rejection limit in Eq.(2),

$$AVR = Min(|AVR+|, |AVR-|) \quad . \tag{3}$$

At least mild skewness will be corrected in this way. If the distribution is symmetric, operation is normal.

3. TESTS OF THE ADAPTIVE MEDIAN FILTERING

The first test set was obtained from satellite laser range observations to the distant LAGEOS- satellite at Metsähovi, Fig. 2a. This is a mixture of good and bad observations. The points on the shorter range side arose from the shape of the laser pulse (Paunonen 1989). The short 4.5 ns pulse was cut by an electro-optical shutter from a 20 ns long ruby laser pulse. However, the shutter operation was not perfect and sometimes some leakage due, for instance, to changing temperature, may have occurred. This leakage, which was less than 10 per cent, looks like a pedestal on which a short pulse is riding.

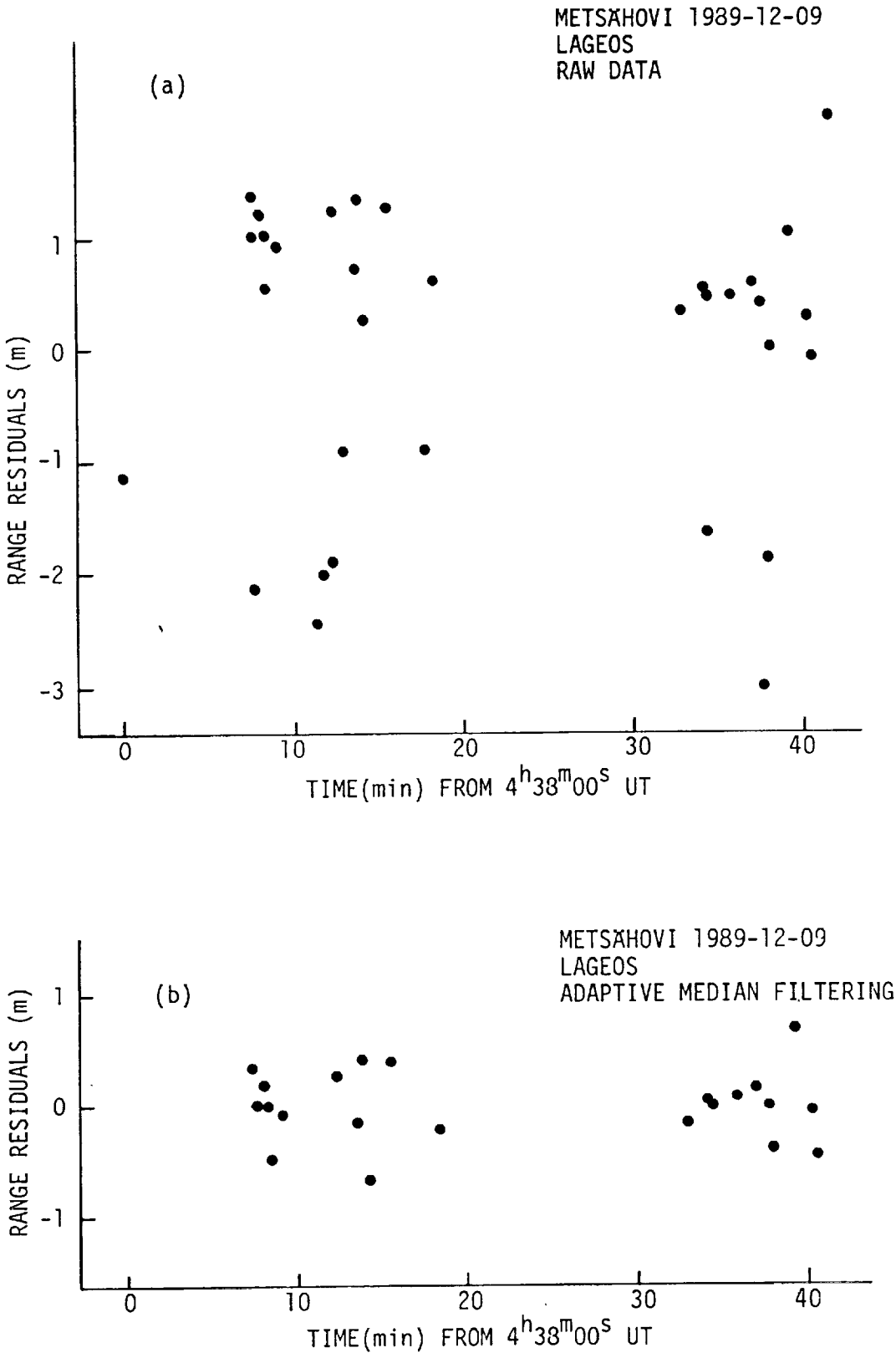

Fig. 2. a) Unscreened range residuals in a LAGEOS pass
b) Range residuals after adaptive median filtering (linear fit).

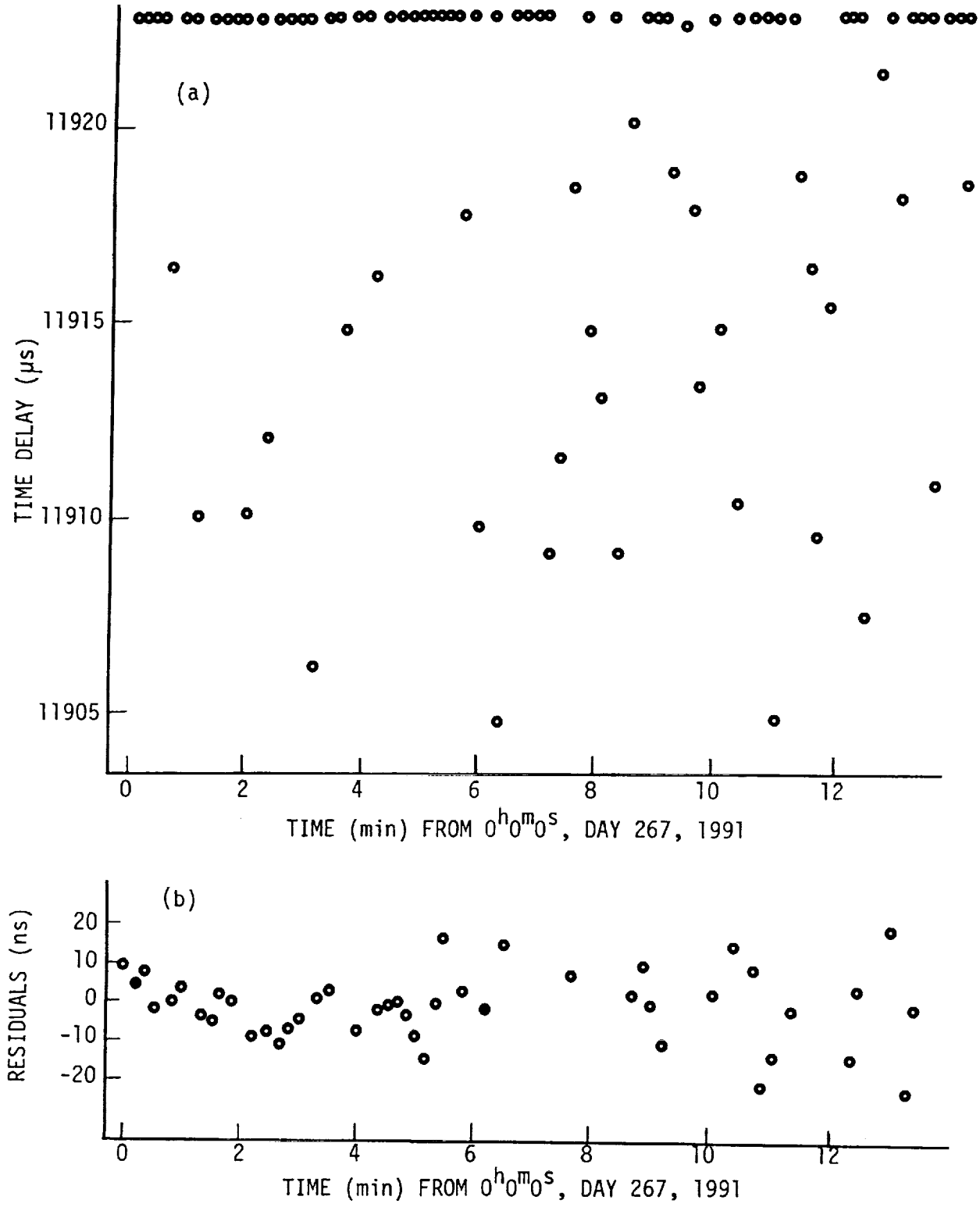

Fig. 3. a) Unscreened time measurements from a TV satellite
b) Time residuals after adaptive median filtering (parabolic fit).

The energy ahead of the main pulse may stop the time interval counter. The adaptive median filter selected 22 observations from the 33 available ones (Fig. 2b). The initial data set is not random, because similar results were also obtained at the calibration line. The result is also plausible, because its width corresponds to the laser pulse width. The earlier method for testing one observation at a time (Paunonen 1982) would be of little value, without knowing what to seek.

Another test set originated from recent TV satellite time measurements (Fig. 3a). Here the second tick from the station clock started the time interval counter and the horizontal syncronization pulse from a satellite TV receiving system (50 Hz rate) stopped it. The large number of badly timed pulses propably originated from the encrypting method the TV transmission (program RAIUNO on the EUTELSAT 1-F5 satellite) is using. This set was also cleared well with the adaptive median filter (Fig. 3b). The r.m.s. value of the residuals was 11 ns.

4. DISCUSSION AND CONCLUSIONS

The adaptive median filter has proved to be versatile and to save time. It can safely remove several outliers, however large they are. This is a big advantage over the least squares method, in which all large outliers must be removed before any useful operations can be obtained. Polynomials should be used with care also in median filtering. End points in particular may behave peculiarly. The median program sets the value of some residuals at zero (this number is same as the degree of the polynomial), which is artificial. The asymptotic estimation efficiency of median is also usually worse than that of the mean (Eadie, et.al.,1971). It seems therefore best to use the median in the data screening phase and to use the normal least squares method for final extraction of the results. Use of the least squares is then well justified, because the distribution of the screened data is nearly normal.

REFERENCES

Appleby, G.M. and A.T. Sinclair (1991). Formation of on-site normal points. Satellite Laser Ranging Newsletter, SLR Subcommission of the CSTG (International Coordination of Space Techniques for Geodesy and Geodynamics), April 1991, pp. 25-28.

Barrodale, I. and F.D.K. Roberts (1974). Solution of an overdetermined system of equations in the l1 norm. Communications of the ACM, Vol. 17, No. 6, pp. 319-320.

Eadie, W.T., D. Dryard, F.E. James, M. Roos, B. Sadoulet (1971). Statistical Methods in Experimental Physics. North-Holland Publishing Company, Amsterdam 1971, 296 pp.

Paunonen, M. (1982). Studies on the Metsähovi satellite laser ranging system. Reports of the Finnish Geodetic Institute, 1982:2, Helsinki 1982, 47 pp.

Paunonen, M. (1989). Use of the L1-norm in screening laser range observations to satellites. Proc. of the 18th INTERKOSMOS Symposium on the Use of Artificial Satellite Observations for Geodesy and Geophysics, June 12-17, 1989, Cracow, Poland, (Ed. WL. Goral, Polish Academy of Sciences, Observations of Artificial Satellites of the Earth, No 27, Warsaw 1990), pp. 359-362.

SATCOP MISSION PLANNING SOFTWARE PACKAGE

S. BUCEY
Bendix Field Engineering Corp.
Seabrook, MD

New laser ranging capabilities, additional satellites, and changing priorities are making it more difficult to determine the most efficient method of operations for NASA's CDSLR Network. A software package called SATCOP (Satellite Ranging Coordination Programs) has been developed to assist in mission support and planning operations. Its uses range from planning daily station operations to conducting pre-launch satellite visibility studies. SATCOP provides a listing and graphics output of satellite visibility for a given occupation site for any time period. SATCOP may also be used to determine the optimum ranging scenario for a station, taking into account satellite ranging priorities and station operational requirements. Finally, SATCOP may be used to illustrate simultaneous satellite visibility for multiple stations.

Introduction

As the CDSLR Network grows into the 1990's it is undergoing many changes in both its capabilities and requirements. On the one hand great progress has been made in terms of increasing the SLR systems' performance. Upgrades to the onsite computer and improved laser ranging hardware have greatly increased the number of satellite passes which can be acquired during an operating shift by reducing the amount of time needed for operations other than actual ranging. On the other hand, more requirements have been placed on the systems. Many more satellites have become available, with more scheduled for launch, thus increasing the likelihood of simultaneous satellite visibility. In addition, the possible scenarios required for ranging these many satellites are changing frequently, with conflicting priorities and needs.

It became apparent that some tools needed to be developed to assist the planners in determining Network ranging priorities. Such tools have been developed at Bendix under the direction of NASA's Dynamics of the Solid Earth Project (DOSE) for both long range planning and routine operations to maximize the amount of data collected. This paper will review some of these tools and describe their uses.

The SATCOP software package has several parts which are used for both routine operations and pre-launch scheduling. The use of such software helps determine pre-mission requirements such as ground track determination, forecasted station performance, predictions of optimum system locations, and predicted satellite visibility. SATCOP also produces graphs of ground tracks of acquired passes; determines availability of simultaneous ranging opportunities; schedules operating hours for maximum visibility; and produces automated single station scheduling for daily station activities.

Figure 1 is a time plot of satellite visibility for a given station. This figure demonstrates that even with just 6 satellites considered the opportunities for laser ranging are abundant. Such plots, and others like it, are used for operational scheduling of station activities and for the determination of operational requirements for future missions or locations. Typically such a plot is done for a 7 day period, but the number of satellites and number of days is user determined. The plot consists of a time scale in hours GMT across the top, and a day scale down the left. A subscale of each day is present, dividing each day into a line for each satellite. For each satellite, a two letter satellite identifier indicates the horizontal line across which the satellite could be visible (refer to Figure 8 to identify the satellite associated with each two letter identifier). Across the plot a solid line indicates when a satellite is visible, and a total number of minutes for that day is printed on the right. On the last day of the plot a column on the right also indicates the total number of minutes visible during the time period of the plot.

Figure 2 illustrates the number of possible sightings of two satellites over a four day period at 5 locations. Such graphs are used when extended time periods are considered, and can be used to compare satellite visibility at several stations simultaneously. Such graphs are useful for determining the best of several possible station locations and the expected visibility at a given location, and can include several satellites. Often it is also desired to know the number of possible simultaneous sightings of a satellite for several locations. Figures 3 and 4 demonstrate the tools used for determining this number. Figure 3 is a matrix showing the number of mutual sightings possible at several locations. The number of such sightings for a given pair of stations is found by cross indexing between the two desired stations to find the result within the matrix; as an example for MOBLAS 4 (7110) and MOBLAS 8 (7109) the number of such sightings is found to be 130. Figure 4 is a listing of all possible subsets of the desired stations which can range, along with the times of mutual availability. The user can determine the minimum number of stations desired for simultaneous ranging, and the time period for consideration.

The SATCOP software package has been developed to provide support for other purposes as well. Figure 5 is a plot which shows the distribution of acquired LAGEOS passes reported as quicklook data for the time period May 2 to May 14, 1992. This type of plot allows the user to quickly

determine the geographic distribution of data reported during the indicated time period. Figure 6 is used to compare sightings for two or more stations over a 24 hour period, and is read similarly to Figure 1. Such a graph is convenient for quickly determining the opportunities for coordinated activities between two or more locations with one or more satellites.

A major use for the SATCOP package is single station scheduling for daily activities. The purpose of such scheduling is to assist the station crew in conducting laser operations by considering as many of the requirements and opportunities presented to the station as possible, and then producing a schedule which is a possible 'optimum' solution for the day's activities.

To perform such scheduling many parameters are considered. A major requirement is to resolve ranging opportunities when two or more satellites are visible simultaneously. SATCOP considers satellite priority, ranging limitations such as a maximum time limit on a satellite pass, and day or night ranging restrictions. If two satellites of the same priority are available then the software ensures that ranging is as evenly distributed between the two during the day as possible, based on available minutes of data. Activities which may exclude laser activities are taken into account, such as data preprossessing and calibration time. If the system has the multi-satellite calibration capability then the software determines a best sequence for calibration and ranging.

As an example a schedule generated for MOBLAS 4 at Monument Peak will be considered, using the time period covered by Figure 1. Some of the parameters used for generating the schedule are illustrated in Figures 7 and 8. As an aid to readability only two days will be scheduled, but normally a regular workweek is considered. The hours of operation were determined previously using other methods described earlier. From this information the schedule sent to the station is graphically shown in Figure 9. Looking at the plot for each day there is a line corresponding to each satellite plus an additional line showing laser calibration, denoted by 'C1'. Since this system is using the multi-satellite calibration capability data may be acquired on several satellites between calibrations. Also, since the overhead time has been greatly reduced by this, and other, upgrades true interleaving of passes is possible when a high priority short pass occurs at the same time as a low priority long pass. The thick line represents the time that the station is actually ranging (or calibrating), while the thin line represents the time the satellite is actually visible (the thick line corresponding to the ranging of a given pass is located above the thin line).

Conclusion

In the future the requirements for SLR activities will only become greater. New satellites, new ranging scenarios, and new station abilities will require changes to be made to the methods used to schedule operations. Recent examples are the ETALON campaign and the multi-

satellite upgrade. Of course, many possible parameters have yet to be considered. Obviously it is impossible to account for poor weather conditions deterring laser activities on a given day, but plans are being considered to include long term weather effects as a statistical modification of the predicted station performance. And it would be similarly difficult to account for system down time due to component failure. But the use of this package, and its continued improvement, has allowed Bendix to more efficiently coordinate the NASA CDSLR network activities.

SATELLITE VISIBILITY: mobl4 (MT PEAK)

FIGURE 1

9/18/92 – 9/19/92

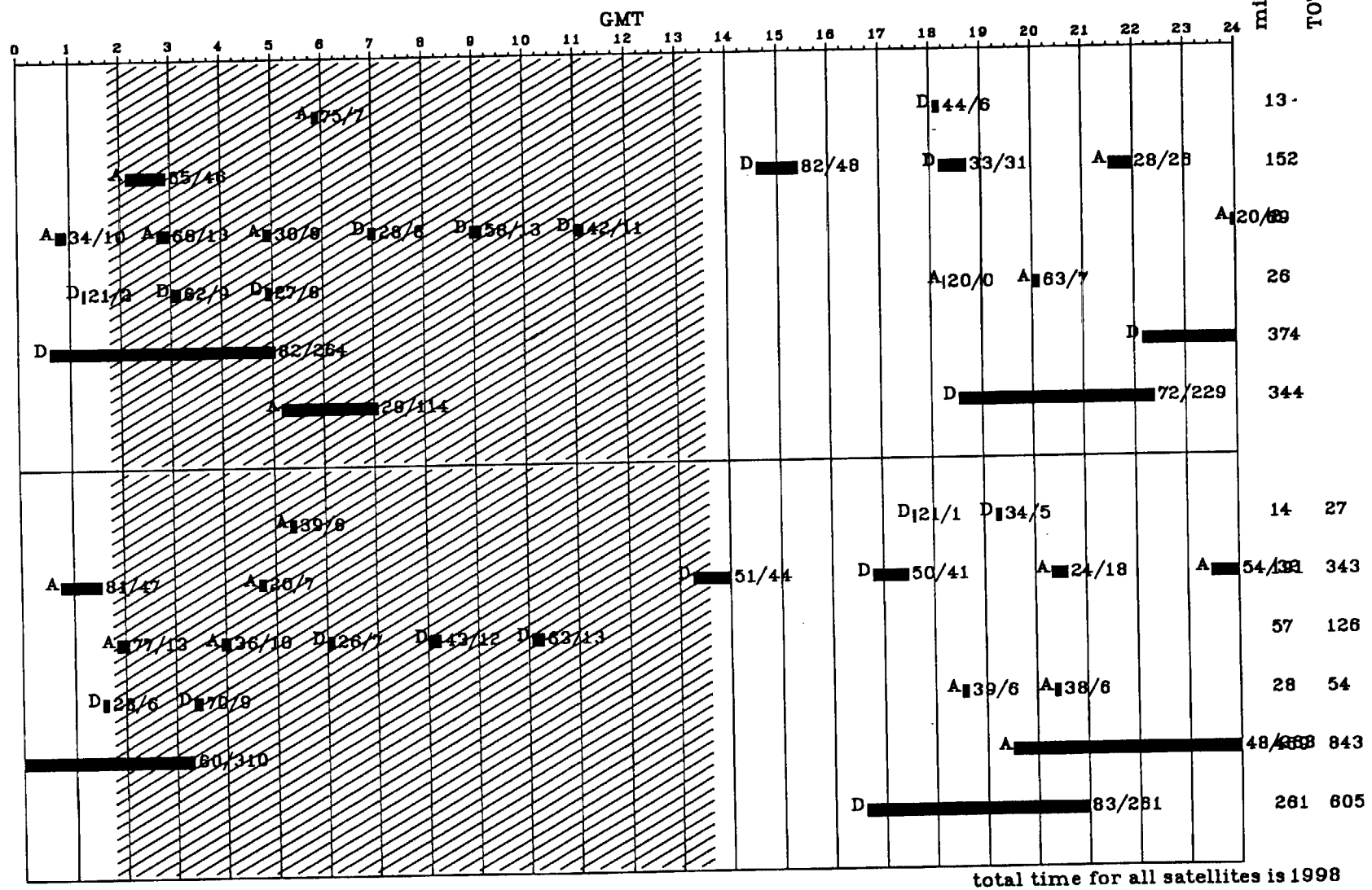

2-55

total time for all satellites is 1998

date created: 9/15/92

CDSLR/OAS

BUCEY

letter on curve indicates ascending/descending

SHADED SECTION IS NIGHT

NOTATION ON PASS IS MAXIMUM ELEVATION–

AND NUMBER OF MINUTES

PASSES BY STATION AND SATELLITE

FIGURE 2

	511 517		518 524		525 531		601 607			Totals	
7110	LAG	AJI	LAG	AJI	LAG	AJI	LAG	AJI		LAG	AJI
DAY	15	0	11	4	15	8	12	16			
TWILIGHT	2	0	4	2	1	3	1	2		137	161
NIGHT	18	40	19	35	19	28	20	23			
7090	LAG	AJI	LAG	AJI	LAG	AJI	LAG	AJI		LAG	AJI
DAY	15	9	15	16	15	19	12	23			
TWILIGHT	1	2	0	2	1	0	1	3		130	150
NIGHT	17	27	18	20	15	18	20	11			
7105	LAG	AJI	LAG	AJI	LAG	AJI	LAG	AJI		LAG	AJI
DAY	14	3	12	9	13	15	11	21			
TWILIGHT	2	2	2	2	1	2	1	3		127	138
NIGHT	16	30	18	23	18	18	19	10			
7109	LAG	AJI	LAG	AJI	LAG	AJI	LAG	AJI		LAG	AJI
DAY	14	0	11	1	15	6	12	14			
TWILIGHT	3	0	3	2	1	3	1	2		134	152
NIGHT	17	38	19	35	18	28	20	23			
7080	LAG	AJI	LAG	AJI	LAG	AJI	LAG	AJI		LAG	AJI
DAY	17	5	13	10	16	18	14	22			
TWILIGHT	3	3	3	2	1	2	1	3		159	205
NIGHT	20	43	24	39	23	32	24	26			

Mutual sightings of LAGEOS by any two stations FIGURE 3
for the period 920511.0 to 920607.0

The upper diagonal is number of mutual trackings.
The lower diagonal is minutes of mutual trackings.

	7080	7090	7105	7109	7110	7112	7123	7210	7843	7939
7080	0	0	119	130	133	0	52	81	0	14
7090	0	0	0	0	0	0	0	0	113	0
7105	3326	0	0	105	106	0	0	18	0	60
7109	5109	0	1997	0	130	0	45	77	0	0
7110	4719	0	1847	4337	0	0	45	74	0	0
7112	0	0	0	0	0	0	0	0	0	0
7123	1057	0	0	420	521	0	0	70	38	0
7210	2369	0	74	1908	1788	0	1431	0	14	0
7843	0	2783	0	0	0	0	668	54	0	0
7939	168	0	413	0	0	0	0	0	0	0

****

FIGURE 4

these 4 stations can track on the sighting date 920511
during the common sighting time 00:20:10.00 to 00:34:43.00
7110 00:05:52.00 to 00:34:43.00 start az: 15. ang: 20. end az:296. ang: 20. max el: 31.
7109 00:01:34.00 to 00:39:16.00 start az: 27. ang: 20. end az:278. ang: 20. max el: 44.
7080 23:48:34.00 to 00:40:56.00 start az: 40. ang: 0. end az:291. ang: 0. max el: 24.
7210 00:20:10.00 to 01:02:15.00 start az: 10. ang: 20. end az:243. ang: 20. max el: 52.

---

these 2 stations can track on the sighting date 920511
during the common sighting time 01:14:01.00 to 01:50:09.00
7843 01:01:28.00 to 01:50:09.00 start az: 31. ang: 20. end az:207. ang: 20. max el: 87.
7090 01:14:01.00 to 01:52:20.00 start az: 84. ang: 20. end az:192. ang: 20. max el: 43.

---

these 4 stations can track on the sighting date 920511
during the common sighting time 03:23:43.00 to 03:43:45.00
7105 03:06:19.00 to 03:43:45.00 start az:125. ang: 30. end az:337. ang: 30. max el: 73.
7110 03:23:23.00 to 03:51:47.00 start az: 63. ang: 20. end az:346. ang: 20. max el: 31.
7109 03:23:43.00 to 03:58:34.00 start az: 69. ang: 20. end az:331. ang: 20. max el: 39.
7080 03:01:36.00 to 04:00:45.00 start az: 98. ang: 0. end az:331. ang: 0. max el: 36.

---

these 5 stations can track on the sighting date 920511
during the common sighting time 06:59:19.00 to 07:06:41.00
7105 06:52:48.00 to 07:06:41.00 start az:239. ang: 30. end az:283. ang: 30. max el: 33.
7210 06:59:19.00 to 07:23:26.00 start az: 71. ang: 20. end az: 13. ang: 20. max el: 27.
7110 06:39:10.00 to 07:27:03.00 start az:146. ang: 20. end az:334. ang: 20. max el: 87.
7109 06:43:49.00 to 07:31:46.00 start az:145. ang: 20. end az:333. ang: 20. max el: 89.
7080 06:24:30.00 to 07:33:54.00 start az:158. ang: 0. end az:336. ang: 0. max el: 74.

Figure 5

QUICK-LOOK ANALYSIS REPORT

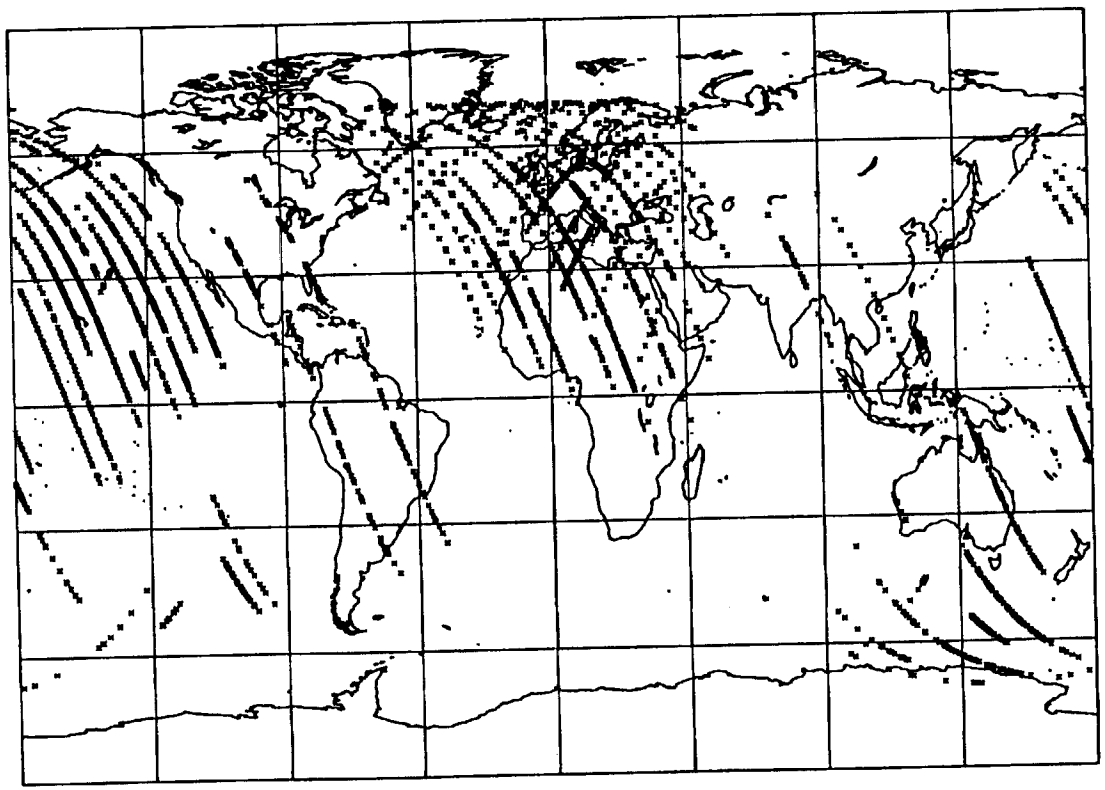

AUG 1 - AUG 7 1992

ALLIED-SIGNAL AEROSPACE/BENDIX FIELD ENGINEERING CORP. CDSLR/DSG/OAS

SATELLITE VISIBILITY: 92/ 9/14

FIGURE 6

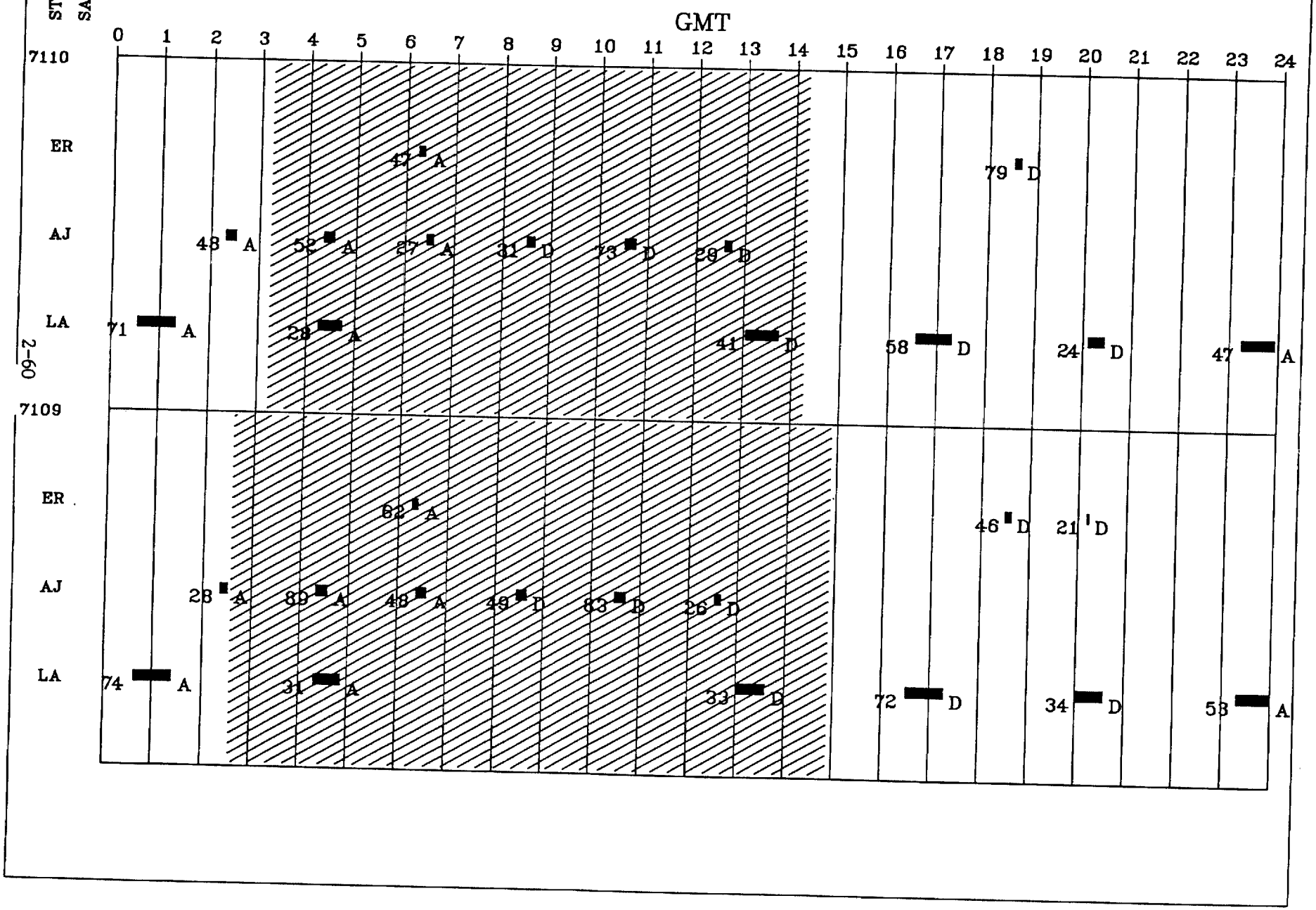

FIGURE 7

SYSTEM TRACKING PARAMETERS FOR MOBLAS 4 AT MT. PEAK.

1. MAY TRACK BOTH DAY AND NIGHT.
2. REQUIRES ABOUT 7 MINUTES FOR PRE/POST-PASS EXTERNAL CALIBRATION.
3. MINIMUM TRACKING ANGLE IS 20 DEG.
4. SYSTEM ABLE TO PROCESS ACQUIRED DATA IN PARALLEL WITH OTHER OPERATIONS.
5. SYSTEM USING MULTI-SATELLITE CALIBRATION CAPABILITY.
6. THE SATELLITE PRIORITIES, MINIMUM TRACK AND OTHER PARAMETERS ARE CHOSEN FOR DEMONSTRATION BUT MAY VARY WITH SATELLITE AND STATION.

FIGURE 8

SATCOP INPUT PARAMETERS

1. TRACKING PERIOD: SEP 18 - SEP 19, 1992.

2. STATION AVAILABILITY: 24 HOURS/DAY.

3. "WORK WEEK": 2 DAYS.

4. SATELLITE PRIORITIES:
   1: ERS-1 (E1 OR ER)
   2: LAGEOS (L1 OR LA)
   3: AJISAI (AJ)
   4: STARLETT (ST)
   5: ETALON 1 (MT)
   5: ETALON 2 (NT)

NOTE: ETALON TRACKING LIMITED TO 45 MINUTE SEGMENTS.

SATELLITE VISIBILITY: MOBL4 (7110)
9/18/92 – 9/19/92 SHIFT NUMBER 1

FIGURE 9

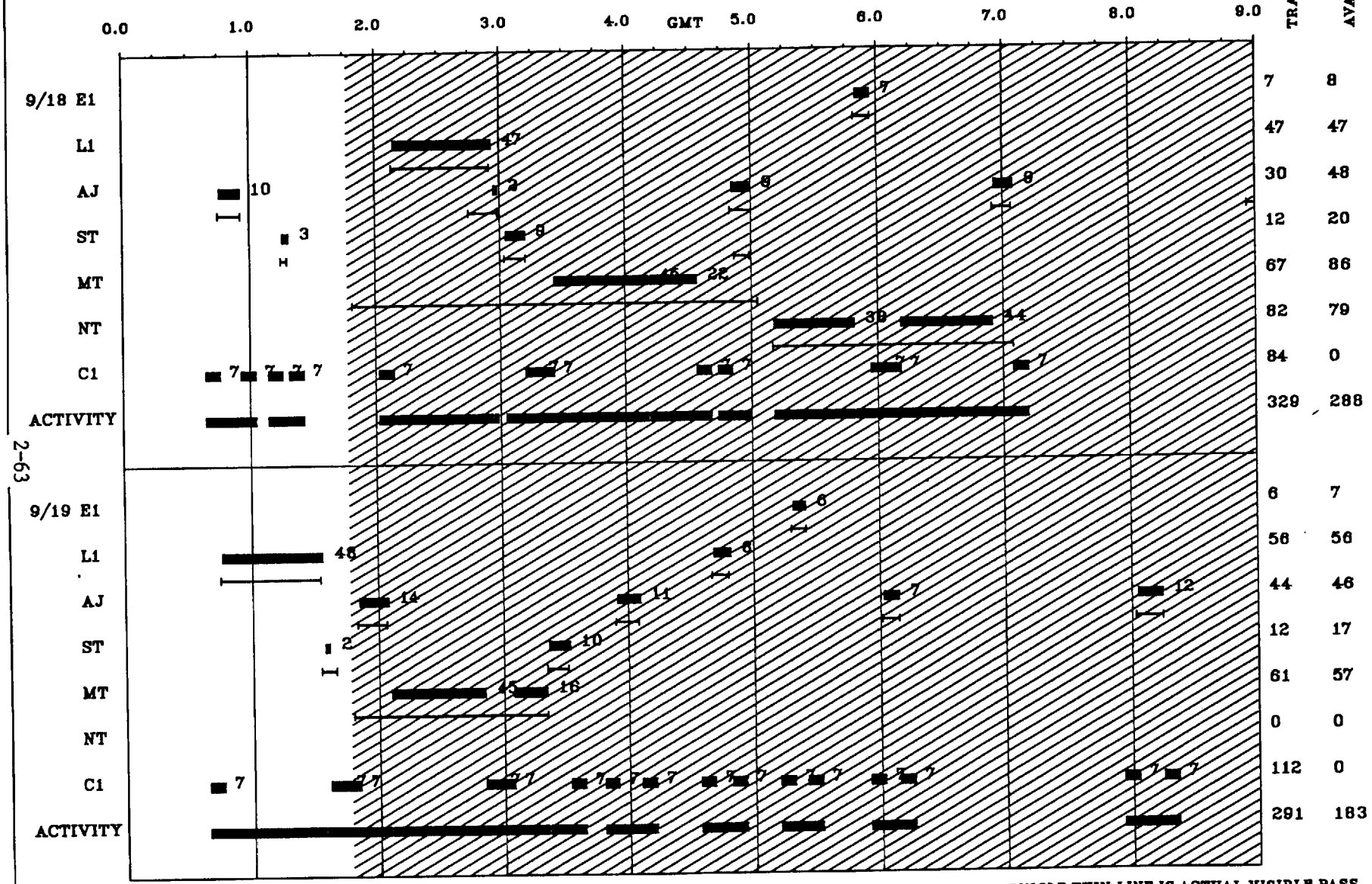

date created: 9/15/92

BFEC/CDSLR DSG Bucey
Conklin

THICK SOLID CURVE IS ACTUAL TRACKING.

ATTACHED THIN CURVE IS PRE/POST CAL TIMES.

NOTATION ON PASS IS MINUTES OF PASS TRACKED.

SINGLE THIN LINE IS ACTUAL VISIBLE PASS.

SHADED SECTION IS NIGHT.

Laser Technology

Nd:YLF Laser for Airborne/Spaceborne Laser Ranging

J.L. Dallas, M.D. Selker
NASA - Goddard Space Flight Center

Abstract - **In order to meet the need for light weight, long lifetime, efficient, short pulse lasers a diode-pumped, Nd:YLF oscillator and regenerative amplifier is being developed. The anticipated output is 20 mJ per 10 picosecond pulse, running at a repetition rate of 40 Hz. The fundamental wavelength is at 1047 nm. The oscillator is pumped by a single laser diode bar and modelocked using an electro-optic, intra-cavity phase modulator. The output from the oscillator is injected as a seed into the regenerative amplifier. The regenerative amplifier laser crystal is optically pumped by two 60W quasi-cw laser diode bars. Each diode is collimated using a custom designed micro-lens bar. The injected 10 ps pulse from the oscillator is kept circulating within the regenerative amplifier until this nanojoule level seed pulse is amplified to 2-3 millijoules. At this point the pulse is ejected and sent on to a more standard single pass amplifier where the energy is boosted to 20 mJ. The footprint of the entire laser (oscillator - regenerative amplifier - amplifier) will fit on a 3' by 4' optical pallet.**

I. INTRODUCTION

There are a number of programs at NASA's Goddard Space Flight Center which are driving the need for compact, efficient, diode-pumped lasers. These programs fall within the headings of Ranging, Altimetry, Metrology, LIDAR, and Communications. One of the primary leaders in this technology push has been the Geodynamic Laser Ranging System (GLRS) which proposed to perform both sub-centimeter ranging to retro-reflectors placed at geodynamically interesting regions as well as sub-decameter altimetry to the Earth's surface, ice sheets, cloud tops, etc.[1] The original requirements were for a spaceborne, 5 year lifetime, diode-pumped, Nd:YAG laser having an output of 200 mJ in 100 ps at the fundamental wavelength (1064 nm). This light was then frequency doubled and tripled to produce a resultant 100 mJ at 1064 nm (IR), 60 mJ at 532 nm (green) and 40 mJ at 355 nm (UV). The green and UV light were to be used for 2-color ranging in an attempt to back out atmospheric refraction effects. The IR radiation was for altimetry operations. Due to the complexity of the GLRS instrument and the still unresolved technological challenges, it was decided to divide the instrument into 2 separate instruments. The ranger is now called GLRS-R and the altimeter, GLRS-A. The work being described in this paper deals with the development of a laser source for an aircraft instrument to proceed and be a "stepping-stone" to the GLRS-R instrument. The requirements for this mission were derived and scaled down from the GLRS requirements and are meant to push the technology to produce a proof-of-concept breadboard for the GLRS-R instrument. This GLRS breadboard laser is required to be: diode pumped, compact (fitting on 3' x 4' palette), greater than 6% efficient, low maintenance, long lived (10^8 shots), low cost, and flyable.

II. BREADBOARD DESIGN

The overall design for the breadboard laser is shown in Fig.1. The laser consists of 3 sub-sections: the oscillator, the regenerative amplifier, and a final power amplifier, with the doubling and tripling left as future tasks . The oscillator produces low energy, short pulses which are used to seed the regenerative amplifier, where their energy is amplified 6 orders of magnitude. The output of the regenerative amplifier is sent to a standard amplifier where the pulse energy is increased by a factor of 20. The required output is an energy of 20 mJ per 10 ps pulse occurring at a repetition rate of 40 Hz. Each of the 3 sub-sections are now described in greater detail. The oscillator is a diode pumped, FM mode-locked laser (Fig.2)[2]. The Nd:YLF laser crystal (the choice of Nd:YLF over Nd:YAG will be described later) is end-pumped by a CW SDL-2482 3 Watt laser diode operating at 796 nm. The highly diverging light from the 500 x 1 μm emitting aperture is collimated and focused using a high NA Fujinon F35B compound lens array and a 12.0 mm cylindrical lens. A spot size of less than 500 μm can be maintained for 4 mm leading to efficient end-pumping of the Nd:YLF rod since the cavity mode size at the rod is also 500 μm. The Nd:YLF rod is 12 mm long with a 6.35 mm diameter. The one end is cut flat and anti-reflection coated for the pump wavelength of 796 nm and high-reflection coated for the lasing wavelength of 1047 nm. The opposite end of the rod is Brewester cut. The only intracavity element is an electro-optic phase modulator which FM mode-locks the laser. In order to keep the laser output stable, a feed-back loop has been designed which keeps the RF modulation frequency (200 MHz) of the phase modulator equal to the cavity mode frequency (c/2L). In a previous experiment performed at NASA/GSFC using a Nd:YAG crystal, stable 15 ps pulses were obtained at a modulation frequency of 344 MHz. An output energy of 5 nJ per pulse is expected for the Nd:YLF oscillator.

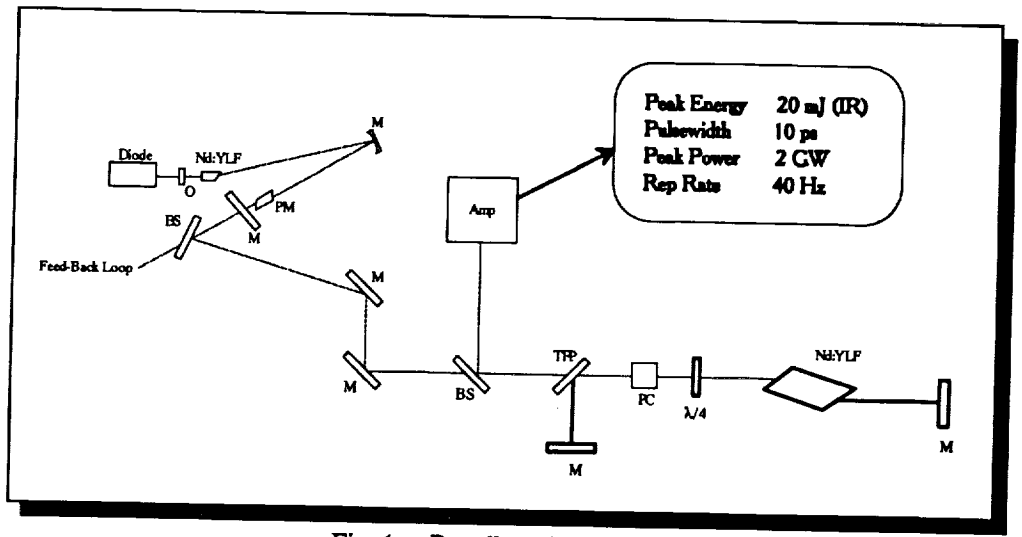

Fig. 1. Breadboard Design

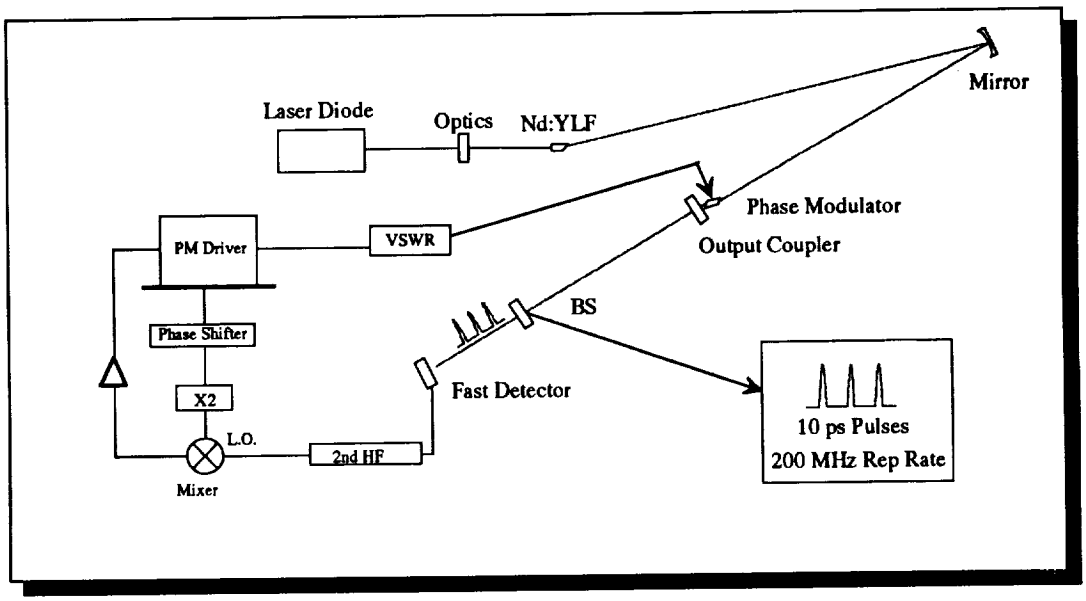

Fig. 2. FM Mode-Locked Laser and Feed-Back Loop

The regenerative amplifier is essentially a Q-switched, cavity dumped oscillator with an injected seed pulse. The seed pulse is trapped electro-optically in the cavity and circulates through the gain medium until the energy of the pulse has been amplified to the desired level. The regen designed for this breadboard (Fig. 3) uses laser diode side-pumped Nd:YLF as the gain medium and a combination of polarizers and a very fast rise-time Pockels cell (3-4ns) to switch the seed pulse into and out of the regen. The laser diodes used to pump the Nd:YLF crystal are Spectra Diode Labs model 3230 which have an output energy of 60mJ within a 500 μs pulse and a repetition rate of 40 Hz at 796 nm. The 10 x 0.001 mm aperture of the diode leads to a divergence of the emitting light of 10° by 40°. In order to collimate this highly diverging light, a unique lens has been utilized that was created at Lawrence Livermore Labs.[3] First the theoretically perfect lens for collimation of the fast axis is created in bulk form. As with optical fibers, this bulk lens is then pulled down to a 200 μm diameter microlens while still retaining the original hyperbolic shape of the bulk lens. Slices of these microlenses are attached to the output facet of the laser diode giving a collimated output of 500 μm at 3 cm. The output from two collimated diodes is delivered through the top of the 2 x 5 x 15 mm Nd:YLF slab (Fig. 4.). The lenses are ~80% efficient leading to ~50 mJ being delivered to the surface of the crystal.

As previously mentioned, control of the number of round trips the seed pulse makes within the regen is accomplished by a very fast electro-optic switch made by Medox Electro-Optics. By rotating the polarization of the traveling pulse through the Pockels cell, the light will either see the Thin Film Polarizer (TFP) as a mirror or a window. After a sufficient number of round trips within the regen, the energy of the seed pulse will have been amplified from 5 nJ to 2mJ. For our design, optical damage puts the ultimate limit on the number of round trips and therefore the gain of the regenerative amplifier.

The third sub-section is a standard single pass diode side-pumped Nd:YLF amplifier which will increase the energy per pulse from 2 mJ to 20 mJ (Fig. 1.).

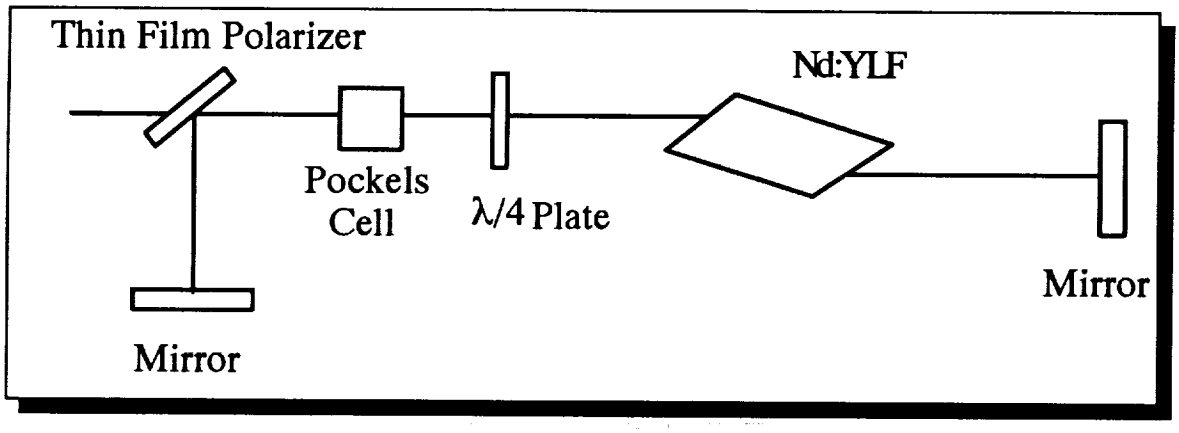

Fig. 3. Regenerative Amplifier

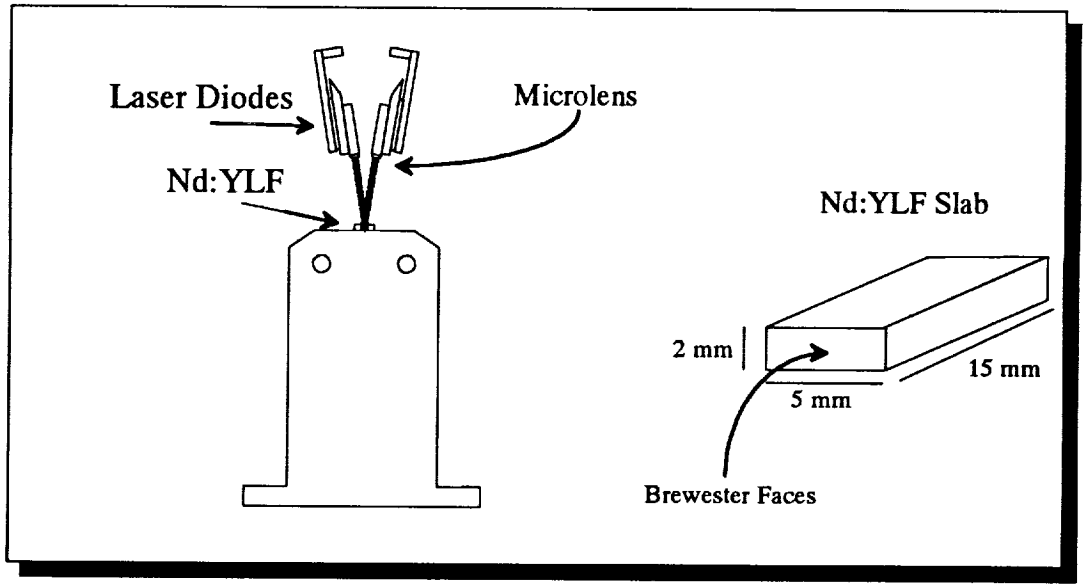

Fig. 4. Diode Collimation and Pump Scheme

III. Nd:YLF vs Nd:YAG

Since the absolute ranging accuracy is increased as the laser pulse width is decreased, the design of this breadboard encompasses the use of Nd:YLF versus Nd:YAG (the crystal of choice in the original GLRS design). From the equation for the pulse width achievable from an electro-optic phase modulated mode-locked laser[4];

$$\tau(FM) = \frac{\sqrt{2\sqrt{2\ln 2}}}{\pi}\left(\frac{g_o}{\delta_c}\right)^{1/4}\left(\frac{1}{f_{m*\Delta f}}\right)^{1/2}$$

where f_m is the modulation frequency, Δf is the bandwidth of the lasing medium, g_o is the gain and δ_c is the effective single-pass phase retardation, it is apparent why it is desirable to use Nd:YLF with a bandwidth of 420 GHz instead of Nd:YAG with a 120 GHz bandwidth for short pulse generation.

	Nd:YLF	Nd:YAG
Lasing Wavelength	1.047 μm	1.064 μm
Stimulated Cross Section	3.0×10^{-19} cm^2	6.5×10^{-19} cm^2
Upper State Lifetime	480 μs	240 μs
Bandwidth	420 GHz	120 GHz

Table.1 Nd:YLF vs Nd:YAG

In addition, Nd:YLF has the advantage of having an upper state lifetime approximately 2.5 times greater than Nd:YAG allowing for approximately 2.5 times the energy storage, hence a larger gain as well. YLF is also naturally birefringent making it resistant to thermally induced birefringence and the concomitant undesired polarization dependent losses. Other advantages include less thermal lensing, and a nonlinear index less than three times that of YAG. Although thermally induced stress fracture has been reported in Nd:YLF, we have not encountered this problem.

IV. SUMMARY

The design for a compact, efficient, diode pumped Nd:YLF laser has been shown. The expected output is 20 mJ per 10 ps pulse at a repetition rate of 40 Hz. The size, weight and power consumption makes this design ideal for aircraft ranging. Some of the areas to be investigated so that this technology may successfully make the transition to a spacecraft instrument include: the reduction of pulse width and its implications to optical damage, shot lifetime of laser diodes, efficient and stable collimation of laser diodes, high voltage Pockels cell driver and mode locker lifetimes, and overall system efficiency.

[1] S.C. Cohen, J.J. Degnan, J.L. Bufton, J.B. Garvin, and J.B. Abshire, "The Geoscience Laser Altimetry/Ranging System," IEEE Trans. Geosci. Rem. Sens., vol GE-25, 581, 1987.

[2] G.T. Maker and A.I. Ferguson, "Frequency-Modulation Mode Locking of a Diode-Pumped Nd:YAG Laser," Optics Letters, vol. 14, **15**, 1989.

[3] J.J. Snyder, P. Reichert, and T.M. Baer, "Fast Diffraction-Limited Cylindrical Microlenses," Applied Optics, vol. 30, **19**, 1991.

[4] D.J. Kuizenga and A.E. Siegman, "FM and AM Mode Locking of the Homogenous Laser-Part I: Theory," IEEE J. Quantum Electron., vol. 6, **11**, 1970.

N94-15564

ALTERNATIVE WAVELENGTHS FOR LASER RANGING

K. Hamal

Faculty of Nuclear Science and Physical Engineering, Czech Technical University
Brehova 7, 115 19 Prague, 1 Czechoslovakia
phone / fax +42 2 848840,tlx 121254 fjfi c,E-mail tjean@csearn.bitnet

To accomplish multicolor laser ranging we should consider :
* the nature of the atmospheric dispersion and absorption,
* the Satellite/Lunar/Ground retro array characteristics,
* Ground/Satellite ranging machine performance.

The existing atmospheric dispersion models [1,2] are perhaps valid up to 1 cm accuracy. It is evident, the higher time interval difference of a chosen pair, the requirements on the ground / satellite instrument are less stringent. The energy balance and jitter budget have to be considered, as well.

The existing Satellite / Lunar retro arrays show serious limitation to accomplish a multicolor experiment [3].

The fieldable picosecond lasers, considered up to now, have the origin on the NdYAG transition (1.06um) and its harmonics (0.53 um, 0.35um), Raman Stokes transition (0.68 um) of 0.53 um in Hydrogen [4,5], Titanium Sapphire (0.8 / 0.4 um) and Alexandrite. We do propose the Raman Stokes / Raman Anti Stokes pair of 0.53 um (0.68 um/0.43 um) and Cr:LiSAF (0.8/0.4 um).

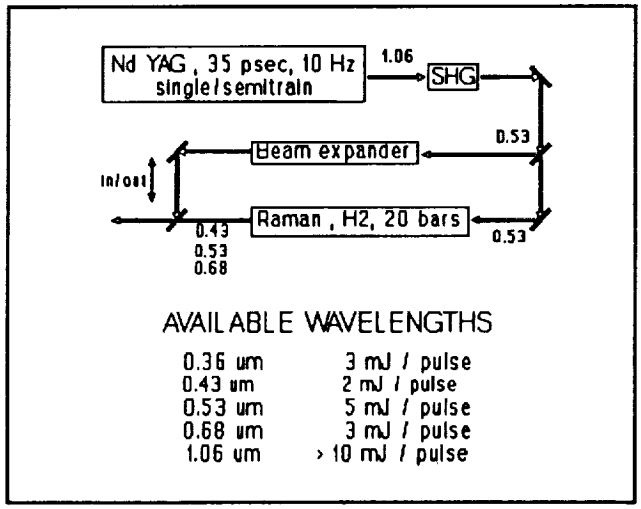

Figure 1 Multiple wavelength laser transmitter
The 3HG may replace the Raman tube

The streak detector experiments carried out in Prague on a ground target (0.53/0.35 um), (0.53/0.68 um) [4], (0.53/1.06 um) and in Graz [5] on Ajisai and Starlette satellites proved the expectancy, however, indicated the complexity. On the other hand, the solid state detector technology offers a remarkable simplicity and compactness with the access to the near infrared. The experiment (0.53/0.68 um) accomplished in Graz [6] indicates a chance, if data averaging requirements will be fulfilled.

Since several years ago, Alexandrite based Fundamental / SHG lasers do not show to much progress. Using the Titanium Sapphire based laser, the scheme is becoming quite complex because of short relaxation time (3 useconds) of the metastable level of the active medium.

The new material Li:SAF [7] tunable around 800 nm, having 66 usec relaxation

time,looks promising related to the spectral response of existing vacuum and solid state detectors and the atmospheric propagation and dispersion, as well.

At the conclusion : the existing Satellite / Lunar retroreflectors seem to be not adequate for the future experiments. The Raman Stokes/Anti Stokes (0.68/0.43um) plus solid state detector look as a promising instrumentation satisfying the Ground/Satellite and Satellite/Ground ranging machine requirements on the precision, compactness and data processing.

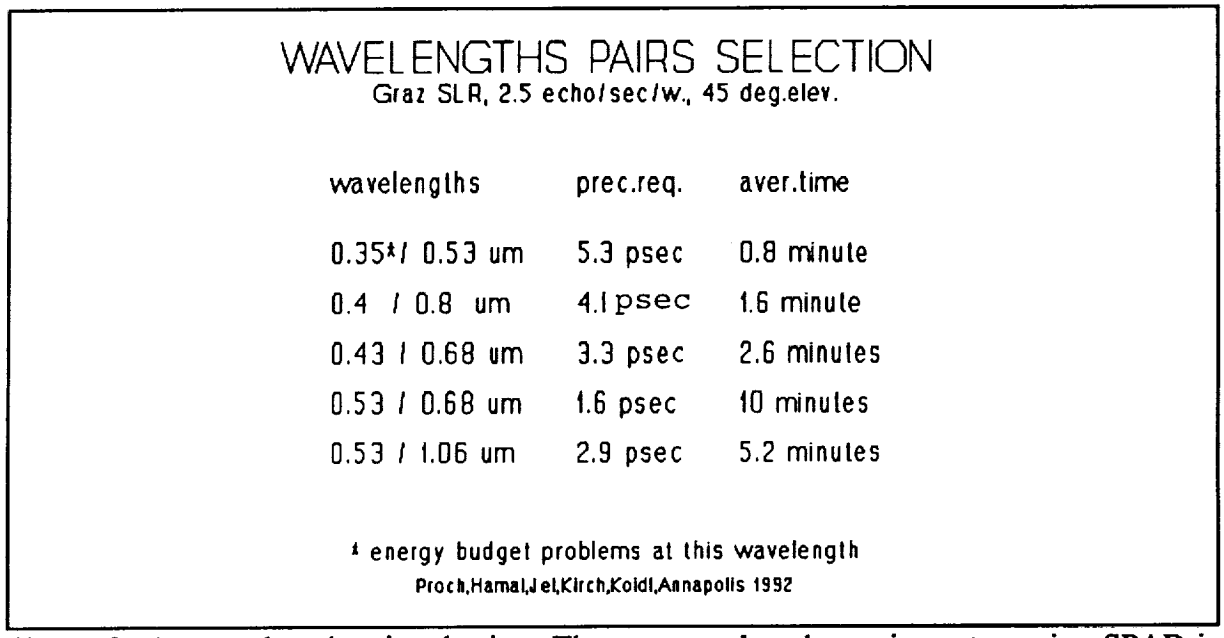

Figure 2 The wavelength pair selection. The two wavelength ranging setup using SPAD is expected, the mean elevation 45 degrees is expected, the SPAD jitter dependence versus wavelength is taken into account.

References:

1. Marrini J.K., Murray C.W., report GSFC X-591-73-351
2. Abshire J., Applied Optics, Vol.19, 1980
3. Prochazka I., in this Proceedings
4. Gaignebet J. et al, Hamal K. et al, Proceedings of the 6th International Workshop on Laser Ranging Instrumentation, Antibes, 1986, p565-577
5. Hamal K et al,to be published at IQEC'92, Vienna, June 1992
6. Kirchner G. et al, to be published at IQEC'92, Vienna, June 1992
7. Hamal K, Richardson M., in this Proceedings

NEW METHODS OF GENERATION OF ULTRASHORT LASER PULSES FOR RANGING

H.Jelinkova,K.Hamal,V.Kubeček,I.Prochazka

Czech Technical University,Faculty of Nuclear Science and Physical Engineering
Brehova 7, 11519 Prague 1,Czechoslovakia
ph/fax +42 2 848840,tlx 121254 fjfi c,bitnet TJEAN@CSEARN.BITNET

INTRODUCTION

To reach the millimeter satellite laser ranging accuracy, the goal for nineties, new laser ranging techniques have to be applied. To increase the laser ranging precision, the application of the ultrashort laser pulses in connection with the new signal detection and processing techniques, is inevitable. The two wavelength laser ranging is one of the ways to measure the atmospheric dispersion to improve the existing atmospheric correction models and hence to increase the overall system ranging accuracy to the desired value.

We are presenting a review of several nonstandard techniques of ultrashort laser pulses generation, which may be utilized for laser ranging:

* Compression of the nanosecond pulses using stimulated Brillouin and Raman backscattering
* Compression of the mode-locked pulses using Raman backscattering
* Passive mode-locking technique with nonlinear mirror
* Passive mode-locking technique with the negative feedback

BRILLOUIN AND RAMAN BACKWARD SCATTERING

The idea of obtaining a single subnanosecond light pulse by temporal compression of a nanosecond laser pulse was suggested in [1] and the compression cascade by backward stimulated scattering of passively Q-switched Nd:YAG laser pulses was experimentally demonstrated in [2]. We had been investigated the generation of monopulse from Q-switched Nd:YAP oscillator [3]. The experimental setup is in Fig.1. The resonator was formed by the concave mirror M1 and the plane output mirror M2 deposited on the front surface of the Nd:YAP laser rod (Nd:YAP1). The b-axis of the crystal Nd:YAP yields linearly polarized light

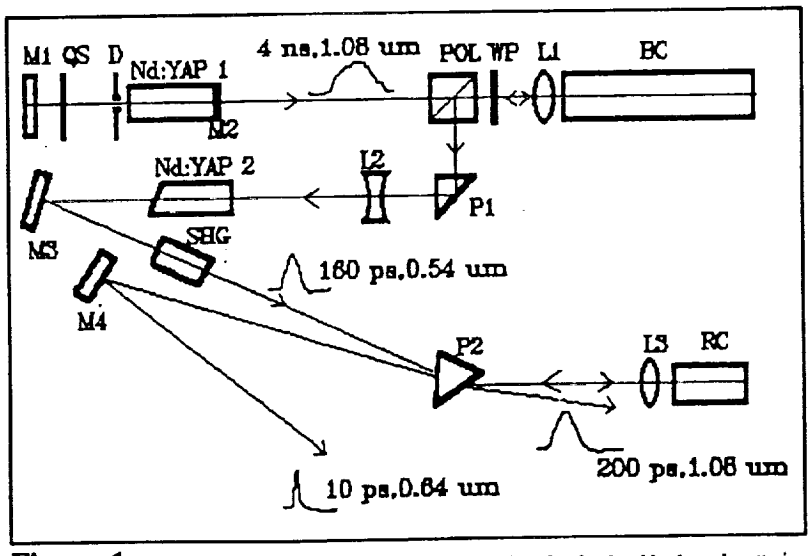

Figure 1 Experimental setup for two-stage pulse compression via stimulated backward scattering

mirror M1 and the plane output mirror M2 deposited on the front surface of the Nd:YAP laser rod (Nd:YAP1). The b-axis of the crystal Nd:YAP yields linearly polarized light output at $\lambda_1 = 1.0795$ μm. Q-switching was performed by the plastic BDN foil QS. The length of the resonator was 20 cm and together with low initial transmission of the Q-switch enable generation of pulses with duration $\tau_1 = 4$ ns (Fig.2a). The pulse energy in TEM_{∞} mode was 7.5 mJ. This setup of short resonator gives most stable output pulses [4].The oscillator radiation passing a cube dielectric polarizer POL and a quarter wave plate WP, was focused by lens L1 into SBS compressor - a 70 cm long cell BC filled with CCl_4. When the necessary condition for SBS was fulfilled, the backward Stokes pulse was generated. The compressed Stokes pulse passing prism P1 and a negative lens L2 is amplified by the single pass Nd:YAP amplifier (Nd:YAP2) to the energy 30 mJ. The diverging beam is recollimated by the concave mirror M3. After frequency doubling in a SHG crystal, the pulse ($\lambda_2 = 0.54$ μm) has an energy of 10 mJ. The radiation at different wavelengths is spatially separated by the dispersion prism P2. The 0.54 μm pulse is then focussed with lens L3 into the second compressor consisting of the Raman cell RC filled with methane at 18 bars.

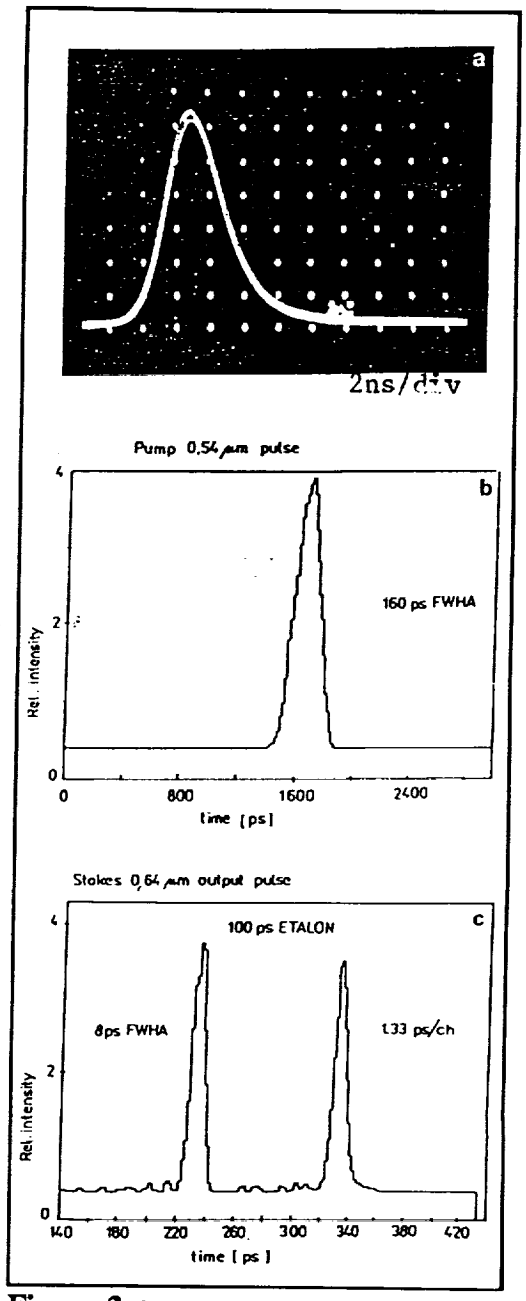

Figure 2 A records of compressed pulses

Temporal characteristics of the pulses in subnanosecond range were measured by the streak camera Imacon 500 with readout system consisting of SIT television camera, single frame memory and computer. The temporal resolution of the whole system was better than 2 ps [5]. Fig.2b shows the pulse after the first stage compression and the frequency doubling ($\lambda_2 = 0.54$ μm). The mean pulse duration was $\tau_2 = 160$ ps. Streak camera record of the backward Stokes pulse ($\lambda_3 = 0.64$ μm) from the Raman cell is on Fig.2c. The mean value of the pulse duration τ_3 for given focussing optics depends on pump energy. The minimum length of pulse τ_3=9 ps was obtained for pump pulse energy 3-5 mJ.

The advantage of this compression technique in comparison to the used mode-locked picosecond lasers, are the absence of the active and/or passive mode lockers used to generate a train of picosecond pulses, and the absence of a fast electrooptical shutter used to select a single pulse from a train of pulses.

RAMAN BACKSCATTERING PULSE COMPRESSION

The generation of single picosecond pulses through backward Raman scattering can start directly from the pulse train generated from a mode-locked laser. The experimental setup composes a passively mode-locked modified SFUR [6] loaded with 1/4"x4" Nd:YAG rod, delivering 30 mJ in a train of 4-5 pulses (FWHM) at $\lambda_1 = 1.064$ μm and with τ_1=24 ps timewidth and an amplitude fluctuation of the highest pulse in the train of 13%. The radiation is then converted to the second harmonic in a KDP crystal using type II configuration, giving 10 mJ and τ_2=17 ps timewidth, with a 20% amplitude fluctuation. The output train is then fed into the Raman cell, focussing it with a 160 mm focal length lens. The Raman cell was filled with 20 bars methane gas. On each shot, signals from fundamental, second harmonic λ_2=0.532 μm and Raman Stokes Backscattering at λ_3 = 0.68 μm were detected and stored for later processing. The Raman signal was checked to be the phase conjugated of the input second harmonic signal. Its energy was measured to be 3 mJ, giving an average green-to-red conversion efficiency of 30%. Time duration of the Raman pulses was τ_3=7.4 ps with a 2.3 compression factor with respect to second harmonic pulses. On Fig.4a is oscilloscope record of the rest of mode-locked train pulses (positive trace) and a single generated Raman pulse (negative trace). Fig.4b shows streak camera records of the overlap of 100 second harmonic pulses (positive trace) and Raman Stokes pulses (negative trace). The second harmonic radiation and Raman output pulses were detected by the independent photodiodes, one of the photodiode output was inverted and both signals have been added on the oscilloscope input.

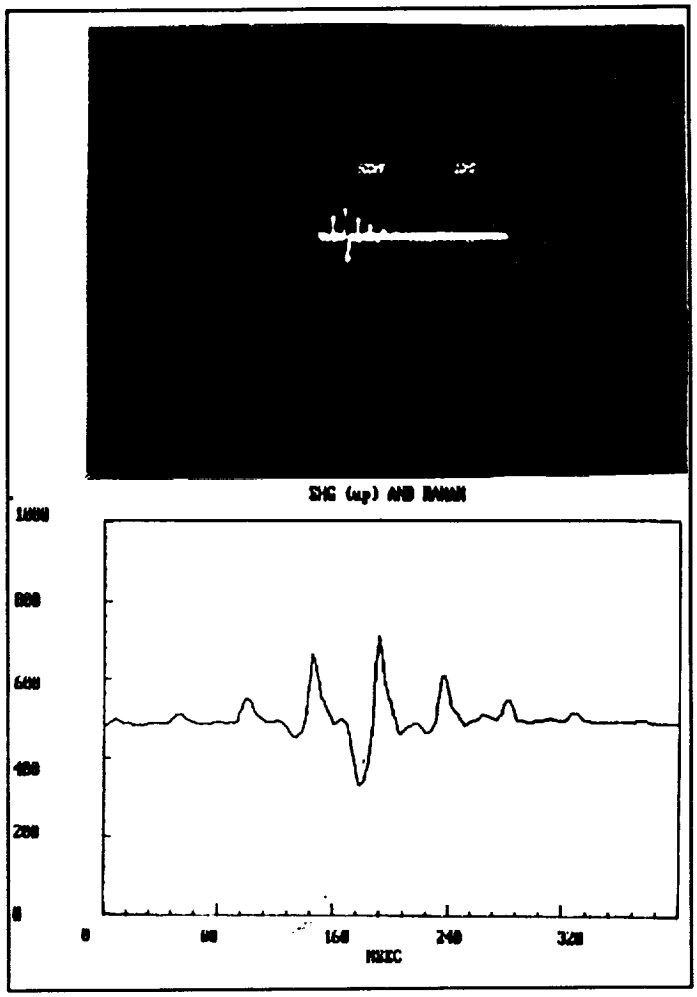

Figure 3 A records of the generated pulses

This technique gives possibility to generate one ultrashot pulse without expensive optical and electronic part as they are Pockels cell, polarizers, high voltage pulse forming circuitry, optostart, high voltage power supply,etc. which are obviously needed to select single picosecond pulse from mode-locked train.

GENERATION OF MODE-LOCKING PULSES USING A FREQUENCY-DOUBLING NONLINEAR MIRROR

The mode-locking technique based on intracavity frequency doubling offers new capabilities for generation of ultrashort laser pulses. A frequency doubler inside the cavity, together with an output mirror with high reflectivity at the second harmonic forms a nonlinear mirror, whose reflectivity at the fundamental wavelength can either increase or decrease when the input light intensity increases. When the phase condition facilitate increasing reflectivity, the device can be used as a passive mode-locker. First experiment with the nonlinear mirror was performed by K.Stankov [8]. With the Nd:YAG laser active medium he got 20 ps length of pulses. We investigated the attractive potential of the second harmonic nonlinear mirror to mode-lock lasers at quite different wavelengths. The laser cavity was formed by the dielectric mirrors. In all cases the rear mirror was a total reflector at the fundamental, the output mirror was dichroic and it was total reflector at the second harmonic and had 20-24% reflectivity at the fundamental wavelength (Fig.4). Using a single 30^0-cut $LiIO_3$ frequency doubler (20 mm long), mode locking at the 1.08 μm and 1.34 μm transitions of pulsed Nd:YAP laser was achieved [9]. Pulses as short as 40 ps and 15 ps at the corresponding wavelength were obtained. Mode-locking was achieved also in Er:YAP laser at 1.66 μm wavelength with pulse duration of 450 ps [10] and in Ti:Sapphire laser at 0.7 μm wavelength with pulse duration of 100-130 ps [11]. A comparative wavelength indicates that the minimum pulse duration is determined by the limited number of round trips only.

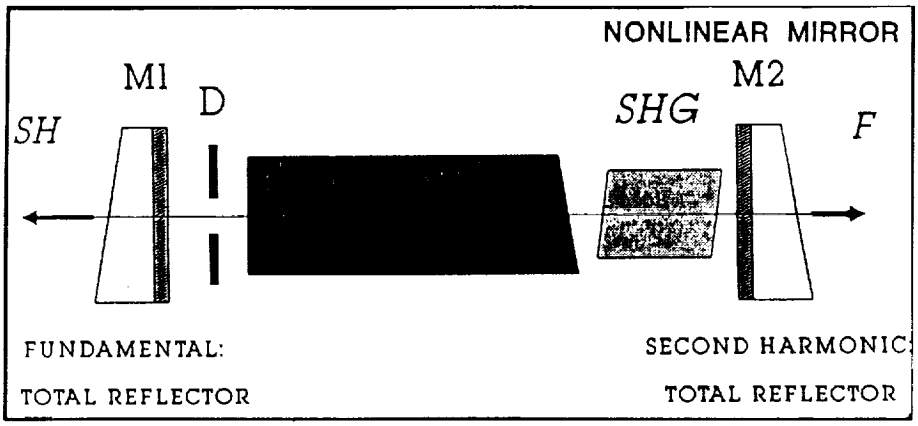

Figure 4 Experimental scheme

This experiment showed that nonlinear mirror technique allows to mode lock a number of solid state lasers ranging in wavelength 0.8 μm (Ti:Sapphire laser) up to 1.66 μm (Er:YAP laser). When the optimalization will be done and shorter pulses will be generated, the advantages of short pulse immediately with the generation of first and second harmonic radiation will be evident.

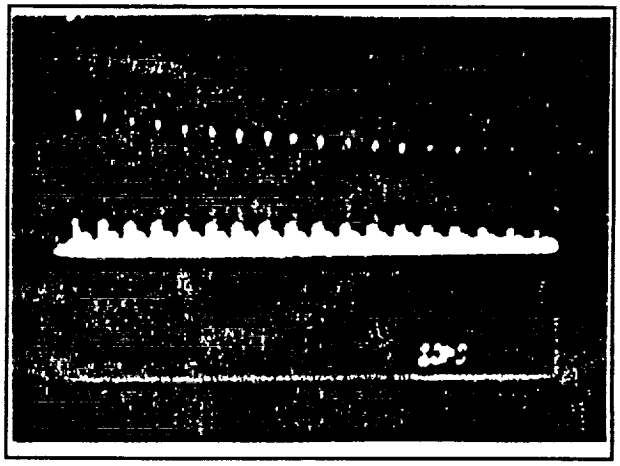
Figure 5 The mode locked Ti:Sapphire laser (10 ns/div)

PASSIVE MODE-LOCKING TECHNIQUE WITH THE NEGATIVE FEEDBACK

The solid state lasers with negative feedback through an electro-optic loss that limits the maximum intensity inside the cavity and prevents the rapid growth of the laser pulse, were successfully used for the generation of shorter reproducible pulses [12,13]. The possibility of using a passive two-photon absorption element instead of the active loss control, was also suggested and demonstrated [14,15,16]. Two-photon absorber (GaAs or CdSe) acts inside the resonator as a passive negative feedback element (NFE). The scheme of experiment with Nd:YAG or Nd:YAP laser is similar and it is schematically shown in Fig.6.

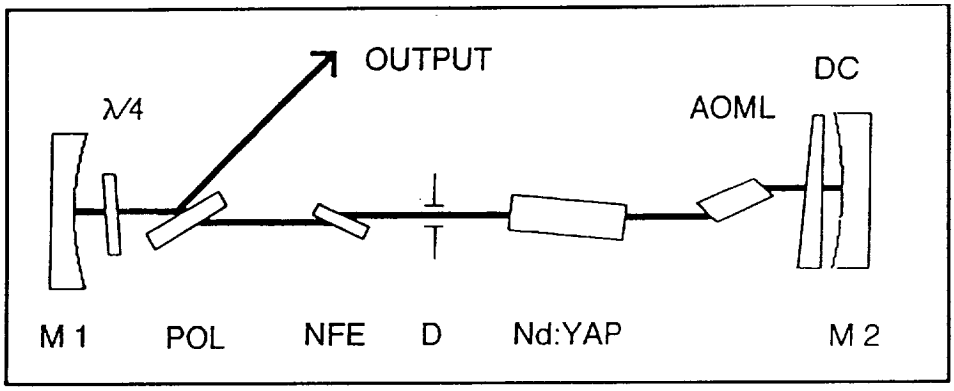

Figure 6 The experimental setup

The Fabry-Perot cavity is formed by concave mirrors M1 and M2(R=10m) having a reflectivity of 99.8%. The mirror M2 is in contact with a 0.5 mm thick dye cell (DC) containing flowing Eastman Kodak 9860 dye in 1,2-dichloroethane (T_0=30% at 1.08 μm). The output coupling of the resonator is achieved by means of a dielectric polarizer (POL), which, in combination with the quarter-wave plate keeps the output coupling at 50%. The active medium was Nd:YAG or Nd:YAP. The cavity round trip time was synchronized to the modulation period of the acoustooptic mode locker. With the Nd:YAG laser long trains of steady-state pulses was generated, with a single pulse time duration of 10 ns and an energy of 10 μJ,with cw comparable stability. The minimum of pulse duration was obtained for Nd:YAP laser with CdSe working as a negative feedback element. In this case, the pulses with 5 ps length was generated with an energy of 1 mJ.The example of the generated pulse trains for different negative feedback elements are in Fig.7.

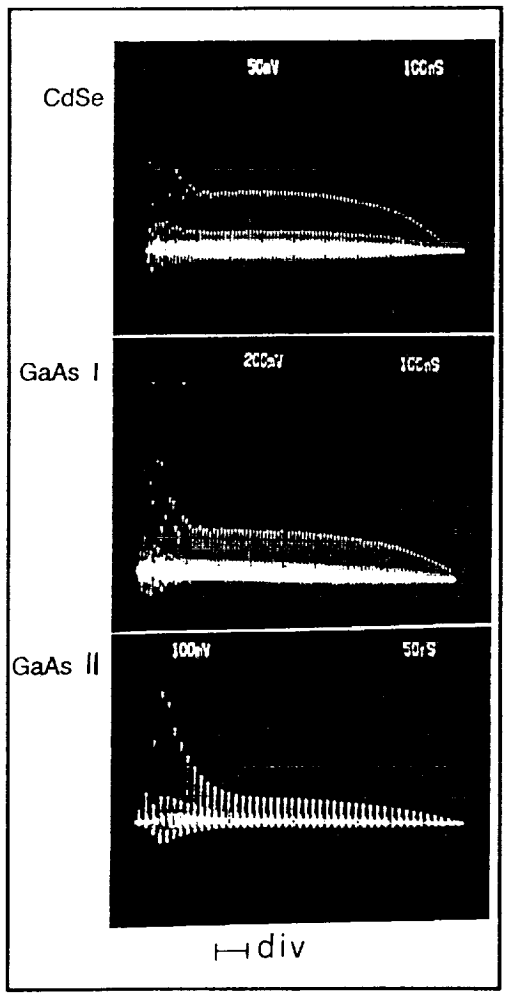

Figure 7 The records of the generated pulses

CONCLUSION

This review article shows some possibilities for generation of short and ultrashort laser applicable in laser ranging.

References

[1] M.Maier,W.Kaiser,J.A.Giordmaine: Phys.Rev.Lett.17 (1966) 1275

[2] R.R.Buzelis,A.S.Dement'ev,E.K.Kosenko: Sov.Journ.Quant.Electron.12 (1985) 2024 (in russian)

[3] V.Kubecek,K.Hamal,I.Prochazka,P.Valach,R.Buzelis,A.Dement'ev: Optics Commun.,vol.73,3 (1989) 251

[4] H.Jelinkova,K.Hamal,M.Vrbova:High Brightness Nd:YAG Oscillator,Preprint Series FJFI No.77/4

[5] I.Prochazka,K.Hamal,H.Jelinkova:Technical Digest Conference on Lasers and Electro-optics (Optical Society of America, Baltimore,MD) (1989) pap.THK42

[6] H.Jelinkova,J.Marek,P.Valach,K.Hamal,G.C.Reali,G.Gabeta:Optics Communications Vol.75,No.5,6,March 1990,p.447

[7] K.Hamal,H.Jelinkova,I.Prochazka,G.C.Reali:Czech Journal Phys.(will be published)

[8] K.A.Stankov:Appl.Phys.B45 (1988) 191

[9] K.A.Stankov,V.Kubeček,K.Hamal:IEEE Journal of Quant.Electron.,vol.27,No.9 (1991) 2135

[10] K.A.Stankov,V.Kubecek,K.Hamal,H.Jelinkova,I.Prochazka:Proceedings of the EQEC,Edinburg,UK,(1991)

[11] K.Hamal,K.A.Stankov,H.Jelinkova,I.Prochazka,M.Koselja:Proceedings of the VIIth Int.Symp. on Ultrafast Proc. in Spect.,Bayreuth,Germany,(1991),TU3-3

[12] K.P.Komarov,A.S.Kuchyanov,V.D.Ugozhayev:Opt.Commun.57,279 (1986)

[13] P.Heinz,W.Kriegleder,A.Lauberau: Appl.Phys.A,43,209 (1987)

[14] K.P.Komarov,V.D.Ugozhyaev: Opt.Spectrosc. 55,564 (1983)

[15] A.V.Babushkin,in Proceedings of Ultrashort Phenomena in Spectroscopy '89, Springer-Verlag,Berlin (1989), PTh20

[16] A.Del Corno,G,Gabetta,G.C.Reali,V.Kubecek,J.Marek:Optics Letters,vol.15, No.13 (1990) July 1,734

Simultaneously Compression of the Passively Mode-Locked Pulsewidth and Pulse Train

Yang Xiangchun, Zhu Xiaolei, Wu Zhaoqing and Sun Zhan'ao
(Shanghai Institute of Optics and Fine Mechanics, Academia Sinica, Lab. of Laser Technology, Shanghai, 201800, P.R. China)

Yang Fumin, Tan Detong, Xiao chikun, Chen Wanzhen and Lu Wenhu
(Shanghai Observtory, Academia Sinica, P.R. China)

Abstract

Simultaneously compression of the passively mode-locked pulsewidth and pulse train have achieved by using a plano-convex unstable resonator hybrided by a nonlinear Sagnac ring interferometer. The >30mJ single pulse energy of alone oscillator and <10ps pulsewidth have obtained. Using this system, the LAGEOS and ETALON satellites laser ranging have been performed successfully.

Key words: Nonlinear Sagnac ring interfereometer,
Simultaneously compression of M-L pulsewidth and train

1. Introduction

In a variety of scientific research and technical applications, laser ranging included, the single mode-locked pulse is necessary. For this reason, the single pulse selector has to be need, and perhaps needs several stages amplifiers in order that achieving necessary energy. Moreover, in outfield applications, not only need smaller and lighter equipments, but need that, the equipment insensitive to mechanical and thermal perturbations, maintaining good aligament over days of operation. Recently years, our group in base on investigations of antiresonant ring hybrided unstable resonator, deeply into investigated the conditions and paramaters of simultaneously compression using an unstable resonator hybrided by nonlinear ring interferometer, and following results have been obtained:
the pulse train compressed to two cavity periods, the mode-locked pulsewidth

compressed to $\leq$10ps, the single pulse energy (alone oscillator) $>$30mJ (Nd:YAG) , the weight and size of the setup (not including power supply) 32Kg and $72\times30\times24Cm^3$ respectively.

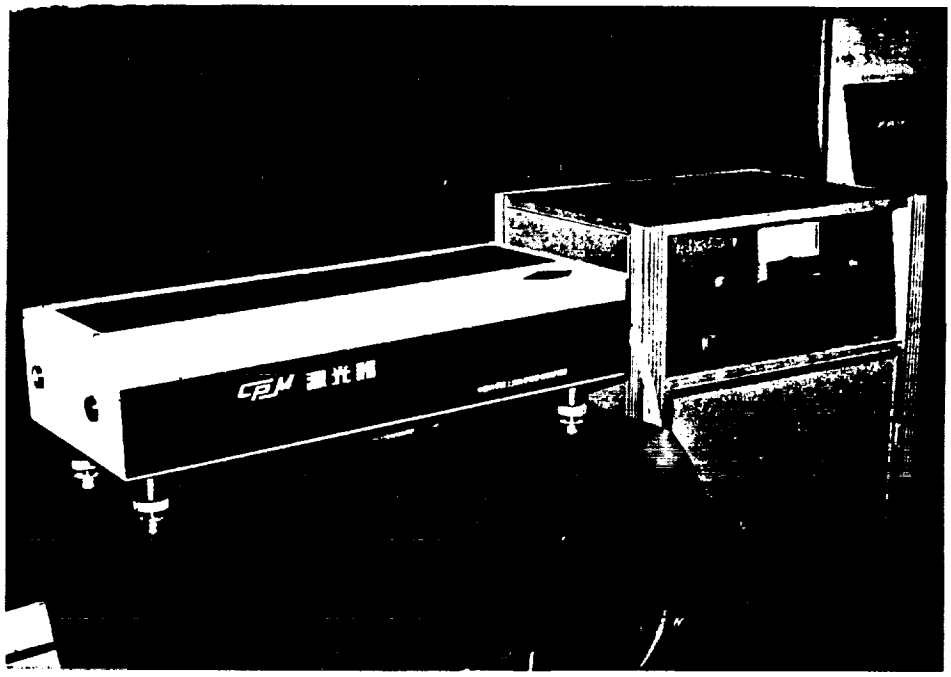

Fig.1 Photograph of the setup

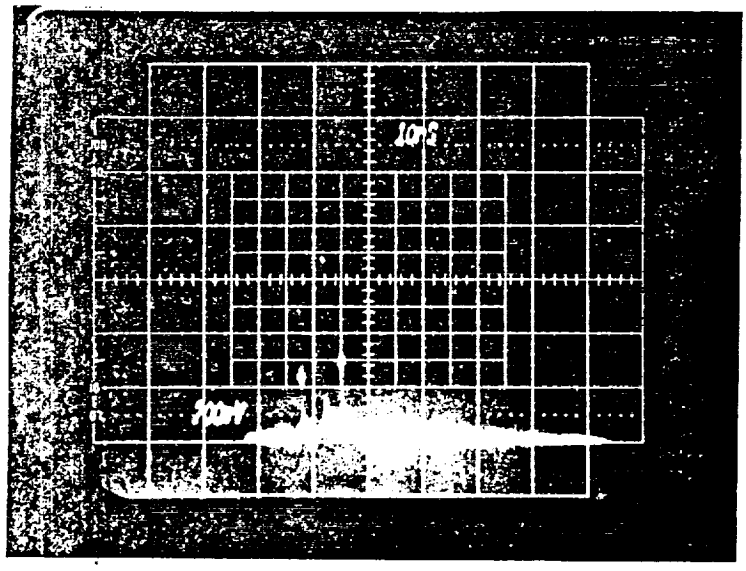

Fig.2 Oscillogram of the M-L pulse train

2. Theroy

Our experiment results exhibit that the mode-locked pulse train and pulse width have achieved compression simultaneously. This can't been explained fully by previous passively mode-locked theroy[1].[2]. Our study believe that true reasons for simultaneously compression should be altributed to the collision interference of the nonlinear ring interferometer, which formed a temporally modulated grating and stationary in space. Therefore, this grating is free from the deleterious atomic motionally induced or frequency-induced "washout" effect. Then, counterpropagation two beams, suffer strongly saturable absorption modulation, and at splitter mirror, again interference, resulting beams, which through a high inversion gain medium, the pulse signal obtain enhanced and compressed by cross-phase modulation. The necessary conditions of the doubly compression by using nonlinear ring interferometer, are Y1 parameter enough large, as that has to be at least one order of magnitude larger than R of [1]. $Y1 \sim |\ln \delta\Omega|$ is the initial amplitude of the stimulated emission, $\delta\Omega$ is solid angle, in which the laser radiation are concentrated. In according to [3], we deduced

$$Y1 = \left(\frac{\delta n}{n}\right)^2 \frac{TV(X1+\mu_a)}{2\zeta}$$

here ζ is the relative excess pump power above the threshold for a closed shutter, $(\delta n/n)$ is the relative excess inversion population, T, cavity period time for mode-locked operation, $(X1+\mu_a)$, X1 is the linear losses per unit optical path, μ_a is absorption coefficient of the mode-locking dye. μ_a must be enough large, as that has to be at least one order of magnitude larger than corresponding value of optimum transmittance of [2]. In proper conditions, sufficient large Y1 can be depleted the δn, and initiated the nonlinear ring interferometer, an overshoot pulse after switching[4], return to a high inversion gain medium, then the pulse signal enhanced and compressed by cross-phase modulation, simultaneously compression of the mode-locked pulses achieved quickly, and a single gaint pulse is obtained.

3. Experiment setup

Experiment setup used in this work is different to [4] slightly. The main difference are addition of interferometer's function.

The nonlinear ring interferometer is composed of a P-polarization 50/50 splitter 1, two totally reflective turning mirrors 2 and 3, and a dye cell 4, which located at the colliding center, fulling pentamethine cyanine dissolve in 1,2-dichloroethane. Two polarizers 5 and 10 used for enhance the polarization purity of the gain medium Nd:YAG, 6, 90mm in length and 6.0mm in diameter, the ends of the rod were angled at 87.5° to the normal of the rod axis. The rear reflector, 11 is a convex mirror, turning mirrors 7 and 8, an aperture 9, output coupled mirror 12 and recollimated lens 13.

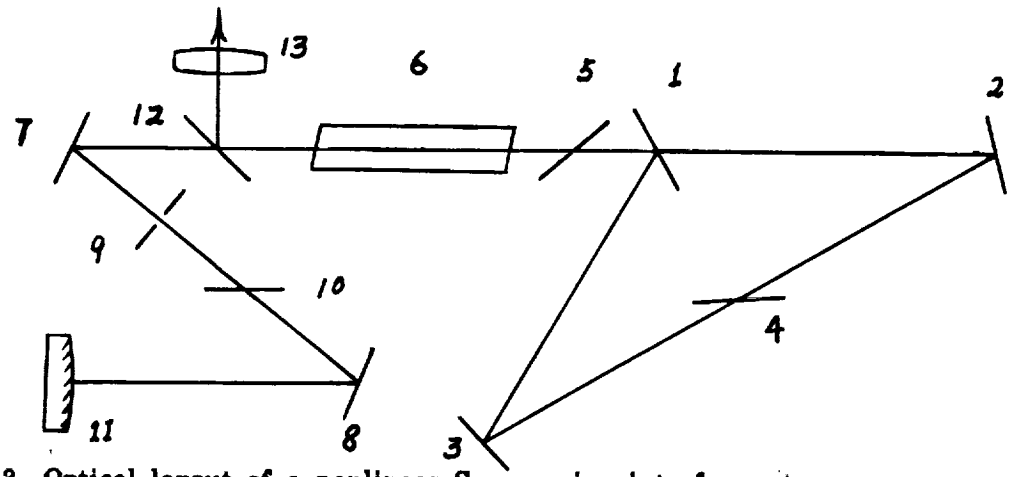

Fig.3 Optical layout of a nonlinear Sagnac ring interferometer.

Since the distance from the splitter mirror to colliding center is equal optical path, for all longitudinal modes $\omega_o \pm m\Delta\omega$, that into oscillated, can be formed interference fringes, stabilzed in space, and thess fringes are insensitive to mechanical and thermal perturbation. Due to the high angle selectivity of this system, so that it may be maintaining good aligenement over days of operation. In this system do not need single pulse selector and A-O modulator, without any amplify, the output energy of oscillator can be achieved >30mJ, pulsewidth <10ps. These performances are sufficient for many applications. For as LAGEOS and ETALON (20,000KM) satellite laser ranging, only need addition to one amplifier and a frequency doupler. More recently, the facts of successful laser ranging of LAGEOS and ETALON in Shanghai Observatory, have showed this point.

4. Conclusions

We have reported the results of a nonlinear Sagnac ring interferometer hybried unstable resonator. The results demonstate that the multiple interference effect quicken the mode-locking process, and the simultaneously compression of the mode-locked pulsewidth and pulse train have been achieved, and a GW level single pulse was obtained. This system have many advantages as that lighter weight, smaller size and insensitive to mechanical and thermal perturbations, particularly applied to outfield utilizations, such as mobile satellite laser ranging, and have great potentialities for heighten precision and distance of laser satellite ranging.

The damage problem of the optical components and improvement of the ratio of the first-second peak of the mode-locked train are currently in the progress.

Reference

[1] G.H.C. New, PIEEE, Vol.67, No.3, PP.380-396, Mar. (1979)

[2] A.L. Max, etal, IEEE JQE., Vol.QE-19, No.4, PP.562-566, Apr. (1983)

[3] A.M. Ratner "Spectral, Spatial and Temporal Properties of Lasers" PP.190-191, Plenum Press, New York-London, (1972)

[4] T. Bischifberger and Y.R. Shen, Physical Review A, Vol.19, No.3, PP.1169-1176, (1979)

[5] Sun Zhan'ao, etal, "Chinese Journal of Lasers", Vol.16, No.5, PP.302-304, (1989)

An improved light source for laser ranging

Karel Hamal
Technical University
Prague, Czechoslovakia
Tel 422 46 23 97
Fax 422 847688

and

Martin Richardson
CREOL
University of Central Florida
Orlando, USA
Tel 407 658 6819
Fax 407 658 6880

Summary

The development of a new laser material, Cr-doped LiSAF makes possible the development of a laser source for satellite ranging systems that is superior in performance capabilities than current Nd:YAG-based laser sources. This new material offers the potential of shorter pulses and more preferrable wavelengths (850nm and 425nm) than multi-wavelength Nd:YAG systems, leading to superior ranging resolution and greater detection sensitivity.

We are embarking on a feasibility study of a two-wavelength , mode-locked laser system based on Cr:LiSAF, providing shorter pulses for improved ranging resolution.

Background

Current satellite multi-wavelength laser-ranging systems operating with Nd:YAG based systems are capable of resolving earth-satellite distances to within a centimeter. The latter limitation is primary set by the minimum pulse-duration available from current field-usable mode-locked Nd:YAG laser systems having diffraction-limited beam divergence. Recent developments in ultrashort laser pulse technology with a new laser material perfected at CREOL in the last two years, now offers the possibility of an improved multi-wavelength laser-ranging system. The principal advantages this new material will offer is in shorter laser pulse durations, down to a few picoseconds, thereby improving ranging accuracy to the millimeter level, and in the use of shorter laser wavelengths permitting detection in a region of higher photocathode sensitivity, thereby improving overall sensitivity.

The new laser material Cr-doped LiSAF[1] has already been extensively studied[2,3], and reliable mode-locked operation has been demonstrated[4]. At the present time most of the technology of Cr-doped LiSAF is resident at CREOL. This has occured as consequence of it's crystal growth development at CREOL, and in a concerted effort being made by CREOL scientists to determine it's optical and physical properties. As a consequence, many laboratories are examining potential applications of this exciting new laser material.

Technical Details

We wish to take advantage of the possibilities offered by Cr:LiSAF in developing a fieldable laser for satellite ranging providing the general properties referred to above. A modelocked Cr:LiSAF laser can be built under this program that would have the principal components shown in fig.1.

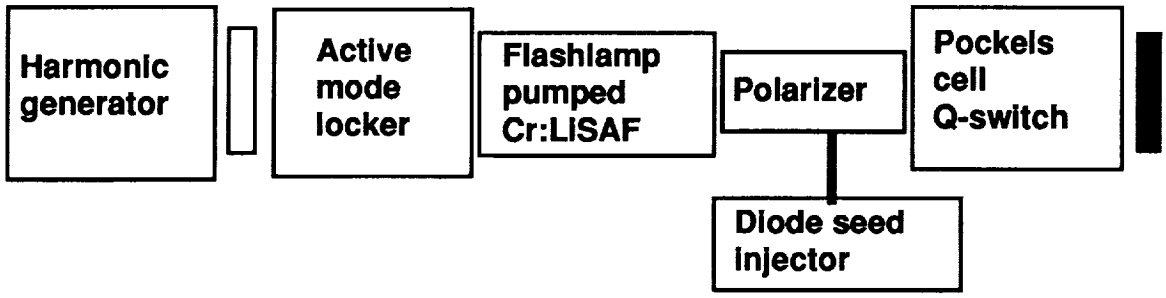

Fig.1. Schematic of an actively modelocked multifrequency Cr:LiSAF laser for satellite ranging

A cw single mode diode laser operating at ~845nm can be used to seed the Cr:LiSAF laser with a specific frequency. This will both control the frequency of the laser, and it's harmonic, and ensure that the modelocked laser has single mode output itself, ensuring diffraction-limited beam divergence. Short pulses wouldbe formed within the laser with the aid of conventional modelocking and Q-switching techniques. With the laser locked to a specific output frequency, efficient, stable, phase-matched second harmonic conversion will be guaranteed. The output performance of the laser will have the following parameters

Energy per pulse-train	500mJ	Wavelength	850nm
Number of pulses	10	Energy per pulse	50mJ
Pulse-duration	30ps	Pulse separation	10ns
Second Harmonic Conv. Eff.	25%	En. @ 425nm	12.5mJ

References

1. S.A. Payne, L.L. Chase, L.K. Smith, W.L. Kway, and H.W. Newkirk, "Laser performance of $LiSrAlF_6:Cr^{3+}$," J. Appl. Phys. **66**, 1051, 1989.
2. P. Beaud, Y-F. Chen, B. Chai, and M. Richardson, "Small-signal gain properties of $LiSrAlF_6:Cr^{3+}$", submitted to Optics Letters.
3. Y. F. Chen, P. Beaud, B. H. T. Chai & M. Richardson, "Small signal gain measurements of Cr-doped LiSAF and LiCAF" Proc. Conf. on Advanced Solid State Lasers Santa Fe (Optical Society of America 1992) to be published.
4. P. Beaud, E. Miesak, Y-F. Chen, B. H. T. Chen and M. Richardson, "A flashlamp-pumped Cr:LiSAF regenerative amplifier" Proc . Conf. on Advanced Solid State Lasers Santa Fe (Optical Society of America 1992) to be published.

Epoch and Event Timing

Preliminary Results from the Portable Standard Satellite Laser Ranging Intercomparison with MOBLAS-7

Michael Selden, Thomas Varghese, Michael Heinick, Thomas Oldham
Allied Signal Aerospace Company,
BFEC/CDSLR
10210 Greenbelt Road
Seabrook, MD 20706
USA

Abstract

Conventional Satellite Laser Ranging (SLR) instrumentation has been configured and successfully used to provide high-accuracy laboratory measurements on the LAGEOS-2 and TOPEX cube-corner arrays. The instrumentation, refered to as the Portable Standard, has also been used for field measurements of satellite ranges in tandem with MOBLAS-7. Preliminary results of the SLR measurements suggest that improved range accuracy can be achieved using this system. Results are discussed.

1 Introduction

The portable standard (PS) is a collection of ranging instrumentation which was originally brought together as a calibration mechanism for the CDSLR network. The system was designed to take parallel measurements with field stations while sharing the existing telescope/mount, system shelter, power, and laser. It is a method to tie and intercompare the worldwide network to a single standard which periodically travels from system to system to maintain the caliber of the satellite laser ranging measurements. A second role for the PS is as a test bed for new instrumentation and SLR techniques. As a constantly improving system, it provides a means of proving new technology prior to implementing changes to the network. A third use of the portable system has been as a troubleshooting mechanism to resolve conflicts during collocation.

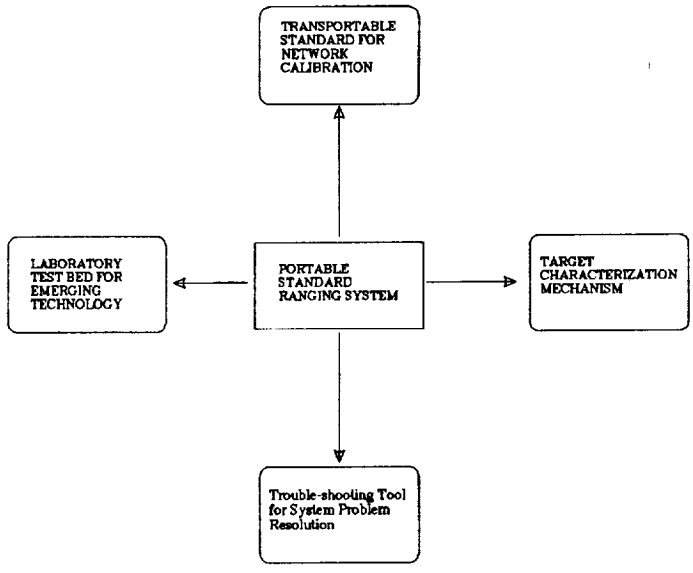

Figure 1 Portable Standard Functions

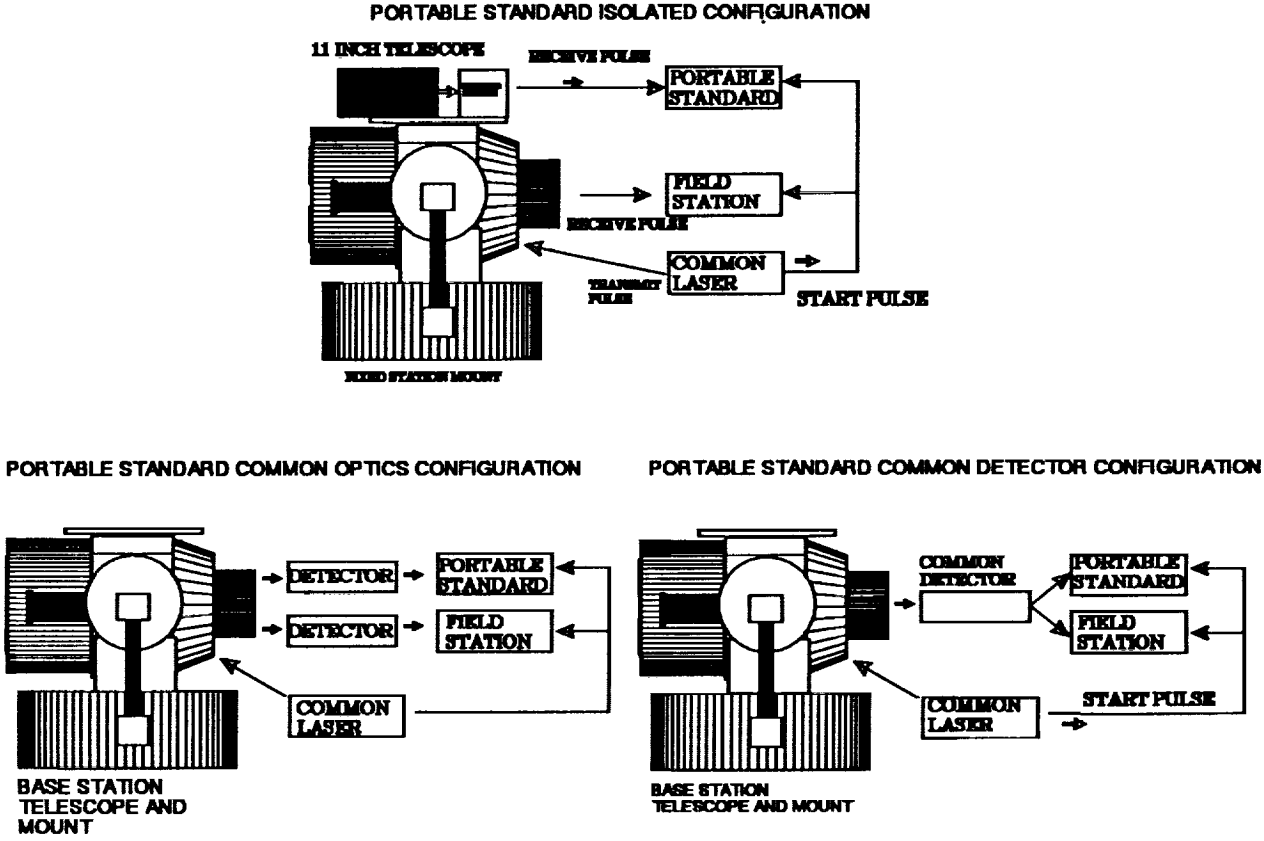

Figure 2 Portable Standard Test Configurations

The PS ranging instrumentation can sample data in parallel with a field system at any measurement point (see figure 2). It can be configured to independently collect the optical signal using a separate detector; share a common detector with the field system but process the signal separately, or share a common detector and signal processor while separately measuring time intervals. The PS is also able to provide a common frequency source to both systems, should this prove desirable.

1.1 History

One use of the PS has been the optical characterization of the LAGEOS-2 satellite and of two TOPEX array segments. These tests enabled us to employ the instrumentation widely used by many of the SLR stations to measure satellite optical response in the time domain. Earlier Laboratory experiments verified that optical range calibration coupled with instrument thermal stability would make it possible to predict and correct the HP5370 nonlinearities over a limited dynamic range (few nanoseconds) and limited time duration (several hours for one calibration). These calibration techniques, improved data statistics, and instrument temperature control made the necessary sub-millimeter instrumental accuracy achievable.

Recently the PS was installed into MOBLAS-7 for performance intercomparison tests. These tests were aimed at measuring the increase in performance which can be gained using multiple time interval counters for increased statistical advantage, calibration of the discriminator time-walk, increased epoch measurement precision, and to test new opto-electronic detectors in a parallel configuration with the existing detector while employing a shot-by-shot comparison. The first series of satellite passes were used to baseline the current performance of the system with respect to MOBLAS-7. The experimental configuration used a common discriminator for both systems, thereby isolating the performance gained using more than one time interval meter. The results of these first tests are described here.

2 Hardware Description

The PS instrumentation is normally rack-mounted in two cabinets, however, due to practical space limitations in MOBLAS-7 the equipment was confined to a single rack. The computer/controller was placed above the tracking console on a plexiglass shelf constructed for these tests. A brief description of the instrumentation used in the PS follows, refer to figure 3 during the description.

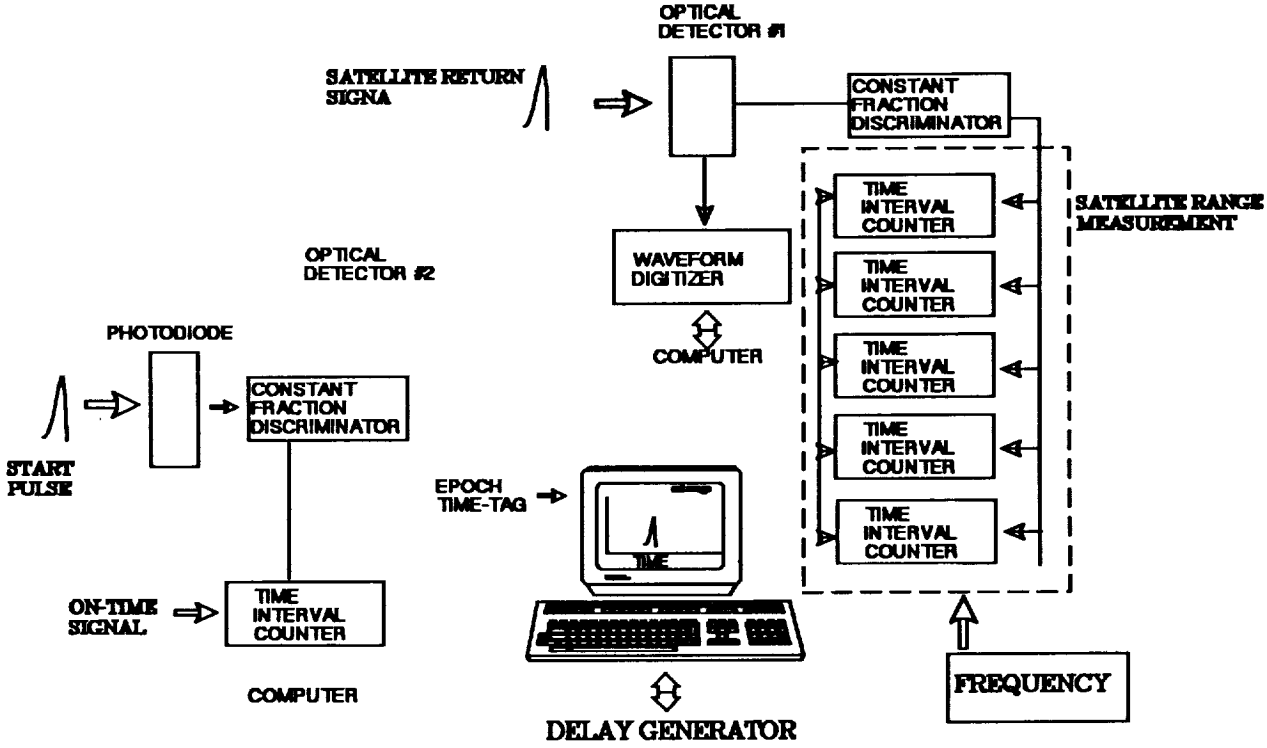

Figure 3 Portable Standard Hardware (SLR Configuration)

2.1 Frequency Source

A Hewlett Packard Cesium beam standard with a high-performance option tube and an Austron disciplined oscillator provide the frequency source for the PS. The disciplined oscillator improves the short-term frequency stability an order of magnitude when compared with use of the Cesium standard alone.

2.2 Time Interval Measurement

Several HP5370 (A & B) time interval counters and two Stanford SR620 time interval counters are available to take range measurements. The time interval counters are arranged to take multiple measurements of the same event to improve the data quality. These counters can also be configured to measure differential time (figure 4) between two return events or a combination of events depending on the application. For these first tests 4 HP5370 counters were used.

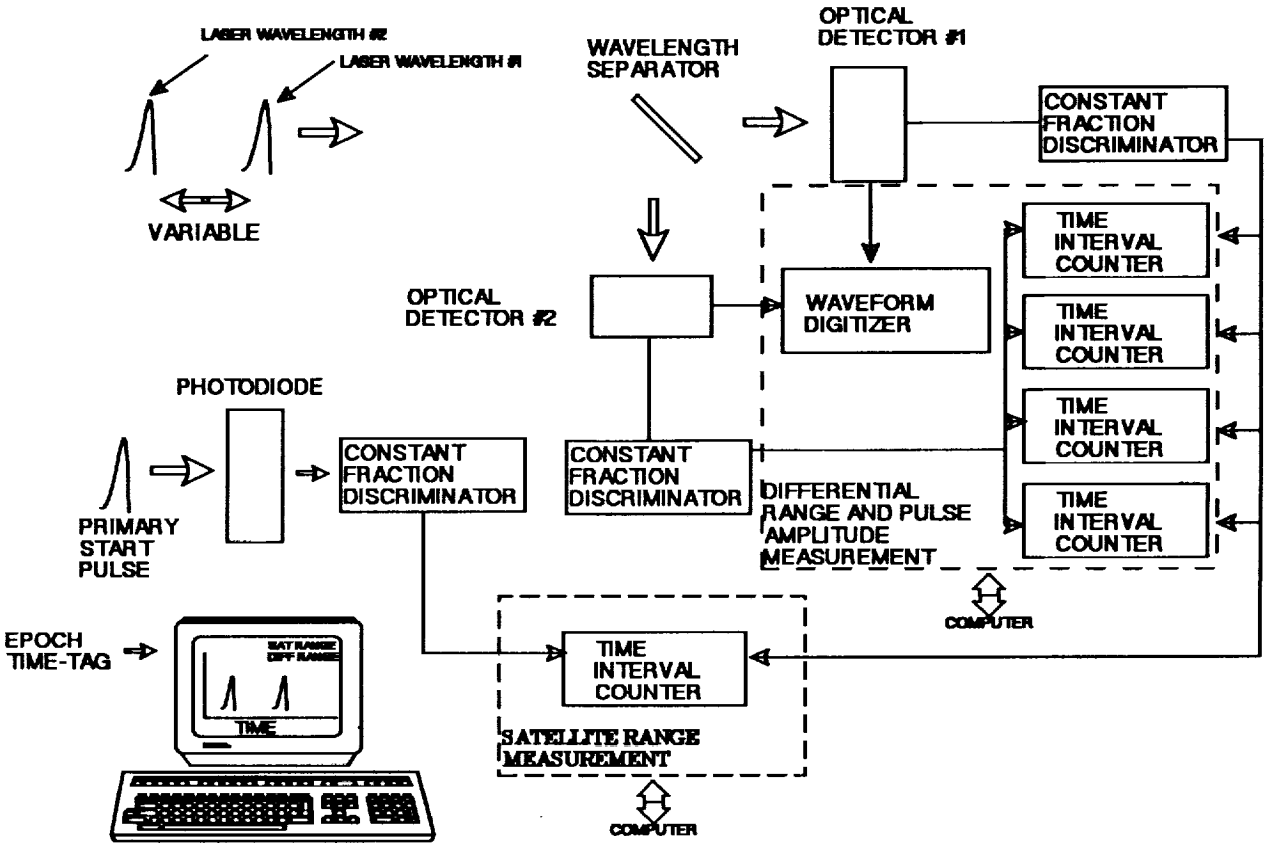

Figure 4 Differential Range Configuration (Two Color etc)

2.3 Signal Processing

A Tennelec constant fraction discriminator (TC-454) is used to process the MCP-PMT detector output. The discriminator is calibrated to remove systematic amplitude-dependent errors (time-walk). For these first tests the MOBLAS-7 discriminator was used and no amplitude measurement was made using the PS.

2.4 Optical Detection

The PS features a detector package which can accommodate several detectors. These may be directly coupled to the optics, or indirectly using fiber-optics. During two-color ranging experiments two MCP-PMT's may be used to separate the wavelenths for differential time measurement. Other types of detectors (PMT, APD, Photodiode) can be used depending on the application, or simultaneously for detection intercomparison. During the first series of passes the MOBLAS-7 MCP-PMT detector was used.

2.5 Amplitude/Waveform Measurement

The output of the MCP-PMT may be digitized using a Tektronix 7912HB (1 GHz bandwidth) digitizer from which amplitude information is extracted. This information can be applied to the range measurements to correct for discriminator time-walk. The digitizer can also be configured to measure the differential time between two pulses while the entire waveform record of each shot is stored on disk. During the TOPEX measurements, a 4.5 GHz bandwidth digitizer coupled to a 60 GHz bandwidth photodiode was substituted for the normal digitizer to map the optical response of the TOPEX array segments.

2.6 Environmental Instrumentation

The thermal environment of the PS instrumentation is monitored and stabilized using microprocessor controlled fans. Thermal sensors are arranged to measure the temperature of the air discharged by the instruments. Thermal stability can be maintained better than 1 degree Centigrade depending on the airconditioning system available. Thermal stability is essential to maintain high data quality.

2.7 Calibration

Optical calibration provides a means to model Time Interval Meter non-linearities for limited dynamic range measurements such as satellite laboratory characterization and two-color differential time interval measurement. The optical calibration mechanism (figure 5) consists of a diode laser, optics and a computer-controlled micropositioner with ~ 2 μm precision. A pulse emitted by the diode laser is split into two pulses, one pulse travels a fixed distance while the second pulse traverses a known but variable range. The two pulses are each detected by a common detector and the signal processed using a common discriminator. The calibration mechanism may be used two ways. For discriminator (amplitude-dependent error) calibration the separation between the pulses is held constant, while the amplitude of one of the pulses is varied using a neutral density filter wheel. A real-time histogram of the varied pulse height is displayed on the computer CRT assuring that a good distribution of data is collected to determine the CFD time-walk curve. For range-dependent error, the amplitude of each pulse is maintained at a constant value, while the pulse-pair separation is varied. A number of data values are collected at each range interval. The variation in separation step size and number of points per position is selectable and is dependent on the desired accuracy. For LAGEOS-2 measurements 0.25 mm instrumental accuracy was desired so an appropriate step size and data volume (500 measurements/position) were used.

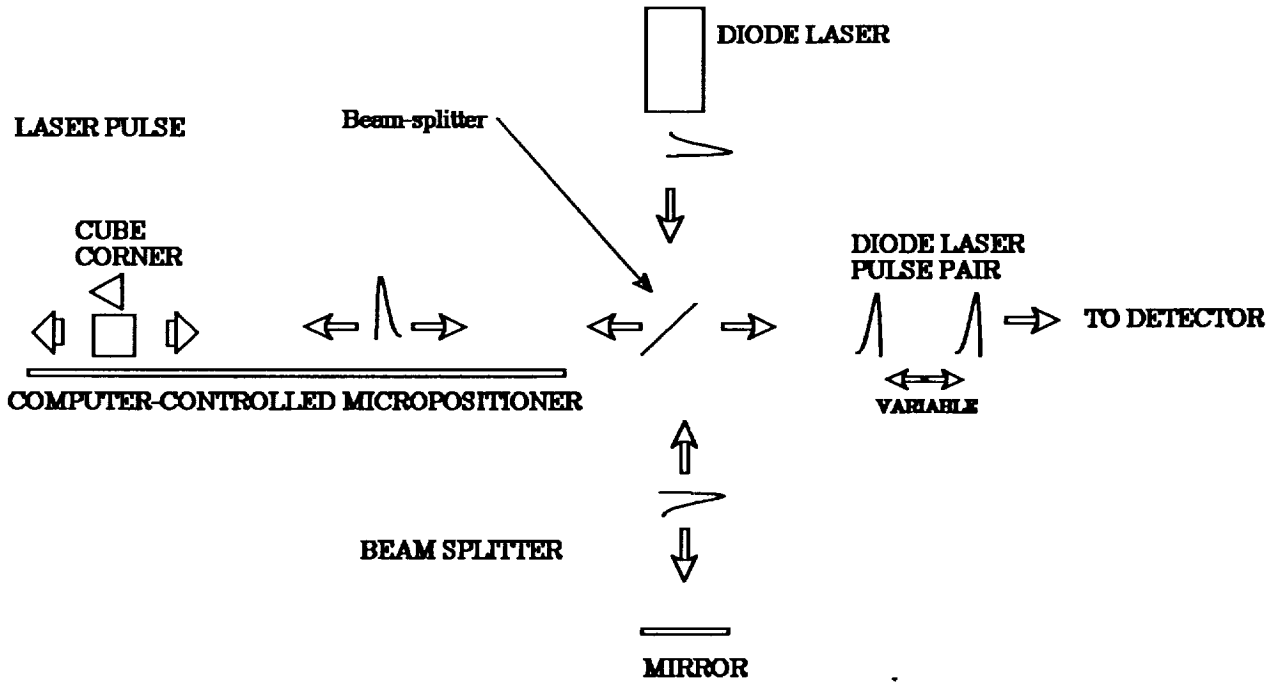

Figure 5 Optical Calibration Mechanism

2.9 Range Gate Generator

A Stanford model DG535 delay generator is used to generate range gates and to perform range simulation for diagnostic purposes. The delay generator may be used to simulate the various ranges encountered during experimental operations. In this mode it is useful for diagnosing internal problems and for software development. The DG-535 uses an external frequency source for enhanced performance.

2.9 Controller

Virtually all instrument control and data acquisition is done using the IEEE-488 interface standard. The controller is a Hewlett Packard model 380 computer which operates using the HP Basic-UX program development environment.

3 Experiment Description

The intercomparison with MOBLAS-7 is a multi-stage experiment. The first stage has been in a common discriminator configuration. One of the output ports of the constant fraction discriminator was divided and fed to four HP 5370 time interval counters. This configuration is the least invasive test and did not affect normal station performance. For this test, no measurement of amplitude was performed, thus, no time-walk correction has been applied to the data. There are two differences to the measurements made by the PS and MOBLAS-7. The PS used its own frequency source (with enhanced short-term stability), and four time interval meters for each event. The choir effect of the counters provides an improvement to the time interval measurement component of the ranging error.

4 Results and Discussion

The resulting satellite data (see table 1) shows significant improvement over MOBLAS-7 data on a shot-by-shot basis. The low-orbit satellite (starlette, ERS-1) trend (see figure 6) shows a somewhat less pronounced improvement when compared to the LAGEOS data. It should be noted that during the period of the intercomparison, MOBLAS-7 was not delivering the level of performance which it is capable of achieving. Historically, MOBLAS-7 has routinely delivered data of 7 - 9 mm single shot rms, whereas, during these tests its typical performance was in the 9 - 11 mm neighborhood. Ground target residuals for the PS varied between 2.5 mm rms (best) and 4.5 mm rms (worst), typically is was in the 3 - 3.5 mm range. There is a consistent bias between the MOBLAS-7 time interval counter and the average of the 4 PS time interval counters. The average of the bias was 3.8 mm with a standard deviation of 1.3 mm. Applying a 3 sigma criteria to the results would eliminate one satellite pass resulting in a mean difference of 3.54 mm with a standard deviation of 0.86 mm. This bias can be largely attributed to the MOBLAS-7 time interval counter. The bias is at a level consistent with HP-5370 counters: agreement better than 1 cm and typically better than 5 mm.

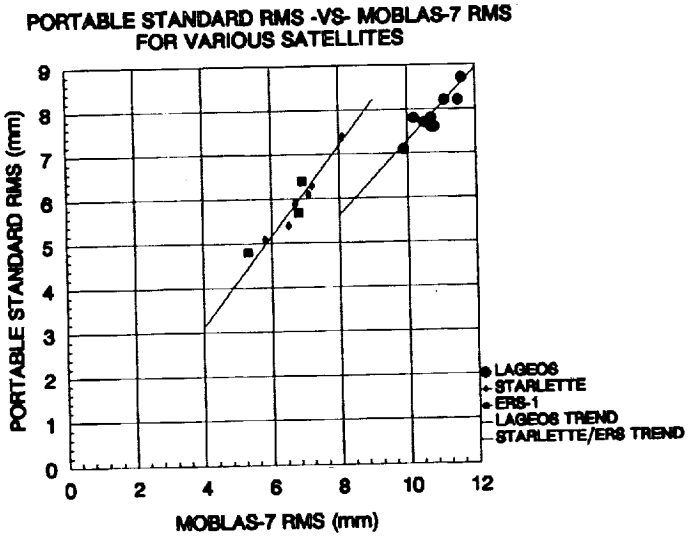

Figure 6

PORTABLE STANDARD PASSES

TAKEN AT MOBLAS 7

DATE	SATELLITE	OBS.	PS RMS (mm)	M7 RMS (mm)	Bias (mm)
19-OCT-91	LAGEOS	8098	7.8	10.7	-3.4
25-OCT-91	LAGEOS	3140	7.8	10.7	-3.4
29-OCT-91	LAGEOS	6478	7.8	10.2	-4.0
29-OCT-91	LAGEOS	989	8.7	11.6	-4.1
30-OCT-91	LAGEOS	2547	8.2	11.1	
31-OCT-91	LAGEOS	2626	7.6	10.7	-3.1
6-NOV-91	LAGEOS	4787	7.1	9.9	-2.6
6-NOV-91	LAGEOS	3591	7.7	10.5	-2.5
6-NOV-91	LAGEOS	829	7.6	10.8	-3.3
29-APR-92	LAGEOS	815	8.2	11.5	-5.4
19-OCT-91	STARLETTE	1343	6.1	7.1	-3.7
29-OCT-91	STARLETTE	443	5.1	5.8	-4.5
29-OCT-91	STARLETTE	598	5.4	6.5	
29-OCT-91	STARLETTE	1443	6.3	7.2	-4.3
30-OCT-91	STARLETTE	881	6.4	6.9	
30-OCT-91	STARLETTE	757	7.4	8.1	
6-NOV-91	STARLETTE	970	5.9	6.7	-7.8
30-OCT-91	ERS-1	463	5.7	6.8	-3.4
30-OCT-91	ERS-1	1062	6.4	6.9	
6-NOV-91	ERS-1	384	4.8	5.3	-1.9

Table 1 Satellite Ranging Intercomparison Results

5 Future Plans

As noted, MOBLAS-7 is not achieving its best performance at this time. For the second stage of the experiment we plan to perform adjustments and fine-tuning of the MOBLAS-7 instrumentation to regain its typical performance, then make the intercomparison again. During the the next series of passes amplitude measurements will also be taken to apply the discriminator time-walk correction to the data. For the third stage of the experiment, we will install a second detector in the MOBLAS-7 receive package for dual-detection tests. The new detector exhibits enhanced bandwidth and jitter characteristics ("Performance Comparison of Microchannel Plate PMTs", Varghese, Selden and Oldham, These Proceedings). We also plan to obtain an APD detection system to perform direct intercomparison measurements between APD and MCP-PMTs at both the multi-photoelectron and single photoelectron level.

Stanford time interval counters will also be used for range measurement. In the past, We have tested the performance of Stanford counters in the laboratory with varying results. Of the five counters tested, two exhibited large and un-predictable (100 ps) jumps in range while the remaining three counters behaved normally and were comparable to the HP-5370 in performance. At least one Stanford SR620 counter which performs well in the laboratory will be used for a shot-by shot comparison with the other time interval meters.

Other plans have begun to perform in-orbit satellite characterization experiments using TOPEX. For these tests the PS will be used in optical isolation mode; a celestron C-11 telescope will be "piggy-backed" on the MOBLAS-7 Contraves telescope for parallel measurement. The test will also provide a comparison between large and small aperture systems on other satellites. Recently, a study of the relative effect of thermal-loading on the two telescopes was done to determine their focal-length stability for small detector (APD) applications.

6 Conclusions

The portable standard, developed and proven through laboratory experiments, has shown improved satellite range residuals through the use of multiple time interval counters over data acquired by MOBLAS-7. Use of its full capabilities should provide even more improvement and test the accuracy limitations imposed by current ranging instrumentation. Sequential testing and replacement of measurement components (detector, signal processor, time interval/event meter, etc.) will offer a controlled measurement baseline and increase our understanding of SLR error sources.

Detector Technology

Performance optimization of detector electronics for millimeter laser ranging

S. Cova[+], *A. Lacaita*[+] *and G. Ripamonti**

[+]Politecnico di Milano, Dipartimento di Elettronica e Informazione and CEQSE-CNR,
Piazza L. da Vinci 32 - 20133 Milano (Italy)

*Universita' degli Studi di Milano, Dipartimento di Fisica
Via Celoria 16 - 20133 Milano (Italy)

(invited paper)

ABSTRACT

The front-end electronic circuitry plays a fundamental role in determining the performance actually obtained from ultrafast and highly sensitive photodetectors. We deal here with electronic problems met working with Microchannel Plate photomultipliers (MCP-PMTs) and Single Photon Avalanche Diodes (SPADs) for detecting single optical photons and measuring their arrival time with picosecond resolution. The performance of available fast circuits is critically analyzed. Criteria for selecting the most suitable electronics are derived and solutions for exploiting at best the detector performance are presented and discussed

I. INTRODUCTION

Laser ranging applications with millimeter resolution require to measure the time of flight of single photons with precision better than 30ps root mean square (rms), that is, with better than 70ps full-width at half maximum (FWHM) of the resolution curve. Two photodetector types can attain single photon sensitivity and picosecond resolution: proximity-focused Microchannel Plates (MCPs) [1-3] and Single Photon Avalanche Diodes (SPADs) [4-7]. In both cases the front-end electronics associated to the detector plays a fundamental role. In order to take full advantage of the detector timing performance, the electronic pulse processing should be carefully optimized.

In set ups where MCPs are employed, the fast preamplifier and the constant fraction trigger circuit (CFT) are by far the most critical electronic components. In this paper we discuss criteria for optimum selection of the preamplifier, taking into account the noise and bandwidth characteristics. We show that preamplifiers with very large bandwidth (3GHz or more) are not to be employed, since they impair the timing performance [8]. We analyze problems met by constant fraction triggers working with

subnanosecond pulses from MCPs. We discuss how the performance of available CFTs can be improved by simple modifications that provide a better adjustment of the relevant CFT parameters and/or by suitable pre-filtering of the MCP pulses [9,10].

SPADs are avalanche photodiodes that operate biased above the breakdown voltage in the so-called Geiger-mode [4-7,11]. Their operation is fundamentally different from that of photomultiplier tubes (PMTs) and of ordinary avalanche photodiodes (APDs). The device does not have a linear internal gain, that is, it does not amplify linearly the primary photocurrent. It instead exploits the avalanche process to behave in a way similar to that of a trigger circuit, rather than an amplifier. When one or more photons are detected at a given time, a fast-rising current pulse is generated, with standard amplitude and shape, independent of the number of photons. The leading edge of this pulse marks with very high precision, down to 20ps FWHM, the time of arrival of the photon that has triggered the avalanche [5].

We analyze limitations met working with SPADs in the simple biasing arrangements that employ a ballast resistor to quench the avalanche, called Passive Quenching Circuits (PQCs) [6,7,11]. In order to fully exploit the ultimate SPAD timing performance, the device should be operated with an Active Quenching Circuit (AQC) [12,13]. We introduce a new AQC model, capable of driving the detector in remote position, connected by a coaxial cable [13]. Special care has been devoted to the design of the input stage, in order to minimize the circuit noise and thus reduce to less than 3ps rms the internal time jitter of the circuit, making negligible its contribution to the overall time resolution.

II. SELECTION OF THE OPTIMUM PREAMPLIFIER FOR MCPs

Since the gain of the MCP is limited to 5 10^5, a fast preamplifier with gain higher than 10 must be used between the MCP output and the pulse-timing trigger circuit. This gain makes the noise of the following circuits negligible, in comparison to that of the amplifier. In order to avoid reflections and ringing in the pulse shape, the MCP output must be terminated on a 50 Ohm resistor R_s , as outlined in the equivalent circuit of Fig.1.

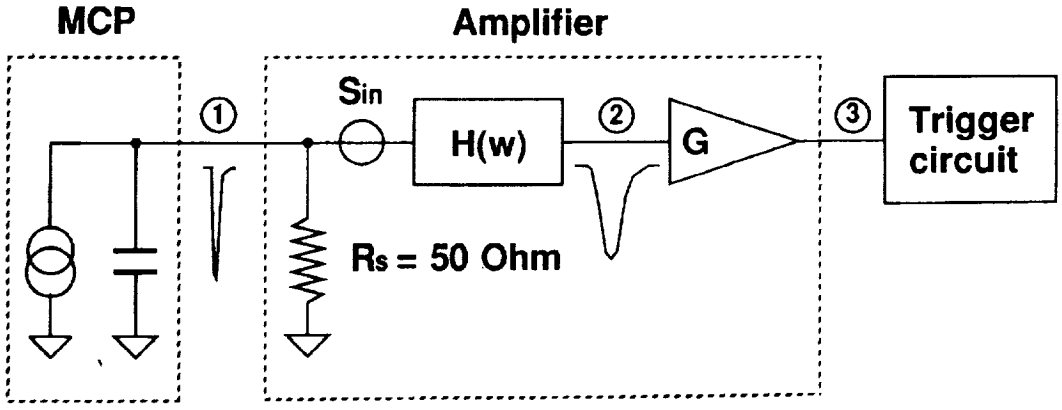

Fig.1 Equivalent circuit for analyzing the effect of the amplifier noise and bandwidth on the pulse time-jitter.

An accurate analysis of the time-jitter contribution arising from the electronic noise has been carried out [8] and we report here the main results. The action of the amplifier on the MCP pulses is described (see Fig.1) by two blocks: a transfer function in the frequency f domain $H_A(f)$, normalized to unity dc gain, followed by a constant gain G. The time-domain impulse response of the amplifier is $h_A(t) = F^{-1}[H_A(f)]$ (where F^{-1} denotes the inverse Fourier transform and $h_A(t)$ is normalized to unit area). S_i is the spectral density of the equivalent input noise generator of the amplifier, assumed to be gaussian. As sketched in Fig.2, the noise causes a random shift of the actual crossing time of the trigger threshold.

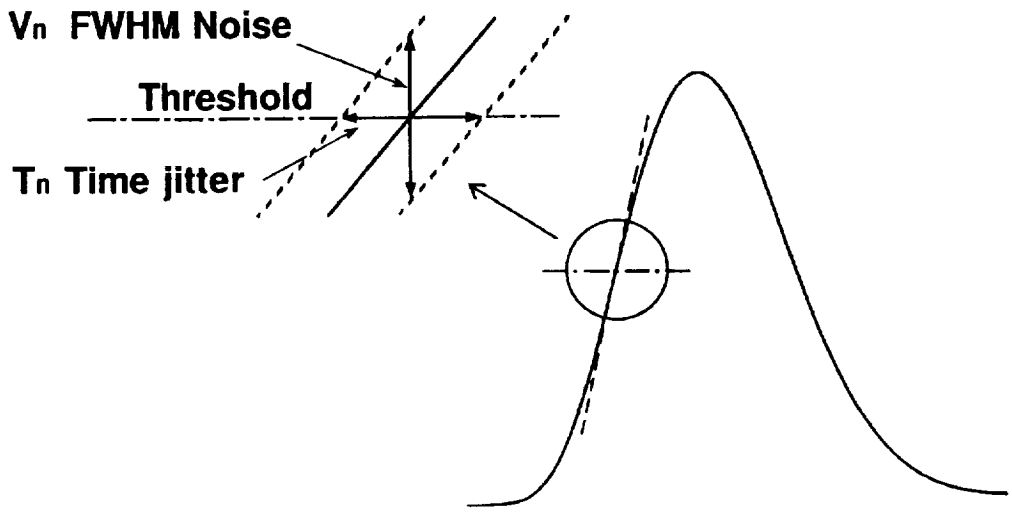

Fig.2 Effect of the electronic noise on the triggering time.

Let us denote by v_n the rms value and by V_n the FWHM of the amplitude distribution of the noise, and by r the slope of the ideal, noise-free pulse at the triggering threshold. The FWHM T_n of the additional time jitter is given by

$$T_n = \frac{V_n}{r} = 2.36\frac{v_n}{r} \qquad (1)$$

This time jitter at the comparator threshold (point 3 in Fig.1) is equivalently evaluated at the input of the gain stage G (point 2 in Fig.1).

In first instance, the noise spectrum can be considered white, that is, with constant spectral amplitude $S_i = a^2$. Let us denote by B_n the noise bandwidth, proportional to the signal bandwidth B_A (3dB down bandwidth)

$$B_n = K_n B_A \qquad (2)$$

with constant K_n depending on the shape of the frequency response $H_A(f)$. We have

$$v_n = a\sqrt{B_n} = a\sqrt{K_n B_A} \qquad (3)$$

The slope r also increases with B_A , and it can be easily seen that there is a minimum in the plot of T_n versus B_A. Let us first consider the high bandwidth side, where the B_A values are high enough to have risetime practically equal to that of the MCP pulse. On that side, T_n goes up as $\sqrt{B_A}$, since the slope r is unaffected and the noise v_n increases as $\sqrt{B_A}$. Let us now consider the low bandwidth side, where the pulse-risetime T_r is fully dominated by B_A, namely, T_r is about $1/(3\ B_A)$. On this side, T_n goes down as $B_A^{-3/2}$ when B_A is increased, since the slope r increases as B_A^2 and noise increases as $\sqrt{B_A}$. A minimum of T_n will therefore be found at an intermediate value of B_A , at which the relative rate of increase of the pulse slope r will be equal to that of the noise V_n. More accurate quantitative results can be obtained by considering the actual voltage waveform. Let us denote by $V_D(t)$ the voltage pulse at the 50 Ohm output of the MCP detector

$$V_D(t) = Q\, h_D(t) \tag{4}$$

where Q denotes the area of $V_D(t)$ and $h_D(t)$ is normalized to unit area. The actual voltage waveform V(t) at the input of the gain stage G (point 2 in Fig. 1), results from the convolution product of the detector pulse $V_D(t)$ and of the amplifier impulse response $h_A(t)$

$$V(t) = Q\, h_D(t) * h_A(t) \tag{5}$$

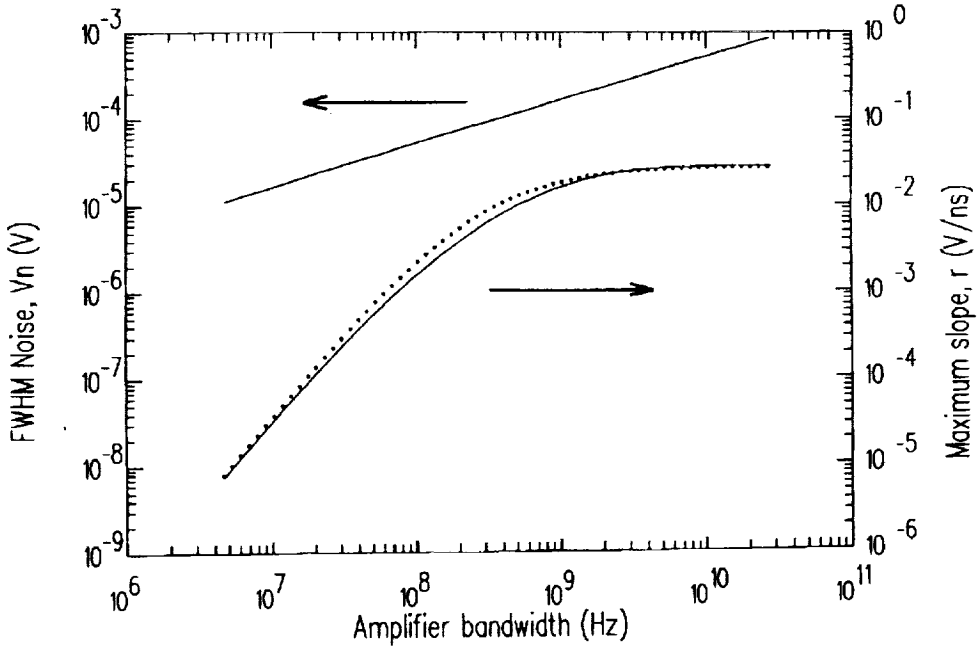

Fig.3 Maximum slope, r, of the amplified pulse and FWHM Vn of the noise amplitude distribution at point 2 in Fig.1 vs amplifier bandwidth B_A. Pulses of a 12μm channel MCP (Hamamatsu R1564U); amplifier having frequency response with two real poles, white input noise generator with rms density $a = 2nV\ Hz^{-1/2}$. Results of detailed computations of the pulse waveform (full line) are compared with the approximation discussed in Ref. [8] (dotted line).

The shape of V(t) and the corresponding maximum slope r can be obtained by numerical computations, accurately taking into account the characteristics of the detector pulse and of the amplifier impulse response [8]. A simple approximation can also be employed to obtain a sufficiently good estimate of r. Essentially, it consists in computing the slope r as result of a weighted average of the corresponding slopes of the detector pulse and of the amplifier impulse response [8]. Fig.3 reports the computed behavior of r and V_n versus amplifier bandwidth for a typical case. Fig.4 illustrates for another case the detailed behavior of the time jitter versus amplifier bandwidth. A broad minimum is found in all cases considered, centered at an optimum bandwidth value B_{Aopt} , which in all cases is well below 2GHz and mostly is around 1GHz .

The analysis carried out with a white noise spectrum leads to definite conclusions. Selecting the amplifier for very high bandwidth and paying minor attention to the noise is not only useless, but even disadvantageous. The noise has primary importance, since the time jitter is proportional to the root-mean square spectral density a. The optimum bandwidth value B_{Aopt} is markedly lower than that suggested by the criterion of keeping the risetime of the amplified pulse very near to the original risetime of the detector pulse. Even for the fastest available MCP detector, B_{Aopt} does not exceed 1.7GHz. Satisfactory results can be obtained with bandwidth values remarkably lower than B_{Aopt}, even by a factor of two. On the basis of these results, it was concluded that amplifiers employing fast bipolar transistors (BJTs) provide better performance than amplifiers based on ultrafast metal-semiconductor field-effect transistors (MESFETs). In fact, the higher bandwidth of MESFETs is not required and, working with a 50 Ohm source, the lower input current noise is not important. Furthermore, MESFETs may have higher components in the low-frequency noise spectrum. However, it must be taken into account that the input noise spectrum of BJTs also contains a high frequency component proportional to f^2. A detailed analysis [8] shows that the f^2 noise component causes a steeper increase of V_n for rising B_A, thereby shifting to lower B_A value the minimum of T_n and making much steeper the rise of T_n on the high B_A side. Fig.5 illustrates a typical case. It is worth stressing that the effect is more marked and the shift of the minimum is greater for transistors having lower white noise component (that is, lower value of a).

These results further support and enhance the conclusions drawn in the white noise analysis. The presence of a f^2 component in the noise spectrum of BJTs i) shifts to even lower value the optimum amplifier bandwidth B_{Aopt} ; ii) makes remarkably more severe the penalty for working with amplifier bandwidths higher than the optimum one ; iii) has almost negligible influence on the results obtained with amplifier bandwidth lower than B_{Aopt}.

In conclusion, the quantitative analysis demonstrates that, by using available low-noise high-frequency bipolar transistors in rationally selected operating conditions, the additional time jitter due to the circuit noise can be kept below 5 ps FWHM. In any case of interest, the behavior of the jitter versus the amplifier bandwidth can be fairly simply analyzed by using the approximate approach introduced in Ref.8. This approach just requires the knowledge of a few numerical parameters characterizing the pulse shapes involved, which can be obtained by analytical representation or by measurements of the waveforms.

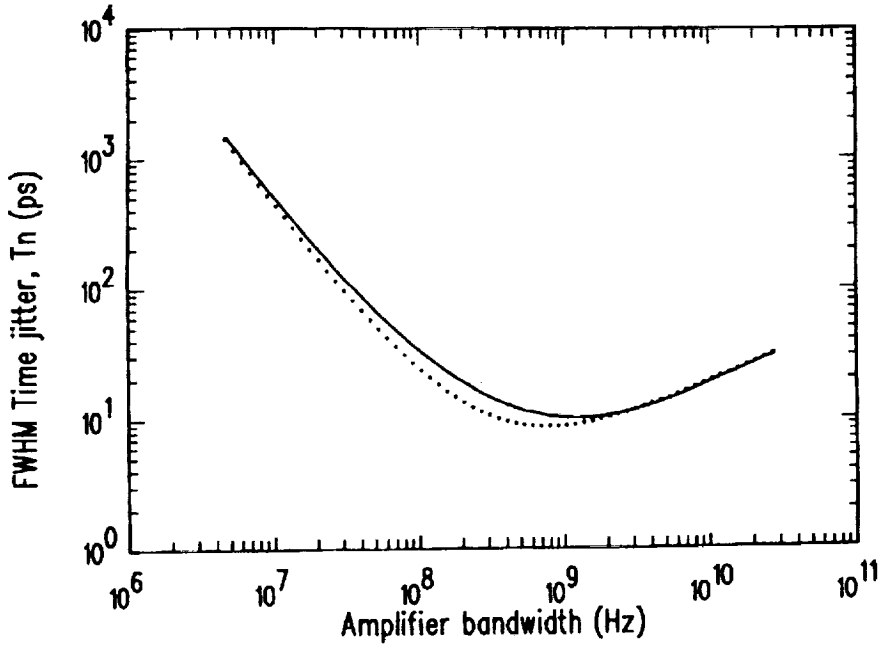

Fig.4 Additional FWHM time jitter T_n due to the noise vs amplifier bandwidth B_A, for the case of Fig.3. Results of detailed computations of the pulse waveform (full line) are compared to the approximation discussed in Ref. [8] (dotted line).

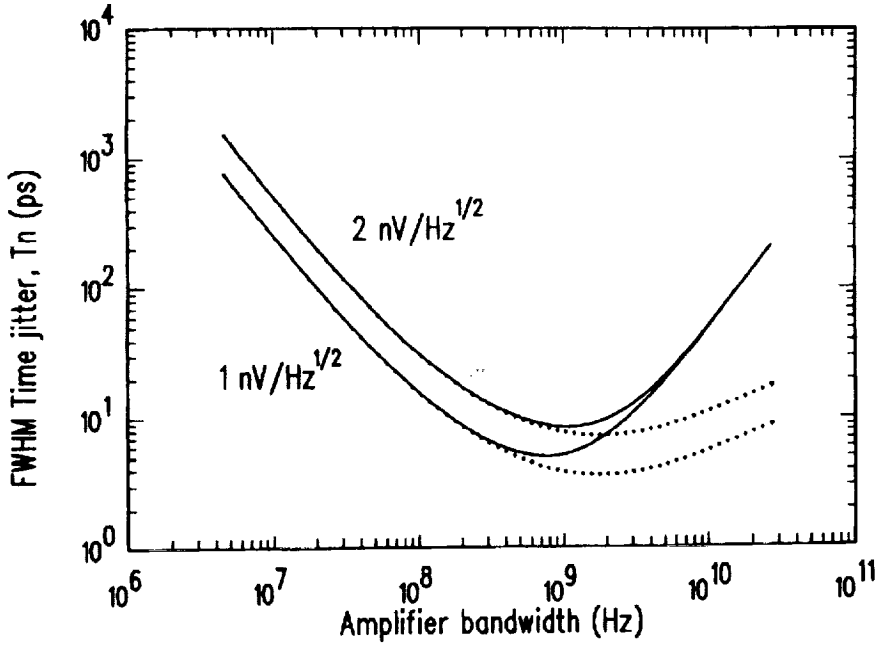

Fig.5 Effect of the f^2 spectral noise component in bipolar transistors (BJT). Pulses of a 6μm-channel MCP (Hamamatsu R2809U). Amplifier with two real poles in the frequency response, input BJT having f_T=5GHz (see Ref.8). Results with the total spectrum (full lines) are compared with those computed with only the white noise term (dotted lines) for two cases: minimum noise a=1nV $Hz^{-1/2}$ and moderately low noise a=2nV $Hz^{-1/2}$

III. CONSTANT FRACTION TRIGGERS WITH MCPs

Since single-photon pulses of photomultiplier tubes (PMTs) have statistically fluctuating amplitude, constant-fraction trigger circuits (CFT) are normally employed for accurate timing [14]. However, with the subnanosecond signals of MCPs non-ideal CFT behavior is observed. A residual amplitude-dependent time-walk sets the ultimate resolution in photon timing. A quantitative analysis of the problem has been carried out and will be here summarized [10].

Fig. 6 illustrates the basic structure and the principle of operation of a CFT circuit. The triggering point of the fast comparator is determined by the crossing of two replicas of the amplified MCP pulse, the first attenuated by a factor k, the second one delayed by a time T_D.

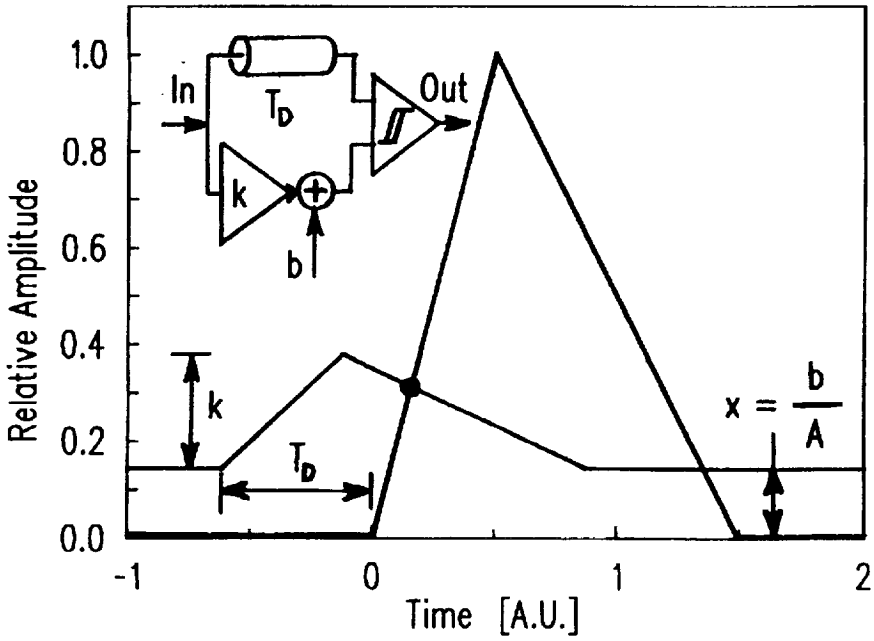

Fig.6 Working principle of Constant Faction Triggers (CFTs) based on a fast comparator with differential input. Block diagram (inset) and pulse waveforms at the comparator inputs (normalized to unit peak amplitude) are depicted in simplified form.

Crossing occurs when the delayed pulse reaches a given percentage of the peak. The time-walk effect is eliminated, since the triggering time is independent of the actual pulse amplitude A. This is strictly true only if the two waveforms have the same baseline level. However, setting both inputs at the same bias voltage level is unacceptable, since it causes the comparator to oscillate. A small dc voltage offset b is necessary; in practice, about 10 mV with modern fast comparators. This constant offset b causes a deviation from the ideal CFT operation, since it causes the crossing time to walk as A is varied. The slower is the rise of the delayed waveform, the larger is the walk. The problem is quantitatively analyzed making reference to the pulse waveform g(t) normalized at unit peak amplitude and to the correspondingly normalized baseline offset x. The pulse-amplitude distribution, with probability density p(A), is transformed in a distribution of

x, with probability density q(x).

$$x = \frac{b}{A} \tag{6}$$

$$q(x) = p(A) \left| \frac{dA}{dx} \right| = p(A) \frac{A^2}{b} \tag{7}$$

The lower threshold level A_L set for accepting the MCP pulses is translated in an upper limit x_H; conversely, the accepted maximum pulse height A_H sets a lower limit x_L. The relation between x and the time walk is readily derived. The crossing time t_c along the waveform g(t) is defined by:

$$x + k\, g(T_D + t_c) = g(t_c) \tag{8}$$

By differentiating with respect to x, we obtain:

$$dx + k \left(\frac{dg}{dt} \right)_{t_c + T_D} dt_c = \left(\frac{dg}{dt} \right)_{t_c} dt_c \tag{9}$$

Denoting by $g'_r = (dg/dt)_{t_c}$ the rising slope and by $g'_f = (dg/dt)_{t_c + T_D}$ the falling slope at the crossing point, we define the intercrossing slope

$$g'_i = g'_r - k\, g'_f \tag{10}$$

and obtain

$$dt_c = \left(\frac{dx}{g'_i} \right) \tag{11}$$

Let us denote by t_o the crossing time for x=0, which corresponds to the ideal CFT case (and is well approximated by the real CFT for pulse amplitude A much higher than the offset b). As A is decreased, the x value is increased and the crossing is shifted from t_o to a later time t_c ; the time walk t_s is $t_s = t_c - t_o$. The equation relating the time walk to x is simply obtained by integrating eq.11. The distribution of x is transformed in a distribution of t_s , with probability density $w(t_s)$. Since $w(t_s)\, dt_s = q(x)dx$ and $dt_s = dt_c$, we obtain from eq.11:

$$w(t_s) = q(x)\, g'_i \tag{12}$$

The actually observed time resolution curve $r_m(t)$ will be the convolution product of this distribution $w(t_s)$ and of the intrinsic resolution curve of the apparatus $r_i(t)$, due to other causes of time dispersion

$$r_m(t) = r_i(t) * w(t) \tag{13}$$

Since w(t) results from an inverse transformation of p(A), it is strongly asymmetric, affected by a long tail towards high t_s values. Its effect in widening the FWHM of $r_m(t)$ is therefore greater than that of a gaussian function having equal FWHM. Taking a linear pulse approximation (as outlined in Fig.6), that is, assuming constant intercrossing slope g'_i, the time walk is proportional to x and the distribution $w(t_s)$ is obtained from q(x) simply by a change of scale. It extends from a lower limit $t_{sL} = g'_i\, x_L = g'_i\, b/A_H$ to an upper limit $t_{sH} = g'_i\, x_H = g'_i\, b/A_L$. With the intercrossing slope g'_i obtained employing the suitable fast preamplifiers (risetime around 400ps, see Sec.II), a fairly small time walk effect would be estimated. For MCP types having 40ps intrinsic FWHM resolution, it would be practically negligible, since the computed FWHM of $r_m(t)$ is less than 45ps. For faster types, having 20ps intrinsic FWHM resolution, it would be moderate, since the computed FWHM of $r_m(t)$ ranges from 25 to 30ps. As a matter of fact, however, in the set-ups actually employed by the experimenters the situation significantly deviates from the linear pulse approximation. As illustrated by Fig.7, this is due to the short duration of the MCP pulses, to their shape and to the CFT setting, in particular to the minimum available value of the delay T_D.

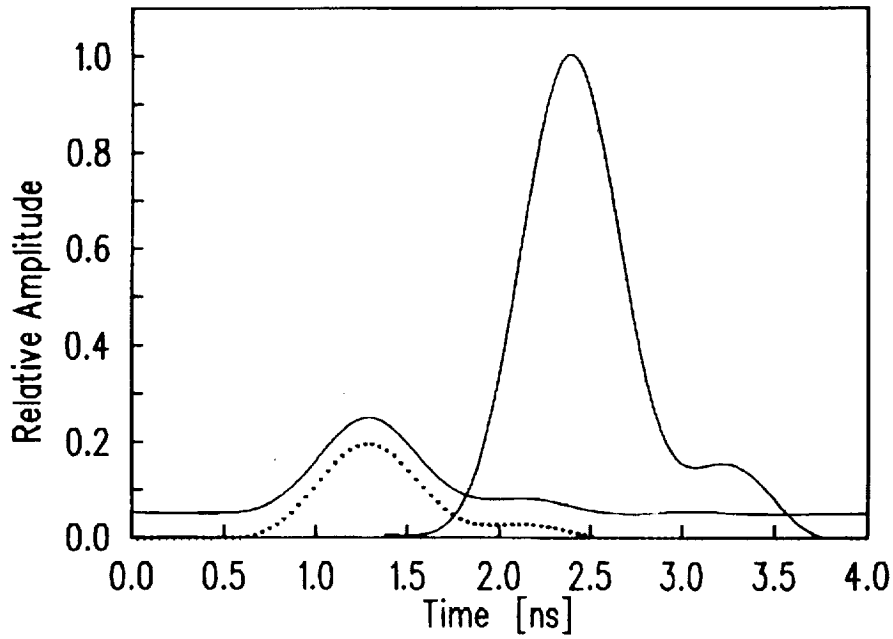

Fig.7 Pulse waveforms at the comparator inputs in the CFT, coming from a 12μm channel MCP (Hamamatsu R1564U), amplified by a HP 8447F fast amplifier. The attenuation is k=0.2, as usual in available CFTs. The delay is T_D=1.1ns, corresponding to minimal external cable length. Actual CFT operation is illustrated by the attenuated pulse with baseline offset (full line); the ideal CFT case is represented by dotted-line waveform.

The intercrossing slope g'_i is a function of the crossing time t_c and cannot be approximated by a constant in eq.s 11 and 12. The transformation from q(x) to $w(t_s)$ is no more linear and a significantly wider $w(t_s)$ results. The situation is particularly bad

when the crossing occurs at the onset of the delayed pulse leading edge, where the rise is slower and the intercrossing slope is correspondingly low. Such a situation can be avoided by making the delay T_D shorter than the duration of the input pulse. In commercial CFT circuits, T_D is mainly determined by the propagation time in a coaxial cable, externally connected to the circuit module and selected by the user. The least obtainable value of T_D is about 1.1ns or slightly less [15], determined by the connectors, the circuit layout and the minimal length possible for the external cable. This was adequate for the pulses of ordinary PMTs, lasting a few nanoseconds, but it is no more sufficient for the subnanosecond pulses of ultrafast MCPs. As illustrated in Fig.7, with T_D=1.1ns the crossing occurs just in the low slope zone of the rising waveform. The operation only roughly approximates the ideal CFT; in fact, it is intermediate between a CFT and a leading edge trigger with small, constant threshold.

Such a situation can be avoided by a suitable selection of parameters in the experiment. The analysis points out the basic criteria for minimizing the time walk effect:

i) the preamplifier gain should be high enough to keep low the value of the upper limit x_H in all cases, even when a small value of the lower threshold A_L is selected for accepting almost all pulses, e.g. 90%of the amplitude distribution p(A).

ii) the delay T_D and attenuation k should be selected for maximizing the intercrossing slope.

The latter criterion is usually not satisfied by industrially produced CFT models. Beside having too long minimum delay, they are normally set to low constant fraction values, around 0.2, which are optimal for timing signals from scintillation detectors of ionizing radiations, but not for timing single photons [10,14]. This is due to historical reasons, since CFTs were originally developed for working with ionizing radiation detectors

A detailed quantitative analysis of the CFT time-walk effect in the conditions of actual experiments can be carried out by means of computer simulation, taking accurately into account the actual shape of the signal waveform processed by the amplifier. It is worth noting that the result of the computation of the crossing time t_c versus normalized baseline offset x can be easily foreseen, by linearly shifting upwards the attenuated waveform in figures like Fig.7 and directly observing the walk of the crossing point. In the following, in order to set in evidence the effects on the time resolution, all the time distribution curves are drawn aligned at the peak value. All FWHM values reported are measured on the complete computed curve $r_m(t)$. In fact, since the shape of the distribution $w(t_s)$ is asymmetrical and far from gaussian, the FWHM value of $r_m(t)$ would be remarkably underestimated by a quadratic composition of the FWHM values of $w(t_s)$ and $r_i(t)$.

Previously published experimental results were analyzed and improvements obtainable by modifying the CFT parameters and/or the pulse shape were evaluated [10]. We first considered cases where a 12micron channel MCP Hamamatsu R1564U is employed with a fast amplifier model HP8447F. The amplitude distribution and signal waveform are reported from Yamazaki et al. [1] and from the manufacturer data sheets

and technical notes [16]. On the basis of published results [1-3] the intrinsic time distribution $r_i(t)$, due to the detector is assumed to be gaussian with 40ps FWHM.

We studied the effect of a filtering stage with a 1ns integrating time constant, interposed between fast amplifier and CFT as proposed and experimented in our laboratory [9]. The wider pulse obtained by filtering makes possible to obtain a higher intercrossing slope with the minimum delay of 1.3ns available in our set up. The computer analysis gives results in perfect agreement with the experiment, confirming that the improvement of the FWHM from 75ps to 55ps was obtained thanks to the reduction of the time walk effect.

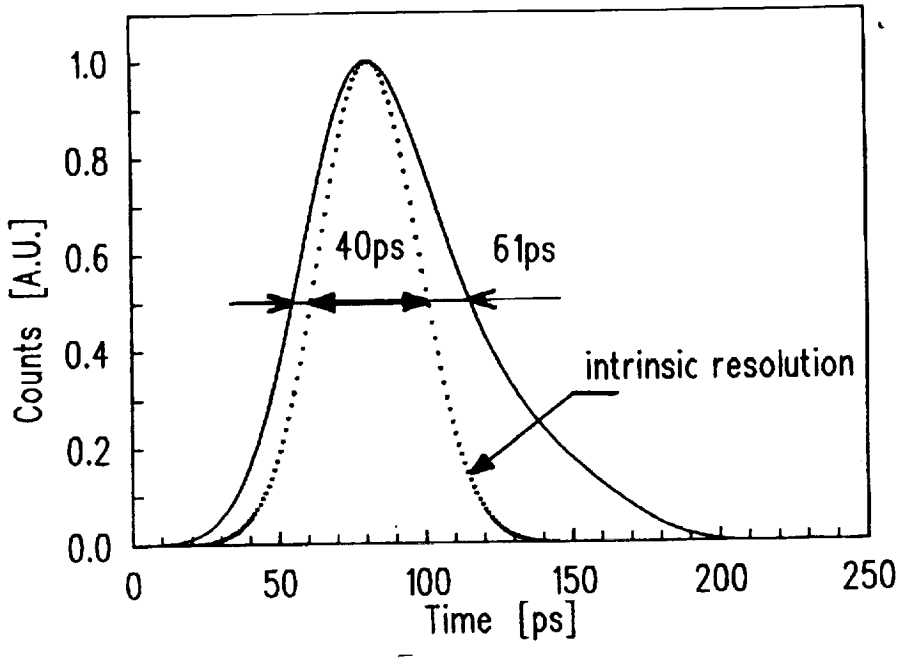

Fig.8 Computed time resolution curve for measurement with low selecting threshold level (accepting almost all pulses), compared to the intrinsic time resolution curve (dotted curve) of a 12 μm channel MCP (Hamamatsu R1564U). The computed FWHM is 61ps; the experimental value in Ref.1 is 63ps.

We analyzed then the experiments reported by Yamazaki et al. [1], where the resolution was measured with two different levels of the auxiliary lower threshold A_L of the CFT, which selects pulses accepted for the time measurement. With low threshold, accepting almost all pulses, they measured 63ps FWHM; the computed value for T_D=1.1ns and k=0.2 was 61ps, as illustrated in Fig.8. The computation also confirmed that with high threshold, accepting only 15% of the pulses, the FWHM suffers negligible degradation with respect to the intrinsic value. For the experiments with low threshold level, we also evaluated the improvement obtainable by reducing the pulse delay T_D and/or the attenuation ratio k, in order to increase the intercrossing slope. It is not difficult to reduce the delay T_D in existing CFTs, without needing to redesign and fabricate new CFT models. The available models can be modified by cutting lines in the printed circuit board and making new internal connections for a shorter delay path, that avoids the external delay cable. By modifying the resistor network that attenuates the prompt waveform (see Fig.6), one can also change the k to higher values. In order to attain k=1, however, major modifications or complete redesigning of the CFT circuit

may be necessary. The results obtained by changing the delay to T_D=0.6ns and/or the attenuation range to k=1 are summarized in Table 1.

We can conclude that with the 12 micron-channel MCP Hamamatsu R1564U it is fairly simple to reduce the time-walk effect to a tolerable or even negligible contribution.

Table 1 FWHM time resolution values obtained in the computer simulation of measurements with Hamamatsu R1564U (intrinsic FWHM resolution 40ps) and CFT circuit with low selecting threshold level (see Fig.8) and different values of the delay T_D and attenuation k.

k	0.2	0.2	1	1
T_D	1.1ns	0.6ns	1.1ns	0.6ns
FWHM	61ps	49ps	50ps	42ps

It is not strictly necessary to design new CFT models, since employing simple auxiliary circuits or making fairly simple modifications to available CFT circuits can be sufficient to the purpose. By employing a simple filter-amplifier to increase the width of the pulse fed to the CFT, without modifying the CFT circuit, the resolution widening can be reduced to less than 40%. By modifying the CFT to reduce the delay, the widening is limited to 22%. If, further to reducing the delay, the attenuation is eliminated (k=1), the widening drops to 5%. It is interesting to note that some older ZCT circuits may therefore be more suitable to single-photon timing than modern CFTs.

We may also note that the results of this analysis suggest how to select a suitable fast amplifier among a set of available models with a given value of the gain-bandwidth product, with criteria in agreement with the conclusions drawn from the analysis of the contribution of the electronic circuit noise to the time jitter. It is clearly better to select a model with moderate bandwidth (1GHz or less) and higher gain, rather than faster models with lower gain. The task of avoiding significant time-walk effect in the resolution becomes tougher with the latest and fastest MCP detectors, having 20ps or better FWHM intrinsic time resolution, such as the 6micron channel MCP model Hamamatsu R2809U. Data for the analysis of this case were obtained from Ref.3 and from the manufacturer data sheet and technical notes [16]. The intrinsic resolution curve $r_i(t)$ is assumed to be gaussian with 20ps FWHM. Since model HP8447F amplifier is very well suited also to this case [8] from the standpoint of the time jitter due to circuit noise, we analyzed set-ups employing such a fast amplifier. Fig.9 illustrates the effect of employing a shorter delay T_D in the CFT. Table 2 summarizes the improvements obtainable with modifications to the CFT circuit.

Table 2. FWHM time resolution values obtained in the computer simulation of measurements with Hamamatsu R2809U (intrinsic FWHM resolution 20ps) and CFT circuit with pulse selecting threshold level set at low level to accept almost all pulses and different values of delay T_D and attenuation k.

k	0.2	0.2	1
T_D	1.1ns	0.6ns	0.6ns
FWHM	50ps	29ps	24ps

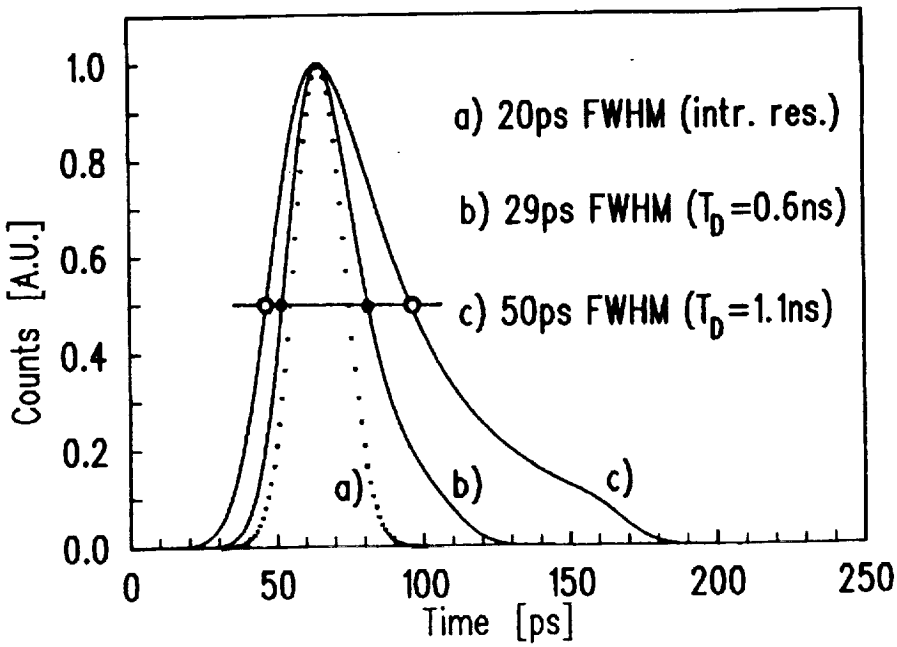

Fig.9 Computed time resolution curves, including effects of amplitude dependent time walk in CFT, for measurement set-ups with MCP model R2809U, fast amplifier HP8447F, CFT pulse selecting threshold set at low level to accept almost all pulses. The dotted curve is the assumed intrinsic resolution curve, having 20ps FWHM. Two cases are reported: a) CFT with the usual attenuation k=0.2 and delay corresponding to minimal external cable T_D=1.1ns (wider curve, 50ps FWHM); b) CFT with k=0.2, but with shorter delay T_D=0.6ns (narrower curve, 29ps FWHM).

It is interesting to compare these results to the corresponding ones for the case of the 12micron channel model R1564U. Essentially, the time walk in the corresponding situations is quite similar in the two cases, but its relative effect on the obtainable performance becomes greater as the intrinsic detector is improved. For the R2809U the actual resolution with the short delay of 0.6ns is remarkable, but 45% wider than the intrinsic one. With delay 0.6ns and no attenuation (k=1) the obtainable resolution is still 20% wider than the intrinsic. Some experimental results point out that the detector intrinsic resolution may be even better than 20ps, possibly 10ps or better.The time walk effect should therefore be considered a major limitation to the ultimate obtainable resolution.

We conclude that there is considerable margin for further improvement. Greater care should be therefore devoted to the electronic pulse processing, in order to take full advantage of the detector intrinsic resolution. It is advisable to work with CFT having k=1 and even shorter delay, possibly with specially studied filter-amplifier input stage. Designing new CFT circuits specially devised for photon counting may be rewarding.

IV. ACTIVE-QUENCHING CIRCUITS FOR SPADs

In early studies on SPADs, the bias arrangement used for the device operation was the so-called *passive quenching* circuit (PQC) [4,5,11]. This circuit employs a high load resistor (in the 100k range) in order to force the diode voltage V to drop down near to the breakdown voltage V_B after each avalanche triggering. This quenches the avalanche. The diode voltage is then slowly restored to the bias voltage, since the diode capacitance is recharged by the small current flowing through the high value resistor. The voltage recovery takes at least some microseconds. A photon can arrive during the recovery from a previous avalanche pulse and trigger the avalanche when the SPAD voltage is at some intermediate level, randomly placed between the breakdown voltage and the correct bias voltage. This has a twofold detrimental effect on the timing performance. First, the intrinsic time resolution of SPADs is strongly reduced as the excess bias voltage $V-V_B$ actually applied to the diode is reduced. Second, at lower excess bias voltage the avalanche current pulse not only has smaller amplitude, but also slower risetime. This causes a walk of the triggering time of the following timing circuit, which is not properly corrected even employing a CFT (CFTs require constant pulse shape to work properly). The intrinsic performance of SPADs can be exploited working with PQCs only in cases where the probability of such events (photons arriving during a recovery from a previous avalanche pulse) is very low, that is, where the rate of repetition of pulses is very low, at best a few kHz. Note that this limitation applies to the total rate of pulses, that is, to the sum of the dark count rate of the SPAD plus the detected photon rate, including unwanted background light.

A partial remedy to such limitations is to apply a pulsed bias voltage to simple passive circuit arrangements, for obtaining a gated operation of SPADs. The additional voltage pulse can be superimposed to the dc bias either by ac coupling or by dc coupling. The ac coupling is very simply implemented, by connecting the junction between SPAD and load resistor to a low-impedance fast pulse generator through a suitable capacitor. The dc coupled gate is obtained by employing a smaller load resistor, typically 1kOhm or less, and applying directly to it the sum of the dc bias voltage plus a pulsed additional voltage. The detailed analysis [18] of such circuit arrangements, however, points out that i) it is possible to detect not more than one photon in the gate interval ii) other specific limitations are associated to each circuit arrangement. With ac coupling, the repetition rate of gating pulses must be low. With dc coupling, the power dissipated in the SPAD may become excessive. In summary, it can be concluded that pulsed-bias passive circuits are of practical interest only for working with gate intervals having short duration, typically below 100ns, and low or moderate repetition rate.

In the early stage of development of SPADs, it became therefore clear that more sophisticated circuits were necessary, in order to fully exploit the device performance. Active quenching circuits (AQCs) were thus conceived and developed in our laboratory [6,12,13]. Essentially, the AQC performs the following operations.

i) It senses the onset of the avalanche current.

ii) It generates an output pulse, synchronous with the avalanche, with the least possible jitter.

iii) It forces the bias voltage of the diode to drop as swiftly as possible below the breakdown voltage. It must therefore have a low-impedance output driver, capable of driving efficiently the capacitance associated to SPADs and connections.

iv) Finally, it restores the initial bias after a well-controlled hold-off time, so that the diode is again ready to detect a subsequent photon. Also the reset transition must be as fast as possible, in order to reduce as far as possible the probability that a photon may arrive during the recovery of the diode voltage, with an associated degradation of the time resolution (see above).

Various problems are met for obtaining a correct AQC operation and severe requirements have to be fulfilled in order to fully exploit the available SPAD performance. A peculiar problem is caused by the large amplitude difference between the avalanche pulse generated by the SPAD and the much larger quenching pulses applied to it and reflected back at the circuit input. The AQC should be sensitive to avalanche pulses of less than 1mA (<50mV over 50), while quenching pulses have amplitude of several Volts (up to 50V in our circuits i.e. 1000 times higher than the avalanche pulse). Unless special precautions are taken in the circuit design, the AQC can be retriggered by the quenching pulse and either be latched in the triggered state or break into a self-sustaining oscillation. Another important requirement is to keep as short as possible the time from the avalanche onset to its quenching. The reason for this is twofold. First, it minimizes afterpulsing effects due to deep levels in the diode junction, acting as charge carrier traps. The charge trapped in deep levels is indeed proportional to the total avalanche charge flowing through the junction. Second, with high voltage devices, the power dissipated in the avalanching state can be fairly high and produce a remarkable variation of the device temperature, with associated variation of the breakdown voltage and of other device parameters. On the other hand, minimizing the delay between the onset of the avalanche and the arrival of the quenching voltage pulse to the SPAD is sometimes conflicting with the requirement of operating the SPAD remote from the AQC, as necessary, for instance, in order to operate a SPAD with cryogenic cooling. For a remotely operated diode, the duration of the avalanche current is inherently increased by twice the transit time in the connecting cables; that is, by 10ns per meter of connecting coaxial cable. The hold-off time must have accurately controlled duration, in order to have a well defined and controlled deadtime (avalanche time plus hold-off time). The actual value of the hold-off time can be very short, a few tens of nanoseconds or less, in cases where photons have to be counted at high rate, up to 10 MHz or more. However, in cases where photon arrival times must be accurately measured and the dark count rate must be minimized, somewhat longer hold-off time have to be employed, typically a few hundred nanoseconds, in order to avoid SPAD retriggering due to the delayed release of trapped carriers. For SPAD devices working with high excess bias voltage $V-V_B$, the quenching pulse must have large amplitude, up to 50V and possibly more, so that the transition times are limited by the slew rate attained by the quenching driver. Finally, in order to exploit the time resolution of the fastest SPADs, the jitter between the avalanche onset and the output pulse should be much lower than the intrinsic resolution of the detector, that is, it must be limited to a few picoseconds. This means that the input stage of the circuit should be designed for minimum noise. Obviously, it is not possible to fulfil at best all these requirements at the same time. Different AQC parameter setting, or even different AQC models are therefore employed for optimizing the most important performance in different cases. In our laboratory, various generations of AQC have been developed, starting in 1975 from the earliest simple model [17] and progressively increasing the performance by a steady evolution of the design [4,6,12,13,18]. Such evolution has produced an AQC design that provides remarkable flexibility for different applications and can work a SPAD in remote position (connected

by a coaxial cable) exploiting at best the device performance. With a minimum-noise input stage, the circuit has intrinsic timing jitter well below 10ps FWHM; it can work at more than 10MHz repetition rate and, with suitably designed output quenching driver, it can provide a 50V quenching pulse.

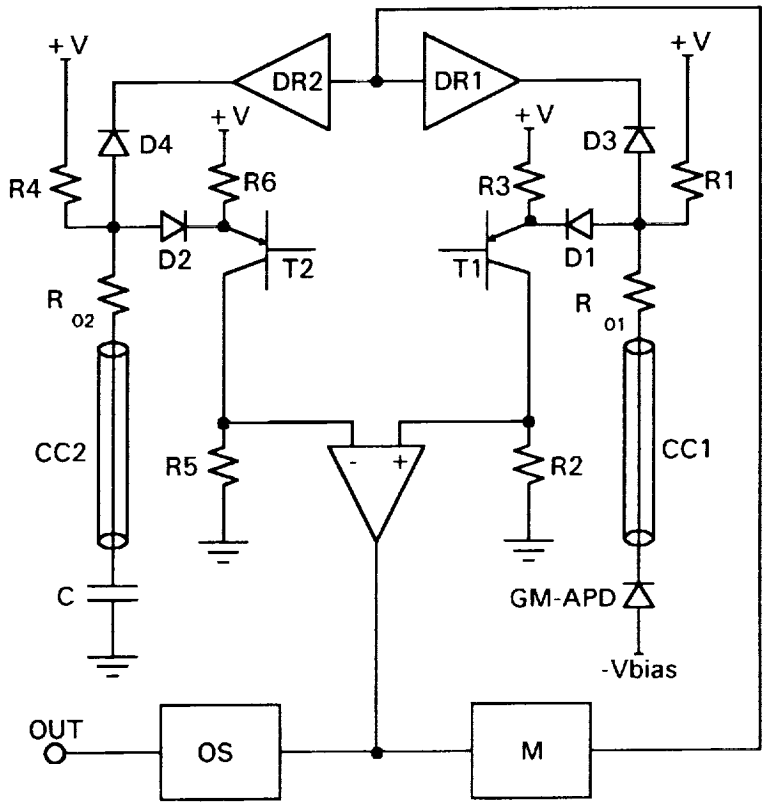

Fig.10 Simplified block diagram of the most recent AQC generation, described in the text. Note the symmetry of the circuit.

The circuit design approach, covered by international patents [13], will be here illustrated making reference to the simplified circuit diagram in Fig.7. The figure illustrates the high degree of symmetry of the circuit. Thanks to this symmetry, the fast comparator can have a low threshold level, as required to sense the avalanche pulse, and at the same time be insensitive to the quenching pulse, avoiding spurious retriggering (see above). The avalanche pulse is applied asymmetrically (only to the non-inverting terminal of the comparator): it is therefore a differential-mode signal that triggers the comparator. The quenching voltage pulse is symmetrically applied (to both input terminals of the comparator), so that it is a common mode signal and does not trigger the comparator. In order to obtain this, the symmetry should be maintained also in the voltage transients, including reflections, overshoots or ringing caused by the load connected to each circuit input. It is therefore necessary to connect to the non-inverting input of the AQC a passive load, in order to match that given by the SPAD, connected to the other input. This normally means a simple capacitor C, with capacitance value equal to that of the SPAD (a trimmer capacitor of a few pF is normally employed). In case of remote SPAD operation, care must be taken of maintaining the

symmetry by connecting with coaxial cables (CC1 and CC2) having equal length the SPAD and the matched load. The cables are terminated at the circuit inputs through the resistors R01 and R02. The avalanche signal flows through the diode D1 and the common-base transistor T1, reaching the comparator input. The role of T1 is twofold. First it establishes a low impedance input, to which the cable-matching resistor R01 is connected. Second, it provides amplification of the voltage signal fed to the comparator, which is important for minimizing the intrinsic time-jitter of the circuit, due to its electronic noise. In stationary conditions, diodes D1 (and D2) is conducting, diodes D3 (and D4) is instead not conducting. When an avalanche is triggered, the current is sensed by the comparator, whose output changes state. This signal triggers a monostable multivibrator, M, that sets the duration of the quenching pulse. In order to obtain the desired amplitude of the quenching signal, a suitable voltage driver stage, DR, is employed. When the quenching voltage pulse is applied by DR, the voltage through D3 becomes direct, the diode conducts and the quenching pulse reaches the photodiode. At the same time the diode D1 is driven to reverse bias condition and prevents the high voltage pulse (up to 50V) from reaching T1. If diode D1 were not present, the entire quenching pulse would be applied to the base-emitter junction of T1, causing it to break down. Another important effect of the two diodes is to break the positive feedback loop of the circuit, thus reducing the risk of oscillations. The AQC output pulse is derived from the comparator, through an output stage OS.

By employing this kind of AQCs, the timing performance of SPADs has been verified down to 20ps FWHM [5]. The flexibility and performance of the circuit have been extensively tested in many different experiments, carried out in a wide variety of conditions, with SPAD working either embedded in the circuit or remote from it and operating in different ambients over a wide range of device temperatures, including cryogenic cooling.

ACKNOWLEDGMENTS

Work supported in part by ASI (Italian Space Agency), CNR (Italian National Research Council) and MURST (Italian Ministry of University and Research). The author wish to thank N.Carbone and S.Masci for their technical support in the development of Active Quenching Circuits.

REFERENCES

1 I.Yamazaki, M.Tamai, H.Kume, H.Tsuchiya and K.Oba, Rev. Sci. Instrum **56**, 1187 (1985).

2 D.Bebelaar, Rev.Sci.Instrum. **57**, 1116 (1986).

3 H.Kume, K.Koyama, K.Nakatsugawa, S.Suzuki, and D.Fatlowitz, Appl. Opt. **27**, 1170 (1988).

4 S.Cova, G.Ripamonti and A.Lacaita, Nucl. Instrum. Methods **A253**, 482 (1987).

5 S.Cova, A.Lacaita, M.Ghioni, G.Ripamonti, T.A.Louis, Rev. Sci. Instrum. **60**, 1104 (1989).

6 S.Cova, A.Longoni, and A.Andreoni, Rev. Sci. Instrum. **52**, 408 (1981).

7 A.Lacaita, S.Cova, M.Ghioni, Rev. Sci. Instrum. **59**, 1115 (1988).

8 S.Cova, M.Ghioni, and F.Zappa, Rev. Sci. Instrum. **62**, 2596 (1991).

9 S.Cova and G.Ripamonti, Rev. Sci. Instrum. **61**, 1072 (1990).

10 S.Cova, M.Ghioni, F.Zappa, and A.Lacaita, Rev. Sci. Instrum. to be published.

11 R.H.Haitz, J. Appl. Phys. **35**, 1370 (1964); **36**, 3123 (1965).

12 S.Cova, A.Longoni, and G.Ripamonti, IEEE Trans. Nucl. Sci. **NS-29**, 599 (1982).

13 S.Cova, US.Patent #4,963,727, Italian patent 22367A/88. Industrial licence to SILENA S.p.A. Milano (Italy).

14 P.W.Nicholson, *Nuclear Electronics* p. 259 (J.Wiley, NewYork, 1974).

15 See e.g. Instruction Manual of ORTEC Mod.583 or Tennelec Mod.454.

16 Hamamatsu Photonics K.K., Hamamatsu City, Japan, and Hamamatsu Corp., Bridgewater, N.J. U.S.A., MCP-PMTs data sheets and Technical Informations No. ET-03/Oct.1987.

17 P.Antognetti, S.Cova and A.Longoni, Proc. Ispra Nucl. Electron. Symp. 1975, Euratom Publication **EUR 537e**, 453 (1975)

18 S.Cova et al. Rev. Sci. Instrum. to be published

N94-15570

Tracking capabilities of SPADs for laser ranging

F. Zappa, G. Ripamonti+, A. Lacaita*, S. Cova*, and C. Samori**

* Politecnico di Milano, Dipartimento di Elettronica and CEQSE-CNR,
Piazza L.da Vinci, 32 - 20133 Milano (Italy)

+ Università degli Studi di Milano, Dipartimento di Fisica,
Via Celoria, 16 - 20133 Milano (Italy)

ABSTRACT

The spatial sensitivity of Single-Photon Avalanche Diodes (SPADs) can be exploited in laser ranging measurements to finely tune the laser spot in the center of the detector sensitive area. We report the performance of a SPAD with 100μm diameter. It features a time resolution better than 80ps rms when operated 4V above V_b at -30C, and a spatial sensitivity better than 20μm to radial displacements of the laser spot. New SPAD structures with auxiliary delay detectors are proposed. These improved devices could allow a two dimensional sensitivity, that could be employed for the design of pointing servos.

I. INTRODUCTION

Due to their high quantum efficiency and picosecond time resolution, Single-Photon Avalanche Diodes (SPADs) are gaining acceptance as detectors for laser ranging experiments. In SPADs the onset of the avalanche current, triggered by a photogenerated carrier, marks the photon arrival time. We have recently demonstrated that not only the timing information, but also the position of the photon absorption can be extracted from the avalanche current rising edge, by exploiting the physical mechanisms involved in the device operation [1]. Measurements previously performed on a position-sensitive SPAD with 14μmx140μm rectangular sensitive area showed that these structures are capable of time resolution better than 30ps rms and spatial resolution better than 5μm rms [1].

In this paper we suggest to exploit the position-sensitive capability of SPADs to keep the echo signal from the satellite always in the center of the detector sensitive area. First, we briefly recall the operation of these novel detectors. Then, we discuss the performance of a circular device (100μm diameter) large enough to make possible the first alignment of the telescope and the subsequent tracking of the satellite. Auxiliary electrodes could be used to obtain position sensitive detectors with angular measurement capability.

II. OPERATION OF SPAD POSITION SENSITIVE DETECTORS

Recently, the avalanche dynamics in silicon SPADs has been investigated; high performance detectors have been designed and fabricated [2-4]. To the purpose of our discussion, here we briefly recall the basic operation of SPADs with a depletion layer only a few microns thick [5]. The avalanche photodiode is operated biased above the breakdown voltage, V_b, but no current flows until the first carrier triggers the avalanche in a seed point. Then, the free carrier concentration swiftly rises by impact ionization around the seed point and, in a few tens of picoseconds, the free carrier space charge lowers the local multiplication rate to a self-sustaining level. The carrier density around the seed point cannot increase further, unless the avalanche is triggered in the surroundings by lateral diffusion of avalanching carriers. As the activated area increases, the diode current rises. At the end, when the multiplication process occurs over the whole active area, the avalanche current reaches the final steady state value given by the ratio of the excess bias above V_b and the diode series resistance.

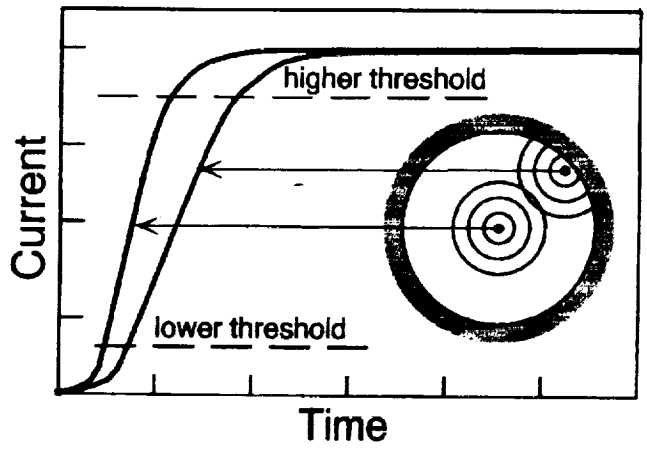

Fig. 1 Avalanche dynamics in a circular device: the curves qualitatively show the dependence of the current rise on the point where the avalanche is triggered. The circle schematically represents the sensitive area of the detector with spreading avalanches. The delay between the crossing times of the two thresholds is proportional to the current rise-time.

The pulse crossing of a discriminator threshold gives the timing information. However, this peculiar dynamics causes the avalanche pulse leading edge to depend on the position where the avalanche is triggered. Fig.1 schematically shows the rise of the diode current in a circular device. The closer is the seed point to the center, the faster is the activation of the whole sensitive area. Therefore, the current leading edge becomes steeper as the seed point moves from the periphery to the detector center. This effect sets a limit to the timing performance of the detector [2,3], but it can also be exploited to get the position

information: the shape of the avalanche leading edge carries the spatial information on the point where the photon was absorbed [1].

III. EXPERIMENTAL DATA

Fig.2 shows the cross section of the tested devices. The avalanching region is the n^+p^+ junction: the depleted region is about 1μm thick. The electric field at the edge is tailored by the n^+p junction with the epilayer. A complete discussion of the structure is carried out in Ref.6. The detector has a 100μm diameter and a V_b of 14.3V.

The rise time of the avalanche current pulses was accurately measured by an Active Quenching (AQ) circuit [7] with two discriminators having different thresholds. The purposes of the AQ circuit are: i) to sense the onset of the avalanche current; ii) to lower the bias of the photodiode below the breakdown voltage, thus quenching the avalanche; and iii) to rapidly restore the bias after a suitable dead time to enable the detection of another photon. The first discriminator is set to sense the avalanche when the current is still low (0.4mA), while the second is triggered when the avalanche is almost saturated. The delay between the output pulses of the discriminators gives the rise time of the avalanche pulse.

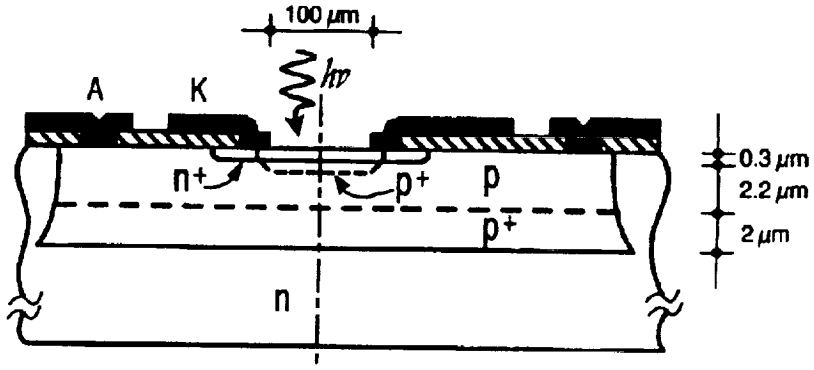

Fig.2 Cross section of the double epitaxial devices tested in the experiments. The active n^+p^+ junction is built in a 10 Ωcm p epistrate. The buried p^+epilayer is 0.3 Ωcm.

In order to reduce the dark count rate, the detector was cooled by a Peltier stage at -30C and operated in gated mode: in stand-by the diode was reverse biased below V_b, and a waveform generator provided pulses at 10 kHz, raising the bias 4V above V_b for 500ns. A 850nm laser diode synchronously emitted a 20ps rms optical pulse, focused to a 10μm spot with a microscope. A Time to Pulse Height Converter measured the delay between the triggering times of the two discriminators. A histogram of the measurements was collected with a MultiChannel Analyzer.

We carried out various measurements by changing the radial position of the light spot. Fig.3 shows the histograms of the delay between the threshold crossing times. The peak shifts 130ps when the laser spot moves from the center to the edge of the detector. The

inset of Fig.3 shows the complete dependence of the peak shift on the spot position. As the laser spot shifts more than 20μm from the device center, the histogram peak moves considerably and a suitable feedback system can react to restore the original centered position.

The time resolution of the device was measured just by recording the delay between the laser shot and the crossing time of the low threshold discriminator. The observed resolution changed somewhat with focusing and with the position of the spot. With the light focused to a 10μm spot size in the center of the sensitive area, the time resolution was 80ps rms.

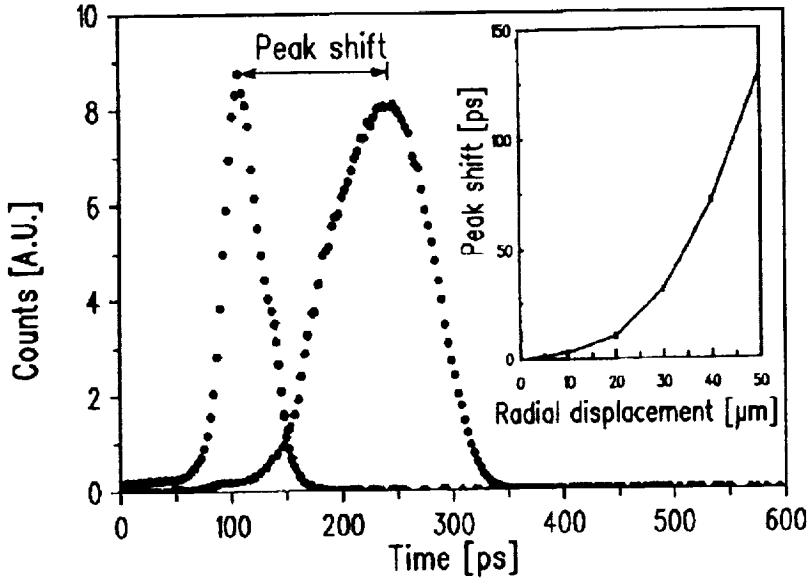

Fig.3 Avalanche pulse rise-time, measured as the delay between the crossing times of the low and the high thresholds of Fig.1. The two histograms correspond to the measurements performed by focusing the laser spot in the center (first histogram to the left) and at the edge of the detector of Fig.2 (histogram to the right). The peak shifts 130ps when the laser spot moves to the periphery of the detector. The inset shows the complete dependence of the peak shift on the spot position.

It is worth noting that photons absorbed at the same distance from the device center generate avalanche pulses with the same risetime. Therefore, these devices cannot give the information on how to operate in order to position the light spot in the detector center, in a single measurement. A trial and error method should be adopted to keep centered the echo light signal.

Fig.4 describes a possible improvement of the technique in order to achieve a complete angular sensitivity. Four SPAD sensors are placed along two perpendicular axes of the main detector, close enough to its boundary to be triggered when the avalanche reaches the corresponding edge. Since the avalanche spreads evenly from the seed point, by measuring the time delay between the current pulses of the sensors one can get the position of the laser

spot over the main sensitive area. Pointing servos could be implemented to correct for misalignement, thus keeping the laser spot always in the center of the main photodetector. It is worth noting that the design of such a device is expected to be critical in the coupling between the delay detectors and the central SPAD. Projects are under way in our laboratories to study suitable stuctures and the most effective coupling arrangements.

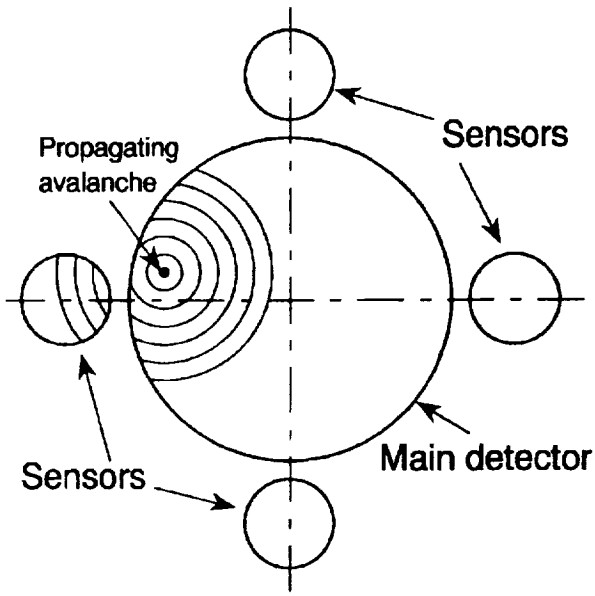

Fig.4 Proposed improvement of the position sensitive detector in order to achieve a complete angular sensitivity. Four SPADs can sense when the avalanche reaches the edge of the central device. By measuring the time delay between the current pulses of the sensors, one can obtain the position of the laser spot over the main sensitive area.

IV. CONCLUSIONS

A position-sensitive single-photon detector with 100μm diameter has been demonstrated. It features a time resolution better than 80ps rms when operated 4V above V_b at -30C, and a spatial sensitivity better than 20μm to radial displacements of the laser spot. The detector provides a continuous sensitive area, free from dead zones, and can be exploited in laser ranging measurements to keep the laser signal always centered into the sensitive area. We have also proposed a more complex SPAD structure, where the introduction of auxiliary delay detectors could allow a complete angular sensitivity of the device. These structures are investigated to overcome the trial and errors method used in pointing with simple position-sensitive SPADs.

ACKNOWLEDGEMENTS

Work supported in part by ASI (Italian Space Agency), CNR (Italian National Research Council) and MURST (Italian Ministry of University and Research). The authors wish to thank ST-Microelectronics for the fabrication of the samples, and S. Masci for his technical support.

REFERENCES

1. G. Ripamonti, M. Ghioni, S. Cova, and M. Mastrapasqua, *IEEE Electron Device Lett.* **EDL-13**, 35 (1992).

2. A. Lacaita, M. Mastrapasqua, M. Ghioni, and S. Vanoli, *Appl. Phys. Lett.* **57**, 489 (1990).

3. A. Lacaita and M. Mastrapasqua, *Electron. Lett.* **26**, 2053 (1990).

4. A. Lacaita, F. Zappa, S. Cova, G. Ripamonti, and A. Spinelli,: *8th International Workshop on Laser Ranging Instrumentation.* Annapolis, MD, May 18-22, 1992

5. S. Cova, A. Lacaita, M. Ghioni, G. Ripamonti, and T.A. Louis, *Rev. Svi. Instrum.* **60**, 1104 (1989).

6. A. Lacaita, M. Ghioni, and S. Cova, *Electron. Lett.* **25**, 841 (1989).

7. S. Cova, A. Longoni, and G. Ripamonti, *IEEE Trans. Nucl. Sci.* **NS-29**, 599 (1982).

N94-15571

How to squeeze high quantum efficiency and high time resolution out of a SPAD

A. Lacaita, F. Zappa*, S. Cova*, G. Ripamonti+ and A. Spinelli**

* Politecnico di Milano, Dipartimento di Elettronica and CEQSE - CNR,
Piazza L. da Vinci, 32 - 20133 Milano (Italy)

+Università degli Studi di Milano, Dipartimento di Fisica,
Via Celoria, 16 - 20133 Milano (Italy)

ABSTRACT

We address the issue whether Single-Photon Avalanche Diodes (SPADs) can be suitably designed to achieve a trade-off between quantum efficiency and time resolution performance. We briefly recall the physical mechanisms setting the time resolution of avalanche photodiodes operated in single-photon counting, and we give some criteria for the design of SPADs with a quantum efficiency better than 10% at 1064nm together with a time resolution below 50ps rms.

I. INTRODUCTION

Solid state photodetectors nowadays employed in laser ranging applications fall into two categories: reach-through avalanche photodiodes (APDs) with a depletion layer about $30 \div 200\mu$m thick [1-3], and shallow junction APDs with a depletion layer about 1μm thick [4-6]. The former are commercially available devices designed for low noise operation in optical communications, while the latter, called Single-Photon Avalanche Diodes (SPADs), are specifically designed for timing applications.

In laser ranging measurements reach-through APDs show several advantages over ordinary Photomultiplier Tubes (PMTs): i) At the operative bias the photodiode is fully depleted and the depletion layer, tens of microns thick, leads to a quantum efficiency higher than 30% at the Nd-YAG emission wavelength. ii) A time resolution of 150ps rms has been demonstrated with RCA C30902S: this value favourably compares with the timing performance of PMTs [7]. iii) The sensitive area diameter (500μm or more) is large

enough to make possible the alignment of the telescope and the subsequent tracking of the satellite.

Indeed, high performance SPADs can attain much better time resolution (8ps rms) [4]. However, these devices have a quantum efficiency lower than 1% at 1064nm and their small active area (5μm diameter) makes impossible their use in laser ranging measurements.

In this paper we address the issue whether a silicon SPAD can be suitably designed to achieve a trade-off between quantum efficiency and time resolution performance. We briefly recall the physical mechanisms setting the time resolution of APDs operated in single-photon counting. We discuss how the performance depends on the device geometry and the junction electric field profile. We give some criteria for the design of SPADs with a quantum efficiency higher than 10% at 1064nm and a time resolution below 50ps rms. This combination of performance cannot be achieved with any commercially available single photon detector, both solid state and vacuum tube.

II. AVALANCHE PHYSICS AND TIME RESOLUTION

Single photon sensitivity is achieved with APDs operated biased above the junction breakdown voltage, V_b. At this bias a single photogenerated carrier can trigger a diverging avalanche process. The leading edge of the avalanche current marks the photon arrival time [1-6]. Any jitter in the delay between photon absorption and the crossing time of the discriminator threshold, impairs the precision in timing measurements [4-6].

The ultimate limit to the timing resolution of a SPAD comes from the thickness of the depletion layer. In fact, the distance between the point where the photon is absorbed and the junction leads to a statistical delay between the photon absorption time and the avalanche triggering. As a rule of thumb, if the photon absorption length, L_a, is longer than the depletion layer thickness, W, and carriers drift at the saturated velocity (v_s=10ps/μm) almost everywhere in the depleted region, the ultimate rms time jitter will be of the order of $W/(3.5v_s)$=2.9ps rms per each depleted micron. Since in silicon the absorption length, L_a, of a photon at 1064nm is 83μm, the choice of a 10μm depletion layer thickness guarantees a quantum efficiency higher than 10%, with an ultimate time resolution less than 30ps rms. Unfortunately, other mechanisms do not allow to reach this limit.

In the device operation the avalanche is triggered by photon absorption in a seed point, then it progressively spreads over the whole detector area. The leading edge of the diode current is affected by the spreading process. In SPADs, with thin depletion layer and small active volume, the avalanche spreads evenly from the seed point to the remaining detector area by transverse diffusion of avalanching carriers [5,6]. This mechanism makes the avalanche propagating with a transverse velocity given by [5]:

$$v_p = 2\sqrt{D/\tau} \tag{1}$$

where D is the average transverse diffusion coefficient of the carriers and τ is the time constant of the avalanche build-up, which increases by increasing the device bias.

Fig.1 helps in understanding how the avalanche spreading impairs the timing performance. In fact, the closer the seed point is to the center of the junction area, the faster is the activation of the whole device. Therefore, in the circular device shown in

Fig.1, the current leading edge becomes steeper as the seed point moves from the periphery to the center. Since a photon can be absorbed everywhere on the detector area, this effect causes a randomness in the pulse crossing of the timing threshold. It follows that the achievable time resolution is related to the difference, Δ, between the crossing times of the fastest and the slowest current pulses. This difference increases by increasing the sensitive area and/or decreasing v_p (i.e. the bias).

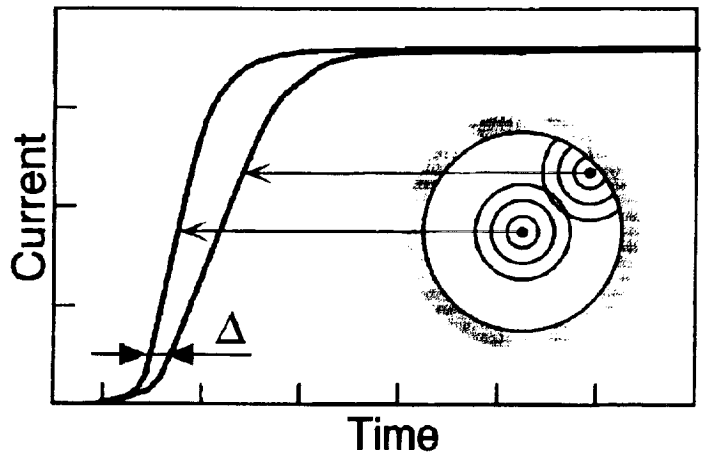

Fig.1 Avalanche dynamics in a circular device: the shift Δ between the crossing times of the fastest and the slowest leading edges sets the limit to the time resolution of the detector. The inset schematically shows the sensitive area of the detector with concentric circles representing the spreading avalanche.

As the detector volume increases, another phenomenon can play a role in the avalanche propagation. Secondary photons, emitted by hot carriers radiative relaxation processes in the avalanching region, can be absorbed in other regions, thus triggering the avalanche even there. Photons with absorption length of a few hundred microns are the most effective in sowing the avalanche. This latter process is dominant in APDs with large sensitive area and thick depletion layer [3].

We have developed a computer simulation of the avalanche dynamics. Fig.2 shows a comparison between the current leading edge of a RCA C30902S APD biased 40V above V_b at room temperature and the result of the computer program. It is worth noting that, due to the intrinsic randomness of the photon-assisted process, the timing performance of the device (170ps rms) is considerably worst than the ultimate limit set by the 30μm thick depletion layer. Moreover, the time dispersion increases by increasing the level of the timing threshold.

In order to reach a reasonable trade-off between quantum efficiency and time resolution, the impairing effects of the photon-assisted spreading have to be overcome. In principle this goal can be achieved in two ways: i) by adopting a timing threshold low enough to sense the avalanche current soon after the avalanche triggering and before the emission of

the first secondary photon; ii) by designing the detector structure so that the lateral carrier diffusion becomes the steering mechanism of the avalanche spreading. The design of fast and sensitive detector circuits is under way in our laboratories. In the next section, we will give some guide-lines on the design of high quantum efficiency SPADs with the avalanche propagation steered by transverse carrier diffusion.

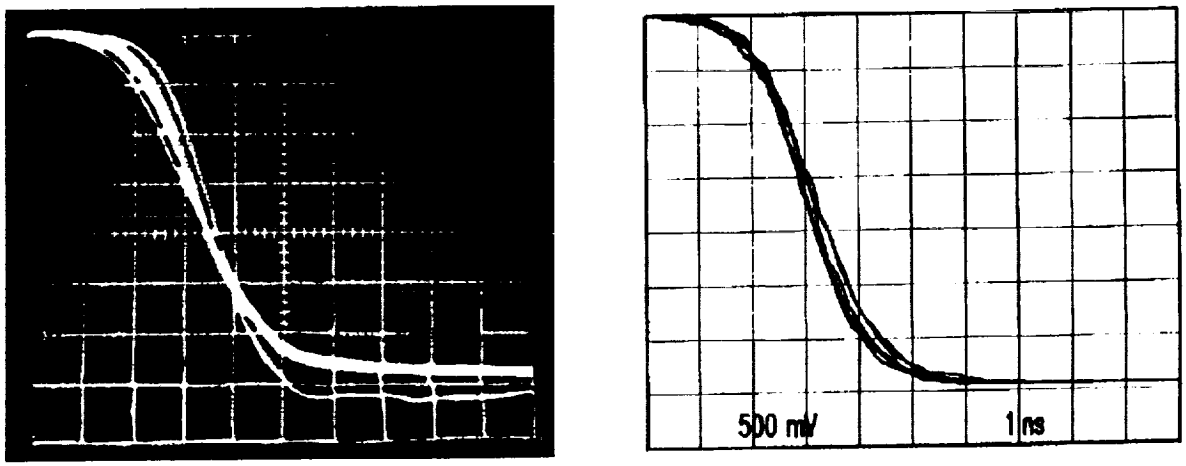

Fig.2 Comparison between the current leading edge of a RCA C30902S APD biased 40V above V_b at room temperature (left) and the result of the computer simulation of the avalanche dynamics (right).

III. DESIGN CRITERIA

In order to make it clear some fundamental design rules, let us compare the expected performance of two devices with 10% quantum efficiency at 1064nm. Therefore, both devices are supposed to have a 10μm depletion layer thickness. The inset of Fig.3 shows the electric field profile of the first device (D#1) at 169V, that is 34V above the estimated V_b=135V. The peak electric field is 3.3x10^{5}V/cm. The high field region is about 3μm thick and, in the remaining part of the depletion layer, the electric field (6x10^{4}V/cm) makes the carriers drifting at saturated velocity. The second device (D#2) has a similar electric field profile (inset of Fig.3) but a high field region only 0.3μm thick and an estimated V_b of 63V. Since the two devices have different V_b, we will compare their performance at the same relative excess bias $(V_0-V_b)/V_b$. Thus D#2 will be operated at 79V and the peak electric field will be 6x10^{5}V/cm.

Fig.3 shows the dependence on the device radius of both diffusion and photon assisted spreading velocities, as obtained from a computer simulation of the avalanche dynamics. The diffusion velocity was estimated from Eq.(1), while the photon assisted contribution was estimated by switching off the diffusion process in the simulation, and then computing the resulting ratio between the device radius and the current risetime. As expected, the role of the photon-assisted process increases by increasing the sensitive area radius; it becomes

eventually dominant in D#1 for a radius greater than 80μm. D#2 has a diffusion velocity more than three times larger and a photon assisted process less effective than in D#1.

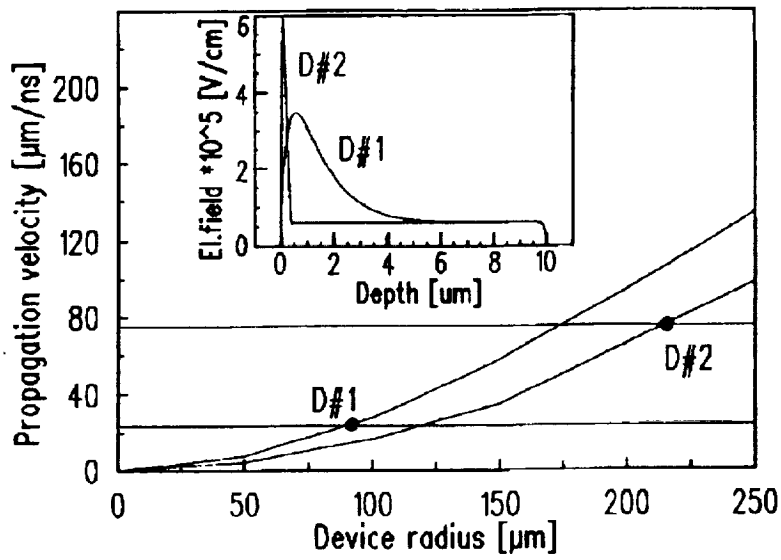

Fig.3 Dependence of the diffusion and the photon assisted spreading velocities on the device radius. as obtained from a computer simulation of the avalanche dynamics in two devices with a 10μm thick depletion layer. The inset shows the electric field profiles assumed in the calculations.

The higher diffusion velocity is due to the steeper electric field profile of D#2. In fact, the avalanche time constant, τ, is proportional to the carrier transit time in the high field region and is inversely proportional to the loop gain of the avalanche feedback process (i.e. the average number of impact ionization events experienced by a carrier crossing the junction). It can be shown that two junctions with similar electric field profile have the same avalanche loop gain when biased at the same relative excess bias. Therefore, in the present comparison, the devices are operated at the same loop gain, and the thinner high field region of D#2 results in a correspondingly shorter multiplication time constant, τ. From Eq.(1) it follows that D#2 is expected to have a faster diffusion-assisted avalanche propagation.

With regard to the difference in the photon-assisted process, it should be noted that D#2 is supposed to work at only 16V above V_b, while D#1 is operated at 34V excess voltage. Both of them have the same depletion layer thickness and therefore the same series resistance. It follows that, at the supposed operating conditions, the current flowing through D#2 is less than that of D#1. Since the photon emission rate is proportional to the current, the photon assisted propagation is less effective in D#2.

These results highlight that, by adopting a suitable steep electric field profile, the diffusion-assisted avalanche propagation can overcome the noisy photon-assisted process even in large area SPADs. We estimated the time resolution of a SPAD detector with 100μm diameter and the electric field profile of D#2 as follows. We computed the leading

edge of the avalanche pulses triggered at the center and at the edge of the detector, assuming that the avalanching area spreads evenly with a radial velocity of 75μm/ns. The time resolution is expected to be proportional to the difference, Δ, between the crossing times of the fastest and the slowest avalanche pulses. By using a timing threshold at 0.3mA, we forecast Δ=87ps. Therefore the time resolution of such a device, defined as the rms value of the timing curve, should be better than 50ps.

IV. CONCLUSIONS

We have discussed the physical mechanisms setting the timing resolution of Single-Photon APDs. In present devices, the timing resolution is limited by the mechanisms involved in the avalanche spreading from the seed point to the entire sensitive area. The best time resolution is obtained when the steering mechanism is the multiplication-assisted diffusion. We have shown that, with a proper design of the electric field profile, the diffusion-assisted process can overcome the photon-assisted spreading also in APDs with a large sensitive area. Therefore, SPAD devices with time resolution better than 50ps rms and a quantum efficiency better than 10% at 1064nm could be obtained. In such devices, the timing resolution would be ultimately limited by the transit time in the thick depleted region.

ACKNOWLEDGEMENTS

Work supported in part by ASI (Italian Space Agency), CNR (Italian National Research Council) and MURST (Italian Ministry of University and Research). The authors wish to thank ST-Microelectronics for the fabrication of the SPADs; EG&G Optoelectronics for providing the reach-through APDs; and S. Masci for his technical support.

REFERENCES

1. P.P. Webb, R.J .McIntyre, and J. Conradi, *RCA Rev.* **35**, 234 (1974).

2. A. Lacaita, S. Cova, and M. Ghioni, *Rev. Sci. Instrum.* **59**, 1115 (1988).

3. M. Ghioni and G. Ripamonti, *Rev. Sci. Instrum.* **62**, 163 (1991).

4. S. Cova, A. Lacaita, M. Ghioni, and G. Ripamonti, *Rev. Sci. Instrum.* **60**, 1104 (1989).

5. A. Lacaita, M. Mastrapasqua, M. Ghioni, and S. Vanoli, *Appl. Phys. Lett.* **57**, 489 (1990).

6. A. Lacaita and M. Mastrapasqua, *Electron. Lett.* **26**, 2053 (1990).

7. D. Bebelaar, *Rev. Sci. Instrum.* **57**, 1116 (1986).

THE SOLID STATE DETECTOR TECHNOLOGY FOR PICOSECOND LASER RANGING

I.Procházka

Faculty of Nuclear Science and Physical Engineering,Czech Technical University
Brehova 7, 115 19 Prague, 1 Czechoslovakia
phone/fax +42 2 848840, telex 121254 fjfi c, E-mail tjean@csearn.bitnet

GENERAL

The millimeter accuracy, multiple wavelength laser ranging to the satellite and long ground baseline is a goal for nineties. Assuming the laser, optics and electronics technology currently available, the optical detectors represent the principal contributions to the ranging error budget in the laser ranging chain. In our group we developed an all solid state laser ranging detector technology [1,2,3], which makes the goal of millimeter accuracy achievable. Our design and construction philosophy is to combine the techniques of : single photon ranging, ultrashort laser pulses and fast fixed threshold discrimination while avoiding any analog signal processing within the laser ranging chain.

The all solid state laser ranging detector package consists of the START detector and the STOP solid state photon counting module. Both the detectors are working in an optically triggered avalanche switching regime. The optical signal is triggering an avalanche current buildup which results in the generation of an uniform, fast risetime output pulse. The fixed threshold discrimination represents no drawback for our application. In connection with the ultrashort laser pulses (35 picoseconds or less), this detection technique introduces the timing jitter of a few picoseconds on the multi photon signal level and less than 15 picoseconds on a single photon signal level. Omitting the fast analog signal processing is simplifying the ranging system and simultaneously increasing its temporal stability.

START DETECTOR PACKAGE

It detects a small portion of the laser output and triggers the time interval unit. The detection structure on silicon is used. The detector is operating in an avalanche switching regime, it is acting as a fixed threshold opto switch generating on its output an uniform current pulse. Its amplitude is typically 8 Volts, length 5 nanoseconds, the risetime is bellow 400 picoseconds. Thanks to the output pulse shape and its uniformity, no additional pulse amplification and discrimination is needed. As no analog signals are propagating along the cables, the detector output is uniform and its amplitude is high, the whole setup is highly resistant to the radio frequency interference and electrical noise problems. This fact is becoming significant in the vicinity of a laser system generating a lot of electrical noise. The detector is capable of operation in three modes :

1. In **linear mode** it may be used as a laser output pulse monitor with the bandwidth of 1 GHz.

In this mode, the optical alignment of the detector may be optimized.
2. The **opto switching mode** described above is used for ranging.
3. In the **self oscillation mode** the detector generates on its output the sequence of uniform output pulses with the repetition rate of about 1 kHz. This mode is and attractive feature for test purpose.

The detector jitter contribution to the overall jitter budget was not measured independently. When it has been used to trigger the streak camera, the overall trigger jitter (detector + streak camera) of 8-16 picoseconds has been observed using the passively mode locked lasers with pulse length 3 - 100 psec FWHM. Thus, the trigger jitter contribution of the START detector itself is well bellow 15 picoseconds for these pulse lengths. Generally, in connection with the active-passive mode locked lasers with pulse lengths bellow 100 psec and the fast response time interval unit input, the jitter contribution of the START detector may be neglected.

SOLID STATE PHOTON COUNTING MODULE

It is used to detect the laser ranging echo signals. The Module is a self consistent detector package, which detects single photons of light over the wavelength range from 0.35 to 1.1 microns. The Module utilizes a unique silicon Single Photon Avalanche Diode (SPAD) [4,2], which is connected in the active quenching and gating circuit and pulse biased above the break. Biasing the diode above the break, the extreme gain of order of 1.10^9 is achieved. This high gain obtained within the semiconductor chip permits to avoid any further amplification of the detector output and the constant fraction discrimination, as well. Simple fixed threshold discrimination technique is used to recognize the detector output and to generate the uniform output NIM pulse. The detector may be gated using the TTL signal, the 'gate on' delay is bellow 25 nanoseconds. The detection diode together with the active quenching circuit, the gating logic, the discriminator, output pulse forming circuit and the light collecting optics in enclosed in one package. It is a cylinder, 120 millimeters long, 40 millimeters in diameter. The optics has an effective focal length 10 millimeters and is optimized for the beam diameter of 8-10 millimeters. Due to the diode relatively small sensitive area (20, 40 or 100 micrometers), the resulting receiver field of view is limited. Using the 100 micrometer diameter diode and the final collecting optics f/D=1, the resulting field of view is 40 arc seconds when installed in the 0.5 meter input aperture telescope. Using the same diode in connection with the 1 meter aperture telescope, the 20 arc seconds field of view is achieved. The 40 um detection chip has been successfully used for SLR at Helwan and Graz, however, the field of view has been to narrow for routine operation. Due to the detection and avalanche buildup mechanisms inside the SPAD chip, the minimal

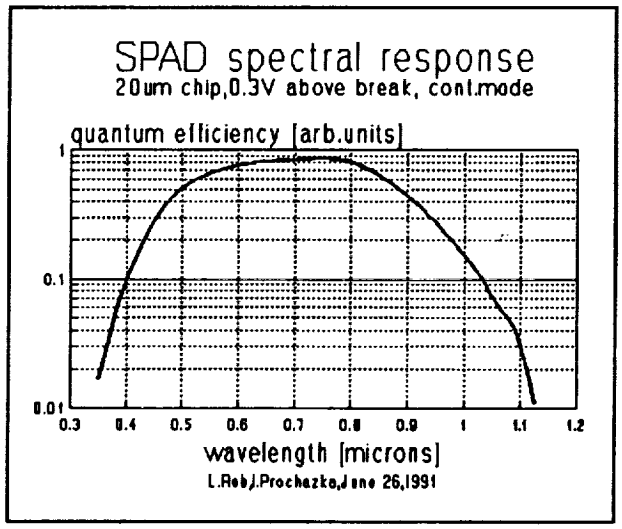

Figure 1 The SPAD relative photon detection probability, 0.3V above the break, + 25°C

detection jitter is achievable when the input photons are focussed on a small spot near to the diode's center. Thus, the good quality light collecting and beam focussing optics together with a careful optical alignment is essential for minimal jitter.

The photon detection probability and its dependence on the wavelength has been measured using the 20 um diameter diode operating in the continuous counting mode. The diode was biased 0.3 Volt above the break. The results are plotted on Figure 1. The detection probability depends on the diode biasing, it increases with the increase of the bias up to 3 Volts above the break. For higher biases, the photon detection probability is not increasing more. The absolute figures of the quantum efficiency have been estimated by comparison to the calibrated photocathode to be 20 % at 0.53 um wavelength and bias 3 Volts above the break. Using the calibrated light source and filters, the quantum efficiency exceeding 20 % at 0.8 um wavelength and biased only 1V above the break has been observed [5].

DETECTORS PERFORMANCE

Since the last Workshop presentation [6], the detectors overall performance has been improved. The SPAD manufacturing technology has been tuned to get lower dark count rates. This is permitting to apply higher voltages above the break and hence to get lower jitter, lower time walk and higher photon detection probability, as well. The active quenching and gating logic has been modified (Prochazka, Kirchner) for this purpose. Cooling the diode using the Peltiere elements down to -25 Centigrades [7] the reduction of the dark count rate is achieved. This proved to be useful for ranging to low satellites suffering of the poor range prediction. Both the detectors are routinely used at the Satellite Laser Station in Graz, Austria since 1989. Most of the application results are based on the data acquired at this site.

The SPAD detector timing jitter and its dependence on the diode biasing is plotted on Figure 2. The jitter values have been computed on the basis of the ground target ranging at the 0.53 um wavelength. At the same figure, the effective dark count rate at the temperatures +25 and -10 Centigrades is plotted. The jitter is depending on the wavelength, it is slightly increasing toward longer wavelengths and reaches 60-70 picoseconds at the 1.06 um when the SPAD is biased 2.5V above the break. The detector package time walk, the detection delay dependence on the signal strength is plotted on Figure 3. The data have been acquired biasing the diode 2.5 Volts above the break and using the semiconductor laser pulser 32 psec FWHM. On Figure 4 there is a plot of evolution of the ranging system single shot precision using the all solid state detector technology together with the list of main upgrades. The ranging system temporal stability is demonstrated on Figure 5, where is a plot of the mean values of ground target calibration runs. It is worth to mention, that this test has been made at the time, when the system single shot precision was 8-9 millimeters. The drift of the 5 picoseconds per hour may be attributed to the

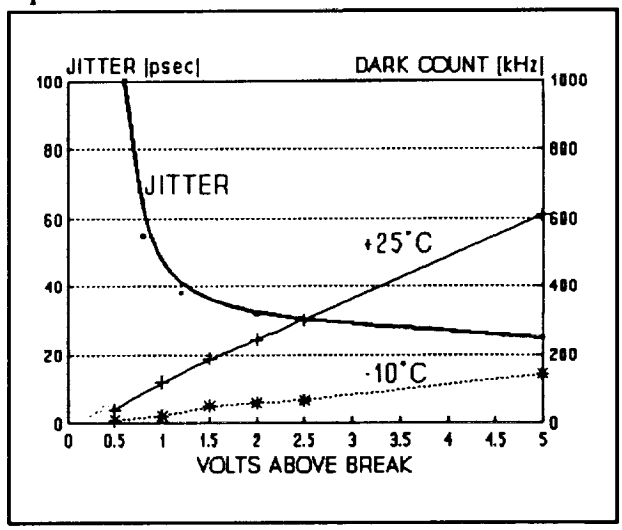

Figure 2 SPAD detector package jitter and effective dark count rate at +25°C and -10°C

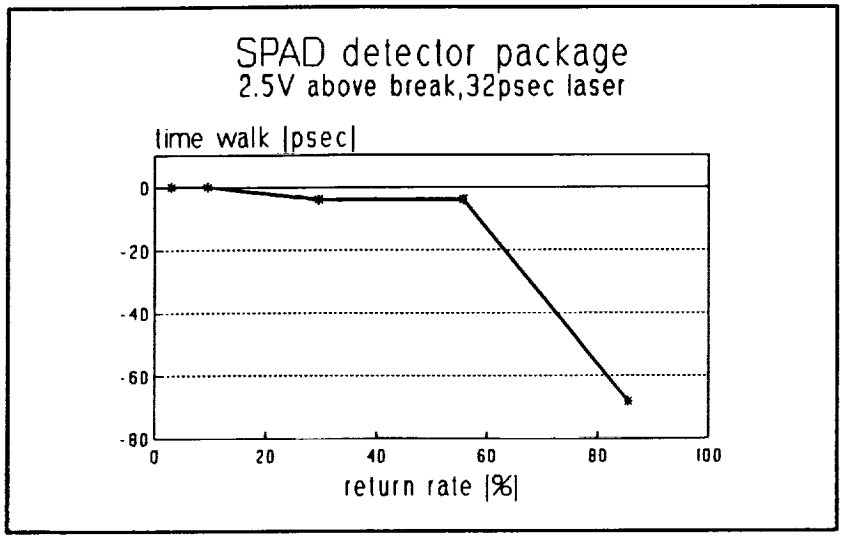

Figure 3 SPAD time walk test,2.5V above break,32 psec laser

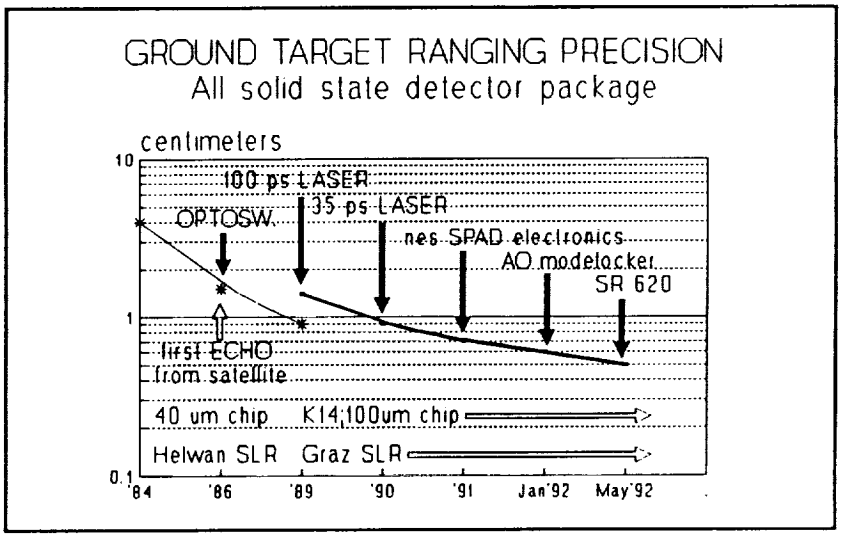

Figure 4 Ground target ranging precision increase

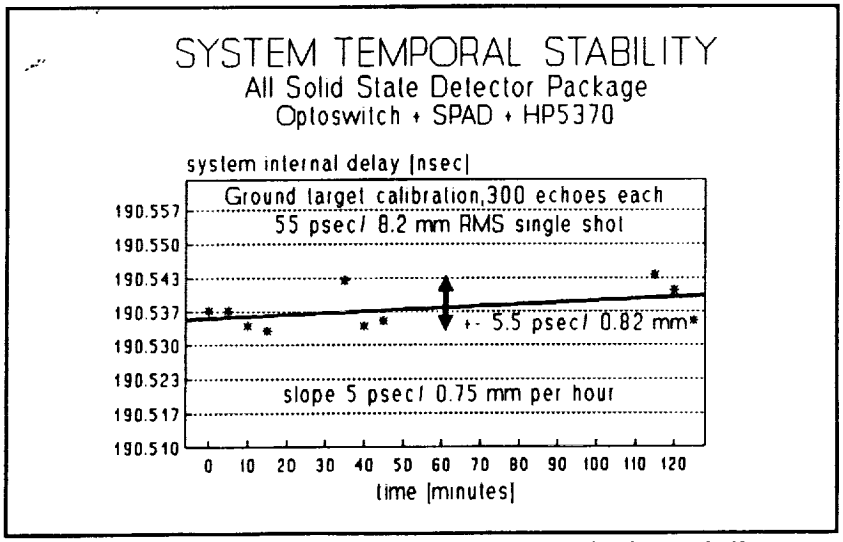

Figure 5 System temporal stability, vert.scale 1mm / div

temperature changes within the control & electronics room and its influence on the ranging counter.

SATELLITE RANGING RESULTS

The all solid state detector package has been used for routine satellite laser ranging since early 1989. Since that time, the ranging precision has been improved from original 2 centimeters to subcentimeter level in 1992.

The satellite signature - its contribution to the echo signal time spread is becoming dominant in the ranging error budget when using the 35 psec laser pulse and single photon detection. On a single photon echo signal level, the ranging precision is limited to 1.5 cm when ranging to Starlette, to 2 cm for Lageos and to 4-5 cm when ranging to Etalon satellites. The effect of the "satellite depth" may be reduced by the use of multiphoton (1-10) return signal strength. In this case, the return photon(s) reflected from the first corner cube is detected. As the detector response time is bellow 20 picoseconds, the photons reflected by the more distant corner cubes are not contributing and are not affecting the detection and discrimination process. Due to this effect, the satellites may be ranged with the return rate exceeding 95% without a detectable time walk and the satellite signature effect on the ranging jitter reduced.

The typical ranging precision obtained in Graz is 8 millimeters for Starlette and ERS-1 satellites, 10 millimeters for Lageos and 12-15 millimeters for Ajisai satellites.

CONCLUSION

The field use of the solid state detector package for satellite laser ranging at various sites over the world : Graz Austria, RGO Great Britain, Shanghai China, MTLRS-1 Germany proved the top performance of the solid state detector technology. The extremely simple, compact and rugged design, the absence of the analog signal processing and the resulting subcentimeter ranging capability and submillimeter temporal stability are the most attractive features. The optical alignment of the SPAD is a difficult task, but it may be solved once the receiver optics is properly designed. The satellite signature and its influence on both the random and systematic error budget is becoming significant from the point of view of millimeter ranging goal.

REFERENCES

[1] I.Prochazka,proc.of 6th Int.Work.on Laser Ranging Instrumentation, Antibes, Sept.1986
[2] K.Hamal,I.Procházka,B.Sopko,G.Kirchner,proc.of Conference on Lasers and Electro Optics, CLEO'90, Anaheim, CA, May 1990
[3] I.Procházka et al,proc.VIIth International Symposium on Ultrafast Processes in Spectroscopy, Bayreuth, Germany, October 1991
[4] S.Cova et al,JQE, Vol.19,630 (1983)
[5] J. Říčka, M.Hoebel, private communication, (1992)
[6] I.Prochazka,K.Hamal,B.Sopko,proc.7th Int.Workshop on Laser Ranging Instrumentation, Matera, Italy, Oct. 1989
[7] G.Kirchner, private communication (1991)

STREAK CAMERA BASED SLR RECEIVER FOR TWO COLOR ATMOSPHERIC MEASUREMENTS

Thomas Varghese, Christopher Clarke, Thomas Oldham, Michael Selden
Allied Signal Aerospace Company,
BFEC/CDSLR
10210 Greenbelt Road
Seabrook, MD 20706 USA

Abstract.

To realize accurate two-color differential measurements, an image digitizing system with variable spatial resolution was designed, built and integrated to a photon-counting picosecond streak camera, yielding a temporal scan resolution better than 300 femtosecond/pixel. The streak camera is configured to operate with 3 spatial channels; two of these support green (532 nm) and uv (355 nm) while the third accommodates reference pulses (764 nm) for real-time calibration. Critical parameters affecting differential timing accuracy such as pulse width and shape, number of received photons, streak camera/imaging system nonlinearities, dynamic range, and noise characteristics were investigated to optimize the system for accurate differential delay measurements.

The streak camera output image consists of three image fields, each field is 1024 pixels along the time axis and 16 pixels across the spatial axis. Each of the image fields may be independently positioned across the spatial axis. Two of the image fields are used for the two wavelengths used in the experiment, the third window measures the temporal separation of a pair of diode laser pulses which verify the streak camera sweep speed for each data frame. The sum of the 16 pixel intensities across each of the 1024 temporal positions for the three data windows is used to extract the three waveforms. The waveform data is processed using an iterative three-point running average filter (10 to 30 iterations are used) to remove high-frequency structure. The pulse pair separations are determined using the half-max and centroid type analysis. Rigorous experimental verification has demonstrated that this simplified process provides the best measurement accuracy. To calibrate the receiver system sweep, two laser pulses with precisely known temporal separation are scanned along the full length of the sweep axis. The experimental measurements are then modelled using polynomial regression to obtain a best fit to the data. Data aggregation using normal point approach has provided accurate data fitting techniques and is found to be much more convenient than using the full rate single shot data. The systematic errors from this model has been found to be less than 3 ps for normal points.

TWO COLOR ATMOSPHERIC MEASUREMENTS

Objectives:

- Measure atmospheric velocity dispersion difference between 532 and 355 nm using short (≤30 ps) pulses, very accurately (2-3 ps).
- Compute atmospheric refraction correction (RC) directly from the differential range.
- Compare this correction with the theoretical one obtained from surface meteorological measurements for agreement/refinement.

Issues of Importance:

- Is there true hydrostatic equilibrium in the troposphere on a local scale ?
- What are the diurnal and seasonal effects ?
- What effect does the local/global temperature gradient have on RC ?

STREAK CAMERA SLR RECEIVER SYSTEM

Desirable Features:

- High Temporal Resolution (ps).
- Good temporal sweep stability.
- High quantum efficiency (> 10%)
- Single photoelectron sensitivity.
- High resolution spatial imaging (< 1 ps/pixel).
- Repetition Rate ≥ 10 Hz.
- Optical calibration source with temporal and amplitude stability.
- Spectral filtering and wavelength isolation.

STREAK CAMERA CHARACTERISTICS

Streak Tube

- Manufactured by Hamamatsu; model C2909, streak tube N2666.
- Sweep: linear
- Maximum MCP gain ≃ 10^6
- Spectral response: 200 - 850 nm
- Phosphor Screen: P20
- Effective Photocathode size: ≃6mm

Input Optics

- Spectral transmission: 200 - 1600 nm
- Transmission efficiency: 65% (350 - 1100 nm)
- Image magnification: 1:1
- Effective F-value: F/4.5

Output Optics

- Image magnification: 1:1
- Effective F-value: F/1.2

Photocathode gating characteristics

- Duration: 0.3 - 100 μs
- Extinction: 10^3

Timing Characteristics

- Maximum sweep ≃ 250 ps/12 mm
- Trigger jitter < 10 ps
- Temporal resolution: 1.4 ps (MCP gain = 1)
- Dynamic range: (30:1 at high gain)

READOUT CHARACTERISTICS

- Vidicon - Plumbicon (North American Philips model 88 X Q)
- Preamplifier gain: ≤80 dB
- Raster Control: flexible, current operation 1024 (time) X 128 (horizontal)
- Sampling rate: 1 M sample/second (max = 16 Msample/second)
- Maximum data transfer to computer: ≃ 700 Kbytes/second (MC-DIO-32)
- Maximum rate (currently) limited by interface card 9.4 Hz
- Maximum Temporal Resolution/pixel: 250 fs
- Data windowing: 3 windows for 3 wavelengths, each operating with 1024 X 16 pixels

TWO COLOR DIFFERENTIAL MEASUREMENT
THEORETICAL AND EXPERIMENTAL LIMITS OF ACCURACY

$$R_0 = R(\lambda_1) - \frac{c}{2}\left\{\left[\frac{f(\lambda_1)}{f(\lambda_2)-f(\lambda_1)}\right]\left[(T_0+T(\lambda_2)) - (T_0+T(\lambda_1))\right]\right\} \quad (1)$$

$$\sigma^2_{R_0} = \sigma^2_{R(\lambda_1)} + \left\{\left[\frac{c}{2}\right]\frac{f(\lambda_1)}{f(\lambda_2)-f(\lambda_1)}\right\}^2 \sigma^2_{\delta T(\lambda_1,\lambda_2)} \quad (2)$$

Where

$$\delta T(\lambda_1,\lambda_2) \triangleq T(\lambda_2)-T(\lambda_1)$$

$$\sigma_{\delta T(\lambda_1,\lambda_2)} = \sqrt{\sum_{i=1}^{2}\left[\frac{\Delta T^2(\lambda_i)\ S(\lambda_i)}{n_{ph}(\lambda_i)\cdot\eta_{QE}(\lambda_i)\cdot A}\right] + \left[\sigma^2_{MCP} + \sigma^2_{sweep}\right]} \quad (3)$$

R_0	=	Absolute range to the satellite
$R(\lambda)$	=	Measured range at wavelength λ
$f(\lambda)$	=	Dispersion factor
T_0	=	Absolute time of flight
$T(\lambda)$	=	Increase in time of flight through atmosphere at wavelength λ
$S(\lambda)$	=	Pulse profile factor
η_{ph}	=	Number of photons
η_{QE}	=	Photocathode quantum efficiency
A	=	Microchannel coupling factor
δT	=	Differential time of flight
σ	=	Standard deviation
$\Delta T(\lambda)$	=	Pulse width at λ

DATA ANALYSIS TECHNIQUES

SMOOTHING (3 POINT) ALGORITHM

$$\langle I_p \rangle^{(m)} = \frac{\left[a\langle I_{p-1} \rangle^{(m-1)} + b\langle I_p \rangle^{(m-1)} + c\langle I_{p+1} \rangle^{(m-1)} \right]}{(a + b + c)} \quad (4)$$

$$\langle I_0 \rangle^{(m)} = \frac{\left[b\langle I_{1022} \rangle^{(m-1)} + c\langle I_1 \rangle^{(m-1)} \right]}{(b + c)} \quad (5)$$

$$\langle I_{1023} \rangle^{(m)} = \frac{\left[a\langle I_{1022} \rangle^{(m-1)} + b\langle I_{1023} \rangle^{(m-1)} \right]}{(a + b)} \quad (6)$$

$\langle I_p \rangle^m$ = Mean intensity of the pixel at location p after "m" iterations

a,b,c = Weighting coefficients

DETECTION:

- Peak
- Half Maximum (Mean Value)
- Centroid

ORIGINAL PAGE
BLACK AND WHITE PHOTOGRAPH

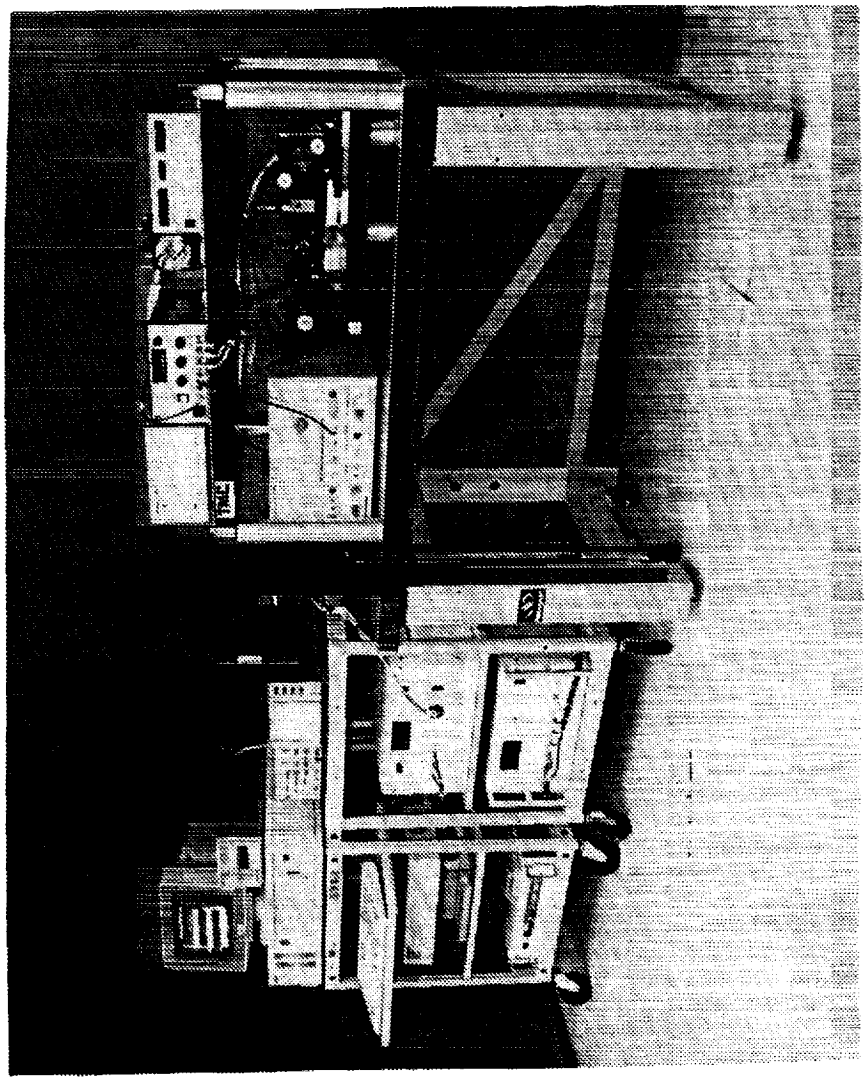

PHOTOGRAPH OF THE STREAK CAMERA BASED SLR RECEIVE SYSTEM.

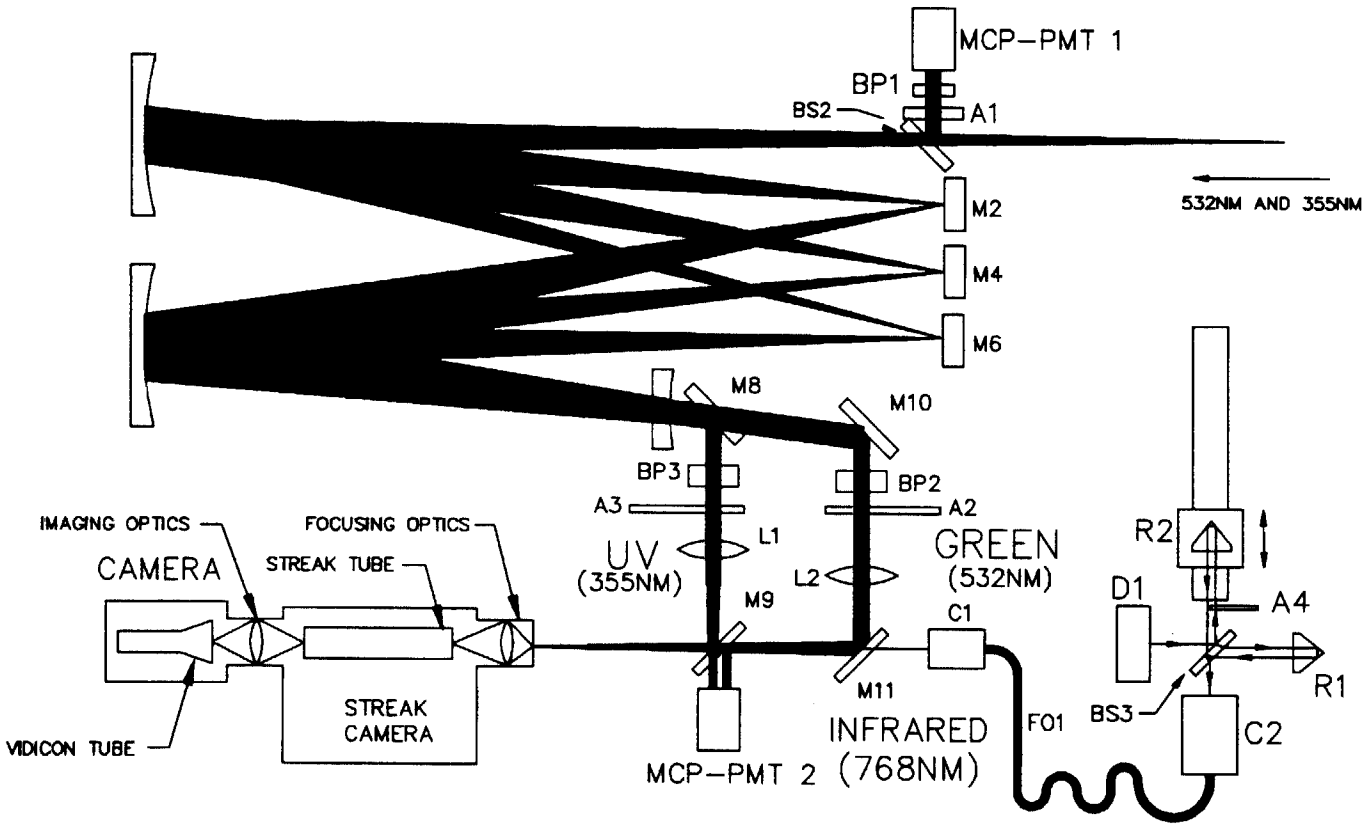

OPTICAL SCHEME OF THE STREAK CAMERA RECEIVER SYSTEM, CURRENTLY USED FOR TWO COLOR MEASUREMENT WITH THE NASA GSFC 1.2 METER TELESCOPE.

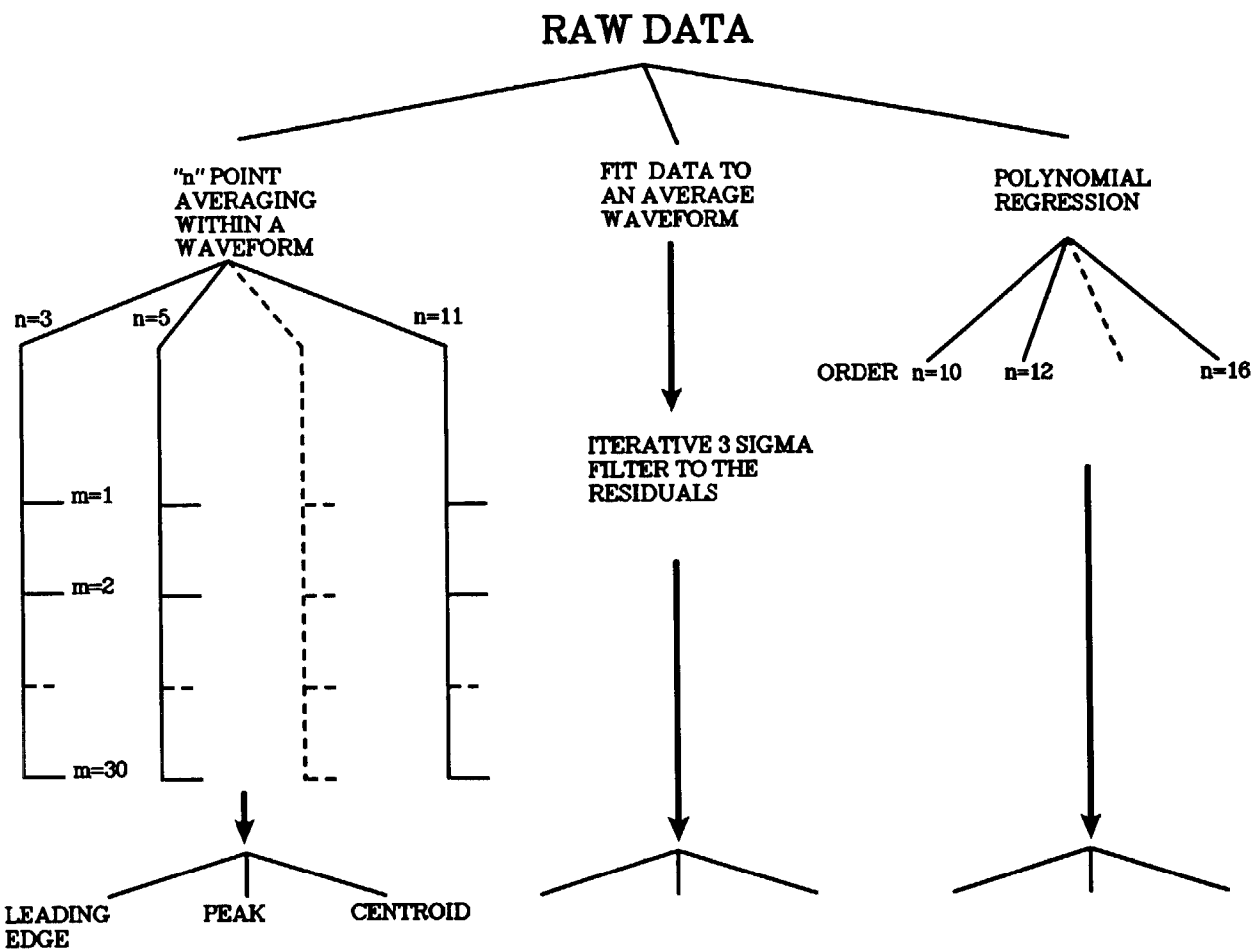

Tree structure illustrating different types of data processing techniques investigated for determination of pulse pair separation. The best results were obtained for data smoothing with n=3 and n=5 while using centroid/leading edge analysis.

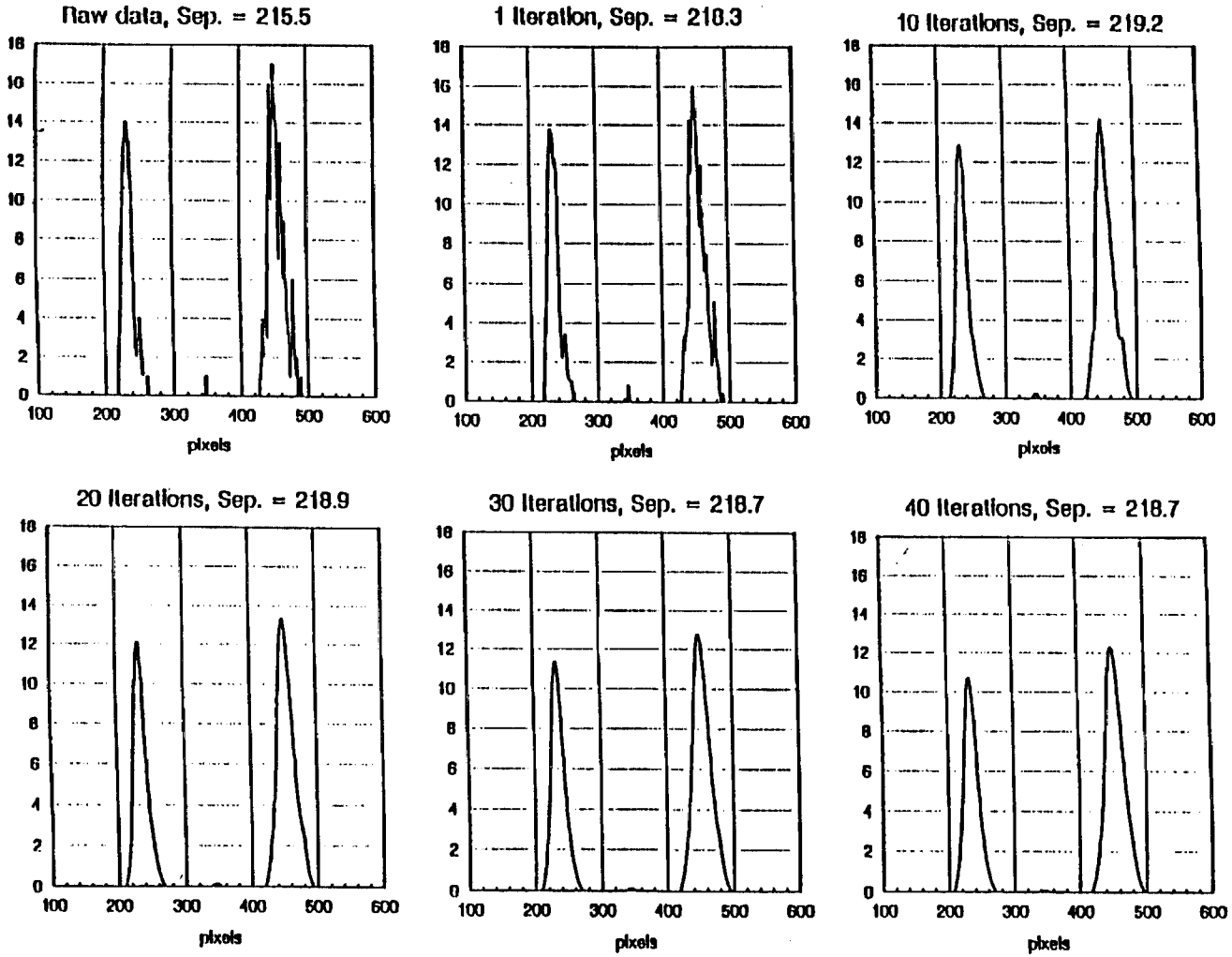

ILLUSTRATION OF THE EVOLUTION OF THE NOISY PULSE PROFILE AS A FUNCTION OF NUMBER OF ITERATIONS OF SMOOTHING (3–POINT). THE PULSE SEPARATION IS STABLE AFTER ABOUT 20 ITERATIONS.

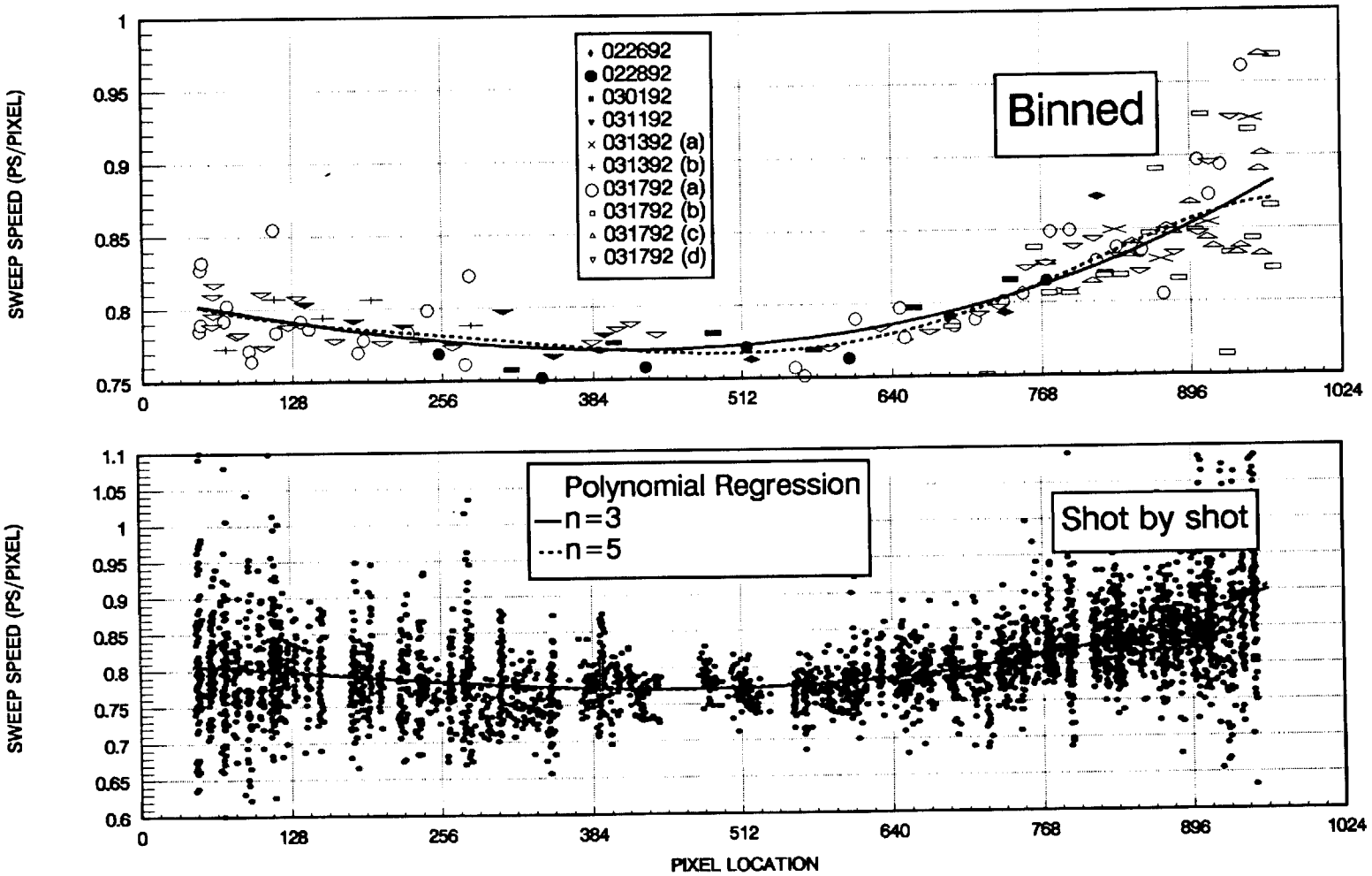

ANALYSIS OF THE NONLINEARITY OF THE SWEEP AS A FUNCTION OF SPATIAL LOCATION. THE TOP PLOT SHOWS NORMAL POINT ANALYSIS FOR A POLYNOMIAL REGRESSION OF N=3 AND N=5 WHILE THE BOTTOM PLOT SHOWS FULL RATE (SINGLE SHOT) ANALYSIS.

SUMMARY

- Single photoelectron sensitive streak camera SLR receive system has been configured with a resolution approaching 250 fs/pixel for high accuracy atmospheric dispersion measurements.
- It has been verified that the streak camera timing characteristics are profoundly impacted by the sweep voltage. The sweep voltage is intrinsically nonlinear in the leading and trailing edges and must be corrected using optical calibration to achieve picosecond timing accuracy. Centroid and half maxima (mean) analyses were found to be superior to peak detection.
- Real-time calibration has been found to be very effective in monitoring the timing performance and would be very advantageous for critical timing measurements.

THE FIRST SATELLITE LASER ECHOES RECORDED ON THE STREAK CAMERA

K.Hamal, I.Procházka

Faculty of Nuclear Science and Physical Engineering, Czech Technical University
Brehova 7,115 19 Prague 1,Czechoslovakia,
Phone/fax +42 2 848840, telex 121254 fjfi c, E-mail TJEAN@CSEARN.BITNET

G.Kirchner, F.Koidl

Austrian Academy of Sciences,Lustbuenel Observatory
A-8042 Graz, Austria, Phone +43 316 472231

ABSTRACT

The application of the streak camera with the circular sweep for the satellite laser ranging is described. The Modular Streak Camera system employing the circular sweep option was integrated into the conventional Satellite Laser System. The experimental satellite tracking and ranging has been performed. The first satellite laser echo streak camera records are presented.

GENERAL

The laser ranging of the artificial Earth satellites, the Moon and the long ground baselines is an attractive and rapidly developing technique. The laser ranging precision and accuracy is gradually increasing, it reaches one centimeter level at present. The goal for nineties, requested by the data users, is the satellite laser ranging to artificial satellites with millimeter accuracy. The existing pulsed laser ranging systems are using short pulse lasers of 20-200 picoseconds at 532 nanometers as a transmitter, the fast microchannel plate photomultiplier tube along with an appropriate electric discriminator or an avalanche photodiode as a return signal detector reaching a time interval resolution of 30 picoseconds. An electronic time interval unit having a resolution of 20-35 picoseconds is used to determine the interval between the laser pulse transmittion and echo signal detection[1].

The limiting factor for the current systems accuracy improvement from centimeter to millimeter level are the currently used detectors and discriminators, time interval meters and the contribution of the target itself. The main contributors to the systematic error and hence limiting the final accuracy is the atmosphere. The existing atmospheric models based on meteorological data permit to predict the atmospheric optical delay with centimeter accuracy. It is expected, that ranging simultaneously on two wavelength and determining the two wavelength propagation time difference, the existing atmospheric models will be improved to millimeter accuracy. However, to obtain the valuable data for atmospheric model improvement, the two wavelength delay must be measured with picosecond accuracy[2] .

The goals of the implementation of a streak camera into a laser ranging system :
The first : the replacement of the existing detectors and discriminators by the streak camera

with and appropriate readout and data processing system. This will increase the time interval resolution of the radar detection chain several times, the echo pulses distortion by the target geometry may be monitored and compensated. The second : the streak camera will be used for two wavelength laser ranging echo signals detection, the two wavelength range delay may be determined with the picosecond accuracy. The third : along with the detector, the streak camera may be integrated into the time interval unit. The picosecond time resolution and a high overall timing accuracy is expected[1].

THE STREAK CAMERA CONSTRUCTION

Designing the streak camera for satellite laser ranging purpose several key problems have to be solved:
- the energy budget of the ranging chain, closely connected to the photocathode and sweep speed used,
- the camera configuration, the type of deflection, input optics configuration,
- the readout system and the output data processing.

Completing the series of indoor and ground target ranging experiments, we have chosen the S25 photocathode, the circular sweep camera setup and a two dimensional TV readout system with a full frame image processing. The linear sweep tube setup reaches higher limiting temporal resolution. However, the necessity of a trigger signal appearing 10-30 nanoseconds prior to the photons to be detected with a subnanosecond jitter and the angular/temporal relation may cause serious difficulties when ranging to satellites. Using the circular sweep tube setup, the trigger signal requirements are moderate : the trigger signal must appear 10-20 microseconds before the optical signal, the jitter of several microseconds is acceptable. The temporal/angular dependence may be monitored, software modelled and compensated.

The PV-006 streak tube having the S25 photocathode and the microchannel plate image intensifier fiber optically coupled together have been used. The streak tube is equipped with two pairs of deflecting plates acting in the mutually perpendicular direction. Applying the RF signal phase shifted to both deflection plate pairs, the circular sweep may be obtained. The 320 MHz signal, 13 Watts of pulsed RF power is used. The maximal RF power applicable on the deflection system is limited by the internal ionization inside the tube. The diameter of the circle was about 6 mm resulting in 155 psec/mm sweep speed. Due to the imperfect impedance matching of the RF driving circuit to the tube deflection system, the deflection is not perfectly circular. Nevertheless, the complex streak image processing and calibration package is able to compensate for these effects. The temporal resolution of 30-35 psec and the range difference jitter 6 psec have been achieved.

The application of the streak camera for ranging purposes is accomplished by the timing and gating circuitry. The deflection signal is ON for only few microseconds before laser transmittion and again few microseconds before expected arrival of the satellite echo. All the remaining time the camera is working in the static image mode and may be used for guiding / alignment purposes, as well. The 320MHz deflection signal is produced by multiplication of the 5 MHz sine wave output of the station Cs beam frequency standard, which is simultaneously acting as an master oscillator for all the station timing electronics. This way, the precise phase synchronism of the radar electronics and the camera circular deflection is maintained. In fact, the camera may be used as a vernier to the time interval unit, rough time interval is derived from the integer number of periods from Start to Stop event, the fraction of the period may be determined from the phase difference of the Start and Stop events[5].

The microchannel plate intensifier gain is controlled in three steps. During the laser

transmittion, the gain is set to minimum to avoid the blinding of the system by the atmospheric backscattered light. Optionally, the mechanical shutter in front of the input photocathode is used. Most of the time the microchannel plate gain is set to 100, a compromise between the static image mode gain and the background noise contribution. At the expected echo arrival time, the gain is set to maximum of 10,000 for 300 microseconds to achieve maximum detection sensitivity.

To readout the tube screen image we use the Silicon Intensified Target (SIT) tube made by Haimann. The output signal was fed to the Visionetics Frame Grabber card (512x512x8bits) inserted in the IBM PC. To solve the problem of a deflection nonsymetry, the software package[3] allows the full frame image processing and accomplishes the software modelling of the image distortion, the sweep nonlinearity, the gain nonuniformity etc. On the end of the image processing procedure the temporal curve consisting of 1000 channels, 8 bits each is generated. Once the center of the deflection circle is identified, for example using the satellite image in the static mode, the temporal/angular effect[4] may be software compensated.

The compact design of the camera, its rugged construction along with its low mass permitted to install it directly on the moving part of the tracking telescope.

SATELLITE LASER RANGING SYSTEM

The streak camera has been integrated to the Satellite Ranging System of the Lustbuehel Observatory, Graz, Austria. The ranging system consists of a modified Quantel laser, passively mode locked NdYAG with the second harmonic generator, delivering pulses of 10 milliJoules, 35 picoseconds in green. Alternatively the semitrain of 5 - 7 such pulses containing totally 60 milliJoules may be transmitted. The telescope is a Contraves laser tracking type. The laser output is transmitted by a 10 cm diameter Galileo telescope, the 0.5 meter diameter Cassegrain optics is used for both return photons collection and visual guiding. The streak camera replaced an original ISIT camera attached to the telescope and dedicated for faint objects visual tracking. The dielectric mirror is directing 99% of the returned photons on the streak photocathode the remaining photons enter the standard detector package based on a single photon avalanche photodiode. All the rest of the satellite laser ranging hard/software remained unchanged. Thanks to the photodiode single photon response capability, the satellite routine ranging capability has been preserved, although with reduced return rate. The streak camera system timing and gating logic has been added.

The streak tube, the image intensifier and the readout have been kept at the temperature + 5 C what resulted in significant dark noise reduction.

RESULTS

The retroreflectors equipped satellites at the distances of 1,000 to 2,300 kilometers have been ranged. The first satellite laser ranging echoes recorded by a streak camera have been obtained January 18,1991 at 21:37 UT from the AJISAI satellite at the distance 2000 km, see **Figure 1**. In this stage, the semitrain of pulses separated by 8.557 nanoseconds has been transmitted. On the image the time interval of 40 milliseconds covering the laser pulse transmittion to echo detection is integrated. The transmitted laser beam backscattered light image is near the center of the pattern displayed in the static image. At this moment the satellite was not illuminated by the Sun. On **Figure 2** there is a streak camera record of the AJISAI satellite echo obtained transmitting single picosecond pulse containing 10 mJ of energy. The temporal profile of the firs part of the trace is included. Please, note the streak camera receiver system saturation by the strong echo signal coming from the first rows of the

corner reflectors. The satellite is a sphere of diameter exceeding two meters covered with retroreflectors. According to numerical simulations, the returned pulse should be spread over the time interval about one nanosecond depending on the satellite orientation. The separate echoes coming from various retroreflectors may be clearly distinguished. The sweep speed nonlinearity has not been compensated on this display. The central spot is an static image of the satellite illuminated by the Sun, thus marking the center of the sweep. The atmospheric backscattered light has been blocked out by the mechanical shutter. The STARLETTE satellite echo record is on **Figure 3**. Single picosecond pulse has been transmitted. The satellite is a sphere covered with retroreflectors of the diameter of about 25 centimeters at a distance about 1,000 kilometers. The echo signal time spread is significantly smaller in comparison to the AJISAI satellite. The temporal profile of the echo is included, as well. The detector saturation may be seen. The system temporal resolution may be demonstrated on the not saturated response from a single corner reflector resulting in a pulse width of 25-30 picoseconds.

CONCLUSION

The first satellite laser echoes have been recorded on the streak camera to our knowledge for the first time. The applicability of a Modular Streak Camera system employing the circular sweep for satellite laser ranging has been demonstrated. The sensitivity of the streak camera has been confirmed to be satisfactory for the purpose : for standard geodetic satellite ranging employing available laser ranging technology.

REFERENCES

1. J.J.Degnan, "Satellite Laser Ranging: Current Status and Future Prospects", IEEE Trans.on Geoscience and Remote Sensing, Vol. GE-23,pp.398-413,July 1985
2. J.Abshire, Applied Optics, Vol.19, No 20,pp.3436-3440, 1980
3. P.Valach," Streak Camera Full Frame Image Processing", proc.of the Seventh International Workshop on Laser Ranging Instrumentation,Matera, Oct.1989, edited by C.Veilet,CERGA,France
4. I.Prochazka, K.Hamal, "Streak Camera as a Laser Radar Receiver, its Performance and Limitations", proc. of the Sixth International Workshop on Laser Ranging Instrumentation, Antibes, Sept.1986, edited by J.Gaignebet,Cerga,France,1987
5. K.Hamal, I.Prochazka, M.Schelev, V.Lozovoi, V.Postovalov, " Modular Streak Camera for Ranging", presented at the 19th International Congress on High Speed Photography and Photonics, Cambridge, UK,Sept.17-21,1991, published in SPIE 1358-55

SATELLITE LASER RANGING

FIRST STREAK RECORDS

AJISAI satellite , diameter 2. meters
range 1 500 km
January 19, 1991 , UT 21:37

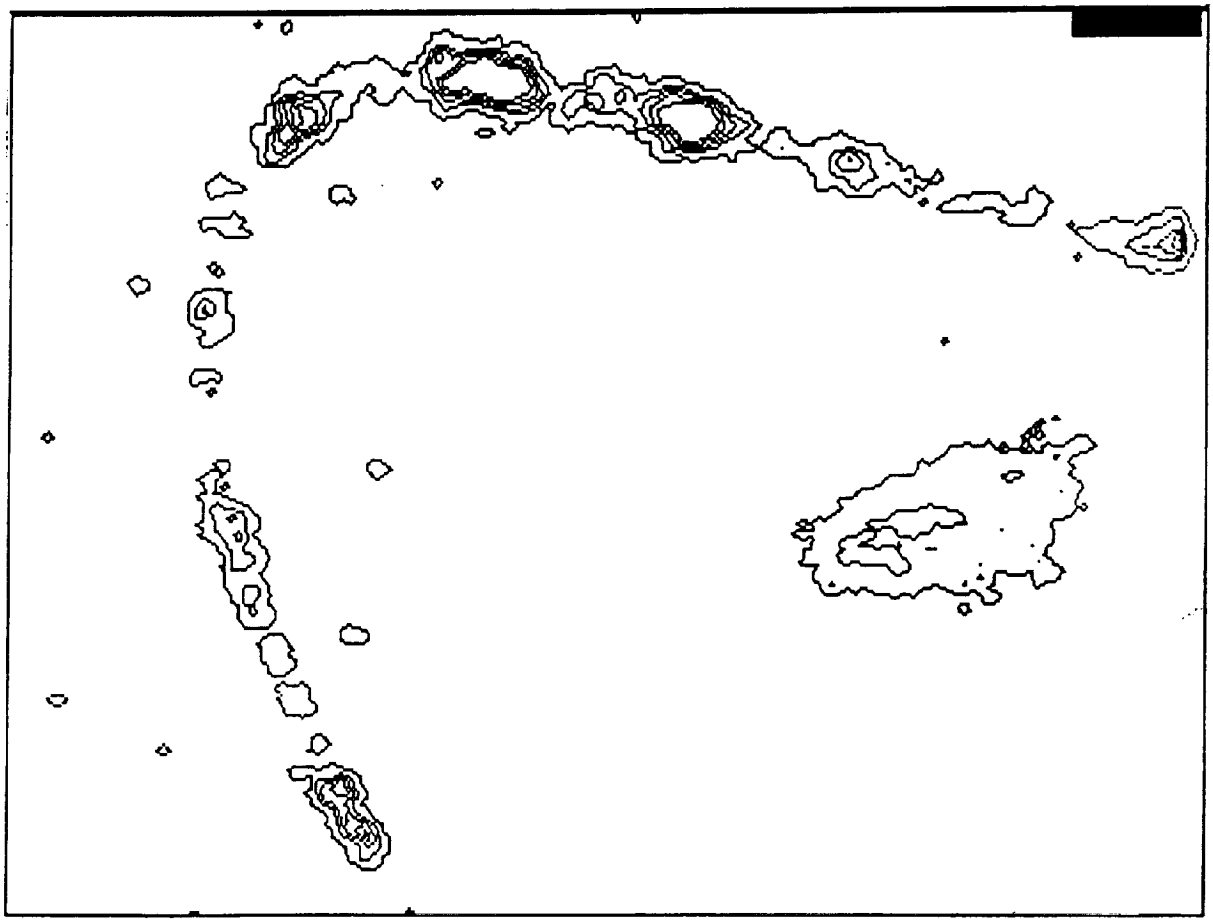

sweep period 3.125 nsec, displayed part 1 nsec

Fig. 1

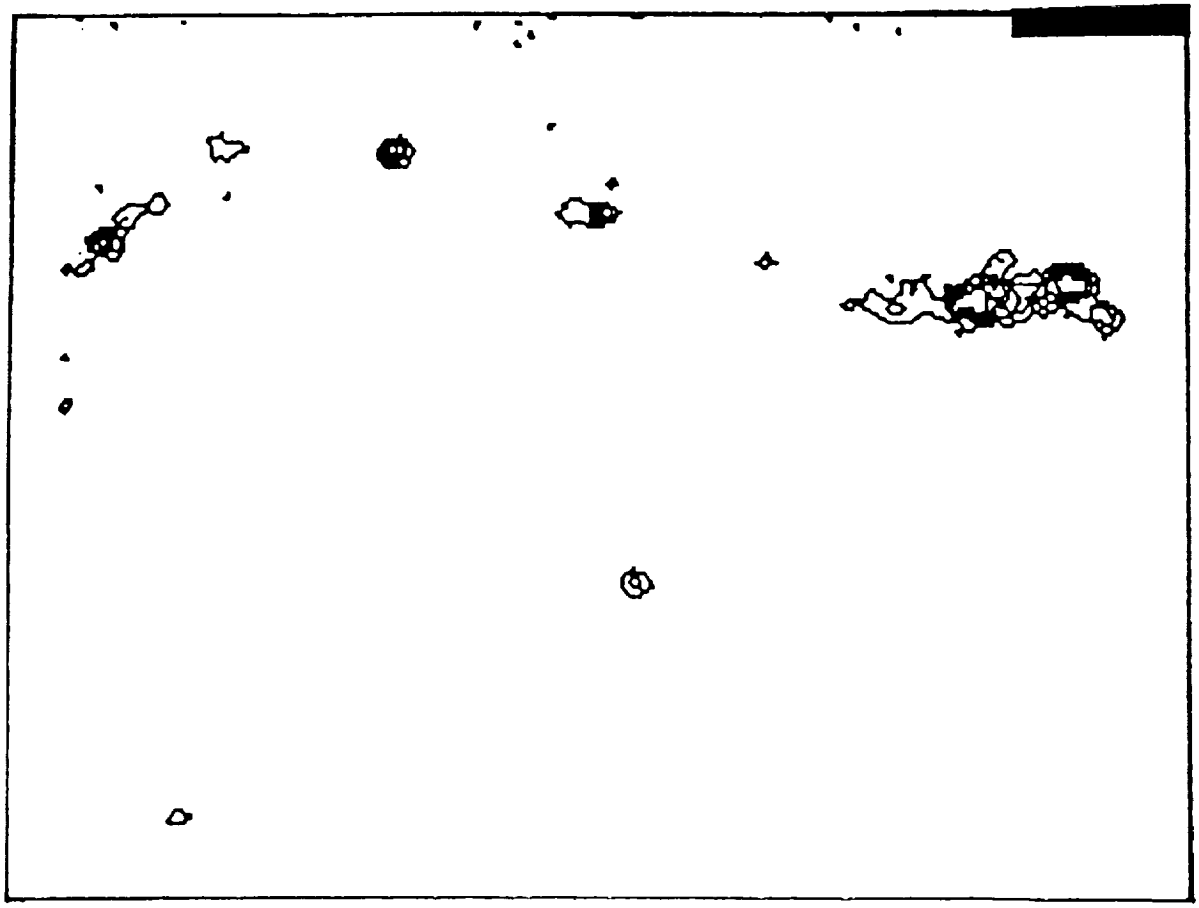

amplitude AJISAI satellite picosecond laser pulse response on streak

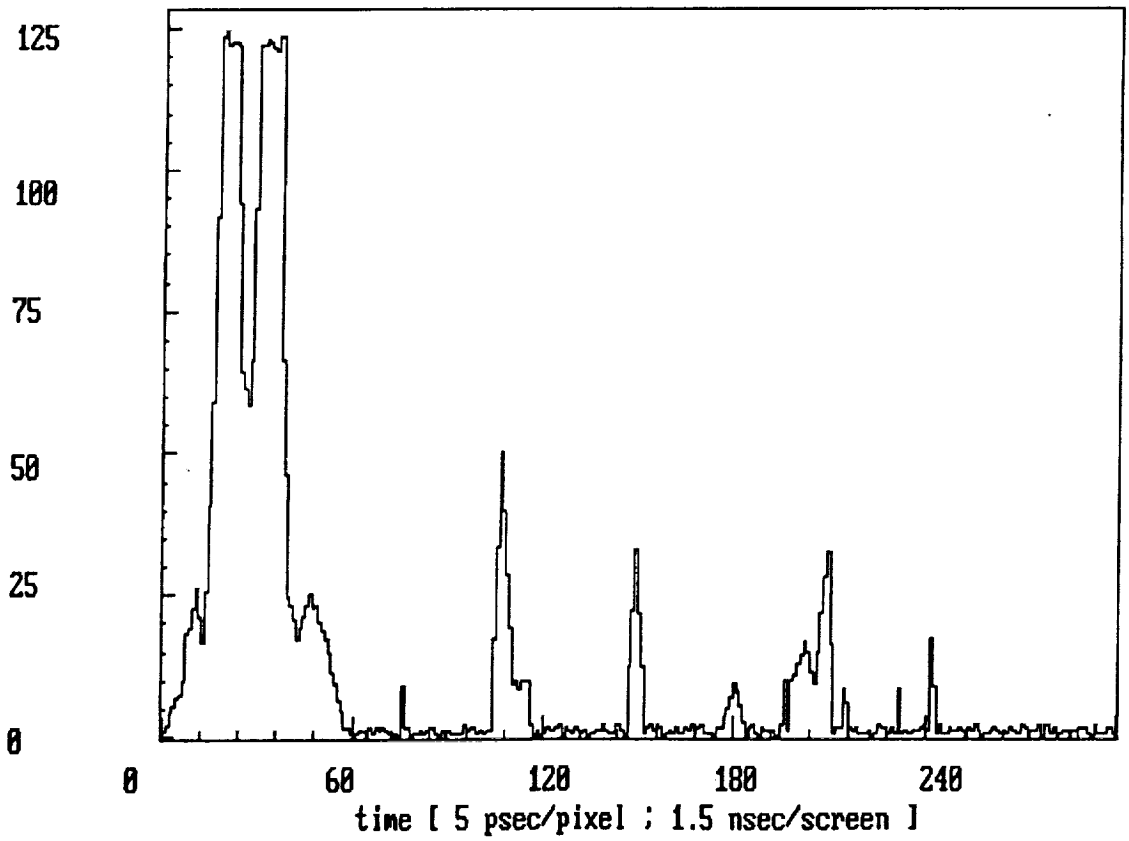

Fig. 2

SATELLITE LASER RANGING

FIRST STREAK RECORDS

STARLETTE satellite , diameter 0.3 meter
range 1 000 km
January 24, 1991 , UT 21:59

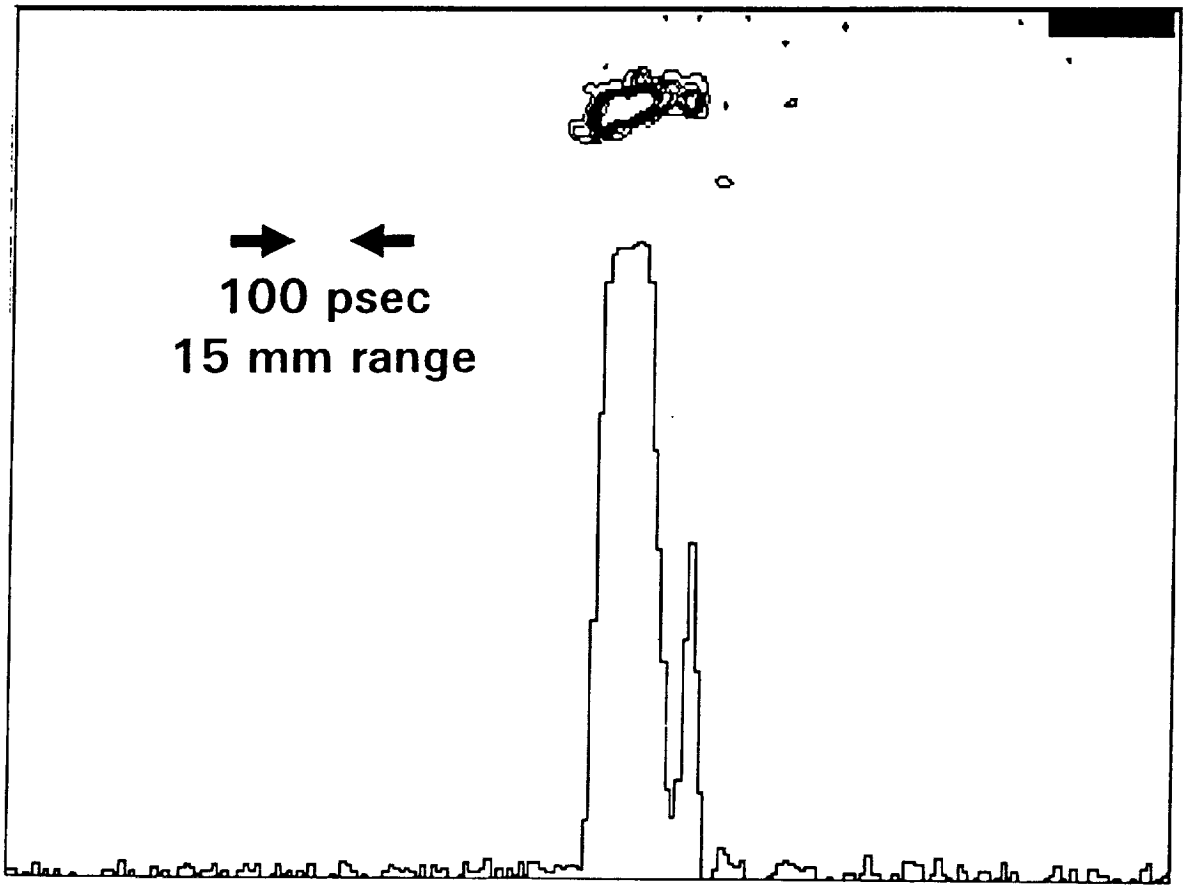

echo signal temporal profile 8 psec / pixel

Fig. 3

Calibration

Techniques/Targets

Experience and Results of the 1991 MTLRS#1 USSR Campaign

P. SPERBER
INSTITUT FÜR ANGEWANDTE GEODÄSIE
FUNDAMENTALSTATION WETTZELL
DER FORSCHUNGSGRUPPE SATELLITENGEODÄSIE
D-8493 KÖTZTING

H. HAUCK
INSTITUT FÜR ANGEANDTE GEODÄSIE
RICHARD-STRAUSS ALLEE 11
D-6000 FRANKFURT/MAIN 70

Abstract. In the fall 1991 the Modular, Transportable Laser Ranging System MTLRS#1 was operating in the USSR for collocation of the SLR systems in Riga, Simeiz and Kazivelli. In this paper we will summarize the results of the collocation experiments and we will show our (positive and negative) experiences, we got during this campaign in the USSR).

1. Introduction

The year 1991 was a special year for the mobile laser ranging systems. Due to the scheduled upgrades of the Modular Transportable Laser Ranging Systems MTLRS#1 (operated by the IfAG, Germany) and MTLRS#2 (operated by the OSG Kootwijk, Netherlands) neither a WEGENER-MEDLAS nor a Crustal Dynamics Project campaign was carried out in 1991.

After the successful upgrade of MTLRS#1 in the first half of 1991 (P. Sperber et al.) the system departed from Wettzell in August to make maesurements at two sites in the USSR.

In Riga/Latvia we operated close to the fixed SLR system, in Simeiz/Ucrainea the place for MTLRS#1 pad was choosen to collocate the two fixed SLR station in Simeiz (300 m distance to MTLRS#1) and Kazivelli (about 3 km distance).

2. Results

An overview about the number and quality of the MTLRS#1 passes is shown in Fig. 1 and Fig. 2.

The system arrived in Riga during week 32. Because the crew was not yet familiar with some new parts of the system, which were installed during the upgrade, it took some days, before the first data were collected successfully.

In week 34 we were faced with a problem, we never had before: In moscow parts of the soviet army putsched against gorbatchov. Due to the unclear and dangereous political and military situation we had to stop our observations again for nearly one week.

During the rest of measurements in Riga we were faced with extremely bad weather conditions. All this problems are showing in an unusual poor performance of MTLRS#1 in Riga. Neither the quantity (number of passes per week) nor the quality (number of normalpoints per pass) was completely satisfying.

After 43 Lageos passes we stopped the observations in Riga on October 3 rd and moved the sytem to Simeiz.

Here the system was able to show its habitual performance. After 53 Lageos passes with more than eleven normalpoints per pass in average the campaign was finished on November 23 rd.

The computation of the collocation was performed by the computing center of the IfAG in Frankfurt/Main. The results are summarized in Fig. 3 - Fig. 5.

Fig. 3 shows the results of the Riga collocation. We got 16 simultaneos Lageos passes with a R.M.S. of 20 cm at the Riga system and 1 cm or 2 cm at MTLRS#1 depending whether a PMT or a single photon avalanche diode (I. Prochazka et al., P. Sperber et al.) was used as receiver.

Out of this 16 passes six passes with good residual overlap (for example: Fig. 4) were selected to calculate the range and epoch bias of the Riga SLR system. There is a small negative tendency in both biases, but compared to the error values and the R.M.S. of the Riga system we can't find a significant bias.

Fig. 5 summarizes the results of the collocation in Simeiz. Because of problems, the fixed stations only were able to observe few passes during the collocation, but all of the passes were simultaneous with MTLRS#1.

The data of the fixed stations are not yet delivered to the network, so until now a computation was not possible.

3. Experience

In this chapter we will summarize our experience during the on-site operartion and the transport of a dedicated geodetic system in the USSR.

2.2. Operation on stations

From the operational point of view there were no problems as long as the system was working near stations. All our requirements concerning electrical power, safety, infrastructure, etc. were fullfilled. In Riga also the supply of fuel and the hotel accomodation were satisfying.

On all stations an independent communication facility like Inmarsat is necessary. The only local data channnel is a very unreliable telex line.

In Simeiz, the hotel, food and fuelsituation is very inconvenient:

- A hotel near the station is far under western standard, an acceptable one is more than 40 km away.
- For fuel a big spare tank is necessary, because fuel is not always available.
- As there are no restaurants near the station, facalities are needed to prepare own food

Additionally most of the people only speak russian language.

In spite of this problems, the operation of a slr system near fixed stations is always possible, if some preparations are made to facilitate the life of the crew members.

2.2. Transport between stations

During the transport of a system from one station to the other the situation becomes very bad compared to the operation on stations.

- Communication channels to foreign countries are not available in short time
- Hotels only exist in big cities. Sleeping facilities for all persons in cars (caravans) are strongly recommended because most of the hotels are full without reservation four weeks in advance.

- Food is only available in hotels, so there are facilities necessary to cook in the cars.
- Security is a big problem, day and night guards are absolutely necessary.
- Fuel is not always availble, therefor big fuel tanks are needed in the cars.
- Car repair is possible, but takes a lot of time and you should have all spare parts with you.

The poeple only speak russian (or sometimes german), but are very friendly and will always try to help if there are problems.

3. Summary

In the second half of 1991 the MTLRS#1 was operating successfully in Riga and Simeiz to collocate the fixed laser ranging stations on this places.

The results of the collocation shows no significant problem at the Riga fixed slr station. The collocation in Simeiz is not yet computed.

To operate and transport a dedicated geodetic system like MTLRS#1 in in the underdeveloped regions of the USSR big efforts and preparations are necessary to become as independent as possible from the local infrastructure.

REFERENCES

P. Sperber, L. Amberg, L. Beyer, G. Blenski, U. Hessels, R. Motz, in this Proceedings, *Results of the MTLRS#1 Upgrade, 1992.*

I. Prochazka, K. Kamal, B. Sopko, Proceedings of the seventh international Workshop on Laser Ranging Instrumentation S. 219, *Photodiode Based Detector Package for Centimeter Satellite Ranging, 1989.*

P. Sperber, U. Hessels, R. Motz in this Proceedings, *The new MTLRS#1 Receiver Package 1992.*

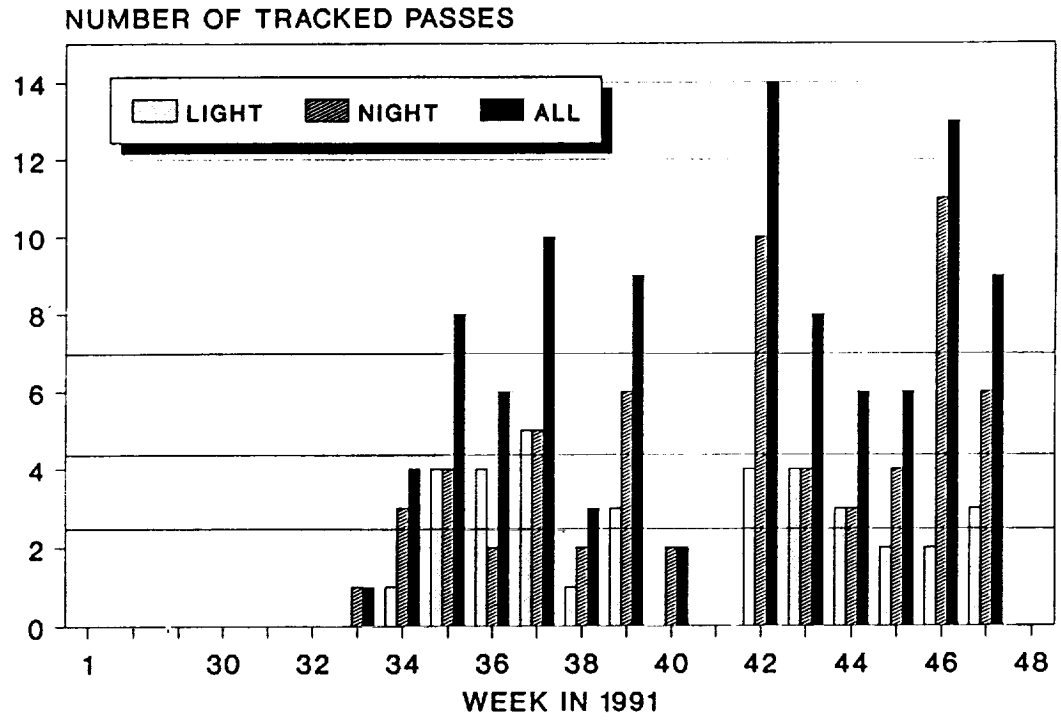

Fig. 1 Number of Lageos Passes in Riga and Simeiz

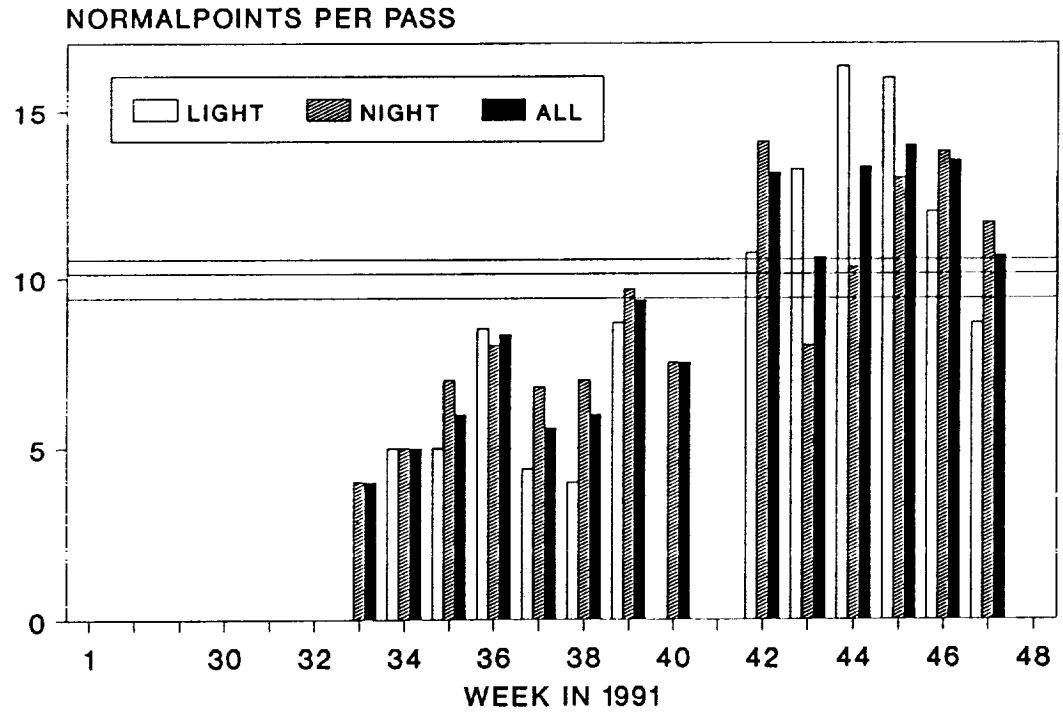

Fig. 2 Number of Normalpoints per Lageos pass in Riga and Simeiz

Results

Riga (1884)	MTLRS#1 (7560)
15868 Returns	27166 Returns (43 Passes)
R.M.S. 20 cm	1 cm (SPAD) - 2 cm (PMT)

Aug. 15 - Oct. 10

16 Simultaneous Passes

Range Bias 7560-1884 in cm	Epoch Bias 7560-1884 in microsec
-6.1	-24
-2.5	-30
-5.1	-58
-16.3	-23
-0.4	-4
-8.4	+66
-6.5 cm +- 5 cm	*-12 microsec +- 30*

Fig. 3 Results of the collocation in Riga

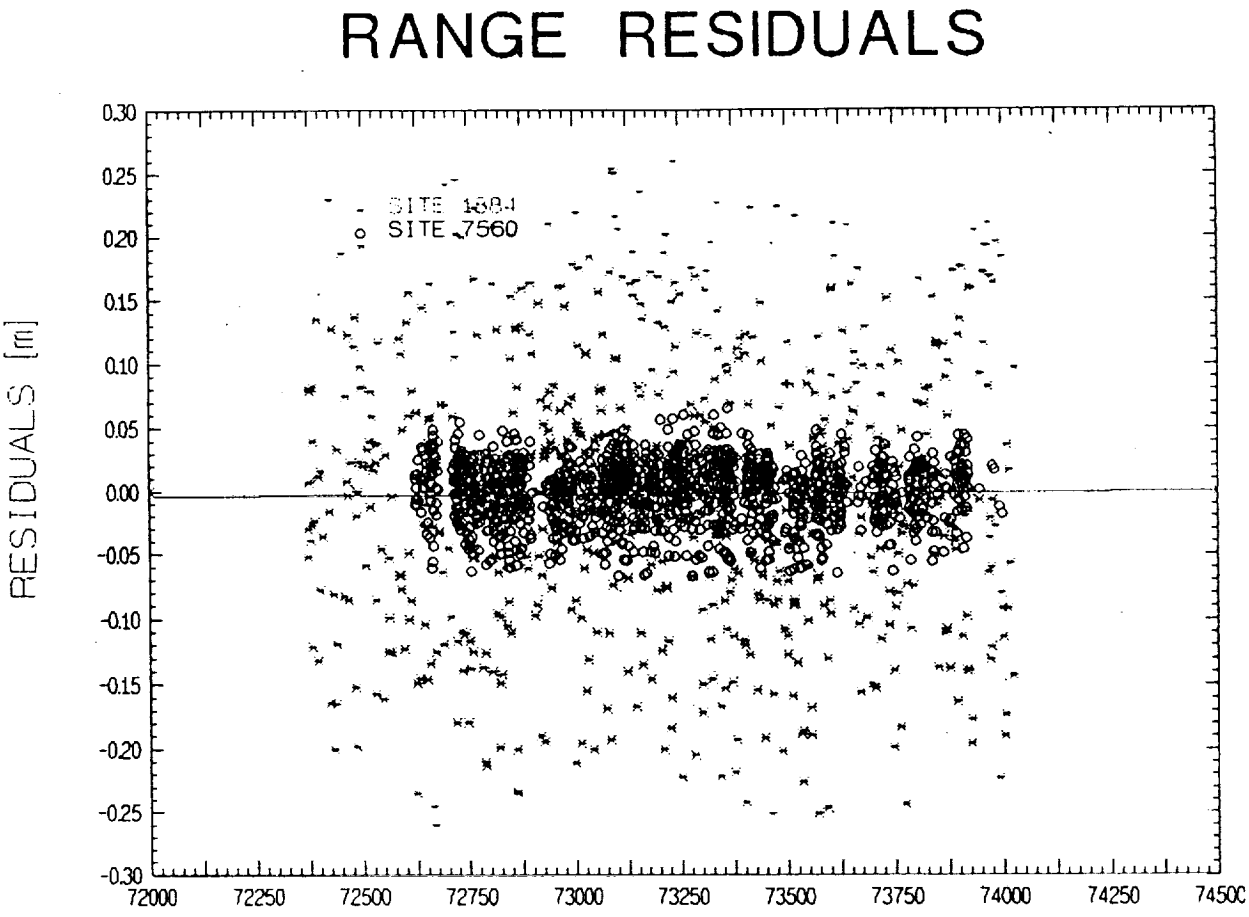

Fig. 4 Example of a Residual plot of a collocation pass between MTLRS-1 and the Riga fixed SLR station

Results

Simeiz (1873)	Kazivelli (1893)	MTLRS#1 (7561)
R.M.S. 10 cm	10 cm	1 cm - 2 cm
10 Passes	20 Passes	53 Passes

Oct. 14 - Nov. 23

Data not yet processed

Fig. 5 Results of the collocation in Simeiz

ETALON-1,-2 CENTER OF MASS CORRECTION AND ARRAY REFLECTIVITY

N94-15576

N.T.Mironov, A.I.Emetz
Main Astronomical Observatory of the Academy of Sciences
Ukraine, 252127, Kiev, Goloseevo
A.N.Zaharov, V.E.Tchebotarev
United Space Device Corporation
Russia, 111024, Moscow, Aviamotornaya st.,53

ABSTRACT. Center of mass correction to be applied to measured ranges to the ETALON-1,-2 satellites are considered. Numerical values of the correction and reflectivity from retroreflector array are computed. The variations of these values with satellite orientation are investigated.

1. INTRODUCTION

In 1989 two identical passive satellites, ETALON-1,-2, developed for precise laser ranging measurements were launched in the Soviet Union into nearly circular high orbits (about 20,000 km). It was reported that the distance between the center of mass and the plane of probable reflection is 558 mm ,Tatevian,1989.

To evaluate the ETALON-1,-2 satellites for Earth rotation applications, the International Earth Rotation Service (IERS) Directing Board has announced an SLR campaign for the tracking of these satellites. The campaign took place for three months period from September 1, 1990 to December 1, 1990.

To discuss the various aspects of analysis of the ETALON-1,-2 laser ranging data carried out at the number of scientific center, the Institute of Astronomy of the USSR Academy of Sciences and the Soviet Mission Control Center organized the International symposium "ETALON-91" which took place in Moscow during June 3-9, 1991. Recognizing the requirement for precise information characterizing the ETALON-1,-2 satellites, the participants of the International Symposium meeting in Moscow recommended

1) that complete design and orbit insertion information on the ETALON-1,-2 satellites be released to the analyst participat-

ing in the international programs,

2) that the international community undertake experiments to measure ETALON satellite characteristics, such as spin rate and direction, photometry, calorimetry and other.

We undertook the study of the center of mass correction and array reflectivity of the ETALON satellites in order to ensure their accuracy.

2. OPTICAL CUBE-CORNER SPECIFICATIONS

The optical cube corners on ETALON-1,-2 satellites have hexagonal entrance faces, each with a width of 27.0 mm across flats. The length from vertex to face is H=19.1 mm. The optical cube-corners are made of fused silica and the reflecting faces are aluminium coated. The index of refraction of the fused silica is n_1= 1.455442 at λ_1=0.6943 μm and n_2=1.460915 at λ_1=0.5320 μm.

The dihedral angles between the back faces have offsets in order to compensate for velocity aberration. The divergence of the cube corner is about 32 μrad for half-maximum level.

3. GEOMETRY OF THE ARRAY

The ETALON satellite is a sphere 1294 mm in diameter with 2146 retroreflectors distributed over the surface (Figure 1). Six of the cube corners are made of germanium for infrared wavelength and the others 2140 are made of fused silica for use at visible wavelength.

The optical cube corners are arranged in 306 lattice frame with 7 cube corners in each one. The lattice frame are mounted over 14 separated zones. Their orientation is shown in Figure 2. The distribution of the lattice frames and cube corners over the zone is illustrated in Figure 3. Table 1 lists such distribution for each zone.

The cube corners are recessed below the surface of the sphere by 5.5 mm. This recession, together with the fact that the front face of a cube corner is flat, places the center of the front face of the cube corner closer to the center of the satellite than 647.0 mm radius of the satellite.

Table 1. Distribution of the cube corners through zones
(+:Yes; 0:No)

System of cube corners	Zones													
	A_1	A_2	A_3	A_4	A_5	A_6	$Б_1$	$Б_2$	$Б_3$	$Б_4$	B_1	B_2	B_3	B_4
0	+	0	+	0	+	+	+	+	+	+	+	+	+	+
0.1-0.6	+	+	+	+	+	+	+	+	+	+	+	+	+	+
1.-3.	+	+	+	+	+	+	+	+	+	+	+	+	+	+
4.1-4.3	0	0	0	0	0	0	+	+	+	+	+	+	+	+
4.4; 4.5	0	0	0	0	0	0	+	+	+	+	+	+	+	+
4.6	0	0	0	0	0	0	+	+	+	+	+	+	+	+
Number of cube corners	133	132	133	132	133	133	175	175	175	175	161	161	161	161

4. OPTICAL CUBE CORNER REFLECTIVITY

The reflectivity E of the ETALON-1,-2 optical cube corners is given below as a function of incidence angle. The angle Φ is measured from the normal N to the front face, and the angle A^1 is the angle to the projection of the incident beam onto the front face; both these angles are shown in Figure 4,5. The variations of the cutoff angles for reflection Φ_c (and refracted angle Φ_c^1) with the azimuth A^1 are illustrated in Table 2 and Figure 6. These variations repeat every 60^o in A^1 and the values Φ_c for 30^o-A^1 are equal to those for 30^o+A^1.

Table 2. Cutoff angles for reflection Φ_c as a function of azimuth A^1

A^1, deg	Φ_{c1},deg	Φ_{c2},deg	Φ_c^1, deg
0	66.965	67.479	39.220
10	61.031	61.421	36.949
20	58.064	58.410	35.667
30	57.147	57.482	35.253

In computing the reflectivity E it was assumed that the cube corners had perfect-metal reflecting faces and no dihedral-angle offset. In Figure 7 each curve is the calculated total reflectivity and is proportional to the active reflecting area.The curves include reflection losses at the front face in entering and leaving the cube corner by laser beam. All curves are normalized to unity at normal incidence. The active reflecting area at normal incidence is 631.33 mm^2 for a hexagonal cube corner whose width W=27.0 mm across flats. The active reflecting area and the reflectivity repeat every 60^o in A^1 In additional, the values E for 30^o-A^1 are equal to those for 30^o+A^1. The curves for the two different wavelengths are fairly similar. The results were used to calculate the center of mass correction and array reflectivity.

5. ARRAY COORDINATE SYSTEM

The coordinate system used to describe the geometry of the array is as follows (Figure 8).As a rule the position and orientation of each cube corner in the array are given by the six numbers: x, y, z B,L,A. The origin of the x-y-z coordinate system is in the center of satellite. X,Y and Z are in the directions of the centers A_1, A_3 and A_2 zones respectively. The angles B and L are given in an $x^1-y^1-z^1$ coordinate system, which is parallel to the x-y-z system and the origin is in the center of front face of each cube corner. The azimuth angles A are given in $\xi-\eta-\zeta$ coordinate system. Its origin is at the center of the front face, its ξ axis normal to the front face, ζ in the direction of increasing B, and η in the direction of increasing L. The orientation angle A is measured counterclockwise from ζ axis to the projection of one of the back edges of the cube corner onto front face, as shown in Figure 8.

The direction of the incident beam V in the array coordinate system is given by the angles φ and λ: both these angles are shown in Figure 8. To compute the incidence angles Φ and A^1 on the cube corner, the vector V must be expressed in the $\xi-\eta-\zeta$ coordinate system (Figure 8). The conversion between the coordinate systems of the array and incident beam is accomplished by rotating the coordinate system of V first about the z-axis by the angle L unti-

clockwise and then about new y-axis by the angle B clockwise.

For the ETALON-1,-2 cube corners the angles A are unknown but the cube corners have been installed so as to give a uniform diffraction divergence independent of satellite orientation. The divergence of the retroreflector array is about 42 μrad for half - maximum level. Taking into account these aspects and the total reflectivity of the ETALON-1,-2 optical cube corners and their recessions,the active reflecting area of each retroreflectors has been averaged for $A^1=0^o$, 1^o,...,30^o.

6.METHOD OF COMPUTING THE CENTER OF MASS CORRECTION

The center of mass correction to be applied to measured ranges is the distance of the centroid of the computed total energy of the return from the center of gravity of the satellite. Computation of the range correction includes a correction for the optical path length of the ray within the cube corner. The correction listed is the one-way correction

$$\rho = \sum_{k=1}^{N} \rho_k E_k \Big/ \sum_{k=1}^{N} E_k$$

where ρ_k is the distance of the apparent reflection point for the k-th retroreflector from the plane through the center of mass of the satellite perpendicular to the incident beam. Constant E_k giving the intensity of the reflection from the k-th cube corner is proportional to the active reflecting area. N is the number of the cube corners contributing to the reflected signal.

The apparent reflection point as a function of the angle Φ between the incident beam and the normal to the front face of the cube corner is given by the expression

$$\rho_k = r\cos\Phi_k - H\sqrt{n^2-\sin^2\Phi_k}\ ,$$

where r=distance from the center of the satellite to the front face of the cube corner (641.7 mm), Φ_k=the incidence angle on the k-th cube corner, H=the length of the cube corner (19.1 mm), n=the index of refraction.

In computing the center of mass correction ρ and array reflectivity $E(=\sum E_k)$, the cube corners have been modeled as isothermal, geometrically perfect reflectors with perfect reflecting coatings

on the back faces. The reflection losses at the front face as the laser beam enters and leaves the cube corners are taken into account.

7. APPARENT REFLECTION POINT AND SPREAD IN RANGE

The cube corners contributing to the reflected signal are contained in a spherical cap whose angular radius (half angle) is the cutoff angle of the cube corner. The earliest possible reflection would come from a reflector directly facing the incident beam, and the latest, from a cube corner near the cutoff angle. Apparent spread in range is the difference between the apparent reflection points for these two cases along the direction of illumination.

Since the cube corners are nonuniformly distributed over the sphere of the ETALON-1,-2 and recessed below the satellite surface there are variations of the earliest and latest reflection points. Table 3 lists the apparent reflection points along the line of sight measured from the center of satellite for various cases: 1) the earliest possible reflection point (a cube corner whose face is normal to the incident beam); 2) the earliest point where an incident beam in the center of A_2 zone could be up to about 4^o from nearest cube corner (replacing an optical cube with an germanium cube); 3) the earliest point where an incident beam could be up to about 8^o from the nearest cube corner (replacing two lattice frame of 14 cube corners with the supporting holder); 4) the last possible reflection point where the active reflecting area goes to zero; 5) the last possible reflection point where there is a sharp decrease in reflectivity because of the recession of the cube corners.

Replacing an optical cube corner in zones A_2 and A_4 with a germanium cubes, which is opaque to visible light, reduces the distance of apparent reflection point by about 1.5 mm. The maximum variation of the earliest reflection point is about 5.9 mm in replacing 14 cube corners with supporting holders in B_1, B_2, B_3 and B_4 zones. The total range spread without taking into account the recession of the reflectors is about 400 mm. The recession reduces the range spread approximately by 2 times. Figure 9 illu-

strates these results.

Table 3. Apparent reflection points for various incident angles

Φ,deg	λ,μm	n	ρ_k,mm	Reflection point
0	0.6943	1.4554	613.9	Earliest reflection point
0	0.5320	1.4609	613.8	Earliest reflection point
3.9287	0.6943	1.4554	612.4	Nearest to the center A_2 zone
3.9287	0.5320	1.4609	612.3	Nearest to the center A_2 zone
7.8574	0.6943	1.4554	608.0	Nearest to the supporting holder
7.8574	0.5320	1.4609	607.9	Nearest to the supporting holder
43.6000	0.6943	1.4554	440.2	Latest recession reflection point
43.6000	0.5320	1.4609	440.1	Latest recession reflection point
66.9650	0.6943	1.4554	229.6	Latest of cutoff angle reflection
67.4790	0.5320	1.4609	224.2	Latest of cutoff angle reflection

8. VARIATION OF THE CENTER OF MASS CORRECTION WITH SATELLITE ORIENTATION

The surface of the ETALON-1,-2 satellites is nonuniformly covered by the cube corners. As a result the center of mass correction and the reflecting properties depend on the satellite orientation. A set of 2522 sampling points were distributed over the surface of the sphere to study the variation of the center of mass correction with ETALON-1,-2 orientation. Table 4 lists these results for two laser wavelengths.

The mean range correction ρ for ETALON-1,-2 is about 576.0mm for all orientations. The standard deviation of range correction $\Delta\rho$ is 3.2mm. The results obtained show the extreme variations in the range correction over all orientations from a high of about 583.4mm to a low of about 567.3mm. The difference between the maximum and minimum range correction is 16.1mm.

The variations of the range correction with the period of 90^0 in λ coordinate for orientation of the ETALON-1,-2 satellites are due to the symmetry in the configuration of the cube corners from different viewing angles.

Table 4. Variation of the center of mass correction with ETALON-1,-2 orientation

λ_1=0.6943 μm				λ_2=0.5320 μm			
Correction		Orientation		Correction		Orientation	
ρ,mm	$\Delta\rho$,mm	φ,deg	λ,deg	ρ,mm	$\Delta\rho$,mm	φ,deg	λ,deg
583.5	7.5	0	$0+90^0$k	583.3	7.5	0	$0+90^0$k
567.5	-8.6	-45	$5+90^0$k	567.1	-8.6	-45	$5+90^0$k
576.1	0.0	45	$75+90^0$k	575.8	0.0	45	$75+90^0$k

where k is digit.

The average range corrections at each longitude and latitude have also been computed to look for systematic effects. Figures 10, 11 illustrate the variations of the range corrections at all longitudes and latitudes. They are contained within 16.1mm interval and have periodical components along φ and λ coordinates.

9. VARIATION OF THE ARRAY REFLECTIVITY WITH SATELLITE ORIENTATION

Array reflectivity over 2522 orientations of the ETALON-1,-2 satellites have been studied. Table 5 lists these results for two wavelengths.

The mean array reflectivity for ETALON-1,-2 is about 65.8 cube corners for all orientations. The standard deviation of the array reflectivity is 3.9 cube corners. The results obtained show extreme variations in the array reflectivity over all orientations from a high of about 74.2 cube corners to a low of about 53.8 cube corners for all orientations. The difference between the maximum and minimum array reflectivity is about 20.4 cube corners that is the variation of the reflected energy is about 30 percents over all orientations.

Table 5. Variation of the array reflectivity with ETALON-1,-2 orientation

λ_1=0.6943 μm				λ_2=0.5320 μm			
Reflectivity		Orientation		Reflectivity		Orientation	
E,c.c.	E,c.c.	φ,deg	λ,deg	E,c.c.	E,c.c.	φ,deg	λ,deg
74.1	8.6	35	$45+90^{0}k$	74.4	8.6	35	$45+90^{0}k$
53.6	-12.0	-45	$5+90^{0}k$	53.9	-12.0	-45	$5+90^{0}k$
65.6	0.0	0	$25+90^{0}k$	65.9	0.0	0	$25+90^{0}k$

where k is digit.

The variations of the array reflectivity with the period of 90 degrees in λ coordinate for orientation of the ETALON-1,-2 satellites are due to the symmetry in the configuration of the cube corners from different viewing angles.

For the purpose of illustrating more detailed studies of the reflectivity properties, the sampling points have been looked at individually to find one whose properties are close to the average for all orientations. The point at $\varphi=45^{0}$, $\lambda=75^{0}$ has nearly the average range correction and reflectivity, so it has been used for above purpose. Figures 12 are histograms of the contribution to the reflected signal from each 1-cm interval along the line of sight starting from the earliest reflection point. The origin of the distance scale is the center of satellite. These histograms are for a direction of illumination given by $\varphi=45^{0}$ and $\lambda=75^{0}$. For this direction the total effective reflecting area is 66.8 times the area of one cube corner, and the mean apparent reflection point is 576.0mm from the center of the satellite. The cube corner shown on the histogram is the closest possible position to the observer.(None of the cube corner points exactly at the observer for this particular direction of illumination. The earliest and latest apparent reflection points for this case are 613.5mm and 440.7mm, respectively). Table 6 lists the data used to plot the histogram: the equivalent number of cube corners at normal inci-

dence, the percentage of the total return and the cumulative percentage in each 1-cm interval,starting from the earliest reflection point.

Table 6. Total return in each 1-cm interval starting from the earliest apparent reflection point

Interval	Equivalent number of cube corners		% of total return		Cumulative %	
	λ_1	λ_2	λ_1	λ_2	λ_1	λ_2
1	16.62	17.24	25.00	25.68	25.00	25.68
2	9.38	7.90	14.11	11.77	39.11	37.45
3	9.22	8.16	13 87	12.16	52.98	49.61
4	5.38	8.87	8.09	13.21	61.07	62 82
5	4.51	5.53	6.78	8.23	67.85	71.05
6	5.23	4.17	7.87	6.22	75.72	77.27
7	3.99	3.58	6.00	5.33	81.72	82.60
8	3.46	3.31	5.21	4.93	86.93	87.53
9	2.78	2.79	4.18	4.16	91.11	91.69
10	2.41	1.98	3.62	2.94	94.73	94.63
11	1.26	1.38	1.89	2.06	96.62	96.69
12	1.21	0.97	1.82	1.45	98.44	98.14
13	0.56	0.77	0.85	1.14	99.29	99.28
14	0.28	0.24	0.42	0.35	99.70	99.63
15	0.12	0.16	0.18	0.25	99.88	99.88
16	0.07	0.06	0.10	0.09	99.98	99.97
17	0.02	0.02	0.02	0.03	100.00	100.00

A quarter of the return energy comes from the first 1-cm interval, over half the return energy comes from the first 3-cm interval, and over 90% comes from the first 9-cm interval. The center of mass correction is at 576.0mm, which is 37.5mm in back of the first reflection point.

The average array reflectivity at each latitude and longitude have also been computed to look for systematic effects. The

variations of the average array reflectivity at all latitudes and longitudes are contained within 21 cube corners and have periodical components. Figures 13 and 14 illustrate these regularities. These variations are similar to ones in the range correction of ETALON-1,-2 satellites.

The effects of the recession of cube corners in concentrating the energy and computing the range correction have been studied. The center of mass correction and array reflectivity, if the cube corners were not recessed, would be 540.7mm and 126.53 cube corners respectively.

10. CONCLUSION

The ETALON-1,-2 center of mass correction is about 576.0mm for both laser wavelengths. This value is 18mm more than value which was published by Tatevian,1989. The range correction has periodical peak-to peak variations of about 2 cm with satellite orientation. These peculiarities give the possibility to derive for ETALON-1,-2 spin rate and direction using the precise laser ranging measurements to the satellites with SLR systems of 3-rd generation.

The mean array reflectivity for ETALON-1,-2 satellites is about 66 cube corners. Difference between the maximum and minimum array reflectivity is about 21 cube corners or 30% over all satellite orientations.

Such regularities in ETALON-1,-2 center of mass correction and array reflectivity are due to the symmetry with respect to the X-axis in the dissemination of the cube corners over the satellite surface.

REFERENCES

Tatevian S.K.Satellite report: ETALON. Satellite laser ranging newsletter.1989,June,p.5.

Pochukaev V.N., Schutz B.E., Tatevian S.K. International symposium on ETALON satellites. Satellite laser ranging newsletter. 1991,April,p.22.

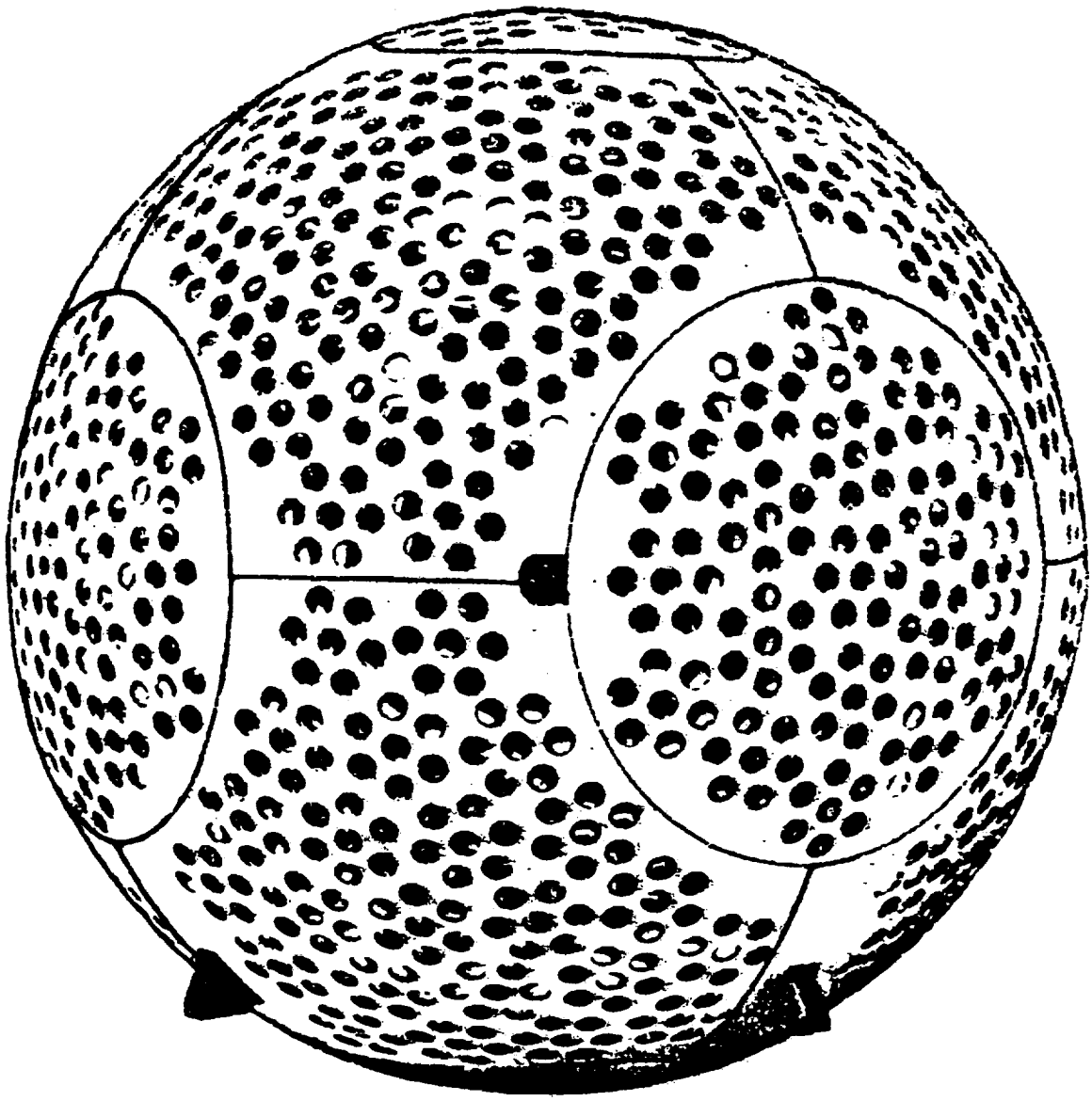

FIG. 1. ETALON-1,-2 SATELLITE

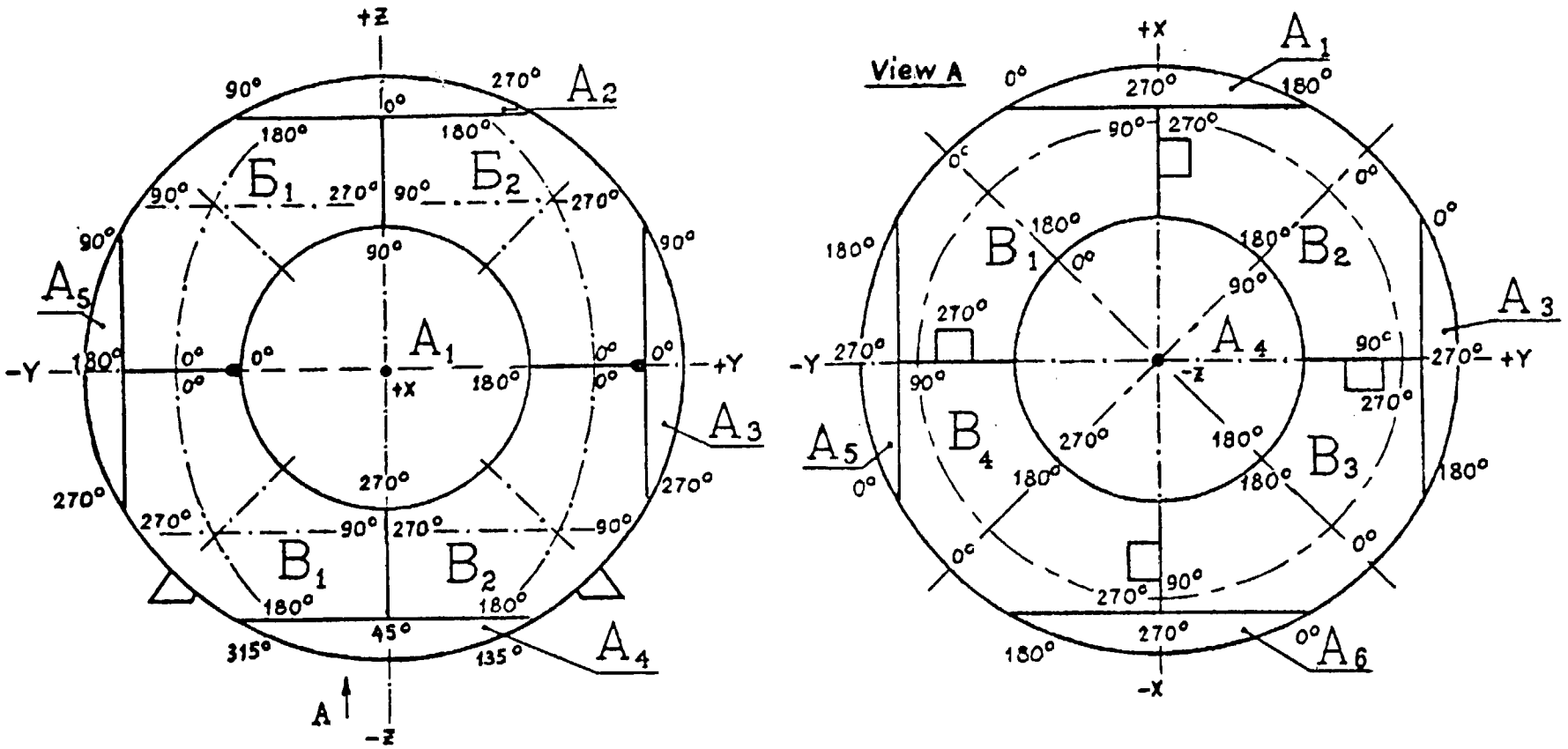

FIG.2. ZONES OF THE RETROREFLECTORS AND THEIR ORIENTATION

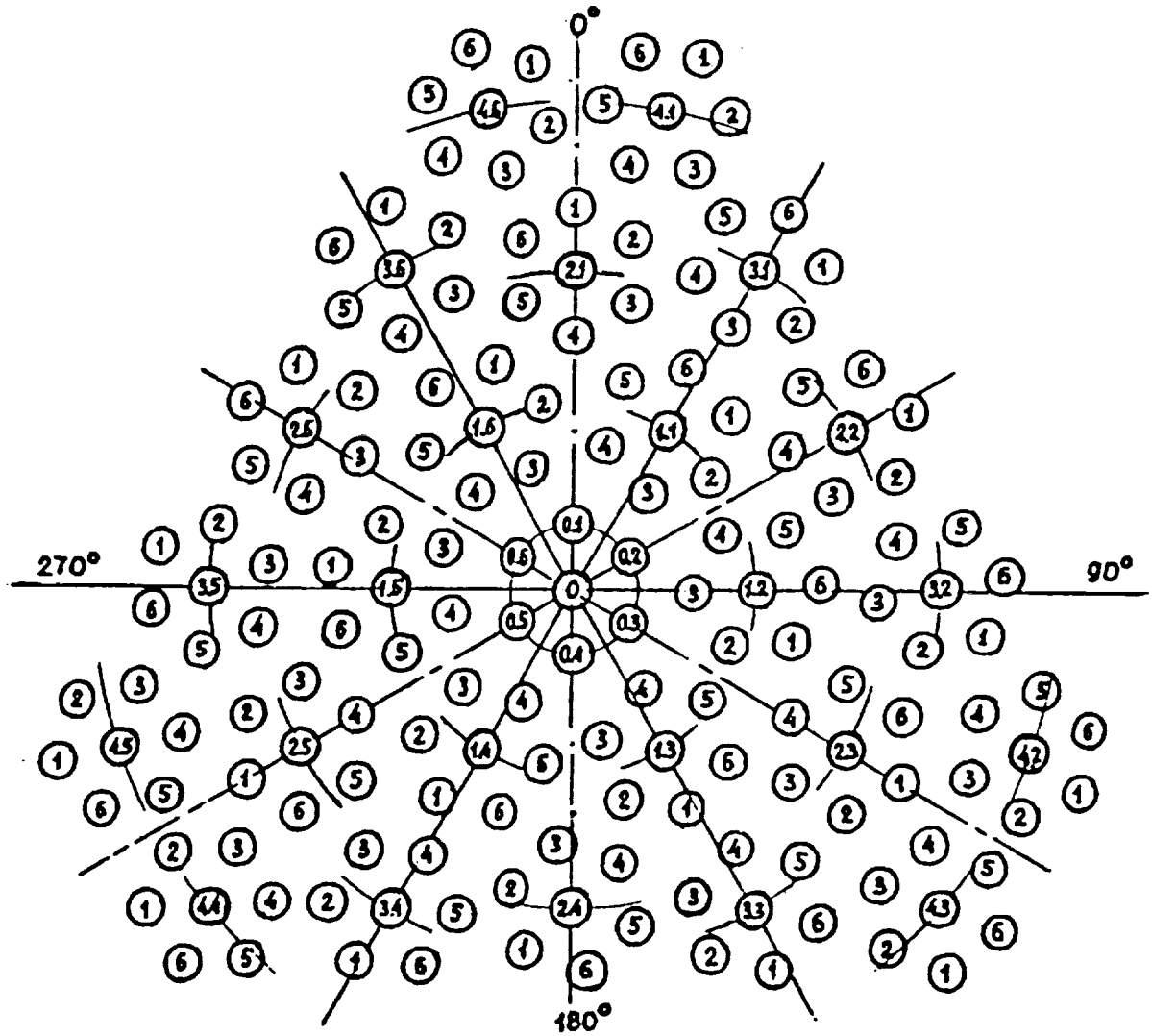

FIG. 3. DISTRIBUTION OF THE LATTICE FRAME AND RETROREFLECTORS OVER A ZONE

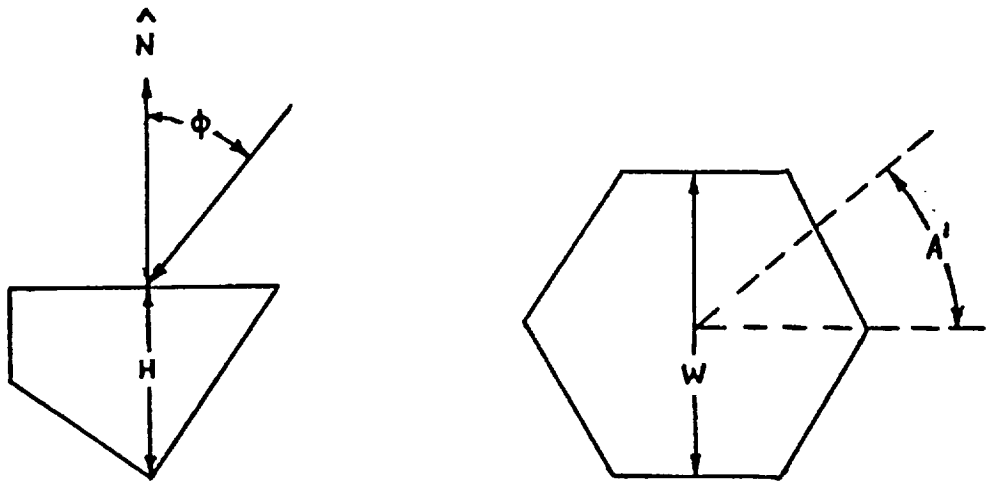

Fig. 4. Direction of incident beam

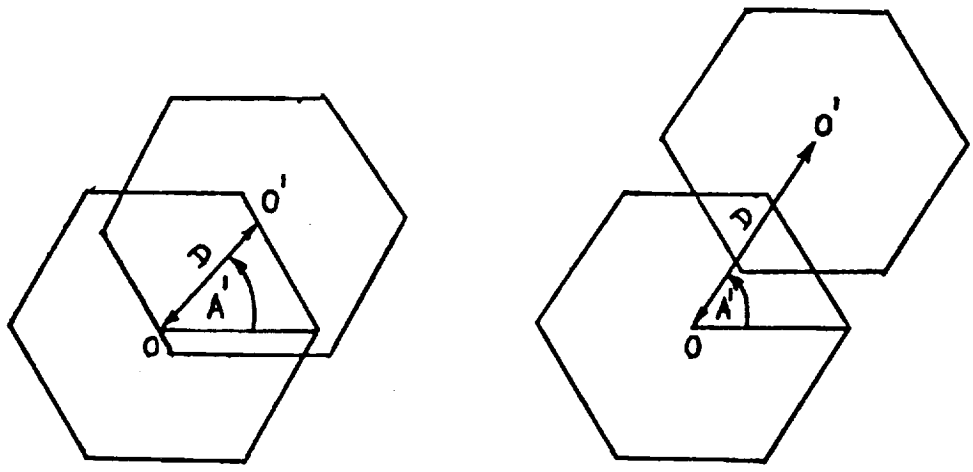

Fig. 5. Active reflecting area: separation of input and output apertures

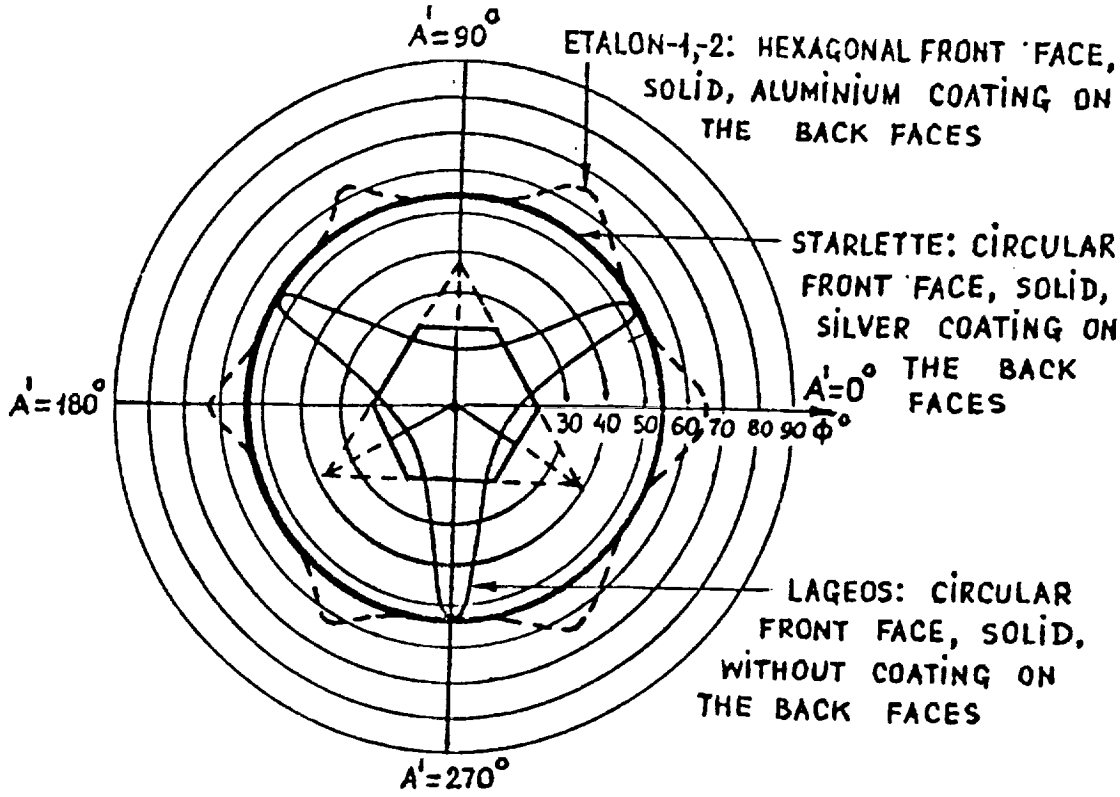

FIG. 6. VARIATIONS OF THE CUTOFF ANGLES FOR REFLECTION Φ WITH THE AZIMUTH A'

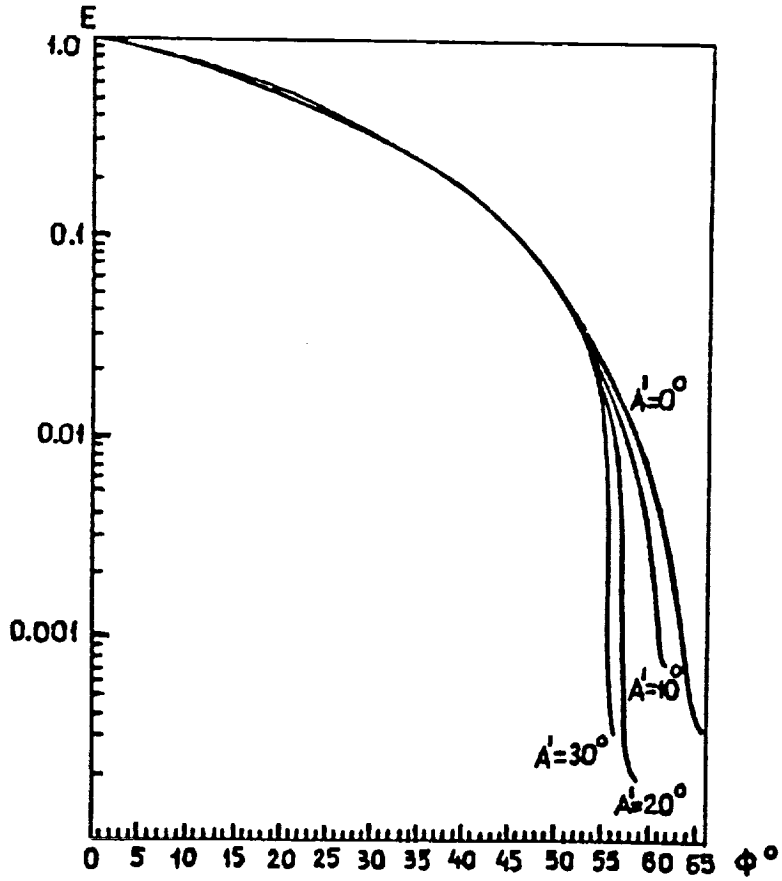

FIG.7. TOTAL REFLECTIVITY OF ETALON-1,-2 CUBE CORNER FOR DIFFERENT AZIMUTHS A', λ=0.6943μm.

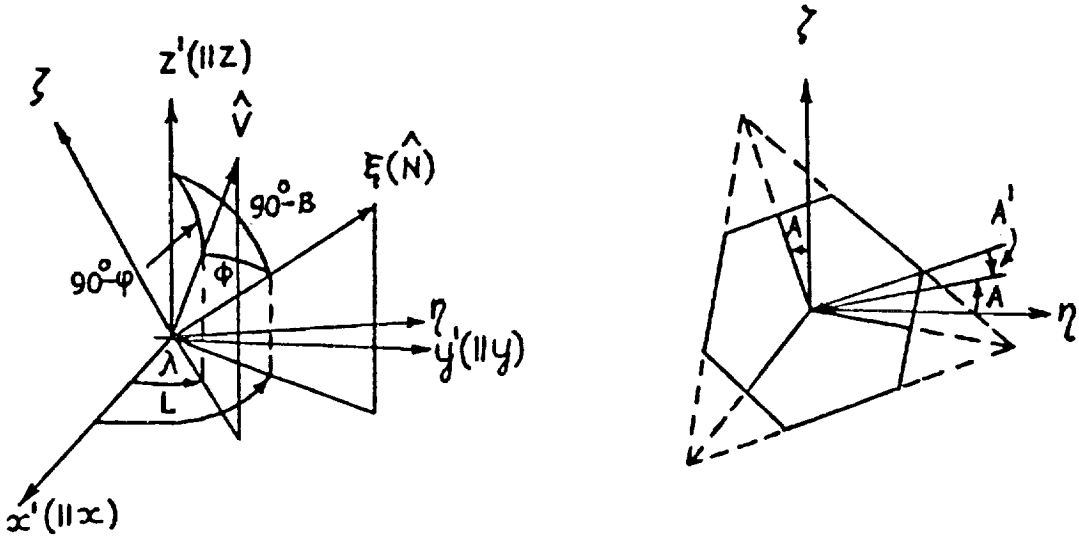

FIG. 8. COORDINATE SYSTEMS FOR RETROREFLECTOR POSITION AND ORIENTATION

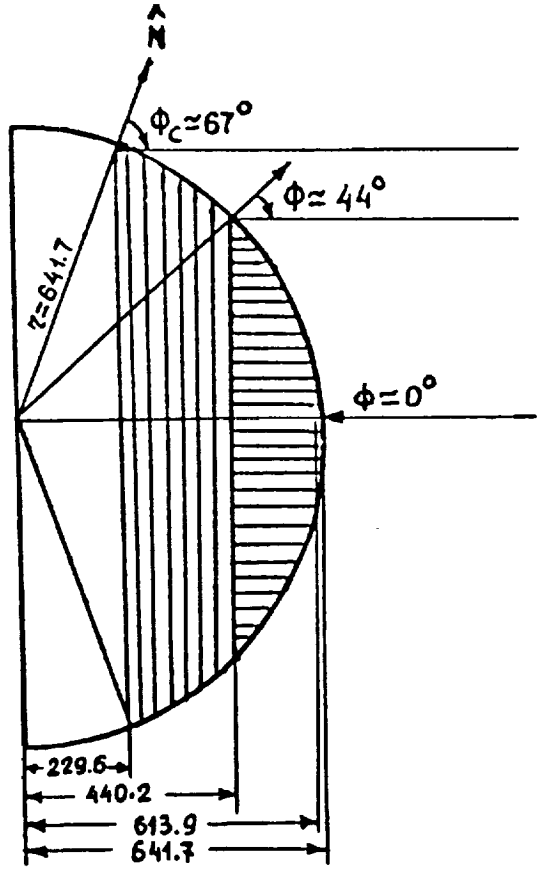

Fig. 9. APPARENT REFLECTION POINTS AND SPREAD IN RANGE

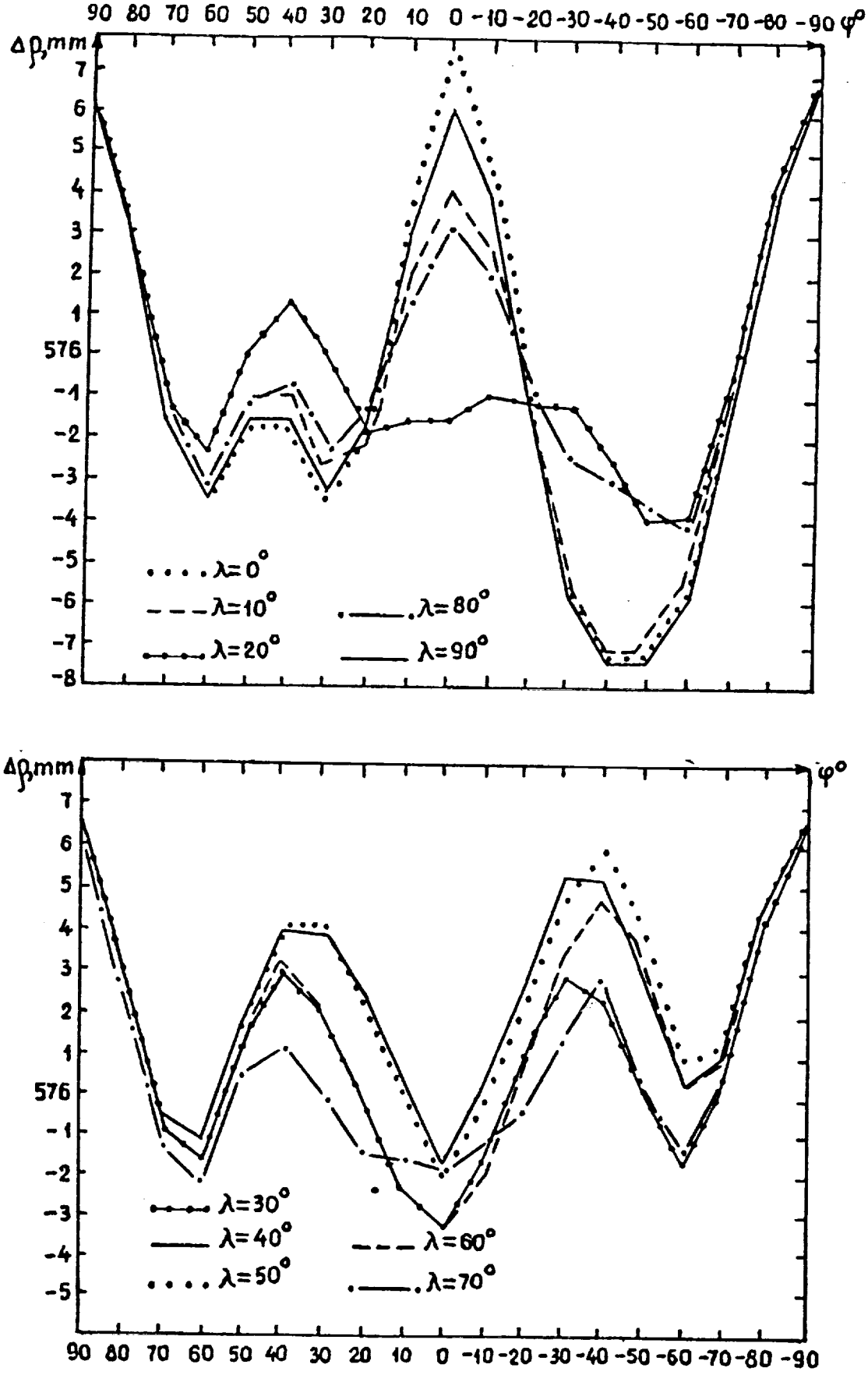

FIG. 10. VARIATION OF ETALON-1,-2 CENTER OF MASS CORRECTION AT EACH LONGITUDE

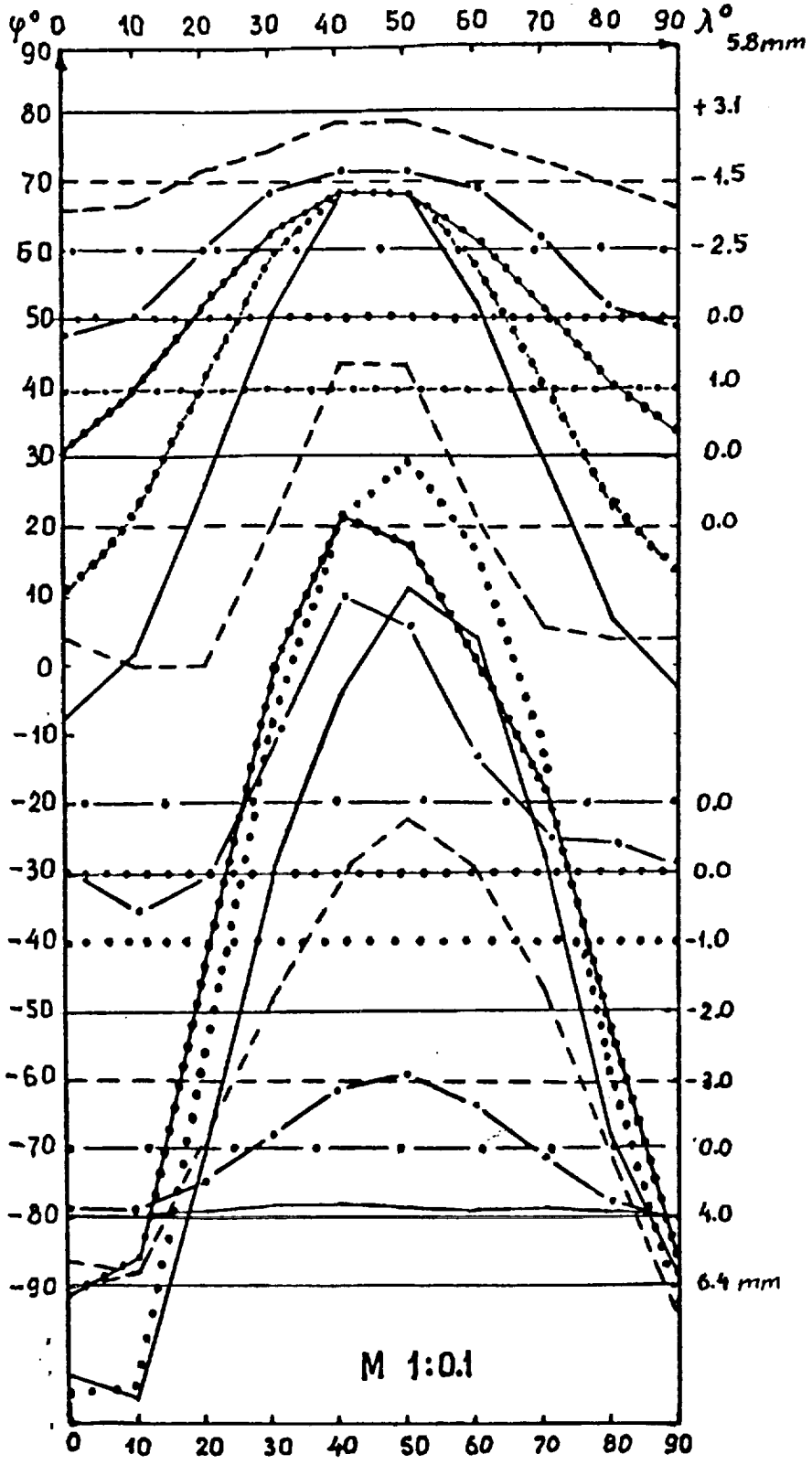

Fig. 11a. VARIATION OF ETALON-1,-2 CENTER OF MASS CORRECTION AT EACH LATITUDE

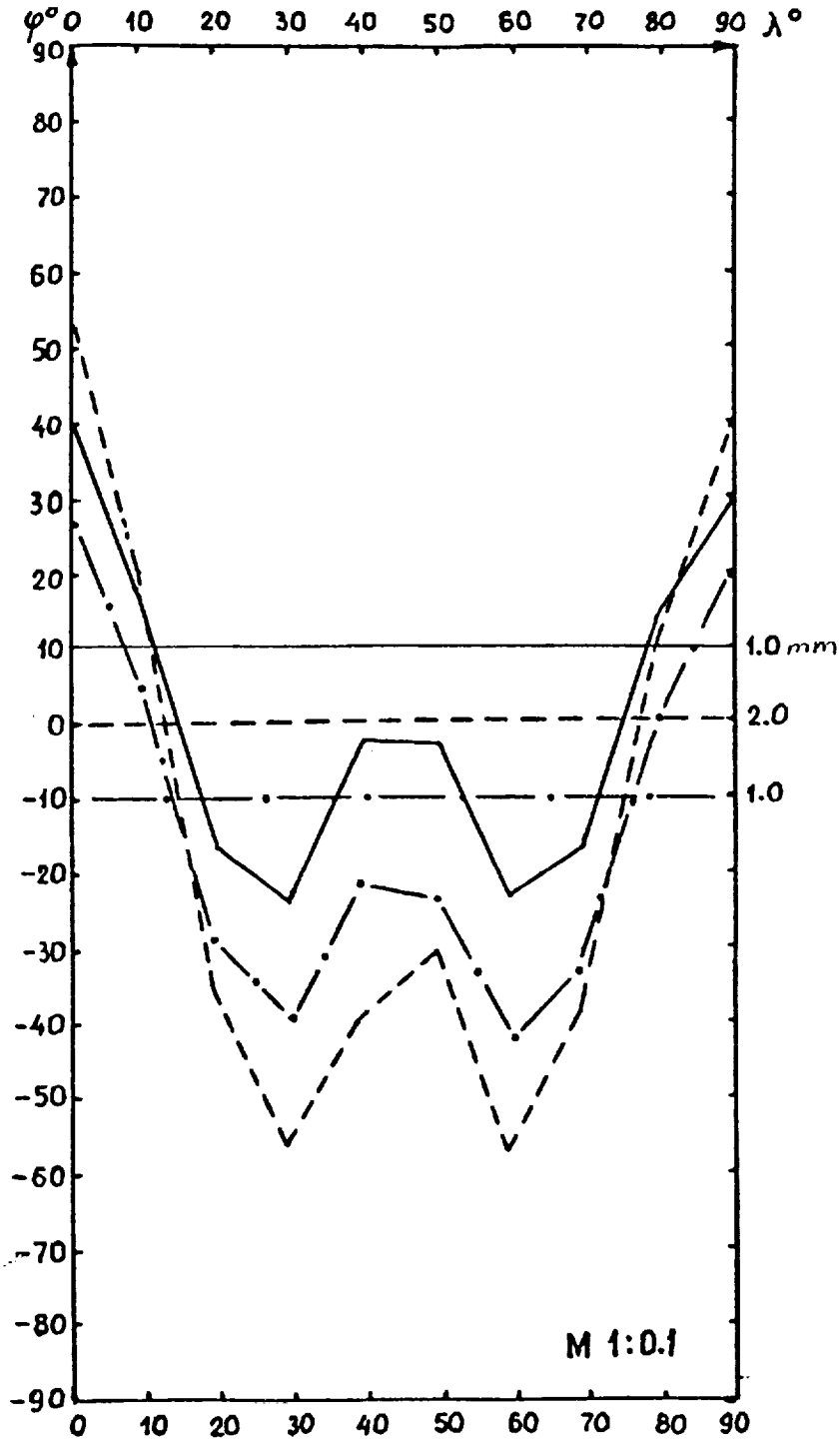

FIG. 11b. VARIATION OF ETALON-1,-2 CENTER OF MASS CORRECTION AT EACH LATITUDE

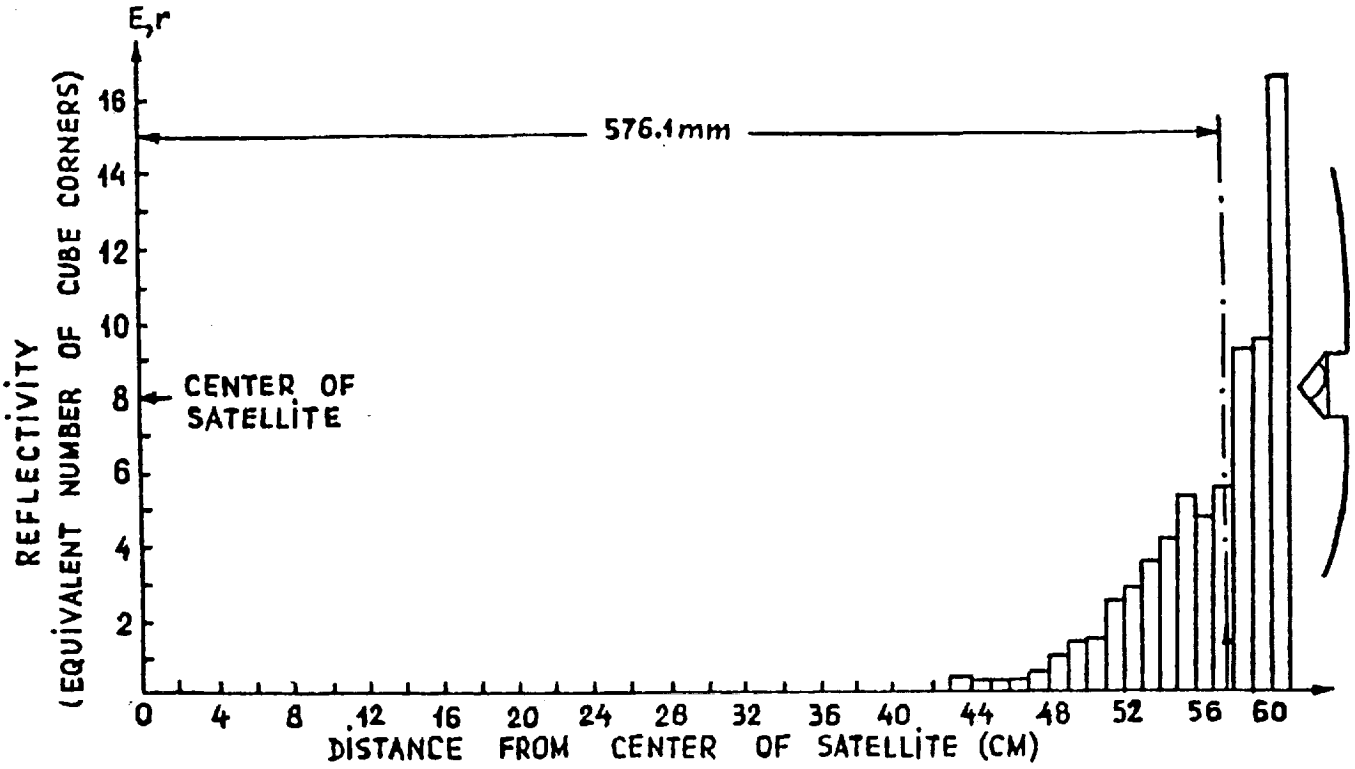

Fig. 12a. Reflectivity histogram of ETALON-1,-2; λ=0.6943 μm

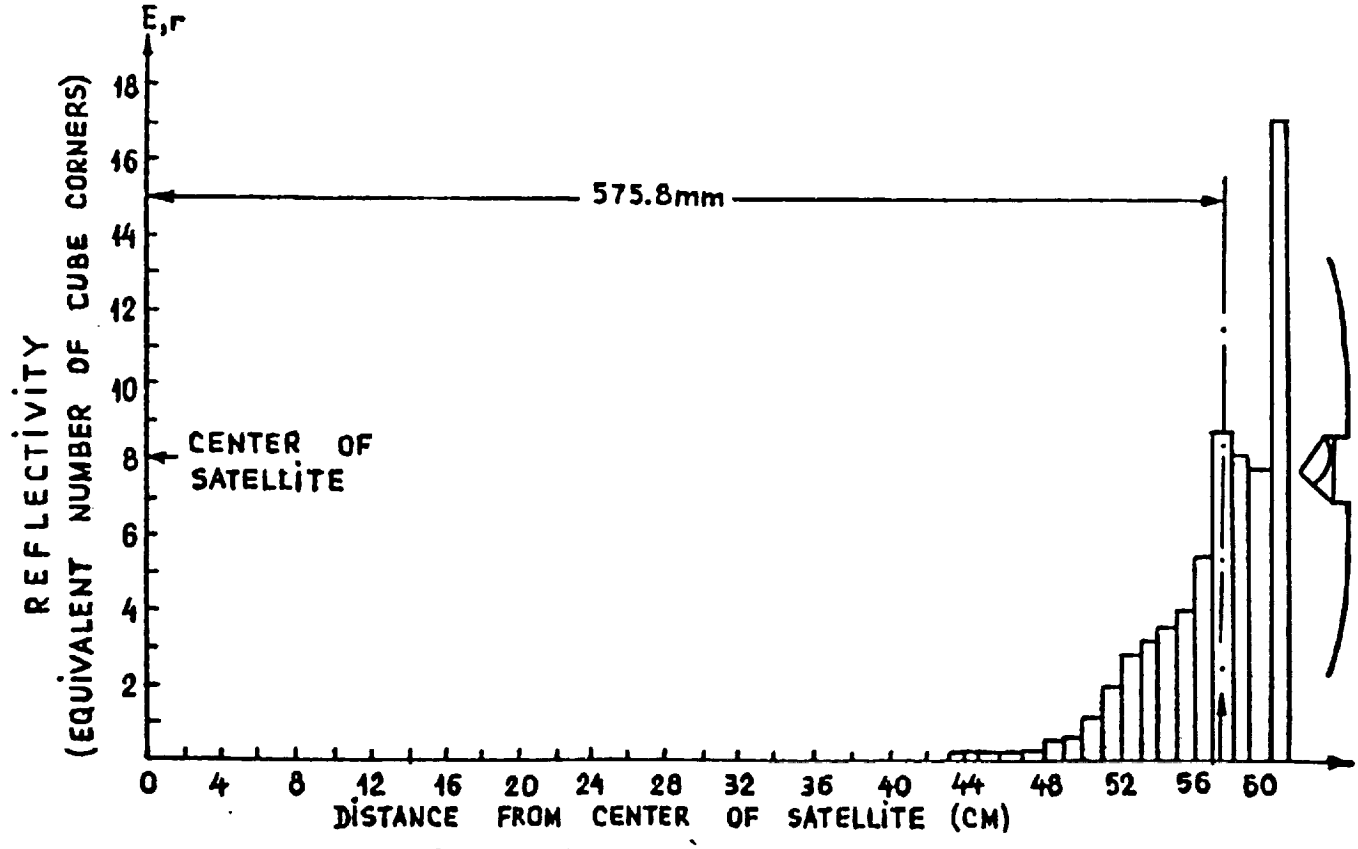

Fig. 12b. Reflectivity histogram of ETALON-1,-2; λ=0.5320 μm

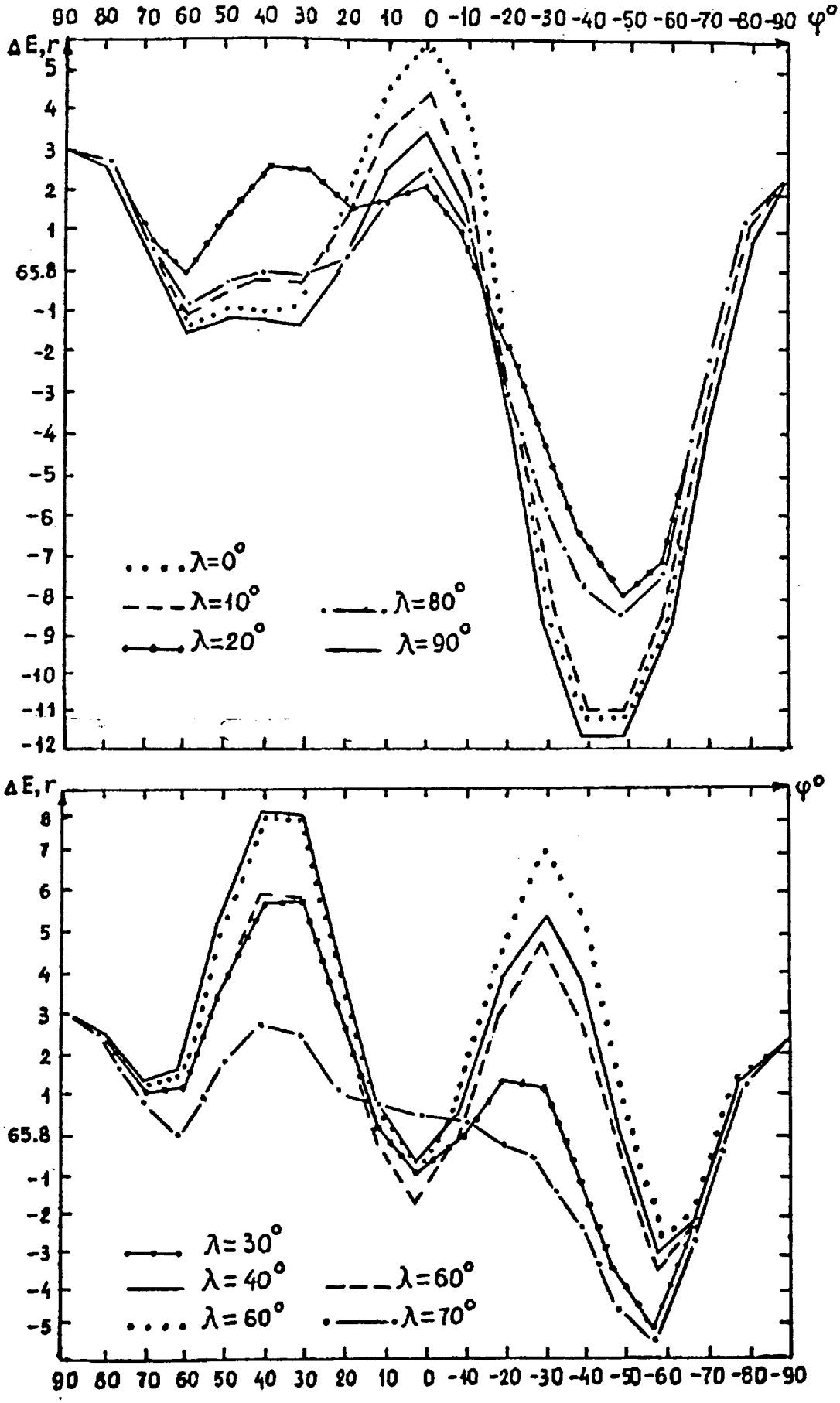

FIG. 13. VARIATION OF ETALON-1,-2 REFLECTIVITY AT EACH LONGITUDE

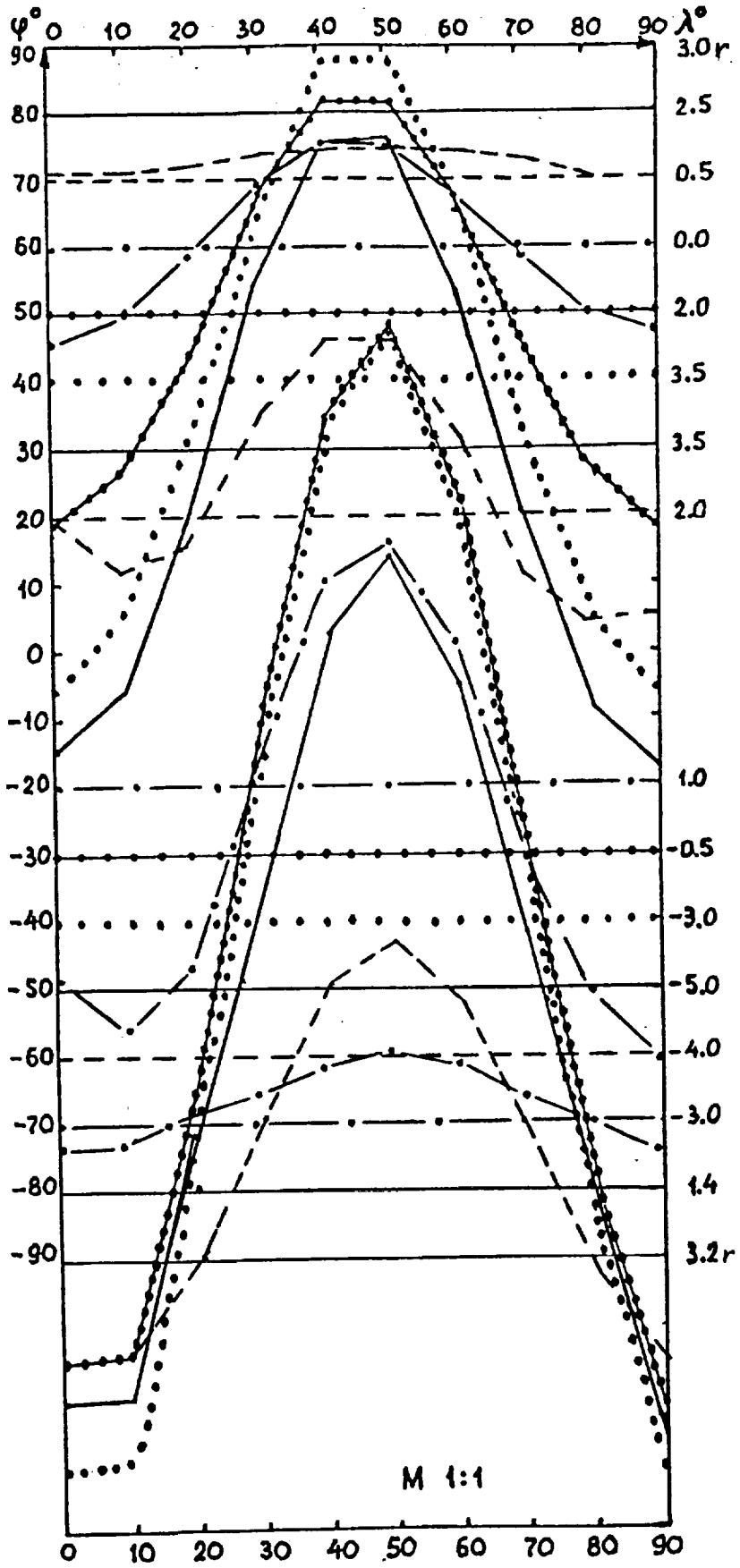

FIG. 14a. VARIATION OF ETALON-1,-2 REFLECTIVITY AT EACH LATITUDE

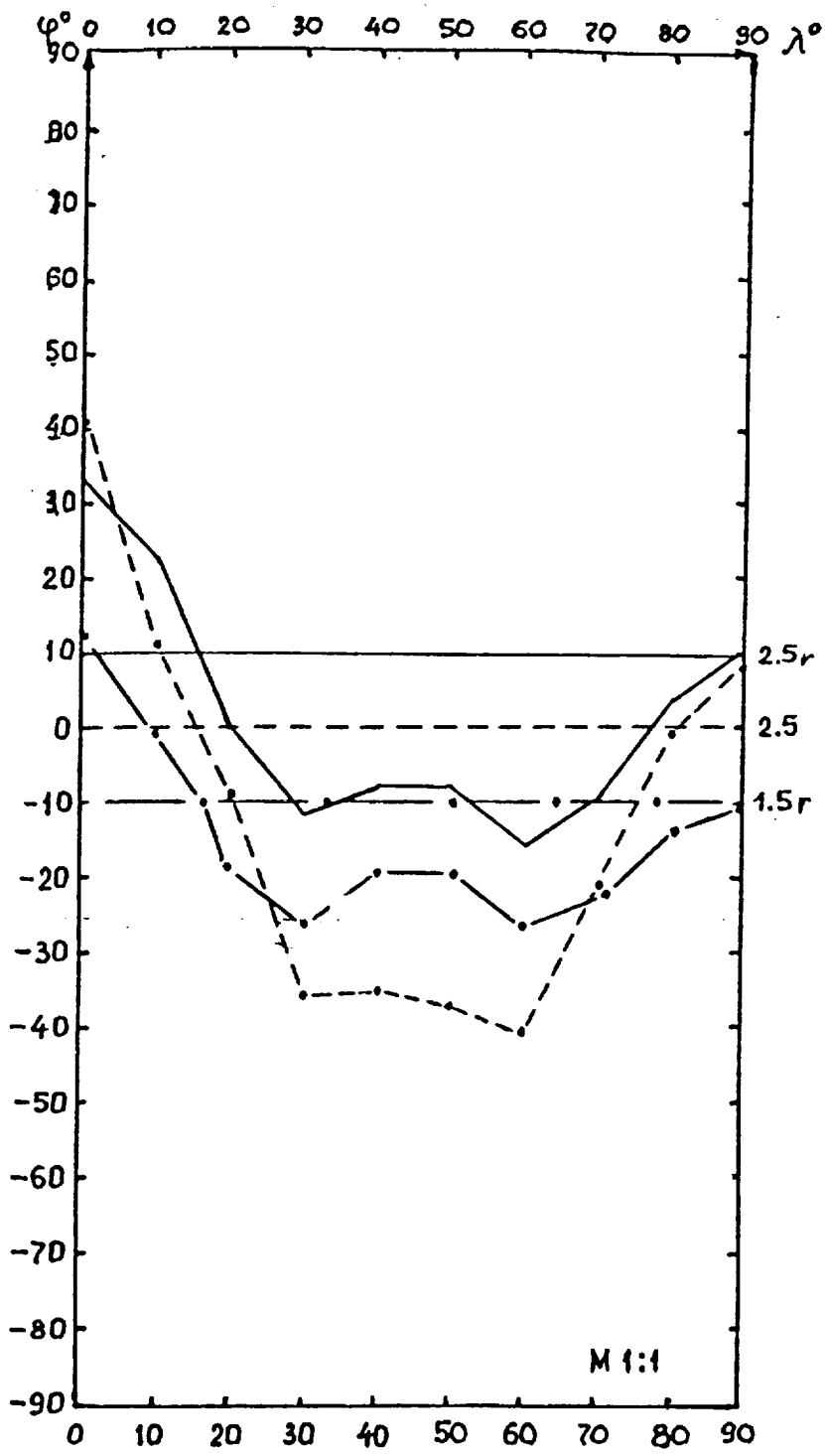

FIG. 14b. VARIATION OF ETALON-1,-2 REFLECTIVITY AT EACH LATITUDE

Test Results from LAGEOS-2 Optical Characterization Using Pulsed Lasers

Thomas Varghese, Michael Selden,Thomas Oldham,Christopher Clarke
Allied Signal Aerospace Company,
BFEC/CDSLR
10210 Greenbelt Road
Seabrook, MD 20706
USA

Thomas Zagwodzki
Photonics Branch
NASA Goddard Space Flight Center
Greenbelt
Maryland, 20770
U.S.A

Abstract

Laser Geodynamic Satellite (LAGEOS-2) has undergone extensive optical testing at NASA Goddard Space Flight Center during 1989. The techniques included measuring the far field diffraction pattern using cw and pulsed lasers. In the pulsed measurement technique, response of the satellite was studied by measuring the FFDP as a function of pulsewidth, wavelength, polarization, position in the FFDP, detector/processing techniques, and satellite orientation. The purpose of the pulsed laser testing was two-fold: (1) Characterize the satellite optical response with the detector and signal processing electronics currently used in most SLR stations using the Portable laser ranging standard, and (2) to characterize the satellite response for various conditions using the highest bandwidth optical detector (streak camera) available for the next generation of SLR technology. The portable ranging standard employed multiple measurement devices and an optical calibration scheme to eliminate range-dependent and amplitude-dependent systematics. These precautions were taken to eliminate/minimize instrumental errors and provide maximum accuracy. For LAGEOS orbit (6000 Km) ground stations are located 34 to 38 μ-radians off the axis of the return signal from the satellite; therefore an optical mask was used to restrict the field of view (FOV) of detection to this annular region of the far-field diffraction pattern (FFDP). The two measurement techniques were implemented using an aperture sharing scheme and complemented each other by providing mutual verification.

The results indicate a variation of range correction as a function of satellite orientation and location within the far-field diffraction pattern. Range correction as a function of wavelength shows a maximum at 532 nm. For other wavelengths, the FFDP of normal-incidence cube-corners is detuned, providing a greater contribution to the integrated response from cube-corners farther away from the observer. Constant-fraction processing of the detected pulse provided more consistent results than peak and leading-edge. Changes in the orientation of the E-vector of the linearly polarized light showed a systematic variation of $\lesssim$ 2mm in the polar regions of the satellite. A consistent difference in RC of $\simeq$ 2 mm between linearly polarized light and circularly polarized light was also observed. The test results showed that a range correction of $\simeq$ 251 mm is applicable to the third-generation SLR systems operating at the multi-photoelectron (MPE) level. The use of short ($\simeq$15 ps) laser pulses and streak cameras would provide time resolved signature of the satellite allowing improved (1mm accuracy) range correction.

BACKGROUND

- LAGEOS-1 launched on May 4, 1976; 5900km orbit; 110° inclination.
- Prior to launch, the satellite was optically tested (532nm, 60ps) at GSFC.
- Remarkable progress in SLR technology over 15 years and the projections for the future required understanding of LAGEOS-2 LRA better than LAGEOS-1.
- Major emphasis to accurately (submillimeter) determine the range offset to satellite CM from the effective reflection point.
- Elaborate experimental schemes with state of the art instrumentation and expanded parameteric study than LAGEOS-1.
- Satellite manufactured by Aeritalia for ASI.
- LAGEOS-2 scheduled for deployment Oct. 15, 1992; 5900km orbit 52° inclination.

SATELLITE FEATURES:

MECHANICAL

- Spherical satellite with a DIAMETER of 599.87mm.
- Two hemispherical shells with outer skin made of aluminum.
- Core of the satellite has brass to improve mass..
- Cylindrical core for preferred spin axis (N-S).
- Total mass 405.38 kgm.
- Hemispherical shells and the brass core held together by a steel shaft.
- 426 cube corner cavities.
- Center of gravity and center of geometry are nearly coinciden (0.078mm)..

SATELLITE FEATURES:

OPTICAL

- 426 cube corners; fused silica (422), germanium (4).
- UV-near IR supported by FS; Ge for infrared ranging..
- FS cubes distributed with symmetry about the polar axis; Ge cubes distributed as a tetrahedron.
- Special grade of FS (Suprasil 1, Special T19) for material homogenity and isotropy..
- Clear aperture 38.1 mm; face to apex depth 27.84mm..
- Dihedral offset of 1.5 arc sec for FS cubes; no dihedral offset for Ge cubes.
- No metallic coating; only TIR to enhance reflection from CCs close to the incoming laser beam.
- TIR cubes are sensitive to polarization affecting FFDP and therefore range correction.

OPTICAL CHARACTERIZATION

PURPOSE

- Range correction to center of mass from effective reflection point.
- Target spread function.
- Lidar cross section.

APPROACH

- Measure the temporal response of the satellite using mode-locked lasers and fast detectors (streak camera, photodiode, MCP-PMT) as a function of wavelength, pulsewidth, polarization, position in the FFDP, satellite orientation, detection bandwidth and, type of signal processing; Compute and deduce the satellite characteristics.

MEASUREMENT PARAMETERS

LASER

- **Wavelength: Pulsed 1064, 532, 355nm**
- **Polarization: Linear (horizontal, vertical), circular**
- **Pulsewidth: 60ps (1064nm); 140ps, 45ps, 25ps (532nm), 30ps (355nm)**

DETECTOR

- **Temporal Resolution: 2.5ps (streak camera); 100ps (photo-diode) 500 ps (MCP-PMT)**
- **Photoelectron Level: 10-100 (MCP-PMT); 1000-10000 (SC); 100000 - (Photodiode)**

SIGNAL PROCESSING

- **Peak**
- **Half Max.**
- **Centroid**
- **Constant Fraction**

SATELLITE ORIENTATION

- **Polar**
- **Equatorial**
- **Others**

Velocity Aberration: Various positions in the annular (34-38 microradian) region of the FFDP.

EXPERIMENTAL APPROACH

PULSE MEASUREMENT

- **Mode-locked laser for illumination.**
- **Temporal detectors in the focal plane.**
- **Detection limited to useful region in the FFDP.**

ADVANTAGES

- **Net effect of coherent/incoherent superposition of FFDPs directly measured.**
- **More direct than cw case since instrumentatiion used is similar to those currently used for SLR; easy to verify spaceborne performance.**
- **Computationally simple.**
- **Less sensitive to air currents, vibration, etc.**

DISADVANTAGES

- **Experimental measurement is complex.**
- **Allows only discrete measurement of the FFDP.**

LAGEOS-2 RESULTS

POLARIZATION EFFECT

- **Although LAGEOS-1 testing showed no significant effect on polarization, analysis of LAGEOS-2 RC using pulsed laser measurement showed ± 1.5mm in the polar region**

- **Pulsed laser measurement showed ≈ 2mm offset between circular and linear polarization consistently for all pulse widths**

PULSE LENGTH/DETECTION METHOD

- **Peak and half max. detection produced increased range corrections (1-2mm) for shorter pulses; at longer pulsewidths, an asymptotic value of ≈ 251mm is reached.**

- **Experimental data on constant fraction discrimination showed decreased range correction for shorter pulses in good agreement with theroretical predictions.**

- **Range correction to center of mass is 250.8mm (gaussian, 200ps pulsewidth, 532 nm, average orientation, plane polarized light, centroid detection/constant fraction detection).**

- **Range correction is a function of orientation, wavelength, pulse length, detection method, coherent effects, and location within the far field diffraction pattern (FFDP).**

WAVELENGTH EFFECT:

- **Range correction is maximum at 532 nm and showed a decrease with increase in wavelength (355 - 1064).**

- **Detuning of the FFDP which is optimized for 532 nm and near-normal incidence; affects longer and shorter wavelengths; cube corners farther from normal incidence contribute more and shift the range correction towards the center of the satellite.**

SUMMARY

- **Detailed investigation of LAGEOS-2 optical characteristics has been completed, algorithms for RC to CM of the satellite have been derived to apply any SLR scenario.**
- **The small departure of LAGEOS-2 results from LAGEOS-1 is currently believed to be due to calibration/instrumentation errors in LAGEOS-1 measurement.**
- **Current estimates of the satellite-limited ranging accuracy is estimated to be < 3mm for the best multi-photoelectron (MPE) SLR station; accuracy approaching 1mm can be obtained with shorter pulses (<15ps) and streak cameras.**

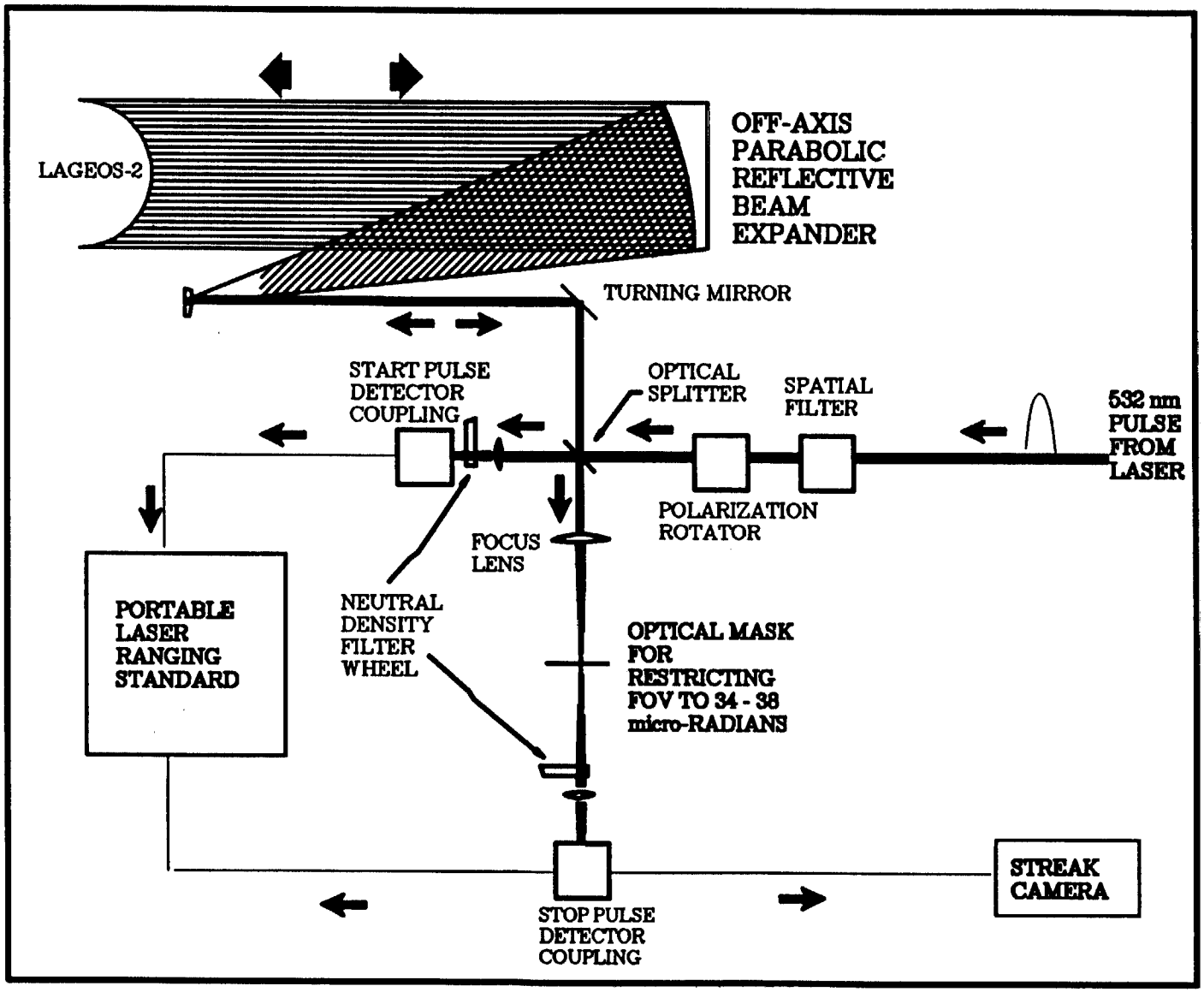

LAGEOS-2 EXPERIMENT OPTICAL SET-UP

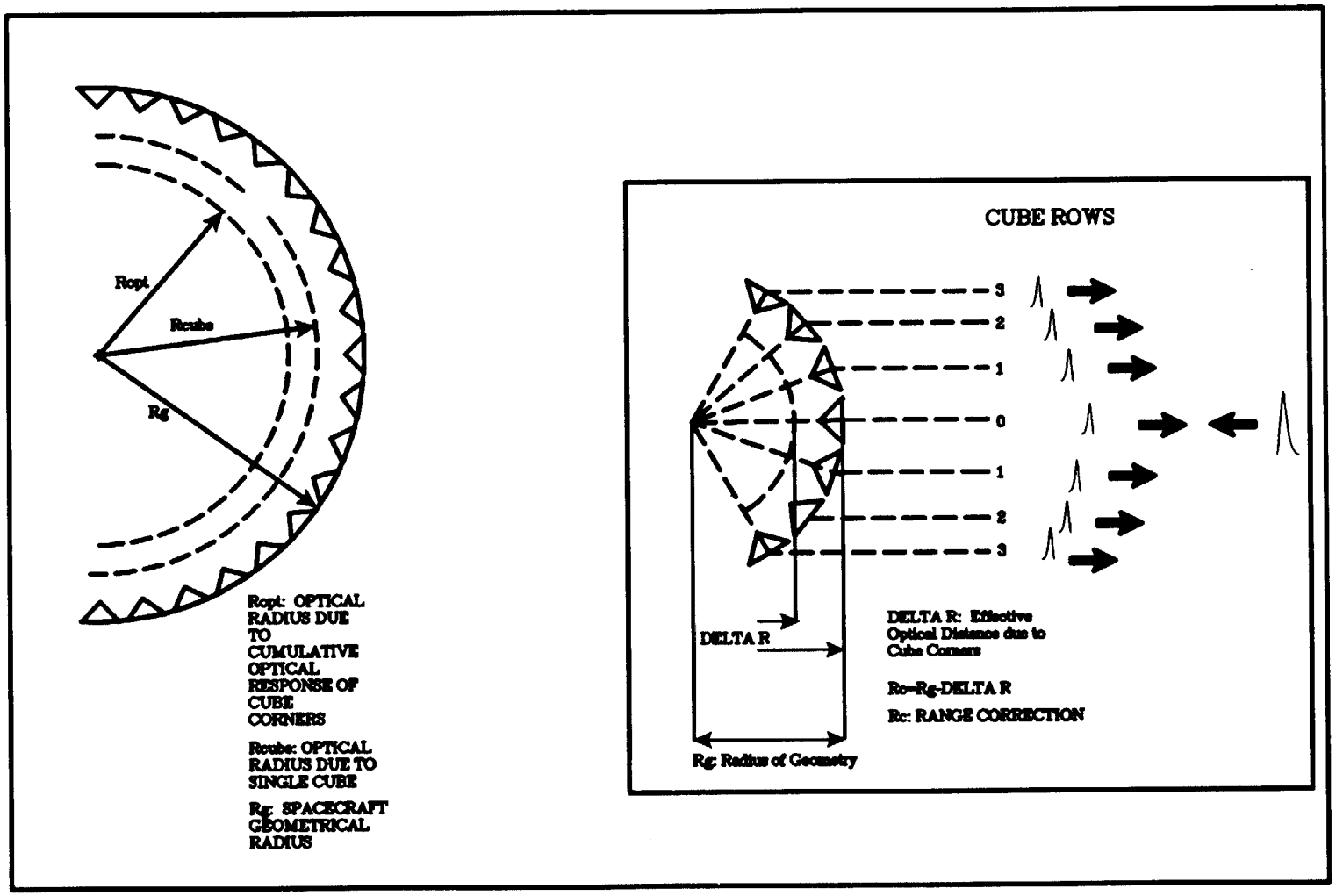

SCHEMATIC OF CUBE CORNER LAYOUT

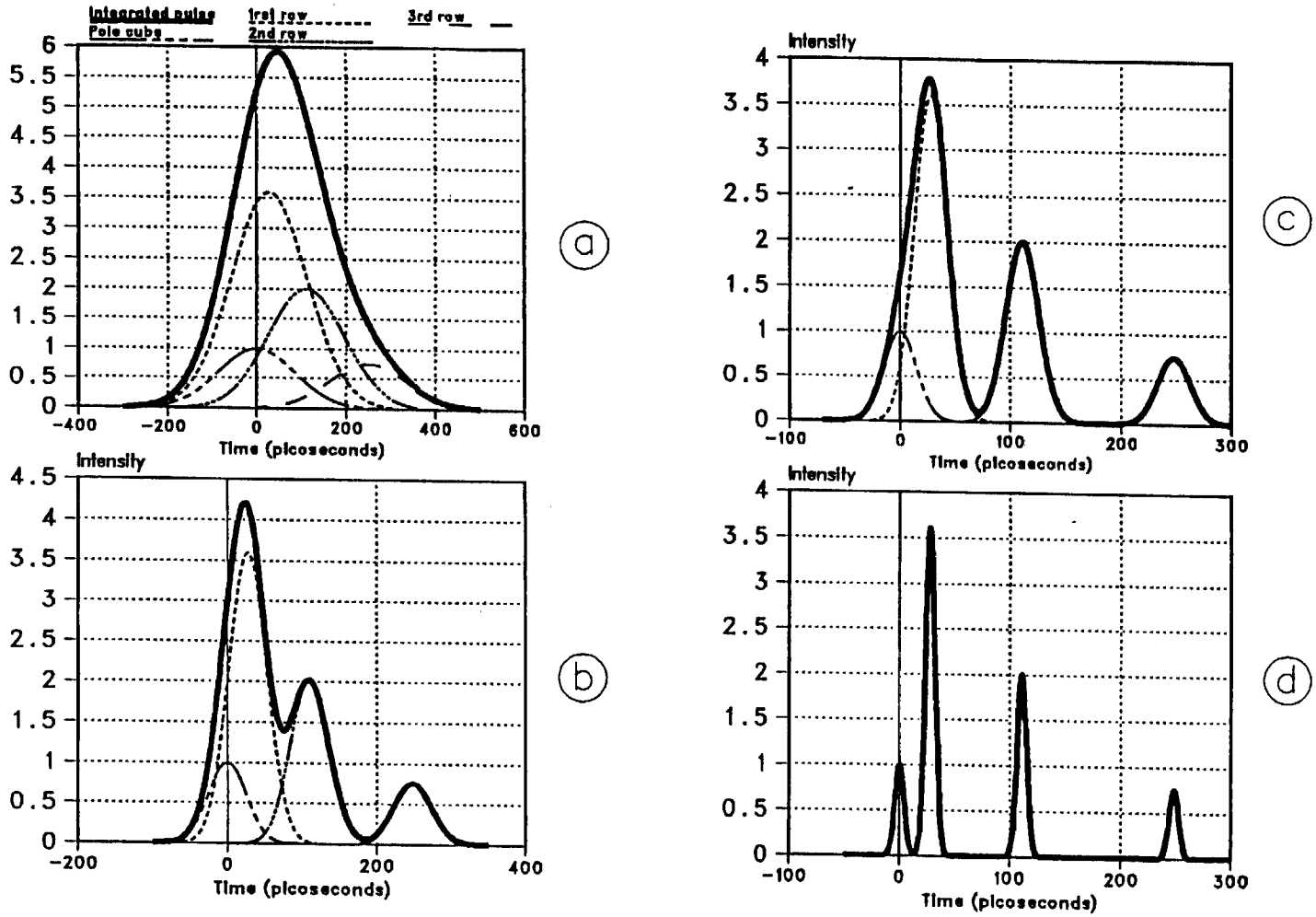

SIMULATION SHOWING INCOHERENT SUPERPOSITION OF THE CONTRIBUTION FROM INDIVIDUAL CUBES IN THE POLAR REGION OF THE LAGEOS-2 SATELLITE AS A FUNCTION OF PULSEWIDTH. THE SIGNATURE OF THE SATELLITE GETS PROGESSIVELY TIME RESOLVED AS THE PULSEWIDTH IS REDUCED FROM APPROXIMATELY 200 PS (a) TO 10 PS (d).

RC-VS-PULSEWIDTH FOR LINEAR AND CIRCULAR POLARIZATION

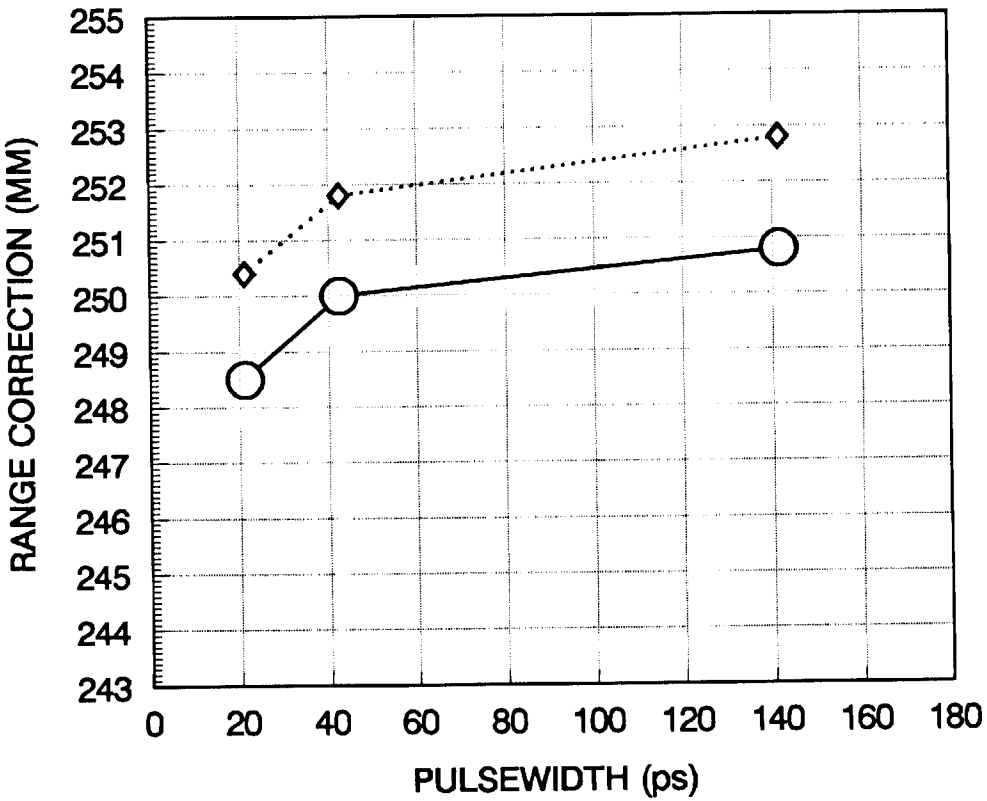

LINEAR POLARIZATION
20 248.5
40 250.0
140 250.8

CIRCULAR POLARIZATION
20 250.4
40 251.8
140 252.8

○ LINEAR
◇ CIRCULAR

Plot illustrating the Range Correction difference between circularly polarized and linearly polarized laser beams for various pulsewidths. An offset of ~2mm was consistently observed in each case.

RC -VS- POLARIZATION DIRECTION

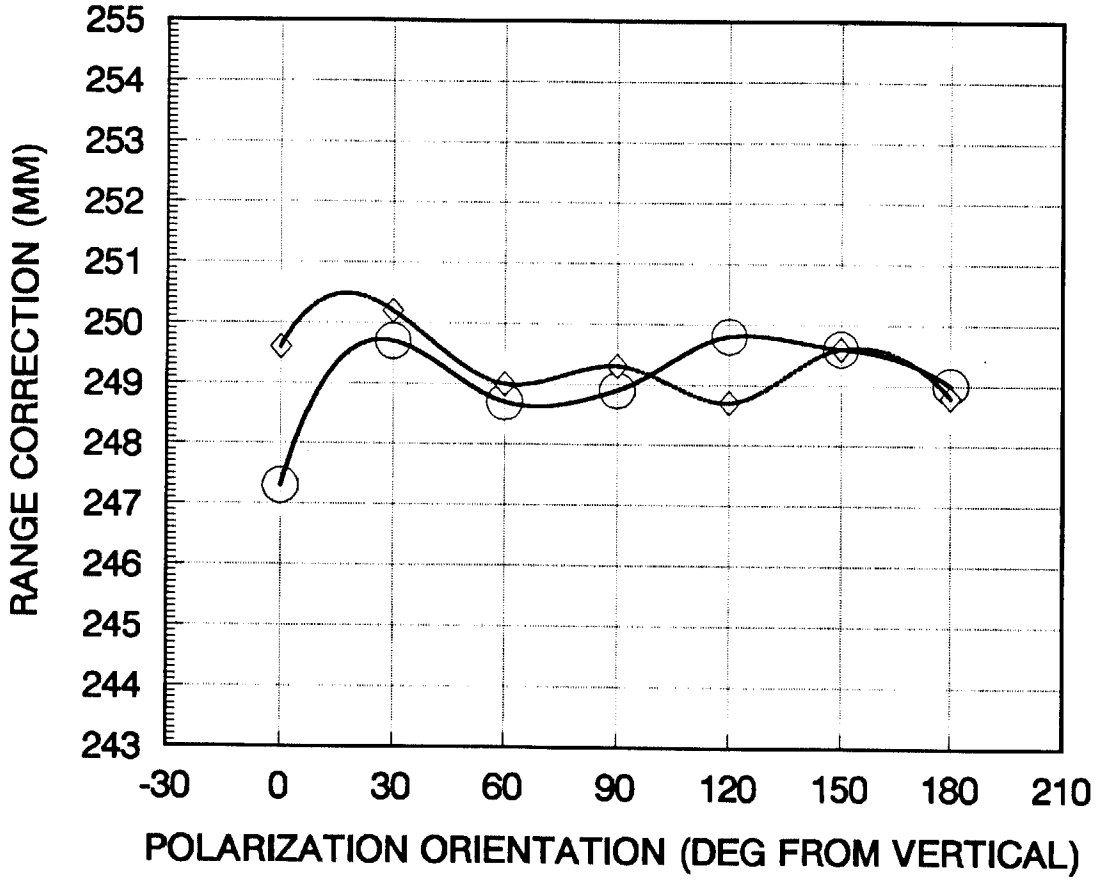

SOUTH:

0	247.3	120	249.8
30	249.7	150	249.6
60	248.7	180	249.0
90	248.9		

NORTH:

0	249.6	120	248.7
30	250.2	150	249.6
60	249.0	180	248.8
90	249.3		

○ SOUTH POLE
◊ NORTH POLE

Plot illustrating the variation of RC as a function of orientation of the E-vector for linearly polarized light. Both polar regions of the satellite showed a similar response.

LAGEOS-2 RANGE CORRECTION -VS- LASER PULSEWIDTH

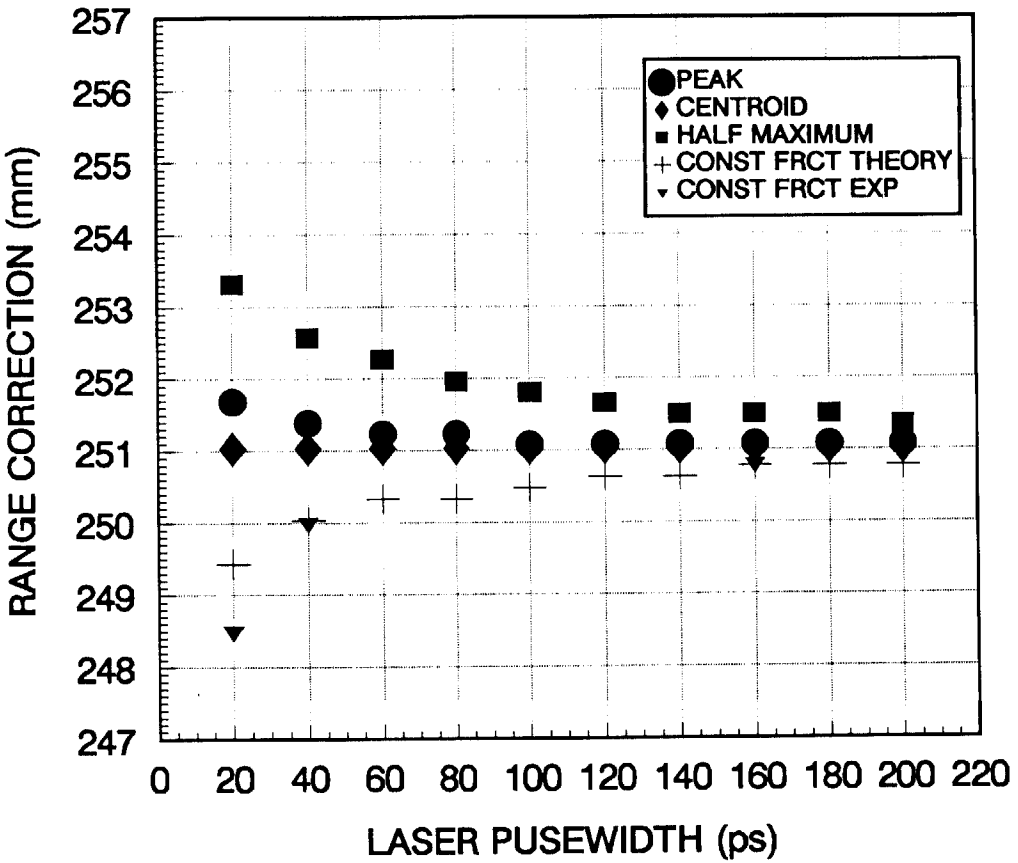

Plot to highlight the dependence of RC on laser pulsewidth as a function of signal processing technique, with special emphasis on constant fraction (CF),which is widely used in the global network. Theoretical values for peak,centroid and CF were computed by P. Minott/GSFC based on a model of the satellite.

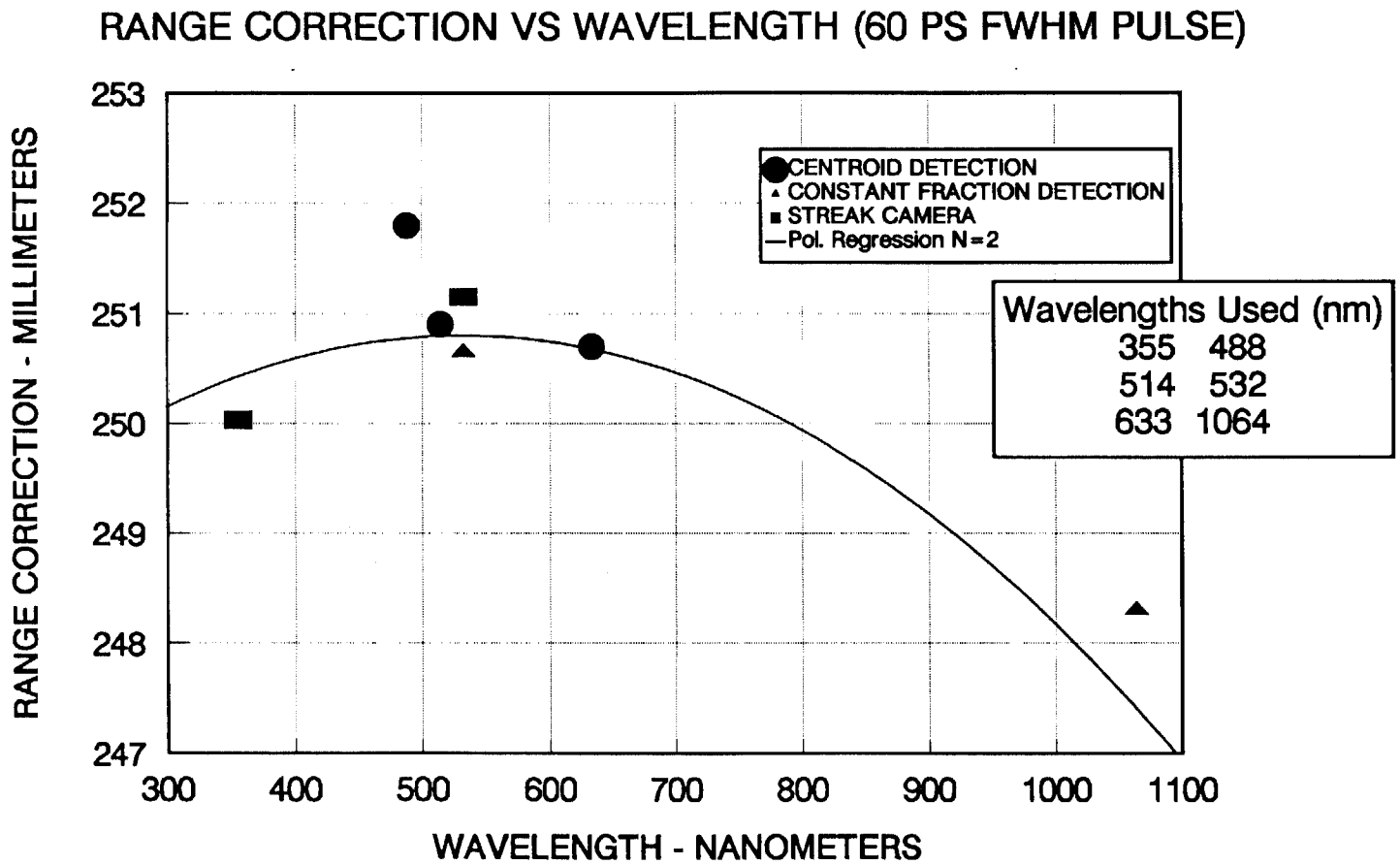

Plot illustrating the dependence of RC on wavelength for various experimental signal processing techniques. The centroid data was computed by P. Minott/GSFC based on a model of the satellite.

ANALYSIS OF TOPEX LASER RETROREFLECTOR ARRAY CHARACTERISTICS

Thomas Varghese
Allied-Signal Aerospace Company
Bendix/CDSLR Network
Seabrook, Maryland 20706
U.S.A.

Abstract:

The joint U.S./French TOPEX/POSEIDON mission was successfully launched on August 10, 1992 for the study of ocean height variation using microwave altimetry. Accurate determination of the satellite orbit is paramount to the determination of the above phenomenon. To accomplish this, using laser ranging, the satellite is equipped with a laser retroreflector array (LRA) around the altimeter antennae. The goal of laser ranging is to obtain precision orbits with a radial accuracy of 13 cm to the Center of Mass of the Satellite. This requires the laser range correction to the LRA reference be known at the sub-cm level and is quite a challenge considering the geometry of the LRA. Detailed studies were initiated by the TOPEX project office (Christensen) under the auspices of the CDP/DOSE project (Degnan) at Goddard Space Flight Center.

The studies included the following:

(1) Theoretical Modelling of the LRA using FFDP data and computation of Centroid tables: P. Minott/GSFC; D. Arnold/SAO

(2) Experimental measurement of the LRA trays using CW techniques: P. Minott/GSFC; Carl Gliniak/EER

(3) Pulsed experimental measurement and modelling: T. Varghese/Bendix

(4) Range Correction tables for Global SLR Tracking Configurations: T. Varghese/Bendix

(5) Data Compression using Fourier Analysis and Satellite Range Correction: A. Marshall/GSFC

This paper provides an overview of items (3) and (4).

c-4

TOPEX LRA OPTICAL CHARACTERIZATION

- **LIDAR CROSS SECTION:** To determine optical link and therefore the photo electron yield for various tracking strategies, detection configurations.
- **TARGET SPREAD FUNCTION:** To study impact on ground ranging hardware configurations, calibration corrections, etc.
- **RANGE CORRECTION:** To deduce the range correction to determine the satellite range to LRA reference center.

LASER RANGING CORRECTIONS FOR TOPEX POD

DETERMINATION OF RANGE TO CENTER OF MASS INVOLVES THE FOLLOWING:

- Range from the station to LRA 'reflection plane'.
- Correction of the reflection plane to the LRA reference center.
- Co-ordinate transformation from LRA reference center to space-craft body-fixed coordinate system origin.
- Center of mass position co-ordinates with respect to the body fixed co-ordinate system origin.

LASER RANGING CORRECTIONS FOR TOPEX POD

FACTORS AFFECTING LASER RANGING CORRECTION

- Satellite elevation angle with respect to the ranging station
- Satellite velocity normal to the line of sight and therefore the location within the FFDP.
- Ranging hardware configuration

    a) Laser wavelength and pulsewidth
    b) Type of detection (peak, leading edge, centroid, CFD)
    c) Detector bandwidth and skew
    d) Detection threshold (spe, mpe, low/high threshold)

Very accurate determination of each of these parameters is required to obtain a laser ranging correction to 0.5 cm (1 sigma).

TOPEX CHARACTERISTICS PERTINENT TO LASER RANGING

- Circular orbit of 1336 km
    - Maximum Range ~ 2700 KM (20° Elevation)
    - Minimum Range ~ 1336 KM (90° Elevation)
- Range of velocity aberration 28-48μr
- Nadir pointing LRA - orientation of the array changes as a function of elevation angle
- LRA consist of 192 hexagonal cubes in a conical ring configuration with 128 cubes in the lower row and 64 cubes in the upper row. There are 16 trays each with 12 cubes
- Lower row diameter - 826.3mm
- Upper row diameter - 852.9mm
- Height of lower row from reference center - 88.6mm
- Height of upper row from reference center - 66.3mm
- Center of mass is away from the LRA reference center by a known distance and varies as a function of expended fuel

TOPEX CUBE CHARACTERISTICS

- **EACH HEXAGONAL CUBE HAS THE FOLLOWING FEATURES:**
  - Material - Corning fused silica #7958
  - Aperture - 38mm
  - Depth - 27.25mm
  - Dihedral Offset - 1.75 $\pm$ 0.25 arc sec
  - Refractive Index - 1.4606
  - Antireflection coating (Mg F2) for the entrance face
  - Protected silver coating for all other sides; total transmission 82%

PULSED LASER MEASUREMENT

- **OBJECTIVE: MEASURE FFDP IN THE ANNUAL REGION USING LINEARLY POLARIZED 60ps LASER PULSES AT 532 nm**
- **MEASUREMENT TECHNIQUES:**
  - Range measurements using portable standard similar to LAGEOS-2
  - Temporal mapping using:
    (a) High speed photodiode (<10ps rise time) and a 4.5 GHz Oscilloscope
    (b) MCP-PMT and 4.5 GHz Oscilloscope
  - Spatial intensity mapping using a CCD Camera and a Frame Grabber
- **MEASUREMENT CONFIGURATION:**
  - Single trays and individual cubes
- **ORIENTATIONS:**
  - Elevation from 0° to 40° in steps of 20°
  - Azimuth from 0° to 45° in steps of 11.25°

The elevation and azimuth here refer strictly to the laboratory setup for mounting the tray

TARGET SPREAD FUNCTION

- Although the leading edge is fairly sharp, the trailing edge is skewed and very long.
- The pulse shape is a function of elevation angle, and the position in the FFDP annulus.
- The presence of two rows of cubes arranged in the form of a conic section produces a skewed return pulse; for the leading edge the skew diminishes monotonically until the elevation reaches 40° at which time the trailing edge picks up the contribution from the upper row of cubes.
- Simulations show that if the predicted contribution from each cube is altered by a process such as thermal gradient, the resulting pulse can have significantly different temporal characteristics.
- The temporal envelope of the pulse affects the range accuracy.

SUMMARY

- Optical characterization of the LRA has been completed and a model has been established to derive the LRA optical parameters such as a Lidar Cross Section, target spread function and range correction to the LRA reference center.
- Range correction is profoundly impacted by type of detection. It is also a function of the input pulse width and the number of photo electrons used for signal definition.
- Since the range varies considerably (3-6cm) within the FFDP, the range correction has to be applied to the satellite data with the knowledge of the satellite velocity and orientation.
- Current efforts to incorporate velocity aberration and ranging instrumentation features into the data correction algorithms should provide data accuracy better than 1 cm.

Acknowledgements

The author acknowledges his deep appreciation to the following colleagues for technical assistance during the course of this project. In strictly alphabetical order, they are Steve Bucey, Christopher Clarke, Brion Conklin, Tony Mann, Tom Oldham, and Mike Selden. He is also indebted to John Degnan for various technical discussions and P. Minott for providing the far field diffraction data of the individual cubes for various orientation of the LRA.

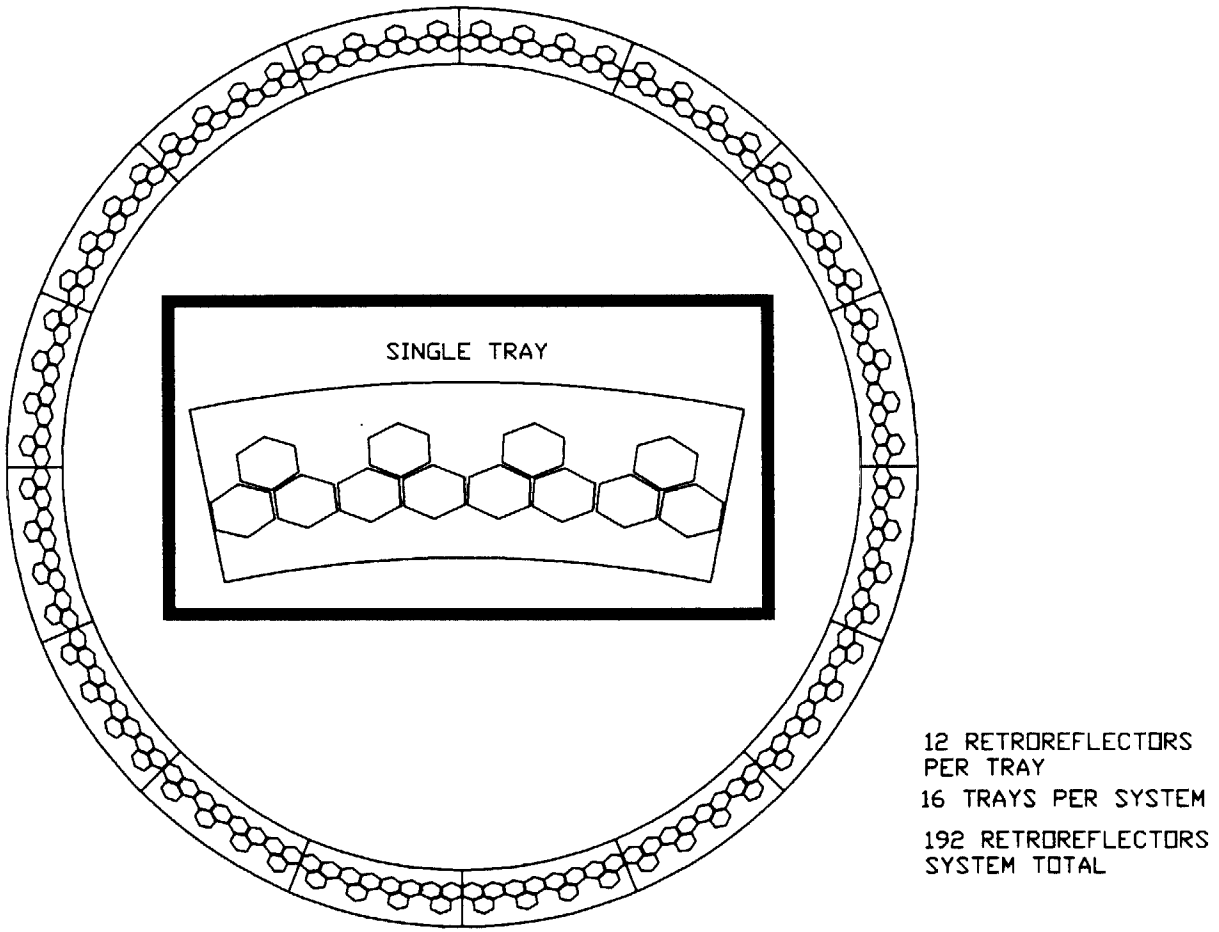

Fig. 1 ILLUSTRATION OF TOPEX LRA AND SINGLE TRAY.

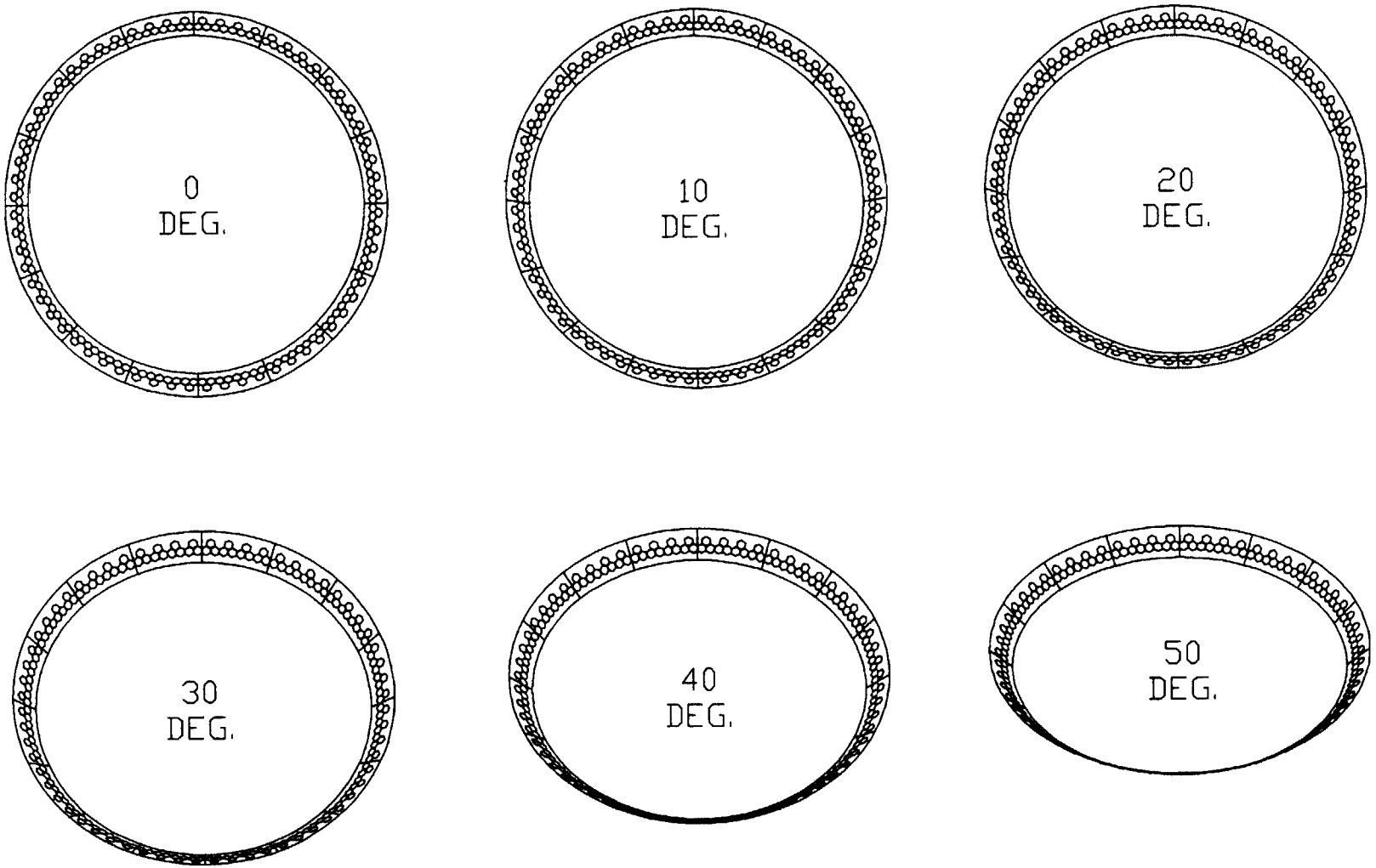

Fig. 2 LRA ORIENTATION AS A FUNCTION OF NADIR ANGLE.

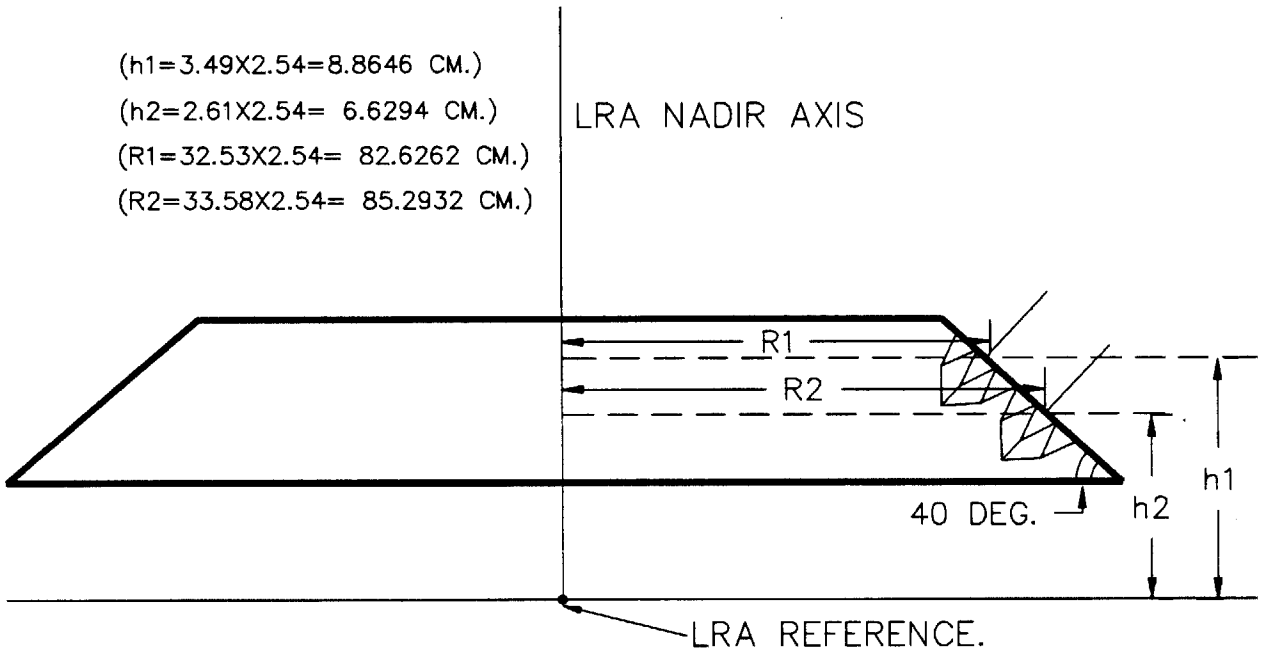

h1=HEIGHT FROM THE CENTER OF THE FRONT FACE OF THE CUBE (LOWER RING; 128 CUBES) TO THE LRA REFERENCE PLANE.

h2=HEIGHT FROM THE CENTER OF THE FRONT FACE OF THE CUBE (UPPER RING; 64 CUBES) TO THE LRA REFERENCE PLANE.

R1=RADIUS (TO THE FRONT FACE OF THE CUBE) OF THE LOWER RING.

R2=RADIUS (TO THE FRONT FACE OF THE CUBE) OF THE UPPER RING.

Fig. 3 TOPEX LRA REFERENCE COORIDINATE SYSTEM.

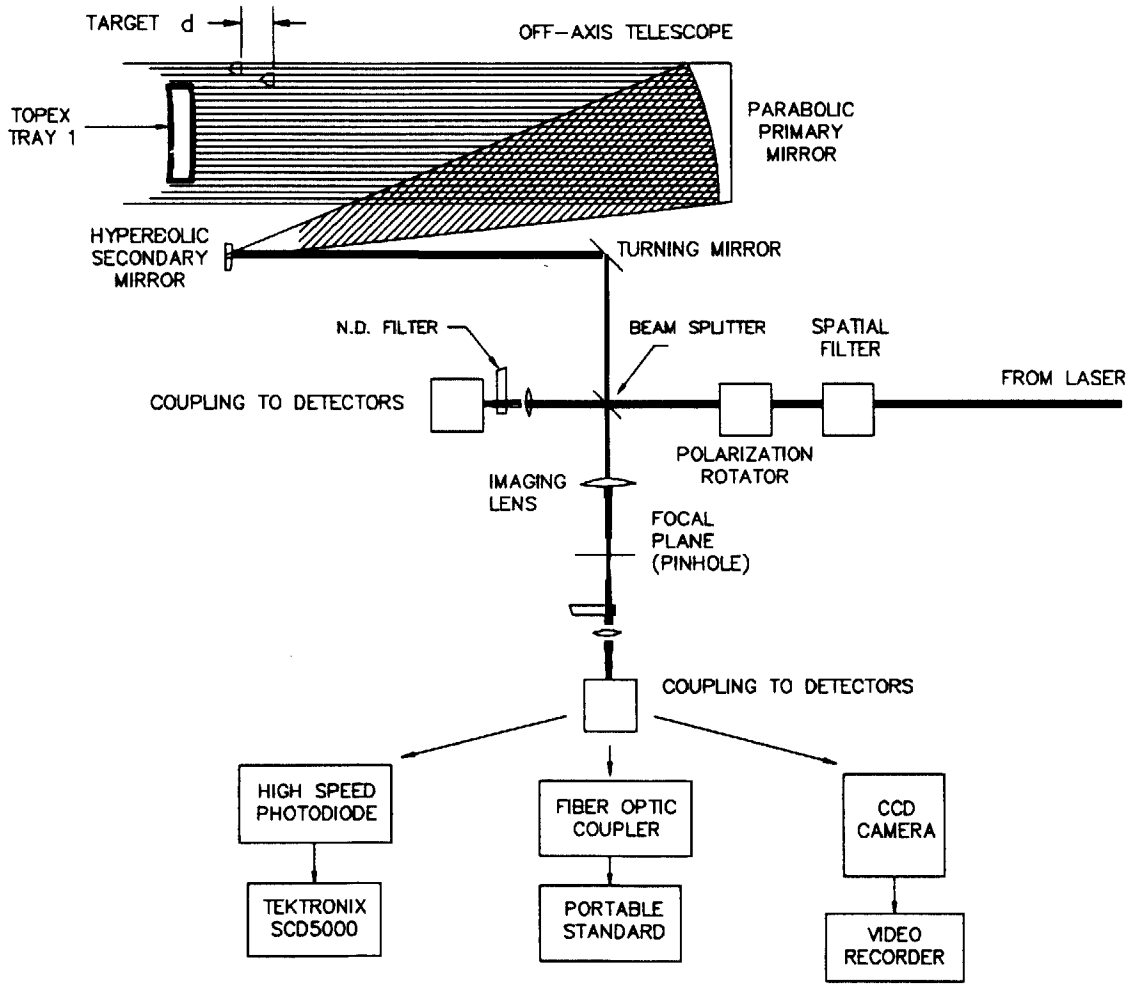

Fig. 4 OPTICAL SCEMATIC FOR TOPEX TRAY MEASUREMENT

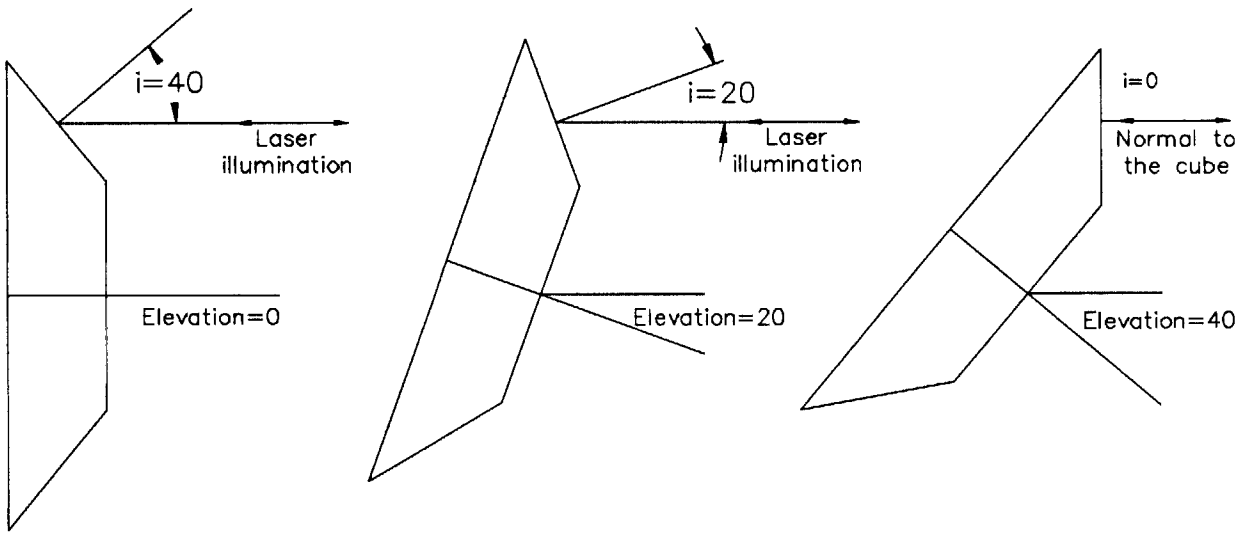

Fig. 5 LABORATORY MEASUEMENTS FOR ORIENTATIONS OF THE TOPEX TRAYS.

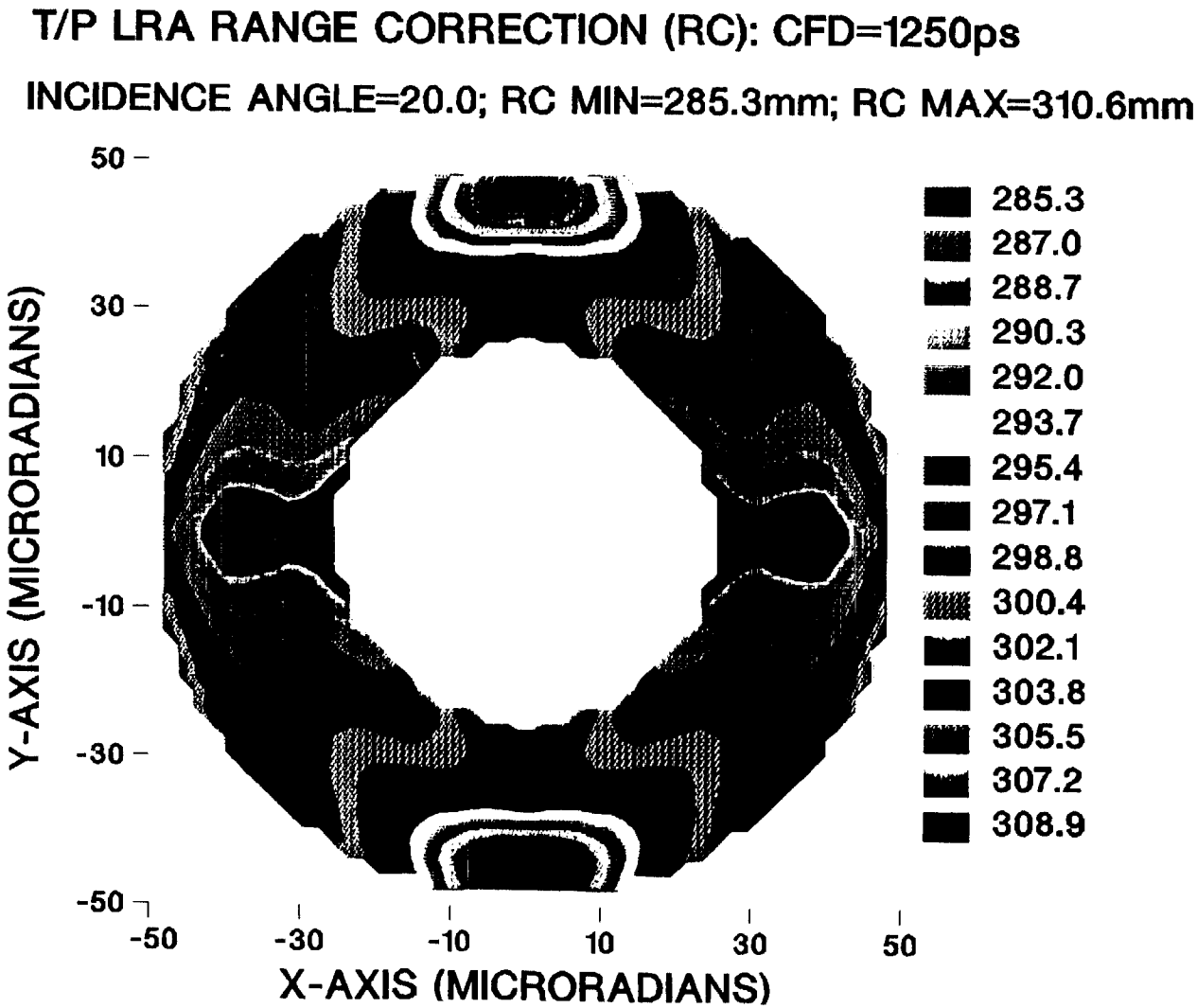

ILLUSTRATION OF THE TOPEX/POSSEIDON LRA RANGE CORRECTION FOR AN INCIDENCE ANGLE (ANGLE BETWEEN LASER LINE OF SIGHT AND NADIR) OF 20 DEGREES FOR CONSTANT FRACTION DISCRIMINATOR BASED SYSTEM. THE RANGE CORRECTION PLOTTED AS A FUNCTION OF THE VELOCITY ABERRATION SPACE SHOWS A COMPLEX PATTERN WITH A MINIMUM VALUE OF 285 MM AND MAXIMUM VALUE OF 311MM.

N94-15579

HISTORICAL MOBLAS SYSTEM CHARACTERIZATION

Van S. Husson

Abstract – This paper is written as a direct response to the published NASA LAser GEOdynamic Satellite (LAGEOS) orbital solution SL7.1 [*Smith et al.*, 1991], in order to close the data information loop with an emphasis on the NASA MOBile LAser Ranging System's (MOBLAS 4,5,6,7,8) LAGEOS fullrate data since November 1, 1983. A preliminary analysis of the supporting information (i.e. satellite laser ranging system eccentricities and system dependent range and time bias corrections) contained in SL7.1 indicated CentiMeter (cm) level discrepancies. In addition, a preliminary analysis of the computed monthly MOBLAS range biases from SL7.1 appear to show cm level systematic trends, some of which appear to be "real", particularly in the 1984 to 1987 time period. This paper is intended to be a reference document for known MOBLAS systematic errors (magnitude and direction) and for supporting MOBLAS information (eccentricities, hardware configurations, and potential data problem periods). Therefore, this report is different than your typical system characterization report [*Pearlman*, 1984], but will be more valuable to the user. The MOBLAS error models and supporting information contained in this paper will be easily accessible from the Crustal Dynamics Data Information System (CDDIS).

1. INTRODUCTION

In the late 1970's, NASA developed five, second generation mobile laser ranging systems in support of the SEa Altimeter SATellite (SEASAT) mission. The goal of the SEASAT mission was to map the surface of the oceans using the onboard satellite altimeter. Satellite Laser Ranging (SLR) data was used to calibrate the SEASAT altimeter. During the 1980's, the MOBLAS systems underwent an extensive upgrade program that improved the data accuracy and precision an order of magnitude, from the 100 MilliMeter (mm) to the 10 mm level. Since the mid-1980's, LAGEOS data has been compressed into 2 minute bins (normal points), which statistically reduces the single shot precision level [*Smith et al.*, 1985]. MOBLAS LAGEOS normal point precision levels have been at the 1-2 mm level since the late-1980's.

During the 1980's, cm level systematic biases were discovered through special and collocation analysis techniques developed by Bendix in support of the Goddard Laser Tracking Network (GLTN) and the Crustal Dynamics Satellite Laser Ranging (CDSLR) mission contracts. When centimeter level systematic errors were discovered in NASA SLR data, the NASA management philosophy was to identify the source of the bias; to eliminate or model the bias; and to document the nature of the bias. Due to cost considerations, historical NASA SLR data were not repaired (in most cases) to remove known cm level systematics. In addition, the documentation of these bias problems was not maintained in a central database and had a limited distribution. The intent of this paper is to provide one reference source for known uncorrected MOBLAS (LAGEOS) systematic errors that will be available from the CDDIS.

The original MOBLAS major hardware components were the General Photonics (GP) q-switched laser, the Amperex dynode-chain PhotoMultiplier Tube (PMT), the Ortec 934 discriminator, and the Hewlett Packard (HP) 5360 time interval counter. In the 1983-1984 time frame, the largest systematic unrecoverable error source, the GP laser, was replaced with a Quantel mode-locked laser. The HP5370 counter was usually incorporated as part of the Quantel laser upgrade. In the 1986-1987 timeframe, the largest systematic error source, the Amperex 2233B and Ortec discriminator, was replaced with the ITT F4129 gated three-stage Micro-Channel Plate (MCP)PMT and Tennelec TC454 discriminators. The systematic error sources associated with the hardware components mentioned above are discussed in *Degnan* [1985] and *Varghese* [1985].

It is virtually impossible to recover any hardware related systematic errors in the GP laser era due to the domination of "wavefront-distortion" errors [*Degnan*, 1985]. In the Quantel laser pre-MCPPMT era, the largest recoverable systematic hardware related error source was signal strength (0-30mm) of the returning pulse [*Heinick*, 1984]. Discriminator and PMT "timewalk" characteristics, coupled with calibration signal strengths not distributed the same as LAGEOS signal strengths induced a systematic bias. The magnitude and direction of the bias was system dependent, and decreased in magnitude as calibration methods improved. A model has been developed to recover this error based on the review of historical calibration and LAGEOS "timewalk" curves. Unfortunately, only a small sample of these curves ever existed. Signal strength effects did vary from pass-to-pass and within a pass. The MCPPMT and dual Tennelec discriminators package developed by *Varghese*, coupled with proper calibration techniques essentially eliminated signal strength as a bias source at the mm level.

In 1988, another recoverable hardware systematic error source was discovered by *See and Sneed.* They discovered the measurement of the laser transmit delay (TDEL) was in error, because the TDEL electronics did not measure the cable delay ($\leq$0.5 microseconds) between the time code generator and the system computer. In addition, they and *McCollums* discovered that the TDEL electronics had other TDEL sub-microsecond accuracy ambiguities, which would have masked this bias. In the 1989-1990 timeframe, the TDEL electronics were modified to remove these sub-microsecond ambiguities. The cable delay has been measured in MOBLAS-4,7,8 and is being modelled in the pre-processing. As of this writing, the MOBLAS-5 and 6 cable delays have not been measured.

Other mm level hardware errors are known to exist in the current MOBLAS hardware (i.e. HP5370 [*Selden*, 1992] and optical path changes as a function of pointing angle [*McCollums*, 1986]), but are presently unrecoverable. Not all systematic error sources in SLR systems are hardware related. Survey of ground targets, survey of monument offsets, atmospheric modelling, data pre-processing, and orbital modelling are other SLR error sources. Fortunately, many of these errors sources can be recovered to the 10-20mm level, using historical processing results.

In the GP laser era, calibration targets were large boards at distances of 2-3 KiloMeters (Km). These boards were mounted on metal poles which were guyed. The height of these poles was system dependent. Cube corners also existed and were mounted on various structures and in most cases were in close proximity (a few meters) to the calibration boards. The reason calibration boards were used versus cube corners was to average the "wavefront-distortion" effects of the GP laser. Historical ground tests results [*Brogdon et. al.*] indicated up to 20cm and 60cm differences in system delay between the board and cube corner, and as a function of pointing angle, respectively. When the mode-locked (Quantel) lasers were installed, ground tests results were dramatically improved, and for the first time, 10-20mm survey errors to the ground targets and 10-20mm ground target movement could be detected [*Wroe et. al.*]. Within a few months of the MCPPMT's (1986-1987) being installed, the primary calibration targets became the original cube corners. In the 1988-1989 timeframe, long (2-3Km) Nelson piers became the primary calibration targets. In the 1991-

1992 timeframe, the primary targets became short (100-200 meters) Nelson piers with the advent of the translator and the short target ranging electronics [*Eichinger et. al.*, 1990].

In the early to mid 1980's, cm level movement of the original targets, coupled with survey uncertainties and infrequent surveys, severely limited the absolute accuracy of MOBLAS data. "Average" target movement and survey uncertainties, in most cases, is recoverable to the 10-20mm level using historical ground test results. In the mid-1980's, surveying equipment and frequency of surveying was improved, but the problem still existed with unstable targets. In the late-1980's, the target stability problem was minimized to the millimeter level, when the current day target calibration structure, the Nelson pier, were used as the primary calibration target.

The MOBLAS eccentricity measurement techniques were improved in the mid-1980's [*Nelson*, 1986]. The infrequency of eccentricity surveys was a mm level systematic error source, because long term temporal changes in the eccentricity data were at this level. Some of these errors are traceable based on MOBLAS log records or special analysis techniques.

Neutral Density (ND) filters have always been used during calibration to attenuate the signal. During satellite ranging the filters were removed, thus inducing a difference in the "effective" calibration and satellite optical paths [*Crawford*, 1985]. This difference was not modelled, but is recoverable to the 1mm level. In 1991-1992 the Optical Attenuation Mechanisms (OAM) [*Silva et. al.*, 1991] were installed in the MOBLAS, which minimizes the use of ND filters. The ND filter bias is currently being modelled in the pre-processing.

Prior to January 1, 1988, the tropospheric range correction applied to the fullrate data was computed based on the MOBLAS elevation encoder measurements. These measurements could be in error by a few millidegrees and would thus induce a systematic error in the tropospheric refraction correction [*Husson et. al.*, 1987]. This correction could be in error up to 20mm. The error was system and satellite dependent, but is fully recoverable to the sub-mm level. To remove this error in pre-1988 MOBLAS data, the applied tropospheric refraction must be removed and reapplied using the computed elevation angle. All MOBLAS data taken after January 1, 1988, were pre-processed using the computed elevation angle from a short arc fit to the ranges.

LAGEOS orbital modelling errors have improved significantly over the last 12 years along with the quality of SLR data [*Smith et. al.*, 1991]. Orbital modelling is limited by the quality and distribution of the global SLR dataset, but in some instances, is the only hope for recovering the "net" historical SLR biases.

In the remainder of this article, each MOBLAS system is addressed individually. Each system's eccentricities and recoverable bias sources are discussed and summarized in tables, which are contained at the end of this article. The bias model tables include the major system configuration changes (laser, PMT, discriminators, counter) and important pre-processing information (i.e. calibration target and calibration range). The tables and this article will be available from the CDDIS.

2. MOBLAS-4

2.1 MOBLAS-4 Eccentricities

Since August 15, 1983, MOBLAS-4 has only occupied one monument/marker (7110). Prior to August 1983, 7110 was occupied by MOBLAS-3. There exists 5 sets of MOBLAS-4 eccentricities and 10 MOBLAS-4 Site Occupation Designators (SOD's) at 7110. SOD's 71100402, 71100403, and 71100410, each have two sets of eccentricities.

The 3mm change in the Up ecc., between the 1985 and 1988, surveys could be caused by settlement of the pad and monument [*Nelson,* 1988]. There were no measurements of the eccentricities between 1985 and 1988. The MOBLAS-4 mount was releveled twice in 1988 (June 16 and December 13), but apparently there was no change in eccentricities, based on the April 1988 and November 1989 surveys. In February 1992, the eccentricities were remeasured prior to the removal of the mount. There was a 2mm unexplained change in the North ecc. In March 1992, the MOBLAS-4 mount was removed from system to be refurbished, and in April 1992, the refurbished mount was re-installed and the ecc. were remeasured. Table 1 contains the recommended set of MOBLAS-4 eccentricities with their corresponding SOD(s) and effective starting dates.

2.2 MOBLAS-4 LAGEOS Biases

The net MOBLAS-4 recoverable biases (range and time) are presented in Table 2. To correct MOBLAS-4 LAGEOS data, the known range and time biases (in Table 2) should be subtracted from the LAGEOS range and timetags, respectively. Any time there is the potential for a change in the bias(es), even though the bias(es) did not change, a new entry has been added. A component breakdown of the biases is presented, followed by a section describing known problem data, and followed by a section describing potential problem data.

2.2.1 MOBLAS-4 ND filters

MOBLAS-4 LAGEOS data was biased short by 3mm $\pm$ 1 and 1mm $\pm$ 0mm from August 15, 1983 through January 17, 1992, and from January 18 through May 31, 1992, respectively, due to ND filters. On January 18, 1992, the OAM was installed in MOBLAS-4 reducing the ND filter bias. After June 1, 1992, this bias has been removed through modelling.

2.2.2 MOBLAS-4 signal strength

MOBLAS-4 LAGEOS data was biased long by 20mm $\pm$ 10, 10mm $\pm$ 5, 6mm $\pm$ 3, and 4mm $\pm$ 2 from August 15, 1983 through June 30, 1984; July 1, 1984 through August 31, 1984; September 1, 1984 through July 31, 1985; and August 1, 1985 through November 19, 1986; respectively, due to signal strength. This bias would vary from pass-to-pass and would have a slight elevation dependence. Low elevation data would be biased longer by several mm than high elevation data. Signal strength effects were reduced as the MOBLAS-4 calibration techniques improved, and were eliminated when the MCPPMT package was installed on November 20, 1986.

2.2.3 MOBLAS-4 elevation angles

Prior to January 1, 1988, the tropospheric range correction applied to the fullrate data was computed based on the MOBLAS-4 encoder measurements. To remove this error in pre-1988 MOBLAS-4 data, the applied tropospheric refraction must be removed and reapplied using the computed elevation angle.

2.2.4 MOBLAS-4 calibration targets/distances

MOBLAS-4 has used 4 different calibration targets (1 board and 3 cube corners) at marker 7110. From August 15, 1983 through December 31, 1987; from January 1, 1987 through January 28, 1988; from January 29 through April 29, 1988; from April 29, 1988 through December 5, 1991; and from December 6, 1991 to the present; the MOBLAS-4 primary calibration targets were the 2Km board, the 2Km cube corner, the 2Km board, the 2Km Nelson pier, and the 200m Nelson pier, respectively.

MOBLAS-4 has been surveyed 5 times (1983, 1985, 1988, and twice in 1992) at marker 7110. Sometime between the 1983 and the 1985 surveys, vandals removed the bracing support of the MOBLAS-4 calibration board tower [*Nelson*, 1985], which could explain the 13mm difference between the 1983 and 1985 calibration board distances. When the new calibration board values were used in data processing, there would be an automatically induced 13mm discontinuity in the MOBLAS-4 range bias. The new board values were used with all data taken after June 20, 1985. Data just prior to June 20, 1985 would have been biased longer by 13mm than data after June 20, 1985 (This 13mm change does not appear in the range bias model, because the exact date of the change is unknown). The cube corner became the operational target in January 1987 (The exact day is unknown at this time).

The distance (2Km) and the design/stability of the original MOBLAS-4 targets (a calibration board mounted on a tower and a cube corner mounted on wooden posts) were limiting factors to surveying accuracy and MOBLAS-4 data accuracy. The survey accuracy of these original targets was at the 10-15mm level [*Nelson*]. Historical ground test results indicate up to 20mm differences in "apparent" system delays between the MOBLAS-4 calibration board and the cube corner, which indicates both targets could move at least 10mm in either direction from month-to-month and from day-to-day. LAGEOS orbital analysis appears to be the only viable means for recovering the "true" average MOBLAS-4 monthly target distance to better than 20mm in the October 1983 to April 1988 timeframe.

Between November 1, 1987 and January 28, 1988, the MOBLAS-4 operational calibration target, cube corner, was very unstable, which caused unusual changes (up to 90mm) in the "apparent" system delay. Individual MOBLAS-4 LAGEOS passes could be biased long (up to 90mm) during this period. *Eanes* [1987] originally discovered this data problem. The bias could change (up to 30mm) from pass-to-pass and from day-to-day. The problem was eliminated when the previous calibration target (board) was used starting January 29, 1988. On April 30, 1988, the MOBLAS-4 calibration target became the 2Km Nelson pier.

2.2.5 MOBLAS-4 TDEL

All MOBLAS-4 data between January 5, 1990 and May 31, 1992 contains a time bias of -0.4 microseconds. To correct this time bias, add +0.4 microseconds to each observation's timetag. This correction is only valid after January 5, 1990, because on this date, the MOBLAS-4 TDEL electronics were modified to eliminate other TDEL sub-microsecond accuracy ambiguities, which would have masked this bias. This bias has been eliminated through modelling, effective June 1, 1992.

2.2.6 MOBLAS-4 known problem data

Between April 12, 1984 and May 24, 1984, individual MOBLAS-4 passes contained discontinuities (100mm up to 600mm) due to the range gate window being changed during the pass. The magnitude of the discontinuities depends upon where the return occurred in the range gate window [*Varghese*, 1985]; therefore, data during this period should not be used. This problem was originally detected by *Eanes* [1985] and was resolved when the system adhered to standard tracking procedures.

2.2.7 MOBLAS-4 potential problem data

Between December 29, 1988 and January 27, 1989, MOBLAS-4 LAGEOS data is questionable due to a bad time interval unit (HP5370). The RMS scatter of this data was cyclic and dependent upon the LAGEOS range [*Heinick et. al.*, 1989]. The data is believed to be unbiased and just systematically noisy. This problem was resolved by replacing the HP5370.

3. MOBLAS-5

3.1 Eccentricities

Since July 1, 1979, MOBLAS-5 has only occupied one monument/marker (7090). There exists only 3 unique sets of MOBLAS-5 eccentricities and 12 MOBLAS-5 SOD's at 7090. SOD 70900508 has 2 sets of eccentricities.

The MOBLAS-5 mount was releveled on September 5, 1985. No survey was performed after the releveling til 1987. The 8mm change in the Up ecc., between the 1979 and 1987 surveys, remains unexplained. It is not known how far back the 1987 Up ecc. can be backdated. The MOBLAS-5 mount was also releveled on August 5, 1989, but the eccentricities were not remeasured. In January 1992, the mount was re-installed and the eccentricities were remeasured. Table 3 contains the recommended set of MOBLAS-5 eccentricities with their corresponding SOD(s) and effective starting dates.

3.2 MOBLAS 5 LAGEOS Biases

The net MOBLAS-5 recoverable biases (range and time) are presented in Table 4. To correct MOBLAS-5 LAGEOS data, the known range and time biases (in Table 4) should be subtracted from the LAGEOS range and timetags, respectively. Any time there is the potential for a change in the bias(es), even though the bias(es) did not change, a new entry has been added. A component breakdown of the biases is presented, followed by a section describing known problem data, and followed by a section describing potential problem data.

3.2.1 MOBLAS-5 ND filters

Prior to June 1, 1992, MOBLAS-5 LAGEOS data was biased short by 3mm $\pm$ 1 due to ND filters. After June 1, 1992, this bias has been removed through modelling.

3.2.2 MOBLAS-5 signal strength

MOBLAS-5 LAGEOS data was biased short by 3mm $\pm$ 2 from July 27, 1983 through April 22, 1987, due to signal strength. This bias would be fairly constant from pass-to-pass. This bias was eliminated when the MCPPMT package was installed in MOBLAS-5 on April 23, 1987.

3.2.3 MOBLAS-5 elevation angles

Prior to January 1, 1988, the tropospheric range correction applied to the fullrate data was computed based on the MOBLAS-5 encoder measurements. To remove this error in pre-1988 MOBLAS-5 data, the applied tropospheric refraction must be removed and reapplied using the computed elevation angle.

3.2.4 MOBLAS-5 calibration targets/distances

MOBLAS-5 has used 4 different calibration targets (2 boards and 2 cube corners) at marker 7090. From August 1, 1979 through June 7, 1980; from June 8, 1980 through May 31, 1987; from June 1 through July 31, 1987; from August 1 through August 25, 1987; and from August 26, 1987 through June 30, 1992; the MOBLAS-5 primary calibration targets were the 2Km calibration board, the 3Km calibration board, the 1Km cube corner, the 3Km calibration board, and the 3Km Nelson pier, respectively.

MOBLAS-5 has been surveyed only 3 times in 13 years (1979/80, 1987, & 1992) at marker 7090. Between the 1979/80 and 1987 surveys, the 1Km cube corner and the 3Km board ranges changed by +30mm and -9mm, respectively. The 2Km board was never resurveyed and the 3Km board blew away in August 1987. In early January 1992, the mount was replaced and a new survey was performed.

The system delay differences obtained from the 1Km cube corner and the 3Km board in historical minico tests since June 1985 were 39mm $\pm$ 5 and 0mm $\pm$ 5 [*Husson and Wroe,* 1987] using the 1980 and 1987 surveys, respectively. Therefore, the 1987 survey values can be backdated to at least June 1985, which means MOBLAS-5 data between June 1985 through May 31, 1987 (all board calibrated data) was biased long by 9mm $\pm$5mm. All data since June 1, 1987, until the mount replacement in 1992, was processed with the 1987 surveyed ranges and should be bias free. Research into minico results prior to June 1985 still needs to be performed.

3.2.5 MOBLAS-5 TDEL

The MOBLAS-5 cable delay causing this bias has not been measured as of this writing. On January 30, 1990, the MOBLAS-5 TDEL electronics were modified to eliminate other TDEL sub-microsecond ambiguities.

3.2.6 MOBLAS-5 PMT Gating

Prior to June 8, 1980, MOBLAS-5 LAGEOS data was biased short by 20mm$\pm$5 due to calibration data falling in a non-linear region of the Amperex 2233B PMT gate. This bias was characterized by *Varghese* [1985]. This bias was eliminated, effective June 8, 1980, when a longer calibration board (>3Km) was used.

3.2.7 MOBLAS-5 known problem data

Between December 19, 1991 and January 3, 1992, MOBLAS-5 data quality was degraded due to a stuck bit. The bit was stuck low (100 picosec.) for LAGEOS. It does not appear that this data is recoverable, because of it's unknown effect on calibration data.

3.2.8 MOBLAS-5 potential problem data

Between August 12, 1988 and January 31, 1989, MOBLAS-5 system delays and pre-to-post calibration shifts were erratic [*Heinick et al.*, 1989]. Therefore, the uncertainty in the system delay is increased during this period; however, this should be a random error than should average over several passes. This problem disappeared during February 1989.

4. MOBLAS-6

4.1 MOBLAS-6 Eccentricities

Since March 3, 1983, MOBLAS-6 has only occupied one monument\marker (7122). There exists 4 sets of MOBLAS-6 eccentricities and 9 MOBLAS-6 SOD's at 7122. SOD 71220604 has two sets of eccentricities.

The May 1988 survey sheet had the wrong sign for the East ecc. It should be negative, not positive. Based on the 1991 survey, there was no apparent change in the eccentricities when the MOBLAS-6 mount was releveled on August 5, 1989. Table 5 contains the recommended set of MOBLAS-6 eccentricities with their corresponding SOD(s) and effective starting dates.

4.2 MOBLAS-6 LAGEOS Biases

The net MOBLAS-6 recoverable biases (range and time) are presented in Table 6. To correct MOBLAS-6 LAGEOS data, the known range and time biases (in Table 6) should be subtracted from the LAGEOS range and timetags, respectively. Any time there is the potential for a change in the bias(es), even though the bias(es) did not change, a new entry has been added. A component breakdown of the biases is presented, followed by a section describing known problem data, and followed by a section describing potential problem data.

4.2.1 MOBLAS-6 ND filters

All MOBLAS-6 LAGEOS data was biased short by 3mm $\pm$ 1 due to ND filters.

4.2.2 MOBLAS-6 signal strength

MOBLAS-6 LAGEOS data was biased long by 12mm $\pm$ 4, 10mm $\pm$ 3, and 4mm $\pm$ 2 from May 1, 1984 through March 31, 1986; from April 1 through August 31, 1986; and September 1, 1986 through January 27, 1987; respectively, due to signal strength. This bias would vary slightly (several mm) from pass-to-pass and would have a slight elevation dependence. Low elevation data would be biased longer than high elevation data. Signal strength effects were reduced as system calibration techniques improved, and were eliminated when the MCPPMT package was installed in MOBLAS-6 on January 28, 1987.

4.2.3 MOBLAS-6 elevation angles

Prior to January 1, 1988, the tropospheric range correction applied to the fullrate data was computed based on the MOBLAS-6 encoder measurements. To remove this error in pre-1988 MOBLAS-6 data, the applied tropospheric refraction must be removed and reapplied using the computed elevation angle.

4.2.4 MOBLAS-6 calibration targets/distances

MOBLAS-6 has used 4 different calibration targets (1 board and 3 cube corners) at marker 7122. From May 1, 1983 through March 26, 1987; from March 27, 1987 through August 16, 1988; from August 17, 1988 through October 3, 1989; and from October 4, 1989 through April 30, 1991; the MOBLAS-6 primary calibration targets were the 2Km calibration board, the 2Km cube corner, the first 2Km Nelson pier, and the second 2Km Nelson pier, respectively.

MOBLAS-6 was surveyed 4 times in 8 years (1983, 1988, 1989, & 1991) at marker 7122. In October 1983, several months after the first survey, a hurricane passed through the site. Between the 1983 and 1988 surveys, the ranges to the 2Km cube corner and the 2Km board changed by +6mm and -17mm, respectively. The system delay differences obtained from the these two targets in historical minico tests, since the Quantel laser installation (July 1984), were 33mm $\pm$ 15 and 10mm $\pm$ 15 [*Husson and Wetzel,* 1987] using the 1983 and 1988 surveys, respectively. The 1988 surveyed target ranges for the cube corner and the board are only accurate to the 10mm level. The 10mm difference which remains in the historical minico results can be attributed to survey. Making this assumption and distributing the 10mm difference equally to both targets, the 1988 survey (with adjustment) can be backdated to the hurricane (October 1983). This means MOBLAS-6 data from October 1, 1983 through March 26, 1987; from March 27, 1987 through May 2, 1988; and from May 3 through August 16, 1988; is biased long by 22mm $\pm$ 10, short by 11mm $\pm$ 10, and short by 5mm $\pm$ 10, respectively.

In 1988, the first Nelson pier was built; however, the pier foundation was not built to specifications. The pier moved 14mm between 1988 and 1989 due to a poor foundation and being on a steep slope [*Nelson*, 1989]. *Nelson* believes this movement would have been linear over the 13 months between the 1988 and 1989 surveys. MOBLAS-6 data between August 17, 1989 and June 23, 1989, was biased long by 4mm $\pm$ 1mm/month. On October 4, 1989, the primary MOBLAS-6 calibration target became the second Nelson pier, which eliminated target movement as a MOBLAS-6 systematic bias source.

4.2.5 MOBLAS-6 TDEL

The MOBLAS-6 cable delay causing this bias has not been measured as of this writing. On January 11, 1990, the MOBLAS-6 TDEL electronics were modified to eliminate other TDEL sub-microsecond ambiguities.

4.2.6 MOBLAS-6 known problem data

All MOBLAS-6 satellite RMS's between February 1 and March 1, 1984, were high caused by a bad distribution amplifier [*Oldham*]. Data during this period should not be used. On March 2, 1984, the distribution amplifier was replaced which eliminated the problem.

4.2.7 MOBLAS-6 potential problem data

All MOBLAS-6 data between February 8 and May 12, 1989, was affected by a bad Setra barometer. Setra barometric data was in error by up to 30 millibars. All MOBLAS-6 data during this interval was corrected and believed to be accurate to at least 3 millibars.

All MOBLAS-6 calibration data between April 1 and September 26, 1990, was unusually noisy (twice the normal RMS). The LAGEOS data during this period is suspected to be bias free. The calibration data returned to normal when some adjustments were performed on the HP5370 in late September [*MOBLAS-6*, 1990].

5. MOBLAS-7

5.1 MOBLAS-7 Eccentricities

Since January 1, 1981, MOBLAS-7 has only occupied one monument/marker (7105); however, two other laser systems (TLRS-2, 71051206, and MOBLAS-2, 71050207) have been referenced to marker 7105. There exists 14 sets of MOBLAS-7 eccentricities and 21 MOBLAS-7 SOD's at 7105.

The reason for the 5mm change in the east ecc. between the 1981 and 1984 survey is assumed to be caused by movement of the survey monument to the East or by movement of the MOBLAS support pad to the West [*Nelson*, 1984].

During the 1985 pre-collocation survey of MTLRS-1 and MOBLAS-7, a 2 cm discrepancy was found in the 7105 Up eccentricity [*Nelson*, 1985]. The original determination of the Up eccentricity is suspected to be in error [*Nelson*, private communication]; and therefore, the 1985 Up eccentricity can be backdated to Jan 1, 1981.

Prior to the TLRS-1 and MOBLAS-7 collocation in 1986 [*Nelson*, 1986], MOBLAS-7 eccentricities were measured on three different occasions, once in December 1985 and twice in January 1986 (before and after the MOBLAS-7 mount was releveled on January 18, 1986). There were millimeter level changes between these surveys. This would give SOD 71050709 five unique sets of eccentricities.

During October 1989, a 1-2 cm bias existed between MOBLAS-7 and TLRS-3 [*Varghese and Husson*, 1989] and a follow-up survey indicated cm level movement of the MOBLAS-7 reference point. Polyquick collocation analysis revealed that the movement appeared to have occurred in August 1989; therefore, the October 12, 1989 survey can be backdated to August 25, 1989.

MOBLAS-7 was down for approximately 6 months in early-1990 due to a major slip ring failure. During this period that the slip rings were being repaired, MOBLAS-7 was removed from it's pad in order that the pad could be reinforced. Prior to ranging and after MOBLAS-7 re-occupied marker 7105, the eccentricities were remeasured. Table 7 contains the recommended set of MOBLAS-7 eccentricities with their corresponding SOD(s) and effective starting dates.

5.2 MOBLAS-7 LAGEOS Biases

The net MOBLAS-7 recoverable biases (range and time) are presented in Table 8. To correct MOBLAS-7 LAGEOS data, the known range and time biases (in Table 8) should be subtracted from the LAGEOS range and timetags, respectively. Any time there is the potential for a change in the bias(es), even though the bias(es) did not change, a new entry has been added. A component breakdown of the biases is presented, followed by a section describing known problem data, and followed by a section describing potential problem data.

5.2.1 MOBLAS-7 ND filters

All MOBLAS-7 LAGEOS data was biased short by 3mm $\pm$ 1,1mm $\pm$ 1,3mm $\pm$ 1, and 1mm $\pm$ 1 from January 1, 1981 through July 9, 1991; from July 10 through 23, 1991; from July 24 through October 17, 1991; and from October 18, 1991 through May 31, 1992; respectively, due to ND filters. The OAM was installed on July 10, 1991, removed on July 24, 1991, and reinstalled on October 18, 1991. After June 1, 1992, this bias has been removed through modelling.

5.2.2 MOBLAS-7 signal strength

MOBLAS-7 LAGEOS data was biased long by 30mm $\pm$ 15, 4mm $\pm$ 2, 7mm $\pm$ 3, 30mm $\pm$ 10, 5mm $\pm$ 3, 3mm $\pm$ 2, and 4mm $\pm$ 2 from August 22, 1983 through February 29, 1984; from March 1 through July 31, 1984; from August 1 through September 30, 1984; from October 1, 1984 through January 25, 1985; from January 26, 1985 through March 31, 1985; from April 1, 1985 through March 30, 1986; and from February 1, 1988 through April 30, 1988; respectively, due to signal strength. This bias would vary slightly (several mm) from pass-to-pass and would have a slight elevation dependence. Low elevation data would be biased longer than high elevation data. Signal strength effects were reduced as system calibration techniques improved, and were eliminated when the MCPPMT package was installed in MOBLAS-7 on March 31, 1986.

5.2.3 MOBLAS-7 elevation angles

Prior to January 1, 1988, the tropospheric range correction applied to the fullrate data was computed based on the MOBLAS-7 encoder measurements. To remove this error in pre-1988 MOBLAS-7 data, the applied tropospheric refraction must be removed and reapplied using the computed elevation angle.

5.2.4 MOBLAS-7 calibration targets/distances

MOBLAS-7 has used 3 different calibration targets (1 board and 2 cube corners) at marker 7105. From January 1, 1981 through September 19, 1986; from September 20 through December 5, 1986; and from December 6, 1986 to the present; the MOBLAS-7 primary calibration targets were the 3Km board, the second 3Km cube corner, and the 200m Nelson pier, respectively.

MOBLAS-7 has been surveyed at least once per year since January 1984. The February 1981 and the June 1981 surveyed board ranges were incorrect, causing all MOBLAS-7 data from March 1 through June 30, 1981 and from July 1 through December 31, 1981 to be biased long by 49mm $\pm$ 20 and 22mm $\pm$ 20, respectively.

Between the 1984 and 1985 surveys, the board range changed by 17mm, however; historical minico results support the 1984 survey value [*Heinick*, 1985] for the board range (not the 1985 value). On February 7, 1986, the guy wires were tensioned on the calibration board before the board was resurveyed (12mm change); however, the new surveyed calibration board range was not used until March 2, 1986. Therefore, all MOBLAS-7 LAGEOS passes from August 1, 1985 through February 6, 1986, and from February 7 through March 1, 1986, is biased long by 17mm $\pm$ 20 and short by 12mm $\pm$ 20, respectively, except for the LAGEOS passes in Table 9. Occasionally due to ground fog conditions, the board could not be ranged, so the secondary calibration target, the 3km cube corner, was used. All passes in Table 9 were calibrated using the original 3Km cube corner and are believed to have the correct calibration distance. Between the January and October 1989 surveys, the Nelson pier target range changed by 15mm due to movement of the MOBLAS-7 reference point. Apparently, the MOBLAS-7 reference point moved around August 25, 1989 based upon intercomparison with TLRS-3 [*Varghese and Husson*, 1989]. All MOBLAS-7 data from August 25 through October 11, 1989 is biased short by 15mm.

5.2.5 MOBLAS-7 TDEL

All MOBLAS-7 data from July 13, 1989 through September 27, 1990, and from September 28, 1990 through May 31, 1992 contains a time bias -0.5 and -0.3 microseconds, respectively. This correction is only valid after July 13, 1989, because on this date, the MOBLAS-7 TDEL electronics were modified to eliminate other TDEL sub-microsecond accuracy ambiguities, which would have masked this bias. On September 28, 1990, the cable length causing this bias was shortened, which caused a decrease in the magnitude of the bias. This bias has been eliminated through modelling, effective June 1, 1992.

5.2.6 MOBLAS-7 known problem data

All MOBLAS-7 data between January 13 through January 17, 1986, has a reference frequency problem and should not be used. The HP5370 frequency was on internal frequency during this period of time.

5.2.7 MOBLAS-7 potential problem data

All MOBLAS-7 LAGEOS data between June 7 and June 13, 1984 was noisy (100-130mm) and should be used with caution. The cause of the high noise is unknown.

All MOBLAS-7 LAGEOS data between September 25 and October 5, 1984 was noisy (80-120mm) and should be used with caution. The cause of the high noise is unknown.

6. MOBLAS-8

6.1 MOBLAS-8 Eccentricities

Since October 1, 1981, MOBLAS-8 has only occupied one monument/marker (7109). In July 1982, the MOBLAS-4 and MOBLAS-8 moms vans were switched. There exists 9 sets of MOBLAS-8 eccentricities, and 15 MOBLAS-8 SOD's at 7109.

On August 4, 1982 the system was releveled, but there was not a follow-up survey until 1984, which indicated a 17mm change in the Up ecc. *Nelson* [1984] recommends that the 1984 survey be backdated to 1982. There was a 4mm change in the Up ecc between 1985 and 1988, possibly due to settlement of the laser support slab [*Nelson* ,1985]. Table 10 contains the recommended set of MOBLAS-8 eccentricities with their corresponding SOD(s) and effective starting dates.

6.2 MOBLAS-8 LAGEOS Biases

The net MOBLAS-8 recoverable biases (range and time) are presented in Table 11. To correct MOBLAS-8 LAGEOS data, the known range and time biases (in Table 11) should be subtracted from the LAGEOS range and timetags, respectively. Any time there is the potential for a change in the bias(es), even though the bias(es) did not change, a new entry has been added. A component breakdown of the biases is presented and followed by a section describing known problem data.

6.2.1 MOBLAS-8 ND filters

All MOBLAS-8 LAGEOS data was biased short by 3mm $\pm$ 1 and 1mm $\pm$ 1 from September 1, 1981 through April 7, 1992, and from April 8, 1992 through May 31, 1992, respectively, due to ND filters. On April 7, 1992, the OAM was installed in MOBLAS-8 reducing the ND filter bias. After June 1, 1992, this bias has been removed through modelling.

6.2.2 MOBLAS-8 signal strength

MOBLAS-8 LAGEOS data was biased long by 5mm $\pm$ 3, 10mm $\pm$ 5, 6mm $\pm$ 3, and 3mm $\pm$ 2 from August 4, 1982 through December 31, 1983; from January 1 through March 31, 1984; April 1 through July 31, 1984; and from August 1, 1984 through September 25, 1986; respectively, due to signal strength. This bias would vary slightly (several mm) from pass-to-pass and would have a slight elevation dependence. Low elevation data would be biased longer than high elevation data. Signal strength effects were reduced as system calibration techniques improved, and were eliminated when the MCPPMT package was installed in MOBLAS-8 on September 26, 1986.

6.2.3 MOBLAS-8 elevation angles

Prior to January 1, 1988, the tropospheric range correction applied to the fullrate data was computed based on the MOBLAS-8 encoder measurements. To remove this error in pre-1988 MOBLAS-8 data, the applied tropospheric refraction must be removed and reapplied using the computed elevation angle.

6.2.4 MOBLAS-8 calibration targets/distances

MOBLAS-8 has used 5 different calibration targets (2 boards and 3 cube corners) at marker 7109. From September 1, 1981 through August 19, 1985; from August 20, 1985 through December 31, 1986; from January 1, 1987 through March 22, 1989; from March 23, 1989 through April 7, 1992; and from April 8, 1992 to the present; MOBLAS-8 primary calibration targets were the original 2Km board, the second 2Km board, the second 2Km cube corner, the 2Km Nelson pier, and the 200m Nelson pier, respectively.

MOBLAS-8 was surveyed 7 times (1981, 1982, 1984, 1985, 1988, and twice in 1991) at marker 7109. During August 1985, new calibration targets (a 2Km board and 2Km cube corner) were built to replace the vandalized 2Km board and 2Km cube corner [*Nelson*, 1985]. The guy wires had been cut on both targets. The newly constructed board became the operational target, effective August 20, 1985. The preliminary board range and the final surveyed board range published in the November 1985 survey sheet were different by 10mm. It is not known at this writing when the "official" number was used for fullrate data processing. Sometime between October 1986 and January 1987, the cube corner became the operational target. In December 1988, these targets were resurveyed along with a newly constructed 2Km Nelson pier. Between the 1985 and 1988 surveys, the board and cube corner ranges changed by 14mm and 11mm, respectively. Historical minico results, since January 1987, suggest that 1985 and 1988 cube corner surveyed ranges were in error by -20mm and -9mm, respectively. Therefore, MOBLAS-8 data was biased long by 20 ± 15 and 9 ± 10mm from January 1, 1987 through December 11, 1988, and from December 12, 1988 through March 22, 1989, respectively. More research is needed into data processing results prior to January 1987.

6.2.5 MOBLAS-8 TDEL

All MOBLAS-8 data from November 22, 1989 through May 31, 1992, contains a time bias of +0.3 microseconds. This correction is only valid after November 22, 1989, because on this date, the MOBLAS-8 TDEL electronics were modified to eliminate other TDEL sub-microsecond accuracy ambiguities, which would have masked this bias. This bias has been eliminated through modelling, effective June 1, 1992.

All MOBLAS-8 data from August 4, 1982 (the date of the moms van swap with MOBLAS-4) through October 26, 1986 was biased late depending on the interval of a second the laser was fired [*MOBLAS-8 crew and Heinick*, 1986]. The transmit delays (TDEL) on the .0, .2, .4, .6, .8 second intervals were reading high by 0.0, 3.2, 6.4, 9.6, and 11 microseconds, respectively, due to a wiring problem. Since MOBLAS-8 data was equally distributed in these different time intervals, a mean offset of 6.0 microseconds can be post-applied to the data. The TDEL wiring problem was fixed on October 27, 1986.

6.2.6 MOBLAS-8 known problem data

All MOBLAS-8 data between January 1 through March 4, 1982, exhibited very high RMS's (300-600mm) due to poor hardware performance. This data probably contains significant biases and should not be used. The hardware was repaired on March 5, 1982, and the RMS's returned to nominal levels.

7. CONCLUDING REMARKS

The present article has been the first attempt to characterize known biases contained in historical MOBLAS LAGEOS data; however, more research into historical ground test results and calibration processing information is needed to resolve potential biases. These bias models and eccentricity information should improve the quality of the historical MOBLAS LAGEOS dataset. We encourage other global data producing centers to characterize their historical biases.

In the 1980-1983 timeframe, the laser was the dominant MOBLAS systematic error source. In the 1984-1986 timeframe, target stability, survey related issues, and signal strength effects were the dominant error sources. In the 1987-1988 timeframe, target stability and survey related issues were the dominant error sources. In the 1989-1992 timeframe, the HP5370 counter and ND filters appear to have been the dominant error sources. Some of the above mentioned systematic errors are recoverable (to some level) using historical processing results; however, orbital analysis may be the only way to unravel the "net" biases in the global SLR dataset to the 10mm level. These bias models will evolve as historical SLR data is better understood by close cooperation of the data producer and the data user.

8. ACKNOWLEDGEMENTS

The material in this article has been amassed through years of close interaction with a highly talented group of colleagues at the Bendix Field Engineering Corporation in Greenbelt and Columbia, Md; at the NASA Goddard Space Flight Center in Greenbelt, Md; and at the Center for Space Research in Austin, Texas, and much of their work is referenced here.

REFERENCES

Brogdon O. L., Heinick J. M., MOBLAS Ground Test Results, Bendix Field Engineering Corporation internal reports, 1980-1983.

Crawford W. F., LTN Data, Bendix Field Engineering Corporation internal report, Nov. 1985.

Degnan J. J., Satellite Laser Ranging: Current Status and Future Prospects, *IEEE Trans. Geosci. Remote Sensing, Vol GE-23 Number 4, pp 398-413*, Jul. 1985.

Eichinger R. A., Oldham T. J., MOBLAS 4, 6, 7, 8 Antiparallax Optical Path Differences, Bendix Field Engineering Corporation internal reports, 1990-1992.

Heinick J. M., Receive Energy Dependence and Correction at MOBLAS 4, 5, 7, and 8, Bendix Field Engineering Corporation, *presented at the spring 1984 AGU*, Feb. 1984.

Heinick J. M, Husson V. S., Wroe S. A., Brogdon O. L., Wetzel S. L., Clarke C. B., Six Month Data Processing Report, Bendix Field Engineering Corporation internal report, Nov. 1989.

Heinick J. M., MOBLAS-7's calibrations using the corner cube and the most recently published calibration board range, Bendix Field Engineering Corporation internal report, Oct. 1985.

Husson V. S., Wroe S. A., MOBLAS-5 Processing Dilemma Update, Bendix Field Engineering Corporation, *presented at the weekly CDPSLR meeting*, Oct. 1987.

Husson V. S., Wetzel S. L., MOBLAS-6 Processing Dilemma Update, Bendix Field Engineering Corporation, *presented at the weekly CDPSLR meeting*, Oct. 1987.

Husson V. S., Wroe S. A., Wetzel S. L., TLRS-1/MOBLAS-7 Collocation Analysis Report, Bendix Field Engineering Corporation internal report, 1987.

McCollums D. L., private communication, Bendix Field Engineering Corporation.

McCollums D. L., Varghese T. K., MOBLAS-7 System Characterization Reports, Bendix Field Engineering Corporation, 1986-1988.

MOBLAS-8 Crew, Heinick J. M., MOBLAS-8 Transmit Delay Investigation, Bendix Field Engineering Corporation internal report, Oct. 1986.

Murphy B., Nelson V. E., MOBLAS 5 Survey Reports, Australian Division of National Mapping, Bendix Field Engineering Corporation, 1979/80, 1987, 1992.

Nelson V. E., MOBLAS 4 Survey Reports, Bendix Field Engineering Corporation, 1983, 1985, 1988, 1992.

Nelson V. E., MOBLAS 6 Survey Reports, Bendix Field Engineering Corporation, 1983, 1988, 1989, 1991.

Nelson V. E., MOBLAS 7 Survey Reports, Bendix Field Engineering Corporation, 1981, 1982, 1984, 1985, 1986, 1987, 1988, 1889, 1990, 1991, 1992.

Nelson V. E., MOBLAS 8 Survey Reports, Bendix Field Engineering Corporation, 1981, 1982, 1984, 1985, 1988, 1989, 1991.

Nelson V. E., private communication, Bendix Field Engineering Corporation.

Nelson V. E., System Eccentricity Measurement Procedures for MOBLAS Systems, Bendix Field Engineering Corporation internal report, 1986.

Oldham T. J., private communication, Bendix Field Engineering Corporation.

Pearlman M. R., Laser System Characterization, Smithsonian Institution Astrophysical Observatory, *Proc. 5th Int. Workshop on Laser Ranging Instrumentation*, Sep. 1984.

Selden M. D., Varghese T. K., Heinick J. M., Oldham T. J., Preliminary Results from the Portable Standard Satellite Ranging Intercomparison with MOBLAS-7, *Proc. 8th Int. Workshop on Laser Ranging Instrumentation*, May 1992.

See D., Sneed R. S., Suggestions for new or improved LRC logic, Bendix Field Engineering Corporation internal report, Oct. 1988.

Silva T. D, Malitson P. H. Eichinger R. E., Optical Attenuation Mechanism, Bendix Field Engineering Corporation internal report, Feb. 1991.

Smith D. E., Kolenkiewicz R., Dunn, P. D., Klosko S. M., Robbins J. W., Torrence M. H., Williamson R. G., Pavlis E. C, Douglas N. B, Fricke S. K., LAGEOS Geodetic Analysis--SL7.1, *NASA Technical Memorandum 104549*, Sep. 1991.

Varghese T. K., Heinick J. M., Sub-cm Multiphotoelectron Satellite Laser Ranging, Bendix Field Engineering Corporation, *Proc. of 6th Int. Workshop on Laser Ranging Instrumentation*, 1986.

Varghese T. K., Husson V. S., TLRS-3: Engineering Upgrades and Performance Evaluation through Intercomparison with MOBLAS-7 from Oct. 88 - Nov. 89., Bendix Field Engineering Corporation internal report, Nov. 1989.

Wroe S. A., Heinick J. M., Brogdon O. L., Wetzel S. L., Clarke C. B, Cheng G. S., Horvath J. E., MOBLAS Ground Test Results, Bendix Field Engineering Corporation internal reports, 1984-1992.

Table 1. MOBLAS-4 Eccentricities for SOD 711004xx

Occ. No.	Start Date	North (M)	East (M)	Up (M)	Revis. Date	Comments
2	08/15/83	-0.033	-0.015	3.209	01Aug92	First survey
2-3	06/20/85	-0.033	-0.015	3.210	01Aug92	1mm change in Up
3-10	04/27/88	-0.033	-0.016	3.213	01Aug92	1 & 3mm change in East and Up
10	02/01/92	-0.031	-0.016	3.213	01Aug92	2mm change in North, no survey sheet published
11	04/21/92	-0.026	-0.019	3.189	01Aug92	Mount replacement

Table 2. MOBLAS-4 LAGEOS Biases at 7110

Time Span	Range Bias(mm)	Time Bias(us)	Revis. Date	Comments
08/15/83 - 04/11/84	17	0	01Aug92	Quantel, 2233B, 5370, Ortec, & board (1954.6037m)
04/12/84 - 05/24/84	17	0	01Aug92	Gating problem causing discontinuous data, see 2.2.6
05/25/84 - 06/30/84	17	0	01Aug92	Data quality returned to normal
07/01/84 - 08/31/84	7	0	01Aug92	Improvement in amplitude modelling
09/01/84 - 06/19/85	3	0	01Aug92	Improvement in amplitude modelling
06/20/85 - 07/31/85	3	0	01Aug92	New target range (1954.5910m), see 2.2.4 para. 2
08/01/85 - 11/19/86	1	0	01Aug92	Improvement in amplitude modelling
11/20/86 - 12/31/86	-3	0	01Aug92	MCP & Tennelec disc. installed
01/01/87 - 10/31/87	-3	0	01Aug92	Cube corner (1955.469m)
11/01/87 - 12/31/87	-3	0	01Aug92	Unstable cube corner, see 2.2.4 para. 4
01/01/88 - 01/28/88	-3	0	01Aug92	Computed angles used, see 2.2.3, unstable cube corner, see 2.2.4 para. 4
01/29/88 - 04/29/88	-3	0	01Aug92	Cal. board (1954.5910m)
04/30/88 - 12/28/88	-3	0	01Aug92	Long Nelson pier (1955.2677m)
12/29/88 - 01/27/89	-3	0	01Aug92	Questionable data, bad counter, see 2.2.7
01/28/89 - 11/06/89	-3	0	01Aug92	New counter installed
11/07/89 - 11/11/90	-3	0	01Aug92	New range (1955.2682m), cube replaced
11/12/90 - 01/04/90	-3	0	01Aug92	Cube vandalized and replaced (1955.2600m)
01/05/90 - 12/05/91	-3	-0.4	01Aug92	Transmit delay modification see 2.2.5
12/06/91 - 01/17/92	-3	-0.4	01Aug92	Translator installed, short Nelson pier (186.9920m)
01/18/92 - 04/20/92	-1	-0.4	01Aug92	OAM installed
04/21/92 - 05/31/92	-1	-0.4	01Aug92	Mount replaced, new target range (186.9986m)

Table 3. MOBLAS-5 Eccentricities for SOD 709005xx

Occ. No.	Start Date	North (M)	East (M)	Up (M)	Revis. Date	Comments
1-8	08/01/79	0.003	0.011	3.185	01Aug92	First survey
8-10	10/15/87	0.003	0.010	3.177	01Aug92	1mm & 8mm change in East and Up
11-12	01/12/92	-0.011	0.020	3.181	01Aug92	Mount replaced

Table 4. MOBLAS-5 LAGEOS Biases at 7090

Time Span	Range Bias(mm)	Time Bias(us)	Revis. Date	Comments
08/01/79 - 06/07/80	-23	0	01Aug92	GP laser, 2233B, 5360, Ortec, & board (2065.491m), gating problem see 3.2.6
06/08/80 - 07/26/83	-3	0	01Aug92	New board (3100.2532m) used
07/27/83 - 05/31/85	-6	0	01Aug92	Quantel & 5370 installed
06/01/85 - 04/22/87	3	0	01Aug92	Suspect 9mm error in target range, see 3.2.4
04/23/87 - 05/31/87	6	0	01Aug92	MCP & Tennelec disc. installed
06/01/87 - 07/31/87	-3	0	01Aug92	Cube corner (1257.9630m) used
08/01/87 - 08/25/87	-3	0	01Aug92	Board (3100.2442m) used
08/26/87 - 12/31/87	-3	0	01Aug92	Long Nelson pier (3116.8969m) used
01/01/88 - 08/11/88	-3	0	01Aug92	Computed angles used, see 3.2.3
08/12/88 - 01/31/89	-3	0	01Aug92	High cal. shifts, see 3.2.8
02/01/89 - 01/29/90	-3	0	01Aug92	Cal. shifts return to normal
01/30/90 - 07/22/90	-3	0	01Aug92	Transmit delay modification, see 3.2.5
07/23/90 - 12/18/91	-3	0	01Aug92	New range (3116.8974m), cube replaced
12/19/91 - 01/03/92	-3	0	01Aug92	Bad data, stuck bit see 3.2.7
01/04/92 - 01/11/92	-3	0	01Aug92	Stuck bit repaired
01/12/92 - 05/31/92	-3	0	01Aug92	Mount replaced, new survey (3116.9047m)

Table 5. MOBLAS-6 Eccentricities for SOD 712206xx

Occ. No.	Start Date	North (M)	East (M)	Up (M)	Rev. Date	Comments
1-4	05/01/83	0.001	-0.007	3.182	01Aug92	First survey
4-7	05/03/88	0.002	-0.006	3.181	01Aug92	1mm change in all eccs., see 4.1
8-9	06/23/89	0.002	-0.006	3.181	01Aug92	No change
9	04/30/91	0.002	-0.006	3.181	01Aug92	No change, final survey

Table 6. MOBLAS-6 LAGEOS Biases at 7122

Time Span	Range Bias(mm)	Time Bias(us)	Revis. Date	Comments
05/01/83 - 09/30/83	-3	0	01Aug92	GP laser, 2233B, 5360, Ortec, & Board (2229.1998m)
10/01/83 - 01/31/84	19	0	01Aug92	Hurricane, suspect target movement, see 4.2.4, para 2
02/01/84 - 03/01/84	19	0	01Aug92	Bad distribution amplifier, see 4.2.6
03/02/84 - 04/30/84	19	0	01Aug92	Distribution amplifier replaced
05/01/84 - 03/31/86	31	0	01Aug92	Quantel laser and HP5370 installed
04/01/86 - 08/31/86	29	0	01Aug92	Improvement in amplitude modelling
09/01/86 - 01/27/87	23	0	01Aug92	Improvement in amplitude modelling
01/28/87 - 03/26/87	19	0	01Aug92	MCP and Tennelec installed
03/27/87 - 12/31/88	-14	0	01Aug92	Cube corner used (2229.4086m)
01/01/88 - 05/02/88	-14	0	01Aug92	Computed angles used, see 4.2.3
05/03/88 - 08/16/88	-8	0	01Aug92	New cube corner range used (2229.4150m)
08/17/88 - 08/31/88	1	0	01Aug92	First Nelson pier used (2229.2215m)
09/01/88 - 09/30/88	2	0	01Aug92	Nelson pier movement, see 4.2.4 para 3
10/01/88 - 10/31/88	3	0	01Aug88	Nelson pier movement
11/01/88 - 11/30/88	4	0	01Aug92	Nelson pier movement
12/01/88 - 12/31/88	5	0	01Aug92	Nelson pier movement
01/01/89 - 01/31/89	6	0	01Aug92	Nelson pier movement
02/01/89 - 02/28/89	7	0	01Aug92	Nelson pier movement, bad barometric data
03/01/89 - 03/31/89	8	0	01Aug92	Nelson pier movement, bad barometric data
04/01/89 - 04/30/89	9	0	01Aug92	Nelson pier movement, bad barometric data
05/01/89 - 05/12/89	10	0	01Aug92	Nelson pier movement, bad barometric data
05/13/89 - 05/31/89	10	0	01Aug92	Barometer repaired
06/01/89 - 06/22/89	11	0	01Aug92	Nelson pier movement
06/23/89 - 11/16/89	-3	0	01Aug92	Second Nelson pier used (2232.7419m)
11/17/89 - 01/10/90	-3	0	01Aug92	New range (2232.7447m), cube replaced
01/11/90 - 03/31/90	-3	0	01Aug92	Transmit delay modification
04/01/90 - 09/26/90	-3	0	01Aug92	Calibration RMS's are high
09/27/90 - 04/30/91	-3	0	01Aug92	Calibration RMS's return to normal levels

Table 7. MOBLAS-7 Eccentricities for SOD 710507xx

Occ. No.	Start Date	North (M)	East (M)	Up (M)	Rev. Date	Comments
1-4	01/01/81	0.016	-0.026	3.169	01Aug92	First survey, Up was in error
5	03/22/84	0.017	-0.031	3.169	01Aug92	1 & 5mm change in North & East
8	05/07/85	0.017	-0.031	3.169	01Aug92	No change
9	07/29/85	0.017	-0.032	3.169	01Aug92	1mm change in East
9	12/13/85	0.017	-0.032	3.170	01Aug92	1mm change in Up
9	01/17/86	0.016	-0.031	3.168	01Aug92	1, 1 and 2mm changes in North, East, and Up
9	01/22/86	0.017	-0.031	3.168	01Aug92	1mm change in North
9-10	03/17/86	0.017	-0.031	3.168	01Aug92	No change
10-11	10/06/86	0.017	-0.031	3.168	01Aug92	No change
11-12	06/18/87	0.017	-0.031	3.168	01Aug92	No change
13	01/09/89	0.017	-0.031	3.168	01Aug92	No change
15-16	08/25/89	0.035	-0.040	3.162	01Aug92	System moved, 18mm, 9mm, 6mm changes in North, East, and Up
17-18	07/25/90	-0.014	-0.033	3.153	01Aug92	Relocation
19-23	12/10/90	-0.014	-0.033	3.153	01Aug92	No change

Table 8. MOBLAS-7 LAGEOS Biases at 7105

Time Span	Range Bias(mm)	Time Bias(us)	Revis. Date	Comments
01/01/81 - 06/30/81	46	0	01Aug92	GP laser, 2233B, 5360, Ortec, & board (3225.460m)
07/01/81 - 12/31/81	19	0	01Aug92	Slyvania laser installed, board (3225.433m)
01/01/82 - 01/31/83	-3	0	01Aug92	Board (3225.411m)
02/01/83 - 08/21/83	-3	0	01Aug92	HP5370 counter installed
08/22/83 - 02/29/84	27	0	01Aug92	Quantel laser installed
03/01/84 - 03/21/84	1	0	01Aug92	Improvement in amplitude modelling
03/22/84 - 06/06/84	1	0	01Aug92	New board (3225.421m)
06/07/84 - 06/13/84	1	0	01Aug92	Data suspect, high RMS's, see 5.2.7
06/14/84 - 07/31/84	1	0	01Aug92	RMS's return to normal
08/01/84 - 09/24/84	4	0	01Aug92	Increase in amplitude dependence
09/25/84 - 09/30/84	4	0	01Aug92	Data suspect, high RMS's, see 5.2.7
10/01/84 - 10/05/84	27	0	01Aug92	Increase in ampl. dependence, high RMS's
10/05/84 - 01/25/85	27	0	01Aug92	RMS's return to normal
01/26/85 - 03/31/85	2	0	01Aug92	Improvement in amplitude modelling
04/01/85 - 07/31/85	0	0	01Aug92	Improvement in amplitude modelling
08/01/85 - 01/12/86	17	0	01Aug92	New range (3225.438m), see 5.2.4 & Table 9
01/13/86 - 01/17/86	17	0	01Aug92	5370 on internal frequency, see 5.2.6
01/18/86 - 02/06/86	17	0	01Aug92	5370 put back on external frequency
02/07/86 - 03/01/86	-12	0	01Aug92	Guy wires on board tensioned, Secondary cal. target new cube corner (3482.552m)
03/02/86 - 03/30/86	0	0	01Aug92	New board range (3225.450m)
03/31/86 - 09/30/86	-3	0	01Aug92	MCP and Tennelec disc. installed
10/01/86 - 12/05/86	-3	0	01Aug92	Cube corner used (3482.547m)
12/06/86 - 12/31/87	-3	0	01Aug92	Nelson pier used (223.385m), antiparallax hardware installed
01/01/88 - 01/31/88	-3	0	01Aug92	Computed angles used 5.2.3
02/01/88 - 04/30/88	1	0	01Aug92	Amplitude dependence (+4mm)
05/01/88 - 01/08/89	-3	0	01Aug92	Elimination of amplitude dependence
01/09/89 - 06/14/89	-3	0	01Aug92	New range (223.3868m)
06/15/89 - 07/12/89	-3	0	01Aug92	New antiparallax hardware installed
07/13/89 - 08/02/89	-3	-0.5	01Aug92	Transmit delay modification, see 5.2.5
08/03/89 - 08/24/89	-3	-0.5	01Aug92	Original antiparallax hardware installed
08/25/89 - 10/11/89	-18	-0.5	01Aug92	Apparent movement of system, see 5.2.4
10/12/89 - 07/23/90	-3	-0.5	01Aug92	New range (223.4018m)
07/24/90 - 09/27/90	-3	-0.5	01Aug92	New range (223.3922m), cube replaced
09/28/90 - 12/09/90	-3	-0.3	01Aug92	TDEL cable shortened, see 5.2.5
12/10/90 - 07/09/91	-3	-0.3	01Aug92	New antiparallax hardware installed
07/10/91 - 07/23/91	-1	-0.3	01Aug92	OAM installed
07/24/91 - 10/17/91	-3	-0.3	01Aug92	OAM removed
10/18/91 - 05/31/92	-1	-0.3	01Aug92	OAM reinstalled

Table 9. MOBLAS-7 Cube Corner Calibrated LAGEOS Passes
(The range biases for these passes would be 0)

Date	Time
08/09/85	5:20
08/09/85	8:51
08/14/85	5:51
08/28/85	4:11
08/29/85	6:16
08/29/85	9:42
08/30/85	8:30
08/31/85	7:08
09/04/85	5:10
09/04/85	8:36
09/06/85	5:55
09/06/85	9:22
09/07/85	4:35
09/07/85	8:03
09/10/85	3:59
09/10/85	7:31
09/11/85	2:52
09/11/85	6:15
09/11/85	9:37
09/17/85	5:04
09/18/85	10:38
09/20/85	8:01
09/21/85	9:59
10/01/85	10:22
10/07/85	12:49
10/08/85	11:24
10/16/85	11:34
10/17/85	13:22
12/03/85	21:32
12/04/85	0:59
02/13/86	22:07

Table 10. MOBLAS-8 Eccentricities for SOD 710908xx

Occ. No.	Start Date	North (M)	East (M)	Up (M)	Rev. Date	Comments
1	09/01/81	0.012	0.011	3.225	01Aug92	First Survey
1	07/22/82	-0.029	0.011	3.124	01Aug92	M8 & M4 mom's van swap
1-2	08/04/82	-0.029	0.011	3.141	01Aug92	System releveled, 17mm change in Up, based on 84 survey
2-3	09/24/84	-0.029	0.011	3.141	01Aug92	No survey sheet
3-5	08/20/85	-0.029	0.011	3.142	01Aug92	1mm change in Up
6-11	12/12/88	-0.027	0.012	3.138	01Aug92	2, 1, & 4mm change in North, East, and Up
12	12/01/91	-0.019	0.005	3.184	01Aug92	Mount replacement
13-15	12/12/91	-0.035	-0.003	3.184	01Aug92	System releveled, 16 & 8mm change in North and East

Table 11. MOBLAS-8 LAGEOS Biases at 7109

Time Span	Range Bias(mm)	Time Bias(us)	Revis. Date	Comments
09/01/81 - 12/31/81	-3	0	01Aug92	GP laser, 2233B, 5360, Ortec, & board (2394.087m)
01/01/82 - 03/04/82	-3	0	01Aug92	Very high RMS's (300-600mm), see 6.2.6
03/05/82 - 08/03/82	-3	0	01Aug92	Hardware repaired, data nominal
08/04/82 - 12/31/83	2	+6.0	01Aug92	M4/M8 van switch, Quantel, HP5370, transmit delay problem see 6.2.5, board (2394.120m)
01/01/84 - 03/31/84	7	+6.0	01Aug92	Increase in amplitude dependence
04/01/84 - 07/31/84	3	+6.0	01Aug92	Improvement in amplitude modelling
08/01/84 - 08/19/85	0	+6.0	01Aug92	Improvement in amplitude modelling
08/20/85 - 09/25/86	0	+6.0	01Aug92	New board used (2389.506 or 2389.496m), see 6.2.4
09/26/86 - 10/26/86	-3	+6.0	01Aug92	MCP & Tennelec disc. installed
10/27/86 - 12/31/86	-3	0	01Aug92	Transmit delay wire connected, see 6.2.5
01/01/87 - 12/31/87	17	0	01Aug92	Cube corner used (2389.519m), see 6.2.4
01/01/88 - 12/11/88	17	0	01Aug92	Computed angles, see 6.2.3
12/12/88 - 03/22/89	6	0	01Aug92	New cube corner range (2389.508m)
03/23/89 - 11/06/89	-3	0	01Aug92	Nelson pier used (2401.1450m)
11/07/89 - 11/21/89	-3	0	01Aug92	New range (2401.1458m), cube replaced
11/22/89 - 11/30/91	-3	-0.3	01Aug92	Transmit delay modification, see 6.2.5
12/01/91 - 12/11/91	-3	-0.3	01Aug92	Mount re-installed, Nelson pier (2401.1392m)
12/12/91 - 04/06/92	-3	-0.3	01Aug92	Mount releveled, Nelson pier (2401.1576m)
04/07/92 - 05/31/92	-1	-0.3	01Aug92	Short range Nelson pier used (207.4742m), OAM installed

Multiwavelength

Ranging/Streak Cameras

OPTIMUM WAVELENGTHS FOR TWO COLOR RANGING

John J. Degnan
Code 901/ Crustal Dynamics Project
NASA Goddard Space Flight Center
Greenbelt, MD 20771

ABSTRACT

The range uncertainties associated with the refractive atmosphere can be mitigated by the technique of two color, or dual wavelength, ranging. The precision of the differential time of flight (DTOF) measurement depends on the atmospheric dispersion between the two wavelengths, the received pulsewidths and photoelectron counts, and on the amount of temporal averaging. In general, the transmitted wavelengths are not independently chosen but instead are generated via nonlinear optics techniques (harmonic crystals, Raman scattering, etc.) which also determine their relative pulsewidths. The mean received photoelectrons at each wavelength are calculated via the familiar radar link equation which contains several wavelength dependent parameters. By collecting the various wavelength dependent terms, one can define a wavelength figure of merit for a two color laser ranging system.

In this paper, we apply the wavelength figure of merit to the case of an extremely clear atmosphere and draw several conclusions regarding the relative merits of fundamental-second harmonic, fundamental-third harmonic, second-third harmonic, and Raman two color systems. We find that, in spite of the larger dispersion between wavelengths, fundamental-third harmonic systems have the lowest figure of merit due to a combination of poor detector performance at the fundamental and poor atmospheric transmission at the third harmonic. Fundamental-second harmonic (~700 nm and 350 nm) have the highest figure of merit, but second-third harmonic systems, using fundamental transmitters near 1000 nm, are a close second. Raman-shifted transmitters appear to offer no advantage over harmonic systems because of (1) the relatively small wavelength separation that can be achieved in light gases such as hydrogen and (2) the lack of good ultrashort pulse transmitters with an optimum fundamental wavelength near 400 nm.

1 INTRODUCTION

With the subcentimeter precisions available from modern satellite laser ranging (SLR) hardware [Degnan, 1985], atmospheric refraction is a dominant error source in the absolute determination of the geometric range from the station to the satellite. While atmospheric modelling is believed to reduce the systematic errors to roughly one centimeter or less, future progress toward millimeter absolute accuracy ranging will rely on the technique of two color, or dual wavelength, ranging.

In the present paper, we attempt to define optimum wavelengths for two color ranging. In order to accomplish this, we must take into account all of the wavelength dependent parameters which influence our ability to make an accurate differential time of flight (DTOF) measurement. As we will see in the ensuing sections, a proper accounting of wavelength dependent terms will include atmospheric dispersion, atmospheric transmission as a function of sea level visibility, transmit antenna and target gains, detector responsivities, transmitter availability and pulsewidth, and the detailed characteristics of the available nonlinear optics techniques for achieving the necessary optical frequency translations.

2 ATMOSPHERIC REFRACTION: THE MARINI-MURRAY MODEL

In the Marini-Murray model of atmospheric refraction [Marini and Murray, 1973], radial variability in the meteorological parameters (i.e. with altitude) is assumed to be governed by the equations for hydrostatic equilibrium, the law of partial pressures, and the perfect gas law. This leads to the following equations for the spherical range correction, SC_{MM}:

$$SC_{MM}(\lambda, E, P_H, T_H, e_H) = \frac{f(\lambda)}{F(\phi, H)} \frac{A(P_H, e_H) + B(\phi, T_H, P_H)}{\sin(E) + \dfrac{B(\phi, T_H, P_H)}{\dfrac{A(P_H, e_H) + B(\phi, T_H, P_H)}{\sin E + .01}}} \tag{2.1}$$

where

$$f(\lambda) = .9650 + \frac{.0164}{\lambda^2} + \frac{.000228}{\lambda^4} \tag{2.2a}$$

$$F(\phi, H) = 1 - .0026\cos 2\phi - .00031H \tag{2.2b}$$

$$A(P_H, e_H) = .002357P_H + .00014\,1e_H \tag{2.2c}$$

$$B(\phi, T_H, P_H) = 1.084x10^{-8}P_H T_H K(\phi, T_H, P_H) + 4.734x10^{-8}\frac{P_H^2}{T_H}\frac{2}{3 - \dfrac{1}{K(\phi, T_H, P_H)}} \tag{2.2d}$$

and

$$K(\phi, T_H, P_H) = 1.163 - .00968\cos 2\phi - .00104T_H + .00001435P_H \tag{2.2e}$$

where λ is the laser wavelength in microns, E is the true elevation angle of the satellite in degrees, ϕ is the station latitude, H is the station height above mean sea level, and P_H, T_H and e_H are the surface pressure, temperature, and water vapor pressure at the station. The water vapor pressure e_H is related to the surface percent relative humidity R_H and surface temperature T_H by the equation

$$e_H(R_H, T_H) = \frac{R_H}{100} 6.11 \times 10^{\left(7.5 \frac{T_H - 273.15}{237.3 + (T_H - 273.15)}\right)} \qquad (2.3)$$

The wavelength dependence of the range correction is contained in the dispersion term $f(\lambda)$ which is plotted in Figure 1. It was arbitrarily chosen by Marini and Murray to have a value of unity at the ruby laser wavelength of .6943 microns.

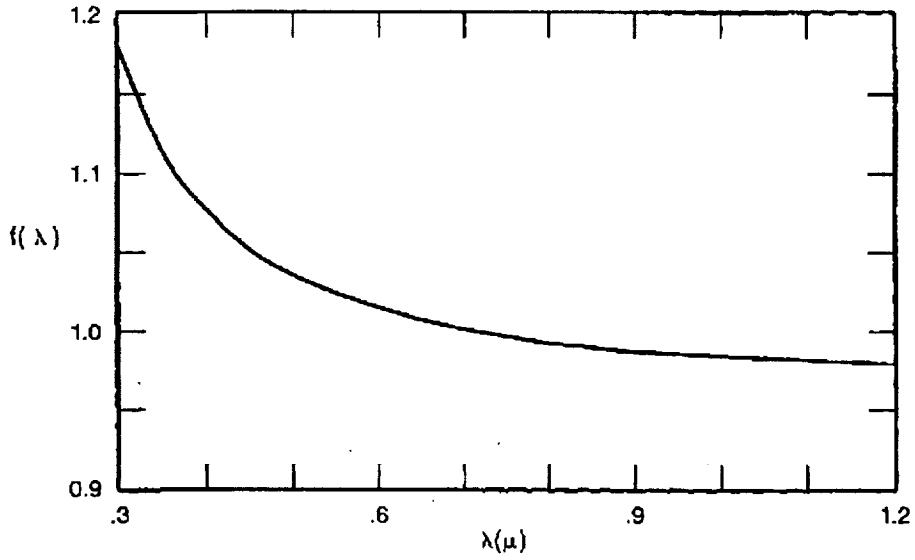

Figure 1. Atmospheric dispersion in a standard atmosphere as a function of wavelength from the near ultraviolet to the near infrared.

3 TWO-COLOR LASER RANGING

By measuring the pulse times-of-flight at two colors and multiplying the results by the velocity of light in vacuum, c, we obtain a measure of the optical path lengths through the atmosphere at the two wavelengths. Thus, the atmospheric refraction correction is given by

$$AC = \gamma(L_1 - L_2) = \frac{\gamma c}{2}(\tau_1 - \tau_2) \tag{3.1}$$

where L_1 and L_2 are the optical path lengths and τ_1 and τ_2 are the measured roundtrip times of flight at the two wavelengths respectively, and

$$\gamma = \frac{n_{g1} - 1}{n_{g2} - n_{g1}} \tag{3.2}$$

where n_{g1} and n_{g2} are the group refractive indices at the two wavelengths. Unfortunately, the wavelength dependence due to the "dry" and "wet" components of the atmosphere are different [Owens, 1968] whereas the expression for the group refractivity N_g used by Marini and Murray assumes no dependence of the water vapor term on wavelength, i.e.

$$N_g(\lambda) = 80.343 f(\lambda)\frac{P}{T} - 11.3\frac{e}{T} \tag{3.3}$$

where P, T, and e are the local pressure, temperature, and water vapor partial pressure respectively. Nevertheless, under normal conditions of modest humidity, γ can be well approximated by the expression [Abshire and Gardner, 1985]

$$\gamma = \frac{f(\lambda_1)}{f(\lambda_2) - f(\lambda_1)} \tag{3.4}$$

where $f(\lambda)$ is given by (2.2a). If we assume that the two times of flight are independently measured, we can express the expected variance in the atmospheric correction as

$$\sigma_{AC}^2 = (\gamma c/2)^2(\sigma_1^2 + \sigma_2^2) \tag{3.5}$$

where σ_1 and σ_2 are the RMS errors in the time of flight measurements at the wavelengths λ_1 and λ_2 respectively. In the ideal limit where the differential timing precision is determined only by the signal strength, one can write

$$\sigma_{AC} = \frac{\gamma c}{2}\left(\frac{\tau_{p1}^2}{n_1} + \frac{\tau_{p2}^2}{n_2}\right)^{1/2} \tag{3.6}$$

where τ_{p1} and τ_{p2} are the laser pulsewidths and n_1 and n_2 are the received photoelectron signal strengths at the two wavelengths respectively.

4 THE RADAR LINK EQUATION

The mean signal flux in a range receiver is obtained from the familiar radar link equation. The mean number of photoelectrons n_{pe} recorded by the ranging detector is given by:

$$n_{pe} = \eta_q \left(E_T \frac{\lambda}{hc} \right) \eta_t G_t \sigma \left(\frac{1}{4\pi R^2} \right)^2 A_r \eta_r T_a^2 T_c^2 \qquad (4.1)$$

where η_q is the detector quantum efficiency, E_T is the laser pulse energy, λ is the laser wavelength, h is Planck's constant, c is the velocity of light in vacuum, η_t is the transmit optics efficiency, G_t is the transmitter gain, σ is the satellite optical cross-section, R is the slant range to the target, A_r is the effective area of the telescope receive aperture, η_r is the efficiency of the receive optics, T_a is the one-way atmospheric transmission, T_c is the one way transmissivity of cirrus clouds (when present), and R is the slant range between the station and the target.

In discussing the link equation, we are primarily concerned with those terms which exhibit a wavelength dependence. While optical coatings certainly exhibit a wavelength dependence thereby affecting the transmit and receive optical efficiencies η_t and η_r, coatings can generally be designed to give approximately equal performance once the operating wavelengths are chosen and hence will not be included in our discussion. Similarly, experimental studies of cirrus cloud transmission have shown no significant dependence on wavelength over the band from 0.317 to 12 microns. Other terms in (4.1) do have a wavelength dependence which we will now discuss.

4.1 TRANSMITTER GAIN

A general expression for the transmitter gain is given by

$$G_t = \frac{4\pi A_t}{\lambda^2} g_t(\alpha_t, \beta, \gamma_t, X) \qquad (4.2)$$

where $A_t = \pi a^2$ is the area of the transmitting aperture and $g_t(\alpha_t, \beta, \gamma_t, X)$ is a geometric factor independent of wavelength [Klein and Degnan, 1974]. Note that, for a given transmit aperture and a well-collimated system, the transmitter gain is inversely proportional to the wavelength squared.

4.2 TARGET OPTICAL CROSS-SECTION

The optical cross-section of an unspoiled retroreflector is given by [Degnan, 1992]

$$\sigma_{cc} = \rho A_{cc} \left(\frac{4\pi A_{cc}}{\lambda^2} \right) \qquad (4.3)$$

where ρ is the cube corner reflectivity, $A_{cc} = \pi R_{cc}^2$ is the light collecting area of the corner cube, and $4\pi A_{cc}/\lambda^2$ is the on-axis retroreflector gain. Even in the presence of complicating factors such as velocity aberration and retroreflector

spoiling, an array of retroreflectors designed to operate at both wavelengths would be expected to retain the same inverse square law dependence on wavelength exhibited by (4.3).

4.3 ATMOSPHERIC ATTENUATION

In the near-ultraviolet to visible spectral band between 0.3 and 0.7 μ, atmospheric attenuation is dominated by aerosol (Mie) scattering but molecular (Rayleigh) and ozone absorption also play a role [RCA, 1968]. In the near infrared beyond 0.7μ, the plot of atmospheric transmission versus wavelength (see Figure 2) is modulated by strong absorption features of various molecular constituents in the atmosphere, notably water vapor, oxygen, and carbon dioxide.

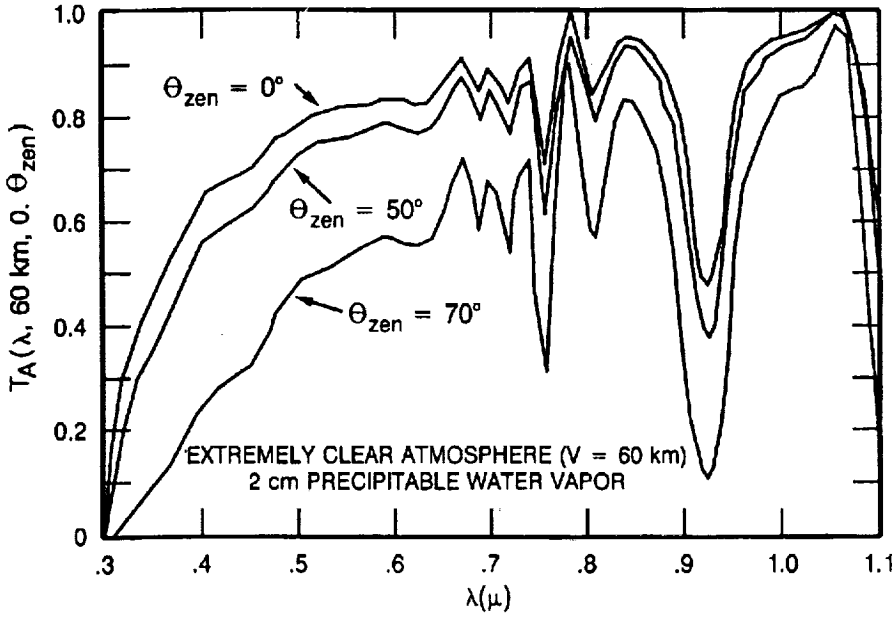

Figure 2. Atmospheric transmission as a function of wavelength under extremely clear conditions with 2 cm of precipitable water vapor at zenith angles of 0, 50, and 70^{o} (corresponding to 1, 2, and 3 air masses) respectively.

The transmission curve presented in Figure 2 corresponds to excellent "seeing" conditions (80 Km visibility) and 2 cm of precipitable water vapor. It should be noted that atmospheric seeing conditions vary widely from day to day and from site to site and are usually characterized by "sea level visibility" expressed in kilometers. Plots of the sea level attenuation coefficient versus wavelength (from 0.4 to 4 μ) as a function of sea level visibility can be found in the RCA Electro-Optics

Handbook [RCA,1968]. For the purpose of this analysis, however, we will consider only the extremely clear atmosphere depicted in Figure 2.

4.4 OPTICAL DETECTORS

Finally, the availability of high quantum efficiency optical detectors at the two laser wavelengths is important. If a common photocathode is to be used, such as in most streak camera schemes for performing differential timing, the photocathode must be sensitive at both wavelengths. However, since the images of the two return pulses can be spatially separated in the entrance slit of the streak camera, one can conceive of specially constructed streak tubes containing more than one photocathode material to obtain the highest sensitivity at both wavelengths. It may also be possible, at some future date, to do the necessary timing via electronic means, such as high speed GaAs technology, without resorting to streak camera technology although this capability has not yet been demonstrated.

A) "BEST" PHOTOEMISSIVE DETECTOR RESPONSIVITIES

WAVELENGTH (μ)	RESPONSIVITY	PHOTOCATHODE (+ WINDOW) MATERIAL
.3	50	S20
.35	60	K-Cs-Sb + (LIME GLASS)
.40	80	K-Cs-Sb + (LIME GLASS)
.45	70	K-Cs-Sb + (LIME GLASS)
.50	63	K-Cs-Sb + (LIME GLASS)
.55	64	GaAs (+ 9741 GLASS)
.60	65	GaAs (+ 9741 GLASS)
.65	67	GaAs (+ 9741 GLASS)
.70	68	GaAs (+ 9741 GLASS)
.75	69	GaAs (+ 9741 GLASS)
.80	70	GaAs (+ 9741 GLASS)
.85	68	GaAs (+ 9741 GLASS)
.90	13	GaAs (+ 9741 GLASS)
.98	9	GaInAs (+ 9741 GLASS)
1.02	.8	GaInAs (+ 9741 GLASS)
1.1	.2	S1

B) COMPOSITE GRAPH OF PHOTOEMISSIVE DETECTOR RESPONSIVITY

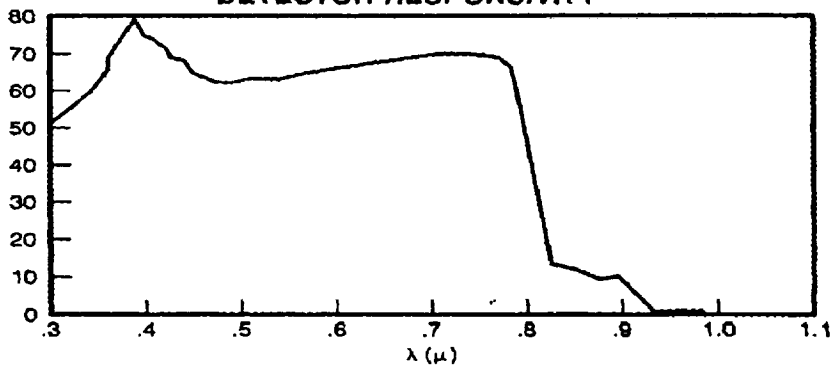

Figure 3. Summary of "best" photoemissive detector responsivities from the near ultraviolet to the near infrared.

Detector sensitivity at a particular wavelength is usually expressed as "spectral responsivity" in milliamperes/Watt. It is related to quantum efficiency by the equation

$$\eta_q(\lambda) = R(\lambda)\frac{hc}{\lambda e} \tag{4.4}$$

where $R(\lambda)$ is the detector spectral responsivity at wavelength λ, h is Planck's constant, and c is the velocity of light. A composite responsivity curve, which is the envelope of individual responsitivity curves for some common visible and near infrared photoemissive detectors[Slater, 1980; Zwicker, 1977] is illustrated in Figure 3.

5 "OPTIMUM" WAVELENGTHS FOR TWO COLOR SLR

In choosing "optimum" candidate wavelengths for successful two color ranging, there are a variety of technical issues the engineer must consider. These will be discussed in the ensuing subsections. As we shall now see, equation (3.6) for the RMS error in the atmospheric correction for the photon-limited case, combined with the radar link equation (4.1), points the way to the selection of a set of optimum wavelengths. Since we want to minimize σ_{AC}, the inverse of (3.6) can serve as an overall system figure of merit.

5.1 ATMOSPHERE

The dependence of (3.6) on the atmospheric dispersive function $f(\lambda)$ illustrates the need for adequate atmospheric dispersion between the two wavelengths in order to reduce the severity of the timing requirements. The atmospheric dispersion curve in Figure 1 strongly suggests that one wavelength be chosen to lie in the near ultraviolet. On the other hand, atmospheric attenuation in the spectral band between 0.3 and 0.7 microns, resulting from the combined effects of molecular (Rayleigh) and aerosol (Mie) scattering and ozone absorption, also increases rapidly in the near ultraviolet as shown in Figure 2. This will negatively impact the timing precision by lowering the photoelectron count at the UV wavelength. Furthermore, in choosing a laser wavelength, it is probably wise to avoid the strong water absorption lines in the spectral regions between 0.7 and 1.0 microns and beyond 1.1 micron. The high variability of water vapor total burden would impact both the day-to-day signal strength and cause the pulse group velocity to vary via the anomalous dispersion effect near an absorbing feature.

5.2 LASER TRANSMITTER

The availability of lasers capable of generating high peak powers and ultrashort pulsewidths on the order of 35 picoseconds or less is also a consideration. Preference is generally given to solid state lasers because of the practical difficulties of using liquid dye lasers in the field. Over the

past decade, much progress has been made in the development of highly tunable solid state lasers such as Alexandrite (700 to 810 nm) and Titanium-doped sapphire (600 to 900 nm). The wide bandwidths of these new materials are capable of supporting subpicosecond pulsewidths whereas today's workhorse, Nd:YAG, is limited to about 10 picoseconds by it's relatively narrow linewidth (120 GHz). However, high bandwidth comes at a price - i.e. lower gain - making the construction of high peak power Ti:Sapphire and Alexandrite devices more difficult.

Generally, the wavelengths in two color systems are generated from the fundamental wavelength λ_f via nonlinear optical techniques such as harmonic generation in crystals or Raman shifting in gases. This assures simultaneity of emission and eliminates (thankfully) the need to synchronize the firings of two separate lasers with picosecond precisions. However, reliance on nonlinear teqhniques implies that the two wavelengths cannot be chosen independently of each other. In the case of harmonic generation, the second and third harmonic wavelengths are given by

$$\lambda_2 = \frac{\lambda_1}{2} \qquad \lambda_3 = \frac{\lambda_1}{3} \tag{5.1}$$

respectively.

In Raman shifting, a portion of the incident radiation at input frequency, ν_o is shifted by some fixed amount ν_s (the "Stokes shift") toward longer wavelengths relative to the fundamental. One also obtains frequencies at longer ("Stokes") and shorter ("Anti-Stokes") wavelengths, but these are generally too weak to supply sufficient energy for satellite ranging. Large Stokes frequency shifts, and hence high dispersion between wavelengths, are obtained by Raman shifting in light gases. Hydrogen produces the largest shift of 4155 cm^{-1}, and photon conversion efficiencies as high as 80% have been reported. For example, one proposed two color SLR system uses the second harmonic of Nd:YAG (532 nm) in hydrogen to obtain a second wavelength output at 680 nm [Gaignebet et al, 1986].

A second consequence of harmonic or Raman generation is that the pulsewidth of the secondary wavelength is generally shorter than the pulsewidth of the fundamental. From the theory of harmonic generation [Degnan, 1979], the harmonic pulsewidths are approximately given by

$$\tau_{2h} \sim \frac{\tau_1}{\sqrt{2}} \qquad \tau_{3h} \sim \frac{\tau_1}{\sqrt{3}} \tag{5.2}$$

for low to moderate energy conversion efficiencies (< 50% - the usual case). Raman generation depends on third order nonlinear processes, and the pulsewidth dependence is identical to that of third harmonic generation.

5.3 WAVELENGTH FIGURE OF MERIT

In order to treat all potential system configurations on an equal basis, some assumptions are in order. We will assume that the fundamental laser, from which all other wavelengths are derived, is characterized by an energy E and a pulsewidth τ_p which is constant for all wavelengths. Thus, Equation (3.6) becomes

$$\sigma_{AC} = \gamma c \tau_p \sqrt{\frac{1}{\beta_1^2 n_1} + \frac{1}{\beta_2^2 n_2}} \tag{5.3}$$

where β_1 and β_2 are pulsewidth scale factors which depend on the nonlinear process used to generate them as in (5.2). In addition, we recognize that wavelengths derived via nonlinear processes are obtained with some typical energy efficiency which we will denote by η_1 and η_2 respectively. If the fundamental wavelength is used as one of the two wavelengths, we will assign values of $\beta_f = 1$ and $\eta_f = 1$. For second and third harmonic generation in the ultrashort pulse regime, typical conversion efficiencies are $\eta_{sh} = .5$ and $\eta_{th} = .2$ respectively.

In order to derive a wavelength figure of merit, we must now bring together all of the wavelength dependent terms in equations (4.1) and (3.5). We obtain for the figure of merit

$$F(\lambda_1, \lambda_2, E) = \frac{f(\lambda_1) - f(\lambda_2)}{f(\lambda_1)} \left[\frac{\lambda_1^4}{\eta_1 \beta_1^2 R(\lambda_1) T_a^2(\lambda_1, E)} + \frac{\lambda_2^4}{\eta_2 \beta_2^2 R(\lambda_2) T_a^2(\lambda_2, E)} \right]^{-\frac{1}{2}} \tag{5.4}$$

where $f(\lambda)$ is the wavelength dispersion term in the Marini-Murray atmospheric correction formula, η_1 and η_2 and β_1 and β_2 are the energy conversion efficiencies and pulsewidth reduction factors respectively for the relevant nonlinear process, $R(\lambda)$ is the spectral responsivity, and $T_a(\lambda, E)$ is the one way atmospheric transmission as a function of wavelength and elevation angle. The factor of λ^4 comes from the combined inverse square law dependence of the transmitter and target (retroreflector) gains on wavelength. The additional factor of λ associated with converting detector quantum efficiency to spectral responsivity cancels with a similar factor in (4.1) which converts transmitter laser energy to the number of transmitter photons. In plotting (5.4), we will use the envelope of the individual photoemitter responsivity curves in Figure 3 so that we present each wavelength in its most favorable light.

6 CONCLUSIONS

Figure 4 provides plots of the wavelength figure of merit as a function of the fundamental (laser) wavelength and elevation angle for the extremely clear atmosphere depicted in Figure 2. Parts (a), (b), and (c) correspond to elevation angles of 90, 45, and 20 degrees respectively. The three curves within each plot compare systems which use: (1) the fundamental and second harmonic wavelengths; (2) the fundamental and third harmonic wavelengths; and (3) the second and third harmonic wavelengths.

In spite of their greater dispersion, fundamental-third harmonic systems have the lowest figure of merit at all elevation angles due to a combination of poor detector performance at the fundamental and poor atmospheric transmission at the third harmonic. The performance of these systems peaks at a fundamental wavelength of about .97 microns independent of elevation angle.

At zenith, fundamental-second harmonic systems, operating at wavelengths of 670 and 335 nm, have the highest figure of merit (F = 1.75) but second-third harmonic systems, operating at wavelengths of 525 and 350 nm (fundamental = 1050 nm), are almost as good (F = 1.6). As one progresses to smaller elevation angles, atmospheric attenuation in the ultraviolet begins to dominate and the optimum fundamental wavelength is shifted toward longer wavelengths with a corresponding reduction in the wavelength figure of merit. Thus, the Nd:YAG laser, with a fundamental wavelength of 1064 nm and a very mature technology, is a near-optimum choice for a second-third harmonic system. However, a fundamental-second harmonic system which utilizes a Ti:Sapphire laser operating in the near infrared beyond 670 nm is a possible alternative.

Figure 5 suggests that a fundamental wavelength of about 400 nm is optimum for a hydrogen Raman-shifted laser and that these systems offer no real advantage over harmonic systems because of their lower wavelength figure of merit. This conclusion is further supported by the fact that there are no high power solid state lasers operating in the near ultraviolet. The principle short wavelength devices are excimer ("excited dimer") gas discharge lasers. At present, excimers cannot achieve ultrashort pulsewidths on the order of picoseconds, typically operate in the high atmospheric attenuation region of the spectrum below 360 nm, and are operationally less desirable than high power solid state lasers. Doubling or tripling solid state lasers to achieve a near ultraviolet wavelength prior to Raman shifting only decreases the overall wavelength figure of merit further by reducing the values for the energy efficiency factors η_1 and η_2. However, this effect is partially offset by the slight reduction in pulsewidth (increased β values) resulting from nonlinear generation.

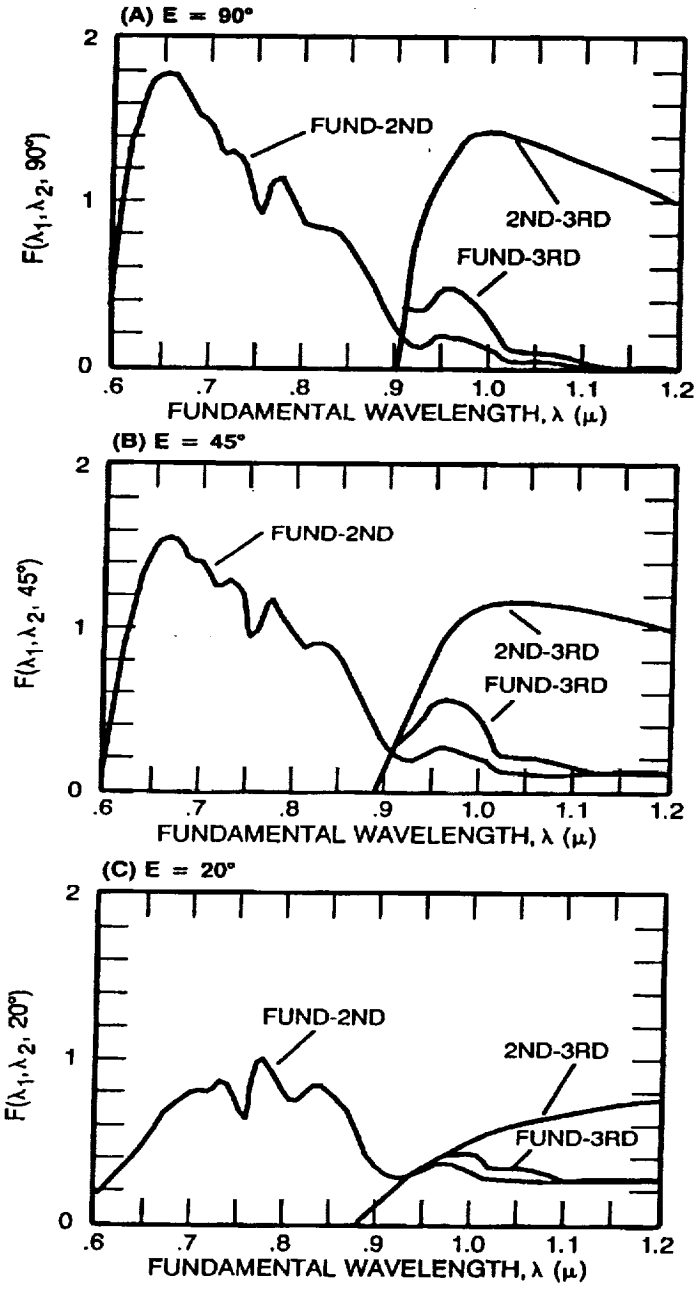

Figure 4. Two color wavelength figure of merit for fundamental-second harmonic, fundamental-third harmonic, and second-third harmonic systems operating in an extremely clear atmosphere at elevation angles of (a) 90°, (b) 45° and (c) 20° respectively.

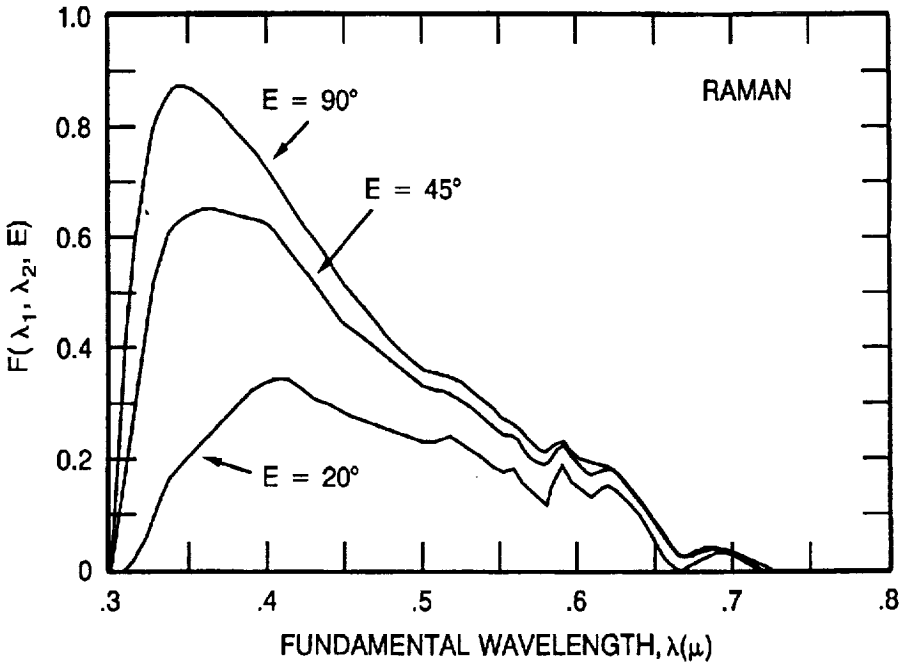

Figure 5. Two color wavelength figure of merit for Raman systems operating in an extremely clear atmosphere at elevation angles of 90°, 45° and 20°.

7 REFERENCES

Abshire, J. B. and C.S. Gardner, "Atmospheric refractivity corrections in satellite laser ranging", IEEE Trans. on Geoscience and Remote Sensing, GE-23, pp. 414-425, 1985.

Degnan, J. J., "Physical processes affecting the performance of high-power, frequency-doubled short pulse laser systems: analysis, simulation, and experiment", Ph.D. Dissertation, University of Maryland, College Park, MD, May 1979.

Degnan, J. J., "Satellite Laser Ranging: Current Status and Future Prospects", IEEE Trans. on Geoscience and Remote Sensing, GE-23, pp. 398-413, 1985.

Degnan, J. J., "Millimeter Accuracy Satellites for Two Color Ranging", these proceedings (1992).

Gaignebet, J., F. Baumont, J. L. Hatat, K. Hamal, H. Jelinkova, and I. Prochazka, "Two wavelength ranging on ground target using Nd:YAG 2HG and Raman 0.68 μm pulses", Proceedings of the Sixth International Workshop on Laser Ranging Instrumentation, Antibes-Juan Les Pins, France, September 22-26, 1986.

Klein B. J., and J. J. Degnan, "Optical antenna gain. 1. Transmitting antennas", Applied Optics, 13, pp. 2134-2140, 1974.

Marini, J. W. and C. W. Murray, "Correction of laser range tracking data for atmospheric refraction at elevations above 10 degrees", NASA Report X-591-73-351, Goddard Space Flight Center, 1973.

Owens, J. C., "Optical refractive index of air: Dependence on pressure, temperature, and composition", Applied Optics, 6,51-58, 1967.

RCA Electro-optics Handbook, Technical Series EOH-10, RCA Commercial Engineering, Harrison, NJ, 1968.

Slater, P. N., Remote Sensing: Optics and Optical Systems, Chapter 13, Addison-Wesley Publishing Co., Reading, Massachusetts, 1980.

Zwicker, H. R., "Photoemissive Detectors", in Optical and Infrared Detectors, Ed. R. J. Keyes, Springer Verlag, New York, 1977.

Two Color Satellite Laser Ranging Upgrades At Goddard's 1.2m Telescope Facility

Thomas W. Zagwodzki
Jan F. McGarry
John J. Degnan

NASA/Goddard Space Flight Center
Greenbelt, Maryland 20771

Thomas K. Varghese

Bendix Field Engineering Corporation
Seabrook, Maryland 20706

Abstract

The ranging laboratory at Goddard's 1.2m telescope tracking facility has recently been upgraded to include a single photoelectron sensitive Hamamatsu streak camera-based range receiver which uses doubled and tripled Nd:YAG frequencies for satellite laser ranging. Other ranging system upgrades include a new Continuum laser, which will deliver up to 30 millijoules (mJ) at both 532 and 355 nm at a pulsewidth of 30 picoseconds (FWHM), and replacement of both ranging and tracking computers with COMPAQ 386 based systems. Preliminary results using a photomultiplier tube based receiver and waveform digitizer indicate agreement within the accuracy of the measurement with the theoretical Marini and Murray model for atmospheric refraction. Two color streak camera measurements will be used to further analyze the accuracy of these and other atmospheric refraction models.

INTRODUCTION

Satellite laser ranging efforts at the 1.2m tracking telescope at Goddard's Geophysical and Astronomical Observatory (GGAO) have evolved over the past few years in response to the demand for more accurate SLR data. This includes a frequency-tripled Nd:YAG laser system and a streak camera based range receiver. The laboratory which houses the Experimental Satellite Laser Ranging System (ESLRS) adjoins a azimuth-elevation mount multi-user facility designed to support the scientific community at the Goddard Space Flight Center. Two of six facility experimenter port locations are dedicated to the laser transmitter and the streak camera based receiver for ranging applications. The ESLRS is a ranging laboratory where new instrumentation, hardware and software are investigated and characterized for planning and developing next generation systems. The SLR data gathered by the ESLRS is considered engineering data and is not archived as is other NASA laser tracking network data. The end users of the ESLRS data are the experimenters and their goal is to use this information to better understand system problems and to help transition laboratory systems more efficiently to field SLR operations. Other system upgrades include a new 386 based tracking computer, a new 386 based ranging computer, and physical plant upgrades at the facility.

The ESLRS has been operational since 1983 except for periods in which high priority flight programs within the Instrument Electro-Optics Branch left the facility without crew support. The initial SLR system [McGarry et al, 1986] included a Quantel YG 402 DP frequency-doubled Nd:YAG laser, a two stage ITT F4128 microchannel plate photomultiplier tube (MCP-PMT), Ortec 934 and later Tennelec TC 453 constant fraction discriminators (CFD's), and a developmental time interval unit (TIU) built by Lawrence Berkeley Laboratory. This system operated at a 5 hertz rate at the doubled YAG wavelength (532nm) and yielded data at the 1 to 2 centimeter level on LAGEOS with a very high return-to-fire ratio.

PROGRAM GOALS

Goddard Laser Tracking Network (GLTN) systems currently operating at or below the 1 cm level RMS must still rely on models of atmospheric range correction which assume certain altitude profiles for temperature, pressure, and possible gradient effects. Knowledge of atmospheric range correction on a shot-to-shot basis is therefore uncertain, and must be addressed to eliminate atmospheric concerns. The best way of accounting for the atmospheric range correction is to measure it on a shot-to-shot basis. The time of flight measurement is made in the conventional manner with a MCP based receiver using the 532nm pulse, while a differential time of flight between the 532nm and 355nm pulses is made with a streak camera based receiver. In making a streak camera differential measurement accurate at the few picosecond level, the atmospheric range correction can be recovered at the few millimeter level. Work in improving ground-based SLR accuracies closely parallel work on planned next generation space-based laser ranging systems. Efforts in the ranging laboratory at the 1.2m facility have been concentrating on both programs in this parallel effort.

SYSTEM UPGRADES

The extension from single color to two color operation at the 1.2m facility required significant system upgrades, one being an improvement in low mirror reflectivities in the UV. Recoating of all telescope mirror surfaces was required since previous coatings revealed mirror reflectivities in the UV of typically 50 to 60% and one as low as 40%. For a 6 mirror coude focus system used in common optics configuration, UV operation was prohibitive. New aluminum mirror coatings with an SiOx overcoating (peaked at 355nm) improved surface reflectivities to typically 92% at 355nm and 88% at 532nm while maintaining broadband characteristics required by other experimenters at the facility.

Return signal levels from LAGEOS are not adequate for two color streak camera-based operation with the present system. Therefore we have opted to use low earth orbiting satellites such as STARLETTE, AJISAI, and ERS-1 for two color data collection. As an acquisition aid for sunlit passes, two TV camera systems have been added to the mount, and a third low light level RCA silicon intensified target (SIT) camera has been used in the system prime focus.

Facility upgrades include the replacement of the PDP 11/24 tracking computer with a COMPAQ 386/20 based system, and new meteorological instruments including air pressure, temperature, and relative humidity. The ranging computer, a LSI 11/23 (MINC), was also replaced with a COMPAQ 386/20 system.

Ranging instrumentation upgrades include both laser transmitter and receiver. The laser available for use at the 1.2m facility for ranging from 1983 to March of 1992 was a Quantel passively mode locked Nd:YAG system model number YG402 DP. This laser system generated up to 60 mJ of doubled YAG at 532nm and about 15 mJ of tripled YAG at 355 nm in a 140 picosecond pulse (FWHM). To make differential measurements accurate at the picosecond level laser pulsewidths must be narrowed considerably, and target satellites with low pulse spreading must be used. The Quantel laser was replaced with a Continuum model PY-62 YAG with doubling and tripling capability. The new Continuum laser outputs 30 picosecond pulses with about 30 mJ of energy at both 532nm and 355nm. The laser fire rate is currently 4 hertz, with work underway to increase it to 10 hertz.

The laser is housed in a clean room approximately 10 meters from the base of the mount. The output beam is coupled into the telescope system with a negative lens (negative focal length matching the F28 ray bundle of the 1.2m system) and a 45 degree aperture sharing 'holey' mirror just inside the system focal plane. The outgoing laser beam is translated approximately 1.25 cm from the optical axis of the telescope to avoid the shadowing by the central obscuration (secondary mirror) in the telescope. The output beam is approximately .4m in diameter, exits the system cleanly between the primary and secondary mirror, and travels around that annulus as the system tracks in azimuth. This configuration results in the least amount of loss in the outgoing beam. In the common optics mode the return path at the 45 degree mirror is folded across an NRC table top to another mirror, splitter, and receiver package. In the prime focus of the system is a field stop, to limit the receiver field of view, and a high speed shutter.

The receive signal is split between a two stage ITT model F4128 MCP PMT and a Hamamatsu streak camera. Shown in Figure 1 is a simplified block diagram of the system that was used for both aircraft and Relay Mirror experiments as well as current SLR activities. The streak camera in use up until the Spring of 1992 was

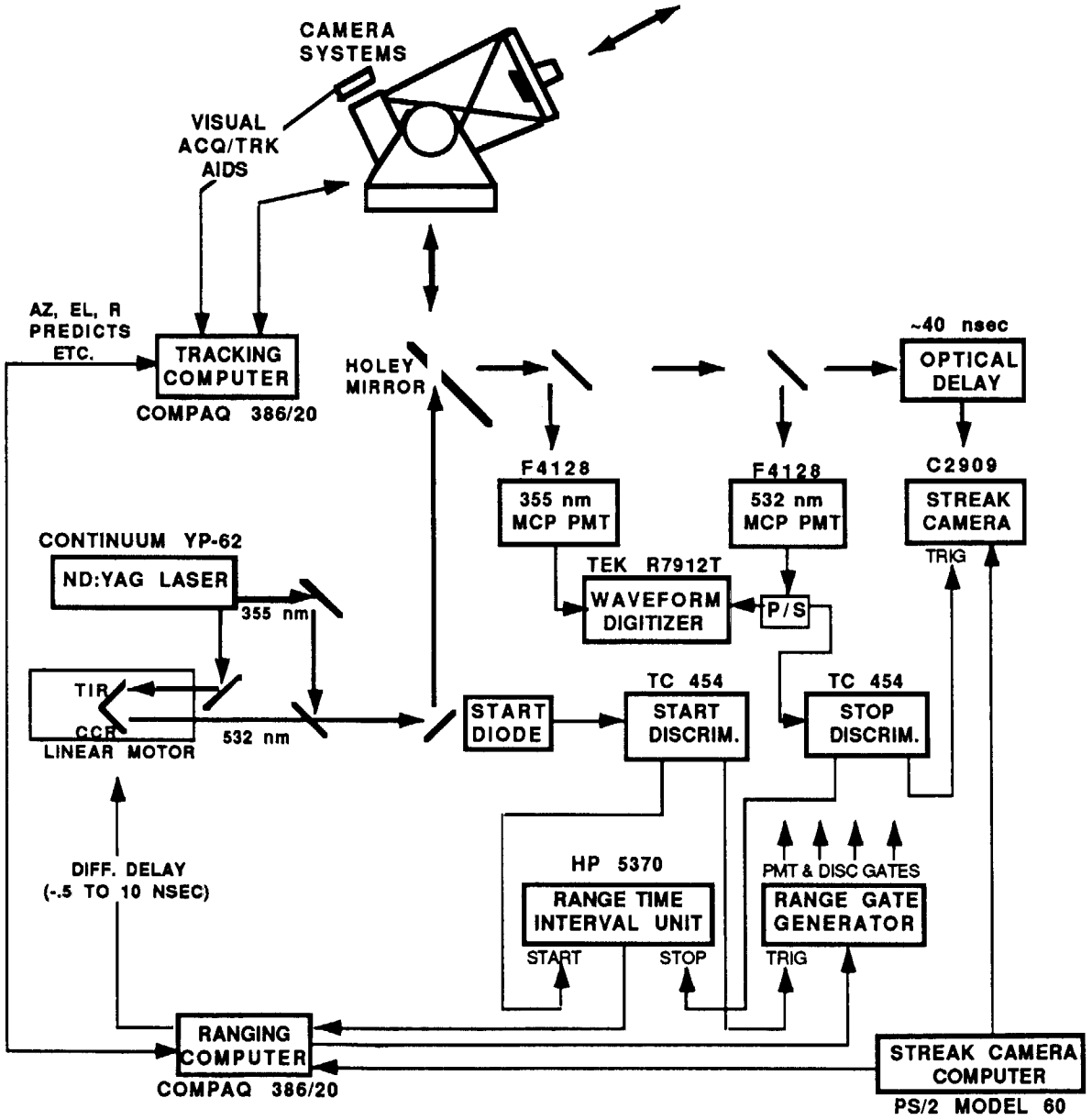

Figure 1. Two Color SLR Simplified Block Diagram

a 2 picosecond resolution Hamamatsu model 1370. This unit was integrated into the system in support of two color experiments which included both aircraft and the NASA/Air Force Relay Mirror Experiment (RME) programs. The signal threshold for the Hamamatsu 1370 streak camera is estimated at several thousand photoelectrons and could be used only for ground work, aircraft, and the RME program where signal levels were extremely high. The Hamamatsu 1370 streak camera has since been replaced with a newer Hamamatsu model 2909 which has an additional internal microchannel plate intensifier giving the unit single photoelectron sensitivity. A summary of upgraded system parameters is given in Table 1.

Table 1. Laser Ranging System Parameters and Instrumentation

Laser	Continuum PY-62, active/passive mode-locked	
Energy	30 mJ @ 532 nm, 30 mJ @ 355 nm	
Pulsewidth	30 picoseconds (FWHM)	
Beamwidth	.0057 degree (FWHM)	
Telescope	1.2 meter diam., f/28 Cassegrain Common optics configuration	
Trans/Rec Sw	Aperture shared	
System trans	60%	
Detector	ITT F4128 MCP PMT	
Discriminator	Tennelec TC 454	
Time Interval Unit	HP5370, 20 ps resolution	
Streak Camera	Hamamatsu model 2909	
Minicomputers	COMPAQ 386/20:	Tracking
	COMPAQ 386/20:	Ranging
	PS/2 model 60:	Streak camera

In the ranging mode a small fraction of the return signal is detected with the MCP PMT, discriminated with a CFD, and triggers the streak camera sweep. Both streak cameras require a pretrigger of 25 to 40 nanoseconds dependent on the sweep speed selected. Sweep speeds available in both cameras are .3, 1, 2, 5, and 10 nanoseconds full scale. The pretrigger is accomplished by delaying the optical return by one of two means. The streak camera input signal is delayed with either a white cell optical delay, or a spot to slit 10m multimode fiber optic bundle. Each technique has it's own advantages and

disadvantages. The fiber optic bundle is easy to align and has the largest field of view, but introduces pulse spreading, while the white cell has the best throughput, no pulse spreading, but is difficult to align. To maintain the best differential timing capability at the receive end an artificial delay on the 532nm pulse is introduced at the laser transmitter. This delay is a dogleg optical path into a total internal reflection (TIR) cube corner on a Compumotor linear motor stage. The linear translation stage provides the differential delay control from -.5 to 10 nanoseconds additional optical path length for the 532nm pulse so that both return pulses can be maintained within the 1 nanosecond sweep window. The linear motor stage under computer control uses the differential delay predicted by differencing the Marini & Murray model delays at 355nm and 532nm The optical delay is adjusted so that the two spatially separated pulses are incident in the streak camera slit at approximately the same time. This minimizes nonlinearity problems in the streak camera sweep. To resolve simultaneous pulses in the PMT based receiver using the waveform digitizer two PMT'S must be used.

PRELIMINARY RESULTS

The NASA/Air Force two color RME experiment mentioned earlier generated the first streak camera returns for the ESLRS [Zagwodzki et al, 1992]. The RME satellite was very attractive for several reasons. The RME satellite represented an active, single cube corner response target with an extremely high lidar cross section (~$6x10^9$ m^2). With a short pulse laser transmitter and streak camera based receiver, the individual cube corners on the satellite, separated by 41.2 mm, could be resolved in time. In the Fall of 1991 the only streak camera available at the 1.2m facility for the RME program was the Hamamatsu model 1370. The high threshold of several thousand photoelectrons for this streak camera made the RME the only viable satellite target. Shown in Figure 2 are streak camera return waveforms from the RME satellite at 532nm only. Three cube corners on the satellite could clearly be resolved in time (separation of 41.2mm). The horizontal sweep speed was 1.2 nanoseconds in time and the laser pulsewidth was 140 picoseconds. Unfortunately satellite control problems ended the experiment prematurely before UV operation began.

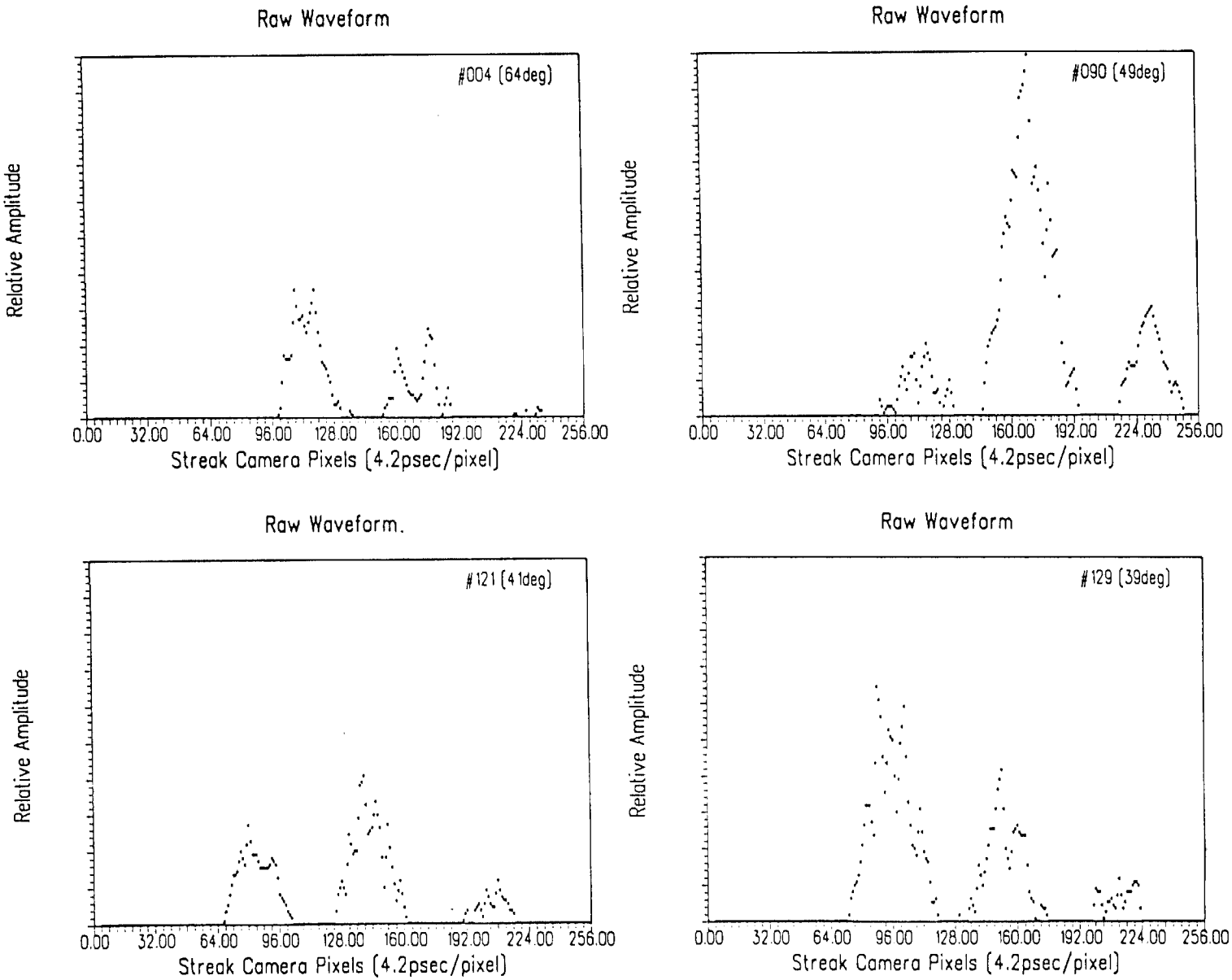

Figure 2. 532nm streak camera returns from the RME

The loss of the RME as a target meant satellite streak camera work had to wait for the installation of the more sensitive Hamamatsu 2909 unit. In the interim, two color efforts have continued at the 1.2m facility using the MCP PMT based receiver with a 1 Ghz bandwidth Tektronix model 7912 waveform digitizer. The ranging system can be configured with two PMT's (one each for 532nm and 355nm) or a single PMT (usually the 355nm). For night time operation, when no bandpass filters are required, a single PMT is used. Since the UV link is the weakest, the PMT with peaked quantum efficiency at 355nm is used. To resolve two distinct pulses with the single UV PMT the differential delay at the transmitter is set to allow at least two nanoseconds offset between the peaks of the two pulses. This assures adequate separation of return pulses at the receiver, but reduces the temporal resolution of the differential time-of-flight measurement.

Figure 3 shows a comparison plot of the theoretical differential delay versus the measured delay calculated from the two color returns as seen by the Tektronix 7912. The theoretical differential delay was calculated by differencing the 355nm and 532nm delays computed using the Marini and Murray model. The Marini and Murray calculations used the weather conditions from the log file taken during the pass. This weather information was taken in real-time, so the actual temperature and pressure were not constant. The pressure changed minimally (1006.27 to 1006.31 millibars) as did the temperature (14.24 to 14.48 C). The gaps (thinner lines) in the Marini and Murray curve represent times that no weather information was available, and so the data had to be interpolated for those regions.

For this pass the linear translator was fixed at 6 nanoseconds. This necessitated a slow sweep setting on the 7912 waveform digitizer in order to capture both frequency's return waveforms during the entire pass. Setting the green delay at 6 nanoseconds always placed the 355nm return ahead of the 532nm return and caused the UV pulses to move toward the green as the elevation decreased.

The measured differential delay was computed by taking the inverted raw 7912 waveforms (no smoothing) and computing the pixel locations of the highest two peaks. The location of these two pixels was differenced, converted to nanoseconds, and subtracted from the fixed 6 nanosecond green delay. This was a "quick-look" at the data so no interpolation was performed between pixels, and

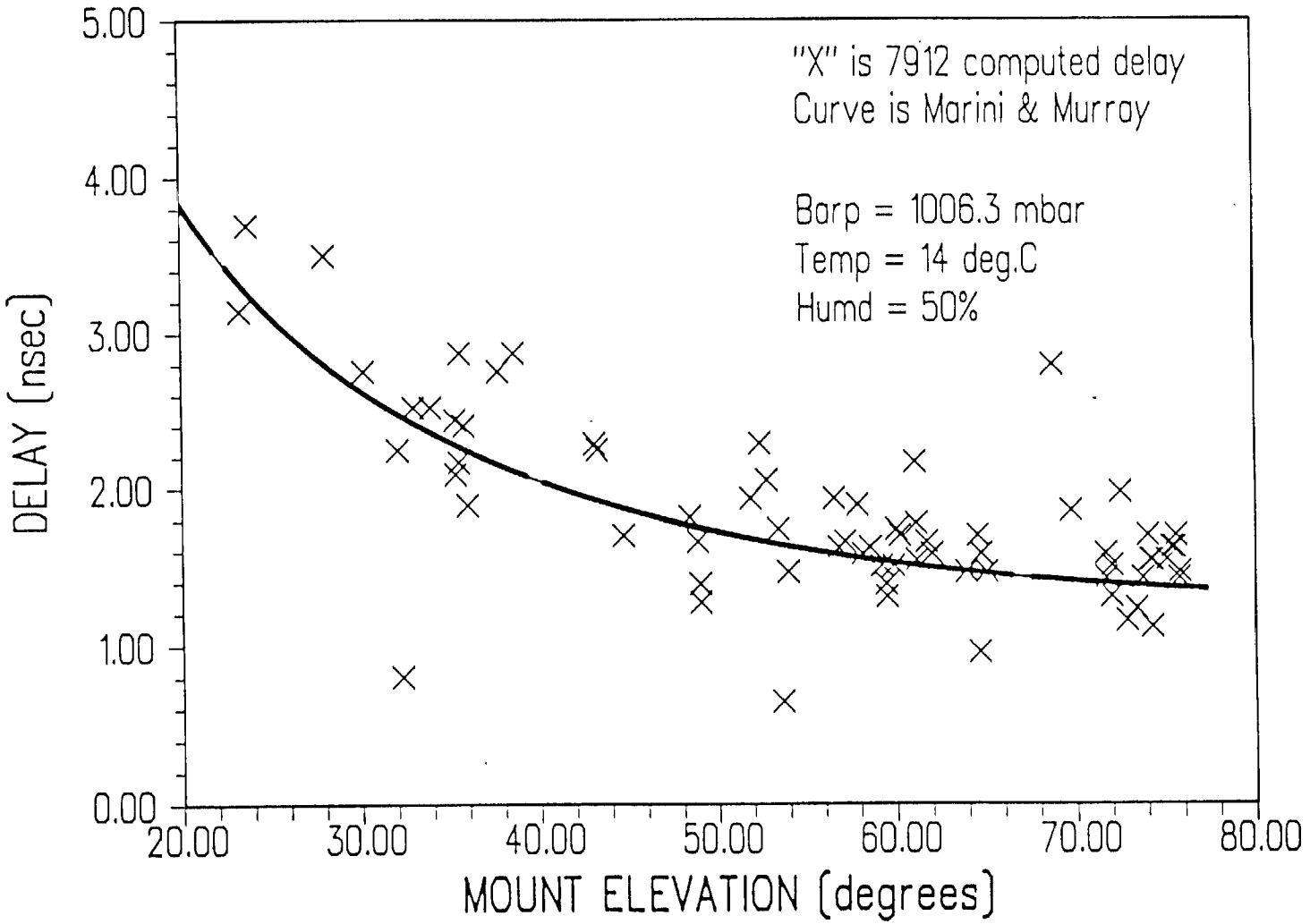

Figure 3. Two color differential delay comparison of AJISAI pass of June 27, 1992.

there was no 7912 calibration data used to correct any nonlinearities in the sweep.

The calibration of the linear translator was not performed as accurately as it will be for streak camera data. The actual zero point of the translator for the 7912 data was good to approximately +/- 200 picoseconds. Actual raw 7912 return waveforms at different elevations are shown in Figure 4. In these plots the 7912 data is inverted, but not smoothed in any way.

FUTURE WORK

Two color laser ranging activities will continue at the 1.2m facility to complete the installation of the streak camera based receiver with single photoelectron sensitivity. This will enable tracking of all low earth orbit satellites in two colors and will yield a good data set for atmospheric model comparisons. Investigative work will begin in the areas of system automation, and optical time interval units. [Degnan, 1985]

ACKNOWLEDGEMENTS

The authors wish to thank the Strategic Defense Initiative Organization Office of Directed Energy for use of the Relay Mirror Experiment satellite, the Phillips Laboratory of Albuquerque, New Mexico for their coordinating efforts, and the Consolidated Space Test Center of Sunneyvale, California for their work in providing NASA the satellite maneuvers for optical engagements.

We would like to thank Arnie Abbott of NASA for his services in maintaining the 1.2m facility, and Tammy Bertram for her operational support. We would also like to thank Bendix Field Engineering Corporation crew members Dick Chabot, Jim Fitzgerald, Dave Grolemund, Mike Seldon, Tom Oldham, and Jack Cheek of Hughes- STX for their continued effort in support of this program.

REFERENCES

J.J. Degnan, "Satellite Laser Ranging: Current Status and Future Prospects", IEEE Trans. on Geoscience and Remote Sensing, GE-23, pp. 398-413, July, 1985.

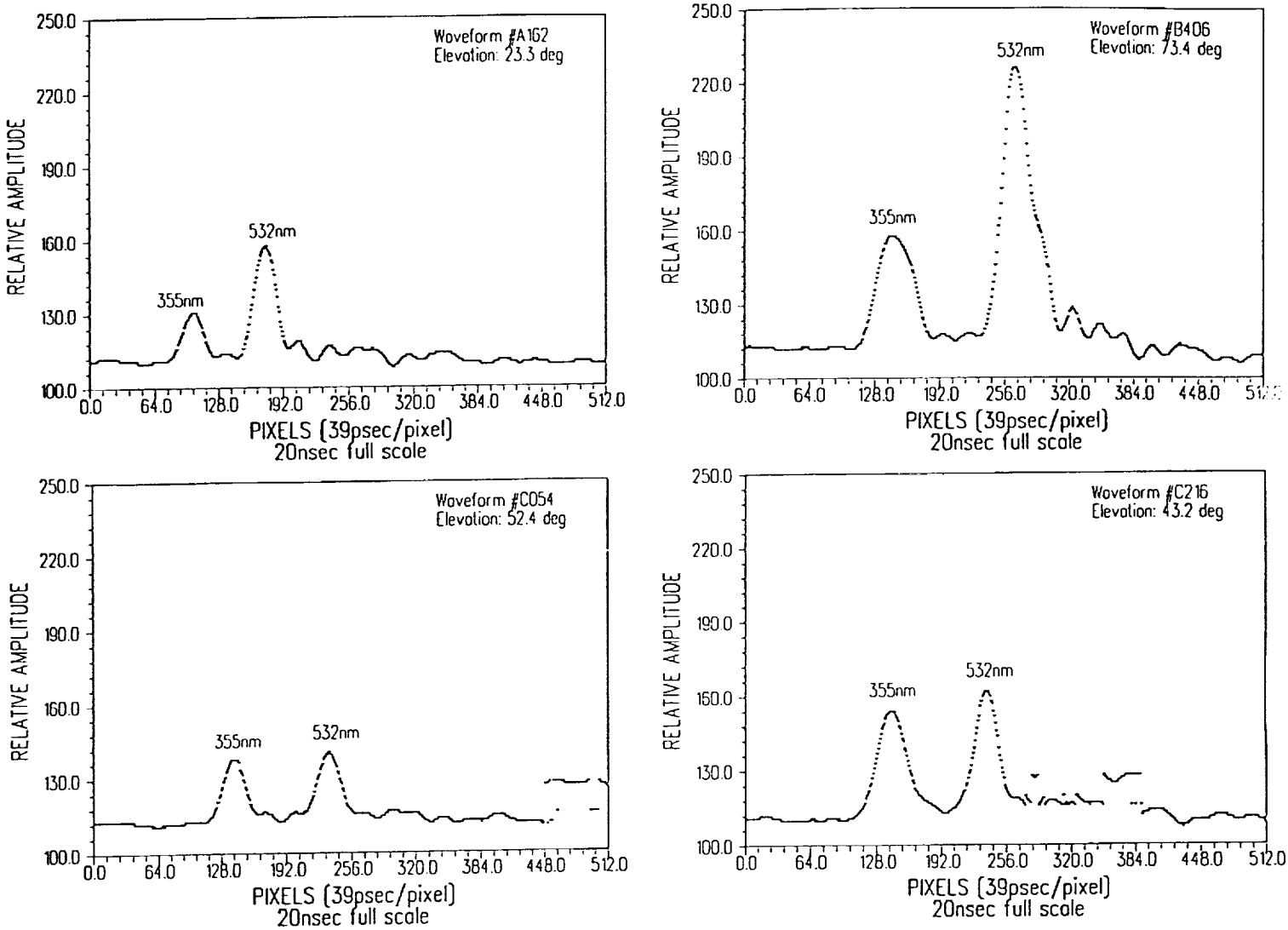

Figure 4. Two color return waveforms from AJISAI pass of June 27, 1992.

J. L. McGarry, T. W. Zagwodzki, J. J. Degnan, "Large aperture high accuracy satellite laser tracking," in Proc. of S.P.I.E. Acquisition, Tracking, and Pointing, Orlando, Florida, April, 1986.

T.W. Zagwodzki, J.F. McGarry, A. Abbott, J.W. Cheek, R.S. Chabot, J.D. Fitzgerald, D.A. Grolemund, "Laser Ranging to the Relay Mirror Experiment (RME) Satellite from Goddard Space Flight Center's 1.2m Telescope Facility", to be published in the *Journal of Geophysical Research*.

Measuring Atmospheric Dispersion With WLRS In Multiple Wavelength Mode

U. Schreiber[1]
Forschungseinrichtung Satellitengeodaesie
Fundamentalstation Wettzell
D - 8493 Koetzting

K. H. Haufe R. Dassing,
Institut fuer Angewandte Geodaesie
Fundamentalstation Wettzell
D - 8493 Koetzting

Abstract

The WLRS (Wettzell Laser Ranging System) allows the simultaneous tracking of satellites on two different wavelengths. These are the fundamental frequency of Nd:YAG at 1.064 μm and the second harmonic at 532 nm. Range measurements to the satellite LAGEOS were carried out with different experimental set- ups, after developing a detector unit based on a silicon avalanche photodiode in Geiger mode, which is sufficiently sensitive in the infrared domain. An approach towards a quantitative interpretation of the data is suggested and discussed briefly.

1 The effect of atmospheric dispersion on satellite ranges

The varying index of refraction of the atmosphere can be considered one of the most important contributions to the error sources for satellite ranges. Following a model of Marini and Murray [1], the additional time for the laser pulse passing through the atmosphere under an elevation angle of 90 degrees is as much as 8 ns. This model assumes rotational symmetric atmospheric layers with respect to the geocenter and has been established with the help of ballon experiments. Inputs to to this model are atmospheric pressure, temperature and humidity, which are measured around the ranging station. In general it can be said that the calculated corrections are very precise, so that the requirements for an experimental improvement are extremly high [2]. However, orbit fitting procedures on the basis of complex programs often show a small systematic error, depending on the pointing elevation of the ranging station. Therefore a better determination of the atmospheric influence is desirable.

2 The experimental set- up

2.1 The 'two-' detector experiment

When the WLRS telescope was designed [3], care had been taken to optimise the signal path for the fundamental (1.064 μm) and second harmonic (532 nm) wavelength of the Nd:YAG

[1]Techn. Universitaet Muenchen, Arcisstr. 21 D - 8000 Muenchen 2

laser. The remaining optical components of the ranging equipment were replaced to allow transmission and reception of these 2 frequencies. In the beginning it was not known if the second harmonic generating crystal (KD^*P) would laterally displace the pulses of the 2 frequencies so far, that there would not be a sufficient overlap of the two signals at the location of the satellite. During the experiments a weak dependance of the return rate of each detector with respect to the pointing was noticed. However, the overlap was found to be acceptable. The WLRS- system uses the same telescope for transmitting and receiving, therefore the photodetector was placed behind the transmit/receive- switch inside the thermocontrolled laboratory. This gives the advantage of high signal stability and an easily accessible working enviroment. Figure 1 outlines the experimental set- up. The receive signal is split into its two different frequency components at a dichroic mirror. The signal with a wavelength of 532 nm is reflected towards a microchannel plate (MCP), while the infrared part of the satellite echo is focused onto the active area of an avalanche photodiode (APD: SP114) placed in Geiger mode. In its present state, the WLRS is capable of recording one stop event per outgoing laser pulse only. This causes the detection of either an event from the MCP or the APD. To achieve a high number of echos from both channels, a constant delay- line of 44.9 ns was added to the MCP output, before recombining both signal lines at an impedance matched T - junction and feeding them to the eventtimer. There are two stops for each measured roundtrip possible, only one of them will be recorded, as the electronics gets disactivated after processing one event. The delayline places the less favourable signal channel to be detected first. When the measured return residuals are plotted versus time one can see two signal tracks (fig. 2) separated in range by the delay of the additional cable. This can be noticed during tracking and indicates, if there are enough recordings for both laser frequencies. The contribution to each wavelength has to be separated during the analysis, as all the range information goes to one datafile.

2.2 The 'one-' detector experiment

A slowly varying instability (i.e. drift) in the detector characteristics would be indicated during the ranging run, as a shot by shot calibration to a fixed target is carried out. To exclude such effects generally, the experiment was altered to use just one detector. The dichroic mirror (ref. fig. 1) was removed and the APD recorded both frequencies. The sensitivity of the diode is higher on 532 nm than on 1.064 μm but, because of the dispersion of the atmosphere, the infrared signal reaches the detector first. Therefore, a sufficient amount of data for both signal frequencies can be obtained. For the present this kind of experiment is restricted to the night hours, as there are no suitable spectral filters for this application. During tracking, the operator notices the formation of one track only, as both satellite tracks are separated by their differential atmospheric dispersion delay only, which contributes as much as 0.6 to 1.8 ns. In figure 3 there is a residual plot for such a measurement. In the analysis the two tracks also have to be seperated. To calibrate this measurement a circuit has been developed, which detects the starting oscillation in the laser after the fire command and forms a trigger signal to gate the APD into the Geiger mode before the calibration return hits the diode. This process is extremly time critical. Measurements to the local ground target demonstrate the proper operation of this set- up.

3 Analysing the satellite data

In this approach the question of wether the simultaneous use of different laser frequencies would result in the same satellite range information and, under the condition that a large amount of ranges have been measured, whether the measurements would allow for a correction of the employed atmospheric model were of interest. Therefore the analysis is limited to the differences in the range residuals of the two spectral components. In the following, the measurements obtained at a wavelength of 532 nm are taken as a reference to correct for other satellite ranging side effects; a non linear least squares fitting procedure is employed to fit a polynomial up to the order of 12 to the reference data. In the second step, the range residuals of the measurement in the infrared spectral domain are analysed. It was assumed that this data can be represented by the same polynomial when the additional contribution by the atmospheric dispersion and, if applicable, the extra cable delay is taken into account. Under the condition that the model of Marini and Murray gives a good representation of the atmospheric influence, so that there can be a minor modification to it only, it is:

$$r(t)_{\lambda=1.064\mu m} = r(t)_{\lambda=532nm} - \alpha\mathcal{M}(\omega) - \beta,$$

where $\mathcal{M}$ represents the contribution of the difference of the atmospheric dispersion of the two used laser frequencies depending on the elevation angle ω. α is a dimensionsless scaling factor around the value of 1 and β yields the constant value of the introduced extra delay. The measured range depending on the epoch is given by r. A curve fitting result of $\alpha = 1$ gives the exact representation of the Marini- Murray model. It is a known fact that a possible range correction for this pair of frequencies contributes with a value of only a few ps to the difference between the two used laser frequencies at a given pointing elevation (i.e. a fixed pathlength through the dispersive medium). This can not be taken from the range residual distribution. However, the characteristic elevation dependence of the difference of the ranges of the two laser frequencies places a constraint on the model, such that it might allow an interpretation of the ranging results, especially when a wide range of elevation angles has been spanned by the measurements. At low elevation angles, the separation of the two frequency components is largest, so it is desirable to range down to very low elevation angles. The model has been tested by creating a data set, introducing $\alpha = 1.05$ to an arbitrarily chosen data set of ranges artificially. After running through the evaluation procedure $\alpha = 1.05002$ was obtained as a result. This shows, that a small additionally introduced effect could be well extracted by this procedure. However, this can not be taken as sufficient proof for the applicability of the suggested model modification.

4 The experimental results

Up to now there are two series of measurements, one for each experimental set- up. In figures 4 and 5 the obtained range residuals are plotted versus the angle of elevation. In the lower part of each diagram the fitted data of the reference wavelength ($\lambda = 532\ nm$) is displayed, while the upper half shows the satellite returns taken at the other laser frequency. In all cases a satisfying residual distribution around the fitted curve was obtained. As a side effect, figure 5 shows a higher sensitivity of the photodiode in the infrared spectral range. This was unexpected because the system is at least one order of magnitude more sensitive around 532 nm. The results are summarized in table 1:

Date:	Type	α	$\beta[ns]$
4. Oct. 91	MCP/APD	0.92	44.89
8. March 92	APD	1.02	-0.027

Table 1: The results of the parameter fitting procedure of the 2 LAGEOS passages

In both cases a good representation of the expected contribution of the second laserpulse with a different wavelength was obtained. The passage of LAGEOS, measured in Oct. 1991, shows a small offset from the Marini- Murray formula, but , it is beyond the point of interpretation within the frame of this work. More experience with this measurement technique and much more data are necessary to judge the applicability of this approach. A higher resolution in the measurement of the satellite ranges is also desirable. Therefore, a modification of this experiment using a streak camera is in preparation. The goal is a higher precision in measuring the time difference in the roundtrip between the two spectral components simultaneously. Furthermore, the measurements will be extended to lower elevation angles and the search for APD's with less jitter and noise will also be continued.

Summarizing the present state of the simultaneous ranging on two different laser pulse frequencies, one can say that the obtained ranges under normal atmospheric conditions do not depend on the wavelength of the employed laser.

References

[1] Marini, J. W.; Murray, C. W.; *Correction of Laser Range Tracking Data for Atmospheric Refraction at Elevations above 10 Degrees* NASA X- Document 591-73-351 (Nov. 1973)

[2] Abshire J. *Pulsed multiwavelength laser ranging system for measuring atmospheric delay* Aplied Optics / Vol. 19, No. 20 / 15 October 1980

[3] Schlueter, W.; Hauck, H.; Dassing, R.; Schreiber, U.; Mueller, J.; Egger, D.; *Wettzell Laser Ranging System (WLRS) — First Tracking Results to Satellites and to the Moon, paper presented at the Crustal Dynamics Project Meeting, held in Pasadena, spring 1991.*

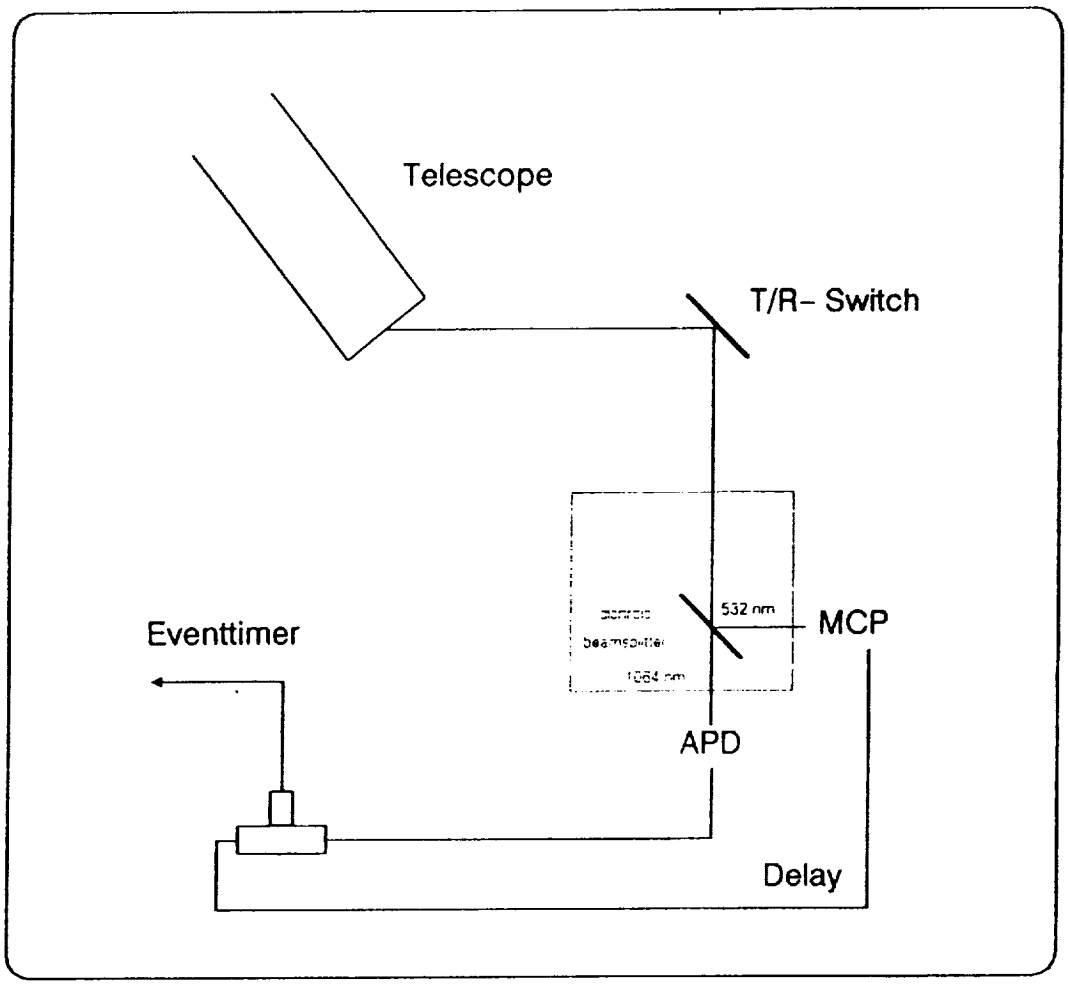

Figure 1: Block diagram for the two detector set- up

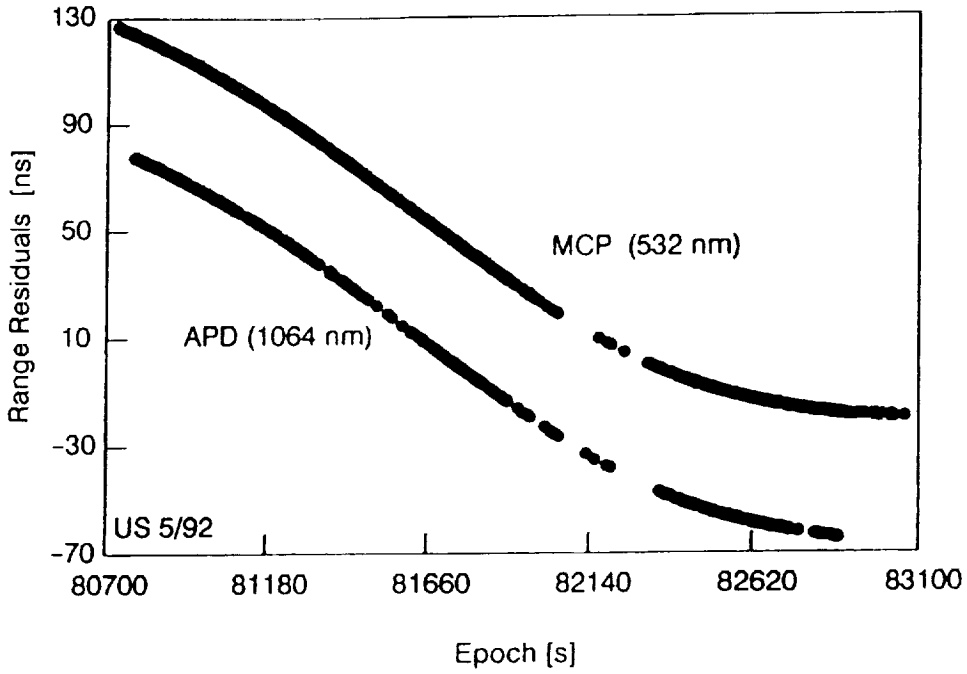

Figure 2: Residual plot of the measured LAGEOS pass from Oct. 4th 1991 after the screening process. The lower track was recorded using the Avalanche photodiode SP114, while the upper track was obtained using a microchannel plate ITT: F 4129 f

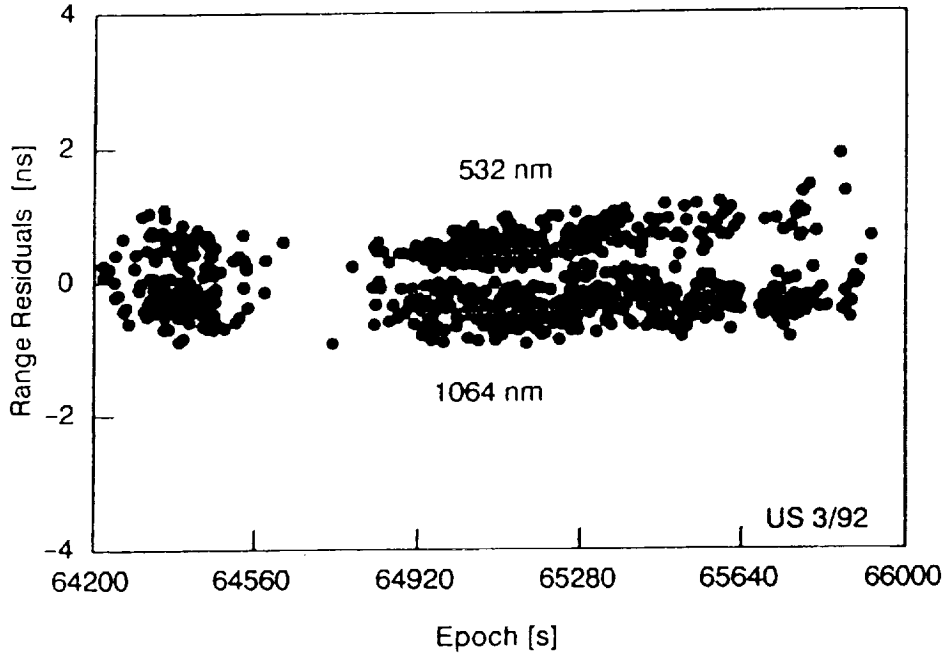

Figure 3: Residual plot of the measured LAGEOS pass from March 8th 1992 after the screening process. Both frequency components were recorded, using the Avalanche photodiode SP114

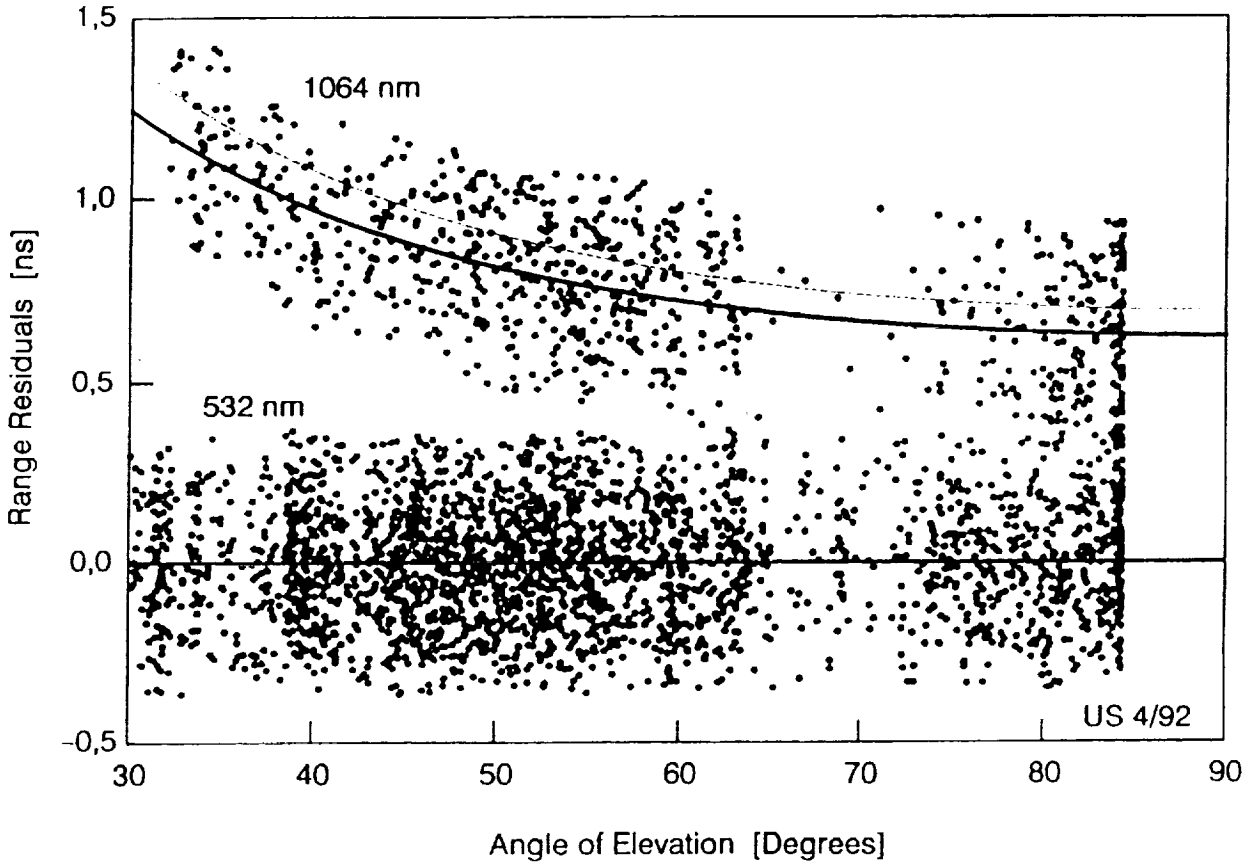

Figure 4: The range residuals of the two different frequency components plotted versus the angle of elevation (satellite: LAGEOS Oct. 4th 1991)

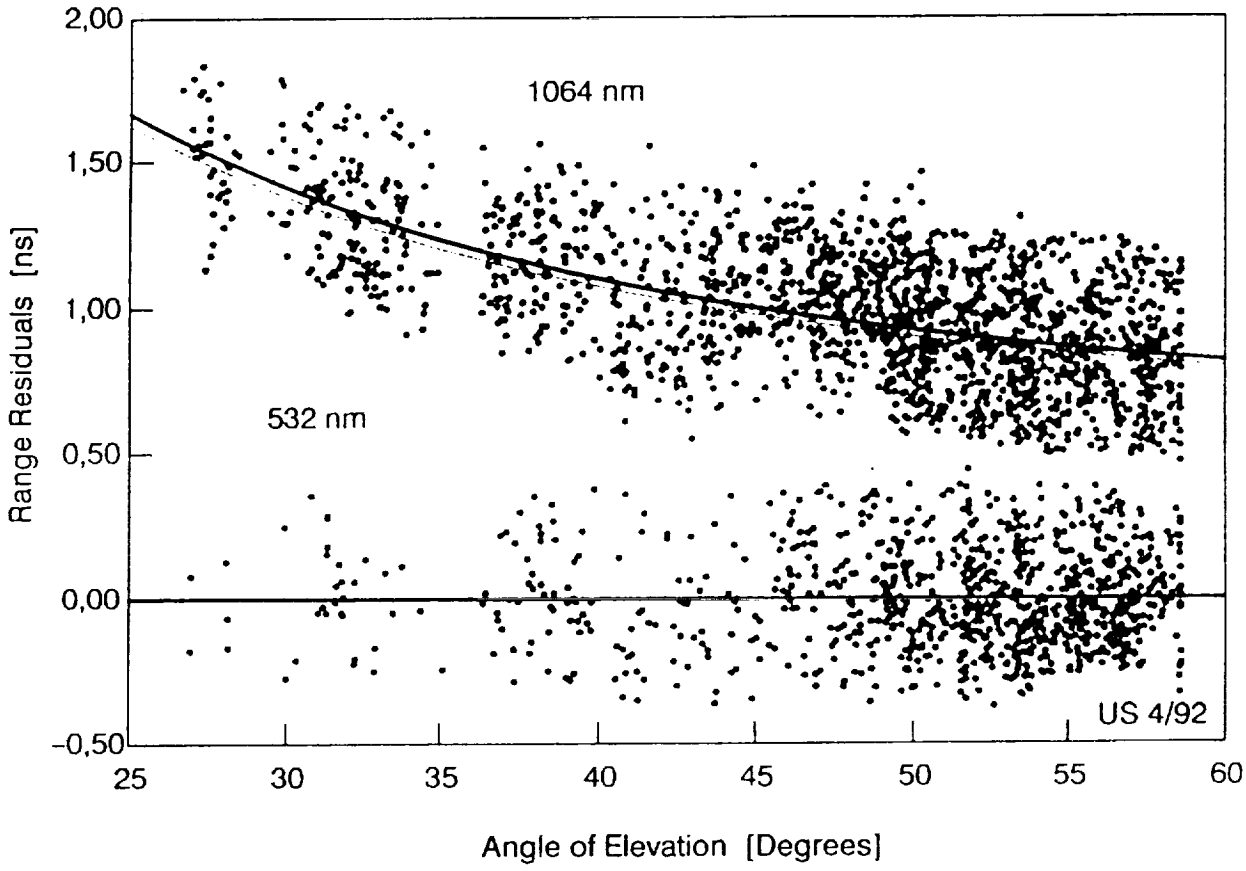

Figure 5: The range residuals of the two different frequency components plotted versus the angle of elevation (satellite: LAGEOS Mar. 8th 1992)

MILLIMETER ACCURACY SATELLITES FOR TWO COLOR RANGING

John J. Degnan
Code 901
NASA Goddard Space Flight Center
Greenbelt, MD 20771 USA

ABSTRACT

The principal technical challenge in designing a millimeter accuracy satellite to support two color observations at high altitudes is to provide high optical cross-section simultaneously with minimal pulse spreading. In order to address this issue, we provide, in this paper, a brief review of some fundamental properties of optical retroreflectors when used in spacecraft target arrays, develop a simple model for a spherical geodetic satellite, and use the model to determine some basic design criteria for a new generation of geodetic satellites capable of supporting millimeter accuracy two color laser ranging. We find that increasing the satellite diameter provides: (1) a larger surface area for additional cube mounting thereby leading to higher cross-sections; and (2) makes the satellite surface a better match for the incoming planar phasefront of the laser beam. Restricting the retroreflector field of view (e.g. by recessing it in its holder) limits the target response to the fraction of the satellite surface which best matches the optical phasefront thereby controlling the amount of pulse spreading. In surveying the arrays carried by existing satellites, we find that European STARLETTE and ERS-1 satellites appear to be the best candidates for supporting near term two color experiments in space.

1 INTRODUCTION

A companion article in these proceedings [Degnan, 1992] demonstrates the benefits of utilizing and maintaining ultrashort pulsewidths in performing two color ranging measurements to satellites. Unfortunately, even if one starts with a very short pulsewidth (e.g. 35 psec), most of the existing satellites will broaden the pulse significantly thereby degrading the precision of the differential time-of-flight measurement. This is especially true for the high altitude satellites, such as LAGEOS and ETALON, which are the primary targets for space geodesy applications. The principal technical challenge in designing a millimeter accuracy satellite to support two color observations at high altitudes is to provide high optical cross-section simultaneously with minimal pulse spreading. In order to address this issue, we provide, in this paper, a brief review of some fundamental properties of optical retroreflectors when used in spacecraft target arrays, develop a simple analytical model for spherical geodetic satellites, and use the model to determine some basic design criteria for a new generation of geodetic satellites capable of supporting millimeter accuracy two color laser ranging.

2 RETROREFLECTOR CHARACTERISTICS

For normally incident light, a single unspoiled retroreflector has a peak (on-axis) optical cross-section σ_{CC} defined by

$$\sigma_{cc} = \rho A_{cc}\left(\frac{4\pi A_{cc}}{\lambda^2}\right) \tag{2.1}$$

where ρ is the cube corner reflectivity, $A_{cc} = \pi R_{cc}^2$ is the light collecting area of the corner cube, and $4\pi A_{cc}/\lambda^2$ is the on-axis retroreflector gain. For a circular entrance aperture, the far field diffraction pattern (FFDP) of the reflected wave is the familiar Airy function given by [Born and Wolf, 1975]

$$\sigma(x) = \sigma_{cc}\left(\frac{2J_1(x)}{x}\right)^2 \tag{2.2a}$$

where

$$x = kR_{cc}\sin(\theta_1) \tag{2.2b}$$

The Airy pattern consists of a main central lobe surrounded by weak rings. The angular half-width from the beam center to the first null is given by the first nonzero root of the Bessel function J_1 which, with (2.2b), yields the formula

$$\theta_{null} = 1.22\frac{\lambda}{D_{cc}} \tag{2.3}$$

where λ is the wavelength and $D_{CC} = 2\ R_{CC}$ is the diameter of the retroreflector.

At arbitrary incidence angle, the area in (2.1) is reduced by the factor [Minott, 1974]

$$\eta(\theta_{inc}) = \frac{2}{\pi}(\sin^{-1}\mu - \sqrt{2}\mu\tan\theta_{ref})\cos\theta_{inc} \tag{2.4}$$

where θ_{inc} is the incident angle and θ_{ref} is the refracted angle determined by Snell's law, i.e.

$$\theta_{ref} = \sin^{-1}\left(\sin\frac{\theta_{inc}}{n}\right) \tag{2.5}$$

where n is the cube index of refraction. The quantity μ is given by the formula

$$\mu = \sqrt{1 - 2\tan^2\theta_{ref}} \tag{2.6}$$

Thus the peak optical cross-section in the center of the reflected lobe falls off as

$$\sigma_{eff}(\theta_{inc}) = \eta^2(\theta_{inc})\sigma_{cc} \tag{2.7}$$

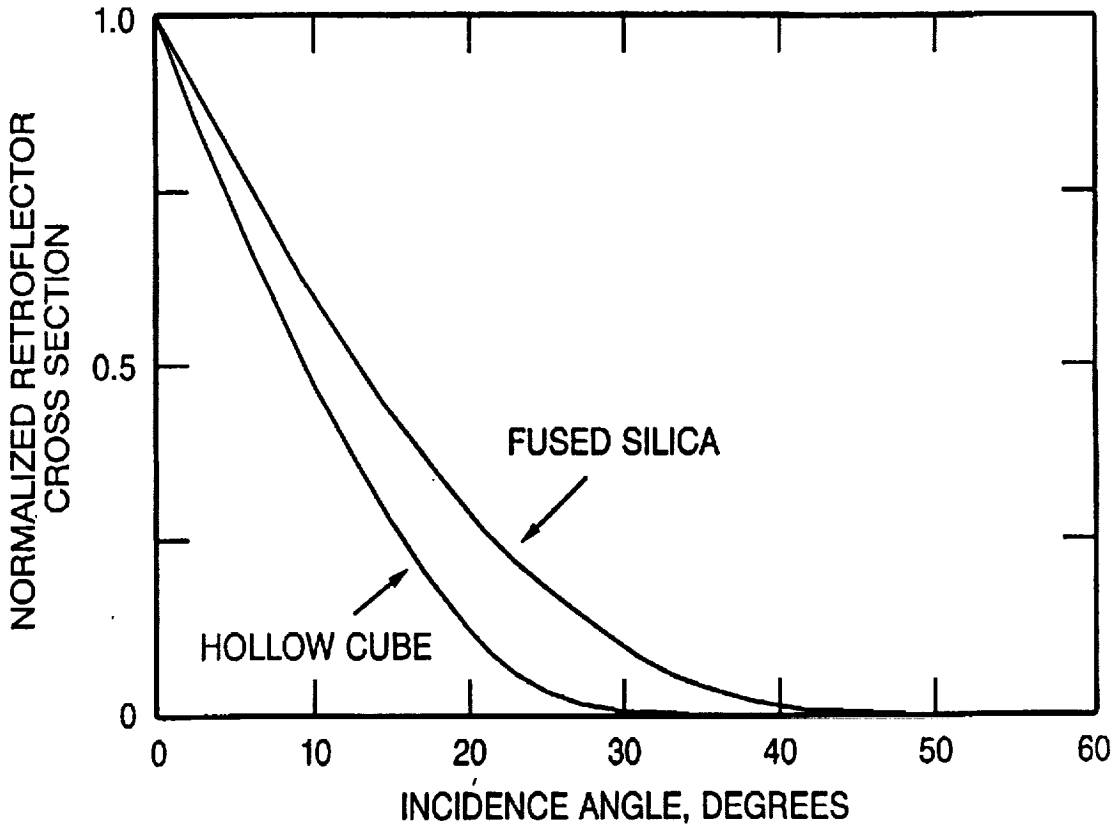

Figure 1: Normalized peak optical cross-section as a function of incidence angle for an unspoiled retroreflector.

Figure 1 shows the falloff of optical cross-section with incidence angle for the two most common retroreflectors - hollow (n=1) and quartz (n=1.455). Note that, for a solid quartz cube, the optical cross-section falls to half its on-axis value at roughly 13° incidence angle and is effectively zero beyond about 40°. The cross-section for a hollow cube corner falls to half its normal incidence value at about 9° and is effectively zero beyond about 30°.

One can further limit the effective incidence angle over which the retroreflector responds by recessing the reflector in its holder. It can be easily shown that the incidence angle at which the retroreflector response is zero is given by

$$\theta_{max} = \cot^{-1}\left(\frac{d}{D_{cc}}\right) \tag{2.8}$$

where d is the depth of the recess.

3 VELOCITY ABERRATION

As mentioned previously, the far field diffraction pattern (FFDP) of a cube corner with a circular entrance pupil function corresponds to the familiar Airy pattern consisting of a single main lobe surrounded by low intensity rings. If there were no relative motion between the satellite and the target, the center of the FFDP would fall on the instantaneous line of sight between the target and satellite. However, due to the relative velocity between the satellite and the target, the coordinates of the FFDP are translated. The magnitude of the angular displacement in the FFDP is given by the equation [Minott, 1976]:

$$\alpha(h_s, \theta_{zen}, \omega) = \alpha_{max}(h_s)\sqrt{\cos^2\omega + \Gamma^2(h_s, \theta_{zen})\sin^2\omega} \tag{3.1}$$

where the maximum value, α_{max}, is given by the expression

$$\alpha_{max}(h_s) = \frac{2}{c}\sqrt{\frac{R_E^2 g}{R_E + h_s}} \tag{3.2}$$

and

$$\Gamma(h_s, \theta_{zen}) = \sqrt{1 - \left(\frac{R_E \sin\theta_{zen}}{R_E + h_s}\right)^2} \tag{3.3}$$

and R_E is the Earth radius, g = 9.8 m/sec^2 is the gravitational acceleration at the surface, h_S is the satellite height above sea level, c is the velocity of light, and the angle

$$\omega = \cos^{-1}[(\hat{r} \times \hat{\rho}) \cdot \hat{v}] \tag{3.4}$$

where $\hat{r}$, $\hat{\rho}$, and $\hat{v}$ are all unity length vectors corresponding to the satellite position vector (relative to the Earth center), the line-of-sight vector between station and satellite, and the satellite velocity vector respectively. Since $\Gamma(h_s, \theta_{zen})$ is always less than unity, equation (3.1) has an effective "minimum" value for a given θ_{zen}, when $\omega = \pi/2$. Thus,

$$\alpha_{min}(h_s, \theta_{zen}) = \alpha_{max}(h_s)\Gamma(h_s, \theta_{zen}) \tag{3.5}$$

The maximum and minimum angular displacements of the FFDP are plotted as a function of satellite height in Figure 2 assuming a maximum θ_{zen} of 70^{o}. It should be noted from the figure that the angular displacement decreases with altitude and that the maximum and minimum values converge for high satellites. At ETALON altitudes (19,000 Km), for example, the angular displacement is roughly constant at about 26 μrad.

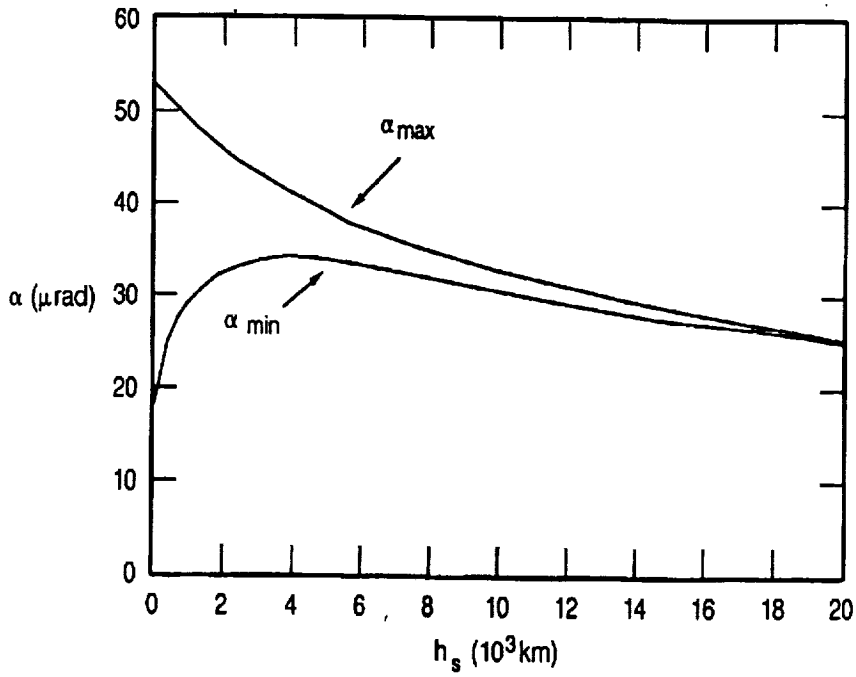

Figure 2: Maximum and minimum angular displacements in the retroreflector far field diffraction pattern caused by the velocity aberration effect as a function of satellite altitude above the Earth's surface.

If the target FFDP is angularly narrow relative to the size of the velocity aberration displacement, the receiver will lie on the low signal edge of the FFDP or even lie outside the FFDP entirely. For example, consider a moving retroreflector whose face is normal to the ranging system line-of-sight. The cross-section is given by (2.2a) with $x = kR_{cc}\sin(\alpha) \sim kR_{cc}\alpha$ where alpha is the instantaneous angular displacement caused by velocity

aberration. If $\alpha \ll \alpha_{null}$, the reduction in cross-section is negligible. However, if α is large, the reflected beam will "miss" the receiver and low or nonexistent signal levels will result. For non-normal incidence angles, the reflected FFDP is no longer circularly symmetric since the collecting (and transmitting) aperture of the retroreflector appears as an ellipse to the range receiver. The FFDP peak is again along the instantaneous receiver line-of-sight, but the FFDP is now given by the two-dimensional Fourier transform of the elliptic entrance aperture of the corner cube. The velocity aberration causes the retroreflector response to be reduced relative to the peak value given by (2.7). This reduction is greater for velocity vectors which are parallel to the long axis of the ellipse because of the faster falloff of the FFDP with angle in this direction.

4 RETROREFLECTOR "SPOILING"

To reduce the effects of velocity aberration in large retroreflectors, the retroreflector is often "spoiled". The goal of "spoiling" is to concentrate more reflected energy into the annular region bordered by α_{max} and α_{min}. Ideally, one would like to uniformly spread the energy within the annular ring yielding an optimum cross-section given by

$$\sigma_{ideal} = \rho A_{cc}\left(\frac{4\pi}{\Omega_{cc}}\right) = \rho A_{cc}\left(\frac{4}{\alpha_{max}^2 - \alpha_{min}^2}\right) \qquad (4.1)$$

where the quantity in parentheses is the effective target gain and Ω_{cc} is the solid angle subtended by the annular ring of interest. However, conventional spoiling techniques generally result in average optical cross-sections which agree only within an order of magnitude with the ideal limit described by (4.1).

Spoiling is usually accomplished by introducing slight variations into the cube corner dihedral angles (typically less than two arcseconds). This creates a complicated FFDP which, for an incident beam normal to the cube face, breaks the initial single main Airy lobe into 2N lobes (where N = 1 to 3 is the number of spoiled dihedral angles) distributed within an angular annulus. The mean angular radius of the annulus increases linearly with the dihedral offset angle from a perfect cube and, from diffraction theory [see (2.3)], one expects the effective width of the various lobes to depend inversely on cube diameter.

Each of the 2N lobes originates from a different sector of the retroreflector entrance aperture. In fact, the FFDP of each lobe is determined by the two-dimensional Fourier transform of the projection of the $180^{o}/2N$ sector of the (assumed) circular retroreflector entrance aperture into a plane perpendicular to the line-of-sight between the satellite and the station. The distribution of energy within this "annulus" is therefore highly nonuniform. Furthermore, the effective area for each lobe is reduced to:

$$A_{eff} = \eta(\theta_{inc}) \frac{A_{cc}}{2N} \tag{4.2}$$

Substituting the latter expression into (2.1), we obtain an approximate expression for the peak optical cross-section at the center of one of the 2N lobes for the spoiled retroreflector at arbitrary incidence angle

$$\sigma_{peak}(\theta_{inc}, N) = \eta^2(\theta_{inc}) \frac{\sigma_{cc}}{(2N)^2} \tag{4.3}$$

One can also "spoil" the retroreflector by placing or grinding a weak lens onto the entrance face. This approach retains the single central lobe of the unspoiled cube corner while reducing its peak amplitude and spreading the energy over a wider solid angle, Ω. This yields a peak cross-section given by

$$\sigma_{lens} = \rho A_{cc} \left(\frac{4\pi}{\Omega} \right) \tag{4.4}$$

and can be an effective approach when velocity aberrations are sufficiently small.

5 SATELLITE OPTICAL CROSS-SECTION

As noted previously, the optical cross-section which can be achieved with a single retroreflector is limited by the need to compensate for velocity abberation effects. Received SLR signals can only be enhanced by summing the contributions of several retroreflectors. Modern geodetic target satellites (e.g., STARLETTE, LAGEOS, and ETALON) are all designed to be spherical in shape in order to avoid the large pulse spreading caused by earlier flat panel arrays when viewed at non-normal incidence. The spherical shape also simplifies the modelling of nonconservative forces acting on the satellite.

Satellite array size is largely determined by the satellite altitude since more retroreflectors are required to achieve reasonable signal-to-noise ratios over longer slant ranges. Thus, STARLETTE (960 Km), LAGEOS (5900 Km), and ETALON (19,200 Km) have diameters of 12, 60, and 129.4 cm and average optical cross-sections of .65, 7, and 60 million square meters respectively.

Let us consider a spherical satellite which is uniformly covered with retroreflectors. The density of cube corners, as a function of incidence angle, is easily seen to be

$$N(\theta_{inc}) d\theta_{inc} = \frac{N}{2} \sin\theta_{inc} d\theta_{inc} \tag{5.1}$$

where N is the total number of reflectors on the satellite. To obtain a simple expression for the overall target cross-section σ, we approximate the sum over all of the retroreflectors within the allowed range of incidence angle by the following integral

$$\sigma = \sigma_{cc} \int_0^{\frac{\pi}{2}} d\theta_{inc} N(\theta_{inc}) \eta^2(\theta_{inc}) \tag{5.2}$$

where we have used (2.7). If the retroreflectors are not recessed in their holders, $\eta(\theta_{inc})$ is given by (2.4). If their angular response is limited by the recess, the variation can be well-approximated by the expression

$$\eta(\theta_{inc}) = 1 - \frac{\theta_{inc}}{\theta_{max}} \tag{5.3}$$

where θ_{max} is given by (2.8). Actually, (5.3) is an excellent approximation to (2.4) as well provided we choose θ_{max} equal to .54 rad (31°) for hollow cubes or .75 rad (43°) for solid cubes respectively (see Figure 1). Substituting (5.2) and (5.3) into (5.2) and evaluating the resulting integrals yields

$$\sigma = \frac{\sigma_{cc} N}{2} \left[1 - \frac{\sin^2\left(\frac{\theta_{max}}{2}\right)}{\left(\frac{\theta_{max}}{2}\right)^2} \right] \tag{5.4}$$

Let us now examine the validity of (5.4) by substituting LAGEOS values. The LAGEOS satellite has a radius R = 29.8 cm and is imbedded with 426 retroreflectors (422 fused quartz and 4 germanium) with a clear aperture diameter D_{CC} of 3.81 cm. Ignoring the fact that four cubes are germanium, we choose N = 426 and a value of θ_{max} = .75 rad for solid quartz cubes. We now use a value σ_{cc} = 2.834 x 10^6 in agreement with the input values to the RETRO computer program as determined during LAGEOS testing and evaluation [Fitzmaurice et al, 1977]. Substituting the latter values into (5.4) yields

$$\sigma_{LAGEOS} = 9.8\sigma_{cc} = 2.78 x 10^7 m^2 \tag{5.5}$$

This is roughly equal to the peak value computed by the much more detailed RETRO program which showed a range of values between .54 and 2.7 x 10^7 m^2. Equation (5.4) tends to overestimate the actual cross-section because it includes only geometric, and not velocity aberration, effects. Equation (5.5) also implies that the LAGEOS array cross-section is roughly 9.8 times that of a single cube corner at normal incidence.

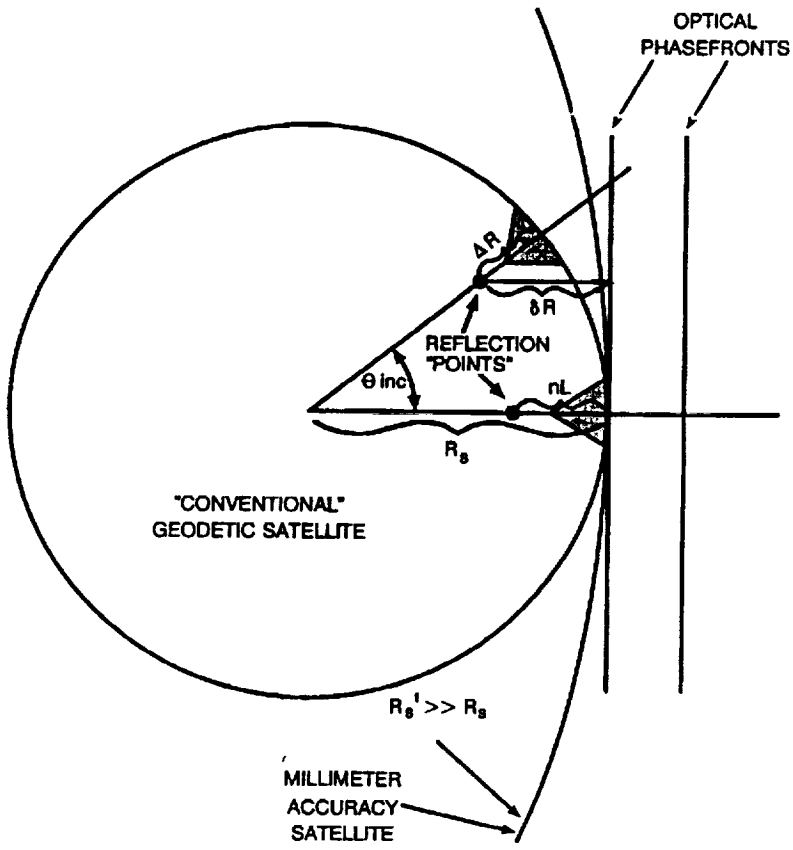

Figure 3: Diagram of a spherical geodetic satellite defining the variables used in the analysis.

6 SATELLITE IMPULSE RESPONSE AND TARGET SPECKLE

An individual retroreflector responds as a point source and hence does not spread the laser pulse in time. However, with a typical array of retroreflectors, the laser pulse arrives at the "reflection center" of each retroreflector at a slightly different time leading to a broadening of the received pulse [Degnan, 1985]. The location of the "reflection center" for an individual solid cube corner reflector is given by [Fitzmaurice et al, 1977; Arnold, 1978]

$$\Delta R(\theta_{inc}) = nL\sqrt{1-\left(\frac{\sin\theta_{inc}}{n}\right)^2} = nL\cos\theta_{ref} \qquad (6.1)$$

where $\Delta R(\theta_{inc})$ is measured from the center of the front face of the cube corner to the reflection point, L is the vertex to front face dimension, n is the refractive index of the corner cube material, θ_{inc} is the angle of incidence, and θ_{ref} is the corresponding refraction angle. From Figure 3, it can be seen that a

cube at an angle θ_{inc} to the incident wave produces a time delay, relative to the surface of the satellite closest to the ranging station (θ_{inc} = 0), given by

$$\Delta t(\theta_{inc}) = \frac{2}{c}\{R_s - [R_s - \Delta R(\theta_{inc})]\cos\theta_{inc}\} = \frac{2R_s}{c}\left\{1 - \cos\theta_{inc}\left[1 - \frac{nL}{R_s}\cos\theta_{ref}\right]\right\} \quad (6.2)$$

where R_s is the satellite radius. It should also be noted that the differential delay between target reflection points also introduces a random phase delay between individual reflectors. Thus, if the temporal profiles from multiple cubes overlap at the range receiver, the electric fields will interfere with each other in a random way from shot to shot resulting in target "speckle". On average, however, the return waveform from the satellite should behave as if each of the retroreflectors is an incoherent source. This was an implicit assumption in our derivation of target optical cross-section in Section 5.

In the same spirit, the time-averaged satellite impulse response can be estimated by summing the weighted (incoherent) returns from each of the retroreflectors. Using the simple model for a spherical satellite introduced in Section 5, the impulse response can be shown to be

$$I(t) = \sigma_{cc}\frac{N}{2}\int_0^{\frac{\pi}{2}} d\theta_{inc}\sin\theta_{inc}\eta^2(\theta_{inc})\delta[t - \Delta t(\theta_{inc})] \quad (6.3)$$

where the geometric weighting factor is given by (2.4) or (5.3), $\Delta t(\theta_{inc})$ is given by (6.2), and the delta function $\delta[t - \Delta t(\theta_{inc})]$ represents an infinitely short laser pulse waveform incident on the satellite. From (6.2), we see that the delta function is nonzero only when the condition

$$\cos\theta(\tau,\epsilon,n) = \frac{1-\tau}{1-\epsilon\sqrt{1-\frac{1}{n^2}+\left[\frac{\cos\theta(\tau,\epsilon,n)}{n}\right]^2}} \quad (6.4)$$

holds where we have defined the new variables

$$\tau = \frac{ct}{2R_s} \qquad \epsilon < \tau < \tau_{max}$$

$$\epsilon = \frac{nL}{R_s} \qquad \tau_{max} = 1 - \cos\theta_{max}\left[1 - \epsilon\sqrt{1-\frac{1}{n^2}+\left(\frac{\cos\theta_{max}}{n}\right)^2}\right] \quad (6.5)$$

The variable τ is a normalized time, expressed in units of the roundtrip transit time from the surface of the satellite to the center and back, and ϵ is the ratio of the optical depth of the cube to the satellite radius. The minimum and maximum values of τ

are determined by setting θ equal to zero and θ_{max} respectively in (6.4) and solving for τ. The total pulse duration, measured at the baseline, is given by $\Delta t = t_{max} - \epsilon$.

From (5.3) and (6.3), the satellite impulse response can now be expressed as a function of the variables τ, ϵ, n, and θ_{max}, i.e.

$$I(\tau,\epsilon,n,\theta_{max}) = \sigma_{cc}\frac{N}{2}\sin\theta(\tau,\epsilon,n)\left[1-\frac{\theta(\tau,\epsilon,n)}{\theta_{max}}\right]^2 \tag{6.6}$$

where $\theta(\tau,\epsilon,n)$ is defined by (6.4). In the limit of large satellite diameters ($\epsilon \to 0$), (6.4) reduces to the simple form

$$\theta(\tau,0,n) = \cos^{-1}(1-\tau) \tag{6.7}$$

and (6.6) becomes

$$I(\tau,0,n,\theta_{max}) = \sigma_{cc}N\sqrt{\frac{\tau}{2}\left(1-\frac{\tau}{2}\right)}\left[1-\frac{\cos^{-1}(1-\tau)}{\theta_{max}}\right]^2 \tag{6.8}$$

The quantity ϵ is typically small and, for nonzero values of ϵ, (6.4) can be easily solved by iteration using (6.7) as a starting point, i.e.

$$[\cos\theta(\tau,\epsilon,n)]_{j+1} = \frac{1-\tau}{1-\epsilon\sqrt{1-\frac{1}{n^2}+\left[\frac{[\cos\theta(\tau,\epsilon,n)]_j}{n}\right]^2}} \tag{6.9}$$

until it converges.

As an illustration, let us use (6.6) to estimate the impulse response of the LAGEOS satellite. Substituting n = 1.455 (fused silica), L= 1.905 cm, and R_S = 29.8 cm into (6.5b), we obtain a value ϵ = .093. We recall that, for solid cube corners, we can use a value θ_{max} = .75 rad. Now, using (6.6) and (6.9), we obtain the plot of the LAGEOS impulse response shown in Figure 4(a). The profile shows the characteristic fast rise and long tail of the LAGEOS response. Furthermore, if we compute a center-of-mass correction from the centroid of this impulse response profile, we obtain a value of 250.2 mm which is in excellent agreement with the accepted LAGEOS value of 249 $\pm$ 1.7 mm [Fitzmaurice et al, 1977].

The impulse response in the large satellite limit, given by (6.8), is shown in figure 4(b) for the case of solid quartz and hollow cubes. Note that both the temporal width of the reflected pulse and the target optical crossection is smaller for the hollow cubes than for the solid cubes because of their smaller field of view.

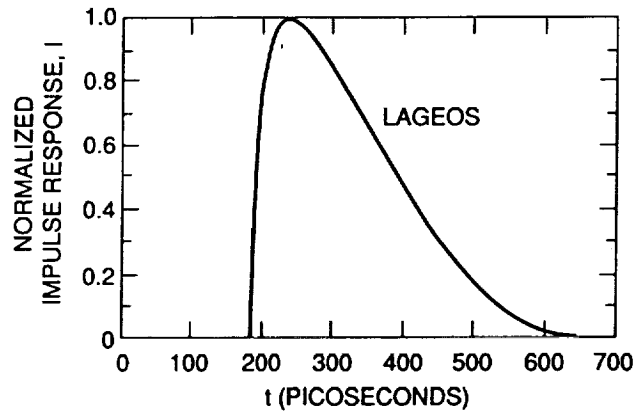

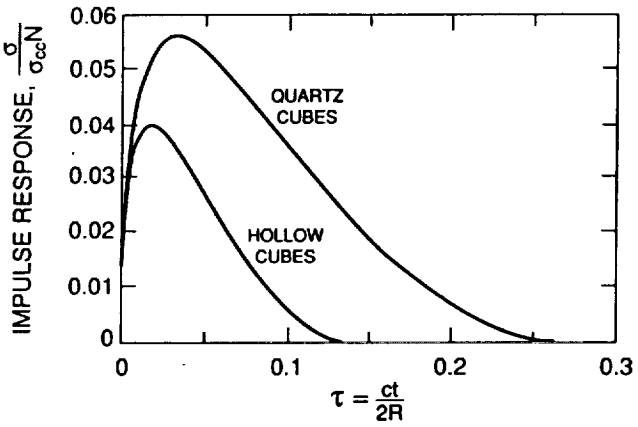

Figure 4: (a) Impulse response of the LAGEOS satellite as computed by our simple analytical model. (b) Impulse response in the large satellite limit for both hollow and solid quartz cubes.

7 FEASIBILITY OF MILLIMETER ACCURACY SATELLITES

We will now demonstrate that, in order to achieve high optical cross-section simultaneously with minimal pulse spreading with a spherical satellite, we must increase the satellite diameter and/or retroreflector density and simultaneously restrict the response to retroreflectors within a relatively small solid angle on the satellite surface about the station line of sight.

The total time duration of the reflected pulse (0% to 0% intensity points) can be determined from (6.5), i. e.

$$\Delta t = \frac{2R_s}{c}(\tau_{max} - \epsilon) = \frac{2R_s}{c}\left\{2\sin^2\frac{\theta_{max}}{2} + \epsilon\left[\cos\theta_{max}\sqrt{1 - \frac{\sin^2\theta_{max}}{n^2}} - 1\right]\right\} \tag{7.1}$$

which, in the limit of small maximum incidence angles, reduces to

$$\Delta t \sim \frac{R_s}{c}\theta_{max}^2\left[1 - \epsilon\left(1 + \frac{1}{n^2}\right)\right] \tag{7.2}$$

In the same limit, Eq. (5.4) for the satellite optical cross-section reduces to

$$\sigma \sim \frac{\sigma_{cc} N}{24}\theta_{max}^2 \tag{7.3}$$

As mentioned earlier, the angular response can be restricted by recessing the retroreflectors in their holders. Substituting (7.2) into (7.3) yields

$$\sigma = \frac{\sigma_{cc} N}{24}\frac{c\Delta t_{max}}{R_s\left[1 - \frac{nL}{R_s}\left(1 + \frac{1}{n^2}\right)\right]} \tag{7.4}$$

We can now express the total number of retroreflectors as

$$N = 4\beta\frac{R_s^2}{R_{cc}^2} \tag{7.5}$$

where β is a "packing density" (= .435 for LAGEOS) which represents the fraction of total surface area occupied by the cube faces. Substituting (7.5) into (7.4) yields our final result

$$\sigma \sim \frac{\sigma_{cc}}{6R_{cc}^2}\frac{\beta R_s c\Delta t}{\left[1 - \frac{nL}{R_s}\left(1 + \frac{1}{n^2}\right)\right]} \tag{7.6}$$

The product $\beta R_s c\Delta t$ in (7.6) quantifies our earlier statement that, if we wish to reduce the amount of pulse-spreading Δt by some factor (via reduction of the retroreflector field-of-view), we must increase the retroreflector packing density -satellite radius product (βR_s) by the same factor to retain a similar target cross-section.

8 CONCLUSION

As mentioned previously, the principal technical challenge in designing a millimeter accuracy satellite to support two color observations at high altitudes is to provide high optical cross-section simultaneously with minimal pulse spreading. Increasing the satellite diameter provides: (1) a larger surface area for additional cube mounting thereby leading to higher cross-sections; and (2) makes the satellite surface a better match for

the incoming planar phasefront of the laser beam as in Figure 3. Simultaneously restricting the retroreflector field of view (e.g. by recessing it in its holder) limits the target response to the fraction of the satellite surface which best matches the optical phasefront thereby reducing the amount of pulse spreading.

For near term experiments, the small radius of STARLETTE makes it an attractive target for testing and evaluating two color systems or for testing atmospheric models. Furthermore, its low altitude (960 Km) and moderate target cross section results in relatively high received signal levels. AJISAI, also in a relatively low 1375 Km orbit, consists of small clusters of retroreflectors separated by large reflecting panels and has comparable signal strength to STARLETTE. Unfortunately, the satellite is quite large and simultaneous returns from several retro clusters results in a complicated satellite signature [Prochazka et al, 1991]. From Figure 4, LAGEOS spreading is in excess of 150 picoseconds FWHM in agreement with [Fitzmaurice et al, 1977] although, with sufficiently short laser pulses (<50 psec), individual retro rings should be resolvable via streak cameras at certain satellite orientations. (Note that the simple satellite model presented here gives an average response over the full range of satellite orientations and shows none of the structure expected from a particular orientation). The LAGEOS pulse spreading combined with relatively low signal returns, measured at the few to several tens of photoelectron level for most systems, would make the necessary differential timing very difficult [Degnan, 1992].

Another useful target for two-color system evaluation is the recently launched European Earth Remote Sensing satellite, ERS-1. It flies at a relatively low altitude (<800 Km) and has a small compact target consisting of one nadir-viewing retroreflector surrounded by a uniformly spaced ring of eight identical cube corners at a nadir angle of 50^{o}. Approximate modelling of this satellite by the author indicates that sharp returns consisting of one or two peaks (well separated) can be obtained from most viewing angles as illustrated in Figure 5. At nadir angles between 0^{o} and 15^{o}, the nadir viewing cube is dominant whereas, for nadir angles between 30^{o} and 70^{o}, the ring provides a sharp return at virtually all azimuthal angles. At nadir angles between about 15^{o} and 30^{o}, there is some overlapping of returns and pulse distortion.

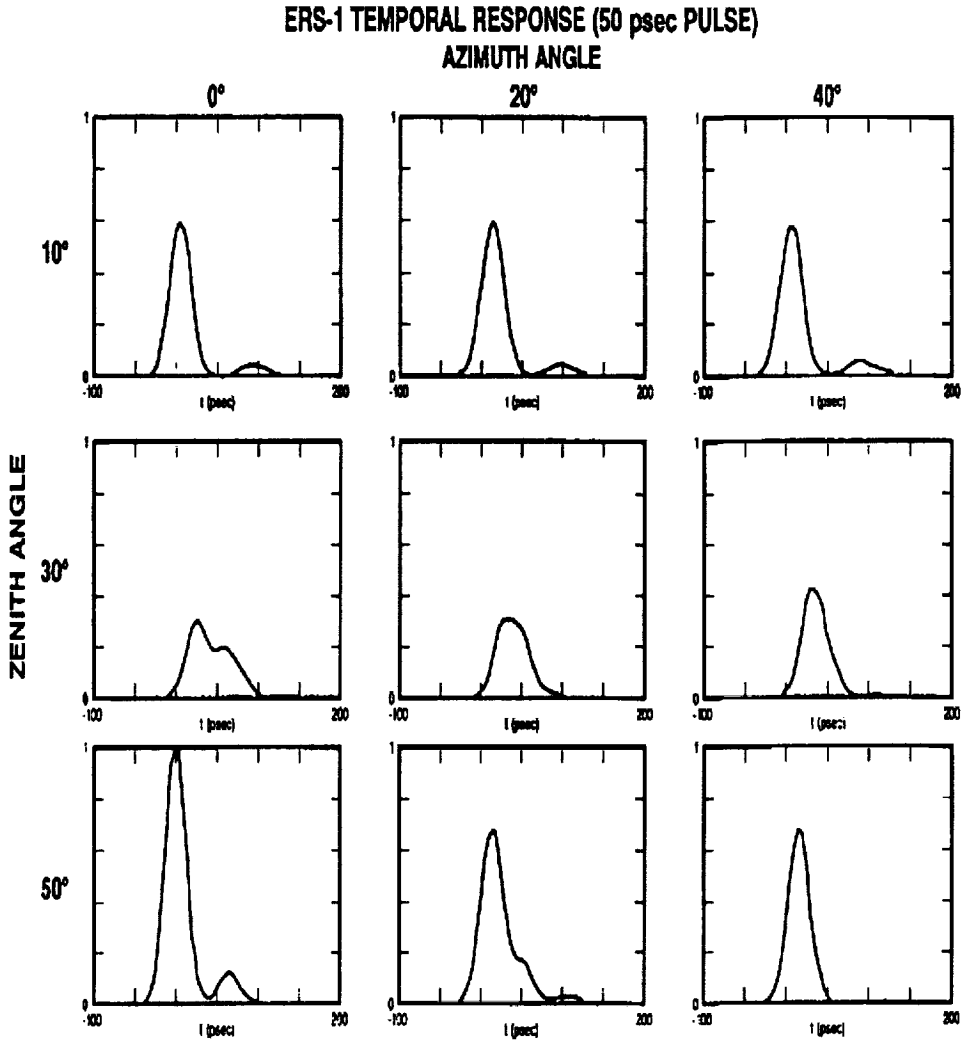

Figure 5: Approximate (geometric) response of the ERS-1 satellite to a 50 picosecond pulse as a function of nadir and azimuthal angle.

9 REFERENCES

Arnold, D. A., "Optical and infrared transfer function of the LAGEOS retroreflector array", Final Report NASA Grant NGR 09-015-002, Smithsonian Institution Astrophysical Observatory, May 1978.

Born M. and E. Wolf, "Principles of Optics", Chapter 8, Pergamon Press, New York, 1975.

Degnan, J. J., "Satellite laser ranging: current status and future prospects", IEEE Trans. on Geoscience and Remote Sensing, GE-23, pp. 398-413, 1985.

Degnan, J. J., "Optimum wavelengths for two color ranging", these proceedings, May 1992.

Fitzmaurice, M. W., P. O. Minott, J. B. Abshire, and H. E. Rowe, "Prelaunch testing of the Laser Geodynamic Satellite (LAGEOS)", NASA Technical Paper 1062, October 1977.

Minott, P. O., "Design of retrodirector arrays for laser ranging of satellites", NASA TM-X-723-74-122, Goddard Space Flight Center, March, 1974.

Minott, P. O., "Reader's Guide to the RETRO Program Output", NASA TM-X-722-76-267, Goddard Space Flight Center, September, 1976.

Prochazka, I., K. Hamal, G. Kirchner, M. Schelev, and V. Postovalov, "Circular streak camera application for satellite laser ranging", presented at SPIE Conference on Electronic Imaging, San Jose, California, Feb. 24-27, 1991.

TWO WAVELENGTH SATELLITE LASER RANGING USING SPAD

N94-15584

I.Prochazka, K.Hamal, H.Jelinkova

Faculty of Nuclear Science and Physical Engineering,Czech Technical University
Brehova 7, 115 19 Prague 1, Czechoslovakia
phone/fax +42 2 848840, tlx 121254, bitnet TJEAN@CSEARN.BITNET

G.Kirchner, F.Koidl

Lustbuehel Observatory,Lustbuehel str. 46,A-8042 Graz,Austria
phone +43 316 472231, fax +43 316 462678

GENERAL

When ranging to satellites with lasers, there are several principal contributions to the error budget : from the laser ranging system on the ground, from the satellite retro array geometry and from the atmosphere. Using a single wavelength we have been routinely achieved a ranging precision of 8 millimeters when ranging to the ERS-1 and Starlette satellites. The systematic error of the atmosphere, assuming the existing dispersion models, is expected to be of the order of 1 cm. Multiple wavelengths ranging might contribute to the refinement of the existing models. Taking into account the energy balance, the existing picosecond lasers and the existing receiver and detection technology, several pairs or multiple wavelengths may be considered. To be able to improve the atmospheric models to the subcentimeter accuracy level, the Differential Time Interval (DTI) has to be determined within a few picoseconds depending on the selected wavelength pair [1].

There exist several projects, based on picosecond lasers as transmitters and on two types of detection techniques : one is based on a photo detectors like photomultipliers or photodiodes connected to the time interval meters [5]. Another technique is based on the use of a streak camera as a echo signal detector,temporal analyzer and time interval vernier. The temporal analysis at a single wavelength using the streak camera showed the complexity of the problem [2].

EXPERIMENT SETUP

We are reporting on the novel concept of ranging to satellites at two wavelengths using a single solid state photon counter. The block scheme is plotted on Figure 1. The receiver package is based on the Silicon avalanche photodiode [4] capable of single photon detection. The receiver and detector is common for both wavelengths, the different color returns are separated in time due to the atmospheric dispersion. In principle, the use of common detector for both wavelengths results in system simplicity, stability and accuracy, as well. Most of the DTI measurement error contributions cancel out by averaging. The system calibration is simple and straightforward.

The experiment has been accomplished at the Satellite Laser Ranging Station Graz, Austria, employing the 0.5 meter aperture Contraves tracking telescope. Considering the available laser technology, the satellite laser telescope transmitter and receiver optics, namely

the Coude path dielectric coatings, and the detector sensitivity, we have chosen the wavelength pair of 0.532 μm and 0.683μm proposed by J.Gaignebet [3]. The laser transmitter consists of the passively mode locked Quantel Nd:AG laser including the second harmonic generator, modified by inserting a Raman cell filled by Hydrogen at 25 Bars, delivering 15 mJ/35 psec at 0.532 μm and 5 mJ/25 psec at the 0.683 μm Stokes waves. Additionally, the anti Stokes radiation at 0.45 μm having the energy of 1-3 mJ is generated.

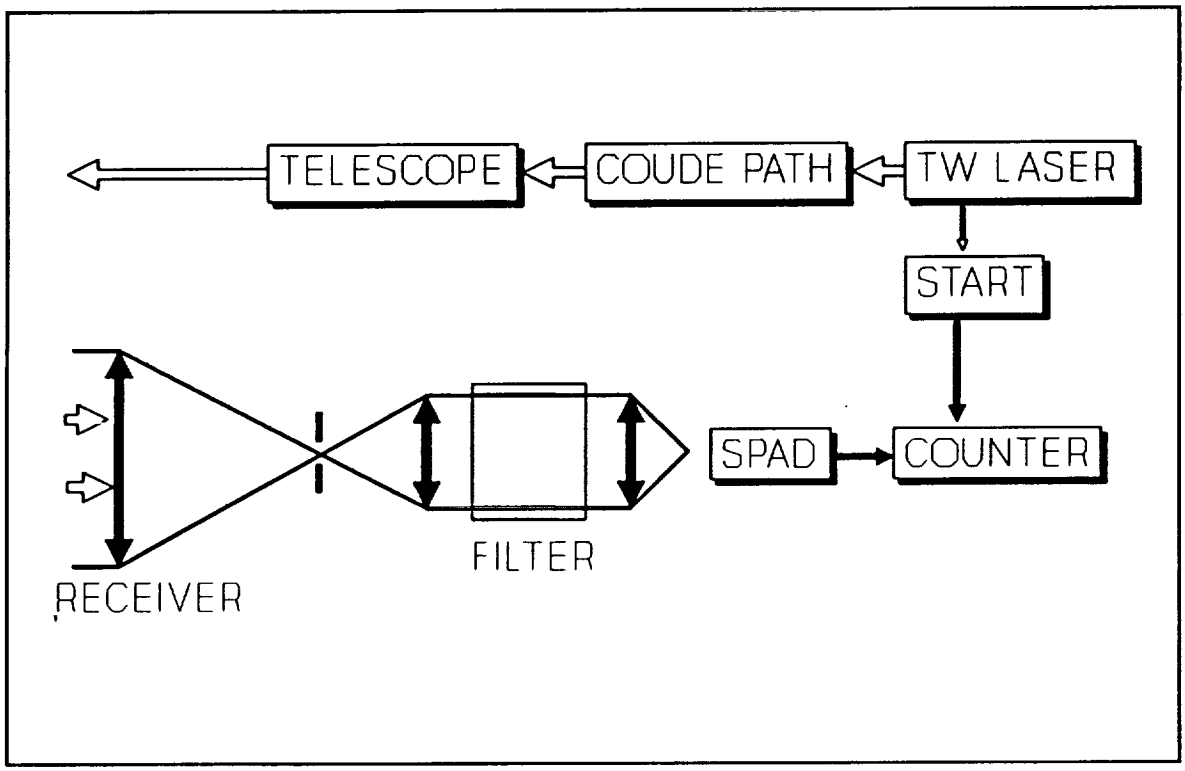

Figure 1 Two wavelengths laser ranging system setup using SPAD

RESULTS

Ranging to several ground targets we obtained a ranging precision of 42 picoseconds at 0.532 μm and 56 picoseconds at 0.683μm. The detector quantum efficiency at both these wavelengths reaches 20 %. The 6 kilometer distant ground target ranging results is shown on Figure 2. The first peak corresponds to 0.683 μm echoes, the second one to the 0.532 μm echoes. The measured DTI was 303.3 picoseconds. Taking into account the data of the atmosphere at this time, the calculated value is 299.4 picoseconds. The precision estimate of our DTI measurement is 4 picoseconds, if 400 returns per color are accumulated.

The first results of two wavelength laser ranging to the Ajisai satellite is on Figure 3, where the range residuals to the fitted orbit are plotted.The lower trace corresponds to the 0.683μm echoes, the upper one to the 0.532μm echoes. The DTI value variation along the pass is caused by changes in the satellite elevation and hence the atmospheric path difference. Up to now the satellites Lageos, ERS-1 and Ajisai have been ranged with two wavelengths. Typically a few hundreds of returns per pass and per wavelength have been collected when the system has been operating at 2.5 Hz. Averaging the two wavelengths data over the whole pass, the two wavelengths differential time interval has been determined with the precision typically 7 picoseconds.

2-COLOR RANGING TO TARGET

RESIDUALS of 532/683 nm Pulses

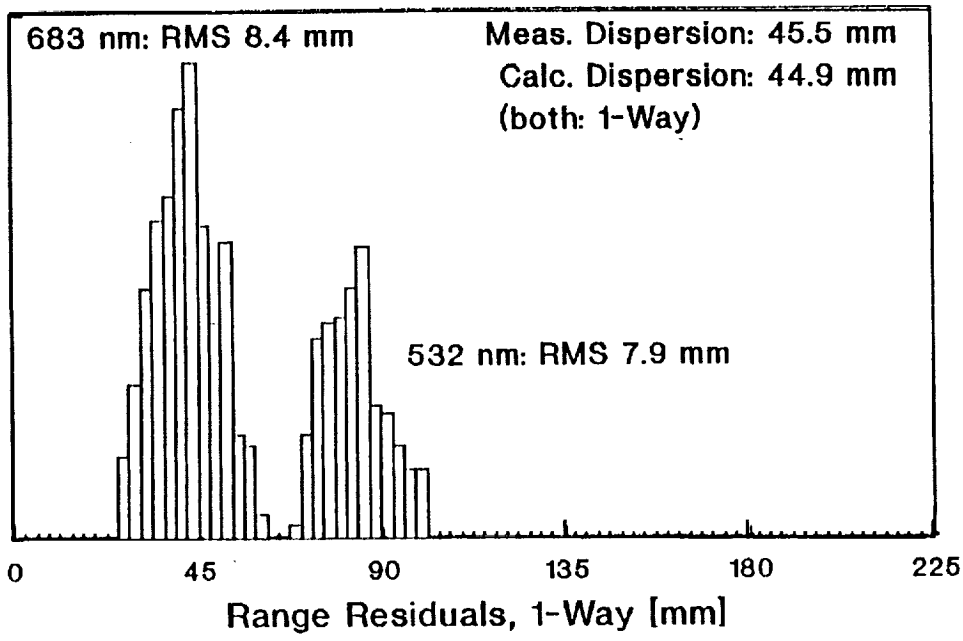

1991-12-12

Fig. 2

Satellite AJISAI

2-Color Ranging: 532 and 683 nm

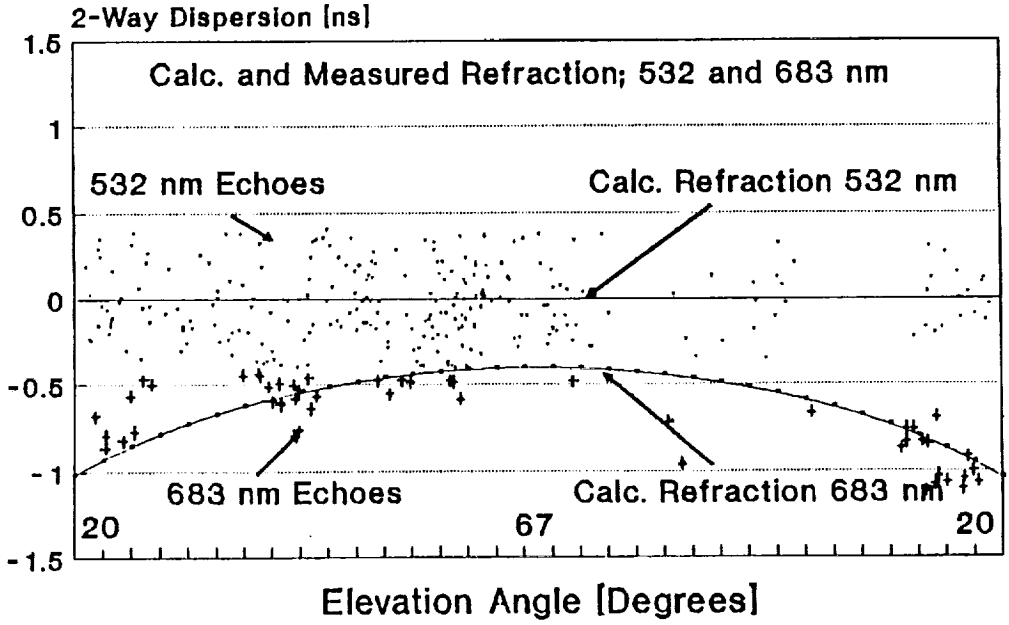

1991-12-12

Fig. 3

The energy budget, the number of returns per wavelength and hence the differential time interval precision has been limited by the system ranging repetition rate of 2.5 Hz, which is determined by the station ranging electronics. Additional limitation is the chromatic aberration of the transmitter refracting telescope, which limits the minimal divergence achievable simultaneously on both wavelengths. These two limitations are expected to be resolved within 1992.

CONCLUSION

Taking into account the energy budget when ranging to a satellite, assuming the data rate requested for two minute burst averaging and the ground target ranging results, one may conclude, that the picosecond accuracy of the two wavelength time difference interval is achievable using this technique. Comparing to the other two wavelengths ranging techniques, the simplicity, stability and the simple calibration is obvious. Some other wavelengths pairs, namely the Raman Stokes and anti Stokes, resulting in a considerably higher value of DTI may be considered. However, the telescope transmitter beam delivering optics has to be reconstructed.

References

1. J.B. Abshire, Applied Optics, Vol.19,No.20,1980, p34-36
2. I.Prochazka,K.Hamal,G.Kirchner,M.Schelev,V.Lozovoi,V.Postovalov, SPIE 1449-40
3. J.Gaignebet et al, Technical Digest of the Conference on Lasers and Electro Optics, CLEO 89, Baltimore, MD, 1989
4. I.Prochazka et al, technical Digest of the Conference on Lasers and Electro Optics, CLEO 90, Anaheim, CA, May 1990
5. B.Greene,proc.of the 6th International Workshop on Laser Ranging Instrumentation, Antibes,France, 1986

NEW PERSPECTIVES FOR HIGH ACCURACY SLR WITH SECOND GENERATION GEODESIC SATELLITES

Glenn LUND
Optical Department
AEROSPATIALE - Space & Defense Division
100 Boulevard du Midi
06322 CANNES LA BOCCA
FRANCE

ABSTRACT

This paper reports on the accuracy limitations imposed by geodesic satellite signatures, and on the potential for achieving millimetric performances by means of alternative satellite concepts and an optimised 2-colour system tradeoff.

Long distance laser ranging, when performed between a ground (emitter/receiver) station and a distant geodesic satellite, is now reputed to enable short arc trajectory determinations to be achieved with an accuracy of 1 to 2 centimeters. This state-of-the-art accuracy is limited principally by the uncertainties inherent to single-colour atmospheric pathlength correction. Motivated by the study of phenomena such as post-glacial rebound, and the detailed analysis of small-scale volcanic and strain deformations, the drive towards millimetric accuracies will inevitably be felt.

With the advent of short pulse (< 50 ps) *dual* wavelength ranging, combined with adequate detection equipment (such as a fast-scanning streak camera or ultra-fast solid-state detectors) the atmospheric uncertainty could potentially be reduced to the level of a few millimeters, thus exposing other less significant error contributions, of which by far the most significant will then be the morphology of the retroreflector satellites themselves.

Existing geodesic satellites are simply dense spheres, several 10's of cm in diameter, encrusted with a large number (426 in the case of LAGEOS) of small cube-corner reflectors. A single incident pulse thus results in a significant number of randomly phased, *quasi*-simultaneous return pulses. These combine coherently at the receiver to produce a convolved interference waveform which cannot, on a shot to shot basis, be accurately and unambiguously correlated to the satellite center of mass.

The present paper proposes alternative geodesic satellite concepts, based on the use of a very small number of cube-corner retroreflectors, in which the above difficulties are eliminated whilst ensuring, for a given emitted pulse, the return of a single clean pulse with an adequate cross-section.

1 RECENT AND IMMINENT ADVANCES IN SLR ACCURACY

Many SLR groups have reported, during the course of the present workshop, considerable progress in their laser station equipment, as well as in the performance of data reduction and orbital modeling.

Laser technology has made considerable progress since the days of the first ruby lasers, and most stations are now equipped with a doubled Nd:YAG. Pulse widths down to 50 ps, with an output power of ~ 30 mJ and a repeat rate of ~ 10 Hz are now being reported and can be expected to become routine performances in many stations. The temporal width of such pulses is now responsible for much less of the return signal duration than the optical depth of the satellite itself.

The technology of ultra-fast SPAD (Silicon Photo Avalanche Diode) detectors would seem very promising for picosecond event timing. Streak cameras, despite the considerable expense involved in their exploitation, are recognised not only for their single picosecond capacity but also for their ability to record single or multiple waveforms (eg. for 2-colour differential flight time measurements). K. Hamal has reported streak camera satellite signature recordings from AJISAI and STARLETTE.

The accuracy of atmospheric models, used to correct for the delay in pulse flight time, is considered to be limited by the small amount of meteorological data exploited and from which the entire atmospheric profile is implicitly defined. Although single-colour SLR makes use of a single *in situ* measurement of temperature pressure and water vapour pressure, 2-colour ranging is expected to enable a considerable improvement to be achieved by virtue of differential flight time correction. The residual error with this technique lies in the range of 2 to 3 mm.

Although several authors have reported improvements in the modeling used to take into account both gravitational and non-gravitational (radiation, thermal, drag) orbital influences, the residual bias in the determination of LAGEOS' orbit is estimated as 2 to 3 cm for 1 month of data and 1 cm for a year of data (R. Eanes). Many sophiticated data reduction and collation procedures have been elaborated, but the limit in rms baseline accuracy nevertheless appears to saturate at the level of 1 cm.

2 RETURN SIGNAL CONVOLUTION BY MULTIPLE ECHOS

The time domain behaviour of a round-trip SLR pulse can be thought of as an initially narrow Gaussian pulse which is convolved successively by the atmospheric transfer function (due to refractive index dispersion - typically ~ 10 ps), the "forest" of Diracs corresponding to each of the satellite reflectors "visible" at the ranging instant, the atmospheric transfer function for a second time, and finally the detector transfer function. Whereas the emission, detection and atmospheric functions could well provide a global received pulse FWHM of ~ 50 ps (7.5 mm), the satellite signature, determined by the overlapping reflector echos within its apparent optical depth, is typically an order of magnitude greater in duration.

The practically indeterminant and undeconvoluable nature of the resulting signature imposes a practical limit in residual range uncertainty varying between 1 and 5 cm (depending on the size and characteristics of the ranged satellite), even after several months of data accumulation. This uncertainty is represented by σ^2_{sat} (~ ≥ 100 ps) in expression (1) of §3.

In an effort to eliminate the drawbacks of such complex signatures, a novel geodesic satellite concept is proposed in which a very small number of retroreflectors, exhibiting very little or no local FOV overlap, is arranged in such a way as to ensure the unicity (or at least unambiguous identifiability) of the detected return waveforms. Ideally, the apexes of each retroreflecting cube corner would be mutually co-located at the satellite's centre of mass. In practice, this requirement cannot be exactly met, implying either some form of attitude stabilisation and/or deterministic correction between measured and true (centre of mass) ranges. The residual uncertainty in range correction should be no more than 1 or 2 mm.

Velocity aberration is a parameter of considerable importance, and the means used to achieve appropriate correction would depend on the implementation (or not) of attitude stabilisation.

Finally, an adequate systems approach to high accuracy SLR would require a careful tradeoff to be made between the mean satellite reflector cross-section (i.e. related to the cube corner size, mean incidence angle and diffraction lobe pattern) and station parameters such as (dual colour) laser wavelength choice, pulse energy and width, and receiving telescope size. The latter considerations are adressed on the following section.

3 LINK BUDGET REQUIREMENTS AND SYSTEM CONSIDERATIONS

The parameters which exert an influence on range accuracy include not only the retroreflector characteristics, but also the laser station design. Range accuracy and link budget analyses are thus needed in order to ascertain an optimal approach to the specification of high accuracy SLR satellites and 2-colour ranging stations, as set out below. The uncertainty in the absolute value of a 2-colour corrected normal point can be expressed as;

$$\sigma^2_{norm.pt.} = K_1 \left\{ \sigma^2_{sat} + \frac{\sigma^2_{noise}}{N_{shot}} + A^2 \left(\sigma^2_{sc} + \frac{1}{N_{shot}} \left(\frac{\sigma^2_{pulse}}{N_{det(\lambda 1)}} + \frac{\sigma^2_{pulse}}{N_{det(\lambda 2)}} \right) \right) \right\} \qquad (1)$$

where ;

- σ^2_{sat} is the unaccountable satellite center-of-mass bias,
- σ^2_{noise} is the cumulated random variance of the timing system,
- N_{shot} is the number of shots used to establish a normal point,
- K_1 is a conversion factor from ps to mm,
- σ^2_{sc} is the unaccountable Streak Camera bias (typically 1 to 2 ps),
- σ^2_{pulse} defines the received pulse width (σ = 0.425 FWHM),
- A is the 2-colour correction sensitivity (related to λ_1 and λ_2), and
- $N_{det(\lambda)}$ is the number of detected photons at wavelength λ.

The expected number of detected photons at a given wavelength is derived from the link budget analysis as follows :

$$N_{det} = K_2 \left\{ \lambda . \frac{1}{R^4(z)} . \frac{1}{\omega^2} . (1 - \theta/40) . T^2_{atm}(z) . QE(\lambda) \right\} \times \left\{ \frac{E_{emit} . \Phi^2_{tel} . \Phi^2_{cc}}{\Omega^2} \right\} \qquad (2)$$

where ;

- K_2 is a constant including geometrical factors optical efficiencies,
- R is the station to satellite range,
- ω is the emitted beam divergeance,
- θ is the local incidence angle of the ranging beam relative to the reflector normal. $(1- \theta/40)$ gives a close approximation to the cube-corner cross-section falloff as a function of incidence angle),
- T_{atm} is the 1-way atmospheric transmission, depending on range angle Z,
- QE_λ is the receiver detector quantum efficiency at wavelength λ,
- E_{emit} is the emitted pulse energy,
- Φ_{tel} is the station receiving telescope diameter,
- Φ_{cc} is the retroreflector diameter, and
- Ω is the equivalent angular diameter of the retroreflector diffraction pattern.

Expression (2) has been grouped into two parts of which the first includes non-system or typically invariant parameters, whereas the second contains those variables which depend on the station (laser, telescope) and satellite (retroreflector size, diffraction pattern) designs.

The term σ_{pulse} in (1) is also considered as a system parameter, and has been combined with the second group of variables in (2) to form the quantity X_{syst} :

$$X_{syst:\,\sigma,E,\Phi_{tel},\Phi_{cc},\Omega} = \frac{E_{emit}.\Phi_{tel}^2.\Phi_{cc}^2}{\Omega^2.\sigma_{pulse}^2} \qquad \left(J.m^4.rad^{-2}.s^{-2}\right) \qquad (3)$$

Tradeoff analysis of the satellite and laser station characteristics can be made on the basis of the numerical evaluation of this quantity. Although the factor A is also a system-related parameter, its numerical value happens to be very similar for the 2 cases treated below and is there-fore not included in the above expression. In the following, it is assumed that Ω is <u>not</u> dependant on $\varnothing_{CC}$, but rather on an engineered diffraction lobe pattern; a conservatively large value of Ω is taken, corresponding to diffraction into a uniform ring 2.5 arcsecs in width, at a mean distance of 9 arcsecs from the incoming beam direction.

Figures (1) and (2) thus illustrate the computed variation of the 10-shot ranging accuracy $\sigma_{Norm.Pt.}$ (exp. 1) as a function of $X_{syst.}$, for a 800 km circular orbit and negligeable center-of-mass bias (σ_{sat}), at four values of zenith ranging angle : 0°, 20°, 40° & 60° (assuming 10 km Standard Atmosphere visibility), and for two different cases of dual wavelength laser configuration :

Fig.1 Doubled & tripled Nd:YAG,
Fig.2 Fundamental & doubled (eg. Ti-Sapphire) wavelengths @ 800 & 400 nm.

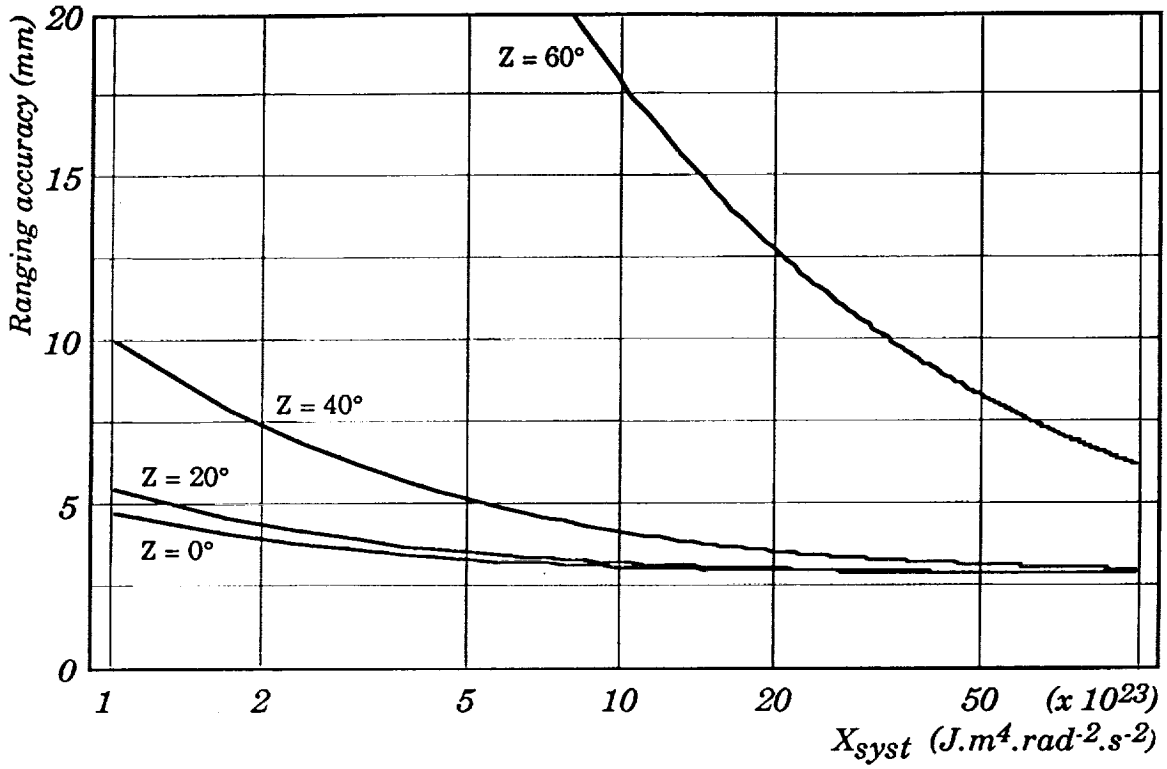

Figure 1. Nd:YAG 2-colour ranging accuracy as a function of the system input parameter X (= $E.\Phi^2_{tel}.\Phi^2_{cc} / \Omega^2.\sigma^2_{pulse}$) and zenith ranging angle Z.

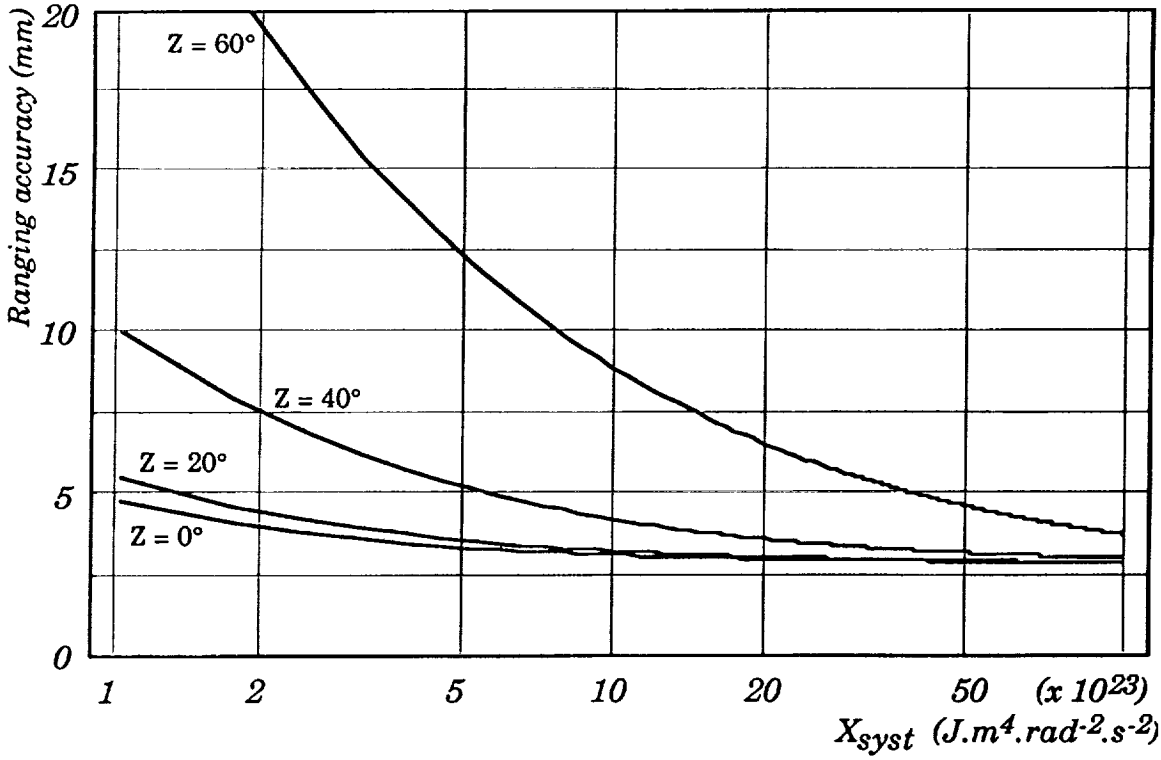

Figure 2. 400 / 800 nm 2-colour ranging accuracy as a function of the system input parameter X (= $E.\Phi^2_{tel}.\Phi^2_{cc} / \Omega^2.\sigma^2_{pulse}$) and zenith ranging angle Z.

The resulting curves show (for example) that if sub-centimetric ranging accuracies are to be achieved with 2-colour systems up to zenith angles of 60°, one could accept a value of $X_{syst.} \geq 7.10^{23}$ from the fundamental/doubled system, whereas a factor of ~ 8 improvement would be needed for comparable performance from a Nd:YAG station.

The above example supposes *normal* incidence at the retroreflector, and could be provided by the following numerical values for a 800 / 400 nm system and a *single* cube-corner retroreflector :

- E_{emit} = 40 mJ
- Φ_{tel} = 30 cm
- Φ_{cc} = 4 cm
- σ_{pulse} = 43 ps ($FWHM_{pulse}$ = 100 ps)

By shortening the emitted pulse FWHM to ~ 50 ps, one could achieve the same performance at local retroreflector incidences up to *30°*. An additional factor of ~ 3 improvement in telescope or reflector diameter would be required to achieve the same result with a Nd:YAG laser (assuming 40 mJ and 50 ps FWHM to be near to the practical limits for the emitted pulse power).

Further improvements could be achieved with still shorter pulses (in the case of a broad bandwidth amplification medium), or a larger number of pulses per normal-point. At the satellite level, larger retroreflectors, or more confined diffraction lobe patterns could be considered, without having to resort to the classical multiple reflector solution.

The strong link budget dependance on orbital height ($\propto R^{-4}$) would probably render single-reflector satellites unsatisfactory for orbits higher than a few 1000 km, if sub-centimetric accuracies were to be expected at high zenith angles and with a small number of pulses per normal point.

These considerations are encouraging, as they suggest that millimetric center-of-mass determinations could well be achieved with dual-colour SLR, provided appropriate consideration is given to the design of future geodesic satellites.

4 SECOND GENERATION REFLECTOR SATELLITE CONFIGURATIONS

It has been pointed out at the beginning of this paper that in the interests of a clean return signature and unambiguous center-of-mass determinations, the "ideal" geodesic satellite should exhibit non-overlapping reflector FOVs in order to inhibit multiple echo returns, whereas the link budget calculations given in § 3 show that a *single* retroreflector of reasonable dimensions could provide adequate return signal strength for millimetric range determination accuracies.

A parameter of considerable importance in the retroreflector design is that of velocity aberration correction, in which an appropriate trade-off is needed between link budget considerations (influenced by the value of Ω) and stabilisation of the reflector orientation relative to the orbital plane. Two fundamentally different approaches could thus be used, according to the choice between ultimate satellite simplicity and optimal link budget performance, as set out in the examples below :

4.1 UNSTABILISED OMNIDIRECTIONAL RETROREFLECTOR SATELLITE

An *omnidirectional* diffraction pattern, as used in the example in § 3 and in the case of existing geodesic satellites, relieves the spacecraft from any attitude stabilisation requirements, and thus results in the simplist form of satellite configuration. In the example shown in figure (3), the satellite is composed of 8 cube corner retroreflectors (solid or hollow, depending on thermal, optical and dimensional constraints), each designed to provide an annular diffraction lobe.

If the ranging system and satellite were designed so as to meet the link budget requirements for local incidence angles up to 30°, it can be shown that any emitted pulse would have a 55% probability of returning to the reciver with adequate signal strength. When compared with the potential advantage of highly accurate range determinations, the drawback of intermittently weak return signals does not appear to be of significant concern.

Although the finite thickness of the cube corner walls would lead to a small residual uncertainty in the satellite center-of-mass determination, this effect is found to be negligeable for wall thicknesses up to ~ 2 cm.

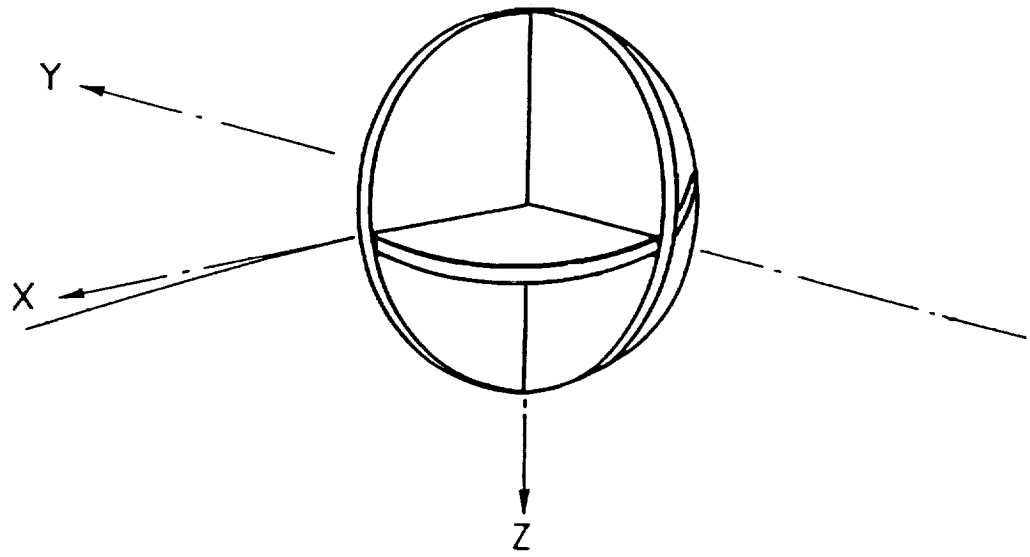

Figure 3 Passive geodesic satellite design for millimetric range determinations.

4.2 STABILISED DIRECTIONAL RETROREFLECTOR SATELLITE

The link budget performance of the previous design could be considerably improved by concentrating the diffracted energy into 2 small lobes (i.e. by reducing Ω), as is the case with the proposed GLRS-R ground target design (reported elsewhere in these proceedings). This approach could only be implemented if the direction of the diffraction lobes were appropriately maintained in alignment with the direction of relative movement between emitter and reflector.

In Figure (4), such a satellite design is shown, in which spin stabilised attitude control is used to maintain one of each of the cube corner dihedral angles in a direction perpindicular to the orbital plane. These dihedral angles would be slightly spoiled from perpindicularity so as to generate two small diffraction lobes in opposite directions, of sufficient amplitude to correct for the velocity aberration. A gain of - 10 or more in return signal strength, compared with the annular diffraction lobe design, could be expected.

Although a *spin* stabilisation is shown here, *3-axis* stabilisation could also be envisaged - thus requiring a smaller number of cube corners. In both cases the attitude control would not have to be very precise (typically - $\pm$ 5° should be adequate), and could be achieved using virtually passive systems such as magnetic torquers. A further possibility would be to use a completely passive 3-axis stabilisation system based on gravity masts.

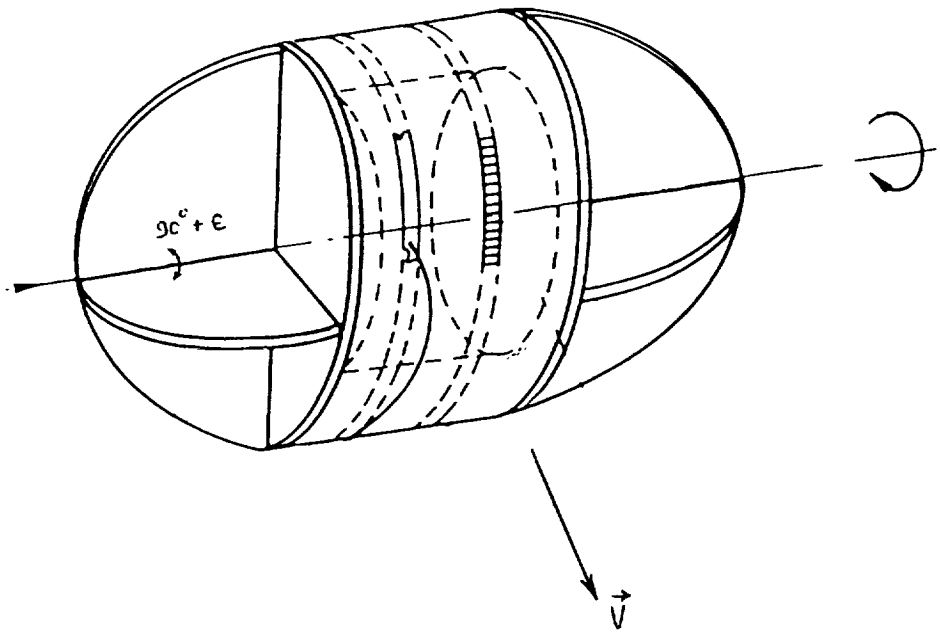

Figure 4 Spin-stabilised geodesic satellite design for millimetric range determinations.

5 CONCLUSIONS

It has been shown from link budget analyses that, when coupled with an appropriate satellite configuration, realistic *single* retroreflector dimensions could enable millimetric absolute accuracies to be achieved with future 2-colour SLR, through the removal of center-of-mass uncertainties in the range determination.

The engineering of retroreflector velocity aberration corrections is an important factor in the design of a geodesic satellite and in the link budget performance to be expected from the complete ranging system.

Two approaches to the design of second generation geodesic satellites have been suggested. Although these might imply the use of non-spherical orbiting bodies, with consequently higher atmospheric drag and solar radiation pressure imbalances than for existing satellites, they could nevertheless enable excellent geometric mode (short arc) range determinations to be achieved, and could be expected to provide very good long arc performance for high altitude orbits.

SLR Data

Analysis/Model Errors

STATE-OF-THE-ART SATELLITE LASER RANGE MODELING FOR GEODETIC AND OCEANOGRAPHIC APPLICATIONS

S.M. Klosko
Hughes ST Systems Corporation Lanham, MD 20706

D.E. Smith
NASA/GSFC, Greenbelt, MD 20771

Abstract

Significant improvements have been made in the modeling and accuracy of Satellite Laser Range (SLR) data since the launch of LAGEOS in 1976. Some of these include; improved models of the static geopotential, solid-Earth and ocean tides, more advanced atmospheric drag models, and the adoption of the J2000 reference system with improved nutation and precession. Site positioning using SLR systems currently yield ~2 cm static and 5 mm/y kinematic descriptions of the geocentric location of these sites. Incorporation of a large set of observations from advanced Satellite Laser Ranging (SLR) tracking systems have directly made major contributions to the gravitational fields and in advancing the state-of-the-art in precision orbit determination. SLR is the baseline tracking system for the altimeter bearing TOPEX/Poseidon and ERS-1 satellites and thusly will play an important role in providing the Conventional Terrestrial Reference Frame for instantaneously locating the geocentric position of the ocean surface over time, in providing an unchanging range standard for altimeter range calibration and for improving the geoid models to separate gravitational from ocean circulation signals seen in the sea surface. Nevertheless, despite the unprecedented improvements in the accuracy of the models used to support orbit reduction of laser observations, there still remain systematic unmodeled effects which limit the full exploitation of modern SLR data.

1. INTRODUCTION

The analysis of Satellite Laser Ranging (SLR) data requires precise dynamic modeling of a rapidly moving near-Earth orbiting target. Through the application of the theory of motion for an orbiting object, both the satellite position and the SLR observing sites can be located in a common reference frame through the accurate determination of the satellite ephemerides. The principal model needed for the computation of a satellite's trajectory is that of the gravitational field which accurately reflects the inhomogeneous distribution of the Earth's mass, and the temporal changes in the field due to tidal and presently unmodeled climatological sources. Depending on the orbit of interest and the area-to-mass ratio of the satellite, non-gravitational forces arising from the effects of

atmospheric drag and solar radiation are also important. Ground tracking systems provide an accurate means of sensing the perturbed motion of satellites. The primary advance in SLR geophysical applications comes through improvements in gravitational field modeling. By modeling the SLR measurements within global orbit solutions from many satellites, the broad features of the gravity field have been unambiguously determined. When combined with other less accurate forms of satellite tracking, satellite altimetry and surface gravimetry, the gravity field is sensed over an extensive spatial bandwidth. Using all these measurements has yielded comprehensive models of the Earth's gravity field in the form of spherical harmonic coefficients. These solutions describe the complex shape of the geoid as well as the resulting variation in the gravitational potential at altitude which perturbs the orbits of near-Earth artificial satellites.

SLR-based geodesy has benefitted from three achievements over the last 15 years. The first and certainly the most important is the advancement in laser tracking hardware. Since the launch of LAGEOS in 1976, laser systems have improved from 50 cm to centimeter level accuracies. With this rapid change in technology and an expanding global network, the laser data themselves were able to directly contribute to geophysical modeling. However, although great advances have been made, the SLR methodology has always been and continues to be geophysical and measurement model limited.

Laser systems are currently the most accurate and advanced means of precision satellite tracking. These ranging systems have substantially evolved, undergoing nearly a threefold improvement in system precision every five years during the last 15 years. The evolution of laser systems in monitoring the motion of near-Earth satellites has in turn resulted in much more stringent demands for geophysical models being used for representing the data to the sub-centimeter level.

Today the precision of existing SLR measurements is less than a cm for the best instruments. The process of forming laser normal points, a type of compressed data, effectively eliminates spurious observational noise of the current measurements. For all the laser data, there are systematic errors which are not eliminated in the normal point computation process. The effects of atmospheric propagation, especially horizontal gradients in the atmosphere which are not detectable by the surface meteorological measurements made at the laser sites, are the largest source of systematic error. Estimates of these errors are in the 0.5 to 2 cm range (Abshire and Gardner, 1985). Electronic errors, non-linearities in the tracking electronics as a function of signal strength, errors in the distance to the calibration targets, together with remaining spurious effects all result in a range system capable of 1-2 cm absolute accuracy for the current SLR data (Degnan, 1985) with further improvements in tracking hardware in progress.

2. IMPROVED GEOPOTENTIAL MODELING

Since the launch of LAGEOS, the gravity model has been improved through the analysis of millions of laser ranges acquired on satellites which span a wide range of orbital inclinations. Knowledge of the geopotential field has improved in accuracy by an order of magnitude or more, especially for the longest wavelength portion of the field.

Closely coupled with the improvement in the gravity field was the development of ancillary force, environmental, and measurement models which enabled the exploitation of these data closer to their precision. Advanced solid Earth and ocean tidal models, descriptions of site motion due to various sources of loading, and improved realization of a geocentrically referenced Conventional Terrestrial Reference System all played an important role in the more accurate representation of SLR data in the orbit determination process. The very significant impact of the precise SLR data on the gravity solution was demonstrated when LAGEOS observations first were included in the GEM-L2 solution. This solution used 2.5 years of measurements acquired by third generation laser systems from 20 globally distributed stations. Given the stability of the LAGEOS orbit against the influences of solar radiation pressure and atmospheric drag, a well isolated gravitational signal was available for geopotential modeling. While complex non-conservative orbital effects are seen on the LAGEOS orbit leading to numerous important studies (e.g. Rubincam et al., [1987]; Rubincam, [1988,1990]; Afonso et al., [1985]; Scharroo et al., [1991]), these effects are far smaller and much better modeled than are the non-conservative effects on less stable lower orbiting satellites. For example, Starlette, like LAGEOS, is a small dense sphere. However, this satellite at its 800-1200 km altitude, it is subjected to atmospheric drag perturbations of several m/day^2 in the along track direction depending on atmospheric conditions whereas the along track "drag" (including thermal, neutral density and charged particle) on LAGEOS is approximately 2 cm/day^2. The GEM-L2 solution contained 630,000 laser measurements, about 70% of which were the high quality ranges to LAGEOS. During the time interval of 1979-1981 where the LAGEOS data used in GEM-L2 were taken, the best systems operated at single shot precision levels of approximately 5-cm. The LAGEOS range measurements were by far the most precise satellite observations used in GEM-L2 and the significant improvement seen in this model is directly attributable to LAGEOS' contribution.

In the mid-1980's, preparation for orbit determination support for the TOPEX/Poseidon Mission began in earnest with the goal being to achieve 10 cm RMS radial orbit modeling. This necessitated a complete reiteration of the GEM solutions requiring recomputation of all of the normal equations in order to benefit from modern constants and models. It was also essential to significantly increase the size of the gravity field to realize the full benefit of better modeling available at this time. Further improvements in laser tracking technologies (e.g. single photon tracking using more sensitive detection technologies with multi-channel plates), required consideration of force and measurement models addressing effects at the cm level. New models were introduced to meet advancing laser tracking precision. The recent GEM-T2 solution (Marsh et al., 1990) is an example of the new series of GEM solutions. It contained over two million observations from 1130 arcs spanning 31 satellite orbits. There was also a significant improvement in the laser data included in the GEM-T2 solution. Third generation SLR observations from Starlette, Ajisai, LAGEOS, BE-C, GEOS-1 and GEOS-3 were included. Second generation data sets included SEASAT and GEOS-2. Early laser data taken on BE-B, D1-C, D1-D and PEOLE were also used. GEM-T2 effectively exploited the available historical satellite tracking database available for geopotential recovery. GEM-T2 extended the truncation limits of the satellite solution for certain resonance and zonal orders to degree 50. The GEM-T3 solution (Lerch et al., [1992]), which combines satellite models with surface gravimetry

and satellite altimetry from GEOS-3, SEASAT and GEOSAT, represents the most robust treatment of these diverse data sets within the GEM models.

2.1 IMPROVEMENTS IN SUPPORTING GEOPHYSICAL MODELS

Additional model improvements have significantly contributed to improved representation of the SLR data within orbital solutions. These improvements fall mutually into two categories. The first entails improvement of the other geophysical models effecting orbit determination and the time-dependent positioning of the observer within a well defined Conventional Terrestrial Reference System (CTRS). The second category concerns model optimization, and the ability to extract the best signal from the diverse observational data set available for geopotential recovery. The first category will be reviewed below.

SLR-geodesy is based on the exploitation of the functional relationships between very precise observations and the underlying model parameters. These parameters are either part of a model used to environmentally correct the data or are part of the physical models which describe the perturbations acting on a satellite and observer-to-satellite positioning. Model parameters are classified in two groups; *arc parameters* which are orbit-specific including the initial satellite state-vector, atmospheric drag coefficients, solar radiation modelling parameters, measurement related parameters such as measurement biases etc.; and *common parameters* which are satellite-invariant including tracking station positions and their motions (tectonic and environmental), reference frame parameters including polar motion and Earth rotation, nutation and planetary ephemerides, and the geophysical force models representing the static and time-dependent gravitational field.

Improved modeling of satellite tracking data over the years has progressively contributed to the accuracy of SLR solutions. Table 1 shows that recent GEM models have significantly increased the number and complexity of the models used to compute orbital motion due to temporal gravitational effects and those used to position an Earth-fixed observer. This development parallels that used at GSFC in the overall analysis of SLR. These models are required to support cm-level geodesy which has resulted in large increases in the size of various models. By increasing the number of harmonic coefficients in both the static and tidal gravity models, the truncation effect on low orbiting satellites is reduced. For example, based on the evaluation of the TOPEX orbit by Casotto (1989), the ocean tide model required for TOPEX to reduce omission effects below the one cm RMS radial error has required us to develop and employ ocean tide models containing more than 7000 terms spanning 96 discrete tidal lines. Along with improved and more complete models of tidal changes in the geopotential fields, reliance on space-based determinations of Earth orientation parameters, creation of SLR normal points, and improved accommodation of non-conservative force model effects have all made significant contributions to recent solutions.

These supporting models were not available for earlier studies or for the supporting site positioning and Earth orientation recovery. The attendant model error created systematic errors in both the orbits and the recovered parameters over a large range of spatial and temporal scales. To reduce these errors, temporal averaging was extensively applied. For example, early GSFC site positioning solutions focused on annual solutions

(Christodoulidis et al., 1985). Earth orientation parameters were recovered using 5-day averaging. With the current level of supporting models, less averaging is needed. Recent GSFC solutions (Robbins et al., 1992) now yield monthly station positions and daily values of Earth pole and length of day variations. Also, the improved stability of the long period reference frame has permitted direct recovery of horizontal site velocities which are much less distorted by the former neglect of some important long period force modeling effects which cause a drift in the orbital frame with respect to Conventional Terrestrial Reference Frame.

The importance of these models are quantified by mapping them into the space of the laser observations on Starlette and LAGEOS (Table 2). The contribution to the variance of the range residuals of numerous models which have been introduced into the analysis of the SLR observations are tabulated. The level of modeling has been systematically stepped back to that which was used to develop GEM-L2. Simulated laser ranging from a global network was generated using all of the current TOPEX standard models (Wakker, 1991). These models were then eliminated to demonstrate the sensitivity of the satellite ranging to each model in turn. These two satellites are at widely separated altitudes largely spanning the geodetic orbits currently available. While cm-level modeling is still a goal, Table 2 demonstrates that a great many effects must be considered when this level of modeling is required. Since many of these effects are similar to the signal arising from the static gravitational field, some aliasing will occur within geopotential solutions due to the limitation and/or neglect of these and other supporting models. Developing models which support mm level ranging will require further advances in the understanding of the geophysical response of the Earth. For example, Figure 1 presents a comparison of the laser site motion due to ocean loading using two independent models (Ray and Sanchez, 1989 vs IERS Standards, 1990) for the largest M2 constituent at the Maui, Hawaii site. While these models are suitable to support cm level geodesy, mm level data precision is rapidly approaching and will require extensive (especially environmental) modeling improvements.

The current gravity models cannot be expected to yield orbit errors at the overall accuracy level of the laser data themselves. The projections from solution covariances reflect instead, our overall ability to fit these data *a posteriori* as reviewed in Table 3. This limitation in our ability to model the laser ranges is a vexing problem for there are many unmodeled error sources which contribute to the post-solution data fits. Among likely candidates, we have some evidence that the error attributable to the static or tidal gravitational field is no longer the major contributing factor to the observation residuals. This conclusion is reached by taking individual satellite data sets like the laser data acquired on Ajisai and giving these data extremely high weight in test solutions. When such solutions are then tested, there is little improvement in the Ajisai orbital fit. This indicates that other effects are playing a significant role. Yet this inability to fit the data at their noise levels has important consequences.

It has long been observed that precise SLR observation residuals from orbit solutions exhibit systematic behavior within each pass, even after adjustment of the gravity field. An analysis of 600 passes of Starlette SLR data reveal that over 90% had apparent biases of 3 cm or more. This residual characterization is dominated by orbit modeling rather

than observation shortcomings. As a result of large (as compared to SLR nominal data accuracy) unmodeled effects in the residuals, their variance is much higher than that of a random effect. Thus, not all of the geodetic information can be extracted from these precise data. For example, gravitational signals which would otherwise be detectable at the cm level are obscured. If these data could be fully modeled with their gravity signal exhausted, there would be a considerable improvement in the accuracy of the SLR geodetic products produced using these data.

From the previous discussion, gravitational and orbit positioning solutions based upon near-continuous inter-satellite tracking have certain advantages. They largely eliminate the need to make complex media corrections to the observations since they are made above the atmosphere. Of course, force modeling errors effecting the orbit arising from solar radiation pressure and atmospheric drag still require further improvement. However, a word of caution is warranted. While continuous high precision tracking above the atmosphere like GPS tracking of TOPEX will eliminate many sources of systematic modeling error, the basic parameterization of the gravity field as a static and tidally varying physical system may itself have significant shortcomings. Only now are we coming to realize that there are a great number of environmental sources of mass redistribution arising from meteorological sources, such as variations of the atmospheric pressure field (Chao and Au, 1991) and continental water storage (Chao and O'Connor, 1988) which require much more attention in current orbit determination processes. These meteorological fluctuations, although having strong seasonality, are rather erratic in nature on shorter time scales. A recent report by Nerem et al., (1992) shows significant changes in the LAGEOS sensed zonal harmonics of the gravitational field related to atmospheric mass redistribution within monthly solutions. Evidence is mounting that these sources of unaccommodated signal are being sensed well above the noise level exhibited by modern SLR/GPS tracking systems. Treatment of these effects will require extensive evaluation of in situ data sources many of which are currently insufficient for the modern needs of precision orbit modeling. Neglect of these effects can limit the detection of signals of great general interest, such as the changes in the geopotential field due to post-glacial rebound, tectonic movement, and core activities.

3. SLR SUPPORT OF OCEAN APPLICATIONS

Satellite Laser Ranging will be used to support oceanographic science through the tracking support provided on recent satellite altimeter missions. Both TOPEX/Poseidon (launched in August 1992) and ERS-1 (launched in July 1991) are heavily dependent on SLR data for precise orbit determination. The accuracy of the orbital reference provided by SLR directly impacts the ability of these missions to geocentrically monitor the ocean surface over time needed for studying global ocean circulation.

From the analysis of the climatological models, the sea surface is known to depart significantly (±70 cm) from the geoid, and is offset in its center of figure with respect to the earth's center of gravity by as much as 25 cm. The absence of perfect symmetry of the dynamic height field with respect to the geocenter gives rise to non-zero degree one terms in the spherical harmonic expansion of the ocean topographic field (see Figure 2). The degree one terms in the absolute ocean height models are essential for

understanding long term changes in the character of the dynamic height field. C,S (1,1) describe the east-to-west slope of the ocean topography across the major ocean basins. The C(1,0) has implications for understanding the seasonal thermal expansion of the oceans. Each of these terms has an important physical basis. The values for the first degree terms from climatology imply that on average over the past 70 years, the southern oceans are more dense than their northern counterparts, and that the western portion of the major gyres are more energetic than that of the east; each of these observations are seen in the in situ data record. It is therefore important to verify that these terms are accurately determined within the satellite analyses. These terms are of special concern for they are of the 1 CPR spatial scale of the dominant orbit error.

The orbital motion of a an altimeter satellite exhibits an integrated response to the forces generated by the inhomogeneous mass distribution on and within the Earth, the density of the atmospheric medium it traverses, by the size and orientation of the satellite surfaces exposed to the Sun and Earth and the response of these surfaces to this incident radiation. There are many additional, although less significant, forces acting on the satellite which require consideration. It is important to characterize the likely errors in these models, and their effect on the radial position over time of an orbiting altimeter satellite. Through this assessment, significant insight can be gained into the role of highly accurate SLR tracking in the recovery of satellite's orbital ephemerides and by inference, in the recovery of the ocean's dynamic height.

Much of the orbit error signal is at or near to 1 Cycle Per Revolution (CPR). At longer periods, principally errors in the odd zonal geopotential harmonics and errors in modeling satellite surface forces are capable of producing a modulation of the 1 CPR error over the orbital arc length. This is the so called "bow-tie" error effect. Moreover, there are important ocean topographic signals on the spatial scale of the 1 CPR orbit errors. The only hope for separating these signals from those of the 1 CPR orbit errors, is through the dense, global distribution of highly accurate tracking data which allows parameters in the orbit determination process to eliminate these errors. Again, TOPEX/Poseidon, with simultaneous tracking provided by satellite laser ranging and DORIS, offers the promise that this separation of signals can effectively be accomplished. The complete spatial correlation of the orbit and oceanographic effects at 1 CPR and the existence of weak tracking data sets supporting previous altimeter missions has limited the understanding of the change in ocean topography on this spatial scale to date.

Secondly, the best "standard" in existence for precise ranging is provided by SLR. Both of these altimeter satellites will overfly ocean/sea oil platforms allowing simultaneous tracking from the SLR and altimeter systems. The SLR ranges will be used to position the satellite with respect to the platform location (using GPS ties). Through tide gauges on the platform, the satellite altimeter is accurately located with respect to the instantaneous ocean surface based on the absolute scale provided by SLR. The altimeter range is calibrated through this method. In this way, the altimeter measurements can be assessed and monitored over the course of these missions to prevent instrument drift being confused with long period sea level changes.

4. SUMMARY

Since the launch of LAGEOS, our ability to model the range data to this and other satellites has improved by more than an order of magnitude. The accuracy and precision of the existing SLR systems has made an enormous contribution to the modeling of the static and tidal geopotential fields. Primarily, through the employment of millions of laser ranges, great progress was seen in the modeling of the gravity field at GSFC as well as at UT/CSR and DGFI/GRGS. These data are capable of detecting the gravity and tidal signals to unprecedented accuracy levels. However, with data of this precision, the further need for supporting geophysical and environmental models of improved accuracy is evident. These underlying models are themselves of considerable scientific interest. Currently, given *a posteriori* data fits which are inferior to the accuracy of SLR, the accuracy of SLR systems are yet to be fully exploited in current solutions, and geodetic signals otherwise detectable at the cm-level, are being obscured by these modeling shortcomings. With improvement, SLR data will be better able to detect temporal changes in many physical systems, like that of the geopotential field. This is important for example, for monitoring mean eustatic conditions apart from postglacial crustal rebounding.

Focus on improving underlying geophysical models, improving data treatment and incorporation of in situ data bases to describe short-term and erratic meteorological sources of mass transport are required objectives for future SLR geodetic investigations.

The SLR observations are also playing an increasingly important role in supporting satellite-based oceanography. Through the tracking support being provided to ERS-1 and TOPEX/Poseidon, these data and their supporting models, will be the basis for defining the absolute geocentric location of the instantaneous ocean surface to better understand the Earth's climatological system and ocean circulation. The SLR data will also be invaluable in the continuous calibration of the altimeter instruments over the lifetime of these and other altimeter missions.

REFERENCES

Abshire, J.B., S. Gardner, Atmospheric Refractivity Corrections in Satellite Laser Ranging, IEEE Trans. on Geoscience and Remote Sensing, GE-23, 4, 414-425, 1985.

Afonso, G., F. Barlier, C. Berger, F. Mignard, and J.J. Walch, "Reassessment of the Charge and Neutral Drag of LAGEOS and its Geophysical Implications", J. Geophys. Res., 90. 9381-9398, 1985.

Barlier, F., Berger, C., Falin, J., Kockarts, G. and Thuillier, G, "A Thermospheric Model Based on Satellite Drag Data", AERONOMICA ACTA, A-No. 185, 1987.

Casotto, S., Ocean Tide Models for TOPEX Precise Orbit Determination, PhD Thesis, University of Texas, Austin, Texas, 1989.

Chao, B.F., W.P. O'Connor, Global Surface-Water-Induced Seasonal Variations in the Earth's Rotation and Gravitational Field, Geophys. J., 94, 263-270, 1988.

Chao, B.F., A.Y. Au, Temporal Variation of the Earth's Low-degree Gravitational Field Caused by Atmospheric Mass Redistribution: 1980-1988, J. Geophys. Res., 96, B4, 6569-6575, 1991.

Christodoulidis, D.C., D.E. Smith, R.G. Williamson, and S.M. Klosko, Observed Tidal Braking in the Earth/Moon/Sun System, J. Geophys. Res., 93, B6, pp. 6216-6236, 1988.

Degnan, J.J., Satellite Laser Ranging: Current Status and Future Prospects, IEEE Trans. on Geoscience and Remote Sensing, GE-23, 4, 398-413,1985.

Engelis, T., Global Circulation from Seasat Altimeter Data, Mar. Geodesy, 9, 1, 1985.

Jacchia, L.G., "Revised Static Model of the Thermosphere and Exosphere with Empirical Temperature Profiles", Special Report 332, SAO, Cambridge, MA, 1971.

Lerch, F.J., S.M. Klosko, R.E. Laubscher, C.A. Wagner, Gravity Model Improvement Using GEOS-3 (GEM-9 and 10), J. Geophys. Res., 84, 3897-3915, 1979.

Lerch, F.J., S.M. Klosko, and G.B. Patel, Gravity Model Development From Lageos, Geophys. Res. Letters, 9, (11), pp. 1263–1266, 1982.

Lerch, F.J. et al., Geopotential Models of the Earth from Satellite Tracking, Altimeter and Surface Gravity Observations: GEM-T3 and GEM-T3S, NASA Tech. Mem. 104555, January, 1992a.

Marsh, J.G., et al.,A New Gravitational Model for the Earth From Satellite Tracking Data: GEM-T1, J. Geophys, Res., Vol. 93, No. B6, pp. 6169-6215, 1988.

Marsh, J.G., Lerch, F.J., Putney, G.H., Felsentreger, T.L., Sanchez, B.V., Klosko, S.M., Patel, G.B., Robbins, J.R., Williamson, R.G., Engelis, T.E., Eddy, W.F., Chandler, N.L., Chinn, D.S., Kapoor, S., Rachlin, K.E., Braatz, L.E., and Pavlis, E.C., The GEM-T2 Gravitational Model, J. Geophys. Res., 95, B13, 22043-22070, 1990.

Nerem, R.S., B.F. Chao, A.Y. Au, J.C. Chan, S.M. Klosko, N.K. Pavlis, R.G. Williamson, "Temporal Variations of the Earth's Gravitational Field from Satellite Laser Ranging to LAGEOS", Geophys. Res. Let., in press, 1992.

Ray, R.D. and B.V. Sanchez, Radial Deformation of the Earth by Oceanic Tidal Loading, NASA Tech. Mem. 100743, July, 1989.

Robbins, J.W., P.J. Dunn, M.H. Torrence, R. Kolenkiewicz, D.E. Smith, "Direct Estimation of Horizontal Velocities of Satellite Laser Tracking Sites from the SL8 LAGEOS Analysis", presented at the 1992 European Geophysical Society Meeting, Edinburgh, Scotland, 1992.

Rubincam, D.P., "Yarkovsky Thermal Drag on LAGEOS", J. Geophys. Res., 93, 13,805-13,810, 1988.

Rubincam, D.P., "Drag on the LAGEOS Satellite", J. Geophys. Res., 95, 4881-4886, 1990.

Rubincam, D.P., P. Knocke, V.R. Taylor, and S. Blackwell, "Earth Anisotropic Reflection and the Orbit of LAGEOS", J. Geophy. Res., 92, 11,662-11,668, 1987.

Scharroo, R., K.F. Wakker, B.A.C. Ambrosius, and R. Noomen, "On the Along-Track Acceleration of the LAGEOS Satellite", J. Geophys. Res., 96, 729-740, 1987.

Smith, D.E., Kolenkiewicz, R., Dunn, P.J., Robbins, J.W., Torrence, M.H., Klosko, S.M., Williamson, R.G., Pavlis, E.C., Douglas, N.B., Fricke, S.K., Tectonic Motion and Deformation from Satellite Laser Ranging to LAGEOS, J Geophys Res, 95, B13, 22013-22041, 1990.

Wakker, K.F., "Report by the Subcommittee on Intercomparison and Merging of Geodetic Data for the TOPEX/Poseidon Science Working Team", Technical University of Delft, Report LR-638, May, 1990.

Table 1. Chronological parameterization of GEM models

NAME (DATE)/ NO. OF SATS	FIELD	MOST RECENT SLR DATA:*	REF SYS/ NUTATIONS	SOLID TIDES	OCEAN TIDES	CTRS	DRAG
GEM-9/10(1977) /30	20x20	76S	1950/Wollard no relativity	None	None	CIO	J71 w/24 hr Ap
GEM-L2(1983) /30	20x20	81L,S	↓	k_2=0.29 e_2=2.018^0 h_2=0.60 l_2=0.075	None	↓	↓
GEM-T1(1987) /17	36x36	84L,S	J2000/Wahr no relativity	k_2=.30 e_2=o^0 h_2=.609 l_2=.0852 Frequency dependence	32 lines (600 coef)	"zero-mean"	↓
GEM-T2(1990) /31	36x36	87L,S,A	↓	↓	↓	↓	+ DTM w/3 hr kp
GEM-T3(1991) /31 T3S	50x50	89L,S,A	↓	↓	↓	↓	↓
Pre-Launch TOPEX Model (1992)/34	70x70	90L,S,A 91E,R_1,R_2	J2000/ Wahr w/relativity	↓	96 lines (6000+coef)	IERS with dynamic polar motion	+ MSIS w/3 hr kp

* L LAGEOS
S Starlette
A Ajisai
E ERS-1
R1, R2: Etalon (USSR) -1 and -2

Key for CTRS: CIO - mean figure axis referenced to the Conventional International Origin; "zero-mean" - mean figure axis reference obtained from the LAGEOS polar motion series; IERS - new international standard definition of the Conventional Terrestrial Reference System (McCarthy, 1989).
Key for Drag: DTM - Barlier et al., (1987); MSIS - Hedin (1986); J71 - Jacchia (1971); 3 hr kp - model uses 3 hour values of the kp magnetic index; 24 hr Ap - model uses daily values of the Ap magnetic index.

Table 2. Estimated contribution of geophysical models to SLR range signal

FORCE MODELS	STARLETTE RMS (cm) Residual: 6^d arc	LAGEOS RMS (cm) Residual 30^d arc
• rotational deformation/ dynamic polar motion	4.9	0.2
• ocean tides:[1] extensive sideband, non-resonance tidal terms	5.8	3.2
• ocean tides	21.8	13.3
• frequency dependency [2] of solid Earth tides	21.6	5.0
• Earth albedo/IR reradiation	4.8	3.3
• Earth tides[3]	150.7	213.7
• GEMT3 v. GEML2 static gravitational model	206.1	7.0
meas. models		
pole tide	0.2	
ocean loading	0.5	
solid Earth tides (geometric)	6.5	

[1] sideband contribution from over 80 tidal lines using linear admittances to scale dominant tide line.

[2] from Wahr (1979): departure of K_2 from .30 within principally semi-diurnal band.

[3] using K_2 = .30 for frequency invariant model.

Table 3. Typical satellite laser ranging orbital fits in cm from various GEM solutions

Gravity model	Lageos	Ajisai	Starlette
GEM-9	33.3	95.1	116.0
GEM-L2	19.9	79.7	100.0
GEM-T1	5.5	12.3	21.2
GEM-T2	5.3	9.4	13.3
GEM-T3	5.2	9.0	11.8
Overall laser ranging precision	3.8		

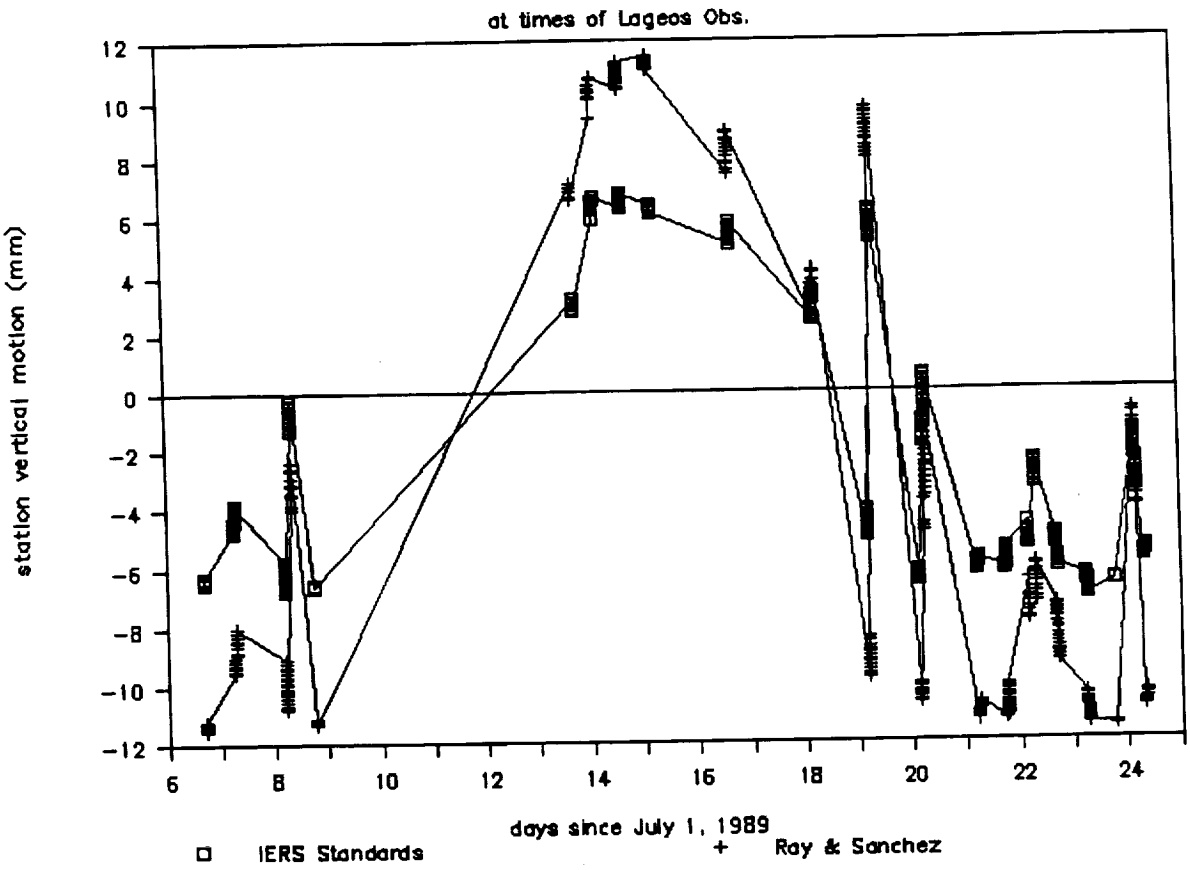

Figure 1. Comparison of models for ocean loading correction for the M2 tide at Maui, Hawaii

Figure 2.

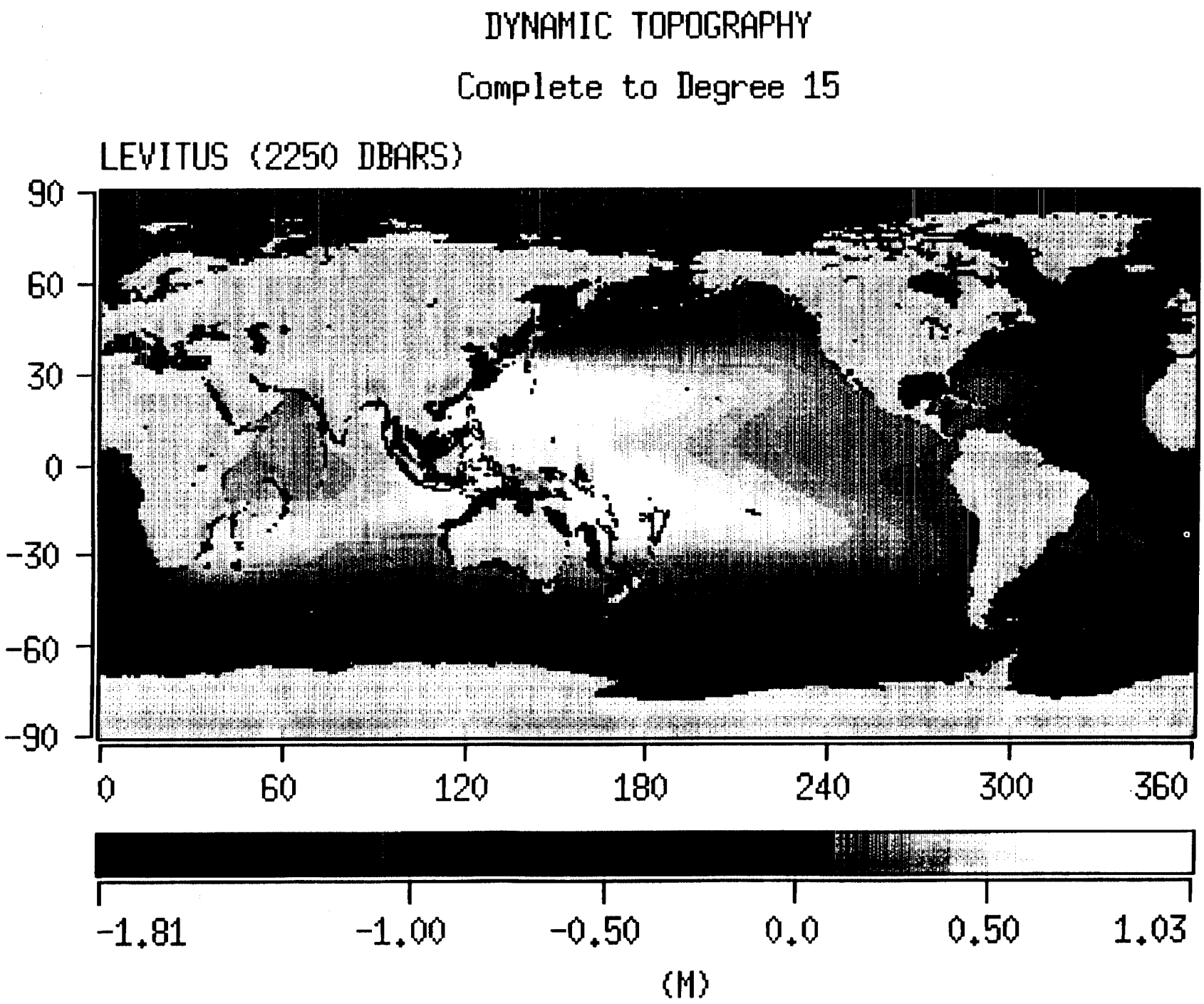
DYNAMIC TOPOGRAPHY
Complete to Degree 15
LEVITUS (2250 DBARS)
90
60
30
0
-30
-60
-90
0
60
120
180
240
300
360
-1.81
-1.00
-0.50
0.0
0.50
1.03
(M)

GEOMETRIC ANALYSIS OF SATELLITE LASER RANGING DATA

B. CONKLIN, S. BUCEY, V. HUSSON, W. DECKER
Bendix Field Engineering Corporation
Seabrook, MD

J. DEGNAN
Code 901/Crustial Dynamics Project
NASA Goddard Space Flight Center

The analysis of simultaneous laser data is investigated using the method of trilateration. Analysis of data from 1987 to 1992 is presented with selected baseline rates and station positions. The use of simultaneous Etalon data is simulated to demonstrate the additional global coverage these satellites provide. Trilateration has a great potential for regional deformation studies with monthly LAGEOS American solutions between 3 - 12 millimeters.

In the 1970s the precision of laser data was about 10 - 15 centimeters and the global distribution of satellite laser ranging stations was poor. Since that time the international laser ranging community has expanded and the precision of the data has improved substantially. Most laser ranging stations now produce data with a single shot precision on LAGEOS below 2 centimeters and much of that data has a single shot precision below 1 centimeter.

During the 1970s the mathematical methods to determine satellite positions using geometric data analysis were improved. The term used for that method is trilateration. The primary advantage of the trilateration technique is independent of orbit. It provides a means of analyzing station positions and data quality in such a way as to lower other outside influences such as satellite drag, radiation pressure, and gravity models that are used in the orbit determination methods. The major disadvantages to trilateration include the need for simultaneous ranging data, the difficulty in separating range biases from the station height, and the fact that the method does not allow for the extraction of the gravity field and other information that can be determined from an orbit determination process. Trilateration is also susceptible to low signal-to-noise ratio and low precision data.

Our method of trilateration requires simultaneous data from four or more laser ranging stations. There are several preprocessing steps that must occur to prepare the data for analysis. The process starts with a monthly LAGEOS fullrate release tape. Software selects the passes in which 4 or more stations have observations during the same timeframe. Once a timeframe has been found a polynomial is fit to the fullrate data for each pass. These polynomials, and other information such as the polynomial statistics and meteorological information, are written to an output file. The process continues through the entire data tape. After all of the polynomials have been determined, simultaneous data points are created at 30 second intervals from the pass polynomials. Poorly fitted passes are removed so that they don't corrupt the solution, although this rarely occurs. Any time intervals

within the selected passes that have fewer than 4 stations are deleted. A summary output of the available stations and data yield is also produced at this step. Finally, the remaining LAGEOS tracking data is separated into two sections. One section is for Europe, North Africa, Commonwealth of Independent States. The other section is for the Americas, Easter Island, and Huahine.

To analyze the data geometrically, each section of LAGEOS ranging data is read in by the software. Apriori station positions and station velocities are used to compute each stations position at the middle of the month. The satellite position is determined for each observation so that angle dependent corrections are computed and applied to the data. Once all the data has been corrected an iterative process is started. The observed minus computed values (O-Cs) from each satellite position are determined for each epoch along with an average satellite position. The O-Cs are then edited using a 6-sigma editing criterion and the average satellite position is recomputed. A summary of each stations mean and rms are written to the run summary file along with the total number of observations per station and the number of edits. A sensitivity matrix is then generated. This is done by applying small offsets to each of the station position vector elements and determining what effect each offset has on the O-Cs for all of the epochs. This procedure is performed for each coordinate (ie. 12 times for 4 stations). A P transpose P matrix is generated and then inverted, where P is the matrix of partial derivatives of the O-Cs with respect to the adjusted station position. The O-Cs are then multiplied by the resulting partials and a matrix is then computed. These corrections are applied to the station positions and a new set of average satellite positions are computed and new O-Cs determined. Again these O-Cs are multiplied by the P matrix and reiterated. This iterative process is repeated until the delta rms of the O-Cs between consecutive iterations is less than one percent, or six iterations have been reached. The total change of the station position is determined for both x,y,z and latitude, longitude and height. The baseline lengths are determined for only the stations involved in the solution and saved in a database. This database also contains the month and the number of simultaneous observations between the two stations. A sample summary for a one month period for a European solution is shown in Figure 1. A by-product of the solution is the point distribution plot, a sample of which is shown in Figure 2. Baseline rates are generated from the baselines and a least-squares linear fit of each of the station combinations is computed by weighting the monthly baseline with the number of observations during that month. Some sample baseline rates are illustrated in Figures 3-5.

The method of trilateration also lends itself to doing long term solutions. In this method both the initial station position and the station velocities are determined. This method of analysis is still under development.

The requirement for simultaneous ranging data from 4 stations requires geographic coverage over a broad area, which in turn requires high altitude satellites. The Etalon satellites offer great potential because of their high altitude and visibility to a larger number of stations at one time. However, the Etalon satellites have had a low

global ranging priority so they are rarely ranged by more than two stations at any one time. An intense Etalon campaign was performed during May and June of 1992 to determine how well these satellites can be used for Crustal Dynamics research and geometric data analysis. Unfortunately, because of the low Etalon priorities, the campaign yielded no simultaneous ranging data sets from 4 stations and only 1 data set where 3 station ranged simultaneously. LAGEOS 2, scheduled for launch in October 1992, offers the next best opportunity to obtain a large simultaneous ranging data set. In addition, at an inclination of about 65 degrees, there will be an opportunity to obtain simultaneous trans-atlantic data sets on a high priority SLR satellite.

In the future, we expect that simultaneous geometric analysis of data from LAGEOS, LAGEOS2, and Etalon1 and Etalon 2, spread over a period of a few days, will accurately determine baselines and velocities. Future modifications to the geometric analysis software are expected to include the additional determination of range and time biases from individual data sets.

```
SOLUTION FOR  5/90 VERSION 3.1
THE STATIONS BEING SOLVED FOR ARE   7835  7839  7840  7834  7939  7810  1181  1884
THE TOTAL NUMBER OF THIRTY SECOND POINTS =  547
ITERATION  1 MEAN =    0.0005 RMS =  0.0381 M EDITS =   82
7835 POINTS =  243 EDITS = 19 MEAN =   0.61(CM) RMS =  2.79(CM) GRASSE,FRANCE
7839 POINTS =  308 EDITS = 14 MEAN =  -2.14(CM) RMS =  4.98(CM) GRAZ,AUSTRIA
7840 POINTS =  401 EDITS = 25 MEAN =   1.04(CM) RMS =  2.49(CM) ROYAL GREENWICH OBSERVATORY,ENGLAND
7834 POINTS =  251 EDITS =  2 MEAN =  -3.53(CM) RMS =  4.06(CM) WETTZELL,GERMANY
7939 POINTS =  433 EDITS = 15 MEAN =   1.58(CM) RMS =  2.98(CM) MATERA,ITALY
7810 POINTS =  407 EDITS =  7 MEAN =  -0.23(CM) RMS =  3.21(CM) ZIMMERWALD,SWITZERLAND
1181 POINTS =   97 EDITS =  0 MEAN =  -0.02(CM) RMS =  3.86(CM) POTSDAM,GERMANY
1884 POINTS =  258 EDITS =  0 MEAN =   2.01(CM) RMS =  2.77(CM) RIGA,LATVIA
ITERATION  2 MEAN =    0.0003 RMS =  0.0294 M EDITS =   83
ITERATION  3 MEAN =    0.0001 RMS =  0.0260 M EDITS =   83
ITERATION  4 MEAN =   -0.0001 RMS =  0.0238 M EDITS =   79
ITERATION  5 MEAN =    0.0001 RMS =  0.0221 M EDITS =   81
ITERATION  6 MEAN =   -0.0001 RMS =  0.0220 M EDITS =   78
ITERATION  7 MEAN =    0.0000 RMS =  0.0211 M EDITS =   78
ITERATION  8 MEAN =    0.0000 RMS =  0.0209 M EDITS =   74
ITERATION  9 MEAN =    0.0002 RMS =  0.0214 M EDITS =   68
7835 POINTS =  243 EDITS = 15 MEAN =   0.18(CM) RMS =  2.36(CM)
7839 POINTS =  308 EDITS = 14 MEAN =  -0.08(CM) RMS =  2.20(CM)
7840 POINTS =  401 EDITS = 17 MEAN =   0.04(CM) RMS =  1.22(CM)
7834 POINTS =  251 EDITS =  7 MEAN =  -0.09(CM) RMS =  3.26(CM)
7939 POINTS =  433 EDITS =  8 MEAN =   0.05(CM) RMS =  1.36(CM)
7810 POINTS =  407 EDITS =  7 MEAN =  -0.02(CM) RMS =  2.05(CM)
1181 POINTS =   97 EDITS =  0 MEAN =  -0.10(CM) RMS =  3.77(CM)
1884 POINTS =  258 EDITS =  0 MEAN =   0.09(CM) RMS =  1.91(CM)

 7835 OFFSET IN CENTIMETERS   -0.8250  -4.5956   2.2171
 7839 OFFSET IN CENTIMETERS  -12.5536   1.6383  -3.0958
 7840 OFFSET IN CENTIMETERS    3.7155   2.1842   0.9769
 7834 OFFSET IN CENTIMETERS  -15.0631 -10.3012  -3.5499
 7939 OFFSET IN CENTIMETERS    6.5119   0.9027   2.9142
 7810 OFFSET IN CENTIMETERS    1.1438  -0.5387  -0.6604
 1181 OFFSET IN CENTIMETERS   11.1416  -0.7329  -5.1856
 1884 OFFSET IN CENTIMETERS    3.4161  -0.6365   3.8376

STATION 7835 TO STATION 7839 =   764437.0501 M # OF 30 SECOND PTS =  91
STATION 7835 TO STATION 7840 =   932884.7705 M # OF 30 SECOND PTS = 142
STATION 7834 TO STATION 7835 =   753159.1604 M # OF 30 SECOND PTS = 124
STATION 7835 TO STATION 7939 =   877290.0126 M # OF 30 SECOND PTS = 225
STATION 7810 TO STATION 7835 =   349661.2268 M # OF 30 SECOND PTS = 119
STATION 1181 TO STATION 7835 =  1060757.9395 M # OF 30 SECOND PTS =  11
STATION 1884 TO STATION 7835 =  1890491.9961 M # OF 30 SECOND PTS =  87
STATION 7839 TO STATION 7840 =  1183242.7342 M # OF 30 SECOND PTS = 218
STATION 7834 TO STATION 7839 =   302138.4442 M # OF 30 SECOND PTS = 137
STATION 7839 TO STATION 7939 =   719404.9253 M # OF 30 SECOND PTS = 205
STATION 7810 TO STATION 7839 =   610840.0036 M # OF 30 SECOND PTS = 238
STATION 1181 TO STATION 7839 =   616033.6433 M # OF 30 SECOND PTS =   0
STATION 1884 TO STATION 7839 =  1242790.6872 M # OF 30 SECOND PTS = 166
STATION 7834 TO STATION 7840 =   917334.0128 M # OF 30 SECOND PTS = 188
STATION 7840 TO STATION 7939 =  1694490.9600 M # OF 30 SECOND PTS = 311
STATION 7810 TO STATION 7840 =   685045.3282 M # OF 30 SECOND PTS = 299
STATION 1181 TO STATION 7840 =   895488.7178 M # OF 30 SECOND PTS =  96
STATION 1884 TO STATION 7840 =  1683599.7109 M # OF 30 SECOND PTS = 152
```

Fig. 1

JUNE 1988 LAGEOS POINTS

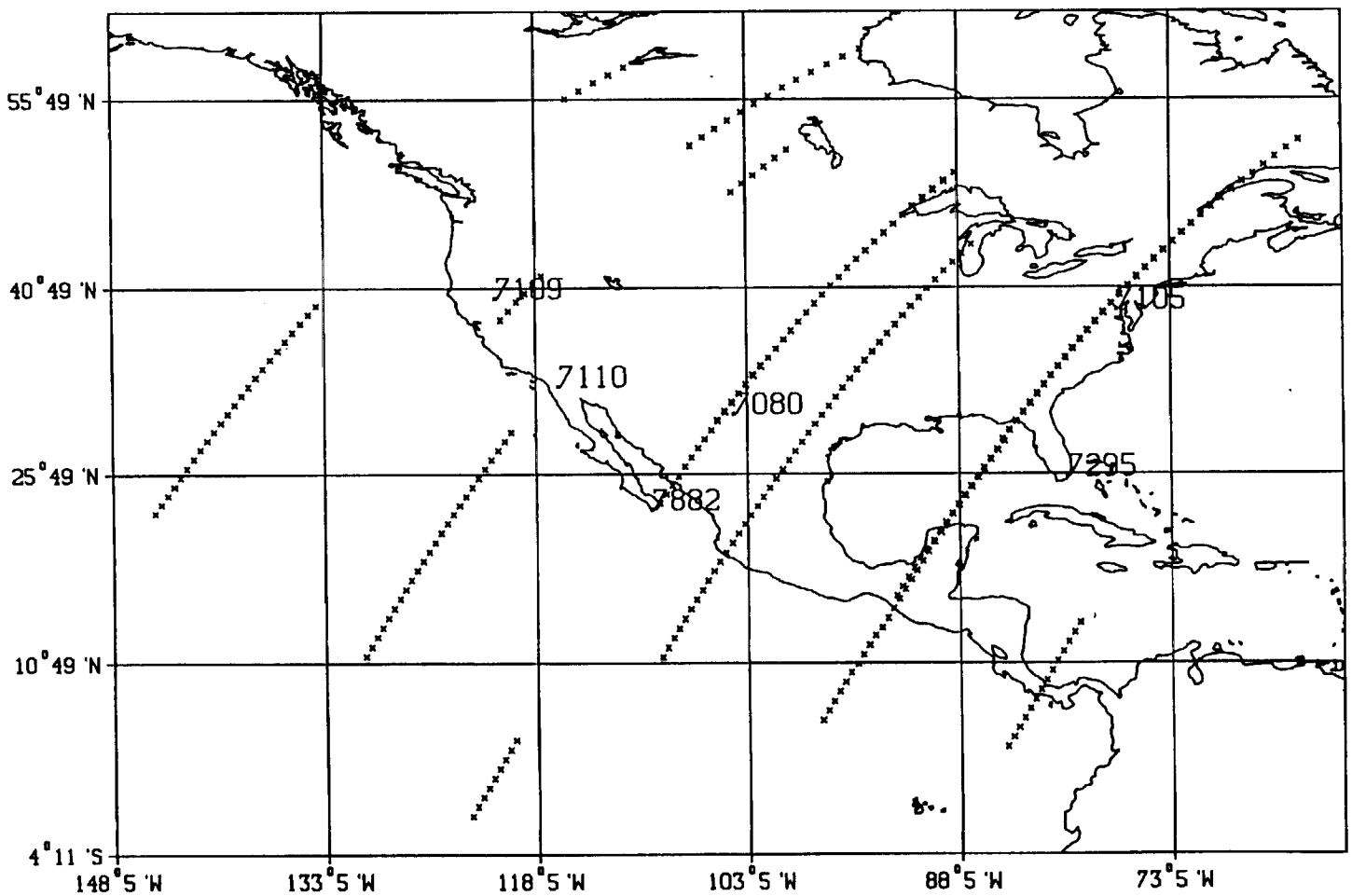

Fig. 2

GREENBELT - MONUMENT PEAK DATES 7/87 - 12/90
BASELINE = 3559741 (M) RATE = -2. (MM/YR)

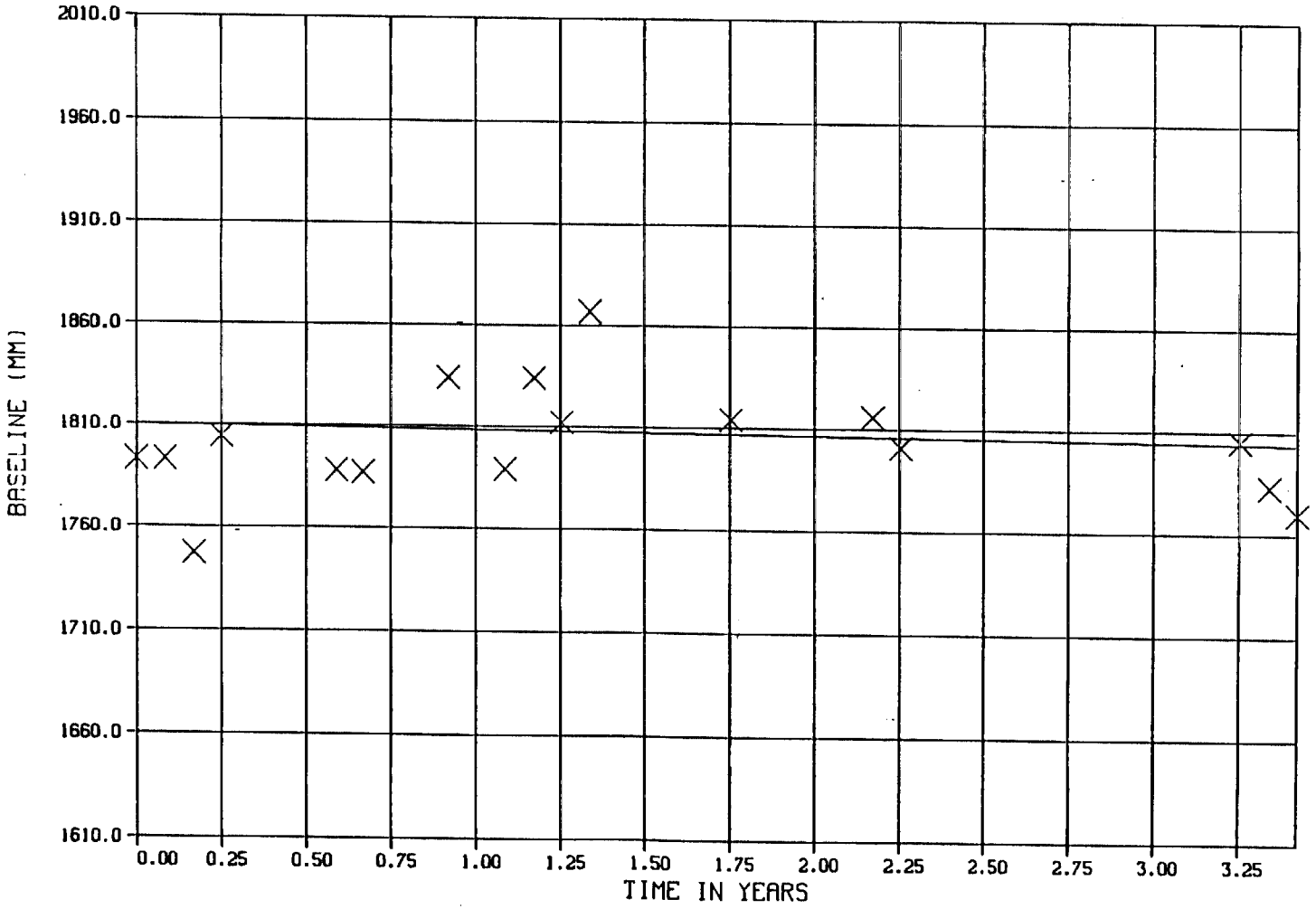

Fig 3

QUINCY - MONUMENT PEAK DATES 7/87 - 12/90
BASELINE = 883601 (M) RATE = -33. (MM/YR)

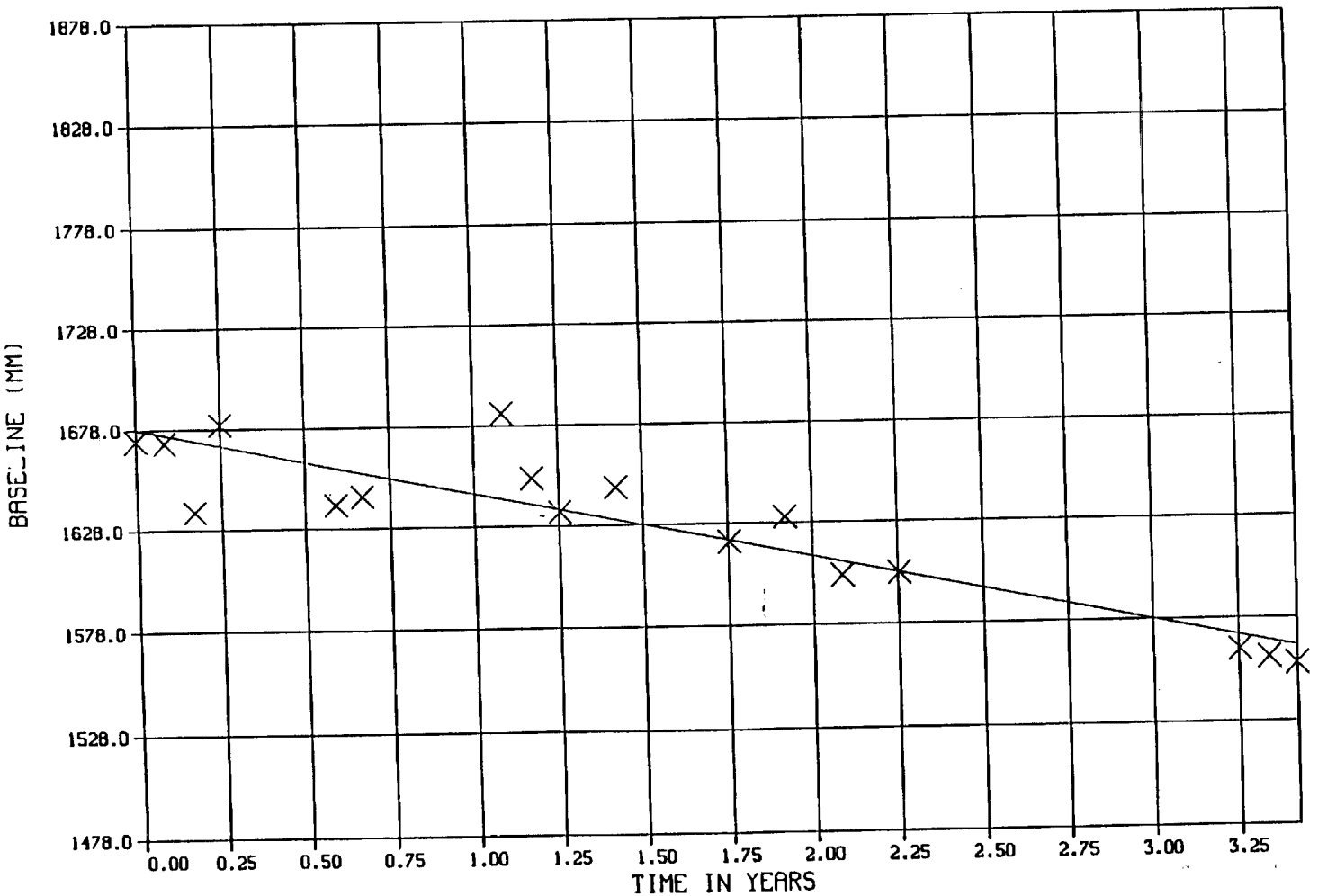

Fig 4

DIONYSOS - HERSTMONCEUX DATES 7/87 - 1/90
BASELINE = 22324305 (M) RATE = 21. (MM/YR)

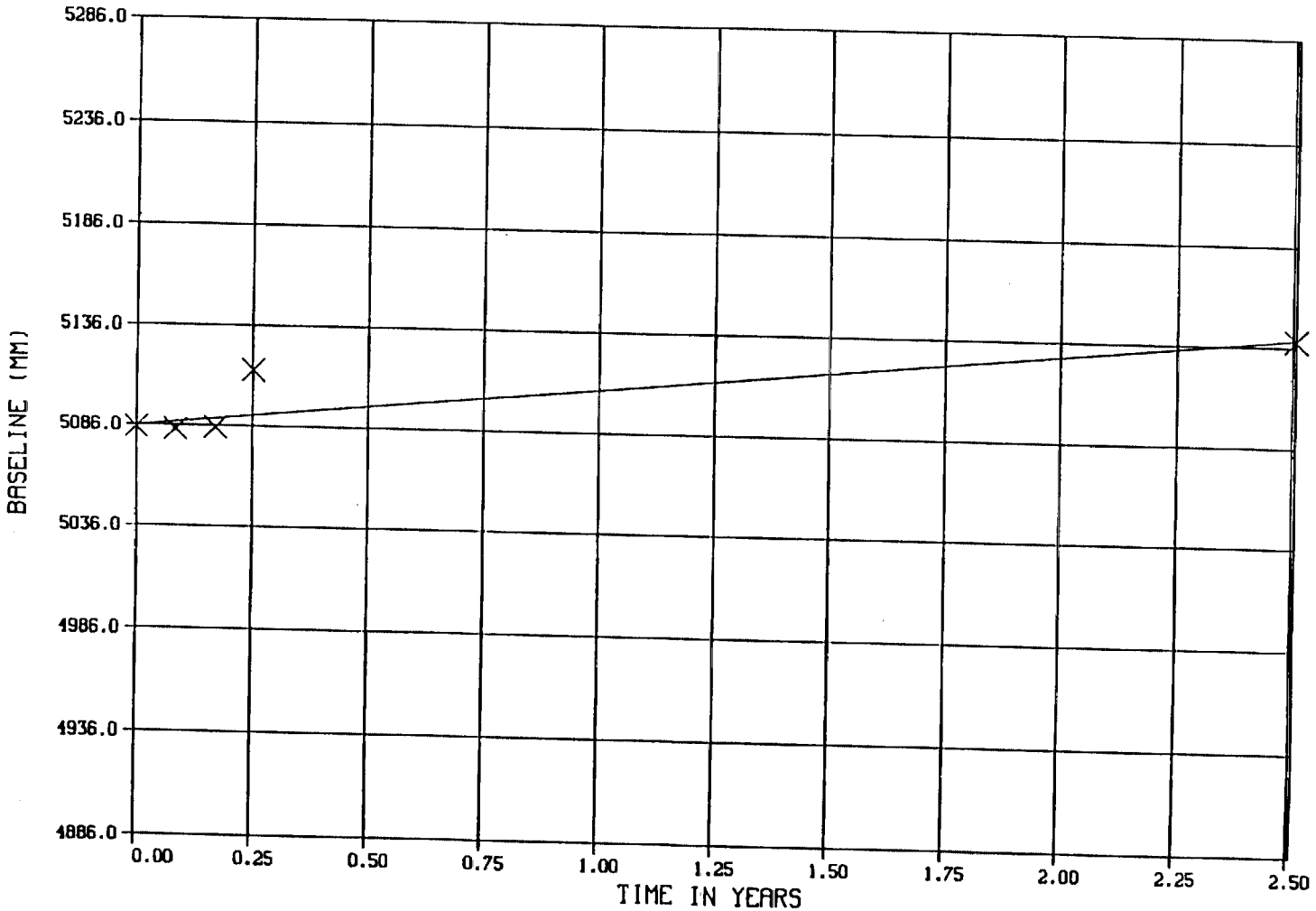

Fig. 5

8th International Workshop on SLR Instrumentation

Session: Mobile System Upgrades / Developments

IMPROVEMENT OF SLR ACCURACY, A POSSIBLE NEW STEP

M. KASSER, ESGT, 18 Allée J. Rostand, BP 77, 91 002 EVRY France

Abstract

The SLR technology experienced a large number of technical improvements since the early 1970ies, leading now to a millimetric instrumental accuracy. Presently it appears as useless to increase these instrumental performances as long as the atmospheric propagation delay suffers its actual imprecision. It has been proposed since many years to work in multiwavelength mode, but up to now the considerable technological difficulties of subpicosecond timing have seriously delayed such an approach.

Then a new possibility is proposed, using a device which is not optimized now for SLR but has already given good results in the lower troposphere for wind measurement: the association of a radar and a sodar. While waiting for the 2-λ methodology, this one could provide an atmospheric propagation delay at the millimetre level during a few years with only little technological investment.

I/ INTRODUCTION

It has been pointed out since a long time that all space geodesy techniques have to deal with the same general problem, i. e. the crossing of the atmosphere to reach either an artificial satellite, or the moon, or a star, or a quasar, etc...

Nevertheless, if it is the same atmosphere for every techniques, the effect is known to be quite different for radiowave and for optical methodologies, the first ones suffering more than the other ones from the crossing of ionosphere (but this is corrected classically by two-frequencies methods) and from the troposphere transit (because of the atmospheric water vapor content which is quite unpredictable and has a strong impact on propagation of radio waves and not on optical ones). Considering these aspects, the general advantages of radio techniques compared with optical ones in geodesy are their all-weather capabilities, and their drawbacks are linked with their poor tropospheric correction quality.

As long as the instrumental accuracies were at a few centimeters level, this meteorological aspects were of secondary concern. This is no longer the case since many years with VLBI, who had to use costly water vapor radiometers to upgrade the tropospheric correction to an excellent level (and since this period, VLBI has got the best positioning precision among all space geodesy techniques). Since a few years too it is no longer the case with satellite laser ranging, which is able of an

internal instrumental precision of a few millimeters, to be compared with the final positioning accuracy of 2-3 cm. Of course the tropospheric corrections are not the only problems biasing the results (consider for example the poor world coverage of SLR stations), but significant improvements of this parameter must be researched. Many teams have pointed out that multiwavelength methodology could provide this required amelioration. Anyway it is quite clear that this will ask for a tremendous technological effort and will probably not be operational since some years. For that reason we have looked for a new solution, able to give better tropospheric correction with up-to-date techniques, even if probably not as efficient as 2-colour method, but immediately available.

II/ THE ATMOSPHERIC CORRECTION FOR SLR

If n is the index of refraction, $n = c_0 / c$ (c_0 is the light celerity in vacuum and c in the atmosphere).

Classically we define the co-index of refraction as

$$N = (n - 1).10^6$$

and for optical wavelengths, using for example Essen's formula:

$$N = A_\lambda (P_a / T).\{ 1 + (a - b.t).P_a \} - B_\lambda (P_v / T)$$

where P_a is the atmospheric pressure, P_v is the water vapor pressure, T is the absolute temperature and t is the centigrade temperature, A_λ and B_λ are λ-dependant parameters, and a and b are constants. With a 10^{-7} precision it is acceptable to use the simplified formulation:

$$N = A'_\lambda (P_a / T) - B_\lambda (P_v / T)$$

We define also the geometric length of the optical ray L_g , the optical path L_o , and the geometric distance L between two points s_0 and s_1 being one at the ground level and the other beyond the atmosphere, at the satellite level:

$$L_g = \int_{s_0}^{s_1} ds \qquad L_o = \int_{s_0}^{s_1} n(s) . ds$$

If we call $\Delta L = L_0 - L$, it is a function of the angle α between the vertical and the direction of the satellite. We notice that:

$$\Delta L = (L_0 - L_g) + (L_g - L)$$

As the curvature of the ray path is low, and as this curvature is experienced only on a small range (a few tens of kilometers), the difference $L_g - L$ is generally considered as negligible. On another hand, ΔL can be expressed as:

$$\Delta L = f(\alpha) \ . \ \Delta L_{vertical}$$

And the function $f(\alpha)$ may be found in (Berrada-Baby *et al.*, 1987 or Akhundov et Stoskii, 1992). We have now to deal with ΔL for $\alpha = 0$. h_0 being the elevation of the SLR station above "sea level".

$$\Delta L = \int_{h_0}^{\infty} N(h).dh$$

Considering the very low dependance of the result regarding the water vapor for these optical wavelengths, we will focus on the "dry" part of this expression ΔL_d :

$$\Delta L_d = \int_{h_0}^{\infty} A \frac{P_a}{T}.dh$$

And, $\rho(h)$ being the air density, $T(h)$ the absolute temperature, $P(h)$ the atmospheric pressure and $g(h)$ the acceleration of the pesanteur at the elevation h, with R = 287 J.kg/°K

* $P_a = \rho(h) \cdot R \cdot T(h)$

* $d\,P(h) = \rho(h) \cdot g(h) \cdot dh$

so that,

$$\Delta L_d = \int_{h_0}^{\infty} \frac{dP(h)}{g(h)}.A.R$$

At this level we may have different assumptions:

1st hyp. $g(h) = g_0$ = constant. Then $\Delta L_d = A.R.P_0 / g_0$

2nd hyp. $g(h) = g_0 / (1 + 2.h/r_0)$ closer to the reality. We find then:

$$\Delta L_d = \frac{A.R.P_0}{g_0}\left(1 + \frac{2R\beta}{r_0.\frac{\beta}{T_0}(g_0 + R.\beta) - 2.g_0}\right)$$

(β is the gradient of T). For P_0 = 1000 mbar, we find $\Delta L_d \simeq$ 2,3 meters

And the difference between these two models is below 1 cm : various studies show (Berrada-Baby, 1987) that this discrepancy is around 5 mm, and is quite stable and thus easy to model. On another hand, the differences between the second model and real data deduced from (Cira 1965) campaigns are quite small (1 mm typically).

So we conclude that it is extremely important to measure P_0 with an excellent precision (1 mbar of error induces 2.3 mm on the atmospheric correction). And one must take into account the fact that the function $f(\alpha)$ (that is the air-mass number) will multiply these values by numbers up to 2.5 in operationnal SLR measurements.

If the temperature is measured in the first 5 kilometers, looking at fig. 1 and fig. 2, we observe that half the total correction is already acquired (fig. 1), and that the upper layers are quite well defined by the profile in the troposphere. If we compare these facts with the abovementionned value of 5 mm, whose noise is around 1-2 mm, multiplied by the air-mass value (1 to 2.5), i. e. less than 5 mm, it is clear that any temperature profile of good precision acquired in the troposphere will leave a residual error on the atmospheric correction at the millimeter level.

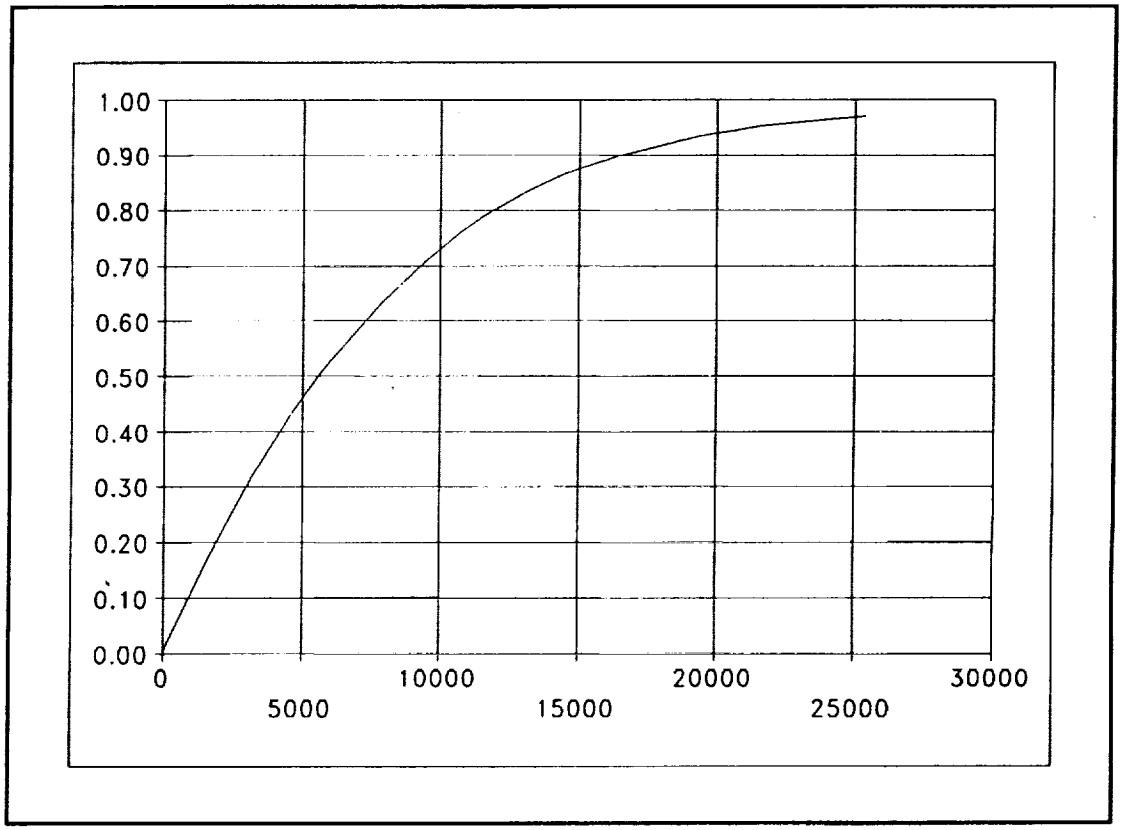

Fig. 1: Fraction (Y-axis) of the total atmospheric correction for a vertical transit of a laser pulse, from the ground level up to a given altitude (X-axis, in meters). Computed from an observed radio-profile in Greece, 1990.

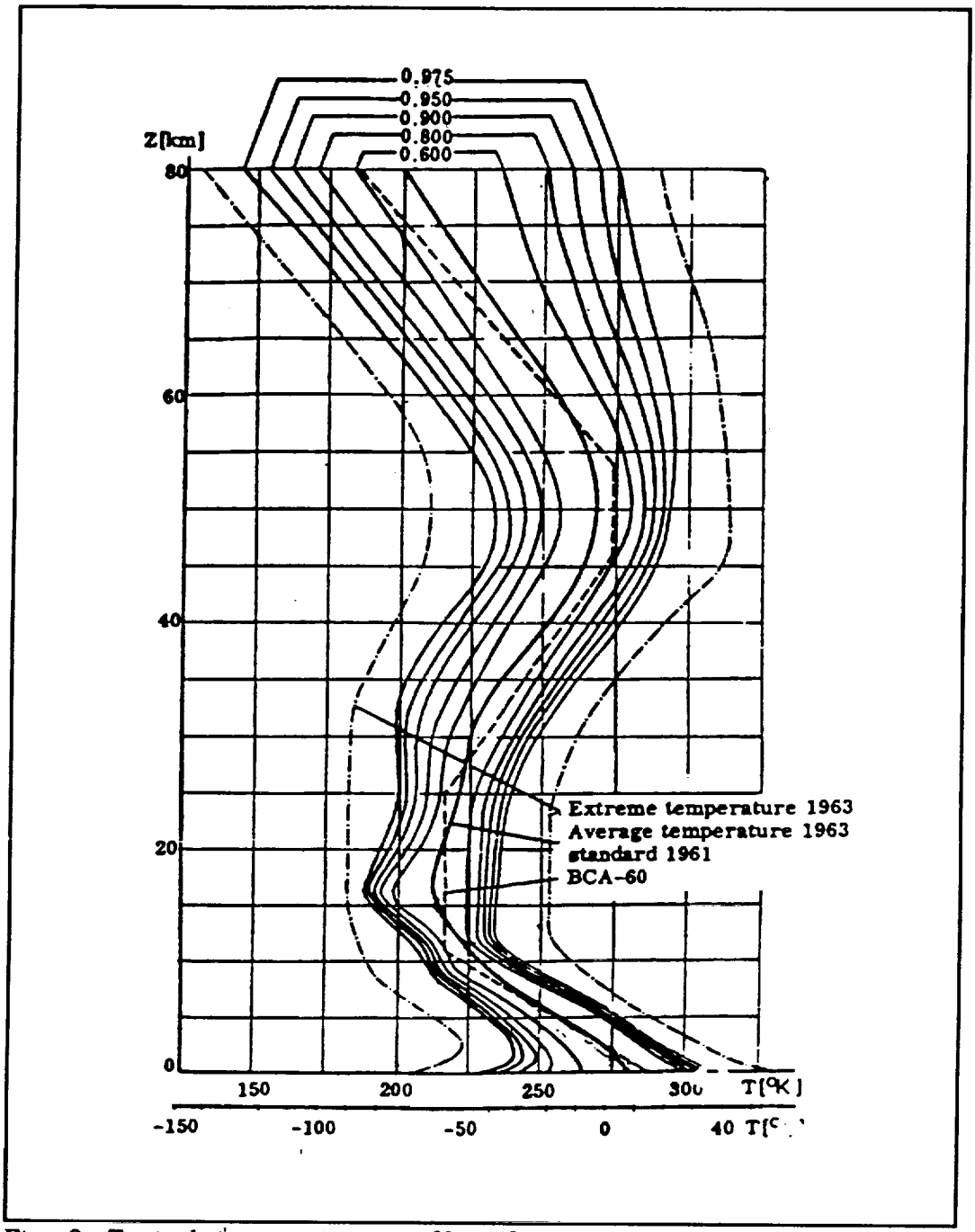

Fig. 2: Typical temperature profiles (from CIRA 1965). If the possible variations are quite large, it is also noticeable that the profiles have the same topological aspects and are quite "parallel", with no intersection from one to another.

III/ PROPOSITIONS

The first one is obviously to measure P_0 quite carefully. It is necessary to calibrate often the barometers employed, to measure preferably the pressure close to the level of the axes intersection of the telescope (it is generally the case). *It must be possible to measure the pressure with an absolute precision < 0.2 mbar.*

Considering the efficiency of barometric levelling, whose precision may reach one meter, we observe that it means that constant pressure surfaces are quite horizontal, so that it is useless to measure the horizontal gradient of P_0 in order to correct its effect in the direction of the sight, provided the weather is reasonably quiet.

Anyway, it seems mostly advisable to improve the correction by a good measurement of **T(h)** in the direction of the satellite, at the 0.1°C level, up to an elevation of 3 to 10 km.

In these conditions, one may be sure to get an atmospheric correction better than 1 mm. It is easy to notice that such a precision with 2-wavelength SLR will require a 20 times better precision on the differential time-of-flight measurement between the two colors (i. e. 0.5 picosecond), which is quite uneasy to reach.

The solution we propose for an easy measurement of the temperature profile along the line of sight is a SODAR (Acoustic LIDAR) associated with a RADAR, the acoustic and the radio wave having the same wavelength. The radar is used to track the acoustic wave, so it allows to measure the speed of the sound in the atmosphere, which in turn provides an excellent temperature profile (at the 0.1 °C level). Such instruments (e. g. Remtech) are now used close to airports, in order to measure winds and wind shears, and this technology is already available. The common ranges are 3 to 5 km, but large instruments may reach 10 km.

IV/ CONCLUSIONS

We propose that an experiment be carried with a radar/sodar equipment close to an up-to-date SLR station in order to check the possible improvements that such data could provide to the laser data. This solution is probably an excellent alternative allowing to wait for the 2-wavelength generation of SLR stations.

On another hand, we insist on the necessity to check quite carefully the barometric equipments used in SLR stations, as the P_a parameter is by far the most important to perform a good atmospheric correction.

BIBLIOGRAPHY

H. BERRADA-BABY, P. GOLE & J. LAVERGNAT
Effets de la troposphere sur les mesures de distance Terre-Satellite. Application au projet DORIS.
CRPE/158 Technical note. June 1987
RPE/ETP, 38-40 rue du Général LECLERC, 92 131 ISSY-LES-MOULINEAUX, France

CIRA 1965
North-Holland Publishing Company, Amsterdam Edition, 1965

T. A. AKHUNDOV, A. A. STOTSKII
Zenith angle dependance of path length through the troposphere
Proceedings of the symposium "Refraction of transatmospheric signals in geodesy", Den Haag, 19-22 May 1992, pp 37-41

REMTECH Company, technical papers on acoustic wind profilers.
Remtech Inc., 1040 Townley Circle, Longmont, CO 80 501, USA

Operational Software Developments

On the Accuracy of ERS-1 Orbit Predictions

presented at
8th International Workshop on Laser Ranging Instrumentation
Annapolis, MD USA
May 18-22, 1992
by

R. König, H. Li, F.-H. Massmann, J.C. Raimondo, C. Rajasenan, Ch. Reigber
Deutsches Geodätisches Forschungsinstitut, Abt.I (DGFI) and
German Processing and Archiving Facility (D-PAF)
Münchner Str. 20
D-8031 Oberpfaffenhofen
Germany

Summary

Since the launch of ERS-1 (first European Remote Sensing Satellite) the D-PAF (German Processing and Archiving Facility) provides regularly orbit predictions for the worldwide SLR (Satellite Laser Ranging) tracking network. The weekly distributed orbital elements are so-called tuned IRVs and tuned SAO-elements. The tuning procedure, designed to improve the accuracy of the recovery of the orbit at the stations, is discussed based on numerical results. This shows that tuning of elements is essential for ERS-1 with the currently applied tracking procedures.

The orbital elements are updated by daily distributed time bias functions. The generation of the time bias function is explained. Problems and numerical results are presented. The time bias function increases the prediction accuracy considerably.

Finally the quality assessment of ERS-1 orbit predictions is described. The accuracy is compiled for about 250 days since launch. The average accuracy lies in the range of 50-100 ms and has considerably improved.

1. Background and Introduction

Since the very first days when ERS-1 began his mission in space, the D-PAF is sending orbit predictions to the SLR community. The orbit predictions are produced in form of the well established IRVs and SAO-elements. The procedure is given in chapter 2. Though these orbital elements are very compressed forms of complicated orbit trajectories, they optimally represent the orbit. The trick to achieve this is called *tuning* of elements. In chapter 3 the problem is illuminated from the numerical point of view.

Very soon after launch it became clear that the ERS-1 trajectory is extremely affected by solar and geomagnetic activities. The orbit predictions lost accuracy mainly in along-track direction. The D-PAF therefore introduced the time bias function which is generated and disseminated daily. Meanwhile the time bias function has become an accepted tool in the SLR community. Some features of the time bias function and related topics are explained in chapter 4.

The extremly high solar activity in the first months of the mission brought extraordinary events such as a geomagnetic storm of nearly singular type. Though SLR tracking was almost lost for two days, the D-PAF orbit prediction system (and the SLR community in turn) gained at the end. The software system got more backup solutions and the quality checks were largely extended. Chapter 5 tells more about quality assessment and quality checks.

Finally the orbit prediction system has developed to a reliable system in SLR tracking. This becomes obvious from the course of the average accuracy of the orbit predictions shown in the more detailed analysis in chapter 5.

2. Generation of Orbit Predictions

In a first step the orbital parameters are estimated by differential orbit correction with the DOGS-OC (DGFI Orbit and Geodetic parameter estimation System - Orbit Computation) software. Laser ranges are mainly used as observations for the least squares procedure and in few cases also RA FD data (Radar Altimeter Fast Delivery) (*Massmann, F.-H. et.al., 1992*). The use of PRARE data (Precise Range And Range rate Equipment) was also planned prior to launch.

Orbit perturbation models used are state of the art ones. The gravitational forces are mainly represented by the GRIM4-S2 gravity field model (*Schwintzer, P. et.al., 1992*). The major non-gravitational perturbations of the low altitude orbit stemm from surface forces. DOGS-OC adopts a macro modell of the surface of ERS-1 for albedo, direct solar radiation and drag. Earth's high atmosphere is represented by the CIRA'86 model where solar and geomagnetic activity is needed as input.

In a second step the orbit is integrated forward by the DOGS-OC software with the parameters derived before. Adopted are the same perturbation models but now solar and geomagnetic activity are predicted for the respectiv time period. And this indeed is the major error source that degrades the accuracy of ERS-1 orbit predictions. Also the ERPs (Earth rotation parameters) are predicted for the time period of the forward integration. The accuracy of ERP predictions is quite good for the lifetime of ERS-1 orbit predictions, the effect can therefore be neglected.

In the third step DOGS-PD (PD for Predictions) compresses the orbit to dedicated forms and formats of orbital elements which can easily be disseminated worldwide via various telecommunication channels. In addition these elements are tuned so that the user will recover the orbit in an optimal way. So-called tuned IRVs (Inter-Range Vectors) and tuned SAO-elements (Smithsonian Astrophysical Observatory) are delivered to the SLR community, PRARE-elements to the PRARE system.

3. Tuning

The orbit is recovered at the SLR sites by simple programs intended for use on low capacity computers. These programs adopt low degree and order gravity fields and do not consider nongravitational forces as drag. The IRVINT integrator written at the university of Texas starts from the IRVs. The ancient AIMLASER program applies analytical orbit theory to recover the orbit from the SAO-elements.

Because of these severe neglections, D-PAF tunes IRVs and SAO-elements. This means that despite of simple perturbation modelling onsite the orbit is recovered in an optimal way. The optimum is a minimum difference in the least squares sense of the recovered orbit to the full perturbation model orbit or reference orbit. The IRVINT and AIMLASER programs have to run then in a defined mode. D-PAF assumes for IRVINT a 60s integration step size and the GEM10N gravity field coefficients up to degree and order 18. The AIMLASER program should run in the RGO version (Royal Greenwich Observatory) with dedicated GEM10B. coefficients.

Fig. 1 shows the along-track error if an un-tuned IRV is integrated by IRVINT. The example holds in general. Due to the missing drag forces modelling the error grows during the day to ca. 1400m in along-track position or ca. 200ms in time bias which would prevent tracking of the satellite.

Fig. 2 displays the error after tuning. Maxima are now ca. 20ms around midnight and around noon. The remaining along-track errors are similar day by day, the maxima are dependent on the solar activity. They could be accounted for by a function giving the error for 24 hours of a day. The more proper way of course would be to model drag in the integrator. Anyway the remaining errors are in a range that can be accepted for tracking.

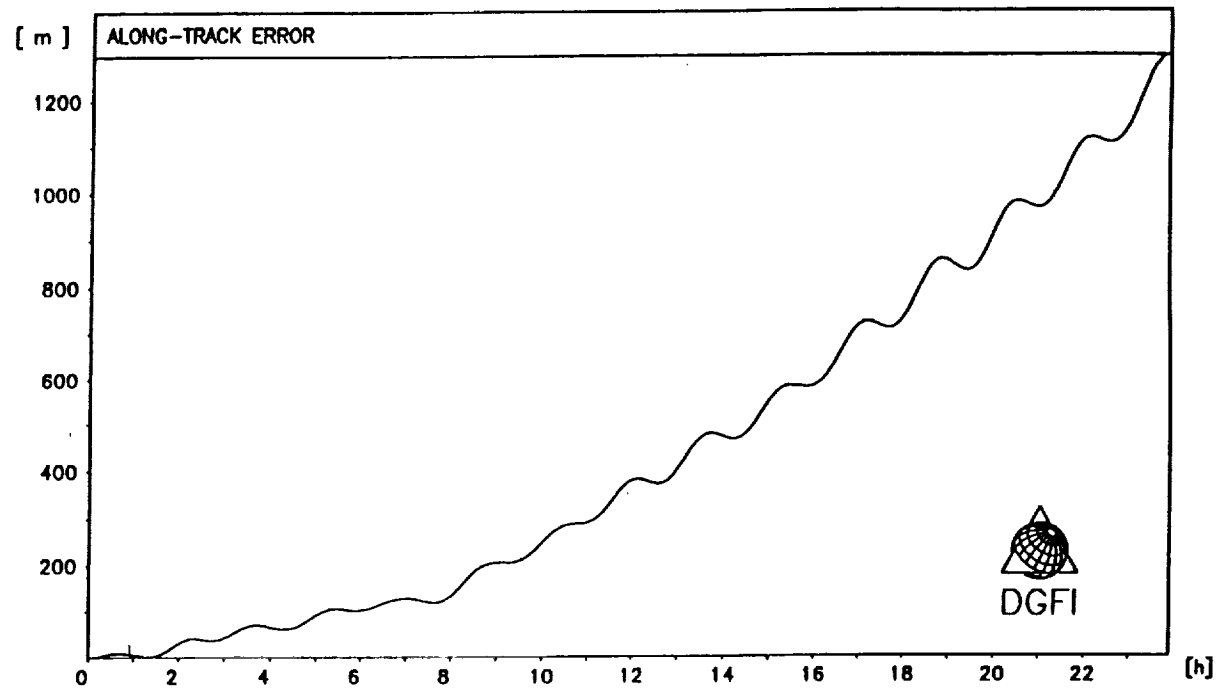

Figure 1 Along-track error from un-tuned IRVs

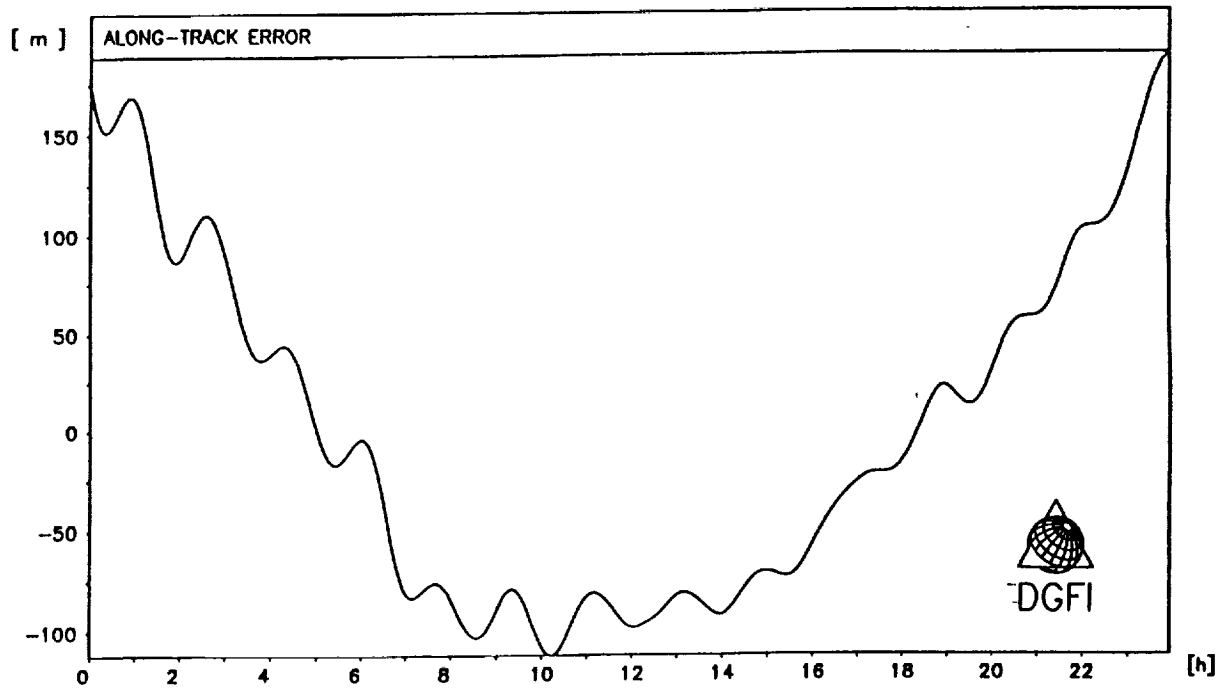

Figure 2 Along-track error from tuned IRVs

The accuracy of tuning, that is the difference of the recovered orbit to the reference orbit, can be seen in Table 1 where the typical differences are given as RMS-values in meters for both types of prediction elements. Again the values are largely dependent on the solar activity.

	IRVs 1d	SAO-elements 10d
radial	3-5	10-20
across-track	3	10
along-track	20-60	20-100

Table 1: Tuning accuracy (in m)

The SAO-elements show less accurate recovery because they represent the whole prediction period (normally 10d) whereas the IRVs are given each day. All values are within a range that can be accepted for tracking.

4. Time Bias

D-PAF generates and disseminates weekly prediction sets containing IRVs and SAO-elements. Due to the sensitivity of ERS-1 to variations of the high atmosphere the predictions loose accuracy mainly in along-track direction. This is also known to the stations as so-called time bias i.e. the satellite rises too late or the satellite rises too early. The determination of the time bias provides a quick and simple update of the orbit predictions.

Therefore D-PAF generates and disseminates daily a time bias function from new Q/L (Quick Look) Laser ranges. For every pass over all stations having observed ERS-1, a time bias is computed relative to the last prediction set. A third order function in time is fitted by LS (Least Squares) to these time bias values. In the LS procedure the time bias values are checked for outliers and the parameters are checked for significance leading all in all to a best approximating function. The function fits to the time bias values within 1ms for up to four days.

A typical example of time bias values is given in Fig.3. Fig.4 shows the fitted function after removing the outliers and after the significance check of the parameters.

The time bias function represents the time bias values of the last few days. More important it is capable of predicting the along-track error.

The EDC (European Data Center) provides another important tool to handle the time bias problem. Stations can store the observed time bias immediately after the pass in the data base. Currently Graz, Potsdam, RGO, Santiago de Cuba and Wettzell do so. This time bias is nearly in real-time available to other stations. The stations can then compare the results with their own computations and with the D-PAF time bias function. This all this together should yield to more confidence in the time bias that is going to be used for the next upcoming pass.

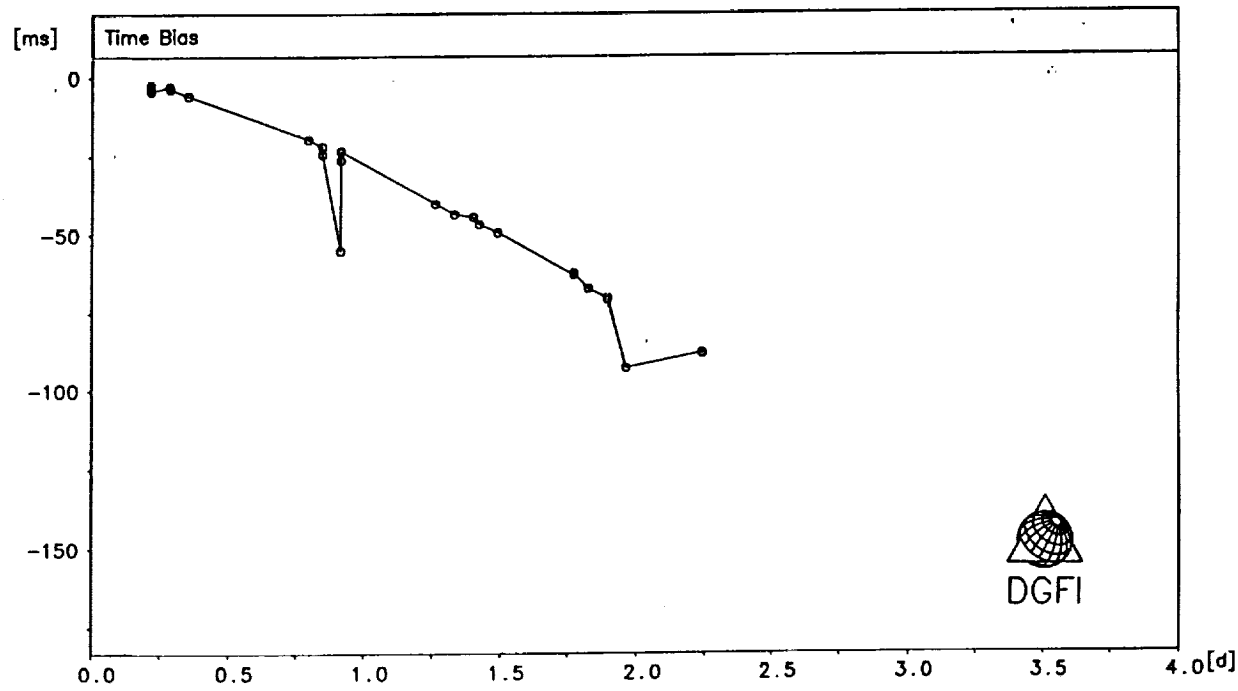

Figure 3 Time bias values

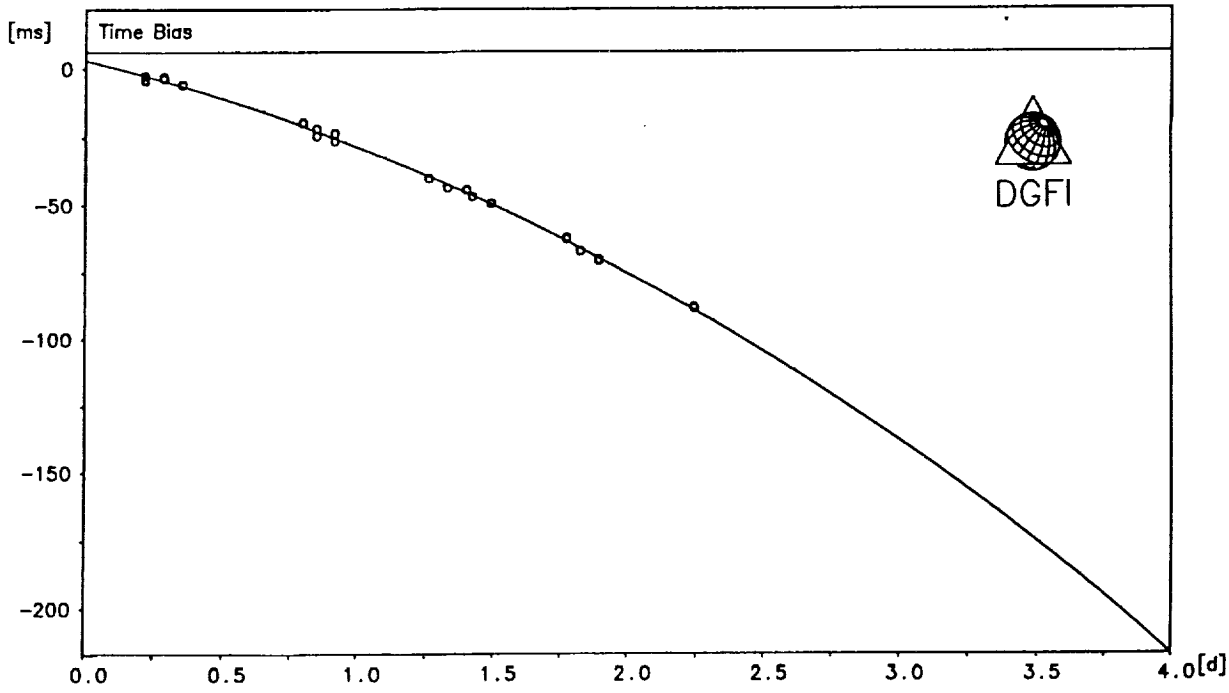

Figure 4 Time bias function

5. Quality

The quality of the ERS-1 prediction products is indicated to the users by a quality flag. In case of orbit predictions the quality flag is computed from the fit of observations in the orbit analysis (step 1 in chapter 2), from the comparison of overlapping arcs and from the tuning accuracy. The quality of the time bias function is assessed from the approximation error of the function and the data coverage.

Of course the quality flag gives only an idea on how the quality of the products can be. By nature predictions go into the future and nobody can determine what will be. Particularly the accuracy of ERS-1 orbit predictions is heavily influenced by unpredictable solar activity. Anyway the quality flag shows the current knowledge of the quality. It convinces the generator that he did a good job and it gives a first indication to the user in case he has problems.

All prediction products are subject to permanent quality checks. Daily the time bias of newly incoming Q/L Laser passes are determined relative to the actual prediction orbit which leads to the time bias function. The prediction orbit is also compared to the MMCC orbit (Mission and Management Control Center). The MMCC orbit is generated by an independent group in ESOC (European Space Operation Center), Darmstadt, from S-band observations and radar altimeter fast delivery ranges. The comparison with such a completely external source provides more confidence in the results.

On a weekly basis when new orbit predictions are generated the new prediction orbit is compared to the old one. The differences in along-track direction should exactly reflect the old time bias function. The differences in radial and across-track direction normally stay within a few meters.

The internal quality checks proceed in a closed loop from prediction set to prediction set. The external checks give an independent judgement. So the reliability of the orbit prediction system has reached a quite high level.

Fig.5 displays the along-track errors of ERS-1 orbit predictions since launch. The first 100d are clearly affected by large solar activities. In addition a manoeuvre was missed. Meanwhile these cases are taken care of. In the right half of Fig.5 it can be seen that the mean accuracy steadily improves, but is clearly degraded by the frequent manoeuvres.

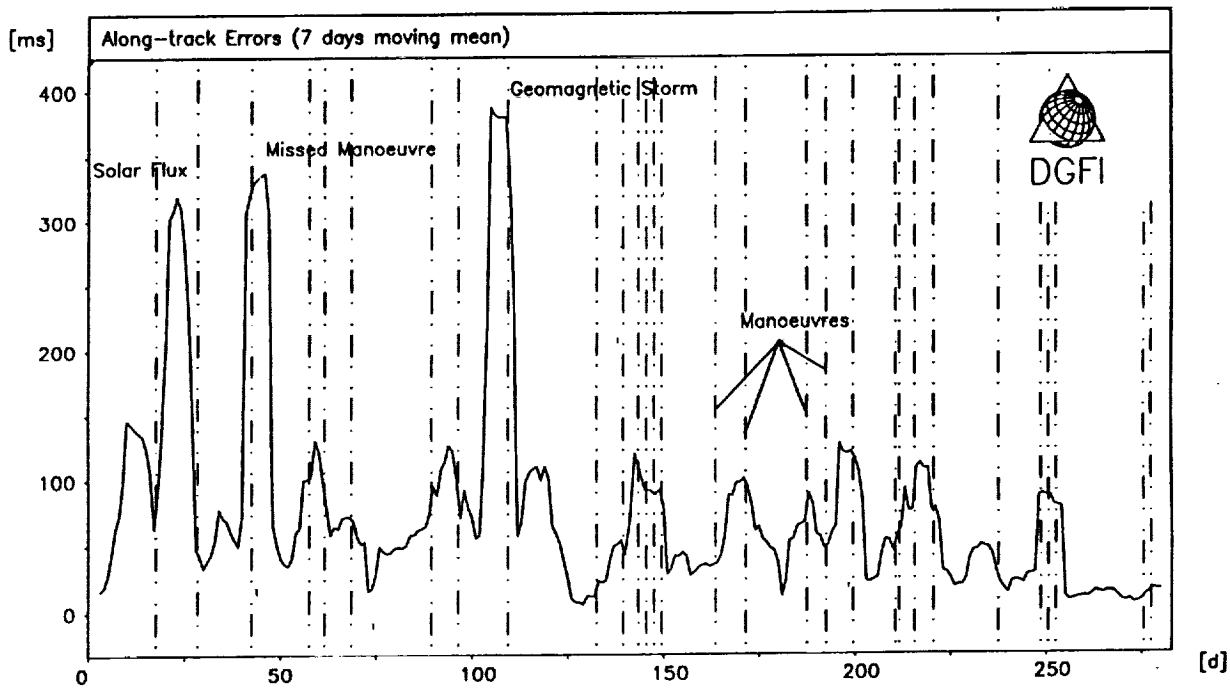

Figure 5 Accuracy of ERS-1 orbit predictions

6. Conclusions

It has been shown that tuning of orbit predictions is essential for ERS-1. D-PAF provides daily time bias functions that account for the along-track error of the predictions. The quality of ERS-1 prediction products is assessed and indicated to the users. The predictions are permanently checked internally and externally. The average accuracy has considerably improved since launch.

7. Literature

Massmann, F.-H., Reigber, Ch., Li, H., König, R., Raimondo, J.C., Rajasenan, C. and M. Vei: *Laser Ranging Network Performance and Routine Orbit Determination at D-PAF*, this proceedings

Schwintzer, P., et. 14 al.: *GRIM4 - Globale Erdschwerefeldmodelle*, Zeitschrift für Vermessungswesen 117, pp. 227-247, 1992

COMPENSATION FOR THE DISTORTION IN SATELLITE LASER RANGE PREDICTIONS DUE TO VARYING PULSE TRAVEL TIMES

Matti Paunonen

Finnish Geodetic Institute
Ilmalankatu 1A
SF-00240 Helsinki, Finland
Telefax:358-0-264995

ABSTRACT

A method for compensating for the effect of the varying travel time of a transmitted laser pulse to a satellite is described. The "observed minus predicted" range differences then appear to be linear, which makes data screening or use in range gating more effective.

1. INTRODUCTION

Accurate range predictions are necessary in satellite laser range measurements when the operation takes place in daylight. Then the range gate, where the return pulse detector is active, can be set very narrow to effectively discriminate against noise. Data screening of the observations is often done using "observed minus predicted" (O-C) range differences. The predicted satellite times are generally equally spaced, as are the transmit times. But the true hitting times are not equally spaced because of the varying pulse travel times. This leads to distortion of the O-C differences which can be as high as 10-20 m. A polynomial of suitable degree is used in screening. It is well known that the polynomial should be of low degree so as to avoid an artificially good fit or end effects. If the travel time distortion is removed, the O-C deviations are nearly constant with time for high quality orbit predictions. This paper describes and tests a simple correction method.

2. METHOD OF RANGE CORRECTION

The range from the laser station to the satellite varies approximately parabolically with time, Fig. 1. When the satellite is passing the closest point, a small time change does not affect the range much. At the far end of the pass the range changes several kilometers per second.

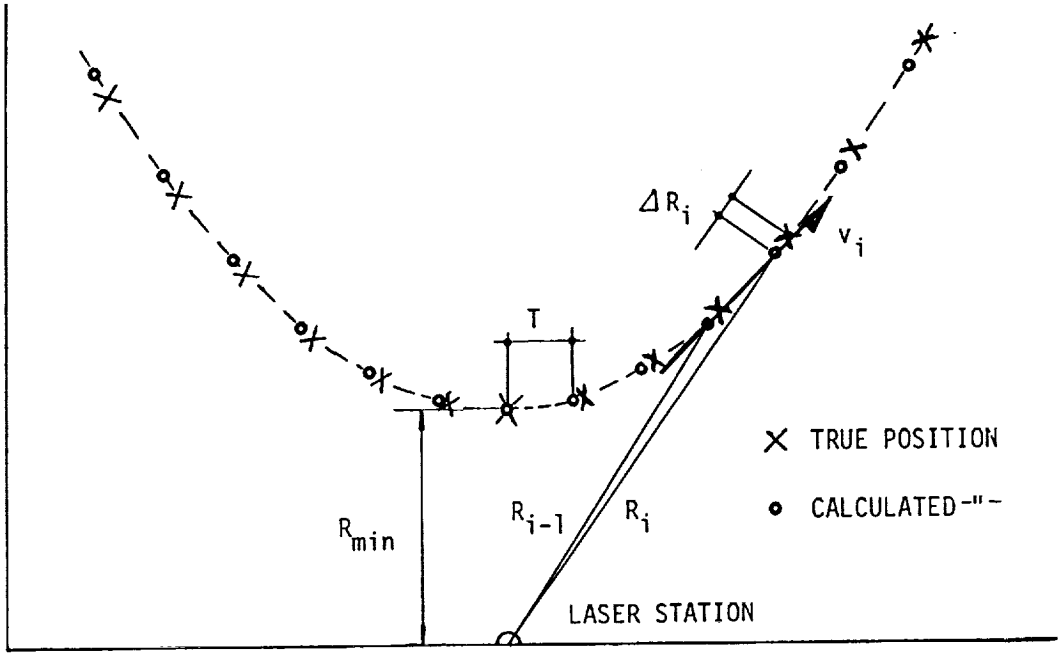

Fig.1 Conceptual scheme for the origin ot the travel time distortion in ranges.

This rate , v_i , can be calculated together with the ranges, or it can be approximated from the change between the successive predicted ranges R_{i-1} and R_i

$$v_i = (R_i - R_{i-1}) / T , \quad (1)$$

where T is the time step (often 1 s).

The travel time difference between the minimum range R_{min} , and the instantaneous range R_i is

$$\Delta t_i = (R_i - R_{min}) / c , \quad (2)$$

where c is the speed of light. Then the travel time correction ΔR_i to be added to the predicted range is

$$\Delta R_i = v_i * \Delta t_i . \quad (3)$$

3. RESULTS AND DISCUSSION

A test with real data is shown in Fig. 2. This LAGEOS pass involved relatively few observations (21). The prediction program used highly accurate long-term IRV predictions /1/. A 220 ms time correction was used in the calculation.

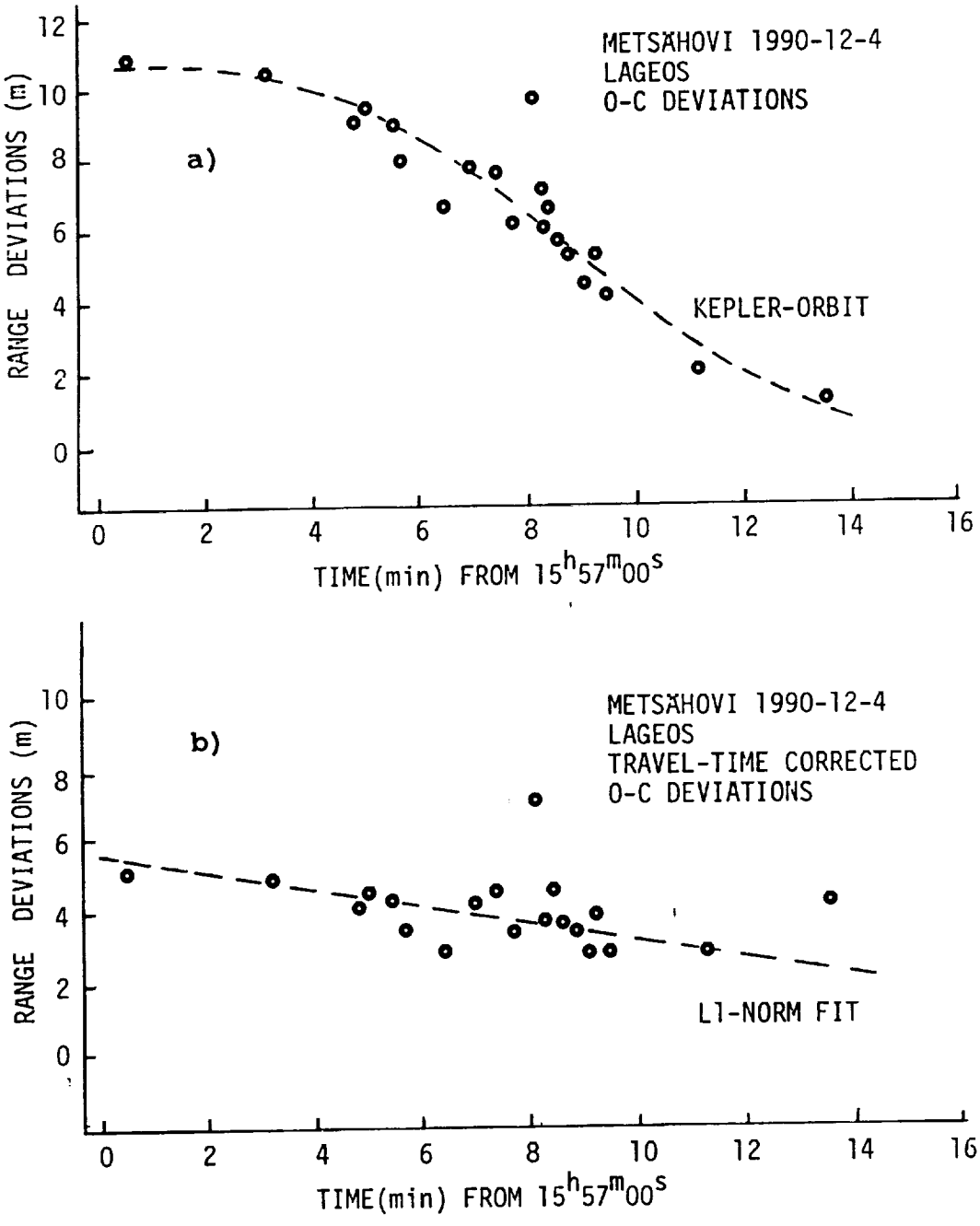

Fig. 2. a) 'Observed-predicted' (O-C) deviations of a measured LAGEOS pass. A Kepler orbit fit is also shown. b) O-C deviations after the travel time correction. A linear median fit is shown.

The time error varies slowly with time, and is normally known from earlier observations. The O-C deviations are shown in Fig. 2a. A simple Kepler orbit /2/ fits the observations quite well, and only one outlier is indicated. In polynomial fitting determination of the order is not easy. The first point would be rejected in a linear fit.

The situation becomes considerably clearer after application of the travel time correction method described (Fig.2b). The fit using the linear L1-norm /3/ eliminated the last point as well as the known outlier. Because the model is now linear, it is not necessary to use higher order polynomials.

This example shows that a very narrow range window is possible in ranging to LAGEOS. A 50 ns window corresponds to 7.5 m of range. This would help considerably in implementing daylight satellite laser range-finding. As has been seen, the method can also help resolve difficult data screening tasks. Good orbit elements and a good orbit are essential for this method.

Note that recalculation of the orbit after the pass, using the satellite hit times, produces approximately the same O-C deviations as the method described.

REFERENCES

1. The Texas University, long term IRV- predictions for LAGEOS satellite; a satellite prediction program ORBIT developed at the Royal Greenwich Observatory, Herstmonceaux, England.

2. J. Kakkuri, O. Ojanen, M. Paunonen, Ranging precision of the Finnish satellite laser range finder. Reports of the Finnish Geodetic Institute 78:8, Helsinki 1978, 11 p.

3. M. Paunonen, Use of the L1-norm in screening laser range observations to satellites. Proc. 18th Intercosmos Symposium on the Use of Artificial Satellite Observations for Geodesy and Geophysics, June 12-17, 1989, Cracow, Poland (Ed. Wl. Goral, Observations of Artificial satellites of the Earth, No 27, 1989, Polish Academy of Sciences, Warsaw 1990),pp.359-362.

Timebias corrections to predictions

Roger Wood and Philip Gibbs

Satellite Laser Ranger Group
Herstmonceux Castle, Hailsham
East Sussex, BN27 1RP, UK

Abstract *This talk aims to highlight the importance to an SLR observer of an accurate knowledge of the timebias corrections to predicted orbits, especially for low satellites. Sources of timebias values and the optimum strategy for extrapolation are discussed from the viewpoint of the observer wishing to maximise the chances of getting returns from the next pass. What is said may be seen as a commercial encouraging wider and speedier use of existing data centres for mutually beneficial exchange of timebias data.*

Introduction

The real behaviour of low satellites is never in exact agreement with even the best predictions. The principal reasons are that modelling the effect of atmospheric drag is difficult, and the perturbations due to solar radiation pressure are not predictable in advance. ERS-1 is much larger and somewhat lower than either Starlette or Ajisai and consequently presents the biggest headaches in making predictions. Despite the problems, detailed elsewhere in these proceedings, the prediction teams do an excellent job in providing orbits and thereby give observing stations the best possible chance of tracking the satellites successfully. Fortunately, most of the deviation from the predicted orbit appears as an along-track error and can be corrected by applying a suitable timebias to the predictions (as has been done very successfully for Lageos for many years now). For a particular set of predictions observing stations can, for each satellite, model the history of the behaviour of the timebias with time and extrapolate to predict the timebias at the time of observation of the next pass.

At Herstmonceux we have been working to improve the accuracy of our extrapolation of timebias values. This talk outlines our findings, indicates the benefits to be gained from increased use of the data centres and shows how helpful good timebiases can be if you have English weather and are trying to keep us with Grasse!

Why do we need accurate timebiases?

We see three distinct advantages:

Ease of satellite acquisition. This is always important, at whatever stage of the pass the satellite is first acquired. But it is especially important at the very beginning of a pass, necessarily at low elevation, when accurate pointing helps to minimise the time spent in searching for returns. Ease of acquisition is also important when there has been a break of a few days in the sequence of observations, because of cloud or technical downtime, where accurate knowledge of the timebias correction can lead to immediate recovery of the satellite. This second point emphasises the usefullness of having access to continuous records of timebias data in order to base any extrapolation on the best available data set.

Improved telescope tracking. If an incorrect timebias is used to compute the telescope position during a pass, the offsets from the reference position on the detector will depend on time and the observer will have to insert ever-changing manual corrections in order to keep the satellite image. By contrast a correct timebias results in little or no guiding, provided that the pointing model for the telescope is well-determined.

Better noise elimination. When the timebias is exactly right the returns from the satellite always appear at the same place in the range window. This means that the window can be made very small and so the amount of noise reaching the detector can be drastically reduced. This improvement in the ratio of signal to noise is particularly valuable for daylight ranging.

The second and third advantages can still be gained (even in cases where an accurate timebias is not available beforehand) if the first few good returns from the satellite are used in real time to convert a range offset into a timebias correction. This technique is routinely applied for multi-photon detection systems where the identity of true returns is not in doubt. But for single photon detection in daylight, or using an intrinsically noisy detector such as a SPAD, it is not always easy for the software to pick out the track, and some form of manual intervention may be required.

Where can we get timebiases?

Originally we used only our own history of passes to make extrapolations to current behaviour. This was quite satisfactory during periods of continuous good weather, but was often very frustrating when trying to recover satellites after a break of two or three days due to cloud or instrumental problems.

Then, for Ajisai and Starlette, we tried using Bendix's timebias data from many stations in addition to our own. We immediately found a great improvement in the quality of our extrapolation and could use narrower range windows right at the start of the pass. We also found that the change from using elements to using IRVs gave better consistency in the timebias histories.

When ERS-1 was launched we, like everyone else, had mixed success in finding it. When we had a reasonable history and the solar activity was not too wild, we got good passes. But at other times, once we had failed to get passes for a day or two, it became increasingly difficult to recover the satellite. We were very pleased when DGFI agreed to use the pass data that they receive from many stations to produce timebias functions for ERS-1. This gave, and continues to give, valuable additional weight to timebias trends.

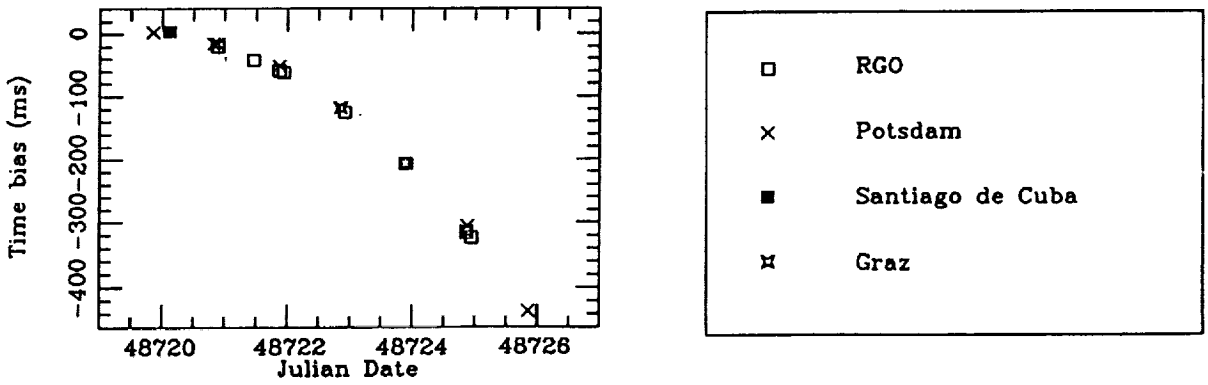

Figure 1: *ERS-1 timebiases from EDC for IRV set A920407 and symbol key*

Since then, following the establishment of the European Data Centre (EDC), a small number of stations have begun to make regular deposits of their timebias data for ERS-1 soon after the observations. We often get EDC data from Graz and Potsdam—and occasionally from Wettzell and Santiago de Cuba. Figure 1 shows a plot of the data deposited for IRV set A920407 at the beginning of 1992 April. The interagreement between the values from different stations is striking and gives great confidence that all timebiases have been reduced to a common system. But, with all the stations close together in Europe, it is clear that the data are clumped together in time: indeed, sometimes they are all clouded out simultaneously! The addition of more data points from other stations at other longitudes around the world would give much better "round the clock" coverage.

How can we best use timebias histories?

ERS-1 Over the last two or three months we have been investigating how best to predict future timebias values from whatever timebias history we had available on a particular day. This usually consisted of a small number of values covering a few days.

First we looked at the timebiases shown in Figure 1 which cover a period of about a week and are all referred to the same IRV set from DGFI. Our approach was to see, in retrospect, how well the observed values available up to a certain day could be used as predictors for the points which followed. The results of our trial fits are shown in Figure 2. First we fitted to data for the first two days only; next we used data for the first three days; then the first four days and so on. For each

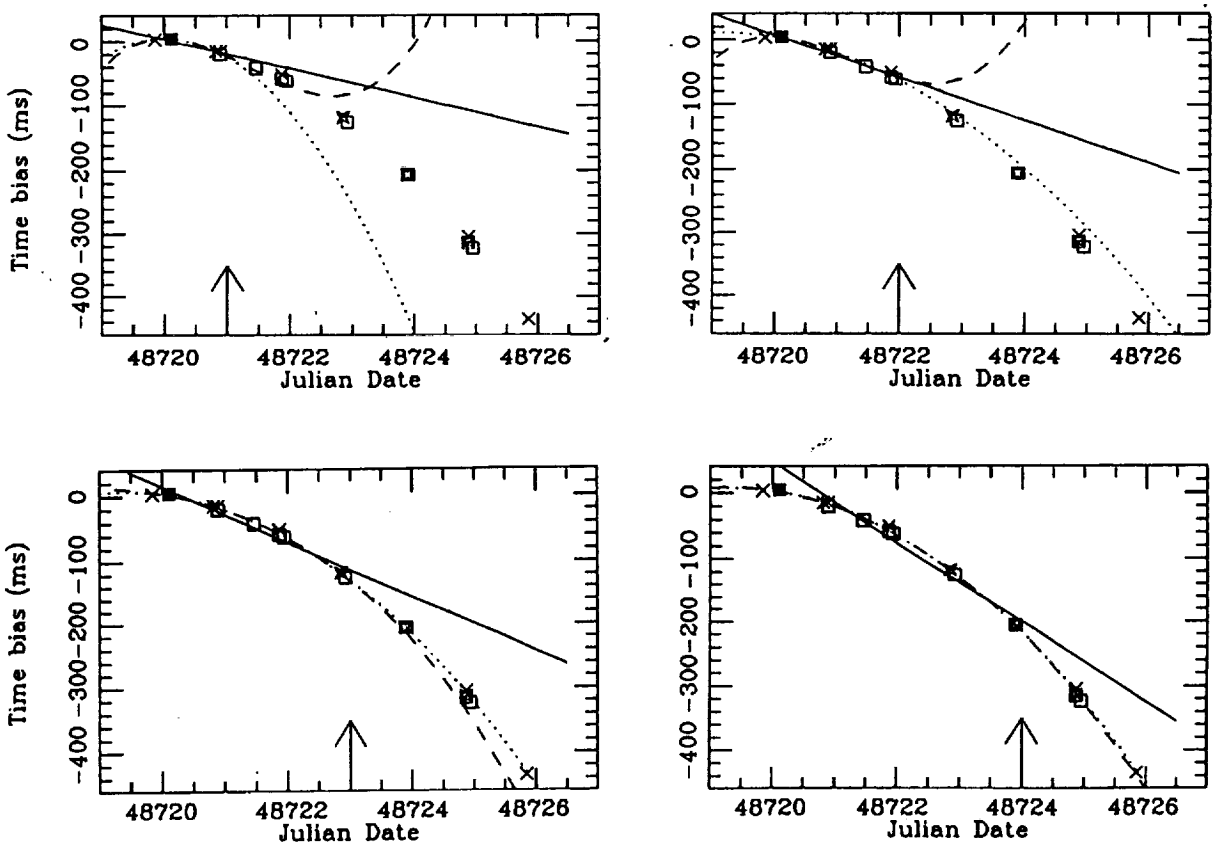

Figure 2: *Successive fits to ERS-1 timebiases from EDC*

trial we fitted the data with functions of three different orders—linear (represented by a solid line in Figure 2), quadratic (dotted line) and cubic (dashed line). Only points to the left of the vertical arrow at the bottom of each plot were included in the fit. We then looked at the next few points to the right of the arrow to see how well, or how badly, each of the attempted fits represented the data which followed. From this examination we drew a number of preliminary conclusions:

- Use the simplest function which gives a *reasonable* fit to the data (even if it is not the *best* fit)—it will generally be better for extrapolation than a higher order function;
- Use only linear fits for the first 2 or 3 days—there are too few data points to justify anything fancy;
- It would be helpful to have quick timebias deposits by all stations and better longitude coverage. This would:
  - fill the gaps in the European data;
  - add data points to strengthen the fit;
  - provide actual timebias values closer to the time of observation than are available now.

More recently we tried a new experiment based on normal point data for ERS-1 passes extracted from the CDDIS database and reduced to give timebiases. [We had hoped to use directly the Bendix values, but there are currently unexplained discrepancies between their derived values of timebias and ours, so we have worked entirely from the normal point data. This effect also appears to exist in the Bendix timebiases for Ajisai and Starlette, but to a lesser extent which does not prevent their use in revealing long-term trends]. In this case we took the data set shown in Figure 3 which covers a week in early May and is referred to IRV set A920505 from DGFI. It is clear that

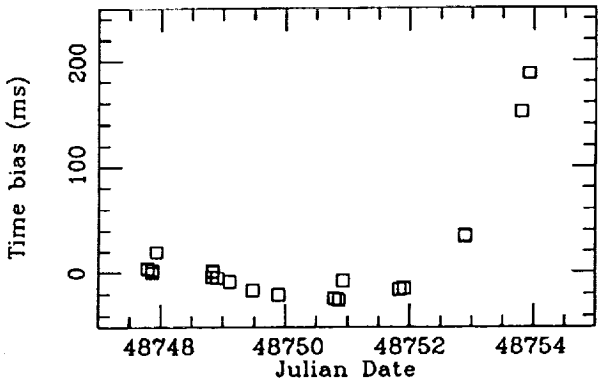

Figure 3: *ERS-1 timebiases from CDDIS normal points*

the longitude coverage is more uniform and the daily density of points is higher. However, there is a drawback as far as immediacy is concerned in that the turn round time for data input can be longer than for EDC, so that some of the data are relatively old. We then followed the same procedure that we used for the EDC data and made trial fits to subsets of the data to see how well the extrapolated curves acted as predictors for what was subsequently observed. The plots in Figure 4 again show that the higher order fits are wildly ineffective for the first few days, and only begin to make more sense later. But around day 48752 the data take a wholly unexpected turn towards large positive values and the trends evident in the early points are no longer relevant. This sudden change of behaviour is probably due to solar activity, and in such circumstances it is wise to abandon the early points of the data set and start the fit again from part way through.

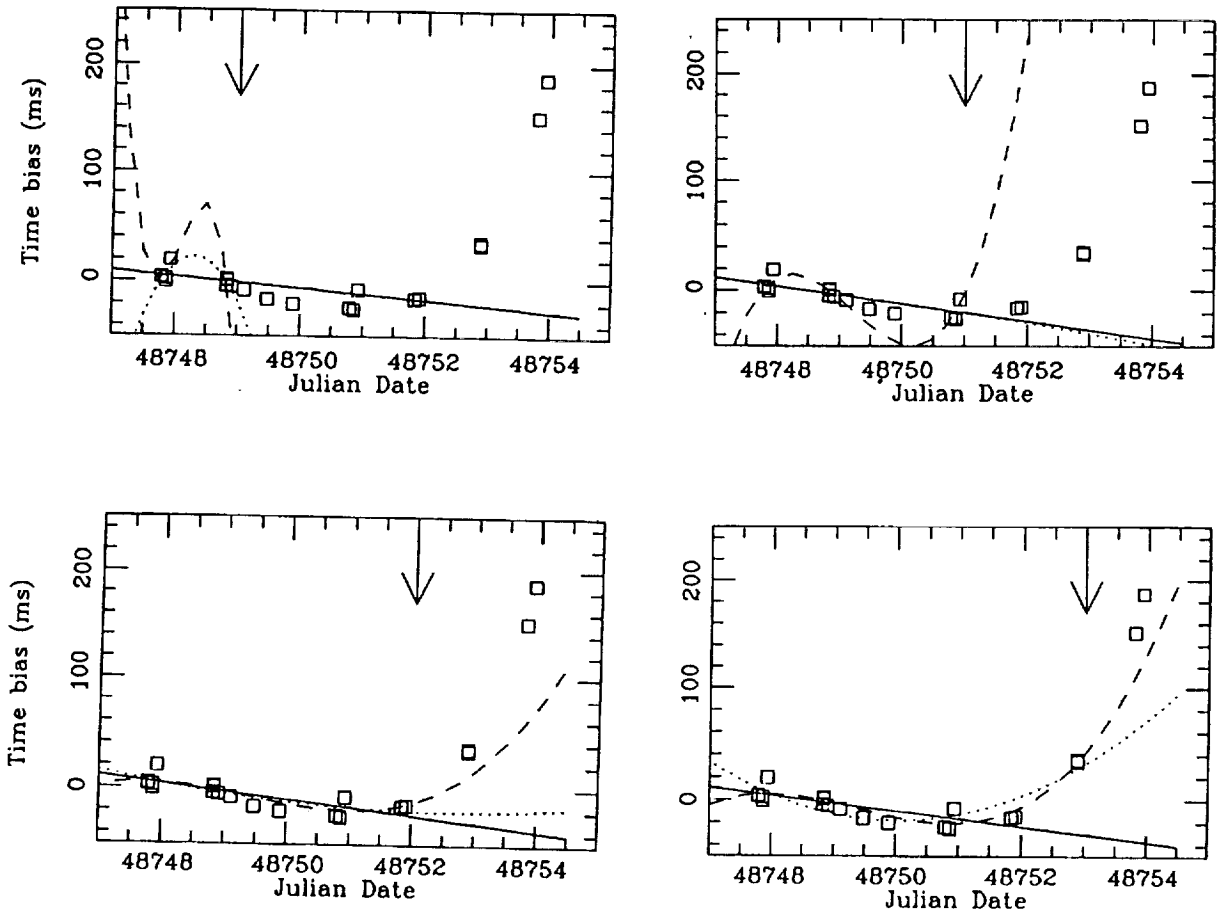

Figure 4: *Successive fits to ERS-1 timebiases from CDDIS*

Our additional conclusions as a result of this exercise were:

- For ERS-1 it is necessary to examine the data and functions daily in order to pick up unexpected trends in good time;
- Better longitude coverage is essential for early warning of departures from previous behaviour;
- Access to the raw data is very useful for making value judgements on the quality of the fit of any functions!

Ajisai and Starlette Generally the prediction of timebiases for these satellites is much more straightforward than for ERS-1 since they are relatively unaffected by atmospheric drag and solar radiation pressure. Indeed orbit predictions can run quite satisfactorily for several weeks so that a long timebias history can be established for one IRV set. Over such an interval timebias corrections usually behave sensibly and, even when the corrections get quite large, a good history with respect to one set of IRVs allows meaningful extrapolation to get accurate values.

What can be done to improve?

We think that all stations can share the clear benefits to be gained from the daily examination of trends in timebiases for ERS-1 by depositing their timebias values with data centres as soon as possible after the pass has ended. Then, by retrieving a comprehensive set of timebiases obtained

worldwide, and using it as the basis for extrapolation, the "hit rate" can be significantly improved. Alternatively, but probably with greater delay, stations can retrieve normal point data and derive timebiases from them.

It would be very worthwhile to extend the system to include Ajisai and Starlette; and to make sure that provision is made for rapid feedback of Topex/Poseidon data.

Finally the proper commercial: we think that timebiases are just like washing powder—use the right one and your whole life is transformed for the better!

Figure 5: *"New improved Timebias"*

Acknowledgements

We wish to thank the staff of the prediction and data archiving centres for advice and data. Special thanks go to Brion Conklin of Bendix for his speedy and cheerful responses to our many requests. We greatly appreciate assistance from Rolf Koenig of DGFI and Wolfgang Seemüller of the European Data Centre.

Formation of on-site Normal Points

G.M. Appleby and A.T. Sinclair
Royal Greenwich Observatory
Madingley Road
Cambridge CB3 0EZ, UK

Abstract.

We describe our methods of fitting a smoothing function to observational range differences from a predicted orbit, by deducing corrections to the orbit in the radial and along-track directions. The method has been used on observations of a variety of satellites, and using predicted orbits computed both by numerical integration using IRVs as starting values and analytically from orbital elements. The along-track corrections to the predicted orbit have been succesfully used in the form of time biases to improve subsequent predictions, and a statistical test has been devised to ensure that the range residuals may be used to form unbiased quicklook normal points.

1. Introduction.

It was recommended at the Fifth International Laser Ranging Instrumentation Workshop held at Herstmonceux, UK, that laser range normal points should be formed by the stations shortly after each satellite pass and transmitted as quicklook data (Gaignebet, 1985). The final version of the quicklook normal point format was agreed by the SLR Subcommission of the CSTG and published in the April 1990 Satellite Laser Ranging Newsletter (Schutz, 1990). The process of forming normal points consists of 2 stages; (a) fitting a smoothing function to the observational range differences from a predicted orbit and subtracting the function in order to form a flat track of residuals, and (b) rejecting noise and outliers and forming the mean values of the accepted residuals in bins spread through the pass. The values of the smoothing function and the predicted orbit at the epoch of an actual observation nearest the mean epoch of the bin are then added to the mean value of the residuals in the bin. The resulting normal points are then virtually independent of both the smoothing function and of the predicted orbit.

In this report we detail the processes adopted to carry out stage (a) of the process; methods for rejecting noise and forming unbiased normal point bin means are developed by Sinclair (these proceedings)

2. Development of the Smoothing Function.

During the observation of a satellite pass, differences from the predicted range are computed for all events detected within the range gate and displayed in realtime, true satellite returns appearing as a track of correlated values among the randomly distributed noise events. An example of such a plot is given in Figure 1, which shows a pass of ERS-1. The rejection of gross noise events is carried out visually using the plot, and the subsequent set of satellite

range measurements and some noise events are passed to the next stage of processing.

At an early stage of the development of the preprocessing software, the decision was taken to use the pass-by-pass observations to solve for corrections to the predicted orbit, and in particular to monitor the along-track error, in order to improve subsequent prediction accuracy. Thus the possible use of an arbitrary polynomial for the smoothing function was not considered. However, corrections to the predicted orbital elements of the satellite would be difficult to apply to orbits computed by numerical integration and using IRVs as starting values, and similarly corrections to the IRVs would not be applicable to orbits computed analytically. Thus it was decided to express orbital corrections as along-track, across-track and radial displacements to the predicted position. Such corrections are then readily applied to the geocentric orbit during the solution iteration process, and the derived along-track correction can be expressed as an orbital time-bias for improving subsequent predictions.

During the prediction process an orbit in the form of geocentric rectangular satellite coordinates and velocities at 1-minute time intervals and in units of Mm and Mm/day, is computed and stored. For each observational epoch, we use 8th order Lagrangean interpolation to compute the instantaneous position **r** and velocity **v** of the satellite. Let **r** = (x,y,z), and **v** = (v_x, v_y, v_z), and let the magnitudes of these vectors be r and v respectively. The reference frame used is different depending upon the source of the orbit being considered; for an orbit generated by numerical integration and using IRVs, the coordinates are given with respect to the true equator and mean equinox at 0hrs UT of the epoch of the IRVs. For an analytically-derived orbit, the coordinates are given with respect to the mean equator and equinox of date. At the observational epoch, we compute the coordinates of the observing station in the same reference frame. Let the station coordinates be **s** = (x_s, y_s, z_s). Then the predicted topocentric coordinates of the satellite are

$$x_T = x - x_s, \quad y_T = y - y_s, \quad z_T = z - z_s \quad ,$$

and the predicted range is the magnitude of this topocentric vector. We thus form the difference of the observed from the predicted range, and in order to solve for corrections to the predicted orbit we require partial derivatives of range with respect to the along-track, across-track and radial components of the displacement of the predicted orbit.

2.2 Partial Derivatives.

(a) Let the along-track displacement or time-bias be ΔT.

Then the displaced range R is given by

$$R^2 = (x + v_x\Delta T - x_s)^2 + (y + v_y\Delta T - y_s)^2 + (z + v_z\Delta T - z_s)^2$$

Then

$$R\frac{\partial R}{\partial \Delta T} = v_x(x + v_x\Delta T - x_s) + v_y(y + v_y\Delta T - y_s) + v_z(z + v_z\Delta T - z_s),$$

or approximately

$$\frac{\partial R}{\partial \Delta T} = (v_x x_T + v_y y_T + v_z z_T)/R$$

(b) Let the across-track displacement be Δ Q

The across-track direction is

$$\frac{\mathbf{r} \times \mathbf{v}}{\mathbf{r} \cdot \mathbf{v}} = (l, m, n) \qquad \text{, say.}$$

So,

$$l = (y v_z - z v_y)/rv$$

$$m = (z v_x - x v_z)/rv$$

$$n = (x v_y - y v_x)/rv$$

So the displaced range R is given by

$$R^2 = (x + l\Delta Q - x_s)^2 + (y + m\Delta Q - y_s)^2 + (z + n\Delta Q - z_s)^2$$

So,

$$R\frac{\partial R}{\partial \Delta Q} = l(x + l\Delta Q - x_s) + m(y + m\Delta Q - y_s) + n(z + n\Delta Q - z_s)),$$

or approximately

$$\frac{\partial R}{\partial \Delta Q} = (l\, x_T + m\, y_T + n\, z_T)/R$$

(c) Let the radial displacement be Δr

So the displaced coordinates of the satellite are $x + x\Delta r/r$, etc.

So the displaced range R is given by

$$R^2 = (x + \frac{x\Delta r}{r} - x_s)^2 + (y + \frac{y\Delta r}{r} - y_s)^2 + (z + \frac{z\Delta r}{r} - z_s)^2$$

Then as before we calculate the approximate partial derivative

$$\frac{\partial R}{\partial \Delta r} = (x\, x_T + y\, y_T + z\, z_T)/(rR)$$

2.3 Solutions.

In practice it was found that the across-track correction was always highly correlated with the radial correction, and in many cases the solution was indeterminate. Hence both could not be solved-for, and so it was decided to suppress the solution for across-track, and solve for a radial correction only, which would thus absorb the across-track error. It was also found that simple constant along-track and radial corrections to the predicted orbit did not in general absorb all the error in the orbits, and that the set of parameters to be determined for a particular pass should be selected from along-track and radial displacements and their time rates of change and accelerations. We denote these parameters $T, \dot{T}, \ddot{T}, R, \dot{R}, \ddot{R}$. The partial derivatives of range with respect to the rates of change and accelerations of these parameters were formed from those of the constant terms by mutiplication by t and t^2, where time t is the epoch of each observation relative to the mid-time of the pass. Such a definition for the origin of t is optimum in reducing correlations between the unknowns. It was usually found necessary to solve for only 4 of the possible six parameters, but occasionally all six were required to remove all trends from the observational residuals.

Initially a scheme was devised to automatically check for very high (>0.999) correlations among the 4 unknowns $\dot{T}, \ddot{T}, \dot{R}, \ddot{R}$, and to supress any one or two of them in order to obtain a determinate solution, consistent with obtaining a flat track of residuals. However experience showed that the values determined for these 4 parameters were always quite small, of the order of 0.1 ms/minute for $\dot{T}$ and 1.0 cm/minute for $\dot{R}$, and of similar magnitude for the accelerations. We thus imposed a-priori standard errors of these magnitudes upon the 4 parameters, and allowed the program to solve for all six unknowns.

In order to iterate the solution, at each stage we replace the predicted coordinates of the satellite by the displaced coordinates as determined from the previous solution. So for example

$$x = x + v_x \Delta T + l \Delta Q + x \Delta r / r$$

and similarly for y and z. It was found that 4 or 5 iterations were usually sufficient, where outliers of magnitude greater than 3 × rms were removed at each stage.

A selection of some plots of observational residuals is given in Figure 2, where it is clear that all trends have been removed; these residuals are readily used to form normal points using the Herstmonceux algorithm.

As a final check that the track of residuals is indeed statistically flat, we have introduced a single-factor analysis of variance test on the residuals. This test checks for significant differences between the means of residuals grouped into normal point bins; any differences indicate that not all trends have been removed from the residuals, and a warning is given that normal points should not be formed until the cause of the problem is traced. It is anticipated that this test may prove useful for the detection of system calibration changes during a pass.

3. Conclusion.

The scheme was found to be determinate for a wide range of satellites and pass durations and quality of predictions, and has been adopted at Herstmonceux. An earlier version of the software is also in use at several European SLR stations. The deduced values of time bias are used to good effect for improving subsequent predictions, and additionally the software has been used to generate time bias values from the quicklook observations from other SLR stations, as described by Wood and Gibbs (these proceedings).

4. References.

Gaignebet, J. (Ed) 1985. Recommendation 84A, Normal Points, in *Proc. 5th Int. Workshop on Laser Ranging Instrumentation.* CERGA, France.

Schutz, B.E. (Ed) 1990, April *Satellite Laser Ranging Newsletter*, Center for Space Research, University of Texas at Austin, USA.

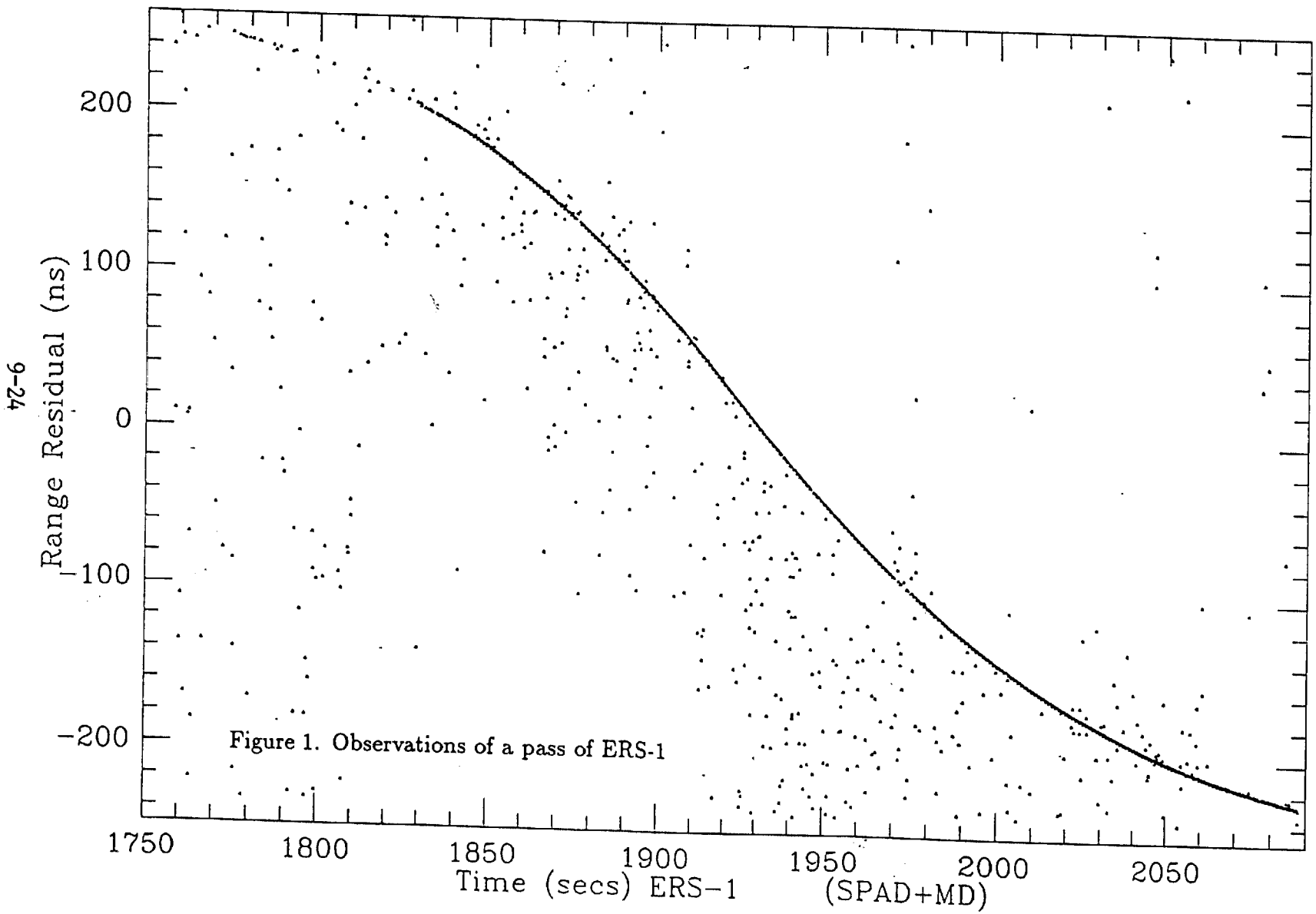

Figure 1. Observations of a pass of ERS-1

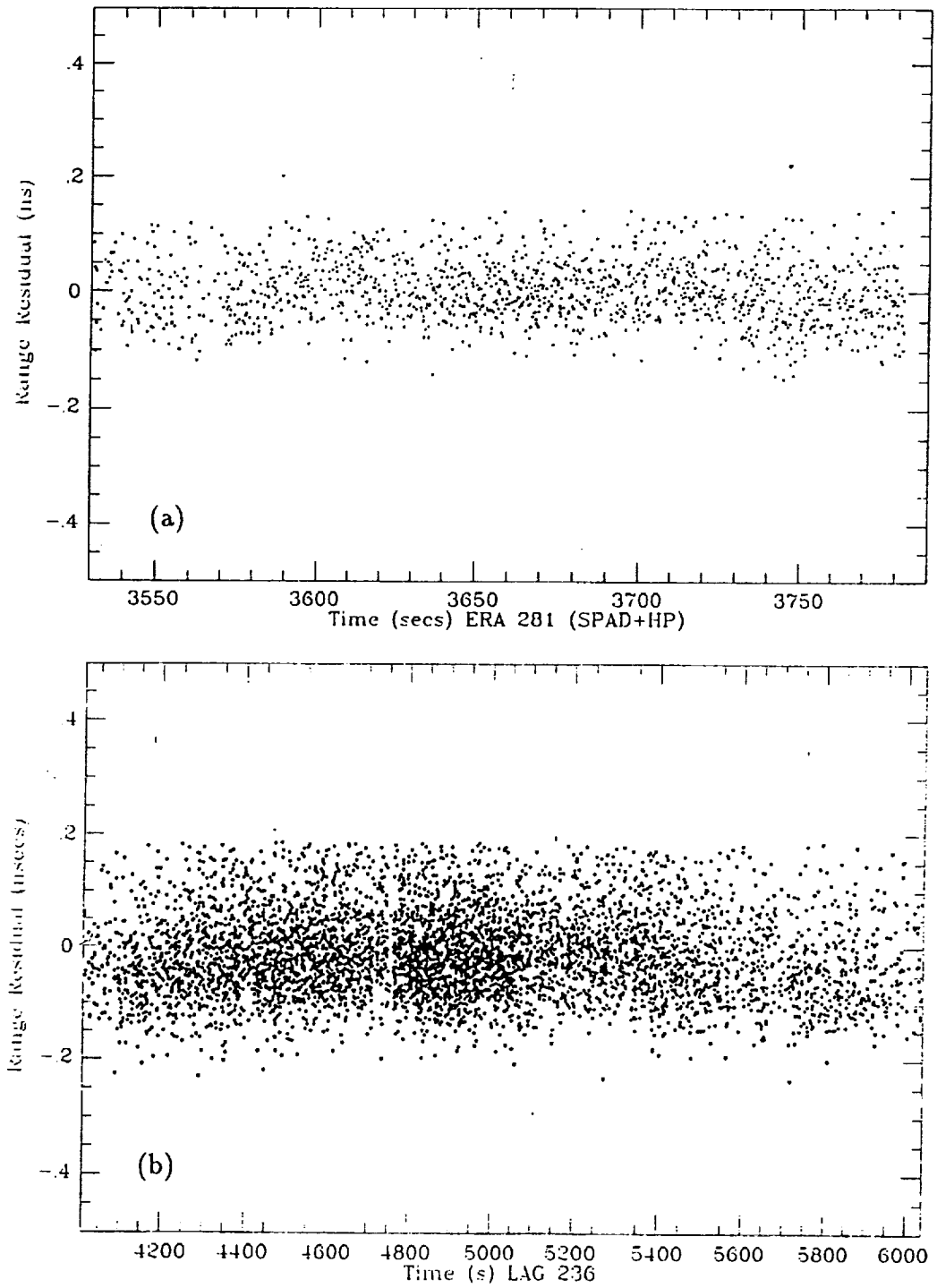

Figure 2. Range residuals from a pass of ERS-1 (a) and Lageos (b).

Poisson Filtering of Laser Ranging Data

by

R. L. Ricklefs and P. J. Shelus
McDonald Observatory, University of Texas, Austin, TX 78712

The filtering of data in a high noise, low signal strength environment is a situation encountered routinely in lunar laser ranging (LLR) and, to a lesser extent, in artificial satellite laser ranging (SLR). The use of Poisson statistics as one of the tools for filtering LLR data is described first in a historical context. The more recent application of this statistical technique to noisy SLR data is also described.

Introduction

Routine LLR operations began at McDonald Observatory in August, 1969 as a part of the NASA Apollo Lunar Ranging Experiment (LURE), using the newly-commissioned 2.7-m astronomical telescope to range to the retro-reflector array placed upon the lunar surface by the Apollo 11 astronauts. During the next several years, additional arrays were left on the moon during the Apollo 14 and Apollo 15 missions, and by two Soviet unmanned soft landing vehicles. Routine LLR operations continued on the 2.7-m telescope until the mid-1980's when these operations were transferred to the dedicated 0.76-m aperture McDonald Laser Ranging Station (MLRS).

It is important to realize that the return signal strength ratio, neglecting all parameters except distance, for a near-Earth artificial satellite and the Moon is something like 3×10^{12}. Thus, it is more than a trillion times more difficult to range to the Moon than it is to range to, say, Ajisai. In the extremely low signal strength environment of LLR it was (and continues to be) necessary to operate largely at the single photon-electron level. However, this means that a very large number of "volunteer" photons from any number of background noise sources may trigger the detection electronics, even though very narrow spatial, spectral and temporal filters are routinely employed in the receive package. Since all incoming photons are indistinguishable from one another, identifying the valid returns from the moon has been a difficult task. From this experiment's inception, the reliance on statistical filtering methods, in addition to the physical ones, had been always assumed.

The application of Poisson statistics to the LLR data filtering problem provided an effective tool for dealing with high-noise, low signal data. The technique has now been expanded and adapted to handle marginal SLR data as well and has proven to be especially effective when applied to data from single or low-multiple photo-electron systems during daylight passes and data from all stations when they are ranging more difficult targets like Etalon-1, Etalon-2, and MP-2. Figures 1 and 2 show samples of noisy data, displayed by MLRS onsite software, for which the Poisson technique is required.

Background

Let us consider the mathematical concept of the Poisson distribution, which gives the probability that a certain integer number, k, of unit rate random events from a population, n, will occur in a given interval of time, x, within some total interval of time. The operative equation is:

$$P(k) = \frac{x^{[k]}\, e^{-x}}{[k]!}$$

where [k] is the largest integer less than k. For x large enough, this function has a bell shape comprised of many rectangular steps. Multiplying the computed probability by the number of bins in the entire sample time gives the number of bins which contain exactly k events.

In a descriptive sense, Poisson statistics states that if one has "n" observations of some independent variable defined over some range of "m" bins of uniform width, and if those observations are random, one can compute, in a statistical sense, how many of those bins will contain exactly k observations. For example, for some specific experiment of, say, 16 independent observations of some value, one might compute from the above equation that 3 of the bins will be empty, 4 of them will contain exactly 1 observation, 3 of them will contain exactly 2 observations, 2 of them will contain exactly 3 observations, and no bins will contain 4 or more observations. Then, if one looks at the actual histogram of measurements and finds that one of the bins contains 8 of the 16 observations, one might safely assume that those observations are indeed not from a random distribution and that something systematic has occurred. In the case of LLR or SLR observations, where the measurement is an (o-c) range residual, it is assumed that the bin (or bins) containing a statistical excess of observations are probably valid returns from the target or the result of some systematic effect in the ranging equipment. As another example, figure 3 represents the statistics from the lunar data in figure 1. The predictions indicate that there should be no bins with more than 21 points. One bins has 22 points, which is probably not significant, but there is another bin with 47 points, which is significant. That bin contains the lunar data.

This technique is routinely applied to the filtering of McDonald Observatory LLR data and is fully described in "Laser observations of the Moon: Identification and construction of normal points for 1969-1971 by Abbot, Shelus, Mulholland and Silverberg (Astron. J., Vol. 78, No. 8, pp 784-793, October, 1973).

Current state of affairs

In the routine application of the Poisson technique to data filtering it must be noted that, in order to have the best possible chance of isolating signal from noise, one should use the narrowest bin width possible, keeping in mind at all times, of course, the quantity being measured. Narrow bins will maximize the signal to noise ratio since, in a narrow-bin environment, a relatively small number of noise photons will be found in any one bin. Further, it is absolutely required that the data be flattened before a histogram is formed, i.e., trends must be removed from the data as much as is possible, so that signal will not "spill over" into many adjacent bins and, again, be lost in the "noise". This problem has been addressed in a straightforward way in the current data screening implementation at the MLRS, as shown in figure 4. All bins are scanned sequentially through a predetermined range of slopes, the plan being that the signal will appear at a significant peak at a slope that matches the inherent slope of the data. This technique is especially important for LLR data when signal strength is low and for SLR data when orbits are not well known. Of course, in altering the slope of the data, one must take care to exclude, or compensate for, those bins which will be incomplete due to clipping. In its present implementation at the MLRS, the Poisson screening software also allows multiple segments of a pass, or a run, to be treated separately. This handles the natural change in residual slope over an extended observation session.

Although personnel at the MLRS are now applying the Poisson filtering technique for both lunar and artificial satellite data, the LLR and SLR screening systems are somewhat different. Both systems provide user interaction to allow the selection of the parameters of the Poisson fit, placement of the time bins, maximum and minimum slopes, and a maximum and minimum residual for data to be accepted as "real". For lunar data, we employ fairly strict limits on acceptable slopes and allowable residuals. Earth rotation and polar motion are major contributors to slope and residual for lunar data, so the earth orientation predictions are kept as fresh as possible. Further, there is considerable latitude in selecting time bins to reflect the observed clumping of MLRS LLR data. Ultimately, the Poisson filter is relied on to provide the LLR data compression, i.e., normal pointing, software with a set of acceptable data.

For the SLR case, the Poisson algorithms serve as a preliminary filter and suggest to the polynomial fitting algorithms in the normal pointing packages a set of data with which to start. The polynomial fit, in its job, can then return previously rejected data back into the fit or remove data suggested to it by the Poisson filter, if either of these tasks are warranted. Also, the polynomial fit, working on the entire pass, can pull in data that might be missed or misinterpreted when the Poisson filter was working on only shorter segments of a pass.

The independent time segments, into which an SLR pass is broken, allow the software to follow changes in slope during a pass and minimize the effect of anomalous distributions of data in short segments. We are examining the desirability of having several software checks that require the slopes and average O-C residuals to be smoothly varying over the pass. However, in the cases where there are breaks in the data and other unusual distributions, this may not be practical.

Results

In the case of LLR data, the presently implemented Poisson filtering technique works well, especially with a bit of interactive help from the user, although, in marginal cases, it would be preferable to use all runs taken over a lunar pass to aid in the filtering . This particular extension is now being examined. As time permits we are also pursuing more elaborate filtering techniques such as jack-knifing and bootstrapping to see if they hold merit.

In the case of SLR, the technique has been used successfully at MLRS for about a year now. In that time our experience has been that the combination of the Poisson filter and the polynomial fit produces good results virtually all of the time. The marginal cases can usually be satisfactorily processed, after the fact, by altering some of the parameter of the Poisson fit or by eliminating from consideration extremely noisy parts of the pass. Of course, most of the anomalies usually occur with weak passes, especially Etalon-1, Etalon-2 and ERS-1. The Poisson filter algorithms are being upgraded so that each satellite uses a parameter set tailored to it. Tests indicate that this will allow successful batch processing of virtually all passes that previously required special handling. Also, an interactive tool similar to the Lunar Data Editor is being developed to help the observing crews to quickly recover passes that were improperly processed. The Laser Tracking Network operated by the Bendix Field Engineering Corporation will soon install the MLRS "batch" Poisson code into their processing software.

Conclusion

The Poisson filtering technique has proven itself to be an extremely valuable tool for both LLR and SLR operations at the MLRS. This technique is being optimized for each ranging target, and in the future provision will be made for routine, near-real-time observing crew interaction with the filter. In addition, new filtering techniques such as jack-knifing and bootstrapping will be evaluated as to suitability for laser ranging data filtering.

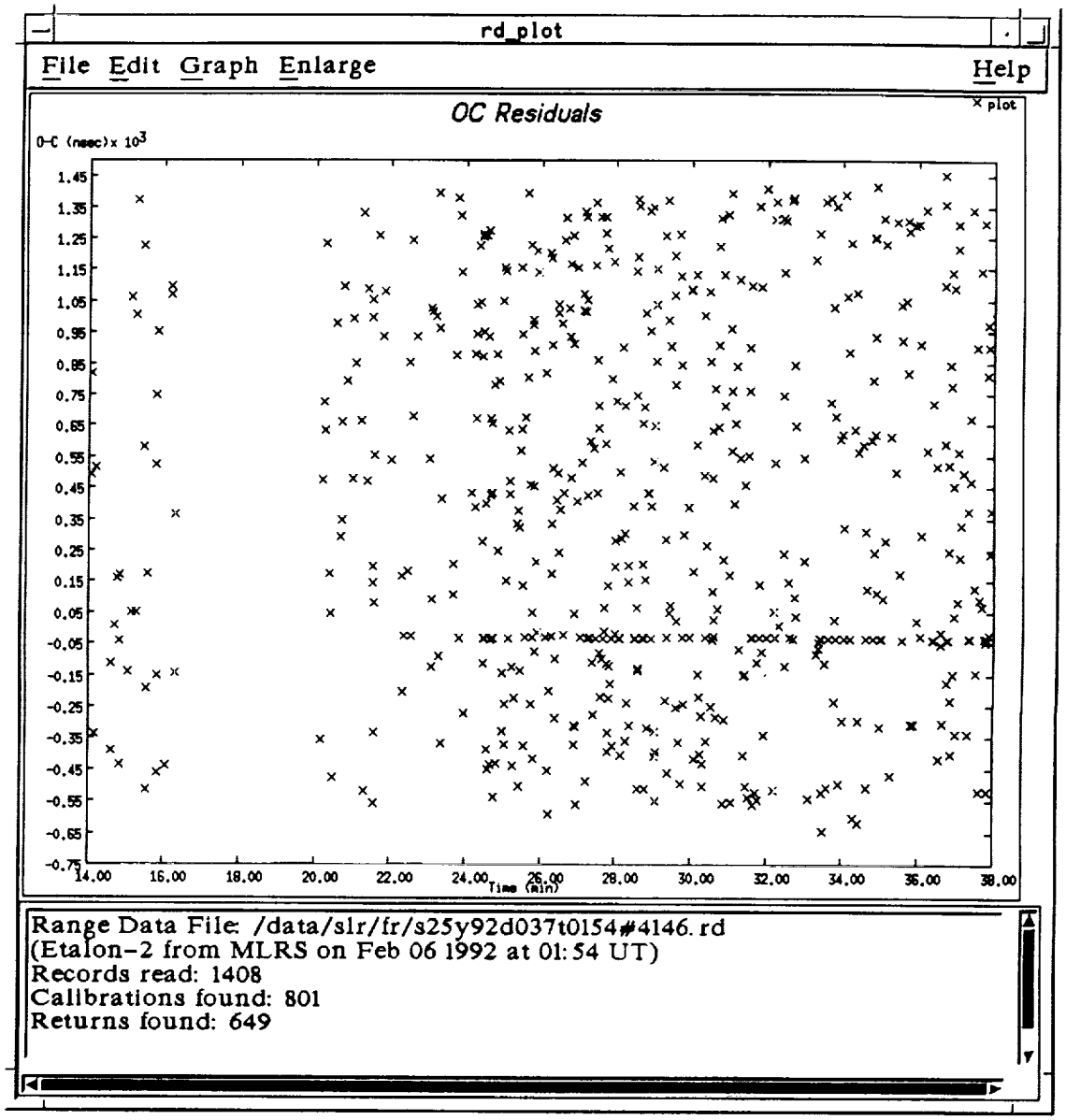

Figure 1 - Noisy Artificial Satellite Data

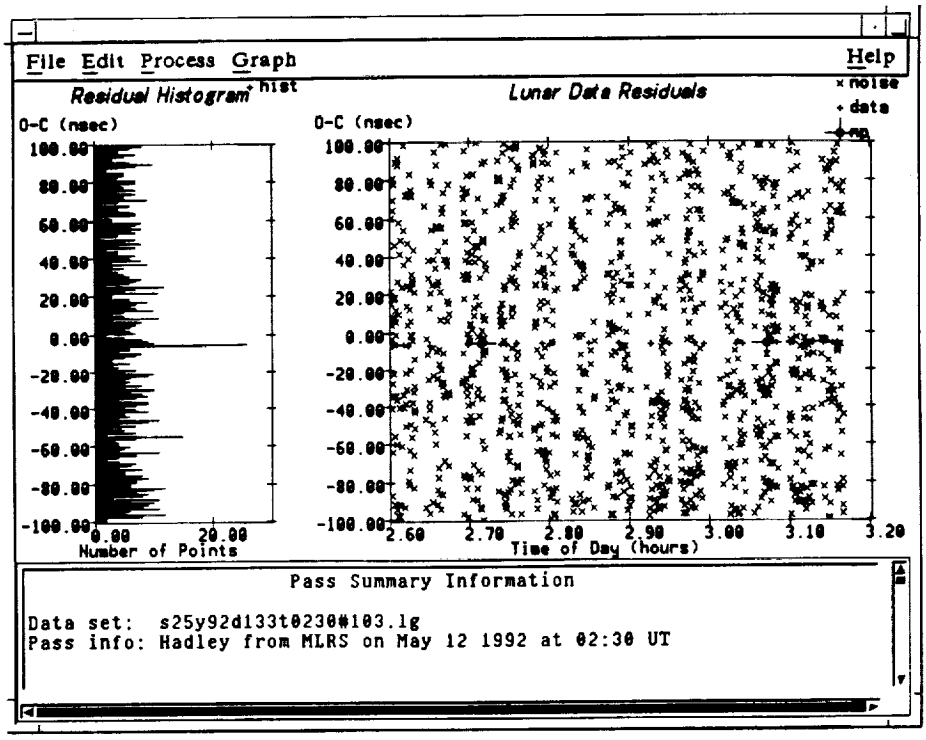

Figure 2 - Noisy Lunar Data

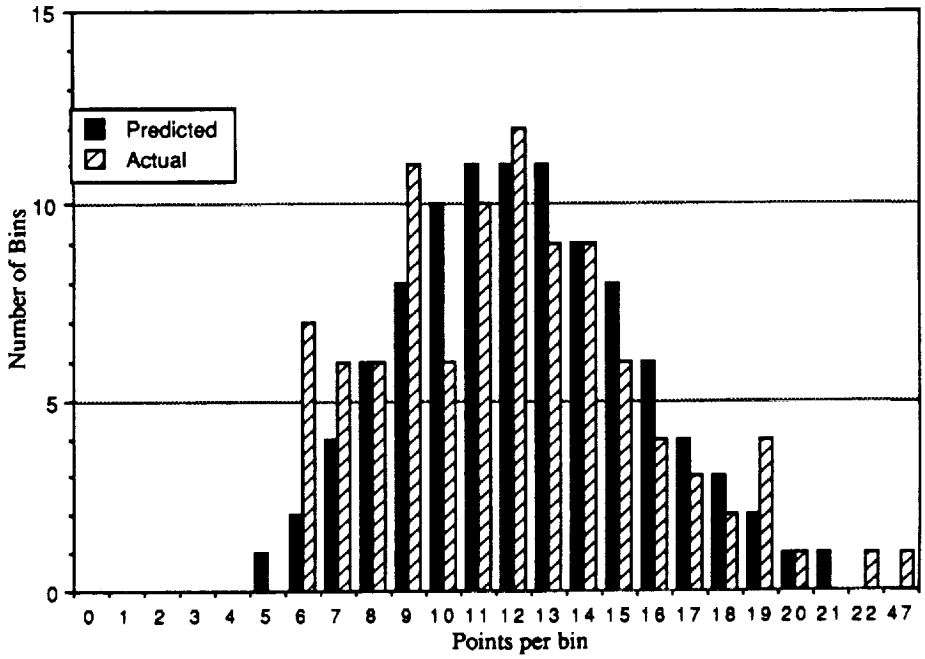

Figure 3 - Poisson Statistics for Sample Lunar Run

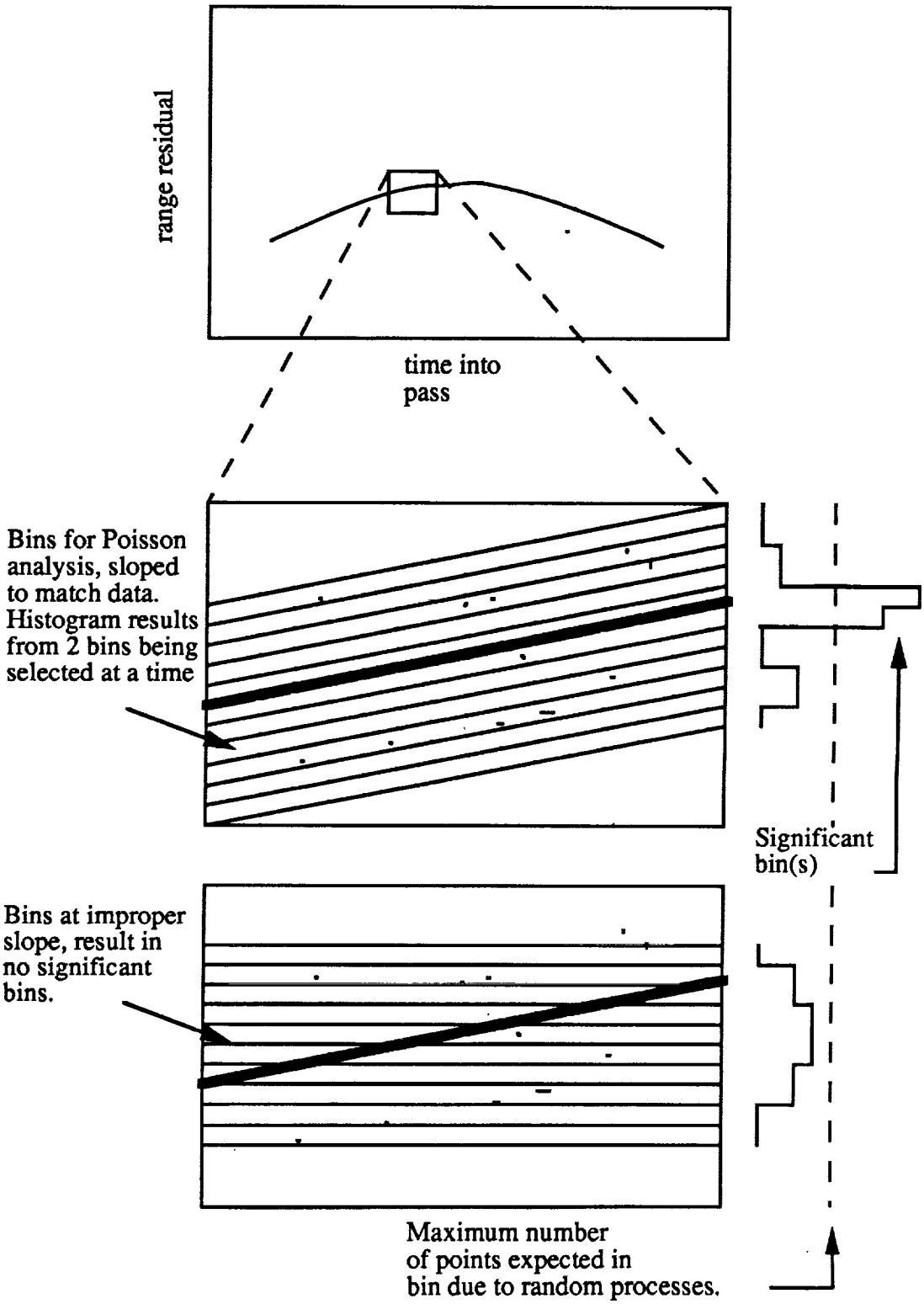

Figure 4 - Effect of Tilting Bins

Computer Networking at SLR Stations

Antonín Novotný[1]
Czech Technical University, Prague
Czechoslovakia

Eighth International Workshop on Laser Ranging Instrumentation
Annapolis, MD USA
May 18–22, 1992

Abstract

There are existing several communication methods to deliver data from SLR station to the SLR data centre and back: telephonmodem, telex and computer networks. The SLR scientific community has been exploiting mainly INTERNET, BITNET/EARN and SPAN. 56 countries are connected to INTERNET and the number of nodes is exponentially growing. The computer networks mentioned above and others are connected through E-mail protocol.

The scientific progress of SLR requires to increase the communication speed and amount of the transmitted datda. The TOPEX/POSEIDON test campaign required to deliver Quick Look data (1.7 kB/pass) from a SLR site to SLR data centre within 8 hours and Full Rate data (up to 500 kB/pass) within 24 hours.

We developed networking for remote SLR station in Helwan, Egypt. The reliable scheme for data delivery consists of: compression of MERIT2 format (up to 89%), encoding to ASCII file (files); e-mail sending from SLR station — e-mail receiving, decoding and decompression at the center.

We do propose to use ZIP method for compression/decompression and UUCODE method for ASCII encoding/decoding. This method will be useful for stations connected via telephonemodems or commercial networks.

The electronics delivery could solve the problem of the too late receiving of the FR data by SLR data center.

[1]e-mail: TJEAN@CSEARN.bitnet
TJEAN@earn.cvut.cs

The Name of the Game

The computer network backbone has spread all over the world.

Nowadays we may claim three axioms on network data exchange:

Axiom 1. *All non-local networks are connected to InterNet.*

Axiom 2. *All non-local networks have common protocol — mail protocol.*

Axiom 3. *The longer file is transferred, the longer it takes a byte to get through the network.*

Networking within the SLR Community

The most commonly used non-commercial networks are BITNet, InterNet, SPAN, UUCP. All are used on the satellite laser ranging facilities over the World.

The CSTG SLR Subcommission Meeting in Passadena, CA USA, March 12, 1992 agreed that "InterNet will be implemented to all of the SLR and other DOSE related stations. This includes the stations in Russia and some of the other Commonwealth states that participate in the global network."

We will propose the new computer network standard for data handling between SLR data center and SLR stations. The following two figures schematically show one of the possible configurations.

Results handling at SLR stations

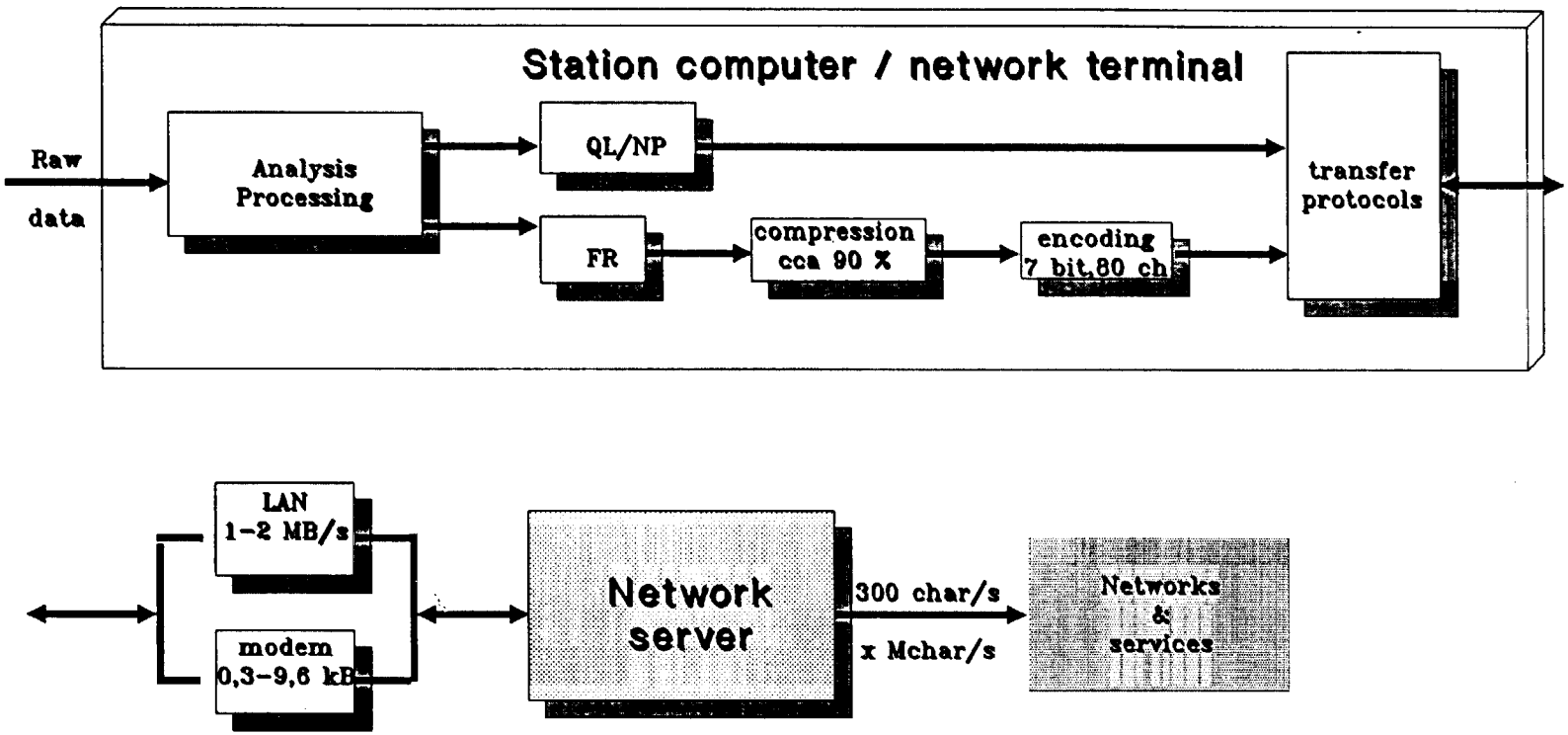

Remark: NP/QL data are redundant.

Results handling at data center

NASA/BENDIX, Eurolas/DGFI

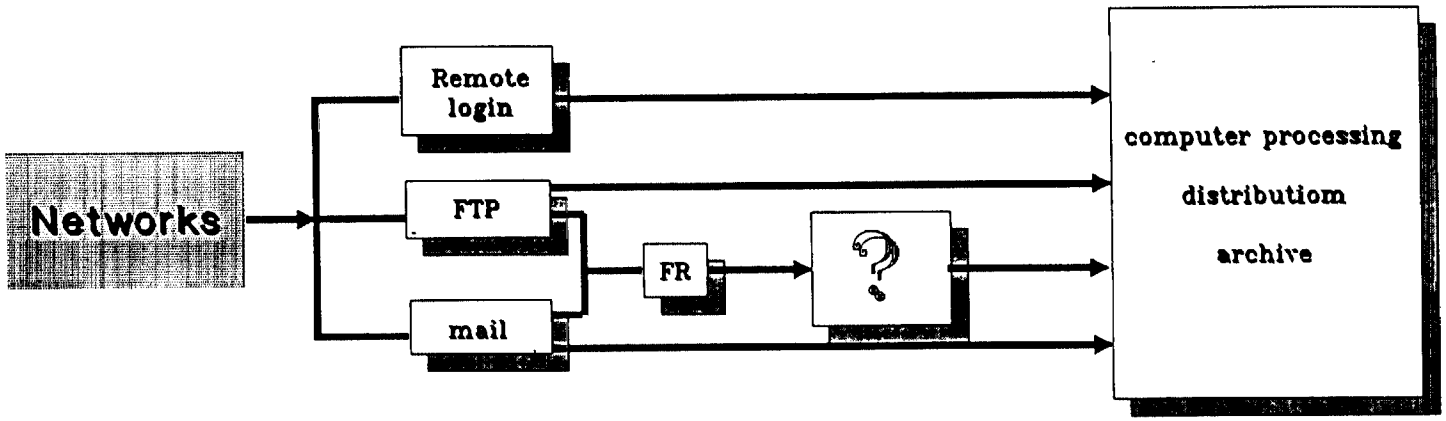

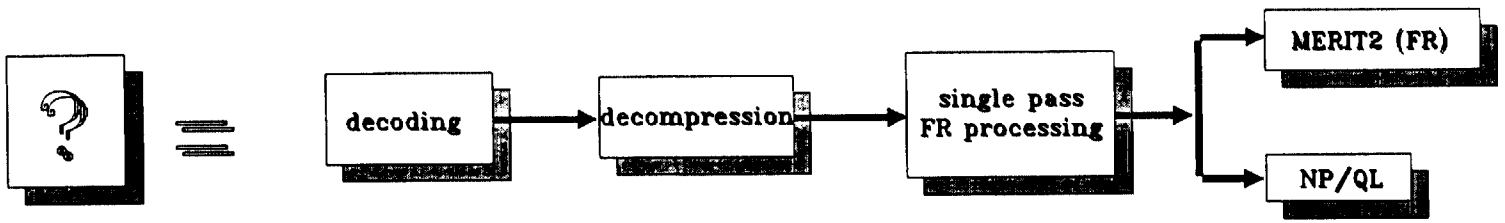

Networks Data Exchange

Mail at other networks

From the other networks, the files are sent to InterNet (and back) as a mail without any difficulties. The possibility of FTP (*File Transfer Protocol*)is strongly reduced to the use of mail servers.

Selection of Large networks [2]

applelink	Apple Computer, Inc.'s in-house network
bitnet/earn	international academic network
bix	Byte Information eXchange: Byte magazine's commercial BBS
bmug	Berkeley Macintosh Users Group
compuserve	commercial time-sharing service
connect	Connect Professional Information Network
envoy	Envoy-100 (Canadian commercial mail service)
fax	Facsimile document transmission
fidonet	PC-based BBS network
geonet	GeoNet Mailbox Systems (commercial)
ieee-compmail	A DIALCOM system supporting IEEE users
internet	the Internet
mci	MCI's commercial electronic mail service
mfenet	Magnetic Fusion Energy Network
nasamail	NASA internal electronic mail
peacenet	non-profit mail service
sinet	Schlumberger Information NETwork
span	Space Physics Analysis Network
sprintmail	Sprint's commercial mail service
thenet	Texas Higher Education Network
usdamail	A DIALCOM system for USDA researchers

The more detailed information on mail network-to-network access see[2].

InterNet data transfer protocols

FTP: (*File Transfer Protocol*) Allows a user to connect to host computer and with reduced set of commands get and/or put files. FTP is essentially inaccessible from other nets. Getting files from FTP sites may be provided by mail servers (they retrieve the file and send it as a mail). Putting files by mail servers isn't supported. FTP is unfortunately slow (approx. 500 bytes/second, for longer files 200 bytes/second), the transfer rate depends on traffic in the network. The terminal must stay on-line while putting/receiving.

Mail: A convenient way for sending a file. A user has no possibility to receieve files via mail (in sense that somebody must send the file, it can't send itself).

[2] © 1990 John J. Chew, available as EMAILGUI.ZIP at SIMTEL and TRICKLE archives

The transfer rate is a bit slower, but it does not keep local terminal busy as FTP does. Files longer than 50000 bytes are regarded as "huge" and sent only when the network is free.
Mail is essentially 7-bit protocol, 80 characters per line. Formatted or binary data can be converted to fit.

TelNet: Allows a remote login. Usefull for remote user access to any computer on the InterNet. Unusable for sending/retrieving files. User has to know remote computer's operating system.

Unfortunately, lots of SLR stations are not connected to InterNet and won't be connected soon. What's more, most stations have to use modems to connect to networks (which naturally slows down the transmission). That's why we should figure out how to send shorter files and how to send them from other networks.

What Kind of Data Is Exchanged?

1. From SLR center to SLR stations

   - Prediction (IRV or SAO) $\approx$ 5 kB
   - Whole year IRV - Lageos $\approx$ 100 kB
   - Comments on operation $\approx$ 2 kB
   - Bendix QL analysis $\approx$ 1 kB
   - Reports $<$ 25 kB

   Suggestion: I would suggest the center to deliver these files to SLR stations as a regular mail to an automatic list of addressees. FTP makes the server at SLR center very busy while everybody is trying to receive the files. Due to the network software, when the network breaks down, it takes the biggest care of mail — it is almost always delivered. The FTP data might be easily lost or corrupted during breakdown. The non-InterNeters have to use mail-servers (for example `BITFTP@PUCC`) that may become very busy.

2. From SLR stations to SLR center

   - Comments on operation $\approx$ 2 kB
   - QL or NP data $\approx$ 2 kB/pass
   - FR data MERIT2 format
     130 chars/line, 1 line/point $\Rightarrow$ huge file
     up to 500 kB/pass
     This file is almost undeliverable via mail — it has more than 80 chars/line and

it has more than 50 kB. The Rules of a Network User say that user should never overload the network. In fact this file should never appear in mail! (And it might take several days/weeks to get through the networks.)

- **or** FR data compressed MERIT2 format and UUENCODEd — (compression 89%)
  This way of transmitting FR data solves almost all of the problems mentioned above.

General Overview of Compression Techniques

- The good compression program must be easy to use, commonly used on different OS, must provide fast algorithm and high compression ratio
- Possible techniques:

  ZOO: Not very common, not very high ratio; source code available

  LHA: Not very common; very high ratio

  TAR.Z: Causes problems on non-UNIX OS, not very easy to use (on MSDOS), not very high ratio; very common on UNIX (supported by VAX/VMS)

  ARC: Out-of-date, slower than PKZIP; very common on many OS

  ARJ: New, not free for institutional use; very fast, the highest compression ratio, useful switches, starting to be used on lots of BBS's

  PKZIP: *Recommended*; very fast, good compression ratio, commonly used on most OS, sources available

Encoding & Decoding

General rules for e-mail transmission:

- Convert 8-bit file and/or formatted file into 7-bit 80 chars/line file
- Split huge files (< 50 kB)
- Standard ENCODE/DECODE (UU & XX) programs are available for all network mainframes

Very comfortable shareware UUXFER program (with C sources) is available from D.M.Read (`readdm @ dopey.cc.utexas.edu`)

Features of UUXFER:

- Encoding UU, XX, using external table
- Decoding UU, XX (automatically detected)
- Optional splitting of huge files to user-defined size
- Merge file options
- Interactive/command-line commands
- User friendly
- Supports most of mainframes

Conclusion

According to the Monthly Report on ERS-1 FR Laser Tracking Data Preprocessing, DGFI/D-PAF October 1991 (issued April 1992), it took up to three and half a month to deliver FR data from Simosato, Japan to the SLR Center (on the magnetic tape), and it took five (!!) months to deliver data from Maidanak, CIC on floppy disks!!! This MUST BE CHANGED.

The electronic delivery via computer networks is the effective method to avoid the late delivery results from SLR sites..

A. Requirements

- All SLR stations can access computer network
- Accepted standard for compression and/or coding
- Files have standard names for automatic processing at data center
- Sufficient operating hours of the involved networks including holidays
- Defined deadline time schedule for FR data delivery (in case QL, NP data would be sent by spare channel)

B. Goals of computer networking at SLR world network

- NP/QL/FR data available for processing at SLR centers within less than 24 hours (hopefully)
- FR data would be transmitted instead of redundant NP and/or QL data
- Increased effectiveness when using data (delivered reliably and in time)
- Much cheaper data exchange

Appendix

Network data exchange of huge data files was successfully tested from Helwan and from Prague during spring 1992

- Helwan — BITNET/EARN
- Prague — BITNET/EARN
  InterNet (the same mainframe)
- München — InterNet

The Prague IBM mainframe was used as data center emulator

1. Helwan — compression, encoding
2. Helwan–Cairo VAX — by KERMIT ($\approx$ 30 B/s)
3. Cairo–Prague — BITNET (file transfer)
   BITNET–InterNet (mail)
4. Prague — decoding, decompression
5. Prague–München — FTP huge file transfer ($\approx$ 100–700 B/s)

All FR data from Helwan were delivered to `Eurolas/DGFI` by e-mail/FTP.

The communication facilities at SLR Helwan are described on the Figure.
Remark: After the workshop, the problem was discussed with Dr. W. Seemüller. The Eurolas Data Center is ready to accept FR data as e-mail (compressed using PKZIP, encoded using UUENCODE/XXENCODE). I expect that all FR data from Helwan SLR will be delivered to EDC compressed and by e-mail from BITNet network.

Communication facilities
SLR Helwan

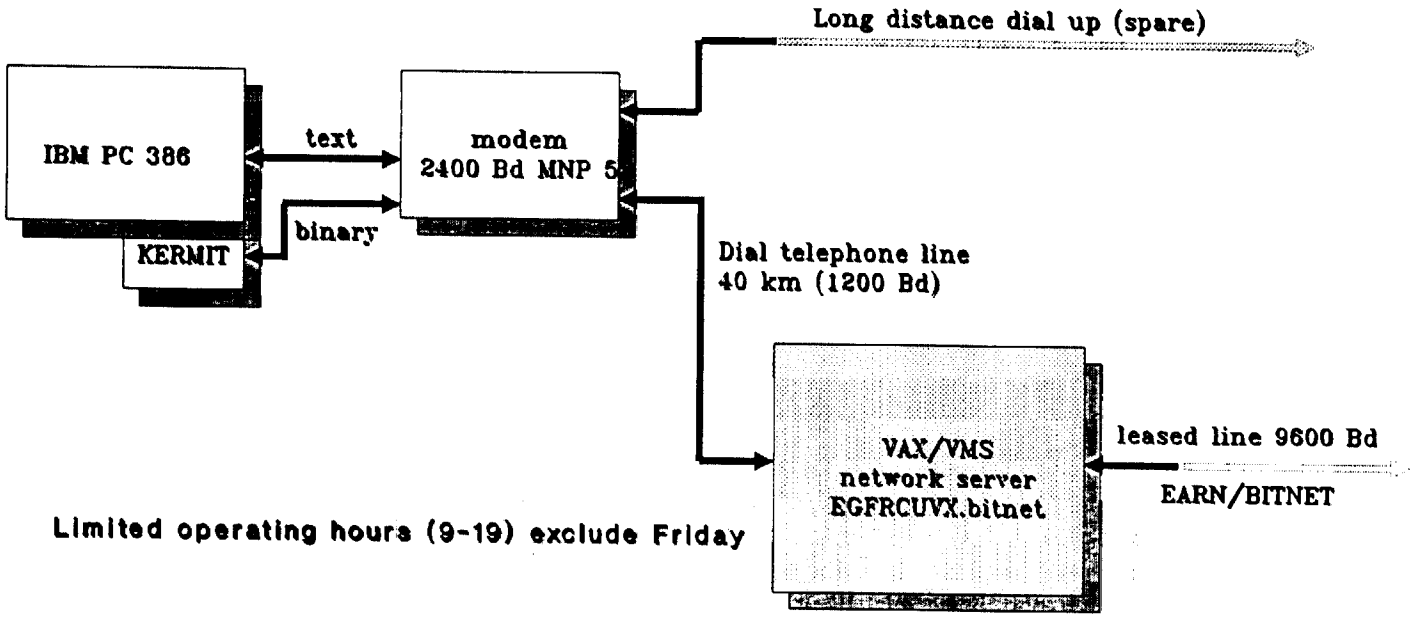

Spare:

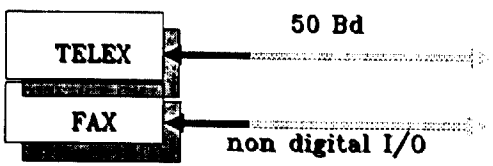

Upgrading NASA/DOSE Laser Ranging System Control Computers

by
Randall L. Ricklefs
McDonald Observatory, University of Texas, Austin,Texas 78712

Jack Cheek
Hughes-STX, Lanham, MD 20706

Paul J. Seery, Kenneth Emenheiser,William P. Hanrahan
Bendix Field Engineering Corp., Seabrook, MD 20706

Jan F. McGarry
NASA Goddard Space Flight Center, Greenbelt, MD 20771,

Laser ranging systems now managed by the NASA Dynamics of the Solid Earth (DOSE) and operated by the Bendix Field Engineering Corporation, the University of Hawaii, and the University of Texas, have produced a wealth of inter-disciplinary scientific data over the last three decades. Despite upgrades to the most of the ranging station subsystems, the control computers remain a mix of 1970s-vintage minicomputers. These encompass a wide range of vendors, operating systems, and languages, making hardware and software support increasingly difficult. Current technology allows replacement of controller computers at a relatively low cost while maintaining excellent processing power and a friendly operating environment. The new controller systems are now being designed using IBM-PC-compatible 80486-based microcomputers, a real-time Unix operating system (LynxOS), and X-windows/Motif graphical user interface. Along with this, a flexible hardware design using CAMAC, GP-IB, and serial interfaces has been chosen. This design supports minimizing short and long term costs by relying on proven standards for both hardware and software components. Currently, the project is in the design and prototyping stage with the first systems targeted for production in mid-1993.

Introduction

In the more than two decades of laser ranging, the observational accuracy of the NASA-funded laser stations has dropped from tens of centimeters to a centimeter or better. To achieve this, most parts of the ranging system have been upgraded a number of times. It has long been recognized that the computer subsystems are antiquated and unable to keep up with the requirements for ever-more-precise range measurements and an ever-growing list of targets. In the last year, a plan of action has been formulated to upgrade these systems in such a way as to minimize both short and long term cost by making extensive use of standard hardware and system software. The stations involved are the DOSE-operated GSFC 1.2m telescope, the Bendix Field Engineering Corporation-operated MOBLAS 4-8 and TLRS 2-4, the University of Hawaii-operated HOLLAS station, and the University of Texas-operated MLRS

History

The controller computers on the DOSE network laser stations are late-1970s minicomputers produced by vendors such as Modcomp, Data General, and DEC. While they were real workhorses in their day, they are now eclipsed by faster, more expandable microcomputers an order of magnitude less expensive. Much of the code on these machines is written in archaic versions of FORTRAN which fail to meet even the FORTRAN 66 standards. A great deal of code is also written in the native assembly language of these machines. Many approximation and shortcuts were required to fit complex allgorithms into these low-capacity computers. In some cases the operating systems are 'homebrew', while in other cases extensive changes have been made to no-longer-supported proprietary operating systems. If key personnel were to leave these organizations, the computer systems would be virtually unsupportable.

In addressing these issues, the CDP SLR Computer Committee decided in 1988 to off-load the data formatting, communications, and prediction functions of the existing controlling computers to dedicated Hewlett-Packard Unix workstations. These workstations were to also take on the tasks of data filtering and normalpointing. It was recognized at that time that replacing the controllers was a necessary task, but was too complex for the timetable necessary to support the burgeoning list of satellite targets. Figure 1 is a schematic of the current dual-computer system at the stations, with a serial line linking the computers. Since the process of implementing the new computers in the network laser stations is nearly complete, work has begun on the task of replacing the controller computers, a task made easier by the off-loading of many tasks to the workstations.

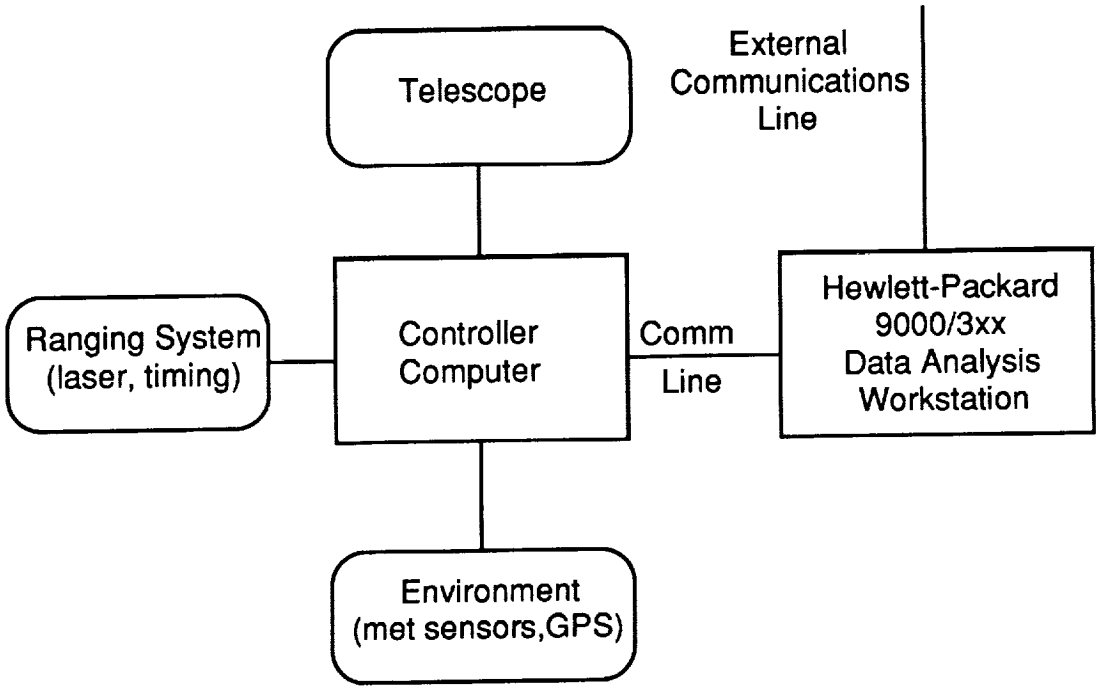

Figure 1: On-site Computer Configuration

Hardware Environment

The new controller system must accommodate many of the vagaries of 7 or so laser systems' designs and philosophies and must be flexible enough to permit expansion of these systems in various ways. For instance, most of the Bendix-operated systems and the University of Hawaii system fire their lasers at 5 or 8 Hz, use external pre- and post-calibrations, and use Hewlett-Packard 5370 counters as time interval units. MLRS on the other hand, fires at 10 Hz, uses internal calibrations and uses a TD811 time digitizer as the finest part of its 3-tiered epoch timing system. The MOBLAS and transportable systems are limited to satellites up to the orbits of the Etalons. The GSFC 1.2m research system accommodates many experimenters, and ranges to aircraft as well as to satellites. MLRS ranges all currently targeted CDP satellites as well as MP-2 (in geostationary orbit) and reflectors on the moon. Some systems use CAMAC interfaces, while others use a proprietary bus interface standard. Some incorporate GP-IB (IEEE-488), and most use serials ports for various devices.

To replace the current controller computers, a new computer must be identified that can talk with each of the existing interfaces and that is likely to be supportable for the foreseeable future. It must support one or more real-time operating systems, and must be fast enough to meet all near term needs. Proprietary architecture and all the danger that implies must be avoided. In addition, the new system must be inexpensive. The obvious choice is the ubiquitous IBM-PC-compatible microcomputer. Boards exist that interface the PC to almost any variety of hardware; the upgrade path to an even faster machine than the prototypical 80486 33 MHz system is expected to be virtually painless; it is relatively inexpensive; and there are a number of reasonable real-time operating systems available.

A prototype systems design was developed which includes an IBM-PC clone containing a 33 Mhz Intel 80486, 16 Mb of RAM, a 330 Mb SCSI hard disk drive, 3 1/2" and 5 1/4" floppy disk drives, a 16 bit ethernet card, high resolution (1024 x 768) video display and a 16" monitor. Interface cards for CAMAC, GP-IB, and a serial mux board were also included. To save cost and space, the preliminary configuration will have the PC use both the printer and erasable optical disk on the HP workstation across the ethernet network.

To standardize the system interfaces and to limit dependence on specific vendors, it was decided to use the CAMAC, IEEE-488 (GP-IB), and RS-232 serial interfaces rather than dedicating a bus slot to virtually each device in a ranging station. Along these lines, the MOBLAS systems' obsolete IACC interface will be replaced by CAMAC, thereby removing an important source of maintenance difficulties. The serial ports are probably the easiest of all of these interfaces to accommodate with the PCs; they will be used to bring in environmental sensor data.

Operating System

Each laser system involved in this project has evolved along a different path dictated by different needs. One overarching need now, however, is to create as much commonality as possible and to program for a software environment that will still be viable in 10 years. There were several options available when the search was made for operating systems, including writing it ourselves. Several of the current stations run home-built operating systems. The difficulties with these have been that they are hard to write and maintain. These systems were written because existing operating systems at the time did not offer the combination of speed, performance, and code size that was necessary to make the most

effective use of the hardware in a real-time environment. With fast and (relatively) inexpensive hardware, there are no such needs today.

In the search for an operating system, we considered DOS and DOS add-ons, various versions of Unix, and several proprietary operating systems, such as Digital Equipment Corporation's VMS and the Apple Macintosh Finder. The proprietary operating systems were rejected immediately, due to our need for vendor-independence. DOS and the Digital Research clone DR-DOS are neither multitasking, multiuser, nor realtime. DOS is also targeted to Intel 80x86 microprocessors, violating our requirement for vendor independence. Although products such as Microsoft Windows and DeskView offer some degree of multitasking, they do not claim to be either pre-emptive or real-time.

Unix was chosen because it has become a commonly available operating system with a rich software development environment. It does provide multi-user and multi-tasking capabilities and is available on many types of processors. Although there are several 'flavors' of Unix in the marketplace, the trend towards standards compliance allows well written programs to be transferred among Unix systems. The Hewlett-Packard workstations already available at the network laser stations run in a Unix environment. Standard Unix is not a real-time operating system. However, there are Unix clones and derivatives which do support realtime, pre-emptive multi-tasking and are designed for realtime acquisition and control applications like laser ranging.

A number of Unix and Unix-like systems were considered. These include:

Coherent (Mark Williams)	QNX (Quantum Systems)
REAL/IX (Modcomp)	Unix / Xenix (SCO)
VRTX (RadiSys Corp)	VxWorks (Wind River Systems)

The above were eliminated due to one or more of the following reasons. The operating system

- requires proprietary hardware
- did not mention POSIX or real-time standards compliance
- lacks one or more of the required compilers (FORTRAN, C, or assembler)
- lacks network capabilities
- lacks graphics capabilities

The chosen operating system is LynxOS by Lynx Real-Time Systems, Inc. LynxOS is a Unix-clone (no AT&T code) which complies with the POSIX standard as well as IEEE 1003.4 and 1003.4a draft real-time standards. It also follows the 80386 binary file standards and runs on IBM-PC compatible computers. LynxOS is also available for Motorola 680x0 systems and is being ported to the SPARC engine. C compilers (including one by GNU) are supplied with LynxOS, while FORTRAN is available from a third party. TCP/IP, NFS, X windows and OSF Motif are also available from Lynx. It should be mentioned for completeness that soon after LynxOS was chosen, Venix (Venturcom) was discovered. It uses AT&T system V code modified for real-time applications and also run on IBM-PC compatibles. It appears to be a viable alternative choice for a real-time operating system.

User Interface and Networks

Several requirements for the user interface were advanced during planning. These included the need for a user-friendly interface, more graphics and less text, remote monitoring and control, automation of many hardware settings and seamless integration

with the HP workstation. The emerging standard for network-based, vendor-independent graphical user interface is the X windows system. Since X windows specifies no policy or style, there is no consistency required of applications. For this reason the Open Systems Foundation developed the Motif graphical user interface (GUI) on top of X windows, which does have a particular "look and feel". Open Look, which is another GUI supported by AT&T and Sun, does not seem to be as widely available at this time. Using the constraints of the GUI, user friendly applications can be produced that have many of the features of the familiar Apple Macintosh and Microsoft Windows applications, such as menu bars, pop-up windows, and freedom from a command line interface. Also, since X windows is network based, one can use the on-site software from virtually anywhere in the world via a network connection. Much of the experience gained and code developed in implementing such an interface for the on-site Hewlett-Packardworkstations for the NASA-funded stations will be of great value in constructing the controller system.

Connecting the controller computer and on-site data-reduction workstation via ethernet and TCP/IP opens a world of data and control-sharing possibilities. Data can be recorded on the controller's disk drive in a directory which is mounted on the workstation via NFS (Network File System). The workstation can then have instant access to the data in real time. Sockets, RPC (Remote Program Calls), and remsh (remote shell) can all server as tools for creating a seamless dual computer system.

Preliminary Design

In addition to agreeing on prototype hardware and software platforms, the GSFC 1.2m telescope, Bendix, and the University of Texas groups have all acquired prototype systems. Work is proceeding on the design of the user interface and underlying functions. Device drivers for two critical pieces of equipment - the CAMAC and the timing board (used to provide the computer with 20 Hz interrupts from the station clock) - have been written. The monitor program, which runs at all times and maintains information such as time, weather, and telescope status, and the star calibration program will be the first software package to be implemented, as they fulfil needs common to all stations. Work is also proceeding on replacement of the MOBLAS IACC interface with CAMAC. The goal is to put the first three upgraded systems (GSFC 1.2m, MOBLAS 7, and MLRS) into production with the new controller in mid to late 1993.

A preliminary version of the user interface is shown in figure 2. This shows the common display of station parameters maintained by the monitor program such as date, time and telescope position. Also evident is the pull-down menu and display of graphs and parameters unique to the star calibration program.

Conclusion

The overdue upgrade of NASA ranging station control computers is finally coming about and is making use of the latest technology to produce a flexible, extensible, and maintainable computer platform. The upgrade is based on standard hardware and software components to lessen vendor dependence and enhance software portability. The prototype computer system has been designed and acquired by the principals in this upgrade, who are in the midst of further software design and low level software implementation.

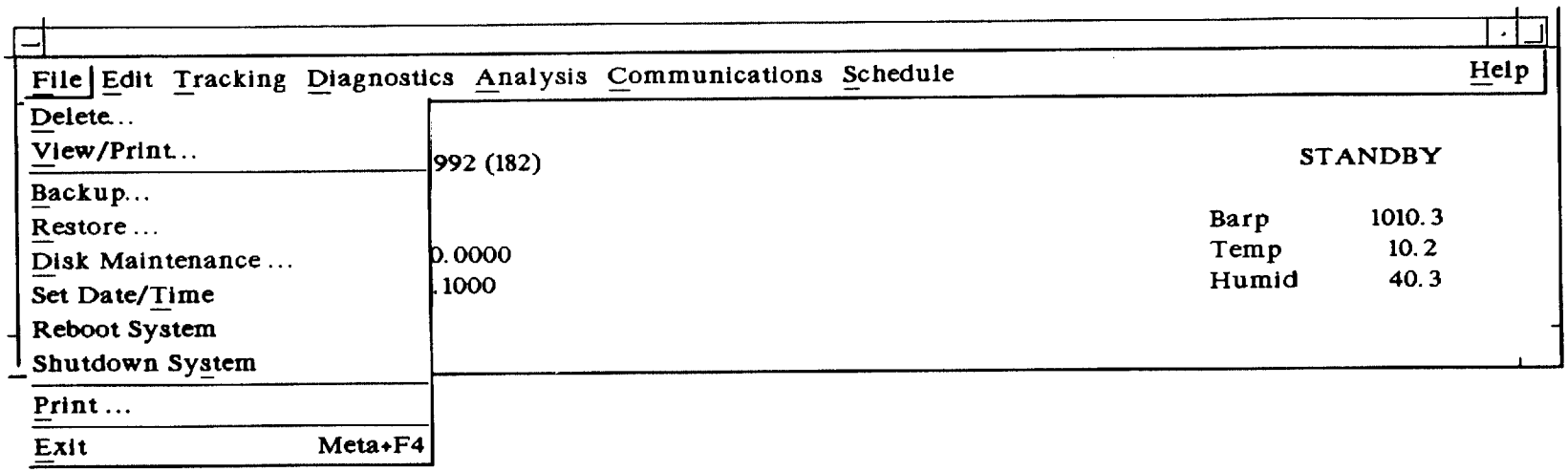

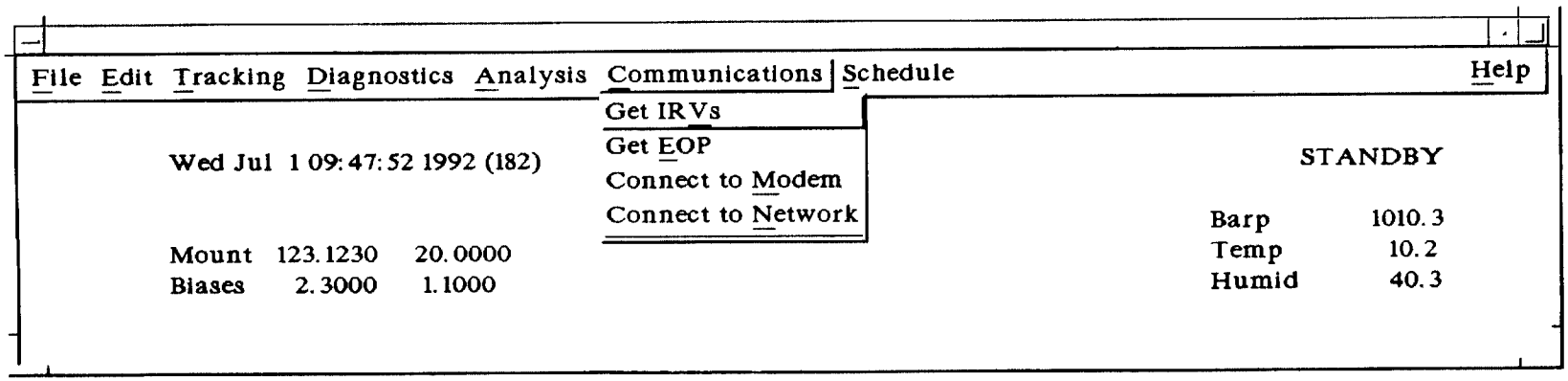

FIgure 2 - Preliminary Monitor program user interface

HP UPGRADE OPERATIONAL STREAMLINING

D. Edge, K. Emenheiser, B. Hanarahan, D. McCollums, P. Seery

Allied-Signal Aerospace Company
Seabrook, Maryland

R. Ricklefs

University of Texas
Austin, Texas

Abstract

New computer technology and resources must be successfully integrated into CDSLR station operations to manage new complex operational tracking requirements, support the on site production of new data products, support ongoing station performance improvements, and to support new station communication requirements.

The NASA CDSLR Network is in the process of upgrading station computer resources with HP UNIX workstations, designed to automate a wide range of operational station requirements. The primary HP upgrade objective was to relocate computer intensive data system tasks from the controller computer to a new advanced computer environment designed to meet the new data system requirements. The HP UNIX environment supports fully automated real time data communications, data management, data processing, and data quality control. Automated data compression procedures are used to improve the efficiency of station data communications. In addition, the UNIX environment supports a number of semi-automated technical and administrative operational station tasks. The x window user interface generates multiple simultaneous color graphics displays, providing direct operator visibility and control over a wide range of operational station functions.

HP UPGRADE OPERATIONAL STREAMLINING

The successful integration of new HP computer resources into the Crustal Dynamics Project (CDP) Satellite Laser Ranging (SLR) Network as part of the HP Upgrade Project has led to critically needed improvements in data system capability and significant gains in network operational efficiency. This paper provides a brief description of the HP Upgrade Project strategy and progress to date in streamlining station operations.

The HP Upgrade Project was initiated in 1987 to prepare the CDP SLR Network to meet the operational challenges presented by multi-satellite tracking operations in the 1990's. The technical approach for the HP Upgrade Project was based on the recommendations of the CDP Computer Panel, which recognized that new station requirements to support up to ten operational satellites and to produce on site normal points could not be supported by existing station computer resources. The existing computer resources recorded tracking data on floppy disk or magnetic tape and required manpower intensive operations to reload the data back into the computer to support station data processing activity. In addition, data processing operations and satellite tracking operations could not be performed at the same time. Therefore, data processing operations had to be scheduled around periods of operational tracking and were typically performed at the end of an operational shift. These problems delayed the production of data products and severely limited network tracking productivity. The basic HP Upgrade Project strategy was to integrate a second computer system into the existing station configuration to provide the required additional computer resources.

In 1988 the first HP computer systems were purchased, and development of HP Upgrade prototype systems started at the Goddard Space Flight Center (GSFC) and at the University of Texas. The development of a parallel prototype at the University of Texas was necessary to address the unique requirements of a lunar tracking station. HP UNIX software development projects were shared between GSFC and the University of Texas to reduce critical software development timelines and to maintain design consistency.

The Moblas 7 and MLRS HP prototype systems were successfully tested in 1990. In 1991, the HP Upgrade was deployed to the remaining network operational Moblas systems and development started on HP Upgrades for TLRS 3, TLRS 4, and Hollas. The TLRS 3, TLRS 4, and Hollas HP Upgrades are expected to be completed in 1992.

In order to reduce the load on critical station manpower and computer resources, the HP data system was designed to provide fully automated data communications and data processing during multi-satellite operations. Figure 1 presents a simplified diagram of HP data system functions. The functions associated with real time tracking operations are divided between the controller and HP computers. Other Non real time HP functions, which include general station operations and automated post tracking functions complete the automated HP Data System Product Cycle. Depending on the number of observations in the pass, the HP Data System was designed to produce the normal point data product 1 to 5 minutes after the operator has closed out the operational data set. The time

required to compress the normal point data set and transmit the data product to headquarters is less than 1 minute.

The HP Data System has built in flexibility which allows interleaving of multiple satellite and calibration sets. The code has been written to allow for many different combinations of hardware settings. This has been accomplished via the use of different levels of ranging activity. By changing levels within the software, the operator may determine which calibration sets (with possibly different hardware characteristics) go with which satellite sets. Up to five different levels may be selected. This feature makes it possible to quickly switch from one satellite to another and back again using calibration sets which may be unique for each satellite. Figure 2 is an example of a single shift of Moblas 4 support scheduling multiple satellite and calibration operations. Scheduled ERS-1, Ajisai, Lageos, Etalon 1, Etalon 2, and Starlette passes are labeled E1, AJ, L1, MT, NT, and ST respectively. Scheduled calibration tracking is labeled C1. The activity scheduled at the bottom is the sum of scheduled satellite and calibration activities. The station is continuously ranging satellites or the calibration target for over 5 hours during the shift. The scheduling of multi-satellite operations has significantly increased the operational productivity of operational laser stations. Additional information concerning the scheduling of multi-satellite tracking operations is presented in another Eight International Workshop on Laser Ranging Instrumentation paper "SATCOP Mission Planning Software Package".

Control of all processing and maintenance operations is provided by a mouse and/or keyboard driven, user friendly multi-level menu interface. These menu controlled operations include data archiving, tuned IRV prediction communications, data product statistics review, station communications, semi-automated daily tracking operations reports, and other general station data communications. The user interface is written in the 'C' programming language and uses the Motif/x windows style and flavor. The use of this industry standard ensures that the user interface is consistent with other operating systems (in addition to UNIX) and is also consistent with widely available off-the-shelf commercial software.

The design prototype for the second "processing" computer system was a UNIX based HP 360 workstation. Low cost upgrades have brought the design prototype up the the current CDP SLR network configuration described in Figure 3. The HP 380 computer configuration includes two 332 MB hard disks to improve efficiency by directing data operations to one disk and operating system functions to the other disk. A 650 MB optical disk is included to provide on line data archiving, a efficient backup media, and to support major software system upgrades. The 67 MB cartridge tape is used as a low cost media for generating weekly full rate mailing tapes. The HP Paintjet printer supports local hard copy requirements. The 19.2k baud modem supports a wide range of station communication requirements including data communications and software system updates. The 16 inch color supports the X-Window environment and is the primary user control interface device for the HP Data System.

The Moblas, MLRS, TLRS, and Hollas systems all have unique controller computer hardware and software environments. Real time control functions may also vary station to station (MLRS is a lunar station, for example). The HP Upgrade development strategy was to minimize the impact on real time controller functions, requiring only real time data communications to the HP "processing computer" and off load as many non real time functions as possible from the controller to the "processing computer". A simplified functional block diagram for TLRS 3/4 is presented in figure 4. The controller

(or tracking) computer performance in managing the real time computer interfaces was a key technical design problem for each station type.

Real time applications were developed in C in the HP UNIX environment to record and manage the flow of raw data measurements from the controller computer to the HP 380. Automated C and Fortran applications assemble, screen, and prepare the raw data measurements for automated data processing. Based on inputs from the system operator, automated data processing functions start as soon as the raw data set is complete.

The HP UNIX software environment, with includes FORTRAN and C applications, was selected to make maximum use of existing operational software, provide multi-vendor hardware portability, and to provide a robust industry x window user interface for station operations. The HP Upgrade Project software strategy was to develop real time applications in C and other data system applications in FORTRAN to make the best use of current operational software. The station user interface was developed in the HP UNIX x window environment to make the best use of the HP 380 workstation resources in controlling station operations.

In order to meet the new station normal point data system requirements and maintain data system integrity, operational data system software was rehosted from VAX/VMS Fortran to HP UNIX Fortran. The field data processing system was designed to use identical data processing algorithms and to perform the same basic data processing and data quality control functions as the operational headquarters system. These data processing functions include quality control of raw data measurements, calibration data processing, computation of satellite ranging corrections, analytical satellite data fitting, and satellite data compression to form normal points. The field data processing system was designed to produce the same operational quality control statistics and data products as the headquarters system. These data statistics and data products were carefully benchmarked against the operational headquarters data system before the HP Data System was declared operational. Some software system utilities used in the VAX/VMS environment had to be replaced with equivalent HP UNIX utilities during software rehosting.

The HP Data System Upgrade has been successfully operating at Moblas 4, Moblas 5, Moblas 7, and MLRS for over a year, producing on site normal points, generated within minutes of operational satellite tracking. Starting in April 1992, multi-satellite operations were successfully integrated into the HP Upgrade Data System, contributing to recent record data production by Moblas 4 and Moblas 8. Upgrades to the HP workstation CPU's have been successfully accomplished in the field without software system modifications and have enabled the HP Data System to accommodate massive increases in data volume associated with multi-satellite operations and two shift network support for TOPEX. Remote software system updates have been performed using modem communications, without impacting station operations. The automation of the Data System has helped free up critical station manpower resources needed to sustain nearly continuous tracking operations associated with multi-satellite support. The HP Upgrade is the first major step in streamlining CDP SLR operations. Strategic technical planning to replace the controller computer, providing necessary computer resources to automate other station functions, is in progress. In addition, direct computer network communications to CDP SLR network stations is expected to be established in the near future, providing advanced communication resources to automate remote software system management activities and global data communications.

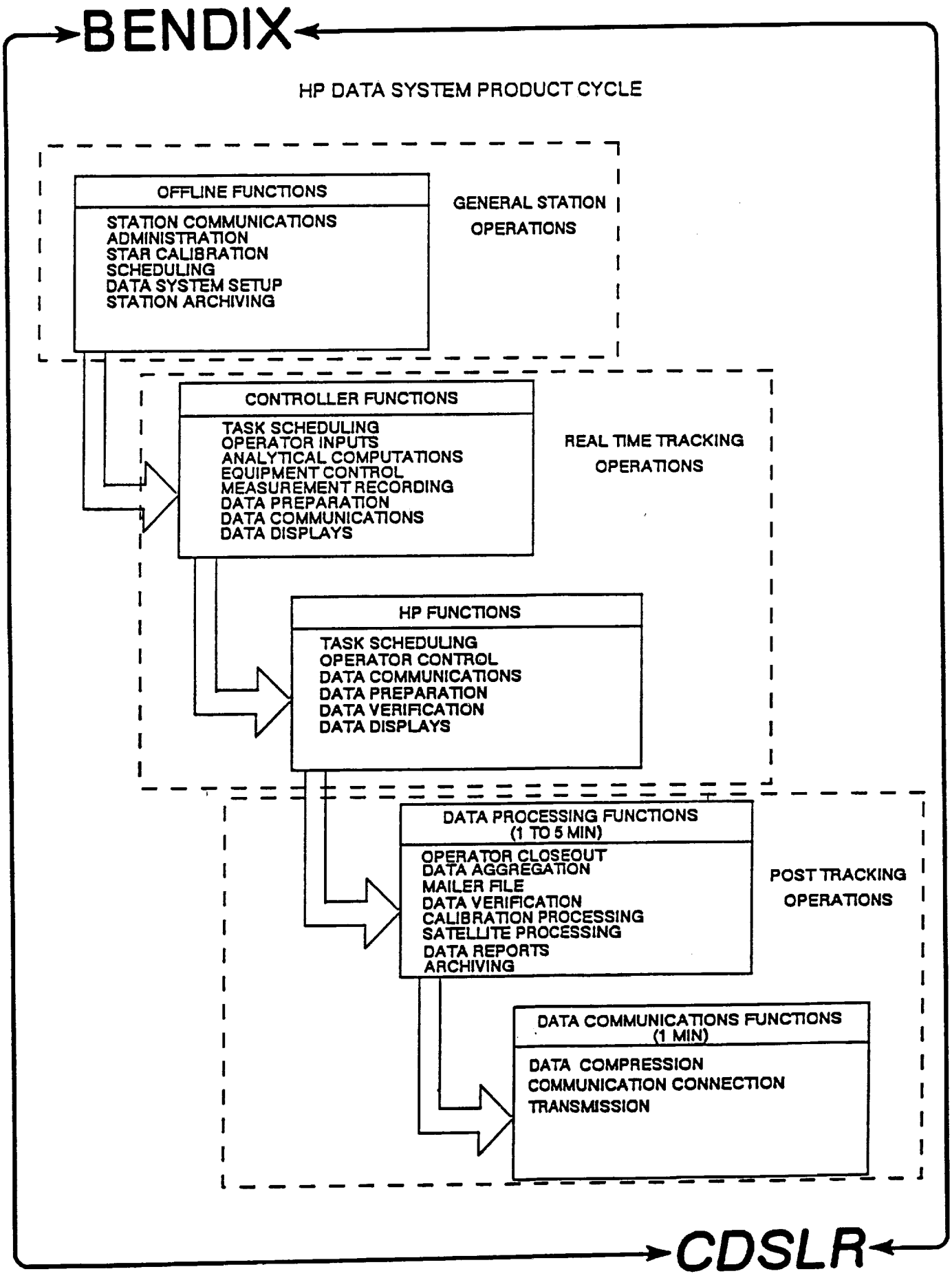
BENDIX
HP DATA SYSTEM PRODUCT CYCLE
OFFLINE FUNCTIONS
STATION COMMUNICATIONS
ADMINISTRATION
STAR CALIBRATION
SCHEDULING
DATA SYSTEM SETUP
STATION ARCHIVING
GENERAL STATION OPERATIONS
CONTROLLER FUNCTIONS
TASK SCHEDULING
OPERATOR INPUTS
ANALYTICAL COMPUTATIONS
EQUIPMENT CONTROL
MEASUREMENT RECORDING
DATA PREPARATION
DATA COMMUNICATIONS
DATA DISPLAYS
REAL TIME TRACKING OPERATIONS
HP FUNCTIONS
TASK SCHEDULING
OPERATOR CONTROL
DATA COMMUNICATIONS
DATA PREPARATION
DATA VERIFICATION
DATA DISPLAYS
DATA PROCESSING FUNCTIONS (1 TO 5 MIN)
OPERATOR CLOSEOUT
DATA AGGREGATION
MAILER FILE
DATA VERIFICATION
CALIBRATION PROCESSING
SATELLITE PROCESSING
DATA REPORTS
ARCHIVING
POST TRACKING OPERATIONS
DATA COMMUNICATIONS FUNCTIONS (1 MIN)
DATA COMPRESSION
COMMUNICATION CONNECTION
TRANSMISSION
CDSLR

FIGURE 1

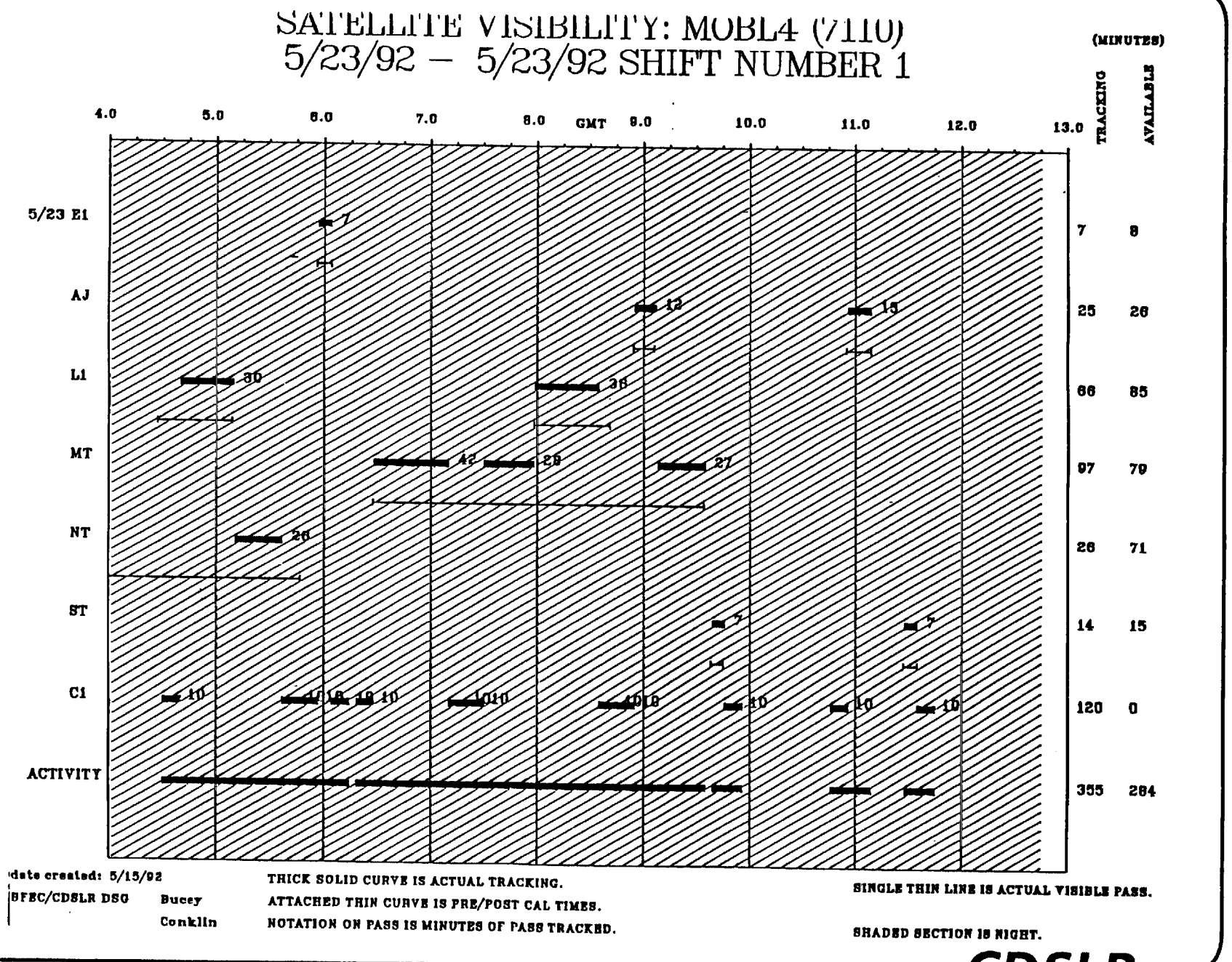
SATELLITE VISIBILITY: MOBL4 (7110)
5/23/92 – 5/23/92 SHIFT NUMBER 1
(MINUTES)
TRACKING
AVAILABLE
4.0
5.0
6.0
7.0
8.0
GMT
9.0
10.0
11.0
12.0
13.0
5/23 E1
AJ
L1
MT
NT
ST
C1
ACTIVITY
7
12
15
30
36
42
29
27
26
7
7
10
10
10
10
10
10
10
10
10
10
7 8
25 26
66 85
97 79
26 71
14 15
120 0
355 284
date created: 5/15/92
GFEC/CDSLR DSG
Bucey
Conklin
THICK SOLID CURVE IS ACTUAL TRACKING.
ATTACHED THIN CURVE IS PRE/POST CAL TIMES.
NOTATION ON PASS IS MINUTES OF PASS TRACKED.
SINGLE THIN LINE IS ACTUAL VISIBLE PASS.
SHADED SECTION IS NIGHT.

FIGURE 2

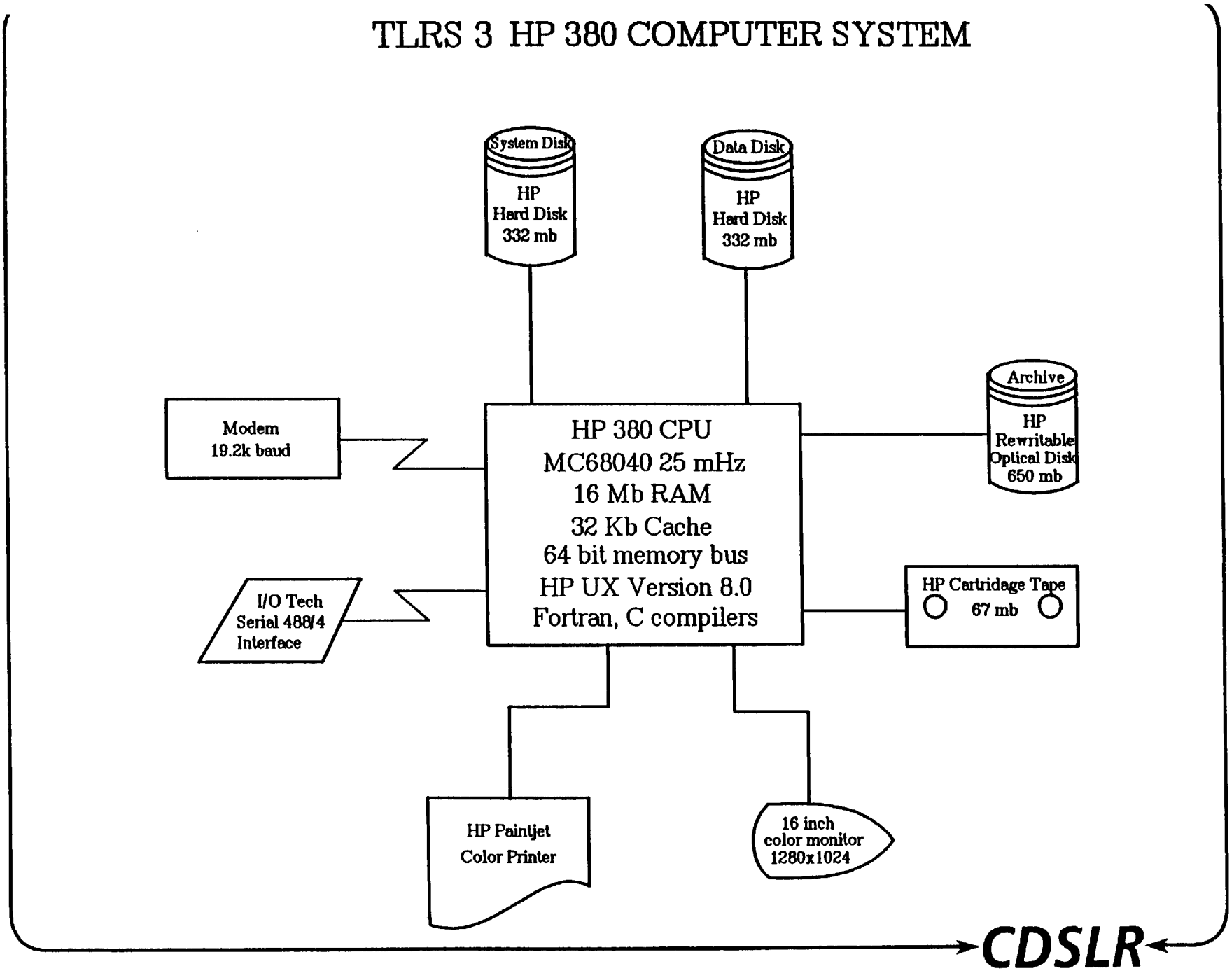
TLRS 3 HP 380 COMPUTER SYSTEM
System Disk
HP
Hard Disk
332 mb
Data Disk
HP
Hard Disk
332 mb
Archive
HP
Rewritable
Optical Disk
650 mb
Modem
19.2k baud
HP 380 CPU
MC68040 25 mHz
16 Mb RAM
32 Kb Cache
64 bit memory bus
HP UX Version 8.0
Fortran, C compilers
I/O Tech
Serial 488/4
Interface
HP Cartridge Tape
67 mb
HP Paintjet
Color Printer
16 inch
color monitor
1280x1024
CDSLR

FIGURE 3

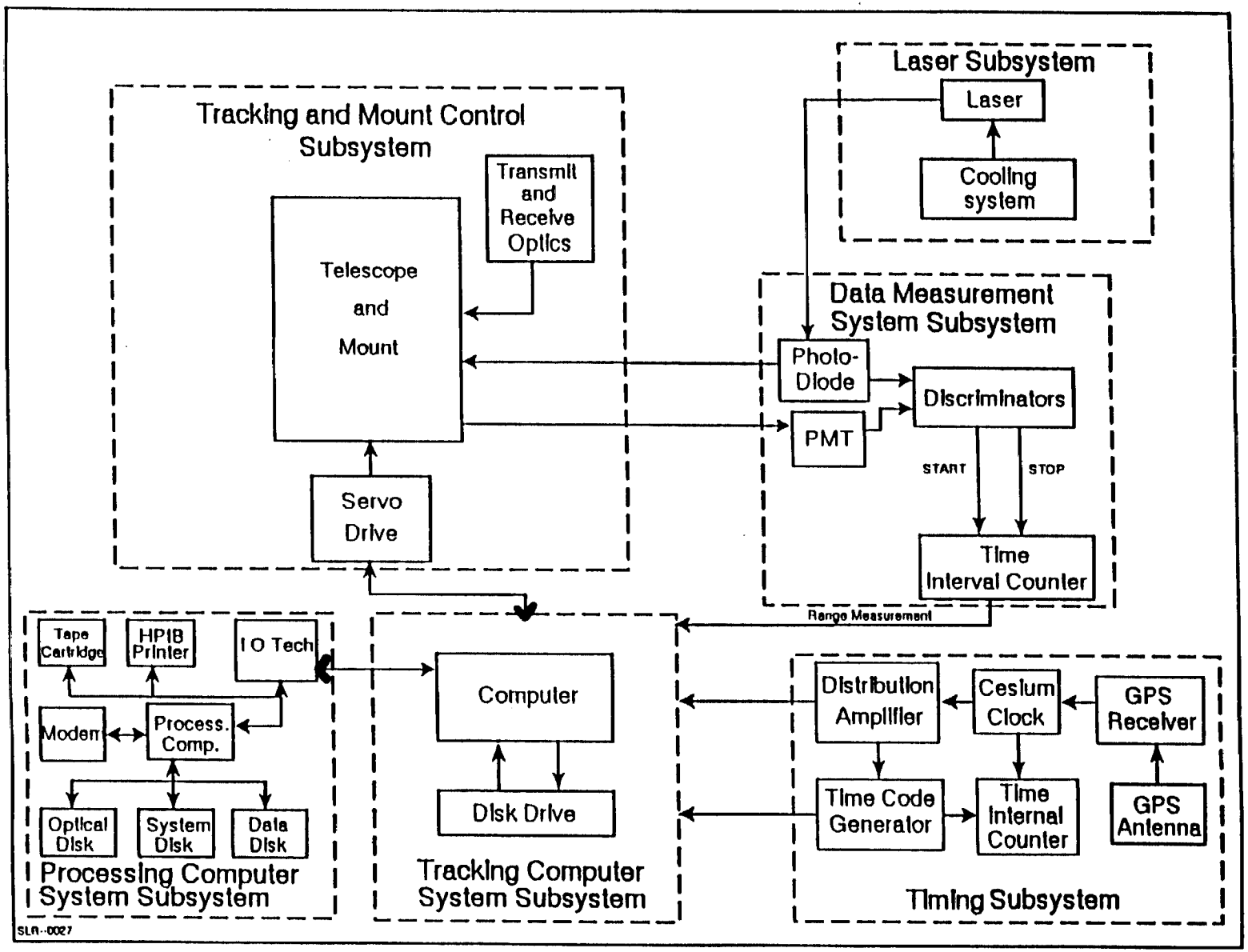
Laser Subsystem
Laser
Cooling system
Tracking and Mount Control Subsystem
Transmit and Receive Optics
Telescope and Mount
Servo Drive
Data Measurement System Subsystem
Photo-Diode
PMT
Discriminators
START
STOP
Time Interval Counter
Range Measurement
Tape Cartridge
HPIB Printer
IO Tech
Modem
Process. Comp.
Optical Disk
System Disk
Data Disk
Processing Computer System Subsystem
Computer
Disk Drive
Tracking Computer System Subsystem
Distribution Amplifier
Ceslum Clock
GPS Receiver
Time Code Generator
Time Internal Counter
GPS Antenna
Timing Subsystem
SLR--0027

FIGURE 4

APPLICATION OF THE ROBUST ESTIMATE IN SLR DATA PREPROCESSING

T. Detong, Z. Zhongping, X. Huaguan
Shanghai Observatory
Academia Sinica

J. Peizhang
Institute of Systems Science
Academia Sinica

ABSTRACT

M-estimator, one kind of robust estimator, has been used in SLR data preprocessing. It has been shown that the M-estimator has 50% or more breakdown point.

APPLICATION OF THE ROBUST ESTIMATE IN SLR DATA PREPROCESSING

Tan Detong, Zhang Zhongping, Xu Huaguan
Shanghai Observatory
Academia Sinica

Jia Peizhang
Institute of Systems Science
Academia Sinica

INTRODUCTION

There are three purposes in preprocessing from a pass of raw satellite range measurements:

a) Correcting system errors for raw SLR data and forming observational files;
b) Fitting a smoothing function to the range residuals from the predicted orbit, rejecting noises and outliers then estimating accurate for this pass;
c) Forming QL, FL and NP data files.

The second term is very impotant for data preprocess, because the smoothing function will have effect on quality of NP data.

The smoothing function we used is simply a polynomial in time. Generaly, the least squares(LS) estimation is used to solve the parameters of polynominal. But, the LS estimation is not a robust estimetion. Sometime, there are a large number of noises in raw SLR data, especialy those passes are in daylight, the solution of the LS estimation will converge to false values.

In this paper, M-estimator, one kind of robust estimator has been used in SLR data preprocessing. It has been shown that the M-estimators has 50% or more breacdown point ε^*. The breakdown point means that, when the probability of noises ε , increases to ε^* ,this method will fail.

M-ESTIMATOR

The linear equation is writen:

$$y_i = X_i^T \theta + e_i \qquad (1)$$

where

y_i are observations

θ is the vector of paramaters to be estimated
X_i is the vector of coefficients
e_i are random errors.

The M-estimator, called Maximum Likelihood Type Estimator, is such an estimator which makes the following objective function minimum:

$$\sum_{i=1}^{N} F\{(y_i - X_i^{\tau}\hat{\theta})/\sigma\} = \min. \tag{2}$$

$\hat{\theta}$ are values estimated for θ
σ^2 is variance
$F\{\cdot\}$ is an even function

Different objective functions have different M-estimator. In this paper we used Hampel estimator, here

$$F(r_i)=\begin{cases} \frac{1}{2} r_i^2 & |r_i| \le \lambda_0\sigma \\ \lambda_0\sigma(|r_i| - \frac{1}{2}\lambda_0\sigma) & \lambda_0\sigma < |r_i| \le \lambda_1\sigma \\ \frac{\lambda_0}{\lambda_2-\lambda_1}(\lambda_2\sigma|r_i| - \frac{1}{2}r_i^2) & \\ \quad -\frac{\lambda_1}{\lambda_2-\lambda_1}\frac{\lambda_0}{2}\sigma^2 - \frac{1}{2}\lambda_0^2\sigma^2 & \lambda_1\sigma < |r_i| \le \lambda_2\sigma \\ \lambda_0(\lambda_2+\lambda_1-\lambda_0)\sigma^2/2 & |r_i| > \lambda_2\sigma \end{cases} \tag{3}$$

$r_i = y_i - X_i^{\tau}\hat{\theta}$
$\lambda_0 = 3,\ \lambda_1 = 4,\ \lambda_2 = 6.$

Equation (2) can be rewriten as:

$$\sum_{i=1}^{N} X_i \Psi\{(y_i - X_i^{\tau}\hat{\theta})/\sigma\} = 0 \tag{4}$$

where

$$\Psi\{\cdot\} = F'\{\cdot\}.$$

Then

$$\hat{\theta} = \left[\sum_{i=1}^{N} X_i W_i X_i^{\tau}\right]^{-1}\left[\sum_{i=1}^{N} X_i W_i y_i\right] \tag{5}$$

and

$$W_i = \Psi(r_i/\sigma)/(r_i/\sigma). \tag{6}$$

From (3) we have

$$W(r_i/\sigma)=\begin{cases}1 & |r_i|\le\lambda_0\sigma \\ \lambda_0\sigma/|r_i| & \lambda_0\sigma<|r_i|\le\lambda_1\sigma \\ \lambda_0(\lambda_2\sigma-|r_i|)/(\lambda_2-\lambda_1)|r_i| & \lambda_1\sigma<|r_i|\le\lambda_2\sigma \\ 0 & |r_i|>\lambda_2\sigma\end{cases} \tag{7}$$

and

$$\hat{\sigma}^2=\frac{1}{N-p}\sum_{i=1}^{N}r_i^2 \tag{8}$$

p is number of the paramaters estimated.

When given the starting values θ_0 and σ_0 , we can solve $\hat{\theta}$ by (5), (6) and (7). The solution is then iterated between (5) and (8), until convergence of the object function.

$$|U^{j+1}-U^j| \;/\; U^j < 10^{-3}$$

here

$$U=\sum_{i=1}^{N}F\{(y_i-X_i^T\hat{\theta})/\sigma\}$$

j is the times of the iteration.

PROCEDURES

The predicted and observed ranges is R_c and R_o at each instant of observation T. After atmospheric correction, center of mass correction and delay calibration, we have the following range residual equation:

$$y_i=\Delta R_i$$
$$=a+b\dot{\rho}_i+e_i. \tag{9}$$

Where a, b are range bias and time bias.

$\dot{\rho}$ is the variability of range.

Reference show a mathod of caculation which have 50% breakdown point.

a) If totel observation data points are N , which are divided into n subgroups equaly and every subgroup inclodes four data points, as:

y_1	y_{n+1}	y_{2n+1}	y_{3n+1}
y_2	y_{n+2}	y_{2n+2}	y_{3n+2}
.....			

y_k y_{n+k} y_{2n+k} y_{3n+k}

.....

y_n y_{n+n} y_{2n+n} y_{3n+n}

n=N/4.

When noise numbers in raw obsrevation data are less then N/2, there must be a subgroup in which contains one noise point at most.

b) For the linear model as (9), we can find the linear estimated value of $\hat{b}_k$ for any subgroup k:

$$\hat{b}_k = \sum_{l=1}^{4} \beta_l y_l \qquad (10)$$

If $\hat{b}_k$ is no-bias, we have:

$$\left.\begin{aligned} &\sum_{l=1}^{4} \beta_l = 0 \\ &\sum_{l=1}^{4} \beta_l \dot{\rho} = 1 \\ &\text{and} \\ &\sum_{l=1}^{4} \frac{1}{\delta_l} \beta_l^2 = \min \end{aligned}\right\} \qquad (11)$$

where

$$\delta_2 = \delta_3 = 1$$

$$\delta_1 = \frac{T_2}{2T_1 + T_2} C \quad \text{(C is a constant to be selected)}$$

$$\delta_4 = \frac{T_2}{2T_3 + T_2} C$$

$$T_l = \dot{\rho}_{l+1} - \dot{\rho}_l \qquad (l=1, 2, 3)$$

By solving equations (11), we get:

$$\beta_l = \delta_l \lambda \tau_l \qquad (l=1, 2, 3, 4)$$

where

$$\lambda = 1 / \sum_{l=1}^{4} \delta_l \tau_l^2$$

$$\tau_l = \dot{\rho}_l - \dot{\rho}_0$$

$$\dot{\rho}_0 = \sum_{l=1}^{4} \delta_l \dot{\rho}_l / \sum_{l=1}^{4} \delta_l$$

$$C = \max\left[\frac{T_2 + T_3}{T_1 + T_2 + T_3}, \frac{T_1 + T_2}{T_1 + T_2 + T_3} \right]$$

Thus, the residuats of k-subgroup are

$$r_{kl}=y_{kl}-\hat{b}_k\dot{\rho}_{kl} \qquad (l=1, 2, 3, 4)$$

c) For each subgroup, the largest and smallest values of r_{kl} are rejeated. And we can get the initial values a_{ko}, b_{ko} from remained two data points through follows:

$$y_{kl}=a_{ko}+b_{ko}\dot{\rho}_{kj} \qquad (j=1, 2)$$

d) Then calcuiation the object function of M-estimate used all observations for every subgroups:

$$U_k=\sum_{i=1}^{N}F\{y_i-a_{ko}-b_{ko}\dot{\rho}_i\} \qquad (k=1, 2, \ldots n)$$

where $F\{\cdot\}$ can be taken from (3), and the initial value of σ can be arbitrarily given, for example 0.5 meters.

e) Select the minimum value from U_k $(k=1, 2, \ldots n)$. Suppose k=m, that is

$$U_m=\min.$$

Then a_{m0} and b_{m0}, those are taken from m-subgrop, can be used as the initial values a_0, b_0. It is sure that the a_0 and b_0 are taken from 'good' observation points.

f) Then we can get

$$r_i=y_i-a_0-b_0\dot{\rho}_i \qquad (i=1, 2, \ldots N)$$

$$\sigma_0^2=\frac{1}{N-2}\sum_{i=1}^{N}r_i.$$

Because a_0, b_0 are obtaied by two data points, they have just lower accuracy. From (5) to (8) and iterated until covergence, the accurate results a, b can be get as above.

g) After correcting range bias and time bias, we can get a polynomial in time as following:

$$\Delta\rho_i'=y_i-a-b\dot{\rho}_i$$

$$=a_0+a_1t_i+a_2t_i^2+a_3t_i^3+\ldots\ldots$$

Useing M-estimator, the parameters of polynomial $a_0, a_1, a_2, a_3\ldots\ldots$ can be solved.

CONCLUSION AND DISCUSSION

Comparing with the LS estimator, M-estimator has its advantage as follows:

a) It can be preprocess observation data that contain a large amount of noises, for example , a pass for LAGEOS in daytime are shown in fig 1, (12/20/1991 8:45 UT). In this pass rate of noise is up to 70%.

b) At same accuracy, the order of polynomial fitting is only 4 using M-estimator, while the order is up to 6-8 or more with LS estimator. Seeing table 1.

c) Noise mixed at the parts near the both ends of the curve can be detected and deleted.

Besides, comparison with the method of screen-processin and LS estimator, one third time is saved with M-estimator.

REFERENCE

J. peizhang On Joint Robust Estimation of The Parameters and The Variance. Acta Astronomica Sinica. Vol. 33. No 1. 1992.

Table 1.
Comparison for Two Estimators(Lageos)

Passes	M-estimator			LS-estimator		
	Order	RMS(cm)	Points	Order	RMS(cm)	Points
Y M D H						
92011011	4	5.8	28	8	5.9	29
92011110	4	5.9	778	8	5.7	752
92011120	4	5.1	452	8	5.4	419
92011317	4	6.0	216	4	6.6	212
92011321	4	4.8	170	4	5.0	169
92011416	4	4.6	169	8	5.1	169
92011419	4	5.9	94	8	5.9	86
92011512	4	5.4	457	8	5.8	453
92022216	4	6.2	187	8	6.1	183
92031116	4	5.6	326	8	6.1	326
92041514	4	5.3	425	8	5.9	422
92041616	4	4.9	419	8	7.0	417
92042011	6	5.6	60	8	5.3	56
92042018	4	5.3	41	4	5.8	41
92042613	4	5.1	583	4	6.4	585
92043015	4	4.1	77	8	5.3	83
92050815	4	3.1	91	8	2.9	91
92052114	4	2.7	212	16	2.7	210
92052312	4	2.6	170	12	2.5	170
92060216	4	3.2	503	8	2.9	471

Fig. 1.
Residual for A Lageos Pass in Daytime

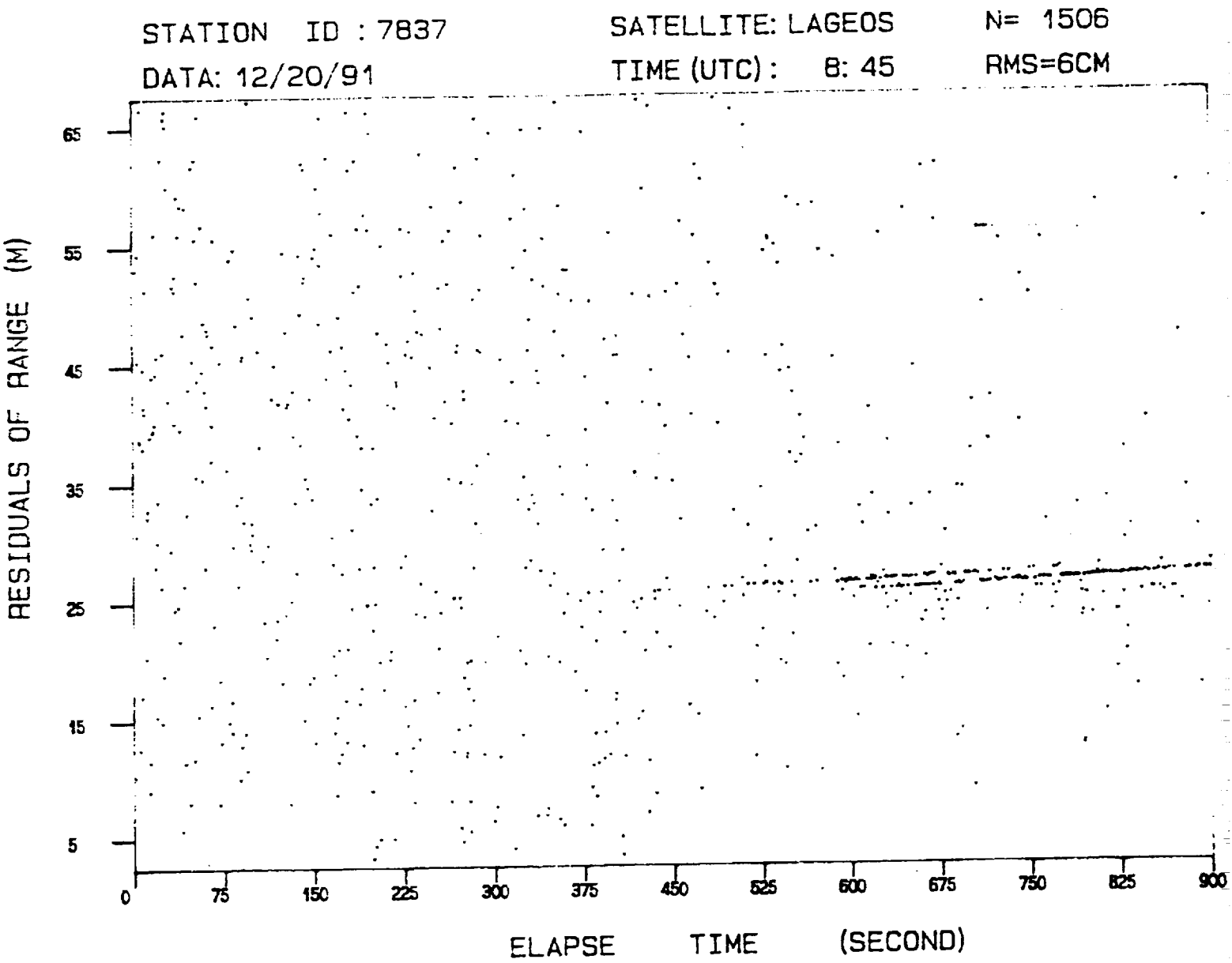

Lunar Laser Ranging

A Computer-Controlled x-y Offset Guiding Stage for the MLRS

by

P. J. Shelus, A. L. Whipple, J. R. Wiant and R. L. Ricklefs
McDonald Observatory, University of Texas at Austin, Austin, Texas 78712

and

Frank M. Melsheimer
DFM Engineering, Inc., Longmont, Colorado 80501

ABSTRACT

The MLRS has experienced excellent success in its lunar and artificial satellite laser ranging operations during its many years of operation, in spite of its relatively small "receive" aperture. We continue to strive, however, for a greater volume of data, together with better accuracy and precision. We have just now completed the design, construction, and implementation of a computer controlled x-y offset guiding stage for the MLRS, analogous to the manual one that had been a part of the original 2.7-m lunar laser ranging system on Mt. Locke at McDonald Observatory. In the past we had been hampered by the lack of a satisfactory hardware design which could fit within the very cramped quarters of the MLRS telescope's tailpiece. Recently, with funding support from the U. S. Naval Observatory and the design and construction expertise of DFM Engineering, Inc., a satisfactory instrument has been specified, designed, built, and installed. This instrument will greatly expand MLRS observational opportunities by allowing the observing crews to actively guide on visible off-axis lunar surface features or background stars while the on-axis lunar surface retroreflector targets are in the dark. This paper describes this instrument and its present implementation at the MLRS.

Introduction

The McDonald Observatory Laser Ranging Station (MLRS) is a dual purpose installation (Shelus 1985) which was designed to obtain laser returns from both artificial satellite and lunar surface retroreflector targets. It was originally constructed to replace the NASA Apollo Lunar Ranging Experiment (LURE) system which had been installed on the McDonald Observatory 2.7-m telescope in the late 1960's (Silverberg 1973) and was used up until the mid 1980's. The MLRS is designed around a 0.76-m x-y mounted Cassegrain/Coudé reflecting telescope and a very short pulsed, frequency doubled, 532-nm wavelength, neodymium-YAG laser, with associated computer, electronic, meteorologic, and timing interfaces. The station was initially erected in the saddle between Mt. Locke and Mt. Fowlkes at McDonald Observatory, near Fort Davis, in far west Texas and first became operational in the summer of 1983. It was soon recognized that wind tunnelling effects in and around this saddle site had very serious effects on what astronomers call atmospheric seeing. A new telescope pad was constructed and the MLRS was moved to its present site atop Mt. Fowlkes in early 1988 (Fig. 1).

Since the mid-1980's, the MLRS observing emphasis has been shifting dramatically from the Moon to artificial satellite targets (Fig. 2) but the Moon has always continued to be an important part of its routine operations (Shelus 1987). Also, attesting to the splendid versatility of the MLRS, in a cooperative effort with the CERGA lunar laser ranging facility in France, we are using the Meteosat P-2 geostationary weather satellite in a laser ranging experiment to study the transfer of time at the sub-nanosecond level over intercontinental distances. Most of the MLRS observing systems are transparent to the observer and it is often the case that through the course of a single 8-hour observing shift an observing crew will routinely range to such diverse targets as Topex/Poseidon, ERS-1, Starlette, Ajisai, Lageos, Etalon-1, Etalon-2, MP-2, and the Moon. The

Figure 1

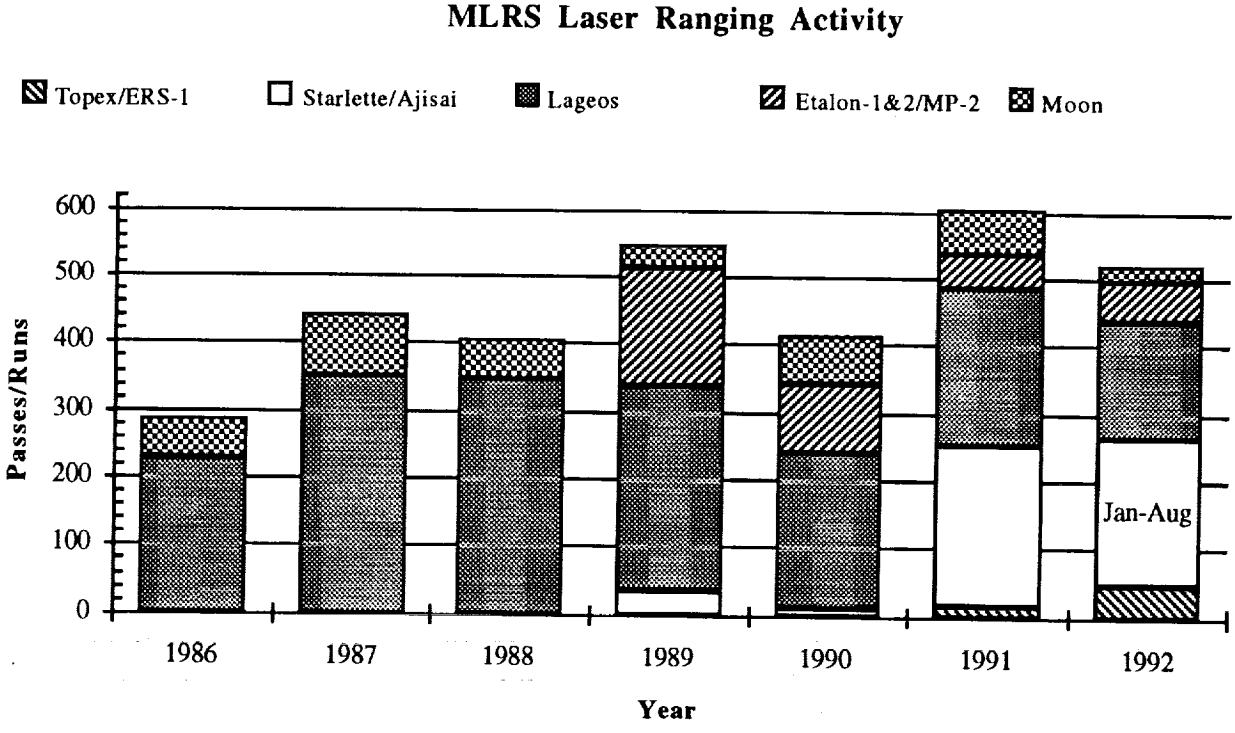

Figure 2

principal differences among all of these observations are the apparent angular speed of the target's motion across the sky and the return signal strength. Of course, low targets move quickly and high targets move slowly. Return signal strength is dictated primarily by the inverse-fourth-power nature of laser ranging. It is extremely important to realize that the return signal strength ratio, neglecting all parameters except the distance, for a near-Earth artificial satellite and the Moon is something like 3×10^{12}. That is to say, it is more than one trillion times more difficult to laser range to the Moon than it is to laser range to, say, Ajisai or Topex/Poseidon.

Increased Data Volume Requirements

In spite of these tremendous handicaps of low signal strength and small "receive" aperture, the MLRS has experienced remarkable success in its lunar laser ranging (LLR) measurements, and the resultant computation of lunar orbit and Earth orientation information therefrom (Whipple et al 1991). However, we are always striving for an even greater number of observations which will, in turn, naturally lead to better accuracy and finer precision. It is evident that we can increase MLRS LLR data volume in at least three ways:

1. spend more time on target;
2. transmit more energy;
3. increase "receive" aperture.

With support from a contract from the U. S. Naval Observatory we have found ourselves in a position to make a viable attempt at implementing the first technique, i.e., spending more time on target, via the design, construction, and implementation of an x-y offset guiding stage for the MLRS.

An Offset Guiding Stage

The concept of an offset guiding stage is one that is commonly used in observational Astronomy and it has surfaced many times during our deliberations about the logical up-grade of the MLRS during the past several years. It is merely the idea of installing an offset guiding stage on the MLRS, analogous to the one that had been in place and in use on the original 2.7-m LLR system at McDonald Observatory. An MLRS x-y offset guiding stage would allow us to routinely guide on a visible off-axis lunar surface feature (or, perhaps, even a star) while the on-axis retroreflector remains in the dark (i.e, it is on the "other" side of the lunar terminator). Not only would there be a much greater number of observing opportunities during the course of a lunation, perhaps, more importantly, ranging data to lunar surface retroreflectors in the dark would be virtually noise free. In our past plannings we had been hampered by the lack of a suitable hardware design which could fit within the very cramped quarters of the MLRS telescope's tail-piece, and the lack of money to actually construct and implement a design if a satisfactory one could be found. Recently, within our interactions with the U. S. Naval Observatory and DFM Engineering, Inc., support has been provided and a new concept has been formulated for just such an MLRS x-y offset guiding stage.

After a very successful series of bid and negotiating sessions, a contract was set up between the University of Texas at Austin and DFM Engineering, Inc. of Longmont, Colorado for design and construction of a x-y stage for the MLRS. Design drawings for the mechanical systems of the stage were received by us in February, 1992. These drawings were reviewed by McDonald Observatory Laser Operations personnel, with support from our McDonald Observatory mechanical engineering colleagues. In general, the overall design was found to be very well thought out and quite workable. A very small number of minor problems and several enhancements were identified during the review. These were conveyed to DFM, Inc. and were incorporated into the final design. Preliminary design drawings for the electrical systems of the

stage were received from DFM, Inc. at the end of March. An internal electrical systems design review which was held at the MLRS during the first week in April. The results of that review were conveyed to DFM, Inc. for implementation. Machining and assembly of the mechanical structures were completed in May at DFM, Inc.. Delivery of the hardware to Austin took place in June and initial testing and shake-down, before its shipment to the MLRS for final installation and implementation, was performed. The instrument was transported to the MLRS at McDonald Observatory in July. After a number of adjustments and relatively minor modifications, installation on the telescope took place at the end of August.

The instrument is a two-axis translation stage (Fig. 3) which mounts directly to the MLRS telescope's back-plate. It provides for the simultaneous mounting of two electronic TV cameras with turning optics to direct the telescope's Cassegrain beam to either of the cameras. The cameras are selectable from within the MLRS operation's trailer via computer control or an auxiliary switch. Each axis is driven by a DC servo motor/encoder combination at speeds in a range 0-8 mm/sec and is directly encoded using digital linear encoders. Positioning of each stage is accurate and repeatable to 5 microns with a travel of more than 125 mm in each axis, centered on the optical axis of the MLRS telescope. The electronics control package includes a dedicated PC-type computer based on an Intel 80386SX processor, a motor controller board inside the PC, together with all of the necessary electronic/computer interfaces and controls. Software provides a closed servo loop between the encoders and the motors and communicates with the external MLRS control computer via a serial port. In addition to the source code, the software deliverable includes the development environment as well, so that future software changes, if necessary, can be accommodated without a need to return to the vendor.

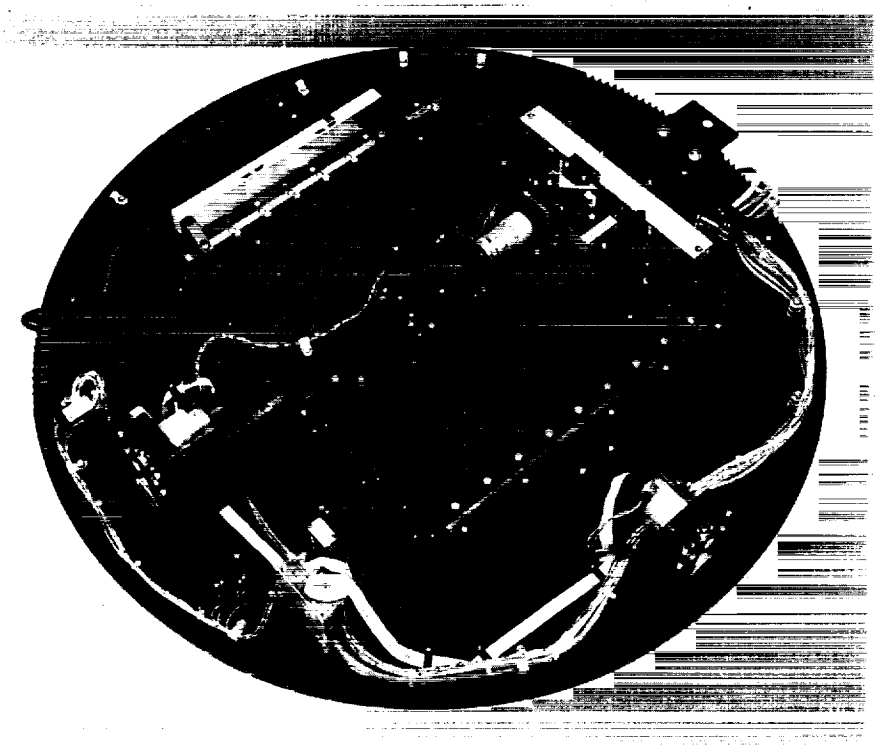

Figure 3

Conclusion

Once in operation, the completed x-y offset guider will have a very positive impact on the quality and quantity of lunar data acquisitions from the MLRS. Sufficient software currently exists to begin immediately the manual operation of the stage at the MLRS. In the coming months and years it is our plan that additional software and hardware will be secured for eventual sem-automatic and completely automatic operation of the stage.

References

Shelus, P. J. 1985, IEEE Trans. on Geosci. and Rem. Sens., Vol. GE-23, No. 4, p. 385
Shelus, P. J. 1987, Discovery, Vol. 10, No. 4, p. 33
Silverberg, E. C. 1974, Appl. Opt., Vol. 13, p. 565
Whipple, A. L., Györgyey-Ries, J., Ricklefs, R. L., Shelus, P. J., and Wiant, J. R. 1991, IERS Tech. Note 8, p. 87

Lunar Laser Ranging Data Processing in a Unix / X Windows Environment

by

Randall L. Ricklefs, Judit G. Ries
McDonald Observatory, University of Texas, Austin, TX 78712

In cooperation with the NASA Crustal Dynamics Project initiative placing workstation computers at each of its laser ranging stations to handle data filtering and normalpointing, MLRS personnel have developed a new generation of software to provide the same services for the lunar laser ranging data type. The Unix operating system and X-windows/Motif provides an environment for both batch and interactive filtering and normalpointing as well as prediction calculations. The goal is to provide a transportable and maintainable data reduction environment. This software and some sample displays are presented.

Introduction

The processes of reformatting, calibrating, filtering and normalpointing lunar ranging data has taken several shapes during the years of University of Texas McDonald Observatory participation in lunar laser ranging. During the days of the 2.7m ranging system, from 1969 to 1985, data was transferred on magnetic tape from the Observatory to Austin, where batch programs on the CDC Cyber computer systems were invoked on an entire month's data. After a good deal of interaction with line printer plots, listings, and punch cards, the data was finally processed and ready for mailing -- on punch cards or magnetic tape.

The part-time lunar ranging facilities on the 2.7m telescope were soon replaced by the dedicated lunar and artificial satellite ranging system MLRS (McDonald Laser Ranging System). From the first lunar observations in 1983 until mid-1990, data was processed interactively on Data General NOVA 4/X computers. There were restrictions as to the amount of computer memory and the speed of processing. Fortunately, the station contained 2 identical NOVAs sharing a hard disk, meaning that the lunar (or satellite) data could be processed on one computer while data was taken on the other. The reduction of the data was totally interactive and in no way automated. In addition, lunar predictions were produced on-site, another first in the effort to down-size historically mainframe-based applications. Extraction of earth rotation parameters was at one time attempted on site in near-realtime.

In 1988, the Crustal Dynamics Project SLR Computer Panel mandated the installation of Hewlett-Packard 9000/360 Unix workstations at each NASA-operated laser ranging station to relieve the aging controller computers of much of their data and communications handling responsibility and to provide on-site data filtering and normalpointing for a growing list of artificial satellite targets. This was seen by MLRS staff as an opportunity to provide a better lunar data processing environment as well.

A New Environment

One of the important goals of the computer panel was to provide a standard environment for data handling that would allow portable code to be written for a non-

proprietary system. To this end Unix as well as X windows were chosen for the software environment. Both of these products can be found on workstations and mainframes from many different vendors. Although there are many "flavors" of Unix, there is enough of a common thread, especially with POSIX, SVID , and other standards to allow fairly portable code to be written. In addition there are many useful tools generally available with Unix, from text editors to file manipulation utilities and operating system shells. The availability of shell scripts to create batch jobs has also eased the task of system development.

X windows (along with OSF/Motif) provide a network-oriented interactive graphical user interface that is quite portable and has been implemented on several operating systems. X-windows is policy free, meaning that there is no implied style imposed on code being written for this interface. The Open Systems Foundation (OSF) Motif graphical user interface was adopted to give a common style to this and other programs written for the X-windows environment.

Lunar Tasks

The process of obtaining lunar data requires several pre- and post-acquisition steps, which are at the heart of this discussion:

1) range and point angle predictions,
2) data calibration and reformatting,
3) data filtering,
4) data normalpointing.

Much of the software for tasks 1), 2), and 4) was implemented in a FORTRAN 66 variant on the NOVA as well as in FORTRAN 77, after a joint port with the Australian National Mapping organization. While the data filtering code also existed on the NOVA, it was not in a form that was readily usable on the Hewlett-Packard workstation. Common to all these steps is the need for a flexible user interface which handles entry of parameters, plotting of data, and display of processing results.

Predictions

The first task of any ranging system is to provide point angle and range predictions. Lunar ranging is no exception. Most of the code required to produce lunar predictions is also required in the production of the filtered lunar data and normalpoints, making the maintenance of code relatively straightforward. This software can use either the MIT/UT PEP ephemeris or the JPL DE-303 ephemeris and its successors. Lunar and planetary predictions as well as lunar librations are included in both of these packages. Since no fit of lunar or solar system parameters is made in the on-site processing, no partial derivatives are needed. Earth rotation data is updated weekly to provide the most accurate predictions possible.

Parameters to run this software are set in the Lunar Data Editor program. The prediction software itself is run automatically on a daily basis from a Unix "cron" script. The program reads the date and time, recognizes whether predictions already exist and produces predictions as appropriate for the next day. The prediction program can also be run interactively from the command line of a terminal window as well as from XControl, the main user interface program, but that is never done in production. Lunar predictions are moved to the ranging system control computer over an RS-232 serial link in the same way as the artificial satellite predictions.

Batch Analysis

The reduction of the lunar ranging data after the moon is observed starts with the same suite of programs as do the artificial satellite reductions. Once the data has been transferred from the controller computer and preliminary reformatting and collating of data has been done a shell script is initated to calculate and apply geometric and electronic calibrations, to filter the data using Poisson filtering techniques, and to normalpoint the data. (See figure 1.) The results of processing are then displayed using the Lunar Data Editor program, giving the crew can get an objective view of the quality of the ranging data.

Interactive Analysis

During the time when lunar data was being entirely reduced on-site with NOVA software, there was manpower available to scrutinize data. We no longer have that luxury. The lunar data is electronically transferred to Austin (using batch uucp over a dedicated line) for final filtering and lunar-network-oriented quality control.

To better interact with the data, the Lunar Data Editor (LDE) was developed. It uses X windows and OSF Motif to provide a modern environment in which to examine and process the lunar data. Pull down menus, pop-up windows as well as both histogram and scatter plots of the data are available for operator use. Figures 2-7 show portions of the user interface through which the user has control over the scale of the plots, the parameters used in the Poisson filtering and normalpointing and the sequence of reduction operations. Also included in the interface are provisions to manage up to 10 sets of station coordinates, lunar ephemeris parameters, and control parameters as well as 5 sets of lunar reflector coordinates. This capability permits easy changes among ephemerides and stations as the situation dictates.

LDE is comprised of several programs with distinct responsibilities. LDE itself is a C language program that handles the user interface, including parameter input and data display. The entire X-windows/Motif interface resides here. It in turn uses the Unix "system" call to invoke the lunar calibration program (C), the Poisson filtering program (FORTRAN), and the normalpoint program (which can also be called to recompute data residuals) (FORTRAN). This has the advantage of breaking up what would otherwise be a huge program into more manageable units. It also provides a way to integrate existing FORTRAN and new C programs in a portable manner. Error codes and messages returned by the called programs are used by LDE to provide pop-up error dialog boxes as needed. Results from each program's execution are shown in the scrolling text box at the bottom of the screen, as can be seen in figure 7. Each of the called programs can also be run individually from the command line, as they are in the batch file.

Since LDE is an X windows program, it can be run across a network. The program itself is run on the HP workstation, but the user can either be at the system console or, as is often the case, running the eXodus X windows server on a Macintosh connected to the workstation over the departmental ethernet network. One can even run this program across internet from thousands of miles away (with some degradation in speed) and still have the advantages of the graphics, pull-down menus and so forth.

It should be noted that none of the above discussion touches on performing quality control by comparing multi-run or multi-station data or the computation of earth orientation parameters from the data. Due to the origins and complexity of that code, it will remain on an IBM mainframe for some time to come.

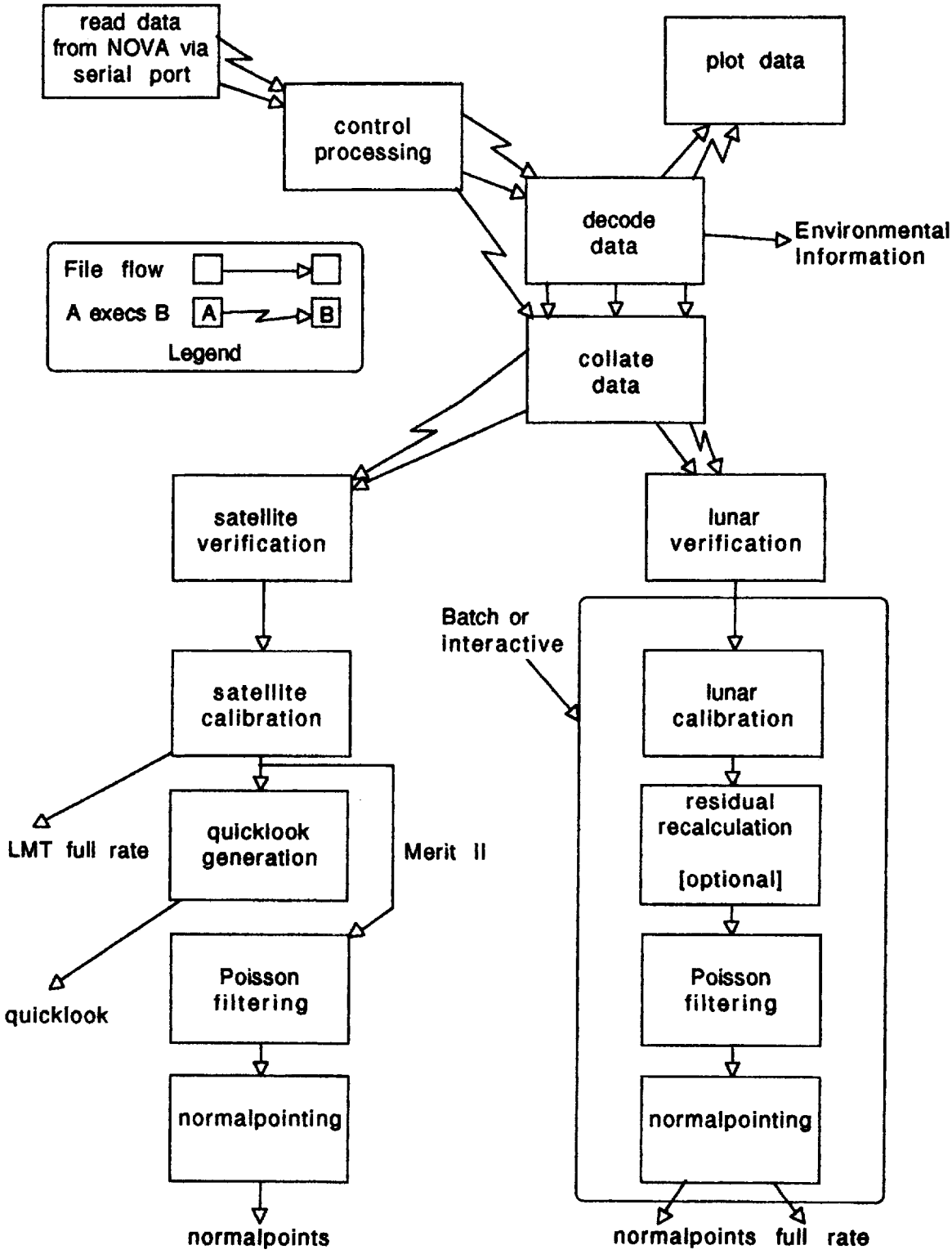

Figure 1 - MLRS Data Flow - HP Workstation

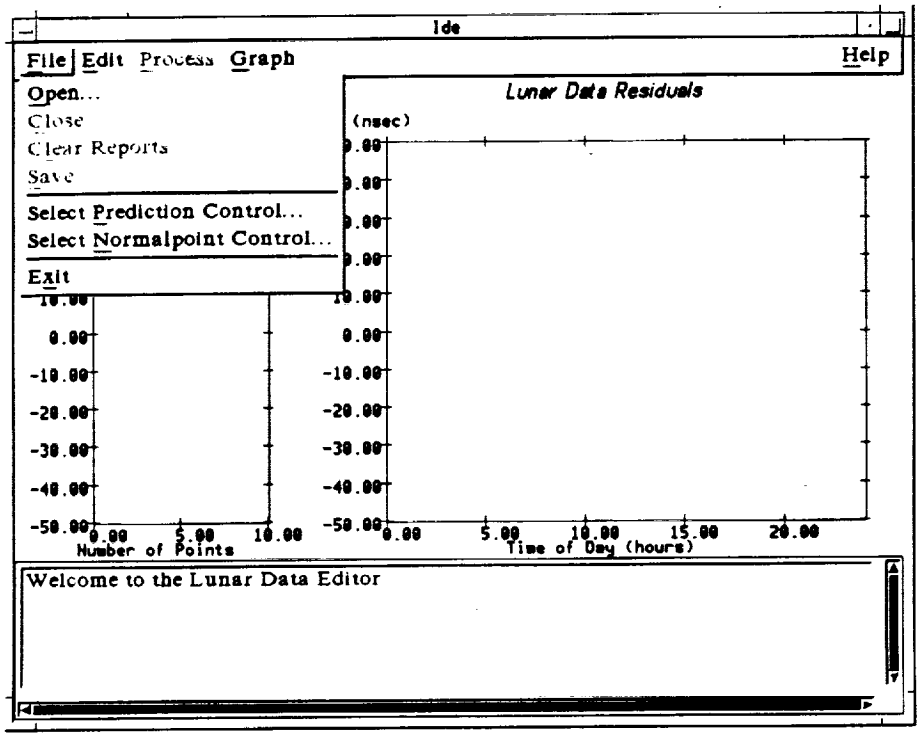

Figure 2 - Lunar Data Editor file menu

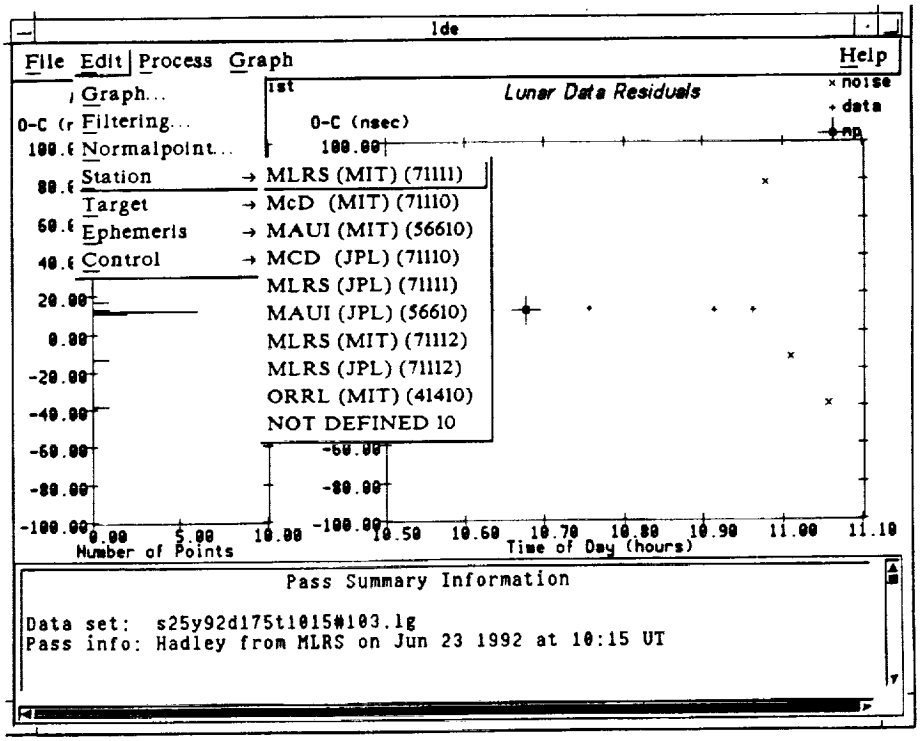

Figure 3 - Lunar Data Editor edit menu

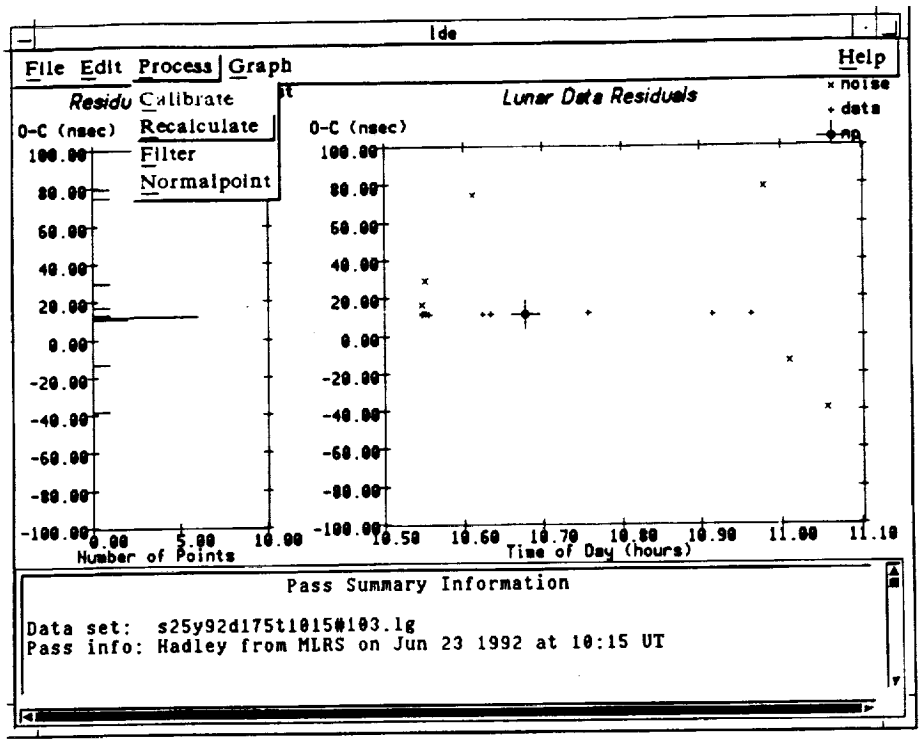

Figure 4 - Lunar Data Editor process menu

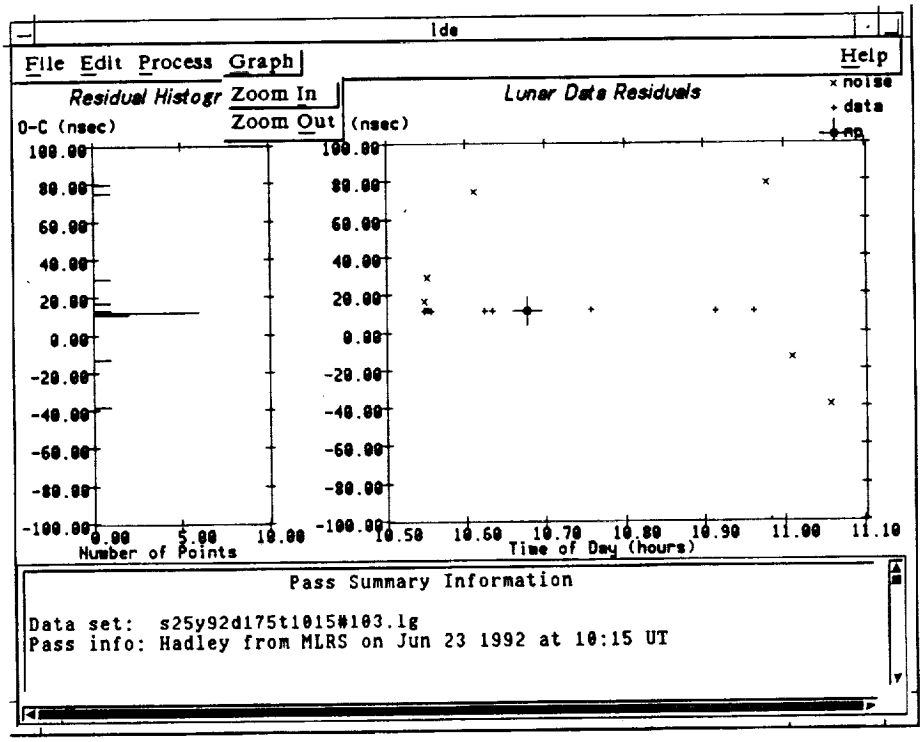

Figure 5 - Lunar Data Editor graph menu

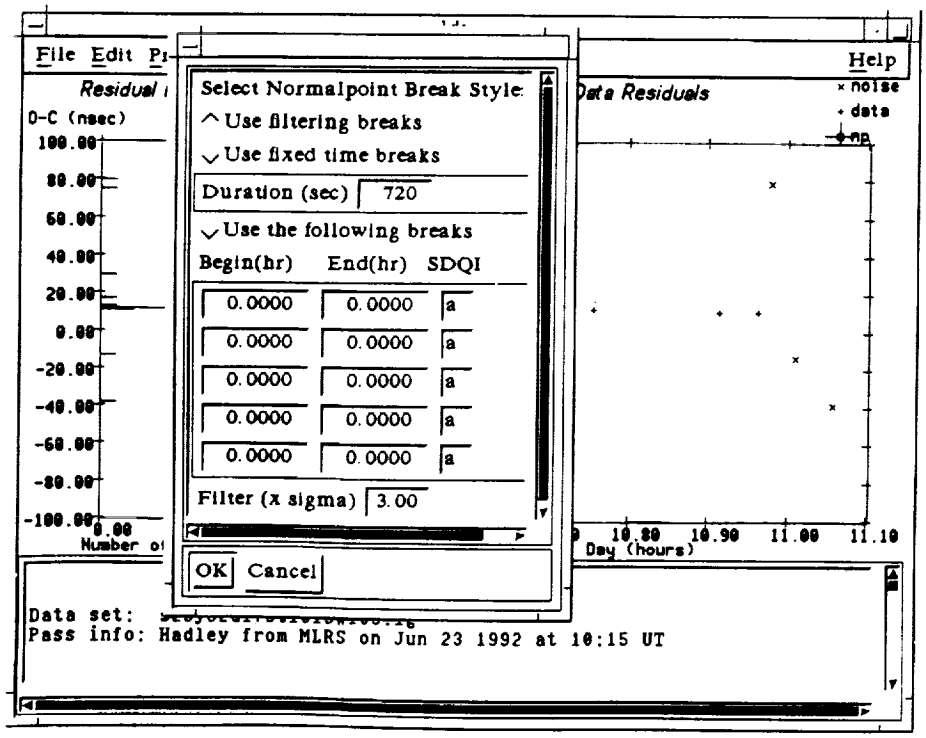

Figure 6 - Lunar Data Editor dialog box for normalpoint parameter edit

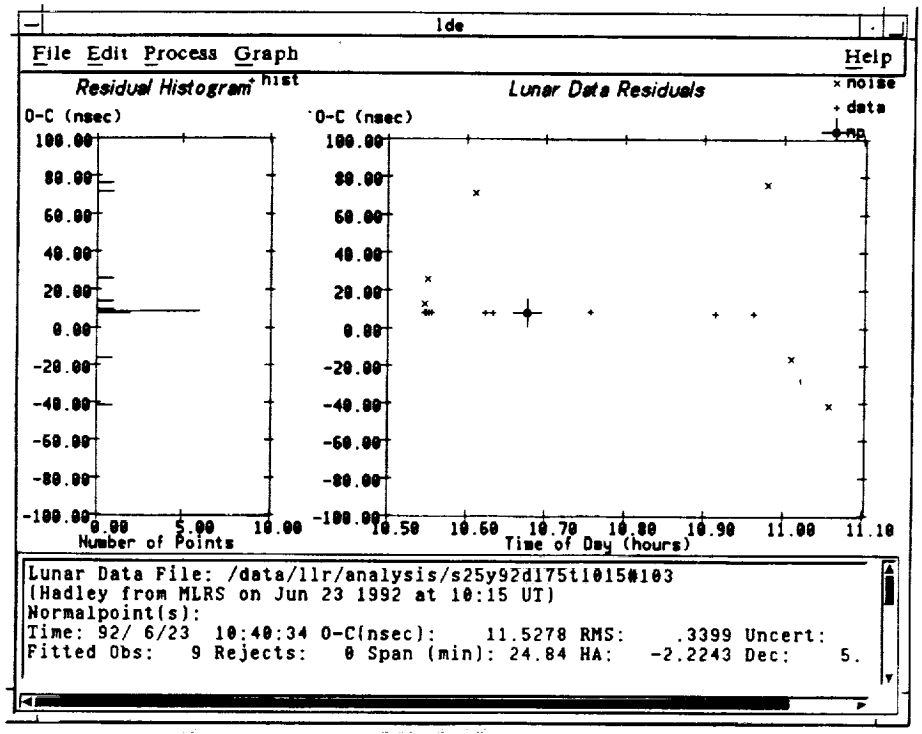

Figure 7 - Lunar Data Editor showing results of normalpointing

Conclusions

The lunar prediction and data analysis at McDonald Observatory have made several big transitions over the years, the latest being a successful move to a X windows/Motif graphical user interface and the Unix operating system. This move has proven to be worthwhile, producing more portable and flexible code and a network-based interactive data reduction environment.

LLR- Activities in Wettzell

U. Schreiber, J. Mueller[1]
Forschungseinrichtung Satellitengeodaesie
Fundamentalstation Wettzell
D - 8493 Koetzting

R. Dassing, N. Brandl, K. H. Haufe, G. Herold, R. Kahn, K. Roettcher, R. Stoeger
Institut fuer Angewandte Geodaesie
Fundamentalstation Wettzell
D - 8493 Koetzting

Abstract

Following the idea of a fundamental station, the Wettzell Laser Ranging Station was designed to range to all types of satellites and to the moon [1]. After obtaining the first lunar echos in October 1990, the system's operation was improved. A short report of lunar ranging activities is given.

1 Ranging to the moon in Wettzell

The WLRS was put to routine operation in the beginning of 1991. It was taking over the task of the old Sylvania Ranging System (SRS). In the beginning it was ranging to LAGEOS and the two ETALON satellites. However, the design was such that it should also allow ranging to the moon. This was shown very early, when in February of 1990 the first ranges from Meteosat P2 were obtained. Unfortunately it took more than half a year to stabilize the operation of this part of the ranging realtime software. For the measurements to the moon a cooled PMT (RCA C 31034a) and a spectral Fabry- Perrot bandpass of 1.5 $\AA$ width around a centerwavelength of 532 nm is used. The laser energy was measured to be 180 mJ with a pulse duration of 200 ps. As the telescope aperture is only 75 cm and the location of the WLRS is on an altitude of only 600 m, there is a poor signal to noise ratio for these measurements. For these reasons the WLRS is usually employing a semipulsetrain for lunar ranging. The semitrain contains 5 individual pulses, the first 3 of them are contributing most to the energy budget. The semipulsetrain gives the additional advantage of producing a known pattern of lunar returns within the random noise from other sources. Ranging to the moon from Wettzell is challenging as the noise counts are usually hiding the lunar returns. This requires a complex post ranging examination procedure, carried out at the Technical University of Munich, to analyse the measurements. At Wettzell LLR has a very high ranging priority. However there were only very few nights during the last year permitting lunar ranging. In these nights hardly any passage of LAGEOS or ETALON was lost as it takes only a few minutes to switch the WLRS from lunar mode to satellite mode and the lunar ranging was interrupted for a short while.

[1]Techn. Universitaet Muenchen, Arcisstr. 21 D - 8000 Muenchen 2

2 Echos from the moon

In figure 1 a successful measurement is shown. Clearly the pattern of the used semitrain can be seen. The high noise rate is also evident. There is a fixed spacing in time between the individual pulses in the semitrain. This separation is depending on the length of the laser cavity and can be measured independendly. For the WLRS laser the pulses are 6.902 ns apart. This relation can be used to fold the lunar returns from the second and the third pulse of the semitrain onto the main pulse to increase the number of returns in the normal point.

3 Status of the WLRS

The WLRS proofed it capability for lunar ranging. However, the ranging to the moon is very complicated and not very well supported by the ranging software, which only provides elementary features. At the present efforts are made to increase the signal to noise ratio and to support blind tracking. The goal is a more efficient use of the few useful observation nights per year in Wettzell.

We would like to thank the lunar ranging team in Grasse (France) for for their help.

References

[1] Schlueter, W.; Hauck, H.; Dassing, R.; Schreiber, U.; Mueller, J.; Egger, D.; *Wettzell Laser Ranging System (WLRS) — First Tracking Results to Satellites and to the Moon, paper presented at the Crustal Dynamics Project Meeting, held in Pasadena, spring 1991.*

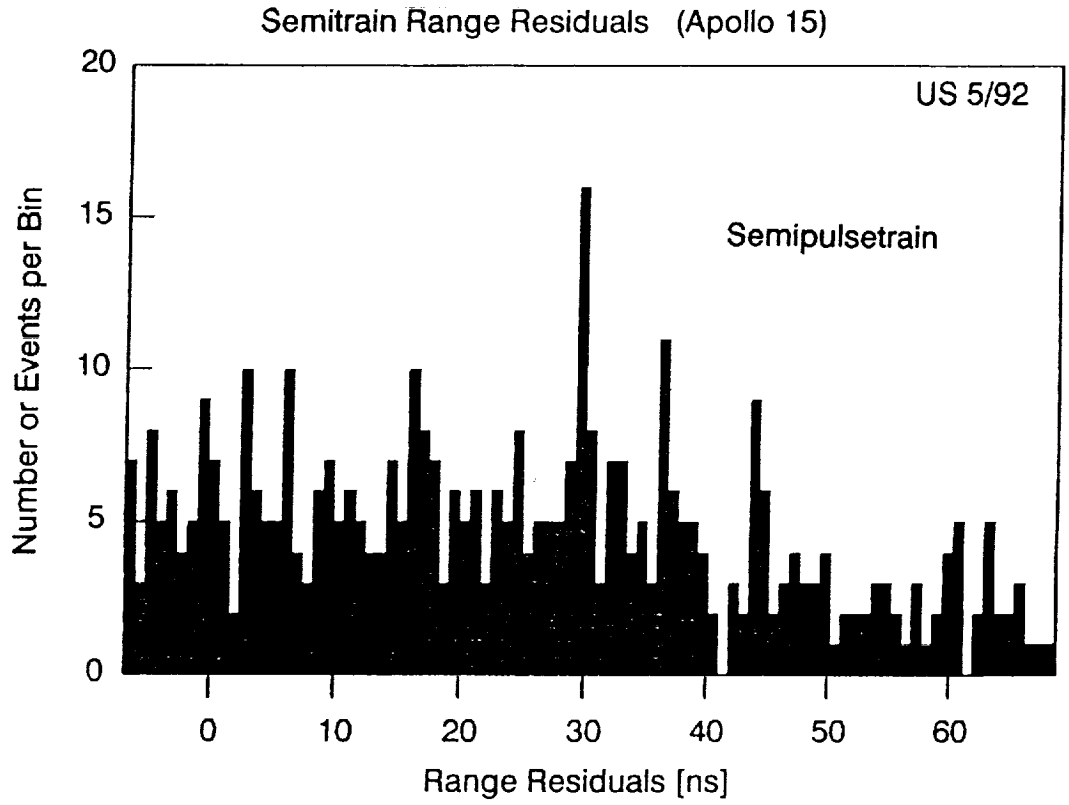

Figure 1: Histogram of the 'semitrain ranges' to APOLLO 15 during the night of Nov. 25th 1991. The session lasted 15 minutes

Fixed Station

Upgrades/Developments

N94-15601

MATERA LASER RANGING OBSERVATORY (MLRO); AN OVERVIEW

Thomas Varghese, Winfield Decker, Henry Crooks
Allied-Signal Aerospace Company
Bendix/CDSLR Network
Seabrook, Maryland 20706
U.S.A.

Giuseppe Bianco
Agenzia Spaziale Italiana/Centro di Geodesia Spaziale
Matera, Italy

Abstract:

The Agenzia Spaziale Italiana (ASI) is currently under negotiation with the Bendix Field Engineering Corporation (BFEC) of the Allied Signal Aerospace Company (ASAC) to build a state-of-the-art laser ranging observatory for the Centro di Geodesia Spaziale, in Matera, Italy. The contract calls for the delivery of a system based on a 1.5 meter afocal Cassegrain astronomical quality telescope with multiple ports to support a variety of experiments for the future, with primary emphasis on laser ranging. Three focal planes, viz. Cassegrain, Coude, and Nasmyth will be available for these experiments. The open telescope system will be protected from dust and turbulence using a specialized dome which will be part of the building facilities to be provided by ASI. The fixed observatory facility will be partitioned into four areas for locating the following: laser, transmit/receive optics, telescope/dome enclosure, and the operations console. The optical tables and mount rest on a common concrete pad for added mechanical stability. Provisions will be in place for minimizing the effects of EMI, for obtaining maximum cleanliness for high power laser and transmit optics, and for providing an ergonomic environment fitting to a state-of-the-art multipurpose laboratory.

The system is currently designed to be highly modular and adaptable for scaling or changes in technology. It is conceived to be a highly automated system with superior performance specifications to any currently operational system. Provisions are also made to adapt and accommodate changes that are of significance during the course of design and integration.

MLRO : An Overview

Objective: Build a state-of-the-art, multi-purpose, laser ranging observatory in Matera, Italy

General Features

- Day and night automated ranging capability on all CCR-equipped satellites (> 400 km) and the moon
- Application of state-of-the-art technology in all sub-systems
- Real time calibration and interleaved multi-satellite tracking
- Multicolor ranging capability
- Advanced computing environment and data analysis tools
- Computerized documentation, with features such as relational database, expert system and hypermedia text

System Specifications

- LAGEOS ranging :
  Single shot precision : ~5 mm
  Normal point precision : <1 mm
- Low orbit satellite (ERS-1, Starlette, etc.) :
  Single shot precision : 3 - 5 mm
- Lunar ranging :
  Single shot precision : ~1 cm
- Real time calibration/ground ranging :
  Single shot precision : <=2 mm
- Range accuracy: Better than 2mm

MLRO : An Overview

Telescope

- Near diffraction limited afocal Cassegrain telescope with a 1.5 meter primary and a 10 centimeter secondary; combination of a tertiary mirror and coude optics for transmission/reception
- Broadband coating for maximum spectral response from UV to near-IR
- Maximum slew rate :
  Azimuth axis : 20 degrees/second
  Elevation axis : 5 degrees/second
- Multiport system for other experiments

Laser

- Diode pumped laser for injection seeding
- Regenerative amplification followed by power amplifiers
- Pulse duration : <125 psec
- Pulse energy (532 nm) : >200 mJ
- Repetition rate : >=10 Hz
- Computer controlled beam divergence
- Modularity for energy scaling / multi-wavelength generation
- Laser firing stability : better than 20 nsec

MLRO : An Overview

Control System

- Software in high level languages
- Automatic recording of all operational parameters
- Automated star calibration, mount modelling
- Computer-assisted optical alignment and verification
- Distributed data acquisition, processing, and control
- Advanced computing/control environment
- Automated system/sub-system simulation and debugging

Transmit/Receive Electronics

- Detection : High Q.E, high speed MCP-PMT/APD
- Signal processing :
  - Speed : 1 - 5 GHz
  - Dynamic range : 20
  - Jitter : <10 psec
- Event timer :
  - Clock frequency : 200 - 1000 MHz
  - Verniers : 4 - 8
  - Time resolution : 1 - 2 psec
  - Accuracy : 5 - 10 psec
  - Jitter : 10 - 20 psec
- Clock : Cesium with disciplined oscillator
- Gating : Range gate adjustable from 10 nsec to 10 μsec

MLRO : An Overview

Current Status (Sept 1992)

- ASI and Bendix proceeding with negotiation/finalization of contract
- Estimated contract start in December 1992
- MLRO delivery in 42 months

N94-15602

PERFORMANCE OF THE UPGRADED ORRORAL LASER RANGING SYSTEM

John McK. Luck
Orroral Geodetic Observatory
Australian Surveying and Land Information Group
Department of Administrative Services
PO Box 2, Belconnen ACT 2616, Australia

1. Upgrade Arrangements

An Agreement 'being in respect of a project to develop Laser and Control Systems Upgrade to Orroral Laser Ranging System' between Electro Optic Systems Pty.Ltd. (EOS) and The Industry Research and Development Board (IRDB) of the Commonwealth Department of Industry, Technology and Commerce was signed on 23 March 1990. On the same day, a corresponding 'Agreement for Collaborative Research and Development of Laser and Control Systems Upgrade to Orroral Laser Ranging System' between the Australian Surveying and Land Information Group (AUSLIG) of the Commonwealth Department of Administrative Services and EOS, was signed. Under these Agreements, the research and development costs were shared between the three parties according to a standard IRDB formula, with AUSLIG having the option to purchase the prototype for its residual value upon successful demonstration. IRDB involvement was directed towards fostering export-oriented Australian high-technology industry.

The old system was de-commissioned on 6 March 1991, although preparatory work such as moving the laser and installing the heads and capacitor banks necessary for conversion to Active-Active mode was completed prior to that date. LAGEOS I was acquired a month later, on 10 April, and AJISAI on 12 April 1991 in Orroral's first-ever attempt at a 'low' target. The following eight months were spent in debugging and refining the new system and preparing for the ill-fated attempt to measure the geodetic baseline between the Orroral Laser Ranging System (OLRS) and the Saudi Arabian Laser Ranging Observatory (SALRO) set up at the Camberra Deep Space Communications Complex, Tidbinbilla to complement terrestrial and GPS surveys and to link SLR at Orroral with VLBI at Tidbinbilla.

The upgraded OLRS was deemed by AUSLIG to be operational from 1 January 1992, and final payment to EOS for purchase of the residual prototype was made in June 1992. A contract for software maintenance and further development was awarded to EOS in November 1992.

2. System Prior to 1991

The original system was the Orroral Lunar Laser Ranger (LLR), lent to the Division of National Mapping (Natmap) in 1973 under a Memorandum of Understanding involving NASA, Smithsonian Astrophysical Observatory and US Air Force Geophysical Laboratory. It was upgraded to include ranging to artificial

satellites under a contract from NASA signed in 1981, the first returns from LAGEOS-I being acquired in mid 1984. Some verified returns from the moon were received in 1985, and ranging to ETALON I & II started in 1990. It was not really possible to expect results for two-way ranges less than 35 milliseconds, which is one of the main reasons for embarking on the upgrade being described here.

Note : Natmap was merged with another Commonwealth agency in August 1987 to form AUSLIG.

DOME : The 9 metre diameter hemispherical dome by Ash Domes of Plainfield,IL was installed atop the original cylindrical Observatory building in 1973. Its AC motors for rotation during observing were manually controlled by a Left-Off-Right lever.

TELESCOPE : 1.5 metre aperture Ritchey-Chretien reflecting telescope, optics by University of Arizona. The tailpiece at the Cassegrain focus carries an eyepiece mounted on an X-Y stage for star observations and to facilitate offset guiding for lunar ranging.

The telescope is used both for transmitting and for receiving. It is depicted in figure 1.

TELESCOPE MOUNT : The telescope tube is by Astro Mechanics of Austin,TX. The original equatorial mount was replaced in 1981-2 by an X-Y ("alt over alt") mount by Contraves, and a Coude Path and the Contraves MPACS drive and readout systems were added. The drive accuracy is better than 0.002 degrees and encoder resolution is 0.0001 degrees.

An interface/controller was built, and all interface drivers and control and mount modelling software were written, by Natmap.

COUDE PATH : The Coude path incorporates a Matching Assembly consisting of two lenses whose combined focal point coincides with the focal point of the telescope. These lenses are in the East bearing of the telescope's inner axis. The Coude path connects the telescope with the laser, transmitter and receiver assemblies which are mounted on Newport optical benches in environmentally stable rooms. A Times 5 Beam expander by Special Optics,NJ on the Coude bench expands the transmitted beam prior to injection to the telescope through mirrors in the North bearing.

TRANSMIT/RECEIVE ASSEMBLY (T/R) : A rotating aluminized mirror with two holes in it, co-rotating 'dogbone' holding two ND filters and CAMAC-controlled stepping motors constituted the T/R assembly purchased from McDonald Observatory,TX in 1983. Laser firing was triggered by optically sensed notches in the rim of the rotating mirror.

The mirror was replaced in 1987 by an 'Appler mirror' in which the holes were just glass left uncoated (glass-hole), and which permitted positive, unambiguous ranging to a ground target and,

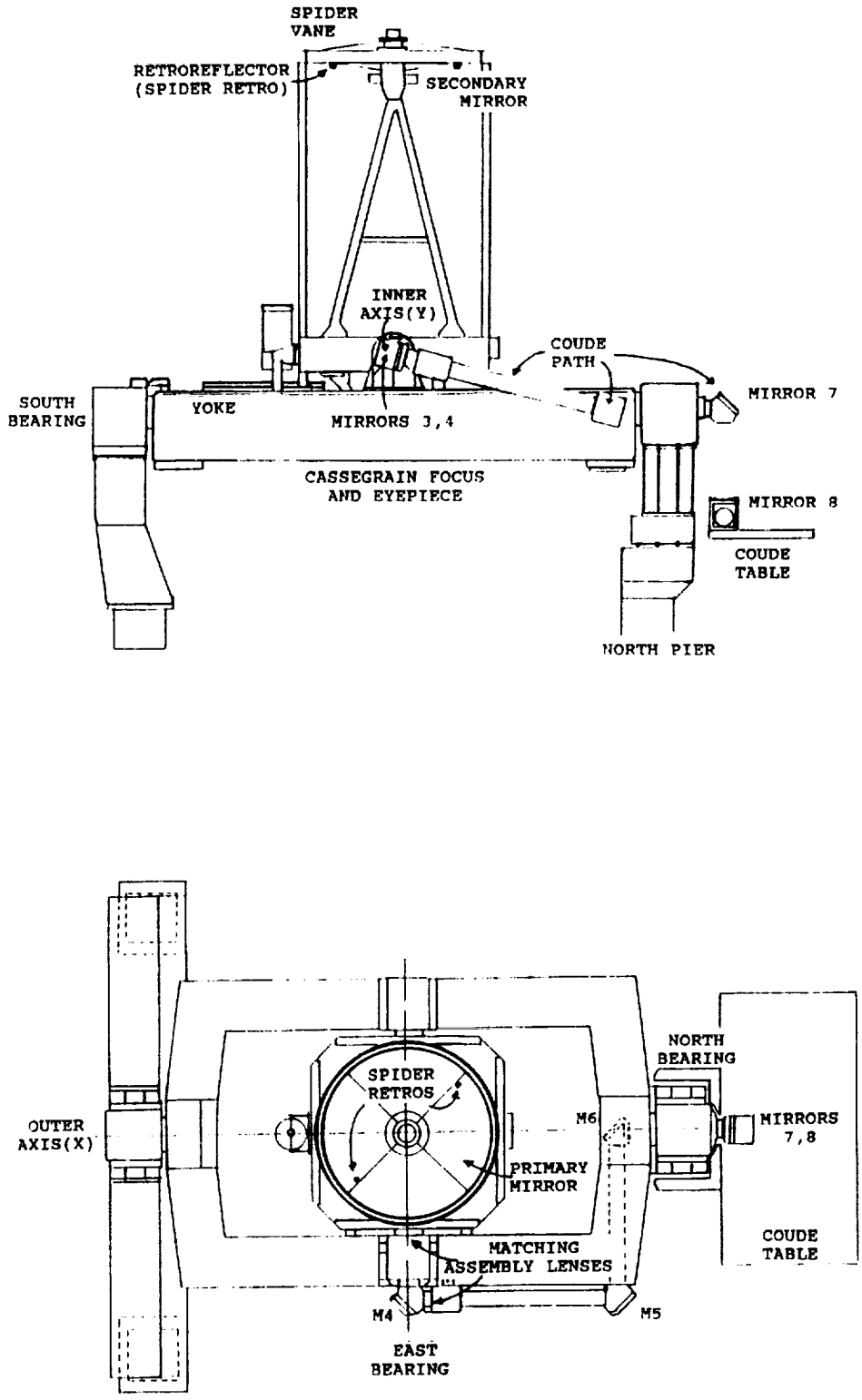

Figure 1: Orroral Laser Ranging System telescope - elevation and plan. (Derived from Contraves 'NLRS Telescope Manual.)

for real-time internal calibrations, to geodetically accessible retro-reflectors placed on the spider vanes holding the telescope's secondary mirror.

The interface was controlled by the CAMAC bus system, and driver and high-level software was written by Natmap in collaboration with the University of Texas.

RECEIVER/DETECTOR : A light-tight box containing a turret of 5 pinholes (spatial filters), a turret with a 10 A^{o} filter and a hole, focussing optics and detector mount was provided by McDonald Observatory. The detector mount was replaceable by an eyepiece for star alignments.

The detector was an RCA 31034A PMT until 1986, when the first of a series of ITT F4129f z-plate MCP PMTs was installed.

LASER : A Quantel YG 402 DP Nd:YAG laser frequency doubled to 532nm output wavelength was purchased as part of the 1981-3 upgrade. Its Q-switching and pulse slicing were accomplished passively, the mode locking being active/passive. Two amplifiers combined to produce in excess of 250mJ per pulse at ten pulses per second when needed. The pulse slicer was replaced by a Quantel solid-state slicer model SPS411 in 1987.

The laser was removed from its Quantel plate in the Coude room and relocated to an RF-shielded room one floor lower in the Observatory building in August 1990. Its components were bolted directly to a Newport optical table.

[The original Hughes 6943A^{o} ruby laser of the Orroral LLR prior to 1981 was bolted to the side of the telescope tube.]

LASER RANGING CONTROLLER (LRC) : This main interface/controller was designed and built by Natmap. It set windows and gates, controlled laser firing, and managed the epoch timing system.

EPOCH TIMING SYSTEM : Range measurements were accomplished by measuring the 'epoch' (time of day) of separate events, rather than depending upon a Time Interval Counter. The LRC time base was driven by a high spectral purity Oscilloquartz 2200 quartz frequency standard at 10MHz, and its clock synchronised at the start of each pass to an external Hewlett-Packard caesium beam frequency standard whose own clock was kept within 1 microsecond of UTC. The LRC Clock was used to time tag events to 100 nanosecond resolution.

Each laser shot produces at least three events to be time tagged: start diode pulse, internal calibration pulse from MCP/PMT, and one or more satellite returns from MCP/PMT (the quest to detect more than one 'satellite' return per shot was abandoned in the mid-1980's). The epoch timing system philosophy theoretically enables many events to be recorded per shot using identical equipment, limited only by instrumental reset/read times.

Two channels were used in practise to obtain fine resolution, one for start diode and one for MCP/PMT. Each comprised a separate channel of the Tennelec 454 Quad Constant Fraction Discriminator (CFD), a LeCroy 4202A Time to Digital Converter (TDC), and a pair of 8-channel LeCroy 2228A TDCs as verniers covering different 50ns sections. The 8 78-picosecond resolution channels of each 2228A were majority voted and meaned to improve resolution to about 28ps. A standard calibration routine was run with each pass to relate the intrinsic 2228A delays to each other, with the scale factors being calibrated periodically against the 4202A TDCs.

All TDCs were read via the CAMAC bus system. Software for these tasks was written by Natmap.

RECEIVE ENERGY MONITOR : A LeCroy 2249A Analog-to-Digital Converter (ADC) ('charge digitiser') was installed on the MCP line in March 1990. It is controlled and read through the CAMAC bus system, and is gated by the 'AND' of the range gate window and of the discriminator output pulse delayed appropriately. Its input signal is amplified by a Stanford Research SR440.

OPERATING SOFTWARE : Apart from the lunar prediction package based on EULER and the satellite prediction package based on IRVINT, which were imported with the aid of Randall L. Ricklefs, all interface drivers, control and operations software, predictions, post-processing, mount modelling, simulation and test software was written by Natmap.

SYSTEM CALIBRATION : Until the end of 1987, the internal calibration pulse was picked off each transmitted laser pulse by a minutely reflecting 'feedback plate' in the T/R box and fed to the MCP/PMT through ND filters in the co-rotating 'dogbone'. The optical and electronic delays between this feedback plate and the epoch timing system were thus well calibrated, but the delay between the feedback plate and the system reference point was not well known, so it was not possible to assess system accuracy properly as it was found impossible to measure or even estimate the length of the convoluted Coude path (with its five refracting elements as added complications) to better than 10cm.

The advent of the 'Appler mirror' in 1987 made it possible to range to the 'Spider Retros' simultaneously with distant targets. The effective reflection points of the retro-reflectors were related to the instrumental reference point and external survey marks early in 1988 with 3mm accuracy by precise survey, enabling accurate correction constants to be calculated.

A ground target was installed at a distance of 1.1km across a valley in November 1987, and surveyed in along with 'Spider Retros'. A session of ranging to this target accompanied each LAGEOS-I pass, and provided a check on the accuracy of the correction constants referred to above. It is also invaluable for assessing such things as the effect of signal strength on range accuracy and the actual precision obtainable at any given time.

3. Elements of the Upgrade

DOME : Automated rotation was provided through hardware and interface controllers. Two DC variable-speed motors were installed in 1991 and new variable-speed controller, interface and software are now under development.

TELESCOPE and COUDE PATH : Not affected by the upgrade.

TELESCOPE DRIVE : A new interface/controller for the MPACS, and corresponding interface driver and high-level software, were provided, as were two new handpaddles with their interface, controller and driver.

TRANSMIT/RECEIVE ASSEMBLY : A completely new box was provided (figures 2,3). The T/R mirror has two genuine holes, and is connected to the co-rotating 'dogbone' by a shaft incorporating a clutch unit. Rotation rates up to 20 revs/second are possible, and are controlled directly from the MRCS. Laser firing is triggered by notches on the T/R mirror rim as before. Laser fire commands may be inhibited through a 'divide by' facility so that only every first, second, third or fourth notch actually causes a shot.

A minutely-reflecting wedged feedback plate (FBP) directs part of the transmitted pulses to targets on the Coude Table for the optical calibration of the timing system and, optionally, for a real-time internal calibration target ('Table Target'). The wedge also reflects a small part of return pulses through ND filters in the 'dogbone' to the detector; this facility is routinely used for the spider retro and ground target returns, the bulk of whose energy passes back through the T/R hole and is lost. Such returns therefore traverse a different path inside the T/R box than do satellite returns which take 1.644ns longer.

An electrically controlled PLZT optical attenuator is placed between the feedback wedge and the 'dogbone' to aid in matching calibration and ground target signal strengths to satellite return signal strengths. A special circuit ('wobbulator') can sweep through the voltage range with 3 second period to give varying energies when adjusting discriminator walk.

RECEIVER/DETECTOR : A new Receiver Box (figures 2,4) contains a new 4-pinhole turret, separate ports for MCP mounting (with 10A^{o} filter built in) and eyepiece/RCA PMT mounting, a flip mirror to switch between ports, a flip mirror to access a CCD camera, a LED pulser to aid MCP characterisation, and new focussing optics. The flip mirrors can be software controlled via the MRCS.

To date, only ITT F4129f MCPs have been used, while the CCD camera and LED Pulser have not been used at all.

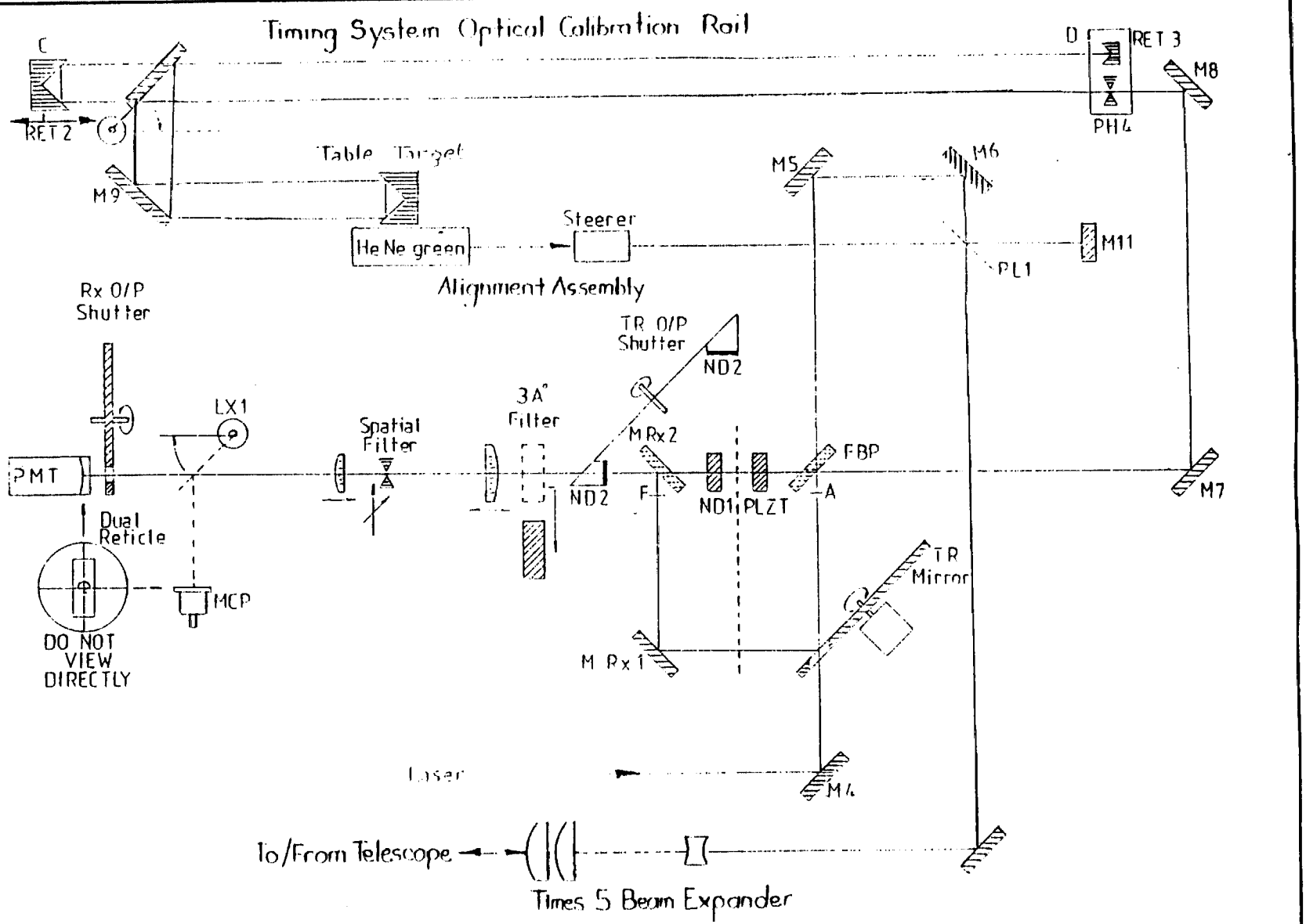

Figure 2: Coude table layout - schematic. (Based on EOS plans.)

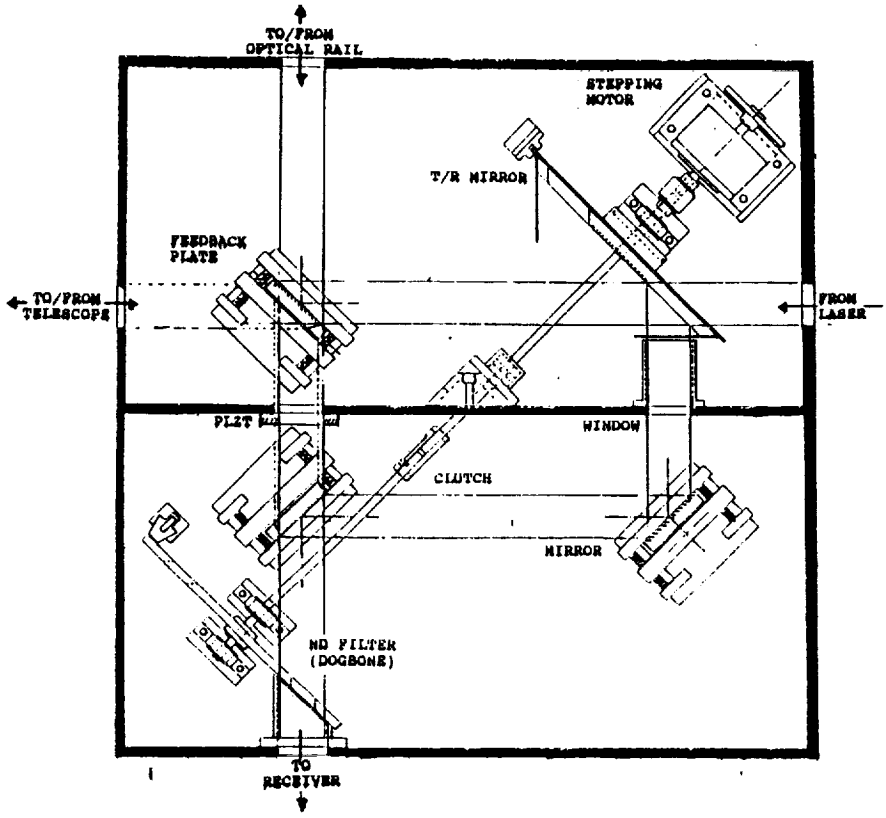

Figure 3: EOS Transmit/Receive assembly. (From EOS drawings.)

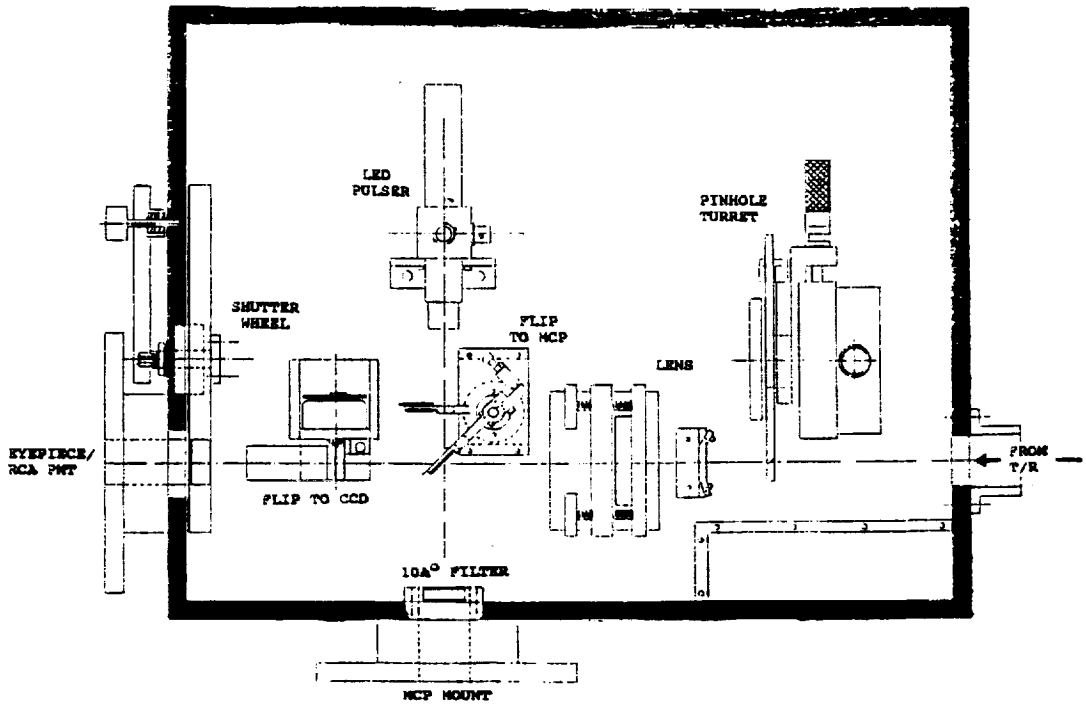

Figure 4: EOS Receiver assembly. (From EOS drawings.)

LASER : The oscillator was converted to Active Q-switching, Active mode-locking to a design by the Centre for Laser Physics of The Australian National University licenced to and developed by EOS. The SPS411 is also connected to the Active-Active circuitry to give positive pulse selection.

It was found necessary in 1990 to replace the laser heads with high-efficiency heads, and the capacitor banks with new units having simmer circuits. This work was supported by IRDB and completed in January 1991 with the installation of a CB632 and two CB631 units, and SF606-4, SF611-07 and SF611-09 heads, all made by Continuum. Later, a Continuum MV 70 RF generator for the Acousto Optic Modulator was also purchased, modified and installed, and other components have needed replacement.

The Upgrade Specifications required a third amplifier, or alternatively, the first amplifier would be double-passed through a spatial filter to keep the beam clean. Neither option has been invoked, yet the laser has achieved its overall goal of 250mJ per shot at 532nm when everything is working properly.

MASTER RANGING CONTROL SYSTEM (MRCS) : Replaced the LRC. It is based on EPLD chips, and sets windows and gates, controls T/R rotation and laser firing, manages all clock and epoch timing functions, and contains a full range of test and simulation facilities. The MRCS communicates extensively with the Hewlett Packard A900 1000-series minicomputer as shown in figure 5.

50 MHZ MULTIPLIER : The MRCS operates at 50MHz, so a box was provided to multiply up the 10 MHz output from the Oscilloquartz 2200 crystal.

EPOCH TIMING SYSTEM : The basic philosophy of 'epoch' event timing has been retained, and is accomplished by the MRCS Clock down to 20ns with EOS-modified LeCroy 2229A TDC verniers providing fine resolution. The intermediate 4202A TDC units are no longer necessary, and only one 2229A TDC is needed on each of the start diode and MCP lines. Each of the 8 channels of a 2229A TDC has a resolution of 25ps (nominal), the average giving 10ps (typical) resolution and precision.

The scale units (ns/count) of the verniers can be calibrated in three ways:

. Programmable delay lines within the MRCS;
. LeCroy 4202A TDC verniers, assumed accurate;
. Optical delay line. In a pseudo-ranging operation, part of a transmitted laser pulse is reflected from the feedback wedge in the T/R Assembly and directed to a retroreflector which slides along a calibrated optical rail, thence back through the wedge to the MCP (see figure 2). The change in TDC reading is then related to change in retroreflector position.

The average offset of each vernier with respect to the first vernier is calibrated daily by injecting a sequence of simulated laser pulses generated within the MRCS into all the verniers.

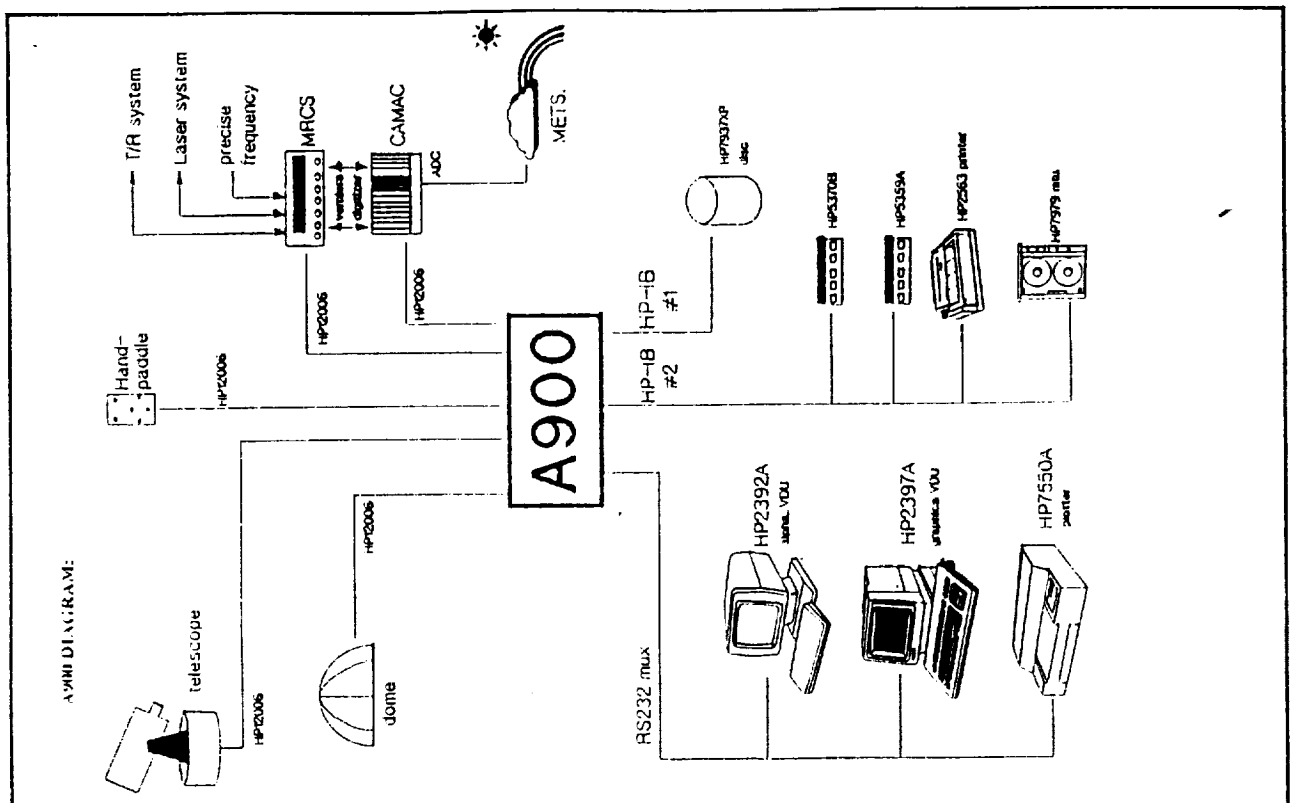

Figure 5: EOS Laser Ranging System. (EOS Operations Manual,V2.0)

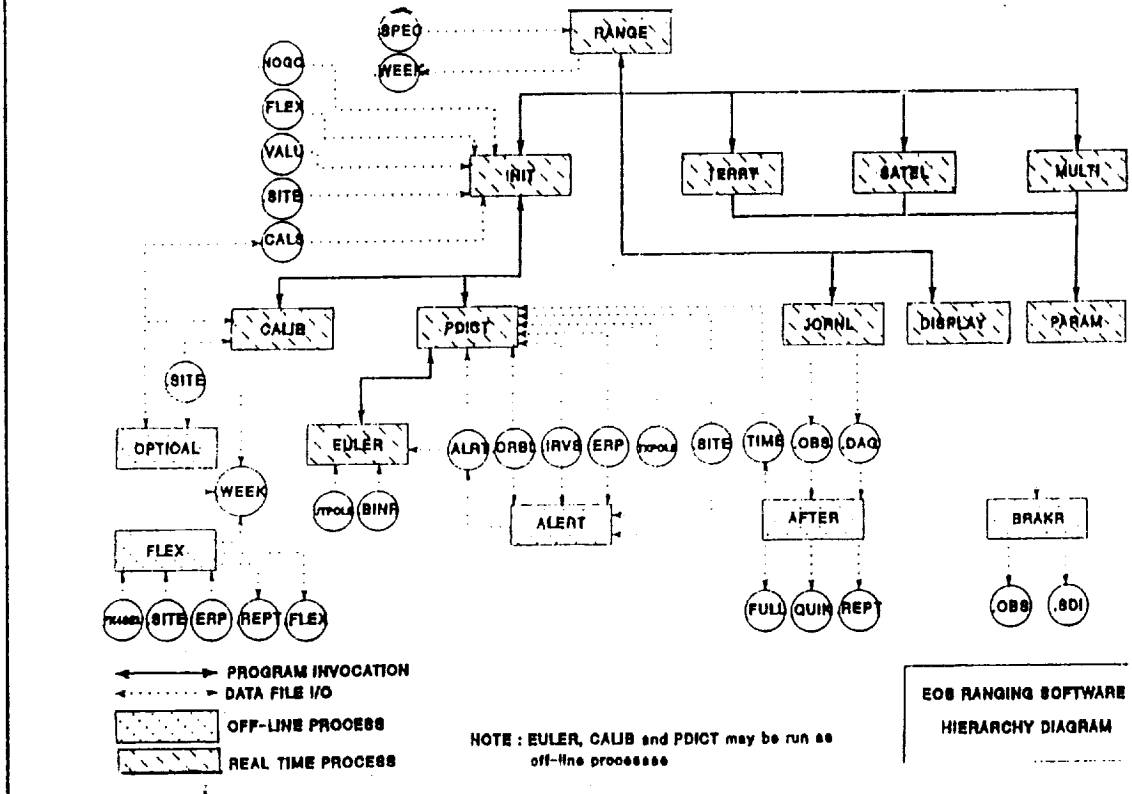

Figure 6: EOS Software Hierarchy. (EOS Operations Manual,V2.0)

RECEIVE ENERGY MONITOR : The previous system based on a LeCroy 2249A ADC has been retained, with hardware gating as above. The EOS software contains an option for automatic gating.

DISCRIMINATOR : As before, Tennelec 454 CFD units are used. EOS has experimented extensively with high-speed comparator chips, delay lines and 'cascade' configurations, but to date Orroral prefers to use unmodified single channels. The upgrade has also provided several potentially useful features for establishing the Z-walk on each channel, such as the PLZT 'wobbulator' and software, which are still being evaluated.

OPERATING SOFTWARE : The upgrade software provided, which is summarised in figure 6, includes mount modelling observations and analysis, pass predictions from receipt of IRV/ORBEL files, revamped EULER and IRVINT, ranging operations, post-processing to generation of normal point, full-rate data and time bias files, timing system calibration, file repair, diagnostic and reporting software. Source code was not included. The original software release was designed to apply 'generically' to all EOS systems; it has required considerable tailoring to Orroral's specific configurations, peculiarities, environment and requirements and has necessitated considerable re-education from an entrenched laser ranging 'culture'. Orroral prefers to use its own post-processing software, modified from the Natmap software to handle the new file structures.

Each interface driver is accompanied by a program demonstrating all its calls and providing extensive diagnostic and simulation capabilities. They cover CAMAC, MRCS, MPACS, PADDLE and DOME.

Ranging operations are built around three separate programs that handle ground targets, satellites out to about 70ms two-way range, and 'multiple shots in flight' targets such as ETALON and the moon, respectively.

SYSTEM CALIBRATION : To date, the same methods for real-time internal calibration and ground target ranging have been used as were used during 1987-91. The 'Table Target' on the Coude Table has been tested inconclusively; its signal strengths are expected to be controllable much better than those from the spider retros.

4. Laser Performance

An assessment was performed in April-May 1991 by Dr Barry Luther-Davies of the Laser Physics Centre, Australian National University. The results and many quotations given below are taken from his report (Luther-Davies,1991). The upgrade to an active/active oscillator and high-efficiency simmered heads has clearly provided very satisfactory performance.

PULSE DURATION : Output from the Second Harmonic Generator was measured using a Hadland Photonics IMACON 500 S20 streak camera

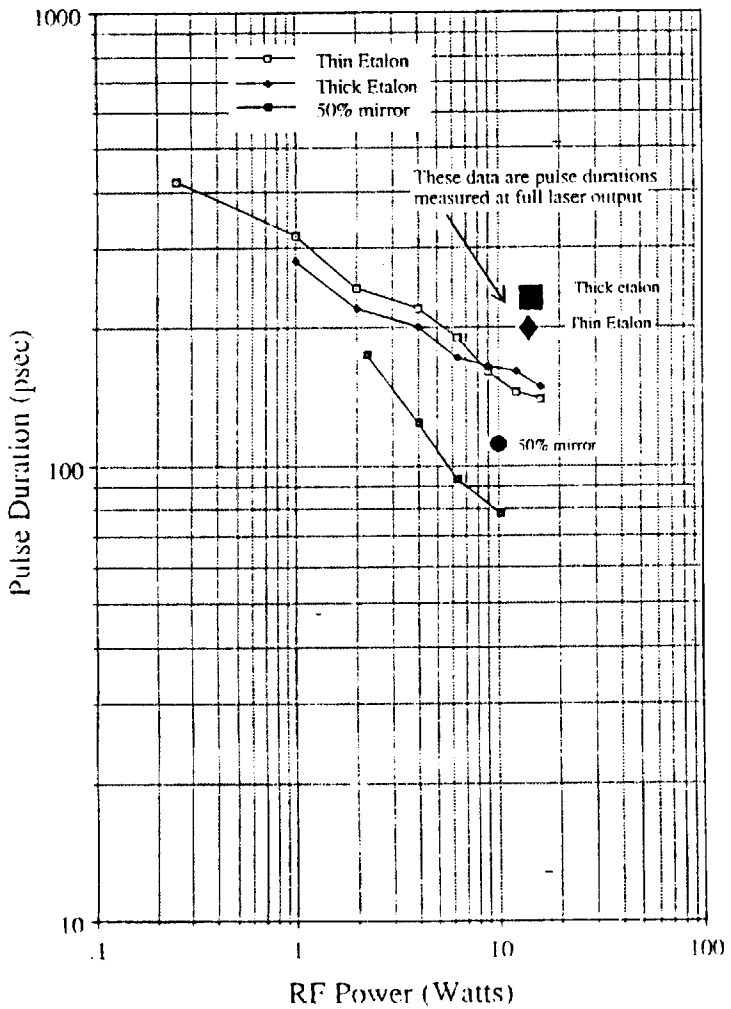

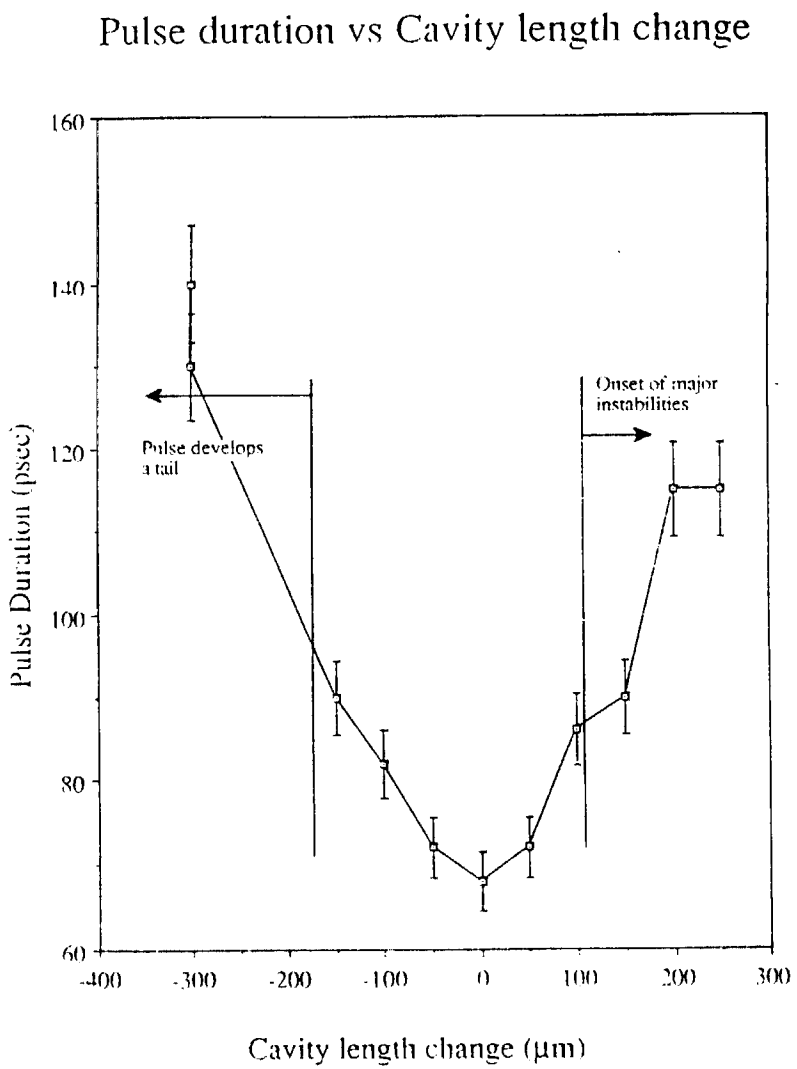

Figure 7: Active-active laser pulse duration- (a) vs RF power to AOM; (b) vs cavity length change. (Luther-Davies,1991)

whose negatives were digitized with a CCD camera. Three different oscillator output reflectors were tested: a "thin" (3mm) Quantel etalon, a "thick" (6mm) Quantel etalon, and a 50% reflecting dielectric mirror. Pulse durations were measured as functions of RF drive power level to the AOM (figure 7(a)) and of cavity length (50% mirror only - figure 7(b)).

Minimum pulse durations at maximum appropriate RF drive power and full laser power were:

with 50% mirror : 110 +/- 5 ps
with thin etalon : 200 +/- 10 ps
with thick etalon : 240 +/- 12 ps.

The 50% mirror was subsequently adopted for normal use, and it was concluded that the oscillator is relatively insensitive to thermal expansion, +/- 5^{o}C on a steel base being tolerable.

LASER OUTPUT ENERGY : Measured with a Scientech volume absorbing calorimeter, with the laser firing at 10 p.p.s. The results are summarised in Table 1. Two settings of the quarter-wave plate between the first and final amplifiers were used, with about a five degree rotation between the settings, to demonstrate the effect of thermally induced birefringence in the amplifiers.

TABLE 1 : Orroral Average Laser Output Energy

Position	Energy (mJ)	Comments
Oscillator,pre-lase	0.8	Osc.voltage 1660,RF drive 9.5W
Oscillator,full-train	5.56	Includes pre-lase, 4 pulses
Pulse slicer	1.1	Main pulse switched
Final amplifier, IR	>226.0	Amp.voltage 1420
SHG, green	> 56.0	Amp.voltage 1420, 1/4 wave "1"
SHG, green	> 67.0	Amp.voltage 1420, 1/4 wave "2"
SHG, green	>113.0	Amp.voltage 1570, 1/4 wave "2"

STABILITY : Output power stability was measured at 10 p.p.s. using the Scientech calorimeter or a silicon photodiode as appropriate, connected to a Hewlett Packard chart recorder. The results are given in Table 2. RMS jitter would be 3-4 times smaller than the peak-to-peak values quoted.

TABLE 2 : Short-term Stability of Orroral Active/Active Laser

Position	Av.Power (mW@10pps)	Jitter (p-p,%)	Period (mins)	Detector
Oscillator,full train	60	+/- 0.8	15	Calorimeter
Pulse slicer	11	1.4	15	Calorimeter
Pulse slicer	11	0.7	2	Photodiode (integrated)
Pulse slicer	11	0.8	120 shots	Photodiode (single shots
Final amplifier,IR	2290	1.2	5	Photodiode (integrated)
Final amplifier,IR	2290	1.6	15	Calorimeter
SHG,green	600	2.0	15	Calorimeter

Worst-case RMS instability lower than 0.5% is inferred.

During these tests, over 100,000 shots were fired and no laser misfires were observed, nor was evidence seen of failure of the mode locking system to generate stable bandwidth limited pulses when the oscillator was correctly aligned.

BEAM PROFILES : The shape of the 532nm output pulse at 1 metre from the SHG was measured with a Pulnix CCD camera. The profiles in figure 8 were obtained: (a) at 40mJ average green energy, at which the beam is quite uniform; (b) at 80mJ, showing a four lobe structure and decreased diameter due to thermal lensing; and (c) at 113mJ with the quarter-wave plate rotated about 5^{o} to emphasise the cross-like pattern caused by thermally induced birefringence in the amplifiers which in turn causes a spatially dependent depolarization of the beam and a variation of the frequency doubling efficiency across it.

5. Timing System Performance

Dr Ben Greene of EOS optimised the 2229A verniers of the epoch timing system in March 1992, and by means of pulses generated internally by the MRCS to simulate start diode and spider retro calibration returns, assessed their stability independently of the influences of MCP, discriminator and signal strength. The results of a 36 minute run where the data is binned in 30 second normal points of approximately 300 simulated shots each, are shown in figure 9. RMS about the mean was 6.2ps (0.93mm), which thus represents the intrinsic precision limit of the system during a LAGEOS pass.

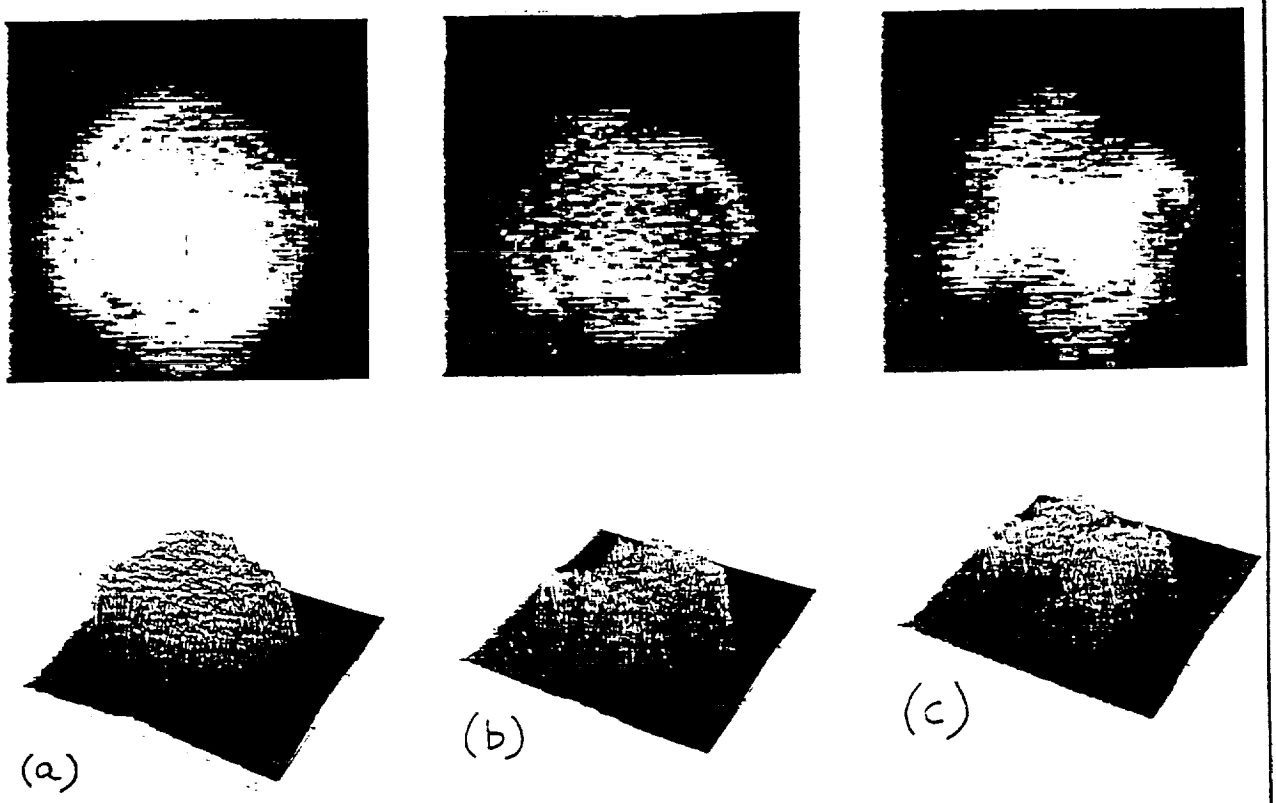

Figure 8: Laser beam profiles, 532nm green output 1m from SHG- (a) 40mJ/pulse in the green; (b) 80mJ/pulse green; (c) 113mJ/pulse green, quarter-wave plate rotated 5^{o}. (Luther-Davies,1991)

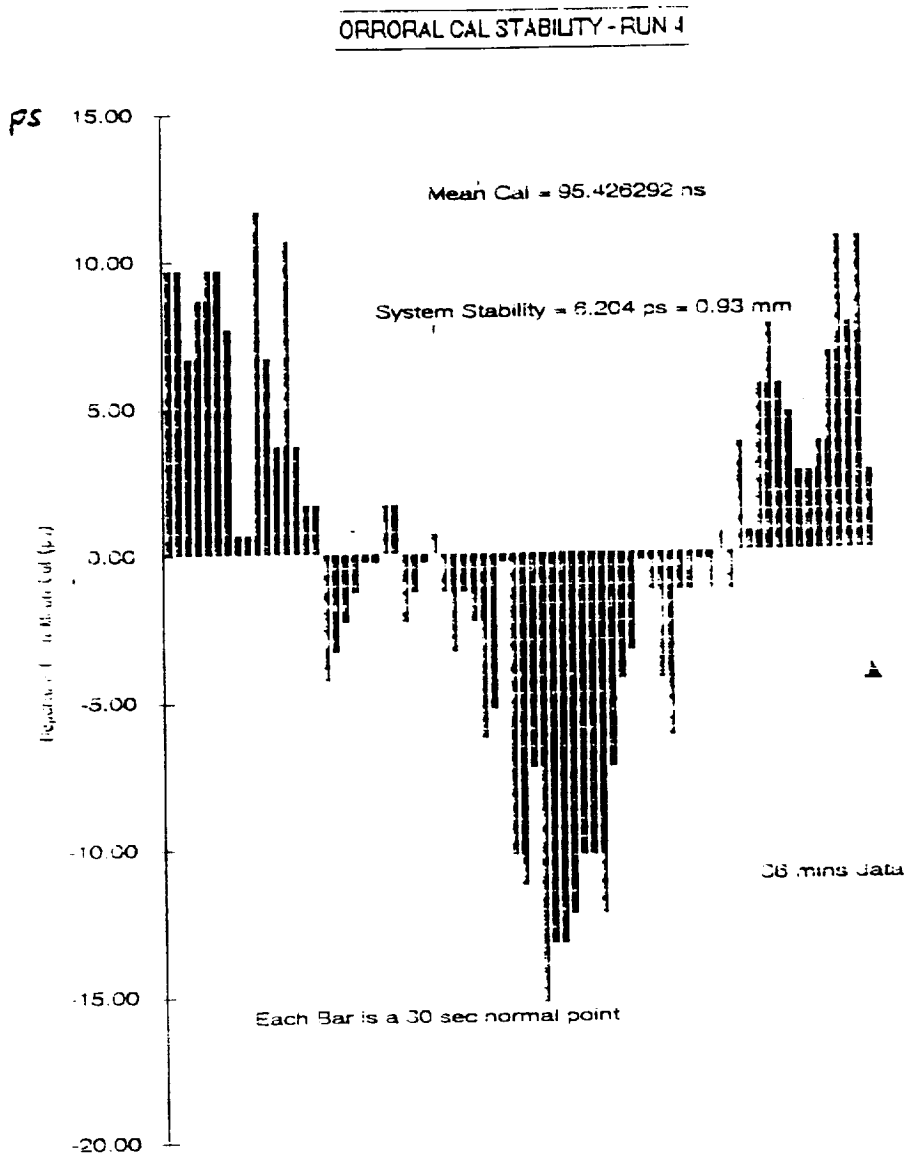

Figure 9: Timing system stability- residuals from mean of 36 minutes of simulated internal calibration data, binned at 30 second intervals (300 shots).

A systematic variation visible in figure 9 may be due to temperature variations in the CAMAC modules. The residuals from a 20 minute run were more random, with RMS 2.4ps (0.36mm).

An estimate of long-term stability is obtained from the daily calibration of the relative delay between verniers. In a 50 day period analysed during which the vernier scale units (ps/count) were held fixed at their values determined at the start of the period, the RMS variation of the delay difference between the two units actually used in ranging was 6.6ps (1.0mm).

It is thus evident that the precision and stability of the system, given perfect discriminator outputs, are 1mm or better. Because range calculations necessarily involve only vernier differences, this value also represents the accuracy limit of the system.

Data on the optical rail method of timing system calibration in situ at Orroral has not been obtained.

6. Pass Productivity

In figure 10(a), the growth in the number of passes acquired per quarter as a result of the upgrade is demonstrated. Prior to March 1991, only LAGEOS I and ETALON I & II (from June 1990) were observable. With the upgrade, STARLETTE, AJISAI and ERS-1 were immediately acquirable, with TOPEX/POSIDON and LAGEOS II being added in the second half of 1992. It is notable that the upgraded Orroral system was the first station to get returns from LAGEOS II, on 24 October. Monthly statistics for January to October 1992 are given in figure 10(b).

An unexpected consequence of the upgrade is that, in view of the enormous increase in number of passes available and the far greater reliability of the upgraded segments of the OLRS, more operational staff are needed in spite of greater system efficiency, and more technical staff are needed to maintain the other segments and bring them to an equal state of reliability and efficiency.

7. System Precision

The evolution of single-shot precision estimates for LAGEOS I ranging from Orroral is shown in figure 11. The data prior to the upgrade come from analyses of full-rate data by Peter Dunn of STX, and from in-house analysis thereafter. The failure to achieve the upgrade's sub-centimetre potential is ascribed to deterioration in laser alignment leading to longer pulses, to the difficulties encountered in optimising the MCP-Discriminator combination, and to a clear dependence of delay upon signal strength. Every effort is made to equalise signal strength distributions from satellite returns, spider retro cals and

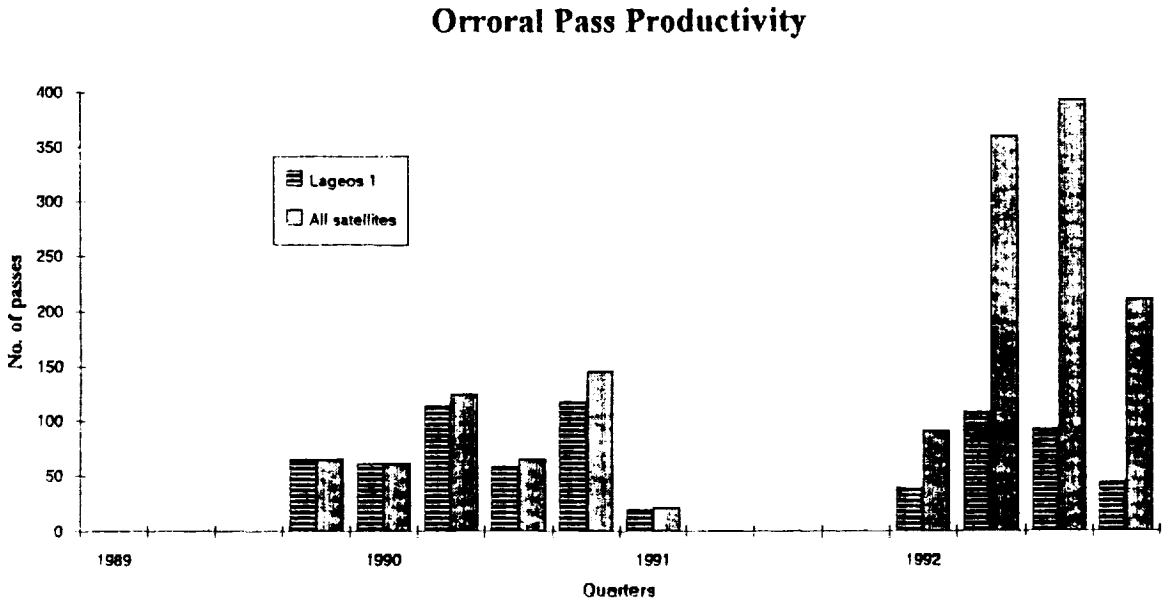

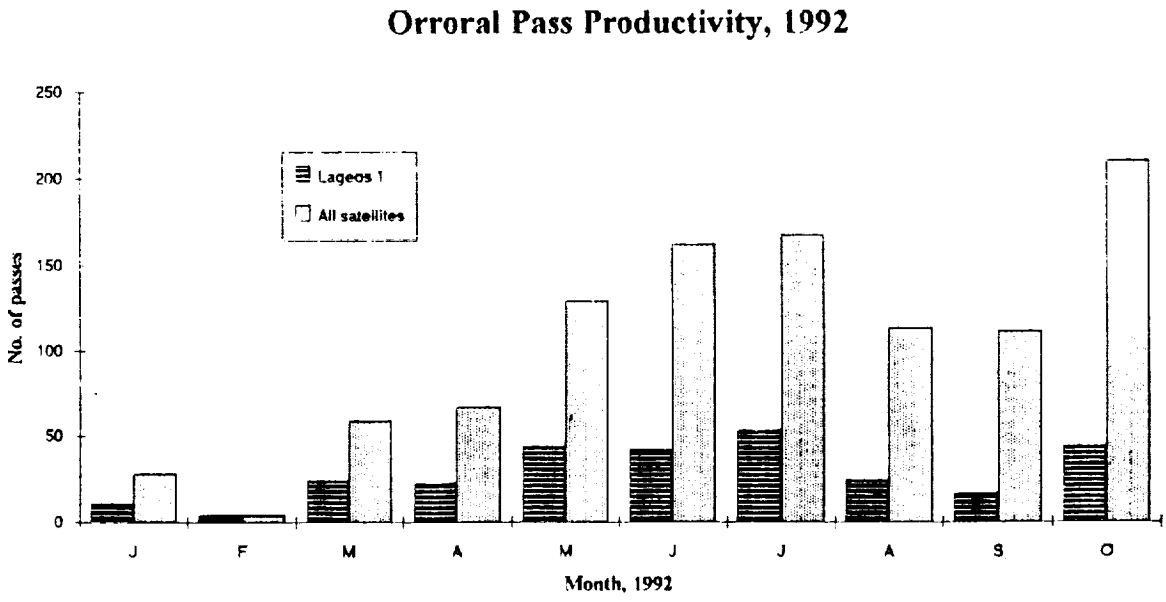

Figure 10: Number of usable passes from OLRS-
(a) Quarterly,1990-2; (b) Monthly,1992.

ground target returns by judicious manipulation of the PLZT and telescope pointing, but it is difficult to do this in practice.

Ground target ranging offers more control over signal strengths. RMS values of 30ps (4.5mm) have been obtained in 5 minute sessions both for raw ground target returns uncorrected for refraction, and for internal calibrations. About 7mm is normal when everything is working properly, as illustrated for a good month in figure 13.

8. System Accuracy

Agreement with external standards is assessed two ways. It has not been possible to organise a co-location experiment.

COMPARISON WITH GROUND SURVEYS : The distance from the ground target retroreflector to all relevant instrumental points was measured by precise geodetic survey in late 1987 and repeated by independent methods and operators in late 1989. The formal one-sigma uncertainty of each survey was 3mm, and agreement was 8mm. The value adopted for the distance between the ground target and spider retro #1 from the more recent survey is 1141624mm.

The same distance is estimated from laser ranging by subtracting the calibration result from the raw range measurement, and applying a refraction correction based on EDM theory and meteorological readings (Rueger,1980). No other corrections for delays inside the telescope are needed. Results for the first ten months of 1992 are displayed in figure 13. The extent to which improvements in signal strength control and laser pulse duration control will decrease the scatter and mean error, remains to be seen.

LAGEOS I RANGE BIAS : Figure 12 shows the range biasses before and after the upgrade, relative to LAGEOS I orbits computed by the Center for Space Research, University of Texas (Eanes,1992). There is evidence of a jump of between 20 and 60mm, but it is inconclusive as there could be contamination from orbit errors, station position errors, inclusion of data from 1991 when the upgrade was still being de-bugged, and truncation at May 1992. There has been no change in the constants and procedures used to reduce raw ranges to the adopted instrumental reference point (Coude mirror 7 - see figure 1), nor in the refraction algorithm applied to quick-look data. The Orroral reduction procedure is given in Appendix 1.

9. Telescope Pointing

MOUNT MODELLING : The analytical model developed previously for the Contraves mount and MPACS encoder system was specially coded into the generic EOS software. There are 10 parameters for each axis. It is solved from star observations by a non-linear process with observed encoder readings as the basic arguments. (The previous implementation by Natmap was solved as a linear

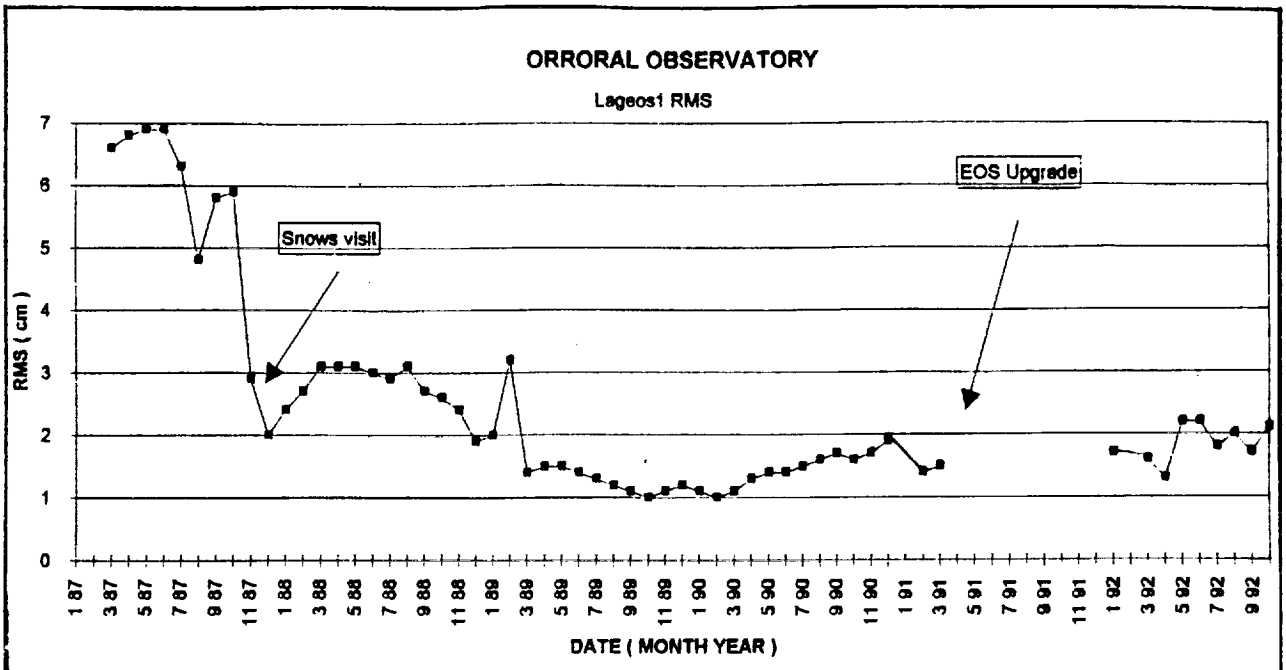

Figure 11: Monthly single-shot precision estimates for ranging to LAGEOS 1 from Orroral.

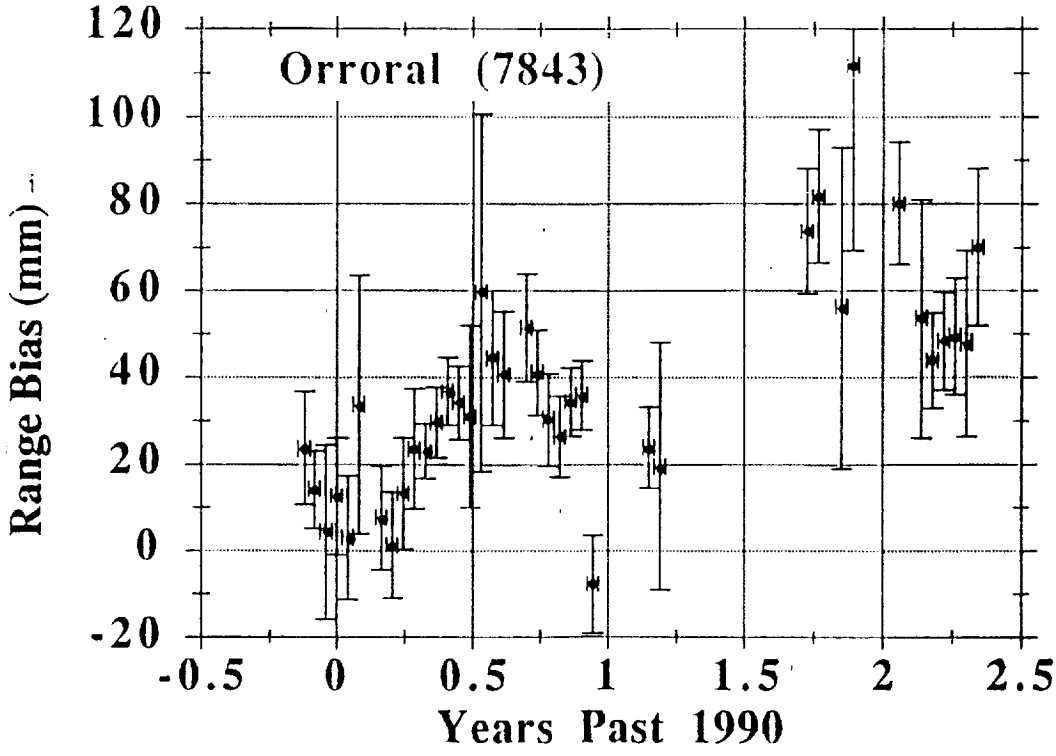

Figure 12: Two-week range bias estimates for ranging to LAGEOS I from Orroral,1989-92. (Eanes,1992)

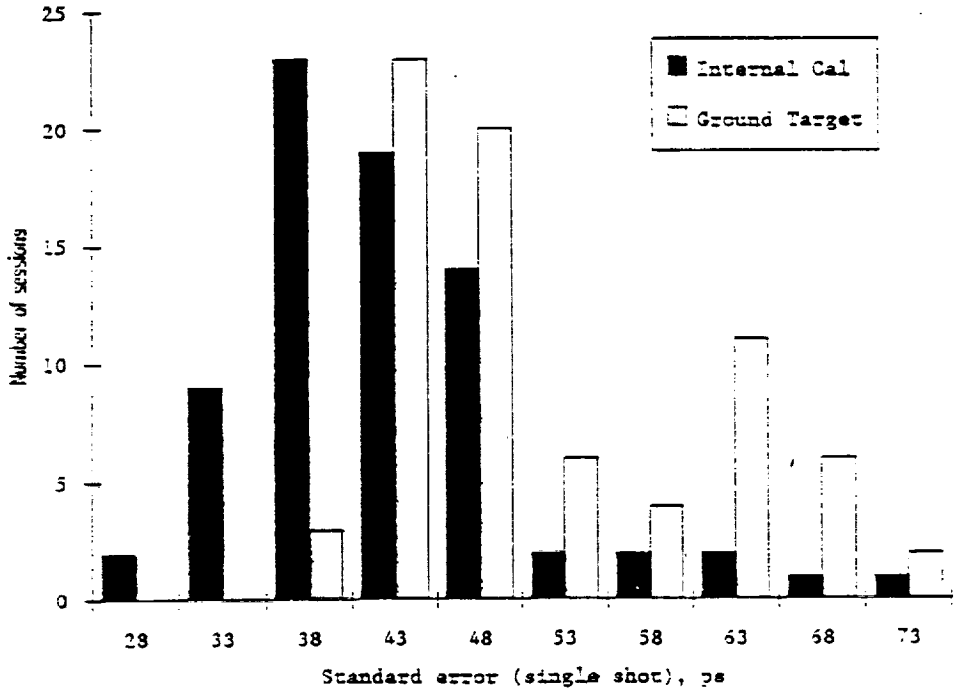

Figure 13: Raw ground target ranging precision (RMS) estimates, for sessions of about 5 minutes each in one month.

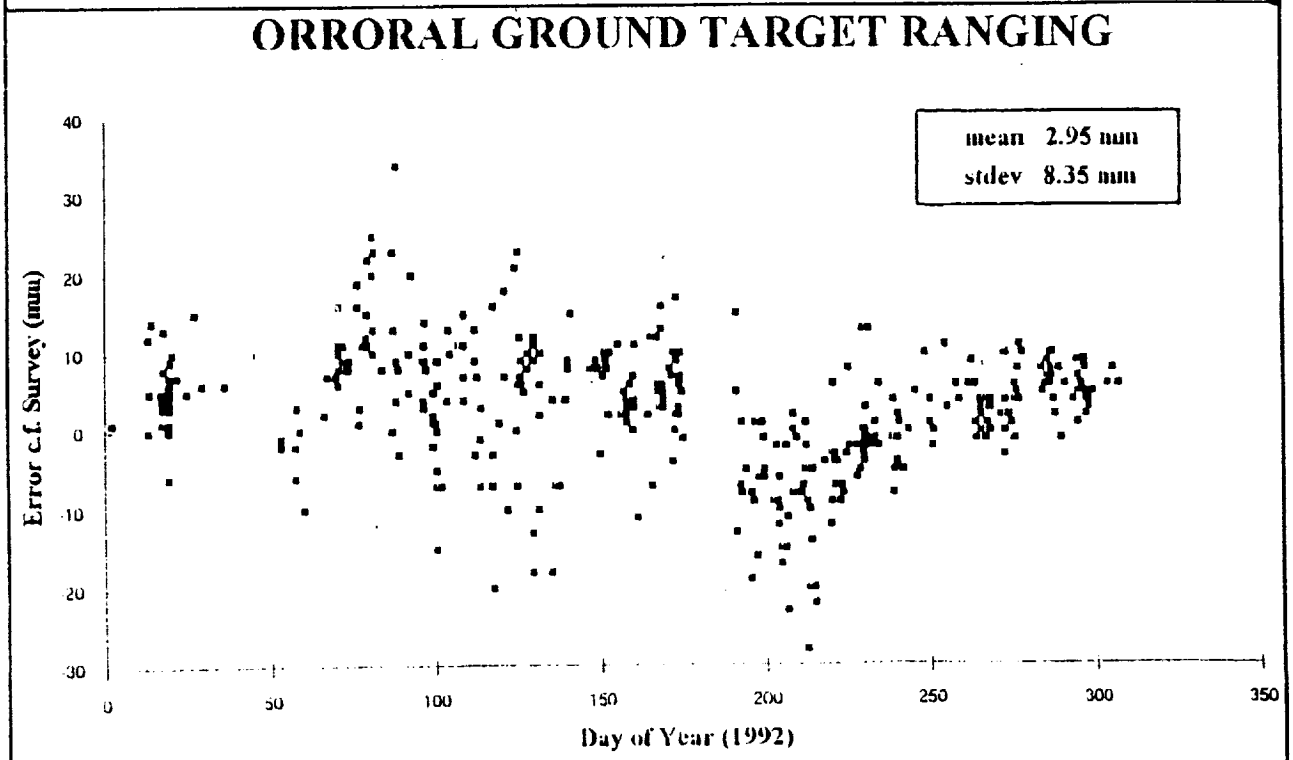

Figure 14: Comparison of reduced ground target ranging results in 1992 against adopted survey values.

model with ideal encoder readings as arguments.) The model is described in Appendix 2.

The star catalogue used is the FK4; previously, we used the homogeneous Perth 70 catalogue, which has a denser distribution.

Star observations are accomplished at the eyepiece at the Cassegrain focus. Star images are set, not on the eyepiece graticule centre but on the image of the coincident 'green spots' formed by returns from the two retroreflectors on the secondary mirror's spider vanes while the laser is firing. Thus the star is set in the direction in which the laser is actually transmitted, which automatically accounts for misalignments in the Coude path.

A feature of the upgraded system is that, between each repeat observation (normally 3) on each star, the telescope is driven off in a random direction to minimise personal bias and any backlash. In other respects, observing speed and the star selection algorithm are inferior to those prior to the upgrade.

HANDPADDLES : For operator convenience in both star observations and ranging, the new handpaddles have thumbwheels to select the resolution of each 'click' of the paddle buttons. This feature has proven very useful.

POINTING ACCURACY AND PRECISION : The post-fit standard error of a full mount model solution from more than 20 stars is typically 3 seconds of arc. The upgrade's solution software does not provide the facility to asses numerically how closely the current model points to stars, so it has to be done at the eyepiece. Our estimate is 5-10 seconds of arc, which is also the typical pointing error to the more distant satellites.

10. Future Upgrades and Extensions

The EOS system is designed to be open-ended for future development. Post-upgrade projects already completed or in-hand include:

- Semi-automatic ranging operations;
- Variable speed dome automation;
- Implementation of 'Table Cals';
- Variable optical attenuation for satellite returns;
- Optical design and fabrication for SPAD installation;
- HP 9000-series Unix workstation for all displays, processing and graphical user interface, leaving the HP A-900 only for instrument control.

while projects made possible in the more distant future include:

- Fully automatic ranging;
- Converting laser to travelling-wave 'ring' design;
- Operating at 40 shots per second;
- Multi-colour ranging.

An important development not directly related to the upgrade but necessary for lunar ranging and desirable for optimum focussing on to a SPAD, is a new telescope secondary mirror which should be installed by July,1993. Its distance from the primary mirror was reduced by 4cm at the 1981 upgrade, which introduced enormous aberrations in the Ritchey-Chretien system because it was inadvertently assumed to be a true Cassegrain at the time (see,e.g.Schroeder,1987). A new optical prescription has been calculated which retains the existing primary mirror, matching assembly and tailpiece optics, reduces the inter-vertex distance by a further 4.5cm, eliminates coma and spherical aberration from the telescope, and reduces them considerably in the matching lens assembly (James,1992).

The heavily aberrated field-of-view at the pinholes in the receiver assembly is essentially zero (James,1992). The layout of assemblies on the Coude Table is being studied, to bring the receiver optically closer to the Beam Expander, if possible, in order to increase the field-of-view somewhat.

11. Acknowledgements

The financial support of IRDB, EOS and AUSLIG is gratefully acknowledged. The Orroral Observatory Advisory Committee chaired by Kurt Lambeck, and AUSLIG management particularly Grahame Lindsay, Wal Lamond, Peter O'Donnell and John Manning, were instrumental in initiating the upgrade. The staff of EOS led by Ben Greene with Grant Moule as Project Manager, and all the staff of Orroral Observatory, worked long and hard to instal and debug the new systems and mate them to Orroral's needs and environment.

Special thanks to John Degnan for his patience waiting for this manuscript, and to Mark Elphick and Steve Cootes for their beautiful drawings and graphs.

12. References

Eanes,R.(1992): Private communication,May.

James,W.E.(1992): "Report on Visit to Orroral Valley Laser Ranging Observatory",Contract Report,James Optics P/L, July.

Luther-Davies,B.(1991): "AUSLIC Laser Operating Manual and Test Data",Contract Report,Australian National University,June

Rueger,J.M.(1980): "Introduction to Electronic Distance Measurement",Monograph No.7 (2nd Ed),The School of Surveying, University of New South Wales,March.

Schroeder,D.J.(1987): "Astronomical Optics",Academic Press Inc.

APPENDIX 1 : CORRECTIONS TO LASER RANGING OBSERVATIONS

Notation

r : Raw range measurement - time interval between start diode epoch and MCP satellite return epoch (2-way, ns)
R : Reduced range from instrumental reference point (Coude mirror 7) to reflection point of target, influenced by atmospheric delay (2-way, ns)
c : Internal calibration - time interval between start diode epoch and MCP spider retro cal epoch (2-way, ns)
a : Excess path length traversed by satellite returns in T/R box over path traversed by internal cal returns (1-way,ns)
h : Distance between spider retro and centre of telescope tertiary mirror, projected on to optical axis (1-way,ns)
s : Distance between centre of telescope tertiary mirror and system instrumental reference point which is the nominal centre of Coude Mirror 7 (outside the North bearing) (ns)
g : Angle subtended at Coude Mirror 7 by the separation between the telescope's inner (Y) and outer (X) axes (rad)
A : Telescope azimuth (ideal, ie assumes all mount model terms are zero)
E : Telescope elevation angle (ideal)
X : Telescope outer axis angle - 0^{o} W, 90^{o} meridian, 180^{o} E
Y : Telescope inner axis angle - 0^{o} N, 90^{o} prime vert, 180^{o} S

Coordinate Transformations

$$\begin{aligned} \cos Y &= \cos E \cos A \\ \cos X \sin Y &= -\cos E \sin A \\ \sin X \sin Y &= \sin E \end{aligned}$$

$$Y = \cos^{-1}(\cos E \cos A)$$
$$X = \tan^{-1}(\sin E / (-\cos E \sin A))$$

Range Reduction

$$R = r - 2*[s*\cos(Y + g) - h] - [c + a]$$

It is left to the analysts to convert to one-way range and to apply refraction and centre-of-mass corrections.

Numerical Values of Constants

s = 10.0389 ns (corresponding to 3.010 metres)
g = 0.16624 rad (corresponding to 9.525 degrees, axis offset 495 mm)
h = 8.9896 ns (corresponding to 2.695 metres)

a = | 1.644 ns (satellite targets)
    | 0.000 ns (terrestrial targets)

APPENDIX 2 : ORRORAL MOUNT MODEL

Notation

X : Encoder reading, actual, outer axis
X_o : Encoder reading, ideal, outer axis
Y : Encoder reading, actual, inner axis
Y_o : Encoder reading, ideal, inner axis
p : $X_o - 90^o$: zero at zenith
q : $Y_o - 90^o$: zero at zenith
c_i, i=1,..,20 : Solution coefficients of mount model,either axis
f_i, i=1,..,20 : Mount model functions,either axis

Linear Model

$$X = X_o + c_1*f_1(p,q) + c_3*f_3(p,q) + c_5*f_5(p,q) + ...$$
$$Y = Y_o + c_2*f_2(p,q) + c_4*f_4(p,q) + c_6*f_6(p,q) + ...$$

Functions

i	Function $f_i(p,q)$	Description	Small Angle Expansion
Outer axis (X)			
1	1	X encoder zero point error	1
3	p	X encoder scale error	p
5	q	Cross scale error (empirical)	q
7	1 - cos p	X encoder de-centering	$p^2/2$
9	-sin p tan q	Outer axis inclination error	pq
11	1 - sec q	Optic axis non-perp to inner axis	$-q^2/2$
13	p - tan p	Yoke (outer axis) flexure	$-p^3/3$
15	cos p tan q - q	Outer axis azimuth error	$-p^2q/2+q^3/3$
17	p - sin p sec q	Telescope tube flexure (sin z)	$p^3/6-pq^2/2$
19	q - tan q	Non-orthogonality of axes	$-q^3/3$
Inner Axis (Y)			
2	1	Y encoder zero point error	1
4	q	Y encoder scale error	q
6	p	Cross scale error (empirical)	p
8	1 - cos q	Y encoder de-centering	$q^2/2$
10	tan p sin q	Empirical	pq
12	1 - cos p	Outer axis inclination error	$p^2/2$
14	q - cos p sin q	Telescope tube flexure (sin z)	$q^3/6+p^2q/2$
16	tan p cos q - p	Empirical	$-pq^2/2+p^3/6$
18	sin q - q	Empirical	$-q^3/6$
20	p - sin p	Outer axis azimuth error	$p^3/6$

Empirical terms were determined by residual analysis. Terms are ordered by small angle expansions around zenith which aids de-correlation of solution parameters especially with few stars.

N94-15603

SUB-CM Ranging and other improvements in Graz

Georg KIRCHNER, Franz KOIDL

SLR Graz / Institute for Space Research
Austrian Academy of Sciences
Observatory Lustbühel, Lustbühelstr. 46
A-8042 GRAZ, AUSTRIA

Tel.: +43-316-472231; Fax: +43-316-462678
E-Mail: kirchner@flubiw01.tu-graz.ac.at

1.0 Introduction

A lot of tests and experiments have been made in Graz during the last 2 years to increase performance and accuracy; using the SPAD from the Prag group as receiver, we have reached now about 5 mm RMS from the calibration target, and about 8 mm RMS from ERS1 and STARLETTE. In addition, routinely using the semitrain, the number of returns has been increased significantly for most satellites.

2.0 Experiments

In January 1991, together with the Prague group, we installed their streak camera as a receiver in the Graz laser telescope, and first echoes from AJISAI and STARLETTE could be recorded.

In December 1991, again together with the Prague colleagues, 2-color ranging experiments were performed, using Raman upshifted red (683 nm) and 532 nm wavelengths; returns of both colors from AJISAI and LAGEOS could be recorded. A detailed description of both experiments is given elsewhere in these proceedings.

3.0 Accuracy Improvements

As stated already during the Matera workshop, the contribution of the SPAD itself to the overall jitter can be decreased by using higher voltages above break (Vab). Modifications of the original SPAD electronics now allow us to increase this Vab to more than 10 V, resulting in a jitter of 5 mm RMS (fig. 1) from the calibration target. In this test, we used an SR620 counter, which also contributes to the lower RMS (the start input of the SR620 handles the output of the start Optoswitch significantly better than our HP5370A).

The well known disadvantage of the high Vab is the increase in noise; while a standard SPAD at 2.5 Vab at room temperature has an acceptable noise of about 200 kHz or less, this increases at 10 Vab to about 1 MHz (fig. 2). To reduce this, we cool the SPAD now with Peltiers to -25°C, reaching again about 200 kHz noise.

Short before the workshop, we had 4 different counters available for test purposes at the SLR Graz: HP5370A, HP5370B, and 2 SR620. The RMS values of these specific instruments are listed in table 1; RMS 1 is measured with asynchronous, random pulses, as it is the case during satellite ranging; RMS 2 is measured with pulses synchronous to the internal frequencies, and is listed here only for completeness.

	RMS 1	RMS 2	Remarks
HP 5370A	22 ps	10 ps	Our standard counter for SLR
HP 5370B	40 ps	12 ps	Available for tests
SR620/1	21 ps	8 ps	Our future counter for SLR
SR620/2	20 ps	8 ps	Same type, available for tests

Table 1: Counter Comparison

Using these counters in our station for calibration tests, we got the results shown in fig. 3. We measured all counters with "good alignment" (the returns focussed as good as possible on the center of the SPAD) and "weak alignment" (focussing of the re-

turns on the SPAD far from optimum). It can be seen that good SPAD alignment (together with optimizing all start/stop input pulse rise times, pulse forms, trigger thresholds etc.) is of the same importance than selecting the proper counter.

4.0 Routine use of the Semitrain

Since summer 1991, we routinely use the second half of the pulse train (semitrain), delivered from our Nd:YAG laser, for all SLR measurements. The software has been modified to allow for automatic "folding" of the returns. Fig. 5 shows an example pass of LAGEOS, with totally 7 tracks (or pulses from the semitrain) identified later by the software.

By using all returns from the semitrain, the number of returns for most satellites could be increased significantly (fig. 6); for LAGEOS the increase in returns is more than 50%; for the ETALON's, it is more than doubled.

5.0 Acousto-Optic Modelocker

In February 1992, we installed an Acousto-Optic Modelocker in our old Nd:YAG laser oscillator, inceasing reliability and shot-to-shot reproducibility of the laser pulses. Besides increasing the number of valid shots from our previous average of about 70% (it was an old, purely passiv modelocked oscillator!) to more than 99%, the much better stability of the pulses had a noticeable effect on the jitter (Fig. 4); the routine cal. values showed better stability and even slightly lower RMS (the AO-Modelocker was installed after calibration number 98, in fig. 4).

The AO-Modelocker requires temperature stabilization; this is done by slighly heating it to 27°, using the hot side of Peltier elements; the cold side of these elements is used at the same time to cool the Dye Cell to about 10°, which should result in a longer lifetime of the Dye. Results are promising (we used the same dye from February to May), but still have to be verified during the next years.

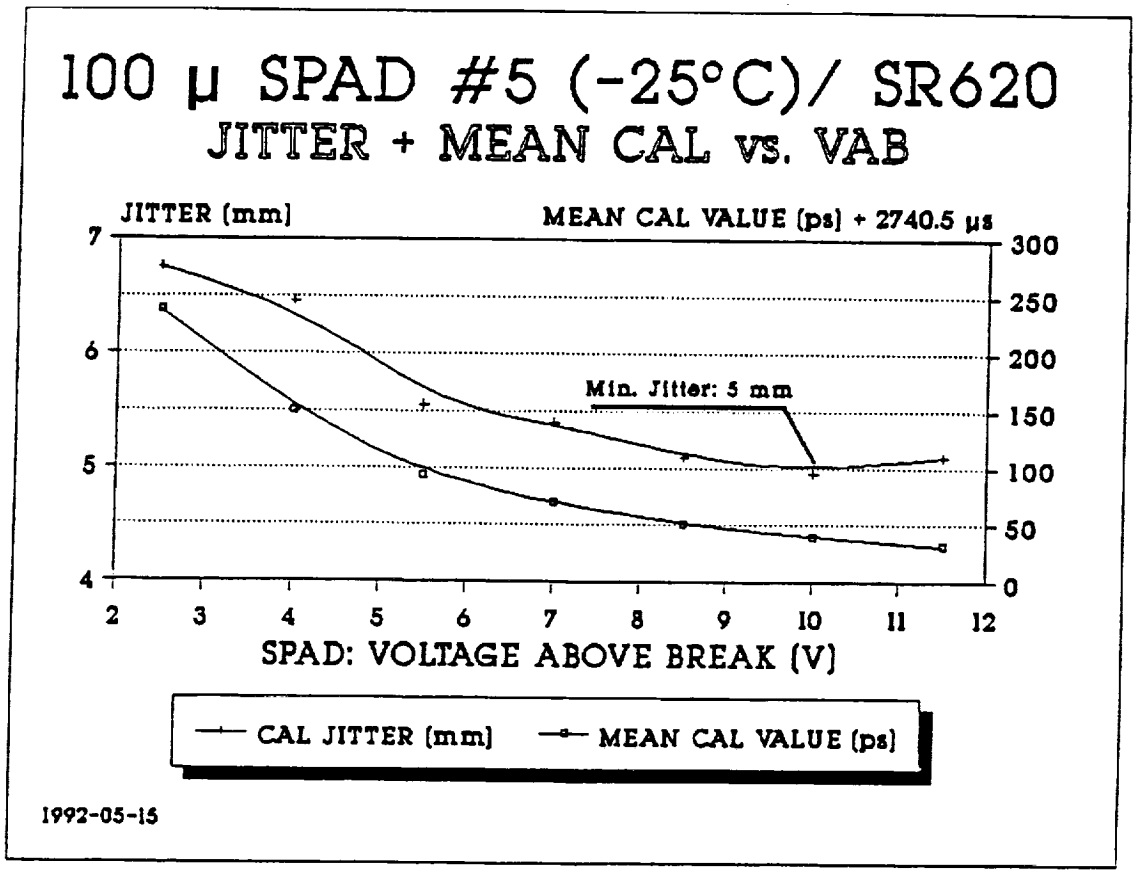

Figure 1: Minimum Jitter from Target is about 5 mm

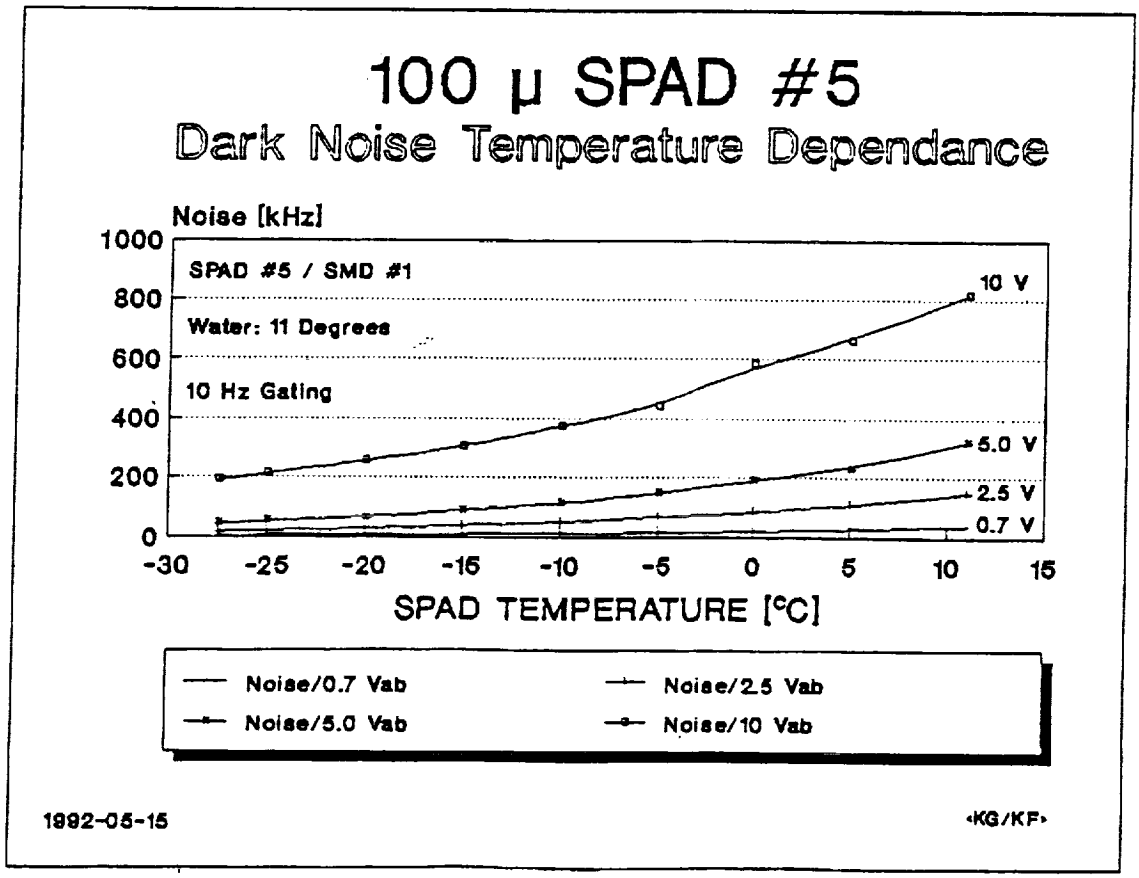

Figure 2: Noise depends on Voltage above break and temperature

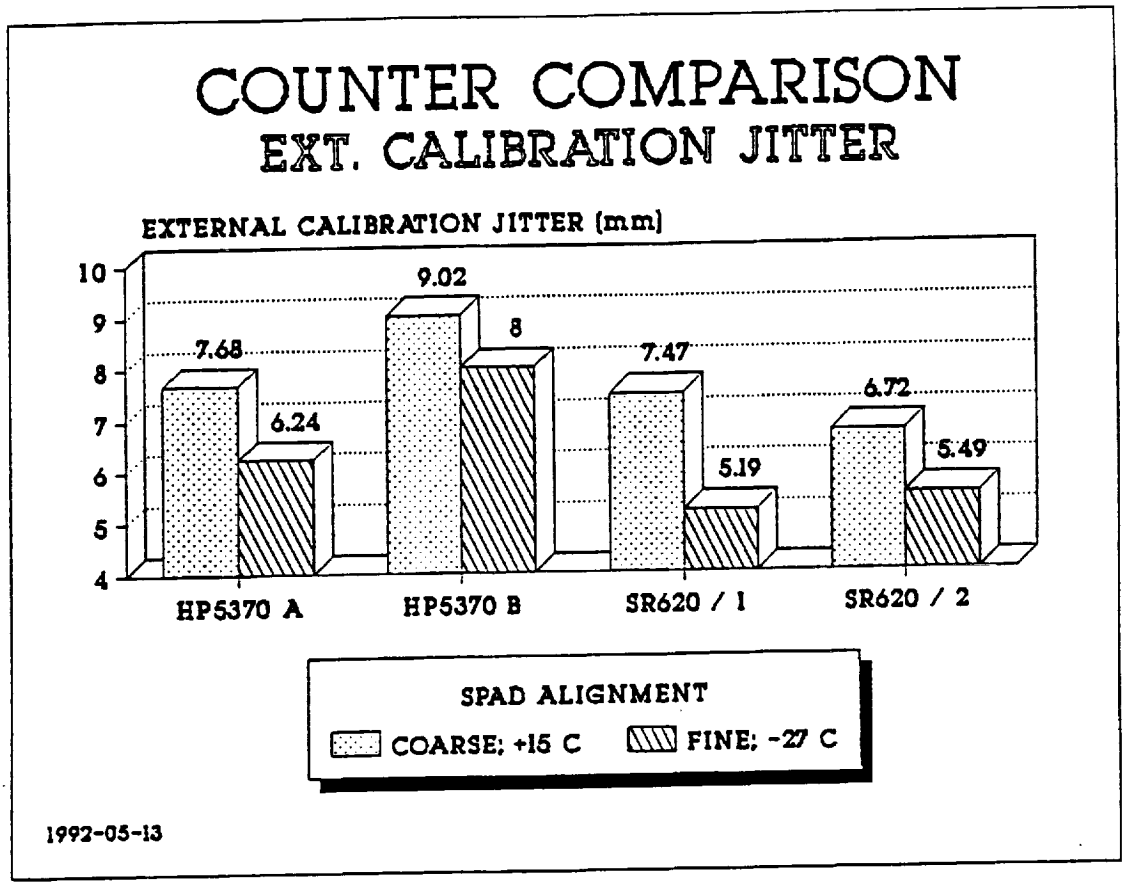

Figure 3: Calibration with different counters and alignments

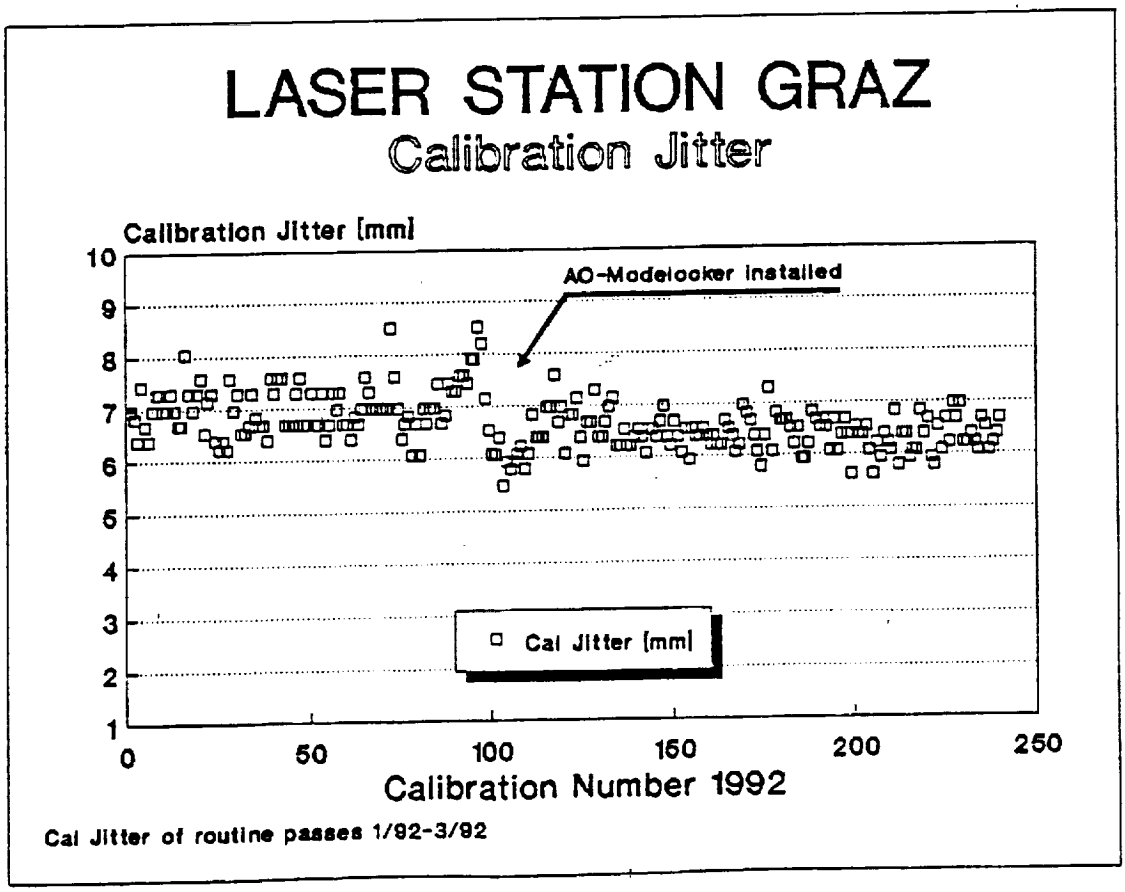

Figure 4: Effect of Acousto-Optic Modelocker on Cal stability

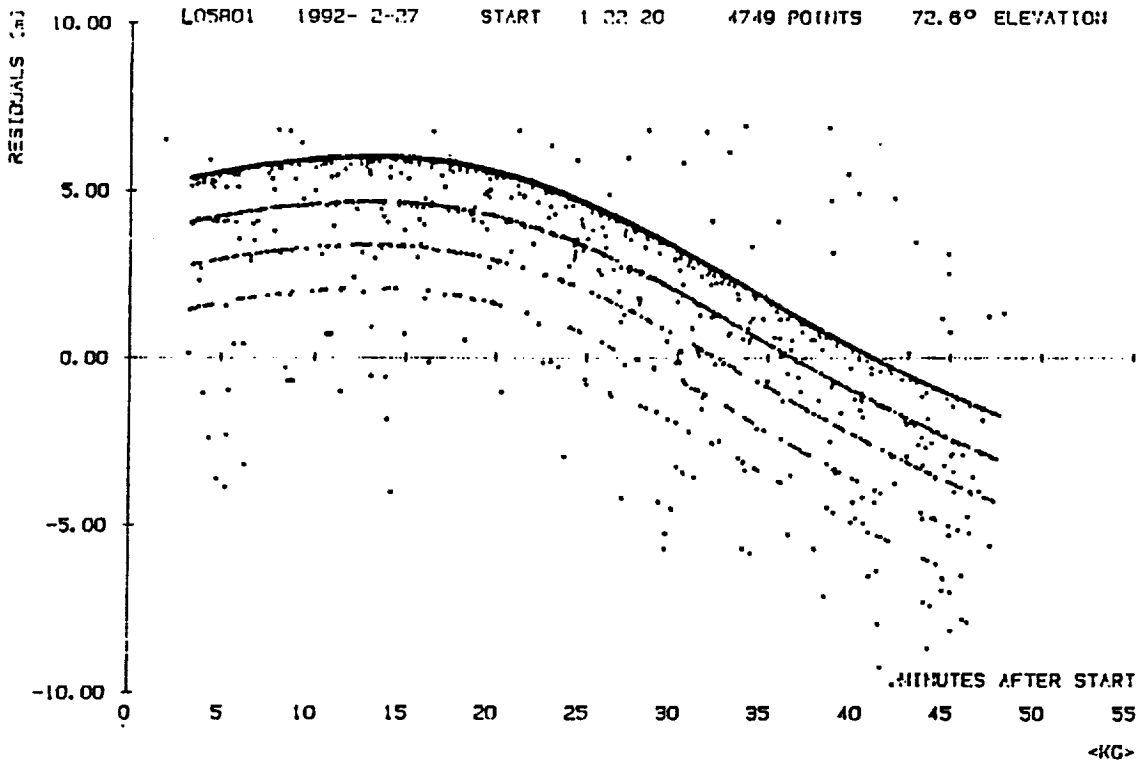

Figure 5: Typical LAGEOS pass, with semitrain returns

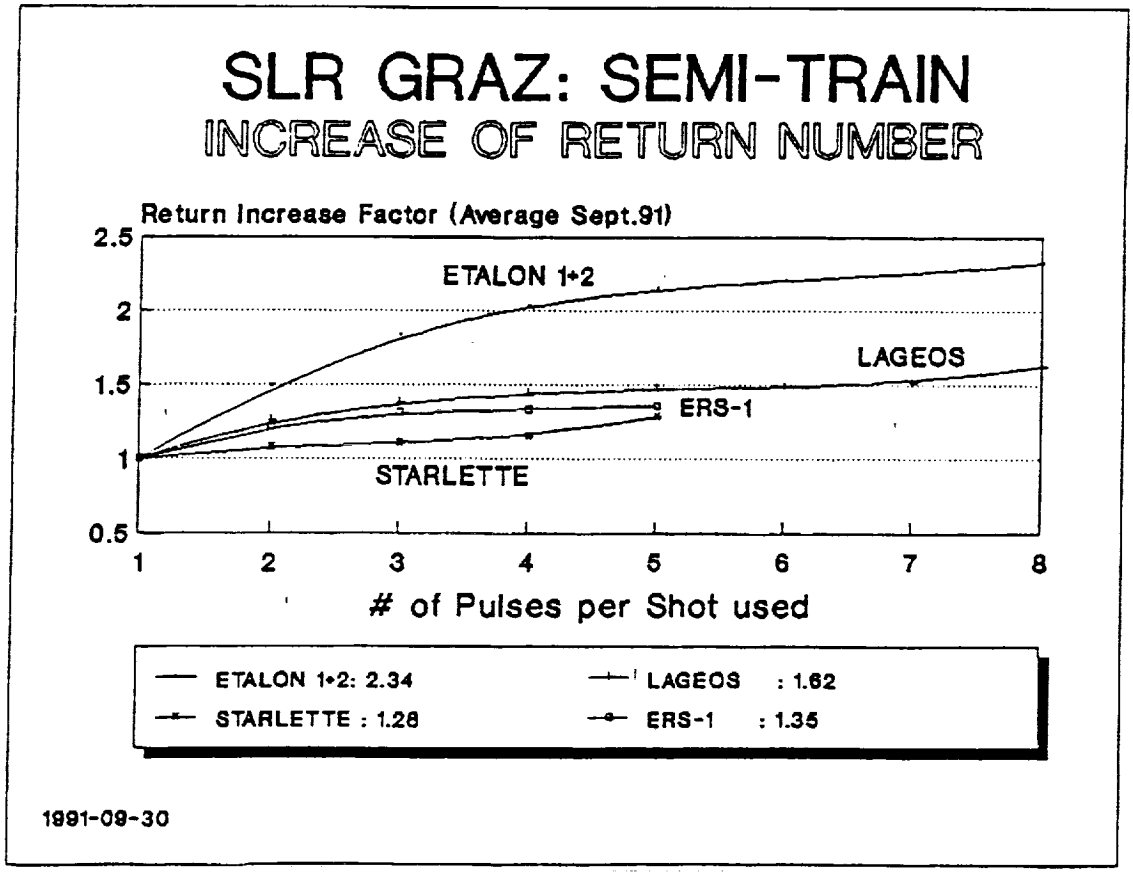

Figure 6: Increase of return number with semitrain

N94-15604

UPGRADING OF THE BOROWIEC LASER STATION

S.Schillak, E.Butkiewicz, J.Wiktorowski
Space Research Center of Polish Academy of Sciences
Astronomical Latitude Observatory
Borowiec 91
62-035 Kornik, Poland

Telephone: (48) 61-170-187
Fax: (48) 61-170-219
Telex: 412623 aos pl

Abstract

The major upgrade at Borowiec SLR since the last Workshop is the new third generation laser, which has been installed in September 1991. Short description of the new CONTINUUM laser and first results of satellites observations are presented. The results confirm expected increase in accuracy (3-5 cm) and in the number of measurements per satellite pass (several hundred).
In addition, information about second Borowiec SLR system is presented. Borowiec No 2 is designated for Tunisia in the next year. System is not yet operational.

1. Introduction.

The Borowiec SLR System is operating since 1988 (Schillak, 1991). During this time the system has provided observations to satellites LAGEOS, Ajisai, Starlette, GEO-IK-1 and ERS-1. The system has only night-time tracking capability. The single shot precision was estimated to be about $\pm$20 cm. Our activity were strongly limited by bad weather conditions and technical problems (Fig.1).

Since the last workshop several upgrading in the system has been done;

- 1990, February, transmitter telescope has been added and divergence of laser beam changed 8X,
- 1990, October, generation of normal points onsite,
- 1990, October, replacement of the photomultiplier FEU-87 by the RCA 8852,
- 1991, June, a received energy detector has been introduced,
- 1991, September, new third generation laser has been installed,
- 1991, October, new real-time software has been introduced,
- 1992, January, microcomputer PC/AT has been used for pre- and post-observation programs, real-time graphic program on PC/AT has been added.

The main upgrading of the system was installation of the new laser.

2. Laser CONTINUUM.

The Nd:YAG laser type CONTINUUM PY-62-10 has been employed in September, 1991. The scheme of the laser transmitter is shown in Fig.2. The laser is a cavity dumped active/passive mode-locked system. The cavity dump consist of the electro-optic Pockels cell triggered by a photodiode. The selected output single pulse is ejected via polarizer when the predetermined intensity level is reached. The oscillator delivering about 3-5 mJ at 1064 nm. The oscillator and preamplifier are pumped by the same flashlamp. A telescope for beam expansion is placed before main amplifier. The amplifier has four flashlamps. A type II $KD^{*}P$ crystal is used for

doubling.
The laser can be operated in two different modes;
- with ETALON (100 ps, 110 mJ at 532 nm),
- without ETALON (35 ps, 65 mJ at 532 nm).
The pulse repetition rate can be varied from 1 to 10 Hz (10 Hz is optimum). Pulse stability - 7%, diameter of output laser beam - 12 mm, divergence - 0.4 mrad, jitter of ext. trig. $\pm$10 us.

3. Results.
The last pass with old 4 ns laser was performed on August 18, 1991, first pass with new CONTINUUM laser on September 28, 1991. The results of SLR using new laser are shown in Table 1. The table shows results of two periods of activity; I - October, November, II - December, January. First period was dedicated to the introducing of new real-time software , second one to achieve maximum efficiency in actual station configuration. The last results show that single shot RMS is equal to 3-5 cm and further increasing of accuracy is limited by classic photomultiplier RCA 8852 (jitter is about 1 ns). Maximum number of returns per one pass was about 1500 for LAGEOS and more than 3000 for Ajisai. The Fig.3 and 4 shows the advantages of new laser in comparison to the old one. To further improve the single shot RMS the photomultiplier needs to be changed to a micro-channel plate or an Avalanche photodiode.

Table 1. Results of the observations performed with CONTINUUM laser from September 28, 1991 to January 31, 1992.

SATELLITE	PERIOD	PASSES	RETURNS	RETURNS/ ONE PASS	RMS cm
LAGEOS	Oct-Nov	8	416	52	7.0
AJISAI		12	5313	443	4.8
LAGEOS	Dec-Jan	8	3516	440	5.0
AJISAI		13	17268	1328	4.0

Problems;
- delay of the mount as result of the short steps (100 ms), step by step mode of the mount should be changed to continuous mode, problem is especially hard for low satellites as ERS-1,
- small operational memory of old computer limits our possibility to maximum 2500 returns per pass, also breaks of about 1 min appeared due to 5 min bursts, microcomputer PC/AT must be attached for real-time operations.

4. Status and parameters of Borowiec-2 SLR system.
The second SLR system has been installed in Borowiec Observatory in 1990. The system is destined to place in Tunisia. The parameters of actual configuration are presented in Table 2.

Table 2. The actual parameters (1992) of Borowiec-2 SLR system.

Laser - Nd:YAG
  pulse energy - 250 mJ (green)
  pulse width - 4 ns
  repetition rate - 1 Hz
Mount - Az-El computer controlled
  tracking - continuous
  tracking possibility - low satellites, Lageos, Etalons
  encoder resolution - 1.8 arcsec
  laser in Coude
Transmitting optics
  diameter - 20 cm
  gain - 8x
  output divergence - 10 arcsec
Receiver - Cassegrain
  diameter - 65 cm
  diameter of secondary mirror - 20 cm
  field of view - 5 arcmin
Guide telescope - Maksutov
  diameter - 20 cm
  field of view - 1^{o}

Photomultiplier - RCA 8852
Time Interval Counter - PS-500, 60 ps accuracy
Discriminator - Tennelec 454, or B-6
Time Base - GPS Time Receiver
accuracy - 100 ns
Computer - PC/AT
Software - Real Time tracking programs, IRVINT and ORBMESS predictions, initial analysis programs, star programs
language - C
Calibration - Pre and Post, external
Expected overall accuracy of the system - $\pm$15 cm
Operating staff - 2 persons

The current 4 ns laser should be exchanged for the better third generation system in the near future. System is not yet operational. The first target calibration is expected this year and system will be operational at Borowiec in 1993.

5. Localization in Tunisia.
Installation of the SLR station in Tunisia is realized in cooperation between Office de la Topographie et de la Cartographie, Tunisie and Space Research Center of Polish Academy of Sciences. Station will be placed in new geodynamical center 10 km north from town Medenine in south part of Tunisia. The Borowiec-2 SLR system will be operational in Tunisia probably in 1994.

Acknowledgments.
The authors thank technical staff of Borowiec laser group; Ms. Danuta Schillak, Mr. Wojciech Rzanny and Mr. Stanislaw Zapasnik for their important participation in new laser installation and performance of observations.

References.
Schillak S., 1991, Borowiec Laser Station 1986-1990. Artificial Satellites, Planetary Geodesy, No. 15, Vol. 26, No. 1, Warsaw, Poland, pp. 13-18.

Fig. 1 OPERATING PERIODS IN 1990
(284 DAYS)

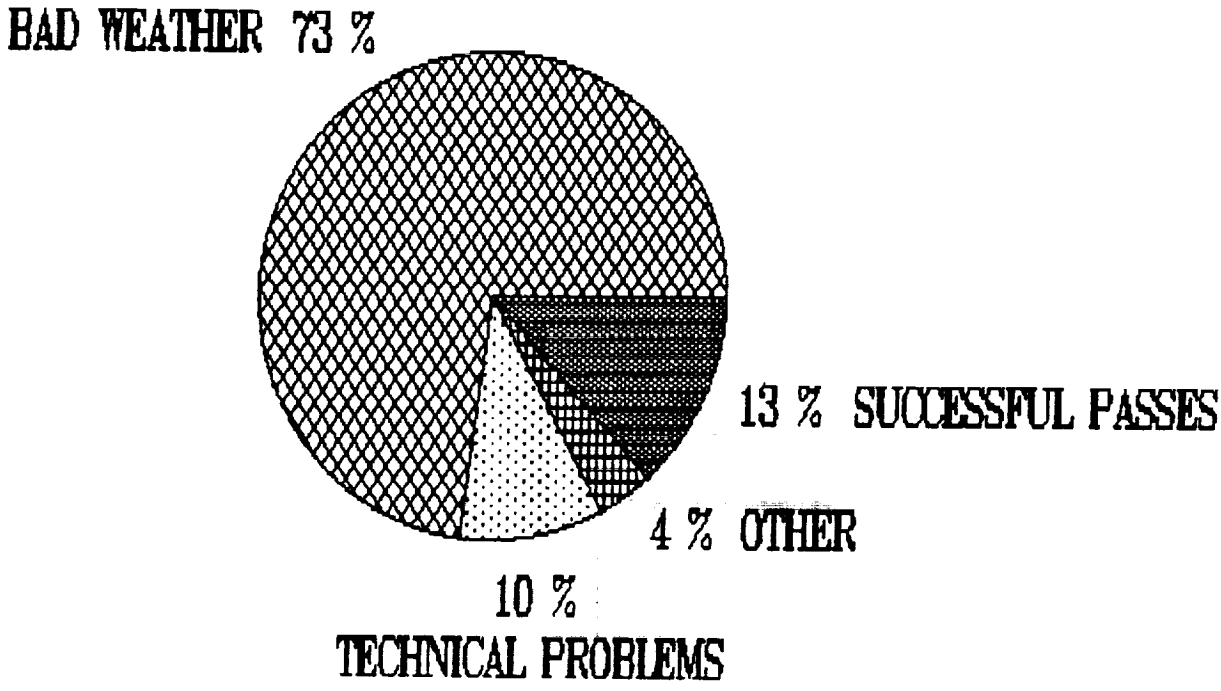

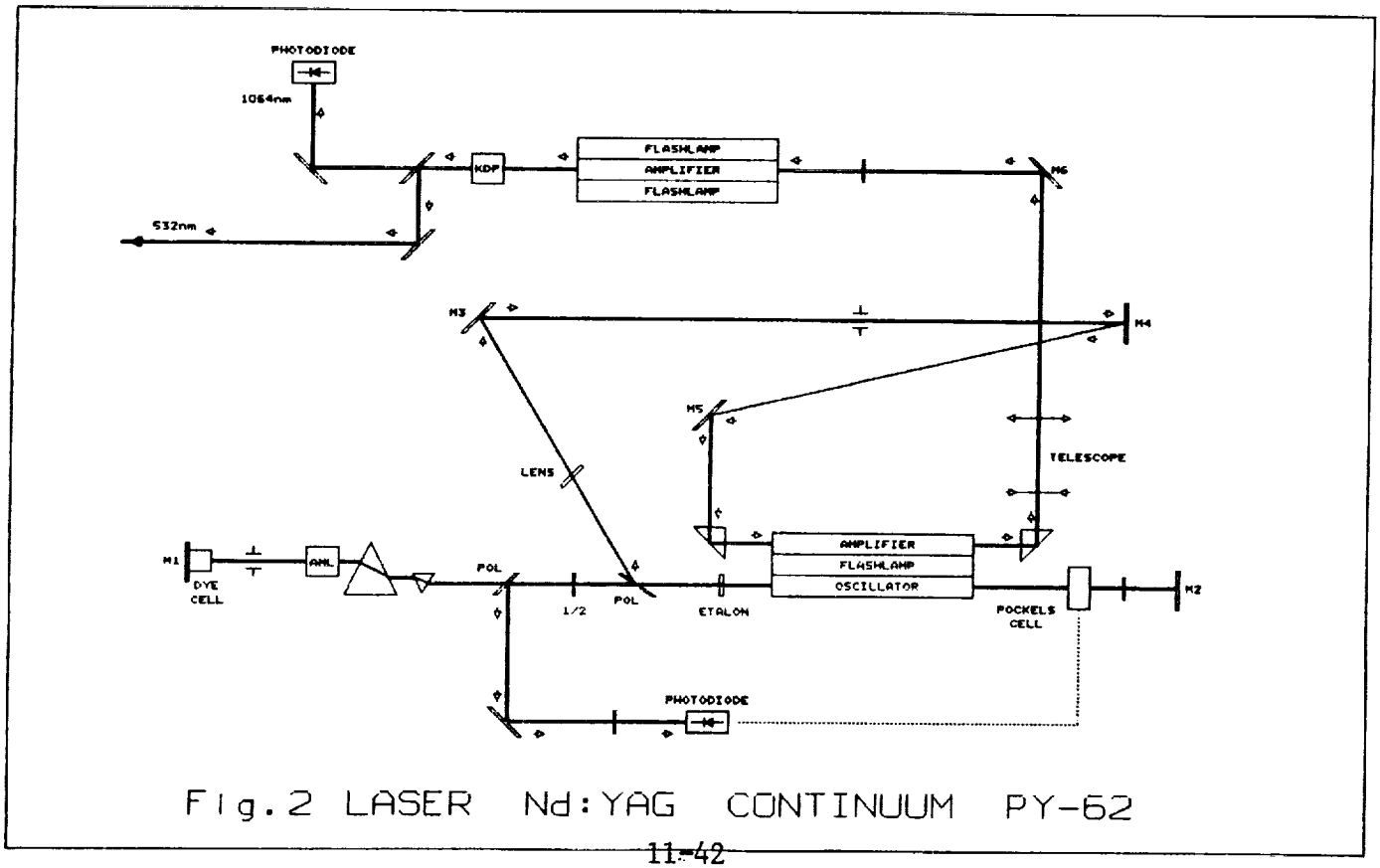

Fig. 2 LASER Nd:YAG CONTINUUM PY-62

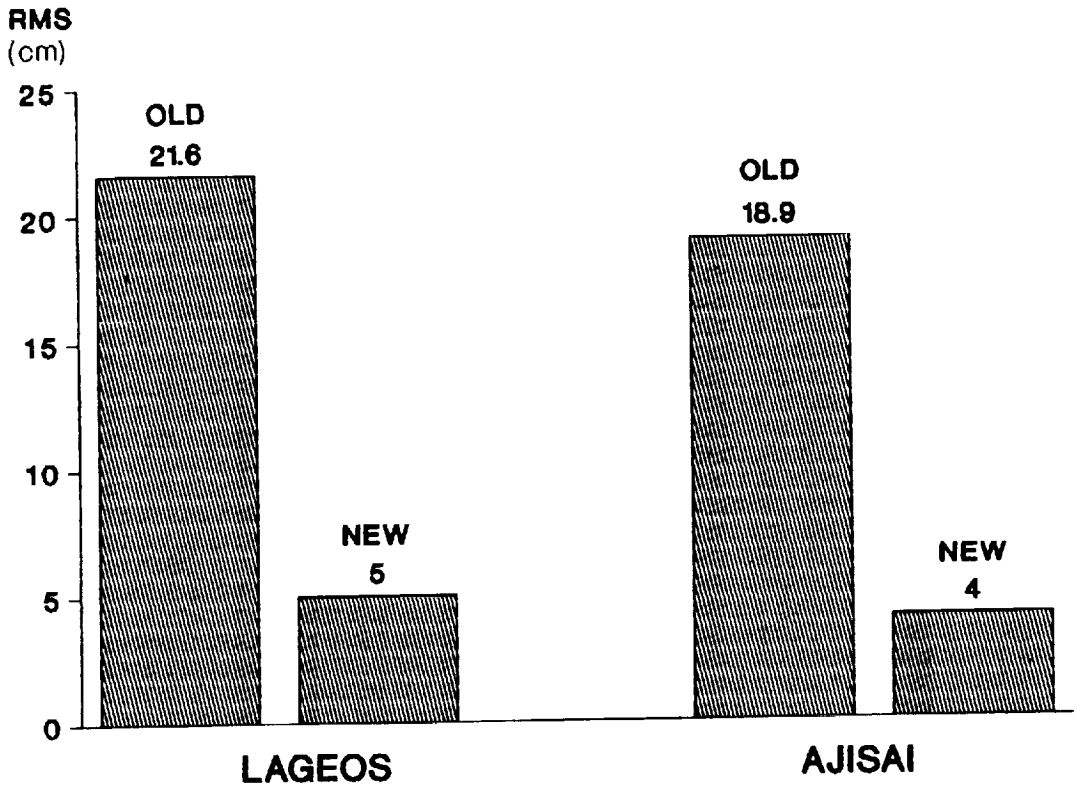

Fig.3 Single shot RMS - old and new laser.

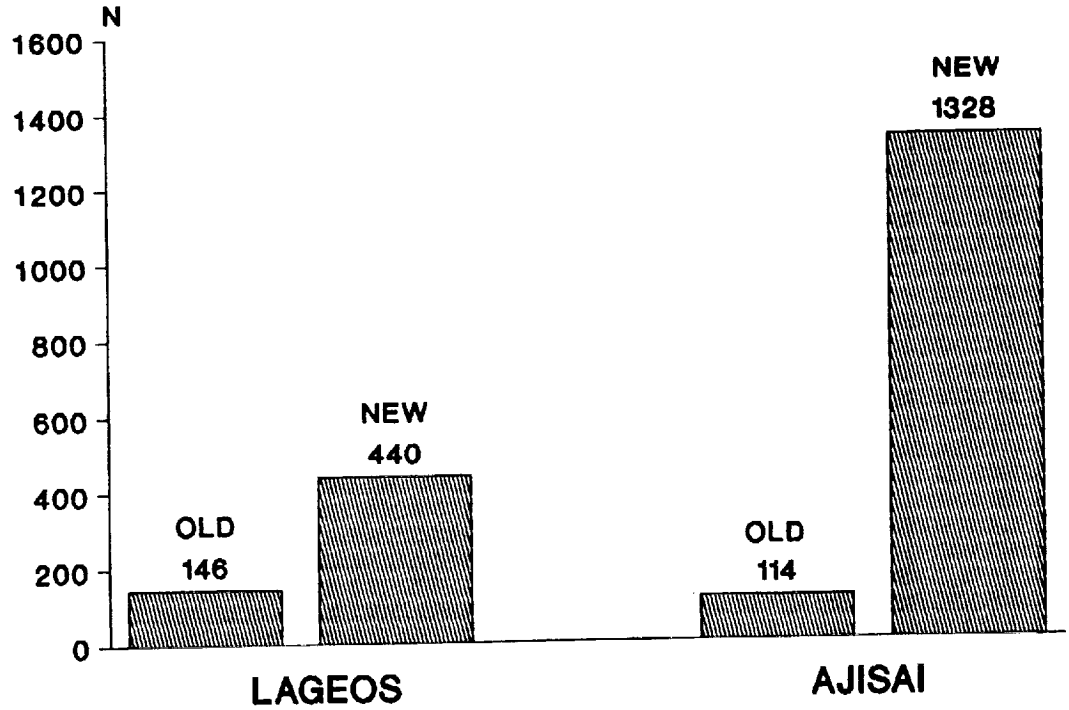

Fig.4 Returns per one pass - old and new laser

Development of Shanghai Satellite Laser Ranging Station

F.M.Yang, D.T.Tan, C.K.Xiao, W.Z.Chen, J.H.Zhang
Z.P.Zhang, W.H.Lu, Z.Q.Hu, W.F.Tang and J.P.Chen

Shanghai Observatory, Academia Sinica
80 Nandan Road, Shanghai 200030, China
Telex: 33164 SHAO CN
Fax: 86-21-4384618
Phone: 86-21-4386191

1. Improvement of the System Hardwares

1.1 Computer control subsystem

An IBM/286 computer control system was set up during August 1989 to March 1990. After three months, the realtime display of range residuals (O-C) on the computer screen was completed. Since then, only one operator has been needed for the routine observation. The operator can control the whole ranging system by using the computer keyboard during the observation and can watch the image of the satellite while illuminated by the sunlight on the monitor of a SIT TV camera side by side. The system automation and reliability has been greatly improved.

1.2 Laser Subsystem

The Nd:YAG mode-locked laser, which was made by the Shanghai Institute of Optics and Fine Mechanics and installed at the station in 1986, contains an oscillator and three single-pass-amplifiers and can usually produce 50 mj (green) and 180 psec width.

Many work have been done in order to improve the stability on both the laser beam direction and the output energy. A new chiller was installed in November 1991. The repetition rate is 1-2 Hz for Lageos and Etalon ranging, and 2-4 Hz for low orbit satellites ranging. The divergence of the laser is about 0.4 mrad. So, the optimum beam divergence from the transmitting telescope which has a magnification of 6 is about 13 arcseconds. That is good for Etalon satellites ranging. The divergence can be adjusted up to 3 arcminutes for the low orbit satellites ranging.

1.3 Receiver

The ordinary PMT (Type GDB49A, China-made) has been adopted from the set up of the system in 1983 to May 7,1992 when a single photon avalanche diode (SPAD) receiver made by the Czech Technical University has been installed. The voltage for the diode is about 30 V and the break down voltage is about 27.5 V. The field of view of the new receiver is about 45 arcsec. The noise rate of the SPAD working at above condition is 200-300 KHz even in the nighttime.

A 0.15 nm narrow band filter in a theomostat has been tested in November-December 1991 and has been shown with good performance.

2. Upgrading of the Softwares

2.1 The prediction of the satellite range

The IRV ephemerides for Lageos and Etalon-1,2 from Texas/CSR, the IRV for ERS-1 from DGFI and the SAO elements (Kepler orbital elements) for Ajisai and Starlette From NASA/GLTN have been used for the routine observations. The range residuals of prediction for Lageos is about 5-10 meters by introducing the corrections of the Time-bias (monitored by ourselves) and UT1 prediction from USNO Bulletin.

2.2 An error model of the tracking mount for reducing the systematic errors has been built. After the star calibration, the pointing accuracy of the mount is about 5 arcsec.

2.3 On-site normal point generation

The program of the on-site normal point generation was finished in March 1992. Since then, these normal points of the routine observation have been transmitted to the data centers.

2.4 New pre-processing program

A M-estimate program for better noise rejection purpose has been developed in stead of the least-squares estimate [Tan Detong, et al, this proceedings]. The new program has a stronger capability to deal with those passes which contain more noises and especially with the "end effect" of the fit curve, it means the noises at the both ends of the observation curve can be easily edited.

3. The Observation Status

3.1 The summary of the observations

After the above efforts, especially on the system automation, the performance of the laser ranging has been greatly improved, and the quantity of the observation passes has been dramatically improved since July 1990, even in Shanghai--the poor whether area. The observation staff works pretty hard, 14-16 hours per day and 7 days per week, if the whether permitting.

* The maximum number of passes obtained in one month — 98 passes (Jan. 1992)
* The maximum number of passes obtained in one night — 12 passes
* The maximum number of points obtained in one pass — 4265(Eta-2) 2865(Lageos)
* The estimate of range precision (single shot,rms) from 1988---up to May 7,1992 is about 4-5 cm.

* Fig.1 & 2 are the O-C residuals of Etalon-2 and Lageos passes.

Summary of SLR Observations at Shanghai (7837)

Year / Satel.	1988		1989		1990		1991		1992*	
	pass,	point	pass,	point	pass,	point	pass,	point	pass,	point
Lageos	37,	2625	33,	2555	162,	73782	137,	35071	89,	22409
Ajisai	41,	4033	74,	4323	158,	30594	134,	33183	48,	12637
Starlette	4,	142	12,	332	44,	6135	59,	9122	35,	2946
Etalon-1					38,	22222	21,	3888	13,	1579
Etalon-2					35,	10402	26,	7430	22,	1737
ERS-1							25,	2088	24,	3074
TOTAL	82,	6800	119,	7210	437,	143135	402,	90782	231,	44382

* up to May 9, 1992

3.2 **Multi-satellite tracking capability**
The typical time interval for the system to transfer from one satellite to another is about one minute, including the telescope moves back to the zero point and then travel to the prediction position of another satellite. The shortest time interval from the last return of Lageos pass to the first return of Etalon pass was only 126 seconds.

4. Preliminary Daylight Tracking Capability

After having the above-mentioned improvements, the daylight tracking to Lageos had been tested during November and December, 1991. The first returns in the daylight was obtained on December 20, local time 16:47 P.M. (Fig. 3)
The aperture of the receiving telescope is 600 mm, and the field of view of the receiver is 60 arcsec, 0.15 nm (FWHM) filter, PMT Type GDB-49A, the noise rate of the sky background was about 800 KHz.

5. Testing the New Type Laser

In April and May, 1992, a new Nd:YAG laser with an unstable resonator hybrided by nonlinear ring interferometer has been tested for satellite ranging at Shanghai station. Another paper [Yang Xiangchun et al, this Proceedings] introduces the technique for simultaneously compressing of

the passive mode-locked pulsewidth and pulse train. For SLR application, one amplifier and one frequency doubler were added to the oscillator. Without the single pulse selector, the output of the laser system was in pulse train containing only 1-2 giant pulses, and the total energy of the pulse train is about 18 mj (green), 10 psec width, 0.4 mrad beam divergence, 2-4 Hz repetition rate. During May 8-9, the new laser system and the SPAD receiver has been successfully used for Lageos and Etalon-1 ranging. The 2 cm range accuracy has been achieved in both satellite and ground target ranging. (Fig. 4 & 5)

6. Future Plans

6.1 Routine daylight ranging to Lageos and other low orbit satellites.

6.2 Single shot range accuracy will be improved to better than 2cm for routine operation.

6.3 **Development of the millimeter level accuracy SLR system**
A cooperative plan between Shanghai Observatory and Xi'an Institute of Optics and Precision Mechanics has been set up to develop a mm- level SLR system based on a circular-scan streak tube. A prototype tube has been made by Xi'an Institute in March 1991. The main characteristics of the tube is as follows:

* Photocathode:	Type S-20, Sensitivity	67 μA / lm
	Spectrum response	200-850 nm
	Effective area	12 mm
* Sensitivity of deflection		10 cm / KV
* Double MCP internal intensifiers		
* Gain		1×10^6
* Spatial resolution		24 lp / mm
* Temporal resolution		4.8 psec
* Dynamic range		390:1

This project has been supported by the Chinese National Science Foundation and the Chinese Astronomical Committee, and expected to be operational in 1994.

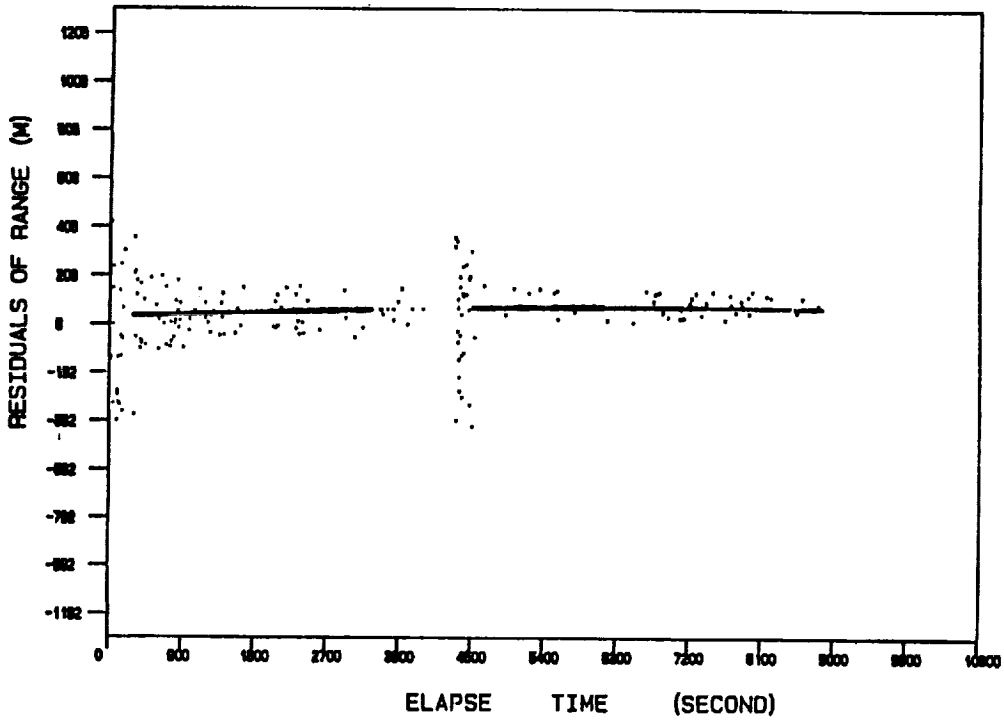

Fig.1 One pass of Etalon-2 on August 13,1990, 4138 Observations
Time (UTC):11:47 Accuracy(rms): 6cm

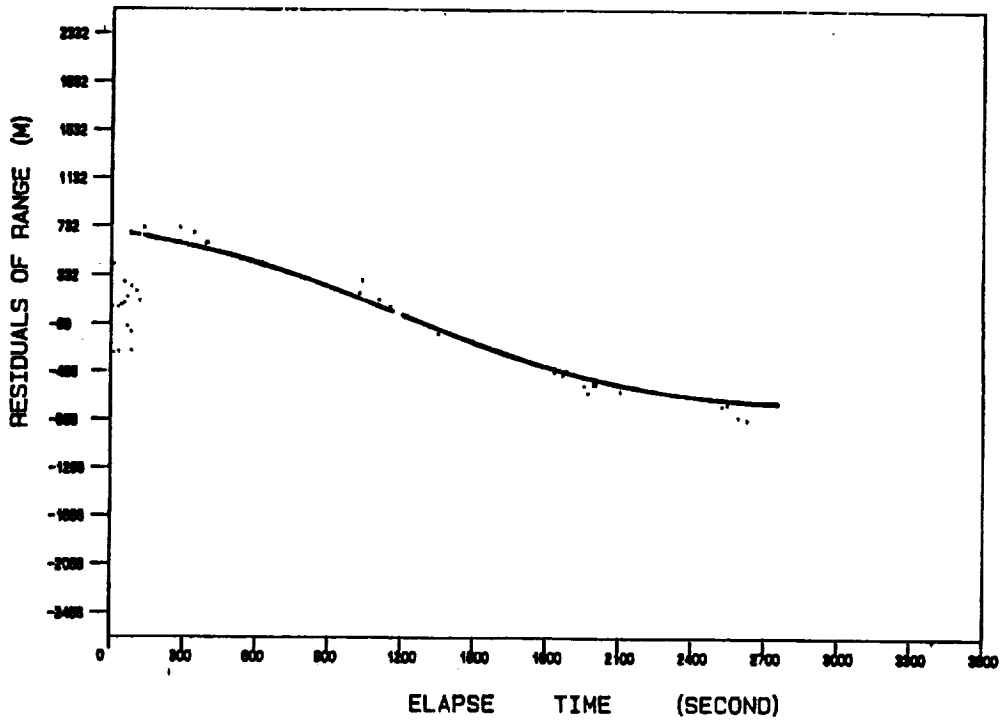

Fig.2 One pass of Lageos on July 28,1990, 2865 Observations
Time (UTC):18:17 Accuracy(rms): 5cm

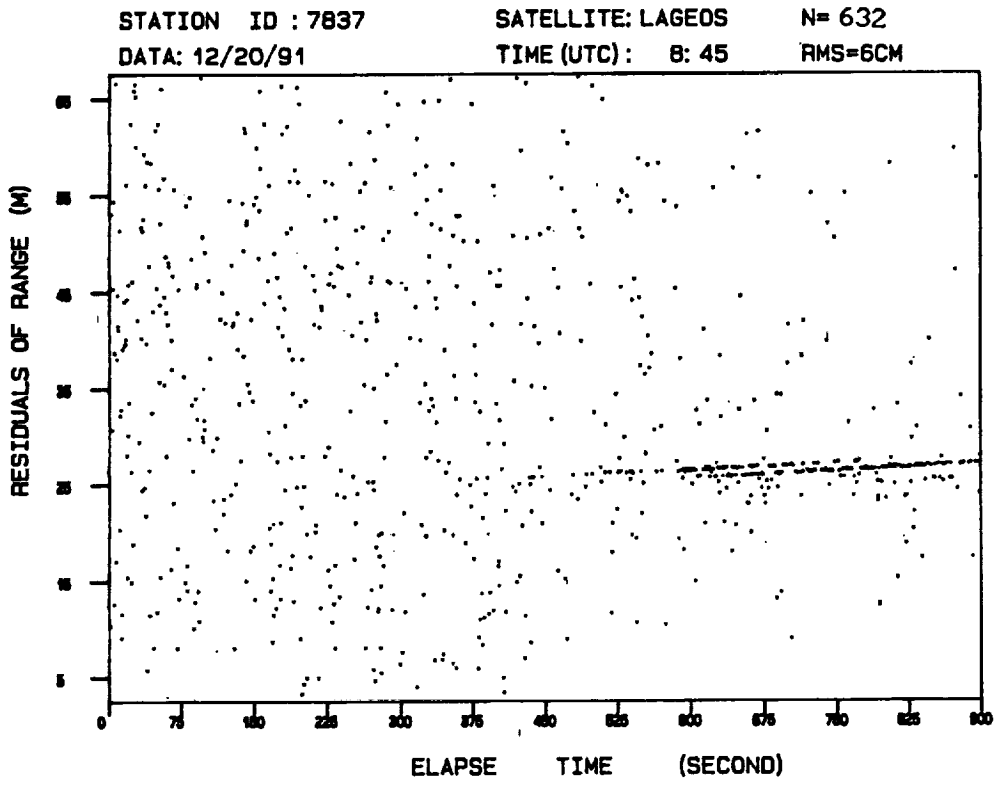

Fig.3 Daylight tracking to Lageos on December 20,1991

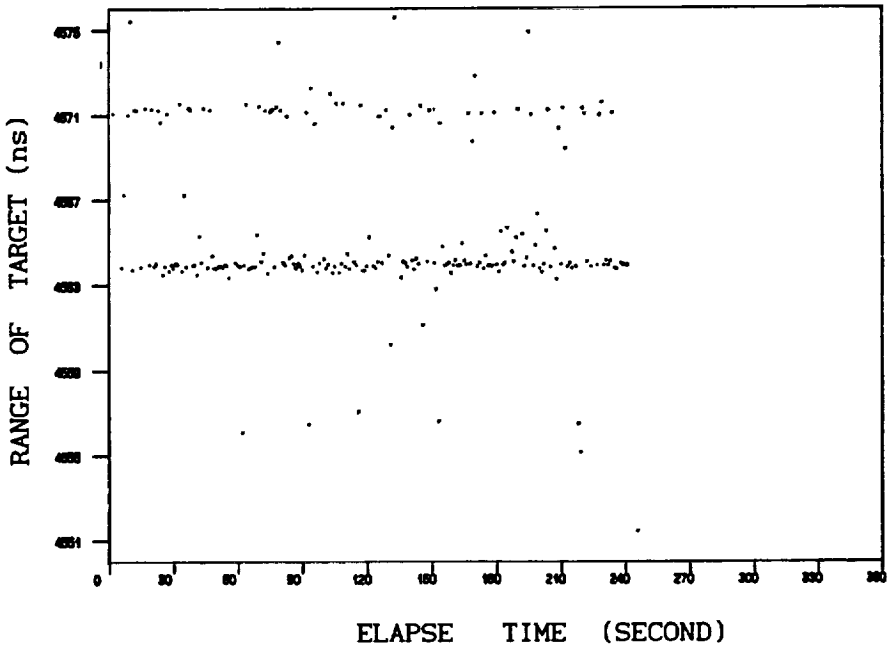

Fig.4 Ground target calibration on May 9,1992
with 10 psec laser train and a SPAD receiver

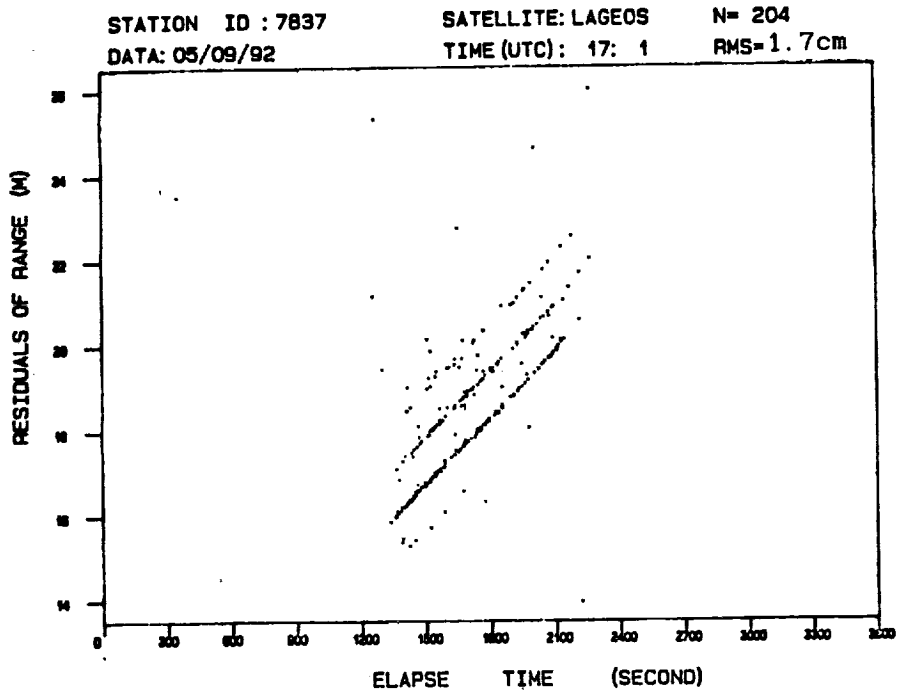

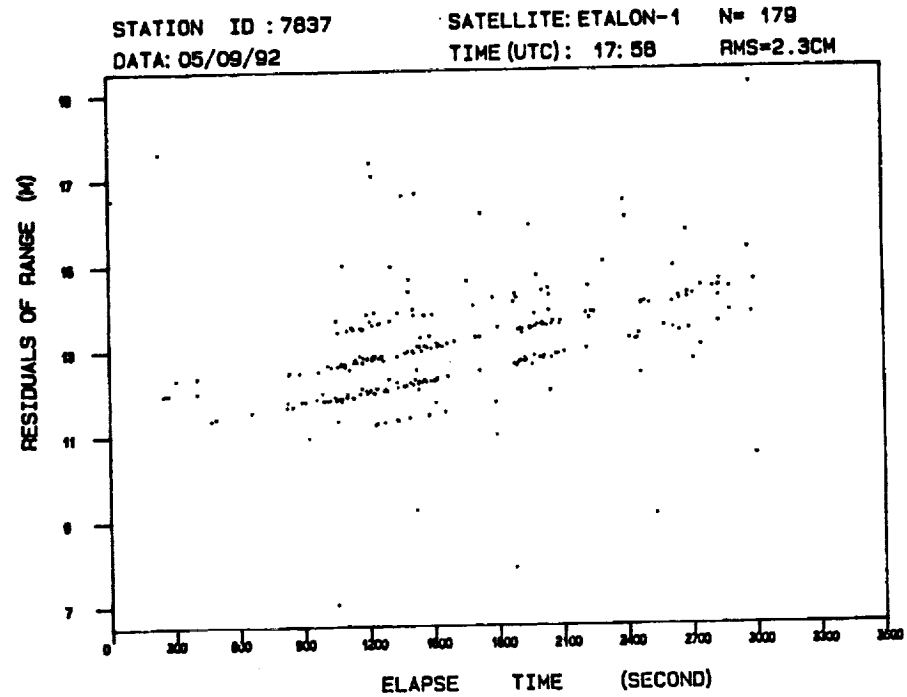

Fig.5 Results of ranging to Lageos and Etalon-1 with a 10 psec laser and a SPAD receiver (May 9,1992) Single shot accuracy(rms): 1.7--2.3 cm

C-7

N94-15606

STATUS-REPORT on WLRS

R. Dassing, W. Schlüter
Institut für Angewandte Geodäsie
Fundamentalstation Wettzell
D - 8493 Kötzting

U. Schreiber*
Forschungseinrichtung Satellitengeodäsie
Fundamentalstation Wettzell
D - 8493 Kötzting

Abstract

The Status-Report of WLRS gives an overview of its set up and the developments necessary to make the system operational.

1 History

After setting up the new Wettzell laser ranging system WLRS in the year 1989 the system got its first successful returns from LAGEOS at 29th January, 1990 (see table 1). As these returns were not calibrated they were only of "engineering use". The system showed that it was able to track to Etalon-type satellites and to METEOSAT P2. Before the first attempts to the moon were started the system was set up to a reliable and calibrated state. In order to guarantee continous observations from Wettzell a co-location between SRS and WLRS has been carried out. The old SRS-system is now replaced by WLRS.

At the beginning of 1991 WLRS started to track on a routine basis to the satellites LAGEOS, ETALON-1 and ETALON-2. During the first six month of year 1991 the WLRS-System was operated by one shift mostly during night times. Since 1st July 1991 there were enough educated observers to track 24 hours a day. This can clearly be seen in the amount of observed passes (see table 1). The number of returns per LAGEOS-pass ranged from several hundred up to 6000. At the end of 1991 the operators had enough experiences to track AJISAI, STARLETTE and ERS-1 satellites.

The first (calibrated) measurements from the moon were obtained in July 1991. In November 1991 a series of 52 echos from the moon could be measured, which resulted in one normalpoint.

*Technische Universität München, Arcisstr. 21, D - 8000 München 2

Jan., 29th, 1990	First echos from LAGEOS
Feb., 21st, 1990	First echos from ETALON-2
Feb., 23rd, 190	First echos from METEOSAT P2
Oct., 1990	First echos from APOLLO-15 reflector
Oct.1990 - Jan.1991	Collocation between SRS and WLRS
Feb.1991 - Jul.1991	Operational tracking system to LAGEOS, ETALON-1 and ETALON-2 during night time.
Jul.1991 - today:	Operational tracking system to *all* satellites and to the moon on 24 hours per day.

Table 1: Highlights of setting up WLRS

Month	Lunar	LAG	E-1	E-2	AJI	STARL	ERS1	sum
01'91	-	19	-	4	-	-	-	23
02'91	-	4	-	1	-	-	-	5
03'91	-	2	3	2	-	-	-	7
04'91	-	7	10	7	-	-	-	24
05'91	-	4	9	4	-	-	-	17
06'91	-	13	7	16	-	-	-	36
07'91	1	57	26	19	-	-	-	102
08'91	-	64	33	27	-	-	1	125
09'91	-	49	19	19	-	-	2	89
10'91	-	60	8	17	-	-	-	83
11'91	1	18	9	6	-	-	-	33
12'91	-	22	1	2	-	-	-	25
01'92	-	30	1	3	14	-	-	46
02'92	-	32	8	7	16	-	-	63
03'92	-	39	6	9	29	3	3	86
04'92	-	38	4	6	20	-	4	72

Figure 1: Number of passes during 1991 and 1992 of WLRS.

2 Developments

The following modifications and extension were carried out:

- WLRS is controlled by a HP1000/A900 computer. The observations during 24 hours a day restricted the computation time for non realtime tasks. Therefor the processing capacity was extended by an UNIX-based computer HP9000/835. The A900 and the HP9000 were connected to the local area network (LAN) of the Wettzell station.
- To track low orbiting the realtime software had to be modified:
  - To drive the telescope within its full capability under computer control the telescope driving process needed to be replaced.
  - An algorithm was written to drive the telescope "smoothly" into a pass which already has passed the tracking horizon.

  - The transmit/receive switch between outgoing and receiving laser pulses is realized as a rotating mirror with two holes. To fire the laser with 10 Hz the mirror must rotate with 5 Hz. To track to low orbiting satellites the software to ramp up and control the rotating frequency of the T/R-switch up to 10 Hz was replaced.
  - To track low orbiting satellites a 'time bias' was built into the realtime software. This 'time bias' moves the current epoch for the calculations of azimuth, elevation and range.
- During winter 1991/1992 the analysists of the University of Texas and Bendix found a sudden range bias of about 1.75 m. This was caused by the replacement of an amplifier of MCP.
  The reason was found in the dead time of the detection electronics. The electronic needs about 68 ns to be able to detect the realtime calibration pulse after the detection of the start pulse of the laser. This means that the calibration return must take more than 68 ns to be recorded by the event timer. As the return signal from the calibration retro was very close to 68 ns it was not obvious that the electronic detected the "dead-time" instead of the real calibration echo. Now, the calibration return moved away from this critical region to avoid any collisions.
- The quicklook-data generation was replaced by a normal point generation. An orbit fitting algorithm is used.
- Experiments in 2-color ranging have been carried out by measuring several LAGEOS-passes simultanously in green and infrared [Schreiber et al.].

3 Summary

After setting up WLRS in 1989 some essential modifications were carried out:

- High data acquisition rate (up to 6000 Returns per LAGEOS pass);
- Normalpoint precision of 3 - 5 mm (BEFC);
- A laser ranging system which can track all targets — from ERS-1 to the moon.

4 References

[Schreiber et al.] U. Schreiber, K.H. Haufe, R. Dassing, "Measuring Atmospheric Dispersion With WLRS In Multiple Wavelength Mode", published in this proceedings

GROUND BASED LASER RANGING FOR SATELLITE LOCATION

by

G. C. Gilbreath
Optical Systems Section
Naval Center for Space Technology
Naval Research Laboratory

and

Harold D. Newby
Malabar Test Facility
Phillips Labs (AFMC)

ABSTRACT

In this article, we describe a new satellite laser ranging capability which is a joint effort between the Naval Research Laboratory and Air Force Optical Tracking Facility at Malabar, Florida. Initial measurements off LAGEOS indicates that uncorrected radial range rms values of 8mm are readily achievable. Number of photoelectron counts are on the order of 180 which are off by an order of magnitude from predicted values.

I. INTRODUCTION

A new SLR capability designed and implemented by the Naval Research Laboratory is now operational at the Air Force Optical Tracking Facility in Malabar, Florida. The configuration is based on the monostatic design utilized by a number of the NASA systems in the geoscience network. The laser itself is more powerful than those used by the NASA network and electronics are somewhat different. The system was designed for experimental efforts in tracking unenhanced satellites (those satellites without retroreflectors), plumes, and other targets which may or may not have large laser ranging cross sections.

II. CONFIGURATION

A. Tracking & Acquisition:

Tracking and acquisition was done by the optical tracking facility at Malabar, Florida. Malabar's facility provided a bistatic optical acquisition capability when tracking in "terminator" mode. In this mode, a platform is sunlit but the tracking station is in the dark. The initial acquisition is done passively with the 1.22 m aperture telescope. Once trained on

the satellite in question, the0.61 m aperture telescope can track the target within 5-10 μR of accuracy. All vectors, offsets, and tracking is done under computer control using a MicroVax III. Video recordings of a laser ranging event is made in addition to a digitized record of tracking vectors and related offsets.

The transmitter/receiver design is monostatic although acquisition is bi-static. Once the 0.61 m telescope is trained on the target, laser ranging commences. A diagram of the overall method is shown in Figure 1.

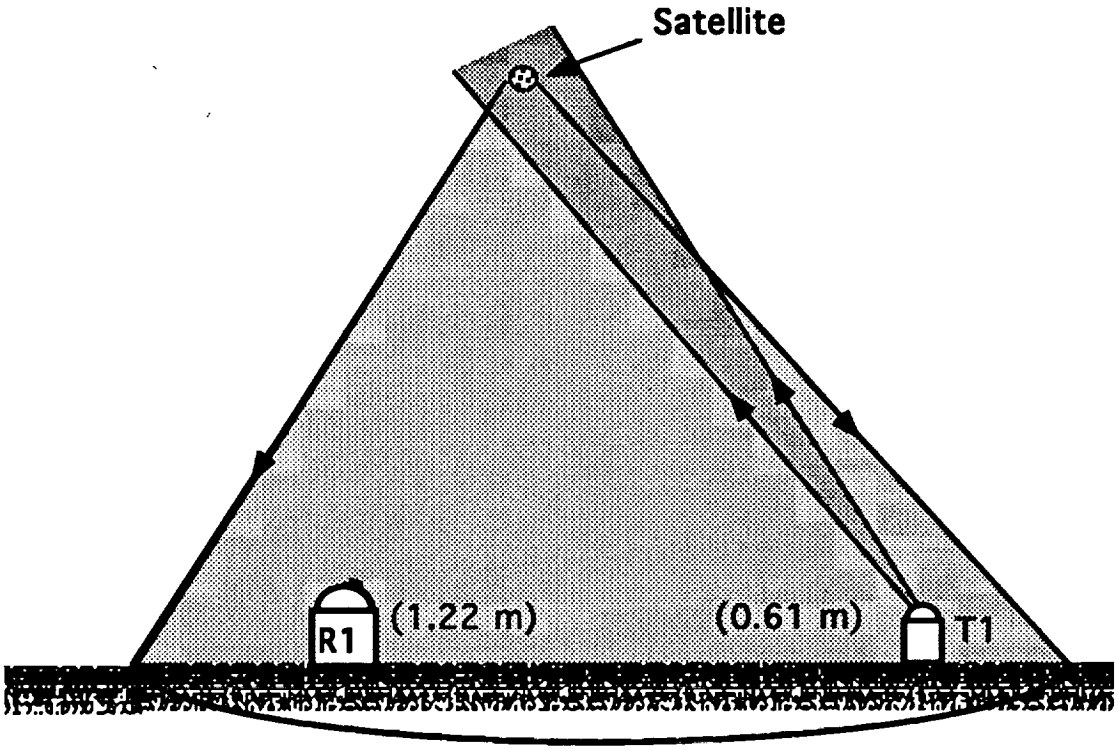

FIGURE 1. NRL/Malabar Satellite Laser Ranging Acquistion Diagram. Initial Acquisition is bistatic when platform is acquired in "Terminator Mode". Once acquired by R1, T1 tracks. The laser ranging T/R is monostatic using T1.

The return signal is collected by the telescope and directed back through the optics where the light is directed to a MCP/PMT using a specially designed annular mirror. The return signal, if strong enough, is split, where part is sent to the time interval counter, and part is sent to a wideband oscilloscope (4Ghz) for waveform capture. An overall system block diagram is shown in Figure 2.

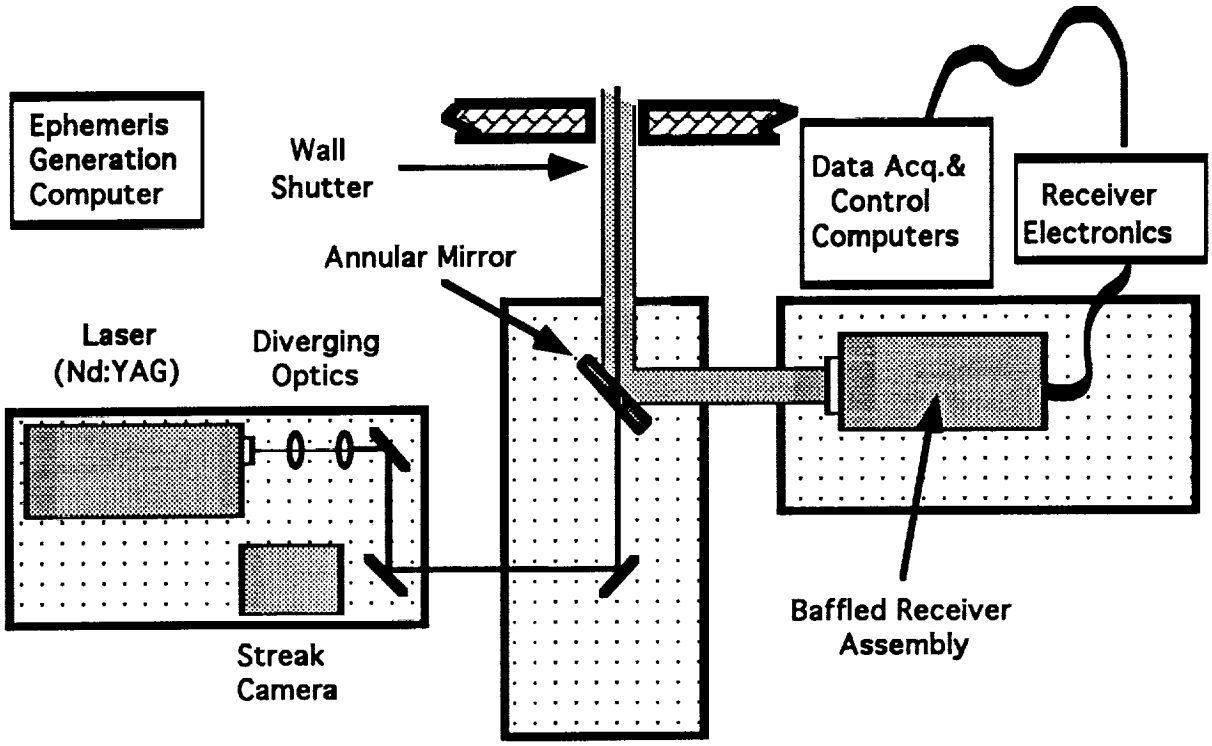

FIGURE 2. NRL/Malabar Satellite Laser Ranging Block Diagram. Configuration shows laser and transmit optics directed through an annular mirror; returned signal is directed via the mirror to the baffled receiver assemby where time differences and waveforms are recorded digitally for off-line analysis.

B. Transmitter:

The laser was designed for the effort by Continuum and is a doubled-YAG, Q-switched, mode-locked laser . The cavity design is "active-active" in that a pulse slicer is used rather than a dye to select desired modes. The configuration includes an oscillator stage and two single-pass amplification stages. The laser provides 300 mJ per pulse in a 250 ps pulsewidth. The pulse repetition rate is 10 Hz. The beam divergence is approximately 10 times the diffraction limit.

Initial alignment in the active-active mode has proven to require careful adjustment. For this reason, a streak camera is configured into the testbed. It was found that initial diagnostics are required at start-up but good alignment is maintained thoughout a given ranging session.

Scattered infrared light is focused onto a PIN detector and the output is directed through a constant fraction discriminator (CFD). The signal is then split and sent to a SR 620 time interval counter and to the IRIG board in the HP 9836 Controller, which time-tags the event.

C. Optics:

Adjustable "zoom" optics are installed to vary the divergence of the beam though computer control. The range of variability is designed for an output at the antenna of 10μRad-100μRad.

A special annular mirror was designed such that the transmitted beam passes through a 4.57 cm hole in the 20.32 cm mirror. The return beam is collimated by the telescope to present a ~11.4 cm beam to the flat. The return beam is then directed to the baffled receiver assembly.

D. Receiver:

The return signal is directed through a 1 m focal length lens to a mirror which can be switched in and out of the optical path. When in place, this mirror directs the light toward a Fairchild intensified CCD which enables verification of proper optical alignment of the receive optics. When this mirror is switched out, the beam is focused onto a 500mm pinhole and directed into the gated ITT F4129 PMT/MCP detector. This detector has a quantum efficiency of 16% with a gain of ~10^6 at 532nm. The detector itself is gated to reduce noise using a programmable delay/width generator. The gatewidth can vary from several hundred nanoseconds to 10 μs.

The output from the PMT is amplified, inverted, and passed through a constant fraction discriminator. The output is time-tagged by the SR 620 time interval counter and the difference stored in the computer. A portion of the output is also directed to a Tektronix SCD 5000 4 GHz wideband oscilloscope which digitizes and stores the waveform for later analysis. A block diagram of the electronics is shown in Figure 3.

III. LAGEOS CALIBRATION

The system was calibrated by ranging off LAGEOS for a series of passes. Radial RMS ranges (uncorrected) were estimated to be ~8mm using the system. Detected photoelectron counts were on the order of 50-190. We initially estimated returns on the order of 1100 p.e.'s. It is possible that the divergence convolved with pointing accuracy has a greater error than anticipated. However, scatter loss is most likely to have been the major contributor to the lower returns.

IV. CONCLUSION

The Naval Research Laboratory and the Air Force Optical Tracking Facility have installed a new satellite laser ranging

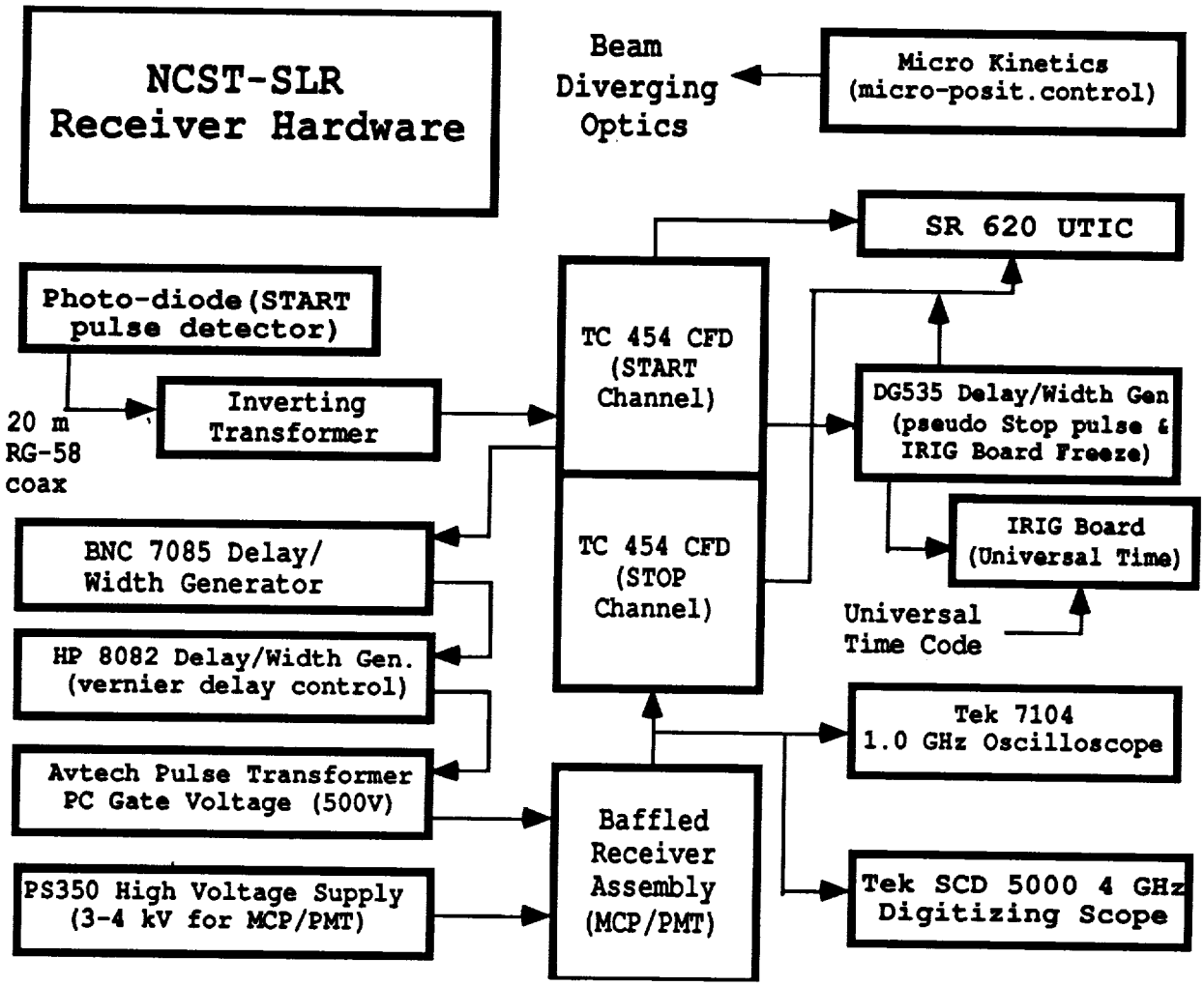

FIGURE 3. NRL Satellite Laser Ranging Receiver Hardware Block Diagram.

capability in Malabar, Florida. The system is based on the NASA monostatic designs used by MOBLAS and other ground sites. The laser itself is a 300 mJ/pulse, 250 ps, 10Hz, Q-switched, mode-locked, active-active design. The detection system includes a gated ITT F4129 PMT/MCP detector and a 4 GHz wideband Tektronix digitizing oscilloscope.

Initial mesurements off LAGEOS indicates that an 8mm uncorrected radial range rms is easily achievable. However, actual p.e. counts are smaller than predicted by an order of magnitude. . This may be due to larger than anticipated divergence and/or to back scatter.

Future efforts will require direct measurement of the divergence in the far-field using the "dithering" technique common to MOBLAS users. Corrections to divergence can be made using the computer-controlled zoom optics in the transmit

optical train. Anticipated experiments will include ranging off of platforms which may not have enhanced laser ranging cross sections and ranging off plumes.

V. ACKNOWLEDGMENTS

We would like to thank John Degnan, Tom Varghese, Tom Zagwodski, and the other NASA personnel who were so generous with their time and advice. We would also like to acknowledge the MacDonald Observatory, and especially Jerry Wiant whose suggestions were invaluable.

We would especially like to acknowledege both the NRL and Malabar teams, without whose the dedication, hard work, and creativity, the system could not have been designed, integrated, and calibrated in such a timely manner, including W. C. Collins, W. L. Lippincott, J. Pirozzoli, T. Murphy, S. Peterson, A. Clement, J. Kobesky, R. Dasenbrock, R. Betz, T. Knox, M. Baciak, P. Patowski, and R. Orcutt.

NEW PROGRESS OF RANGING TECHNOLOGY AT WUHAN SATELLITE LASER RANGING STATION

Xia Zhizhong, Ye Wenwei, Cai qingfu
Institute of Seismology State Seismological Bureau
430071 Wuhan China

ABSTRACT

A satellite laser ranging system with an accuracy of the level of centimeter has been developed successfully at the Institute of Seismology, state Seismological Bureau with the cooperation of the Institute of Geodesy and Geophysics, Chinese Academy of Science. With significant improvements on the base of the second generation SLR system developed in 1985, ranging accuracy of the new system has been upgraded from 15cm to 3-4cm. Measuring range has also been expanded, so that the ETALON satellite with an orbit height of 20,000Km launched by the former U. S. S. R. can now be tracked.

Compared with the 2nd generation SLR system, the newly developed system has the following improvements:

(1) A Q modulated laser is replaced by a mode-locked YAG laser. The new device has a pulse width of 150ps and a repetition rate of 1-4pps.

(2)A quick response photomultiplier has been adopted as the receiver for echo, for example, the adoption of MCP tube has obviously reduced the jitter error of the transit time and therefore has improved the ranging accuracy.

(3)The whole system is controlled by an IBM PC/XT Computer to guide automatic tracking and measurement. It can carry out these functions for satellite orbit caculation, real-time tracking and adjusting, data acquisition and the preprocessed of observing data etc. , the automatization level and reliability of the observation have improved obviously.

INTRODUCTION

Satellite laser ranging(SLR) is a new measurement technology established with the advancement of laser, optoelectronics, computer, and space science. It has been widely applied in geoscience. Its observing date have already been used in many scientific fields such as geody-

namics, geodesy, astronomy and earthquake prediction.

It has especially shown its importance in monitoring the movements of global plates and reginal crust, determining geocentric coordinates, and studing of earth rotation parameters and gravitational field model. The 2nd generation SLR system finished in 1985 at the Institute of Seismology. The system has a measuring range of 8000Km and the accuracy of 15cm. In order to upgrade the equipment from 2nd to 3rd generation. So that the observing data of Wuhan SLR station can meet the need of monitoring crustal movements and the research of earth rotation parameters and solid earth itself, the Institute of Seismology and Institute of Geodesy and Geophysics established cooprative relation.

The 3rd generation system tracked satellite AJISAI of Japan and Lageos of US successfully several times in June 1988. After the preprocessed of observing data, the accuracy of single shot attained 5—7cm. Since August 1989, the quick-look data of the ranging results have been sent to GLTN of NASA. The accuracy of Lageos observing date of Wuhan SLR station back from GLTN is also about 5-6cm.

In April of 1990,F4129 micro-channel plate(MCP) is used to replace PM2233B photo multiplier and the accuracy reaches 3-4cm. At the same time ETALON-2 and ETALON-1 satellite with an orbit height of 20,000Km launched by the former U. S. S. R. in 1989 were also observed.

Measuring Principle of System and Performance of the Individual Parts

The ranging principle of the Wuhan SLR system is as follows: the ephmeris (provided by GLTN or CSR of Teaxs University) is input into an IBM PC computer before observation, in order to caculate and interpolate the satellite orbit. A real-time clock in the computer sends out a series of order signals to control the automatic tracking of the mount, to shoot laser beam, to pre-set range gate, to correct the pointing direction of telescope and range gate in real time and to collect observing data. At the moment of shooting laser the main pulse is sampled as the open signal for time interval counter. The echo from the retroreflectors of the satellite is received by a telescope with an aperture of 60cm. The optical signal is converted to an electronic pulse by MCP tube and then amplified to close the time interval counter and the time interval measurement is completed. Meanwhile, observing data is collected by the computer. , The whole measuring process is shown on the computer display. Observing object,caculating satellite position, or ways of interpolation and measurement can all be selected on the menu. Fig. 1 and Fig. 2 show the telescope and computer, control and electronic measurement system respectively. Table 1 is the performance of the main parts in the system.

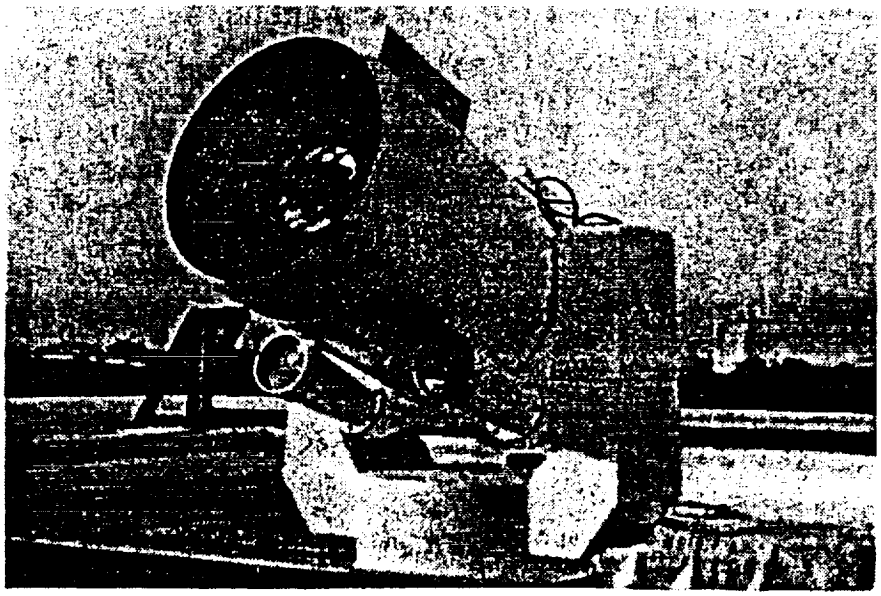

Fig. 1 The mount of Wuhan SLR system

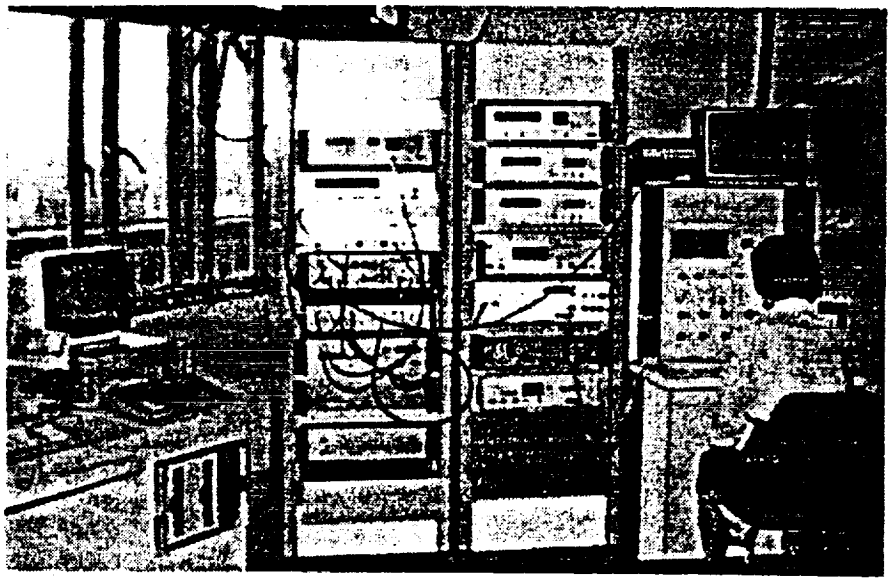

Fig. 2 Receiving electronic equipment, computer and clock subsystem

Table 1 Specification of the satellite laser ranging system at Wuhan

Subsystem	Specification
Mount	
Configuration	elevation-azimuth
Tracking velocity	18 arcsec—0.5° per second
Synchronistic inductor	resolution 1 arcsec
Drive	DC torque motors
Orthogonality	±4 arcsec
Laser	
type	Nd:YAG
Wave length	0.532μm
Energy	50mj
Pulse width	150ps
Repetition	1-5pps
Receiving telescope	
Type	Cassegrain
Diameter	60cm
Field of view	1′-6′or 1°(use for sighting satellite)
Filter	1nm
Transmitting telescope	
Type	Galilean
Diameter	10cm
Beam divergence	0.6′-3′ can adjustable
Sighting telescope	
Diameter	15cm
Field of view	3°
Receiving electronics	
PMT	ITT F4129 MCP
Amplifier	H/P 8447 D
Discriminator	Canberra 1428A
UTC clock	
Type	Cesium H/P 5061A
Stability	1×10^{-12}
Accuracy	2μs
Time interval counter	
Type	5370B
Resolution	20ps
Micro computer	IBM PC/XT

Main Improvements

1. Nd : YAG ultra-short pulse mode-locked laser is used

An active and passive mode— locked laser with Nd : YAG as laser material is used in the new SLR system. Fig. 3 is block diagram of laser. Infrared light output of 100 mJ in energy, 1. 06μm in wavelength, and 150ps in pulse width is got from laser with one stage oscilator and three stage optical amplifier. It is converted to green light of 50mJ in energy, 532nm in wave length and 1-4pps adjustable in repetition rate. Compared with the Q modulated device(4. 5ns inpulse width, 0. 25J in energy) used in the 2nd generation system, The new laser improved the ranging accuracy, because the pulse width is reduced greatly Table 2 shows the comparision of ranging accuracy between adopting Q modulated device and mode-locked device, while other conditions are the same.

Table 2. The Comparision of ranging accuracy between Q modulated and mode—locked laser from LAGEOS

DATE	TIME	OBS	Wuhan RMS(cm)	GLTN RMS(cm)	LASER
1985. 08. 02	23:44	103	13. 9		YAG Modulated Q
8. 03	22:20	370	15. 8		
8. 14	21:26	131	14. 6		
8. 16	22:21	105	15. 4		
9. 11	22:01	280	14. 9		
9. 28	20:02	320	14. 7		
10. 05	21:03	101	16. 1		
10. 07	21:50	170	15. 7		
1989. 11. 27	18:50	471	5. 7	5. 1	YAG Mode-Locked
11. 28	17:34	431	5. 7	5. 1	
11. 28	21:07	303	5. 7	6. 5	
12. 01	17:04	144	6. 1	6. 5	
12. 01	20:28	483	6. 3	6. 5	
12. 02	19:04	176	7. 3	5. 1	
12. 03	17:44	330	7. 5	5. 3	
12. 03	21:18	438	6. 7		

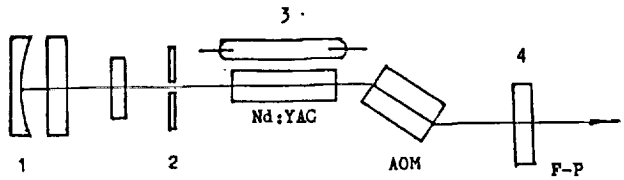

High Repetition Rate Ultra-short Pulse Oscillator
1-Rear mirror contacted by dye cell with circulating system. 2-Transverse mode selecting aperture.
3-Xe flash lamp. 4-Front mirror.

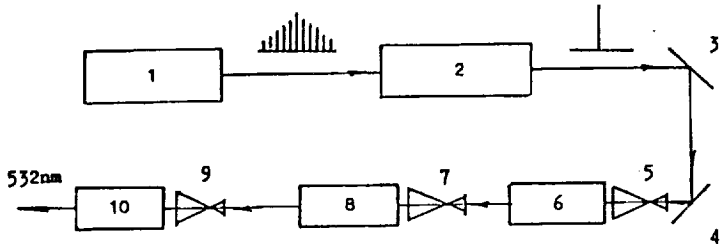

1-Ultra-short pulse oscillator. 2-Single pulse selector. 3,4-45° mirrors. 5,7,9-Beam expanders. 6-First stage of amplifier. 8- Two stage of amplifier. 10-Harmonic generator.

Fig. 3 Schematic Diagram of Repetition Rate Ultra-short Pilse Laser System

2. Improvement of opto-electronic detector PM2233B photomultiplier is employed as detector for main and echo pulse in the 2nd generation SLR system, the transit time of electron in the whole tube is relatively long so the jitter error will become very important for precise ranging. In order to overcome this shortcoming, F4129 MCP photomultiplier with 1ns transit time is used for detecting echo in the 3rd generation system. The jitter error is sharply reduced because the distance between the cathode and micro-channel plate is just 0. 6μm . Table 3 shows the observing results before and after the photomultiplier is replaced. Data processing by GLTN, Delft University and ourselves, all show that the ranging accuracy has upgraded from 5-7cm to 3-4cm.

Table 3. the Observing results before and after the photomultiplier is replaced from LAGEOS

DATA	AOS	LOS	OBS	Wuhan RMS(cm)	GLTN RMS(cm)	DELT1 RMS(cm)	PMT
SAT. LAGEOS							
90. 3. 6	17:55:15	18:17:48	81	8. 1	5. 6	6. 4	PM 2233B
3. 7	16:24:58	16:51:52	210	7. 1		6. 4	
4. 4	13:32:14	14:11:08	308	8. 4		7. 2	
4. 12	13:11:49	13:50:55	47	8. 8	7. 8	8. 0	
4. 13	15:25:13	15:56:08	265	7. 5	4. 7	6. 1	
4. 19	14:16:44	14:57:38	675	6. 4	5. 4	6. 1	

4.25	13:04:01	13:44:19	312	4.5	4.4	4.9	F4129 MCP
4.26	11:48:11	12:19:58	346	6.3	6.1	4.9	
4.26	15:18:14	15:47:42	387	4.6	4.8	4.9	
5.4	11:49:50	12:00:50	40	4.1	3.7	3.5	
5.4	15:01:39	15:26:16	274	3.9	5.0	3.5	
5.5	13:36:30	14:11:07	643	3.8	3.2	3.3	
5.6	12:17:38	12:41:51	123	3.9	2.9	3.3	
5.9	11:50:05	12:06:31	252	4.0	3.4	3.3	
5.17	14:54:44	15:16:12	355	3.8	2.1	1.6	
5.18	13:26:49	14:05:00	1050	3.8	2.2	2.8	
5.19	12:07:34	12:37:50	530	3.8	2.2	2.0	
5.24	12:22:27	12:54:50	630	3.6	4.4	2.8	
5.25	14:37:25	14:55:54	163	4.1	2.3	2.0	
5.27	12:07:14	12:24:11	114	3.8	2.0	2.0	
6.1	12:02:29	12:35:54	491	3.8	1.3	1.8	
6.8	13:13:31	13:31:57	294	3.6		1.8	
6.10	13:54:12	14:16:18	164	4.3		1.8	

3. Automatization and reliability greatly improved with the use of IBM personal computer.

Though the 2nd generation system at Wuhan SLR station has realized automatic track for the first time in China. "Automatic" only means the numerical guiding of the mount since only two 8-bit single board micro-computer is used for real-time control while orbit elements of the satellite(one set for every 20 second) is caculated by VAX-750 computer and is input from Keyboard manully. Heavy work loud, low information convey speed, frequent handling error are among the shortcoming. the 3rd generation SLR system adopts IBM PC as its control center. Real-time clock range, gate controller, data acquisition and laser shooting controller, etc. which are originally in the instrument cabinet are extended in programmable functions and are reduced in volume, so that they combined on two extending boards to be installed in the extension slot of IBM PC computer. With these change, the structure is compacted and reliability raised. Software regarding ephemeris, data processing, numerical track guiding, software managing,etc. are all transplanted to IBM PC computer. While working, the telescope is automatically guided towards the satellite by the track control part with the caculating result from ephemeris. In order to improve tracking accuracy, tracking parameters(time, azimuth, elevation) can be displayed and corrected in real time during the observation. Observing results and o-c difference are also displayed in both digital and graphical ways, so that the operator can understand working state and correct parameter to improve hit rate. Once observation end, the preprocessing is selected to analyze ranging data. By the manner of the menu

the operational course are simplified greatly. These improvements decreased the misoperation and raised the efficiency. Fig. 4 shows the display of some parameters on computer screen during the operation.

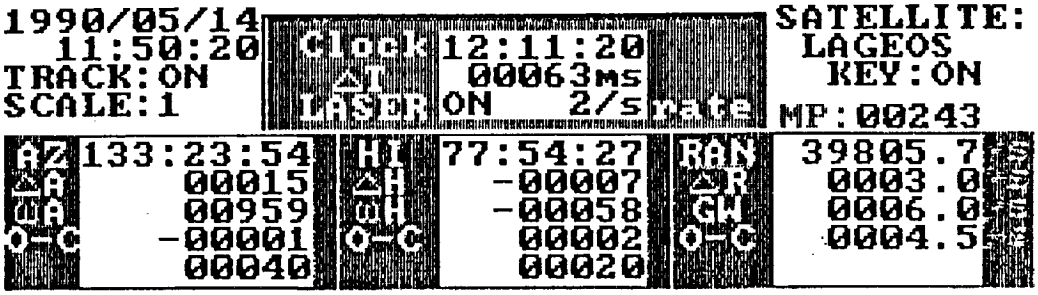

Fig. 4 The display of some parameters on computer screen during the operation

In addition, other improvement are also carried out e. g. 5370 B time interval counter is instead of old one and stability of laser output and the accuracy of mount pointing are also improved. We are also striving to realize daytime observation and to improve other performance of system to better the use of SLR technology for geoscience research.

Reference

1. Xia Zhizhong, Ye Wenwei, Cai Qingfu. "A satellite laser ranging system for tracking LAGEOS" proceedings of China- United states symposium on crustal deformation and earthquake, 1985 Wuhan China.

2. John J. Degnan " Satellite Laser Ranging: Current status and Future Prospects" IEEE Transactions on geoscience and remote sensing, Vol. GE—23 No. 4 July 1985.

3. Ye Wenwei, Xia Zhizhong, Liu Hangang, "Study on Improving Ranging Accuracy in Wuhan SLR Station" in Chinese 1990. 10.

4. Guo Tangyong, et al. "A Track-Control and Data-process System for the Satellite Laser Ranging" in Chinese, 1990. 10

Mobile System

Upgrades/Developments

Allied Signal

TLRS-3 SYSTEM UPGRADES

Richard Eichinger, Grace Cheng, Bill Crawford, Don Cresswell,
Henry Crooks, Bud Donovan, Dave Edge,
Ken Emenheiser, Bill Hanrahan, Mike Heinick,
Herb Hopke, Van Husson, Toni Johnson, Mark Levy, Paul Malitson,
Dennis McCollums, Alan Murdoch, Tom Oldham, Don Patterson,
Paul Seery, Mike Selden, Charles Steggerda, Tom Varghese,
Scott Wetzel, Anne Wheeler

Allied Signal Aerospace Company
BFEC/CDSLR
10210 Greenbelt Road
Seabrook, MD 20706
USA

Abstract

This presentation describes the upgrades to the Transportable Laser Ranging System, serial number three (TLRS-3), and the impact that these upgrades will have on the TLRS-3 performance in the field. The four major areas of system upgrades are the HP-380 computer, the Optical Attenuation Mechanism (OAM), the upgraded spatial, spectral and temporal filtering for improved daylight ranging capability, and the software upgrade to enable the system to track the Etalon satellites.

The TLRS-3 was returned to the Goddard Geophysical and Astronomical Observatory (GGAO) in December 1991 for system upgrades in preparation of the TOPEX/POSEIDON campaign scheduled to begin in the summer of 1992. Many system upgrades were incorporated into the system while interleaving planned facility maintenance making TLRS-3 a more versatile and more dependable laser ranging system.

The TLRS-3 was initially baselined with the MOBLAS-7 via simultaneous satellite ranging on the LAGEOS, Ajisai, Starlette and ERS-1 satellites. During the upgrades and following completion of the system upgrades intercomparisons with the MOBLAS-7 were made to verify the integrity and accuracy of the system changes.

Several other groups of personnel participated in the TLRS-3 upgrade and they are: the Survey Section, the Precision Measurement Equipment Laboratory, the Architectural and Engineering Services Department, the Precision Timing Section and the station personnel at TLRS-3 and MOBLAS-7.

Allied Signal

OBJECTIVES AND GOALS

HP-380 COMPUTER UPGRADE

OPTICAL ATTENUATION MECHANISM UPGRADE

DAYLIGHT TRACKING CAPABILITY

ETALON RANGING CAPABILITY

FACILITY MAINTENANCE

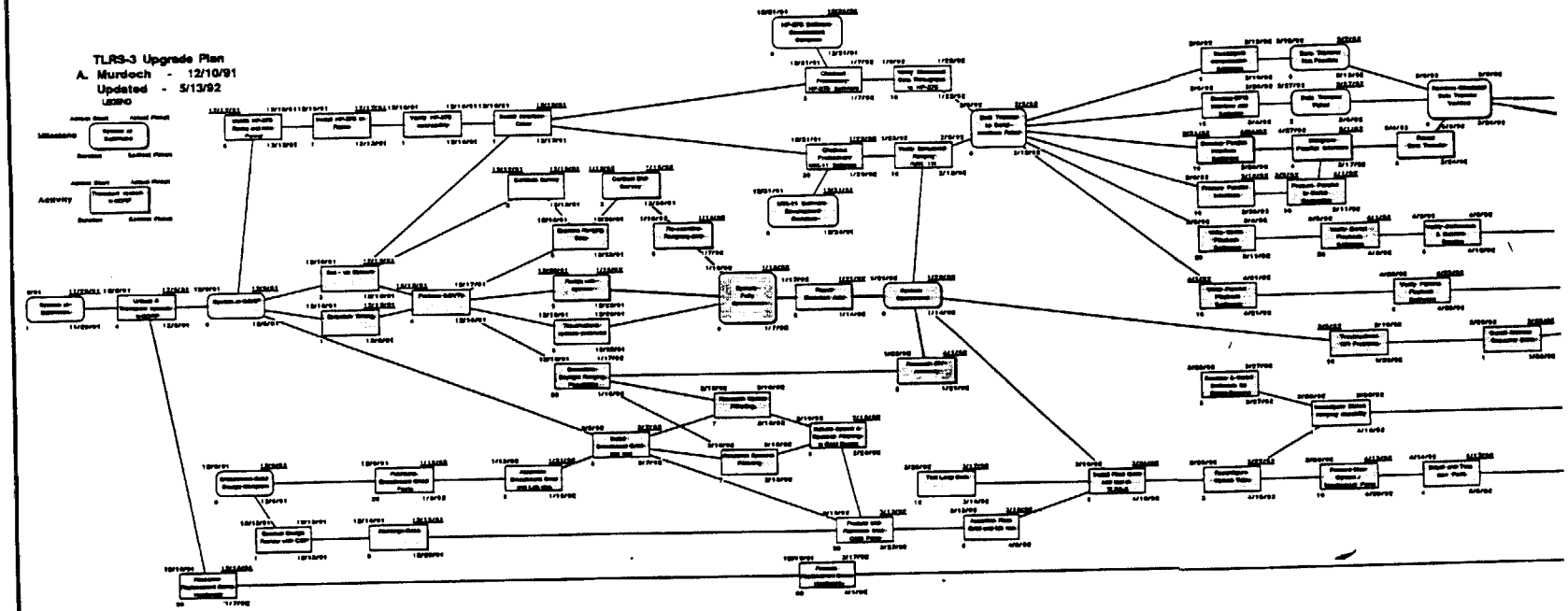
TLRS-3 Upgrade Plan
A. Murdoch - 12/10/91
Updated - 5/13/92

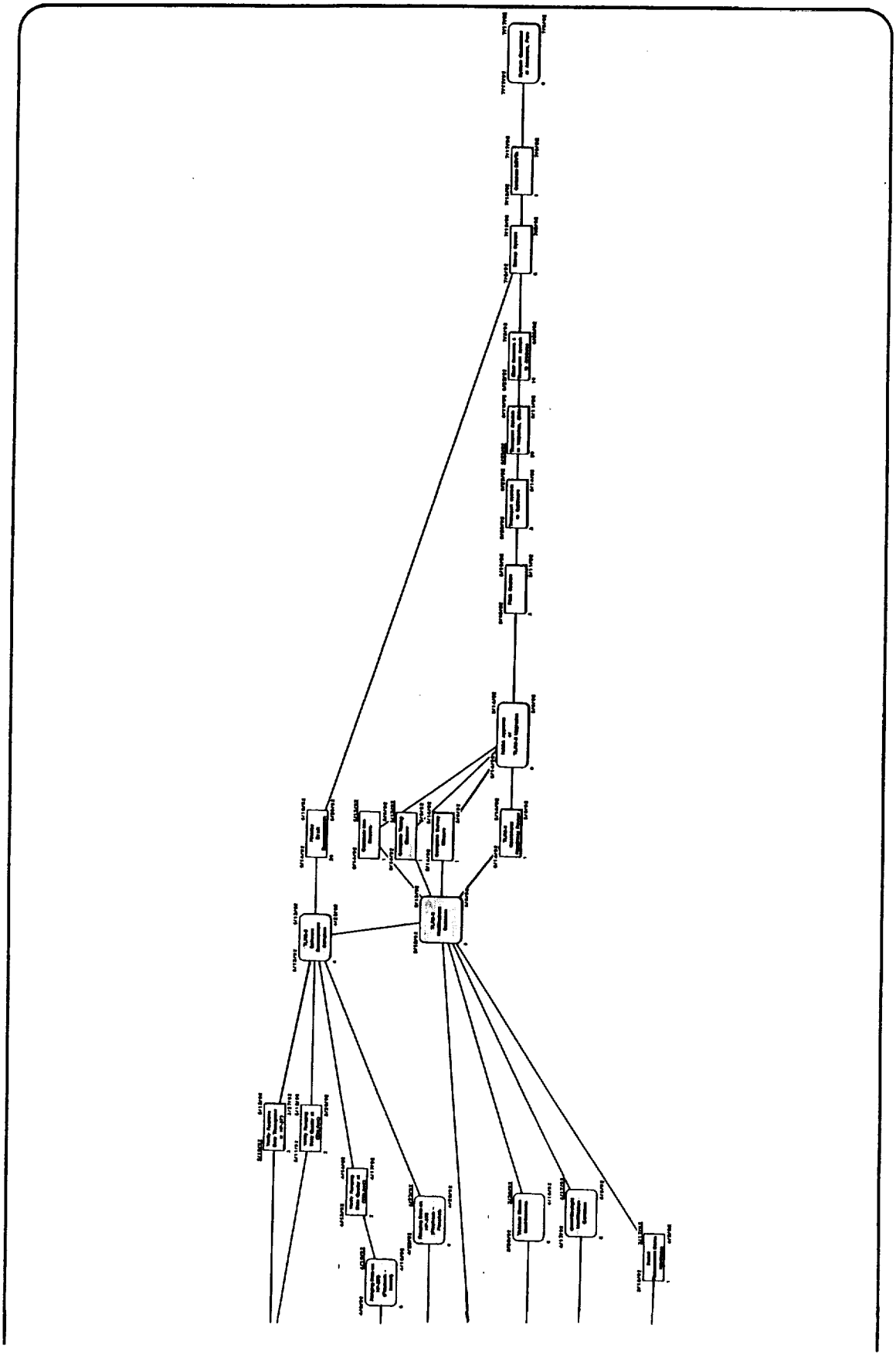

Allied Signal

HP 380 COMPUTER FEATURES

HP 380: 16MB RAM, 660MB HARD DISC, 330MB OPTICAL DISC, HP UX 8.0

REAL TIME DSP PARALLEL INTERFACE TO MIK-11/2 COMPUTER

INCLUDED MULTI-SATELLITE/MULTI-LEVEL OPERATIONS CAPABILITY

IMPROVED STAR CALIBRATION PROGRAMS (FK5, GLOBAL/KALMAN, 70 STARS)

ETALON RANGING CONTROL AND DATA AQUISITION

TUNED IRVs; ie TEMPORAL FILTER IMPROVEMENT

Allied Signal

OPTICAL ATTENUATION MECHANISM FEATURES

MANUAL CONTROLLED OPERATION

COMPUTER CONTROLLED OPERATION

SOLENOID ACTUATED TRANSMIT ND FILTER: FIXED VALUE

VARIABLE RECEIVE ND ATTENUATION RANGE: 0.01 to 4.0 ND

SOLENOID ACTUATED DAYLIGHT FILTER

Allied Signal

DAYLIGHT TRACKING

SPATIAL FILTER APERATURE REDUCED to 500 MICRONS

DAYLIGHT SPECTRAL FILTER REDUCED FROM 10 to 3 ANGSTROMS

ALIGNMENT COLLIMATOR MAKES DAYLIGHT STAR CALIBRATION POSSIBLE

TELESCOPE FOCUS MUST BE ADJUSTED FOR DAYTIME/NIGHTTIME TRACKING

Allied Signal

ETALON TRACKING

CAPABLE OF 5 pps OPERATION TO 135 MILLISECOND RANGE

DATA AQUISITION CHANGES TO 2.5 pps FOR GREATER THAN 135 ms

LOW SIGNAL AMPLITUDE RETURNS WHEN TESTED AT GGAO

Allied Signal

TLRS-3 IMPROVEMENT SUMMARY

- HP-380 COMPUTER SYSTEM
- OPTICAL ATTENUATION MECHANISM
- AUTOMATED TRANSMIT ND FILTER
- AUTOMATED 3A SPECTRAL FILTER
- COLLIMATOR ALIGNMENT TELESCOPE
- SIMMERED CAPACITOR BANK FOR LASER OSCILLATOR HEAD
- TEMPORAL FILTER REFINED
- SPATIAL FILTER TIGHTENED
- TRANSMIT/RECEIVE OPTICS RECONFIGURED
- BORESIGHT AND COELOSTAT ALIGNMENT PROCEDURES REDEFINED
- CESIUM FREQUENCY STANDARD REPLACED
- FREQUENCY STANDARD UPS REPLACED
- DOME AND VAN REPAIRED
- AC POWER RECONFIGURED

SATELLITE RESIDUALS

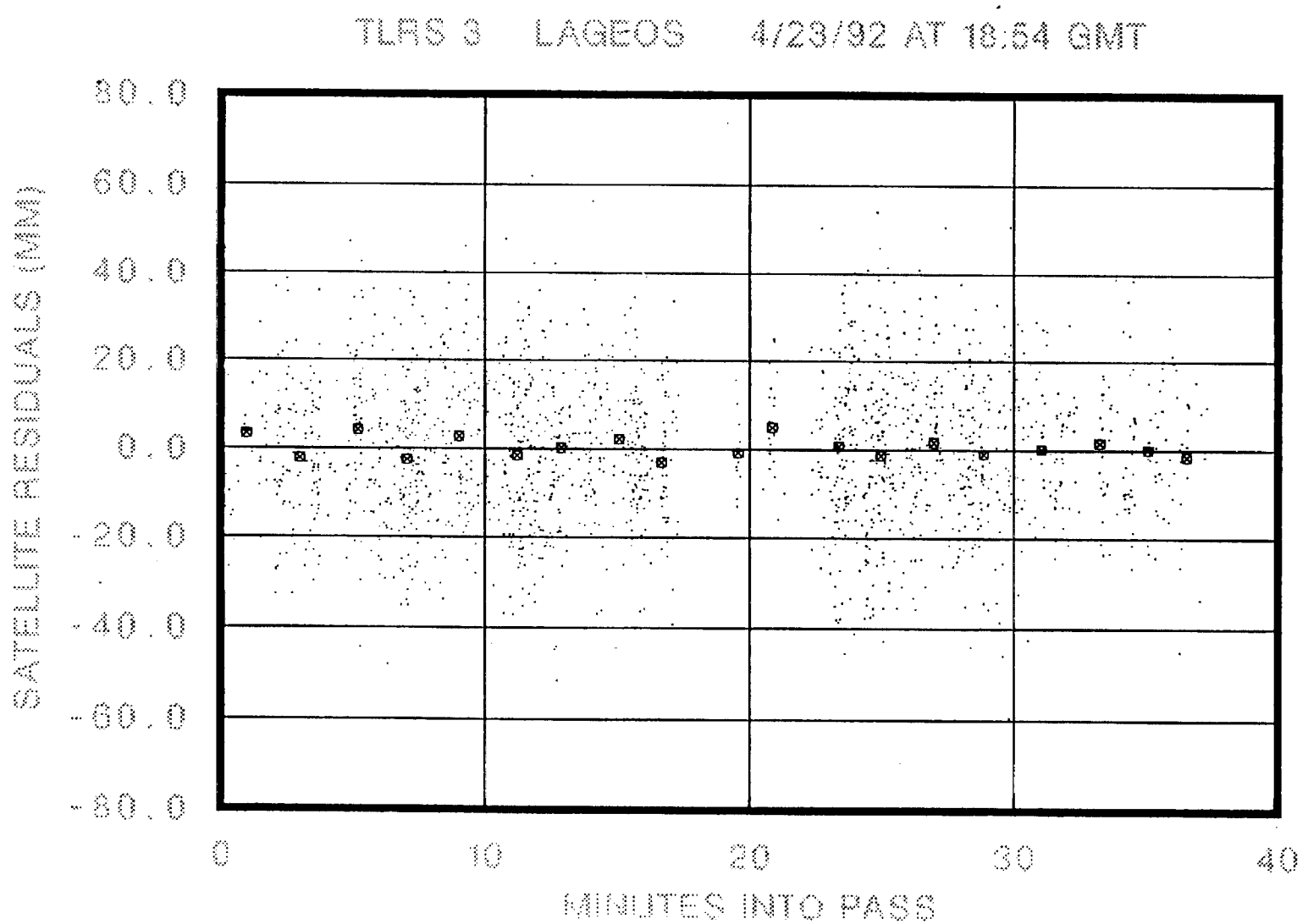

SATELLITE RESIDUALS

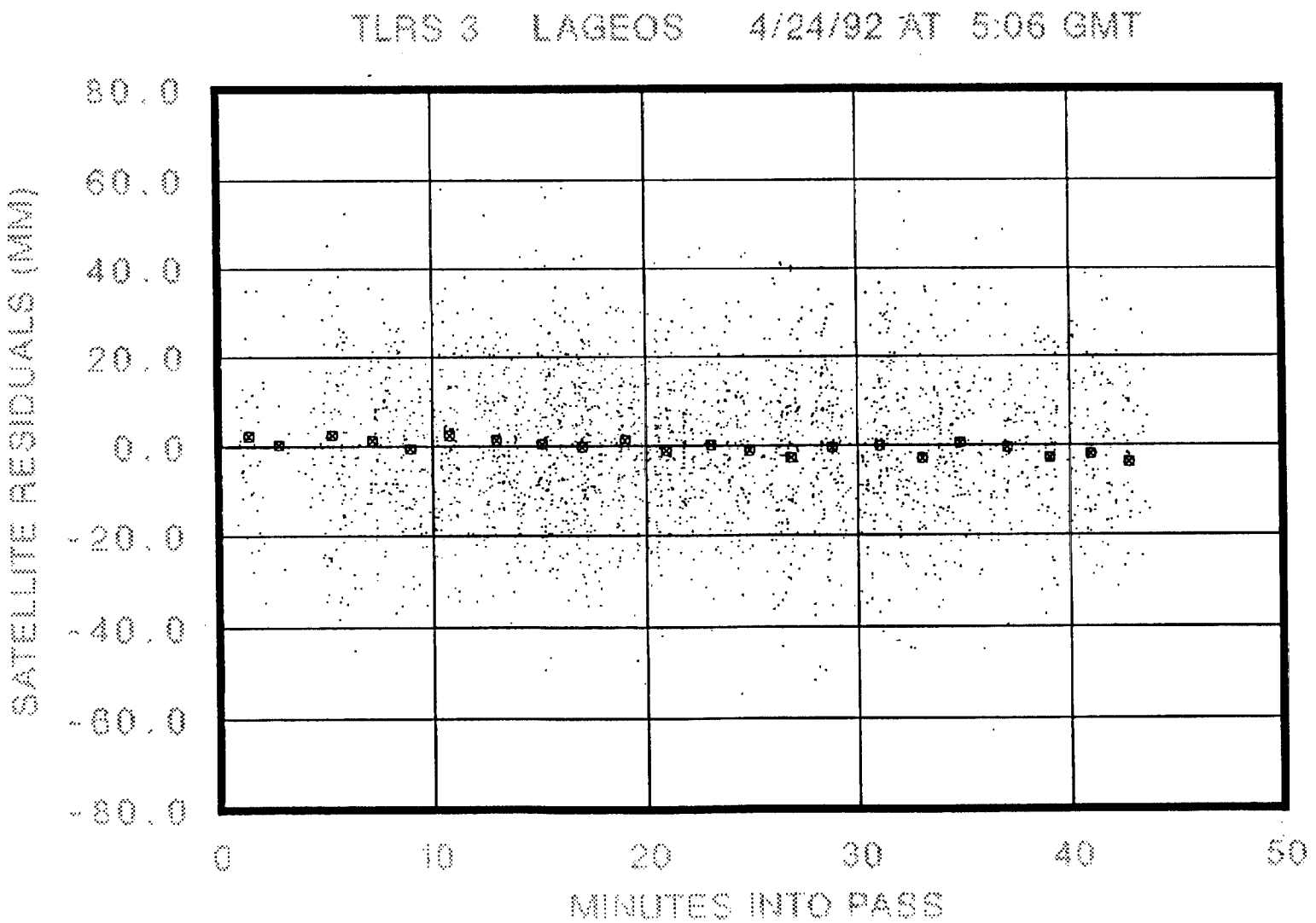

TLRS-3 vs. MOBLAS 7 GORF INTERCOMPARISON

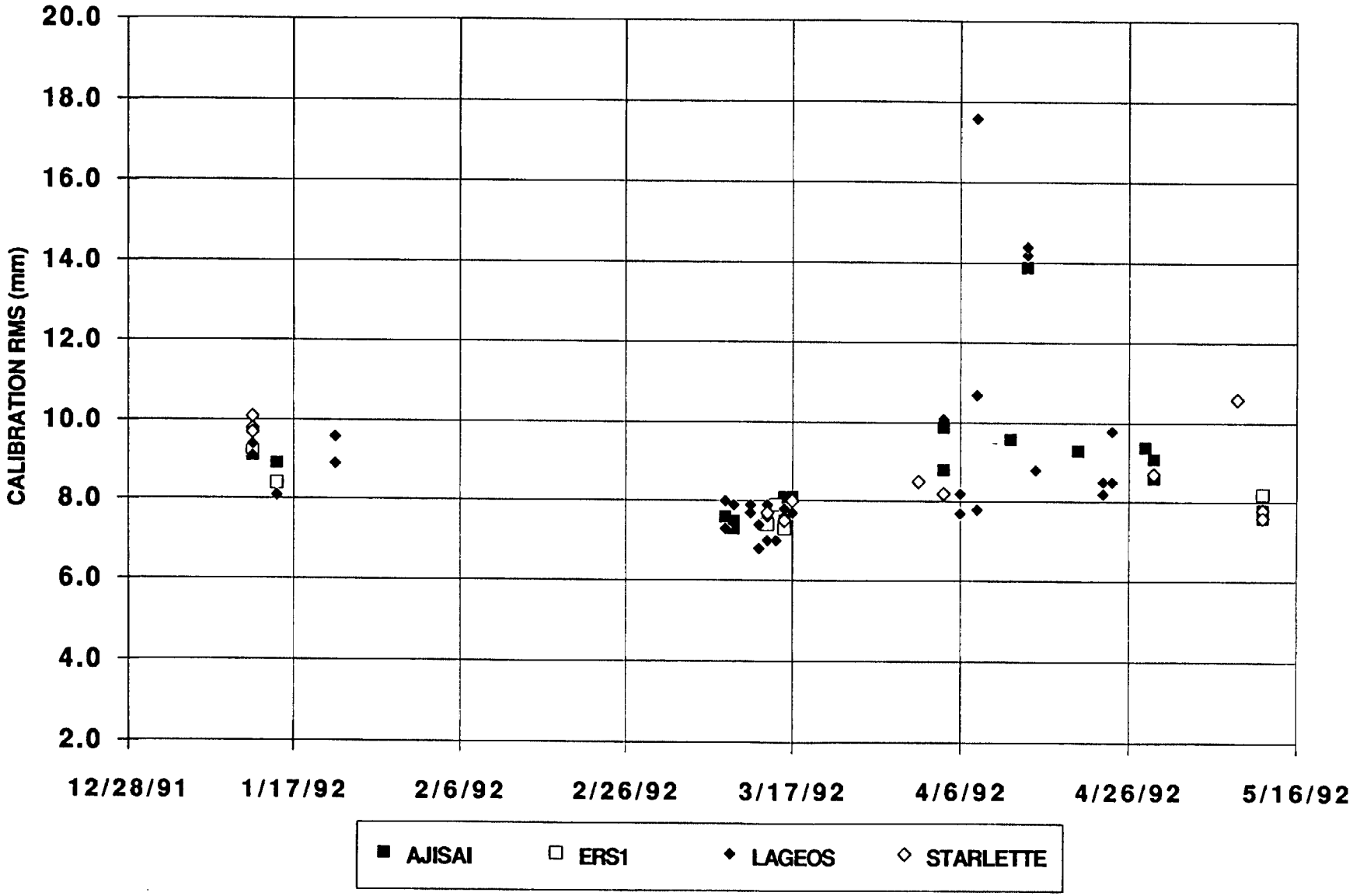

CDSLR/NES/S.WETZEL

5/13/92

TLRS-3 vs. MOBLAS 7 GORF INTERCOMPARISON

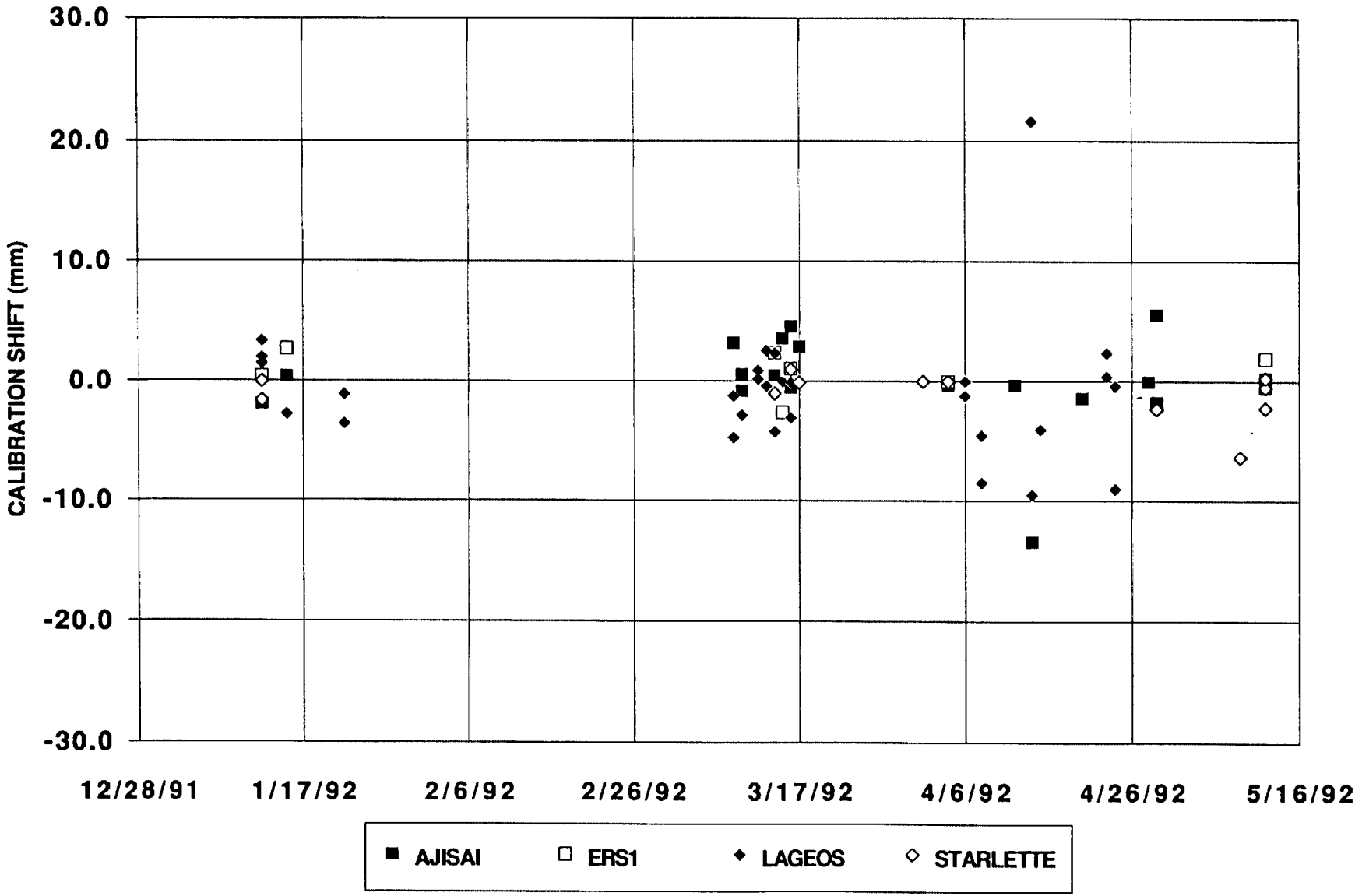

CDSLR/NES/S.WETZEL

5/13/92

TLRS-3 vs. MOBLAS 7 GORF INTERCOMPARISON

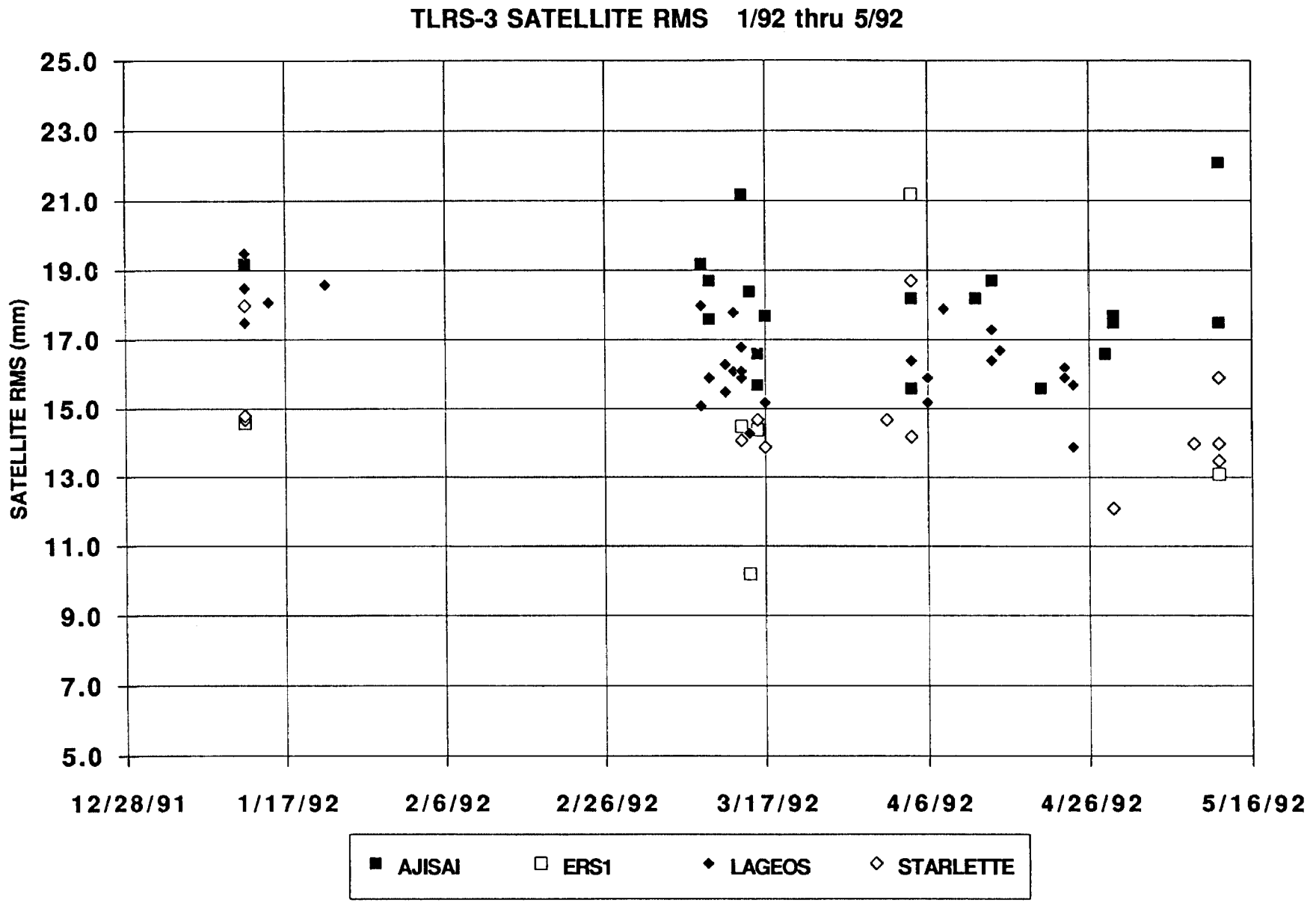

CDSLR/NES/S. WETZEL

5/13/92

TLRS-3 vs. MOBLAS 7 GORF INTERCOMPARISON

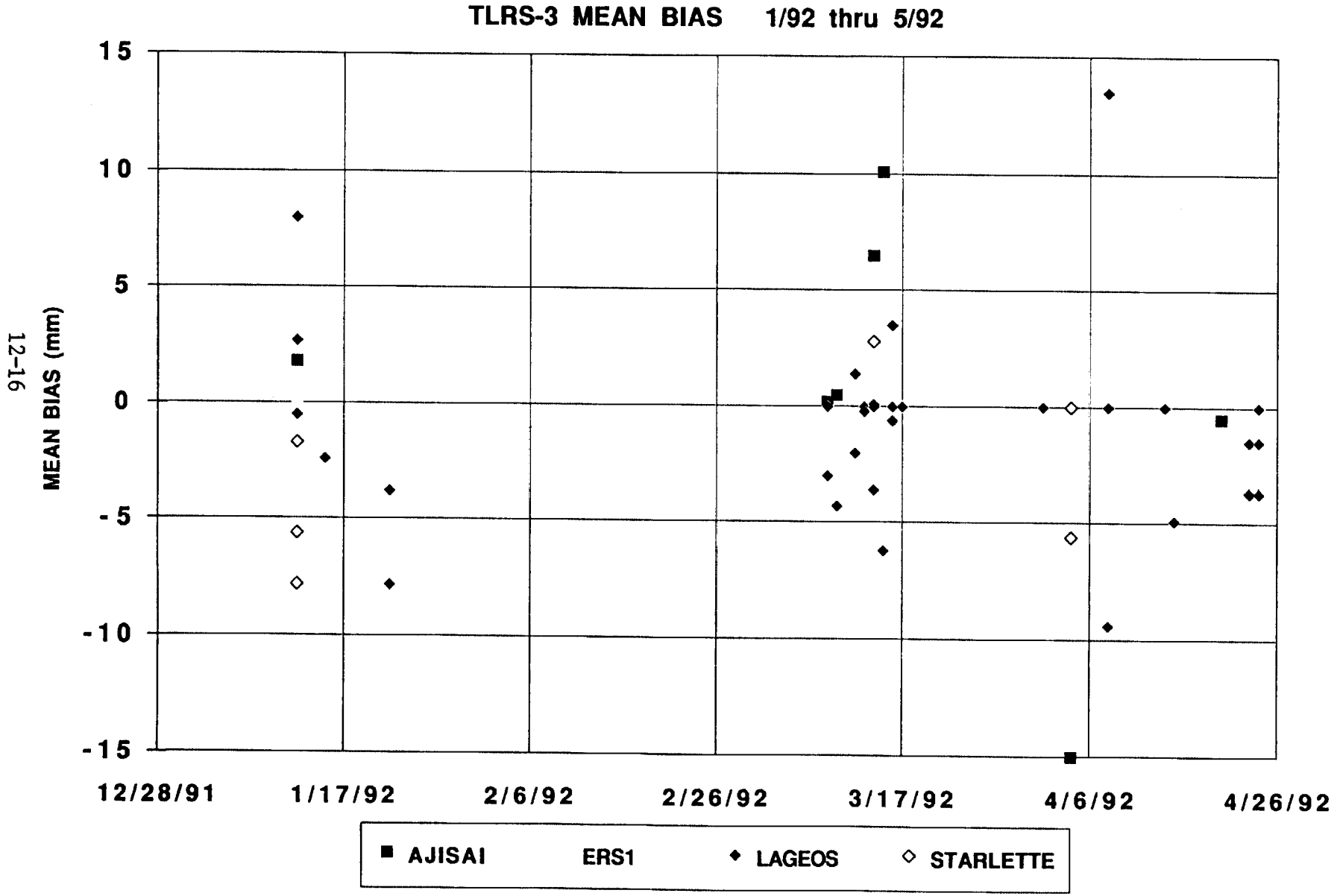

12-16

CDSLR/NES/S.WETZEL

5/13/92

Results of the MTLRS-1 Upgrade

P. SPERBER, L. AMBERG, L. BEYER, G. BLENSKI, W. ETLING, U. HESSELS, R. MOTZ,
INSTITUT FÜR ANGEWANDTE GEODÄSIE
FUNDAMENTALSTATION WETTZELL
DER FORSCHUNGSGRUPPE SATELLITENGEODÄSIE
D-8493 KÖTZTING

Abstract. In this report the results of the upgrade of the German Modular Transportable Laser Ranging System MTLRS#1 are summarized. A short description of the new components and their influence on the system accuracy is given. It is shown, that the single shot accuracy of the MTLRS#1 has been improved from 5 cm to 1 cm.

1. Introduction

The German Modular Transportable Laser Ranging System MTLRS#1 has been operated successfully since 1984. From 1985 to 1990 the system was employed in the Central and Eastern Mediterranean area and in the U.S.A., contributing to the WEGENER-Medlas and the NASA Crustal Dynamics project.

In order to improve the system reliability and the ranging accuracy from 5 cm to 1 cm a major system upgrade was performed from December 1990 to July 1991.

This upgrade was planned and carried out in five steps:

- Exchange of the Laser
- Exchange of the Start Detector
- Exchange of the Receiving System
- Exchange of the Single Photon Detector
- Improvements in Periphery and Software

In this paper we will summarize the technical specifications of the new systems and show first tracking results.

2. Technical description of the upgrade

2.1. The Laser

The duration and the energy of the emitted laser pulses are critical elements in the determination of the accuracy and the number of returns produced by a satellite laser ranging system. To improve this two points, we exchanged the original Nd:YAP Laser (Pulseduration: 370 ps; Pulseenergy at 536 nm: 10 mJ) for a new Nd:YAG Laser (Pulseduration: 30 ps, Pulseenergy at 532 nm: 30 mJ). To ensure a good reliability of the laser in field, we made use of the self filtering unstable resonator (SFUR), described by R. Bianchi et.al. and K. Hamal et.al, which has a very simple optical layout.

This setup has three major adventages:

- insensitive to inaccurate adjustment
- homogenious spatial energy distribution
- very high pulse energy in the resonator.

The realisation of the optical setup of the laser delivered by Laser Valfivre is shown in Fig. 1. To save place, the resonator M1 - M2 is folded over the prism PR. The laser is cavity dumped through a pockelscell PC and a polarizer PO. An active-passive configuration (acustooptic modelocker ML and dye cell with Kodak 9860 in 1,2-Dichlorethan) is used to generate picosecond pulses.

In the SFUR configuration, the energy of the pulses in the resonator is already reasonable high, therefore a Single Pass Amplifier (AMP) is sufficient to generate a pulseenergy of about 100 mJ in the infrared which gives about 30-40 mJ in the Second Harmonic.

Due to the good isolation of the laser head and the power electronic to environmental influences and due to remote control facilities in the laser head, we are able to operate the laser over long period without opening the shielding.

2.2. The Start Detector

To take full advantage of the short laser pulses it is neccessary to use a start diode with very fast risetime to generate the start signal for the counter. As each component between diode and counter gives some additional jitter we were looking for a solution with a very simple electrical layout. Mainly we tried to find a way where it was no longer neccessary to use a constant fraction discriminator to compensate the amplitude fluctuations of the diode signal.

Therefor we integrated an optically triggered avalanche diode (I. Prochazka et.al.) as start detector. This diode generates an electrical signal, which is independent from the energy fluctuations of the laser pulses. This signal is directly used as start signal for the counter.

The signal has a risetime of 300-400 ps (Fig. 2), the jitter between laserpulse and electrical pulse is less than 20 ps.

To obtain high stability and to have also the possibility to vary the pulse energy during tracking the new start diode is placed before the amplifier to detect the infrared signal. In the previous design the diode detected the green light after the second harmonic generation.

2.3. Receiving Package

In contrast to other SLR System the MTLRS is using an echelle grating for the spectral filtering of the received light. Compared to the common used interference filters this has the advantage to be insensitive to environmental influences. Unfortunately an echelle grating generates a time spread of a pulse due to the different light paths over the grating.

In the old grating this was compensated with an accuracy of about 1 cm by sending the diverse parts of the beam to different mirrors. Due to this splitting of one pulse into several beams, the outcoming beam has not the high optical quality which is necessary for focusing on the small active area ($100\mu m$) of an avalanche diode.

In the new package a second echelle grating in opposite position is used to make full compensation. The excellent optical quality of this configuration results in a very homogeneous beam which is necessary to generate small focal spots.

Additionally a remote controled field-of-view pinhole and a better isolation against straylight is installed in the new package. The sketch of the whole receiver is seen in Fig. 3. (H. Visser)

At the input the beam coming from the telescope is directed by a prism to an optical package in which a rotating shutter and some small prism are used for filtering and guiding of the beam. The light has to travel through the rotating shutter and is directed to an echelle grating. After that the pulse is spread in time and frequency. An adjustable pinhole is used for the field of view filtering and for selection of the correct wavelength. To compensate the time spread the beam now

propagates a second time to the echelle grating before two lenses form a parallel, 8 mm diameter output beam.

2.4. Single Photon Detector

A major improvement in the accuracy of the time interval measurement was achieved by the exchange of the photomultiplier for a single photon avalanche diode (SPAD) (I. Prochazka et.al., G. Kirchner).

The signal out of the SPAD is independent of the signal strength, so the use of a constant fraction discriminator is not necessary.

A description of the technical details is given in Sperber et.al.

3. System Accuracy

The main reason for the upgrade of the MTLRS was the demand to improve the system accuracy from 5 cm to about 1 cm single shot r.m.s.

In Fig. 4 the developement of the accuracy during each step of the upgrade is depicted. The main influence to the accuracy came from the exchange of the laser and the single photon detector. The start detector has minor effect and the importance of the new receiver package can be seen in the good optical quality which finally allows the usage of the SPAD.

The contribution of each single component of the system to the system accuracy is shown in Fig. 5 for the old and the new configuration. The r.m.s of all components has now about the same size. Further improvements are probably possible at the laser (10 ps) and at the counter. More accurate start and stop detectors are not available at the moment.

The plot of a typical pass before and after the upgrade is given in Fig. 6. Here the significant decrease of the system r.m.s is conspicious.

All this data are showing, that the single shot accuracy of the MTLRS#1 is now 1 cm or less, if all components (mainly start diode, SPAD and laser) are optimally adjusted.

Under field conditions we demonstrated (P. Sperber, H. Hauck) a system accuracy of 1 cm - 1.5 cm and a normalpoint accuracy of a few mm.

3. Perspectives into the next years

The receiving and transmitting part of MTLRS#1 is now again state of the art. To bring the whole system to a status comparable with modern SLR systems two additional upgrade steps are under discussion.

- Installation of a new control electronic and software, designed for future demands to Laser Ranging Systems. IfAG has decided to develop such a control system based on a transputer network in cooperation with MTLRS#2 (OSG Kootwijk). The integration in the MTLRS#1/2 is scheduled for 1993 (E. Vermaat et. al.)
- The Laser and the Receiving system are now prepared to make two color ranging. Only the telescope does not meet the specifications for two color ranging as the reflecting mirrors are optimized only for a wavelength of 532 nm. A further upgrade for two color ranging capability depends strongly on the demand of the international SLR community for two color ranging data.

5. Summary

After the upgrade of MTLRS#1 performed from December 1990 to Juli 1991 a system with the following modified specifications is now available.

- 30 ps laser pulse-width with 30 mJ/pulse at 532 nm
- Optically triggered avalanche diode to start the time interval counter
- Compensated echelle grating filter
- Single Photon Avalanche Diode
- In field normal point generation

As a result of these modifications MTLRS#1 is now capable of tracking high and low satellites day and night with a single shot r.m.s. of about 1 cm.

REFERENCES

Laser Valfivre, *Specifications of a laser system for MTLRS#1 , 1989.*

A. Bianchi, A. Ferrario, P.G. Gobbi, C. Malvicini,G.C. Reali, SPIE 701, p.132, *1989.*

K. Hamal, V. Hraskova, H. Jelinkova, CLEO'85 Proceedings p.82, WE 4, *1987.*

I. Prochazka, K. Hamal,, *Subcentimeter Single Photon Ranging All Solid State Detection Package, 1990.*

G. Kirchner, Proceedings of the seventh international Workshop on Laser Ranging Instrumentation p. 123, *1989.*

P. Sperber, U. Hessels, R. Motz in this Proceedings, *The new MTLRS#1 Receiving System 1992.*

P. Sperber, H. Hauck, in this Proceedings, *Experience and Results of the 1991 MTLRS#1 USSR campaign, 1992.*

E. Vermaat, J.W. Offierski, K.H. Otten, W. Beek, C. van Es, P. Sperber, in this Proceedings, *A Transputer Based Control System for MTLRS, 1992.*

H. Visser, Technisch Physische Dienste (TPD), Delft private communication, *Design of a new MTLRS#1 receiver package, 1990.*

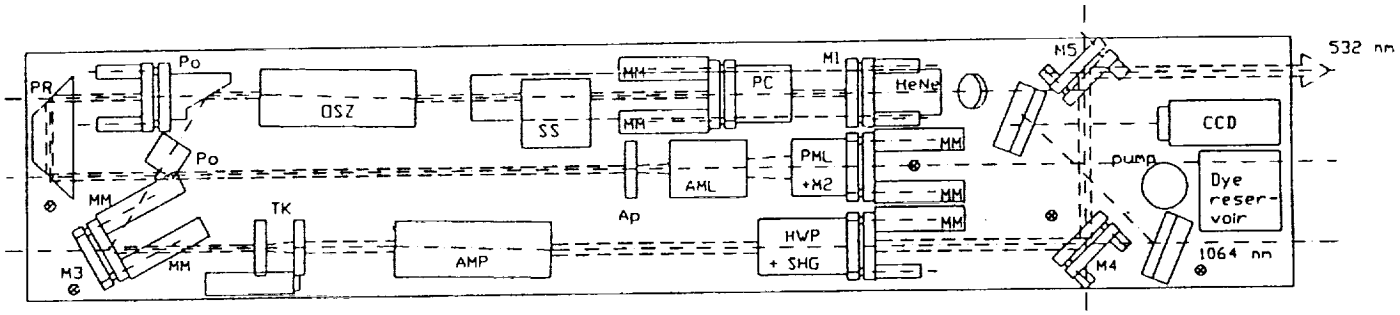

M1 - M5	Mirrors	OSZ	Oscillator	SS	Safety shutter	HWP	half wave plate
MM	Motor-Mikes	AMP	Amplifier	Ap	Aperture	SHG	Second harmonic gen.
Po	Polarizer	AML	Active mode-locker	PC	Pockels-cell	HeNe	He-Ne alignment laser
Pr	Prism	PML	Passive mode-locker	Tk	Telescope	CCD	CCD camera
⊗	Diagnostic diodes						

Fig. 1 - Schematic of Laser Head

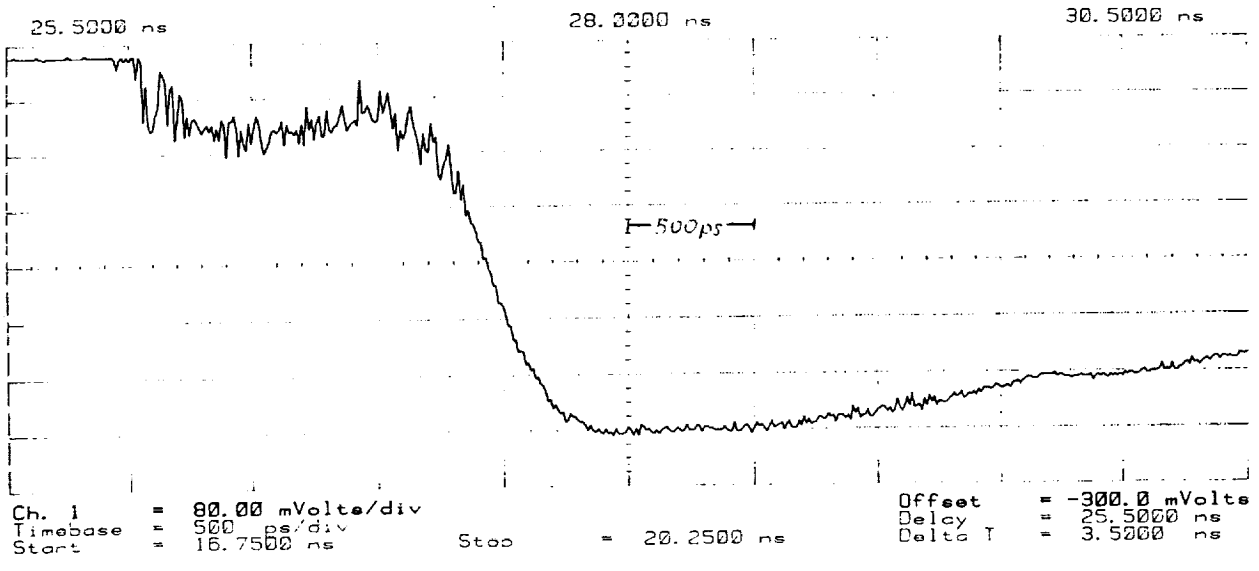

Fig. 2 - Signal of the Start Diode

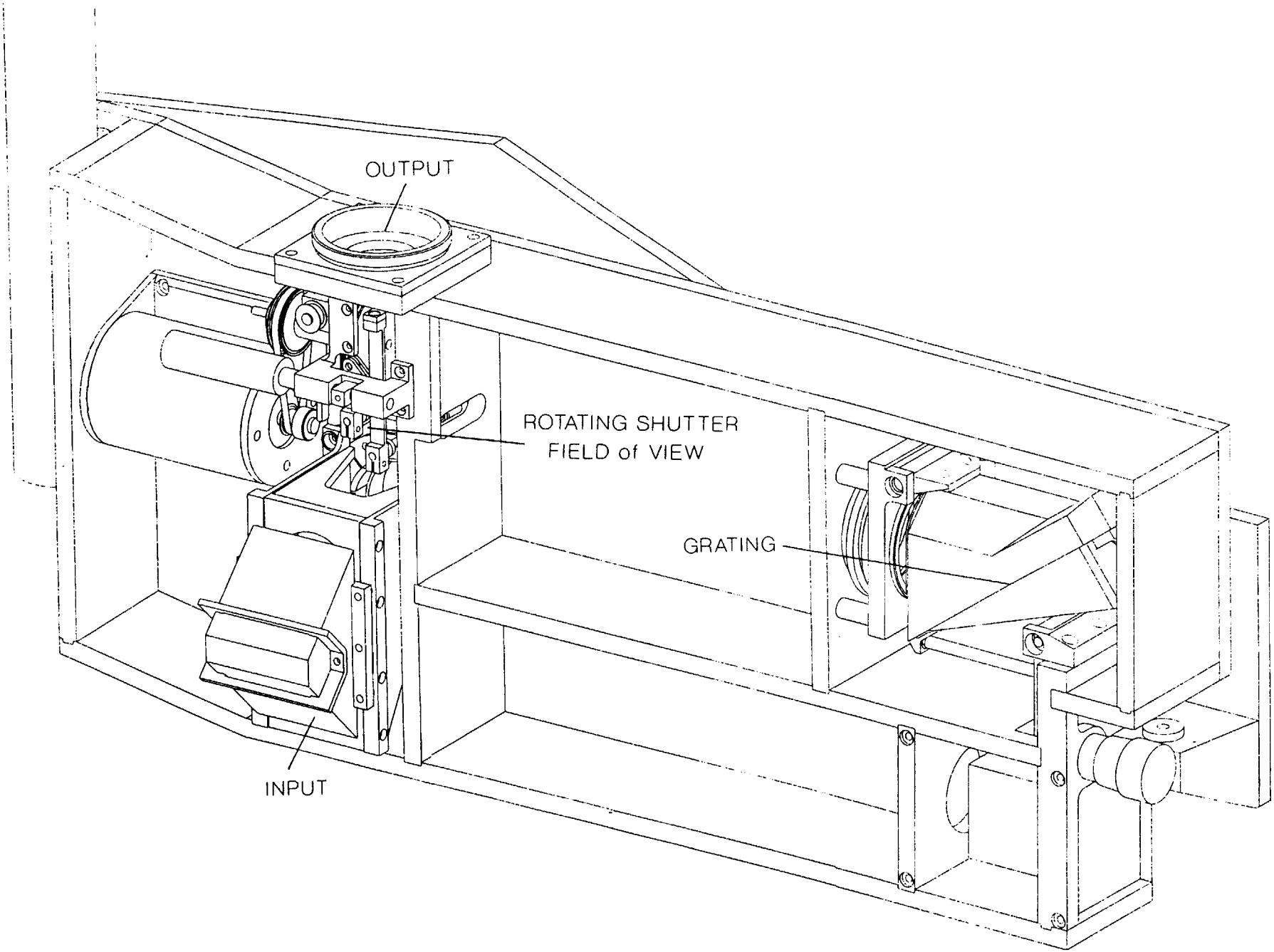

Fig. 3 Mechanical Layout of the MTLRS#1 Receiver Package

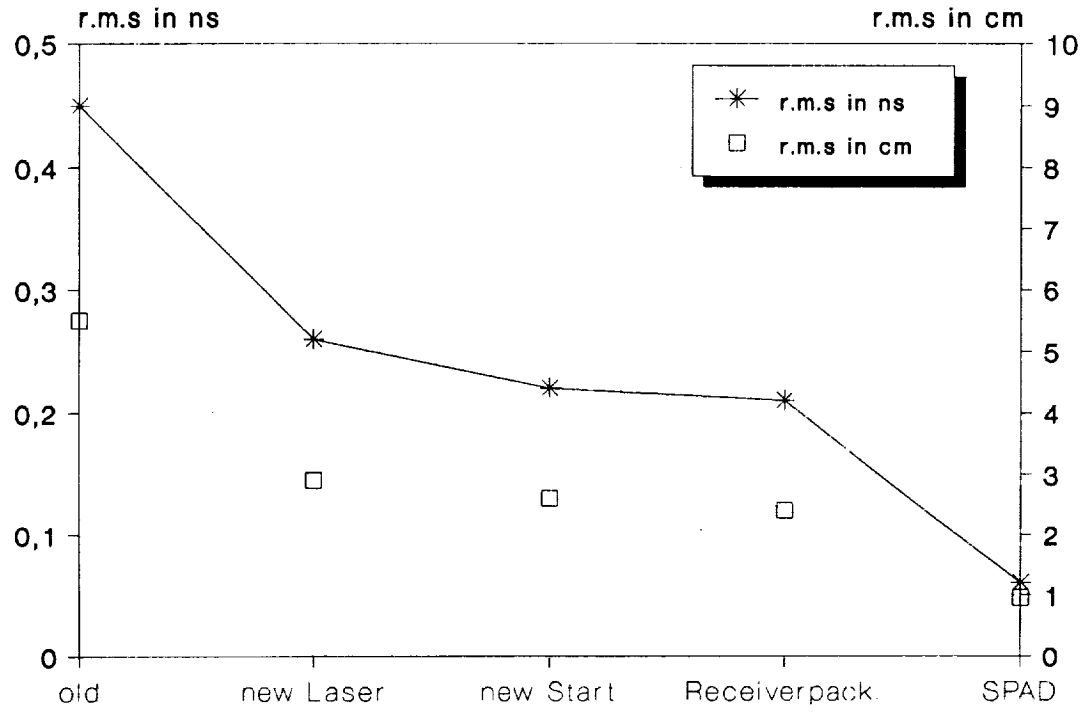

Fig. 4: Decrease of the single shot r.m.s. during upgrade

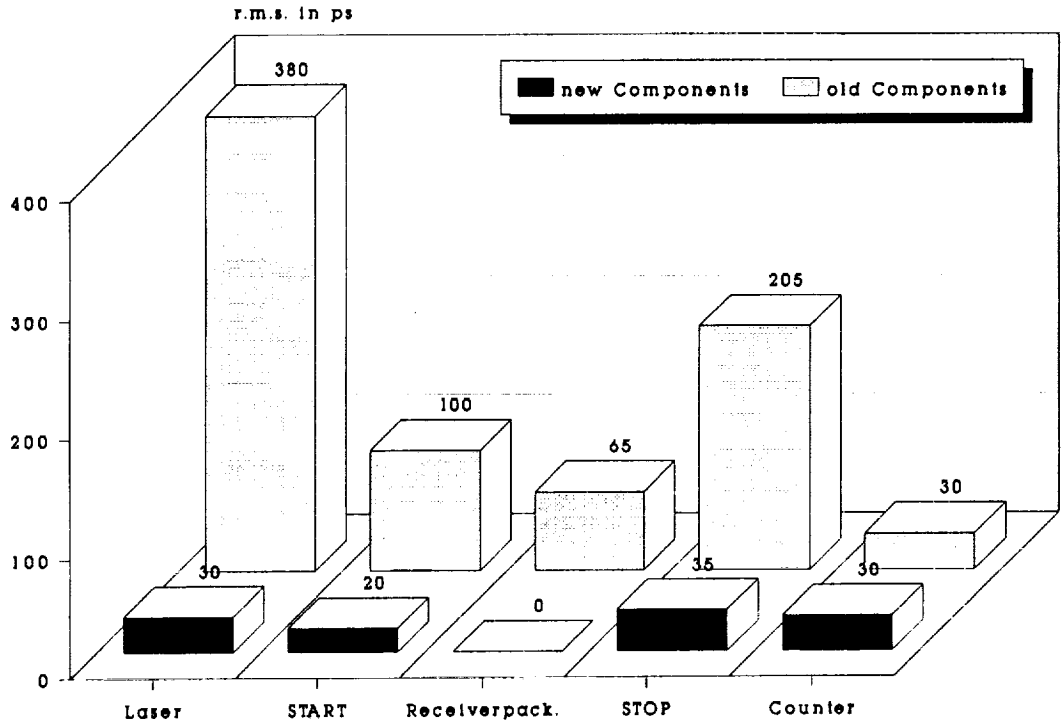

Fig. 5: Single shot r.m.s before and after upgrading

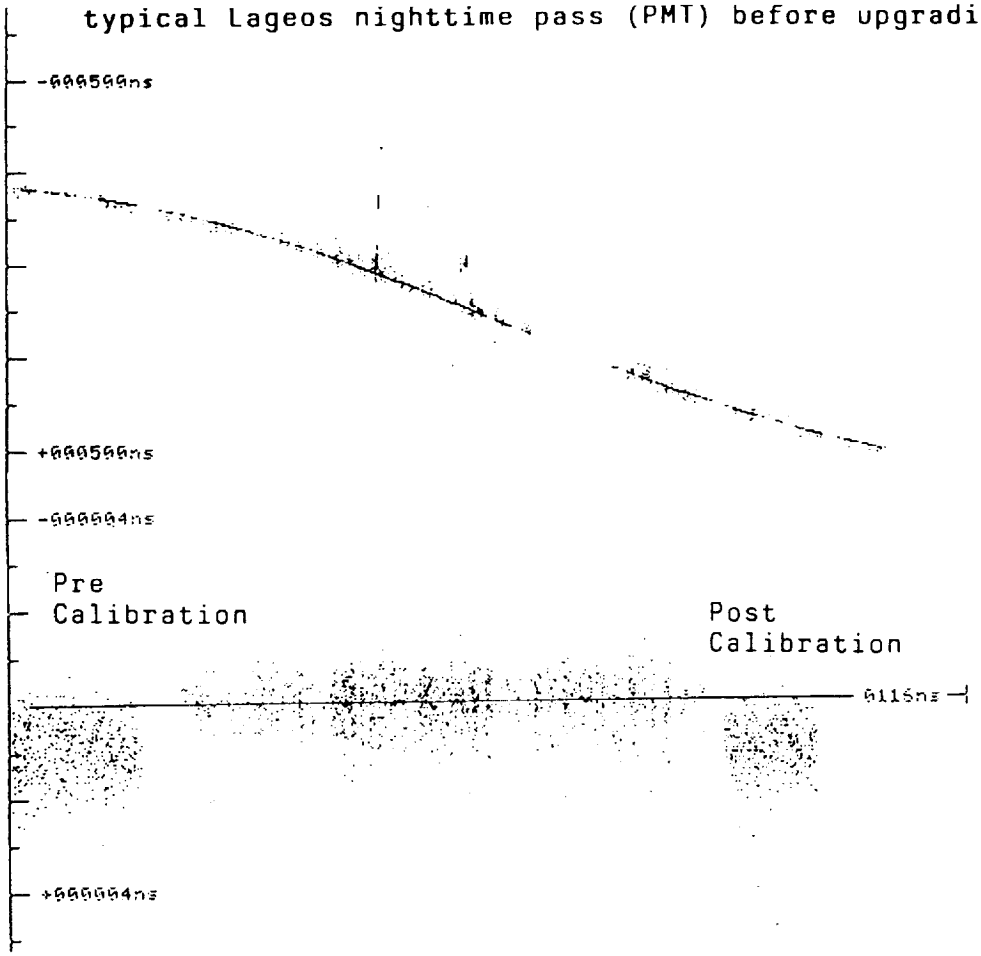

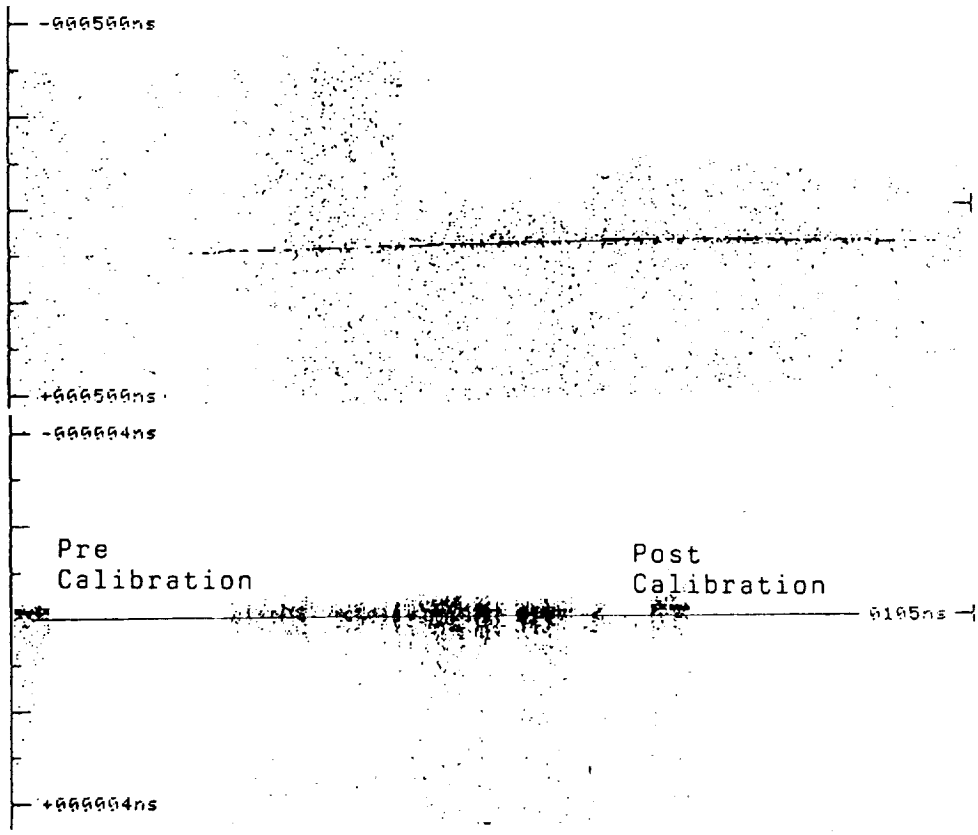

Fig. 6 - Lageos Pass before and after upgrading

The new MTLRS#1 Receiving System

P. SPERBER, U. HESSELS, R. MOTZ,
INSTITUT FÜR ANGEWANDTE GEODÄSIE
FUNDAMENTALSTATION WETTZELL
DER FORSCHUNGSGRUPPE SATELLITENGEODÄSIE
D-8493 KÖTZTING

H.-M. GÜTHER
HOECHST AG, MATERIALFORSCHUNG
D-6230 FRANKFURT AM MAIN 80

Abstract.
In this report we are giving a detailed description of the new receiving system of the German Modular Transportable Laser Ranging System MTLRS#1 consisting of a spectral time and field of view filter and a Single Photon Avalanche Diode (SPAD) as single photon detector. The system gives full day and night ranging capability to all satellites with cm accuracy.

1. Introduction

In order to improve the ranging accuracy and the sensitivity of the German Modular Transportable Laser Ranging System MTLRS-1 a major system upgrade was scheduled and performed from Dec. 1990 to July 1991 (P. Sperber et.al.). Together with the exchange of the whole transmitting part (Laser and Start Diode) (P. Sperber et.al.) the installation of a new receiving system was the main point of the upgrade.

The receiving system has two parts, which will be shown in detail

- Filter (Frequency, Range, Field of View)
- Single Photon Detector.

2. Receiving System

To extract reflected photons from the satellite from noise photons which are entering the telescope mainly in daylight, a powerful filter equipment has to be installed in SLR systems.

This filtering in modern systems is realized in three steps

- Range (time interval) filter: A rotating shutter is commonly used to supress straylight during laser firing and to open the detector at the time, the echo from the satellite is expected.
- Field of View: A pinhole ensures, that only light coming from a small angle around the telescope axis can hit the detector.
- Spectral Filter: The most effective filtering process is the filtering in frequency which allows just light of the well defined laserwavelength to propagate.

The new receiver package of MTLRS#1 is a very compact, field qualified realization of this three requests, deliverd by Technisch Physische Dienste (TPD), Delft, Netherlands.

The setup is shown in Fig. 1.

The light from the telescope is focussed to a field of view pinhole, which is remote adjustable with a motor driven micrometer from 0 to about 30 millidegrees. Connected to the field of view filter there is a rotating shutter, synchronized to the predicted range window, which opens the receiving system 10 times per second for about 3 ms and mainly protects the single photon detector from straylight during laser firing.

The spectral filtering is done by an echelle grating (efficiency: 55 %) used in 7 th order, which gives a bandwidth of 0.2 - 0.65 nm depending on the opening of the filed of view pinhole. The grating has a surface of almost 100 mm top-top in air, therefore the range difference of the beams over the grating surface is not neglegible. To compensate this range difference the grating is used a second time in opposite order. At the end of the receiving package a lens is generating a 8 mm diameter, parallel beam with excellent optical quality.

3. Single Photon Detector

To see the full advantage of the short laser pulses and of the errorfree receiving package a single photon detector with high accuracy is necessary. In the world of SLR two types of high accuracy receivers are used in the moment:

- Microchannel Plates
- Avalanche Diodes.

We decided to install a single photon avalanche diode (SPAD) (I. Prochazka et al.) developed by the Czech Technical University in our system. The reasons for this decision were:

- High ruggedness under field conditions
- High Quantum Efficiency (20 %)
- Low jitter (35 ps)
- Low operating voltage (25 V)
- High dynamic range and neglectable influence of signal strength to the range measurement
- No additional electronics (CFD) between detector and counter.

The housing for the diode has to meet some demands:

- Adjustable in three dimensions in the μm range.
- Possiblity to cool the diode below $-10°$ C.
- Protection against humidity (condensation).
- Flexible for usage of different types of diodes.

The cooling of the diode is necessary because of the high termal noise (some 100 kHz) at room temperature. The temperature of $-30°C$, which is possible with this setup will decrease the noise far below 100 kHz (Fig. 2) and therefor make the search for satellites at night more easy.

To meet all this points, we designed a new housing (Fig. 3) with the following specifications:

- adjustement accuracy in each dimension: $5 - 10\mu m$

- input beam: 5-10 mm diameter, parallel
- optics: effective focal length: 11 mm
- field of view in our system (100 μm diode): 30 mrad
- cooling: to $-30°C$ with peltier cooler and water ($5°C$)
- good mechanical stability under field conditions (temperature change, humidity)

The housing is made from aluminium, the inner moving part which makes the termal isolation of the diode to the housing is DELRIN.

For the fixing of the diode a very special material with high mechanical stability, high thermal conductivity and good electrical isolation was necessary.

To get a thermal equilibrium even at high outside temperatures we decided not only to cool the diode, but the whole fixing plate with powerful peltiers (the hot side of the peltier is water cooled). As some diodes (mainly the diode we use) needs an electrical isolator around it, a material with the mentioned specifications was necessary.

In cooperation with the Material Research Departement of Hoechst AG, a new ceramic material - Aluminium Nitride- was selected. The important properties of this are its high thermal conductivity of 170 W/mk (comparable to pure Aluminium) and its dielectric constant of about 8.5 (good insulator). The powder, together with a sintering aid, are prepared for pressing. The cold isostatic pressed parts, in the form of rough discs, are then turned to improve their finish and a hole is bored in the centre. The binder is then burned out. The samples are sintered at $1840°C$ for 3 h under a nitrogen atmosphere in a special graphite crucible. After the heat treatment the ceramic parts were finished. They were grond with diamond wheels in all directions to get the high dimensional accuracy and surface smoothness for installation of the measuring diode and for the mounting of the peltier elements. The specifications of the material are given in table 1.

Due to the flexibility and the good experience with this housing in the last field campaign it is now also used at the new Wettzell Laser Ranging System (WLRS) for the tests of different diodes.

3. Summary

The new receiving system of MTLRS#1, consisting of a filter package for field of view, time and spectral filtering and a single photon avalanche diode as detector gives the possibility of SLR with cm accuracy during night and day. The whole system is build very modular and flexible, so easy exchange or usage in other SLR systems is possible.

All parts are designed and manufactured in a way, that even under extreme environmental changes in field an adjustement is not necessary.

In the last field campaign the new receiver proved to work very reliable and satisfactory.

REFERENCES

P. Sperber, L. Amberg, L. Beyer, G. Blenski, U. Hessels, R. Motz, in this Proceedings, *Results of the MTLRS#1 Upgrade, 1992.*

P. Sperber, U. Hessels, R. Motz, W. Beek, in this Proceedings, *The new MTLRS Transmitting System, 1992.*

I. Prochazka, K. Kamal, B. Sopko, S. 219, *Photodiode Based Detector Package for Centimeter Satellite Ranging,.*

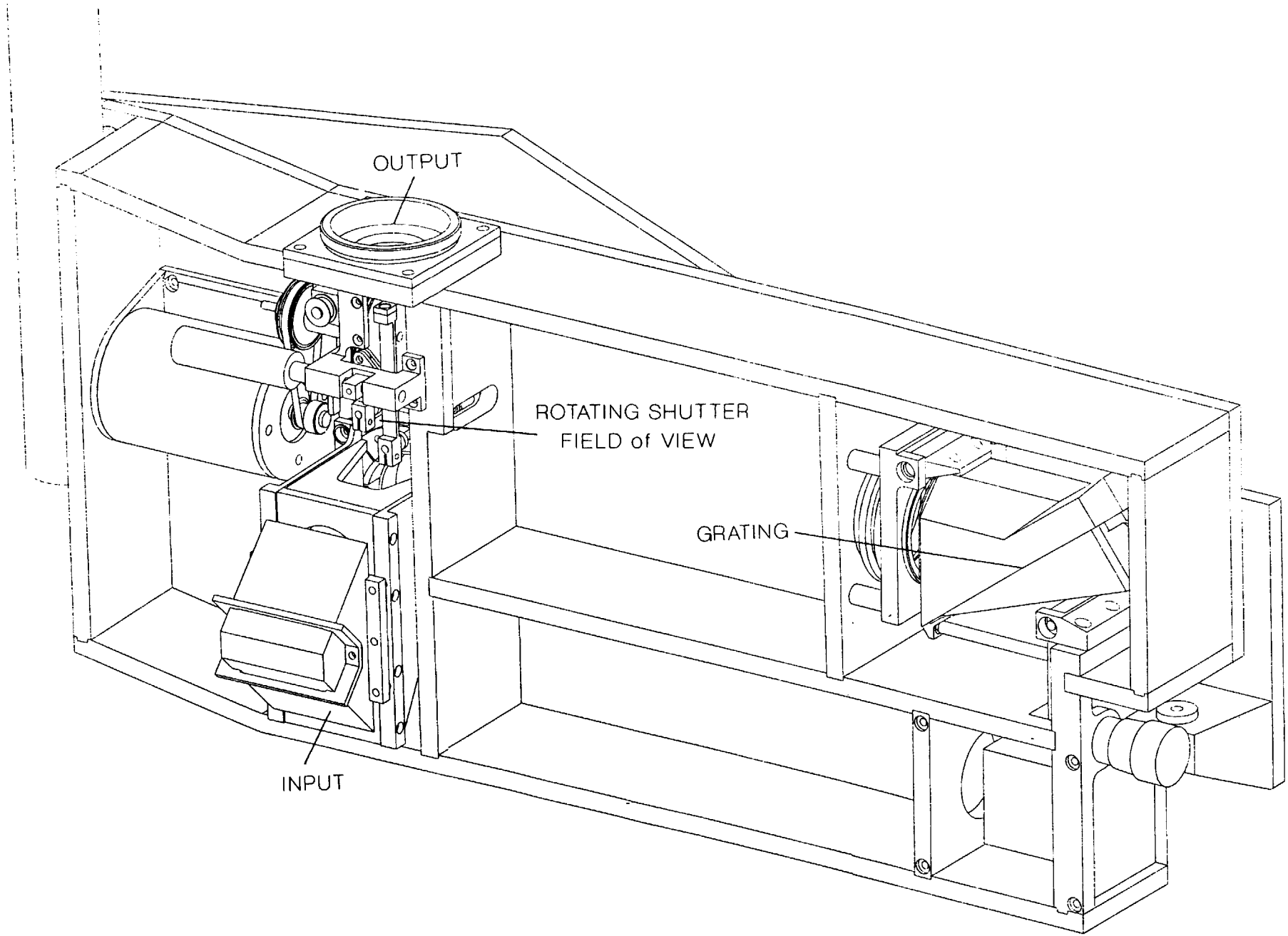

Fig. 1 Mechanical Layout of the MTLRS#1 Receiver Package

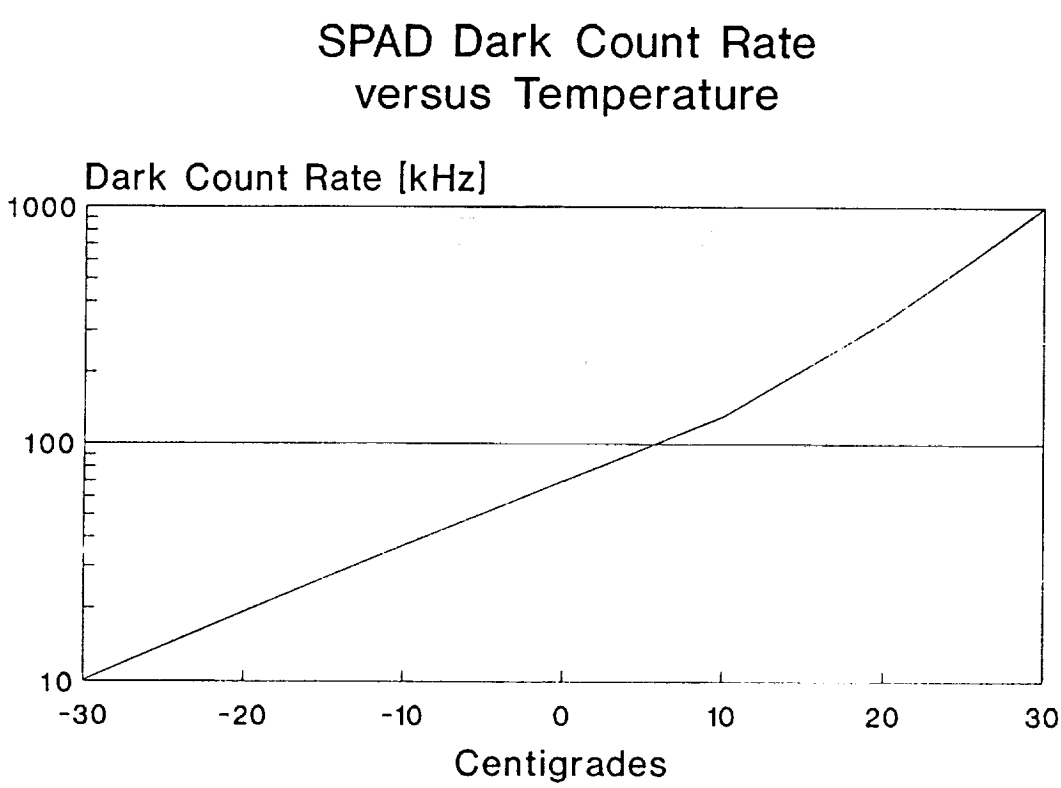

Fig. 2 SPAD Dark Count Rate versus Temperature (2.5 V above Break)

- Density	3,3 g/cm³
- Termal Conductivity	170 W/m K
- Specific Heat	738 J/kg K
- Flexural Strength	300 - 400 MPa
- Electrical Resistivity	> 10^{14} Ohm cm
- Dielectric Constant	8,5 - 9

Table 1 Specification of Aluminium Nitride

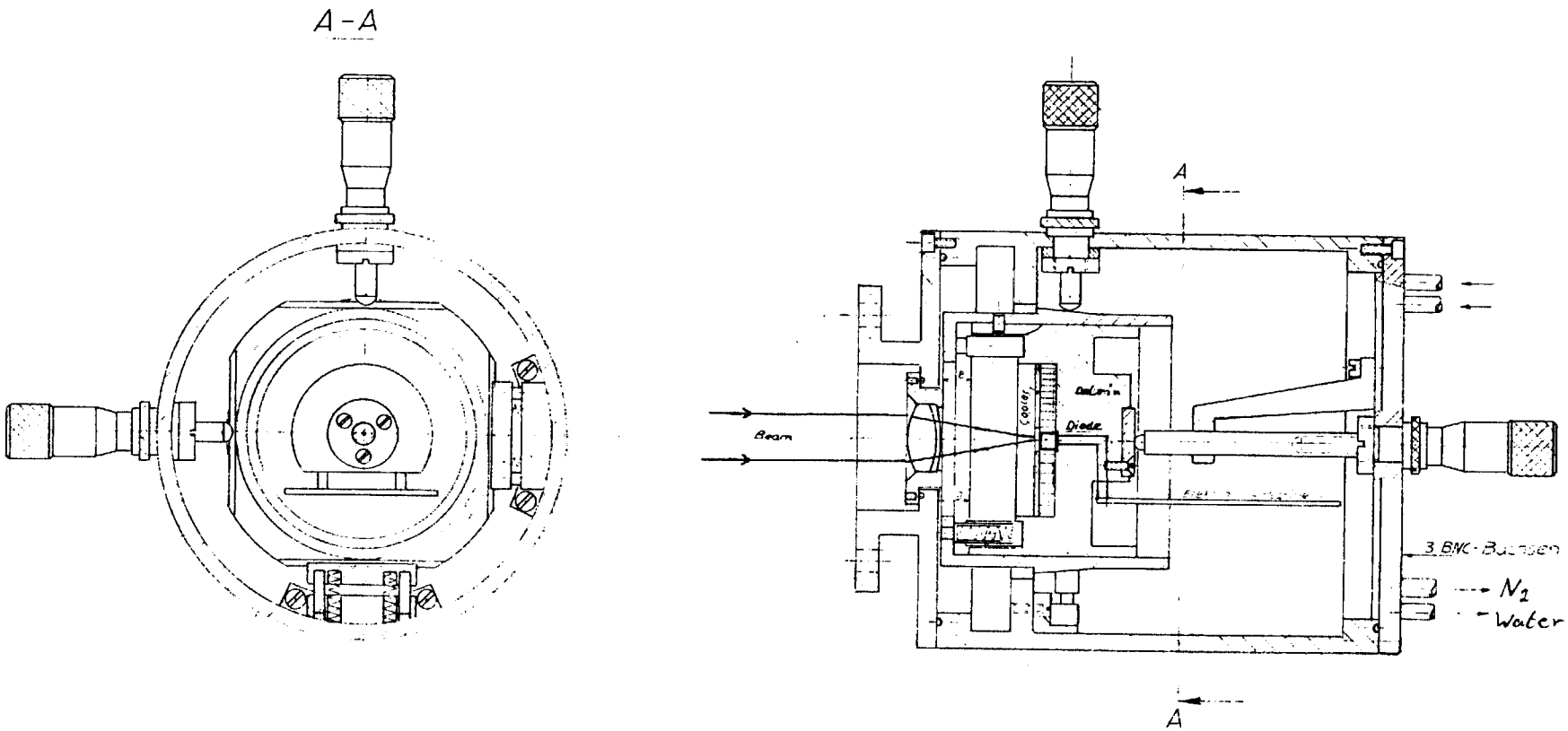

Fig. 3 Housing of the Single Photon Avalanche Diode

N94-15612

The new MTLRS Transmitting System

P. SPERBER, U. HESSELS, R. MOTZ
INSTITUT FÜR ANGEWANDTE GEODÄSIE
FUNDAMENTALSTATION WETTZELL
D-8493 KÖTZTING
GERMANY

W. BEEK, J.W. OFFIERSKI, C. VAN ES
DELFT UNIVERSITY OF TECHNOLOGY
KOOTWIJK OBSERVATORY FOR SATELLITE GEODESY
POSTBOX 581, 7300 AN APELDOORN
THE NETHERLANDS

Abstract

This paper presents a detailed description about the new transmitting system of the Modular Transportable Laser Ranging Systems MTLRS-1/2. A simplified theory of the Self Filtering Unstable Resonator (SFUR) is explaned. Laser design details are discussed concerning the extreme environmental conditions in which these mobile systems are operating. Details are given concerning the new avalanche START detector. The new SFUR laser and START detector are necessary parts in order to bring both mobile systems towards 1 cm ranging accuracy.

1. Introduction

Since 1984 the two European Modular Transportable Laser Ranging Systems MTLRS-1, operated by the Institute for Applied Geodesy (IfAG, Germany), and MTLRS-2, operated by the Delft University of Technology (DUT, The Netherlands), have supplied the international network with laser ranging data from sites in Europe, CIS (former USSR) and North America. To improve the ranging accuracy from 5 cm to the 1 cm level, both systems carried out a major upgrade in 1991. The main part of this upgrade was the exchange of the transmitting system consisting of the Laser and the Start Detector (The German MTLRS-1 system also upgraded the receiver package [1].

2. The Laser

The accuracy and the number of returns produced by a satellite laser ranging system is mainly influenced by the duration and energy of the emitted laser pulses. To improve these two points, the original Nd:YAP laser (370 ps FWHM pulse-duration, 10 mJ pulse-energy at 539 nm) was exchanged for a new Nd:YAG laser (30 ps FWHM pulse-duration, 30 mJ pulse-energy at 532 nm). To realize this high demands with a simple and reliable optical configuration, a new resonator setup, the Self Filtering Unstable Resonator (SFUR) [2,3] was used. Together with a simple optical setup, this resonator has the advantage to be less sensitive to optical adjustments and operates with a very homogeneous spatial pulse-shape, minimizing the danger of destroying optical components at high resonator energy output levels.

2.1 Simplified SFUR Theory [4]

Fig. 1 shows the principle of the SFUR resonator.

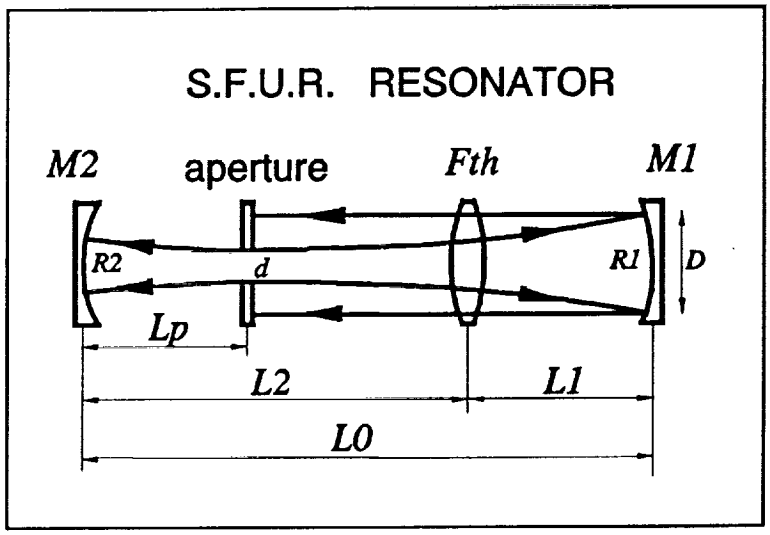

Fig. 1

Two mirrors M_1 and M_2 are forming an instable, confocal resonator:

$$R_1 + R_2 = 2 \cdot L_o$$

R_1 and R_2 are the (concave) radii of the mirrors and L_o the optical resonator length. This resonator configuration generates a spot in the resonator, which usually destroys optical elements. If a small pinhole is placed in this focal point this problem disappears and some major advantages can be seen. The diameter d of the aperture has to be chosen in a way, that only the central lobe of the Airy pattern (generated by mirror M_2) propagates to M_1.

$$d = \sqrt{2.44 \cdot f \cdot \lambda}$$

(f: focal length of M_2, λ: laser wavelength)

The mode, generated by the central maximum of the Airy pattern has a smooth, nearly Gaussian shape, with zero intensity at radius r_0 where

$$r_0 = - M \cdot \frac{d}{2} \qquad \left(M = - \frac{R_1}{R_2} \right)$$

If the parameters of the resonator are correct, the mode is exactly filling the whole volume of the active medium. Therefore nearly all the energy stored in the rod is converted into the laser pulse. The outcoupled pulse-energy is much higher compared to usual resonator configurations. The aperture (typical diameter $d \leq 1$ mm) gives a strong spatial filtering at

each round trip smoothing the energy distribution in the beam and avoiding hot spots. In an exact analysis of the SFUR configuration the influence of the thermal lens (f_{th}: focal length) in the laser rod has to be taken into account.

$$L_0 = L_1 + L_2 - \frac{L_1 \cdot L_2}{f_{th}}$$

$$g_1 = 1 - \frac{L_0}{R_1} - \frac{L_2}{f_{th}}$$

$$g_2 = 1 - \frac{L_0}{R_2} - \frac{L_1}{f_{th}}$$

$$g = 2 \cdot g_1 \cdot g_2 - 1$$

$$M = g - \sqrt{g^2 - 1}$$

(L_1 and L_2 are the distances of M_1 and M_2 to the virtual position of the thermal lens). The optimum position L_p (distance from M_2) of the aperture, the diameter d of the aperture and diameter D of the laser beam are given by:

$$\frac{1}{L_p} = \frac{1}{R_2} + \frac{\sqrt{g^2 - 1}}{2 \cdot g_1 \cdot L_0}$$

$$d = \sqrt{4.88 \cdot L_p \cdot \lambda \cdot \left(1 - \frac{L_p}{R_2}\right)}$$

$$D = 1.5 \cdot M \cdot d \cdot \left(1 - \frac{L_2 - L_p}{\frac{1}{\frac{2}{R_2} - \frac{1}{L_p}} - L_p} \right)$$

2.2 Technical Realization

The laser system consists of four separate units, the laser head, the power supply with electronics, an external dye-cooling unit and the control panel.

A schematic drawing of the laser head is shown in Fig. 2. To save place, the SFUR Resonator M_1 - M_2 is folded over a prism PR. Picosecond pulses are generated with an acousto-optic modulator AML and a bleachable dye (Kodak 9740 in 1,2 Dichloroethane) (PML). The intense 30 ps long pulse is cavity dumped by the pockelscell PC and two polarizers PO. Because of the high energy of the output pulse of a SFUR resonator a single stage amplification (AMPL) is sufficient to get 100 mJ per pulse in the infrared. The second Harmonic Generator SHG converts about 40% of the energy into green light at 532 nm. The two wavelengths are separated by the dichroic mirror M_4. The excessive use of diagnostic diodes and motor driven micrometers allows the fine adjustment of the laser without opening the dust cover. Even the spatial shape of the pulse is monitored by a CCD - Camera. For maximum mechanical stability, the whole laser head is built on a temperature controlled, reinforced invar plate.

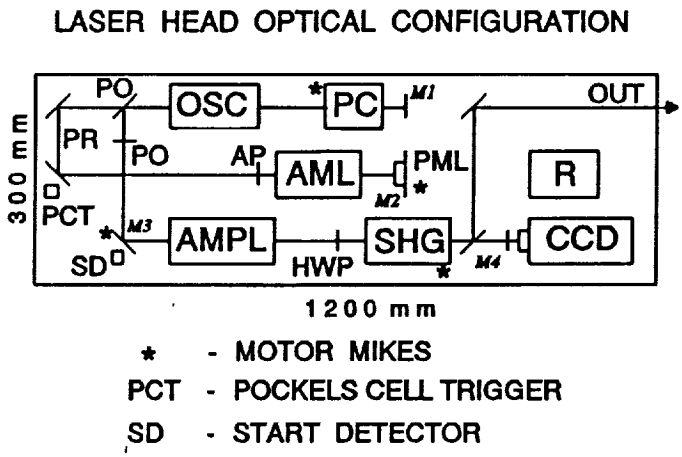

Fig. 2

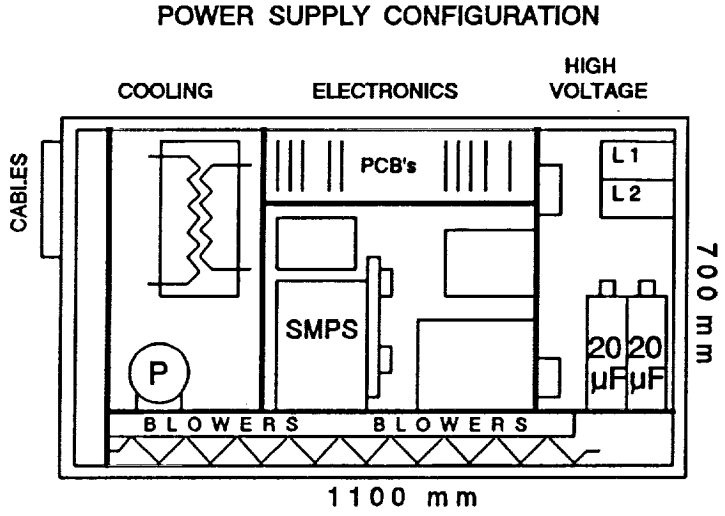

Fig. 3

Fig. 3 shows an inside picture of the power supply. The power supply and control electronics are also built in an isolated, temperature stabilized housing. The laser switches automatically between 380 V/50 Hz and 460V/60 Hz input, and the 3 phase power consumption is 5 KVA. Two independent control panels for the laser can be used; one for the Cabin, in use during ranging, and another one in the Cart for maintenance purposes.

Fig. 4 shows the laser temperature control system. The telescope together with the laser are built in the Cart which is located in full sunshine in the middle of the concrete platform (Pad). During satellite tracking this Cart is open and because of extreme environmental conditions (-20°C to +40°C), considerable attention is given to the stability and reliability of the laser (komacel-isolation of the head and power supply, excellent mechanical stability of all optical components). The heat generated by the flashtubes in the secondary cooling system is exchanged to the primary cooling system by means of an internal water to water heat exchanger connected to an external water flow with temperatures between 5-16°C.

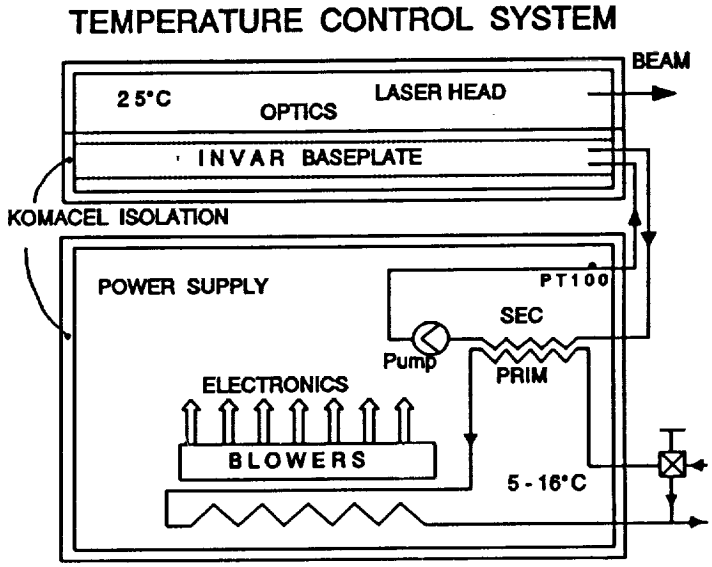

Fig. 4

The laser was first tested under field conditions during the campaign of MTLRS-1 in CIS (Common wealth of Independant States - the former USSR). The experiences were excellent.

The specifications of the laser are summarized in Fig. 5.

LASER SPECIFICATIONS	
Wavelength	532 nm
Pulse energy	30 mJ
Pulse width	30 ps
Rep. rate	20 pps (max)
Divergence	0.4 mrad
Mode locking	active + passive
SHG	KD * P
Beam diameter	7 mm
Environment	- 20°C to +40°C
Power	5 kVA
Voltage	380/460 - 5A/ph.

Fig. 5

3. Start Detector

To start the time interval counter with high accuracy, the optical output signal of the laser has to be converted with minimum jitter to an electrical pulse, which is used in the start channel of the counter. Until 1990 this problem was solved in the MTLRS in the conventional way: a part of the green pulse was sent to a fast photo diode which generates an electrical pulse with an amplitude corresponding to the energy of the laser pulse which is fluctuating from shot to shot. These amplitude fluctuations were compensated by a constant fraction discriminator. Changes in the temporal pulse shape and strong energy fluctuations in this setup caused errors in the start-channel of the counter.

To minimize these errors, an optically triggered avalanche diode **[5,6]** was integrated into the system. This diode delivers an output signal with a constant amplitude independent on the energy of the laser pulse. The output signal is directly used as startsignal for the counter, a constant fraction generator is superfluous. Furthermore, to introduce high stability and the possibility to vary the pulse energy during tracking, the start diode is placed before the amplifier (behind mirror *M3* in Fig. 2) to detect the infrared light. Fig. 6 shows the output signal of the start diode which has a risetime of 300 - 400 ps and the jitter between optical and electrical pulse is less than 20 ps.

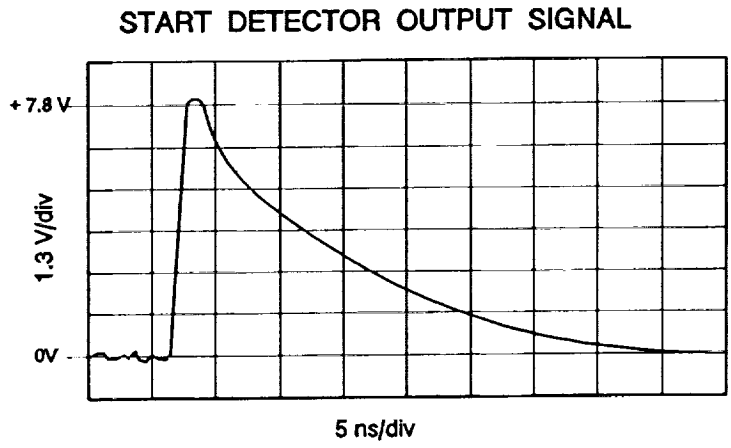

Fig. 6

In order to get stable results from the avalanche start detector under field conditions, the fibre together with the electronics have to be built inside the laser head where the temperature of the optical bench is stabilized at 25°C.

4. Summary

The upgrade of the transmitting part of MTLRS-1/2 formes the basis to improve the ranging accuracy of the systems significantly and makes them again some of the most advanced SLR systems worldwide.
First tracking results **[7]** show, that the system's single shot accuracy is about 1 cm after the upgrade of the receiver package which is already completed in MTLRS-1.

References:

[1] The new MTLRS-1 Receiving System, 1992 by P. Sperber, U. Hessels, R. Motz, in this Proceedings.

[2] Paper 1989 by A. Bianchi, A. Ferrario, P.G. Gobbi, C. Malvicini, G.C. Reali, SPIE 701, p.132.

[3] Paper 1987 by K. Hamal, V. Hraskova, H. Jelinkova, CLEO'85 Proceedings p.82, WE 4.

[4] Paper 1989 by C. Malvicini, A. Ferrario, G. Gabetta, G.P. Banfi, G.C. Reali, Proceedings of the seventh international Workshop on Laser Ranging Instrumentation p. 181.

[5] Paper 1990 Subcentimeter Single Photon Ranging All Solid State Detection Package, by I. Prochazka, K. Hamal, B. Sopko.

[6] Paper 1989 by I. Prochazka, K. Hamal, B. Sopko, Proceedings of the seventh international Workshop on Laser Ranging Instrumentation p. 219.

[7] Results of the MTLRS-1 Upgrade by P. Sperber, L. Amberg, L. Beyer, G. Blenski, W. Etling, U. Hessels, R. Motz, in this Proceedings.

Transputer Based Control System for MTLRS

E. Vermaat, J.W. Offierski, K.H. Otten, W. Beek, C. van Es
Kootwijk Observatory for Satellite Geodesy
Delft University of Technology
P.O. Box 581
7300 AN APELDOORN
THE NETHERLANDS

P. Sperber
Institut für Angewandte Geodäsie
Fundamental Station Wettzell
8493 KÖTZTING
GERMANY

Introduction

The Modular Transportable Laser Ranging Systems (MTLRS-1 and MTLRS-2) have been designed in the early eighties and have been in operation very successfully since 1984. The original design of the electronic control system was based on the philosophy of parallel processing, but these ideas could at that time only be implemented to a very limited extent. This present system utilizes two MOTOROLA 6800 8-bit processors slaved to a HP A-600 micro-computer. These processors support the telescope tracking system and the data-acquisition/formatting respectively. Nevertheless the overall design still is largely hardware oriented. Because the system is now some nine years old, aging of components increases the risk of malfunctioning and some components or units are outdated and not available anymore.
The control system for MTLRS is now being re-designed completely, based on the original philosophy of parallel processing, making use of contemporary advanced electronics and processor technology [Beek, 1989]. The new design aims at the requirements for Satellite Laser Ranging (SLR) in the nineties, making use of the extensive operational experience obtained with the two transportable systems.

Design goals

Major considerations followed in the design are to bring down the operational costs, to ensure full capability for all present and future SLR satellites and to facilitate future modifications and alternative applications through a highly structured and modular approach.

I. Optimize cost of operations

Deploying SLR systems is quite expensive, in particular in transportable mode. A modern design aiming at minimizing these costs, must minimize crew size, increase the mean-time-between-failure (MTBF) and facilitate trouble shooting and repair.

a. Minimize crew size
The default mode of operation will be fully automatic. This means that the system will initiate and perform all basic tasks, e.g. maintaining satellite alert information, ephemeris calculation, initiate and perform calibration and tracking procedures, data screening, Normal Point calculation and data mailing. The routine task for the operator (if any) will be to monitor system performance and to respond to problems. Manual mode of operation is always possible through operator intervention.

b. Reliability

Increasing the MTBF will be primarily accomplished through defining a maximum of all functions in software, running in a multiprocessor parallel architecture. The remaining hardware will be built from high quality, highly integrated components, including Programmable Gate Array (PGA) logic. Integrated components also allow a great deal of miniaturization.

c. Self-diagnostics capability

Diagnostic tasks running concurrently with the control tasks will enable rapid detection and localization of problems. Parallel processors are very convenient for hosting these functions.

d. Modular hardware design

The hardware is designed with an optimum number of printed circuit (PC) boards. Same processor-functions at different locations use identical PC-boards. Different application-functions are realized with a minimum number of different PC-boards. Interface-functions are accomplished by separate PC-boards in order to optimize hardware portability. Most spares will be available at PC-board level which enables rapid replacement, reducing system down-time under field conditions.

II. All-satellite capability

a. Satellite altitude

This decade a variety of high and low SLR satellites are or will become available. Typical extreme altitudes are ARISTOTELES (200 km) and METEOSAT (geostationary). A design goal is to eliminate any logical restriction to the satellite range in the control system (e.g. by accommodating time interval measurement and event timing).

b. Satellite interleaving

Because the system will be designed for automatic ranging, the implementation of decision schemes in software for interleaving observations to different satellites will be relatively easy.

III. Flexible design

The design of the control system must simplify future modifications in view of new or modified requirements as well as implementation of more advanced technologies. This calls for a highly structured design in software and hardware, which may also enhance the portability of the design to other SLR stations, with different hardware environments.

a. Adaptation to modifications

Hardware. The general electronic design is separated into three major types of functions: 1. interfaces, 2. applications and 3. processors. These different types are physically separated in PC-boards which are individually exchangeable. The hardware uses PGA logic, which can be easily modified (by software).

Software The RT-software system is strictly separated into three independent layers: 1. global (functional), 2. device dependent, 3. interface dependent. In this way, modifications can be implemented locally in the related module at one layer, without affecting other layers.

Because of this high level of structurization it is feasible to implement this design in SLR systems which are quite different from the MTLRS concept, with a minimum of

modifications, primarily in software.

b. Expanding processor capability

If new requirements dictate additional computer power (e.g. RT-filtering, Frame Grabbing) this capability can be easily implemented in the structured design by adding standard processor boards hosting additional software tasks. To enable implementation of different types of (parallel) processors than the transputer which has been selected in the present design, all software is written in ANSI based high-level languages and no RT-program modifications have to be made because the 3L-compiler [3L] supports different processors.

c. Highly manufacturer independent

Custom made hardware usually increases the dependence on particular manufacturers. This is avoided by full restriction to standard bought-out components and self-designed PC boards.

The parallel processor set-up eliminates the necessity of selecting a vendor dependent RT operating system and thus ensures the flexibility of adopting any brand of (future) parallel processor. In the current design the INMOS transputer (see below) has been selected because of its early availability and its capabilities. Any future transition to another parallel processor is possible and will basically only require the exchange of the ***T805*** credit card size processor board.

Lay-out of the design

I. Hardware

In SLR the great progress in (opto-)electronics of the last decades has been applied to aspects such as detection, laser technology and timing, but seems to have largely by-passed the issue of Control System design. Here state-of-the-art electronics is introduced in the MTLRS Control System, resulting in a modular design with a high level of reliability, miniaturization and flexibility.

Probably the most dominant feature in the design is the application of a parallel processor architecture. This choice supports most of the design goals in a unique way, in particular the issues of modularity and of adaptivity to future requirements for extended computing power.

The INMOS transputer

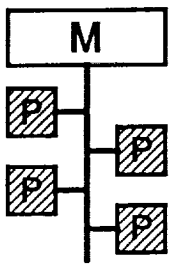

Fig 1

Parallel-processing computers [BYTE nov '88] can be divided into two basic architectures; the shared-memory multiprocessor (fig. 1) and the multicomputer type (fig. 2). All existing microprocessors can be used in the first architecture which will be limited in practice to about 4 processors due to the so called "von Neumann" bottleneck. This bottleneck arises when one processor reads or writes to the shared-memory while the other processors have to wait during this time till the "shared-memory bus" is free! Only few processors like the INMOS T800 transputer family [INMOS 1989] and the Texas Instruments TMS320C40 [TMS User guide] can make an optimal use of the multi-computer architecture because these processors possess high

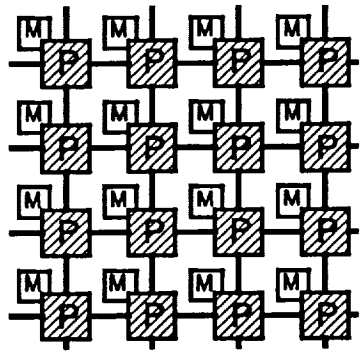

Fig 2

speed communication ports besides their standard address and data busses. Through these ports (links) the processors communicate with each other in a network where each processor possesses its own memory and thus eliminating the von Neumann bottleneck. In a practical multicomputer network the number of processors can be almost unlimited.
The INMOS transputer family consists of T2.., T4.., T8.. and T9... processors supported by link-crossbarswitches and periferal link-adapters. All INMOS processors are equipped with 4 links. Each link consists of one serial transmitting wire and one serial receiving wire both having an unidirectional speed of 20 Mbaud. If a link sends and receives data at the same time, the total data transport will be limited to 23.5 Mbaud/link. The T9000 will be available at the end of 1992 and has a peak performance of 200 MIPS and 25 MFLOPS with link speeds up to 100 Mbaud.

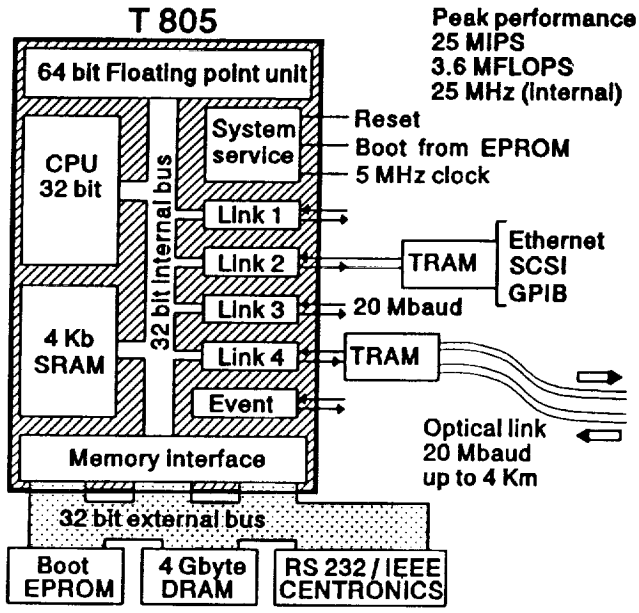

Fig 3

For the MTLRS Control System the T805 has been selected and is running at an internal clock speed of 25 Mhz giving 25 MIPS and 3.6 MFLOPS peak performance. The external 5 Mhz clock is internally multiplied by 5. Fig. 3 illustrates how the processor can be interfaced to the outside world in a flexible way. The present Control System is designed around a minimum of 5 transputers T805 which are interconnected through their links. A link is connected to a server-program running on a host-PC and through this link all the different programs are distributed through the network and loaded to a particular transputer. Each program is started automatically after it is loaded onto the destination processor. The design makes no use of the boot-EPROM facility but this makes the processor also very powerful for embedded designs. The word TRAM is an abbreviation for TRAnsputer Module which is an off-the-shelf interface board delivered by several manufacturers.
For parallel processor networks the software can be programmed in various ways; one task can be cutted into pieces which run in parallel at different processors, different tasks can run in two or more processors so that each processor runs a different task. Also multitasking in one processor can be programmed in a partly parallel way because the T805 can perform processes like cpu- operation, link-communication, timing and memory-IO concurrently. This means that while e.g. one task is busy with link-communication, the cpu is free for other tasks, scheduled in a sequential way following task priority. When a task consists of a number of processes, running concurrently in different processors, process-synchronization can be accomplished by the use of channel I/O (inter process data exchange) and semaphores.
Part of the internal CASH of 4 Kb SRAM is used to hold all registers for up to 99 different tasks and internal processes. If more than 99 modules are running concurrently, external DRAM is also used to hold registers. In contrast to conventional processors where the cpu has to share time to all processes, the T805 is doing this partly parallel which leads to a much higher performance.

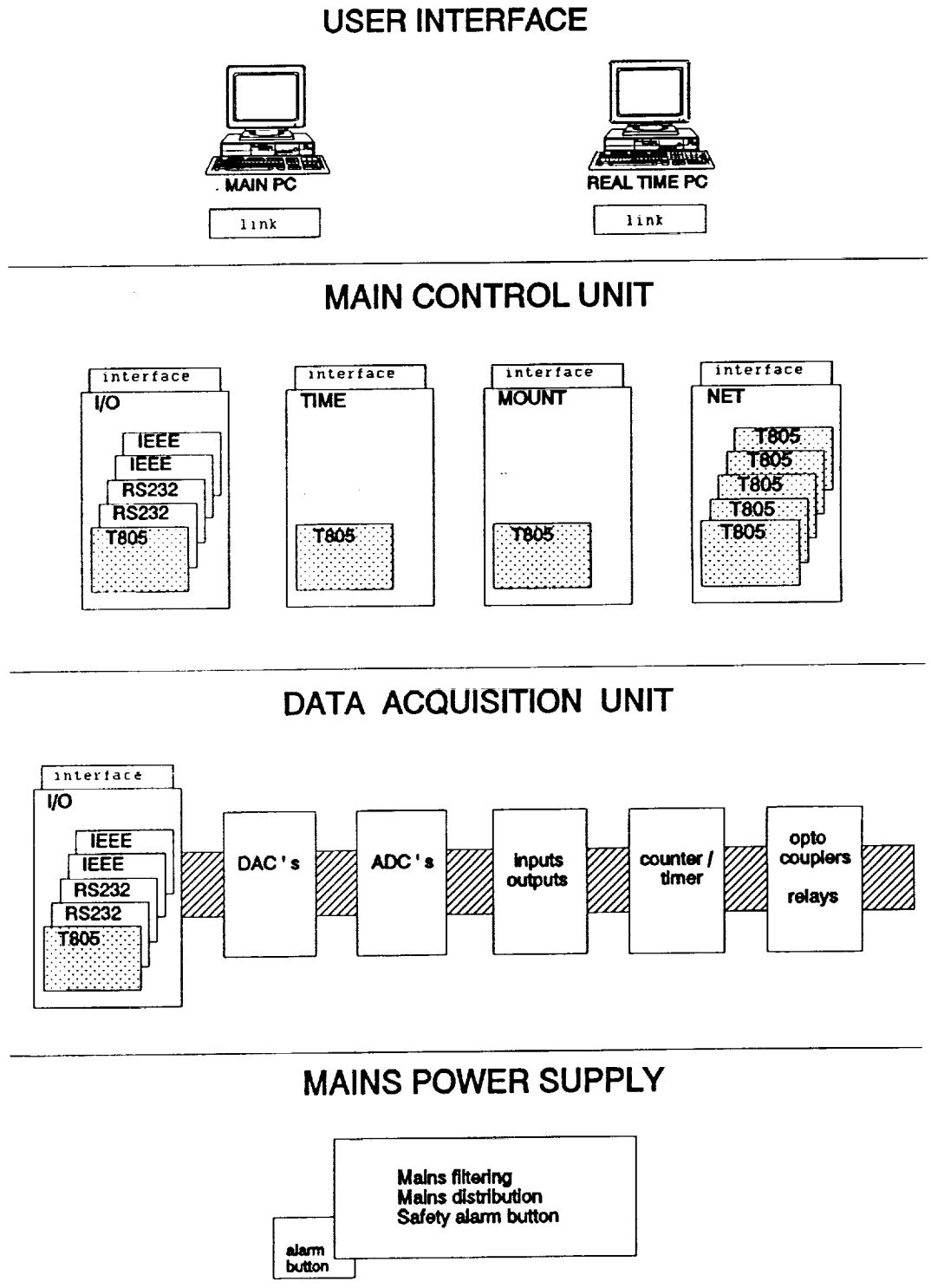
USER INTERFACE
MAIN PC
link
REAL TIME PC
link
MAIN CONTROL UNIT
interface
I/O
IEEE
IEEE
RS232
RS232
T805
interface
TIME
T805
interface
MOUNT
T805
interface
NET
T805
T805
T805
T805
T805
DATA ACQUISITION UNIT
interface
I/O
IEEE
IEEE
RS232
RS232
T805
DAC's
ADC's
inputs
outputs
counter /
timer
opto
couplers
relays
MAINS POWER SUPPLY
Mains filtering
Mains distribution
Safety alarm button
alarm
button

Fig 4

The hardware lay-out

The hardware system can be separated into four major units, the user interface, the main control unit, the data acquisition unit and the mains power supply (fig. 4). It consists of several printed circuit boards, which largely demonstrate the modularity of the design and make it flexible to future modifications.
The basic board is the processor board ***T805***. On this creditcard size board the T805 transputer is placed, which is dedicated to parallel processing (see above). In addition this processor board contains 4 MByte memory, a special reset system for checking that the processor is still alive (EMI protection) and four 20 MBaud serial link drivers.
Other creditcard size boards in the system are ***IEEE-488*** and ***RS-232*** interfaces for connection to standard devices. These creditcard size boards are daughter boards to the extended eurocard size boards of the Main Control Unit and the Data Acquisition Unit.

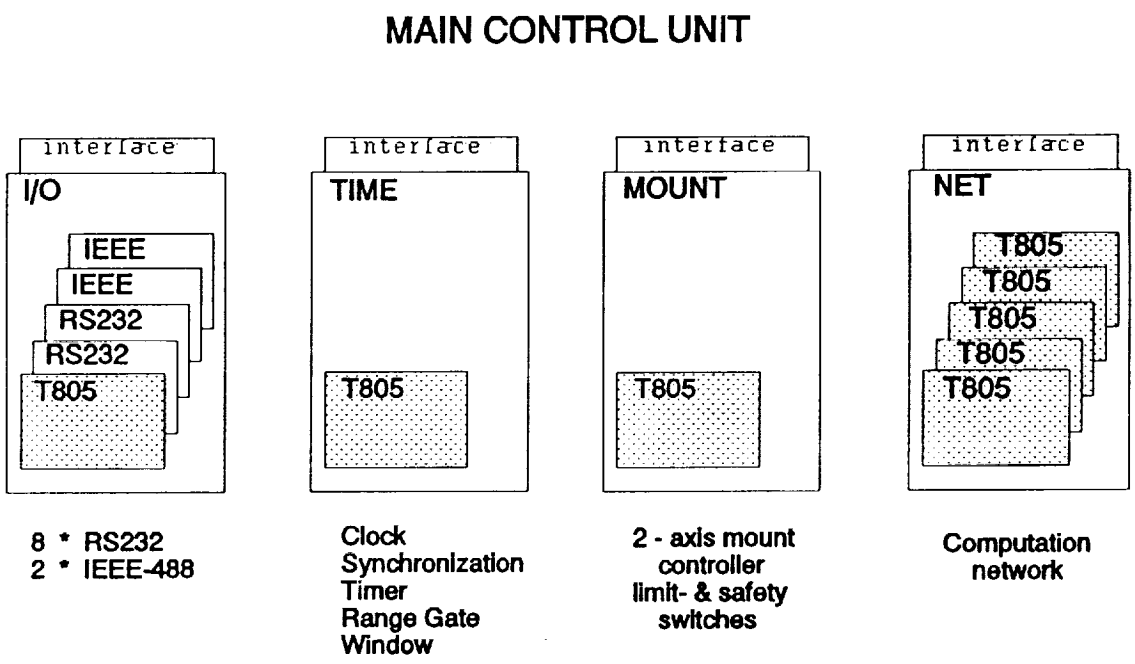

Fig 5

The ***Main Control Unit*** (fig. 5) is made up of four extended eurocard size boards:

1) the ***I/O*** board for connecting the processor to IEEE, RS-232 devices.

2) the ***TIME*** board for all time dependent tasks:
   - 4 channel event counter (low accuracy 20 ns),
   - range gate programmable generator (400 ps one shot accuracy),
   - window programmable generator (20 ns resolution),
   - programmable generator/synchronizer for the shutter, independent from window,
   - RT-clock with battery backup,
   - programmable synchronization for all required signals (e.g. laser firing).

   The ***TIME*** board requires 10 Mhz and 1 pps input signals.

3) the ***MOUNT*** board for driving a 2-axis telescope. The specifications for both axes are:
   - 32 bit position and 16 bit velocity and acceleration controlling,
   - three 16 bit coefficient programming for PID filter,
   - DC and DC-Brushless motors driving,
   - position and velocity mode of operation,
   - interface for quadrature incremental encoder with index pulse,
   - absolute encoder up to 32 bit,
   - limit-, safety switches, etc. ports,
   - joystick connection,
   - nonvolatile RAM for storing position, offset, etc. during power off, without battery backup.

4) the ***NET*** board with a minimum of one processor board with the possibility of extending computer power up to five processor boards. Additional ***NET*** boards can be implemented for expanding the network even further.

Instead of one big backplane interface, four individual backplane ***interface*** boards are designed. The design of each small backplane is dedicated to the typical hardware application, e.g. dependent on the type of encoders etc.
Each backplane can easily be modified to different input signal levels e.g. negative, positive, NIM, TTL, 50 Ω, ...

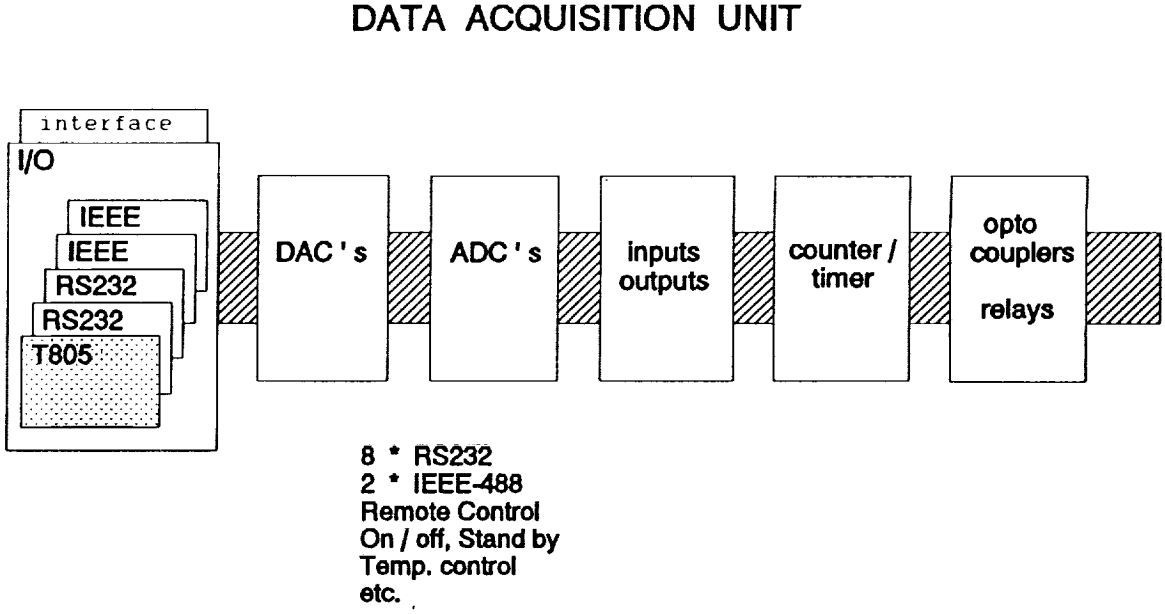

Fig 6

The ***Data Acquisition Unit*** (fig. 6) will be used for controlling additional hardware for the purpose of automation e.g. DC-motors, stepper-motors, temperature control, contacts checking and on/off-switching of equipment. It consists of an ***I/O*** extended eurocard size board which is identical to the one in the main control unit, together with several Data

Acquisition boards like:

- 12 bit D/A-converter (multiplexed for 8 outputs) with programmable range and offset.
- 12 bit A/D-converter (multiplexed for 8 inputs) with programmable range, offset and auto-calibration.
- 24 parallel input/output ports.
- Counter/timer for controlling counting/timing functions.
- Galvanic separation by opto-couplers and solid state relays.

The ***User Interface*** (fig. 4) consists of two identical 486 Personal Computers (PC) which are linked to the transputer network by means of 20 Mbaud ***link*** extension boards located in each PC. At this level the system can also be connected to Local and Wide Area Networks by adding standard interface boards to the PC-ISA bus, utilizing standard protocols.

Finally the ***Mains Power Supply*** (fig. 4) is designed for distribution, switching and filtering mains. It also features an alarm button for safety.

II. Software

General aspects

The computer configuration includes a transputer network and two identical PC-486AT's, the ***Main PC*** and the ***Real-Time PC***, each connected to the transputer network by a so called 'link'(fig. 4). On both PC's the operating system MS-DOS is running together with the highly efficient and friendly Microsoft WINDOWS which is a widely accepted industry standard graphical environment for PC's. In the transputer network the RT-software is running without any operating system. On both PC's the WINDOWS TRANSPUTER FILE SERVER is running. The ***Main PC*** hosts the off-line software and is used for data storage. Tasks like: site installation, preparing predictions, real time processes, data screening, normal point calculations and data mailing are initiated from or performed by the ***Main PC***. The ***Real-Time PC*** interacts with the ranging process as a terminal through the on-line Real-Time (RT) windows transputer file server program, supporting graphics capabilities for the transputer network during all real time processes like: satellite ranging, target calibration, telescope alignment and diagnostics. Through the ***Real-Time PC*** the operator interacts with all ranging related processes. The transputer network is built around several transputers where the actual RT-software is running in order to directly control the hardware. Modification of (default) input parameters for the various modules by the operator is based on WINDOWS dialogue boxes and menus which are on both PC's supported by extensive help information. In case of malfunctioning of one of the PC's, the software is designed to run on one PC only, with minimum inconvenience to the operator. Thus each PC is a back-up unit for the other one.

The off-line software

This software is largely based on the original MTLRS system and will be updated for compatibility with the PC-hardware platform under MS-DOS. The software will be embedded in the WINDOWS graphical environment. Error handling is supported by supplying help information and by allowing operator intervention in run-time whenever feasible. Primarily the new software package has been re-written in C, whereas individual existing modules are kept in FORTRAN-77, callable from C-programmes. Both the C- and the FORTRAN coding are based on to the ANSI-standard to ensure maximum portability of the software. All data files have been

defined in ASCII-format, unless specific requirements dictated the use of a binary format.

The RT-software

The transputer software system consists of a set of communicating processes, logically combined in functions. To make the software usable for other ranging systems and to facilitate future developments, the software has been structured into three layers:

a. the GLOBAL, SLR SYSTEM independent software
b. the DEVICE or data format dependent DRIVER software
c. the INTERFACE type dependent DRIVER software

Diagnostic capabilities are integrated in all three layers of the RT-software and are running concurrently by default or can be activated to run concurrently.

a. Global system

The global system includes all functions of the present MTLRS RT-software. The current MTLRS limitations concerning the observation range, the correction domain and the fixed firing epoch have been eliminated. Interleaving satellite ranging is made possible. To optimize this, the coarse pass prediction integration and the fine prediction interpolation are moved into the RT-software. This also allows firing epoch dependent range residual calculation to speed up data filtering. The meteo data and the UTC-GPS time are made available to the RT-time system.

b. Device driver

A device driver prepares the standard information from the global system to meet the requirements of the device and vice versa. It executes a device function by preparing a device command according to the operational device protocol and by calling interface drivers for data transfer. Device drivers are available for all external devices to be accessed by the global software.

c. Interface driver

An interface driver transfers the data from the transputer network through a hardware interface to each device and vice versa. No modifications are applied to the data. Interface drivers are available for each type of interface and protocol used by the external devices. Event interrupt processing is supported for devices which are capable of asserting the transputer event signal.

International design standard

Because of the structured approach to the design of this control system it is hoped that this activity will contribute to the establishment of an international standard for SLR control systems.

References

- Beek, W. and K.H. Otten, "MTLRS-2 Upgrade", Proceedings Seventh International Workshop On Laser Ranging Instrumentation, Matera, 1989, OCA/CERGA, Grasse, France.
- INMOS, "The Transputer Databook", Second Edition, document No.72 TRN 203 01, 1989, Redwood Burn Ltd, Trowbridge.
- TMS User guide, Texas Instruments Data Book: TMS320C40 User guide.
- BYTE: November 1988, Parallel Processing in depth, T800 and counting.
- 3L Ltd. Peel House, Ladywell, Livingston EH54 6AG SCOTLAND, UK Telefax: -506-415944.

Airborne and Spaceborne Systems

AIRBORNE 2 COLOR RANGING EXPERIMENT

Pamela S. Millar
James B. Abshire
Jan F. McGarry+
Thomas W. Zagwodzki*
Linda K. Pacini*

Experimental Instrumentation Branch, Code 924
NASA/Goddard Space Flight Center
Greenbelt, Maryland 20771

+Crustal Dynamics Project, Code 901
*Photonics Branch, Code 715

ABSTRACT

Horizontal variations in the atmospheric refractivity are a limiting error source for many precise laser and radio space geodetic techniques[1-7]. This experiment was designed to directly measure horizontal variations in atmospheric refractivity, for the first time, by using 2 color laser ranging measurements to an aircraft. The 2 color laser system at the Goddard Optical Research Facility (GORF) ranged to a cooperative laser target package on a T-39 aircraft. Circular patterns which extended from the southern edge of the Washington D.C. Beltway to the southern edge of Baltimore, MD were flown counter clockwise around Greenbelt, MD. Successful acquisition, tracking and ranging for 21 circular paths were achieved on three flights in August 1992, resulting in over 20,000 two color ranging measurements.

INTRODUCTION

Atmospheric refractivity is a limiting error source in precise satellite laser ranging (SLR). Several models have been developed to correct SLR measurements for the increased optical path length caused by atmospheric refraction[1-3,8,9]. The first three formulas assume that atmospheric refraction is spherically symmetric, and require surface meterological data at the laser ranging site. A higher order model developed by Gardner [8,9] can, in principle compensate for spatially varying atmospheric refraction by utilizing pressure and temperature measurements at many locations near the laser ranging site. However, this model depends on the surface measurements being strongly correlated to atmospheric density at higher altitudes.

A more accurate method for determining the atmospheric correction is to directly measure the atmospheric dispersion with a two color laser ranging system[4-7]. In the two color ranging approach, the single color range and the differential delay between the two colors is measured. Due to atmospheric dispersion, the differential delay is proportional to the path-integrated atmospheric density, and therefore it can be used to estimate the atmospheric correction. In 1980, Abshire proposed to measure the magnitude of the horizontal gradients in atmospheric refraction by making dual color ranging measurements to an aircraft equipped with a retroreflector. We have developed and successfully carried out such an airborne two color ranging experiment. We expect that data from this experiment will improve our knowledge of gradients in the refractivity, and could contribute towards improving atmospheric models.

APPROACH

Our experiment utilized Goddard's 2 color ranging system at the 1.2 meter (m) telescope facility with a cooperative laser target package on a T-39 aircraft. A simplified diagram of the experiment is shown in Figure 1. The ground-based laser system tracked and ranged to the aircraft as it circled Greenbelt, MD. With this circular flight pattern, the aircraft passed partially over two major cities, Washington D.C. and Baltimore, and land near the Chesapeake bay. It is likely that variations in the terrain temperatures will cause horizontal gradients in the air density directly above, which could be measured by the experiment.

The initial step in the experiment is to acquire the aircraft's approximate location. A realtime GPS data relay link was developed for this purpose. A GPS receiver on the T-39 relayed the aircraft position every 3 seconds through an RF digital packet link to the ground telescope. The telescope's tracking program then determined the pointing angles to the aircraft by extrapolating the aircraft's position from the GPS data.

Once acquired, we closed an automatic tracking loop by using a CCD camera and frame grabber which commanded the 1.2 m telescope to automatically track the aircraft's 810 nm laser diode beacon. The aircraft target package was manually pointed to the ground from inside the aircraft by viewing the ground beacon which was modulated at 5 Hz.

To determine the optical path length we measured the range to the aircraft at 355 nm with a 20 psec resolution laser ranging system. For the differential delay measurement, we used a streak camera-based receiver which recorded the reflected 355 & 532 nm pulses within a 1.2 nanosecond (nsec) time window.

AIRCRAFT INSTRUMENTATION

Figure 2 shows the T-39 aircraft based at (Wallops Flight Facility) used in this experiment, along with the flight crew. The T-39 is a two engine, 4 passenger, jet aircraft capable of maintaining 12 kilometer (km) altitude. The three science flights were limited to 6 - 7 km altitudes due to high cirrus clouds near 7 km. The target package was located beneath the nadir port of the aircraft just aft of the air brake.

On the aircraft we used a combination of laser and electro-optic instrumentation for pointing the target package with two radio transceivers for data and voice communications to the ground laser facility. A photograph of the target configuration is shown in Figure 3. The target package consisted of a cube corner array (CCA), a laser diode beacon and a CCD camera with a narrow bandpass filter. The package was secured to a commercial pan and

tilt camera mount and was controlled with a joystick inside the aircraft. The entire package was protected by an aluminum enclosure which incorporated a 1/4" thick quartz window to transmit the optical signals at 355, 532 and 810 nm. This window was tilted ~3°, with respect to the aircraft nadir, so that the beams would transmit through at right angles to the window. We used baffles on both the laser diode beacon and the CCD camera to reduce scattering of the laser beacon from the window into the camera. The baffles extended close to the enclosure window. The target package components and parameters are listed in Table 1.

We used several techniques to control the target package's temperature. To avoid condensation on optical surfaces, tape heaters were attached to the inner walls of the CCA housing and around the filter adaptor tube on the CCD camera. Resistive heaters were installed on the back mounting plate of the target package. An AD590 temperature sensor was placed on the filter adapter of the CCD camera. The sensor indicated that at 7 km altitude the target package stayed at 10°C for the flight duration. Dry nitrogen was flushed into the target enclosure before takeoff and during ascent, descent and landing to displace water vapor, which could condense on cold optical surfaces.

The target package could be pointed in azimuth ±5° from port, parallel to the left wing and in elevation +5° to -15° from horizontal. The operator who moved the target package via joystick could instruct the pilots to adjust aircraft attitude if the ground beacon was moving outside of the CCD camera's 10° field of view (FOV). This was necessary particularly in azimuth during flights with strong cross winds.

The flight crew consisted of two pilots and two science team members. One person pointed the target and communicated with the pilots, while the other operated the GPS control software and maintained radio communication with the ground ranging site. The GPS receiver was used to receive the aircraft's lattitude, longitude, altitude and time. The GPS receiver relayed its information to the flight computer via a RS232 port, as well as to the packet radio. The packet information was transmitted in bursts every 3 seconds. The flight computer allowed the operator to verify that at least four satellites were in the receivers FOV and that the GPS data being sent was correct. An aircraft LORAN unit was used as a backup to initialize the GPS receiver in the event of a computer crash.

The ground packet radio receiver relayed the aircraft's position to the DEC PDP 11/24 computer. This mount control computer pointed the 1.2 m telescope to the aircraft. While flying the circular pattern, the pilots used a TACAN transceiver which gave them slant range to GORF where another TACAN transceiver was located.

GROUND-BASED RANGING & TRACKING INSTRUMENTATION

The airborne two color laser ranging experiment was one of several projects which have used Goddard's 1.2 m telescope ranging & tracking facility. This facility was developed for satellite laser ranging. We tried to design the aircraft experiment to minimize the impact to the ongoing satellite ranging program, so that only slight system modifications were made to convert from satellite mode to aircraft mode. A simplified block diagram of the system is shown in Figure 4, with system parameters given in Table 2.

For the aircraft experiments the Nd:YAG laser was operated at 10 mJ at 355 nm and 0.3 mJ at 532 nm to avoid damaging the telescope optics. The laser was housed about 10 meters from the base of the telescope. Figure 5 shows the laser transmitter and two color optics. The experimenters area is located at the base of the telescope near the telescope focal plane. This area contains the range receiver electronics, aft optics and streak camera. The aft optics

for the aircraft configuration is shown in Figure 6. The laser output is directed through a hole in the 45° bifurcated mirror through the telescope and to the aircraft.

The ranging operation can be described by referring to Figure 4. A start diode samples the outgoing laser pulse to initiate the time interval measurement sequence. The aircraft return pulses are then reflected at the 45° birfurcated mirror and into the aft optics receiver. In the receiver a small percentage of the return is split and detected by the MCP photomultiplier tube. This generates the stop signal for the time-of-flight measurement as well as the pre-trigger for the streak camera.

The majority of the received signal was then separated into 532 nm and 355 nm paths by a dichroic mirror and bandpass filters. Each color was focussed into a fiber optic delay line. The optical delay was required to allow pre-triggering the streak camera with respect to the optical pulse's arrival time. The delay fiber bundle was composed of 27 fused silica fibers with 100 μm core for each color which were round at the input side and formed into a single row at the output side. The signals were then imaged onto the streak camera photocathode by the streak camera's input lens. The streak camera's 1.2 ns sweep speed setting was calibrated and used to achieve ~4 psec/pixel resolution. During pre-flight tests the detection threshold for optical pulses transmitted through the fiber optic cable to the streak camera was measured to be 6,600 photoelectrons at 355 nm and 4,200 photoelectrons at 532 nm.

At the transmitter, an optical delay was added to the 532 nm pulses to allow both 532 and 355 nm received pulses to be recorded within the 1.2 ns sweep window. The 532 nm pulse was delayed with respect to the 355 nm pulse by using a total internal reflection (TIR) cube corner mounted on a computer controlled linear motor stage. This time offset was used to compensate for the additional ~2.7 nsec round trip atmospheric delay at 355 nm. Each streak camera waveform pair was digitized to 256 time pixels by 8 bits amplitude and was recorded on hard disk. The streak camera waveforms were stored on the PDP LSI 11/23 at a 2 Hz rate. Each file consisted of the optical waveform pair, the 355 nm time-of-flight measurement, the transmitter 532 nm delay setting, telescope azimuth and elevation angles, and other relevant tracking information.

The aircraft was acquired by using the GPS measured aircraft positions which were relayed to the tracking computer. Every 20 msec, the computer tracking program extrapolated the aircraft's present angular position from the three most recent GPS data points and directed the mount to that angular location. GPS tracking was usually sufficiently accurate to keep the aircraft position within the CCD camera's ~0.3° FOV. The tracking loop was closed by reading an X-Y digitizer which determined the angular offset of the aircraft's 810 nm laser diode beacon within the CCD FOV. In this mode the mount was driven so that the beacon's angular position stayed within the center of the CCD FOV. Optical background from bright stars, the moon and other aircraft were suppressed with a 5 nm FWHM bandpass filter in front of the tracking camera. The telescope was able to track the aircraft to a precision of ~200 microradians, and successfully tracked the aircraft across the face of a full moon.

STREAK CAMERA CALIBRATION

When making two color ranging measurements at 532 and 355 nm, the differential delay is ~1/12 the 532 nm delay. The differential delay must be measured to better than 5 psec for 1 cm single color corrections[10,11]. The streak camera's sweep speed had to be carefully calibrated to permit this accuracy.

The first step involved finding the zero delay setting in the transmitter. A cube corner was placed in the optical path in front of the telescope to avoid any atmospheric effects. Then the transmitter's 532 nm delay was adjusted to a position where the 532 and 355 nm pulses arrived at the streak camera simultaneously. This was denoted the zero reference position. Next an optical delay of 100 picoseconds was set at the transmitter. Each waveform pair was smoothed and peak positions were computed along with the difference between the peaks. The 100 psec optical delay setting was then divided by the peak difference (in pixels) to yield an inverse velocity measurement. This dt/dx value (psec/pixel) was then plotted at the x position which was at the midpoint of the two peaks.

This process was repeated several hundred times as the pulse pairs were moved across the streak camera window. The coefficients for the sweep speed were computed as the best fit to the inverse velocity versus midpoint plot as shown in Figure 7. To check the calibration, and to process the flight data, the time difference between the 355 and 532 nm pulses were computed by integrating the inverse velocity profile [5]. The calibration was checked by displacing the TIR cube corner to other known values for comparison with calculated optical delays. The system's calibration was tested either before or after each aircraft experiment, and agreement was typically ~4 psec.

SUMMARY:

On the evenings of August 5, 6 and 7, 1992 we conducted a two color ranging experiment to an aircraft. Each ranging experiment lasted about 2.5 hours as the aircraft circled the ranging system at an altitude of 6 to 7 km and a slant range of 20 to 25 km. This resulted in 7 to 8 full rotations around the ranging site per flight. About 6,000 to 8,000 two color laser ranging measurements were recorded on each flight. In total 30 Mbytes of calibrated 2 color ranging data were collected.

An example of a waveform pair from 8/05/92 is illustrated in Figure 8. Both smoothed and raw data for the green and UV are shown. The waveforms are smoothed for analysis by convolving with a raised cosine pulse. Most of the waveforms had pulse widths wider than the transmitter. Some pulse broadening was caused by modal dispersion in the multimode fiber delay lines. Additional broadening on some signals may be due to saturation of the streak camera. However, in most cases, the sharp leading edges of the optical pulses were preserved in the waveforms. Our work to date shows that timing to the pulse's leading edges appears to have the least timing jitter.

We are currently in the process of normalizing the data for varied range and elevation angle as well as optimizing our method for calculating the differential delay between the 2 color pulses. These results will be compared to atmospheric models[3,8,9] and published upon completion.

ACKNOWLEDGEMENTS

The authors wish to thank NASA Headquarters Code SEP, the Crustal Dynamics Project and the EOS GLRS instrument project for supporting this work. We are indebted to Arnie Abbott, Jonathan Rall, Richard Chabot, Jack Cheek, Kent Christian, Jimmie Fitzgerald, Dan Hopf, Bill Krabill, Earl Frederick, John Riley, Robert Gidge, George Postell, Virgil Rabine, Dave Pierce, Evan Webb and John Degnan for their many contributions towards the completion of this project.

REFERENCES

1. Bender, P. L. and J. C. Owens, "Correction of Optical Distance Measurements for the Fluctuating Atmospheric Index of Refraction," J. Geophys. Res., 70(10) pp. 2461-2462, May 1965.

2. Marini, J. W., and C. W. Murray, Jr., "Corrections of Laser Range Tracking Data for Atmospheric Refractions at Elevations above 10 Degrees," NASA X-591-73-351, Nov. 1973.

3. Herring, T. A., "Marini and Murray Atmospheric Range Correction Formula," *Report to the CSTG SLR Subcommission meeting NASACDP Principal Investigators meeting*, Munich, October 1988.

4. Abshire, J. B., "Plan for Investigation Atmospheric Errors in Satellite Laser Ranging Systems," *NASA X-723-80-10*, January 1980.

5. Abshire, J. B., and C. S. Gardner, "Atmospheric Refractivity Corrections in Satellite Laser Ranging," *IEEE Trans Geoscience & Remote Sensing*, **GE-23**(4) pp. 414-425, 1985.

6. Degnan, J., J., "Satellite Laser Ranging: Current Status and Future Prospects," *IEEE Trans. Geoscience & Remote Sensing* **GE-23**(4) pp. 398-413, 1985.

7. Bender, P. L., "Atmospheric Refraction and Satellite Laser Ranging," submitted to: *Symp. on Refraction of Transatmospheric Signals in Geodesy*: The Hague, May 19-22, 1992.

8. Gardner, C. S., and B. E. Hendrickson, "Correction of Laser Tracking Data for the Effects of Horizontal Refractivity Gradients," *Radio Research Laboratory* **478**, University of Illinois, Urbana Illinois, December 1976.

9. Gardner, C. S., "Correction of Laser Tracking Data for the Effects of Horizontal Refractivity Gradients," *Appl. Optics* **16**(9) pp. 2427-2432, September 1977.

10. Im, K. E., C. S. Gardner, J. B. Abshire, and J. F. McGarry, "Experimental evaluation of the performance of pulsed two-color laser-ranging systems," *J. Opt. Soc. Am. A* 4(5) pp. 820-833, 1987.

11. Zagwodzki, T. W., J. F. McGarry, A. Abbot, J. W. Cheek, R. S. Chabot, J. D. Fitzgerald and D. A. Grolemund, "Streak Camera Returns from the Relay Mirror Experiment (RME) Satellite at Goddard space Flight Center's 1.2m Telescope Facility," submitted to: American Geophysical Union Monograph, Space and Geodesy and Geodynamics, Fall 1992.

Table 1. Aircraft Instrumentation Parameters

1. Cube Corner Array Target	23 element array, 2.5 cm cube corners, 5 arc second accuracy, UV coated, R=78% @355 nm.
2. Laser Diode Beacon	SDL-2460 AlGaAs Array, 780 mW at 810 nm, 7° azimuth by 8° elevation divergence.
3. CCD Camera	Philips model 56471 camera, 25 mm lens, f/0.7, 10° FOV, Bandpass Filter: 810 ± 2.5 nm.
4. Pan & Tilt Camera Mount	VICON model V353APTV variable speed drive system and tilt controller, 8" by 12.75" mounting plate
5. GPS Receiver	Motorola EagleVIII, 4-channel, simultaneous L_1 C/A code carrier tracking, <25 m spherical error probability.
6. Packet Radio Controller	AEA, Inc. Model PK-87 Controller ICOM IC-37A FM Transceiver 217.55 MHz, 25 Watt.
7. Minicomputer	Compaq 386 for GPS data control and display.
8. Voice Radio	ICOM IC3SAT FM Transceiver 219.45 MHz, 5 Watt.

Table 2. Two Color Laser Ranging Aircraft Experiment System Parameters

1. Laser Transmitter	Continuum PY62 Cavity Dumped, mode-locked, Nd:YAG System: 355 nm: 10 mJ, 150 μrad 532 nm: 0.3 mJ, 300 μrad Pulsewidth: 30 psec FWHM.
2. Telescope	1.2 meter diameter, f/28 Cassegrain.
3. Detectors:	
PMT	ITT F4128, Microchannel Plate.
Streak Camera	Hammamatsu model C1370, 2 psec resolution, 256 elements by 8 bit digitization.
4. Time Interval Unit	Hewlett Packard HP5370, 20 psec resolution.
5. Minicomputers:	DEC PDP 11/24, Pointing. DEC LSI 11/23, Tracking, Streak Camera.

AIRBORNE 2 COLOR RANGING EXPERIMENT

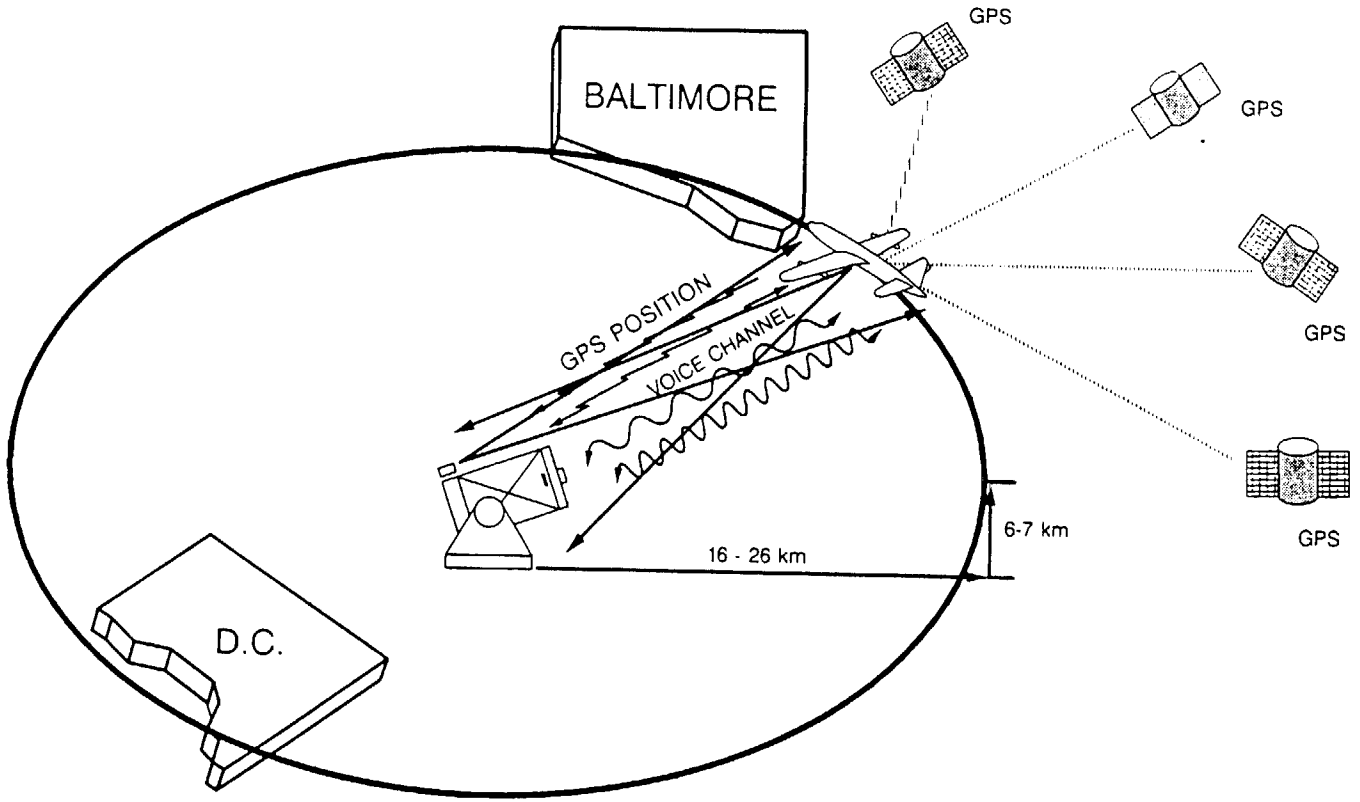

Figure 1. The 1.2 meter 2 color ranging facility centrally located in the flight pattern tracks and ranges to the aircraft. Coarse tracking is accomplished with GPS and fine tracking utilizes the diverging laser diode beacon on the aircraft. 2 color ranging is represented by the two sinusoidal bidirectional lines. The jagged lines imply radio transmission. The aircraft is able to point the cube corner target by tracking the ground laser diode beacon.

ORIGINAL PAGE
BLACK AND WHITE PHOTOGRAPH

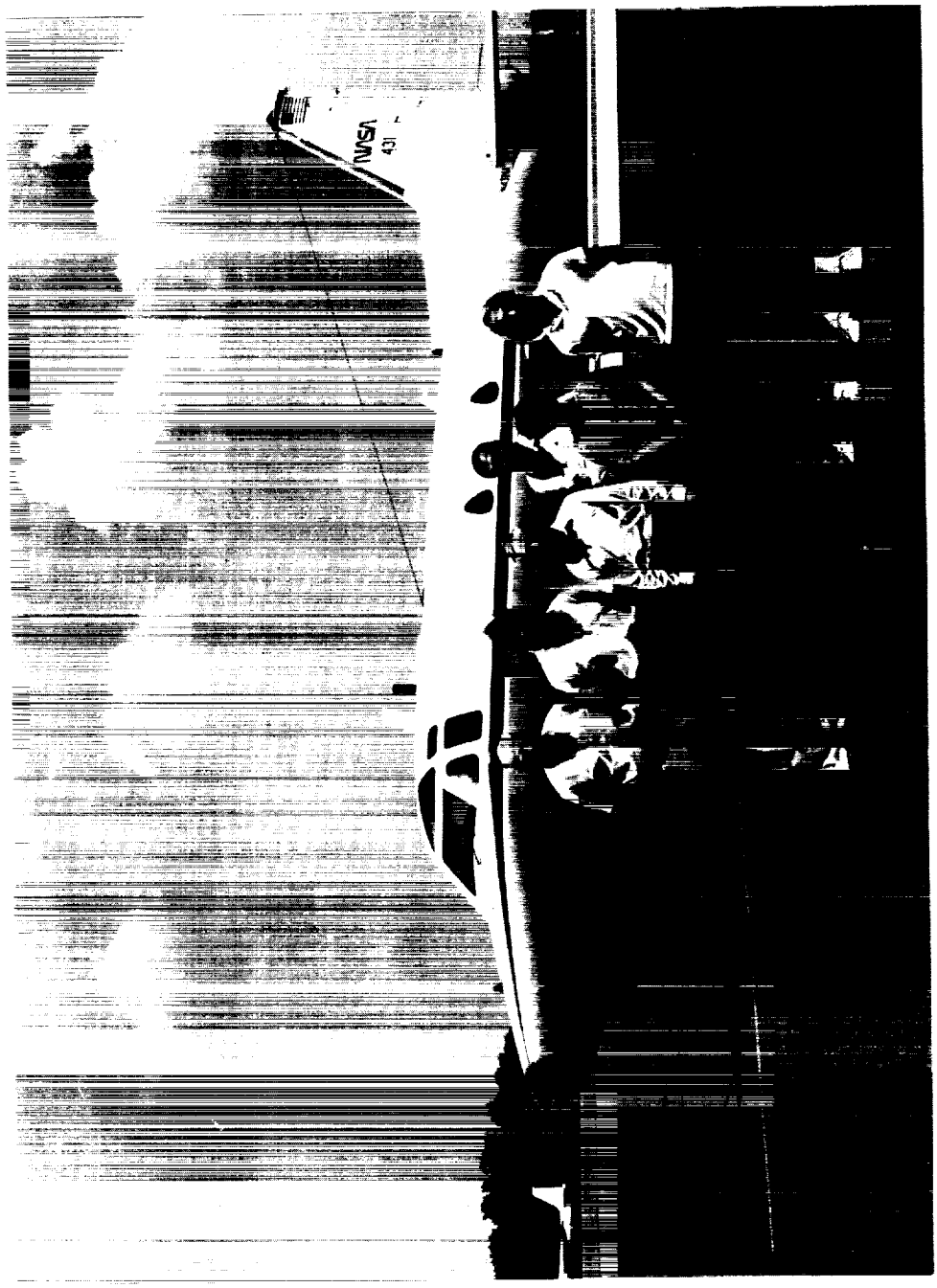

Figure 2. NASA T-39 aircraft and airborne 2 color laser ranging flight crew at Wallops Flight Facility.

ORIGINAL PAGE
BLACK AND WHITE PHOTOGRAPH

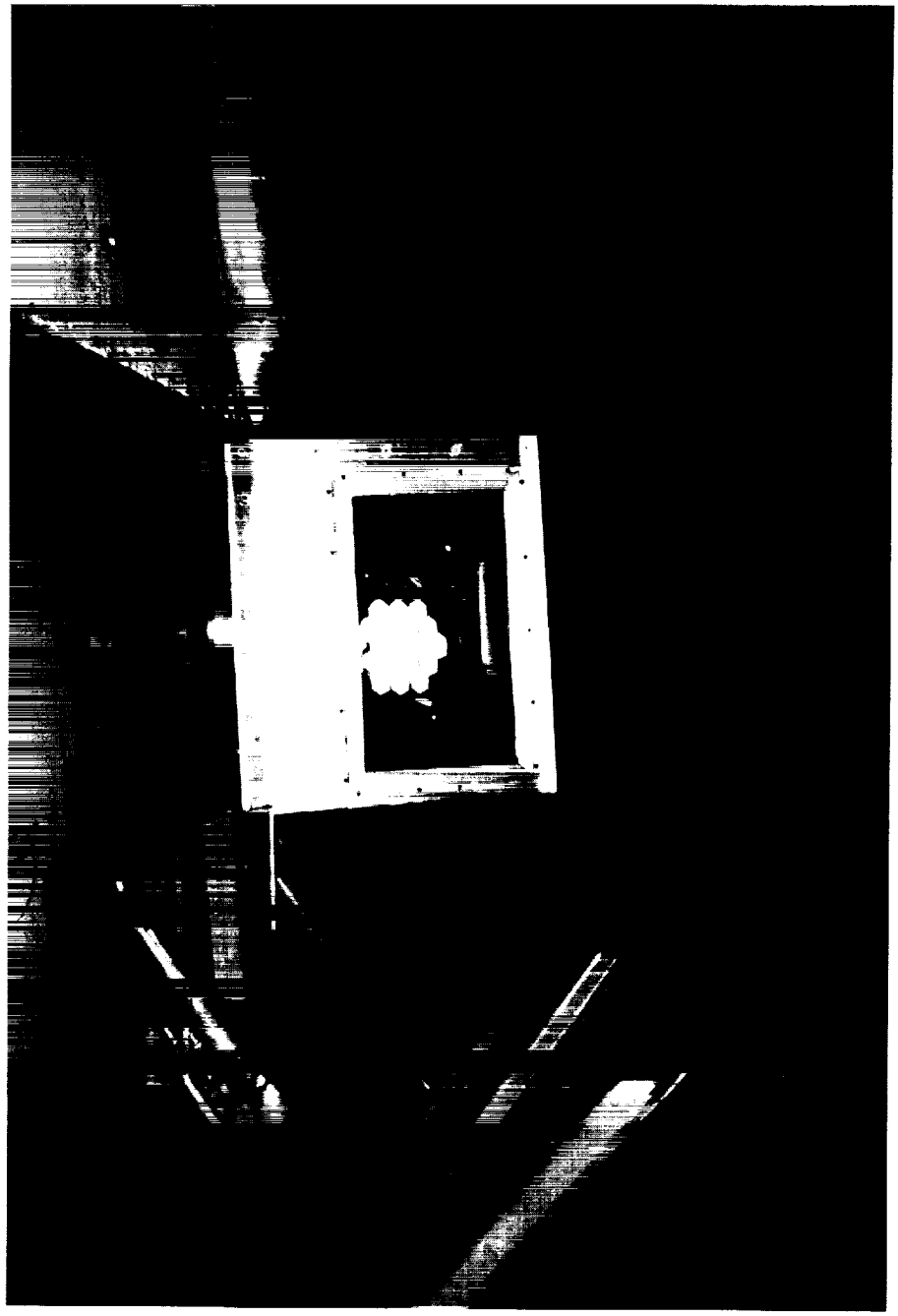

Figure 3. Aft of the T-39 airbrake is the protective enclosure and target package which is mated to the nadir port of the aircraft. The package assembly consists of a cube corner array, and a 1 Watt laser diode beacon above a CCD camera with 25 mm lens and bandpass filter. A pan & tilt mount (not visible) can point the target ± 5° in azimuth and +5° to -15° in elevation .

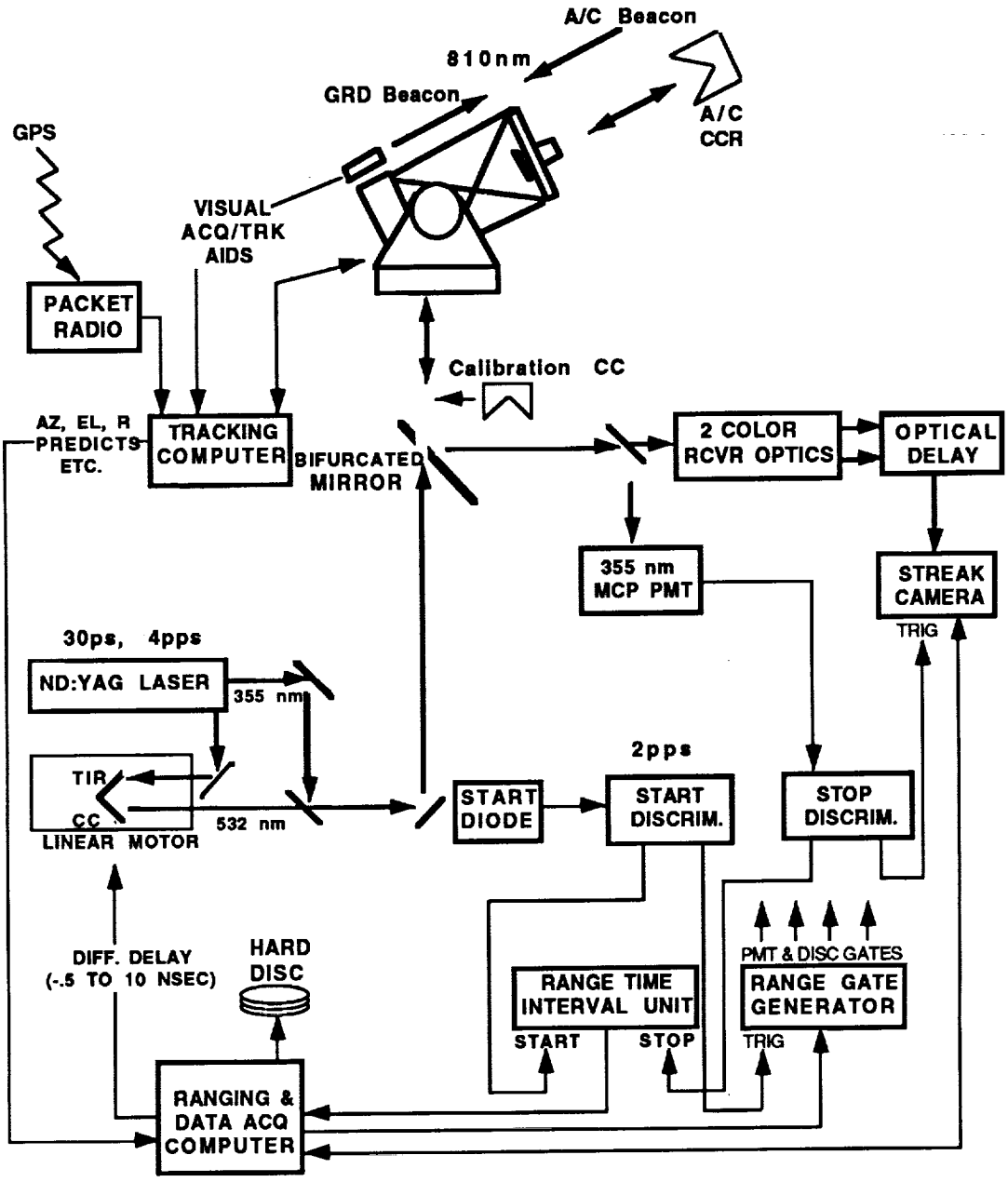

Figure 4. Simple block diagram of 1.2 m ranging and tracking facility in Greenbelt, MD. Thick lines represent optical signals while thin lines indicate electrical signals. The system operated at 2 Hz (or pps). Single color range was measured at 355 nm with conventional time of flight instrumentation. Differential time between the 355 and 532 nm pulses was measured with a streak camera based receiver. System calibration was performed by inserting a corner cube in front of the telescope and setting known delay in the 532 nm path with the TIR cube corner (cc).

A/C = aircraft, ACQ = acquisition, DISCRIM. = discriminator,
MCP PMT = microchannel plate photomultiplier tube, TRK = Tracking

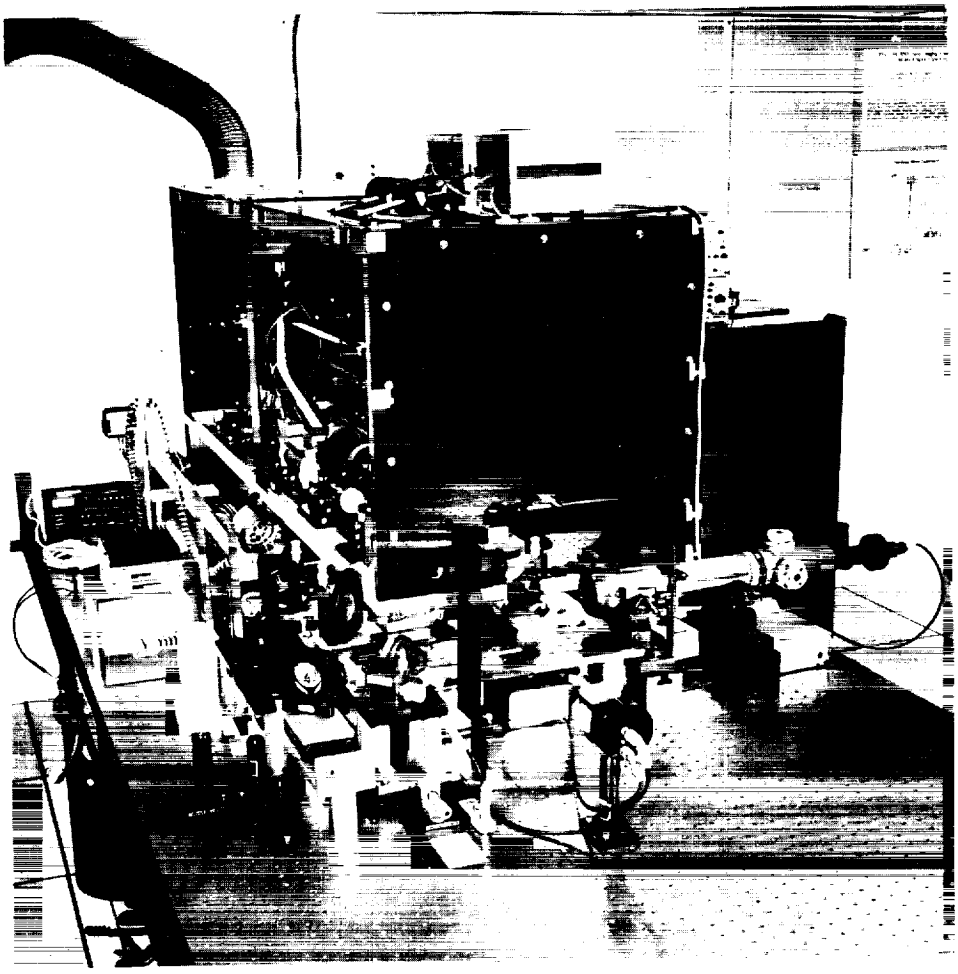

Figure 5. Laser clean room housing the 30 ps Continuum PY62 cavity dumped, mode-locked, doubled and tripled Nd:YAG laser. This system has two amplifier stages. The TIR cube corner variable delay in the green path is shown on the left side of the optical table. Alignment and two color optics are located outside of the primary, plexiglass, laser housing.

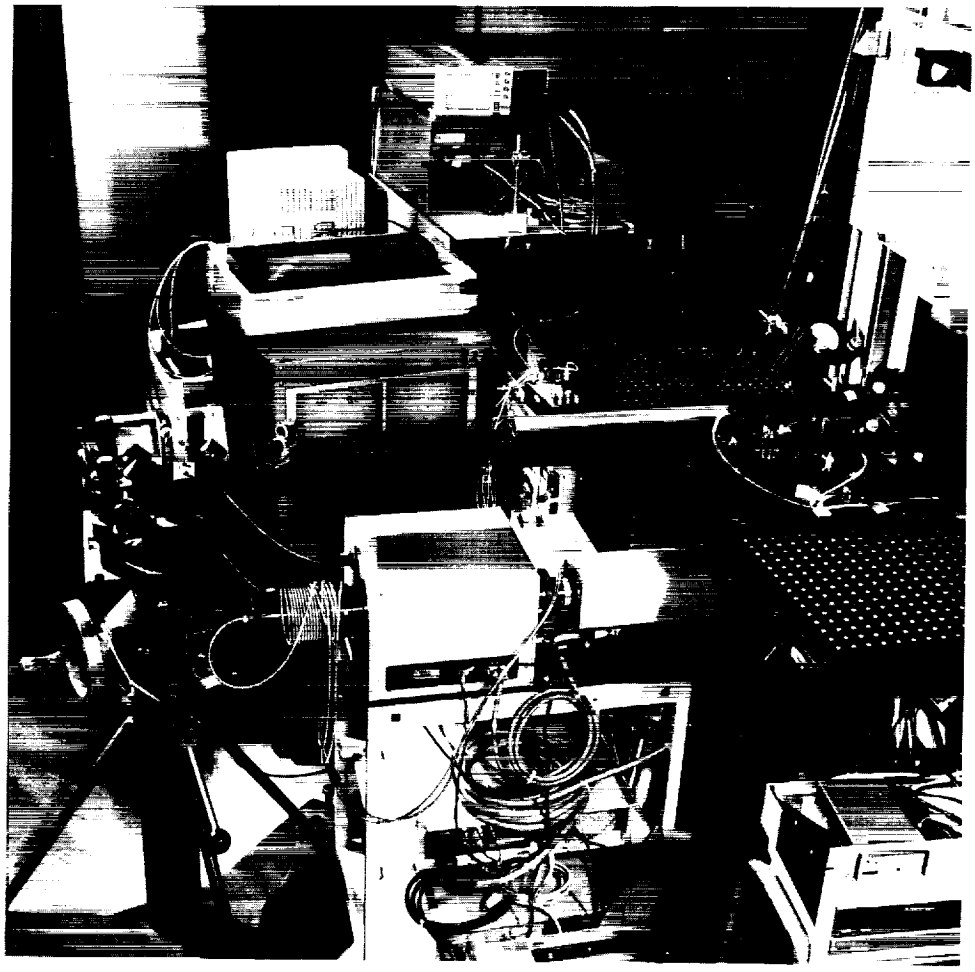

Figure 6. Receiver electronics including MCP PMT, Hammamatsu model 1730 streak camera, fiber optic delay lines, two color aft optics fastened to small breadboard at the base of the 1.2 m telescope.

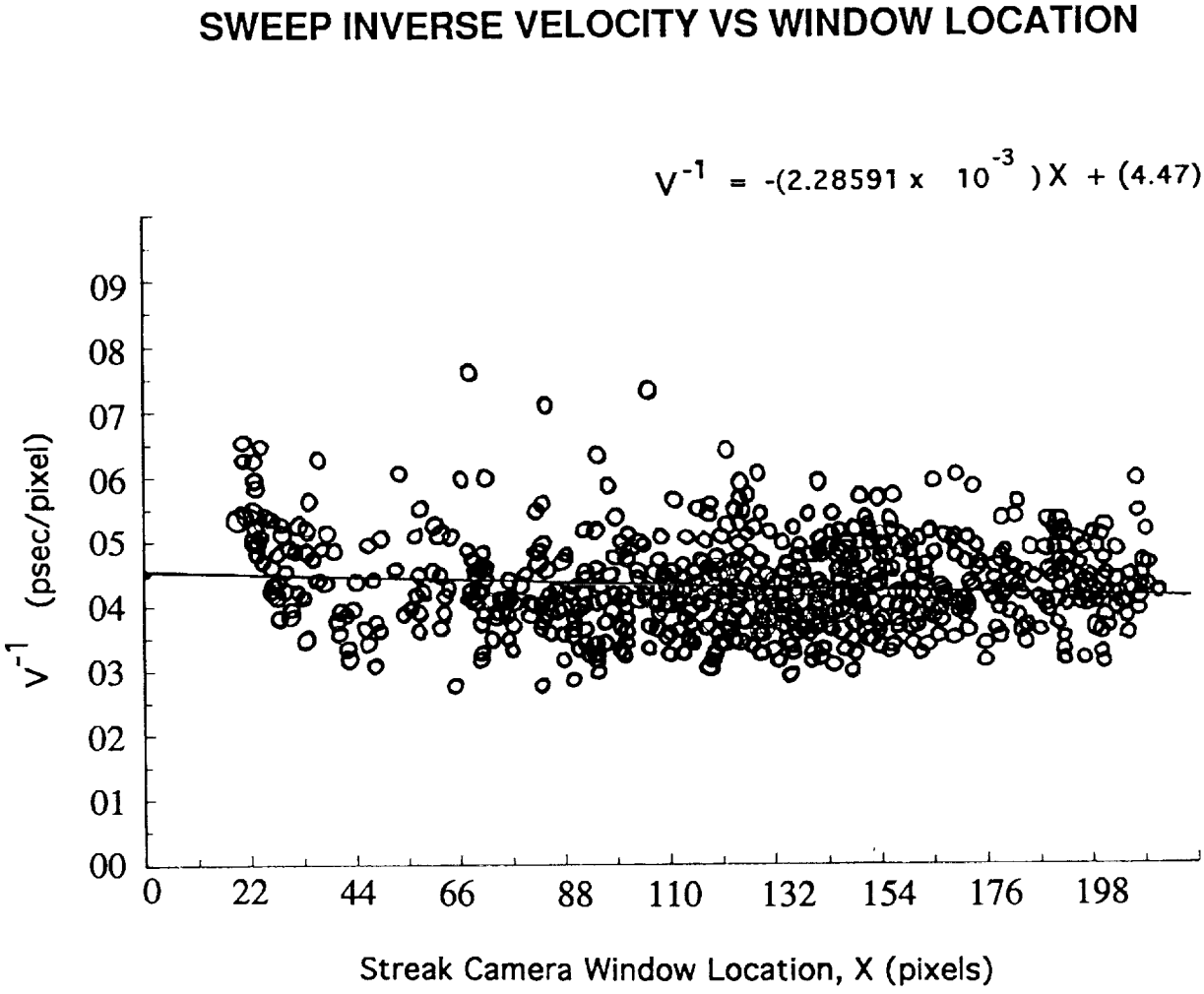

Figure 7. Streak camera sweep speed calibration for 2nsec sweep using data taken 3/24/92. The linear fit using 100 data points is displayed in the upper right hand corner of the plot. The units of inverse velocity are psec/pixel.

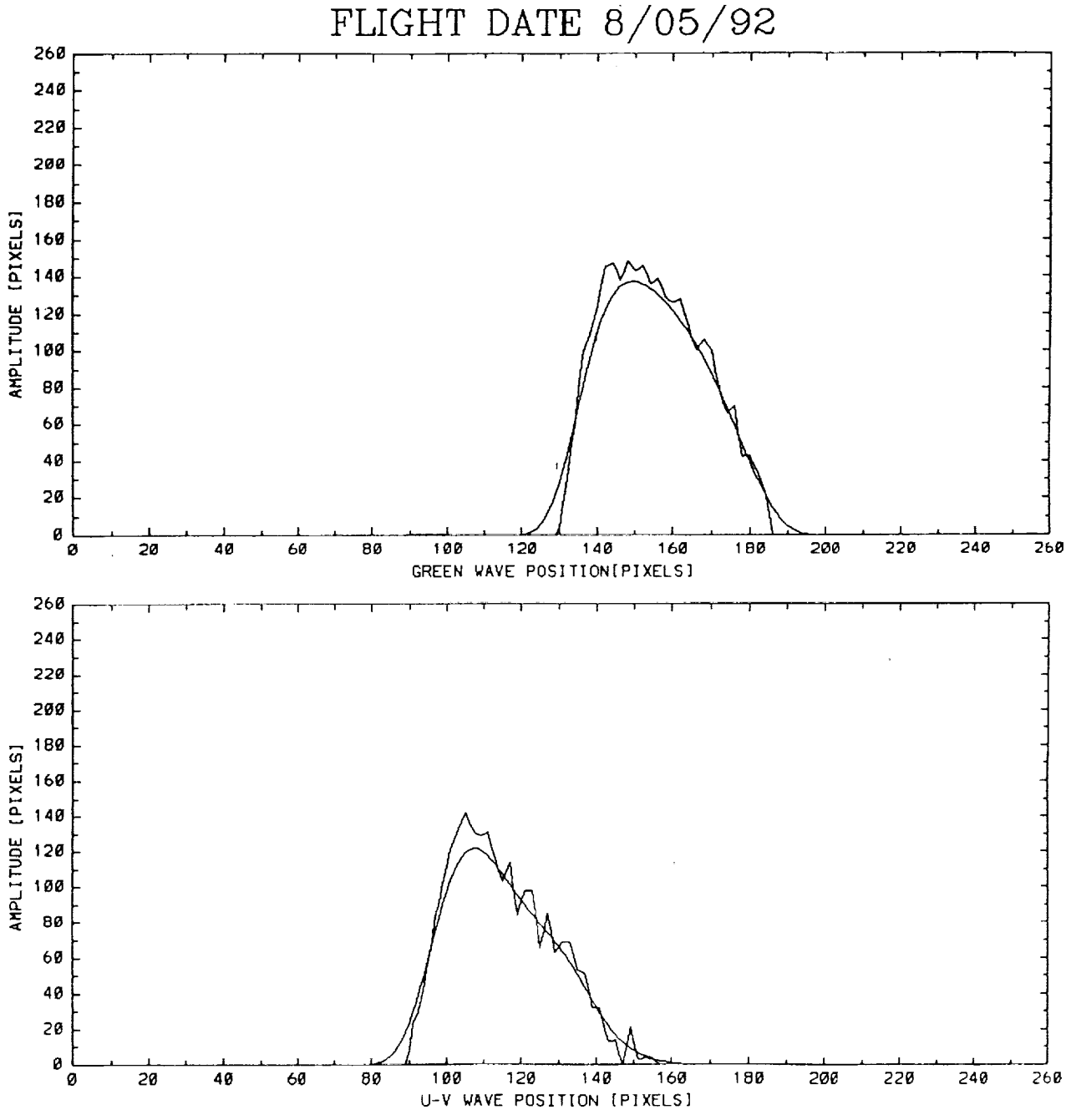

Figure 8. Two color waveform pair recorded by Hammamatsu model C1370 Streak Camera. Each waveform is shown in both raw and smoothed form. The horizontal scale factor is about 4.2 ps/pixel determined by calibration. For this pulse pair, the differential delay (including the optical delay set in the 532 nm path) was 2.667 nsec.

GLRS-R 2-COLOUR RETROREFLECTOR TARGET DESIGN AND PREDICTED PERFORMANCE

Glenn LUND
Optical Department
AEROSPATIALE - Space & Defense Division
100 Boulevard du Midi
06322 CANNES LA BOCCA
FRANCE

ABSTRACT

This paper reports on the retroreflector ground-target design for the GLRS-R spaceborne dual-wavelength laser ranging system.

The described passive design flows down from the requirements of high station autonomy, high global FOV (up to 60° zenith angle), little or no multiple pulse returns, and adequate optical cross-section for most ranging geometries. The proposed solution makes use of 5 hollow cube-corner retroreflectors of which one points to the zenith and the remaining four are inclined from the vertical at uniform azimuthal spacings.

The need for fairly large (~ 10 cm) retroreflectors is expected (within turbulence limitations) to generate quite narrow diffraction lobes, thus placing non-trivial requirements on the vectorial accuracy of velocity aberration corrections. A good compromise solution is found by appropriately spoiling just one of the retroreflector dihedral angles from 90°, thus generating two symmetrically oriented diffraction lobes in the return beam. The required spoil angles are found to have little dependance on ground target latitude.

Various link budget analyses are presented, showing the influence of such factors as point-ahead optimisation, turbulence, ranging angle, atmospheric visibility and ground-target thermal deformations.

1. BASIC GROUND TARGET REQUIREMENTS

During the various study phases investigated during the course of the GLRS project, the Ground Target (GT) requirements established to be of most significant importance were the following :

- Choice of a multiple-retroreflector, passive target concept.
- As nearly full coverage of the sky as possible, up to local zenith angles of at least 60°.
- Avoidance of ambiguous (multiple) pulse returns.
- Adequate velocity aberration correction, in keeping with the link budget requirements.
- Adequate photon budget for sub-centimetric ranging accuracies under most clear atmospheric conditions.
- Moderate cost and high reliability.

The requirement of a *passive* GT design leads to the choice of a *multiple* fixed Retroreflector (RR) concept where full sky coverage is achieved by the summation of several contributing RR FOVs.

The inherent difficulties in this approach result firstly from the *non*-uniform reflected energy diagram of a static RR, and secondly - because of the gradual fall-off of this diagram - from the requirement of inter-RR crosstalk (i.e. multiple pulse return) avoidance.

The adopted solution must therefore achieve an acceptable compromise between somewhat conflicting requirements and the need for accurate range measurements to be achieved under *most* conditions.

In the following sections the proposed GLRS-R GT design is described, and its numerically simulated performance is illustrated as a function of several important system variables.

2. BASELINE GLRS-R TARGET CONCEPT

The baseline 5-retroreflector GT design illustrated in Fig. 1 provides a good compromise between full sky coverage, minimal FOV overlap and minimal number of RRs. The individual retroreflectors have a useful diameter of 100 mm, and will need to be of hollow construction in order to minimise thermally induced wavefront deformations. Although good thermal performance is achieved (in space applications) with small solid cube-corners, there are practical limits in *size* and *temperature excursion* beyond which

the resulting refractive-index gradients will generate unacceptable wavefront distortions.

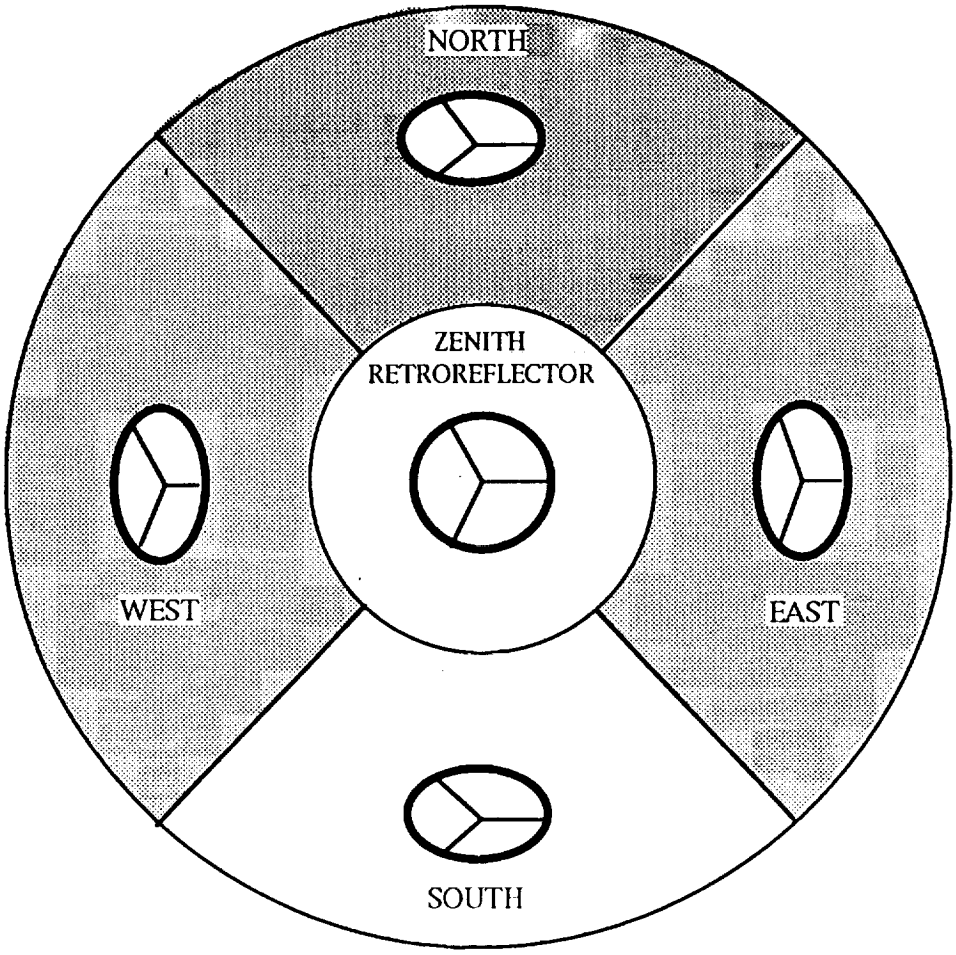

Figure 1. Proposed baseline 5 - cube corner ground-target

As shown in § 10p, thermo-mechanical effects can also lead to wavefront distortions in hollow retroreflectors, although they are expected to be an order of magnitude smaller than those induced under comparable conditions in a refractive medium. For reasons of resistance to environmental influences, the hollow reflectors will need to be covered by a protective (optical quality) window.

Preliminary thermo-mechanical analysis has shown that the GT *support structure* can be made of common materials which would give rise to reflector location stabilities of ~ 3 mm, for temperature excursions of ± 50° C (± 90° F). If required, partial correction for these excursions could probably be made using epoch and climatic data together with an appropriate thermo-mechanical model for support structure deformations.

As explained in §3 and §4, velocity aberration correction is achieved by designing the RR far-field diffraction patterns to exhibit a symmetrical *twin-lobe* structure. Each of the RRs must be oriented (about its local normal) in a particular direction with respect to the overhead spacecraft tracks, in order to achieve appropriate alignment of the reflected lobes.

Although a 45° inclination of the peripheral reflectors provides good overall FOV coverage and has been assumed in the following analyses, the choice of this value is somewhat arbitrary. Parametric analysis could reveal a more favourable inclination, depending on the criteria used to trade link budget performance at high zenith-angles against FOV overlap limitations. Variants involving more than 4 peripheral reflectors could also be considered, although they would incur an increase in the extent of FOV overlap, and higher overall GT costs.

It is assumed that the spacecraft (S/C) ranging strategy will inhibit operation for the small percentage of geometries where crosstalk effects are expected to be strong and determines, for any *allowed* ranging operation, which of the RRs must be providing the return signal. An appropriate deterministic correction then relates the measured RR range to a common GT reference point.

3. PRINCIPAL INFLUENCES IN LINK BUDGET PERFORMANCE

As shown in Fig.2, there several quite different influences which can affect the system link budget performance. Those which are considered or referred to in the present paper are listed below :

- Two-way atmospheric transmission, depending on visibility conditions, local zenith angle and GT altitude.
- Atmospheric turbulence, characterised by wavelength and the mean *long*-exposure turbulent energy ($\int C_n^2\ (h).dh$).
- Ranging geometry, as determined by local zenith angle, local RR incidence angle, satellite azimuth and range.
- Velocity aberration, depending on ranging geometry and satellite height and velocity.
- Retroreflector characteristics such as size, optical quality and dihedral angle spoiling.
- Detection techniques, which in the case of GLRS-R imply the use of a receiving telescope, transfer optics and a streak camera.

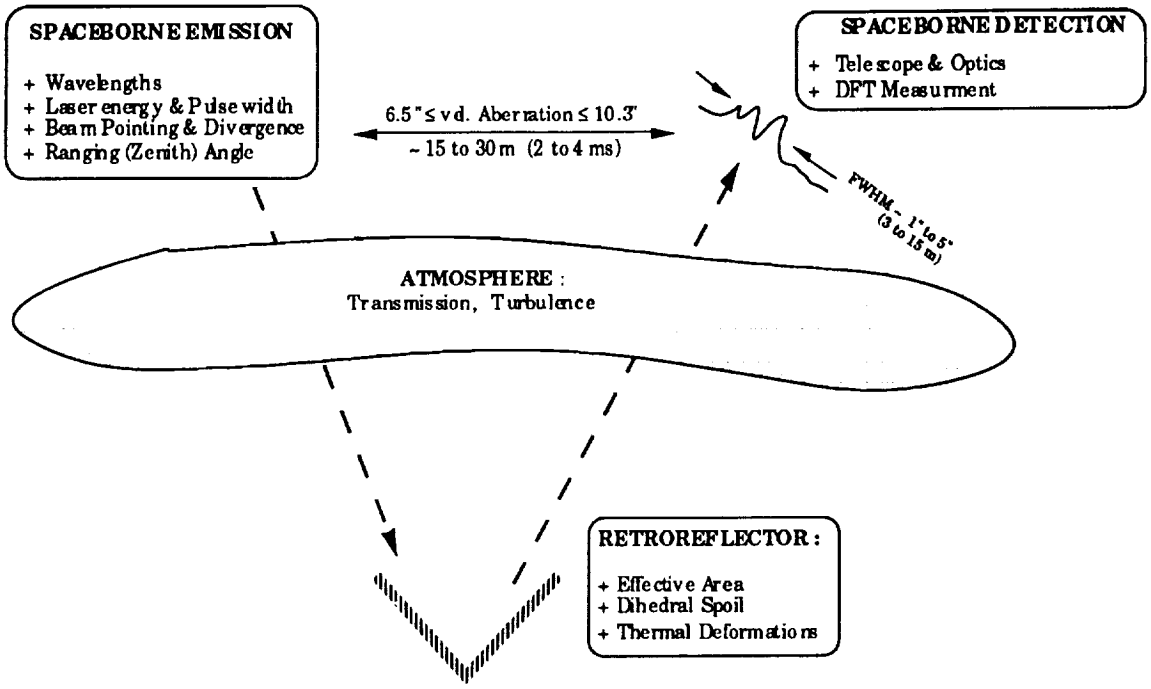

Figure 2. Factors contributing to link-budget performance

The schematic depicts an emitted (laser) beam of given wavelength, energy, pulse width and divergence which, on traversing the earth's atmosphere, is attenuated and degraded in wavefront uniformity. The RR returns the incident beam, introducing *vignetting* (defined by the intersected aperture and local incidence angle), additional *thermal* (and/or *manufacturing*) wavefront perturbations, a certain degree of *energy loss* (due to the reflectivity of the RR mirror surfaces) and a small *point-ahead* correction (by virtue of the dihedral angle spoil). The point-ahead is designed to compensate for the angular displacement of the S/C during the return propagation time of the emitted pulse. Having once *again* traversed the turbulent atmosphere, the reflected wavefront diffracts into space to form a resulting *speckle* pattern (characterised by the path-integrated turbulence strength). The mean received energy at the ranging telescope can be related to the mean *spread* of the speckle pattern and to the *pointing residual* - defined as the angular *difference* between the spacecraft and nominal reflected beam directions at the instant of pulse return.

The accuracy of the resulting range determination depends not only on the respective numbers of collected photons (at the doubled and tripled Nd:YAG wavelengths - 355 & 532 nm), but also on the implemented detection and signal processing techniques. Although these GLRS-R design features are not presented in greater detail here, they are implicitly included in the range accuracy calculations presented in § 9.

4. POINT-AHEAD CORRECTION OF VELOCITY ABERRATION

As shown in the above figure, at the GLRS-R orbit the S/C is displaced by an angular distance ranging between 6.5 and 10.3 arcseconds (equivalent to ~ 15 - 30 m) during the 2-way propagation time. The FWHM of the return beam is however, for a 100 mm RR, of the order of 1 to 5 arcseconds. The ambition of the point-ahead correction is thus to compensate as well as possible for this effect.

Fig. 3 illustrates the approach used in the GLRS-R GT concept, in order to achieve acceptable velocity aberration correction by means of a small degree of point-ahead applied to the retroreflected beams. Both diagrams are scaled in arcseconds as viewed from the RR, with the center corresponding to the direction of any given incoming beam. The central spot would thus also correspond to the required *return* beam direction if the S/C had no transverse velocty with respect to the RR.

The left-hand diagram illustrates (relative to the origin defined at the instant of pulse emission) the angular loci of the S/C at the instant of pulse *arrival* back at the S/C. The amplitude of any particular locus is commonly referred to as *velocity aberration*. The size and shape of these loci depend on the transverse (relative to the instantaneous line of sight) vectorial components of S/C velocity, within the foreseen limits of ranging geometry. The presence of two loci subsets results from the approximately opposite directions in which the S/C can move, as observed from the ground (i.e for *ascending* or *descending* tracks). These regions change and increase in size at increasing GT latitudes, in accordance with the wider range of directions of apparent S/C trajectory.

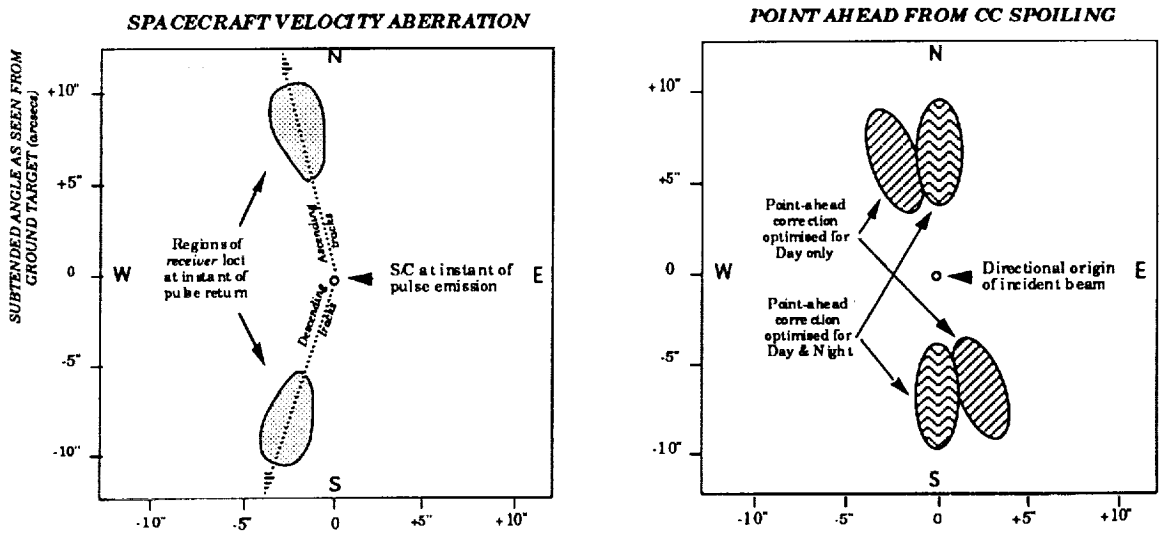

Figure 3. Point-ahead correction of velocity aberration.

The right-hand diagram illustrates how the RR point-ahead "attempts" to compensate for velocity aberration, by generating two return beams, offset in equal and opposite directions with respect to the incoming beam. The wavefront fold is achieved by what is commonly referred to as "dihedral angle spoiling", whereby one (or more) of the 3 RR dihedral angles is offset from the nominal value of 90.000°. Spoiling of a single angle leads to 2 reflected beams, whereas uniform spoiling of all 3 angles will (as is the case for most geodetic satellite reflectors) generate 6 evenly distributed return beams. The exact shape of the retroreflected directional loci is a geometrical consequence of the local incidence angles of the incoming beam with respect to the cube-corner retroreflector and to the orientation of its spoiled dihedral angle(s). The inclination of the two loci shown here can be modified in order to optimise the return signal strength during either *day* (ascending) or *night* (descending) S/C tracks. An alternative solution, as illustrated in Fig.3, would be to incline the RR so as to achieve a compromise compensation for both day and night tracks.

The degree to which velocity aberration is adequately compensated for, at a given ranging geometry, is referred to here as the beam *pointing residual*. It is expressed, in arcseconds, as the difference between the *required* (velocity aberration) direction and the *applied* (point-ahead) direction. In general, the smaller the domain of ranging geometries for which the RR point-ahead compensation is designed, the smaller the mean value of pointing residual.

Other factors influencing this mean performance are local RR incidence angle and orientation, GT lattitude, and the choice between day (or night)-only and day+night E/R track compensation.

5. GLRS-R GROUND TARGET OPTIMISATION AND PERFORMANCE

In the following link budget analyses, the GT performance is expressed in terms of *cross-section* profiles, which are derived take into account the appropriately computed *pointing residuals*. Although other performance criteria could have been chosen, these tend to be more difficult to characterise with a single curve, as they can depend on extrinsic influences such as turbulence and wavelength.

Fig. 4 illustrates, for the required GLRS ranging geometries, the variation in optimal values of dihedral spoil angle as a function of GT latitude and RR orientation. The optimisation process is designed to determine (for a given GT, S/C and latitude characteristics) the dihedral spoil which minimises the quadratic sum of pointing residuals.

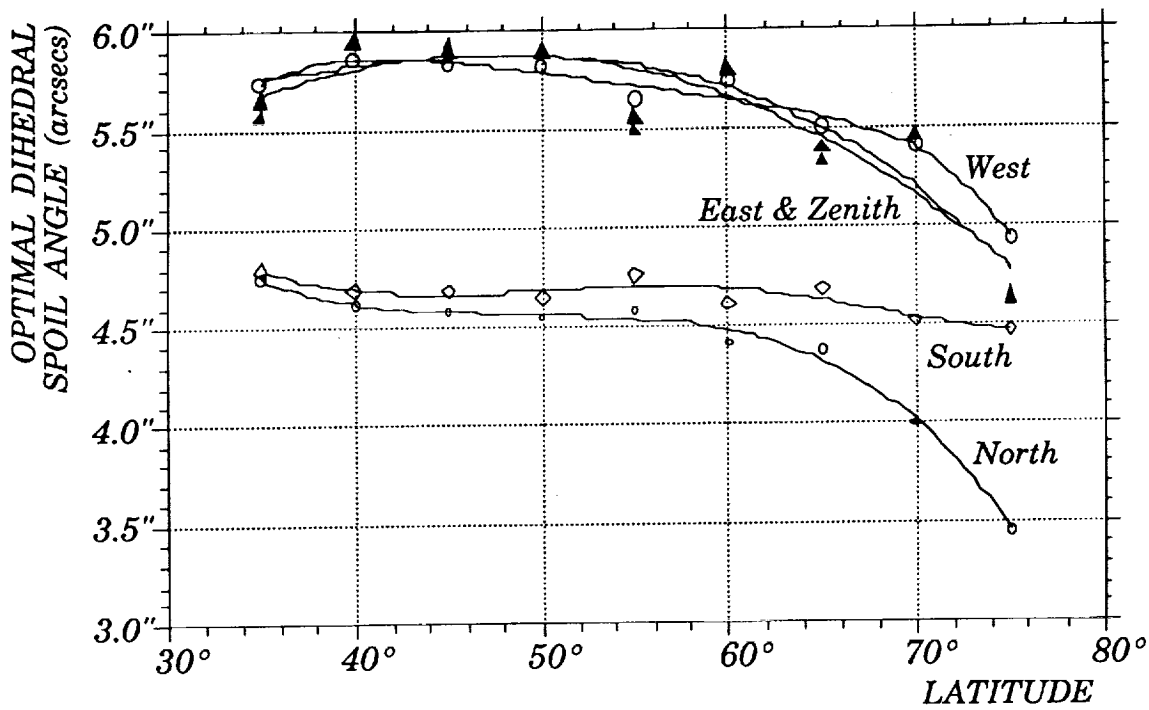

Figure 4. Optimal dihedral angle spoil as a function of latitude.

The curves shown here correspond to the nominal GLRS orbit and to a day/night optimisation of the pointing residuals. The following two figures illustrate the expected GT performance at a GT latitude of 35°, in terms of optical *cross-section*. The choice of this quantity is partly due to its similarity to the familiar notion of radar cross-section, and partly to its physical significance; the RR cross-section can be thought of as the equivalent surface area of a perfectly white (albedo = 1) Lambertian diffuser. Such a diffuser, if exposed to a uniform illumination equal in intensity to that intersected by its equivalent retroreflector, would give rise to the same far-field luminous flux as that produced by the retroreflector in the considered point-ahead direction. For a perfect RR, on-axis and in the absence of turbulence, the theoretical cross-section can be shown (for a 2-lobe diffraction pattern) to be :

$$\zeta = (\pi^3/16).(\phi^4/\lambda^2) \sim 1500.\ 10^6\ m^2$$ (~ 100 x greater than in Fig.5)

In practice, the RR is rarely ranged to directly on-axis, and atmospheric turbulence induces considerable beam-spread. A certain degree of spreading is in fact desireable since the retroreflected beam would otherwise be extremely narrow (~1 arcsec in the above example), with a consequently dramatic fall-off in received energy at pointing residuals beyond about 2 arcsecs.

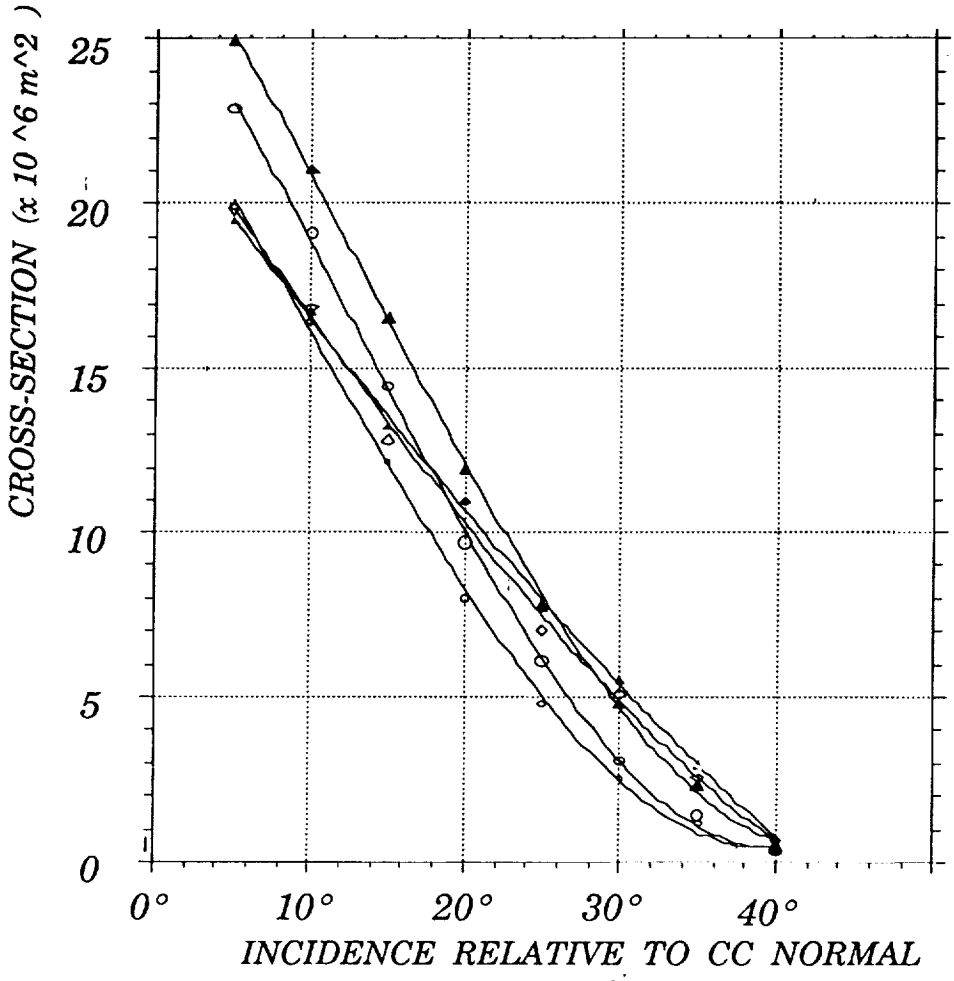

Figure 5. Mean cross-section profiles vs. local incidence angle

The variation of cross-section profile, as shown here, is given as a function of local incidence angle and CC orientation, for a "moderate" degree of turbulence (see also § 7) and at λ = 532 nm. The disparities in cross-section profile, from one RR orientation to another, can be largely explained by differences in the range of velocity aberration vectors to be corrected for within each individual FOV.

For most purposes, the fall-off in CC cross-section with increasing incidence angle can be adequately approximated by a straight line with 40° zero-crossing. This fall-off is nevertheless a factor of considerable importance when considering the global GT performance; the most probable CC incidence angle is that of least mean cross-section.

6. THE CHOICE BETWEEN DAY AND NIGHT TRACK OPTIMISATION

In the GT design process, the choice can be made between a preference for ranging during one only (Day/Night) or both (Day and Night) of the S/C tracks (see also Fig. 3). The corresponding point-ahead corrections are then computed to provide the least overall pointing residuals.

In Fig. 6 the expected mean variations of RR cross-section are traced for the above 2 cases, and for the unfavourable case of ranging at *night* (*day*) to a *day* (*night*) -optimised GT. It can be seen that the latter case gives rise to a considerable degradation in mean cross-section. Alternatively, a good compromise can be achieved between day and night optimisations, as shown by the curve with full triangles. Such an approach has the advantage that it does not restrict the ranging opportunities to just half of the S/C overhead tracks.

It could also be argued that night-time turbulence is in general much lower than that encountered under hot daytime conditions, thus compensating for the potential disadvantage of ranging at night to a *day*-optimised GT.

For any given GT location, the choice of track optimisation could forseeably be made, in accordance with an amalgum of site-specific parameters, so as to enhance the global probability of accurate range measurements.

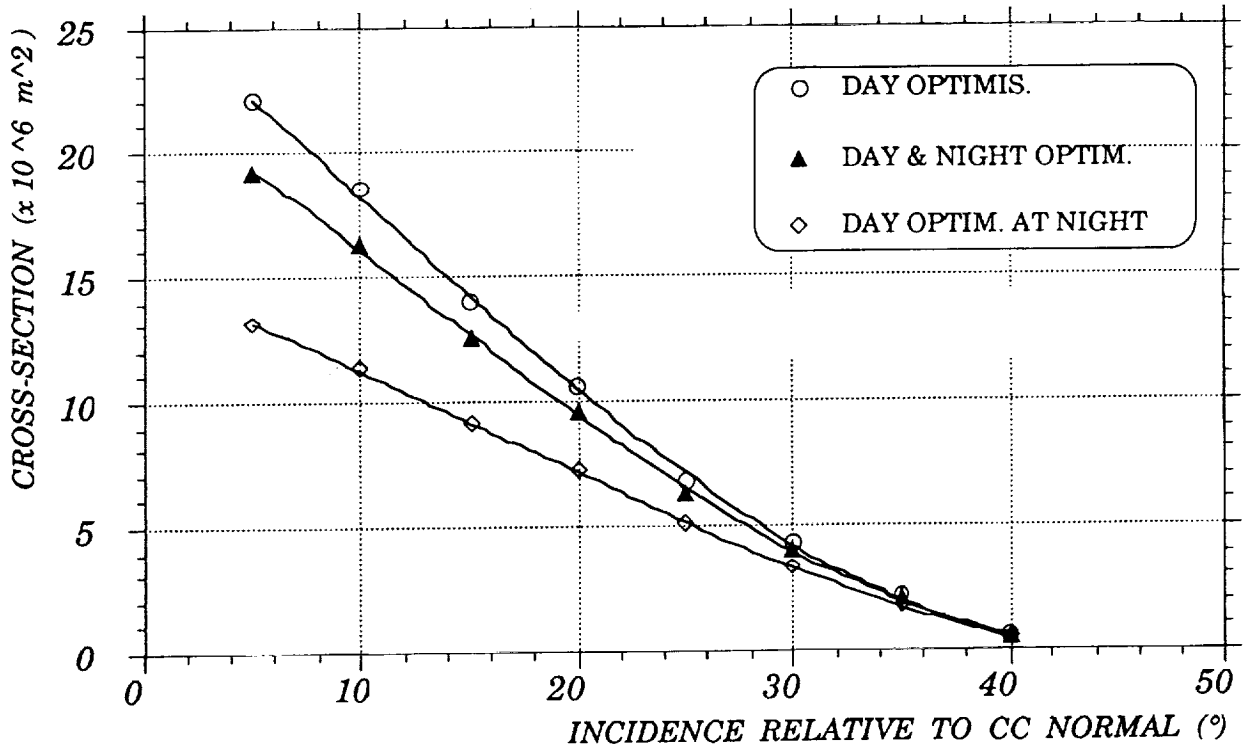

Figure 6. Mean peripheral retroreflector cross-section vs. track optimisation.

7. INFLUENCE OF ATMOSPHERIC TURBULENCE ON GT PERFORMANCE

The role of turbulence in the GLRS-R link budget performance is of considerable importance, as it can introduce strong changes to the overall system performance.

In Fig. 7, the expected mean peripheral cross-section profiles are traced for 3 values of atmospheric turbulence strength, considered to represent (respectively) low, moderate and high levels of turbulence; 10, 50 & 100 x 10^{-13} $m^{1/3}$. Good night-time conditions might correspond to the "low" level, whereas high temperature daytime conditions could generate even worse turbulence than that assumed under "high" conditions.

The unit of turbulence strength used here is that of refractive index structure (or turbulent energy) integral :

$$\int C_n^2 \, (h) \, . \, dh \quad (m^{1/3})$$

The choice of this quantity, rather than Fried's parameter r_o or *Seeing*, has been made because of its independance from wavelength. Table 1 provides conversions between these units, for a few selected values of extreme and typical turbulence integral.

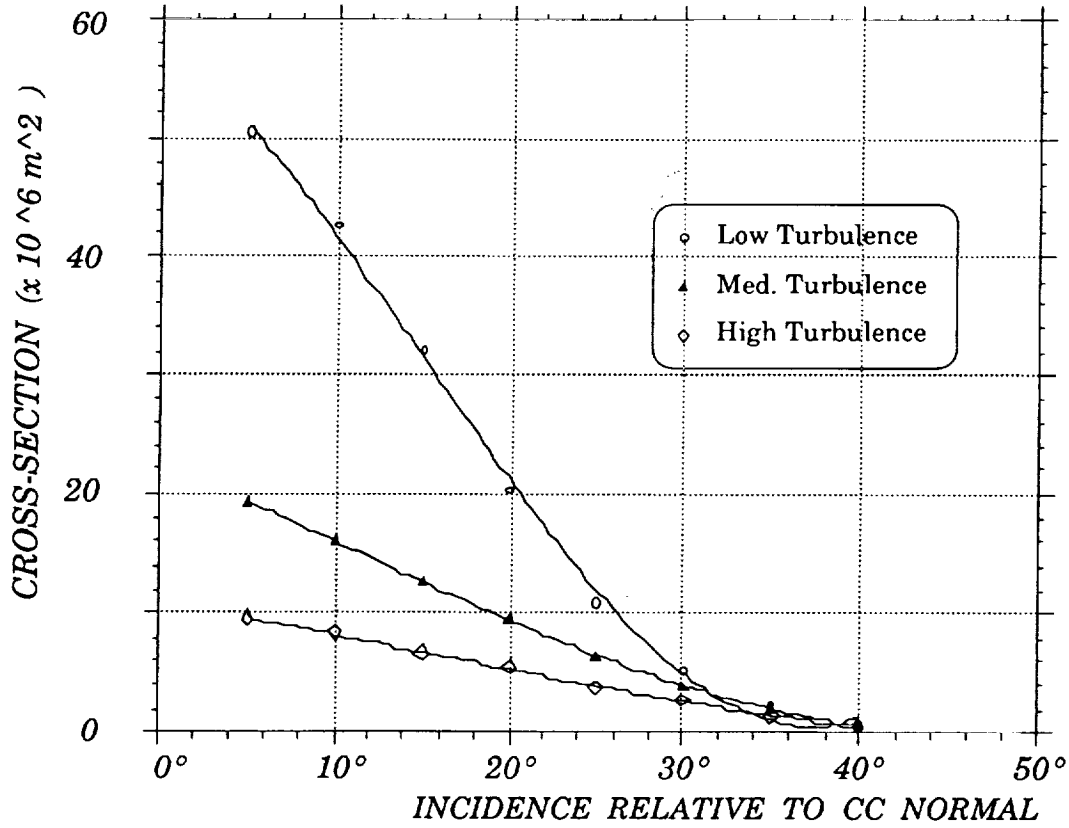

Figure 7. Variation of mean peripheral cross-section as a function of turbulence.

$\int C_n^2$ (h) .dh	r_o (355 nm)	r_o (532 nm)	Seeing (355nm)	Seeing (532nm)
(m 1/3)	(cm)	(cm)	(arcsec)	(arcsec)
$1. 10^{-13}$	21.	34.	0.35	0.32
$5. 10^{-13}$	8.	13.	0.92	0.85
$10. 10^{-13}$	5.3	8.6	1.4	1.3
$50. 10^{-13}$	2.0	3.3	3.7	3.4
$100. 10^{-13}$	1.3	2.1	5.6	5.2

TABLE 1. Fried's parameter r_0 and seeing as a function of turbulent energy integral $\int C_n^2(h)$. dh.

As can be seen in Fig. 7, strong atmospheric turbulence can give rise to a considerable drop in the overall cross-section performance of the GT retroreflectors due to overspreading of the reflected diffraction patterns.

8. CROSSTALK EFFECTS AND SYSTEMATIC BIAS

The 3D plot shown in Fig. 8 illustrates the notion of inter-RR crosstalk, expressed in terms of range measurement bias, which results from the detection of retroreflected energy originating from more than one RR.

The bias is determined at the level of the Streak Camera differential flight time measurement, where the (temporal) barycenters of the Green and UV return pulses are calculated. In the case of multiple returns, the Streak Camera detection algorithm can be confused by the presence of more than one pulse within the streak scan time-window (typically ~ 10 ns). Assuming the strongest pulse to be that of interest, the influence of a secondary echo is evaluated here in terms of the (distance) bias it would introduce into the timing determination.

The four crosstalk zones, generated by peripheral FOV overlap, correspond in fact to ranging geometries of reduced interest because of the weak return signal strength to be expected at the edge of any of the RR's local FOV (see 3 previous charts). In the bias zones corresponding to overlap between the zenith RR and any of the peripheral RRs, either one of the two following strategies would need to be applied :

1 The GLRS system ranging controller software would forbid ranging at this limited set of geometries.

2 The detection data processing would be designed to account for the deterministic bias effects, giving preference to the range determination based uniquely on the (clearly strongest) pulse returns originating from the nearest RR.

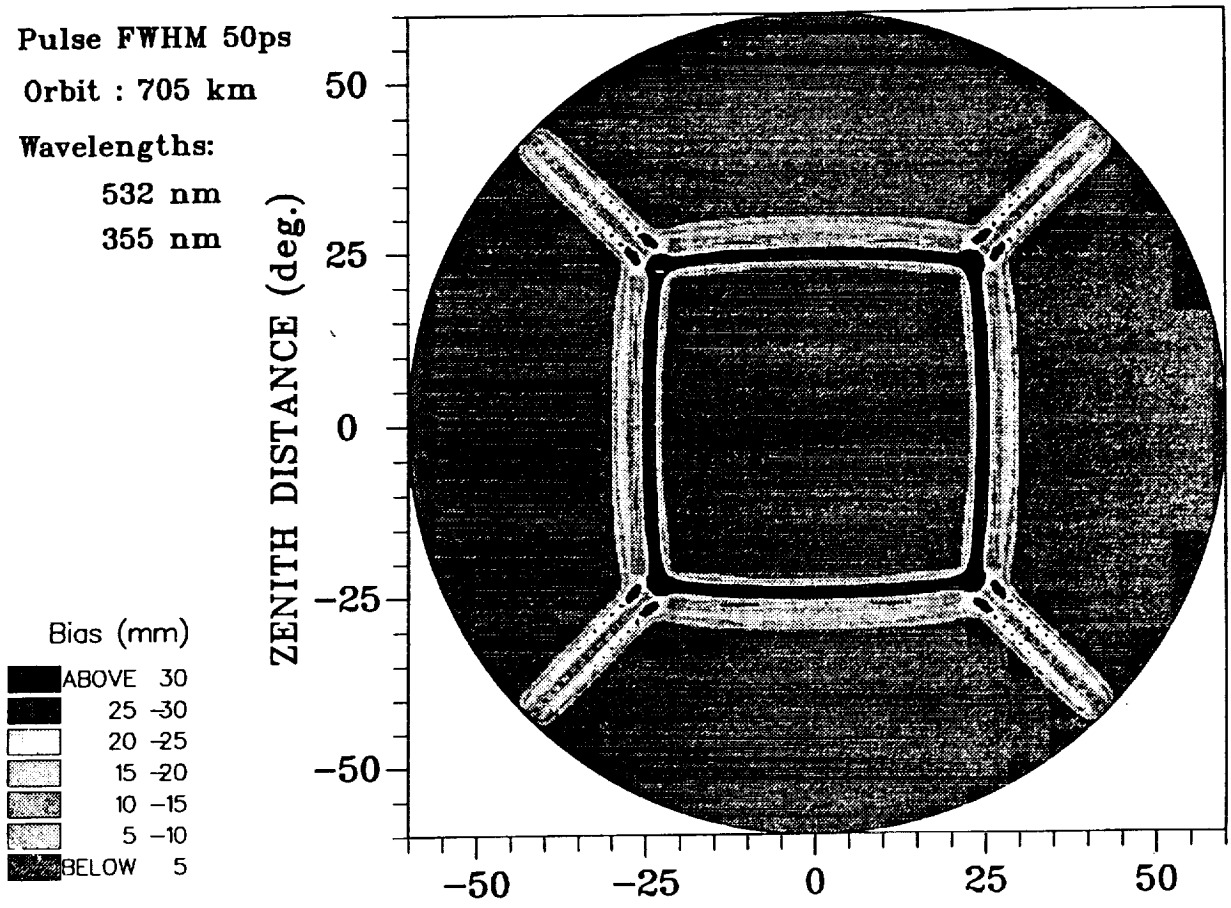

Figure 8. Systematic bias related to multiple pulse returns arising from FOV overlap.

9. LINK BUDGET CALCULATIONS AND EXPECTED RANGE ACCURACY

Although the GT performance has been expressed, in Figs. 5 - 7, in terms of cross-section, these figures need to be translated into photons in order to assess the system range measurement performance. The correspondance between these 2 quantities depends on the following factors :

- Emitted pulse wavelength, energy and beam divergence.
- Two-way atmospheric transmission at the given range angle **Z**.
- Emitter - GT - receiver range (also a function of **Z**).
- Receiving telescope diameter.
- Miscellaneous optical component efficiencies.

The curves shown in Fig. 9 express the expected numbers of received photons at the GLRS detector as a function of **Z**, at the least transmitted (355 nm) wavelength, for two values (*5km* and *23km*) of standard atmospheric visibility and selected values of cross-section. It can be seen that at high zenith angles there is a sharp drop in received energy and a widening gap between the 5 and 23 km performances.

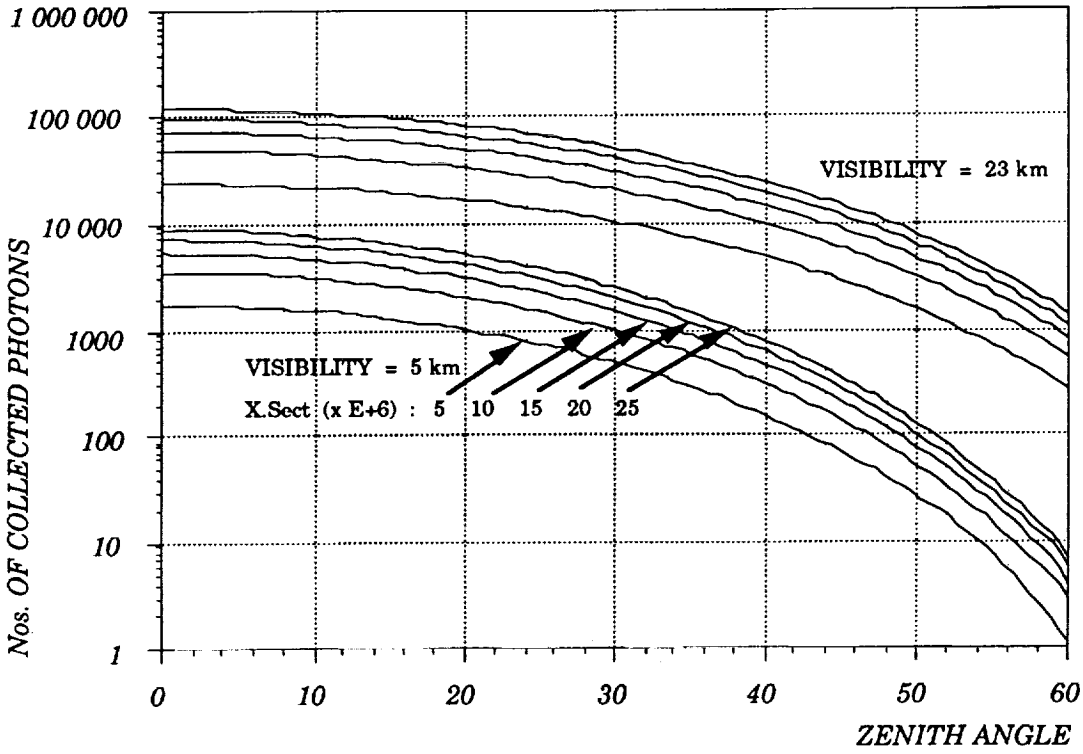

Figure 9. Received photons @ 355nm as a function of zenith angle, visibility and cross-section.

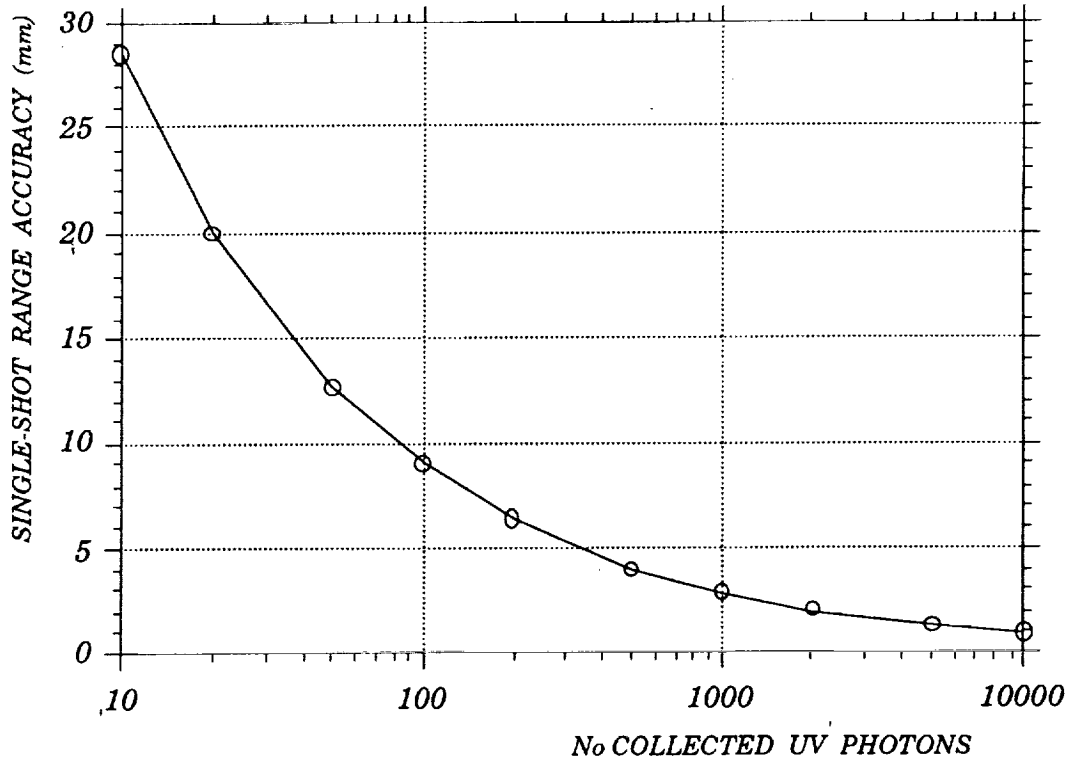

Figure 10. Range accuracy as a function of collected uv photons.

10. INFLUENCE OF THERMAL EXTREMES ON DIFFRACTION PATTERNS

In all of the preceeding analyses, atmospheric turbulence has been the only influence considered in terms of a potential source of wavefront deformation. However, thermal distortions of the RR itself, under conditions of extreme ambient temperature or midday solar illumination, could also be expected to introduce some degree of change into the retroreflected beams. These effects have been simulated firstly by running Nastran finite element simulations of the structural distortions of an assumed mechanical RR design. The resulting deformations of the reflecting surfaces were then introduced into the optical code used to generate retroreflected wavefronts and their corresponding far-field diffraction patterns.

The diffraction pattern shown in Fig. 11 has been derived from the simulated conditions of low ambient air temperature (-15°C) in the absence of solar illumination (midnight), and shows that there is indeed some spreading of the return beams. Various other simulations have also been run, and show that extreme heat can also have a detrimental effect on the retroreflected beam quality. These simulations are of course highly (thermo-mechanical) model dependant, but nevertheless show that under conditions of moderate ambient temperature (-5° to +25°C) there is no significant degradation of the diffaction lobes.

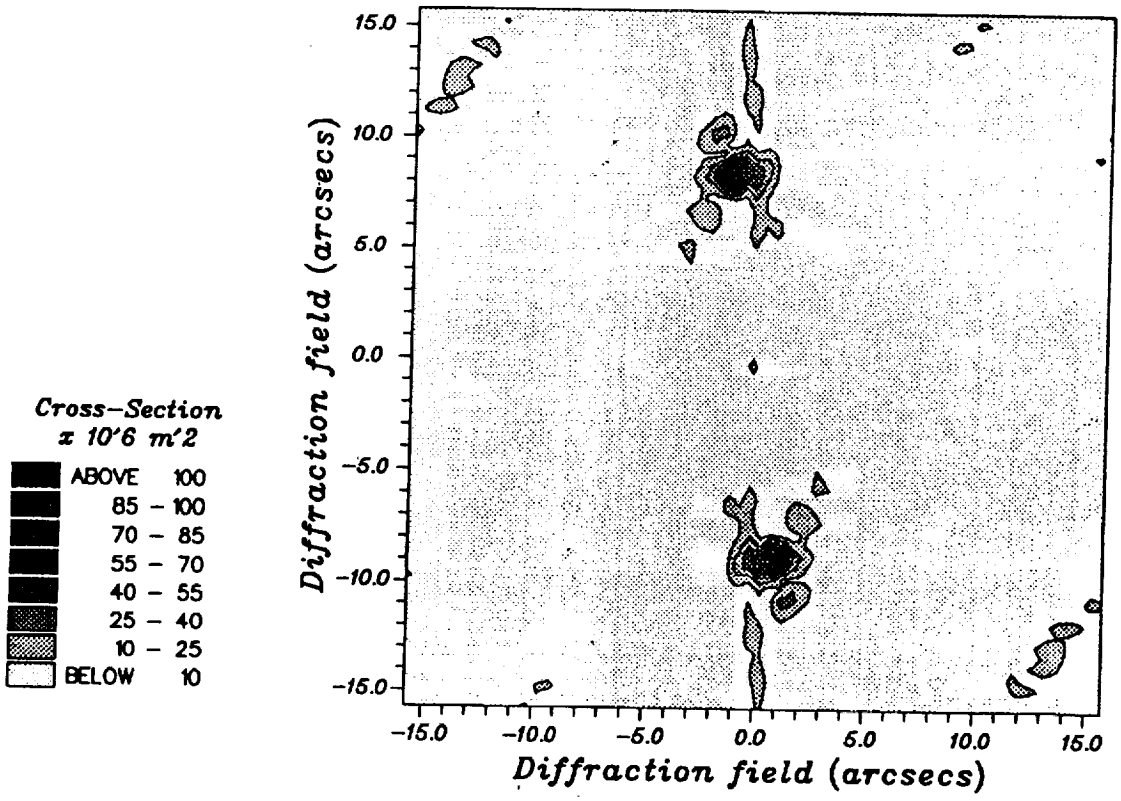

Figure 11. Simulated GLRS diffraction lobe distortion at -15°C.

11. CONCLUSIONS

The GLRS-R Ground Target design approach and analyses described in the present paper are found to satisfy the system requirements under most ranging conditions, as summarised by the following points:

- A relatively small number of retroreflectors can satisfactorily cover the observable sky up to zenith angles of 60°.
- Minimal zones of undesireable crosstalk are achieved.
- Appropriate spoiling of the retroreflectors can enable good correction of velocity aberration to be assured while maintaining high return signal strength at most rangiong geometries.
- Just 2 values of dihedral spoil angle are needed for most practical latitudes, thus leading to considerable simplification of their manufacture, assembly and testing.
- The Ground Target performance is found to have a minimal dependance on site location, for latitudes up to 65° (north or south).
- The system performance is quite strongly dependant on atmospheric turbulence.
- Thermal influences can become non-negligeable under extreme ambient temperature conditions.
- The overall link budget performance is found to be such that under typical conditions, a single-shot ranging accuracy of 1 cm or better can be expected.

Effects of Turbulence on the Geodynamic Laser Ranging System

James H. Churnside
NOAA Wave Propagation Laboratory
Boulder, Colorado 80303

1. INTRODUCTION

The Geodynamic Laser Ranging System (GLRS) is one of several instruments being developed by the National Aeronautics and Space Administration (NASA) for implementation as part of the Earth Observing System in the mid-1990s (Cohen et al., 1987; Bruno et al., 1988). It consists of a laser transmitter and receiver in space and an array of retroreflectors on the ground. The transmitter produces short (100 ps) pulses of light at two harmonics (0.532 and 0.355 μm) of the Nd:YAG laser. These propagate to a retroreflector on the ground and return. The receiver collects the reflected light and measures the round-trip transit time. Ranging from several angles accurately determines the position of the retroreflector, and changes in position caused by geophysical processes can be monitored.

The atmosphere will have several effects on the operation of the GLRS. The most obvious atmospheric factor is cloud cover. When there are clouds between the satellite and a particular retroreflector, no measurement from that reflector is possible. Fortunately, most of the geophysical processes of interest are slow enough that many cloud-free observations are expected before significant motion is observed. The next factor to consider is refraction because of the overall temperature gradient in the atmosphere. This can be corrected using the dispersion of the atmosphere, and is the reason for using two colors of light (Querzola, 1979; Abshire, 1980; Abshire and Gardner, 1985).

The final atmospheric factor to consider is refractive turbulence. This is a random phase perturbation of the optical field as it propagates through a random field of refractive index inhomogeneities in the atmosphere. Possible effects on the optical field include a random time delay, pulse spreading, beam wander, beam spreading, and irradiance fluctuations or scintillation. Gardner (1976) and Abshire and Gardner (1985) calculated the amount of random time delay and found it to be negligible for the GLRS configuration. The pulse spreading has also been calculated (Muchmore and Wheelan, 1951; Bramley, 1968; Brookner, 1969; Brookner, 1970) and is also negligible ($<<$ 1 ps) for the GLRS case. The other effects are considered in this report.

2. TURBULENCE CHARACTERISTICS

At optical frequencies, the refractive index of air can be approximated by

$$n = 1 + 7.76 \times 10^{-7}(1 + 7.52 \times 10^{-3}\lambda^{-2})P/T, \quad (1)$$

where P is the atmospheric pressure in millibars, T is the temperature in Kelvins, and λ is the wavelength of light in micrometers. Thus, small changes in temperature cause small changes in the refractive index. Small changes in temperature exist in the atmosphere because of turbulent mixing of air parcels.

Refractive turbulence in the atmosphere can be characterized by three parameters. The outer scale, L_0, is the length of the largest scales of turbulent eddies. The inner scale, l_0, is the length of the smallest scales. For separations greater than the inner scale and less than the outer scale, the structure function of refractive index is given by

$$D_n(\rho) = C_n^2 \rho^{2/3}, \quad (2)$$

where ρ is the separation of two observation points at positions p and $p + \rho$, and the structure function is defined by

$$D_n(\rho) = \langle [n(p) - n(p + \rho)]^2 \rangle . \quad (3)$$

This implies that C_n^2 is a measure of the strength of refractive turbulence.

In the lowest few hundred meters of the atmosphere, turbulence is generated by radiative heating and cooling of the ground. During the day, solar heating of the ground drives convective plumes. Refractive turbulence is generated when these warm plumes mix with the cooler air surrounding them. At night, the ground is cooled by radiation and winds mix the cooler air near the ground with warmer air higher up. Periods of extremely low turbulence exists at dawn and dusk when no temperature gradient exists in the lower atmosphere. Turbulence levels are also very low when the sky is overcast and solar heating and radiative cooling rates are low.

Values of turbulence strength near the ground vary widely. Lawrence et al. (1970) measured values from less than 10^{-16} to greater than 10^{-12} $m^{-2/3}$ at a height of about 2 m. These values are typical of what we see at this height. At 2.5 m, Kallistratova and Timanovskiy (1971) measured values from less than 10^{-17} to almost 10^{-13} $m^{-2/3}$. Under certain conditions, the turbulence strength can be predicted from meteorological parameters and characteristics of the underlying surface (Holtslag and Van Ulden, 1983; Thiermann and Kohnle, 1988; Andreas, 1988).

Using a theory introduced by Monin and Obukhov (1954), Wyngaard et al. (1971) derived a theoretical dependence of turbulence strength on height above flat ground in the boundary layer. During periods of convection (generally clear days), C_n^2 decreases as the -4/3 power of height. At other times (night or overcast days), the power is nearly -2/3. No theory for the turbulence profile farther from the ground exists. Measurements show large variations in refractive turbulence strength. They all exhibit a sharply layered structure, where the turbulence appears in layers of the order of 100 m thick with relatively calm air in between. In some cases, these layers can be associated with orographic features; that is, the turbulence can be attributed to mountain lee waves. Generally, the turbulence decreases as height increases to a minimum value at a height of about 3-5 km. The level then increases to a maximum at about the tropopause (10 km) and decreases rapidly above the tropopause.

Based on these type of data, Hufnagel and Stanley (1964) and Hufnagel (1974) developed a model of an averaged profile of C_n^2 for altitudes of 3-20 km. It is probably the best available model for investigation of optical effects. To extend the model to local ground level, one should add the surface layer dependence (i.e., $h^{-4/3}$). To see the general dependence of C_n^2 on altitude, we plotted the average Hufnagel profile in Fig. 1. It has been extended to ground level using a $h^{-4/3}$ dependence with a value of 10^{-12} $m^{-2/3}$ at a height of 2 m. Note that this type of combination of models generally leaves a step in the profile at h = 3 km. Although this is not physical, it does not prevent the model from producing valid results in optical propagation problems.

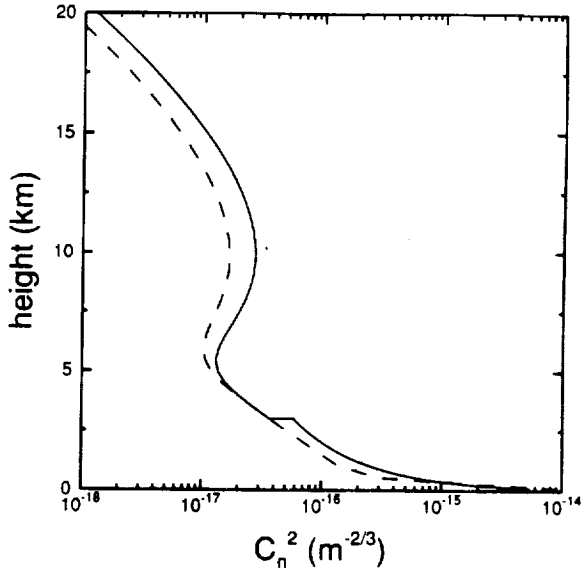

Fig. 1. Typical height profile of the refractive turbulence structure parameter C_n^2. The solid line is the Hufnagel model with a -4/3 height dependence near the ground. The dashed line is the Hufnagel-Valley model with 5-cm coherence length and 7-μrad isoplanatic patch.

Another attempt to extend the model to ground level is the Hufnagel-Valley model (Sasiela, 1988), referred to as the $HV_{5/7}$ model because it produces a coherence diameter (separation required for two receivers on the ground to observe incoherent fields from a source at zenith) r_0 of about 5 cm and an isoplanatic angle (angular separation required for two mutually coherent sources at zenith to produce mutually incoherent fields at a point on the ground) of about 7 μrad for a wavelength of 0.5 μm. It is plotted as a dashed line in Fig. 1. Although it is not as accurate at modeling turbulence near the ground, it has the advantage that the moments of turbulence profile important to propagation can be evaluated analytically (Sasiela, 1988).

Less is known about the vertical profiles of inner and outer scales. Over flat grassland in Colorado, we typically observe inner scales of 5-10 mm near the ground (1-2 m). Banakh and Mironov (1987) report calculated values of 0.5-9 mm at similar heights. Larger values (up to ~10 cm) are expected higher in the atmosphere.

Near the ground, the outer scale can be estimated using Monin-Obukhov similarity theory (Monin and Obukhov, 1954). For typical daytime conditions, the outer scale is about one-half the height above the ground. Above the boundary layer, the situation is more complex. Weinstock (1978) calculated that L_0 should be about 330 m in moderate turbulence in the stratosphere. Barat and Bertin (1984) measured outer scale values of 10-100 m in a turbulent layer using a balloon-borne instrument.

3. BEAM WANDER

The first effect to consider is the wander of an optical beam caused by refractive inhomogeneities in the atmosphere. This wander is generally characterized statistically by the variance of the angular displacement. Both the magnitude of the displacement and the component along a single axis are used. For isotropic turbulence, the variance of the magnitude is simply twice the variance of the component.

For the downlink, the beam wander variance can be written as

$$s^2 = 2.92\phi^{-1/3}H^{-7/3}\sec^{2/3}\theta\int_0^\infty dh h^2 C_n^2(h), \tag{4}$$

where ϕ is the full-angle beam divergence, θ is the zenith angle, and H is the orbital height. For the GLRS system, ϕ is about 100 μrad, H is 824 km, and θ is between 0° and 70°. Using the C_n^2 profile of Fig. 1 with no inner or outer scale effects, the rms beam wander at 70° is 7.7 nrad. This is much less than the beam divergence and can be neglected.

For the uplink, the beam wander variance can be approximated by

$$s^2 = 2.92 D^{-1/3} \sec\theta \int_h^\infty dh' \, C_n^2(h') , \tag{5}$$

where D is the diameter of the retroreflector and h is its height above the ground. If h is set to zero and a pure power law dependence of C_n^2 on height is used, the integral does not converge. The simplest solution to this mathematical problem is to assume that the retroreflector is at some height above zero.

For the GLRS system, we will assume a 10-cm-diameter retroreflector at a height of 1 m. For a C_n^2 value of 10^{-12} $m^{-2/3}$ at a height of 2 m and a -4/3 dependence, the beam wander varies from 6.8 μrad at a zenith angle of 0° to 11.6 μrad at a zenith angle of 70°. The diffraction angle for this size reflector is about 13 μrad for the green wavelength and about 8.7 μrad for the ultraviolet wavelength, so the uplink beam wander can be a significant fraction of the beam size.

Since the wander from the uplink alone cannot be neglected under the strongest turbulence conditions, it is necessary to consider the effects of the correlation between the turbulence on the downlink with that on the uplink. Although the beam wander on the downlink can be neglected, there is also an angular deviation or tilt across the retroreflector induced by the downlink turbulence. This would result in a wander component at the receiver. However, the beam is reversed by the retroreflector and then propagates back through the atmosphere. If the propagation were through the exact same portion of the atmosphere, the tilt from the downlink would exactly cancel the wander induced on the uplink and there would be no wander. If the two propagation paths are not identical, only partial cancellation is obtained (Churnside, 1989). In the case of the GLRS, the two paths are slightly different because of the motion of the satellite during the propagation of the pulse. The retroreflector is not a true retroreflector, but has been designed to accomodate this path separation. This case has not been treated in the literature.

The derivation can be done using a geometric optics analysis following Churnside and Lataitis (1987, 1990) and Churnside (1989). For small values of α, the angle between the incident and reflected beams, the wander variance can be expanded in a Taylor series in α. For a circular orbit of 824 km, the orbital period is about 100 min and the orbital velocity is 7.44 km s^{-1}. The round trip time of a light pulse is 5.49 ms at zenith and increases to 16.1 ms at a zenith angle of 70°. The beam separation angle varies from 49.6 μrad at zenith to 27.5 μrad at 70°. We calculated the rms beam wander for a 10-cm retroreflector using the high turbulence profile (solid line) of Fig. 1. The result was less than 1 μrad at any zenith angle and beam wander effects can be neglected.

4. BEAM SPREADING

The next effect to consider is the turbulence-induced spread of an optical beam as it propagates through the atmosphere. Here we are talking about the short-term beam spread, which does not include the effects of beam wander. The primary effect of beam spreading is to spread the average energy over a larger area. Thus, the average value of the on-axis irradiance is reduced and the average value of the irradiance at large angles is increased. Since beam spreading is a statistical quantity, the amount of the spreading fluctuates in time. This aspect has not been treated in depth in the literature.

We can consider beam wander to be caused by turbulent eddies that are larger than the beam. Beam spread is caused by turbulent eddies that are smaller than the beam. There are more small eddies in the beam at any time, which implies that the beam spread at any instant is averaged over more eddies. Thus, the fluctuations of beam spread are smaller than those of beam wander. Also, the smaller eddies are advected across the beam more quickly, and changes in beam spread are faster than changes in pointing angle. The long-term beam spread is defined as the turbulence-induced beam spread observed over a long time average. It includes the effects of the slow wander of the entire beam. The short-term beam spread is defined as the beam spread observed at an instant of time. It does not include the effects of beam wander, and is approximated by the long-term beam spread with the effects of wander removed, although the two are not identical.

Yura (1973) and Tavis and Yura (1976) used the extended Huygens Fresnel principle to calculate the short-term spread of a Gaussian beam. The results are collected and summarized by Fante (1975, 1980). For ρ_0 and l_0 much less than D, the short-term beam spread is approximately given by

$$p_s = \left\{ \frac{4}{k^2 D^2} + \frac{D^2}{4L^2}\left(1 - \frac{L}{F}\right)^2 + \frac{4}{k^2 \rho_0^2}\left[1 - 0.62\left(\frac{\rho_0}{D}\right)^{1/3}\right]^{6/5} \right\}^{1/2}, \tag{6}$$

where

$$\rho_0 = \left[1.46\, k^2 \int_0^L dz \left(\frac{z}{L}\right)^{5/3} C_n^2(z)\right]^{-3/5} \tag{7}$$

If ρ_0 is much greater than D, the turbulence-induced component of beam spreading can be neglected.

Valley (1979) presents more complicated integral expressions that include inner-scale and outer-scale effects. Breaux (1978) performed numerical calculations for the case of a truncated Gaussian beam with a central obscuration. By curve fitting, he obtained the following approximation:

The high-turbulence values of coherence length may be less than the aperture diameter of the reflector. If so, the reflected beam will not be diffraction limited even before it propagates back through the atmosphere. Propagation back through the atmosphere will further spread the beam. If ρ_0 is greater than D, the effects of turbulence are small compared to diffraction effects. If ρ_0 is less than $D/2$, the beam reversal in the retroreflector will translate most points in the field by more than ρ_0. These points will then propagate back through a perturbation that is uncorrelated with the initial perturbation. Therefore, it is reasonable to consider the effects of the downlink and the uplink statistically independent. As turbulence effects get larger, this approximation gets better. We can include the effects of uplink and downlink turbulence by multiplying C_n^2 by 2 in Eq. (10).

The ratios of the round-trip, short-term beam spread to the diffraction beam spread are plotted in Fig. 2 for the high turbulence profile of Fig. 1 and a 10-cm-diameter reflector at a height of 1 m. The solid lines use the Gaussian aperture formula of Eq. (6) with D = 7.07 cm [an exp(-2) intensity diameter of 10 cm]. The dashed line is the uniform circular aperture formula of Eqs. (8) and (9) with a 10-cm aperture diameter. In the ultraviolet and at large zenith angles in the visible, D/r_0 is greater than 7.5 for this turbulence profile, and the uniform aperture formula does not apply. Where both are valid, the numbers are fairly similar after normalization by the diffraction limit.

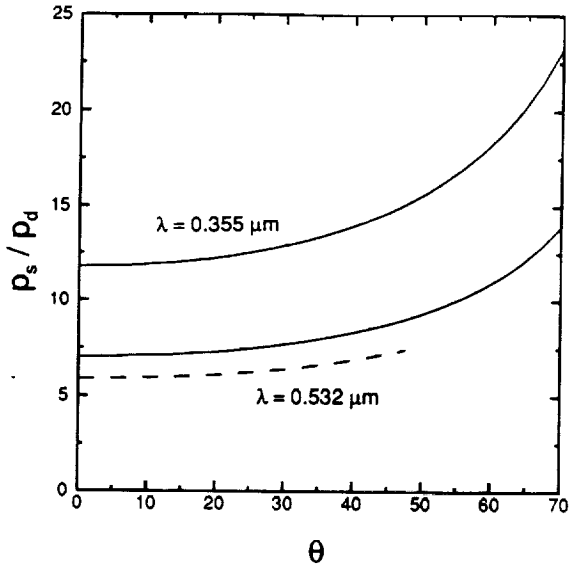

Fig. 2. Ratio of short-term beam spread to diffraction-limited value as a function of zenith angle ρ for Gaussian-aperture formula (solid line) and circular-aperture formula (dashed line).

$$p_s = \left(1 + 0.182 \frac{D^2}{r_0^2}\right)^{1/2} p_d , \tag{8}$$

where D is the effective aperture, $r_0 = 2.099\ \rho_0$, and p_d is the diffraction limited value. This expression is valid for $D/r_0 < 3$. For $3 < D/r_0 < 7.5$, the expression is

$$p_s = \left[1 + \left(\frac{D}{r_0}\right)^2 - 1.18\left(\frac{D}{r_0}\right)^{-5/3}\right]^{1/2} p_d . \tag{9}$$

These expressions agree fairly well with available data (Dowling and Livingston, 1973; Cordray et al., 1981; Searles et al., 1991) and are similar to the previous calculations.

For the GLRS downlink, the beam spread is calculated using the point source phase coherence length for propagation from the ground to the satellite. If we use the turbulence profile of Fig. 1 and a zenith angle of 70°, we estimate that the phase coherence length is about 13 m for the 532-nm wavelength and about 8 m for the 355-nm wavelength. The corresponding long-term beam spreads are 13 nrad and 14 nrad. Thus, we conclude that beam spread on the downlink can be neglected.

For the uplink, we calculate ρ_0 for propagation from space to the earth. The formula is

$$\rho_0 = \left[1.46\, k^2 \sec\theta \int_h^\infty dh'\, C_n^2(h')\right]^{-3/5} . \tag{10}$$

For the turbulence profile of Fig. 1, the coherence length for propagation from a satellite at 70° zenith angle to a height of 1 m is 4.0 mm at 355 nm and 6.6 mm at 532 nm. The formula assumes that ρ_0 is much greater than the inner scale, which may not be valid under the conditions of this example. However, these values of ρ_0 are not much less than expected l_0 values and are not expected to be too far off.

For the 532-nm wavelength at zenith, the Fried coherence length r_0 is about 26 mm using the profile from Fig. 1. Fried and Mevers (1974) used astronomical data to infer r_0 values at two sites. They found a log-normal distribution of values ranging from about 30 mm to about 350 mm. Walters et al. (1979) observed values of about 20 mm to about 300 mm, also at an astronomical site. Walters (1981) made measurements at mountain and desert sites and found a similar range of values. Thus, the turbulence profile used seems to be a reasonable high-turbulence limit.

The big difference in the numbers is in the diffraction. Equation (6) implies a diffraction limited beam spread of $\lambda/\pi D$, where D is the exp(-1) intensity diameter of the transmitter. If we convert from exp(-1) values to exp(-2) values and convert to the full angle divergence, the corresponding beam spread is $4\lambda/\pi D$. The full angle to the first minimum for a uniform aperture is $2.44\lambda/D$, which is almost twice as high. The difference is partly due to the difference in definitions of beam divergence and partly due to the fact that a Gaussian beam will be diffracted less than a uniform one. In the visible, $2.44\lambda/D$ = 13 μrad; the turbulence-induced beam spread can be six or seven times this, even at zenith. In the ultraviolet, the diffraction is less, but turbulence has more of an effect. The net result for this example is that the beam spread will be on the order of 100 μrad for both wavelengths near zenith.

We note that the beam spread depends on the 1/3 power of the height of the retroreflector above the ground under conditions of high turbulence. This implies that the irradiance in the center depends on the 2/3 power of reflector height. Thus, doubling the height will increase the average power at the center of the beam by almost 60%. This may be worth considering at sites where daytime surface turbulence is expected to be severe.

5. SCINTILLATION

The refractive index perturbations that distort the optical phase front also produce amplitude scintillations at some distance. The first cases to be considered were plane and spherical wave propagation through weak path-integrated turbulence. The weak turbulence condition requires that fluctuations of irradiance be much less than the mean value. Tatarskii (1961) used a perturbation approach to the wave equation. Lee and Harp (1969) used a more physical approach to arrive at the same results. These results are summarized in a number of good reviews (Lawrence and Strohbehn, 1970; Fante, 1975, 1980; Clifford, 1978).

For propagation from the satellite to the ground, the plane wave formula is valid. The variance of irradiance fluctuations (normalized by the mean irradiance value) is given by

$$\sigma_I^2 = \exp\left[2.24\, k^{7/6} \sec^{11/6}\theta \int_0^\infty dh h^{5/6} C_n^2(h)\right] - 1. \qquad (11)$$

For the GLRS downlink, the rms fluctuations vary from 62% for the 0.532 μm link at zenith to 308% at 70° and from 83% for the 0.355 μm link at zenith to 650% at 70°. Near zenith, these values are small enough that the weak turbulence approximation is probably not too bad. Off zenith, the available theory is much more complex. Note that the visible values are similar to measured values of stellar scintillation (Jakeman et al., 1978; Parry and Walker, 1980), as one would expect.

For the uplink, the effects of the finite beam must be considered. Kon and Tatarskii (1965) calculated the amplitude fluctuations of a collimated beam using the perturbation

technique. Schmeltzer (1967) extended these results to include focused beams. Fried and Seidman (1967), Fried (1967), and Kinoshita et al. (1968) used these results to obtain numerical values for a variety of propagation conditions. Ishimaru (1969a, 1969b, 1978) used a spectral representation to obtain similar results.

The case of interest, however, is not a collimated beam transmitted from the ground. Turbulence on the downlink adds scintillation. It also adds phase distortion at the reflector that creates additional scintillation as the beam propagates back up to the satellite. The case of a retroreflector embedded in refractive turbulence can be treated in the same weak-turbulence approximation that has been used throughout. Most work in this area has been done in the Soviet Union. An excellent review of this work is given in Banakh and Mironov (1987).

One interesting feature of the results of retroreflector calculations is that the fluctuations in the reflected light are maximum at the optical axis and decrease as the observation point moves off the axis. This effect might tend to counteract the tendency of a beam wave to have minimum fluctuations on the axis. However, these calculations are all for uniform turbulence and do not account for the propagation to the far field. They have also only been done for reflectors that are very large or very small in comparison to the Fresnel zone size.

For observation points near the center of the returned beam,

$$\sigma_I^2 = \exp\left\{8.70\, k^{7/6} L^{11/6} \int_0^1 du\, C_n^2(u)\, Re\left[4g_2^{5/6} - 4g_1^{5/6} + \frac{5}{12}\left(g_3 g_1^{-1/6} - g_3 g_2^{-1/6} + 2ig_4\left(ig_1 - ig_2\right)^{-1/6}\right)\frac{k\rho^2}{L}\right]\right\} - 1, \tag{12}$$

where

$$g_1 = \frac{1}{2}\frac{\delta u^2}{1+\delta^2}, \tag{13}$$

$$g_2 = g_1 + i\left[u(1-u) + \frac{1}{2}\frac{\delta^2 u^2}{1+\delta^2}\right], \tag{14}$$

$$g_3 = \frac{\delta^2 u^2}{(1+\delta^2)^2} - \left(1 - u + \frac{\delta^2 u}{1+\delta^2}\right)^2, \tag{15}$$

$$g_4 = \frac{1+\delta^2-u}{(1+\delta^2)^2}\,\delta u. \tag{16}$$

Representative values of σ_I^2 have been calculated using this expression. In Fig. 3, we have presented the variance as a function of the distance of the observation point from the beam axis for vertical propagation. From this figure, we see that the variance is reduced as the observation point moves off the optical axis, in agreement with previous reflected beam results. It does not increase as with the upward propagating beam case. Thus we conclude that the round-trip propagation effects must be included to properly account for turbulence in the GLRS.

Figure 3 includes values for one reflector at a height of 1 m above the ground and one at a height of 10 m. We see a significant difference at both wavelengths. In the center of the ultraviolet beam, the improvement obtained by raising the reflector is about a factor of 2 in the variance. Of course, the turbulence profile considered here is for strong daytime turbulence near the ground. At night, the improvement would be less.

In Fig. 4, we investigated the zenith angle dependence of the visible wavelength with a reflector at 1 m. At a zenith angle of about 30°, the variance begins to increase rapidly. At these scintillation levels, the weak turbulence approximation of this theory is invalid. Investigation of the scintillation at these levels must be done with a numerical simulation of the type done by Lightsey et al. (1991).

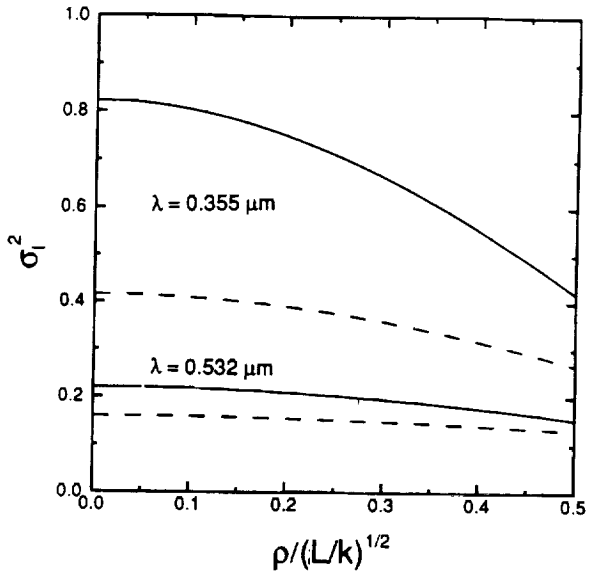

Fig. 3. Irradiance variance σ_I^2 for the GLRS geometry as a function of the distance of the observation point from the optical axis ρ divided by the Fresnel zone size $(L/k)^{1/2}$. Solid lines are for a retroreflector height of 1 m and dashed lines for a height of 10 m.

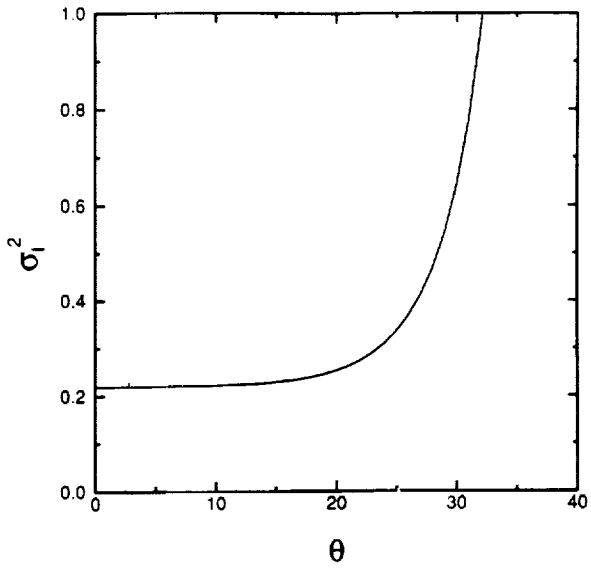

Fig. 4. Irradiance variance σ_I^2 for the GLRS geometry as a function of zenith angle θ for the visible wavelength sand a reflector height of 1 m.

6. CONCLUSIONS

The first conclusion is that the effects of beam wander can probably be neglected.

The next conclusion is that turbulence-induced beam spreading will probably be significant under conditions of high turbulence. The available theory can be used to make reasonable estimates of the magnitude of this effect.

The most significant conclusion of this report is that substantial scintillations can be expected. The round-trip propagation geometry must be taken into consideration when scintillation levels are evaluated; the uplink beam propagation calculation is qualitatively unable to predict the effect of moving the point of observation off of the optical axis. Furthermore, the weak-turbulence theories that have been developed for scintillation are not valid under the strong-turbulence conditions that can be expected at times in the GLRS system. A numerical simulation will probably be necessary to calculate values for various cases.

We recommend that a numerical simulation be performed to evaluate the scintillation for round-trip propagation to a retroreflector in the case of strong turbulence near the reflector. Following this, an experiment should be performed to verify the results. A first experiment could be done in the laboratory with a layer of artificially generated turbulence in front of the reflector. This could be followed by an aircraft experiment using atmospheric boundary layer turbulence in a configuration similar to the actual GLRS geometry.

REFERENCES

Abshire, J. B., 1980: Pulsed multiwavelength laser ranging system for measuring atmospheric delay. *Appl. Opt., 19*, 3436-3440.

Abshire, J. B., and C. S. Gardner, 1985: Atmospheric refractivity corrections in satellite laser ranging. *IEEE Trans. Geosci. Remote Sens., GE-23*, 414-425.

Andreas, E. A., 1988: Estimating C_n^2 over snow and sea ice from meteorological data. *J. Opt. Soc. Am. A, 5*, 481-494.

Banakh, V. A., and V. L. Mironov, 1987: *Lidar in a Turbulent Atmosphere*, Artech House, Boston.

Barat, J., and F. Bertin, 1984: On the contamination of stratospheric turbulence measurements by wind shear. *J. Atmos. Sci., 41*, 819-827.

Bramley, E. N., 1968: Correlation of signal fluctuations at two frequencies in propagation through an irregular medium. *Proc. IEEE, 115*, 1439.

Breaux, H. J., 1978: Correlation of extended Huygens-Fresnel turbulence calculations for a general class of tilt corrected and uncorrected laser apertures. U.S. Army Ballistic Research Laboratory Interim Memorandum Report No. 600.

Brookner, E., 1969: Limit imposed by atmospheric dispersion on the minimum laser pulse width that can be transmitted undistorted. *Proc. IEEE, 57*, 1234.

Brookner, E., 1970: Atmospheric propagation and communication model for laser wavelengths. *IEEE Trans. Comm. Tech., COM-18*, 396.

Bruno, R. C., W. W. Chapman, and P. W. Kwong, 1988: Ranging and Altimetry Link Assessment for the Geodynamic Laser Ranging System, Stanford Telecommunications, Inc. Report TR880142.

Churnside, J. H., 1989: Angle-of-arrival fluctuations of retroreflected light in the turbulent atmosphere. *J. Opt. Soc. Am. A, 6*, 275-279.

Churnside, J. H., and R. J. Lataitis, 1987: Angle-of-arrival fluctuations of a reflected beam in atmospheric turbulence. *J. Opt. Soc. Am. A, 4*, 1264-1272.

Churnside, J. H., and R. J. Lataitis, 1990: Wander of an optical beam in the turbulent atmosphere. *Appl. Opt., 29*, 926-930.

Clifford, S. F., 1978: The classical theory of wave propagation in a turbulent medium. In *Laser Beam Propagation in the Atmosphere*, J. W. Strohbehn, ed. (Springer-Verlag, New York), 9-43.

Cohen, S. C., J. J. Degnan, III, J. L. Bufton, J. B. Garvin, and J. B. Abshire, 1987: The geoscience laser altimetry/ranging system. *IEEE Trans. Geosci. Remote Sens., GE-25*, 581-591.

Cordray, D. M., S. K. Searles, S. T. Hanley, J. A. Dowling, and C. O. Gott, 1981: Experimental measurements of turbulence-induced beam spread and wander at 1.06, 3.8, and 10.6 μm. *Proc. SPIE, 305*, 273-280.

Dowling, J. A., and P. M. Livingston, 1973: Behavior of focused beams in atmospheric turbulence: Measurements and comments on the theory. *J. Opt. Soc. Am., 63*, 846-858.

Fante, R. L., 1975: Electromagnetic beam propagation in turbulent media. *Proc. IEEE, 63*, 1669-1692.

Fante, R. L., 1980: Electromagnetic beam propagation in turbulent media: An update. *Proc. IEEE, 68*, 1424-1443.

Fried, D. L., 1967: Scintillation of a ground-to-space laser illuminator. *J. Opt. Soc. Am., 57*, 980-983.

Fried, D. L., and G. E. Mevers, 1974: Evaluation of r_0 for propagation down through the atmosphere. *Appl. Opt., 13*, 2620-2622.

Fried, D. L., and J. B. Seidman, 1967: Laser-beam scintillation in the atmosphere. *J. Opt. Soc. Am., 57*, 181-185.

Gardner, C. S., 1976: Effects of random path fluctuations on the accuracy of laser ranging systems. *Appl. Opt., 15*, 2539-2545.

Holtslag, A. A. M., and A. P. Van Ulden, 1983: A simple scheme for daytime estimates of the surface fluxes from routine weather data. *J. Clim. Appl. Meteor., 22*, 517-529.

Hufnagel, R. E., 1974: Variations of atmospheric turbulence. In *Technical Digest of Topical Meeting on Optical Propagation through Turbulence* (Optical Society of America, Washington).

Hufnagel, R. E., and N. R. Stanley, 1964: Modulation transfer function associated with image transmission through turbulent media. *J. Opt. Soc. Am., 54*, 52-61.

Ishimaru, A., 1969a: Fluctuations of a beam wave propagating through a locally homogeneous medium. *Radio Sci., 4*, 295-305.

Ishimaru, A., 1969b: Fluctuations of a focused beam wave for atmospheric turbulence probing. *Proc. IEEE, 57*, 407-414.

Ishimaru, A., 1978: The beam wave case and remote sensing. In *Laser Beam Propagation in the Atmosphere,* J. W. Strohbehn, ed. (Springer-Verlag, New York), 129-170.

Jakeman, E., G. Parry, E. R. Pike, and P. N. Pusey, 1978: The twinkling of stars. *Contemp. Phys., 19*, 127-145.

Kallistratova, M. A., and D. F. Timanovskiy, 1971: The distribution of the structure constant of refractive index fluctuations in the atmospheric surface layer. *Izv., Atmos. Ocean. Phys., 7*, 46-48.

Kinoshita, Y., T. Asakura, and M. Suzuki, 1968: Fluctuation distribution of a Gaussian beam propagating through a random medium. *J. Opt. Soc. Am., 58*, 798-807.

Kon, A. I., and V. I. Tatarskii, 1965: Parameter fluctuations of a space-limited light beam in a turbulent atmosphere. *Izv. VUZ Radiofiz., 8*, 870-875.

Lawrence, R. S., and J. W. Strohbehn, 1970: A survey of clear-air propagation effects relevant to optical communications. *Proc. IEEE, 58*, 1523-1545.

Lawrence, R. S., G. R. Ochs, and S. F. Clifford, 1970: Measurements of atmospheric turbulence relevant to optical propagation. *J. Opt. Soc. Am., 60*, 826-830.

Lee, R. W., and J. C. Harp, 1969: Weak scattering in random media, with applications to remote probing. *Proc. IEEE, 57*, 375-406.

Lightsey, P. A., J. Anspach, and P. Sydney, 1991: Observations of uplink and retroreflected scintillation in the relay mirror experiment. *Proc. SPIE, 1482* (in press).

Monin, A. S., and A. M. Obukhov, 1954: Basic laws of turbulent mixing in the ground layer of the atmosphere. *Trans. Geophys. Inst. Akad. Nauk. USSR, 151*, 163-187.

Muchmore, R. B., and A. D. Wheelan, 1951: Frequency correlation of line-of-sight signal scintillations. *IEEE Trans. Antennas Propag., AP-11*, 46.

Parry, G., and J. G. Walker, 1980: Statistics of stellar scintillation. *J. Opt. Soc. Am. 70*, 1157-1159.

Querzola, B., 1979: High accuracy distance measurement by two-wavelength pulsed laser sources. *Appl. Opt., 18*, 3035-3047.

Sasiela, R. J., 1988: *A Unified Approach to Electromagnetic Wave Propagation in Turbulence and the Evaluation of Multiparameter Integrals*, Technical Report 807 (MIT Lincoln Laboratory, Lexington).

Schmeltzer, R. A., 1967: Means, variances, and covariances for laser beam propagation through a random medium. *Quart. Appl. Math., 24*, 339-354.

Searles, S. K., G. A. Hart, J. A. Dowling, and S. T. Hanley, 1991: Laser beam propagation in turbulent conditions. *Appl. Opt., 30*, 401-406.

Tatarskii, V. I., 1961: *Wave Propagation in a Turbulent Medium*, (McGraw-Hill, New York).

Tavis, M. T., and H. T. Yura, 1976: Short-term average irradiance profile of an optical beam in a turbulent medium. *Appl. Opt., 15*, 2922-2931.

Thiermann, T., and A. Kohnle, 1988: A simple model for the structure constant of temperature fluctuations in the lower atmosphere. *J. Phys. D: Appl. Phys., 21*, S37-S40.

Valley, G. C., 1979: Long- and short-term Strehl ratios for turbulence with finite inner and outer scales. *Appl. Opt., 18*, 984-987.

Walters, D. L., 1981: Atmospheric modulation transfer function for desert and mountain locations: r_0 measurements. *J. Opt. Soc. Am., 71*, 406-409.

Walters, D. L., D. L. Favier, and J. R. Hines, 1979: Vertical path atmospheric MTF measurements. *J. Opt. Soc. Am., 69*, 828-837.

Weinstock, J., 1978: Vertical turbulent diffusion in a stably stratified fluid. *J. Atmos. Sci., 35*, 1022-1027.

Wyngaard, J. C., Y. Izumi, and S. A. Collins, Jr., 1971: Behavior of the refractive-index-structure parameter near the ground. *J. Opt. Soc. Am., 61*, 1646-1650.

Yura, H. T., 1973: Short-term average optical-beam spread in a turbulent medium. *J. Opt. Soc. Am., 63*, 567-572.

Development of the Mars Observer Laser Altimeter (MOLA)

Bertrand L. Johnson, Jr. et. al.
NASA-Goddard Space Flight Center
Experimental Instrumentation Branch, Code 924
Greenbelt, Maryland 20771

The Mars Observer (MO) spacecraft payload scientific mission is to gather data on Martian global topography, gravity, weather, magnetic field and its interaction with the solar flux, surface chemistry and mineralogy over one Mars year (≈2 Earth years). In mid-1988 the need for a replacement altimeter as part of the payload complement arose. The MOLA was proposed by GSFC as an in-house effort and shortly afterward was "conditionally" accepted. Constrains on funding (fixed price cap), schedule, power and mass were imposed with periodic reviews during the instrument development to authorize continuation. MOLA was designed, tested, and delivered in less than 36 months (August '88 to July '91) and integrated with the spacecraft. During spacecraft payload testing the laser failed due to contamination in the laser cavity. In only 6 months the laser was removed, rebuilt from spare parts, retested and the instrument reassembled, realigned, requalified, and again delivered for spacecraft integration.

The spacecraft will arrive at Mars in October 1993, begin orbit insertion and reach its final 250 mile orbital altitude about 3 months later. MOLA will measure the laser pulse round-trip flight time from the spacecraft to the Martian surface, providing relative surface topography data to 1.5 meters for examining features of particular interest. Over the 2 year period a 0.2 X 0.2 degree global topographic grid of Mars will be generated with a vertical accuracy of 30 meters (mainly a function of orbit position accuracy knowledge) providing data on geophysics, geology and atmospheric circulation. By examining the return pulse through the four filter channels, surface slope will be inferred. Comparing transmitted energy with return energy will give surface reflectivity at 1.064 microns (the laser wavelength). These data will contribute to analyses of global surface mineralogy.

The transmitter is a lithium niobate Q-switched, Nd:YAG laser, pumped by a 44 bar aluminium gallium arsenide (AlGaAs) laser diode array. Pulsewidth is 7.5 nsec at 10 Hz. and 1.064 microns wavelength. At launch the measured output energy is greater than 40 millijoules. At the expected rate of degradation the output will be 30 millijoules at end of

mission, still providing sufficient link margin to meet measurement requirements. Power consumption of the laser transmitter is 14 watts, only about half of total instrument consumption. The laser was developed by McDonnell Douglas Electronic Systems Inc. of St. Louis, MO.

A 100 MHz clock is the standard by which the time interval unit measures the laser pulse round-trip flight time. The flight computer is set-up to begin ranging as soon as the instrument is powered on. Laser firing provides the range timing start pulse. The center of the laser beam is sampled optically and focused onto a fiber optic cable which carries the pulse to the PIN diode start detector. This starts the time interval unit (TIU). The clock provides timing for the laser firing as well as the TIU. Laser output energy is inferred from the start detector output.

The laser signal return from the Mars surface is received by a 50 cm. diameter beryllium telescope and focused on a silicon avalanche photo diode (40% quantum efficiency at 1.064 microns). In addition to focusing optics, the aft optics contain a bandpass filter to minimize solar background and a solar rejection filter for reducing solar input if the sun is viewed. The signal is amplified and passes through 4 low pass filters. Filter widths were selected to optimize detection probabilities for Mars footprint-scale surface slopes of 1.7, 5, 15 and 39 degrees. The flight computer continuously updates receiver channel thresholds, maximizing detection probabilities and establishing a fixed rate of false alarms.

Physically the instrument is about 2' tall and its baseplate is triangular, about 2' on a side. It weighs 28 kg. and draws 30 watts including heater power. The telescope sun shield is attached to the laser/telescope interface plate, acting as a radiator to cool the laser. Thermostatically controlled heaters are mounted to the laser for additional thermal control.

The MOLA instrument underwent full environmental testing at the Goddard Space Flight Center (thermal balance, thermal vacuum, vibration, acoustic, and EMI/EMC) as well as thermal vacuum, EMI/EMC, and acoustic testing while integrated with the spacecraft. The Mars Observer Spacecraft is scheduled for launch in Sept./Oct. 1992.

For a comprehensive description of the MOLA experiment refer to the paper by M.T. Zuber et. al., The Mars Observer Laser Altimeter Investigation, *Journal of Geophysical Research*, vol. 97, No. E5, Pages 7781-7797, May 25, 1992.

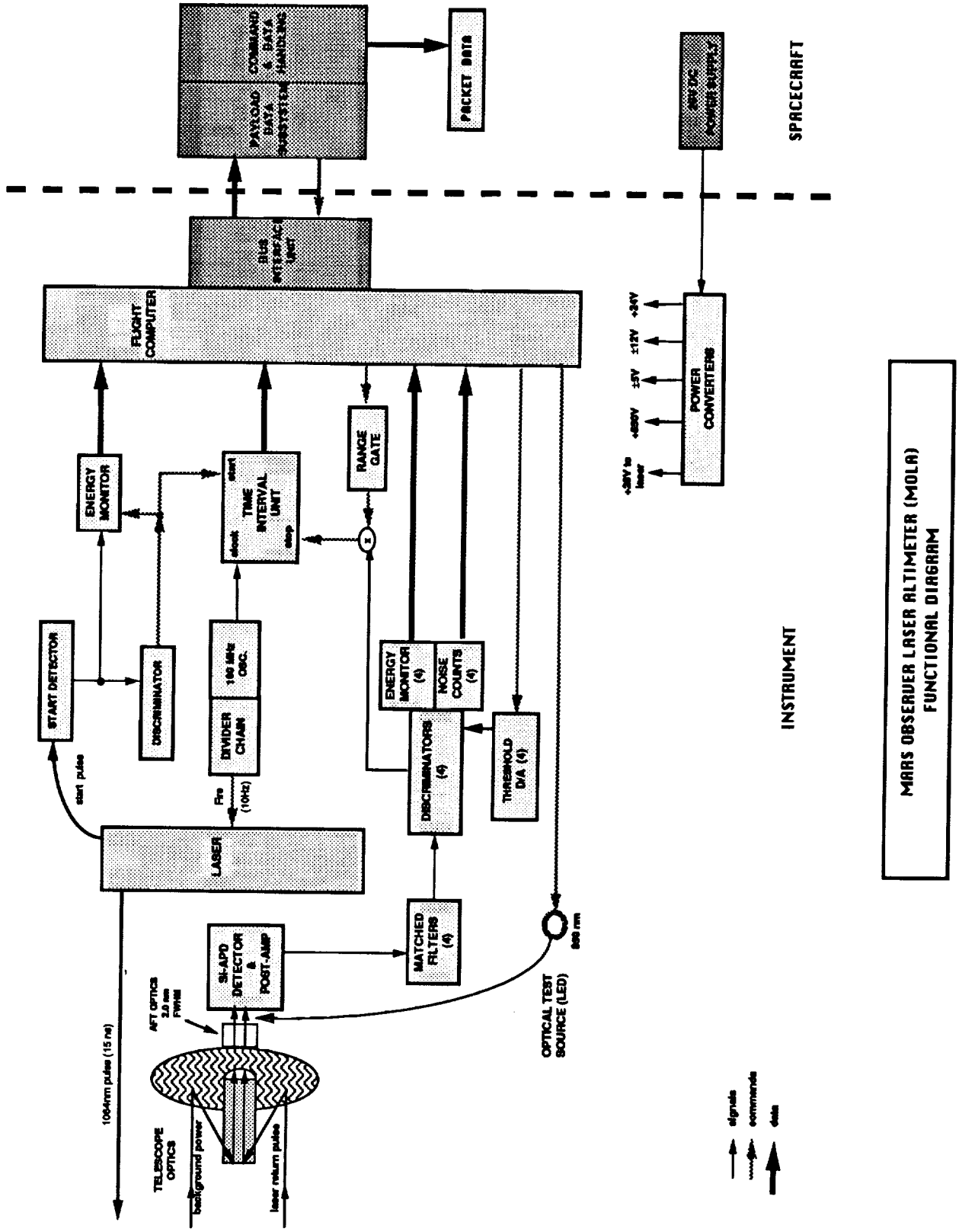
COMMAND & DATA HANDLING
PAYLOAD DATA TRANSMITTER
PACKET DATA
SPACECRAFT
BUS INTERFACE UNIT
FLIGHT COMPUTER
POWER CONVERTERS
+34V
±12V
±5V
+28V
+28V to laser
ENERGY MONITOR
TIME INTERVAL UNIT
start
clock
stop
RANGE GATE
START DETECTOR
DISCRIMINATOR
DIVIDER CHAIN
100 MHz OSC.
start pulse
Fire (10Hz)
ENERGY MONITOR (4)
NOISE COUNTS (4)
DISCRIMINATORS (4)
THRESHOLD D/A (4)
LASER
MATCHED FILTERS (4)
SI-APD DETECTOR & POST-AMP
AFT OPTICS 2.0 m FWM
TELESCOPE OPTICS
1064nm pulse (15 ns)
background power
laser return pulse
OPTICAL TEST SOURCE (LED)
800 nm
INSTRUMENT
signals
commands
data
MARS OBSERVER LASER ALTIMETER (MOLA)
FUNCTIONAL DIAGRAM

Bench Checkout Equipment for Spaceborne Laser Altimeter Systems

September 17, 1992

James C. Smith
NASA/Goddard Space Flight Center
Laboratory for Terrestrial Physics
Experimental Instrumentation Branch - Code 924
Greenbelt, MD 20771

Gregory C. Elman
Ressler Associates, Inc.
14440 Cherry Lane Court - Suite 212
Laurel, MD 20707

Kent D. Christian
Bendix Field Engineering
One Bendix Road
Columbia, MD 21045

John F. Cavanaugh
NASA/Goddard Space Flight Center
Laboratory for Terrestrial Physics
Experimental Instrumentation Branch - Code 924
Greenbelt, MD 20771

Luis Ramos-Izquierdo
NASA/Goddard Space Flight Center
Laboratory for Terrestrial Physics
Experimental Instrumentation Branch - Code 924
Greenbelt, MD 20771

Dan E. Hopf
Science Systems Applications, Inc.
5900 Princess Garden Parkway - Suite 300
Lanham, MD 20706

LIST OF FIGURES

Figure	Title
1	BCE System Block Diagram
2	BCE Target Assembly
3	ATU Functional Block Diagram
3a	ATU Optical Bench Layout
3b	ATU Optical Head Position on the Target Assembly
3c	ATU Optical Head Detail
4	LDU Functional Block Diagram
5	LDU Optical Path Layout
6	GPS Functional Block Diagram
7	BCE Controller Operation Flow Diagram
8	Data Analysis Performance Chart

ACRONYM LIST

A/D	Analog to Digital
ATU	Alitmetry Test Unit
BCE	Bench Checkout Equipment
CCD	Charge Coupled Device
D/A	Digital to Analog
DSA	Digital Signal Analyzer
EMC	Electromagnetic Compatibility
EMI	Electromagnetic Interference
GPS	Ground Power Supply
GSFC	Goddard Space Flight Center
JPL	Jet Propulsion Laboratory
LDU	Laser Diagnostics Unit
LEC	Laser External Cooler
LED	Light Emitting Diode
MB	Mega Byte
MO	Mars Observer
MOLA	Mars Observer Laser Altimeter
MOSCS	Mars Observer Spacecraft Checkout Station
MSB	Most Significant Bit
NASA	National Aeronautics and Space Administration
OTS	Optical Test Source
PC	Personal Computer
PDS	Payload Data Sub-systems
RX	Receive
S/C	Spacecraft
SCS	Spacecraft Checkout Station
Si-APD	Silicon Avalanche photo-diode
TBD	To Be Determined
TBS	To Be Specified
TIU	Time Interval Unit
T/V	Thermal Vacuum
TX	Transmit

INTRODUCTION

This paper addresses the requirements for testing and characterizing spaceborne laser altimeter systems. The Bench Checkout Equipment (BCE) system, test requirements and flow-down traceability from the instrument system's functional requirements will also be presented. Mars Observer Laser Altimeter (MOLA) and the MOLA BCE are presented here as representative of a 'typical' laser altimeter and its corresponding test system. The testing requirements of other or future laser altimeter systems may vary slightly due to the specific spacecraft interface and project requirements.

MOLA, the first solid-state interplanetary laser altimeter, was designed to be operational in Mars orbit for two Earth years (687 days). MOLA transmits a 7.5 ns pulse at a wavelength of 1.064 μm with a 0.25 mr beam divergence and a pulse repetition rate of 10 Hz. The output energy is specified at 45 mj at the beginning of mapping orbit and 30 mj at the end of one Martian year (687 Earth days). MOLA will measure the laser pulse transit time from the spacecraft to the Mars surface and return to a resolution of 1.5 meters.

BCE FUNCTIONAL REQUIREMENTS

Functional requirements of an instrument and the associated performance specifications are generated to accomplish specific scientific requirements of a project. The science team or principal investigator work closely with the system engineer to develop instrument functional requirements that will collect the necessary data to address the science requirement. These functional requirements are usually a compromise between the best instrument that can be built and what is minimally acceptable to obtain the required science data.

Typical functional requirements for a laser altimeter will address range resolution, laser energy, pointing accuracy, etc.. Verifying that an instrument meets these functional requirements becomes the Bench Checkout System (BCE) system functional requirements.

"A set of bench checkout equipment (BCE) is identified as that hardware equipment and software, if applicable, necessary for performing a complete functional checkout of a flight instrument. The BCE must be capable of simulating all functional spacecraft electrical interfaces, exercising all normal instrument operating modes, and providing a hard copy record of instrument output data in a form suitable for determining whether or not the instrument is performing consistent with the environment in which it may be operating. The BCE also includes all cables and instrument stimuli necessary for performing these functions.

The BCE will interface with the instrument primarily through those electrical connectors that normally interface with the spacecraft. The BCE may, in addition, interface with special test-access connectors located on the instrument.

The BCE also consist of stimuli (if applicable), stimuli controls, and whatever equipment is necessary for monitoring essential internal instrument functions that cannot be monitored via spacecraft telemetry when mounted on the spacecraft. The BCE also consist of all cables between the instrument and/or stimuli and the system test complex. When on the spacecraft, the BCE may

interface with the instrument directly only through special test-access connectors located on the instrument."[1]

In addition, the BCE should be capable of " ... isolating equipment (instrument) faults or malfunctions to an assembly level. Monitor and evaluate equipment performance during spacecraft systems tests."[2] The BCE should also continuously monitor Health and Welfare of the instrument during spacecraft level testing via instrument telemetry data provided by the Spacecraft Checkout Station (SCS).

Given the above project specific formal definition of the BCE , the following is a grouping of the BCE functional requirement categories. These should be addressed individually with regard to thoroughness and required complexity as separate requirements at the onset of the BCE design. These tasks must be weighed against practical considerations such as instrument schedule, budgets, and required project and spacecraft interfaces. Above all, the agreed upon BCE design and performance specifications must be consistent with the requirement to validate the instrument system functional requirements.

1) Validate the Instrument System Functional Requirements - This is the primary reason for instrument system level testing and therefore is the primary BCE system requirement.

2) Perform Instrument calibration and/or performance characterization - The level of precision and accuracy required of the BCE System performance will dictate the overall system cost and complexity.

3) Provide system interfaces during all phases of testing (EMI/EMC, T/V, S/C integration., etc.) - This mostly involves cabling, connectors and logistics of the BCE system. Particular attention must be given to interfacing with the EMI/EMC and thermal vacuum test facilities. These facilities often have very specific and unique requirements, but these interfaces are usually straight forward and can be well defined in advance.

4) Monitor instrument sub-system performance - In a situation when instrument performance severely degrades during system level testing it is extremely useful to know exactly which sub-system is malfunctioning. This knowledge will be crucial in determining the strategy for any corrective engineering efforts.

[1]Mars Observer Payload Policies and Requirements Document, JPL 642-40, Appendix C, pp. C-1
[2]Mars Observer Spacecraft General Interface Specification Document, JPL 642-SE-001, Section 4.1.a.1,2, & 3

Instrument (MOLA) Functional Requirements and BCE Testing Requirements flow-down:

The following is a representative list of how the MOLA Functional Requirements flowed-down to form the BCE Functional Requirements (i.e. Testing Requirement traceability).

I. Instrument Functional Requirement:

Maintain a laser non-operating lifetime of two years and a operational lifetime of three years. The three years operational lifetime is allocated to two years Mars orbit operation plus pre-launch testing.

Testing Requirement: Monitor the MOLA laser output energy with an integration sphere and energy meter combination. Monitor MOLA packet data and recover the Laser Start-Detector readings. Average these readings over TBD shot intervals. Record and monitor laser transmit energy to establish an output energy trend to validate an "expectation" of >30 mj laser output at end of Mars mission. In order to track total accumulated laser shots, a Laser Shot Record Book will be maintained to record all laser "on" times. To help manage and conserve laser life, each test will have a specific run-time allocation .

II. Instrument Functional Requirement:

Maintain an approximate 100 meter Mars surface laser illuminated footprint.

Testing Requirement: Monitor the far-field energy pattern of the laser output beam with a CCD camera system. Record the laser beam divergence, and energy uniformity (peak-to-average). These data and statistical readings will be taken as required.

III. Instrument Functional Requirement:

Maintain a laser firing rate of 9.9999 Hz in order to achieve a greater than 30% along-track coverage; assume nominal spacecraft orbit altitude of 380 km and orbital velocity of 3.3 km/sec..

Testing Requirement: Monitor MOLA packet data to correlate the spacecraft time and the laser fire offset interval timer with the 140 shots per packet constant rate (9.9999 Hz) to identify long or short term drifts between the expected offset constants. This data will be averaged over the total time for any given test length. Monitor the oscillator temperature data within the MOLA packet to correlate timing changes due to temperature.

IV. Instrument Functional Requirement:

Acquire range timing measurements with 10 ns resolution (1.5 m).

Testing Requirement: Provide simulated range delay pulse returns (1.064 μm) over the expected Mars orbital values corresponding to distances of 360-410 km. Provide range

delay pulse returns to simulate various Mars topographic profiles. These simulated topographies will vary in range delays between suitable for evaluating the function of the time interval unit (TIU), TIU counter transition boundaries, range gate, and acquisition/tracking software.

V. Instrument Functional Requirement:

Employ four (4) receiver channel filters matched to 20 ns, 60 ns, 180 ns, and 540 ns pulse returns which correspond to Mars terrain variations of 3 to 80 meters over the laser footprint.

Testing Requirement: Utilize a light emitting diode (LED) source and programmable pulse generator to simulate variable laser pulse width and pulse amplitude return signals. Generate a sufficient number amplitude and pulse width combinations to verify proper four channel discrimination. These LED pulse inputs will also provide a data base necessary to address the time-walk correction factors for each channel at different background thresholds and return energy levels.

VI. Instrument Functional Requirement:

Measure laser transmit and received pulse amplitudes.

Testing Requirement: Utilize a fiber optic pick-off and integration sphere combination to monitor the MOLA laser output beam pulse width and energy values. The MOLA start detector value and the BCE data will be independent measurements for correlation of laser transmit energy. The BCE pulsed 1.06 um laser source will supply variable receiver pulse amplitudes that will encompass the Mars expected conditions. The MOLA packet data will be reviewed for proper receive energy readings and correlated with the energy monitor readings within the BCE data.

VII. Instrument Functional Requirement:

Provide a 90% orbit average ranging probability - Ch#1 and Ch#2 only. Provide 50% orbit average ranging probability for Ch#3 and 10% orbit average ranging probability for Ch#4. These probabilities are valid only during non-disturbing atmospheric conditions (no dust storms, etc.).

This functional requirement encompasses a variety of hardware and software design features which require testing. Listed below are the functions which will require specific verification

A. Bore-sight alignment - maximum deviation ±100 μr

Testing Requirement: Monitor the far-field energy pattern of the laser output beam with the BCE CCD camera. Record the laser energy centroid location (bore-sight alignment stability), centroid pointing jitter, divergence, and energy uniformity (peak-to-average). These data and statistical readings will be taken on shot averages as required. Also, the Ch#1 and #2 energy readings obtained during the "zero range delay" operation mode will also be compared

with the Laser Start Detector energy reading contained in the MOLA packet data to help correlate alignment status.

The "absolute" laser-to-detector alignment verification will be performed with a set of adjustable Risley wedges and a retro-reflector corner-cube combination (BCE hardware).

B. 3 dB link margin at Mars orbit

Testing Requirement: Provide simulated expected Mars background day/night 1.06 μm power levels and associated return pulse energies using the BCE test hardware. The test hardware will provide expected Mars signal conditions (with margin). The MOLA laser , electronics box and detector assembly operating temperatures will be varied over the expected operational ranges to verify adequate link margin.

C. Maximization of detection probabilities

Testing requirement: Provide the instrument with simulated return stimulus necessary to verify proper discriminator threshold settings, range delays (360-410 km orbit altitude), range windows (+/- 10 km tracking) and validate the flight software acquisition/tracking algorithms.

Ranging profiles, background power and return pulse energies will be varied to simulate loss of signal and verify correct re-acquisition software algorithms. Also "within norm" terrain profiles, background power and expected return pulse energies will be tested to validate the normal tracking software algorithms.

MOLA Flight software algorithms and parameters will be modified via up-link commanding to verify software "patch" capabilities. Science and Maintenance Mode operations will be validated.

D. General Housekeeping Data

Testing Requirement: These data will normally be retrieved within the MOLA packet data during all MOLA "on" testing states and generally require no special testing requirements other than periodic monitoring. These data need only be verified for proper levels/contents for the given test conditions. All current, voltage and temperature monitors will be cataloged into an appropriate trend files establishing the "norms". This data will also be used to establish temperature correction factors for energy readings, time-walk corrections, timing drifts, internal optical test source (OTS) output levels, all D/A threshold levels, A/D conversions, detector responsivity, etc..

VIII. Instrument Functional Requirement:

Comply with Mars Observer Project Requirements

A. Spacecraft Interfaces - Software

Testing Requirements: The packet data will be reviewed to verify the packet format and validate proper MOLA Science and Maintenance Mode packet data contents. All MOLA commands will be sent and validated by reviewing the MOLA packet data (Science and Maintenance Modes) that the command has been properly executed. All MOLA packet status data will be validated against the expected values particular to the test conditions. All Spacecraft broadcast commands will be relayed to MOLA and packet reviewed to validate the required action or no-action was taken.

B. Spacecraft Interfaces - Electrical

Testing Requirements: The MOLA +28V power consumption will be measured to verify compliance with the power allocation as specified in the Interface Control Document (ICD). The MOLA +28V power bus transient and ripple content will be measured to verify compliance with the ICD.

C. Spacecraft Interfaces - Mechanical

Testing Requirements: The MOLA will be weighed to verify compliance with the mass allocation specified in the ICD. MOLA will also be measured to determine mass, center of gravity, and mass moment of inertia to verify compliance with the ICD.

D. Spacecraft Interfaces - Thermal

Testing Requirements: The MOLA instrument must be fully functional according to the S/C environment specified by the ICD. The MOLA cruise phase replacement and operational heaters along with the associated quad-redundant KLIXON thermostats will be tested during system level thermal testing.

TESTING OBJECTIVES

The MOLA Instrument System consist of several sub-systems. These sub-systems have certain performance specifications that need to be monitored and validated in order to ensure the instrument meets it functional requirements and in the case of the power sub-system, the spacecraft bus interface.

The following is the list in outline form of sub-systems for the MOLA instrument and the associated parameters requiring testing, validation, and characterization.

Altimetry Electronics:

I. Define acquisition and tracking performance
   A. under simulated Mars conditions
      1. wide test parameters to show performance margins past expected Mars day/night conditions
   B. limited test conditions
      1. parameters suited for collecting data to characterize corrections for range walk
      2. TX and RX pulse energy calibration

II. Define operational parameters
   A. acquisition
      1. probability of measurement
      2. probability of false alarm (miss)
   B. tracking
      1. tracking window sensitivity
   C. altimetry
      1. altimetry accuracy (timing)
      2. return pulse width discrimination
      3. time walk variations (pulse width and amplitude)
   D. reflectance measurement
      1. start/stop pulse energy readings (pulse width and amplitude)
      2. background noise counters

III. Temperature monitors - (packet data)

Computer:

I. Spacecraft commands
   A. command execution
      1. single word
      2. multi-word

II. Science and Maintenance mode commands (MOLA)
   A. command execution
      1. single word
      2. multi-word

III. Temperature monitors - (packet data)

IV. Current and Voltage monitors - (packet data)

Power Supply:

I. MOLA power usage - +28V
    A. turn on transient (250 kHz sampling)
    B. total power
        1. steady state
            a. science mode
            b. maintenance mode
    C. ripple spec
        1. steady state
            a. science mode
            b. maintenance mode

II. Temperature monitors - (packet data)

Laser:

I. Spatial characteristics
    A. divergence
    B. energy uniformity
    C. shot-to-shot jitter (pointing)

II. Pulse parameters
    A. energy
    B. width
    C. repetition rate

III. Power consumption
    A. science mode
    B. maintenance mode

IV. Temperature monitors - (packet data)

Optics:

I. Laser and receiver boresight alignment stability
    A. acceptance/verification level testing
    B. thermal vacuum testing

Thermal:

I. Allowable temperature ranges - Instrument on and off states
    A. launch and earth orbit
    B. inner and outer cruise phase
    C. anomalous spacecraft safe hold conditions
    D. transition and mapping orbits

BCE SYSTEM DESCRIPTION

BCE System Block Diagram:

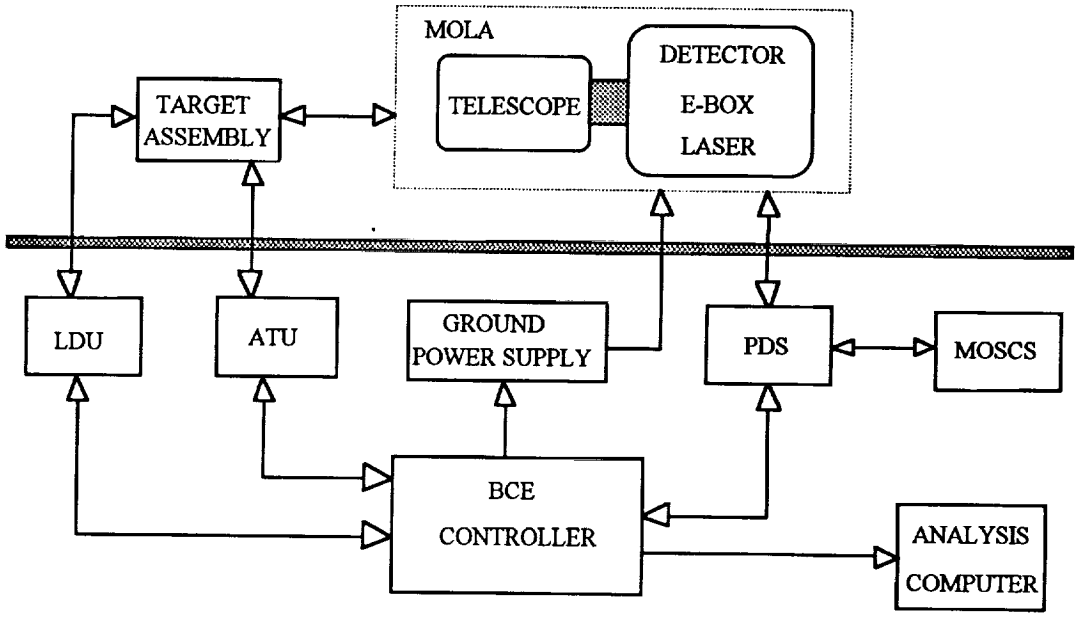

Fig. 1 (BCE System Block Diagram)

Figure #1 shows the MOLA BCE system block diagram. The central point of the BCE system is the BCE Controller which coordinates the testing stimulus provided by the BCE sub-systems and the MOLA instrument. In test configurations where power is not provided by the spacecraft, the MOLA operational power (+28V) is supplied via the Ground Power Supply (GPS). The Altimetry Test Unit (ATU) provides MOLA with simulated expected Mars background and range delay return signals. The Laser Diagnostic Unit (LDU) monitors the MOLA laser beam energy, temporal and spatial characteristics. During instrument testing the BCE controller commands and receives data from the ATU and the LDU. The Target Assembly is positioned directly over MOLA and provides the ATU and LDU optical interface to MOLA. MOLA packet telemetry data is collected and transmitted to the BCE Controller by the Payload Data Sub-system (PDS). The BCE controller commands and coordinates data exchanges to MOLA via the PDS and/or directly to the Mars Observer Spacecraft Checkout Station (MOSCS).

Target Assembly:

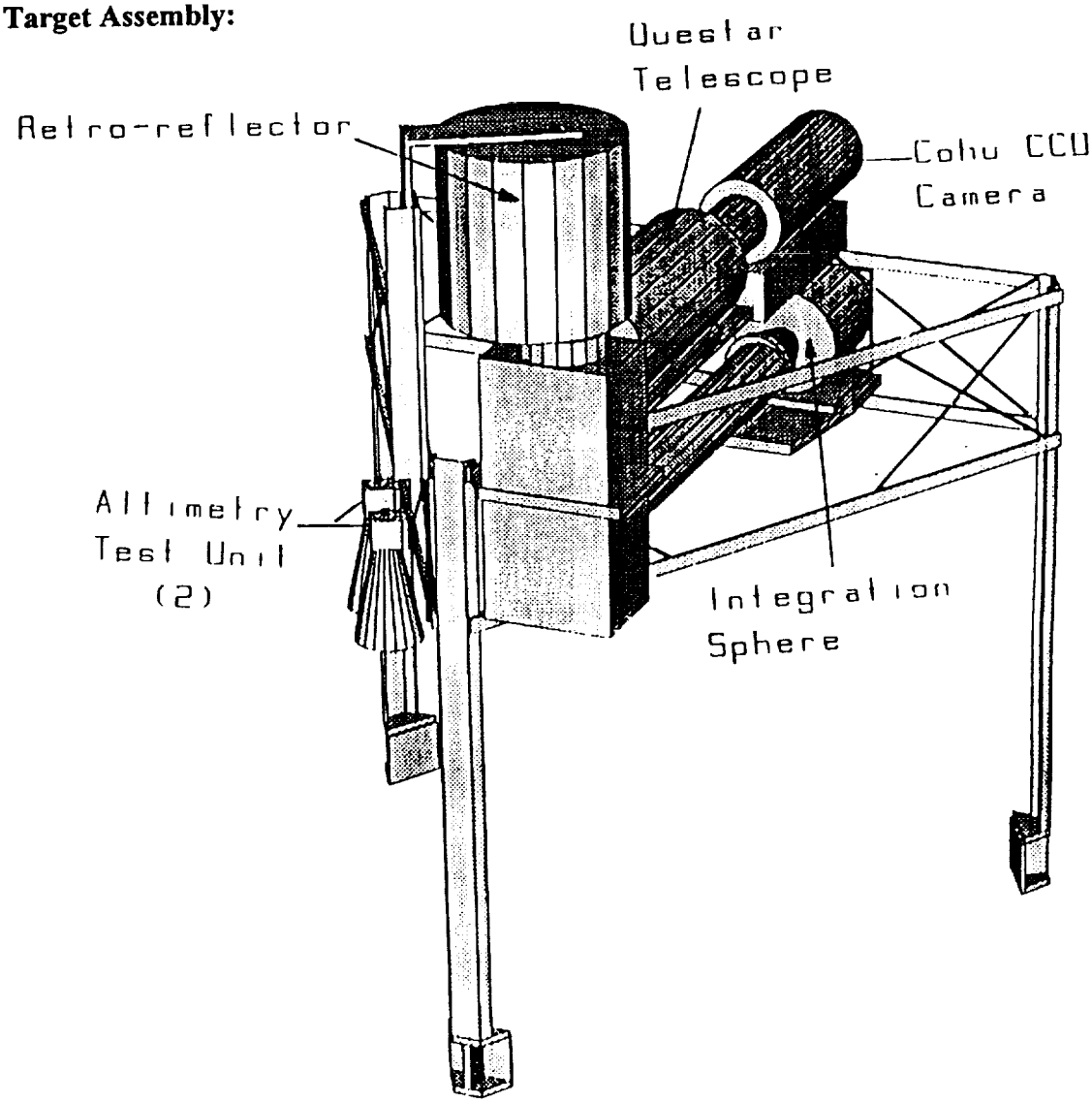

Fig. 2 (BCE Target Assembly)

The BCE Target Assembly is a mechanical test fixture (figure #2) that is mounted over the MOLA instrument and holds the ATU and LDU testing apparatus. These apparatus will be discussed in more detail under the ATU and LDU sections that follow. The three legs of the Target Assembly are designed to have a ball-and-cup mounting interface with the MOLA instrument. The MOLA instrument has three cup-like holding sockets located at the perimeter corners of the instrument base mounting plate. The ends of the Target Assembly legs are rounded to provide a ball mounting surface. This ball-and-cup mounting arrangement provide an easy and self-aligning mechanism to ensure alignment repeatability over the MOLA instrument. The Target Assembly is constructed of Invar and was designed for use within the thermal vacuum chamber over wide ambient temperature ranges (+60 °C to -30 °C). The Target Assembly also houses a combination of retro-reflector corner-cube and Risley adjustment wedges that are used to verify the MOLA laser transmitter and telescope receiver boresight alignment.

Altimetry Test Unit (ATU):

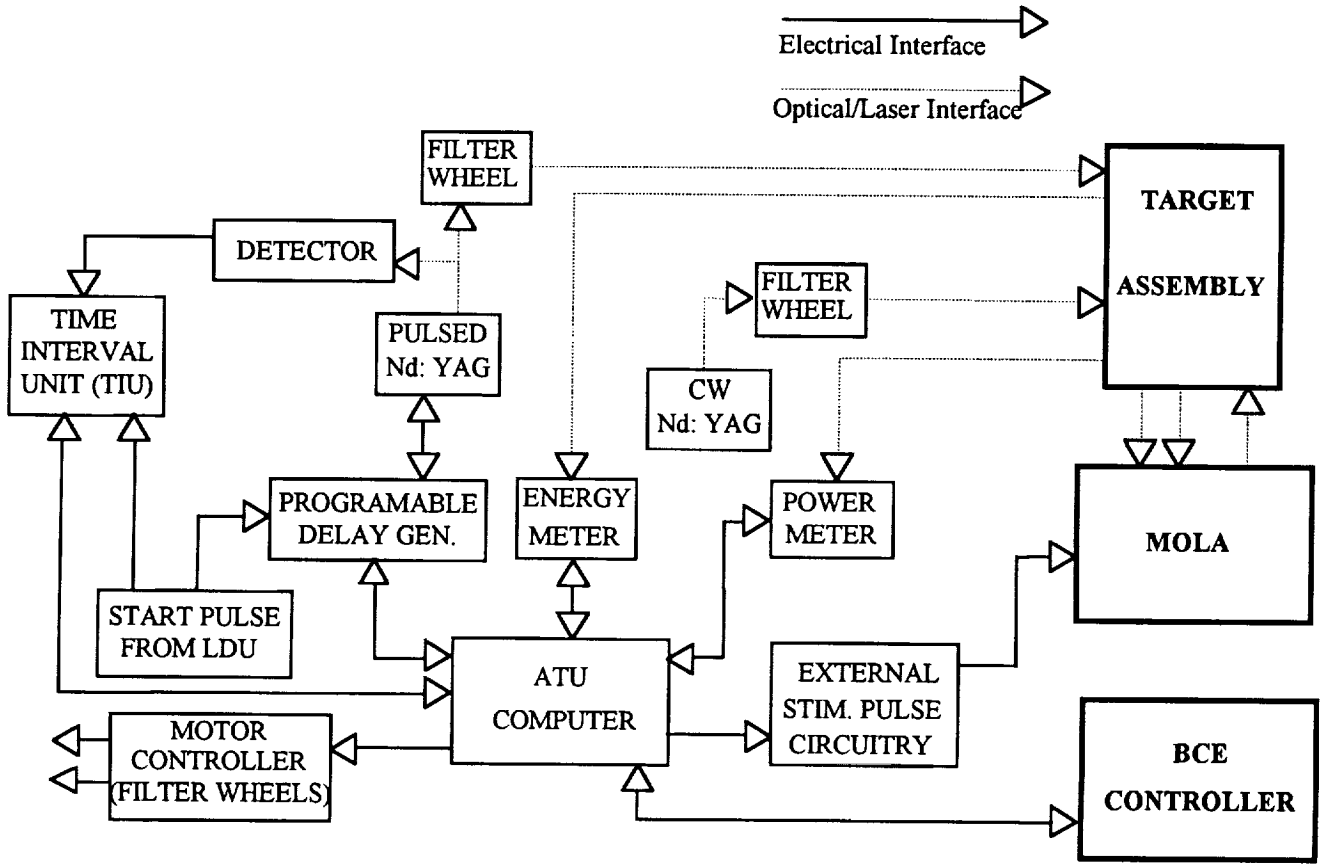

Fig. 3 (ATU Functional Block Diagram)

Figure #3 shows the ATU sub-system block diagram. As stated earlier, the primary ATU function is to provide the MOLA with simulated Martian flight conditions which include stimuli that tests the instrument's ranging electronics, range gate, discriminator thresholds, return pulse energy and background noise counters.

The ATU has three main sub-systems. The first is the background simulator, a CW laser (1.064 μm) that is directed into the MOLA telescope and simulates the reflected sunlight from the surface of Mars that would be in the MOLA receiver field of view (Fig. 3b). The luminance level of this signal can be selected, via commands from the BCE controller, from 16 discrete levels on a shot-to-shot basis. This is accomplished by passing the laser light through a sixteen position neutral density filter wheel driven by a stepper motor (Fig. 3a).

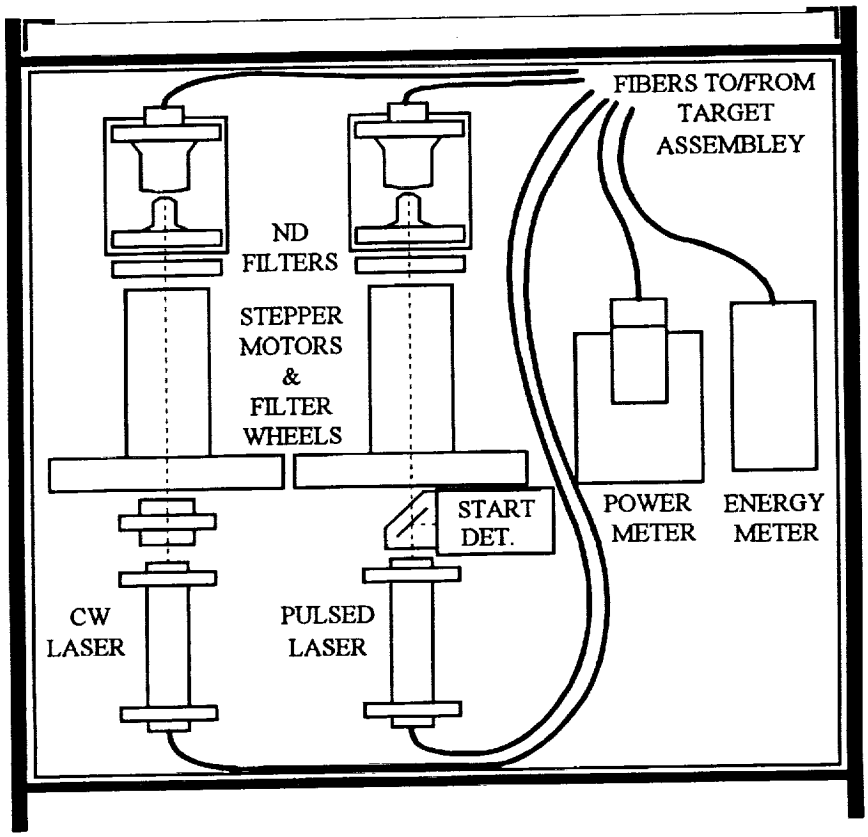

Fig. 3a (ATU Optical Bench Layout)

These filter wheel positions are programmed to provide simulated background levels ranging from Mars night to twice the Mars expected daylight (average) levels. This feature exercises the MOLA background noise counters, adjustable threshold discriminators, and the flight software that autonomously adjust the receiver discriminator threshold levels to provide a predetermined constant false alarm rate.

The second ATU sub-system provides a 35 ns laser pulse (1.064 μm) directed into the MOLA telescope and is also located on the Target Assembly adjacent to the background simulator (Fig. 3b).

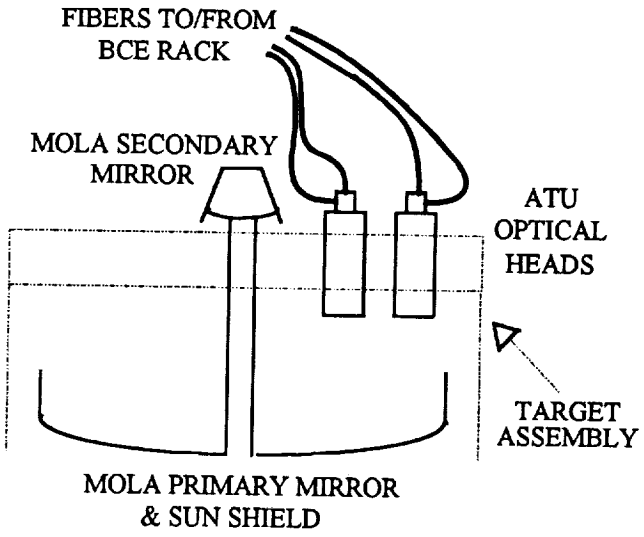

Fig. 3b (ATU Optical Head Position on the Target Assembly)

This pulse simulates the laser return signal from the surface of Mars and exercises the altimetry electronics return pulse energy monitors and ranging related functions. The luminance of this signal can also be selected from 16 discrete levels on a shot-to-shot basis in the same manner as the background simulator (Fig. 3a).

The third sub-system involves hardware and software programming that coordinates and synchronizes these two laser test sources. This feature allows for simulated 'real-time' Mars terrain topography profile data to be input into the MOLA receiver telescope thus providing an end-to-end system functional test. This is accomplished by using a digital programmable delay generator providing the pre-programmed fire control signals to the pulsed laser. This 'canned' topographic profile provides a means to evaluate MOLA range tracking performance, time interval counter (TIU), range gate, and the flight software signal acquisition and tracking algorithms.

The ATU also monitors and records the test laser output power and energy that is sent into the MOLA telescope on a shot-to-shot basis (Fig. 3c). It also measures the actual delay of the pre-programmed delay times of the simulated return pulses.

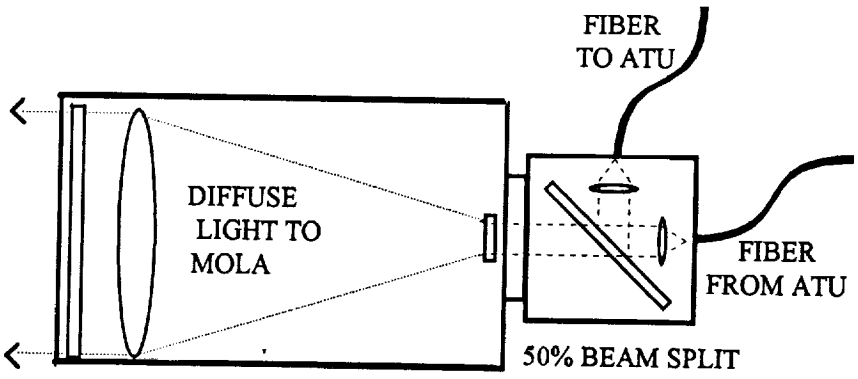

Fig. 3c (ATU Optical Head Detail)

The simulated Mars return pulses, background stimuli, and monitor data are relayed to and from the ATU optical heads located on the BCE Target Assy and the ATU instrument rack via 200 ft. fiber optic cables (200 μm core diameter n = 1.4997 @ 1.064 μm).

The control and data acquisition of the ATU sub-systems are performed by the ATU computer which interfaces to the BCE controller. The ATU computer translates test parameters sent by the controller into a coordinated process of setting delays to simulate terrain patterns, moving motors to set the filter wheels simulating different terrain albedos and reading the monitored data. The ATU computer then organizes the stimulus and monitor data in a shot-to-shot format so that it can be aligned and compared against the MOLA performance results thereby providing a means of characterizing and calibrating the MOLA instrument altimetry electronics performance for each test environment.

Laser Diagnostic Unit (LDU):

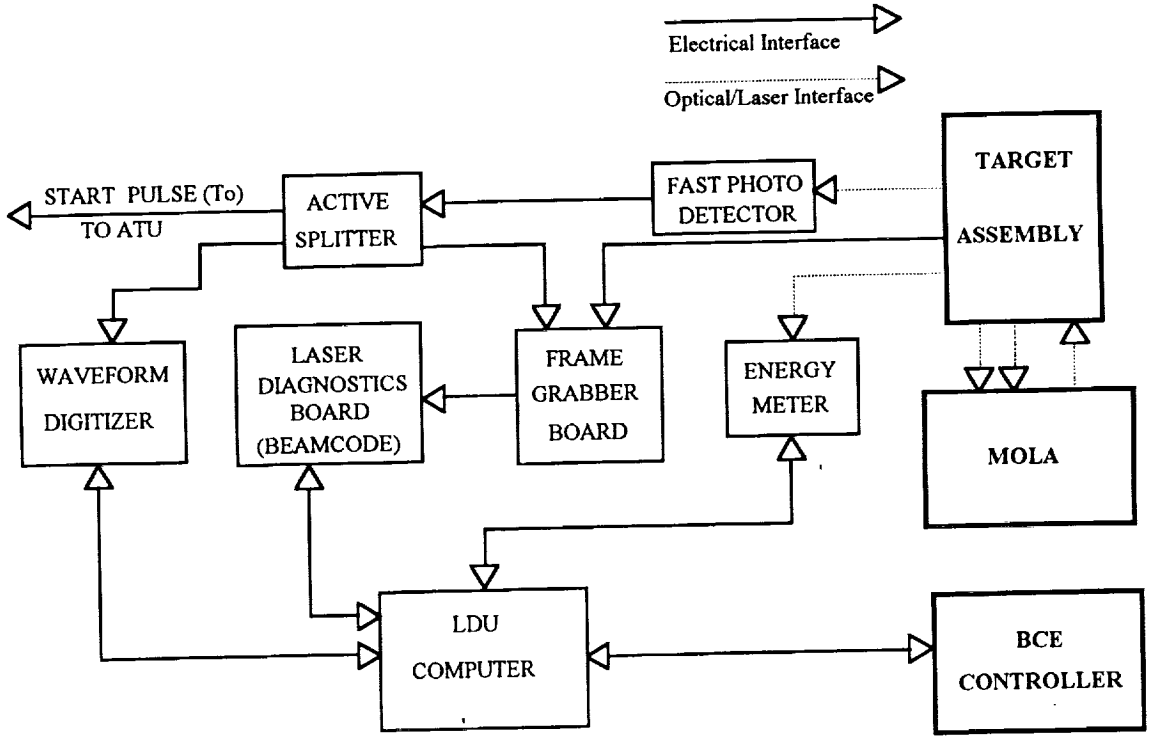

Fig. 4 (LDU Functional Block Diagram)

The LDU system block diagram is shown in Figure #4. The primary purpose of the LDU is to acquire data detailing the performance of the MOLA laser transmitter output. These data consist of laser pulse spatial and temporal characteristics as well as laser pulse energy. Optical and electronic instrumentation to sample the transmitted laser pulse is mounted on the MOLA Target Assembly. The Target Assembly itself is attached to the MOLA instrument during testing and evaluation (see Target Assembly section). Signals from the Target Assembly instruments are transmitted via optical fibers, coax and wire cables to the data acquisition hardware which may be located up to 45 meters away from the MOLA instrument. The data acquisition instruments are housed in a 19" electronics rack. All data acquisition hardware is connected to the LDU computer, a Compaq™ 386/20 MHz PC.

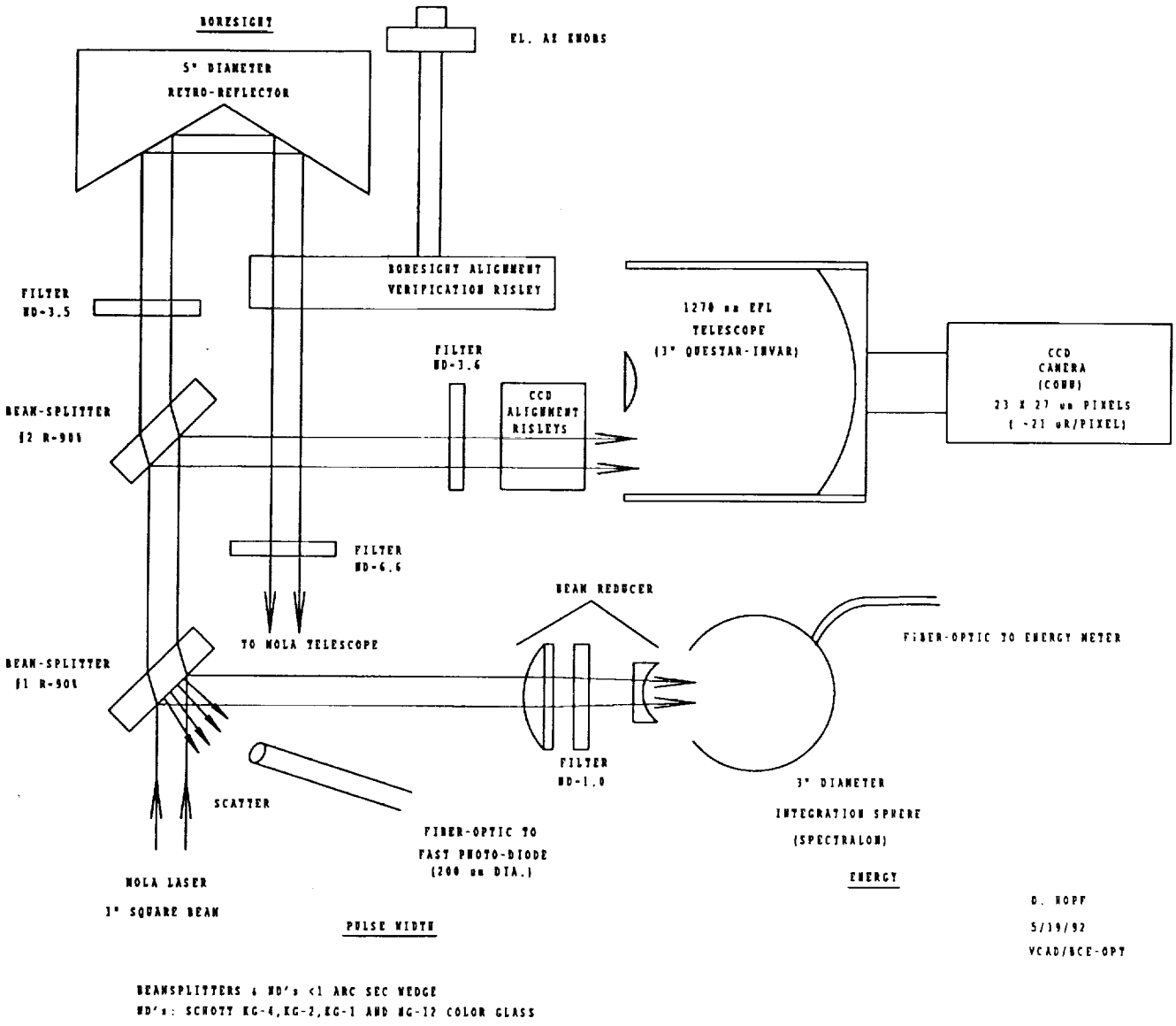

Fig. 5 (LDU Optical Path Layout)

Referring to figure #5, beam-splitter #1 directs 90% of the transmitted energy through beam attenuation and reduction optics and into a Spectralon™ integrating sphere manufactured by Labsphere™. The sphere is utilized to remove spatial non-uniformity in the laser beam while sampling the pulse energy. An optical fiber (200 μm core, n = 1.5, length = 45 m) is coupled to the integrating sphere and transmits a portion of the energy to a Molectron™ J3S 10 mm silicon photo diode connected to a Molectron™ JD2000 energy meter. The JD2000 computes the average and standard deviation of 99 laser pulse energy readings for transmission to the LDU computer.

A second optical fiber (200 μm core, n = 1.5, length = 45 m) transmits a portion of the diffuse reflection from beam-splitter #1 to a high speed silicon avalanche photo-diode (Si-APD) and amplifier manufactured by OptoElectronics™ Inc.. A screw-type attenuator is used to adjust the optical throughput to the Si-APD. The Si-APD and amplifier bandwidth is 1 GHz. The pulse output of this detector is digitized at 2 GSamples/s and stored with a Tektronix™ DSA 602 Signal Analyzer. The DSA 602 averages 100 pulses and calculates pulse width, peak voltage, rise time and fall time.

The Si-APD signal is split after the amplifier to provide a T_0 reference for the ATU and a trigger for the Molectron™ JD2000 energy meter.

Beam splitter #2 again splits the remaining energy. 90% of this energy is directed into a 1270 mm EFL Invar Schmidt Cassegrain telescope manufactured by Questar™. The telescope focuses the far-field beam pattern onto a 8.7 x 6.4 mm COHU™ CCD camera. Neutral density filters are used to limit the beam intensity and a Risley alignment prism assembly adjusts the beam displacement. A typical beam cross section illuminates approximately 30 x 30 pixels on the camera (each pixel is 23 x 27 μm). Power, synchronization and video signals are transferred to the LDU rack over a 45 meter long wire cable. Camera scans are captured at the LDU computer with an AT Vista™ video frame grabber and Big Sky Beamcode™ software. The software computes diameter, centroid and peak positions of the beam cross section.

The remainder of the pulse energy is transmitted through beam splitter #2 to a five inch retro-reflector which displaces and reflects the pulse back into the MOLA telescope. The MOLA receiver detects this pulse and the signal is used to verify alignment of the MOLA receiver and transmitter. A Risley prism assembly is used to manually translate this return pulse across the detector field-of-view for alignment verification. This alignment check procedure is performed each time after the instrument has been significantly relocated, vibration, thermal vacuum testing etc. to verify the internal laser-to-detector alignment is still within specification.

Ground Power Supply (GPS):

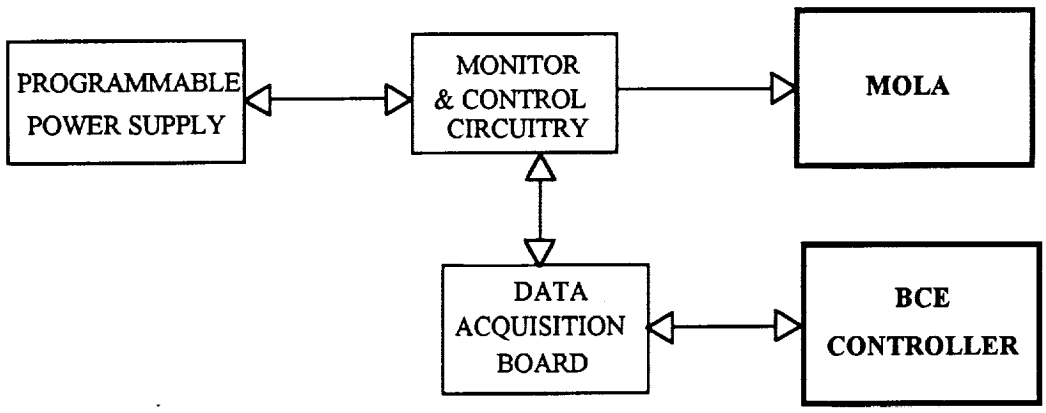

Fig. 6 (GPS Functional Block Diagram)

A block diagram of the BCE GPS is shown in Figure #6. The GPS system consists of a programmable power supply controlled and monitored (voltage and current) by custom circuitry consisting of a current sensor, latching relay and accompanying electronics interfaced to a Data Translation™ 2821 data acquisition board. The GPS system provides adjustable DC power to MOLA, captures the instrument's current and voltage turn-on transients, and simulates over/under voltage surges on the spacecraft power bus due spacecraft events such as battery switching, etc..

The GPS is used to verify that MOLA functions as designed over the possible range of spacecraft over/under voltage levels and transient events.

BCE Controller:

The BCE Controller consists of PC based hardware and custom menu driven software that coordinates and controls the operation of the other BCE sub-systems with the related spacecraft systems. The BCE Controller software provides the primary interface between a test conductor/operator and the sub-systems shown in figure #1. Resident in the BCE Controller software is a series of standard instrument tests.

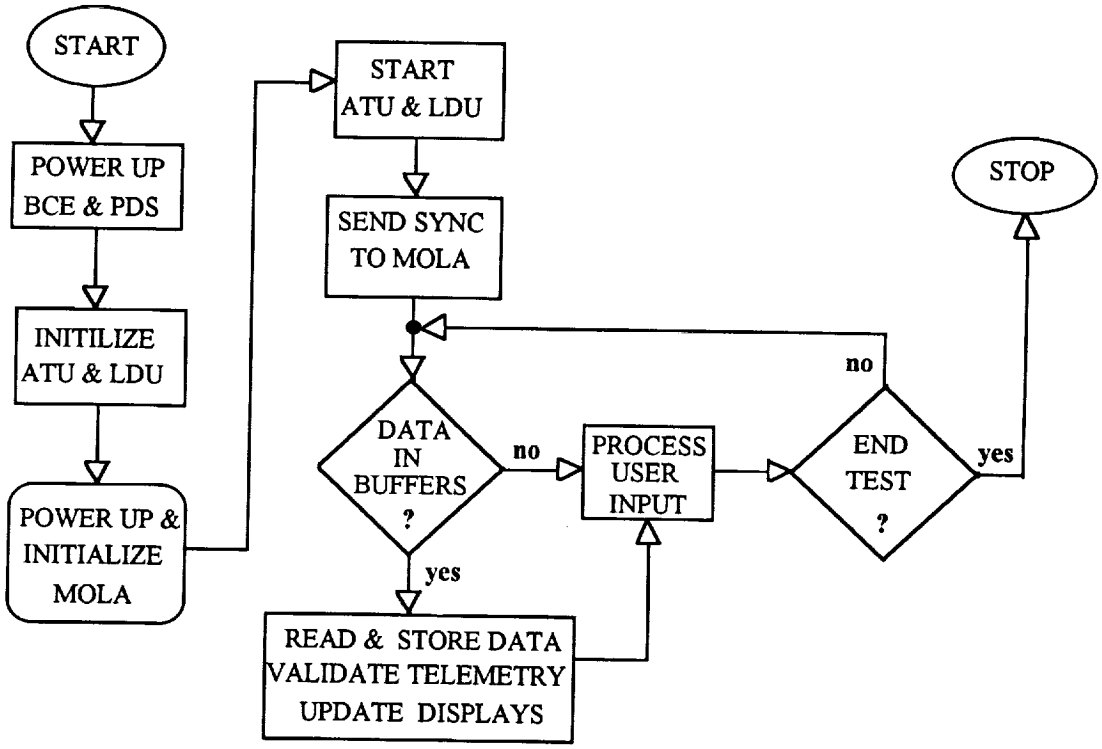

Fig. 7 (BCE Controller Operation Flow Diagram)

As shown in Figure #7, a typical test scenario begins with the power-up and initialization of all of the BCE systems and the PDS. The BCE controller software sends test setup information to the ATU and LDU software. After acknowledging the controllers setup commands the ATU and LDU initialize their various components and then wait for a start command from the controller. At this time the controller will either energize a relay to provide power to MOLA via the GPS or monitor the MOLA telemetry data packets from the PDS to determine whether MOLA is operational. Once MOLA is turned on and in the correct configuration the controller will command the ATU and LDU to start and execute a test. Immediately after the start command is received the ATU sends a pre-defined ranging pattern to MOLA which provides a means to align the BCE stimulus (ATU) and laser monitor (LDU) data with the MOLA packet telemetry data. The ATU software then sets its filter wheels, delay circuits and pulse generators to the settings required for the specific test. As the test continues the controller acquires and processes the

stimulus, laser monitor and telemetry data from the ATU, LDU and PDS. The controller continues to acquire, monitor telemetry and archive test data until the end of the test is reached or until the test is stopped by an operator. At the end of a test the BCE Controller software updates test logs and creates backup copies of all the data files generated from that test. The BCE test data can then be fully processed off-line by the Analysis Computer.

Analysis Computer:

The Analysis Computer sub-system consist of data processing hardware and performance assessment software. This BCE sub-system receives MOLA and BCE sub-system testing data from the BCE Controller on 20 MB removable hard disk media (Bernoulli®). Raw test packet data from MOLA and BCE sub-system stimulus data is then merged and aligned by post-processing software on the analysis computer to form spreadsheet data files. These data files are then processed to form summary data product files and hardcopy performance sheets (graphs and tables). These summary performance data files are archived to form the data base for the instrument performance trend analysis. The summary data products are used to quantitatively determine the MOLA performance and determine that MOLA is meeting the instrument functional requirements during that specific series of instrument tests. The instrument performance trend data is continuously monitored for anomalous indications. The performance data base will allow the MOLA data analysis team to evaluate mission data and predict instrument performance trends (i.e. laser energy output, etc.).

Shown in figure #8 below is a representative data analysis performance chart displaying the MOLA range and range gate tracking performance to a triangular topographic profile provided by the BCE/ATU stimulus.

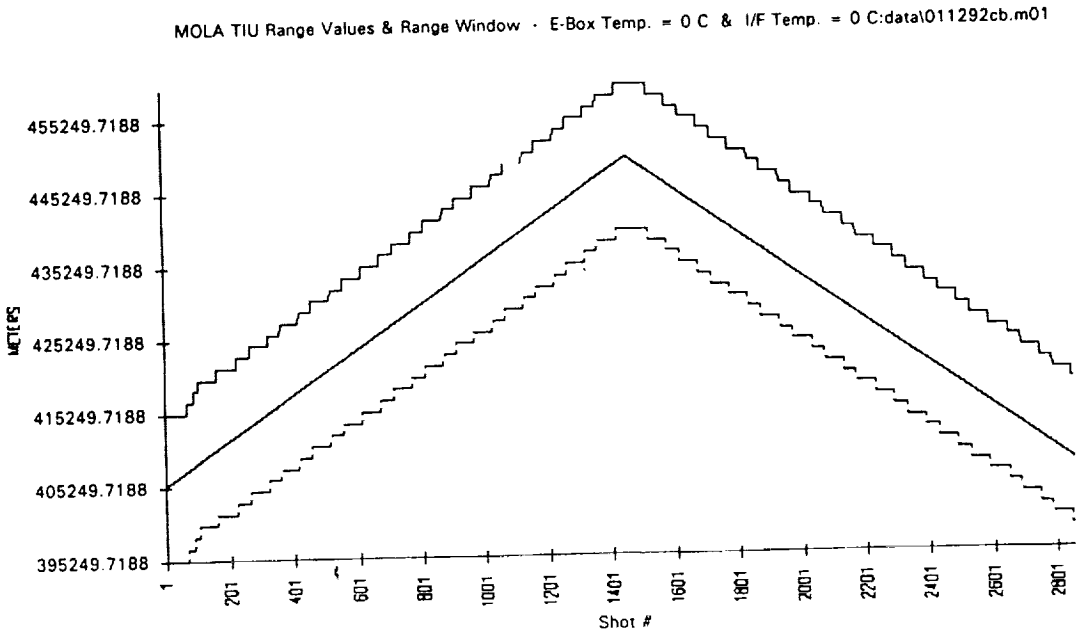

Fig. 8 (Data Analysis Performance Chart)

FINAL COMMENTS

There are a few BCE sub-systems that were used with the MOLA instrument that bear mentioning. These were not include in the main text of this paper because they were too MOLA specific and may not be necessary or of the same design (implementation) on future altimeter instrument systems.

The Laser External Cooler (LEC) was an off-the-shelf chiller that we used to cool a plate that was used to conductively couple (clamped) to the side of the laser box to remove the heat generated by the laser pumping diodes. This allowed operation the laser at or above normal room temperatures preventing the overheating of the diodes and subsequent lifetime degradation. Also, by varying the chiller temperature over a small range we were able to characterize the laser output energy and pulse width as a function of temperature. For future spaceborne solid state laser instruments, consideration should be given to having the cooling manifold integral to the laser box. The added mass overhead will more than be compensated for by the increased operational flexibility, simplification of hookup, and added system level safety considerations.

The laser cavity purge system was used on MOLA to prevent a laser cavity burst disk assembly from rupturing during system level thermal vacuum testing. The burst disk assembly was designed into the box wall of the laser cavity and is intended to rupture during the spacecraft launch and thus venting the laser cavity to deep space. This is necessary to avoid the critical pressure region because of the high voltage used to operate the Lithium Niobate Q-switch. The Class 100 cleanliness requirements of the laser cavity made this a very difficult task to manage. Consideration should be given to future applications to implement a totally sealed laser cavity box - fully pressurized or totally evacuated and maintained for the life of the system.

In conclusion, it is important to maintain an overall BCE system that is fairly flexible and modular. There will always be testing anomalies and BCE component failures that will occur. The ability of the BCE to absorb and accommodate these events must be planned for in advance. In the end, this will greatly reduce testing cost and schedule impacts.

ACKNOWLEDGMENTS

We would like to express our deep appreciation to Mr. Roger Ratliff of Code 727.3 who spent long hours and many evenings completing the mechanical design of the MOLA BCE Target Assembly. His innovative ideas and skilled craftsmanship are solely responsible for the success and simplicity of an extremely complicated testing apparatus.

MARS LASER ALTIMETER BASED ON A SINGLE PHOTON RANGING TECHNIQUE

I.Prochazka, K.Hamal, B.Sopko
Faculty of Nuclear Science and Physical Engineering, Czech Technical University
Brehova 7, 115 19 Prague 1, Czechoslovakia
ph/fax +42 2 848840, tlx 121254 fjfi c, bitnet TJEAN@CSEARN.BITMET

S.Pershin
Space Research Institute,Moscow,Russia

GENERAL

The MARS 94/96 mission [1] will carry, among others, the balloon probe experiment. The balloon with the scientific cargo in the gondola underneath will drift in the Mars atmosphere, its altitude will range from zero, in the night time, up to 5 km at noon. The accurate gondola altitude will be determined by an altimeter. As the balloon gondola mass is strictly limited, the altimeter total mass and power consumption are critical, maximum allowed is a few hundreds grams and a few tens of mWatts of average power consumption, only. We did propose, design and construct the laser altimeter based on the single photon ranging technique.

PRINCIPLE OF OPERATION

The system operation is based on the single photon laser ranging technique : the short and low power laser pulse is transmitted in the nadir direction, the signal reflected from the planet surface is collected by the receiver lens and detected by the photon counting device. The light time of flight is measured. Completing the series of measurements, the altitude, the range to the surface, may be evaluated. The number of individual laser fires needed for one altitude determination is limited by the altitude itself, the background illumination intensity and hence the signal to noise ratio and the balloon gondola vertical velocity. Thanks to the relatively high repetition rate of the laser transmitter (currently 7 kHz, the 25 kHz version is expected to be available in the near future), one altitude measurement may be completed within fractions of a second.

The single photon ranging technique has several key advantages in this application :

* the low power, high repetition rate diode laser may be used as a transmitter,
* the wavelength of such a transmitter well coincides with the maximum sensitivity of the semiconductor photon counting detector,
* no analog signals are treated within the device, all the information is obtained from the statistical treatment of the set of range measurements. This fact is resulting in overall simplification of the device and its performance stability within a wide temperature range. All the electronics may be based on digital, low power CMOS circuits only, what is resulting in low mass and low power consumption,
* the laser ranging system may be used, for the atmospheric clouds, haze and aerosols monitoring, as well.

ALTIMETER CONSTRUCTION

As a transmitter, the integrated laser diode pulser LDI 91 is used. It delivers uniform, fast risetime pulses at 880 nanometers wavelength 100 nanoseconds long with the energy of 2 microJoules. The receiver consists of a Single Photon Avalanche Diode detector package [2], its operating voltage is controlled by a newly designed circuit in a wide temperature range -60 to +20 Centigrade. The diode's quantum efficiency reaches 20 % at this wavelength range. The transmitter and receiver share the same optics of 40mm aperture, the optical path is separated by a polariser. To keep the optics as simple as possible, the diode aperture and hence the receiver field of view is not perfectly matched to the laser transmitter one. By this compromise the optics mass and alignment precision requirements have been significantly reduced on the expense of the energy budget link. The bandpass filter 5 nanometers wide having the transparency of 60% is used to reduce the background illumination. The altimeter electronics consists of a flying time counter having 33 nanoseconds resolution, the programmable range gate generator, the control logic and interface to the board computer.

To facilitate the single photon ranging even under the Mars daylight conditions, the combination of the detector limited field of view, optical bandpass filtering, the adjustable range gate electronics and the data processing software have to be applied. One out of three main strategies may be selected for setting up the range gate :

1. 'Start from scratch' all the possible range gate settings are consequently applied, the echo signal is recognized. This is an emergency solution not requiring any a priori knowledge of the altitude to be measured.
2. ' Morning take off' starts from the range gate interval 0 - 150 meters. It is based on the presumption, that the gondola will take off after the sunrise.
3. ' Routine operation ' the range gate setting is predicted on the basis of the previously measured altitude and vertical velocity. The signal search in the +/- 1 range gate interval may be carried out, if necessary.

GROUND TESTS

To proof the feasibility of the device, the experimental system has been constructed at the Space Research Institute, Moscow and tested in a series of ground test at the Czech Technical University. The ultimate single shot range resolution and the measured range dependence on the echo signal strength (the range bias) have been measured. The LDI91 laser diode pulser, the single photon detection package and a high resolution time interval unit has been used. The results are plotted on Figure 1 together with the return rate. From the single shot range resolution of 4-5 meters one can conclude, that the ranging precision of one meter may be obtained averaging more than 25 returns. The ground target ranging within the ranges 0-3.5 km has been obtained using the optics aperture of 17 mm only. The example of the ranging result is on Figure 2,

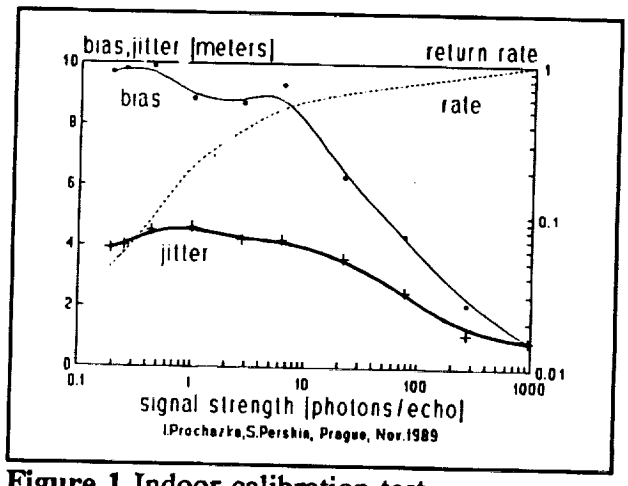

Figure 1 Indoor calibration test

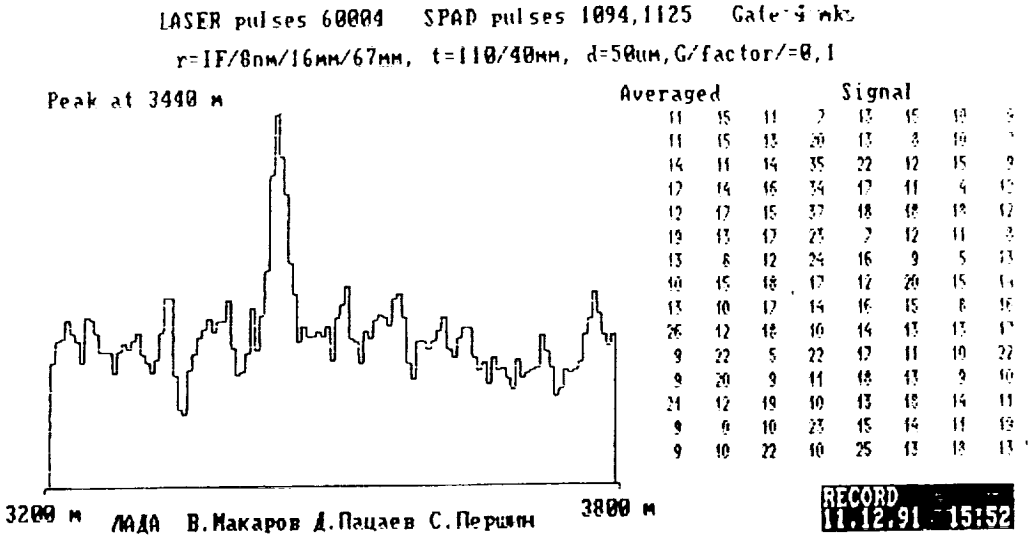

Ground target ranging, 3.5 km distance

Fig. 2

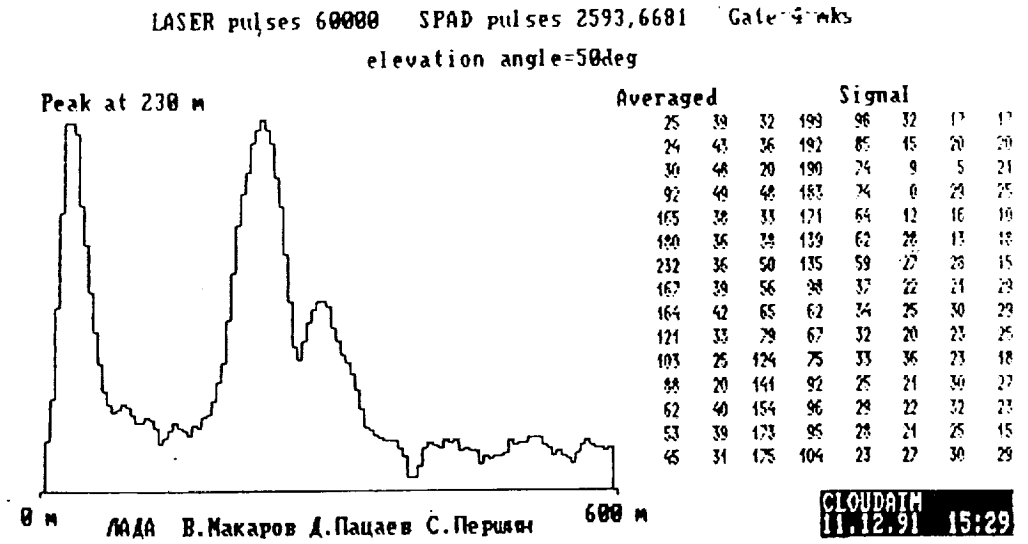

Vertical humidity haze monitoring, daylight multiple haze layer may be seen

Fig. 3

this is a horizontal ranging to the 3.5 km distant target in a light haze visibility conditions. Employing the full 40 mm aperture optics of the final version, the full range will be guaranteed.

The single photon ranging system may be used for the atmospheric transparency/backscatter monitoring [3]. Currently, the proposal, that such a system may be used for the Mars atmosphere monitoring, is under investigations. Either using the independent unit installed in the 'Small Mars Station' [4] or directly from the balloon gondole in the night time, when is it located on the surface and it is not used for altimetry. In another words, the system may be used for the clouds distance and density profile monitoring, as well. On Figure 3 there is an example of the results of the clouds monitoring. The laser rangefinder was pointed to the zenith, the lower cloud boundary and its density profile may be recognized. The clounds may be monitored day and night up to the height of 1 km.

CONCLUSION

The altimeter based on the single photon ranging technique outranged the microwave and Nd YAG laser systems by low weight, low power consumption and the compact design. The mass, dimensions and price of such a system make it attractive not only for Mars mission, but also for mobile, air and space born remote sensing applications. The excellent stability of both the laser transmitter and the single photon detector permits to calibrate the receiver sensitivity to high accuracy and thus to use the system as a precise visibility and surface reflectivity sensor. The applications of a visibility sensor in automated meteo stations, traffic safety, air and ship safety systems seem to be quite promising. In all these applications, the eye safety of the laser transmitter is a significant advantage of the device decsign. The air and space born remote sensing application in agriculture, geology, large area forest monitoring, soil humidity and radioactive Cesium dust monitoring is under consideration.

References

[1] R. Sagdeev, Physics Today, **5**, 30 (1988)
[2] I. Prochazka, K.Hamal, B.Sopko, G.Kirchner, Technical Digest of the Conference on Lasers and Electro Optics, CLEO 91, Baltimore, May 1990
[3] I.Prochazka, K.Hamal, S.Pershin, Capabilities of Single Photon Detection in LIDAR for Atmospheric Studies, International Symposium on Radars and Lidars in Planetology, Cannes, France, Sept. 1991
[4] I.Prochazka, K.Hamal, et al, MARS 94 Mission Backscatter LIDAR for Small Mars Stations, Gound Tests Results, European Geophysical Society XVII General Assembly, Edinburg, April 1992

MULTI-BEAM LASER ALTIMETER

Jack L. Bufton
David J. Harding
Luis Ramos-Izquierdo

Laboratory for Terrestrial Physics
Goddard Space Flight Center
Greenbelt, MD

Laser altimetry provides a high-resolution, high-accuracy method for measurement of the elevation and horizontal variability of Earth-surface topography. The basis of the measurement is the timing of the round-trip propagation of short-duration pulses of laser radiation between a spacecraft and the Earth's surface. Vertical (i.e. surface elevation) resolution of the altimetry measurement is determined primarily by laser pulsewidth, surface-induced spreading in time of the reflected pulse, and the timing precision of the altimeter electronics. With conventional gain-switched pulses from solid-state lasers and sub-nsec resolution electronics, sub-meter vertical range resolution is possible from orbital altitudes of several hundred kilometers. Horizontal resolution is a function of laser beam footprint size at the surface and the spacing between successive laser pulses. Laser divergence angle and altimeter platform height above the surface determine the laser footprint size at the surface; while laser pulse repetition-rate, laser transmitter beam configuration, and altimeter platform velocity determine the spacing between successive laser pulses.

Multiple laser transmitters in a single altimeter instrument provide across-track as well as along-track coverage that can be used to construct a range image (i.e. topographic map) of the Earth's surface. Figure 1 is an illustration of the pushbroom laser altimeter instrument measurement concept that utilizes multiple laser beams. This multi-beam laser altimeter (MBLA) contains modular laser sources arranged in a linear, across-track array. Simultaneous or near simultaneous measurements of range to the surface are possible by independent triggering of the multiple laser pulse transmitters and reception by a single telescope that is staring at nadir and is equipped with a multi-element linear detector array in its focal plane. This arrangement permits alignment of each transmitter output into a separate, dedicated receiver channel. The illustrated configuration is a linear, contiguous across-track array of 30 beams which produces a strip-image range map of the Earth's surface. This MBLA configuration is one possible arrangement to accomplish high accuracy terrestrial topographic mapping near the nadir track in a NASA Earth Probe mission devoted to global topographic measurements. The configuration can be changed in accord with required science products and available resources. Possible modifications in the design include variation of footprint size and/or footprint spacing both along-track and cross-track to produce the desired coverage or sampling density within the sensor swath width.

The illumination pattern incident on the Earth's surface from any one transmitter element is a two-dimensional circular pattern of laser irradiance, with a Gaussian spatial distribution of illumination intensity, that is produced by a single

transverse (spatial) mode of the laser cavity. The transmitted laser pulsewidth is short (i.e. ~ 5 nsec full-width-at-half-maximum). The temporal distribution of laser irradiance in the pulse is approximately Gaussian and is the result of multiple longitudinal laser cavity modes produced by the gain-switched (Q-switched) laser cavity. In an ideal altimeter application (e.g. measurement of a smooth water surface) the backscattered laser pulse retains the shape of the incident pulse. However in the general case, the height distribution (i.e. roughness) and slope of the surface within the laser footprint produce spreading in time of the laser pulse reflected to the receiver. After interaction of the laser footprint with a rough or sloping surface, the backscattered pulsewidth may be expanded to several tens to several hundreds of nsec. The spread pulse degrades range measurement accuracy but analysis of the received pulse shape provides additional information on surface structure.

Figure 2 illustrates the pulse spreading effect and portrays the measurement approach in laser altimetry by providing the time varying amplitude of an altimeter detector that observes both the transmitted and backscattered laser pulse. Pulse spreading, by re-distributing the available pulse energy into a larger time interval, acts to reduce the peak-power signal-to-noise-ratio, thus increasing the probability of error for the range measurement. Pulse spreading also adds timing uncertainty by slowing the rise time of the return signal. Variability in pulse rise time in turn produces a time-walk effect when conventional threshold-crossing time-interval-unit devices are used for the range measurement. The application of GHz-bandwidth digitization or multi-stop time-interval measurement to the receiver pulse waveform provides pulse shape data. Digitization is indicated by the horizontal axis tick marks in Figure 2. The centroid T_S of the pulse shape data is used to make a timing correction that provides the measure of range-to-surface. The centroid is in effect the mean round-trip time-of-flight range to surface features within the laser footprint, weighted by: (1) the input two-dimensional Gaussian illumination pattern; (2) the reflectivity and areal extent of the surface features; and (3) the laser altimeter receiver transfer function.

The pulsewidth (or rms pulse spreading) that is derived from digitizer or multi-stop timing data is used to assess the magnitude of surface slope and/or surface structure within the footprint. Pulse spreading data taken together with along-track and across-track slope information provided by adjacent range pixels, enables calculation of the sub-pixel (footprint) slope or roughness. An analytical expression has been developed (Gardner, 1991) to express pulse spreading (mean square pulse width) in terms of the laser altimeter system parameters, beam curvature, nadir angle of observation, surface slope, surface roughness, and laser receiver operating signal-to-noise ratio.

The total area under the received pulse is proportional to pulse energy and is a measure of surface reflectance at the monochromatic 1 μm laser wavelength. Effective use of this reflectance data requires normalization by laser transmitter energy and consideration for atmospheric transmission. Reflectance data acquired with the pushbroom scan pattern of the laser altimeter provide an imaging capability that supplements the ranging functions. Since this image is acquired with an active sensor that transmits and receives only near nadir (180° phase function, i.e. backscatter mode), the surface illumination angle is fixed within 1° of zenith and the resultant image is free of bidirectional reflectance effects that exist in passive images with variable solar illumination geometries. Surface slope effects

on this reflectance image can also be directly characterized from the associated laser altimeter along-track and across-track range measurement record.

The functional block diagram of the multi-beam laser altimeter instrument appears in Figure 3. The laser transmitter module, receiver telescope, detector package, ranging and waveform electronics, GPS receiver, and pointing attitude measurement components form the major instrument subsystems. These subsystems are packaged into a common structure that provides a rigid platform for the laser transmitter, receiver optical components, and dual star cameras. The size of this structure is primarily dependent on telescope aperture (~ 0.9 m). The key component of the laser altimeter instrument structure is a lightweight, rigid optical bench illustrated in the perspective view of the MBLA Instrument in Figure 4 and the cross-sectional view of Figure 5. The altimeter telescope primary mirror is attached to the nadir-viewing side of the optical bench and the laser transmitter modules, detector package, and dual star cameras are attached to the opposite side. This construction ties all the transmitter and receiver optics together for maintenance of arc sec alignment. Beryllium is the material of choice for fabrication of the telescope optics and structure, optical bench, laser module cases, and the star camera mounting brackets. Beryllium provides a rigid optical platform, superior thermal diffusivity for removal of waste heat, an athermal optical train, and a minimum total mass. With these beryllium components, the design illustrated in Figure 5 has a mass of ~ 60 kg. Mass of the altimetry electronics, instrument computer, thermal, power, and GPS receiver subsystems bring the instrument total to ~ 100 kg.

The pulsed transmitter is based on high-power neodymium (Nd)-doped solid-state laser crystals and employs the Q-switching technique to concentrate laser energy in a short pulse . Each of the 30 laser transmitter modules illustrated in Figure 5 is optically-pumped by separate AlGaAs laser diode arrays that are coupled into the Nd laser crystal by fiber-optic cables. This results in an all-optical laser module that is separated from the electronic and power supply components of the laser subsystem. The majority of thermal dissipation for the laser modules can thus be grouped together and placed at a remote radiator location in the spacecraft instrument. The laser module design is a scaled version of present-day commercial diode-pumped Nd laser technology that is in use in NASA airborne laser altimeter systems. The illustrated array of laser transmitter modules is capable of producing ~ 7000 pulses-per-sec and requires average input electrical power of 1 kW when operational.

Optical backscatter from the Earth's surface is collected by the MBLA telescope that is fixed in orientation at the nadir track of the spacecraft. A series of two optical lenses and optical bandpass filters are used to collimate, filter, and then focus the backscattered radiation on the detector plane. Each laser transmitter element is angle-mapped into a silicon avalanche photodiode detector array element for a continuous two-dimensional range and reflectivity image of the surface. Energy measurements are made for the transmitted and received laser pulses and are affected by the reflectivity and transmission of the various optical surfaces in the instrument as well as detector sensitivity. Optical contamination and degradation for long term exposure to the space environment are potential problems. An on-board laser diode emitter can be utilized as a calibration source and coupled with fiber optics into the optical detectors. This method will maintain calibration for the energy measurement for surface reflectance studies.

Pointing attitude knowledge is generated by dual star cameras. Each camera is a second-generation star tracker that employs a 2-dimensional CCD array that is capable of simultaneous tracking of as many as five stars. On-board Kalmann-filtering is utilized to compare stellar angular position data with a star catalog and provide an output pointing attitude estimate; in principle eliminating the need for an inertial reference unit. Both star cameras are capable of 1 arc sec (total angle) pointing knowledge limited by the quality of the star catalog. The dual star camera system can provide the 2 arc sec total angle (1-sigma) knowledge required for sub-meter accuracy altimetry. Pointing angle data are continuously generated with-respect-to the stellar inertial reference frame. Laser pointing angles are tied to the star camera data through beam angle sensors which sample a portion of one or more output laser pulses and measure the angle (at the arc-sec level) of reflection from reference mirrors on the star cameras. Output laser pulse samples are also coupled with retroreflectors directly into the receiver telescope in order to assess alignment shifts between telescope and lasers.

The pulse timing data, waveform digitizer, and pulse energy data form the basic laser altimeter dataset for each laser pulse. These data points accumulate in a buffer in digital form, are formatted into data blocks or files, and then enter the altimeter platform data stream for recording or telemetry. The expected data rate of the laser altimeter resulting from 1000 - 7000 laser pulse measurements a secondis estimated to range from 10 - 50 kbps. On-board processing is planned for the ranging centroid correction and waveform shape data products. Data telemetry involves range-to-the-surface, waveform shape products, sensor housekeeping, pointing attitude, and GPS position data. Post processing on the ground is used to correct the altimetry data for the precision orbit and spacecraft pointing attitude. The basic data products are a gridded topographic map containing $\geq 10^{10}$ surface elevation measurements with the selected horizontal resolution (grid size) and an image of Earth's surface reflectance at 1 μm wavelength with a similar level of detail. These products will be developed with minimal ground processing, stored on compact optical disks, and made available to the scientific community in a timely fashion. Analysis and use of the topographic data will be done by the end user in the scientific community.

REFERENCE:

Gardner, C.S., "Generalized Target Signature Analysis for Laser Altimeters", Applied Optics, 1992.

ACKNOWLEDGMENTS:

The definition of the MBLA instrument was made possible through the efforts of a number of individuals in the Laboratory for Terrestrial Physics (LTP) at the Goddard Space Flight Center and in the aerospace industry. Notable among these efforts were those of David Rabine in the University Research Foundation of the Maryland Advanced Development Laboratory, Nita Walsh of Science Systems and Applications, Inc., Ying Hsu of the Optical Corporation of America, David Thompson of Spectrum Astro, Inc., and Tom Baer, Spectra Physics, Inc.

MULTI-BEAM LASER ALTIMETER MISSION CONCEPT

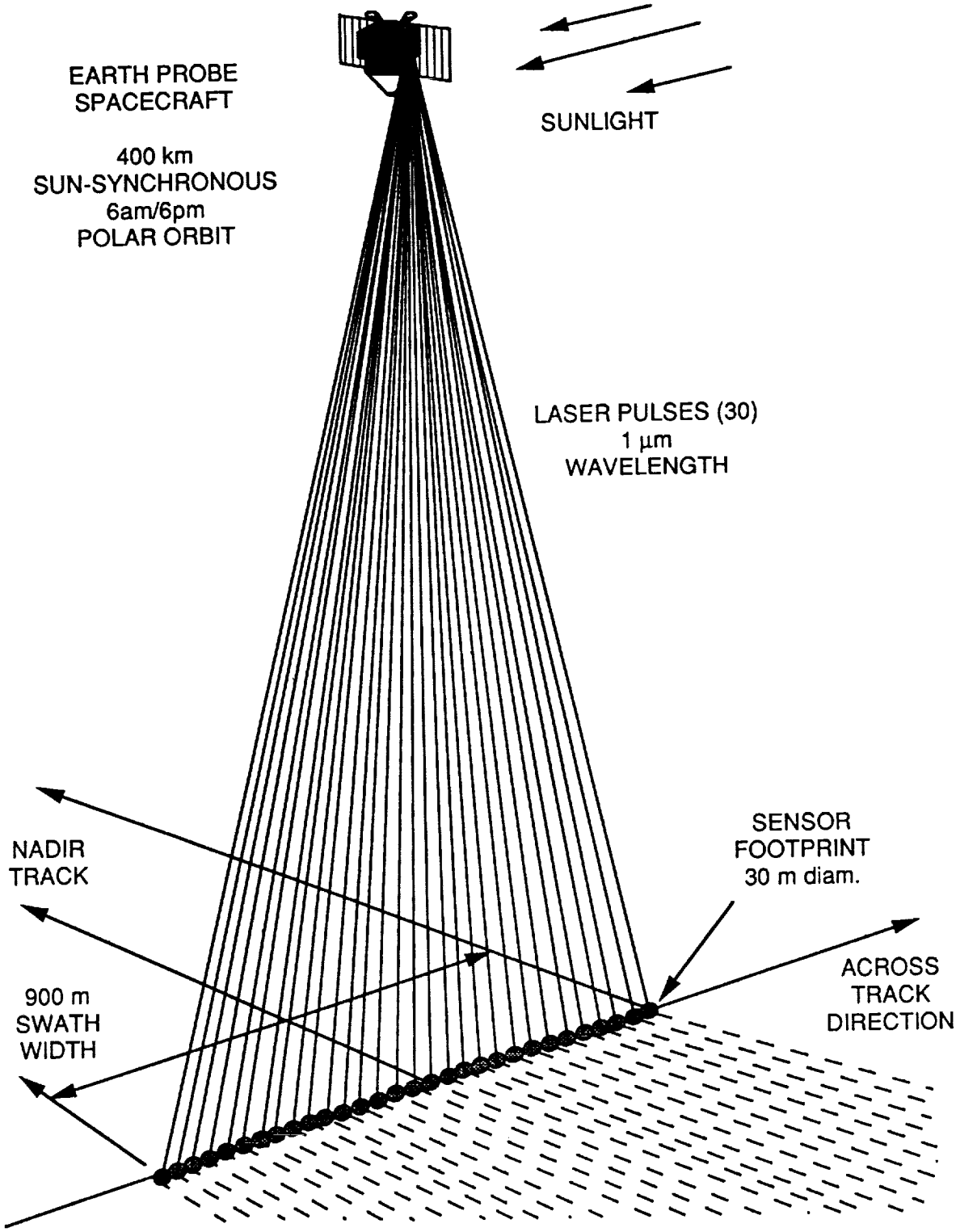

Fig. 1

LASER ALTIMETER PULSE WAVEFORMS

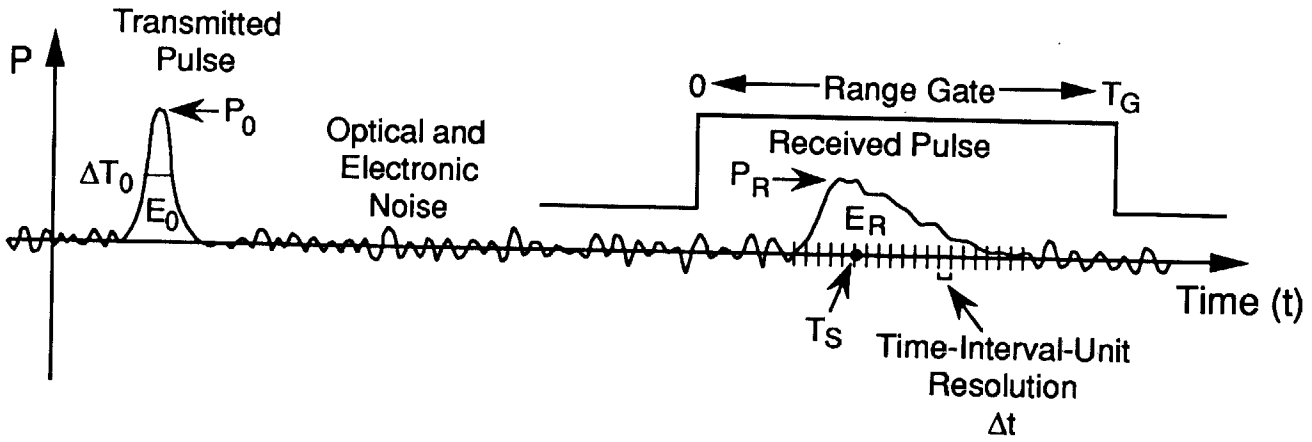

$$\text{Pulse Centroid: } T_S = \int_0^{T_G} (1/TG) \cdot t \cdot P(t)\, dt$$

Fig. 2

MULTI-BEAM LASER ALTIMETER

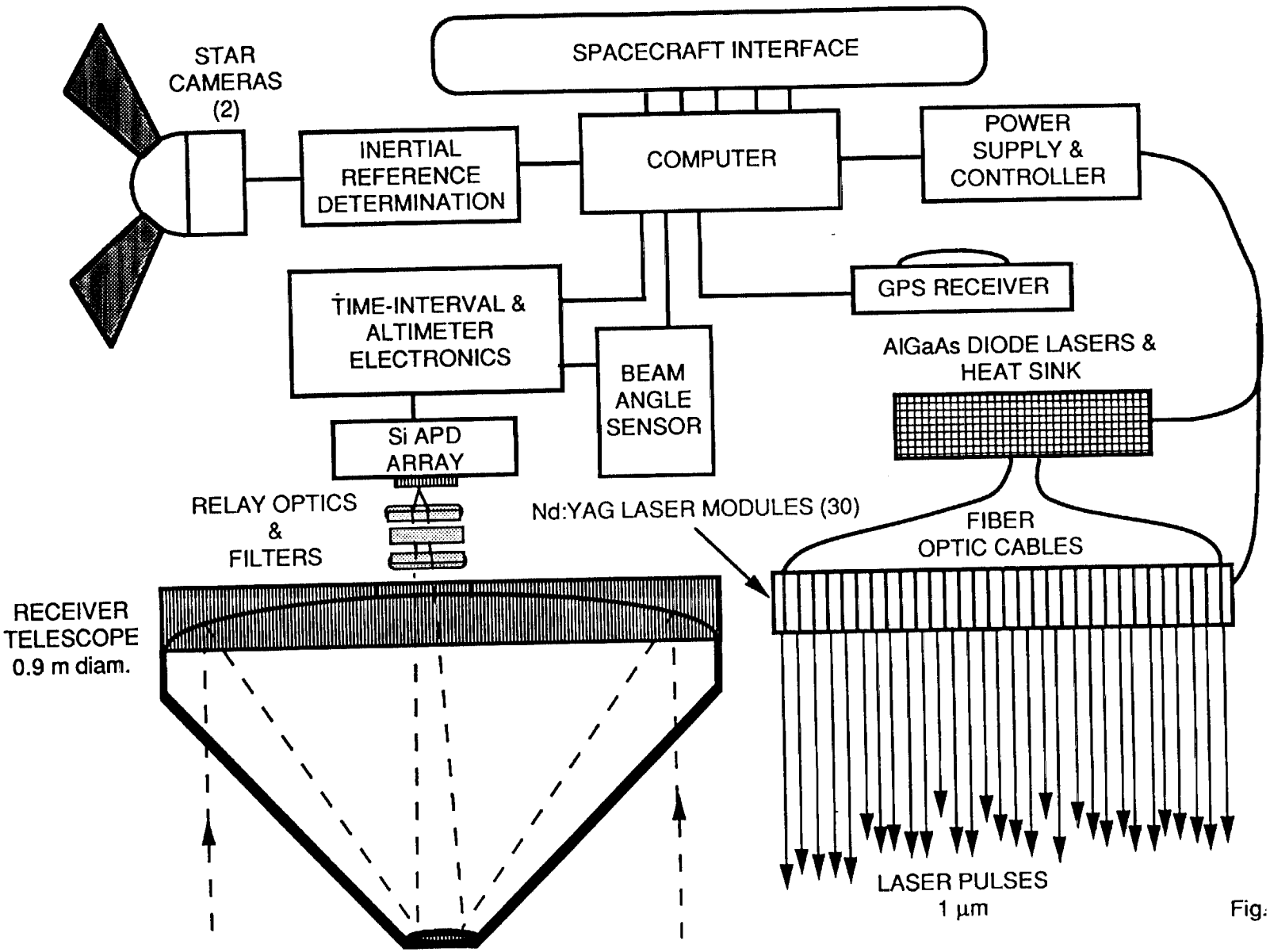

Fig. 3

MULTI-BEAM LASER ALTIMETER

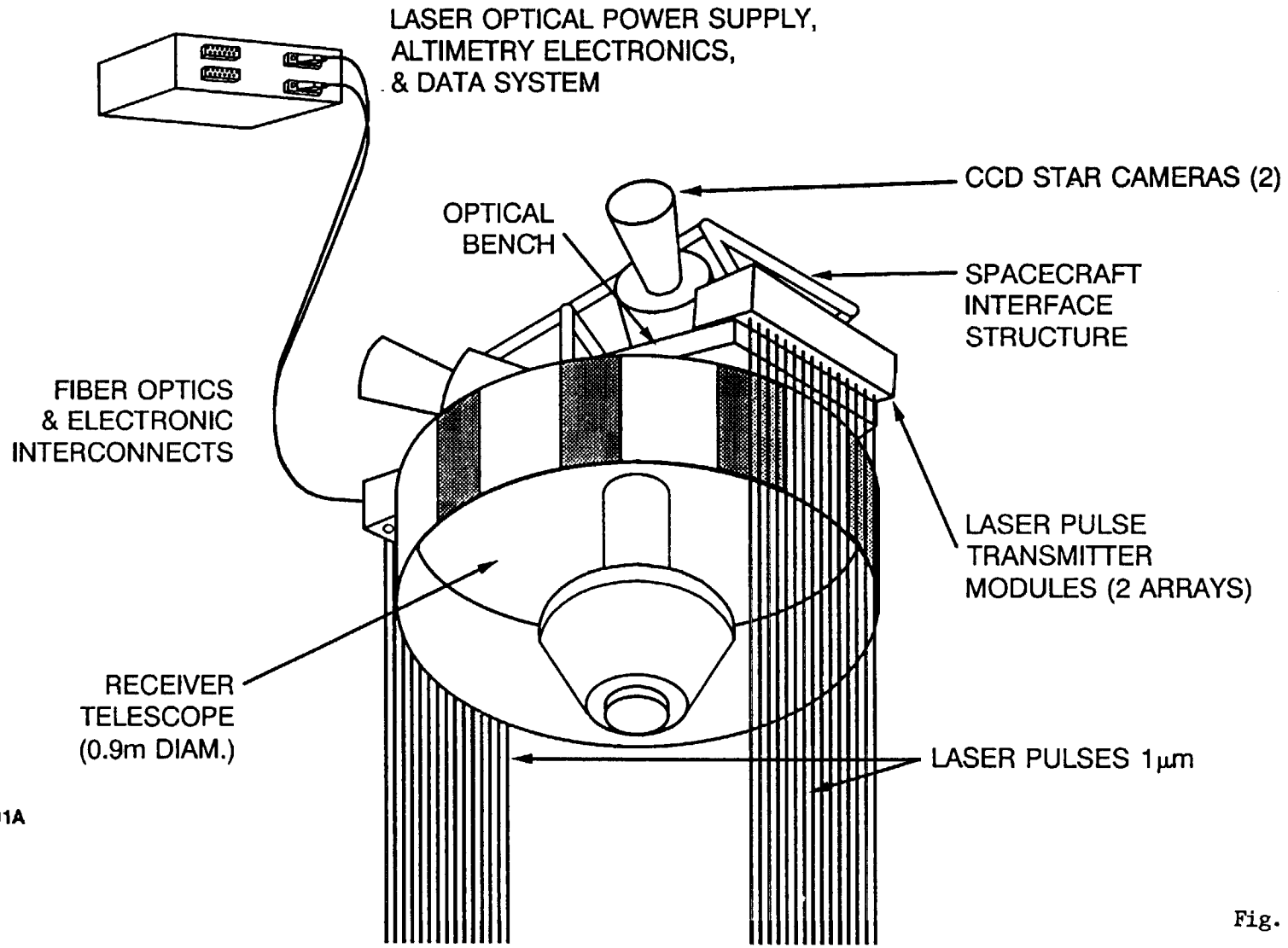

Fig. 4

MULTI-BEAM LASER ALTIMETER
elevation view

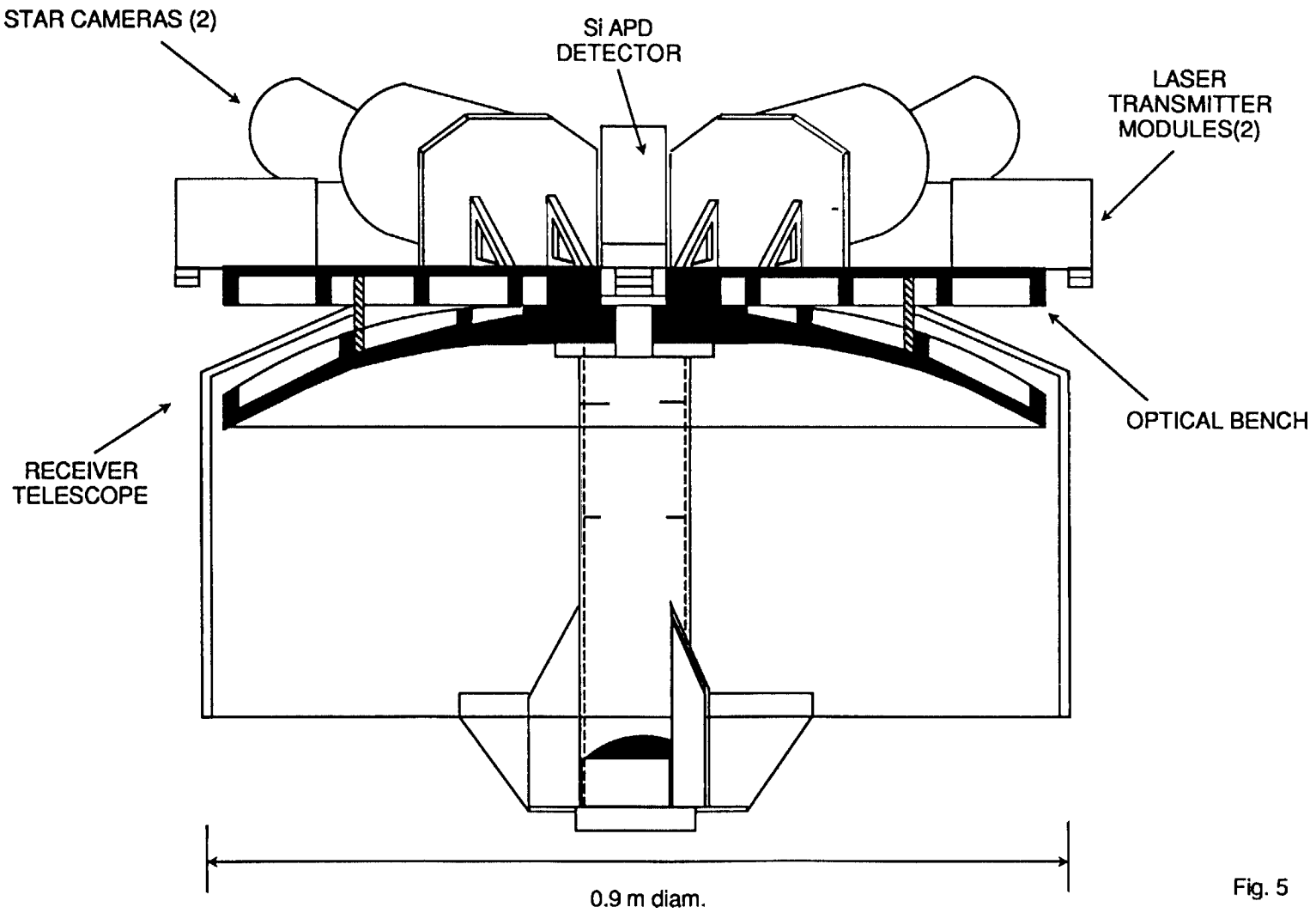

Fig. 5

Poster Presentations

SATELLITE LASER STATION HELWAN STATUS 1992

M Čech, K.Hamal, H.Jelínková, A.Novotný, I.Procházka

Faculty of Nuclear Science and Physical Engineering, Czech Technical University
Brehova 7, 115 19 Prague 1, Czechoslovakia
phone / fax +42 2 848840, telex 121254 fjfi c, E-mail tjean@csearn.bitnet

B.B.Baghos, Y. Helali, M.J.Tawadros

National Research Institute of Astronomy and Geophysics, Helwan, Egypt
phone / fax +20 2 782683, telex 93070 hiag un, E-mail nriag@egfrcuvx.bitnet

GENERAL

The Satellite Laser Station Helwan has been operated jointly by the National Research Institute of Astronomy and Geophysics in Helwan, Egypt and the Czech Technical University in Prague, Czechoslovakia (see Proceedings of the 7th International Workshop on Laser Ranging Instrumentation, Matera, 1989). The station components have been carefully tuned to increase the system overall stability and reliability critical for the remote location. The mount correction model based on the Gaussian smoothing (Kabeláč, 1990) has been implemented to simplify the blind satellite acquisition and tracking. The on-site normal points generation algorithm has been implemented, the station has been connected to the international information network. The ERS-1 satellite has been included into the tracking schedule. The station range capability has been verified by experimental Etalon 1 ranging by April 1992. The ranging precision of 2-3 centimeters is obtained when ranging to ERS-1, Starlette and Lageos satellites.

The station operation has been cosponsored by the DGFI contracts ERS-1/7831/91,92 and the Smithonian Astrophysical Observatory contract, whose support in acknowledged.

Allied Signal

OPTICAL ATTENUATION MECHANISM

UPGRADES

MOBLAS and TLRS SYSTEMS

Richard Eichinger, Toni Johnson, Paul Malitson,
Tom Oldham, Loyal Stewart

Allied Signal Aerospace Company
BFEC/CDSLR
10210 Greenbelt Road
Seabrook, MD 20706
USA

Abstract

This poster presentation describes the Optical Attenuation Mechanism (OAM) Upgrades to the MOBLAS and TLRS Crustal Dynamics Satellite Laser Ranging (CDSLR) systems. The upgrades were for the purposes of preparing these systems to laser range to the TOPEX/POSEIDON spacecraft when it will be launched in the summer of 1992. The OAM permits the laser receiver to operate over the expected large signal dynamic range from TOPEX/POSEIDON and it reduces the number of pre and post calibrations for each satellite during multi-satellite tracking operations. It furthur simplifies the calibration bias corrections that had been made due to the pass-to-pass variation of the photomultiplier supply voltage and the transmit filter glass thickness. The upgrade incorporated improvements to the optical alignment capability of each CDSLR system through the addition of a CCD camera into the MOBLAS receive telescope and an alignment telescope onto the TLRS optical table.

The OAM is stepper motor and microprocessor based; and the system can be controlled either manually by a control switch panel or computer controlled via an EIA RS-232C serial interface. The OAM has a neutral density (ND) range of 0.0 to 4.0 and the positioning is absolute referenced in steps of 0.1 ND. Both the fixed transmit filter and the daylight filter are solenoid actuated with digital inputs and outputs to and from the OAM microprocessor. During automated operation, the operator has the option to overide the remote control and control the OAM system via a local control switch panel.

PHOTOELECTRONS RETURNED BY VARIOUS SATELLITES

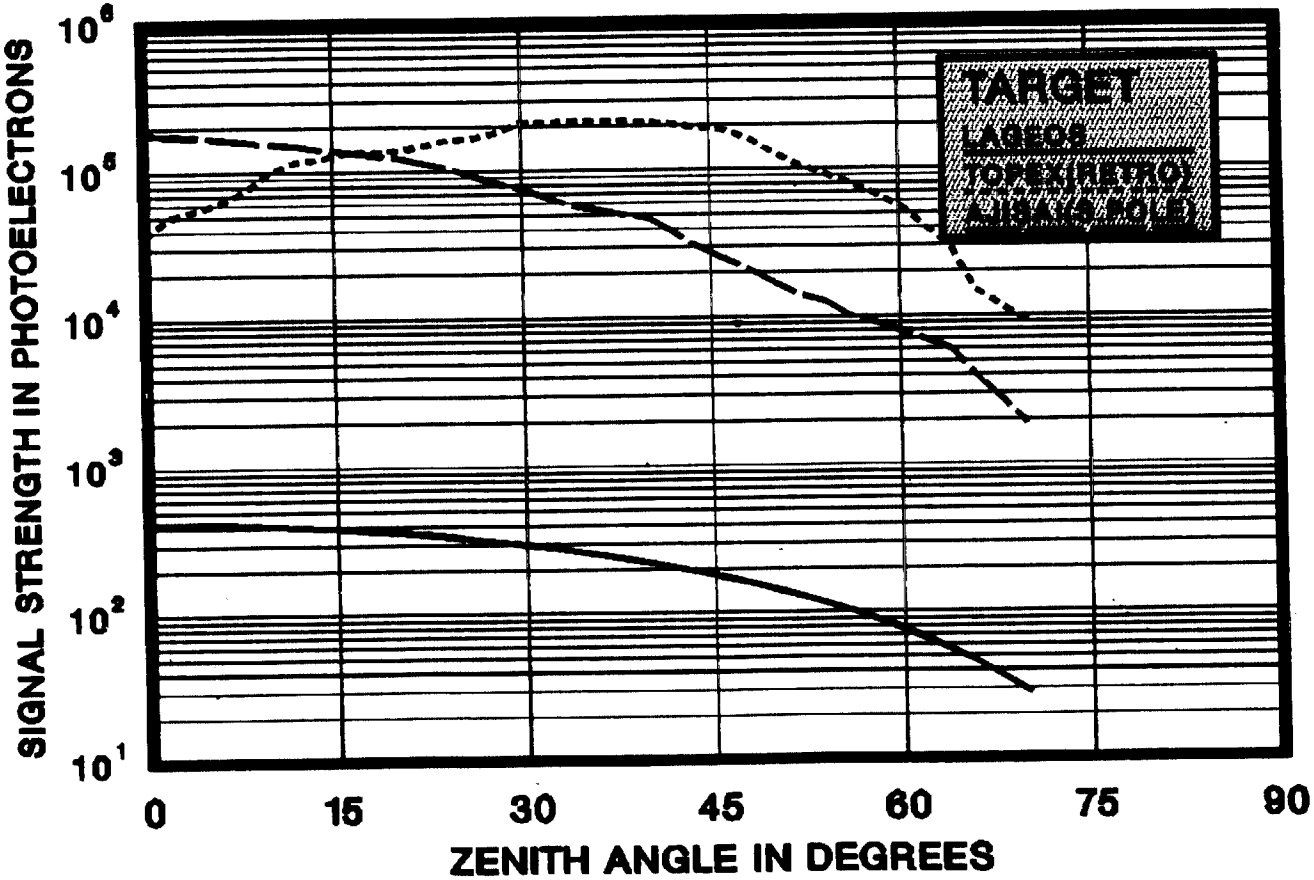

PHOTOELECTRONS RETURNED BY VARIOUS SATELLITES WITH OAM
(TOPEX/POSEIDON: 2.6 ND; AJISAI: 2.2 ND; LAGEOS: 0.0 ND)

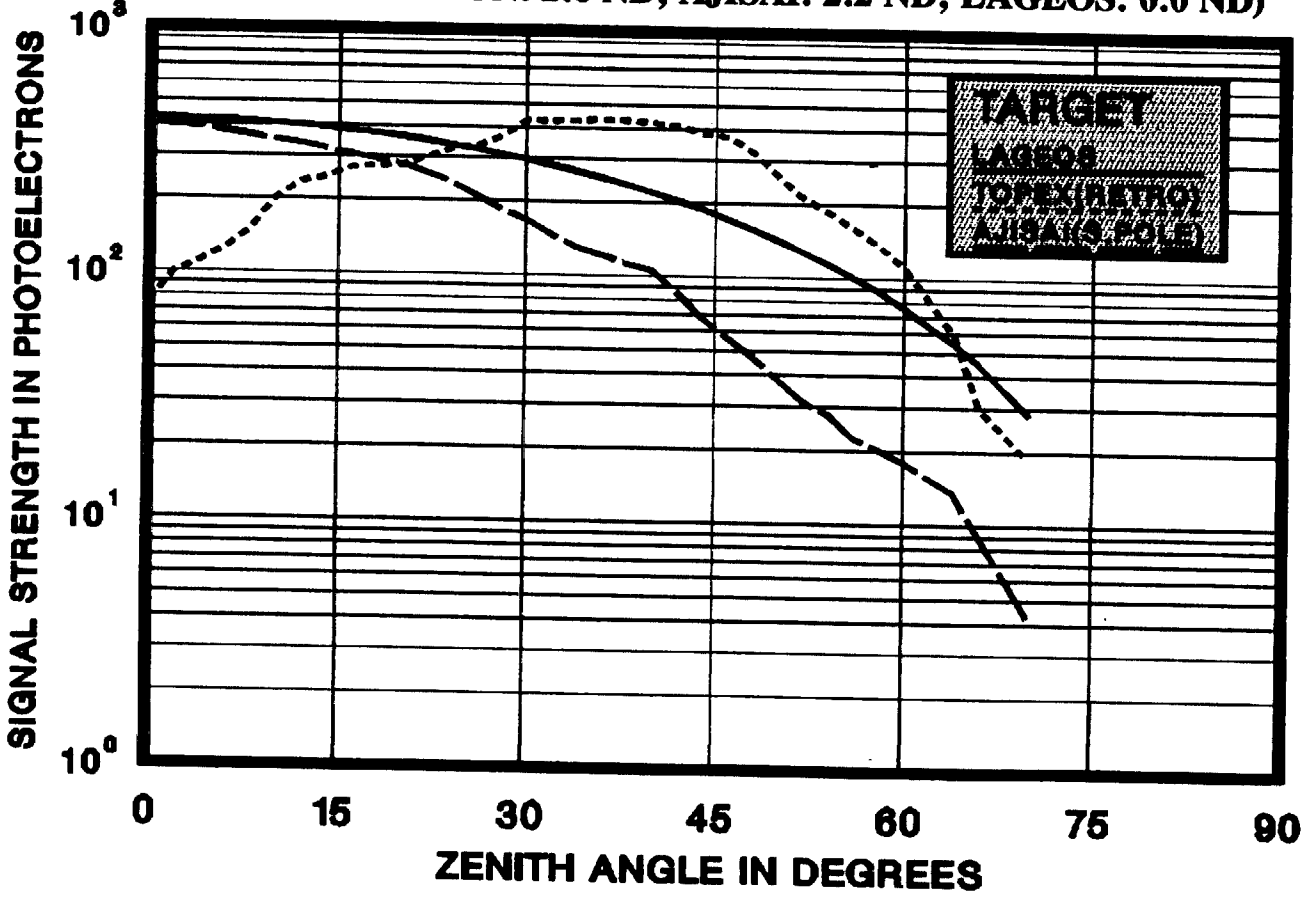

MOBLAS OAM UPGRADE SUBSYSTEM

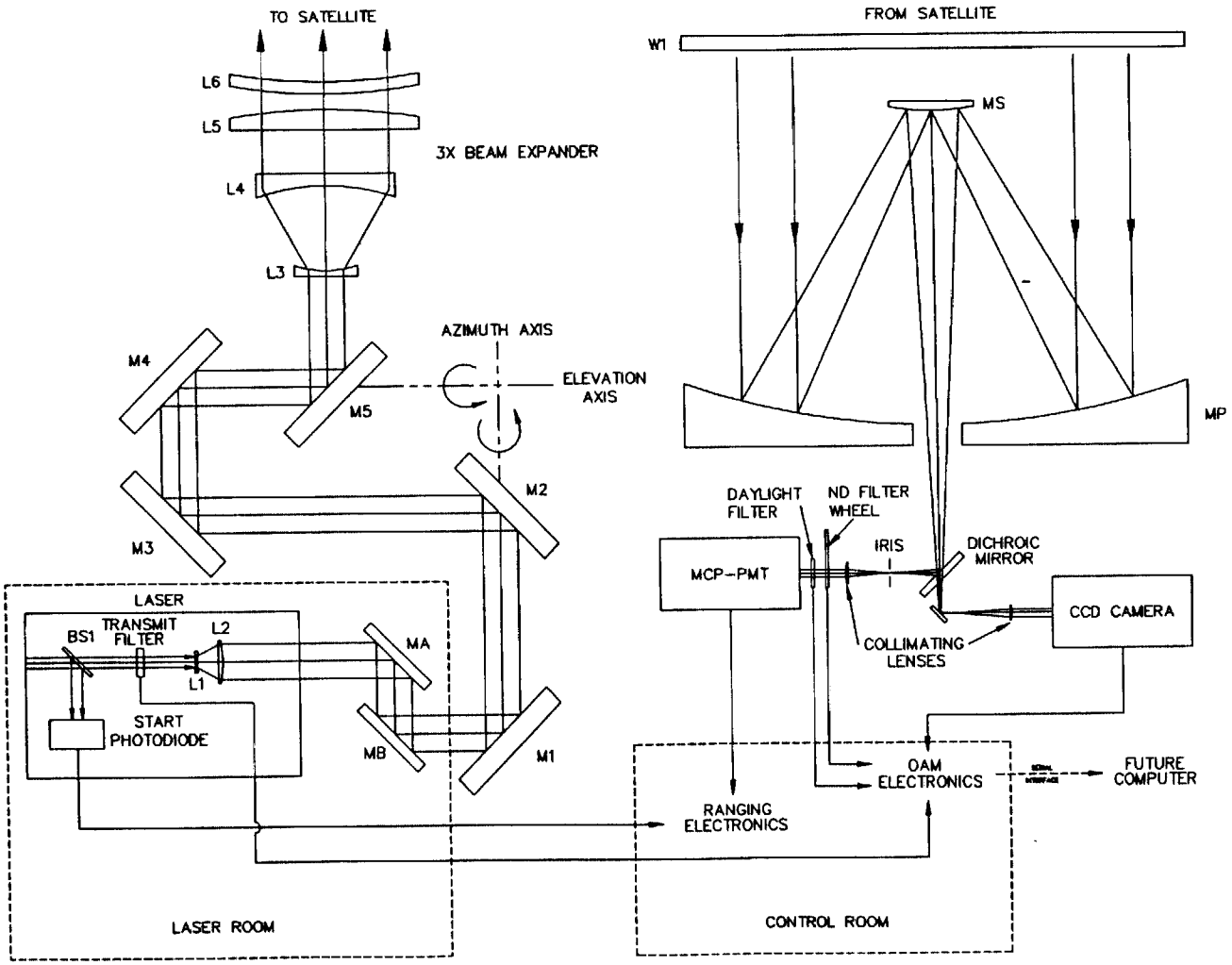

Bendix Field Engineering Corporation

TLRS OAM UPGRADE SUBSYSTEM

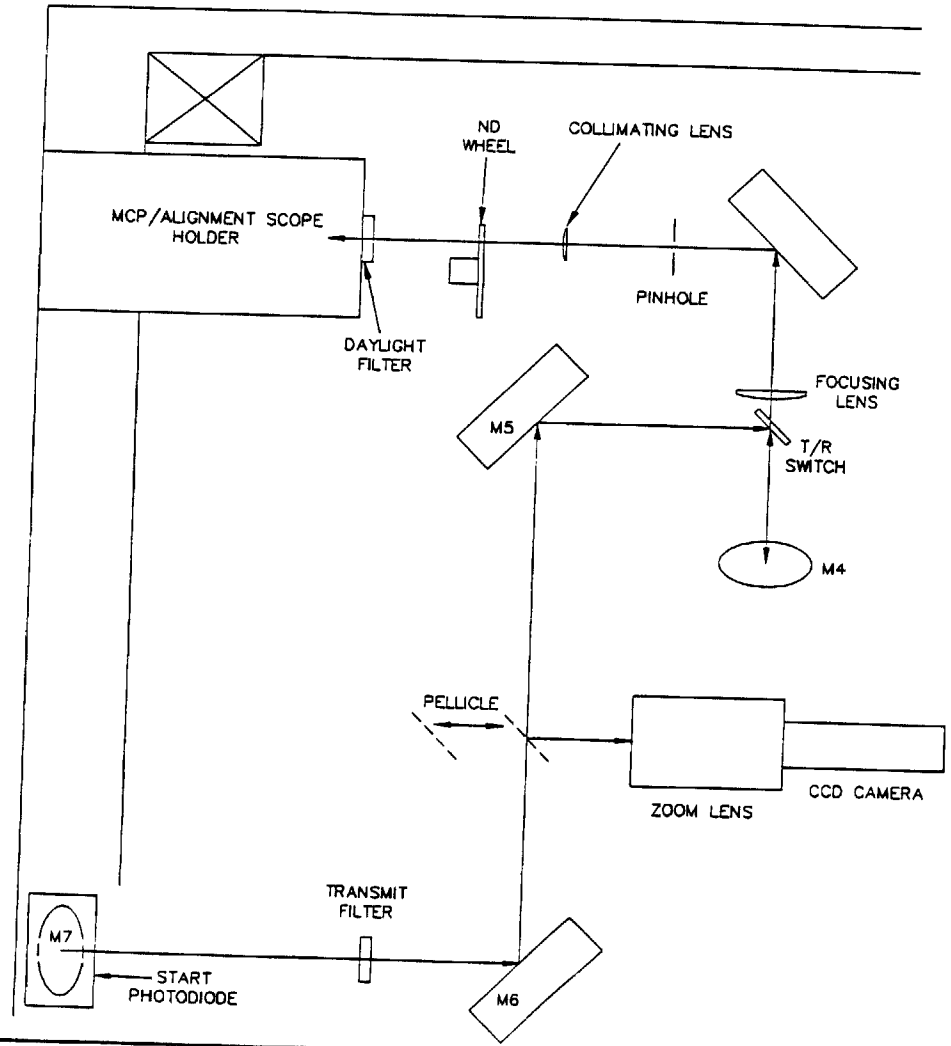

Bendix Field Engineering Corporation

Allied Signal

OAM UPGRADE SPECIFICATIONS

Stepper Motor and Control Electronics:
- Indexer/Controller: Compumotor model 500
  - Max. speed: 40 rps
  - Steps per revolution: 25,000
  - Digital I/O: 13 inputs, 8 outputs
  - Computer interface: EIA RS-232C
  - Software:
    - High level X-language
    - Variable assignments
    - Math functions
    - Conditional branching
    - Max. program locations: 99
    - Memory: 8k RAM
- Motor Drive: Compumotor model CT
- Miniature Stepper Motor: Compumotor model CT25-30

Neutral Density Wheel: Reynard part 522
- 0.0593 to 3.94 ND: 0 to 270 degrees, 7 mm dia. beam
- linearity of density: +/- 5%
- ar (532 nm, normal incidence, both sides): 0.1 % reflective
- substrate: 100 mm dia., BK-7, < 3 arcmin wedge

Dichroic Beam Splitter: Melles Griot substrate, coated by Omega
- 99 % reflective, 532 nm, unpolarized, 45 degree incidence
- approx. 85 nm FWHM relective about 532 nm
- 400 to 800 nm blocking
  - > 532 nm: 80-95 % transmitive
  - < 532 nm: 20-70 % transmitive
- ar (MgF) coating on one side
- substrate: BK-7, lambda/10, 1 arcmin wedge

Daylight Filters:
- Original MOBLAS: 10A @ 532 nm, Oriel
  approx. 40 % trans. (GSFC meas.)
  unknown blocking
- Original TLRS, new MOBLAS: 10A @ 532 nm, Omega
  60-65 % trans.
  uv to 900 nm blocking
- New TLRS: 3A @ 532 nm, Omega
  45 % trans.
  400 to 700 nm blocking

TLRS Pellicle:
- Uncoated: 8 % refl.
- Flatness: 2 lambda per 25 mm

OAM UPGRADE SPECIFICATIONS (continued)

Lenses:

MOBLAS Collimating lens: 36 mm fl, BK-7, ar (MgF)
Field lens: 1000 mm fl, BK-7, ar (MgF)
Achromat lens: 80 mm fl, ar (MgF)
TLRS Focussing lens: 150 mm fl, BK-7, ar (MgF)
Collimating lens: 60 mm fl, BK-7, ar (MgF)

Mirrors:

MOBLAS turning mirror: Edmund Scientific
lambda/8
enhanced aluminum
TLRS turning mirror: CVI
lambda/10
> 99.5 % refl.
BK-7 substrate
< 5 arcmin wedge

Alignment Telescopes, K&E Electro-Optical Products, Cubic Precision

Original MOBLAS: Model 71 2030 Bright Line Alignment Telescope
Magnification: 4x @ zero to 46x @ infinity
Resolving Power: 3.4 arcsec
Field of View: 42 mm @ zero, 37 min @ infinity focus
Effective Aperature: 42 mm
New TLRS: Model 71 2062 Line of Sight Telescope
Magnification: 23x @ 7 in. to 35x @ infinity
Resolving Power: 3.5 arcsec
Field of View: 7.4 mm @ 7 in., 47 min @ infinity focus
Effective Aperature: 38 mm

CCD Camera Systems:

MOBLAS CCD camera: Burle model TC652EA
510 (H) x 492 (V) pixels, EIA RS-170
Horizontal resolution: 383 TVL
Signal-to-noise: 50dB
Lens: 75 mm fl, F/1.4
Lens mount: Standard "C" or "CS"
Video Line Generator: Oracle model 1000
Video Monitor: Panasonic model TR-930B
TLRS CCD Camera: Pulnix model TM840
767 (H) x 483 (V) pixels, NTSC
TV resolution: 580 lines (H), 350 lines (V)
Signal-to-noise: 50 dB
Lens: 11-110 mm zoom
Lens mount: Standard "C"
Video Monitor: Panasonic model TR-930

ORIGINAL PAGE
BLACK AND WHITE PHOTOGRAPH

MOBLAS OAM UPGRADE

ORIGINAL PAGE
BLACK AND WHITE PHOTOGRAPH

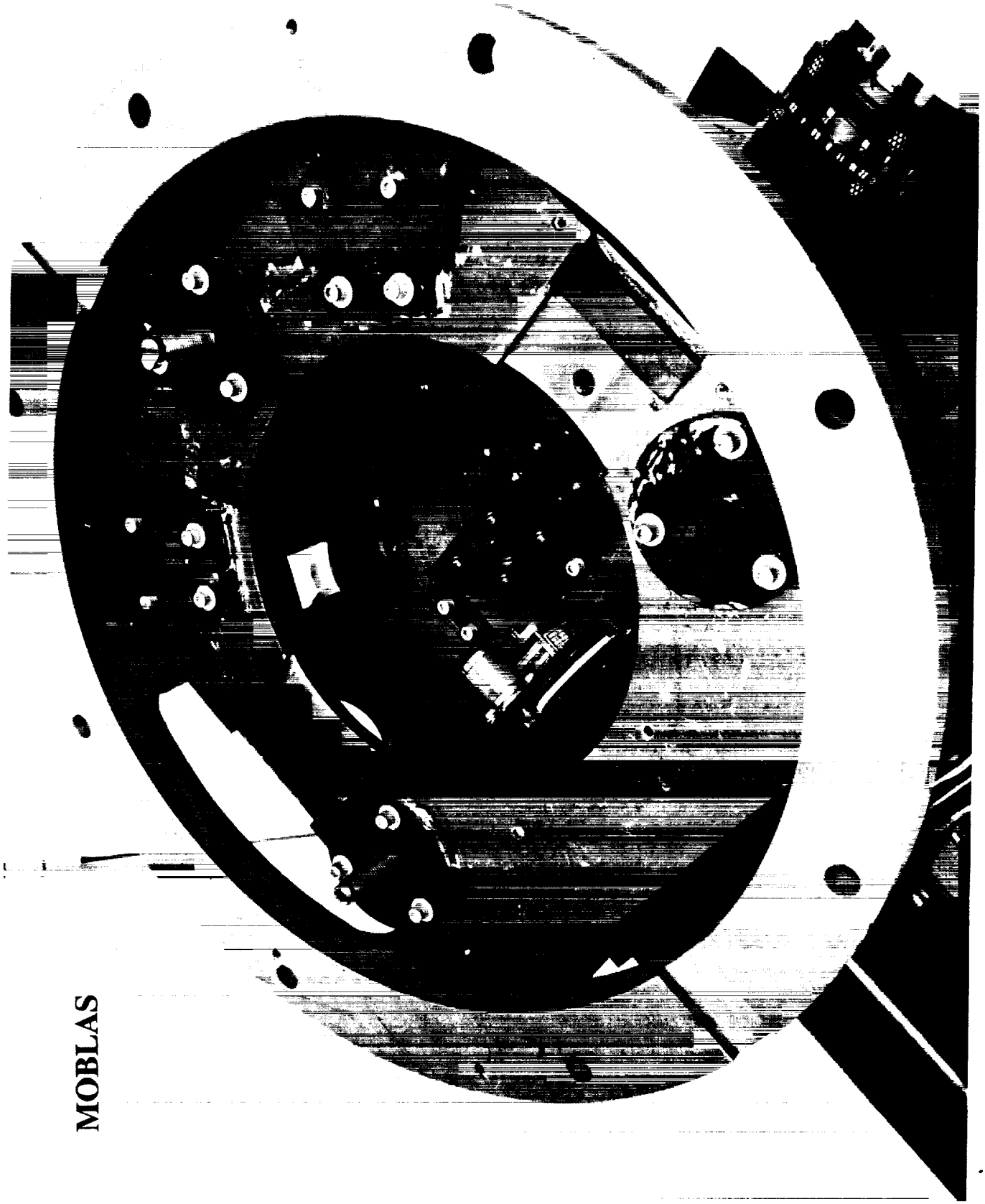

MOBLAS

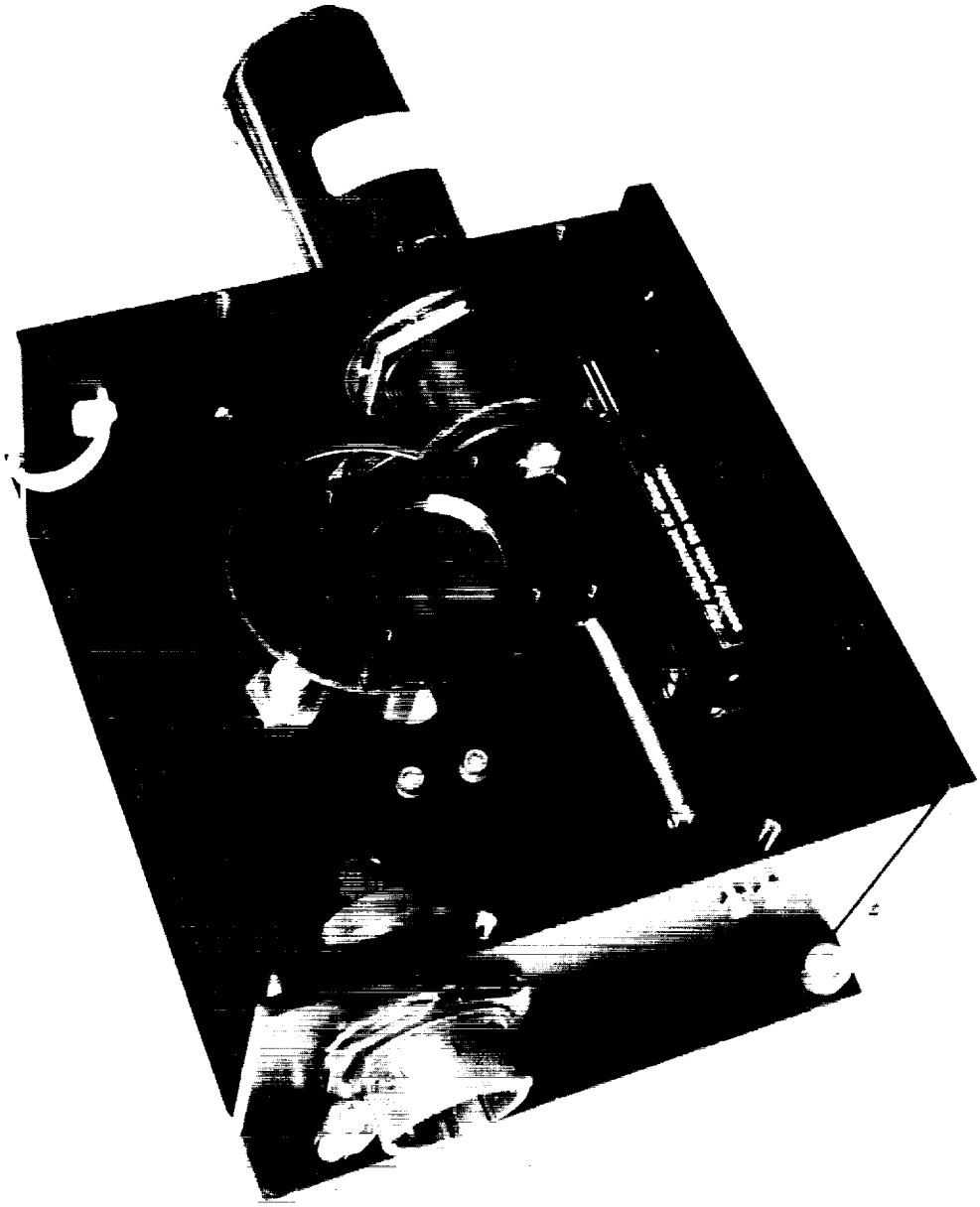

MOBLAS OAM

ORIGINAL PAGE
BLACK AND WHITE PHOTOGRAPH

TLRS OAM UPGRADE

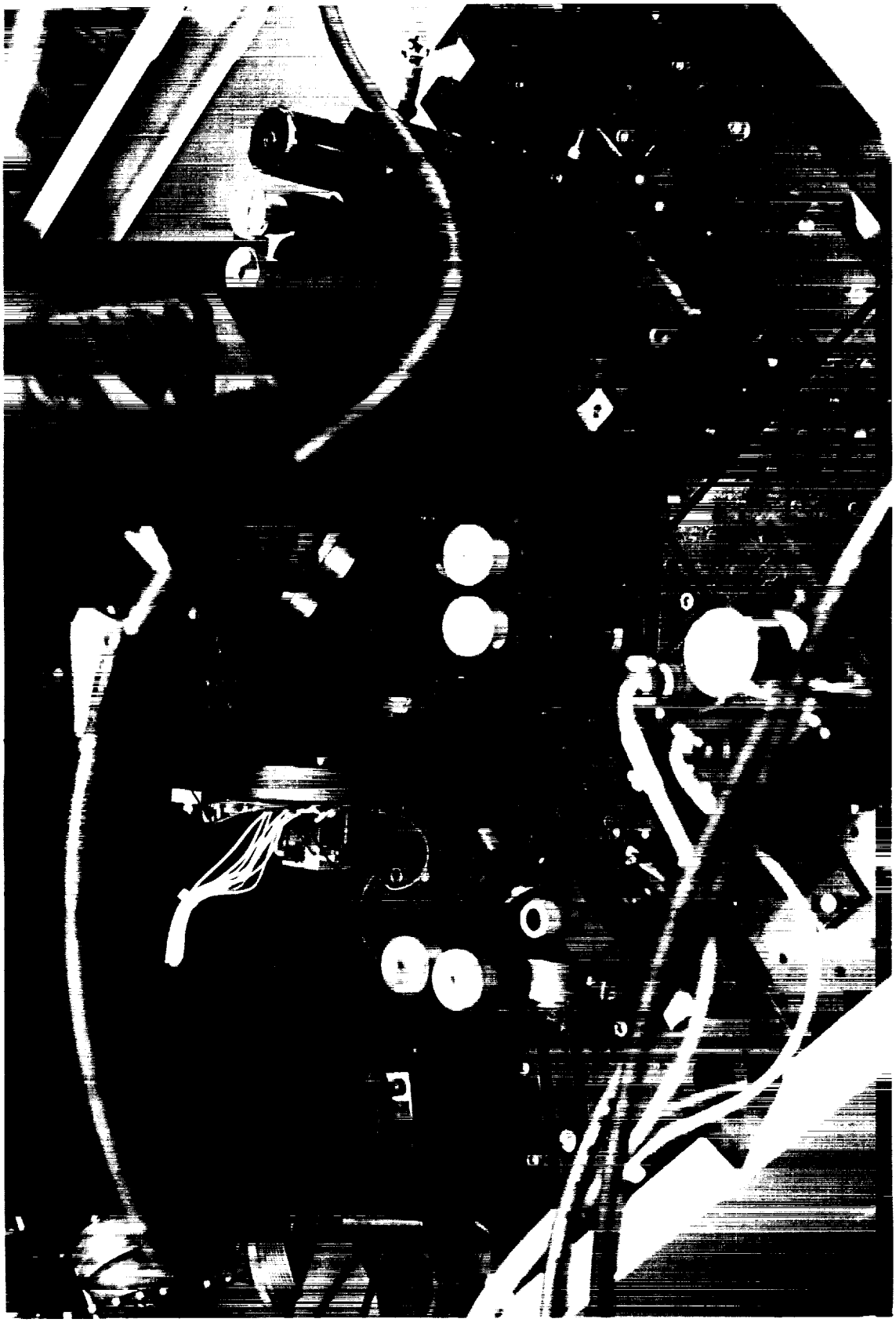

N94-15623

THE THIRD GENERATION SLR STATION POTSDAM NO.7836

H.Fischer, L.Grunwaldt, R.Neubert
GeoForschungsZentrum Potsdam
Telegrafenberg A17, D-O-1561 Potsdam
Phone: (03733)-310-0
Fax: (03733)-310-648
(03733)-22824
E-Mail: lasgrp@gfz-potsdam.dbp.de

The new SLR station Potsdam has been installed during Winter 1991/1992 in an existing dome near to the old ruby laser at Helmert Tower. It has been built around a one-meter-Coude telescope and is equipped by a 50 ps Nd-YAG laser and a SPAD receiver. First successful LAGEOS passes were obtained in May 1992 demonstrating 2-3 cm rms at the single photon level.
The new station will be used for experimental work and selected observation campaigns as well.

HARDWARE SPECIFICATIONS

Mount and Telescope:

One-meter Coude system type TPL (Riga University)
common transmit-receive path switched by rotating mirrors
step motor drives for azimuth and elevation

Receiver Package:

Silicon avalanche photodiode type C 30902 S-TC (integrated Peltier cooling)
operated in the Geiger mode with passive quenching
standard interference filter, spectral width 2 nm

Laser:

Nd-YAG with passive modelocking by dye #3274 (own construction)
KTP frequency doubler
main data at 532 nm: 10-20 mJ, 35-50 ps, 10 Hz

Time Interval Counter:

Stanford Res. Labs. type SR 620

Time Base:

GPS- receiver Datum Inc. type 9390-55134, internal Rb- standard

Control System:

Standard PC (HP Vectra 386) interfaced via IEEE-488 to the
specially designed control unit (step motor controller,
gate pulse generator, epoch counter with 100 ns resolution)

SOFTWARE SPECIFICATIONS

Orbit Reconstruction:

numerical integrator using point mass model for the gravitational field representation (Ch. Foerste)

Input : IRV's
Output: reference points in a space-fixed system, arbitrary time spacing (usually 10 sec)

Real Time Tracking:

Input : reference points, real time corrections
Output: control information with 10 Hz rep. rate
raw data

Prefiltering:

Input : reference points, raw data
Output: filtered data
interactive filtering using the same reference orbit as for tracking, polynomial fitting to the O-C's
(J. del Pino)

Star Calibration:

automatic star identification

Input : star positions (azimuth, elevation, epoch)
Output: mount-error-model parameters

On Site Normal Point Software:

EUROLAS OPAN S/W (Appleby and Sinclair)

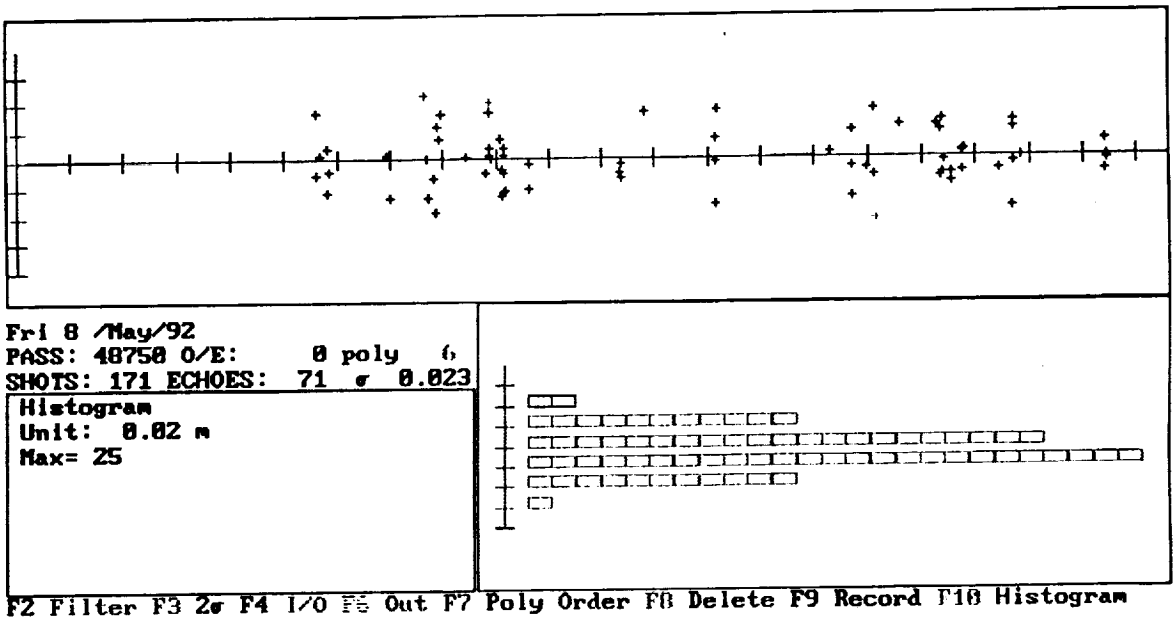

Screen copy of a LAGEOS test pass after filtering and polynomial fitting
upper part: residuals versus time (23 mm rms)
lower right: histogram of the residuals

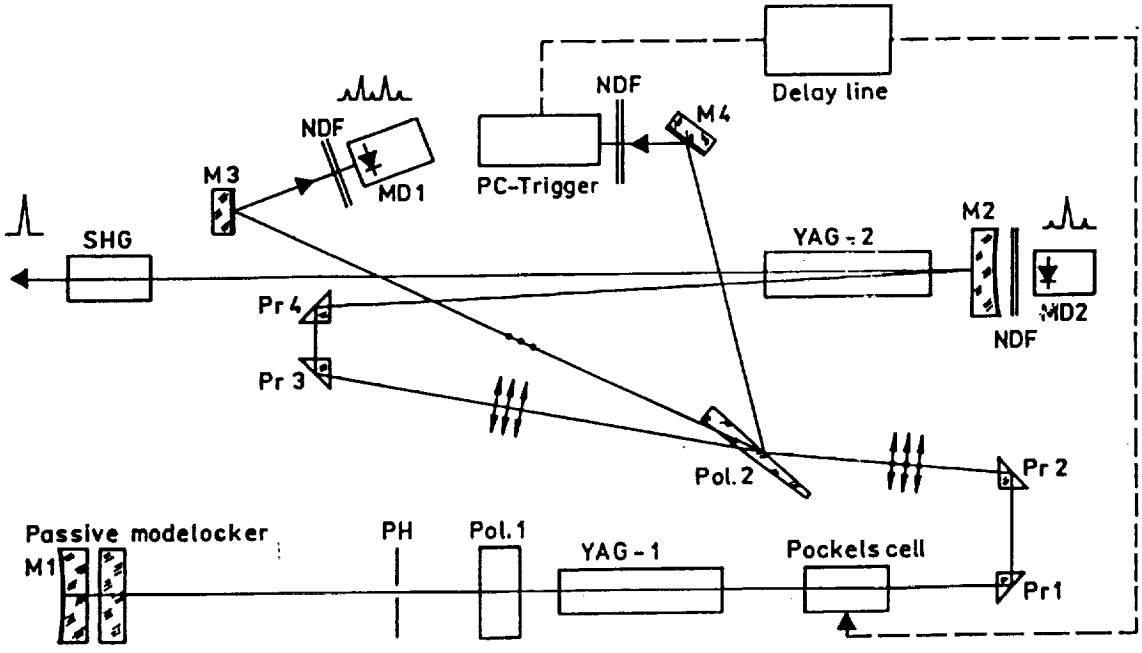

Optical scheme of the laser PLS-5
Symbols: Pr- prisms ; M- mirrors ; NDF- neutral density filters
MD- monitor photodiodes ; Pol- polarizers

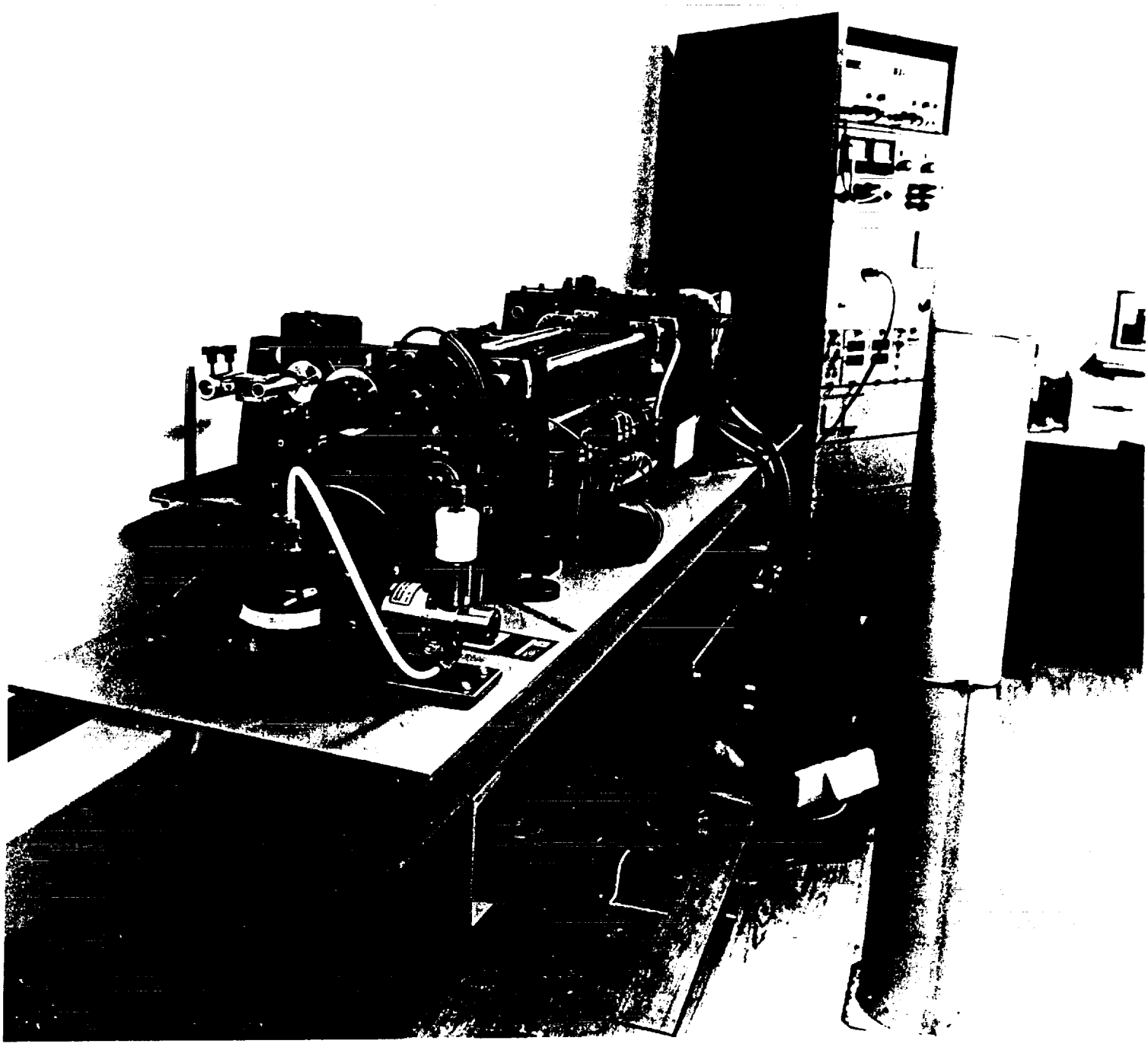

Laser control room

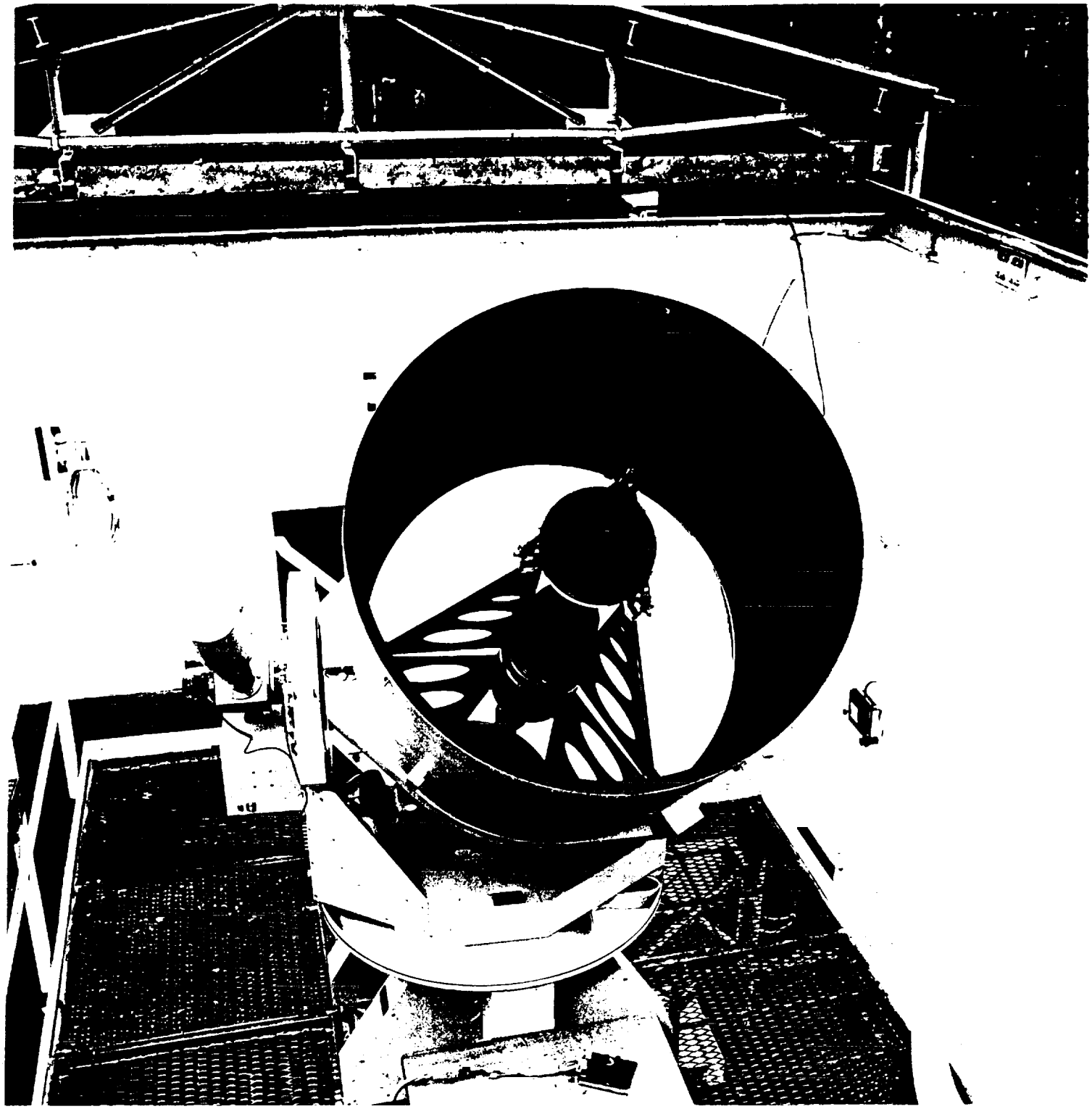

Close-up view of the TPL mount and telescope

N94-15624

PERFORMANCE COMPARISON OF HIGH SPEED MICROCHANNEL PLATE PHOTOMULTIPLIER TUBES

Thomas Varghese, Michael Selden, Thomas Oldham
Allied-Signal Aerospace Company
Bendix/CDSLR Network
Seabrook, Maryland 20706
U.S.A.

The transit time spread characteristics of high speed microchannel photomultipliers has improved since the upgrade of the NASA CDSLR network to MCP-PMT's in the mid 1980's. The improvement comes from the incorporation of 6μm (pore size) microchannels and offers significant improvement to the satellite ranging precision. To examine the impact on ranging precision, two microchannel plate photomultiplier tubes (MCP-PMT) were evaluated for output pulse characteristics and temporal jitter. These were a Hamamatsu R 2566 U-7 MCP-PMT (6μm) and an ITT 4129f MCP-PMT (12μm).

An Opto-Electronics diode laser and a Hewlett Packard 50 GHz digital sampling scope were used to sample a large number of pulses from each tube. The jitter of the sampling scope trigger was independently measured by splitting the diode laser pretrigger signal; one portion of the signal was used to trigger the scope, while the remaining signal was measured by the sampling scope. The scope trigger jitter was found to be about 2.6 ps. The laser pulses were $\simeq$ 40 ps in duration with a wavelength of 764 nm; the pretrigger-to-fire jitter of the diode laser is $\simeq$ 5 ps. During the experiment the pre-fire output of the diode laser control unit was used to trigger the sampling scope while the output responses of each MCP-PMT was captured by the sampling scope.

The optical input from the laser diode was adjusted to produce ~ 7 - 10 photoelectrons on the average. To measure the detector response, several thousand MCP-PMT output pulses were digitized to construct a pulse-distribution for each detector. Measurements were taken around the single (1 - 3 pe) photoelectron level as well as the multi-photoelectron ($\simeq$ 5 - 10 pe) level for each PMT. An average waveform was used to determine pulse rise-time and duration, while the standard deviation of the pulse distributions at the half-maximum point were used to determine the RMS of the temporal distribution within each sample set. Statistical information is printed below each graph. Each MCP-PMT was tested separately but under identical conditions. For the above experimental conditions, the ITT MCP-PMT produced about 36 ps jitter while the Hamamatsu MCP-PMT produced 9.1 ps jitter.

The sampling scope jitter and diode laser jitter has no significant effect on the 12μm PMT measurement while deconvolution improves the jitter of the 6μm tube to ~ 7 ps. The single photoelectron jitter can be estimated from these measurements to be ~ 110 ps and ~ 25 ps respectively for each tube.

The results of these tests suggest that the MCP-PMTs with 6 micron pore size has the potential to offer improved (x 2) satellite laser ranging data quality, especially at low photoelectron levels. Further testing of a gated Hamamatsu MCP tube in MOBLAS-7 in a parallel configuration using the NASA Portable Standard is planned for later this year. These tests will focus on relative performance at various signal levels as well as the response of the constant fraction discriminator to the higher bandwidth detector output.

DEVICE CHARACTERISTICS

FEATURE	HAMAMATSU R 2566 U-7	ITT MCP-PMT 4129f
Microchannel Plate	2-Stage (V-Type)	3-Stage (Z-Type)
Microchannel Dia	6um	12um
Max. Operating Voltage	-4600V	-3700V
Max. MCP Gain	$3x10^6$	$1x10^6$
Rise Time	≈108ps	~350ps
Fall Time	≈100ps	≈500ps
Full Width	≈160ps	≈550ps
Single Photoelectron Jitter	≈25ps	≤100ps

GAIN CHARACTERISTICS

HAMAMATSU R 2566 U-7

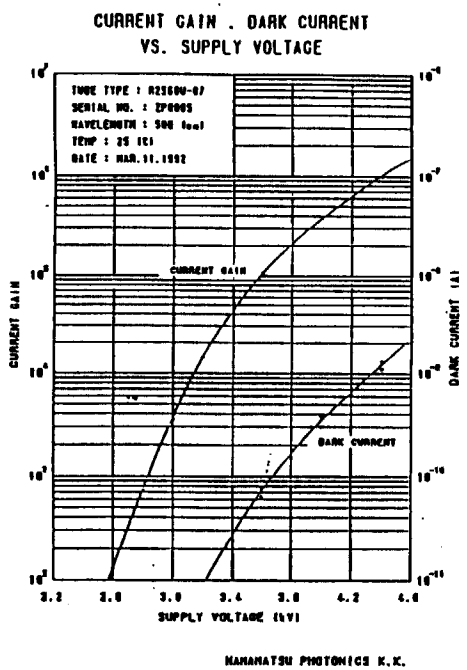

ITT MCP-PMT 4129f

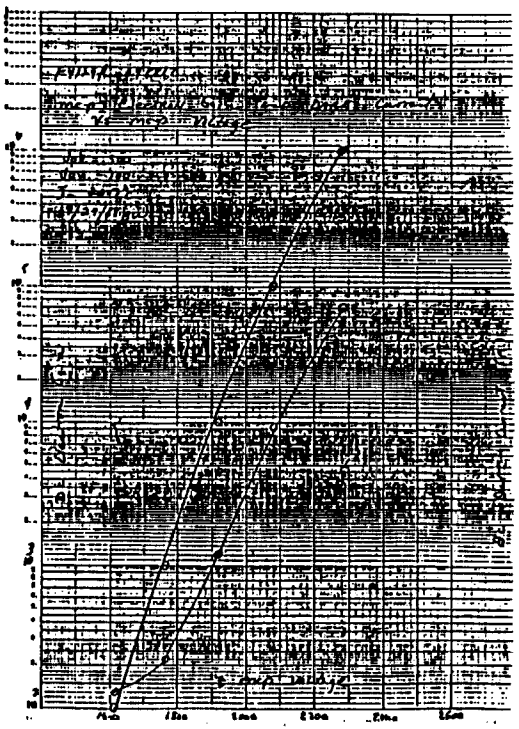

SPECTRAL RESPONSE

HAMAMATSU R 2566 U-7

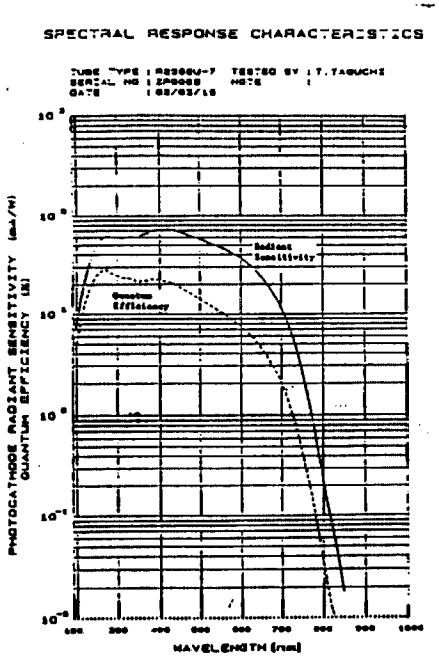

ITT MCP-PMT 4129f

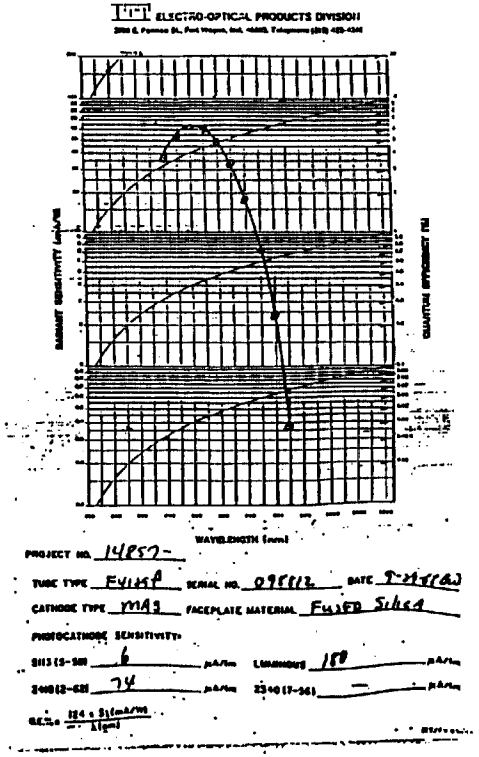

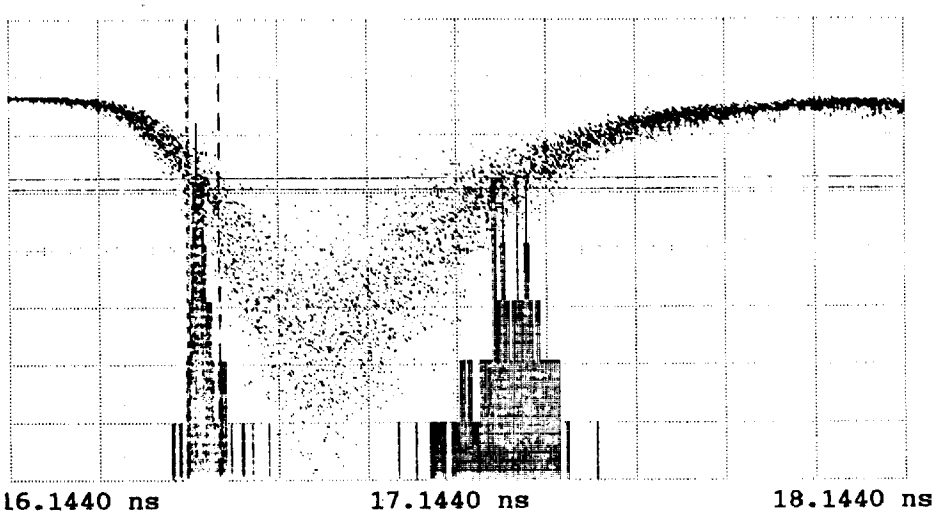

Ch. 1	= 80.00 mVolts/div	Offset	= -204.7 mVolts
Timebase	= 200 ps/div	Delay	= 16.1440 ns
Delta Windo	= 15.000 mVolts		
Window 1	= -105.00 mVolts	Window 2	= -120.00 mVolts
Delta %	= 77.10 %		
Upper	= 86.74 %	Lower	= 9.638 %
Delta T	= 71.9 ps		
Start	= 16.6126 ns	Stop	= 16.5407 ns
# Samples	= 255		
Mean	= 16.5767 ns	Sigma	= 35.9 ps

Trigger on External at Pos. Edge at 409.5 mVolts

MULTIPHOTOELECTON (8–10) RESPONSE OF SAMPLIING SCOPE MEASUREMENTS OF THE ITT MCP–PMT (F4129F).

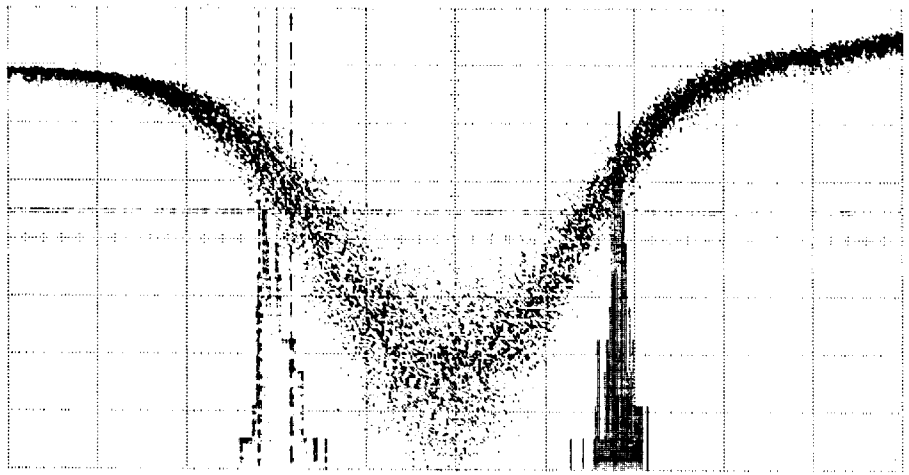

Ch. 1 = 50.00 mVolts/div		Offset = -140.0 mVolts	
Timebase = 50.0 ps/div		Delay = 19.4380 ns	
Delta Windo= 3.1250 mVolts			
Window 1 = -115.62 mVolts		Window 2 = -118.75 mVolts	
Delta % = 66.02 %			
Upper = 83.33 %		Lower = 17.30 %	
Delta T = 18.2 ps			
Start = 19.5960 ns		Stop = 19.5778 ns	
# Samples = 295			
Mean = 19.5869 ns		Sigma = 9.1 ps	

Trigger on External at Pos. Edge at 409.5 mVolts

MULTIPHOTOELECTON (8–10) RESPONSE OF SAMPLIING SCOPE MEASUREMENTS OF THE HAMAMATSU MCP–PMT (R 2566U–7).

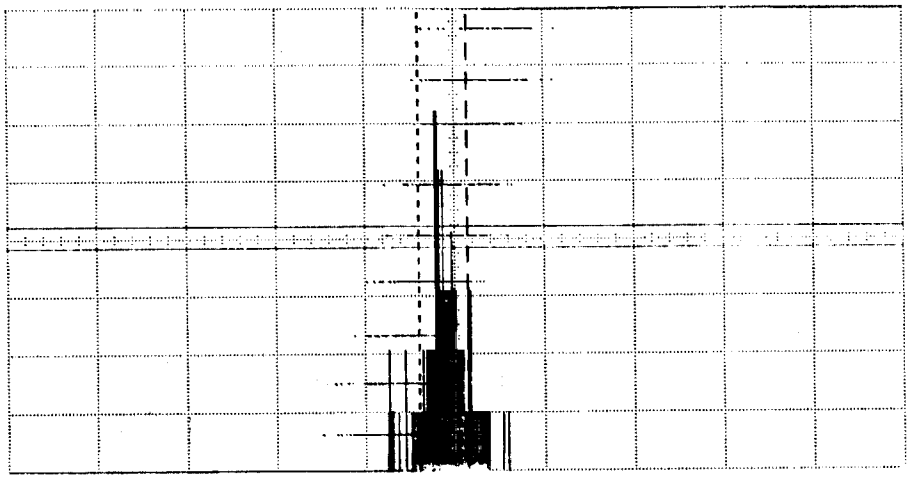

■Ch. 1 = 1.000 mVolts/div		Offset = 237.2 mVolts	
Timebase = 10.0 ps/div		Delay = 18.5280 ns	
■Delta Windo=-375.00 uVolts			
■Window 1 = 237.09 mVolts		Window 2 = 237.46 mVolts	
■Delta % = 71.84 %			
■Upper = 85.43 %		Lower = 13.59 %	
■Delta T = 5.3 ps			
■Start = 18.5794 ns		Stop = 18.5741 ns	
# Samples = 100			
■Mean = 18.5767 ns		Sigma = 2.6 ps	

Trigger on External at Pos. Edge at 409.5 mVolts

SAMPLING SCOPE JITTER CALIBRATION USING PULSES WITH FIXED SEPARATION.

SUMMARY

- 6 um core diameter microchannel plate photomultiplier tubes demonstrate significantly improved (4x) transit time spread than the 12 um core diameter tubes (25 pscosecond vs 110 picosecond)
- The state of the art Hamamatsu MCP-PMT 2566U has a bandwidth of ~3GHz which is approximately 3x better than the 12 um core diameter tubes; this will improve the bandwidth for post detection signal processing and the laser ranging precision.
- Sub-cm single photoelectron ranging to Lageos can be obtained using current SLR instrumentation.
- Advantageous especially for low aperture telescope systems.

STATION REPORT ON THE GODDARD SPACE FLIGHT CENTER (GSFC) 1.2 METER TELESCOPE FACILITY

Jan F. McGarry
Thomas W. Zagwodzki
Arnold Abbott
John J. Degnan
NASA/Goddard Space Flight Center
Greenbelt, Maryland 20771, USA

Jack W. Cheek
Hughes/STX
Lanham, Maryland 20706, USA

Richard S. Chabot
David A. Grolemund
Jim D. Fitzgerald
Bendix Field Engineering Corporation
Seabrook, Maryland 20706, USA

ABSTRACT

The 1.2 meter telescope system was built for the Goddard Space Flight Center (GSFC) in 1973-74 by the Kollmorgen Corporation as a highly accurate tracking telescope. The telescope is an azimuth-elevation mounted six mirror Coude system. The facility has been used for a wide range of experimentation including helioseismology, two color refractometry, lunar laser ranging, satellite laser ranging, visual tracking of rocket launches, and most recently satellite and aircraft streak camera work. The telescope is a multi-user facility housed in a two story dome with the telescope located on the second floor above the experimenter's area. Up to six experiments can be accommodated at a given time, with actual use of the telescope being determined by the location of the final Coude mirror. The telescope facility is currently one of the primary test sites for the Crustal Dynamics Network's new UNIX based telescope controller software, and is also the site of the joint Crustal Dynamics Project / Photonics Branch two color research into atmospheric refraction.

INTRODUCTION

The 1.2 meter telescope is located about 5 kilometers from the Goddard Space Flight Center in the middle of the Beltsville Agricultural Research Center (see Table 1). This telescope has been part of a wide variety of experiments since its development in

1973-74 by the Kollmorgen Corporation (now part of Contraves). It was originally built for Goddard as a highly accurate tracking telescope to use in the development and testing of satellite laser ranging (SLR) systems. Although there was preliminary work done in this area by both T.Johnson (GSFC) and C.O.Alley (University of Maryland), it was not until the mid 1980s that the telescope facility realized its full potential in this area with the development of the Experimental Satellite Laser Ranging System (ESLRS). The telescope's primary usefulness is in the areas of photon gathering and astronomical testing. As an astronomical observatory, it has drawbacks; these include the air bearings which distort the images, and the poor quality of seeing in the Baltimore-Washington region. The proximity to Goddard, however, makes the 1.2m telescope an excellent test facility for astronomical experiments, and the large aperture, highly accurate tracking capability, and excellent laboratory facilities make it an ideal system for developing and testing new ideas in satellite laser ranging.

TELESCOPE CHARACTERISTICS

The 1.2 meter telescope system is a multi-user azimuth-elevation mount housed in a two story dome (see Figure 1). The telescope is located on the second floor above the experimenters' area. The 15 ton assembly, as seen in Figure 2, consists of three sections: the yoke assembly, the trunnion with the primary mirror cell, and the forward tube truss (holding the secondary mirror). Air bearings, which raise the mount 0.005 millimeters above the support, are used for azimuth rotation to avoid the friction caused by roller bearings. The telescope is a six mirror Coude system with an effective system focal length of 33.13 meters (shown in Figure 3). The primary mirror is paraboloidal, 1.2 meters in diameter, with a focal distance of 3.2 meters. The secondary mirror is hyperboloidal, 0.4m in diameter, and is motor driven over a range of approximately 1.5 centimeters, giving the system the ability to focus from one kilometer to infinity. Three other flats direct the light from the telescope down into the experimenters' area below. Here a sixth mirror (the steering or pit mirror) can be rotated to direct the light to any of six experimenters' ports located at equidistant points around the circular pit area. All mirrors have been recently recoated with a broadband aluminum coating and SiOx overcoating. Peak reflectivity ranges from 88% to 92%.

The telescope was designed to meet a 20 arcsecond absolute positioning with a 5 arcsecond repeatability. In the current configuration the pointing is actually around 1 arcsecond due to the 28 term trigonometric error model used by the servo system computer. The servo system computer is a COMPAQ 386/20Mhz with 4Mbytes of memory. The tracking programs are written mainly in FORTRAN and run under the MS-DOS operating system. Timing for the software tasking is provided by 1Hz and 20Hz signals (accurate to 1 microsecond) and by the 36-bit NASA time code generator which

consists of day of year and time of day. The computer closes the servo loop by reading the 22-bit encoders and performing software servo compensation; the telescope drive signals are output at 20Hz to provide a smooth track. The mount is able to track to the 1 arcsecond level at rates of up to 1 deg/sec in azimuth and up to 0.5 deg/sec in elevation. The actual speed of the mount is software limited to under 6 degrees per second in both axes.

The telescope facility has the ability to track satellites, aircraft, planets, the moon, the sun, and the stars. Predictions for satellites can either be in the form of Inter-Range-Vectors or NORADs. Aircraft acquisition uses onboard GPS data relayed to the ground in real-time or just visual observation; tracking is accomplished by using the digitized camera image of an onboard light source (such as running lights or laser diode beacon). The right ascension and declination of stars comes from the FK4 (soon to be FK5) catalog or from operator type-in of apparent position. Planetary prediction data, as well as the moon and the sun, comes yearly from the Flight Dynamics Support Branch at Goddard in the form of Chebyshev polynomials.

Acquisition aids are also available with the telescope. Operators in the dome can view through a 0.3 meter finder telescope boresighted with the main telescope. Also boresighted on the 1.2m telescope are an RCA Silicon Intensified Tube (SIT) camera and a CCD camera. An RCA SIT camera is also located in the pit area below the telescope in the focal plane. This camera was used during the RME experiment (see experiments listed below) and is also used for star calibrations. The video image from all three cameras can be viewed in the telescope control room and can be sent through the Colorado Video X-Y Digitizer for closed loop tracking by the servo computer. Table 2 lists the pertinent information on the finder scope and cameras.

PAST TELESCOPE EXPERIMENTS

PLANETARY OBSERVATION

The telescope served as a field test facility for bread board optical heterodyne spectrometers in the near and thermal infrared. This work was in support of earth and planetary atmospheric observations and was performed in the 1970s and early 1980s by M. Mumma and colleagues at NASA/GSFC.

A Laser Heterodyne Spectrometer for Helioseismology was an experiment performed at the telescope facility in the early 1980s to measure solar oscillations by mixing solar radiation with the output of a frequency stabilized CO_2 laser. D. Glenar of Colgate University was the principal investigator in support of ongoing work at GSFC.

ATMOSPHERIC LIDAR

A laser induced resonant fluorescence experiment took place in the early 1980s. This experiment, conducted by C.Gardner of the University of Illinois Department of Electrical Engineering, measured the density of atomic sodium at altitudes up to 100km using a dye laser mounted to the telescope trunnion.

LUNAR LASER RANGING

The design and testing of a high average power laser and special electronics for lunar ranging was overseen by C.O.Alley of the University of Maryland Department of Physics. Limited lunar ranging from the telescope was also accomplished during the early 1980s.

TIME COMPARISONS

C.O.Alley and colleagues at the University of Maryland set up and operated a laser link to the United States Naval Observatory (USNO) from the 1.2m telescope facility for time comparisons in support of the LASSO experiment. This link provided the highest precision time comparison (30 psec) as of that date (1983).

A comparison of East-West versus West-East one way propagation times of laser light pulses was also performed by C.O.Alley and R.A.Nelson. This was the first experiment to make such a direct measurement and provided the highest precision ever achieved in a time comparison with a transported atomic clock (40 picoseconds to USNO and back).

AUTOMATED GUIDING AND TWO-COLOR REFRACTOMETRY

D.Currie and D.Wellnitz of the University of Maryland Department of Physics developed the Automatic Guider System (AGS) during the period from 1975 to 1978 for automated tracking of continuous light sources. The AGS was used to perform automated star calibrations at the 1.2m telescope during the late 1970s.

D.Currie and D.Wellnitz also developed and tested at the 1.2m telescope a Two Color Refractometer, based on the AGS design, to measure atmospheric refraction. The final experiment performed at the USNO measured atmospheric refraction in a single night to a precision previously requiring one month's observations.

SINGLE COLOR SATELLITE LASER RANGING

The Experimental Satellite Laser Ranging System (ESLRS) operated as an R&D facility from 1982 to 1986. It was one of the first centimeter level, high return to transmit ratio satellite laser

ranging systems. This system was developed by T.Zagwodzki, J.McGarry and J.Degnan of NASA/GSFC.

The NASA/RME experiment in 1991 used the U.S.Air Force low orbiting, high lidar cross-section Relay Mirror Experiment satellite to investigate streak camera returns from satellites, and to develop and test a system design for later two color work. Streak camera waveforms from RME showed clearly resolved responses from the individual cubes on the satellite. This experiment was conducted by T.Zagwodzki and J.McGarry.

TWO-COLOR STREAK CAMERA AIRCRAFT LASER RANGING

The goal of this experiment was to determine the azimuthal variations in the atmospheric induced range delay using doubled (532nm) and tripled (355nm) frequencies from the facility's Nd:YAG laser to a corner cube mounted on the NASA T-39 aircraft. Waveforms were recorded with a Hamamatsu C1370 2-psec resolution streak camera. The aircraft was acquired by using a GPS receiver onboard the aircraft whose output was transmitted to the ground computer via a radio link. Once the aircraft was visually acquired, the ground computer was able to lock onto and track the aircraft's laser diode beacon by digitizing the image seen in a camera mounted on the telescope. This experiment was successfully completed in early August 1992. The principal experimenters were P.Millar, J.Abshire, J.McGarry, and T.Zagwodzki, all of NASA/GSFC.

CURRENT TELESCOPE PROJECTS

TWO-COLOR STREAK CAMERA SATELLITE LASER RANGING

Recent upgrades to the ESLRS at the 1.2m telescope facility have been made to allow measurements of two color differential delay to the ERS-1, STARLETTE and AJISAI satellites using a single-photoelectron sensitive Hamamatsu Streak Camera. Differential two color measurements will be used to analyze the accuracy of existing satellite ranging atmospheric refractivity models. This work is being performed by T.Zagwodzki, J.McGarry, J.Degnan, all of GSFC, T.Varghese of Bendix, and colleagues from GSFC, Bendix and Hughes-STX.

SATELLITE LAUNCH TRAJECTORY TRACKING

In support of the Office of Naval Research and later the Air Force SDIO work, the University of Maryland has been observing the Firefly and Firebird series of launches from Wallops and Cape Canaveral using a wide field camera installed on the 1.2m telescope and the University of Maryland Optical Metric Mapper at the Coude focus. Acquisition is provided by realtime Launch Trajectory Acquisition System (LTAS) data via a high speed direct link. This

work is being performed by D.Currie and D.Wellnitz of the University of Maryland.

SUPPORT OF LASSO EXPERIMENT

Attempts at visual acquisition of the Meteosat satellite (MP2), in order to range to the LASSO experiment, have been attempted using both the RCA Silicon Intensified Target camera on the mount and at the Coude focus, and using the University of Maryland Zibion camera installed on an auxiliary 12-inch telescope mounted to the 1.2m telescope. Due to the low magnitude of the visual MP2 and the poor seeing in the Baltimore-Washington area, all attempts at seeing MP2 to date have been unsuccessful. This work has been a joint effort between the Crustal Dynamics Project at GSFC, the Photonics Branch at GSFC, and the University of Maryland Physics Department.

MONITORING LAGEOS SATELLITE'S SPIN

Evaluation is in progress to determine the feasibility of monitoring the spin vector of the LAGEOS satellite (and later LAGEOS II) to support the prospective experiment to measure the Lense-Thirring Effect predicted by General Relativity. This is a joint experiment involving NASA, the Italian Space Agency, and the U.S.Air Force. The University of Maryland effort is being conducted by D.Currie, D.Wellnitz and P.Avizonis.

SOFTWARE DEVELOPMENT AND CHECKOUT

New CDP Network Telescope Controller Software is being designed to replace all of the telescope computers in the NASA Network with 486 compatible computers. The 1.2m telescope is the primary test system for the new software which will operate in the UNIX environment and will provide a user friendly, menu driven, graphical interface for the crews. The software team consists of J.McGarry (GSFC), J.Cheek (Hughes-STX), R.Ricklefs (University of Texas), P. Seery (Bendix), and K.Emenheiser (Bendix).

ACKNOWLEDGEMENTS

The authors would like to thank Jack Bufton (GSFC), Carol Alley (University of Maryland), and Dennis Wellnitz (University of Maryland) for detailed information on past projects at the telescope. A special thanks goes to the CDP SLR Manager, Larry Jessie, for photographing the telescope.

Table 1: 1.2 meter telescope location

1.2m TELESCOPE LOCATION	North American Datum 1927 CLARK 1866 ellipsoid
LATITUDE (geodetic)	39.02136044 degrees
LONGITUDE (east)	283.31712961 degrees
HEIGHT (above ellipsoid)	0.053198 km

Table 2: Acquisition and Tracking Aids

	Field of View	Dimmest object that can be seen
SIT camera in pier	70 mdeg diameter	8th magnitude
Finder scope	250 mdeg diameter	9th magnitude
CCD camera	200 by 300 mdeg	3rd magnitude
SIT camera on mount	2 by 3 degrees	8th magnitude

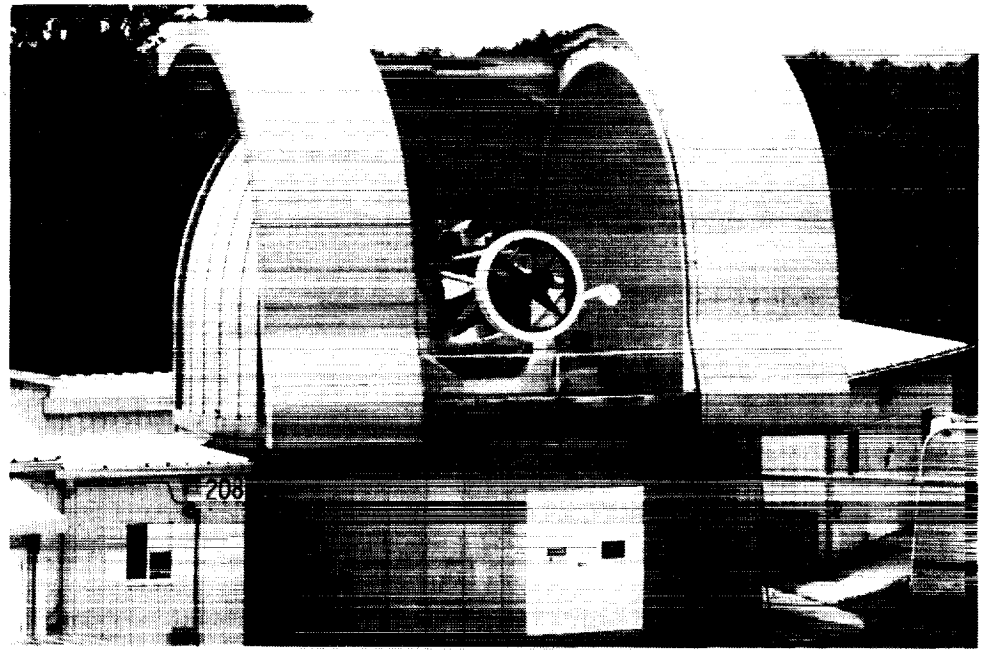

Figure 1: 1.2 meter telescope facility

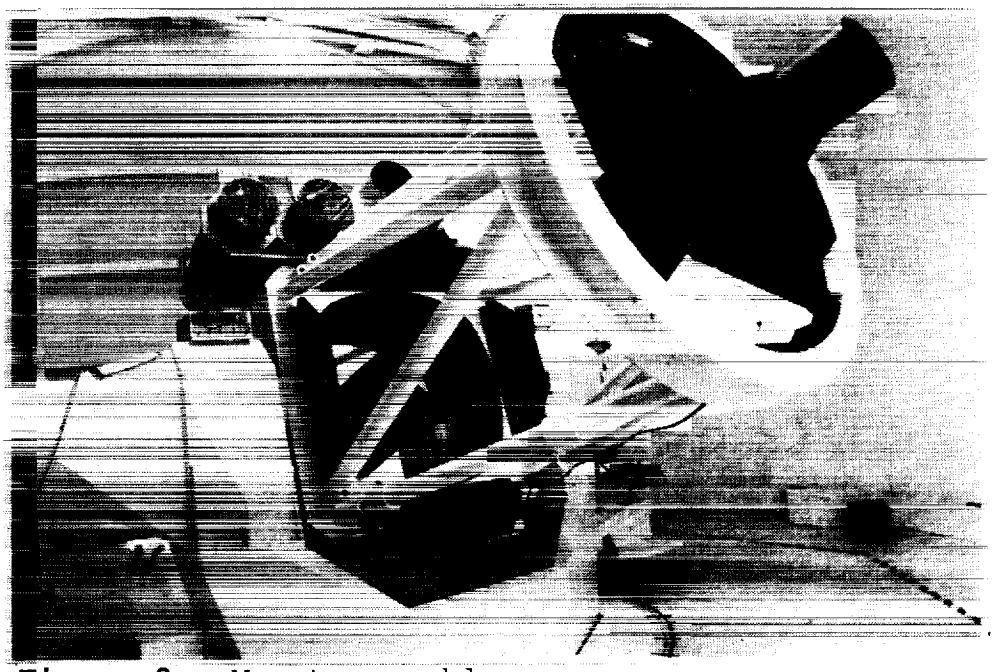

Figure 2: Mount assembly

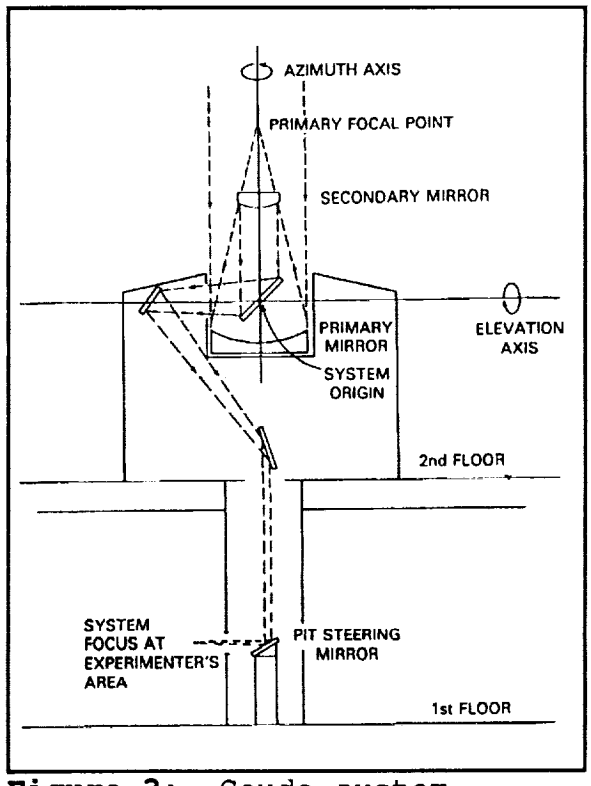

Figure 3: Coude system

Session Summaries

SESSION SUMMARIES

On the last day of the conference, each of the session chairman were asked to summarize, in vu-graph form, major conclusions or observations distilled from the individual talks within their sessions. These vu-graphs are reproduced in the following pages (with some minor editing on my part to improve clarity and eliminate duplication) along with comments made by workshop participants following the formal presentation by the session chairman. I have made no attempt in this record to identify the source of individual comments.

John Degnan

SCIENTIFIC APPLICATIONS AND MEASUREMENTS REQUIREMENTS

Bob Schutz/Richard Eanes

The science applications of SLR were summarized as follows:

Mean Gravity Field

Gravity field improvements - GEM-T3, TIG2, GRIM

Gravity Field Fluctuations/Variability

Longterm J_2
18.6 year tide
seasonal correlation with atmosphere

Terrestrial Reference Frame/Earth Orientation

Polar Motion
0.5 milliarcsecond routine accuracy on X and Y for 3 day values
1 day series available
Rapid Service UT1
Possible use of ETALON to extend to higher frequencies
Motion of network relative to center of mass of Earth/oceans/atmosphere
RMS 1 cm in X,Y; 3 cm in Z
Relative Station Positions
Best: 0.5 cm
Typical: 1-2 cm
Relative Motion
Horizontal velocities: 1 to 10 mm/yr for 40 or 50 sites
Vertical motions: Available for the "best-behaved sites"

Ocean Surface Study with SLR tracked altimetric satellites

ERS-1 orbits controlled by laser tracking

Time Transfer

Preliminary LASSO results from Grasse and MLRS $<$ 100 ps

SCIENCE GOALS AND REQUIREMENTS

GOALS	REQUIREMENTS
Mean Gravity Field 2 cm LAGEOS < 10 cm TOPEX,AJISAI, STARLETTE	Better control of systematic error Better global coverage Satellite campaigns Altimetric satellite tracking
Gravity Field Variations	Continued operations by stable network Multiple targets
Earth Orientation	Continued operations by core network Better coverage of sidereal day Multiple targets
Terrestrial Reference Frame	Continued operations by core network Subcentimeter control of systematics Better Southern Hemisphere coverage
Ocean Topography	More ERS-1 coverage Good TOPEX support
Time Transfer	More attempts with Meteor-P2 Wider participation CRL,OGO

COMMENTS

(1) The breadth of SLR applications is not adequately known in the scientific community.

(2) It is essential that instrumental errors in SLR be minimized at a small level because the scientific analyses based on SLR could be either misled or limited by such systematics.

(3) The global SLR community needs to assist all participants to reach a uniform level of performance and a common operational view.

(4) Developments in two color techniques are important, but the competitiveness, and perhaps survival, of SLR will not be accomplished solely on those efforts. We, as a community, must find the right balance between new developments and conducting operations, i.e. regular and high quality tracking.

(5) SLR should play to its strengths, e.g. gravity and vertical positioning.

(6) The community should establish ties to Global Change.

(7) Carroll Alley reminded the group that lunar ranging was developed to support relativistic and fundamental physics studies whereas the present program appears to be tightly tied to Earth science.

TIMELY ISSUES
Andrew Sinclair

SATELLITE SIGNATURE

Issue has been raised previously
Subject is controversial
Effects of signature have been clearly established by two papers
Signature primarily affects single photon systems
Has consequences for data screening and center-of-mass computations

DATA SCREENING

Simple 3 sigma screening not adequate for skew data
Two methods
- adaptive median filtering
- determine bias of mean from peak

Tasks
- write up details
- develop subroutine for assessment
- CSTG Working Group to consider extra information in data format

MISSION PLANNING

Interleaving of passes

LASER TECHNOLOGY
Helena Jelinkova

LASER TRANSMITTER SUMMARY

Wavelength	0.53 μm (1.06 μm) Nd:YAG
Length of pulses	30 psec to 400 psec
Energy	20 mJ to 300 mJ
Repetition Rate	2 to 10 Hz
Maintenance	1 alignment/pass to 1 alignment/0.5 year (Improving)

GOALS AND ISSUES

Multipulse Transmitter (to maximize energy usage)

- Semitrain
- Full train

Multiwavelength Transmitters

- Doubled and third harmonic
- Stokes and Anti-stokes
- New Active Materials

10 picosecond pulses compression by

- Brillouin + Raman
- Raman
- Negative Feedback
- Colliding Pulse Method

Space use of Diode-pumped lasers

- High efficiency
- Long life

COMMENTS

Billion shot flashlamps have been demonstrated but lamp failure is catastrophic whereas diode arrays degrade.

EPOCH AND EVENT TIMING
Ben Greene

SUMMARY

Streak cameras presently at 2 psec; future resolution and accuracy = 0.5 psec

Electronic timing systems presently at 3 psec; future 1 psec resolution and accuracy

Both technologies are approximating useful levels for 5 mm two color ranging

COMMENTS

General agreement on first bullet

Disagreement on second bullet although new technologies (e.g. GaAs) are becoming available

There has been insufficient vision on the part of the funding agencies in developing this technology

DETECTOR TECHNOLOGY

Thomas Varghese

SUMMARY

High speed single photoelectron detectors (SPADS)

High speed, low jitter microchannel plate photomultipliers (230 psec) benefit from effects

Streak cameras represent the leading edge of high accuracy

COMMENTS

SPADs are useful for lunar ranging

Subcentimeter level ranging has been established on a global level and we are approaching millimeter accuracies

CALIBRATION TECHNIQUES/TARGETS

Jean Gaignebet

SUMMARY

Recommended formation of a study group for the design of improved laser retroreflector arrays. G. Lund offered to chair.

There is a need to monitor and keep records on individual SLR stations and configurations.

An interesting corner cube design based on the Fizeau effect was presented by V. Shargorodsky of Russia.

MULTIWAVELENGTH RANGING/STREAK CAMERAS

Karel Hamal

EXPECTED GOALS	ACHIEVED
Optimum wavelength pair	Preliminary
Two Color Ranging MCP	Not yet
MCP	Some progress
SPAD	single color
Streak Camera	
Optimum Satellite & Fizeau Cubes	Promising
Figure of Merit	Controversial
Laser	Stokes/Antistokes Cr:LiSAF

COMMENTS

Raman systems will never have high figure of merit; frequency shift is relatively small.

A Fizeau target is already in a 620 Km orbit. V. Shargorodsky will send the satellite orbit parameters by telex to the Smithsonian Astrophysical Observatory.

Russians will fly a new target at 1000 Km altitude by the end of the year. Only one cube (Fizeau) is visible at a time.

SLR DATA ANALYSIS/MODEL ERRORS
Ron Kolenkiewicz, Richard Eanes

Dynamic, Semi-dynamic, and Geometric Analyses
Orbital models and nonconservative forces

With increased data precision, the effect of time-varying gravity on the satellites is important, and the tracking site motions due to ocean and atmospheric loading needs to be considered.

Geopotential at the one to two level still exist for LAGEOS. More high quality data should improve this below one cm - especially at new sites or recently improved sites.

Systematic errors in the data due to satellite signature and calibration errors must be reduced to less than one cm.

A large non-gravitational signal affecting the LAGEOS eccentricity and perigee at the few meter level has been detected by the analysis groups at GSFC and UT/CSR. The effect was especially large in 1989 and 1991. The current models that explain the along -track or "drag" acceleration on LAGEOS do not explain the eccentricity anomaly. We need a physical explanation for the once per revolution accelerations on LAGEOS.

An attempt should be made to improve the atmospheric correction for single wavelength SLR by means of acoustic and/or lidar sounding of the atmospheric temperature profile.

There is a need for improved second generation SLR satellites with much more stable and deterministic center-of-mass corrections.

With the increased altitude and number of geodetic satellites (e.g., ETALONS and LAGEOS II), the use of geometric analysis to obtain geophysical parameters should be utilized.

Partly random seasonal fluctuations in the mass distribution of the atmosphere limit our ability to ever completely eliminate gravitational model error. Rather we must consider the error as an opportunity and track the fluctuations over time.

Obtaining successful results for the variations of the vertical component of station positions requires that biases in the SLR data be controlled much better than they have in the recent past. Solutions for range bias show some interesting regionally correlated signals that are evidence of either height variations or of some other model defect that is unknown. However, there are also large sudden changes in the biases that are certainly due to problems at the stations.

OPERATIONAL SOFTWARE DEVELOPMENTS
Georg Kirchner

Software developments are freely exchanged between groups.

Community relies on exchanges, standardized formats, etc.

Conclusions from the Splinter Meeting:

Transputer-based SLR control system has no disadvantages (according to the engineer who built it)

Stations should transmit full rate data by E-mail in compressed form

The community should investigate possible standardization of SLR operating and control systems.

LUNAR LASER RANGING
Christian Veillet

The loss of Haleakala to the LLR community is "very unfortunate".

There are presently only two regularly working lunar stations (CERGA and MLRS).

LLR needs lots of observations in order to adequately support the science.

LLR is important to lunar studies and fundamental physics.

LLR pushes individual station performance to the limit.

LLR stations could range to cubes in lunar orbit.

FIXED STATION UPGRADES/DEVELOPMENTS
John Degnan

There appear to be at least two hardware configurations capable of subcentimeter range accuracy:

150 psec pulse, MCP/PMT, and constant fraction discriminator

35 psec pulse, SPAD

There is a continued international interest in SLR as evidenced by the development of new stations and continued upgrades of established stations

There is a new emphasis on higher degree of automation to drive down operational costs.

Countries continue to sponsor stations outside their national borders (e.g., Poland in Tunisia) which will help to provide better global coverage.

MOBILE SYSTEM UPGRADES/DEVELOPMENTS

Erik Vermaat

Highly transportable systems are now demonstrating the same state-of-the-art quality as larger stations (< 10 mm)

Mobile stations typically operate in the single or few photoelectron regime

Mobile stations are becoming more miniaturized as evidenced by the latest system, the French Transportable Laser System (FTLRS).

Automation is a major driver in reducing costs.

Levels of standardization is a key issue.

Conference

Summary/Resolutions

CONFERENCE SUMMARY/RESOLUTIONS

Michael Pearlman

RESOLUTION

We wish to acknowledge and thank all of the representatives from NASA Headquarters, Goddard Space Flight Center, and Bendix Field Engineering Corporation for their untiring efforts in support of the 8th International Workshop on Laser Ranging Instrumentation. Without the hard work, dedicated backing, and personal interest of each of these individuals, this workshop would not have enjoyed the tremendous successes that it did. The help and support of John Degnan is especially recognized.

RESOLUTION

As satellite ranging develops towards millimeter accuracy and the use of multiple wavelengths, one of the most important contributions to the energy link budget and satellite signature to ranging accuracy is the design of the laser retro array.

The SLR community appreciates the idea and proposal of the Russian Space Device Engineering Institute to compensate for angular velocity aberrations via the Fizean effect.

We strongly recommend the continuation of space experimentation in this field.

The SLR community proposes that SLR stations and experts in this field should participate in the construction and subsequent tracking of a satellite designed for this purpose.

RESOLUTION

Whereas the Workshop participants recognize the importance of improving the global distribution of SLR sites and applauds the efforts of various member nations to extend coverage outside their national borders through:

1. The establishment of fixed station (e.g., USA in South America, Czechoslovakia in Egypt, Poland in Tunisia, and Germany in Cuba).

and,

2. The use of mobile systems (USA, Germany, the Netherlands, and France).

We resolve to encourage all member nations in the SLR community to assist, to the best of their ability, in the development and/or operation of stations outside their national borders and particularly in the Southern Hemisphere.

RESOLUTION

We would like to recommend the creation of a special study group to investigate all possible new generation laser ranging retroreflector concepts for optical signature and (null) center of mass correction.

RESOLUTION

Whereas, future analysis of our laser data products would benefit by a knowledge of the configuration of the hardware and software by which it was obtained, we resolve to document our operational configurations and changes there to and record these at a centralized facility in a manner as to be defined by the CSTG.

RESOLUTION

We resolve to initiate experiments designed to improve the atmospheric correction through the use of real-time temperature profiles based upon acoustic wave tracking (SODAR).

Business Meeting/

Next Workshop

BUSINESS MEETING/NEXT WORKSHOP
Carroll Alley

It was decided by the participants that the next workshop should be held within two years. Three participants offered to host the next workshop. The proposers were John Luck of Australia, Yang Fu Min of the Peoples' Republic of China, and Erik Vermaat of the Netherlands. Sentiment was strong among many of the delegates that the ninth workshop should be held in either Asia or Australia since previous workshops had all been located in Europe or the United States. The delegates decided (in a very close vote) to hold the next meeting in the September to November 1994 time frame in Canberra, Australia. The meeting will be hosted by the Australian Survey and Land Information Group (AUSLIG).

REPORT DOCUMENTATION PAGE

Form Approved
OMB No. 0704-0188

1. AGENCY USE ONLY *(Leave blank)*	2. REPORT DATE	3. REPORT TYPE AND DATES COVERED
	June 1993	Conference Publication

4. TITLE AND SUBTITLE
Proceedings of the Eighth International Workshop on Laser Ranging Instrumentation

5. FUNDING NUMBERS
920.1

6. AUTHOR(S)
Compiled and Edited by John J. Degnan

7. PERFORMING ORGANIZATION NAME(S) AND ADDRESS(ES)
Goddard Space Flight Center
Greenbelt, Maryland 20771

8. PERFORMING ORGANIZATION REPORT NUMBER
93B00079

9. SPONSORING/MONITORING AGENCY NAME(S) AND ADDRESS(ES)
National Aeronautics and Space Administration
Washington, D.C. 20546–0001

10. SPONSORING/MONITORING AGENCY REPORT NUMBER
CP–3214

11. SUPPLEMENTARY NOTES

12a. DISTRIBUTION/AVAILABILITY STATEMENT
Unclassified–Unlimited
Subject Category 19
Report available from the NASA Center for AeroSpace Information, 800 Elkridge Landing Road, Linthicum Heights, MD 21090; (301) 621–0390.

12b. DISTRIBUTION CODE

13. ABSTRACT *(Maximum 200 words)*

The Eighth International Workshop for Laser Ranging Instrumentation was held in Annapolis, Maryland in May 1992, and was sponsored by the NASA Goddard Space Flight Center in Greenbelt, Maryland. The workshop is held once every 2 to 3 years under differing institutional sponsorship and provides a forum for participants to exchange information on the latest developments in satellite and lunar laser ranging hardware, software, science applications, and data analysis techniques. The satellite laser ranging (SLR) technique provides sub–centimeter precision range measurements to artificial satellites and the Moon. The data has application to a wide range of Earth and lunar science issues including precise orbit determination, terrestrial reference frames, geodesy, geodynamics, oceanography, time transfer, lunar dynamics, gravity and relativity. This Proceedings is a compendium of full papers based on material presented at the Annapolis workshop.

14. SUBJECT TERMS
Satellite Laser Ranging, Lunar Laser Ranging, lidar, ranging, optical radar, lasers, optical detectors, timers, satellite tracking, satellite orbits, software, geophysics, terrestrial reference frames, Earth orientation parameters, geodesy, geodynamics, oceanography, time transfer, Moon, gravity, lunar physics, geopotential

15. NUMBER OF PAGES
740

16. PRICE CODE

17. SECURITY CLASSIFICATION OF REPORT	18. SECURITY CLASSIFICATION OF THIS PAGE	19. SECURITY CLASSIFICATION OF ABSTRACT	20. LIMITATION OF ABSTRACT
Unclassified	Unclassified	Unclassified	Unlimited